INFORMATION TO USERS

This manuscript has been reproduced from the microfilm master. UMI films the text directly from the original or copy submitted. Thus, some thesis and dissertation copies are in typewriter face, while others may be from any type of computer printer.

The quality of this reproduction is dependent upon the quality of the copy submitted. Broken or indistinct print, colored or poor quality illustrations and photographs, print bleedthrough, substandard margins, and improper alignment can adversely affect reproduction.

In the unlikely event that the author did not send UMI a complete manuscript and there are missing pages, these will be noted. Also, if unauthorized copyright material had to be removed, a note will indicate the deletion.

Oversize materials (e.g., maps, drawings, charts) are reproduced by sectioning the original, beginning at the upper left-hand corner and continuing from left to right in equal sections with small overlaps. Each original is also photographed in one exposure and is included in reduced form at the back of the book.

Photographs included in the original manuscript have been reproduced xerographically in this copy. Higher quality 6" x 9" black and white photographic prints are available for any photographs or illustrations appearing in this copy for an additional charge. Contact UMI directly to order.



University Microfilms International
A Bell & Howell Information Company
300 North Zeeb Road, Ann Arbor, MI 48106-1346 USA
313/761-4700 800/521-0600

Order Number 9325114

Depositional environments, diagenesis, and burial history of the Antelope Valley Limestone (Lower-Middle Ordovician) in the Great Basin, central Nevada. (Volumes I and II)

Kaya, Ali, Ph.D.

City University of New York, 1993

U·M·I
300 N. Zeeb Rd.
Ann Arbor, MI 48106

DEPOSITIONAL ENVIRONMENTS, DIAGENESIS, AND BURIAL HISTORY OF THE ANTELOPE VALLEY LIMESTONE (LOWER-MIDDLE ORDOVICIAN) IN THE GREAT BASIN, CENTRAL NEVADA

by

ALI KAYA

(VOLUME I)

A dissertation submitted to the Graduate Faculty in Earth and Environmental Sciences in partial fulfillment of the requirements for the degree of Doctor of Philosophy, the City University of New York.

1993

This manuscript has been read and accepted for the Graduate Faculty in Earth and Environmental Sciences in satisfaction of the dissertation requirement for the degree of Doctor of Philosophy.

3/3/93 — Date

Gerald M. Friedman — Chair of Examining Committee

4/7/93 — Date

Daniel Habib — Executive Officer

Prof. Somdev Bhattacharji

Prof. Daniel Habib

Prof. William J. Meyers

Supervisory Committee

THE CITY UNIVERSITY OF NEW YORK

Abstract

DEPOSITIONAL ENVIRONMENTS, DIAGENESIS, AND BURIAL HISTORY OF THE ANTELOPE VALLEY LIMESTONE (LOWER-MIDDLE ORDOVICIAN) IN THE GREAT BASIN, CENTRAL NEVADA

by
Ali Kaya

Adviser: Professor Gerald M. Friedman

In central Nevada, the Lower-Middle Ordovician Antelope Valley Limestone (AVL) resulted, in ascending stratigraphic order, from the vertical and progradational growth of Nuia, Girvanella oncolitic, and oolitic and skeletal shoals on a gently declining shelf-slope profile or ramp.

Nuia particles, problematic algal remains, are the major constituents of the lithologic units of the subtidal Nuia shoal bars, which chiefly represent the Orthidella zone. Absence of ooids in the Nuia shoal units suggests moderately high- to high-energy shoals formed on a nearly flat shelf margin-- analogous of the modern Halimeda shoals in Marquesas Keys in Florida. Girvanella, blue-green algae with coating and perforating habits, flourished on the open seaward- and leeward-extended flanks of Nuia shoal bars.

Girvanella- constituted oncoids are the most common particles in the oncolitic shoal lithofacies of the Palliseria zone. In the oncolitic packstone- and grainstone lithofacies, the occurrence of multiple fining-upward thin beds within lenticular, thick beds suggests a sedimentation below the normal weather-wave base and represents incipiently drowned, moderately high-energy shoals which are analogous to modern Serinella bank in the Nicaragua Rise. Receptaculites bioherms overlying the oncoidal shoal units indicate water depth of 6 to 12 m. Both Nuia shoal and Girvanella-oncolitic shoals were separated from the intertidal flats by well-circulated, wide shelves.

The fine-grained siliciclastic lithofacies of the shelf and slope- and deep-ramp facies represent a storm-countercurrent sedimentation during incipiently-drowned stages of Nuia and Girvanella-oncoidal shoals.

In the Martin Ridge and Ninemile Canyon sections, the oolitic shoals of the AVL evolved from a tidal-bar belt type shelf margin in the lower sections to a mobile sand bar type shoal in the upper sections. Oolitic shoals in lower sections are primarily composed of radial ooid-dominated lithologic units, and the upper section oolitic shoal units are composed of two transitional subunits: (1) lower subunits, chiefly containing radial ooids; and (2) upper subunits, dominated by calcitized ooids. Radial ooids formed on open seaward- extended flanks of oolitic shoal bars where Girvanella-carpeted substrate may have influenced water chemistry by producing organic acids; whereas calcitized ooids (originally tangential ooids) formed in high-energy oolitic shoals, specifically at the crest of oolitic bars.

In the lower intervals of the June Canyon section, the normal-graded bioclastic turbidites are believed to have resulted from storm countercurrent-generated turbidity currents.

Stromatolitic lime mudstone with birdseye texture, flat-pebble conglomerate and desiccation cracks represent the features of subaerial exposure of the AVL under the influence of subtropical to tropical climatic conditions.

Shallowing-upward cycles of the AVL are correlative as far as 40 km normal to depositional strike and 60 km along depositional strike. These cycles, having an average cycle duration 82 000 yrs, represent the climate-forced (glacioeustacy-induced) cyclicity.

The Copenhagen Formation represents the lagoonal lithofacies of the AVL; the Eureka Quartzite represents the siliciclastic shoreline facies of the AVL, particularly where intertidal algal flats were missing.

Nine evolutionary phases of the Whiterockian carbonate platform were recognized. These phases show "keep up", "incipiently drowned", "catch up", "off lap", and "onlap" shelf-margin features and correspond to third-order events of three transgressions, two regressions, and two stand stills.

Submarine calcite cements (radiaxial-fibrous, isopachous cement, cryptocrystalline, and columnar calcite) played an important role for the early lithification of the AVL. Columnar calcite and radiaxial-fibrous calcite cements were originally high-Mg calcite in composition, and their $\delta^{18}O$ composition ranges from -6.66 to -6.77 ‰ PDB which is consistent with the estimated-$\delta^{18}O$ values of Middle Ordovician marine calcites.

The meteoric calcite cements (pendant, equant mosaic, drusy, and syntaxial cements) are

volumetrically the most important cements in the AVL and formed during major progradational events.

Late-diagenetic void- and fracture-filling calcite cements (FFCC) with a depleted-$\delta^{18}O$ composition ranging from -8.4 to - 11. 06 ‰ PDB, and high T_h values represent the deep-burial calcite cements of the AVL. However, one set of late FFCC having exceedingly depleted-$\delta^{18}O$ composition of -18 to -30 ‰ PDB and low salinity two-phase fluid inclusion may have originated from meteoric diagenetic water.

Nine kinds of multistage dolomitization were recognized in the AVL. Dolomite I is marine dolomite; Dolomite II is an early diagenetic supratidal dolomite in stromatolitic mudstones. Dolomite III selectively replaced Girvanella oncoids and postdates calcite- filled fractures of a shallow to intermediate burial depth. Dolomite IV, V are zoned dolomites found only in the Lone Mountain section. Dolomites III, IV and V probably originated from diagenetically modified sea water at shallow- to intermediate burial depths. Dolomite VI, ferroan dolomite, is of deep-burial origin and closely associated with stylolites, and selectively replaced late-diagenetic sparry calcites. Dolomite VII, dolostone units of the AVL, postdates stylolite-induced ferroan dolomite (Dol. VI). Pervasive dolomitization of the AVL may have resulted either from diagenetically modified regional ground-water flow or from basinal brine during the Middle Pennsylvanian and Early Permian uplifting. Dolomite VIII, fracture-filling sparry dolomite, is also of late-diagenetic and deep-burial origin and exhibits two textural relations with Dol. VII: (1) Dol. VIII-filled fractures appear to be syngenetic with Dol. VII, and (2) postdate Dol. VII. Cathodoluminescence petrography and relations between Dol. VII and Dol. VIII suggest that pervasive dolomitization of the AVL resulted from two different basinal solutions. Dolomite XI is fracture-filling saddle dolomite and postdates the dolostone (Dol.VII) of the AVL.

Nonstoichiometry of early-diagenetic Dolomite II suggests that time has no direct control over the dolomite stoichiometry.

Dedolomitization of the AVL is late diagenetic and shows near surface diagenetic features. Iron-rich zones of dolomite rhombs show a fabric-selective dedolomitization.

Cogenetic occurrence of quartz, pyrite, calcite, and dolomite in void-filling cements of chert nodules probably resulted from sulfate-reducing reactions. In chert nodules,

cathodoluminescence study showed that opal-CT transformation to quartz induced dolomitization by releasing Mg form opal-CT phase. Source of silica in chert nodules is primarily biological (from sponge spicules and radiolaria).

Multi-geothermometric methods-- fluid inclusion (FI), oxygen isotope, thermal alteration indices (TAI) of organic matter, and illite crystallinity (CI)-- were used to determine the maximum-burial temperature ranges and corresponding burial depths of the AVL.

Measured TAI values from primarily algal matters correspond to thermal-alteration level which is at least two to three times less than those estimated from FI and IC as well as time temperature index (TTI) from the reconstructed-subsidence curve. The lower thermal alteration level can mainly be attributed to the presence of Kerogen type I, dominated by algal matters.

Formation temperatures estimated from oxygen-isotope are lower for calcite cements and higher for dolomite cements than temperatures measured from the same samples by CI and FI methods. This discrepancy between oxygen-isotope thermometry and FI and CI may have resulted from re-equilibration of parent solutions, isotopic contamination during sampling, and using nonrepresentative $\delta^{18}O$ composition for formation waters in the equilibrium equations.

For FI thermometry, two-phase fluid inclusions were used. In histograms, pressure-uncorrected homogenization temperatures makes several clusters for each vertical section which may indicate different events of heating or different generations of fracture-filling cements. The plots of T_h versus salinity estimated from Tm (melting temperature) show vertical, diagonal, and horizontal trends which suggest that most fluid inclusions were re-equilibrated by undergoing volumetric and compositional changes caused by decrepitation and stretching either due to increased burial depth or uplifting.

Illite crystallinity (CI) shows a good correlation with the fluid-inclusion thermometry. Burial temperatures derived from pressure-uncorrected T_h are 20 to 30 °C lower than temperatures estimated from CI.

FI thermometry and IC suggest a maximum burial depth of 7 to 10 and a total uplifting of 7 to 12 km for the AVL which are comparable with the results of the reconstructed-subsidence curve.

ACKNOWLEDGEMENTS

To Prof. G.M. Friedman, my advisor, I am grateful for offering me several projects and allowing me to choose the one I wanted most. I also owe special gratitude and debt to Dr. Friedman for his advice and suggestions generously given at the every stage of this study.

I wish to thank to members of my thesis committee, Prof. S. Bhattacharji, Prof. D. Habib, and Prof. W.J. Meyers for reading my thesis and suggesting improvements.

My appreciation is expressed to Prof. W.J. Meyers from SUNY at Stony Brook for serving my committee as a coadvisor and allowing me to use the cathodoluminescence lab, and to Prof. Homa from Physics Department of Brooklyn College for letting me use their X-ray diffractometer. I am pleased to acknowledge the help, friendship and fruitful suggestions of Osman Taban and David Hill during the field work.

My thanks are extended to the Northeastern Science Foundation for allowing me to use their equipment and providing funds for my experimental work. Mrs. Sue Friedman's technical assistance during my analytical work at the Northeastern Science Foundation is gratefully acknowledged.

I want to extend my special thanks to Prof. C.E. Nehru, ex-chairman, and Prof. J.E. Chamberlain, present chairman of Department of Geology in Brooklyn College, for providing me teaching assistantship during my study.

Ann Tomo and Lina McClain, our secretaries, deserve my special thanks for their help.

To Dr. Golam Sarwar, I owe special thanks for his friendship and productive discussions relating to thermal history of sedimentary basins. I would like to thank to my room mates, Dr. Faye Males, and Dr. Joachim Amthor, for making life bearable in Troy for a year.

Finally, I would like to extend my most sincere appreciation and gratitude to my mother Pullu Kaya, my in-lows Mr. Pasqualino and Mildred Fasulo, my wife Jo Ann, my brother Mustafa and his wife Senay, and my sister Gülhayat for their moral support and encouragements throughout this study.

TABLE OF CONTENTS

VOLUME I

ABSTRACT iii
ACKNOWLEDGEMENTS vii
TABLE OF CONTENTS viii
LIST OF TABLES xix
LIST OF FIGURES xxiii

PART I: INTRODUCTION, GEOLOGY, AND METHODS 1

CHAPTER 1: INTRODUCTION 2
A. Purpose of study 2
CHAPTER 2: BACKGROUND GEOLOGY 3
A. Geologic history 3
B. Previous study 14
C. Stratigraphy 19
CHAPTER 3: METHODS 25
A. Field work 25
B. Laboratory work 25
a) Staining 25
b) Cathodoluminescence petrography 26
c) Dolomite stoichiometry 26
d) Illite crystallinity and clay diagenesis 28
e) Fluid-inclusion microthermometry 30
f) Oxygen-isotope geothermometry 36
g) Thermal alteration level of organic matter 38

PART I: DEPOSITIONAL ENVIRONMENTS AND CYCLICITY OF THE AVL, AND EVOLUTION OF THE MIDDLE ORDOVICIAN CARBONATE PLATFORM 41

CHAPTER 4: NUIA SHOALS 42
A. Lithofacies 43
Lithofacies 1: Nuia Packstone and grainstone 43
Description 43
Interpretation 52
Lithofacies 2: Nuia-rich peloidal and oncolitic packstone 59

Description 59
Interpretation 62
Lithofacies 3: Rhythmically, thin-bedded siltstone and lime mudstone 63
Description 63
Interpretation 67
Lithofacies 4: Silty quartz-rich, glauconitic lime mudstone 69
Description 69
Interpretation 69
B. Synthesis 71
C. Discussion 73
CHAPTER 5: ONCOIDAL SHOAL FACIES 77
A. Areal distribution of oncolitic shoal units 77
B. Lithofacies 79
Lithofacies 5: Oncoidal packstone and grainstone 79
Description 79
Interpretation 90
Lithofacies 6: Receptaculites bioherms or buildups 95
Description 95
Interpretation 98
C. Synthesis 100
D. Discussion 102
CHAPTER 6: OOLITIC AND SKELETAL SHOAL 107
A. Areal distribution of oolitic and skeletal shoals 107
B. Lithofacies 111
Lithofacies 7: Oolitic packstone and grainstone 111
Description 111
Interpretation 120
Lithofacies 8: Peloidal packstone-grainstone 131
Description 131
Interpretation 133
Lithofacies 9: Crinoidal packstone and grainstone 134
Description 134
Interpretation 137
Lithofacies 5 A: Oncoidal packstone of oolitic shoal 139
Description 139
Interpretation 140
C. Synthesis 141
CHAPTER 7: SHELF FACIES BELT 145
A. Lithofacies 145
Lithofacies 10 A: Bioturbated wackestone lithofacies of the shelf behind Nuia Shoals 145
Description 145
Interpretation 148
Lithofacies 10 B: Bioturbated wackestone lithofacies of the shelf behind the

oncoidal shoals 151
Description 151
Interpretation 152
Lithofacies 10 C: Bioturbated wackestone lithofacies of the shelf behind the oolitic and skeletal shelf 153
Description 153
Interpretation 156
Lithofacies 10 D: Interlayered wackestone and mudstone and shale (Lagoonal Copenhagen Formation) 157
Description 157
Interpretation 161
Lithofacies 11: Fine-grained peloidal packstone (Nearshore bars) 163
Description 163
Interpretation 164
Lithofacies 12: Fine siliciclastics 164
Lithofacies 12 A: Parallel-laminated, silty quartz-rich lime mudstone 164
Description 164
Interpretation 168
Lithofacies 12 B: Massive siltstone 170
Description 170
Interpretation 172
Lithofacies 12 C: Fine-grained, massive quartz arenite 174
Description 174
Interpretation 174
Lithofacies 13: Pelletal oncolitic wackestone 175
Description 175
Interpretation 178
B. Synthesis 180
CHAPTER 8: INTERTIDAL-TO SUPRATIDAL FACIES BELT 182
A. Lithofacies 182
Lithofacies 14: Pelletal and oncoidal mudstone and wackestone 182
Description 182
Interpretation 185
Lithofacies 15: Cryptalgal lime mudstone 185
Description 185
Interpretation 191
B. Synthesis 195
CHAPTER 9: SLOPE- AND MARGINAL BASIN FACIES 196
A. Lithofacies 196
Lithofacies 16 A: Greenish gray shale 196
Description 196
Interpretation 198
Lithofacies 16 B: Shaley limestone 198
Description 198

Interpretation 201
Lithofacies 17 A: Graded-bioclastic packstone 202
Description 202
Interpretation 206
Lithofacies 17 B: Skeletal-grain supported, monogenic, edgewise conglomerate 208
Description 208
Interpretation 211
Lithofacies 18: Rhythmical hemipelagics with shale interlayers 212
Description 212
Interpretation 217
Lithofacies 19 A: Nodular limestone 219
Description 219
Interpretation 221
Lithofacies 19 B: Mottled limestone 222
Description 222
Interpretation 223
Lithofacies 12: Parallel-laminated silty quartz-rich, lime mudstone 224
Description 224
Interpretation 226
Lithofacies 13: Oncoidal wackestone to packstone 226
Description 226
Interpretation 231
Slope- and Basinal Storm Deposits 233
Lithofacies 20 A: Crinoidal packstone to wackestone 233
Description 233
Interpretation 236
Lithofacies 20 B: Normal-graded conglomeratic packstone 238
Description 238
Interpretation 240
Lithofacies 20 C: Nuia-rich oncoidal wackestone 241
Description 241
Interpretation 241
Depositional model for the slope- and basinal storm deposits 243
B. Synthesis 244
CHAPTER 10: CYCLICITY OF THE ANTELOPE VALLEY LIMESTONE . . 248
Introduction 248
A. Shallowing-upward cycles 250
1) Nuia shoal cycles 250
2) Oncoidal shoal cycles 252
3) Oolitic and skeletal shoal cycles 252
4) Shallow subtidal and intertidal algal-flat cycles 255
B. Nonshallowing-upward cycles 255
1) Slope or deep-ramp cycles 255
2) Middle shelf cycles 257

Correlation of shallowing-upward cycles 258
Durations of shallowing-upward cycles 259
Progradation rate of intertidal-algal flat 260
Chronostratigraphy of the shallowing-upward cycles and their relations with third-order changes in sea levels 261
Origin of shallowing upward cycles in the AVL 270
CHAPTER 11: EVOLUTION OF MIDDLE ORDOVICIAN CARBONATE PLATFORM 275
Phase I 275
Phase II 276
Phase III 280
Phase IV 282
Phase V 283
Phase VI 287
Phase VII 288
Phase VIII 291
Phase IX 293

VOLUME II

PART III: DIAGENESIS AND DIAGENETIC HISTORY OF THE ANTELOPE VALLEY LIMESTONE 294

CHAPTER 12: CALCITE CEMENT 295
A. MARINE CEMENT 295
Radiaxial-fibrous cement 295
Description 295
Interpretation 297
Isopachous-bladed cement 301
Description 301
Interpretation 301
Cryptocrystalline high-Mg calcite cement 305
Description 305
Interpretation 306
Columnar cement 307
Description 307
Interpretation 309
B. METEORIC CALCITE CEMENT 313
Pendant calcite cement 313
Description 313
Interpretation 316
Equant blocky cement 318
Description 318
Interpretation 320

Drusy cement 322
Description 322
Interpretation 323
Syntaxial cement 323
Description 323
Interpretation 327
C. DEEP-BURIAL CALCITE CEMENTS 330
Intraooid-, or Oomold-filling calcite 330
Description 330
Interpretation 332
Intercrystalline calcite cement 333
Description 333
Interpretation 334
Void-filling, poikilotopic calcite cement 334
Description 334
Interpretation 338
Neomorphic equant blocky calcite 339
Description 339
Interpretation 342
Neomorphic poikilotopic calcite 343
Description 343
Interpretation 346
CHAPTER 13: DOLOMITE TYPES, CHEMISTRY, AND MODEL FOR PERVASIVE DOLOMITIZATION 349
CHAPTER 13-A: DOLOMITE TYPES 349
Dolomite Type I 350
Description 350
Interpretation 350
Dolomite Type II 353
Description 353
Interpretation 353
Dolomite Type III 355
Description 355
Interpretation 358
Dolomite Type IV 360
Description 360
Interpretation 370
Dolomite Type V 374
Description 374
Interpretation 377
Dolomite Type VI (Ferroan dolomite) 381
Description 381
Interpretation 384
Dolomite Type VII (Mosaic dolomite) 388

Stratigraphic relations and aerial distributions 388
Petrography 393
Cathodoluminescence petrography 402
Stable isotope chemistry 409
Stoichiometry of mosaic dolomite 409
Interpretation 411
Dolomite Type VIII (Fracture-filling dolomite) 420
Description 420
Interpretation 423
Dolomite Type IX (Saddle dolomite) 426
Description 426
Petrography 426
Stable isotope chemistry 426
Interpretation 429
CHAPTER 13-B: DOLOMITE STOICHIOMETRY 431
Introduction 431
Dolostones 431
Results 431
Interpretation 435
Partially dolomitized limestones 437
Results 437
Interpretation 438
CHAPTER 13-C: DOLOMITIZATION MODEL OF THE DOLOSTONE UNITS IN THE ANTELOPE VALLEY LIMESTONE 439
CHAPTER 14: DEDOLOMITIZATION 445
Introduction 445
Nonfabric-selective dedolomitization 445
Description 445
Interpretation 447
Fabric-selective dedolomitization 447
Description 447
Interpretation 449
CHAPTER 15: QUARTZ AND CHERT CEMENTS 453
I. Quartz Cements 453
A. Quartz cement 453
Description 453
Interpretation 455
B. Replacive quartz 455
Description 455
Interpretation 457
C. Authigenic euhedral quartz 458
Description 458
Interpretation 458
II. Chertification 461

A. Selective chertification of allhochems 461
Description 461
a) Crinoids 461
b) Brachiopods 464
c) Bryozoans 465
d) Trilobites 465
Interpretation 465
B. Chert nodules and beds 468
a. Microcrystalline granular quartz 469
b. Length-fast chalcedony 472
c. Megaquartz or mosaic quartz 472
Interpretation and timing 474
C. Source of silica 478
TIMING AND SUMMARY OF DIAGENESIS 481

PART IV: MAXIMUM-BURIAL DEPTH RANGE OF THE ANTELOPE VALLEY LIMESTONE AND THERMAL HISTORY OF GREAT BASIN AT CENTRAL NEVADA 483

CHAPTER 16: ORGANIC METAMORPHISM (ORGANIC MATURATION OR THERMAL ALTERATION 484
A. Introduction 484
B. Results 487
Lone Mountain 487
Data 487
Interpretation 487
Martin Ridge section 488
Data 488
Interpretation 488
Whiterock Canyon 489
Data 489
Interpretation 489
June Canyon sequence 490
Data 490
Interpretation 490
Mill Canyon sequence 490
Data 490
Interpretation 491
Toiyabe Range 491
Data 491
Interpretation 492
Keystone Canyon 493

Data 493
Interpretation 493
Comparison of measured TAI and the estimated thermal alteration levels from TTI and homogenization temperature (T_h) 494
C. Synthesis 498
CHAPTER 17: OXYGEN-ISOTOPE THERMOMETRY 501
A. Introduction 501
B. Results 503
Lone Mountain 503
Data 503
Interpretation 506
Antelope Valley region 506
Data 506
Interpretation 508
The allochthonous units of the AVL in the Whiterock Canyon section, and June Canyon and Mill Canyon sequences 509
Data 509
Interpretation 511
Toiyabe Peak region 512
Data 512
Interpretation 514
Southern localities (Keystone Canyon and Clear Creek Canyon sections) . . . 516
Data 516
Interpretation 518
C. Synthesis 519
CHAPTER 18: FLUID-INCLUSION MICROTHERMOMETRY 524
A. Introduction 524
B. Results 527
Lone Mountain 527
Homogenization (T_h) data 527
Freezing data 529
Interpretation 529
Ninemile Canyon 532
Homogenization (T_h) data 532
Freezing data 534
Interpretation 536
Martin Ridge 541
Homogenization (T_h) data 541
Freezing data 543
Interpretation 543
Keystone Canyon 545
Homogenization (T_h) data 545
Freezing data 545
Interpretation 547

Clear Creek Canyon 548
Homogenization (T_h) data 548
Freezing data 548
Interpretation 548
The Toiyabe Range 551
Toiyabe Peak 551
Homogenization (T_h) data 551
Interpretation 553
Dry Creek Canyon 555
Homogenization (T_h) data 555
Freezing data 555
Interpretation 557
Reeds Canyon 558
Homogenization (T_h) data 558
Freezing data 558
Interpretation 558
Allochthonous units of the Roberts Mountains thrusts 561
1. Whiterock Canyon and June Canyon sequences (The upper tectonic slice of the lower thrust plate) 561
Homogenization (T_h) data 561
Interpretation 561
2. Mill Canyon Sequence (The lower tectonic slice of the lower thrust plate) 564
Homogenization (T_h) data 564
Freezing data 564
Interpretation 566
CHAPTER 19: CLAY DIAGENESIS AND ILLITE CRYSTALLINITY 567
A. Introduction 567
B. Results 570
a) Peak positions of illite 571
b) Peak positions of chlorite and kaolinite 571
c) Clay-mineral assemblages 571
d) Effects of KCl and $MgCl_2$ treatment 575
e) Effects of Glycolation 576
f) Ordering Level of Illite and composition of I/S-mixed layers 578
g) 001 I/ 002 I ratio and Esquiven charts 578
C. Regional distribution of clay-mineral assemblages and their relations with illite crystallinity 583
a) Highly deep-burial diagenetic zones 583
b) Anchizone 588
c) Epizone 588
D. Synthesis 594
CHAPTER 20: COMPARING THE RESULTS OF GEOTHERMOMETRIES . . 598
A. Comparison of geothermometries 598
Antelope Valley region 598

Southern localities (The Keystone Canyon and Clear Creek Canyon sections) 602
Toiyabe Range 605
Allochthonous Units (Whiterock Canyon section, and June Canyon and Mill Canyon sequences 608
B. Synthesis 611
CONCLUSIONS 614
A. Depositional environments and evolution of carbonate platform 614
B. Diagenesis 618
C. Maximum burial depth and burial history of the AVL in the Great Basin . . . 621

APPENDIX I-A: THE MEASURED VERTICAL SECTIONS AND THEIR LOCATIONS 625
APPENDIX I-B: TEXTURAL AND LITHOLOGIC VARIATIONS OF THE ANTELOPE VALLEY LIMESTONE IN THE MEASURED VERTICAL SECTIONS 629
APPENDIX I-C: OCCURRENCE AND GROWTH FORMS OF NUIA (PROBLEMATIC ALGAE) 658
APPENDIX II: SEMI-QUANTITATIVE X-RAY DIFFRACTOMETRY ANALYSIS ON THE STOICHIOMETRY OF DOLOMITE 665
APPENDIX III-A: SUMMARY OF ORGANIC CARBON AND VISUAL KEROGEN DATA 666
APPENDIX III-B: OXYGEN- AND CARBON-ISOTOPE DATA 674
APPENDIX III-C1: PRINCIPLES OF FLUID INCLUSION THERMOMETRY 679
APPENDIX III-C2: HOMOGENIZATION AND FREEZING TEMPERATURE AND SALINITY DATA FROM TWO-PHASE FLUID INCLUSIONS 689
APPENDIX III-D: SEMI-QUANTITATIVE X-RAY DIFFRACTOMETRY ANALYSIS FOR CLAY MINERALS 698
REFERENCES 704

LIST OF TABLES

Table 1. Decompacted- and present-day thickness of Middle Ordovician Rocks in the Antelope Valley region 259

Table 2. Oxygen-isotope composition of the dolomites and other diagenetic products in the crinoidal and oolitic packstone- and grainstone units 370

Table 3. Oxygen- and carbon-isotope composition of the late-replacive mosaic dolomite of the AVL 409

Table 4A. d-spacing and mole % of $CaCO_3$ and $MgCO_3$ in dolomite composition . . . 433

Table 4B. The dolomite content of partially dolomitic limestones, mole percentages of $CaCO_3$ and $MgCO_3$ in the dolomites of dolomitic limestone of the AVL 437

Table 5A. TAI values of the AVL and their correlative Ro%, LOM, Coal Rank values and the estimated temperature range from TAI from each vertical section 495

Table 5B. Estimation of TTI values from Lopatin method (see Waples, 1980) 496

Table 5C. For the AVL, estimated thermal alteration or maturation level of organic matter during the following geologic time periods 497

Table 6. Estimated formation temperatures of the fracture -filling calcite and dolomite cements of the AVL by oxygen-isotope thermometry and comparison with T_h ranges in the Lone Mountain section 504

Table 7. Calculated-$\delta^{18}O$ values and salinity contents of the formation water of carbonate cements by using from T_h range in the isotopic fractionation equation as an equilibrium temperature 505

Table 8. Estimated formation temperatures of carbonate cements of the AVL by oxygen-isotope thermometry and comparison with T_h ranges of the same formation in the Antelope Valley region 507

Table 9. Calculated-$\delta^{18}O$ values and salinity contents of the formation water of carbonate cements by using from T_h range in the isotopic fractionation equation as an equilibrium temperature 508

Table 10. Estimated formation temperatures of carbonate cements of the AVL from the oxygen-isotope thermometry and their comparison with T_h ranges of the same formation in the allochthonous sections 510

Table 11. Estimated formation temperatures of carbonate cements of the AVL from the oxygen-isotope thermometry and comparison with T_h ranges of the same formation in the Toiyabe Peak region 512

Table 12. Calculated-$\delta^{18}O$ values and salinity contents of the formation water of carbonate cements by using from T_h range in the isotopic fractionation equation as an equilibrium temperature 513

Table 13. Estimated formation temperatures of carbonate cements of the AVL by oxygen-isotope thermometry and comparison with T_h ranges of the same formation in the Clear Creek Canyon and Keystone Canyon sections 517

Table 13A. Calculated-$\delta^{18}O$ values and salinity contents of the formation water of carbonate cements by using from T_h range in the isotopic fractionation equation as an equilibrium temperature 518

Table 14. T_h values of two-phase fluid inclusions and the corresponding maximum burial-depth range for the AVL in the Lone Mountain section 531

Table 15. Three major clusters of T_h values and relative positions of the samples, from the base of section, in the Ninemile Canyon section 534

Table 16. Estimated-maximum burial depth range of the AVL from the pressure-uncorrected, maximum Th values from the Ninemile Canyon section 540

Table 17. Estimated-maximum burial depth of the AVL from pressure-uncorrected T_h values at the Martin Ridge section 544

Table 18. Estimated-maximum burial depths of the AVL from the maximum T_h ranges at Keystone and Clear Creek Canyon sections (Surface temperature 20 °C) 551

Table 19. Estimated burial depth range of the AVL from T_h ranges, in the Toiyabe Peak section (Average surface temperature= 20 °C) 554

Table 20. Estimated-maximum burial depth range of the AVL from the max. T_h range, in Dry Creek Canyon 557

Table 21. Estimated-maximum burial depth of the AVL from T_h values, in the Reeds Canyon section 560

Table 22. T_h ranges and corresponding burial-depth ranges, in the Whiterock Canyon section and June Canyon sequence 562

Table 23. Estimated-maximum burial depths of the AVL from T_h values, in the Mill Canyon sequence 566

Table 24. Relative abundance of clay mineral assemblages in the various type section 575

Table 25. Effects of K, and Mg cations and glycolation on 001 illite peaks, illite crystallinity indices and sharpness ratio 577

Table 26. Illite content in I/S-mixed layers and its ordering level 578

Table 27. Crystallinity indices (CI), sharpness ratio (WI) and intensity ratio of 5 Å and 10 Å illite reflections (I 002/ I 001) 579

Table 28. Illite crystallinity indices and half width of chlorite peaks at half height; June Canyon sequence (I), and Keystone Canyon section (K) 586

Table 29. Clay-mineral assemblages and illite crystallinity indices and corresponding pressure-uncorrected T_h values 596

Table 31. Maximum-burial temperatures of the AVL estimated from various geothermometries in the Antelope Valley region 598

Table 32. Maximum burial depths of the AVL, removed post-Devonian strata, and total uplifting of the AVL estimated from maximum T_h range and other geothermometries in the Antelope Valley localities 601

Table 33. Maximum-burial temperatures of the AVL estimated from various geothermometries at southern localities (the Keystone Canyon, and Clear Creek Canyon sections) of this study 602

Table 34. Maximum burial depths of the AVL, removed post-Devonian strata, and total uplifting of the AVL in the Keystone Canyon and Clear Creek Canyon sections, estimated from the range of maximum T_h values and other geothermometries 604

Table 35. Maximum-burial temperatures of the AVL estimated from various geothermometries in the Toiyabe Peak region 605

Table 36. Maximum burial depths of the AVL, removed post-Devonian strata, and total uplifting of the AVL estimated from the range of maximum T_h values and other geothermometries at the Toiyabe Peak region 608

Table 37. Maximum-burial temperatures of the AVL estimated from various geothermometries in the Whiterock Canyon and Iks Canyon regions 610

Table 38. Maximum burial depths of the AVL, removed post-Devonian strata, and total uplifting of the AVL estimated from maximum T_h range and other geothermometries in the Whiterock and Iks Canyon regions 611

Table 39. Summary of organic carbon and visual kerogen data 673

LIST OF FIGURES

Figure 1- A) Major geographic features of the Great Basin. B) Index map of the study area in central Nevada showing the measured-vertical type sections designated A to K 4

Figure 2- Cross section of Precambrian and lower Paleozoic rocks in the central Great Basin (Stewart, 1980) 5

Figure 3- Map of depositional provinces of Ordovician rocks in the Great Basin (Stewart, 1980) 5

Figure 4- Allochthonous units of the Antler orogeny (the Roberts Mountains thrusts): A) At the Petes Canyon window (Toquima Range); B) At the Iks Canyon window (Toquima Range). C) At the Whiterock Canyon section, the lower thrust plate Monitor Range 6

Figure 5- Cross section of upper Paleozoic rocks in the Great Basin: M-Mississippian, P-Pennsylvanian, and P-Permian (Stewart, 1980) 8

Figure 6- Map of depositional provinces of (A) Mississippian rocks, and (B) Permian rocks (Stewart, 1980) 9

Figure 7- Approximated-leading edge of the Roberts Mountain thrusts (Late Devonian-Early Mississippian) and Golconda thrusts (Late Permian-Early Triassic), modified from Stewart (1980) 11

Figure 8- Map of depositional provinces of Triassic rocks and the Lower Triassic Upland in the Great Basin (Stewart, 1980) 12

Figure 9- Index map showing the location of study area and other localities where the AVL was studied by others 15

Figure 10- Columnar section showing the biozones of the AVL in the Antelope Valley region in central Nevada 16

Figure 11- The stratigraphic column of lower Paleozoic rocks in the Antelope Valley region, central Nevada 20

Figure 12- Stratigraphic correlation of Paleozoic rocks in the different tectono-stratigraphic sequences at the northern Toquima Range (McKee, 1976) 21

Figure 13- Stratigraphic correlation chart of Middle Ordovician rocks in the Great Basin, central Nevada (Ross, 1977) 23

Figure 14- X-ray diffractogram showing the sharpness ratio of a 001 illite peak (Sharpness ratio= height of 10 Å illite peak / height of 10.5 Å illite peak) and illite crystallinity index (equal to half width of a 001 illite peak, 10 Å, at its half height, as indicated by arrowheads) 29

Figure 15- Kinds of fluid inclusions and occurrences: (P) primary, Ps) pseudo secondary, and (S) secondary inclusions (Shepherd et al., 1984) 31

Figure 16- Sequence of phase changes in two-phase fluid inclusions during heating stage 32

Figure 17- Phase changes in two-phase fluid inclusions during freezing/heating stages 32

Figure 18- A correlation chart of various maturation parameters of organic matter--generation and destruction zones of oil, modified from Dow (1977), and Hood et al. (1975) 39

Figure 19- Successions of shallowing-upward Nuia shoal cycles and related lithofacies in the Ninemile Canyon and Martin Ridge sections 44

Figure 20- Photomicrographs of Nuia packstone- and grainstone lithofacies 45-46

Figure 21- Field and outcrop photographs of Nuia packstone- and grainstone lithofacies 48-49

Figure 22- Sedimentary structures in the polished slabs of Nuia packstone- and grainstone units 50

Figure 23- Photomicrographs of Nuia-rich peloidal and oncoidal packstone 60-61

Figure 24- Outcrop photographs of the rhythmically thin-bedded siltstone and lime mudstone lithofacies, and a photomicrograph of crinoid-rich, intraclastic Nuia packstone 64-65

Figure 25- Photomicrographs of the parallel-laminated siltstone interlayers of the rhythmically-thin bedded siltstone and lime mudstone lithofacies 66

Figure 26- An outcrop photograph of the parallel-laminated, glauconite-rich lime mudstone lithofacies 70

Figure 27- A) A suggested-depositional model of Nuia shoal and related lithofacies in this study. B) Nuia model by Stricker and Carozzi (1977) 74

Figure 28- Succession of the oncoidal shoal cycles and related lithofacies in the vertical sections 78

Figure 29- Polished slabs of the oncolitic packstone- and grainstone lithofacies . . . 80-81

Figure 30- Photomicrographs of the oncolitic packstone- and grainstone lithofacies 82-83

Figure 31- Kinds of oncoids and oncoidal laminae in the oncoidal shoal units 85

Figure 32- Photomicrographs of Girvanella growth forms and related-concentric laminae 87

Figure 33- Photomicrographs of oncoid laminae and outline of oncoids 88-89

Figure 34- Polished slabs of the Receptaculites bioherm lithofacies and photomicrograph of Receptaculites 96-97

Figure 35- A) Suggested-oncoidal shoal model of this study; B) "Algal ball model" of the oncoidal shoal by Stricker and Carozzi (1977) 104

Figure 36- Vertical columnar sections in Ninemile Canyon and Martin Ridge sections showing successions of shallowing-upward oolitic shoal cycles and related lithofacies . . . 109

Figure 37- Vertical columnar sections show the oolitic and skeletal shoal units of the upper Palliseria and lower and middle Anomalorthis zones 110

Figure 38- Field view of oolitic shoal bars and polished slab of Nuia packstone from oolitic backshoal facies 112-113

Figure 39- Polished slabs of oolitic packstone- and grainstone lithofacies 114

Figure 40- Photomicrographs of oolitic packstone and grainstone lithofacies 116-117

Figure 41- Photomicrographs of radial ooid- and calcitized-tangential ooid-dominated oolitic grainstone subunits 118-119

Figure 42- Oolitic and skeletal shoal packstone- and grainstone unit 121

Figure 43- Photomicrographs of radial ooid-dominated grainstone 129

Figure 44- Photomicrographs of the peloidal packstone- and grainstone lithofacies . . . 132

Figure 45- Crinoidal packstone- and grainstone lithofacies 135

Figure 46- The suggested model for the oolitic shoal and related lithofacies of the AVL by this study 143

Figure 47 I- Vertical section showing the bioturbated-wackestone lithofacies and related lithologic units in the Antelope Valley region and in the Lone Mountain section 146

Figure 47 II- Bioturbated-wackestone lithofacies 149-150

Figure 48- Bioturbated wackestone lithofacies in the Middle and Late Anomalorthis zone 154

Figure 48 D- Polished slab of recycled flat-pebble conglomerate; arrow indicates a fining-upward texture in this unit 155

Figure 49 I- Vertical section showing the interlayered- wackestone /mudstone and shale (the lagoonal lithofacies of the AVL) or the Copenhagen Fm. 158

Figure 49 II- Polished slabs of the lagoonal lithofacies of the AVL, or the Copenhagen Formation 159-160

Figure 50- Photomicrograph of peloidal packstone lithofacies 163

Figure 51- Rhythmically alternating silty quartz-rich parallel-laminated lime mudstone or thin siltstone and lime mudstone interlayers 166-167

Figure 52- Cyclical successions of parallel-laminated, silty quartz-rich lime mudstone lithofacies with a nonshallowing-upward texture in the Keystone Canyon and Clear Creek Canyon sections 171

Figure 53- Model for the sedimentation of nonshallowing-upward fine-siliciclastic cycles in middle and outer open shelves 173

Figure 54- Pelletal lime mudstone and oncolitic wackestone lithofacies of restricted shelf 176

Figure 55- Forms of oncoids and their different kinds of laminae in the restricted-shelf facies 177

Figure 56 I- Vertical sections showing the cryptalgal lime mudstone lithofacies and their cyclical successions in the Ninemile Canyon and Martin Ridge sections 183

Figure 56 II- Photomicrograph of pelletal lime mudstone to wackestone and the polished slab of the stromatolitic oncoidal wackestone unit 184

Figure 57 I- Cryptalgal mudstone lithofacies in polished slabs and a photomicrograph 187-188

Figure 57 II- Cryptalgal mudstone lithofacies 194

Figure 58- Lithofacies of the open shelf facies in the AVL, and their successions in the June Canyon, Whiterock Canyon and Toiyabe Peak sections 197

Figure 59- Shaley limestone lithofacies 199-200

Figure 60- Bioclastic turbidites within the hemipelagics 203-204

Figure 61- Normal-graded, thick-bedded bioclastic and brecciola lithofacies 209-210

Figure 62- Hemipelagic lime mudstone beds and their sedimentary structures . . . 213-214

Figure 63- Photomicrographs of hemipelagic lime mudstone interlayers and outcrop photograph of silty quartz-rich hemipelagic intervals 217

Figure 64- Nodular limestone and mottled-limestone lithofacies 220

Figure 65- Cyclical successions of parallel-laminated, silty quartz-rich lime mudstone and oncoidal wackestone intervals of the open shelf facies of the AVL in the Mill Canyon sequence 225

Figure 66- Oncolitic packstone-wackestone and parallel-laminated, silty quartz-rich lime mudstone units 227

Figure 67- Photomicrographs of open shelf oncoids and their concentric laminae 229

Figure 68- Oncoids of open shelf facies or deep ramp 230

Figure 69- Storm layers of slope and basinal facies 234-235

Figure 70- Grain-supported conglomerate and thin shelly packstone to wackestone units of the open shelf facies of the AVL 239

Figure 71- A) Depositional model for the storm deposits of open slope and basinal facies or deep ramp, and their comparison with storm layers in carbonate shelf. B) Relations between winnowing level and water depth, and corresponding texture in storm layers . . . 242

Figure 72- Model for strong storm currents-induced turbiditic deposits (Hamblin and Walker, 1977) 245

Figure 73- Major cycle types of the different depositional facies of the AVL 251

Figure 74- Interpreted approximate-initiation depth ranges of the following shallowing-upward cycles and their succession patterns in vertical sections: 1) Oolitic shoal in the Martin Ridge section; 2) oncoidal shoal in the Martin Ridge section, and 3) Nuia shoal in the Ninemile Canyon section 251

Figure 75- Algal flat-capped, shallow-subtidal cycles and algal flat cycles and their patterns in vertical sections 256

Figure 76- Correlation of short durational, shallowing-upward Nuia shoal cycles 263

Figure 77- Correlation of short durational, shallowing-upward oncolitic and oolitic cycles 266

Figure 78- Correlation of short durational shallowing-upward algal flat-capped cycles and oolitic shoal cycles of the Anomalorthis zone. B) Correlation of the short durational, nonshallowing-upward middle shelf cycles 268

Figure 79- Proposed model by this study for the evolution of the Middle Ordovician carbonate platform during the formation of the AVL, particularly at the Lone Mountain and Keystone Canyon sections 277

Figure 80- Proposed model by this study for the evolution of the carbonate platform at the Martin Ridge and Ninemile Canyon sections 278

Figure 81- Relations between third-order changes in sea level and sedimentation patterns, and evolutionary phases during the formation of this formation and their correlatives . . . 281

Figure 82- Depositional model of the Antelope Valley Limestone proposed by Taban (1986) 284

Figure 83- Regional Cross section of Whiterockian strata in western Utah and Nevada (Ross et al., 1989) 289

Figure 84- Model for evolution of the Middle Ordovician carbonate platform suggested by Ross et al. (1989) 290

Figure 85- Areal view and outcrop photograph of the Eureka Quartzite 292

Figure 86- Photomicrographs of radiaxial-fibrous calcite cement 296

Figure 87- Photomicrographs of neomorphically altered radiaxial cement 298

Figure 88- Photomicrographs of the interparticle, isopachous-rim cement of Nuia packstone- and grainstone unit 302

Figure 89- Photomicrographs of isopachous-bladed calcite cement 303

Figure 90- Photomicrograph of cryptocrystalline calcite cement 305

Figure 91- Photomicrographs of columnar-calcite cement in oncolitic packstone- to grainstone units 308

Figure 92- Photomicrographs of columnar calcite cement 311

Figure 93- Photomicrographs of pendant or fenestra-filling calcite cement 314

Figure 94- Cathodoluminescence photomicrographs of gravitational pendant cement . . 315

Figure 95- Photomicrographs of equant blocky interparticle cement in the Nuia packstone- and grainstone lithofacies 319

Figure 96- Photomicrographs of syntaxial cement 324

Figure 97- Photomicrographs of syntaxial cement 326

Figure 98- Photomicrographs of intraooid or oomold-filling calcite cement 331

Figure 99- Photomicrographs of interparticle poikilotopic calcite cement 335

Figure 100- Photomicrographs of poikilotopic calcite cement 336

Figure 100- C) Photomicrograph of void-filling sparry calcite cement (c) in the Nuia packstone and grainstone units shows that void walls of this cement are generally sharp 337

Figure 101- Photomicrographs of neomorphic blocky calcite cement 340

Figure 102- Photomicrographs of neomorphic blocky calcite cement of skeletal packstone units in the shelly substorm layers 341

Figure 103- Photomicrographs of poikilotopic neomorphic cement in the skeletal and peloidal packstone to grainstone unit of the oolitic backshoal 344

Figure 104- Photomicrographs of poikilotopic neomorphic cement in skeletal packstone layers of the open shelf 345

Figure 105- Photomicrographs of dolomite type I (Euhedral dolomite rhombs with slightly red brown-staining within the locally concentrated fine-grained siliciclastics in the skeletal sublayers of storm beds) 351

Figure 106- Photomicrograph of dolomite type II 355

Figure 107- Photomicrographs of dolomite type III (Zoned-euhedral dolomite rhombs selectively replaced allochems and calcitized-Girvanella filaments) 356-357

Figure 108- Photomicrographs of dolomite type IV (Luminescently zoned-euhedral dolomite replaced the oomold-filling calcite) 361

Figure 109- Cathodoluminescence photomicrographs of dolomite type IV 363

Figure 110- Photomicrographs of dolomite type IV 364

Figure 111- Photomicrographs of dolomite type IV 365

Figure 112- Photomicrographs of dolomite type IV in the crinoidal packstone- and grainstone unit 366

Figure 113- Photomicrographs showing timing relations among dolomite type IV, fracture-filling calcite cement, and late-replacive dolomite in the same fracture 368

Figure 113 C- A close up photomicrograph shows that late-diagenetic dolomite (r) replaced the fracture-filling sparry calcite (c) and dolomite type IV (s) 370

Figure 114- Photomicrographs of dolomite type V in the skeletal packstone units of the open shelf facies 375

Figure 115- Photomicrographs of dolomite type V and its complete zones 376

Figure 116- Photomicrographs showing diagenetic timing relations between a mechanically broken allochem and dolomite type V 378

Figure 117- Cathodoluminescence photomicrographs of dolomite type V 379

Figure 118- Photomicrographs of dolomite type VI (euhedral ferroan dolomite) in the Nuia

packstone- and grainstone unit 382

Figure 119- Photomicrographs of dolomite type VI in the oolitic grainstone unit 383

Figure 120- Pervasively dolomitized intervals (Dol. VII) of the AVL in the Martin Ridge, Lone Mountain, Keystone Canyon, and Clear Creek Canyon sections 389

Figure 121- A) A field view of E to W trending normal faults in the Martin Ridge section. These faults are responsible for the fault-controlled pervasive dolomitization. B) A polished slab of the pervasively dolomitized oncolitic packstone- and grainstone lithofacies 390

Figure 122 A- The geological map of the Hot Creek Canyon region shows the Antelope Valley Limestone (opc), and E to W and N to S-trending normal faults (Lowell, 1965) . . 391

Figure 122 B- The geologic map of the east Clear Creek Canyon region shows the E to W and N to S-trending normal faults and the Antelope Valley Limestone (Lowell, 1965) . . . 392

Figure 123- Photomicrographs of dolomitized oolitic grainstone units of the AVL 394-395

Figure 124- Photomicrographs showing dolomite type VII (mosaic dolomite) and its relationship with pre- and post-pervasive dolomitic, fracture-filling calcite cements 396

Figure 125- Photomicrographs of a mimicly replaced crinoid by mosaic dolomite 398

Figure 126- Photomicrographs showing mosaic dolomite (dolomite type VII) and its relation with stylolite 399

Figure 127- Photomicrographs of mosaic dolomite and intercrystalline quartz cements . 401

Figure 128- Photomicrographs of mosaic dolomite 403

Figure 129- Close-up photomicrographs of mosaic dolomite 404

Figure 130- Photomicrographs of mosaic dolomite and stylolites 405

Figure 131- Photomicrographs of fracture-filling dolomite and calcite cements in the mosaic dolomite 407

Figure 132- Photomicrographs of mosaic dolomite and stylolite-induced ferroan dolomite 408

Figure 133- Isotope composition of dolomite types and calcite cements of the Antelope Valley Limestone 410

Figure 134- Photomicrographs of fracture-filling white sparry dolomite (dolomite type VIII) 421

Figure 135- Close-up photomicrographs of inclusion-rich zones in the fracture-filling white sparry dolomite (dolomite type VIII) 422

Figure 136- Photomicrographs of void-filling white sparry dolomite cement (dolomite type VIII) 424

Figure 137- Fracture-filling saddle dolomite (dolomite type IX) 427

Figure 138- Photomicrographs of untwinned, neomorphic blocky saddle dolomites . . . 428

Figure 139- Dolomite percentages in dolostones of the Antelope Valley Limestone. The rest of the dolostone composition are mostly calcite, and a few samples are composed of considerably high fine-grained siliciclastics 432

Figure 140- Mole percentages of $CaCO_3$ in the composition of dolomites of the dolostone units of the Antelope Valley Limestone 434

Figure 141- Mole percentages of $MgCO_3$ in the composition of dolomites of the dolostone units of the Antelope Valley Limestone 434

Figure 142- Deep-burial dolomitization model by topography-driven regional ground water, modified from Todh (1980), Hitchon (1984) and Garven and Freeze (1984) 442

Figure 143- Deep-burial dolomitization model by compaction expelled basinal brine . . 442

Figure 144- Photomicrographs of nonfabric-selective dedolomitization 446

Figure 145- Photomicrographs of dedolomitized-euhedral ferroan dolomites 448

Figure 146- Photomicrographs of fabric-selective dedolomitization in zoned dolomite crystals 450

Figure 147 A, B- Photomicrographs of quartz cements 454

Figure 147 C,D- Photomicrographs of replacive quartz cement 456-a

Figure 148- Photomicrographs of authigenic quartz 459

Figure 149- Photomicrographs of a selectively silicified crinoid grain 462

Figure 150- Photomicrographs of selectively-silicified allochems (Brachiopods, trilobites, and bryozoans 463

Figure 151- Photomicrographs of quartz cements in chert nodules and lenses 470

Figure 152- A) Photomicrograph of length-fast chalcedony at the calcitized center of a Girvanella oncoid. Arrowheads point to curvature, a sharp contact between calcite cement (c) and chalcedony (ch). B) Photomicrograph of pervasively silicified Nuia packstone- and grainstone unit 471

Figure 153- Photomicrographs of void-filling mosaic quartz, pyrite, and calcite and dolomite cements in chert nodules 473

Figure 154- Photomicrographs of the zoned-dolomite crystals replaced by quartz and zoned-microdolomite crystals at the margin of chert nodules 475

Figure 155- Photomicrographs of sponge spicules and radiolarias in chert nodules . . . 479

Figure 156- Paragenetic and diagenetic sequence of the Antelope Valley Limestone in the study area. The length of bars does not reflect the duration of diagenetic events and sequences, but the bars does reflect timing relations of diagenetic events 482

Figure 157- R_o versus depth relations of the samples from Well 6464 in Willistone Basin, Dunn County (Price et al., 1986) 499

Figure 158- Intensely folded, calcite-filled large fractures within the slaty units of the Antelope Valley Limestone which originally was a basinal shaley limestone lithofacies 515

Figure 159- Oxygen-isotope compositions of fracture- and void-filling carbonate cements have been used for oxygen-isotope thermometry to estimate the paleo-burial temperature range for the Antelope Valley Limestone 520

Figure 160- Plot of oxygen-isotope composition range of parent fluids of the fracture-filling calcite cements and their salinity content: oxygen-isotope composition of parent fluids estimated from the homogenization temperatures, and oxygen-isotope compositions of host calcite cements. Counter lines are in ‰ SMOW 521

Figure 161- Plot of oxygen-isotope composition range of the dolomitizing fluids. Counter lines are in ‰ SMOW 521

Figure 161 B- Oxygen and carbon-isotope composition range of carbonate rocks (Friedman, 1992) 522

Figure 162- Histogram of homogenization temperatures (T_h) of two-phase fluid inclusions from carbonate cements in the Lone Mountain section 528

Figure 163- Plot of homogenization temperature (T_h) versus salinity content of primary two-phase fluid inclusions in fracture-filling dolomite cement in the Lone Mountain section 528

Figure 164- Histogram of homogenization temperatures (T_h) of primary two-phase fluid inclusions from fracture-filling calcite cement in the Ninemile Canyon section 534

Figure 165- Plot of T_h versus salinity content of primary two- phase fluid inclusions in Ninemile Canyon section 534

Figure 165 A- Plot of T_h versus salinity content explains volumetric and compositional changes on fluid inclusions and suggests possible processes for indicated changes after Shepherd et al. (1985) and Goldstein (1988) 535

Figure 166- Histogram of homogenization temperatures (T_h) of primary two-phase fluid inclusions from fracture-filling calcite cement in the Martin Ridge section 542

Figure 167- Plot of T_h versus salinity content of primary two-phase fluid inclusions in the Martin Ridge section 542

Figure 168- Histogram of homogenization temperatures (T_h) of primary two-phase fluid inclusions from the fracture-filling calcite cement in the Keystone Canyon section 546

Figure 169- Plot of T_h versus salinity content of primary two-phase fluid inclusions in the Keystone Canyon section 546

Figure 170- Histogram of homogenization temperatures (T_h) of primary two-phase fluid inclusions from intercrystalline pore-filling quartz cement in the Clear Creek Canyon section 549

Figure 171- Plot of T_h versus salinity content of primary two-phase fluid inclusions in the Clear Creek Canyon section 549

Figure 172- Histogram of homogenization temperatures (T_h) of primary two-phase fluid inclusions from fracture-filling calcite cement in the Toiyabe Peak section 552

Figure 173- Histogram of homogenization temperatures (T_h) of primary two-phase fluid inclusions from fracture-filling calcite cements in the Dry Creek Canyon section 556

Figure 174- Plot of T_h versus salinity content of primary two-phase fluid inclusions in the Dry Creek Canyon section 556

Figure 175- Histogram of homogenization temperatures (T_h) of primary two-phase fluid inclusions from fracture-filling calcite cement in the Reeds Canyon section 559

Figure 176- Plot of T_h versus salinity content of primary two- phase fluid inclusions in the Reeds Canyon section 559

Figure 177- Histogram of homogenization temperatures (T_h) of primary two-phase fluid inclusions from fracture-filling calcite cement in the Whiterock Canyon section 563

Figure 178- Histogram of homogenization temperatures (T_h) of primary two-phase fluid inclusions from fracture-filling calcite cement in the June Canyon sequence at Iks Canyon 563

Figure 179- Histogram of homogenization temperatures (T_h) of primary two-phase fluid inclusions from fracture-filling calcite cement in the Mill Canyon sequence in Iks Canyon 565

Figure 180- Plot of T_h versus salinity content of primary two- phase fluid inclusions in the Mill Canyon sequence in Iks Canyon 565

Figure 181- Diagenetic evolutionary phases in the Illite Smectite-mixed layers (Velde, 1981) 568

Figure 182- Diagenetic evolutionary phase changes in the I/S mixed layers and chlorite through progressively increasing heat and pressure (Velde, 1981) 568

Figure 183- Position of illite peaks and effects of glycolation (G) on 001 illite peak position (10 Å) of air-dried samples, and effects of potassium (K) saturation on the 001 illite peak (10 Å) 572

Figure 184- Position of illite peaks and effects of glycolation (G) and magnesium saturation (Mg) on the 001 illite peaks (10 Å) of air-dried samples 573

Figure 185- Position of illite, chlorite, and kaolinite peaks, and the effects of K and Mg saturations, and glycolation on the position of their peaks in air-dried samples 574

Figure 186- Plots of illite crystallinity index and I 002/ I 001 ratio (Esquiven chart): relations between Al / Fe+Mg ratio and clay diagenetic and metamorphic zones 580

Figure 187- Plots of illite crystallinity index and I 002/ I 001 ratio (Esquiven chart): Mineral composition of mica minerals in epizone 581

Figure 188- Plots of illite crystallinity index of Kubler (1966) and sharpness ratio of Weaver (1960): Boundaries of clay diagenetic and metamorphic zones 581

Figure 189- Position of illite peaks and assemblages of clay minerals in the K-saturated samples and their correspondence with clay content of the shale limestone samples from the June Canyon sequence 585

Figure 190- Position of illite peaks from K-saturated samples representing the anchizone of this formation in the Mill Canyon sequence 589

Figure 191- Position of 001 illite peaks (10 Å) and clay-mineral assemblages from K-saturated samples, representing the epizone, of this formation in the Toiyabe Peak . . . 591

Figure 192- Photomicrographs showing advanced deformation and recrystallization of fracture-filling calcite cement 592

Figure 193- Photomicrographs showing deformation of calcite cement crystals, slaty texture, and related mineral paragenesis 593

Figure 194- Histogram of homogenization temperatures (T_h) of primary two-phase fluid inclusions from fracture-filling carbonate cements in the Antelope Valley region 599

Figure 195- Histogram of Melting temperatures (Tm) of primary two-phase fluid inclusions from fracture-filling carbonate cements in the Antelope Valley region 599

Figure 196- Burial-history diagram of the Antelope Valley Limestone in the Antelope Valley region and Eureka district. The compaction-corrected subsidence curve was constructed on the basis of calculations given in Angevine and Heller (1987) 600

Figure 197- Histogram of homogenization temperatures (T_h) of primary two-phase fluid inclusions from fracture-filling calcite cement and intercrystalline pore-filling quartz in the southern localities of this study 603

Figure 198- Histogram of melting temperatures (Tm) of primary two-phase fluid inclusions from the indicated cements in the southern localities of this study 603

Figure 199- Histogram of homogenization temperatures (T_h) of primary two-phase fluid inclusions from fracture-filling calcite cement in the Toiyabe Range 606

Figure 200- Histogram of melting temperatures (Tm) of primary two-phase fluid inclusions from fracture-filling calcite cement in the Toiyabe Range 606

Figure 201- Histogram of homogenization temperatures (T_h) of primary two-phase fluid inclusions from fracture-filling calcite cement in the lower plates of Roberts Mountain thrusts 609

Figure 202- Lithology types, sedimentary structures, textures, and faunal and floral content of the Antelope Valley Limestone in the measured vertical sections 629-657

Figure 203- Photomicrographs of various growth forms of Nuia in the AVL . . . 659-660

Figure 204- Reconstructed-growth forms of Nuia by Mamet and Roux (1982): 1) Normal growth; 2) normal dichotomy; 3) embracing dichotomy; 4) encasing growth; 5) external-veneering growth; and 6) budding growth 662

Figure 205- Photomicrographs of Nuia growth forms which were not described by Mamet and Roux (1982) 663

Figure 206- Influence of salinity on the position of the liquid-vapor curves and slope of the isochores in the liquid field for the system H_2O- NaCl (Roedder, 1984; Shepherd et al., 1985) 686

PART I: INTRODUCTION, GEOLOGY, AND METHODS

- INTRODUCTION
- BACKGROUND GEOLOGY
- METHODS

CHAPTER 1: INTRODUCTION

Purpose of Study

The Middle Ordovician Antelope Valley Limestone (AVL) in the Great Basin of central Nevada is the youngest member of the Pogonip Group.

Stratigraphy and paleontology of the Antelope Valley Limestone (AVL) in central Nevada, have been studied in detail since the early 1900's. A detailed examination of this formation is needed due to absence of studies related to depositional environment, evolution of carbonate platforms, diagenetic history, and burial history.

The integrated sedimentologic and diagenetic study of the Whiterockian Antelope Valley Limestone (AVL) includes the following objectives:

(1) Describing and sampling the lithofacies in the vertical sections, and correlating them laterally in order to reconstruct depositional environments.

(2) Defining and estimating durations of shallowing-upward cycles and correlating them basin-wide; determining relations between the short durational sea-level fluctuations and third-order changes in sea level.

(3) Establishing a dynamic sequence stratigraphy for the Middle Ordovician AVL.

(4) Defining diagenetic features and their timing, and relating them to diagenetic environments.

(5) Establishing a diagenetic model for calcite, dolomite and silica cementation.

(6) Establishing a burial history which can be compared with the diagenetic history.

CHAPTER 2: BACKGROUND GEOLOGY

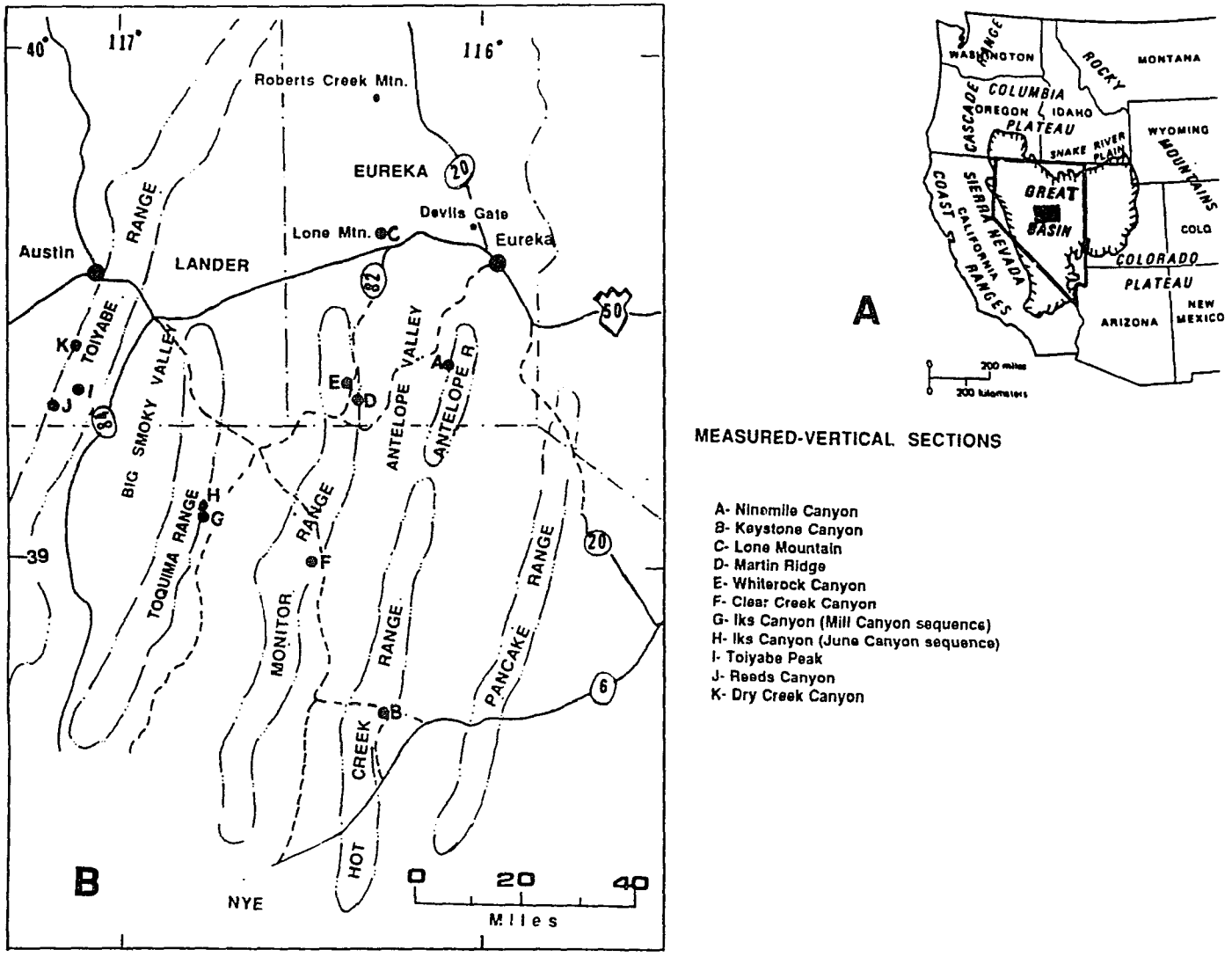
Geologic History

The study area lies within the Great Basin region of the Basin Range physiographic province, in which typical elongated-mountain ranges rise up to 1000-5000 feet above the adjacent valley and transcend more than 50 miles in a north and north east trend (Fig. 1).

From the latest Precambrian to the middle Paleozoic, Nevada is thought to have lain along the western margin of the North American continent. From the latest Precambrian to Early Cambrian times, shallow-water continental shelf sedimentation dominated a westward-thickening clastic wedge (Fig. 2).

However, during Middle and Late Cambrian, clastic sedimentation changed to carbonate-dominated sedimentation which continued until the Antler orogeny of Late Devonian and Early Mississippian age (Fig. 2, Stewart, 1980). From Middle Cambrian to Late Devonian, shallow-shelf carbonate sedimentation became dominant in eastern, central, and southern Nevada, and continental slope and basinal sediments were deposited in western Nevada and in the farther west.

Similarly, Ordovician strata in the Great Basin, from east to west, show westward-deepening four sedimentary provinces (Fig. 3): a) Carbonate and quartz province, including the Antelope Valley Limestone (AVL) and other members of the Pogonip Group, the Copenhagen Formation, Eureka Quartzite, Hanson Creek Formation (Fig. 3); b) Shale and carbonate province, representing outer shelf or upper slope deposits with evenly medium-bedded limestone and alternating shaley intervals; c) Shale and chert province, including the Vinini Formation of Lower and Middle Ordovician age (Fig. 4), consisting of minor shale, chert, quartzite and sparse mafic lava flow and representing the upper plate of Roberts Mountain thrusts of



MEASURED-VERTICAL SECTIONS

A- Ninemile Canyon
B- Keystone Canyon
C- Lone Mountain
D- Martin Ridge
E- Whiterock Canyon
F- Clear Creek Canyon
G- Iks Canyon (Mill Canyon sequence)
H- Iks Canyon (June Canyon sequence)
I- Toiyabe Peak
J- Reeds Canyon
K- Dry Creek Canyon

Figure 1- A) Major geographic features of the Great Basin. B) Index map of the study area in central Nevada showing the measured sections designated A to K.

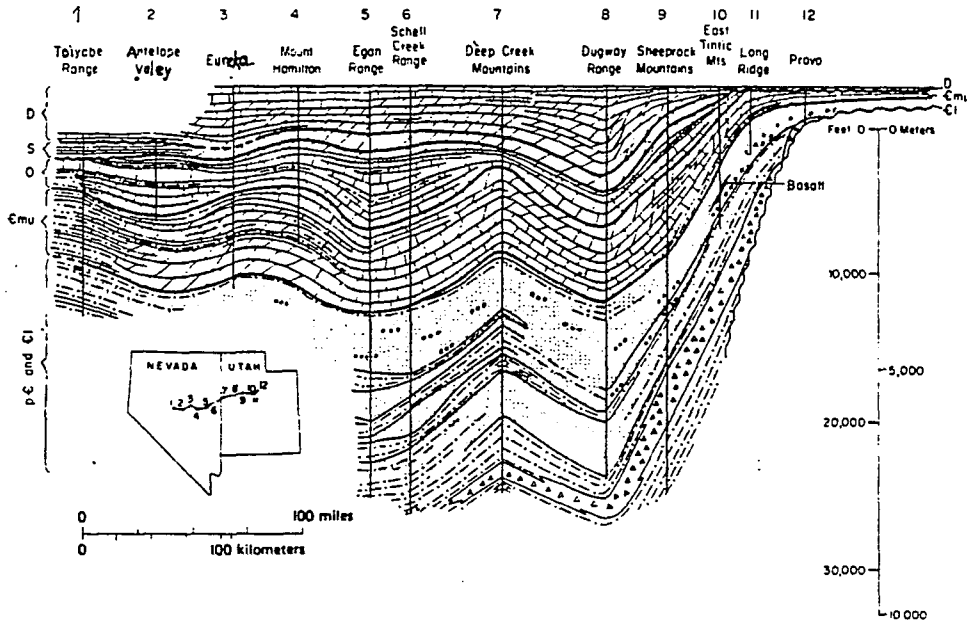
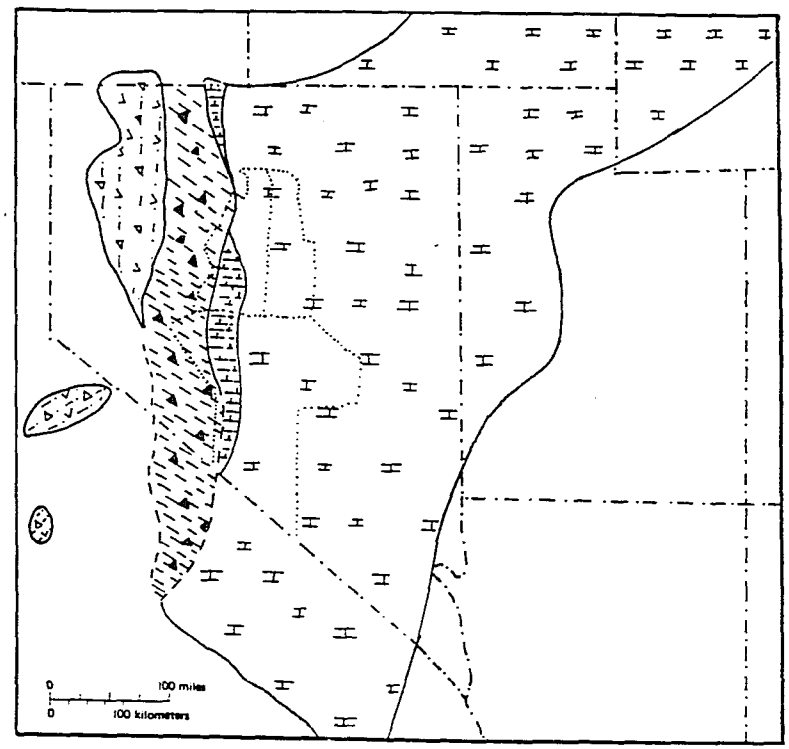


Figure 2- Cross section of Precambrian and lower Paleozoic rocks in the central Great Basin (Stewart, 1980).



EXPLANATION

- Carbonate and quartzite province
- Shale and limestone province
- Shale and chert province
- Chert-shale-quartzite-greenstone province

Figure 3- Map of depositional provinces of Ordovician rocks in the Great Basin (Stewart, 1980).

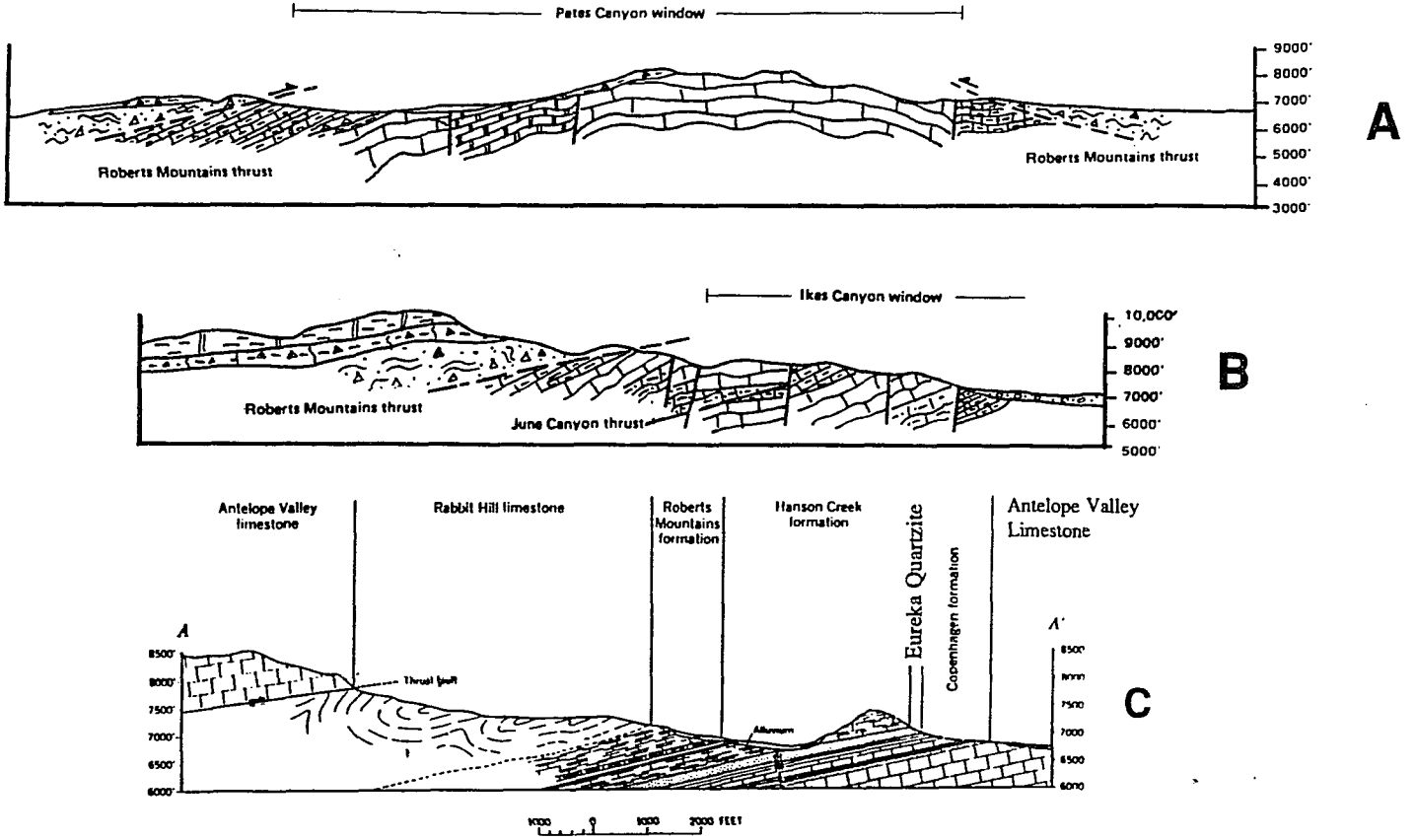


Figure 4- Allochthonous units of the Antler orogeny (the Roberts Mountains thrusts). A) At the Petes Canyon window (Toquima Range), the upper thrust plate (Vinini Formation) overlies the lower thrust plate of the same thrust system. B) At the Iks Canyon window (Toquima Range), the upper thrust plate of the Roberts Mountain thrusts (Vinini Formation) thrusted over the lower thrust plate (June Canyon sequences) of the same thrsut system (McKee, 1976). "6" Tertiary tuffs, "5" Vinini Fm., "4" Roberts Mountains Fm. (Devonian), "3"Hanson Creek Fm., "2" The AVL, and "1" Goodwin Ls. C) At the Whiterock Canyon section, the lower thrust plate overlies the autochthonous Silurian Rabbits Hill Formation (Merriam, 1963).

Antler orogeny; and d) Chert, shale, quartzite and greenstone province consisting of chert, shale, pillow lava, and green stone (McKee, 1976; Merriam, 1963; Ross, 1976; and Stewart, 1980).

During Late Devonian and Early Mississippian times (during the Antler orogeny) open shelf- to deep-water carbonates, siliceous and volcanic rocks ranging from Cambrian to Late Devonian age were thrust eastward as much as 90 miles (145 km) over the platform and shelf carbonates on the western margin of the North American Plate (Stewart and Poole, 1974). These allochthonous units, ranging from Ordovician to Upper Devonian age, are called the Roberts Mountains thrusts of the Antler Orogeny, and they are composed of two-major units: the upper and lower thrust plates. The Vinini Formation is an allochthonous unit on the upper plate of the Roberts Mountains thrusts and overlies the lower thrust plates with a tectonic contact in the Iks Canyon window (Fig. 4A) and Petes Canyon window (Fig. 4B) in the Toquima Range (Kay and Crawford, 1964, McKee and Ross, 1969; and McKee, 1976), in Roberts Mountain and at the Devils Gate of Eureka district (Merriam and Anderson, 1942). The allochthonous units of the lower thrust plate of the Antler orogeny were also reported in the Iks Canyon tectonic windows of the Toquima Range (Fig. 4B) and in the Whiterock Canyon (Fig. 4C), where the lower thrust plate is represented only by the Antelope Valley Limestone (Merriam, 1963). The allochthonous units on the lower plate primarily consist of carbonate and shaley-carbonate rocks from Cambrian to Late Devonian age (Fig. 4A, B, C).

Along the western margin of the North American Continent, the Antler orogeny had created a highland which provided sediments for a deep-adjacent foreland basin from the Mississippian through Permian (Fig. 5A, B). This sedimentary and tectonic pattern was established during the Mississippian and continued into Pennsylvanian and Permian times. Generally, on the Antler highland, the coarse-grained conglomeratic units (molasse facies) of the conglomerate and carbonate province gradually change eastward into the normal-graded beds of terrigenous units (Antler flysch-facies belt) of the terrigenous province, which changes gradually eastward into the shallow carbonates in the carbonate province (Figs. 5, 6). The siliceous and volcanic rock

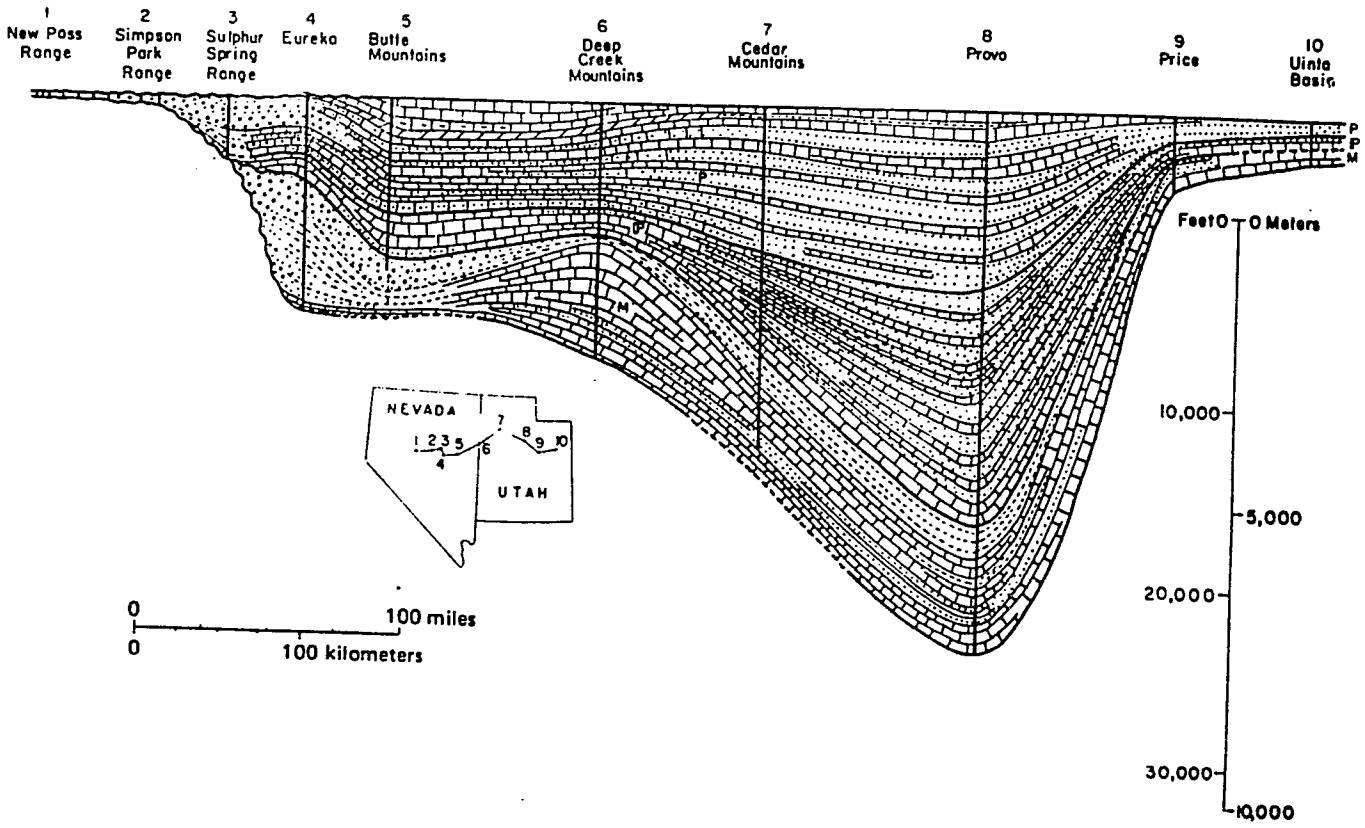


Figure 5- Cross section of upper Paleozoic rocks in the Great Basin: M-Mississippian, P-Pennsylvanian, and P-Permian (Stewart, 1980).

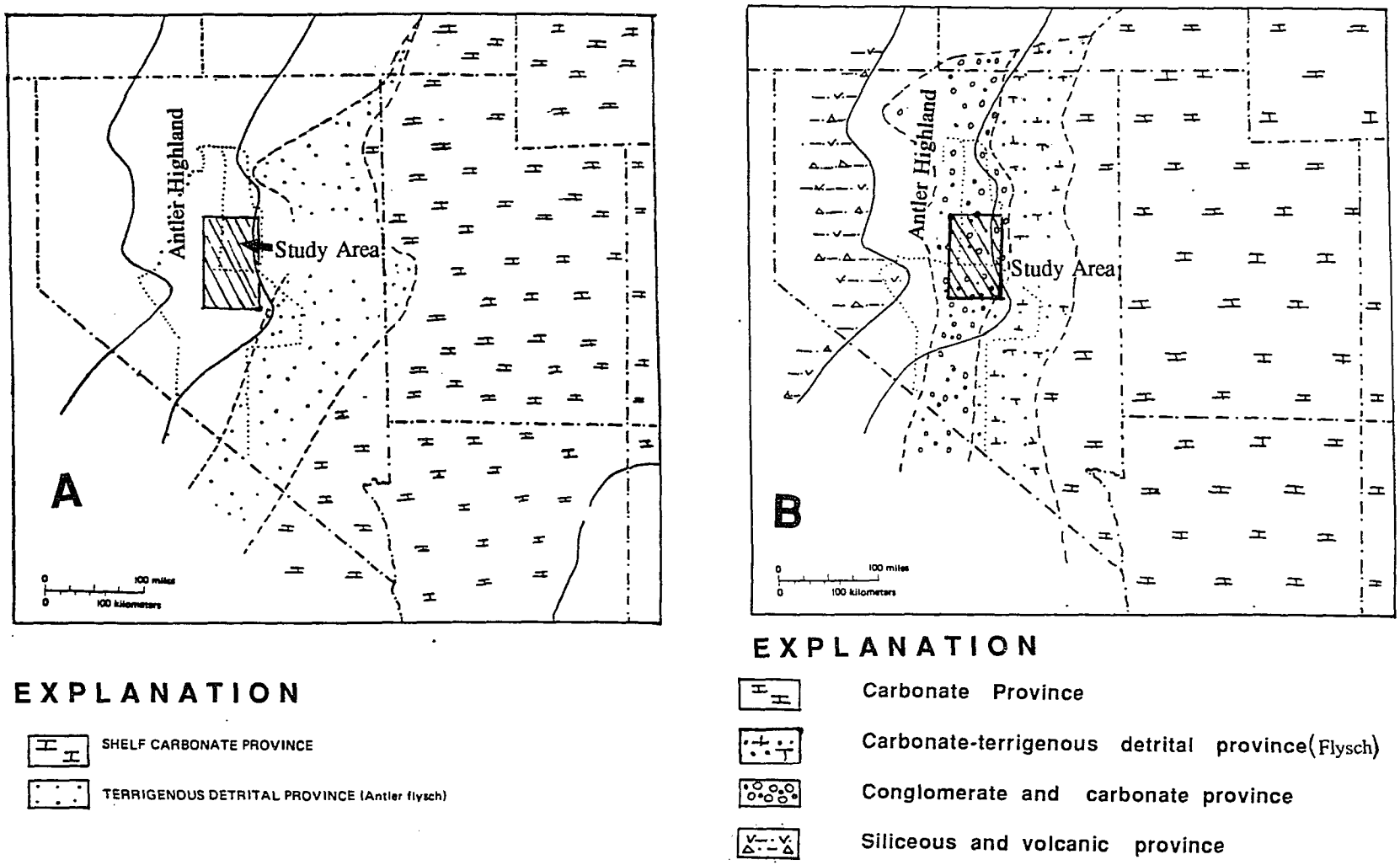


Figure 6- Map of depositional provinces of (A) Mississippian rocks, and (B) Permian rocks (Stewart, 1980).

province to the west of the Antler highland consists of chert and mafic volcanic rocks upward siliceous argillite, silty limestone, sandstone, and conglomerate of deep-marine origin (Fig. 5B).

During the late Middle and early Late Pennsylvanian, much of the central and northeastern Nevada were uplifted and produced a widespread unconformity (Steel, 1960; Roberts, 1964, Nolan et al. 1956; Yochelson and Fraser, 1973; and Ketner and Smith, 1974). This uplifting renewed the influx of clastic sediment from the Antler highland to the eastern foreland basin.

During Late Permian and Early Triassic in Nevada, the Sonoma orogeny took place and generated the eastward-thrusted siliceous and volcanic rocks of the Golconda allochthons as much as 45 miles (72 km) over the shallow-water deposits of early and middle Paleozoic in the Antler highland and produced the Lower Triassic Upland (Fig. 7). The Sonoma orogeny is thought to have occurred by collision of an oceanic arc with the North American continent (Speed, 1971; Burchfiel and Davis, 1972; Silberling, 1973; Churkin, 1974; Speed, 1977 c, 1979; and Stewart, 1980).

Mesozoic sedimentary rocks in Nevada are chiefly of Triassic and Early Jurassic age. The Lower Triassic Upland is believed to have separated the shallow marine carbonates and clastics in the eastern basin from the shallow-water detrital carbonates, deep-water mudstone, and volcanogenic fine-grained detrital sediments in the western basin (Fig. 8). From Triassic to the end of Mesozoic, the shorelines of these basins separated by the Lower Triassic Upland moved farther eastward to the eastern basin (Utah and Colorado) and farther westward into the western basin in California. During the entire Mesozoic, the studied area existed as a highland in which no marine sediments have been reported. In the Antelope Valley region, about 1800 feet of Cretaceous Newark Canyon Formation, reported by Nolan et al. (1957), are mainly composed of conglomerate, sandstone, siltstone, and fresh-water carbonates.

Mesozoic intrusive rocks, mostly granitic (quartsodiorite and monzodiorite), are mostly of Jurassic and Cretaceous ages, and these intrusive rocks are very common in California and western Nevada, and relatively sparse elsewhere. Mesozoic granitic rocks of western Nevada, having considerable economic importance for gold, silver

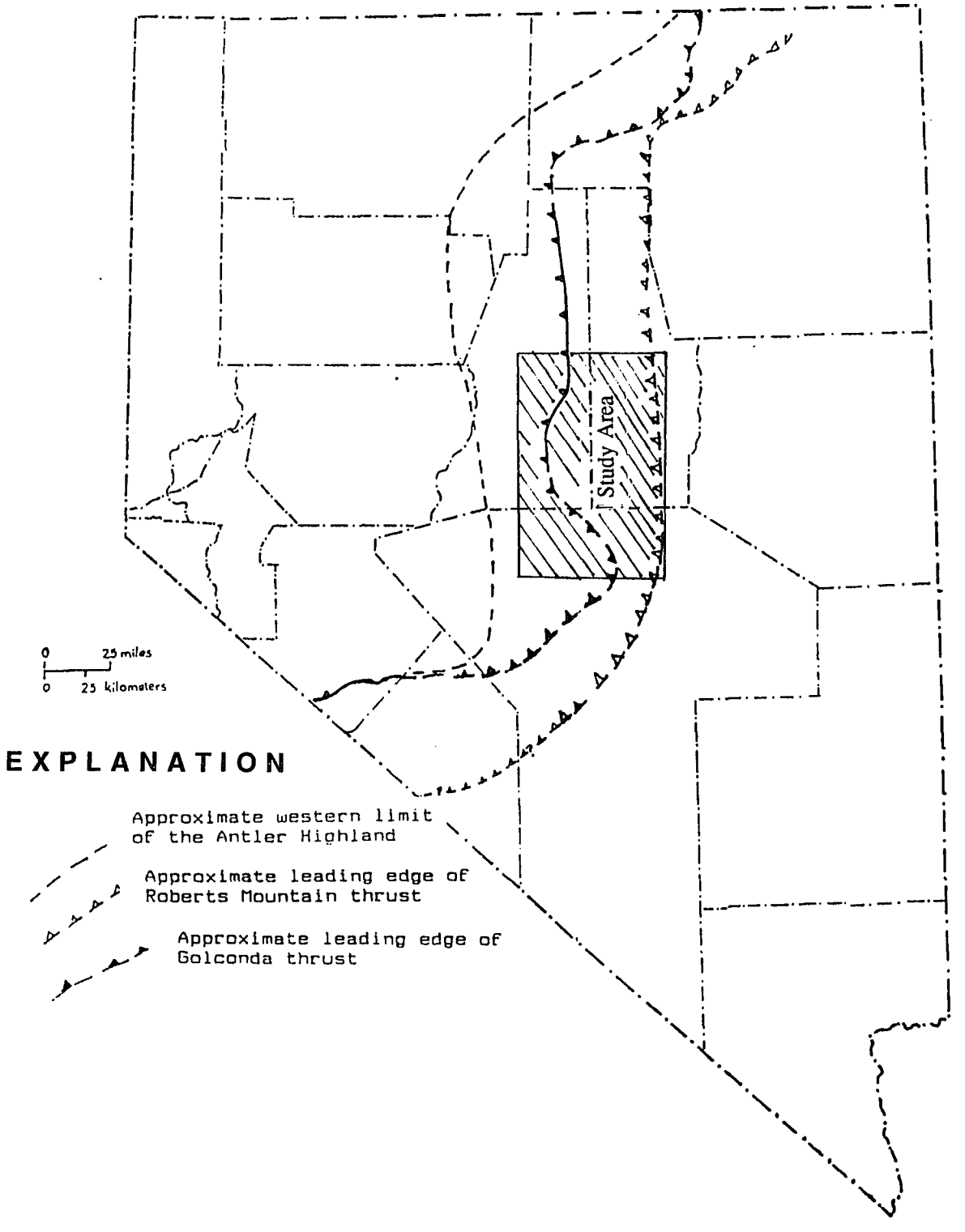
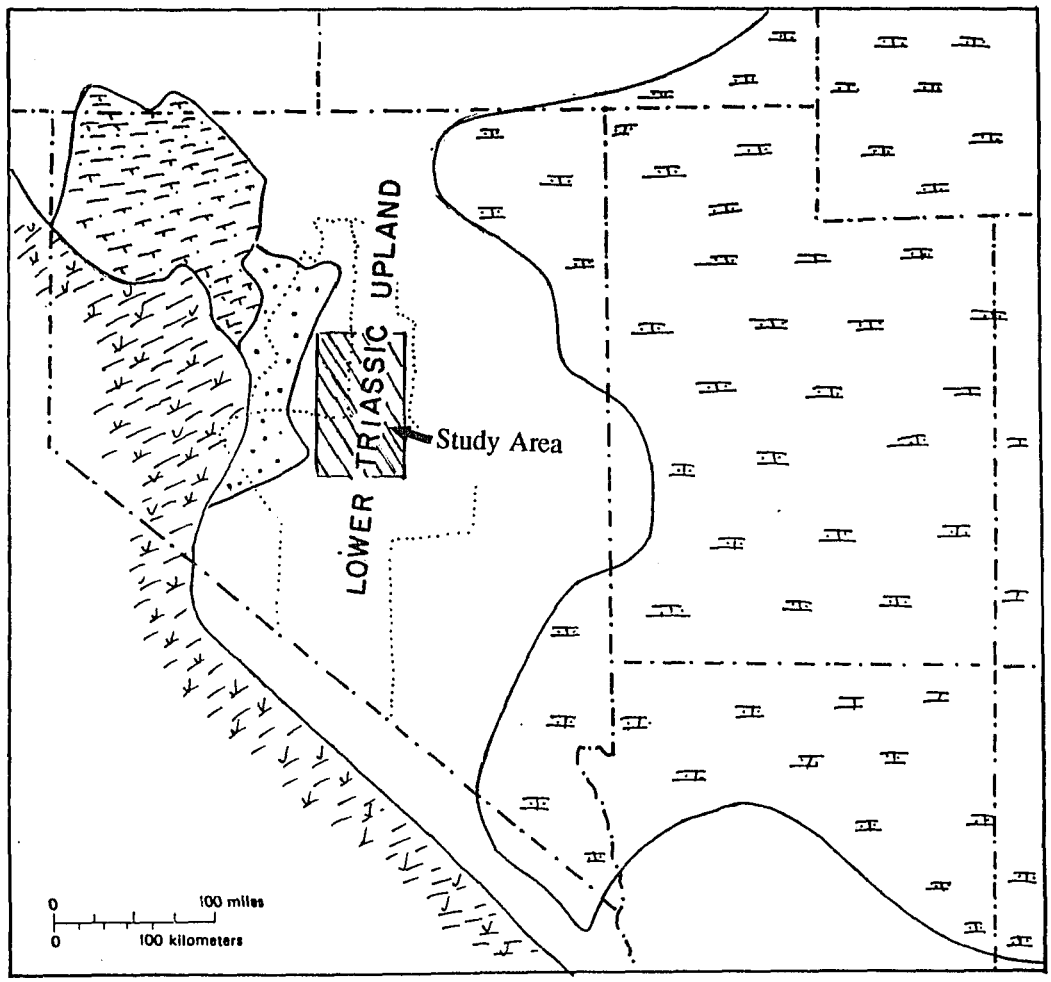


Figure 7- Approximated-leading edge of the Roberts Mountain thrusts (Late Devonian-Early Mississippian) and Golconda thrusts (Late Permian-Early Triassic), modified from Stewart (1980).



EXPLANATION

Lower Triassic marine carbonate rocks and siltstone and Upper Triassic continental sandstones, conglomerates, and bentonitic claystones.

Carbonate and terrigenous detrital rocks, locally thick rock at base

Shale, mudstone, siltstone, sandstone and carbonate rocks

Shale, sandstone, volcanogenic clastic rocks, andesite, rhyolite, and locally thick carbonate units

Figure 8- Map of depositional provinces of Triassic rocks and the Lower Triassic Upland in the Great Basin (Stewart, 1980).

and tungsten, are considered to be a continuation of the Sierra Nevada Batholith (Moore, 1966; Smith et al., 1971; Crowder and others, 1973; and Stewart, 1980).

In addition to magmatic intrusions during the Mesozoic, post-Sonoma orogeny folding and thrusting not being firmly dated, are probably as old as Late Triassic and Early Jurassic in Nevada at 36 and 40 latitude. In western Utah and Southern Nevada, from Middle Jurassic to end of the Mesozoic, north-north east trending large-scale overthrusting and complex folding took place during the Sevier orogeny. Approximate tectonic displacement by thrusts of Sevier orogeny is estimated to range from 21 to 75 miles (Armstrong, 1968; Stewart, 1980).

Paleocene, Eocene, Oligocene and Lower Miocene sediments are chiefly unconsolidated volcanic and conglomeratic rocks scattered in Nevada. Pliocene and Quaternary deposits are dominantly inter-mountain basin-filling sediments which are alluvial fan, valley-flat, and playa-lake deposits.

Igneous activity was widespread throughout Cenozoic time, starting 43 m.y ago in the northern part of the state, and moved southward. Igneous rocks ranging from 43 to 37 m.y. in age are primarily andesitic or rhyolitic in origin. About 34 million years ago in Nevada, a significant change in character of volcanic activity started with voluminous eruptions of siliceous and rhyolitic-ash flow and continued until 17 m.y ago. In Nevada, about 17 m.y. ago, extensional block faulting accompanied by mostly basaltic and minor rhyolite volcanism produced the present-day Basin and Range topography (Stewart, 1980. Since then continental sediments were entrapped within the fault-bounded, inter-mountain basins.

Previous Study

The first geologic investigation in central Nevada was by Henry Engalman in 1859, and the subsequent studies in 1868 were undertaken by the U.S. Geologic Survey in north, east and west of the Antelope Valley region where Paleozoic rocks were examined and reported (Merriam, 1963).

For the first time the " Pogonip Limestone " was introduced by Clarence King for 4000-feet thick group of strata at the north end of the Pogonip Mountain (Fig.9), and later it was redefined by Arnold Hague in 1883 for Ordovician strata (Merriam, 1963). Little knowledge was added to the geology of Paleozoic rocks of the Antelope Valley region and neighboring Eureka district until 1928, when Henry G. Ferguson and Edvin Kirk visited the region. Later (1933-1934), Kirk discussed some aspects of the fossil record in the southern Antelope Range and Monitor Range, calling special attention to Ordovician strata (Merriam, 1963). Merriam and Anderson (1942) investigated the Paleozoic rocks in the Roberts Mountain, Devils Gate, and Lone Mountain regions, where siliceous-and volcanic-assemblage rocks of the upper plate of the Antler orogeny were observed. The revision of the Ordovician in the Antelope Valley and Eureka Mining district was jointly undertaken by Nolan, et al. (1959). Their definitions of the "Pogonip" depart slightly from Hauge's definition, mainly restricting the Pogonip name to post-Cambrian rocks and elevating it to group rank with three-mappable formations, from the youngest to oldest: the Antelope Valley Limestone (AVL), Ninemile Shale, and Goodwin Limestone (see Fig. 9 in the Stratigraphy section). In the Antelope Valley Limestone (AVL), Merriam (1963) defined three distinct biofacies zones: (1) Anomalorthis, (2) Palliseria, and (3) Orthidella (Fig. 10). These biozones are identical throughout central (Antelope Valley region) and southern Nevada.

In southern Nevada, Ross (1964) showed that the Antelope Valley Limestone at the Meiklejohn Peak at the Nevada Test Side and Arrow Canyon Range (Fig. 9) was also

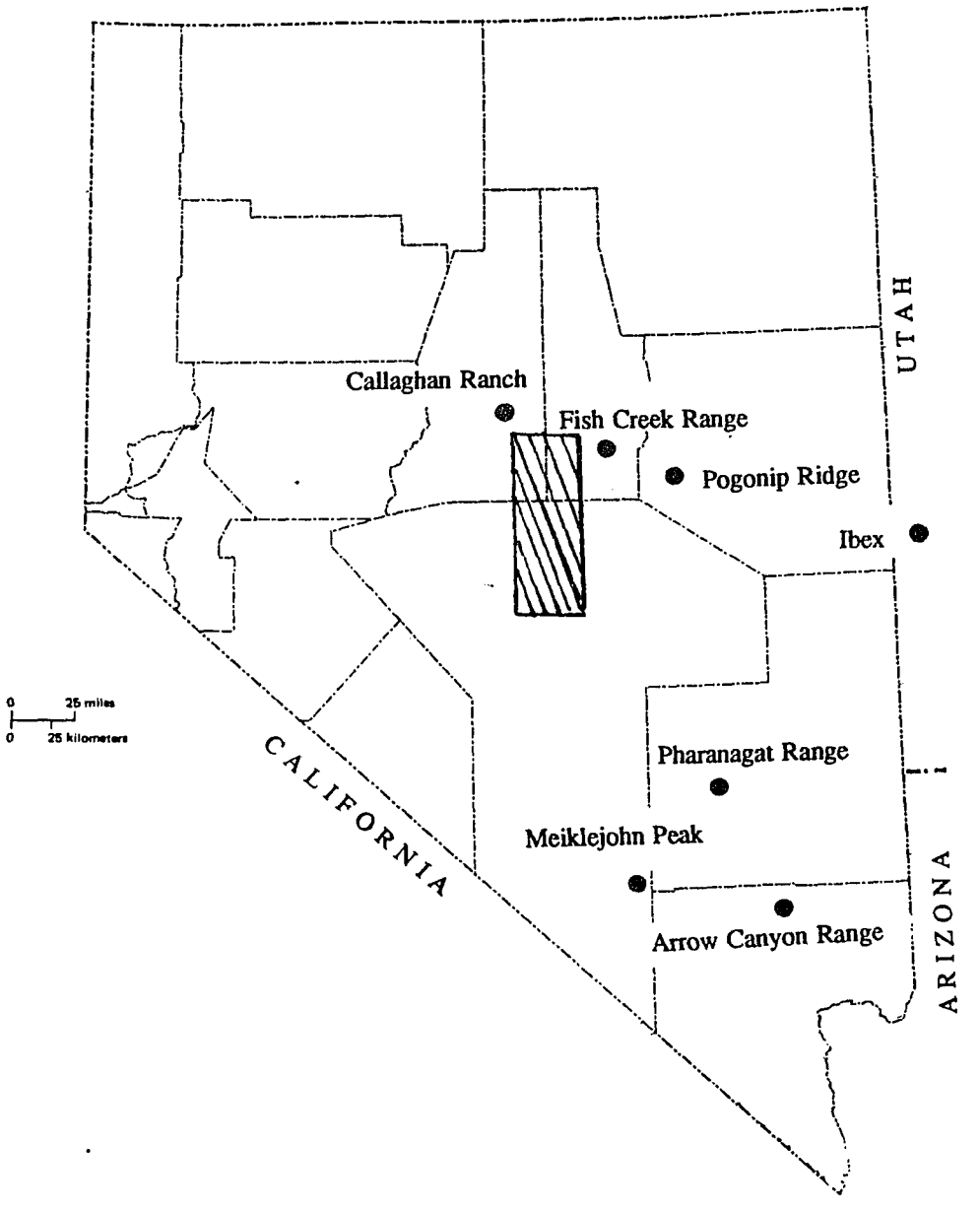


Figure 9- Index map showing the location of the study area and other localities where the AVL was studied by others.

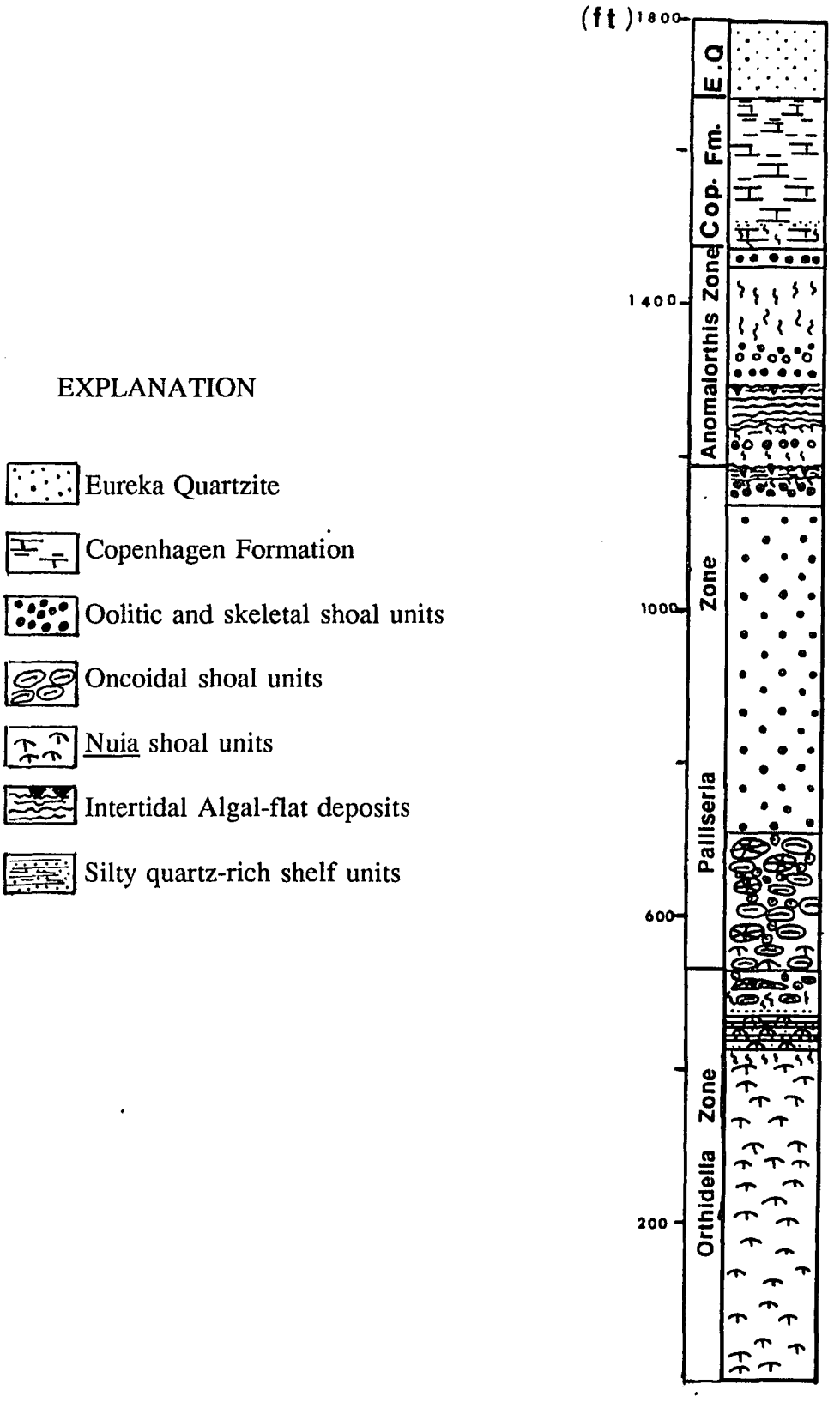


Figure 10- A Columnar section showing the biozones of the Antelope Valley Limestone in the Antelope Valley region, central Nevada.

divisible into those of three-distinct biofacies being identical to those of biofacies defined in central Nevada by Merriam (1961). The Palliseria and Anomalorthis zones were noted within the dolomitic and limestone intervals in the Hot Creek Range and southern part of the Monitor Range by Lowell (1965).

In Iks Canyon window, Ordovician fauna in the open-shelf facies of the Antelope Valley Limestone on the lower thrust plate of the Roberts Mountain thrusts were studied by Bassler (1927), Kirk (1933), Ulrich and Cooper (1936, 1938), and McKee (1976). Ross (1970) undertook a comprehensive study in which he discussed and compared the Ordovician fauna in eastern and central Nevada, especially near the mouth of Iks Canyon.

In the vicinity of Iks Canyon, Kay and Crawford (1964) divided the AVL into three-allochthonous sequences of the lower and middle Paleozoic rocks: the August, Mill, June Canyon sequences (see Figs. 4, 10 in the Stratigraphy section). An additional allochthonous sequence, the Petes Canyon sequence (Figs. 4, 10), was recognized at 24 km north of the Iks Canyon window (Ross and McKee, 1969). The fossil content, particularly brachiopods, trilobites, conodonts, ostracods, and graptolites, of the Antelope Valley Limestone (AVL) was documented in four tectonic sequences by McKee (1976) and Ross (1972). Further westward in the Toiyabe Range, Washburn (1969) observed this formation and interpreted it as a deep-water setting on the basis of its uniform, parallel even laminae, less fossil content and more shaley intervals.

Several studies have carried out microfacies analysis and examined depositional environments of the AVL. In the Arrow Canyon Range (Fig. 9), Stricker and Carozzi (1977) described nine lithofacies and established two-different models in time and space as "the Nuia Model" and " Algal Ball model".

In the Antelope Valley region and the Toquima Range, Morreale (1981) studied depositional environments and stratigraphy of the Antelope Valley Limestone and suggested that this formation consisted of the following facies from west to east,: subtidal / subtidal and intertidal / intertidal and supratidal. Morreale (1981) suggests that these facies characterize, respectively, lower, middle and upper members of the Antelope Valley Limestone. Taban (1986) studied the AVL at the Martin Ridge and

Ninemile Canyon sections and described eight different lithofacies. He suggested that from open shelf to shoreward three-shoal facies, Nuia subtidal offshore bars, oolitic shoal, and skeletal shoal, formed simultaneously in the shallow-epicontinental sea. Also, he suggested that the climate was dominantly arid during the deposition of this formation. Ross (1977) and Ross et al. (1989) regionally evaluated the depositional systems and patterns. Ross et al.(1989) suggested four evolutionary phases for basinal and depositional history. All the studies related to the depositional environment of the AVL and to the evolution of carbonate platforms are either too general (Ross et al., 1989) or based on a few type sections (Morreale, 1981).

Nuia units of the lower Antelope Valley Limestone were studied in detail by Kaya and Friedman, (1987). Ross et al. (1988) reported the Nuia units at the Callaghan Ranch, and Pharanagat Range (Fig. 9).

Stratigraphy

The Pogonip Group consists of three formations, from the youngest to oldest, the Antelope Valley Limestone, Ninemile Shale, and Goodwin Limestone (Fig. 11). In Antelope Valley and Eureka district, the Pogonip group is mainly limestone, and attains approximately 3450 feet of thickness.

In Ninemile Canyon and Martin Ridge, the Antelope Valley Limestone has a gradational lower contact with the Ninemile Shale and a gradational upper contact with the Copenhagen Formation (Fig. 11). The AVL is overlain disconformably by the Eureka Quartzite with a sharp-erosional contact in Lone Mountain. According to Ross (1964), nearly 170 m of the Antelope Valley Limestone were removed by the pre Eureka Quartzite erosion. Similarly, in the Fish Creek Range, the Eureka Quartzite disconformably overlies the Receptaculites zone of the AVL (Webb, 1958). The gradational basal contact of the AVL has been observed only in the Ninemile Canyon and Whiterock Canyon sections; however, this basal contact is covered by basin-fill sediments in other type sections of the Antelope Valley region, such as Martin Ridge and Lone Mountain.

In the June Canyon and Mill Canyon sections, the AVL has a gradational basal contact with the Ninemile Shale and disconformable upper contact with an unnamed-limestone unit consisting of medium- to thin-bedded gray limestone (Fig. 12). However, in these sequences, a hiatus exists between the AVL and overlying-unnamed limestone. In the Petes Canyon sequence, the upper contact of the AVL is disconformable with the overlying Upper Ordovician Hanson Creek Formation where a hiatus exists on the basis of faunal differences of these two formations (Fig. 12; McKee, 1976).

At Ibex in western Utah and eastern Nevada (Fig. 9), the stratigraphic units, in ascending order, the Juab Limestone, Kanosh Shale, Lehman Limestone, Swan Peak Quartzite, and Crystal Peak Dolomite, are correlative with the Antelope Valley Limestone in central Nevada (Fig. 13; Hintze, 1951; 1973).

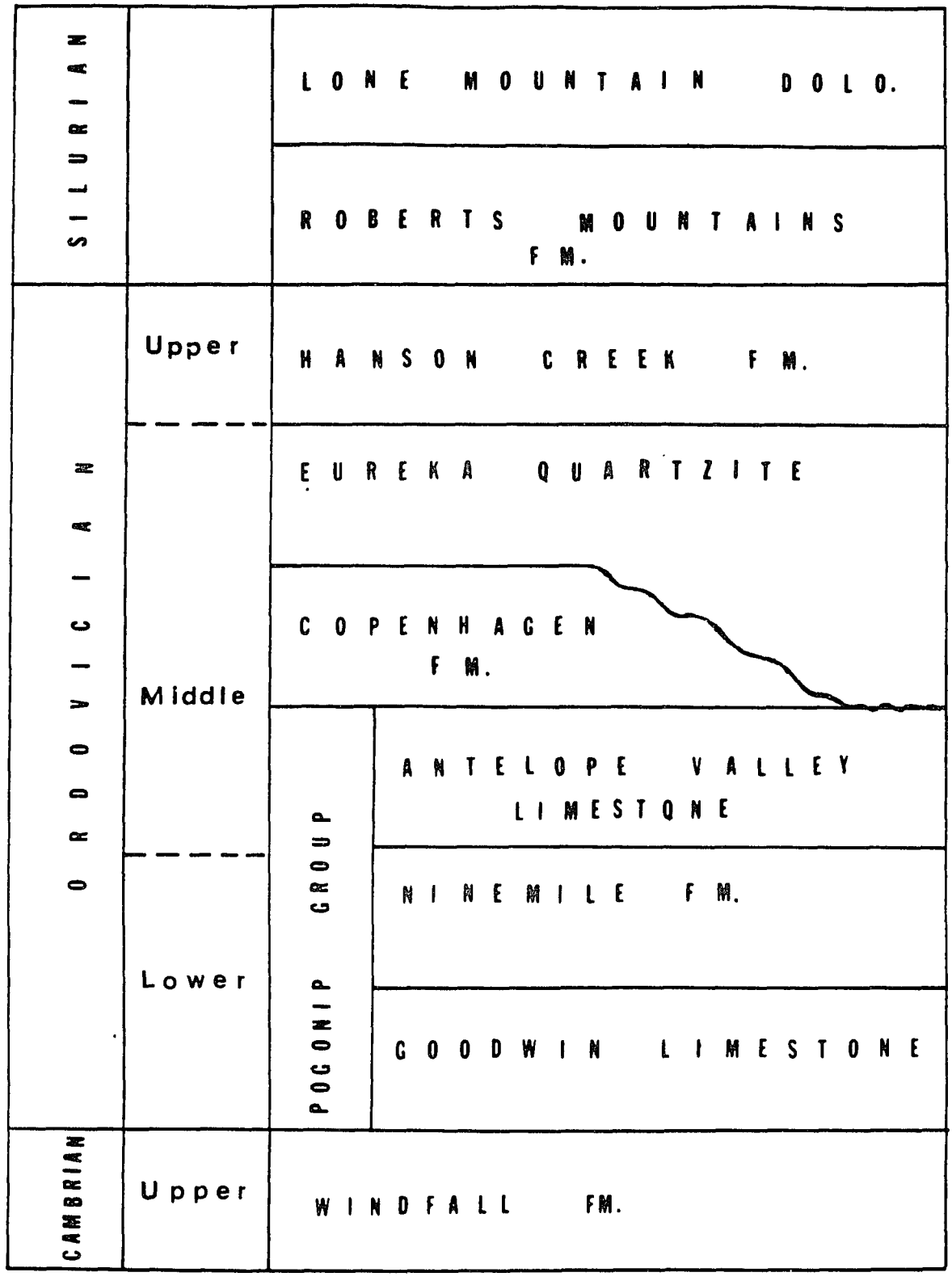
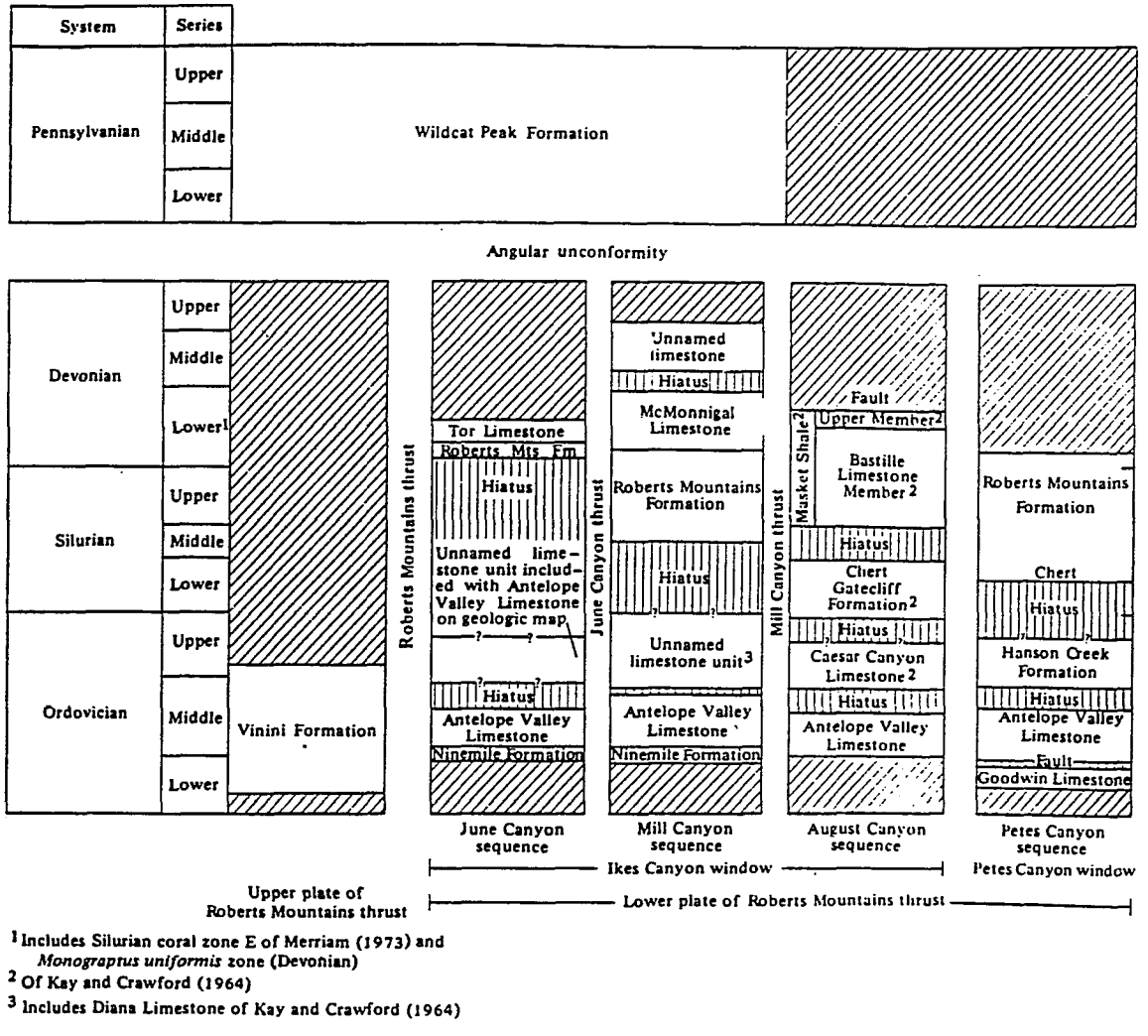


Figure 11- The stratigraphic column of lower Paleozoic rocks in the Antelope Valley region, central Nevada.



[1] Includes Silurian coral zone E of Merriam (1973) and *Monograptus uniformis* zone (Devonian)
[2] Of Kay and Crawford (1964)
[3] Includes Diana Limestone of Kay and Crawford (1964)

Figure 12- Stratigraphic correlation of Paleozoic rocks in the different tectono-stratigraphic sequences at the northern Toquima Range (McKee, 1976).

Copper (1956) studied the brachiopod fauna of this formation and correlated it with the Whiterockian stage. On the basis of faunal content, he also proposed five biozones for this formation, in ascending order: Orthidella, Palliseria, Desmorthis, Anomalorthis, and Rhyosostrophia.

Later, Merriam (1963) identified three well-defined biozones in the AVL; in Antelope Valley region, these biozones approximate the lithologic divisions of the Antelope Valley Limestone (Fig. 10). In descending order, these three bio-zones are the following (Fig. 10):

1-Anomalorthis: occupying nearly 350 feet of the upper AVL and characterized by platy and flaggy mottled limestone consisting of high-spired small gastropods, small orthoid brachiopods, and large Leperditia ostracods and hemispherical bryozoa.

2-Palliseria: forming more massive cliff and characterized by Palliseria and Maclurites (large gastropods) and also containing abundant Girvanella and in places Receptaculites.

3-Orthidella: typical faunal assemblages starting 75 feet above the base of the Ninemile Shale in the Whiterock Canyon section, characterized by Orthis ostracods and bryozoans. Merriam (1963) agrees on Whiterockian stage for the age of the Antelope Valley Limestone (Fig. 13) as proposed by Cooper (1956).

Kay (1962) studied the trilobite and cephalopod faunas of the Anomalorthis zone in the sponge-bearing strata (Bassler, 1941); he also observed that Rhyosostrophia zone (based on twelve genera of brachiopods) in the thick-bedded units (initially interpreted as the Palliseria zone) represented mainly by Girvanella oncoids rest on the Anomalorthis zone. Therefore, Kay (1962) inferred an age younger than Chazy for the Palliseria zone, suggesting that the Antelope Valley Limestone (AVL) in this region was correlative to the formations of Chazian age at Ibex in western Utah and eastern Nevada (Fig. 9), such as the Juab Limestone, Kanosh Shale, Lehman Limestone, Swan Peak Quartzite, and Crystal Peak Dolomite (Hintze, 1951; 1973).

Ross (1964) regionally synthesized the faunal and stratigraphic correlation of the AVL at the Nevada Test site, Meiklejohn Peak, Inyo Range, Toquima Range, and Antelope Valley region (Fig. 13), and he included the Desmorthis zone of Cooper

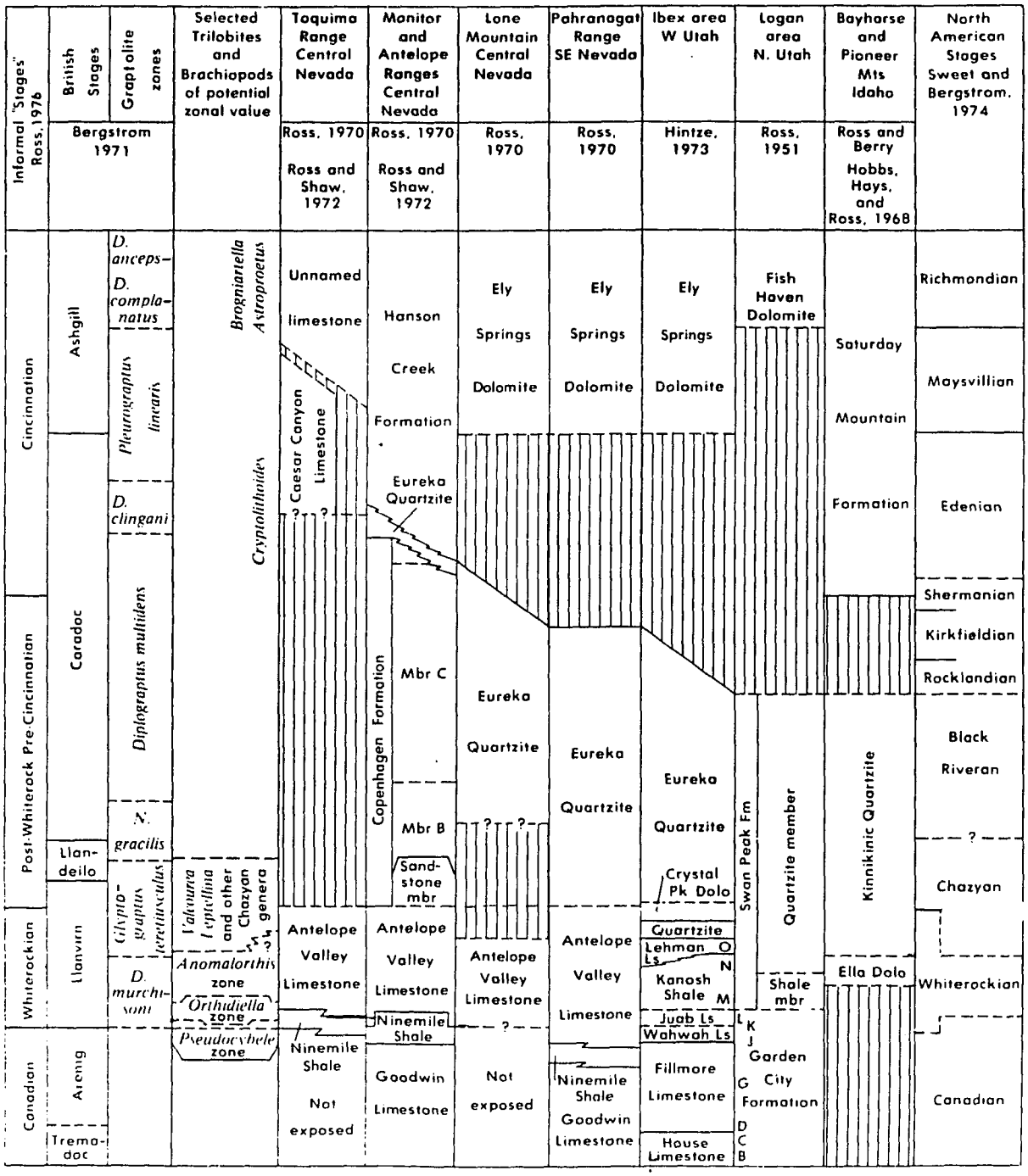


Figure 13- Stratigraphic correlation chart of Middle Ordovician rocks in the Great Basin, central Nevada (Ross, 1977).

(1956) found in Lone Mountain to the Anomalorthis zone. He assigned the Rhyososstrophia zone to the Marmor stage (Crown Point of Chazy), not to Whiterockian as suggested by Cooper (1956). Ross (1964) noted that the Palliseria zone overlies the Rhyososstrophia zone in the Inyo Range and the Anomalorthis zone in the Nevada Test site areas, suggesting that except for the Antelope Valley region and Arrow Canyon, the Palliseria zone westward becomes younger. As a result, he concluded that the Palliseria zone could not be used as stratigraphic marker. The uppermost part of the AVL is represented in the Marmor stage of Chazy (Ross, 1964). However in the Antelope Valley region, the Rhysostrophia zone was observed about 15 feet above the upper Antelope Valley Formation (AVL). Only in this region, the AVL can be restricted to the Whiterockian stage (Fig. 13; Ross, 1964).

CHAPTER 3: RESEARCH METHODS

A. Field Work:

A Jacob's staff and a Brunton compass were used, respectively, for measuring the thickness of lithofacies of the Antelope Valley Limestone (AVL) in vertical sections and inclinations of strata. The AVL was sampled at intervals where lithofacies change occurs and where lithologic and faunal constituents vary in the same lithofacies. Diluted HCl was used for distinguishing dolomite from limestone.

Dunham's classification and nomenclature for carbonate rocks was used for description of collected specimens and lithology in the field.

B. Laboratory Work

a) Staining

About 495 standard-petrographic thin sections were prepared for studying the petrography and diagenesis of the AVL. Two kinds of staining techniques were used to identify carbonate minerals:

(1) Alizarin Red-S added into 1.5 % HCl was used for identifying calcite and dolomite (Friedman, 1959).

(2) 2 gr potassium ferri-cyanide "K_3 Fe (CN_6)" added into 2 % HCl, Alizarin Red-S solution and 1.5 % HCl were applied together to identify ferroan purple-blue calcite cement from non-ferroan red calcite (Friedman, 1959; Dickson, 1966). Two-hundred and five finely polished thin sections for cathodoluminescence study were stained by these solutions.

b) Cathodoluminescence Petrography

This method was used to determine cement stratigraphy, crystal-growth fronts, and other diagenetic features that can not be recognized by standard petrography.

A 1000 grit and $Al_2 O_3$ final polishing powder were used for polishing two hundred and five thin sections. For cathodoluminescence petrography, a Nuclide ELM. 2B luminescope was used and operated under 10-12 kv (kilo volt) and 0.6-0.8 mA (milliampere).

Bright, dull, and non-luminescent zones of calcite and dolomite cements are compositional zones that can represent the evolution of diagenetic solutions, pores and permeabilities of the carbonate rocks during diagenesis. Mn^{+2} is the most important activator detected in bright luminescent zones, whereas Fe^{+2} is the most important quencher found in non-luminescent zones (Meyers, 1974; Frank et al., 1982; and Machel, 1984).

The concept of cement stratigraphy was first introduced by Evamy (1969) and first applied by Meyers (1974). The detection of crystal-growth zones, zonal discontinuities, and truncations between zonal cements can be examined by cathodoluminescence, and are interpreted in a petrographic manner. For correlation of discrete luminescent zones, each zone is believed to represent a different episode of cementation; the order of luminescent zones is assumed to be continuous in a sequential order (Meyers, 1974). If the sequence of luminescent zones is incomplete, then it is assumed that some zones are missing. The missing zones and truncational contacts between luminescent zones probably indicate unconformities (Meyers, 1974).

c) Dolomite Stoichiometry

A total of 63 samples, 48 dolomites and 15 dolomitic limestones were selected for x-ray diffractometer analysis, representing various depositional environments, diagenetic mechanisms and environments, such as stromatolitic dolomites,

fault-controlled sucrosic epigenetic dolomites, ferroan dolomites, and saddle dolomites.

Mortar and pestle were used for crushing the samples to less than 250 mesh (60 μm) powder size for X-ray diffractometer analysis. A Phillips diffractometer was operated under the following conditions: 40 kv and 25 mA; scan mode of 2° per minute; range of 1K*1; and chart speed of 60.

For detailed semi-quantitative X-ray study, the same samples were scanned from 29 to 32° 2θ by a Rigaku (CuK alpha radiation) diffractometer linked to a soft-ware system. Operating conditions of diffractometer measurements from 29.00 to 32.00° 2θ were, as follows: 40 kv and 20 mA, step size 0.010, counting time 1.000, scan speed 2.000. In this range, the two most commonly detected peaks are (1) 30.6-31.8° 2θ (104) peak for dolomite, and (2) 29.0-29.9° 2θ (104) peak for calcite. All analysis were replicated three times.

The peak positions, relative intensity'"I (Rel)" and intensity in count per second " I (Cps) of calcite and dolomite, d-spacing of dolomite and calcite peaks, and their full width half maximum (FWHM) were given by computer print outs during each run. Dolomite concentration in dolostones and dolomitic limestones was calculated by the following expression:

$$Dolomite\ \% = D(I) + C(I) / D(I) \times 100$$

D= Dolomite, *C*= Calcite, and *I*= intensity.

Mole percentage of $CaCO_3$ in the dolomite composition was determined by the following equation:

$$\%\ Ca\ CO_3 = M * d + b$$ (Lumsden, 1980).

M= 333.33, *d*= observed d-spacing, *b*=911.99.

This study did not use (113) dolomite peaks (40.7 and 41.5° 2θ) and (113) calcite peaks (39.1-39.8° 2θ) because all samples contain less than 1% Fe^{+2} (Runnel, 1970). Measured samples were not stained by potassium-ferri cyanide because it may contribute additional Fe^{+2} into sample compositions (Lumsden and Chimahusky, 1980).

Disordered or nonstoichiometric dolomites result mostly from excess Ca^{+2} substituting for Mg^{+2} (Goldsmith and Graf, 1958), as well as some periodic structural modulations (Reeder, 1983).

d) Illite Crystallinity and Clay Diagenesis

About 18 shaley limestone samples (50 gr) were ground in a mortar and sieved through a 2 mm sieve. These ground samples were first treated with 6 % H_2O_2 within a 600 ml beaker for the removal of organic matter. The H_2O_2-treated samples were heated from 25 °C room temperature to 100 °C. This treatment was followed by decantation and successive washing.

The next step was the removal of carbonate minerals: the sieved samples were diluted by the addition of distilled water in a beaker; then 1 N HCl acid was added drop by drop to the distilled-water suspension until pH level reached 3.5 to 4. Until the final removal of carbonate from the samples, these treatments were repeated, the beakers were decanted and successively washed. This was followed by separation of clay-sized particles from fine-grained sand and silt particles for which the well-washed residue was suspended within a 5-cm high distilled-water column for 40 minutes. When fractions larger than clay-sized particles settled to the bottom of beakers, clay-sized particles in suspension were separated by decantation.

In the next step, Na_2CO_3 was added to distilled-water suspension for flocculation until pH level reached 9.5. From the solution of pH 9.5, 2 hours and 50 minutes of gravity sedimentation allowed 2μ-size and finer clay particles to be separated by decantation. After that solutions containing 2μ and finer fractions were separated into three parts for the preparation of air-dried, KCl- and $MgCl_2$-treated samples. Pipets were used for preparing oriented-clay samples on glass slides. A total of 18-air dried, 18 KCl-treated, 7 glycolated-, and 3 $MgCl_2$-treated glass slides were prepared.

These laboratory analyses were based on the procedures described by Jackson (1967) and Moore and Reynolds (1989).

A Rigaku X-ray diffractometer with CuK-alpha radiation, linked to software, was used for clay mineral analysis. And the following working conditions were employed: 40 kv and 20 mA; starting = 3° 2θ; ending = 19° 2θ, Step size = 0.020, scan speed= 1 degree per minute.

Weaver (1960), Kubler (1967), and Dunoyer de Segonzack (1970) documented that

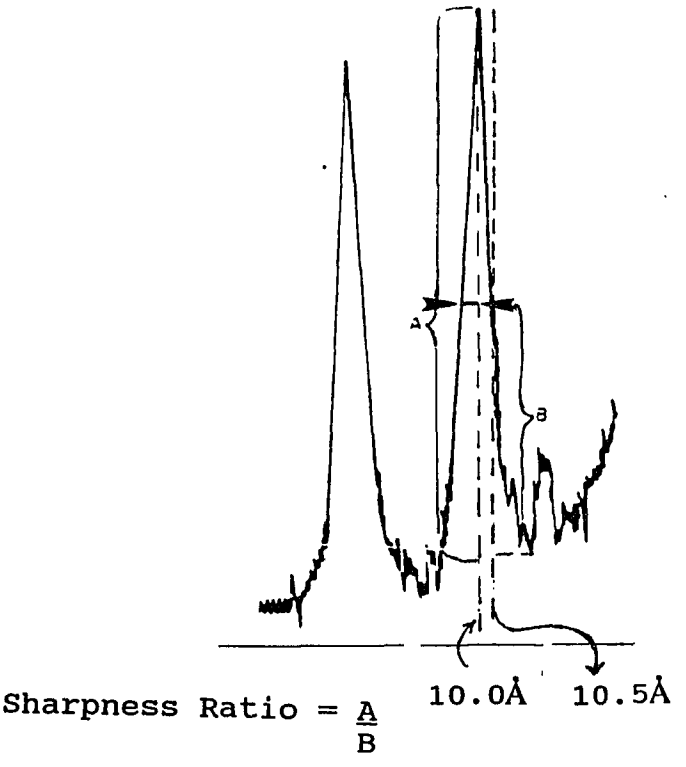


Figure 14- X-ray diffractogram showing the sharpness ratio of a 001 illite peak (Sharpness ratio= height of 10 Å illite peak / height of 10.5 Å illite peak) and illite crystallinity index (equal to half width of a 001 illite peak, 10 Å, at its half height, as indicated by arrowheads).

the intensity and sharpness of 10 Å, or 001 illite peaks increase with increasing crystallinity due to depth of burial. Weaver (1960) introduced "sharpness ratio" which is defined as the ratio of height of 10 Å illite peak to height of 10.5 Å illite peak (Fig. 14). Kubler (1966) introduced "illite crystallinity index" (CI) which is simply the measurement of the 001 illite peak's width at half peak height (Fig. 14). Diminishing of the half peak width of 10 Å illite peaks reflects the increasing crystallinity of illite. Therefore, higher illite crystallinity indices correspond to greater diagenetic and incipient metamorphic changes. In this study, sharpness ratio is generally expressed by mm, and crystallinity index is expressed by both mm and °2θ. For conversion of CI values from mm to °2θ, the following equation was used:
Crystallinity index in °2 θ = *crystallinity index (CI) in mm x 0.079* (Houseknecht et al., 1987).

e) Fluid-Inclusion Microthermometry

A total of 110 samples with calcite- and saddle dolomite-filled fractures and vugs were collected for fluid-inclusion microthermometry. 150 to 200-μ thick, doubly polished thin sections were prepared for fluid inclusion study. Heating and freezing runs were made in a USGS Heating and Cooling stage equipped with a Nikon microscope. Primary and pseudosecondary two-phase fluid inclusions (Fig. 15), having formed during the growth of host crystals (Roedder, 1984), were used for fluid-inclusion thermometry. Secondary two-phase fluid inclusions (Fig. 15) representing the post-crystal fluid entrapment were not useful for fluid-inclusion microthermometry. Secondary fluid inclusions are similar to pseudo-secondary inclusions; however, they form along microfractures which are healed generally long after the termination in growth of host-crystals (Roedder, 1984).

The two-phase inclusions were heated until the homogenization of two immiscible phases (gas and fluid) occurred. Pressure-uncorrected homogenization temperatures (T_h), attained from heating experiments, give the minimum-entrapment temperatures of

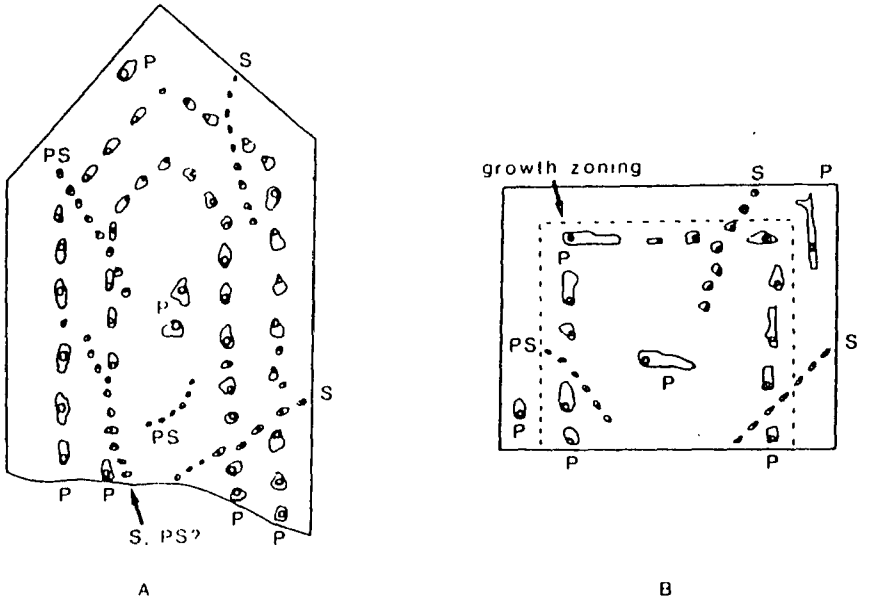


Figure 15- Kinds of fluid inclusions and occurrences: (P) primary, Ps) pseudo secondary, and (S) secondary inclusions (Shepherd et al., 1984).

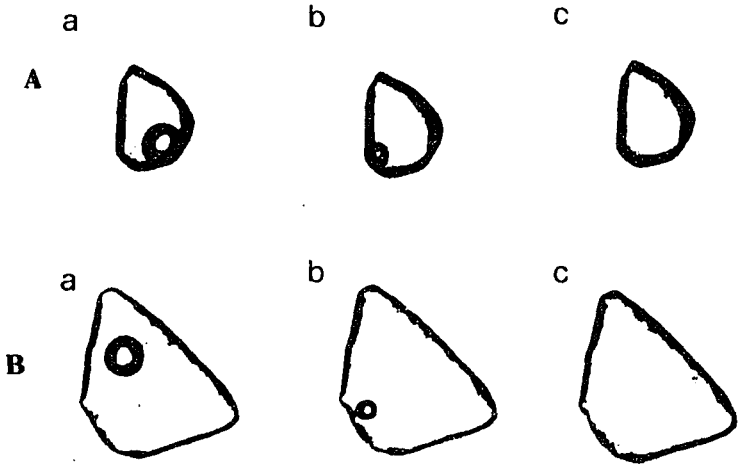


Figure 16- Sequence of phase changes in two-phase fluid inclusions during heating (A) and (B) indicating the homogenization of gas and fluid phases of two-phase fluid inclusions into fluid phase during heating stage; progressive heating results in progressive reduction in the size of gas bubbles, and final disappearance of gas phase marks the minimum-entrapment temperatures (T_h) of two-phase fluid inclusions (Shepherd et al., 1984).

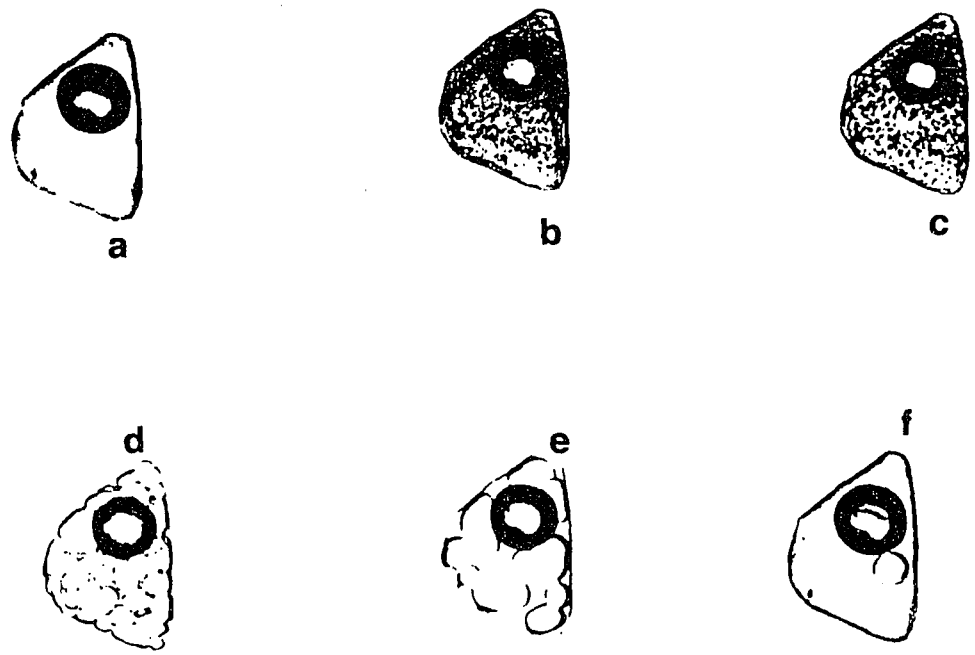


Figure 17- Phase changes in two-phase fluid inclusions during freezing/ heating stages: 1) on freezing, a) complete freezing at 106 °C; and 2) on heating, b) inclusion with a pale-brown color and granular appearance, c) a phase of first ice crystal-melting temperature or eutectic temperature (Te), d-e) progressive melting of ice crystals, and f) melting of the last ice crystal marks the melting temperature (Tm) of fluid.

two-phase fluid inclusions (Fig. 16 A, B).

By freezing-heating experiments, phase changes can be observed during events of the first- and last ice crystal melting. The first ice crystal-melting temperature is called eutectic temperature and can be observed in relatively large and clean, primary two-phase inclusions. Melting of the first ice crystal can not be detected in small inclusions, but it can only be estimated when two-phase inclusions have a fine, granular appearance with pink-brown color (Fig. 17).

The last ice crystal-melting temperature (Tm), on the other hand, can clearly be determined by the first free movement of stationary gas bubbles in two-phase fluid inclusions (Fig. 17). Then, gas bubbles begin to move freely in the fluid inclusions at the melting temperatures of the last ice crystal (Tm).

Data obtained from freezing-heating runs on two-phase fluid inclusions are indicative of the fluids' composition and density because increasing salinity in solutions depresses the freezing points of given solutions (Roedder, 1962; 1963; and Potter et al., 1978). In fluid inclusions, a total salinity which is equivalent to wt. % of NaCl can be estimated from melting temperature by the following equation (Potter et at., 1978) :

$$Ws = 0.00 + 1.76958\,\Theta - 4.2384 \times 10^{-2}\,\Theta_2 + 5.2778 \times 10^{-4}\,\Theta^3\ [\pm 0.028]$$

Ws= the weight percent NaCl in solution

Θ= the freezing point depression (Tm) in °C

The Following practical steps were taken to produce reliable data on homogenization and melting temperatures:

1) On heating stage:

1) The field of view was mapped and sketched.

2) Origin (primary, pseudosecondary, and secondary). of the inclusions were determined.

3) Heating experiments were performed first because it is widely believed that freezing runs decrepitate fluid inclusions by expansion of ice crystals, especially in soft minerals like calcite (Lawler and Crawford, 1983).

4) Visual estimate of vapor / liquid ratio was used to determine which inclusions T_h should be determined first: in viewed areas, two-phase inclusions with the smallest V/L ratio were examined first at relatively lower temperatures.

5) Two-phase inclusions were heated rapidly to just below the lowest temperature at which fluid inclusions appear to be near homogenization. Then these inclusions were heated with 0.5 to 1 °C / minute increments.

6) Fluid inclusions with the lowest T_h values were measured first in order to avoid overheating. During rapid heating, some two-phase inclusions' bubbles become smaller and smaller which is the indication of low-T_h values for those inclusions.

7) Several heating experiments were repeated as temperature was gradually reduced until bubbles reappeared; then inclusions were reheated with the same low-temperature laps (0.5 to 1 °C per minute) in order to determine the stretching of inclusions. The stretching or expansion of host crystals were recognized only by a rise in temperature of subsequent runs.

8) Two-phase inclusions with darker borders were heated repeatedly in order to determine approximate T_h because small bubbles can easily disappear in these dark boundaries.

9) During heating runs, V/L (vapor-liquid ratio) or bubbles gradually decrease, and two-phase inclusions homogenize and become miscible. A sudden increase or decrease in the size of vapor bubbles (in V/L ratios) were interpreted to indicate irreversible fluid inclusion deformations either by stretching or by leaking. Constancy of V/L ratio before and after each heating run is essential in order to determine irreversible fluid inclusion deformations (Roedder, 1984).

13) Leakage of two-phase inclusions during heating was checked by increase or no change in the size of vapor bubbles and significant change in the V/L ratio of the inclusions after each heating experiment.

2) On freezing-heating stage:

1) Two-phase inclusions were frozen until -100 to -110 °C. At this temperature range, if the color of fluid inclusions turns brown, it indicates color change represent a high-salinity fluid. Light color of frozen inclusions, on the contrary, indicates low

salinity fluids.

2) Temperature were allowed to rise until -60 °C or -40 °C very rapidly after which temperature was allowed to rise 0.5 °C per minute in order to determine the first ice crystal-melting temperature (Te). Granular appearance of two-phase fluid inclusions was used to approximate Te values.

3) Temperature was then increased rapidly (5-8 °C) until the last ice crystals melt. Then inclusions were freezed until bubbles became stationary again. From this point, temperature was increased in a 0.5 °C / minute increment until the last ice crystals melted. In order to determine precise Tm values, repeated cooling runs below the melting temperatures were followed by gradual heating runs with a 0.5 °C per minute incrementation.

4) The ice crystals attached to liquid and bubbles cause bubbles to be stationary at the fixed position in inclusions (Fig. 17); as soon as the last ice crystals melt, bubbles leave their fixed positions very rapidly. The temperature at which the last ice crystals melt is called "melting temperature" (Tm).

5) Two-phase fluid inclusions with considerably high-melting temperatures (up to -1 or + 0.1 °C) adjacent to inclusions of much lower melting temperatures (-20 to -10 °C) in the same crystal of carbonate cement, were interpreted to represent hydrohalites ($NaCl.2H_2O$ crystals).

3) Equipment

U.S. Geological Survey' Heating and Cooling stage was used in this study. This equipment is available from the SHE Inc., Arizona 05721-USA. Maximum and minimum temperature ranges for heating and cooling experiments which can be reached are + 700 °C to -196 °C, respectively. Heating of samples is done by passing preheated N_2 gas; cooling of the samples is done by passing-liquid nitrogen and N_2 gas.

Advantages of this stage compared to other available stages are, as follows: (1) it heats very rapidly above room temperature, and rate of heating and cooling can be changed quickly; (2) continuous N_2 flow around sample minimizes thermal gradient

within samples; (3) a relatively large sample area (about 22 mm in diameter) can be measured without major corrections; and (4) the thermocouple of this stage rests directly on samples which minimizes temperature-correction errors.

f) Oxygen-Isotope Thermometry

Fracture- and void-filling calcite and dolomite cements, other calcite cements and dolomite types were sampled for diagenesis and oxygen-isotope thermometry. A total of 46 samples were analyzed for the indicated purposes in the stable isotope laboratory of University of Michigan.

The following analytical procedures were applied. A dental drilling assembled on microscope was used for extracting powdered 0.5 to 1 mg portions of calcite and dolomite from polished slabs. The powdered samples were roasted in *vacuo* at 360 °C for 1 hr in order to remove volatile contaminant, and then they were reacted with anhydrous H_3PO_4 at 55 °C. Calcite samples were reacted in an extraction line coupled directly with the inlet of a VG 602E ratio mass spectrometer. Dolomite samples were reacted in an off-line for 6 hr. All analyses were converted PDB and corrected for ^{17}O enrichment by the procedures described in Carig (1957). No additional correction was applied for dolomite phosphoric acid fractionation. Precision was calibrated by NBS-20, which is better than 0.08 per mil for both oxygen and carbon determination.

Depleted-$\delta^{18}O$ values of carbonate cements are commonly attributed to high-temperature basinal fluids and meteoric water ((Dickson and Coleman, 1980; Land, 1980). Clayton et al., (1965) and Hitchon and Friedman (1969) have shown that under increasing burial depths and burial temperatures, $\delta^{18}O$ values of carbonate cements become progressively depleted, whereas oxygen-isotope composition of parent fluids become progressively enriched with respect to ^{18}O along with progressive increase in the salinity content of parent fluids. For this reason, carbonate cements having considerably depleted oxygen-isotope composition and high-salinity fluid-inclusion compositions were used for oxygen-isotope thermometry in this study.

For estimating formation temperature of carbonate cements from the measured $\delta^{18}O$ values, the following equations were used: (1) Craig's formula were used for the samples which have extremely depleted oxygen-isotope values with respect to heavy oxygen isotope (^{18}O).

$T=16.9-4.41\ (\delta c-\delta w) + 0.14\ (\delta c-\delta w)^2$ *for calcite (Craig, 1965).*

$T=31-5.55\ (\delta d-\delta w) + 0.17\ (\delta d-\delta w)^2$ *for dolomite* (Craig, 1965).

T= formation temperature of carbonate cement in °C, δw= estimated oxygen-isotope composition of parent solution in SMOW, δc= measured oxygen-isotope composition of calcite in PDB, and δd= measured oxygen-isotope composition of dolomite in PDB. (2) Generally, two other equations were used to calculate paleotemperature of dolomite and calcite cements.

$10^3 ln\ \alpha = 3.2 \times 10^6 \times T^{-2}(K)-3.3$ for dolomite cements (Land, 1983).

$10^3\ ln\ \alpha = 2.78 \times 10^6 \times T^{-2}\ (K) + 2.89$ for calcite cements (Friedaman and O'Neil, 1977).

$10^3\ ln\ \alpha = \delta ca-\delta w$

T= formation temperature of carbonate cements, K= Kelvin, δca (calcite or dolomite)= measured oxygen-isotope composition of carbonate cement (SMOW), and δw= estimated oxygen-isotope composition of parent solution (SMOW).

Oxygen-isotope values of cements represent the bulk composition of related cement types rather than specific compositional zones, and they may have been contaminated during drilling by adjacent phases. In addition, late diagenetic alterations at near-surface diagenetic environments modify the original composition of deep burial carbonate cements. Because of the indicated reasons above, paleotemperatures calculated by this method may not represent the accurate formation temperature of related deep-burial carbonate cements.

In this study, for paleotemperature calculations, the oxygen-isotope composition ranging from + 5 to + 9 ‰ SMOW was used for the $\delta^{18}O$ values of parent fluids. Carbonate cements chosen for the oxygen-isotope thermometry are believed to have

crystallized from deep-burial, basinal brines. Approximated $\delta^{18}O$ values of + 5 and + 9 ‰ SMOW for parent fluids are believed to represent mean and maximum oxygen-isotope values of basinal brines. In the Gulf of Mexico, the oxygen-isotope values of basinal brines range from +0.15 to +15 ‰ SMOW (Hanor, 1983). Formation waters of sedimentary basins in western Canada represent the mixing of meteoric and diagenetically modified sea water; the calculated-$\delta^{18}O$ values of formation waters for Upper Devonian at reservoir temperatures range from +2.6 to +9.0 ‰ SMOW (Hitchon and Friedman, 1969).

g) Thermal Alteration Level of Organic Matters

A total of 16 samples were analyzed for thermal alteration indices (TAI) or visual kerogen analysis by Geochem Laboratories, Inc., Houston, Texas. The following analytical method were used. About 10-20 gram of sediments were crushed to peas size and rinsed with water to remove surface dust and dirt. A 20 % diluted-HCl acid was added until the final removal of carbonates. The samples were then washed by a centrifuge. Then 52 % hydrofluoric (HF) acid was added to the residue for removal of silicates, and this stage was followed by washing and decantation. The residue was then mixed with a 20 ml zinc bromide solution (adjusted to the specific gravity of 1.8 gr/cm^3 by drops of 10 % HCl). The organic matter floated to the top of this solution and was removed for slide preparations. Details of this technique have been described by Dow (1976).

Prepared slides were generally examined under the transmitted light by Geochem Labs. Organic matter indicates a color range from yellow to brown, and to dark black due to progressive increase in burial depth (Staplin, 1969; 1977). Stablin correlated the color alteration indices with Coal Rank, LOM (Level of Organic Metamorphism), and vitrinite reflectance (Fig. 18). TAI and vitrinite reflectance data have been correlated with hydrocarbon generation, preservation and destruction stages (Fig. 18) (Waples, 1980; Dow, 1982).

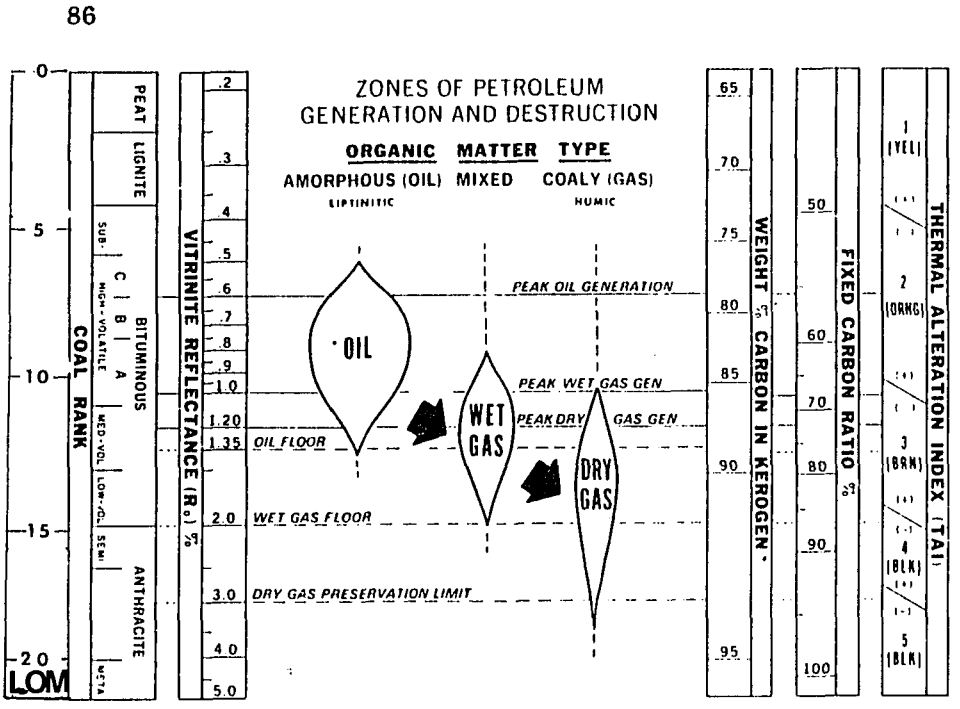


Figure 18- A correlation chart of various maturation parameters of organic matter--generation and destruction zones of oil, modified from Dow (1977), and Hood et al. (1975).

Thermal alteration indices and vitrinite reflectance (R_o %) which increase with increasing temperatures are the function of burial depth, geothermal gradient, time, and kinds of organic matter.

Diagenesis of organic matter is progressive and irreversible; therefore, this method has a great advantage over other geothermometries, such as illite crystallinity, oxygen isotope, and fluid inclusion (Price, 1983; Price and Barker, 1985).

For estimating maximum burial temperature of the AVL, the equation of Price (1983), which is primarily applicable to organic matter of the composition of kerogen type I, was used in this study.

$T = 302.97 \log_{10} x\ R_o\% + 187.33$ (Price, 1983).

T= temperature

$R_0\%$= vitrinite reflectance.

Price's formula in 1983 was compared to the expression of Barker and Pawlewicz (1986):

$ln\ R_{mn} = 0.0078\ x\ T_{max} - 1.2$

R_{mn}= mean vitrinite reflectance. T= temperature °C.

PART II: DEPOSITIONAL ENVIRONMENTS AND CYCLICITY OF THE ANTELOPE VALLEY LIMESTONE, AND EVOLUTION OF THE MIDDLE ORDOVICIAN CARBONATE PLATFORM

- NUIA SHOAL
- ONCOIDAL SHOAL
- OOLITIC AND SKELETAL SHOAL
- SHELF FACIES
- INTERTIDAL- TO SUPRATIDAL FACIES BELT
- SLOPE- AND MARGINAL BASIN FACIES
- CYCLICITY OF THE ANTELOPE VALLEY LIMESTONE
- EVOLUTION OF THE MIDDLE ORDOVICIAN CARBONATE PLATFORM

CHAPTER 4: NUIA SHOAL

The thickest and complete Nuia shoal units occur in the lower part of the AVL and represent the Orthidella zone of Merriam (1963) in the Martin Ridge, Ninemile Canyon, and Lone Mountain sections. In the lower Palliseria zone of the AVL, Nuia shoal lithofacies in the Ninemile Canyon section grades westward into the Girvanella-constituted oncoidal shoal lithofacies. In addition, in the Martin Ridge section, the Nuia packstone lithofacies gradually overlies the oolitic packstone and grainstone lithofacies at the intervals where the oolitic shoal first appears (see Chap. 6).

In the Antelope Valley region, the Nuia shoal units of the Orthidella zone gradually overlie the Ninemile Shale and are separated from the Girvanella-constituted oncoidal shoal by 100- to 150-feet thick Nuia shelf facies.

The major lithofacies of this shoal are (1) Nuia packstone- and grainstone, (2) Nuia-rich peloidal and oncoidal packstone, (3) Rhythmically thin-bedded siltstone and lime mudstone to wackestone, (4) Silty quartz-rich glauconitic lime mudstone, and (5) Nuia-rich bioturbated wackestone (see Chap. 7).

Nuia packstone- and grainstone lithofacies represents the Nuia shoal bars and is gradually overlain and underlain by Nuia-rich peloidal and oncoidal packstone lithofacies. In the upper Nuia shoal units, the rhythmically thin-bedded siltstone and lime mudstone to wackestone lithofacies directly overlies the Nuia shoal bars. The silty quartz-rich glauconitic lime mudstone occurs as a condensed unit between two Nuia shoal bars at intervals of 155 to 165 in the Ninemile Canyon section. Nuia-rich bioturbated wackestone lithofacies gradually overlies Nuia shoal bars and represents the shelf facies of the Nuia shoal (see Chap. 4).

A. Lithofacies

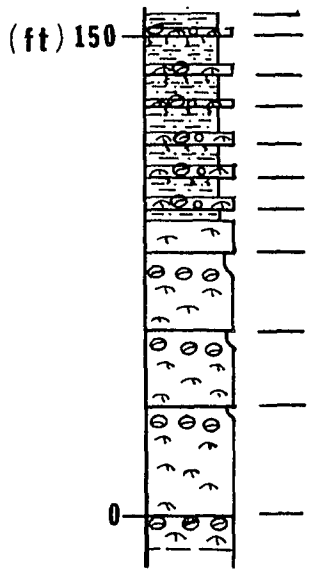
Lithofacies 1: Nuia Packstone and Grainstone

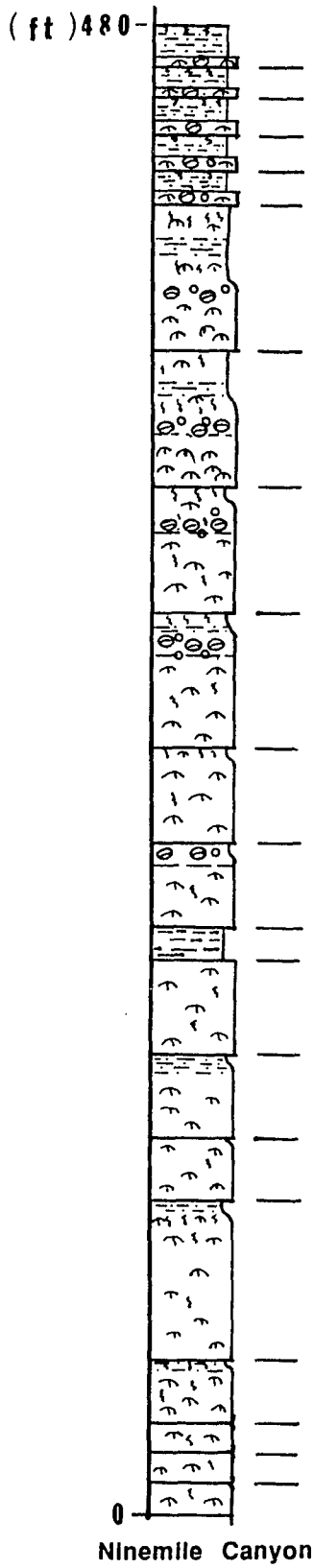
Description:

Tan to light gray Nuia packstone- and grainstone lithofacies occurs mostly in the Orthidella zone (Figs. 19; Appendix I-B); a few Nuia packstone- and grainstone units occur in the lower Palliseria zone (see Fig. 28 in Chapter 5). In Orthidella zone, this lithofacies lies stratigraphically between the underlying-shaley limestone (i.e., transitional facies between the Ninemile Shale and the AVL) and the overlying bioturbated wackestone of a well-circulated shelf. The Nuia packstone and grainstone lithofacies in the shallowing-upward cycles of Nuia shoals occurs at intervals of 0 to 150 feet (0-47 m) and 0 to 480 feet (0-146 m) from the base of the Martin Ridge and Ninemile Canyon sections, respectively (Fig. 19; Appendix. I-B).

Nuia is the remains of the problematic calcerous algae (Maslow, 1954; Johnson, 1966; and Toomey and Klement, 1966). One- to two wall-structured Nuia grains are the major constituents of this lithofacies; multi wall-structured Nuia grains are scarce. These problematic algal remains show a segmentary feature and appear to be finger-like grains. They can commonly be found in three cross sectional forms: circular, ellipsoidal, and elongated (see Appendix I-C for their grain size and growth forms, and for the occurrences and geographic distribution of Nuia).

In the Nuia packstone and grainstone lithofacies, one and two wall-structured Nuia forms are the most common Nuia grains (Fig. 20 A, B). However, multiwall-structured Nuia particles are scarce (Fig. 20 C, D). Interparticle-rim cement is the predominant cement type in this lithofacies, being similar to that of marine-isopachous cement which can clearly be recognized under cathodoluminescence. Besides interparticle-rim cement, some void-filling, radiaxial-fibrous cement was also





EXPLANATION

Nuia packstone-grainstone

Peloidal and oncolitic packstone

Nuia-rich oncolitic packstone

Silty quartz-rich lime mudstone

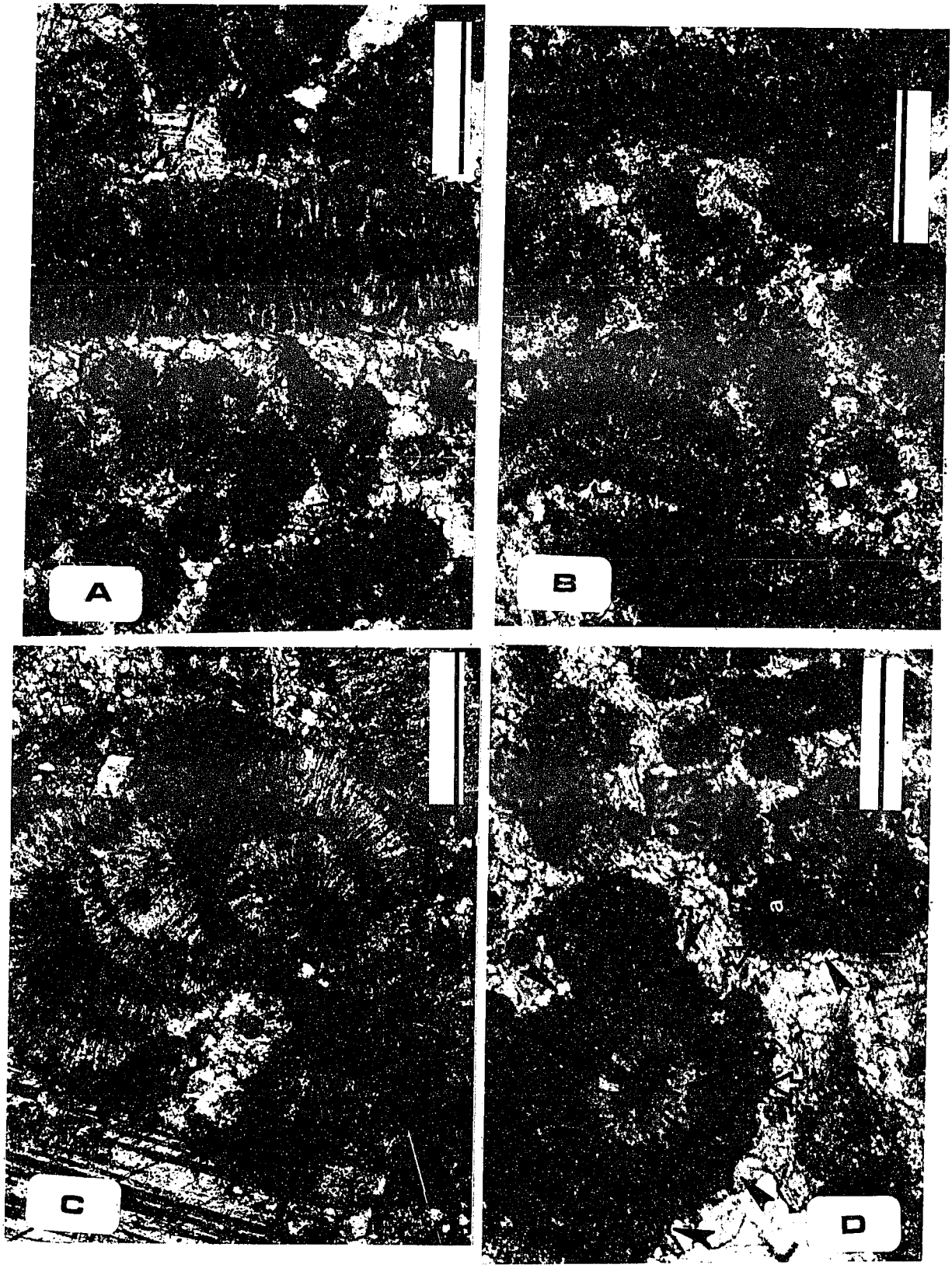
Bioturbated wackestone

Silty quartz-rich, glauconitic lime mudstone

Cycle boundaries

Figure 19- Successions of shallowing-upward Nuia shoal cycles and related lithofacies in the Ninemile Canyon and Martin Ridge sections.

Figure 20- Photomicrographs of Nuia packstone- and grainstone lithofacies. A) and B) show that Nuia packstone-and grainstone units primarily consist of one wall-structured Nuia grains. C) A multiwall-structured Nuia with two central micritic canals indicated by arrows is scarce in this lithofacies. D) Two multiwall-structured Nuia grains indicated by arrows; arrowheads indicating neomorphic replacement of multiple Nuia walls by calcite. With plane-polarized light; scales = 0.5 mm.


A
B
C
D

recognized under cathodoluminescence (see Chap. 12).

Figure 21 A- shows that the packstone and grainstone lithofacies of the Nuia shoal bars are gradually overlain by parallel-laminated, silty quartz-rich lime mudstone units and laterally interfinger with these fine-siliciclastic mixed sediments. Generally, three major bed forms of the Nuia packstone and grainstone units occur in the following stratigraphic successions, in ascending order: (1) the bioturbated, parallel, wavy medium-bedded Nuia packstone intervals alternating with thin glauconite-rich greenish shaley partings; (2) the rhythmical, thin-interbedded siltstone and Nuia packstone to grainstone (Fig. 21 B, C); (3) the thick-bedded Nuia grainstone units (Fig. 21 C, D). Gradual transition occurs in these three-bedded units in the given stratigraphic order (Fig. 21 C, D).

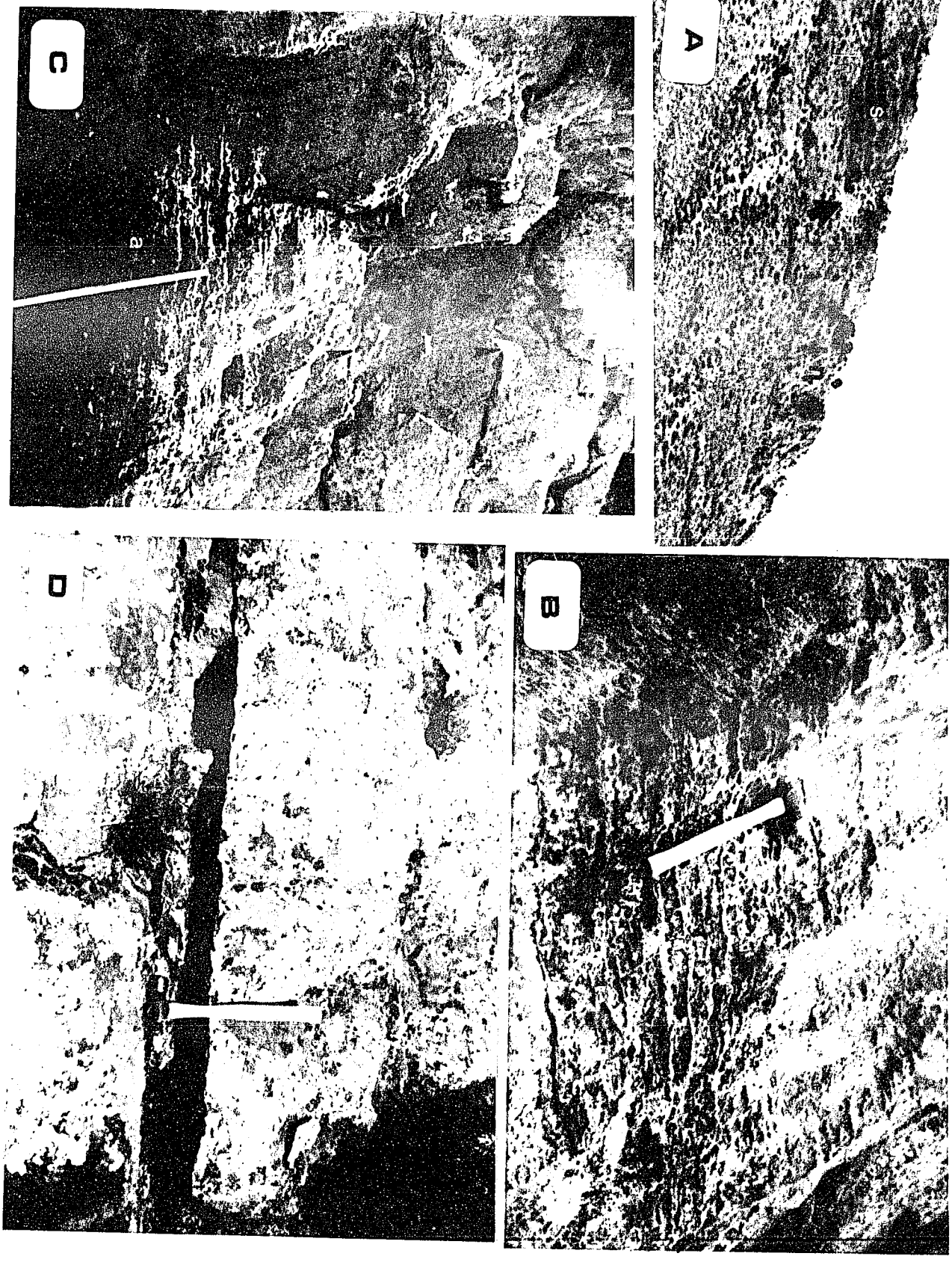
Bioturbation is scarcely common in the thick-bedded and rhythmical thin-bedded Nuia packstone and grainstone units; however, some vertical burrows are commonly filled by yellowish-brown mud (Fig. 22 A, C). Parallel, wavy medium-bedded Nuia packstone units consist of unbroken-, thin-shelled, small gastropods. They show relatively more bioturbation compared to other bedforms of this lithofacies, and their burrows are filled by yellowish-brown, detrital silty quartz-rich mud. These sublithofacies locally show parallel, normal-graded laminae.

However, in the thin rhythmically interbedded Nuia packstone and siltstone sublithofacies or bedforms and the thick-bedded Nuia packstone and grainstone subunits, the parallel even silty-quartz laminae (Fig. 21 B, C, and D) are the most common sedimentary structures in which laminae are accompanied by scarce bioturbation.

Sharp basal and upper contacts occur between the parallel-laminated, thin-bedded siltstone interlayers and the overlying-, thin-bedded Nuia packstone and grainstone interlayers (Fig. 21). These thin, rhythmical bedforms generally occur in the basal part of the superimposed, thick-bedded Nuia packstone-grainstone units (Fig. 21 B, C).

Thick-bedded units overlie one another with a sharp-planar basal contact (Fig. 21 C, D). Upper contacts of these thick and massive beds are also sharp and sometimes contain a very thin-mud veneer or blanket. Nuia remains with different morphologic

Figure 21- Field and outcrop photographs of Nuia packstone- and grainstone lithofacies. A) Nuia packstone- and grainstone units of the interpreted Nuia shoal bars (n) laterally interfinger with fine-siliciclastic sediments (s) of the interbar facies and are gradually overlain by the same fine-grained siliciclastic deposits. B) Rhythmical thin-bedded Nuia packstone and siltstone interlayers occur at the base of the Nuia shoal bars. C) The siltstone interlayers of these rhythmical beds are most commonly found in the base of the Nuia shoal bars and gradually disappear upward into thick bedded-Nuia packstone- and grainstone units of Nuia bar crests; the arrowheads indicate a sharp erosional planar basal contact separating the thick-bedded Nuia packstone- and grainstone units from one another. A 4-foot long stick for scale. D) A planar, sharp erosional contact between two thick-beds of Nuia packstone- and grainstone units.


A
B
C
D

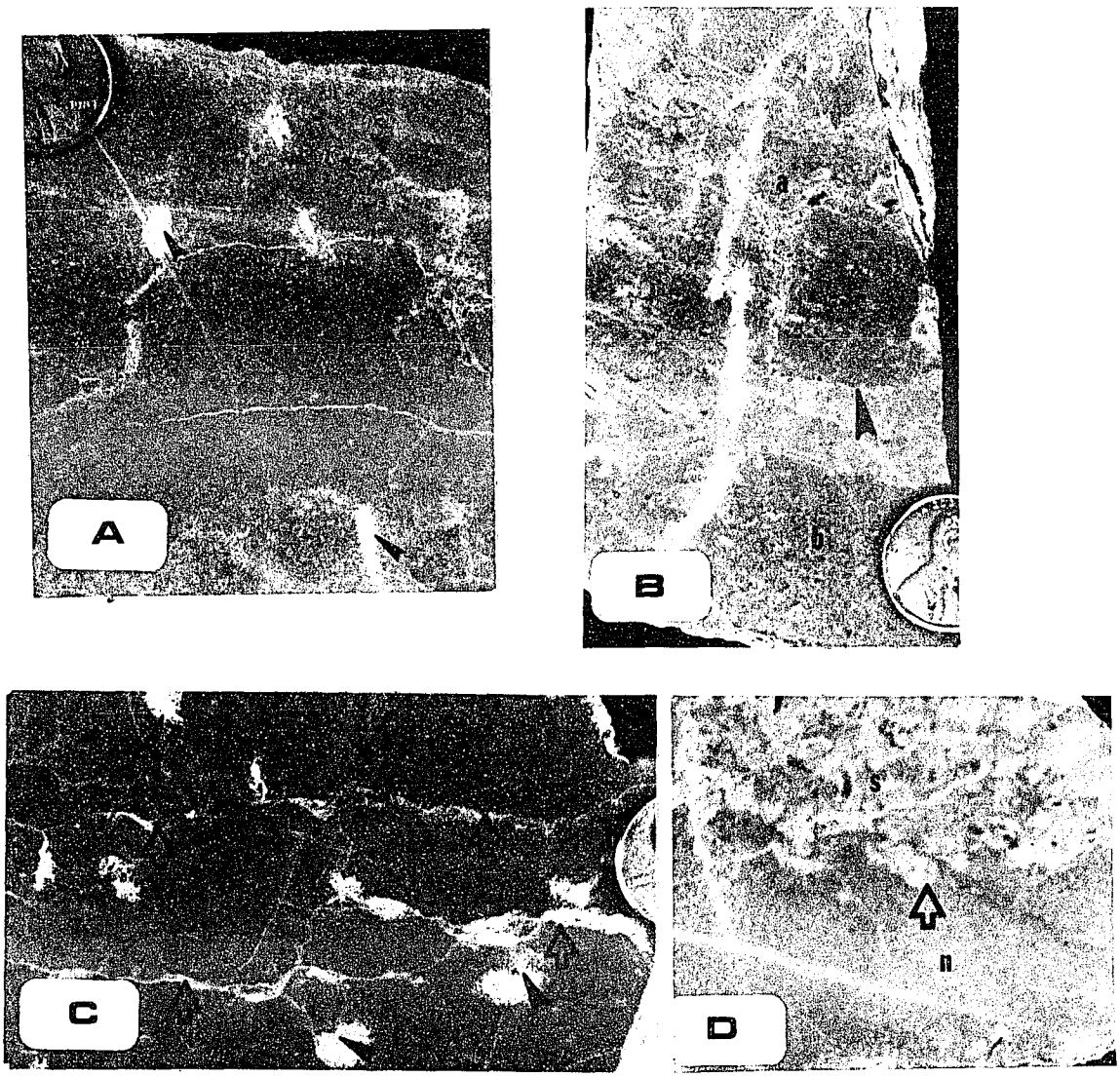


Figure 22- Sedimentary structures in the polished slabs of Nuia packstone- and grainstone units. A) In the Nuia packstone- and grainstone unit, vertical burrows are filled by yellow-brown silty quartz-rich mud, as indicated by arrow heads. B) Thick bedded-Nuia packstone units consist of multiple Nuia-rich shelly layers (a and b) separated from each other by a concave upward truncational basal contact indicated by arrowhead. C) Multiple thin beds in thick-bedded Nuia packstone lithofacies are separated from one another by truncational basal contacts. Yellow brown silty quartz-rich mud concentrates along these basal contacts indicated by arrows and fills vertical and elongated burrows indicated by arrowheads. D) Oncoid and skeletal-rich subunits (s) overlie the Nuia packstone- and grainstone unit (n) with a concave upward truncational basal contact indicated by arrow. Pennies for scale.

forms are the predominant constituents of this lithofacies. The uppermost part of the thick-bedded Nuia packstone to grainstone units consist of more crinoid ossicles, and peloids which are probably micritized-remnants of Girvanella. Thick-bedded Nuia packstone and grainstone units commonly consist of inclined-thin foresets overlying one another with a truncational basal contact, and locally oncoid-rich skeletal sublayers overlying the Nuia foresets with a concave-upward truncational contact (Fig. 22 B, D). Upward, progressively increasing well-rounded peloids (0.2-0.6 mm in grain size) in these thick-bedded Nuia grainstone beds coincide with progressive darkening of these units. Normal-graded texture and oscillation-wave ripples are not present in this lithologic unit.

In cyclical successions, the Nuia packstone- and grainstone lithofacies is gradationally overlain by bioturbated-wackestone lithofacies of backshoal and indicate a shallowing-upward sequence (Fig. 19). Each shallowing-upward cycle has a sharp erosional, basal planar contact and is overlain by a similar basal contact of the subsequent cycle (Fig. 19). Generally, the thick-bedded grainstone units commonly show lenticular bed forms and morphologies (Fig. 21 A, C and D) as each thick bed laterally get thinner from their thickest-mid points to their margins over a lateral distance. The planar erosional basal contact of each cycle and sharp basal contact of a thick-bedded unit constituting basal part of these cycles are consistent, conformable and do not show any angular discordance. The grain supported-Nuia shoal lithofacies become thinner progressively upward, and in cyclical successions, they appear to have a stair-step morphology in which more resistant Nuia packstone-grainstone units represent each ascending step of stairs (Fig. 19).

The visually approximated-average percentages of the constituents from the thin sections of this lithofacies occur in the following ranges: Nuia 60-80 % in the grainstone subunits (Fig. 20 A, B and C), Nuia approximately 45-60 % in the packstone to grainstone subunits. Other constituents are, in order, crinoids 5-12 %, brachiopods 2 %, small ostracods and gastropods 4 %, trilobites 2 %, peloids 15-25 %, and silty quartz 5-8 %. Sponge spicules and conodont fragments are less than 1 %. Glauconite with a very small grain size (fine sand and silt size) is common (less than

2 %) within the relatively silty quartz-rich zones, or laminae.

Interpretation:

In the Nuia packstone and grainstone lithofacies, distributions of Nuia grains and their contributions to sedimentation appeared to have closely been related to variations in water depth and temperature of the Nuia shoals and meadows as well as in substrate. The substrate types are important for the selection of a niche by different Nuia forms. The most common occurrences of one- and two wall-structured Nuia remains within the Nuia packstone and grainstone units of Nuia bars may suggest that these Nuia forms probably preferred a firm substrate. Thus, Nuia, with one- and two wall-structure, may have attached themselves to firm substrate of Nuia sediments in the agitated environmental conditions which probably inhibited Girvanella growth. Hence, Nuia forms with the indicated wall structures are the principal sediment contributing Nuia growth forms. They may have flourished in the moderate- to high-energy environment which led to formation of early lithification by marine cementation in the Nuia shoal. From their predominance in this grain- supported Nuia lithofacies, it can be suggested that during high-energy storms, these dominant Nuia forms demised due to their delicate and articulated natures and that they were transported from the moderately high-energy Nuia meadow to the high- energy Nuia shoal in which these sediments were reworked by tidal currents and waves. On the other hand, abundant multiple wall-structured Nuia grains are often coated by Girvanella and accompanied by a few one and two wall-structured Nuia within the oncoid- and peloid-rich Nuia packstone units. Such abundance of multi wall-structured Nuia in the peloidal lithofacies may suggest that multi wall-structured Nuia probably inhabited the Girvanella-carpeted, soft-bottomed substrata behind the protected side of the active Nuia subtidal bars (see Nuia-rich peloidal and oncoidal packstone lithofacies and Fig. 23 A, C). Therefore, it is possible to suggest that other Nuia forms were probably transported into the protected-subtidal environment, or some one- and two

wall-structured Nuia may have equally adapted to both the soft and firm substrata.

The articulated nature of the problematical algae has been recognized by Toomey and Klement (1966), Toomey and LeMone (1977), Roux (1985), Mamet and Roux (1982), and Ross et al.(1988). Furthermore, Ross (1988) pointed out the similarities between the green alga Halimeda and Nuia, such as their growth forms, life cycles, as well as their ecologic niche. Wiman and McKendree (1975) demonstrated ecological zonation and sediment distributions of Halimeda species in the 1 to 4.5 m bathymetry of the Corsair Patch reef at three miles northeast of Key Largo in the Florida Reef Track: most of the Halimeda flourished on the firm-ground of patch reefs; a few on the Thalassia-carpeted soft substrate of mixed-grass zone which represents a deep- and relatively low-energy environment, and several adopted in both environments.

Hudson (1985) estimated carbonate production rate of a colony of H. opuntia having 25 cm height and a basal area 25x50 cm. He demonstrated that this indicated area produces about 1250 g dry weight of Halimeda segments per square meter per year equal to about 1088 g carbonate products per year. The significantly high-carbonate production rate by Halimeda opuntia is highly comparable with a considerably high-reproduction capacity of Nuia sibrica Maslow: for instance, a nearly 480-feet (146 m) thick Nuia shoal facies was constructed during the Orthidella zone chiefly by Nuia (Fig. 19). Therefore, this can be attributed to Nuia's high-growth rate and its high-carbonate secreting capability as well as its segmentary and articularey nature.

Furthermore, Shinn at al. (1982), and (1990) reported a 12-m thick, subtidal Halimeda predominated the E-W oriented-skeletal shoal, lying in the Quicksands area (47 km long by 28 km wide) west of the Marquesas Keys, Florida. The westward advance of the Quicksands consist of an east-west trending, 2 to 3-m thick subtidal-sand dunes which were shaped by strong tidal currents. Importantly, these Halimeda-tidal sand bars are surrounded by lime muds and silts as much as 7 m-thick and equivalent in age. They are found in the topographically low areas, as well as the south, west and north of the Halimeda shoal. The variation in water depth, from the low-tide level to sediment surface, ranges 1.8 m to 6.9 m with an exception of some tidal-bar crests being exposed during low tide (Shinn et al., 1990).

Another comparable contemporary phenomenon has been studied at the Serranilla Bank of the Nicaragua Rise by Triffleman et al.(1988; 1992). Water depth ranges from 10 to 60 m on this bank, which is dominantly composed of Halimeda, molluscan shells and algal encrusted clasts, and sponge-bound aggregates. Predominantly, Halimeda, sea grass (Thalassia) and other calcareous algae proliferated at the top of this bank. The dominance of the Serranilla Bank by the indicated-algal groups instead of corals has been attributed to this bank's failure to "keep up" with Holocene sea-level rise (Triffleman et al. 1988; 1992).

In spite of many unanswered questions concerning origin of problematical algae Nuia, Halimeda sand shoal facies in the Quicksands are highly comparable to the many aspects of the ancient Nuia shoal units of the Antelope Valley Limestone rather than the Oceanic Serranilla Bank. This can be substantiated by the exclusive predominance of Nuia but not Girvanella, molluscs, and sponges, etc.

Nuia, alone, is the principal sediment contributor of the Nuia shoal bars which provided a great deal of disarticulated-fingerlike or cylindrical segments during the seasonal life cycle of this flora. Predominance of these problematic algal remains in this lithofacies represent an environment where constant turbulence, winnowing, and reworking kept the sediments in constant motion and prevented the blue-green algae Girvanella from forming (e.g, Monty and Gebelein, 1969) and coexisting with Nuia in this shoal. As a result, one can suggest that the energy level of a Nuia-flourished environment was much greater than the energy level of Girvanella-flourished environments which were probably located at the protected and deeper sites.

This study suggests that Nuia meadows may have thrived mainly on the open seaward flank of active subtidal bars where moderately high- to high-energy level prevailed. Consequently, the sites of Nuia bars may not represent the active Nuia growth environment, but represent the accumulation sites to which disarticulated-Nuia segments were transported probably by storm events, and where Nuia-dominated sediments were reworked and redeposited by tidal wave and currents (Kaya and Friedman, 1987). In addition, presence of Nuia in the farther landward and open seaward environments can be attributed to sediment transportation from Nuia shoals

and adjacent areas by storm currents, and storm countercurrents, respectively.

Cathodoluminescence and petrographic studies reveal that interparticle-isopachous cement is the most important cement type in the thick-bedded grainstone units and in the thin, rhythmical-bedded units of the Nuia-subtidal bars. The common occurrences of the isopachous-rim cement represents a very high-energy, marine-phreatic diagenetic environment (Longman, 1980) and suggests that the early marine cementation was responsible for the stabilization of disarticulated-Nuia grains rather than other forms of algal colonization. On the other hand, parallel wavy-bedded Nuia packstone subunits of this lithofacies, containing diverse marine fauna along with crinoid ossicles, and minor isopachous-marine rim cement, are indicative of a lower energy shoal or the open seaward-extended flank of a subtidal-Nuia bar. On the basis of all the criteria above, we can suggest that the Nuia shoal can be analogous to the tidal bars of the Halimeda skeletal shoal in the Quicksands of the Marquesas Keys, southwest Florida rather than the incipiently drowned oceanic Serranilla Bank on the Nicaragua Rise.

Bed and sedimentary structures as well as textural variations of the Nuia packstone and grainstone lithofacies can further elaborate the physical parameters of the Nuia shoal. First, the parallel, wavy-bedded packstone units alternate with the thin glauconite-rich interlayers at the base of this lithofacies. These units are composed of relatively intense bioturbation, sometimes normal-graded laminations, and the small unfragmented-, thin-shelled gastropods. All of these suggests that these bed forms took place below the normal-wave base on the farther seaward extended flanks of the Nuia bars.

Secondly, in the rhythmically thin-bedded Nuia packstone- to grainstone and siltstone interlayers, the grain-supported interlayers probably formed from the high energy storm countercurrents, as suggested by Brenner and Davies (1973), Kelling and Mullins (1975), Kreisa (1981) and Aigner (1982). These thick, grain-supported sublayers alternating with thin glauconitic mud covers or blankets indicate a proximal type of storm deposit forming below the normal-weather wave base and above the normal storm-wave base (Miller et al, 1988). Glauconitic muddy partings may have been deposited from the post-storm suspension after the deposition of the

grain-supported Nuia-rich basal sublayers. Burrow-fillings by yellowish-brownish silty mud (Fig. 22 A, C) represent the storm-induced rapid sedimentation (Wanless et al. 1988).

It is widely accepted that glauconite forms favorably in a moderate to highly oxygenated environment in which wave-induced turbulence and sedimentation rate are minimal (McRea, 1972; Odin and Matter, 1981; Odom, 1982; van Houtten and Purucker, 1984). Hence, glauconite-rich shaley interlayers of these wavy beds were probably deposited during the latest stage of storm countercurrents and normal marine sedimentation on the open-seaward extension of Nuia bars. Thus, glauconites of these wavy beds can be both authigenic and allochthonous in origin.

The rhythmical thin-bedded couplets within the thick and massive beds (Fig. 21 C, D) can be interpreted as amalgamated beds (Aigner, 1981). The similar bedforms have been observed in the low shoreface of the modern clastic-beach environments by Howard and Reineck (1979). Similarly, in the Cambrian muddy shelf of New Mexico, fine to medium-grained sandstone and muddy siltstone couplets change upward into thick-bedded, medium- to coarse-grained sandstone of high-energy shoal and are interpreted to have been the storm layers formed below the normal weather-wave base (Soegard and Erickson, 1985). Like in the Cambrian case, the thin couplets of the Nuia packstone- and grainstone lithofacies represent a short durational high-energy storm deposition in the open seaward extended foreshore environment (i.e., below normal wave base). Therefore, in the amalgamated beds, these couplets represent multiple, high-energy storm events, as suggested by Aigner (1981) and Kreisa (1982). The formation of the sharp truncational basal contact and deposition of coarse-grained Nuia packstone and grainstone layers may have taken place concomitantly during the high-energy storms' peak phase. Parallel-laminated siltstone interlayers, on the other hand, may have been deposited during the post-storm, quiescent phases from the suspension. The absence of bioturbation and the preservation of the parallel laminae in these silty layers probably indicate rapid sedimentation in a low-energy shoal but not in Nuia bar-crest environment.

The thick-bedded-Nuia packstone and grainstone units--consisting of 3-4 mm thick,

silty quartz-rich parallel laminae, a sharp-erosional planar basal contact and very thin-veneered upper contact, as well as with laterally changing bed thicknesses (Fig. 21 C, D) -- suggest that they may have been deposited from the high-magnitude storm floods or landward transportation of disarticulated-Nuia plates in the Nuia shoal. In this respect, the formation of these thick beds are similar to single, strong, storm-induced thick sand waves or dunes in an oolitic shoal facies (Hine, 1977). They are also similar to thick-bedded clastic shoreface deposits consisting of 2-3-mm thick, parallel-laminated silt layers (Kumar and Sanders, 1976).

Tan to light gray, thick-bedded-Nuia packstone- and grainstone lithofacies with isopachous marine cement characterizes a high-energy, well-agitated shoal facies where high-energy storm currents transported sediments and deposited them as sand waves and dunes. The grain-supported texture of this lithofacies suggests that these storm deposits were reworked and winnowed by tide-dominated waves and currents. As a result, increased winnowing and resultant greater permeability finally led to the stabilization of these sediments in shoals by submarine cementation.

In the thick-bedded Nuia grainstone units, the lack of wave-oscillation ripples, and other kinds of tide-induced sedimentary structures at the uppermost part of these beds are closely related to: (1) uniform grain size of Nuia, (2) scouring of the fine-grained blanket and the uppermost part of these thick beds by strong storm-flood currents, and (3) diagenesis which alters the original particles and textures by dissolution and precipitation or by neomorphism.

Rapid depositional features of these thick-bedded units can be inferred from the locally concentrated mud and fine-grained sediments, and glauconites. In addition to the allochthonous origin of glauconites, the in situ glauconites in the thick-bedded Nuia grainstone units can be attributed to very rapid deposition-induced decay of organic matter (i.e., soft tissues of benthic fauna and other algal remains). This decay process is likely to produce adequate oxygen for glauconitization of pellets and other grains in the micro environment (McRea, 1977; Odin and Matter; and van Houtten and Purucker, 1984).

The conformable relations between the basal contacts of the unconformity-bounded

shallowing-upward cycles and of thick successive Nuia beds in these cycles strongly suggest that the deposition of Nuia bank facies took place on a nearly flat, very broad shoal facies extending to a gently declining upper-slope facies.

In vertical sections, the progressively upward thinning of thick-bedded Nuia shoal facies, directly overlain by rhythmical, thin siltstone and lime mudstone or silty quartz-rich mudstone, may represent the progressively deepening of Nuia shoal facies during the short durational sea-level rises. The stair-step morphologies of shoal bars in vertical sections were first described by Gilbert (1880), and he related this phenomenon to transgressions and landward migrations of the bars. However, Kumar and Sanders (1976) related this morphology in vertical sections to rapid sea-level rises and stated that offshore sand bars would remain in place until the breaker or surf-zone interacted with the upper parts of these bars during rapid sea-level rises. As a result of this interaction, the sediments derived from the upper part of the bars would be moved to further landward as retreated bars and / or degraded bars (e.g, Stubbfield et al. 1984; and Swift et al., 1984). The suggestion of Kumar and Sanders (1976) is adopted by this study for the upward progressively thinning Nuia shoal bars, having stair-step morphology. During rapid sea-level rise, some parts of the pre-existing bars of the Nuia shoal were drowned, and some parts were transferred farther landward or retreated. Farther landward-decreased thicknesses of the bar facies suggest that sea-level rise outpaced the sedimentation rate of Nuia or growth rate of Nuia bars (see Chapter 10).

Lithofacies 2: Nuia-rich Peloidal, Oncoidal Packstone

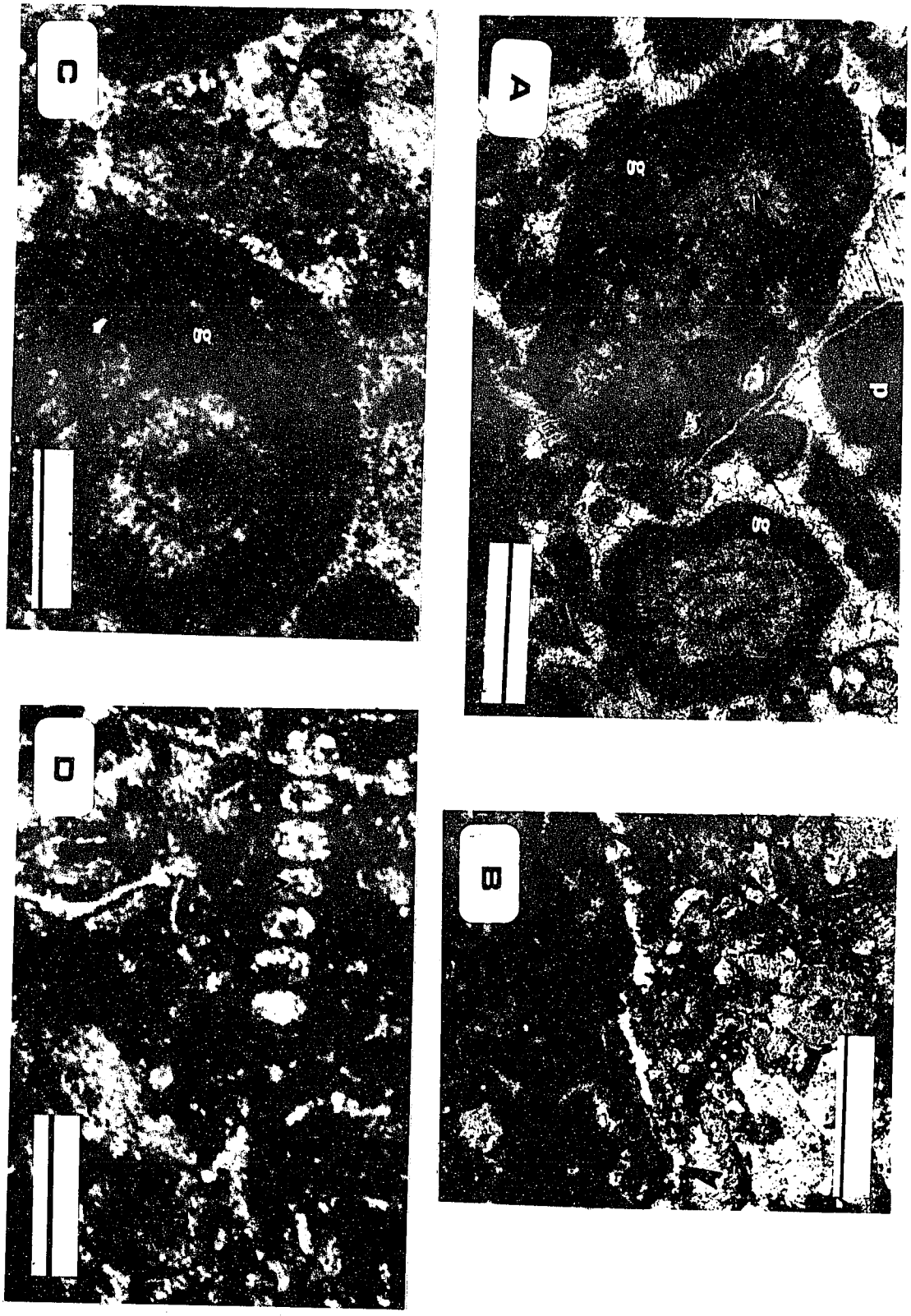
Description:

Gray to slightly dark gray, massive-bedded Nuia-rich peloidal and oncoidal packstone lithofacies gradually overlie the thick-bedded Nuia grainstone units and gradually change upward into the Nuia-rich, bioturbated-wackestone lithofacies. In this packstone lithofacies, bioturbation progressively increases, and color of this lithofacies becomes darker upward from its base. The lowermost part of this packstone lithofacies usually contains abundant Girvanella-derived peloids and one- or two wall-structured Nuia particles (Fig. 23 A, B). However, upward in these beds, one- or two wall-structured Nuia grains and peloids become more and more scarce, while Girvanella oncoids and multiwall-structured Nuia particles progressively become predominant in the same direction (Fig. 23 A, C, and D).

Girvanella-derived peloids and oncoids are commonly well rounded. Girvanella oncoids, with a nearly spherical shape, usually range from 3 to 7 mm in size and have an average grain size of 3-5 mm. These oncoids are usually composed of multiple symmetrical, continuous concentric laminae and commonly include multiwall-structured Nuia as nuclei. This packstone lithofacies in places is missing in some cycles, especially in those thick-bedded Nuia packstone- and grainstone units. In addition, the interparticle-columnar calcite cement is more common in the oncoidal packstone sublithofacies than the basal packstone sublithofacies.

The average percentages of the constituents of the Nuia-rich peloidal and oncoidal packstone lithofacies are oncoids 30-45 %, peloids 8-15 %, Nuia particles 25-40 %. Other skeletal fragments in this lithofacies occur in similar percentages with those of the Nuia grainstone- and packstone units. In addition, Sphaerocodium (encrusting algae) are very common in this lithofacies.

Figure 23- Photomicrographs of Nuia-rich peloidal and oncoidal packstone. A) Girvanella (g)-coated, multiwall-structured Nuia; arrows indicating partially dedolomitized euhedral dolomite rhombs in the coated area, and small arrowheads indicating two-central canals in Nuia which were not described by Mamet and Roux (1982). B) Iron-oxide stained hardground surface between crinoid- and Nuia-rich layers and peloidal packstone units indicated by arrowheads. C) A multiwall-structured Nuia (n) coated by Girvanella (g). D) Sphaerocodium (pointed by arrow) within the Girvanella-rich packstone unit with Nuia (n). With plane-polarized light; scales = 0.5 mm.


A
B
C
D
bg
bg
bg
bg

Interpretation:

Close association between Girvanella and multiwall-structured Nuia suggests that the multiwall-structured Nuia is probably a different Nuia species than the most common single- and two-wall structured Nuia, and it may not be a distinct growth form of the same Nuia which flourished favorably in the relatively low-energy environment. In this packstone lithofacies, an abundance of the coated-, multiwall-structured Nuia along with Sphaerocodium may indicate a Girvanella-carpeted soft substrate behind the Nuia bars. In this respect, the multiwall-structured Nuia would be comparable with the Halimeda species flourishing in soft substrate or the Thallasia mixed-grass zone (e.g., Wiman an McKendree, 1975).

Upward progressively increasing mud and pellet content of the Nuia-rich peloidal and oncoidal packstone lithofacies suggests that this lithofacies may have been deposited in a relatively low-energy, protected environment of the landward subtidal Nuia bars. This Nuia-rich pelodial and oncoidal lithofacies can also be considered analogous to a sand-flat depositional environment where Nuia shoal facies are stabilized and colonized by algal activities and where shoal facies are partly physical barrier for the open-sea water circulations (Harris, 1979).

In Lone Mountain, similar oncoidal and peloidal lithofacies occur beneath the pervasively dolomitized Orthidella shoal units, which are assumed to be the Nuia shoal lithofacies. The Nuia-rich oncoidal packstone lithofacies probably formed both in the protected areas of landward Nuia shoals and in the seaward deep flank of Nuia bars.

Lithofacies 3: Rhythmically Thin-Bedded Siltstone and Lime Wackestone to Mudstone

Description:

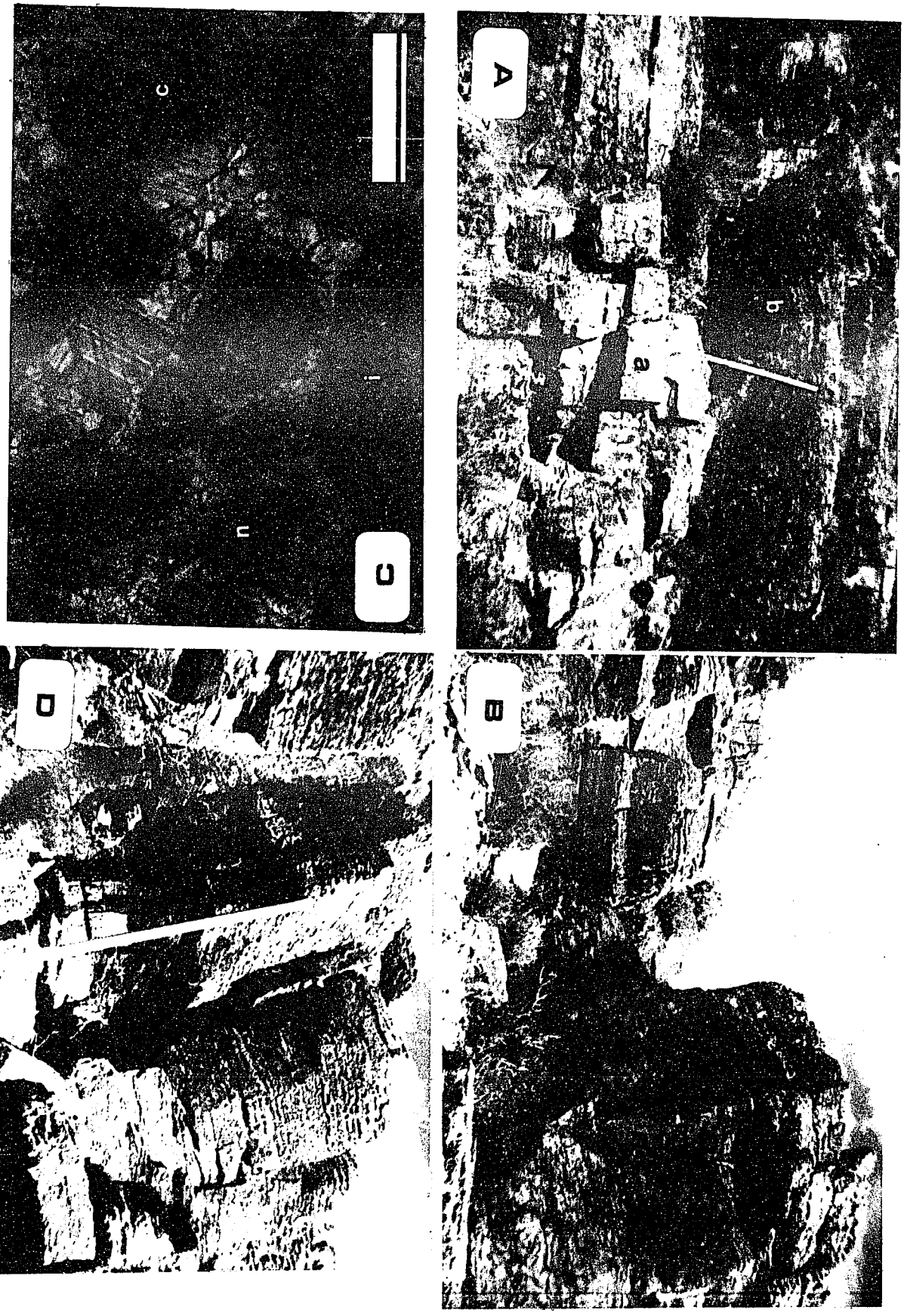
The rhythmically thin-bedded siltstone and lime mudstone lithofacies at some intervals directly overlie the uppermost part of the Nuia-rich oncoidal and peloidal packstone facies (Fig. 24 A). In turn, these rhythmical siltstone and lime mudstone layers are gradually overlain by the Nuia-rich wackestone (Fig. 24 B, and D). The rhythmical lithofacies are separated from the thick-bedded Nuia grainstone units by the peloidal and oncoidal packstone units 3 to 5-feet thick, gradually changing upward into the Nuia-rich, bioturbated-wackestone lithofacies. The upper part of the Nuia shoal bars are directly overlain by these rhythmical-bedded siltstone- and lime mudstone couplets. The thickness of each rhythmic layer varies between 2-4 cm (Fig. 24 B, D). More resistant, parallel-laminated siltstone layers with yellowish-brown color overlie the dark gray bioturbated-lime mudstone and wackestone interlayers with a sharp and truncational basal contact (Fig. 24 A, B, and D). In siltstone interlayers, parallel laminae become gradually more discontinuous upward and scarce due to bioturbation.

The constituents of black and dark gray lime-mud layers are represented by similar diverse faunal content at the Nuia-rich, bioturbated wackestone lithofacies (see Chap. 7). Microcrystalline calcite and dolomite as a cement are equally important, particularly siltstone interlayers. Dolomite replaced the microcrystalline calcite.

Less commonly 4-6 cm thick-intraclastic Nuia-rich packstone and grainstone layers occur within this rhythmical interbedded lithofacies with sharp-planar basal contacts and gradually change upward into the parallel-laminated siltstone layers (Fig. 24 C).

The approximated-average constituents of siltstone are Nuia particles 4-8%; silty quartz 45-65% (Fig. 25 A, B); peloids (probably Girvanella fragments) 2-4%; unbroken brachiopods 4% (Fig. 25 A); crinoid fragments 2%; and some trilobites 2-4%. Euhedral micropyrites crystals are also present in both interlayers; however, they are more abundant in the siltstone interbeds.

Figure 24- Outcrop photographs of the rhythmically thin-bedded siltstone and lime mudstone lithofacies, and a photomicrograph of crinoid-rich, intraclastic Nuia packstone. A) The rhythmically thin-bedded siltstone and lime mudstone lithofacies (b) gradually overlies the Nuia packstone- and grainstone lithofacies (a) at the uppermost part of the Orthidella zone. B) The rhythmical siltstone and lime mudstone lithofacies locally consists of relatively thick, shelly layers which have sharp-planar upper and basal contacts indicated by arrowhead. C) Photomicrograph of the crinoid-rich intraclastic Nuia packstone shows that this packstone interlayer consists of intraclasts (i) of silty quartz-rich lime mudstone, and Nuia (n), and crinoid (c) grains. With plane-polarized light; scale = 0.5 mm. D) The rhythmical siltstone /mudstone unit (b) directly overlies the uppermost part of the Nuia packstone-and grainstone lithofacies (a). A 4-foot long stick for scale.


A
a
b
B
C
c
D

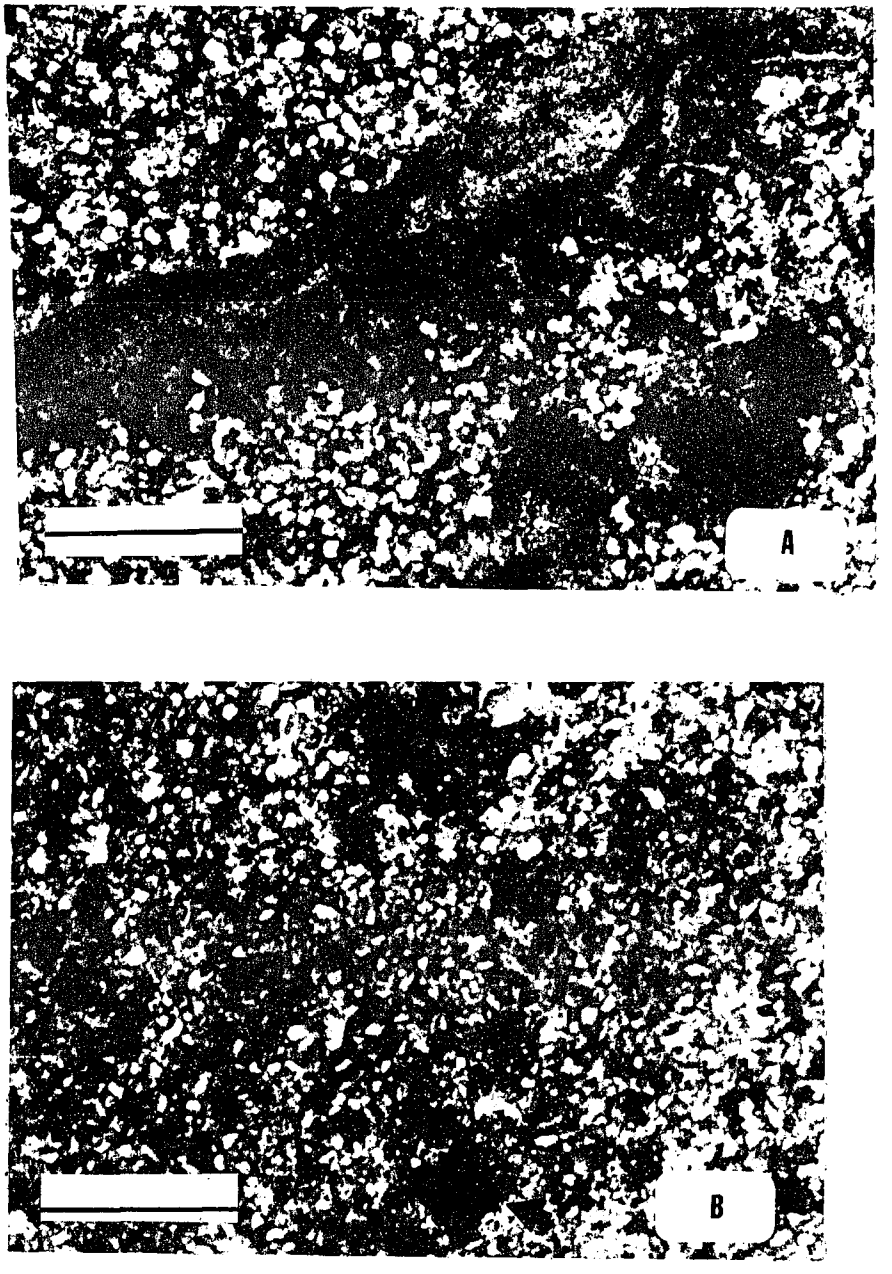


Figure 25- Photomicrographs of the parallel-laminated siltstone interlayers of the rhythmically thin-bedded siltstone and lime mudstone lithofacies. A) Unfragmented brachiopod in a silty quartz-rich lime mudstone or siltstone interlayer. B) In the same siltstone interlayer, red brown euhedral hematite pointed by arrow is probably a pseudomorph of pyrite. With plane-polarized light; scales = 0.5 mm.

The approximated-average percentages of the constituents of the intraclastic Nuia-rich packstone- and grainstone layers are Nuia particles 45-55 %, crinoids 15-25%, brachiopods 5-8%, trilobites 5 %, and silty quartz-rich irregular intraclasts 10 %. Others -- spicules, glauconite, euhedral pyrite crystals-- are less than 3 %.

Interpretation:

In the rhythmical thin-bedded siltstone- and lime mudstone lithofacies, repetitions of these thin siltstone- and lime mudstone couplets with a high frequency may have resulted from short durational, episodic-high-energy events in the predominantly low energy subtidal environment. Discontinuous parallel laminae (due to upward increasing bioturbation), lack of wave-oscillation ripples, and common presence of unbroken brachiopods (specifically in the siltstone interlayers) as well as diverse open-marine faunal composition of the lime mudstone- and wackestone interlayers strongly suggest the presence of rapid sedimentation below the fair weather-wave base which is a low-energy, subtidal-depositional environment. However, this interpretation disagrees with Stricker and Carozzi (1977) and Taban (1986) as they suggest the intertidal- and supratidal-depositional environment for this thin rhythmical lithofacies.

Sharp truncational contacts and a crudely fining-upward feature (from siltstone to lime mudstone) indicate the progressively waned high-energy storm countercurrents in the low-energy, subtidal-depositional environment. Basal truncation was probably caused by erosional work of the storm countercurrents moving open seaward. Therefore, it is possible to suggest that the parallel-laminated siltstone interlayers of these rhythmical lithofacies were deposited rapidly from the fine-grained siliciclastic suspension of the gradually waning storm countercurrents.

Similar bedforms have been noted in the offshore subtidal modern marine environments at 25 m depth, and at 30 km offshore in the Gulf of Mexico (Hayes, 1965) as well as in the North Sea (Reineck and Singh, 1972). In the Early Cambrian muddy shelf by Gevirtzman and Mount (1986) describe similar rhythmical couplets. All the studies above relate the parallel-laminated siltstone interlayers in the very

similar lithofacies to the very rapid sedimentation from suspension load of storm surge currents (storm countercurrents) during the quiescent storm phases.

The preservation of parallel laminae in the siltstone interlayers can be related to the rapid deposition of fine sediments from suspended-silty clouds of the storm surge below the fair-weather wave base. Deposition of siltstone interlayers from the gradually waning storm countercurrents probably may have created a very restricted-, subtidal-depositional environment (silty quartz-rich muddy clouds) for benthic fauna and calcareous algae. Upward decreasing parallel laminae in the siltstone interlayers can be attributed to the infaunal activities, or more specifically to the work of deposit-feeder brachiopods. Therefore, parallel-laminated, thin-bedded siltstone interlayers represent sediments which storm countercurrents deposited, but the dark gray bioturbated-wackestone to mudstone interlayers formed in a low-energy, subtidal-depositional environment. Storm countercurrents probably transported the suspended silty quartz-rich fine sediments from the nearshore areas into the offshore, subtidal-marine environment (Hayes, 1965; Rezak, 1985; and Yancey, 1986).

Less-frequently repeated Nuia-rich skeletal grainstone units (Fig. 25 C), on the other hand, represent relatively high-magnitude storms which were capable of excavating the semi-lithified siltstone intraclasts of these interlayers.

The occurrences of this lithofacies on the transgressive or landward-migrated Nuia bars suggest that this lithofacies represents the post-transgressional, high- frequency storm-induced sedimentation in the predominantly low-energy subtidal environment.

Lithofacies 4: Silty Quartz-rich, Glauconitic Lime Mudstone

Description:

At the lower part of the Ninemile Canyon section (at interval 155 to 165 feet from the base of the section), a 10-foot thick, parallel-laminated silty quartz rich-shaley mudstone lithofacies, as a condensed unit, is bounded unconformably between two Nuia packstone and grainstone units of Nuia shoal (Fig.26).

In this lithofacies, the subaerial features, such as mud cracks, algal chips and fenestral fabrics, are not present, nor do the evenly parallel, continuous laminae exhibit similarity with the crenulated-algal laminae. Micro-euhedral pyrite crystals occur along the pelletal or silty quartz-rich interlayers. The most common constituents of this unit are quartz silt (20-25 %), pellets (15-20 %), and glauconites as pellets (5 %); recognizable trilobite, brachiopod and crinoid fine particles are also present.

Interpretation:

Sedimentary structures in general and the stratigraphic position of this lithofacies (between the two Nuia grainstone- to packstone units) suggest that deposition of this lithofacies may have taken place in a low-energy subtidal depositional environment, where wave energy was not strong enough to destroy these even-parallel laminae. On the basis of the same criteria, it can also be suggested that deposition of this lithofacies probably occurred below the fair weather-wave base during the drowning of the Nuia bars due to a short-lived transgressive event. As a result of this transgression, low-energy, open marine depositional conditions prevailed on the precursor Nuia bars. Lack of bioturbation indicates that rapid deposition from the column of suspension load probably created a restricted-subtidal environment for the benthic fauna which, in turn, resulted in preservation of parallel laminae. In this lithofacies, presence of



Figure 26- An outcrop photograph of the parallel-laminated, glauconite-rich lime mudstone lithofacies. Large arrowhead indicates a sharp-erosional planar contact between the overlying parallel-laminated glauconite-rich lime mudstone (a) and the underlying Nuia packstone- and grainstone lithofacies (b) of the Nuia shoals; and arrows show the sharp planar contacts between thick-bedded Nuia packstone- and grainstone units. Thick bed designated
by "b" is two-feet thick.

glauconite, and absence of mudcracks and fenestral textures substantiate that sedimentation took place below fair-weather wave base within a low-energy subtidal environment. Silt-size glauconite particles represent a low-sedimentation rate in the oxygen-rich open marine environment (McRea, 1977; Odin and Matter, 1981; and van Houtten and Purucker, 1984). Therefore, it can be suggested that these glauconite particles may have formed authigenically during the drowning of Nuia shoals due to a high-sea level rise or transgression.

This transgressive stage probably characterized the flooded tidal flats in which fine-grained sediments were probably no longer trapped and baffled by cyanobacteria (stromatolites) because of submergence. As a result, in the nearshore, storm-flood currents suspended fine-grained sediments by the interaction of the shoaling-storm currents, and storm countercurrents transported them farther seaward.

In conclusion, it can be interpreted that this lithofacies clearly indicates a short durational drowning of the carbonate platform during the early stage of the Orthidella zone.

B. Synthesis:

Nuia packstone- and grainstone lithofacies may have been deposited in storm-and tide-dominated shoals, which occurred on a very broad, nearly flat shelf margin. The Nuia shoals formed and evolved in moderately high- to high-energy environments in which high-energy pulses frequently occurred as a result of storm events. The storm-induced textures and sedimentary structures predominate in all the bedforms (parallel wavy medium beds, rhythmical thin packstone and silt stone beds, and thick packstone-and grainstone beds) of the Nuia packstone- and grainstone lithofacies. In the three bedforms of this lithofacies, the presences of the following textural and sedimentary features are directly related to the high-energy storm events: sharp basal and upper contacts; fine-grained blanket; fining-upward texture; and multiple thin

couplets in amalgamated-beds. However, the lack of normal grading in the Nuia grainstone and packstone units is probably related to the predominance of uniform Nuia grains in this shoal environment.

The medium-wavy beds represent the proximal-storm sediments which may have deposited at the farther open-seaward extension of Nuia shoals, or on the very gentle, nearly flat upper slope.

Thin-rhythmically interbedded siltstone and Nuia packstone- and grainstone couplets probably represent sedimentation by two processes below the fair weather-wave base, specifically in the open seaward-extended flank of the Nuia bars: (1) rapid sedimentation from storm-surge currents, characterizing the parallel-laminated, thin-siltstone intervals; (2) considerably slow normal shelf sedimentation, characterizing mudstone interlayers.

Thick-bedded Nuia grainstone units represent the crest of the Nuia tidal bars in the Nuia shoals despite the lack of tide-dominated oscillation ripples and wave ripples on the uppermost part of these bedforms. The missing tide-dominated sedimentary structures and textures can be attributed to the scouring and erasing effects of the high-magnitude storm currents, to uniform-grained size of Nuia particles, and to diagenetic overprint.

Nuia-rich, (Girvanella-derived) oncoidal and peloidal packstone lithofacies, gradually overlying the thick-bedded Nuia grainstone and underlying Nuia shoal units, characterize the protected-Nuia backshoal and open seaward-extended flank of the Nuia bars. Multiwall-structured Nuia particles are predominant in this Nuia-rich oncoidal and peloidal packstone lithofacies, commonly being coated by Girvanella, and have a very close relation with Girvanella and Sphaerocodium compared to other growth forms of Nuia. The multiwall-structured Nuia was probably a different Nuia species and adapted to soft substrate of relatively low-energy Nuia shoal. In contrast, one and two wall-structured Nuia may have adopted to the high-energy environment and firm substrate.

The parallel-laminated, silty quartz-rich lime mudstone lithofacies, which is bounded unconformably between two Nuia bars, indicates a low-energy, below normal

wave-base sedimentation which took place during a short durational drowning of the Nuia shoal by a high-amplitude sea-level rise.

C. Discussion

There are several studies of the Orthidella zone of the Antelope Valley Limestone, such as Stricker and Carozzi (1977), Morreale (1981), Taban (1986), Kaya and Friedman (1987), and Ross et al. (1988).

Morreale (1981) interpreted the Nuia packstone- and grainstone units as the skeletal-debris deposits of the upper slope derived from the shelf margin by gravity flow. However, this study has demonstrated that the Nuia packstone- and grainstone units, with light gray color, indicated bedforms, sedimentary structures and cement types, imply a storm- and tide-dominated shoal facies rather than gravity flow-induced sedimentation.

Stricker and Carozzi (1977) not only recognized the Nuia but also suggested the "Nuia Model", which is a depositional model for Nuia packstone- and grainstone units. In their model, the crests of the peloidal bars separate the Nuia-offshore subtidal bars from the very broad intertidal algal-flat deposits (Fig. 27 B). Furthermore, Stricker and Carozzi exclude the formation of Girvanella-derived oncoids in the Nuia subtidal-offshore bars. However, this study has clearly shown that oncoidal and peloidal-rich Nuia packstone lithofacies coexisted with Nuia shoal at the protected site of Nuia bars (Fig. 27 A).

The rhythmical siltstone and mudstone couplets and silty quartz-rich, parallel-laminated mudstone have been interpreted to be intertidal deposits (Fig. 27 B) by Stricker and Carozzi (1977). The same rhythmical lithofacies have been interpreted to be the lower-intertidal deposits on the offshore subtidal Nuia bars which were separated from the oolitic shoal by a stressed subtidal setting (Taban, 1986). On the basis of Taban's proposal, it can be assumed that the oolitic shoals and Nuia shoals

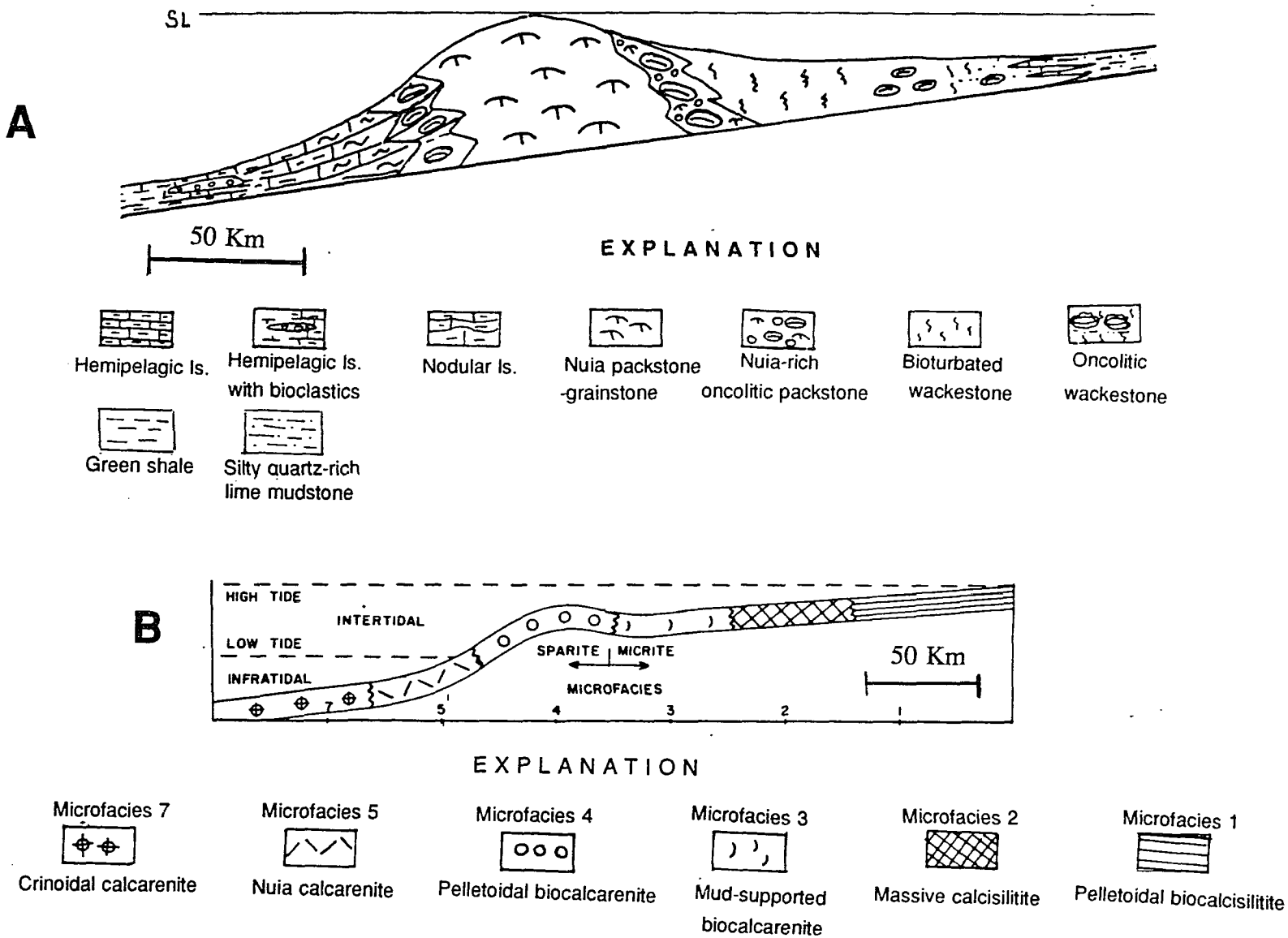


Figure 27- A) A suggested-depositional model of Nuia shoal and related lithofacies in this study. B) Nuia model by Stricker and Carozzi (1977).

existed contemporaneously at the shoreward (east) and openseaward (west) parts of the same carbonate bank, respectively. By contrast, this study suggests that these fine-siliciclastic units were deposited from the episodic storm countercurrents below wave-base in the muddy carbonate shelf (Fig. 27 A)

According to this study, the fine-grained terrigenous units in the Nuia-subtidal zone represent sedimentation that may have taken place during the incipiently drowned Nuia shoal phase. In addition, the fine-grained sedimentary units laterally interfingering with the Nuia grainstone- and packstone lithofacies may represent the topographically low areas or passes between the subtidal-Nuia bars. Moreover, there are no features signifying subaerial exposure in the fine-grained siliciclastic sediments. Thus, the fine-grained siliciclastic lithofacies represents a subtidal, bellow wave base sedimentation rather than an intertidal algal-flat sedimentation. Similarly, no evidence exists to support the assumption that the oolitic shoals and Nuia shoals are synchronous; on the contrary, we interpret that the oolitic shoal evolved from the oncoidal shoal during the mid-Palliseria zone and later.

In Nevada, the Nuia shoal during the Orthidella zone extending from the Arrow Canyon to Callaghan Ranch trending SE-NW (Ross et al., 1988) was probably composed of numerous Nuia tidal bar banks lying perpendicular to the shelf margin. This can be inferred from the lateral facies changes between the Nuia bank deposits and the fine-grained siliciclastic deposits of the topographic low areas or of the Nuia inter bank passes.

The consistency between the sharp erosional planar basal contacts of bedforms of the thick-bedded Nuia packstone- and grainstone units and the erosional, nearly planar basal contacts of the shallowing-upward cycles indicate that a very broad and a nearly flat shelf margin, extending to very gently declining slope, existed during the deposition of Nuia shoal.

Tan to light gray Nuia grainstone- and packstone units with marine-isopachous cement and bedforms are comparable with the oolitic shoals (e.g., Ball, 1967; Hine, 1977; and Halley, et al., 1983) units. However, the absence of ooids in the Nuia shoals can be attributed to a nearly flat Nuia bank which was probably located far from the

shoaling site of the deep-open sea water and the high concentration of the fine-grained suspension in the Nuia shoal water. Therefore, Nuia tidal bars on the nearly flat, very broad shelf margin without ooid formation can be analogous to contemporary Halimeda shoals in the Quicksands of the Marquesas Keys. The lack of ooid formation in the modern Halimeda shoal is related to the following: (a) Halimeda skeletal shoals in the Quicksands are located on a nearly flat substrata and about 10 to 12 km away from the area where strong ocean currents and waves of deep water of Florida Straits shoal, whereas the oolitic shoals of the Bahama Bank are located approximately 1 to 2 km from the shoaling ocean currents and waves; (b) the water is not clear due to suspended-fine materials (Shinn et al., 1990).

In vertical sections, upward progressively thinning Nuia bar facies of the shallowing-upward cycles with a stair-step relationship represent landward-migrated transgressive sand bars (e.g., Gilbert, 1880; Wilson 1975; and James and Mountjoy, 1983).

This study clearly demonstrates that Nuia flourished in the moderately high- to high-energy environment, and probably some Nuia species (growth forms) thrived in the Girvanella-carpeted soft substrate, but not in the low-energy environment as in the sponge-bearing beds reported by Klement and Toomey (1967), Toomey and LeMone (1977), and Alberstadt and Repetski (1990). Later, Toomey (1970) re-interpreted that Nuia-bearing sediments were storm layers in the inter-sponge mound channels.

CHAPTER 5: ONCOIDAL SHOAL FACIES

A. Areal Distribution of Oncoidal Shoal Units

In Antelope Valley region, the oncoidal shoal facies stratigraphically lies between the overlying-skeletal and oolitic shoal facies and the underlying-shelf facies or platform interior facies of the Nuia shoal (Appendix I-B). However, in the Lone Mountain and Keystone Canyon sections, the oncoidal shoal facies are directly overlain by the bioturbated-wackestone lithofacies with a gradual contact (Appendix I-B). In the Whiterock Canyon and June Canyon sections, the oncoidal shoal directly overlie the nodular-bedded lithofacies of upper slope depositional environment (Appendix I-B). The upper part of the oncoidal shoal and the Antelope Valley Limestone are missing in the Whiterock Canyon section. However, in the June Canyon sequence, it is overlain by the mottled limestone of upper-slope or deep ramp. Moreover, in the Ninemile Canyon section, particularly at intervals of 480-500 feet and 515-530 feet, small, biohermlike oncoidal-shoal lithofacies occur in the silty quartz-rich lime mudstone units (see Appendix I-B). Light to dark gray colors dominate this oncoidal shoal facies of the westerly type sections, but in the Ninemile Canyon section, the oncoidal shoal lithofacies are predominantly light gray and light-brownish gray in color.

In the study area, the oncoidal shoal facies were reported in the intervals from the base of the following vertical sections (Fig. 28): (1) in the Martin Ridge section, a 160-foot thick oncoidal shoal at intervals of 240 and 400 feet; (2) in the Ninemile Canyon section, a 100-foot thick oncoidal shoal at intervals of 655 and 750 feet; (3) in the Lone Mountain section, a 140-foot thick oncoidal shoal at intervals of 290 and 430 feet; (4) in the Keystone Canyon, a 125-foot thick pervasively dolomitized oncoidal shoal facies at intervals of 0 and 125 feet; (5) in the Whiterock Canyon section, a 140-foot facies at intervals of 300 and 440 feet; and (6) in the June Canyon sequence,

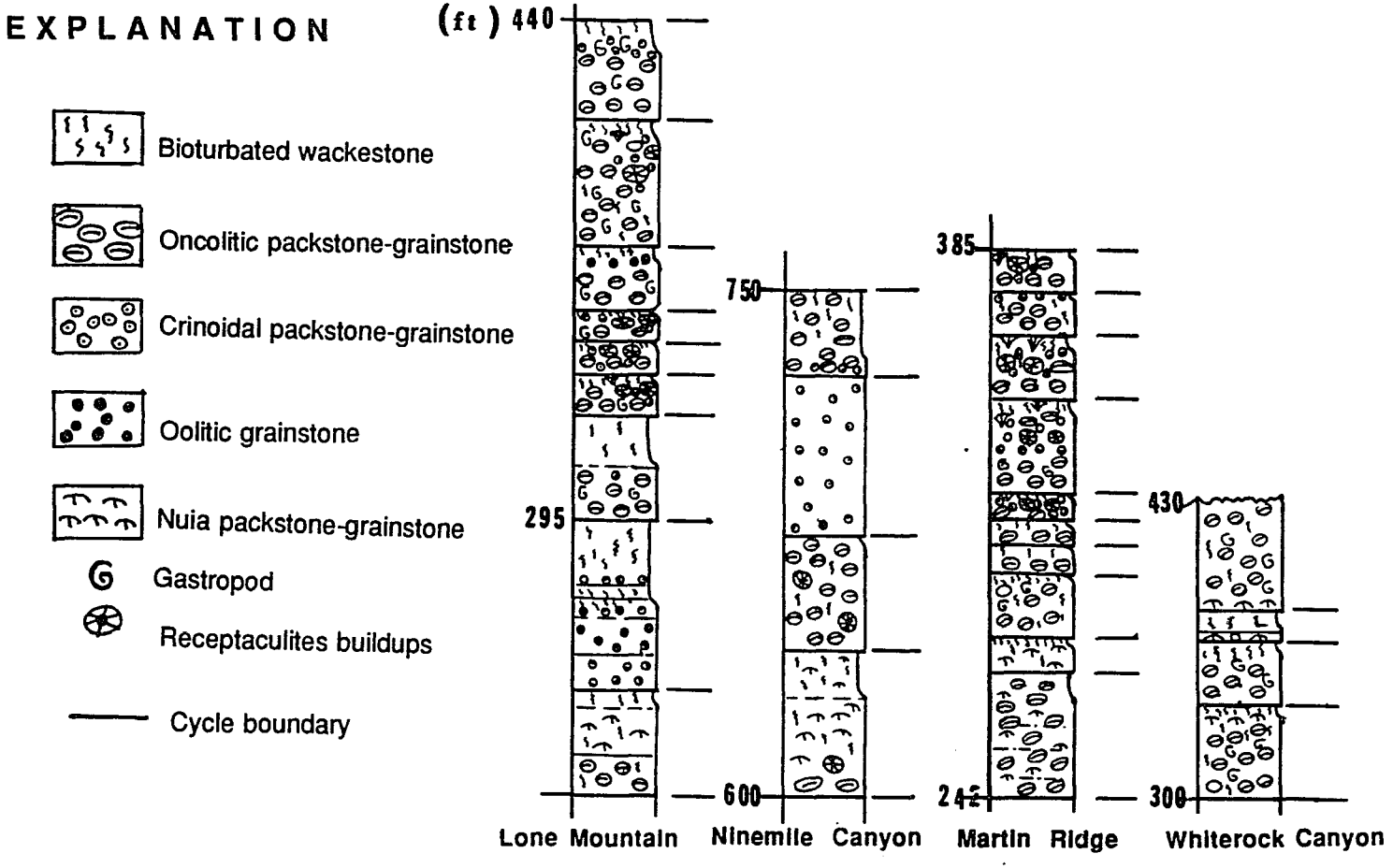


Figure 28- Succession of the oncoidal shoal cycles and related lithofacies in the vertical sections.

a 55-foot thick oncoidal shoal facies at intervals of 635 and 690 feet (see Chap. 9; Appendix I-B).

Generally, in the Ninemile Canyon and Martin Ridge sections, the oncoidal shoal facies are separated from the Nuia shoal units by about 100 to 150-feet thick shelf or platform interior facies of the Nuia shoal (Appendix I-B). A similar sequence appears to be present in the Lone Mountain section; however, the pervasive dolomitization of this formation, and the modern basin-fill sediments at the lower part of this section make such comparison impossible.

B. Lithofacies

Lithofacies 5: Oncolitic Packstone- and Grainstone

Description:

The oncolitic packstone- and grainstone lithofacies usually occur in slightly inclined, thick-to massive-bedded units; however, these cross beds do not show any of the features of the cross-bedded units. Laterally, the thickness of these beds varies and appears to be lenticular. In the oncolitic packstone- and grainstone lithofacies, columnar calcite cements are the principal cement and precipitated on the bottom of large oncoids and intraclasts as a geopetal cement (Fig. 29 A, B, and C).

Each of these thick-bedded oncolitic packstone- and grainstone units changes gradually upward into the wackestone and mudstone units, displaying a fining-upward texture. Similarly, in these oncolitic packstone- and grainstone beds, bioturbation, too, increases upward with increasing mud and quartz silt contents. In places, thin slightly inclined, parallel silty quartz laminae occur in the yellowish-brown, matrix-supported upper subunits (5 to 25 cm thick) of these packstone- and grainstone beds.

The upper and lower boundaries of these thick-bedded units are clearly notable, but

Figure 29- Polished slabs of the oncolitic packstone- and grainstone lithofacies. A) Well-sorted oncolitic packstone- and grainstone unit overlies the oolitic grainstone lithofacies (o) with a concave-upward basal contact which is depicted by line and pointed by arrow. This oncolitic lithofacies consists of calcitized-large gastropod, Maclurites (m), fragments and spherical and ellipsoidal oncoids. Arrowheads point to sheltered-columnar calcite cements occurring beneath or protected sides of oncoids. B) In the oncoidal and intraclastic packstone unit, (i) marks intraclasts, and arrowheads point to Girvanella oncoids. C) In the oncolitic packstone- and grainstone unit, arrowheads point to columnar calcite cement beneath protected sides of oncoids. D) and E) Thick-, massive-beds of the oncoidal packstone- and grainstone lithofacies consist of multiple thin beds which includes basal oncoidal grainstone to packstone sublayers and relatively muddier upper sublayers (a fining-upward texture). Arrows indicate a sharp truncational contact between two thin inner layers, and (m) indicates yellow-mud concentration within the upper fine-grained sublayers. Pennies for scale.

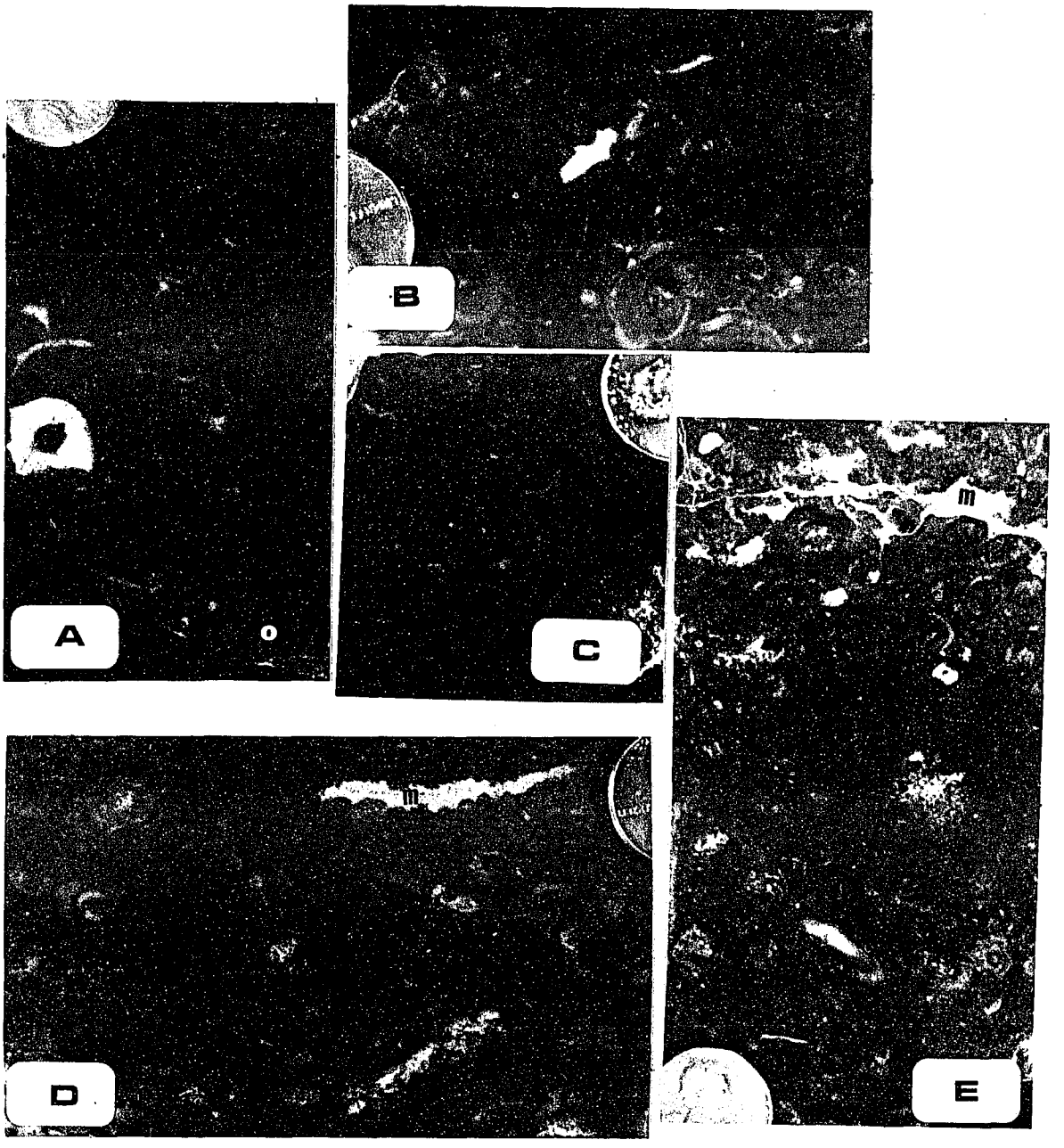
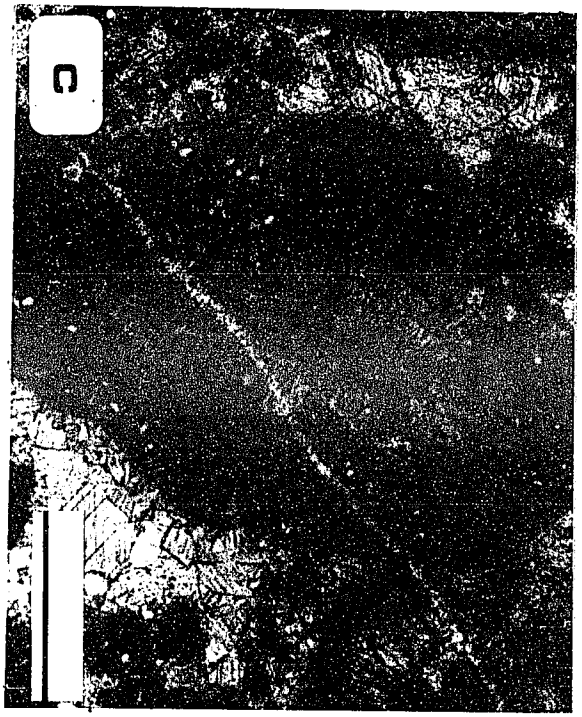

A
B
C
D
E

Figure 30- Photomicrographs of the oncolitic packstone- and grainstone lithofacies. A) In oncolitic packstone- and grainstone, Girvanella-coated Nuia grains (n) and other allochems. B) Nuia grains and calcitized-ooids (o) within the intraclast-rich oncolitic packstone- and grainstone lithofacies. C) Multiwall-structured Nuia as a nucleus within a Girvanella oncoid; arrowhead indicating an euhedral dolomite crystal of type II in the algal coating. D) White arrow indicating the encrusting-green algae "Sphaerocodium" in the oncolitic packstone unit. With plane-polarized light; scales= 0.5 mm.


C


A


B


D

in some intervals, these boundaries are not recognizable due to their massive-bedding appearances. Each of these beds is subsequently overlain by a sharp, erosional-basal contact of the overlying-oncolitic packstone- and grainstone unit.

These thick-bedded grainstone and packstone units consist of several sublayers as much as 4-6 cm thick which show a fining-upward texture. (Fig. 29, D and E). These oncoidal sublayers overlie one another with a truncational basal contact.

In cyclical successions, each shallowing-upward cycle of oncoidal shoals includes a 20- to 25-foot thick oncolitic packstone-and grainstone basal units and the overlying bioturbated-wackestone units (approximately 5 to 8 feet thick). In addition, these oncoidal shoal cycles overlie one another with a sharp erosional basal contact (Fig. 28).

In the Martin Ridge and Ninemile Canyon sections, two types of thick-bedded oncolitic sulithofacies are present: (1) Nuia-rich lower oncoidal shoal units (Fig. 30 A, B and C), and (2) upper oncoidal shoal units with Receptaculites build ups. The lower oncoidal shoal units are very similar to the Nuia-rich peloidal and oncoidal Nuia packstone unit which has been described in the Nuia shoal (Fig. 30 A, B and C). The upper thick-bedded oncoidal shoal units, however, laterally change into the unbedded-bioherm lithofacies, which are made up of Receptaculites, crinoids, Girvanella, Sphaerocodium (encrusting algae) (Fig. 30 D), bryozoans, large gastropods Maclurites, and maybe some stromatoporoids.

In both lower and upper oncolitic packstone units grain size of oncoids occurs in a comparable range, and oncoids and peloids are constituted by the blue-green algae Girvanella (Figs. 31, 32, 33).

In the upper oncoidal shoal lithofacies, oncoids are usually subrounded- and ellipsoidal grains and consist of the fragments of gastropods, crinoids and brachiopods as nuclei, respectively. In contrast, larger multi-wall structured Nuia grains are most commonly found in the nuclei of Girvanella oncoids in the lower part of oncoidal shoal facies at Ninemile and Martin Ridge sections (Fig. 30 A, B, and C). In the Lone Mountain sections, Maclurites are commonly present throughout the oncoidal shoal; however, Receptaculites are not present at the first two oncoidal shallowing-upward

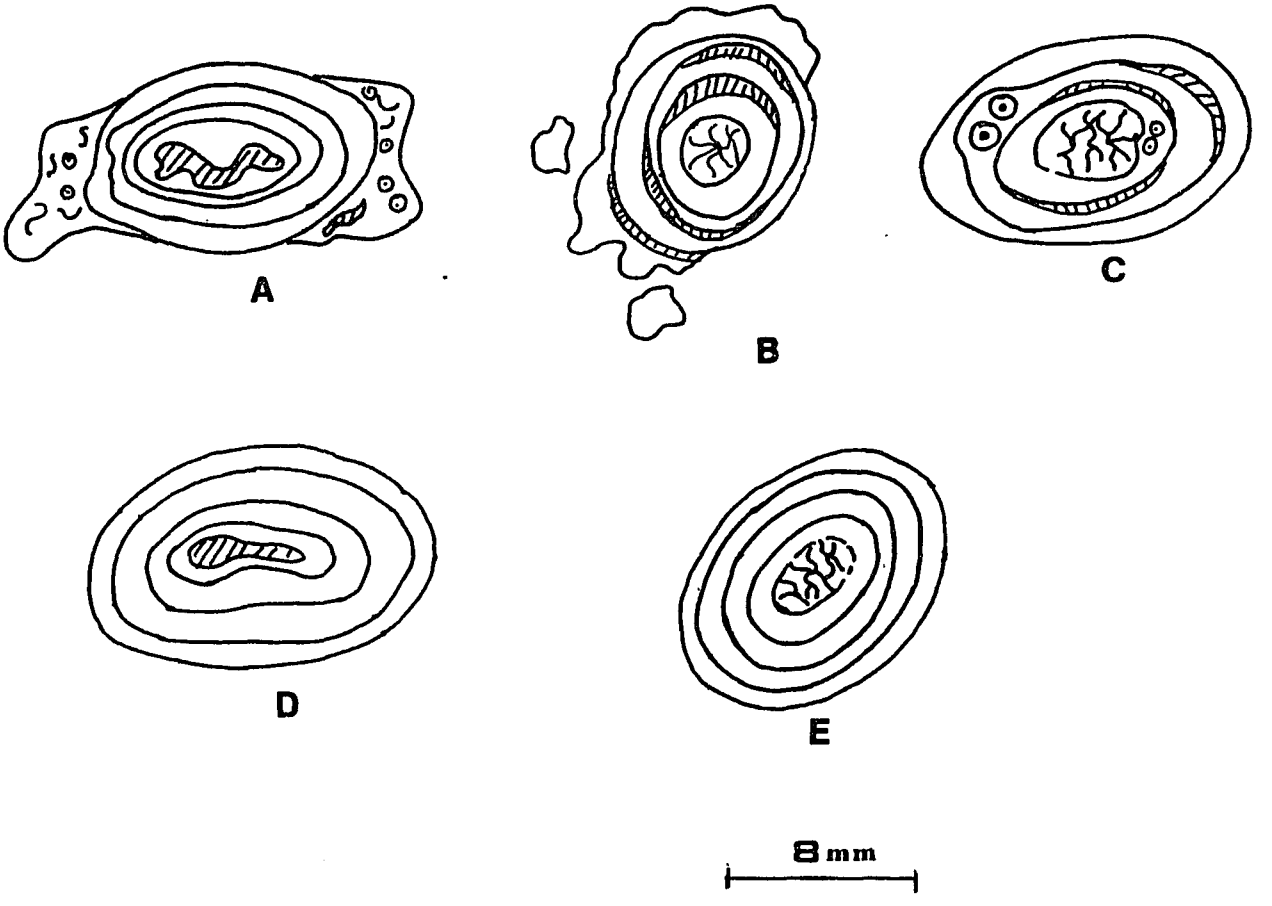


Figure 31- Kinds of oncoids and oncoidal laminae in the oncoidal shoal units. A) A well-rounded ellipsoidal oncoid with irregular, outer skeletal laminae. B) A well-rounded spherical oncoid with semi-concentric inner laminae and digitated outer Girvanella laminae. C) An ellipsoidal oncoid with very thin, discontinuous inner skeletal laminae along with semi-concentric calcite laminae. D) and E) Well-rounded ellipsoidal and spherical oncoids with symmetrical concentric laminae.

sequences.

In places, the upper oncolitic packstone to wackestone lithofacies is overlain by two- to three-foot thick crinoidal grainstone units which appears to occur as flank deposits of the Receptaculites-bioherm facies.

The upper packstone to wackestone oncolitic shoal facies comprise abundant but relatively small Girvanella-derived oncoids, intraclasts and peloids. The presence of Nuia never exceeds 2 % in this upper oncoidal, bioherm-dominated sublithofacies. In contrast, in the lower, thick-bedded oncoidal shoal lithofacies, (beneath the 7 to 12-feet thick subtidal Nuia bar), Nuia is the most important constituents of this lithofacies after the Girvanella-derived peloids, oncoids and intraclasts (Fig. 30 A, B, and C).

The approximated-average percentages of constituents of the lower oncoidal shoal facies are, the following: oncoids 25-45 %, Girvanella-derived peloids 10-25 %, Nuia 20-25 %. Other open marine faunal remains include crinoids, trilobites, brachiopods, and gastropod fragments.

In the upper oncoidal lithofacies, crinoids accompany to Girvanella, and Receptaculites and Sphaerocodium (Fig. 30). Particles of Maclurites are also significantly important in the upper oncoidal shoal facies and in the backshoal lithofacies of skeletal and oolitic shoals.

The oncoids of both the lower and upper oncoidal shoal lithofacies have multiple concentric, continuous, symmetrical coatings (Fig. 31), and they most commonly occur in the lower-basal part of the grain-supported sublayers of the multiple thin beds which constitute the massive-amalgamated beds. These oncoids have generally symmetrical, concentric laminae (Fig. 31 D, E) with or without very fine-grained peloids and Nuia particles (Fig. 31 C). However, the outer coatings of the oncoids in this lithofacies are irregular and partially concentric, and include large skeletal fragments (Fig. 31 A, B).

The grain size of well-rounded, ellipsoidal oncoids ranges from 2.5 to 6 mm; an average is 3-4.5 mm (Fig. 31 D, E). Some oncoids in the uppermost part of the oncoidal shoals and in the overlying-wackestone units have irregular outlines, and irregular inner- and outer-concentric, skeletal fragment-bearing laminae with a

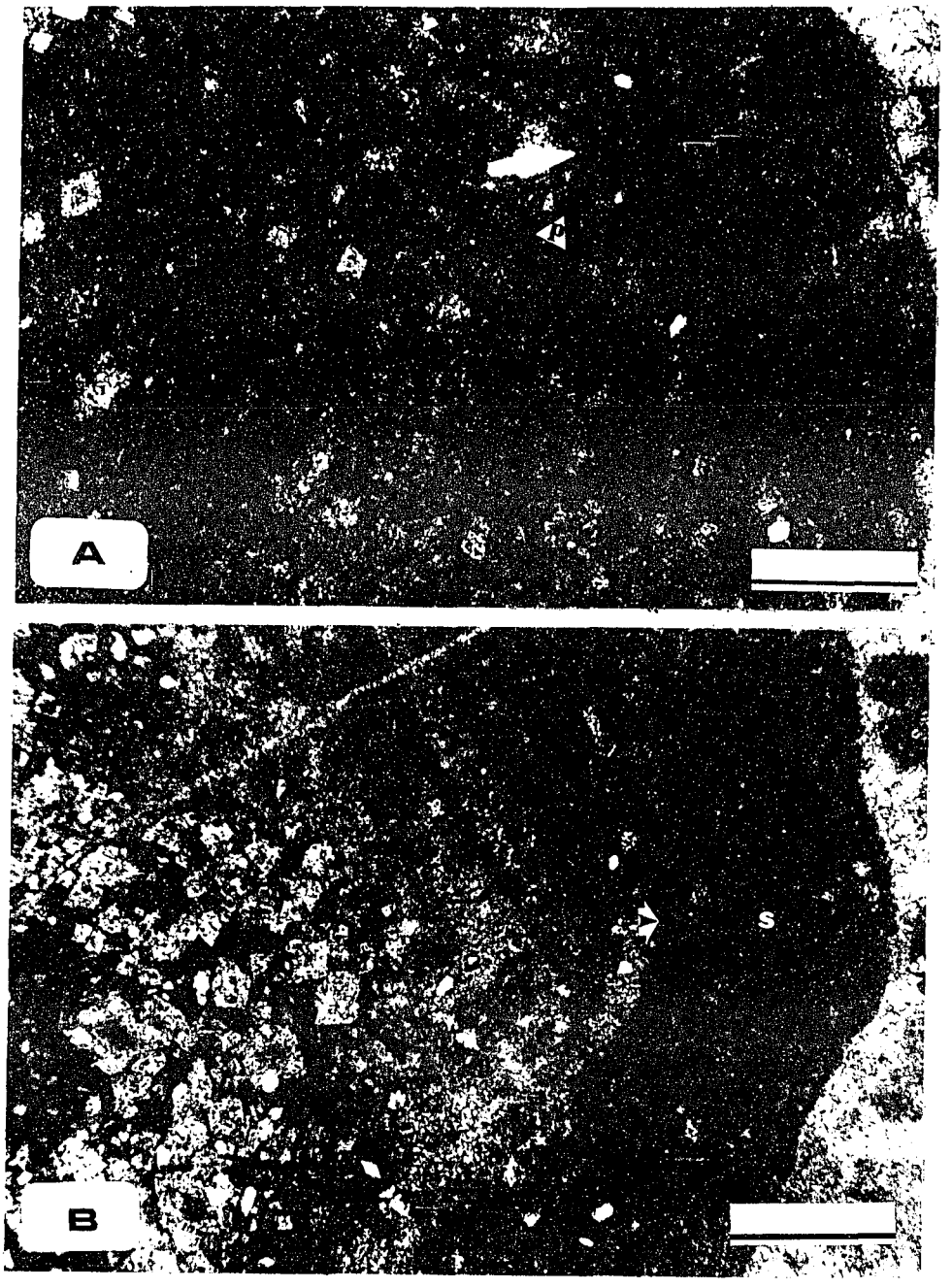
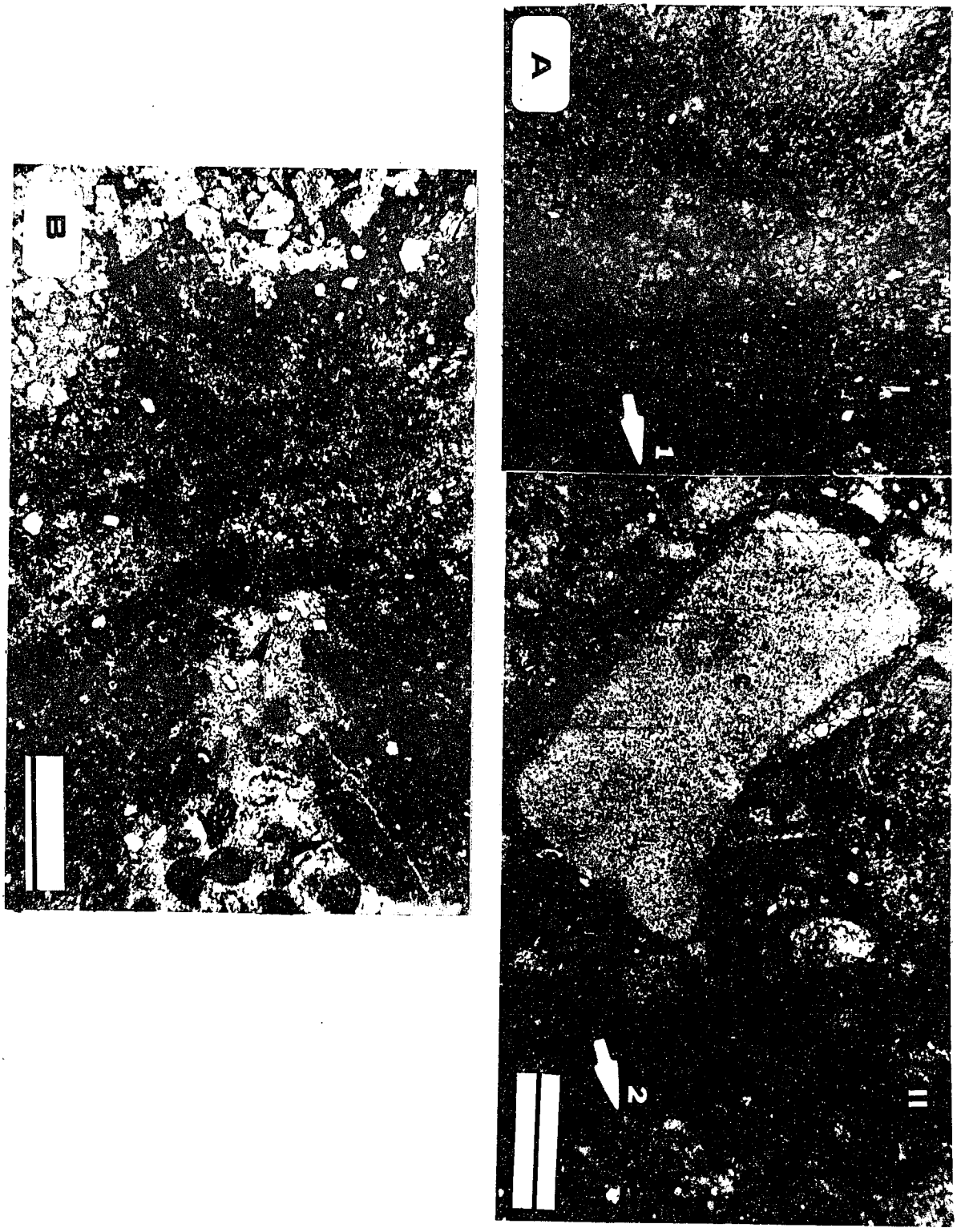


Figure 32- Photomicrographs of Girvanella growth forms and related-concentric laminae. A) Tightly intertwined-Girvanella tubules in concentric laminae of well-rounded oncoids of the oncolitic packstone- and grainstone lithofacies; pyrite (p) and euhedral small dolomite rhombs of dolomite type II indicated by arrow heads are common in algal laminae. B) Upward growth form and tightly intertwined-Girvanella tubules: (1) Upward growth form of Girvanella tubules are partially calcitized and selectively dolomitized at the center of oncoid, and (2) outer-tightly intertwine algal tubules laminae (s). White arrow points to a gradual contact between two growth forms of Girvanella-constituted concentric laminae; authigenic quartz indicated by arrow. With plane-polarized light; scales= 0.5 mm.

Figure 33- Photomicrographs of oncoid laminae and outline of oncoids. A) Well-rounded spherical oncoid (I) is coated by a very thick, outer skeletal concentric laminae (II); arrow 1 points to the regular outline of inner oncoid, and arrow 2 points to the outer skeletal laminae's irregular outline in which crinoids (c) and ostracods are common. B) In a well-rounded oncoid, arrow points the selectively dolomitized part of the upward growth form of Girvanella at center (a); stacking-growth form of Girvanella (b). Arrowheads indicate locally digitated outline of an oncoid. With plane-polarized light; scales= 0.5 mm.


A
1
2
B

considerably larger grain size.

Neomorphically altered mollusc fragments are usually common in the nucleus of the oncoids, and they are selectively dolomitized (Fig. 31 E). The most common concentric laminae of Girvanella-derived oncoids are as follows: (a) only dark and black stacking-growth form of Girvanella filaments (Fig. 32 A) or concentric Girvanella sheets i.e. tightly intertwined filaments (e.g., Coniglioni and James, 1985); (b) partially calcitized upward-growth form of Girvanella (selectively dolomitized) gradually changing into dominantly stacking algal filaments (Fig. 32 B), or only upward growth forms of Girvanella (Coniglioni and James, 1985); (c) skeletal fragment-bearing outer and inner laminae (Fig. 33 A); (d) partially concentric calcitic laminae (Fig. 31 A and C); and e) concentric regular inner laminae and digitated-outer laminae (Fig. 33 B).

Thin-micro calcite spar crystals occur and alternate along with dark micritic or Girvanella-constituted concentric laminae. On the other hand, Girvanella growth forms as laminae are separated from one another by dark organic micritic sublaminae. Locally, stylolites occur between alternating-organic laminations. Calcitization is common in the inter-Girvanella tubules of upward growth forms Girvanella of this alga and reminiscent of **grumeleuse** texture (Fig. 33 A, B; Bathurst, 1975). Local concentrations of calcite filling in the Girvanella tubules appear to be similar to birdseye texture.

Interpretation:

The oncolitic packstone- and grainstone lithofacies, with its columnar calcite cement, probably represents a moderate to high-energy environment in which the energy level was high enough to keep the oncoids in constant motion. The large, sheltered-interparticle columnar calcite cements were probably contemporaneously derived from the super-saturated sea water. Similarly, in the spherical and ellipsoidal oncoids, the common occurrences of the symmetrical, regular concentric laminae and

scarcity of discontinuous skeletal internal laminae also indicate moderately high-energy environmental conditions. These oncoid forms with continuous and symmetrical laminae could be correlative with the high-energy environmental conditions in the oncoid-forming environment (Logan et al., 1962; Dahanayake, 1977; and Bosselini and Ginsburg, 1971).

The well-rounded oncoids containing very thin skeletal-inner laminae (very fine-grained Nuia and peloids) may represent very brief episodes when slight energy decrease may have occurred in this moderately high-energy shoal. During these episodes, the oncoids of the oncoidal shoal were probably resting on the sea floor, and Girvanella bound and baffled the fine skeletal grains at the upper surface of the oncoids. In contrast, the coarse-grained skeletal fragments along the partially concentric inner-laminae may suggest that these organo-sedimentary grains may have experienced relatively long resting periods during which the energy level of the moderately high-energy environment was diminished considerably. Nevertheless, it can be suggested that the energy level was probably strong enough for movement of smaller skeletal fragments but not for such large organo-sedimentary grains. The presence of partially irregular, thick skeletal outer laminae probably represent much longer resting periods compared to other forms of skeletal and inner and outer laminae. Therefore, we can suggest that these thick outer skeletal laminae may have formed during the final settlement of these organo-sedimentary particles. It may also be implied that Girvanella at the upper surface of the oncoids probably continued its daily life activity, while it was resting on the sea floor. As a result, at this final stage, the Girvanella-baffled skeletal grains resulted in the formation of irregular, non-concentric, outer-skeletal laminae which should not, in turn, be correlated with a low-energy or slightly moderate-energy environment. Because this stage appears to represent the stabilization and partial lithification of these organo-sedimentary grains by submarine cementation.

For the above cited reasons, the lamina types, outline of oncoids, presence of outer and inner laminae, texture and bed forms should be taken into considerations together in order to interpret the depositional environment of the oncoid-bearing strata.

In some oncoids, the alternating elongated-encrusting (concentric Girvanella sheet) and upward-Girvanella growth forms may be comparable to daily activity of modern blue-green algae. Monty (1972) described two-growth forms due to phototactic (i.e., movement of an organism in response to stimulus from light) behavior of the modern-blue green algae: (1) tightly intertwined, elongated- encrusting growth habits, forming during the night, and (2) upward growth habits, forming during the day as algal growth being directed to light.

In the subtidal environment of oncoidal shoals, the predominance of tightly intertwined, elongated-encrusting concentric Girvanella laminae may represent periods of relatively dark and deep environmental conditions as well as the episodes of fine-siliciclastic influxes. The upward-growth forms, on the other hand, may represent the light periods either caused by the shallow-water depth or fine siliciclastic influx-free episodes during which the photic zone was deeper than those episodes during siliciclastic influx. The fine-grained siliciclastic suspensions in the water column probably created a shield against sun-light penetration, and reflected sun light back to the atmosphere. Therefore, it is possible to suggest that the episodes of the fine-grained siliciclastic influxes can be correlative with the darker episodes in subtidal environments.

The thin- to medium-bedded oncolitic packstone- and grainstone units, with sheltered-columnar calcite cement, commonly show a fining-upward texture and constitute thick, massive lenticular beds. These thin- to medium-oncolitic beds, which occur as amalgamated bed overlying one another with a sharp-basal contact, suggest that these oncolitic packstone and grainstone lithofacies may have resulted from high-energy storm currents in the moderately high-energy environment. During high-energy storm pulses, the fair weather-wave base level becomes deeper than those of the base levels during the non-storm periods; as a result, the deepened normal wave base can erode. These erosional-basal contacts and upward-decreasing grain size indicate the gradually waning-storm currents, as suggested by Kelling and Mullin (1975), Brenner and Davies (1973), Kreisa (1981) and Aigner (1982).

The lateral variation in thicknesses of the amalgamated-massive oncolitic beds

(lenticular shape) also represent the storm-dominated depositional environment (e.g., Kreisa, 1981; Aigner, 1982). Truncational basal contacts of thin to medium-bedded units in the amalgamated-massive beds are also indicative of the strongest phase of each storm event (Leckie and Walker, 1982). The coarse-grained sediments represent rapid sedimentation which deposited them from storm currents after the formation of erosional surface. The gradual decrease in strength of the storm currents is probably reflected by the formation of the normal-graded beds (Kreisa, 1981; Aigner, 1982; and Leckie and Walker, 1982).

Finally, the fine-grained, muddy sublayers of these normal-graded beds with silty quartz-rich parallel laminae symbolize storm countercurrent sedimentation which commonly occurs during post-stormal tranquil phases.

Darker gray color of these units and their preserved-parallel silty laminae may suggest that deposition of these shoal units most likely took place slightly below the normal weather-wave base. Thus, the oncolitic packstone- and grainstone lithofacies appear to represent the storm-dominated oncoidal shoal environment in which the energy level was ranging from highly moderate to moderately high. In this oncoidal shoal, Girvanella may have inhabited relatively lower energy areas than those environments where these oncoids were deposited. Therefore, it can be suggested that oncoids were transported into their depositional site and farther landward by strong, high-energy, episodical-storm events.

Some intervals of the oncolitic packstone lithofacies are overlain by the crinoidal, oolitic and Nuia packstone and grainstone units, indicating that the oncolitic subtidal bars yielded a short-lived syndepositional topography which interacted with the active tidal waves and currents. Therefore, the progradations of oncolitic subtidal bars brought oncoidal shoals briefly into the tide-dominated shoal sedimentation in the storm-predominated oncoidal shoals. During these brief episodes, on the crest of oncoidal bars, daily tidal wave and current works probably produced the skeletal grainstone units which commonly mark the normal weather wave base (Irwin, 1965; Heckel, 1972; and Laporte, 1978).

In the upper oncoidal shoal facies, the presence of Receptaculites-framed bioherms

and abundant crinoids and thick-shelled gastropods indicate a relatively high-energy environment which was above fair-weather wave base. Therefore, it is important to suggest that the general depositional environment of this oncoidal shoal unit appears to have ranged from slightly below fair-weather wave base to the lower level of the fair weather wave base.

Moreover, the absence of cross beds and oscillation ripples and the preservation of the parallel-laminated, silty quartz-rich upper sublayers imply that these thick-bedded units were probably shaped by storm events or where tidal washing and reworking were ineffective (below fair-weather wave base). Rapid sedimentation from storm-flood currents, and baffling by Girvanella probably did not allow fine-mud fractions to clog the interparticle pores. Relatively thin discontinuous aragonitic, fibrous, transparent concentric laminae alternating with thick, dark-algal, cryptocrystalline laminae were noted in the oncoids of modern hypersaline pools of the Red Sea (Friedman et al., 1973; 1985). The partially concentric calcite inner laminae of the oncoids of this lithofacies are comparable with those oncoids described by Friedman et al. (1973; 1985). In this lithofacies, these partially concentric, inner calcite laminae of oncoids may represent sheltered-cement being formed periodically under the protected site of the oncoids before these organo sedimentary grains' final settlement. Therefore, it is possible that these partial concentric calcite laminae may have formed when the oncoids were resting on the sea floor during the episodically quiescent periods.

At the June Canyon section, Nuia occurs in the oncolitic packstone and wackestone units above the sponge-bearing beds. Generally, thicker wackestone sublayers and thinner basal packstone sublayers probably represent the farther seaward flank of the oncoidal shoal.

Probably Girvanella appears to have favorably inhabited the farther basinward environments of the oncoidal shoal bars from which oncoids may have been transported into the relatively more turbulent oncoidal shoal. In the Lone Mountain section, the oncolitic packstone units of the Orthidella zone gradually change into Nuia packstone units. Nuia-rich oncoidal shoal units of the lower oncoidal shoal in Martin

Ridge are laterally correlative with the Nuia packstone- and grainstone units in the Ninemile Canyon sections (Fig. 28; see Chap. 10). These clearly suggest that the oncoidal shoals represent a depositional environment whose energy level was considerably lower than that of the Nuia shoal. This suggestion can further be supported by the contemporaneous occurrence of the oncoidal shoal at the farther open seaward extension of the Nuia shoal during the early Palliseria zone (see Chaps. 10, 11).

Ruppel and Walker (1982) noted comparable relationships between two Middle Ordovician formations: The Lincolnshire Formation, representing the basinward shoal, is the oncoidal shoal facies and overlain by the crinoidal or skeletal shoal facies known as the Rockdell Formation.

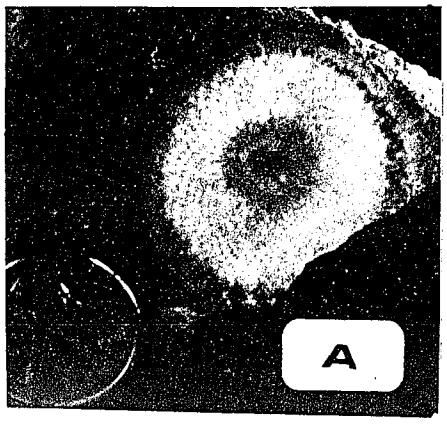
Lithofacies 6: Receptaculites Bioherms or Buildups

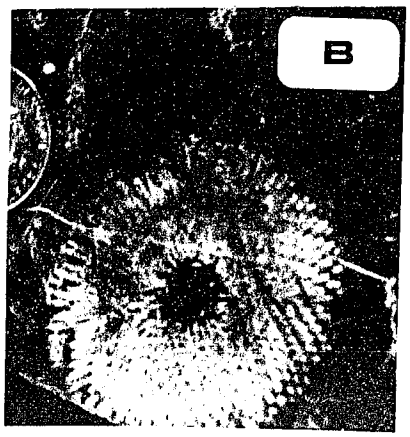
Description:

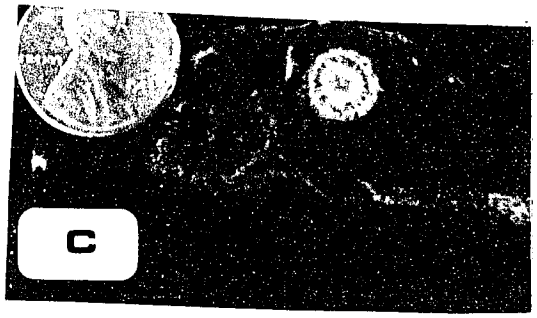
Generally, dark gray to black color, unbedded-massive morphology are distinctive features of this bioherm lithofacies. The Receptaculites bioherm facies is composed of two parts: a) lower subbioherm units, having massive-bedded morphology and changing upward into about 2-3 feet of crinoid-dominated, thick-bedded skeletal packstone and grainstone units; and b) upper subbioherm units, characterized by dark bioturbated-pelletal mudstone to wackestone in which bryozoa remains are recognizable.

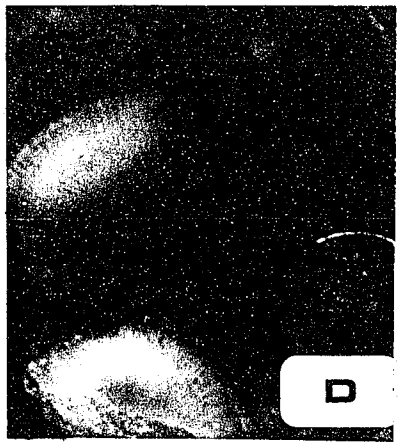
In general, Receptaculites, crinoids and other encrusting algae Sphaerocodium occur in the lower subbioherm units, which gradually change to the bioturbated wackestone which includes the scattered Receptaculites. Bryozoans, stromatoporoids and Sphaerocodiums are commonly present in the intensively bioturbated upper Receptaculites subbioherm facies. The pioneer communities of this bioherm facies are crinoids and Receptaculites, (Fig. 34) as well as Girvanella (cf., Alberstadt et al.,

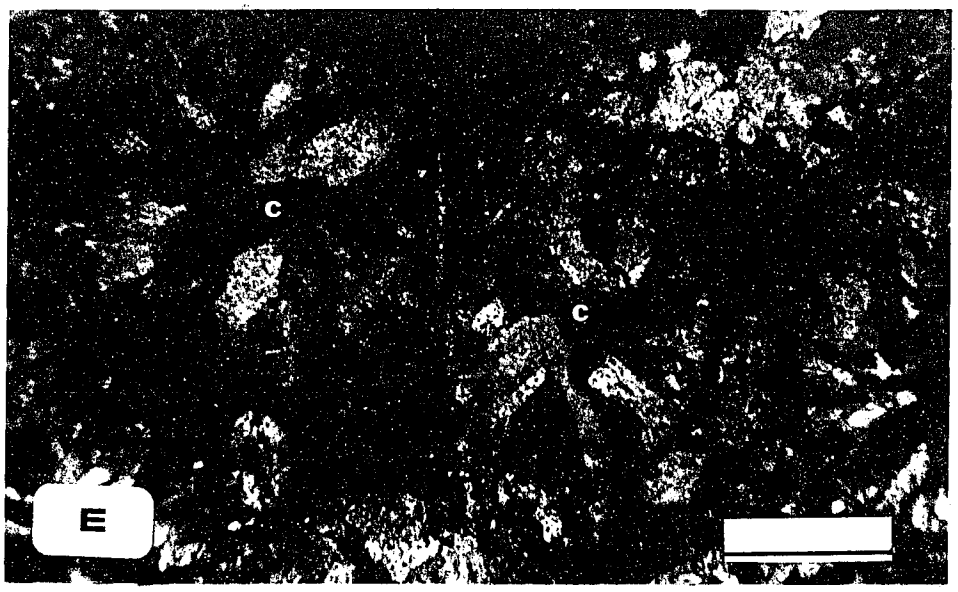
Figure 34- Polished slabs of the Receptaculites bioherm lithofacies and photomicrograph of Receptaculites. A) and B) Arrowheads indicate spherical Receptaculites, which has a micritic central canal from which ossicles radiate. C) Arrowhead point to a conical Receptaculites in the crinoidal packstone. D) Arrowheads point to semicircular or horseshoe-like Receptaculites in the skeletal and oncolitic packstone. Pennies for scale. E) Photomicrograph of calcitized Receptaculites ossicles; calcite cement (c) of the ossicles appears to show a radiaxial texture. With plane-polarized light; scale= 0.5 mm.


A


B


C


D


C
C
E

1974; Alberstadt and Walker, 1976). Bryozoas and stromatoporoids have been determined in the thin sections, particularly, of the upper subbioherm mudstone units. Receptaculites and crinoid-dominated skeletal packstone- and grainstone lithofacies overlie the dark black micritic sublithofacies of the upper subbioherms and laterally grade into the oncolitic packstone units. In addition to crinoids, Girvanella-derived oncoids with peloids and some Nuia grains occur in the lower part of these buildups.

The size of these buildups laterally extends in 6 to 50 m and varies 2-4 m in thicknesses. Each buildup facies with the indicated thicknesses overlies one another with erosional sharp contact like a "stratigraphic reef" or bioherm (e.g., Dunham, 1970).

The crinoidal packstone- to grainstone units (Fig. 34 C, D) at the base and top of the bioherms and the bioherm itself change laterally into the thick-bedded oncolitic packstone- and grainstone units.

Large, unbroken, thick-shelled gastropods (Maclurites) are most commonly present in the lower part of this bioherm lithofacies. In this study, three kinds of Receptaculites have been distinguished in this bioherm facies (Fig. 34): 1) large spherical, 2) half-moon shape, and 3) cylindrical.

Figure 34 A shows that Receptaculites ossicles were replaced by calcite which appears to have a radiaxial cement texture.

Stratigraphically, this bioherm facies is overlain by the skeletal and oolitic shoal facies in the Martin Ridge and Ninemile Canyon sections and by the deep-shelf or platform-interior lithofacies of the oncoidal shelf in the Lone Mountain and Keystone Canyon sections.

Interpretation:

The thick-bedded lower Receptaculites buildup facies represents relatively higher energy conditions than those of the oncolitic packstone to wackestone units. However, pelletal and bryozoa-rich, bioturbated-upper wackestone and mudstone sublithofacies

may have been deposited in relatively low-energy environments or specifically at the protected-leeward site of the Receptaculites bioherms. Encrusting stages of this bioherm were not determined. Therefore, in this study, Receptaculites and crinoids as well as Girvanella constituted organo structures are likely to be bioherms rather than reefs.

Additionally, with other open marine fauna, thick-shelled Maclurites (gastropods) are generally indicative of the high-energy environment (Kendall and Skipwith, 1969). By studying the Girvanella-dominated environments of the Chazy beds, Finks and Toomey (1969) suggested that Maclurites was a grazer and fed on blue-green algae Girvanella. Receptaculites is mostly found in carbonate banks in the North America and Europe, and it has affinity with green algae. Nitecki (1972) proposes that Receptaculites can be analogous to the modern green algae. In addition, a few species have been found in the Arctic, Siberia, Manchuria, Southeast Asia and West Africa, and South America. They are mostly recovered from strata ranging from Lower Ordovician to Permian in age.

Receptaculites are believed to represent the paleoequator due to their affinity with calcareous-green algae (Nitecki, 1972; Heckel and Witzke, 1979; and Beadle, 1988). However, Ahlfelt and Barnisa (1960) reported the Devonian Receptaculites in Bolivia with a cold-temperate and subarctic fauna (Beadle, 1988). Modern dasycladaceans, Bornetalla and Nomeris, which are analogues to Receptaculites, are most commonly found in tropical regions, but they also occur at the mid latitude, such as in the Mediterranean and at high latitude in Chile (Nitecki, 1972; Beadle, 1988).

Nitecki (1972) suggests approximately 6 to 12 m of water depth for the Receptaculites environment because of their coexistence with the green algae, Sphaerocodium. If this is so, these bioherms overlain by crinoidal grainstone or packstone units mark the beginning of sedimentation above the normal-wave base (Irwin, 1965; Heckel, 1972; and Laporte, 1978). From this point, it can be suggested that Receptaculites bioherms formed at the crest of oncoidal bars, where crinoids provided a favorable place for Receptaculites to attach themselves and probably to grow in this moderately high- energy environment. It is possible to consider that the

vertical growth of bioherms on the oncoidal shoal (incipiently drowned shelf margin of the AVL) probably gave rise to the formation of skeletal and oolitic shoals of the Antelope Valley region.

Therefore, one can suggest that the oncoidal-, skeletal- and oolitic shoals existed synchronously on the same shelf margin. Oncolitic shoals at this stage are generally represented by the oncolitic packstone units behind oolitic and skeletal bars and at the farther open-seaward extended-flank of the oolitic bars.

Receptaculites bioherm facies prevailed on the farther-open seaward extended shelf-margin environment, while skeletal and oolitic shoal facies were probably growing on the topographically high precursor subtidal-oncoidal bars and Receptaculites bioherms. For instance, the small Receptaculites bioherms in crinoid-dominated skeletal shoals in the Ninemile Canyon section grade westward (open sea ward) into the Receptaculites-dominated oncoidal shoal in the Martin Ridge section.

The patchy Receptaculites bioherms of the Middle Ordovician Carter Formation at Elk River, in Tennessee (Alberstadt and Walker, 1976) is comparable to the Receptaculites buildups of the oncoidal shoal in the Antelope Valley Limestone in central Nevada. The only difference is that the dark micritic upper Receptaculites bioherm facies of the AVL does not include observable stromatoporoids in the field, even though some stromatoporoids are recognized under the petrographic examination.

C. Synthesis

The presence of blue-green algal oncoids in modern marine environments has been noted particularly in lagoons, backreefs and lower-intertidal environments at a water depth of approximately three-meter (Bathurst, 1975; Ginsburg, 1960; Gebelein, 1977; Logan et al., 1962; Monty, 1977; and Flügel, 1984). In ancient carbonates, oncoids are

also believed to represent the lower intertidal and upper subtidal environments (Flügel, 1984), and the Girvanella-derived oncolitic packstone units were interpreted to represent moderate-energy conditions for the Cambrian rocks (Aitken, 1969).

Ooid and oncoid coexistence in the oolitic shoal facies in the Cambrian carbonates in Australia were reported by Young (1978); he interpreted that the oncolitic packstone probably represented the seaward and leeward flank of oolitic bars in the active oolitic-shoal environment. Similarly, this study agrees with the moderately high-energy environmental conditions that were proposed for the oncolitic packstone facies by Stricker and Carozzi (1977), Riding (1975; 1977), Dahanayake (1983), and Peryt (1981).

Oncoidal shoal facies of the AVL also occur at the very wide depositional realm between the Antelope Valley region and the Toquima Range. Oncoids of the oncolitic packstone and grainstone lithofacies (especially at Martin Ridge, Ninemile Canyon and Lone Mountain sections) consist of complete continuous-concentric laminae and have nearly spherical and elliptical outlines which are supported by interparticle columnar calcite cement. All these criteria probably indicate a moderately-high energy shoal depositional environment. In the Whiterock and June Canyon sections, the oncoids of packstone- and wackestone units consist of continuous and discontinuous, skeletal grain-bearing outer and inner laminae, and gastropods of these units are small, thin-shelled. All these features characterize the open-seaward extended flank of oncoidal shoals, where energy level (i.e., slightly moderate to moderately high energy spectrum) was much lower than the oncolitic shoal formed in Antelope Valley region and Lone Mountain. The common presence of large thick-shelled gastropods, preferably in the oncoidal shoal units of the Antelope Valley region and Lone Mountain sections, suggests that agitation level of the oncoidal shoals was considerably higher than in the oncoidal shoals in the June Canyon and Whiterock Canyon sections. Therefore, from the Antelope Valley region to the June Canyon section, a progressive decrease in the size and abundance of Maclurites provide further evidence to support the westward progressively decreasing-energy level of the oncoidal shoal. Furthermore, this trend suggests progressive increase in the water depth of the

oncoidal shoal.

In the Antelope Valley region, thick-bedded oncoidal shoal lithofacies (consisting of normal-graded thin beds overlying one another with a truncational basal contact and showing fining-upward texture without wave ripples) suggest that deposition of this lithofacies may have taken place under moderately high-energy, storm-dominated open shelf environment. More specifically, physical parameters of this environment correspond to just slightly above or below fair weather-wave base sedimentation. It is possible to suggest that the oncoidal shoal facies formed on the very wide, gentle-slope profile and in the deeper marine environment than that of the Nuia shoal. The oncoidal shoals in places appear to have reached into the skeletal and radial ooid-dominated shoals; however, these periods did not persist because these bars were submerged by a subsequent-sea level rise.

In this formation, water depth of the oncoid-forming shoal probably may have ranged from 6 to 45 meters perhaps even more. As Riding (1977) and Peryt (1981) as well as this study suggest that Girvanella oncoids cannot be independent indicators of bathymetry, or the shallow-water and low-energy environment, but these oncoids indicate a low-sedimentation rate.

The energy level of the Receptaculites-bioherm lithofacies with 6 to 12 m water depth (e.g., Nitecki, 1972) was probably deeper than Nuia shoal facies and shallower than oncoidal subtidal bar facies.

Receptaculites is believed to indicate the position of the paleoequator. This can be inferred from the study of modern, analogous-green algae Bornetella and Nomeris (Nitecki, 1972; Beadle, 1988).

D. Discussion

At Arrow Canyon of southern Nevada, in addition to the Nuia Model, Stricker and Carozzi (1977) put fourth the "algal ball model" (Fig. 35 B) for the oncolitic strata of

this formation. According to them, the uniform slope of the "Nuia Model" was nearly broken down by rapid subsidence below the low-tide level toward the deep-open sea, and as a result, algal subtidal oncoidal bars formed. Stricker and Carozzi (1977) showed that transition from the "Nuia model" to the "algal ball model" took place in a 25-m thick transition zone in which Nuia offshore sand bars were being destroyed and Girvanella and other encrusting algae-predominated oncoidal subtidal bars developed. In the algal ball model as in the Nuia Model, the oncoidal subtidal bars are separated from intertidal algal flat by peloidal bars. Furthermore, in their models, no oncolitic packstone-grainstone facies occur in the Nuia model, and each model excludes the occurrences of lithofacies of the other model. Finally, they suggested that algal balls formed in a moderately high-energy environment which had slightly deeper-and lower-energy conditions than those of the Nuia depositional environment. This study, on the other hand, clearly demonstrated that very close relationships existed between Girvanella and Nuia, in the Nuia-back bars and interbars and, in the lower oncoidal shoal facies. In Chapter 4 and in this chapter (Fig. 35 A.), we have clearly demonstrated that oncolitic packstone and grainstone units commonly occur at the protected side and in the open seaward extension of Nuia bars. In the Ninemile Canyon section, the oncolitic packstone lithofacies is overlain by a 35-45 foot Nuia-bar facies which westward extends into oncolitic packstone- and grainstone units at the Martin Ridge section.

The observations of this study of Nuia and Girvanella-constituted oncolitic lithofacies contradict Stricker and Carozzi's claim concerning total destructions of Nuia during the transition from the Nuia bars to algal ball subtidal bars. The transitional zone described by Striker and Carozzi (1977) represents the drowned and landward-migrated Nuia shoal bars which are gradually overlain by thin-bedded siltstone- and lime-mudstone interlayers or by parallel-laminated, silty quartz-rich lime mudstones. The cyclical repetitions of these units suggest that multiple events of short durational, sea-level rise might have been responsible for the replacement of Nuia-dominated shoals by Girvanella-dominated oncoidal shoals (Fig. 35 A) rather than a single event of subsidence. The Nuia shoal bars, overlying the oncoidal shoal

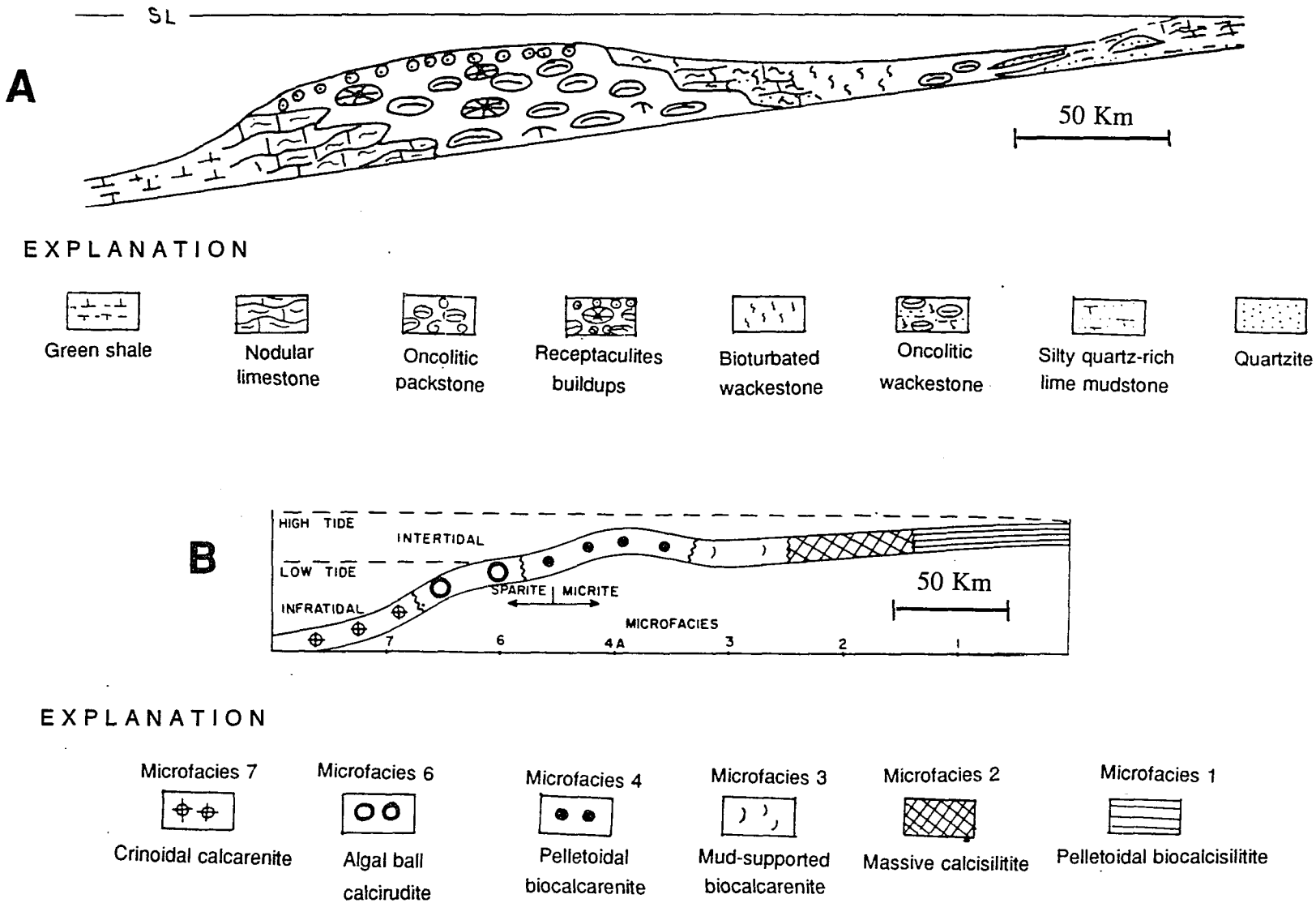


Figure 35- A) Suggested-oncoidal shoal model of this study; B) "Algal ball model" of the oncoidal shoal by Stricker and Carozzi (1977).

units (the Palliseria zone) and gradually changing into the oncoidal shoal bars, suggest that these reconstructed-Nuia bars represent the "Catch Up" phase of the Nuia shoal which extended gradually westward into the relatively deeper oncoidal subtidal shoal environment. Therefore this study clearly shows that these two-depositional environments coexisted during the Orthidella and early Palliseria zones on the N- to S-extending shelf margin in which oncoidal shoal occurred in relatively deeper and lower-energy open- sea environment than those of Nuia shoals. However, during the late-early Palliseria zones, Girvanella, and Receptaculites, with other encrusting algae, dominated the carbonate-shelf margin. In the Lone Mountain and Keystone Canyon sections, the formation of oncoidal shoals very rapidly terminated the existence of the Nuia shoals.

In short, this study suggests that the dominance of these shoals by Nuia and Girvanella was chiefly controlled by the energy level of the environment and relative sea level and the ability of organisms to adapt to indicated changes. This study has interpreted the parallel-laminated lime mudstone units as subtidal lithofacies that formed in a deep middle shelf behind the oncoidal shoal but not in the intertidal-algal flats. According to Stricker and Carozzi (1977), these parallel-laminated, fine-grained siliciclastic lithofacies represent the intertidal algal flat which was separated from oncoidal shoal by peloidal bars. Both Nuia and oncoidal shoals were 250 km away from the paleoshoreline (Ross et al.,1988). In this respect, it is highly unlikely that a 250-km long intertidal flat was separated from the oncoidal and Nuia shoals by the indicated-peloidal intertidal bars.

Taban (1986) and Ross et al. (1989) suggest on the basis of parallel-laminated, fine-grained siliciclastic sediments overlying oncolitic lithofacies that the Girvanella-dominated oncoidal shoal or subtidal bars contemporaneously reached to subaerial exposure. Furthermore, Ross et al. (1989) suggest that contemporaneous karstification presumably was caused by subaerial exposure for the oncolitic shoal lithofacies. Similarly, as suggested by Taban (1986), the occurrences of collapse breccias at the various stratigraphic levels of the Antelope Valley Limestone were also attributed to the dissolution of evaporites during subaerial exposure.

The evidence of this study suggests that indicated parallel-laminated, fine-grained siliciclastic lime mudstone units were not the intertidal-supratidal algal flat deposits. The following criteria, such as absence of birdseye texture, desiccation cracks, algal flat-pebble conglomerate, and evaporite minerals, substantiate the suggestion of this study. It is clearly seen that the parallel-laminated, silty quartz-rich mudstone subunits overlying oncolitic packstone units probably led to this misinterpretation in Taban's (1986), and Ross et al. (1988) studies.

This study also noted that breccias occur in the various stratigraphic levels of the AVL not only in the Palliseria zone but also in the Orthidella and Anomalorthis zones, closely associated with fault-controlled epigenetic dolomitization and dissolution features (see Chap. 13 B).

As indicated before, the oncoidal shoal briefly may have reached the tide-dominated, high-energy shoal environmental conditions. However, this shoal represents storm-dominated, incipiently drowned shoals below the normal-weather wave base. The fining-upward texture, marine columnar calcite cement, undisturbed parallel laminae in the upper mudstone units, and the absence of any features of subaerial exposure are the lines of evidence supporting our findings. With respect to this, the Girvanella shoal of this formation can be analogous to the incipiently drowned Serrinella Bank in Nicaragua which occurs in 10 to 60-m water depth from the low-tide sea level and on which Thalassia, Halimeda, and other encrusting algae and sponges flourish and have constructed the carbonate bank.

On the basis of diverse algal flora and predominance of Receptaculites, this study suggests that the deposition of the Antelope Valley Limestone (AVL) may have occurred in the tropical region (e.g., Nitecki, 1972) rather than a subtropical region and arid climatical conditions. This conclusion concurs with Ross's (1977) findings in about deposition of this formation 10 ° south of the equatorial region.

CHAPTER 6: OOLITIC AND SKELETAL SHOAL

A. Areal and Vertical Relations of the Oolitic and Skeletal Shoals

In the Martin Ridge section, the oolitic shoal facies change eastward into the oncoid-rich, crinoidal packstone and grainstone lithofacies of the skeletal shoal at the Ninemile Canyon section (Fig. 36; Appendix I-B).

The oolitic and skeletal shoal lithofacies, with the overlying bioturbated-wackestone units demonstrate shallowing-upward cyclical features. The shallowing-upward cycles overlie one another with a sharp erosional basal contact (Figs. 36, 37; Appendix I-B). In addition, the relatively low-energy backshoal units of the Ninemile Canyon section are correlative with the high-energy shoal units of the Martin Ridge section. For instance, at interval of 805-816 feet, the oolitic and peloidal shoal lithofacies, overlying the first stromatolitic lime mudstone lithofacies, are correlative with the bioturbated-oncoidal packstone to wackestone lithofacies at Ninemile Canyon section (Fig. 37; Appendix I-B).

The basal components of the shallowing-upward oolitic and skeletal shoal cycles are the oolitic and skeletal packstone- and grainstone units. A complete sequence of the basal component of these cycles includes the following gradually changing sublithofacies, in ascending order: bioturbated-oncoidal wackestone and packstone; dark gray crinoidal packstone and grainstone with oncoids; skeletal and peloidal packstone and grainstone; oolitic packstone and grainstone (as bar-crest subfacies of the oolitic bars); skeletal and peloidal packstone and grainstone, crinoidal packstone to grainstone; and skeletal and oncoidal packstone to wackestone. In addition to typical litho-stratigraphic order of the oolitic and skeletal shoal facies, locally, the large Maclurites-rich oncoidal packstone- and grainstone units overlie the oolitic grainstone- to packstone units with a concave upward, sharp erosional contact. Similarly, in places

the dark gray oolitic and peloidal grainstone units, with varying thicknesses, overlie light gray crinoidal grainstone units with a concave upward, erosional contact. In the Martin Ridge section, the dark gray radial-oolitic units are locally overlain directly by the admixtured-oncoid and radial ooid-dominated packstone to grainstone units at the lowermost part of the oolitic shoal facies (Appendix I-B).

In the Martin Ridge section, the oolitic packstone- and grainstone units (as bar crest subfacies) are laterally (parallel to the strike of paleoshoreline) continuous, and their thicknesses vary between 4 and 7 feet. However, the same lithofacies in the lower part of the same vertical section appear to be laterally discontinuous.

The geometry, thickness, stratigraphy and constituents of the oolitic grainstone units of the Martin Ridge section are different from those of the oolitic and skeletal shoal units at the Lone Mountain and Ninemile Canyon sections (Appendix I-B). For instance, in both sections (without indicated internal order), the oolitic shoal units are thinner and more skeletal-rich in the Ninemile Canyon section compared to the oolitic shoal units of the Martin Ridge section. In the Ninemile Canyon section, at interval 887-904 feet, about four-feet thick, dark gray, bioturbated-oolitic packstone units are overlain by a sharp erosional basal contact of the oncoid and gastropod-rich crinoidal grainstone units (Fig. 36; Appendix I-B).

Another important oolitic shoal facies in the Ninemile Canyon section occurs in the lower and middle part of the Anomalorthis zone where this shoal facies unconformably overlies the very thick, algal-flat deposits of intertidal and supratidal deposits at intervals of 1165-1186 feet (Fig. 37; Appendix I-B). The lower part of this shoal facies is the oncoidal and skeletal packstone lithofacies (a 7-foot thick) and gradually changes upward into the oolitic packstone- and grainstone units. These shoal units of the Ninemile Canyon section are correlative with the peloid-rich skeletal packstone- and grainstone facies of the Anomalorthis zone at the interval of 877-928 feet in the Martin Ridge section (Fig. 37; Appendix I-B).

In Lone Mountain, the oolitic lithofacies is present only at two-stratigraphic levels (from the base of this section): (a) at interval of 352 and 358 feet, dark gray, oncoid-rich skeletal and oolitic grainstone overlying the oncoidal packstone lithofacies;

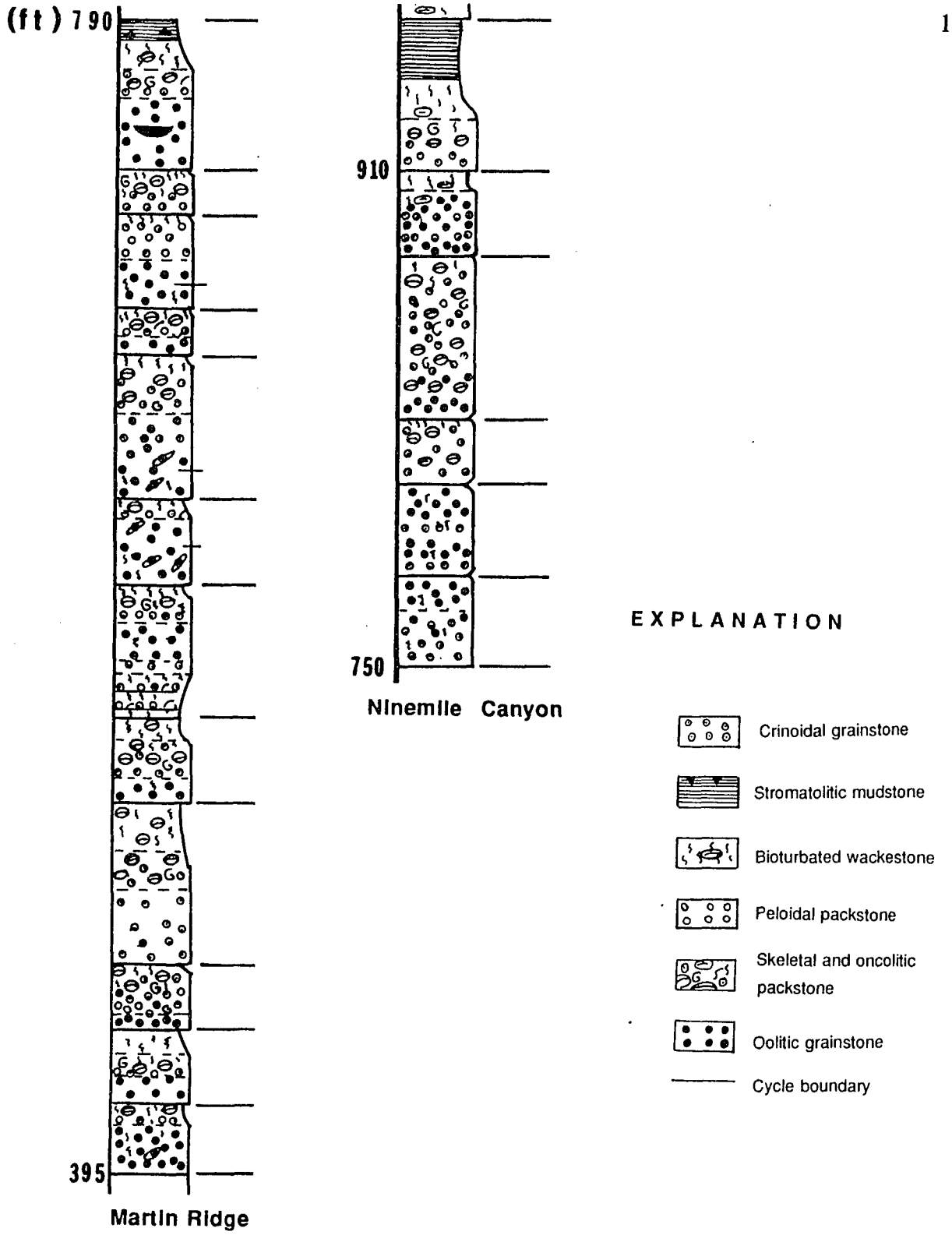


Figure 36- Vertical columnar sections in Ninemile Canyon and Martin Ridge sections showing successions of shallowing-upward oolitic shoal cycles and related lithofacies.

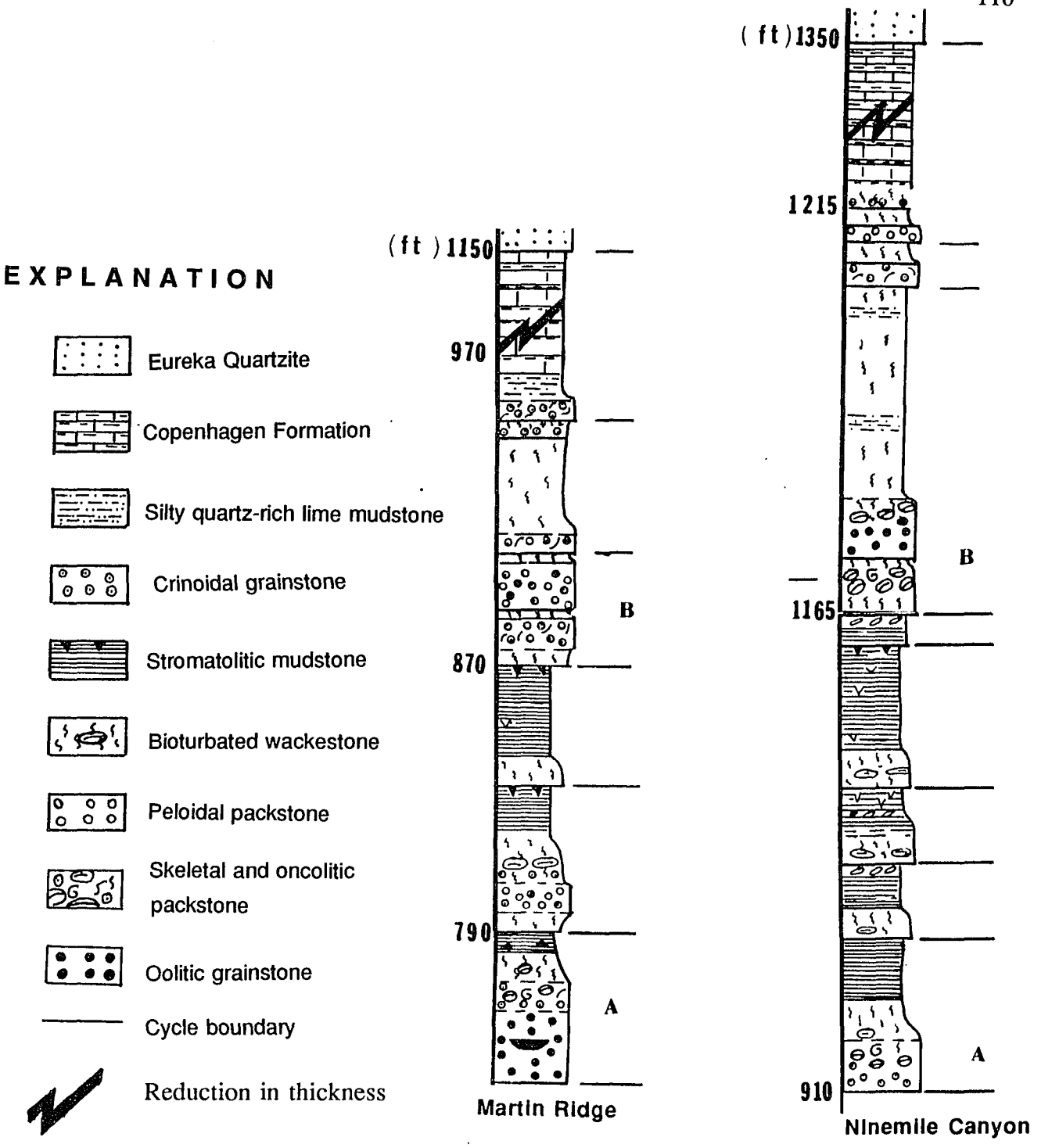


Figure 37- Vertical columnar sections show the oolitic and skeletal shoal units of the upper Palliseria and lower and middle Anomalorthis zones. A) Succession of algal flat-capped oolitic shoal cycles at the upper Palliseria zone and the lower Anomalorthis zone. B) Oolitic and peloidal shoal cycles of the middle and upper Anomalorthis zone unconfomably overlie algal flat deposits and are capped by well-circulated middle shelf lithofacies which are separated from the lagoonal Copenhagen Formation by peloidal nearshore bars.

and (b) at interval of 240-252 feet, the oolitic grainstone overlying the 10 to 12-feet thick crinoidal grainstone unit of the Orthidella zone (see Chap. 4; Appendix I-B).

Unlike other sections, in the Martin Ridge section (approximately one mile south of this type section), a 45-foot thick of bioturbated-Nuia packstone lithofacies directly overlies the oolitic packstone- and grainstone lithofacies at the intervals where the first oolitic shoal units began to form (Fig. 38 A, C). However, this feature is not found in other type sections of the Antelope Valley region.

B. Lithofacies

Lithofacies 7: Oolitic Grainstone and Packstone

Description:

Thick bedded, oolitic packstone- and grainstone units comprise numerous thin-bedded, low-angle cross beds or foresets dipping with 15°-19°. The thin foresets are composed of predominantly either dark gray ooids or light brown ooids (Fig. 39 A). The light brown ooids are predominant in the uppermost part of the oolitic grainstone units. However, the dark gray ooids are commonly predominant in the lower levels of the same lithologic units. A transitional zone occurs between these two prominent oolitic shoal subunits and includes alternating light brown ooid-dominated foresets and dark gray ooid-bearing foresets as well as mixed-ooid layers subunits. The dark gray ooids are radial ooids. On other hand, the light gray to light brown ooids are calcitized and composed of intraooid-calcite cement. thin, low-angle, The light-brown ooid-bearing strata change gradually upward into bioturbated, mixed-peloidal and skeletal grainstone- and packstone subunits (Fig. 39 B).

Commonly, in the lower and middle parts of the light brown ooid-bearing subunits and transitional zone, the dark gray lenticular intraclasts (1-5 cm length and 1-3 cm

Figure 38- Field view of oolitic shoal bars and polished slab of Nuia packstone from oolitic backshoal facies. A) View of fault-displaced Nuia shoal units (n) formed behind oolitic shoal bars (a). B) Steep and cliff-forming oolitic packstone- and grainstone units (a) overlying backshoal facies of the preceding shallowing-upward oolitic shoal cycle (s). C) Polished slab of intensely bioturbated-Nuia packstone lithofacies representing sand-flat facies behind oolitic shoal; arrowheads point to burrows filled by yellow-brown silty quartz-rich mud. Penny for scale.


C


A
a


B
s
a

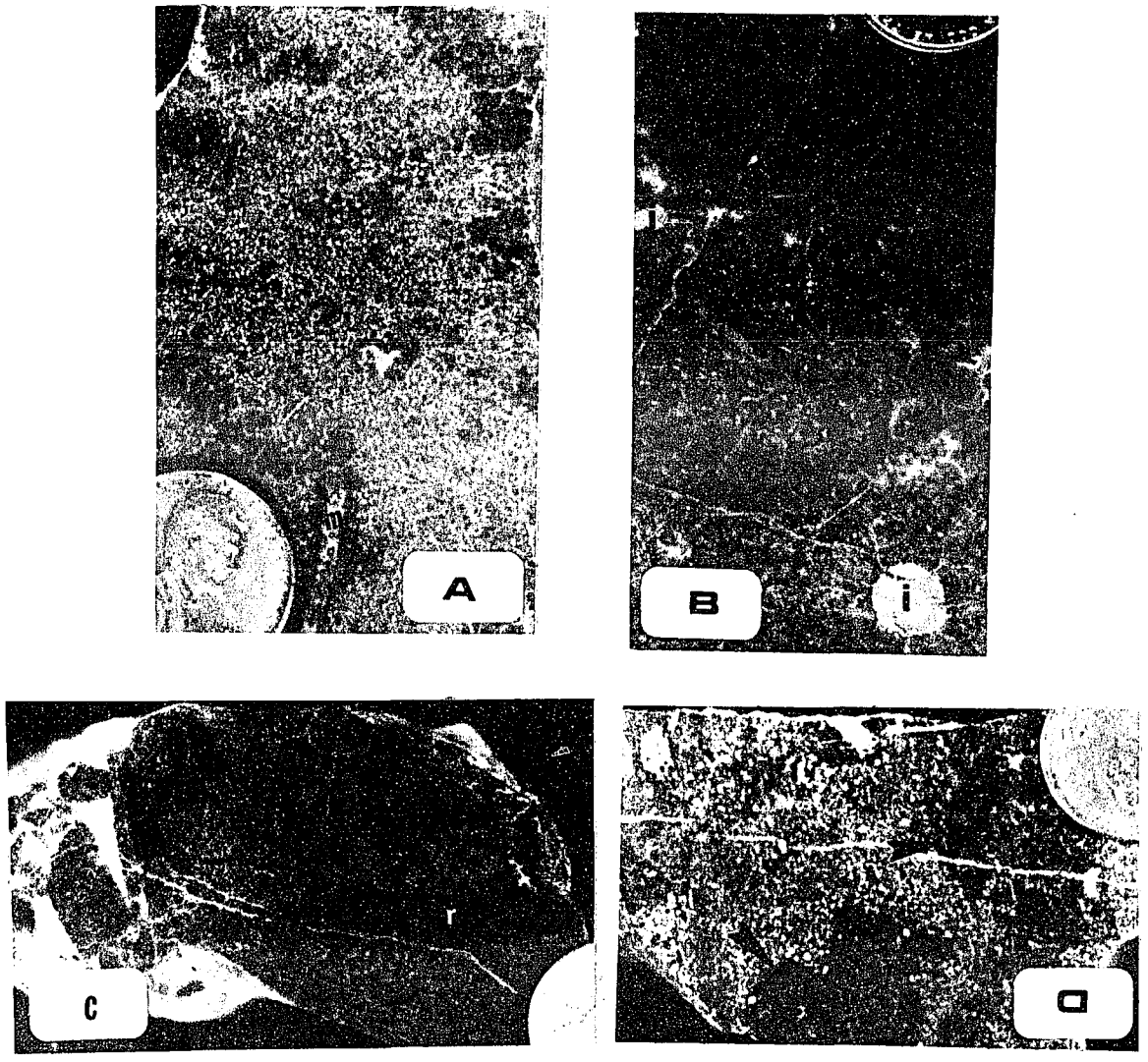


Figure 39- Polished slabs of oolitic packstone- and grainstone lithofacies. A) Polished slab of the oolitic packstone- and grainstone lithofacies shows dark gray radial ooids within the light brown gray ooid-dominated oolitic subunits. B) Light gray ooids are scattered within the dark gray peloidal packstone which gradually overlies the oolitic packstone- and grainstone lithofacies and consists of well-rounded yellow intraclasts (i). C) Patchy dark gray ooids (r) within the radial- and calcitized ooid-mixed oolitic subunits. D) Dark gray intraclasts (i) within light gray, calcitized ooid-dominated subunits. Arrowheads indicate a sharp contact between dark gray radial ooid-constituted intraclasts and the light gray ooid-dominated subunit. Pennies for scale.

thickness) occur with their longer axes parallel to the bedding planes. These dark gray intraclasts consist of predominantly radial ooids with and without yellowish-green mud (Fig. 39 C, D). In addition to dark intraclasts, dark gray radial ooid patches with irregular boundaries are also found in the light brown ooid-predominated strata. Intraclasts display straight and sharp boundaries. Planar, oxidized-hardground surfaces are more common in the dark gray oolitic units than in the light brown ooid-bearing strata. The uppermost radial ooid-bearing layers include dispersed-light brown ooids in minor concentrations (Fig. 40 A); whereas dark ooids are most commonly scattered into the light brown ooid-dominated zones (Fig. 40 B).

Most light brown ooids are filled by calcite spars (Fig. 40 C, D) which are commonly replaced by late ferroan dolomite (Figs. 40 B, 41 A). Commonly, large light brown ooids appear to be filled by single, sparry calcite crystals, or by several twined calcite crystals; however, these intraooid-calcite crystals do not exhibit any dissolution and drusy void-filling features (Fig. 40 C, D). Within the light brown ooid-bearing units, the equant blocky and bladed-interparticle calcite cements are the most common cement type in addition to intraooid-calcite cements. But the void-filling, radiaxial-fibrous and cryptocrystalline calcite cements are absent in these light brown ooid-bearing subunits.

Grain size of the radial ooids usually ranges from 0.4 to 0.6 mm, and some large radial ooids even reach up to 0.8 mm (Fig. 41 B). Grain size of calcite-filled ooids occurs in the range of 0.2-0.8 mm with an average of 0.5 mm. Dark gray radial ooids are usually composed of micritic cores which are similar to the micritized-Girvanella fragments and which rarely include Nuia as a nucleus. Exceptionally, skeletal fragments are found as nuclei in radial ooids which are similar to superficial ooids (Ball, 1967). Generally, in this packstone- and grainstone lithofacies, the radial ooids are better sorted than the light brown ooids (Fig. 41, D).

The dark gray radial ooids commonly exhibit radial fractures (cracking), as described by Halley (1980) for the Great Salt Lake ooids. Some radial ooids have a relatively larger grain size (approximately 0.7 mm) than the average grain size, and these larger ooids in addition to their radial coatings are completed by several

Figure 40- Photomicrographs of oolitic packstone and grainstone lithofacies. A) Well-sorted radial ooids with a few partially dolomitized, light gray ooids indicated by arrow; arrowheads indicate iron-oxide staining and microdolomite rhombs at the center of radial ooids. B) Equally mixed radial- and calcitized ooids (c); selectively dolomitized-calcitized ooids (d). C) Bimodal ooid; arrowhead indicates the outer radial coating around irregular outline of tangential-calcitized ooids. D) Stylolite (arrow) developed along calcitized ooids indicated by arrows; arrowhead indicates the partial micritization of ooid-filling calcite cement, and this micritization postdates the ooid-filling calcite cement and replacive ferroan dolomite. With plane-polarized light; scales= 0.5 mm.

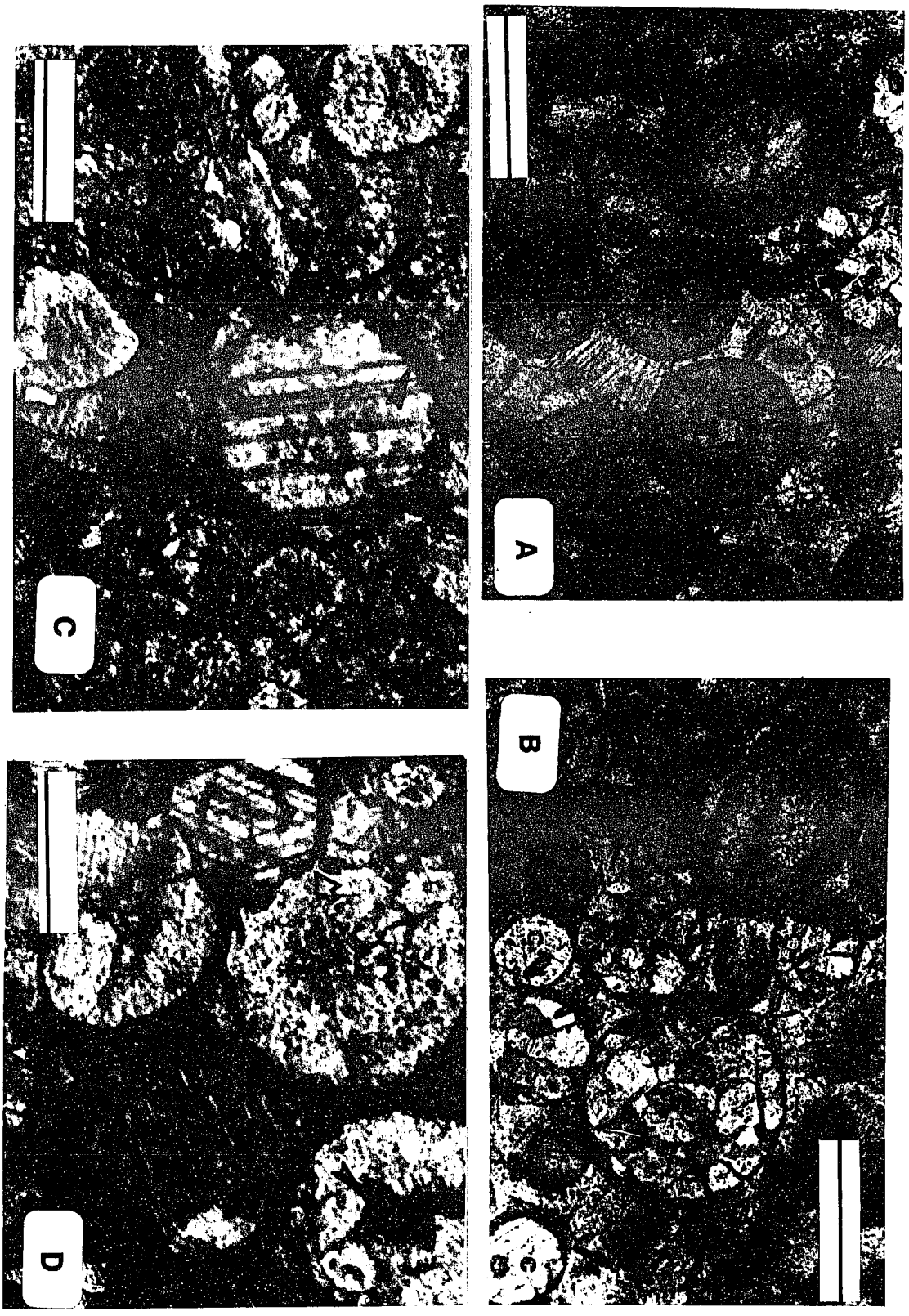
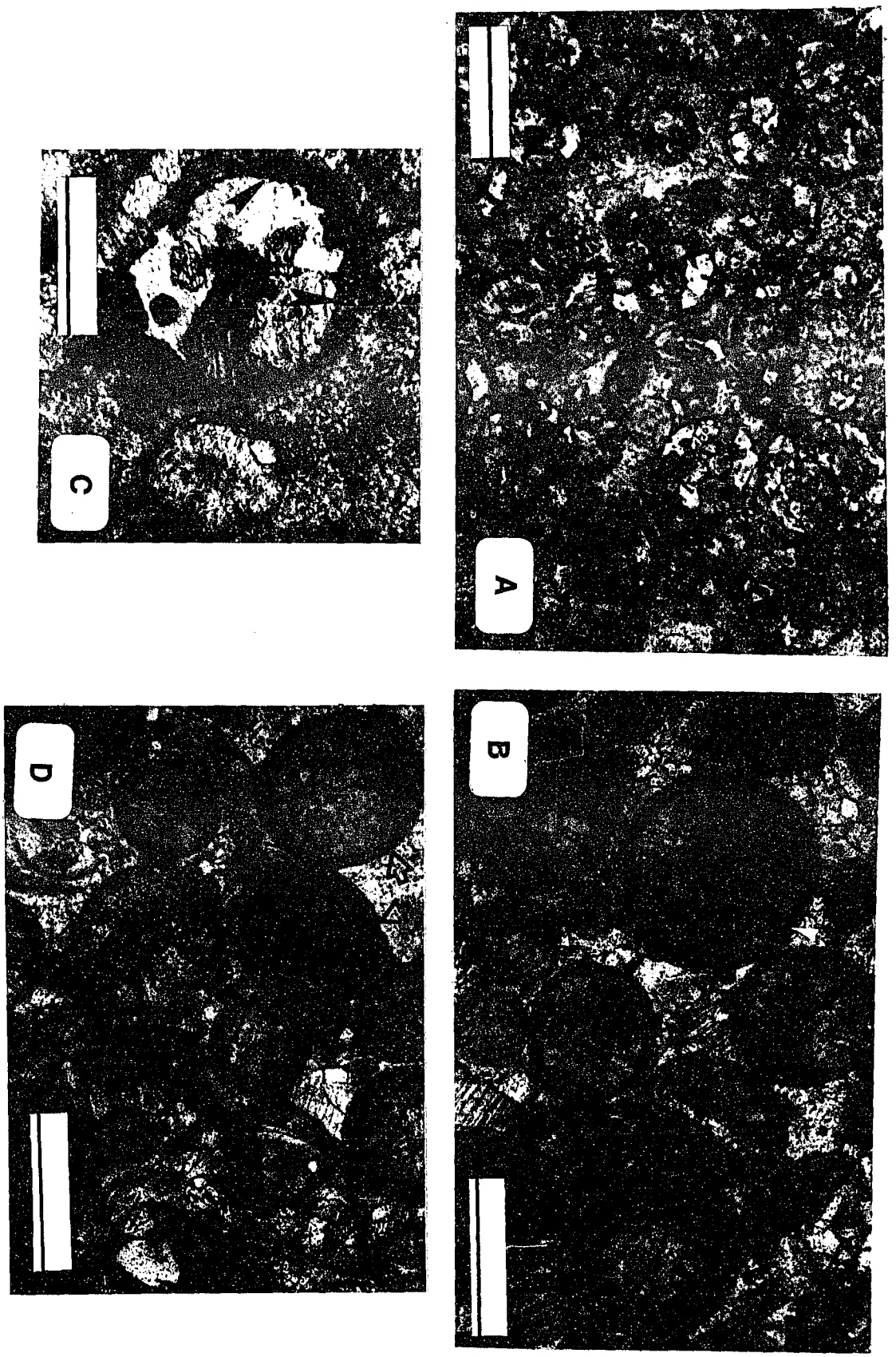

A
B
C
D

Figure 41- Photomicrographs of radial ooid- and calcitized-tangential ooid-dominated oolitic grainstone subunits. A) Selectively dolomitized calcite-filled ooids. B) Well sorted, radial ooid-dominated oolitic grainstone subunit; bimodal ooids are indicated by white and dark arrowheads: a) the largest radial ooid has concentric calcite coating or lamina pointed by white arrowhead; and b) the second largest ooid has a calcitized core with a truncational outline followed by radial coating. C) Photomicrograph of a bimodal ooid. A calcitized ooid with an irregular outline were coated by radial cortices. D) In the radial ooid-bearing sublithofacies, some ooid contains large skeletal fragments (artificial ooids) indicated by arrowhead, and arrows indicate the replacement of interparticle cement by syntaxial overgrowth of a crinoid. With plane-polarized lights; scales = 0.5 mm.


A
B
C
D

calcitized- or micritized-concentric laminae on the truncated outlines of inner ooids (mostly radial ooids; Fig. 41 C, D).

The relict of original texture of radial ooids is preserved despite their high-degree of neomorphism and dolomitization. Red to yellow brown-iron staining and euhedral microdolomite rhombs are also very common at the center of the radial ooids (see Fig. 89 B in Chap. 12 A). Unlike euhedral microdolomite rhombs, late diagenetic ferroan dolomites replaced the radial calcite crystals of these ooids. The isopachous- marine, cryptocrystalline (micritic), and radiaxial-fibrous cements are commonly seen in dark gray radial ooid-bearing substrata (Fig. 42 A). Moreover, the dark gray radial ooid-dominated units are composed of small amount of pellets, ostracods, crinoids, and superficial ooids.

In general, the composition of this packstone- and grainstone lithofacies symmetrically grades upward and downward into peloidal and skeletal packstone- and grainstone units and finally into the bioturbated-wackestone units. This trend coincides with progressively decreasing ooid grain size and ooid content in the indicated sublithofacies of the oolitic and skeletal shoal. For instance, skeletal and peloidal oolitic grainstone has only 20-40 % ooids in its composition, but in oolitic grainstone units, ooid content attains 90-95 % of the total allochems.

Interpretation:

In modern shoals, the formation of ooids usually ranges from 1 to 6 meters of water depth (Nevel, 1960; Ball, 1967; Loreau and Purser, 1972; Bathurst, 1975; and Hine, 1977). In modern oolitic shoals, depth of the most favorable ooid-forming environment ranges from 1 and 1.8 m of water depth below tide (Nevel, 1960; Ball, 1967; Bathurst, 1975; Hine, 1977; and Harris, 1979).

Relatively high-energy backshoal and lateral discontinuity of the oolitic packstone- and grainstone units in the lowermost part of the oolitic shoal facies suggest a tidal-bar belt type of shelf margin. In addition, in the Martin Ridge section, a 45 foot unit of

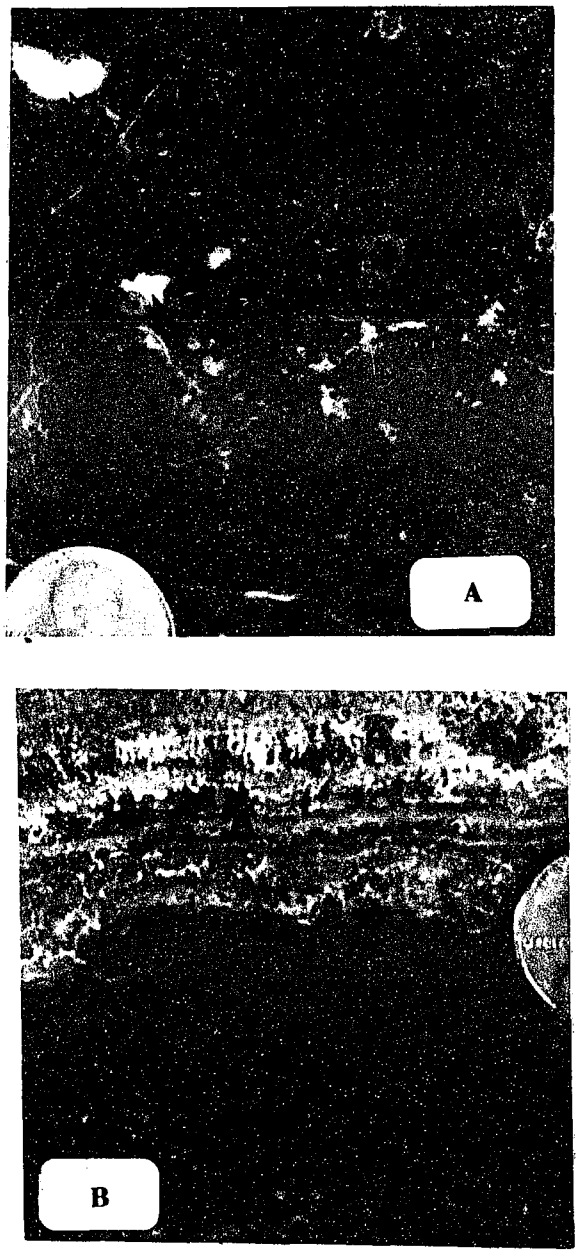


Figure 42- Oolitic and skeletal shoal packstone- and grainstone unit. A) Polished slab of the oolitic grainstone unit; arrowheads indicate radiaxial calcite cement primarily within radial ooid-bearing subunits. In this unit, (t) indicates the mixed-calcitized and radial ooids, and (r) represent dark gray radial ooids. B) A polished slab of skeletal and oncoidal packstone. Small arrowheads indicate a truncational boundary between calichified surface and unaltered-part of this unit, and large arrowhead points to parallel, concentric calichified layers. Pennies for scale.

bioturbated-Nuia packstone overlies oolitic shoal facies (Appendix I-B) and laterally grades into the oncolitic packstone lithofacies at the lowermost part of oolitic shoal facies. This lithologic association indicates that a well-circulated back-shoal facies may have existed during the early evolutionary stages of the oolitic shoal. This shelf margin configuration of the Antelope Valley Limestone (AVL) shows similarity to that of modern-tidal bar belts where oolitic bars are perpendicular to the paleoshoreline (Ball, 1967; Hine, 1977; and Halley et al., 1983). Therefore, the lateral variations (along the strike of paleoshoal) of oolitic bars in the Martin Ridge section clearly supports the existence of the possible tidal-bar belts at the shelf margin during the transition from the oncoidal shoal to the skeletal and oolitic shoal.

From the early evolutionary stage, the oolitic shoal of the AVL may have gradually evolved into a bank barrier or a marine-sand belt stage during the deposition of the middle and upper oolitic shoals. The evolution of the oolitic shoal facies of the AVL may be comparable to modern oolitic shoals and recent Pliocene-Pleistocene carbonate shoal facies (e.g., Harris, 1979; Beach and Ginsburg, 1980; and Evans, 1984).

The well-sorted, medium to coarse-grained oolitic grainstone units of the AVL indicate a high-energy shoal environment. On the other hand, from the oolitic packstone- and grainstone units to upward and downward progressive increase in bioturbation, matrix-supported texture, pelletal and skeletal grain content as well as decrease in ooid content and their size suggest that the energy level of the oolitic shoal appears to have ranged in a very broad energy spectrum. These textural and compositional changes imply that the energy level of the oolitic shoal decreased progressively either from the oolitic bars to windward or to leeward during the deposition of this lithofacies. Similarly, in the contemporary marine-sand belts, the energy level of the oolitic shoals decreases gradually to open seaward and leeward from the active mobile sands. This trend is reflected by the increasing skeletal grain content, bioturbation rate, altered-nonskeletal grains (peloids), and pellets (Ball,1967). All these gradual textural and faunal changes clearly suggest that the oolitic shoal facies of the AVL probably formed in the shelf edge which was similar to the modern

mobile sand belts. The syndepositional topography or the crests of the oolitic sand bars appear to have formed parallel to the paleoshoreline and produced a restricted shelf due to their topographies as physical barriers to the advancing, strong-open sea currents and waves.

The thick oolitic shoal lithofacies at the Martin Ridge section, correlative with the skeletal packstone and grainstone units in Ninemile Canyon section, suggest that oolitic shoal facies may have formed at Martin Ridge. On the other hand, the absence of comparable oolitic shoal units in Lone Mountain and southern localities of this formation suggest that the oolitic shoal from the Martin Ridge area may have gradually plunged below the normal-wave base on the N- to S-extending shelf margin trend.

In Lone Mountain, about two-feet thick oolitic packstone- and grainstone units overlying the oncolitic bar facies and the Receptaculites buildups suggest that oncoidal bars and / or Receptaculites buildups had probably produced a topographic high on which skeletal and oolitic shoal conditions were very briefly established by the active tidal currents. The termination of these short-lived skeletal and oolitic shoal conditions can be attributed to rapid sea-level rise. Consequently, the oolitic or skeletal shoal environment turned into to the predominantly open marine, low-energy oncoidal shoal.

About 2 to 6-feet thick oolitic packstone- and grainstone units in the average of 20-25-feet thick shallowing-upward sequences suggest that more frequent sea-level changes and short-lived depositional episodes were responsible for the formation of the oolitic shoal facies of the AVL.

In the Ninemile Canyon section, the crinoidal grainstone units containing yellowish muddy lenses and pebbles, overlying the dark gray oolitic and peloidal packstone- and grainstone with sharp, erosional basal contacts, represent the high-energy storm-induced very rapid sedimentation or the spill-over lobes on the sand flat, or the farther landward-extended subtidal facies of the sand-flat environment. Very scarce bioturbation in this sand flat lithofacies can be correlated with short durational, low-sedimentation periods and following high-frequency, rapid storm deposition.

The intensity of bioturbation in the sand-flat environment is primarily attributed to

sedimentation rate and the duration of non-depositional episodes in the Miami Limestone by Evans (1984). Besides these two-indicated factors, this study suggests that high-frequency rapid deposition by storm events cover and protect the sand-flat environment from the further mottling.

The Maclurites-rich oncoidal and skeletal packstone to grainstone units, overlying the oolitic units with a concave upward sharp erosional basal contact, represent a tidal or axial-channel facies that cross cut the active oolitic sand belt. Similarly, the mixed oncoids and ooids occurring in the same beds probably suggest that oncoids were probably transported by storm floods into the oolitic shoals where these sediments were later reworked by active tidal wave and currents.

Like in modern shoals, thick-bedded, dark gray radial ooid-bearing lower oolitic shoal units probably represent the farther bankward-migrated ripples or sand waves (Ball, 1967; Hine, 1977), which commonly form during major storm events. However, light brown ooid-bearing, thin, low-angle cross-bedded forsets, at the upper part of the each oolitic shoal unit, probably represent post-storm, daily tidal flood- and ebb-dominated bar-crest subenvironments (see Hine, 1977). The low-angle cross laminae 1-3 cm probably represent the slip face or the avalanching facies of ripples at the crest of the oolitic bars.

In the modern oolitic-carbonate shoals, the locally isolated firm-grounds or the crust zones, about two to three meters in diameter, and large clasts from the fragmented crusts are the common occurrences in the Cat Cay and Shooner Cay described by Ball (1967) and by Dravis (1979), respectively, and in the Lily Bank by Hine (1977). These occurrences are cemented-oolitic crusts that are commonly present everywhere in the depth range from 1 to 11 m except at the continuously agitated oolitic bar crests and proximity areas (Dravis, 1979).

In this packstone- and grainstone lithofacies, the radial ooid-constituted intraclasts are probably the erosional remnants of the hardground crusts that can be inferred from their very thin and considerably longer axes. These clast forms characterize the downward-decreasing lithification of the hardground surfaces. The hardground surfaces generally signify the lithified surfaces before the deposition of the upper units or

sedimentary layers (Bathurst, 1975). Like in the modern active sand shoals, the oolitic crusts of this formation represent the low-energy oolitic shoal where the radial ooids were probably stabilized by the algae and marine-phreatic cements. Therefore, these dark intraclasts in the mixed-dark gray and light gray (brown) oolitic packstone- and grainstone units represent the fragmentation of the crusted surfaces or hardgrounds (Fig. 43 A). The high-energy storm currents must have been responsible for the breakage and transportation of the crusted surfaces to the active shoal facies where these intraclasts were likely to be reworked and redeposited by active tidal wave and currents.

At the open seaward-extended, low-energy oolitic shoal of the Antelope Valley Limestone, the radiaxial-fibrous cement, cryptocrystalline calcite cement and baffling and colonization by Girvanella indicate the early syndepositional lithification and stabilization of the oolitic sand bodies. From this low-energy shoal, the fragmented crusts, semi-lithified fragments, and unlithified-radial dark ooids were transported into the active bank or shoal.

In modern oolitic shoals, aragonitic tangential ooids are the predominant ooid forms; however, the formation of radial ooids is very rare. Radial ooids form in the low-energy subtidal modern shoal environment in the Persian Gulf (Loreau and Purser, 1972); with oncoids in the hypersaline pools of the Red Sea by Friedman et al, (1973; 1985), in Baffin Bay by Land et al.(1979); in the Great Salt Lake by Erady (1958) and Khale (1977). Radial ooids found in all modern carbonate shoals are aragonitic in composition except for ooids of the Baffin Bay, Texas, where radial ooids are high-Mg calcite in composition (Land et, al. 1979). Therefore, it is widely believed that the formation of the aragonitic radial ooids probably has close association with the hypersaline environments. The high-Mg calcite composition, red-iron staining and micron-size dolomite rhombs are common in relic radial ooids which were found along the Australian and Amazon coasts (Brazil), respectively by Marshall and Davies (1975) and Milliman and Barretto (1977).

Loreau and Purser (1972) have shown that in the high-energy environment, grain to grain collisions with strong impacts are responsible for the formation and growth of

tangential ooids in which fibrous aragonite crystals are arranged parallel to concentric envelopes. However, in the radial ooids, aragonite rays grow perpendicular to concentric envelopes and result from the weaker collisional impacts in the relatively less-agitated shoal environment (Loreau and Purser, 1972). Relatively common fragmentation and radial cracking of radial ooids result form the weak crystal support (centerward) of the radial-fibrous aragonite growth in the radial ooid structures, as suggested by (Halley, 1977) for the Great Salt Lake ooids.

In the oolitic packstone and grainstone lithofacies of the AVL, the radial ooids with preserved original textures, despite intensive neomorphism and diagenesis, appear to represent original high-Mg calcite ooids. The textural preservation of Mg-calcite allochems and disappearance of the aragonitic allochems during the transformation of high-Mg calcite and aragonite to low-Mg calcite in the meteoric diagenetic environments have been illustrated by Friedman (1964) and later by Sandberg (1983; 1985). In addition, Rich (1982) has shown that the calcitized mosaic patterns in concentric envelopes of ooids result from the replacement of aragonitic ooids by low-Mg calcite rather than dissolution of original grain and precipitation of low-Mg calcite. The light brown ooids with sparry-calcite fillings or neomorphic replacement in the AVL are most likely to be the original aragonitic ooids of high-energy shoals. The coexistence of radial ooids and calcitized ooids (interpreted to be aragonitic ooids) have been reported in many ancient oolitic shoal lithofacies by Wilkinson et al (1979), Moore and Druckman (1980), Simone (1980), James and Klappa (1983), Tucker (1984), Sternbach and Friedman (1984), Chow and James (1987), and Swiryduczuk (1988).

In the Late Cambrian Conasuga Formation, Sternbach and Friedman (1984) related the coexistence radial and tangential ooids to hypersaline environments on the basis of microdolomites at the center of radial ooids, authigenic quartz crystals interpreted to be pseudomorphs of previous evaporite minerals, and common presence of radial ooids.

The oomolds along with sparry calcite-filled ooids (originally aragonitic ooids) and calcitic radial ooids occur in the different intervals of the Platsburg Limestone in

Kansass (Wilkinson et al., 1984). The different ooid-type dominated strata and the formation of each ooid type in different intervals have been considered to represent, respectively continental emergence, or low-sea level stands for aragonitc ooids and high-sea level stands for calcitic radial ooids (Wilkinson et al., 1984).

In the Smackover Formation of Jurassic, Moore and Druckman (1981) and Swiryduczuk (1988) have reported that two basic ooids and ooid-bearing strata are separated in space, such as (1) the oomold-dominated oolitic strata (originally aragonitic) in the north representing the paleo-shoreward depositional environment, and (2) radial ooid-bearing strata in the south representing the open seaward environment.

Like in the Antelope Valley Limestone, Tucker (1984) and Chow and James (1987) have noted, respectively, in the Mid-Proterozoic Belt Super Group (Montana) and in the Middle and Upper Cambrian platform carbonates in New Foundland, Canada, that the well-sorted radial ooid-bearing lower oolitic shoal units underlie the gray calcite-filled ooid (light brown ooids in this study)-bearing upper oolitic shoal units or sublithofacies which are directly overlain by stromatolites. According to these two studies, the radial ooid-bearing strata to represent a active, high-energy subtidal shoal, and the overlying calcite-filled ooid-bearing strata represent a sand-flat depositional environment in the intra-cratonic shelf margins.

In the Antelope Valley Limestone (AVL), the light brown ooid-bearing strata are gradually overlain by the skeletal or skeletal oncoidal packstone lithofacies of back shoals, but they do not show any associations with stromatolitic mudstone units of the intertidal and supratidal algal flats. Like in the Belt Super Group (Tucker, 1984) and the Middle and Upper Cambrian carbonates (Chow and James, 1987), the dark radial ooids and the related strata are mostly found in the lower oolitic subshoal units of subtidal environment. Furthermore, in this packstone and grainstone lithofacies, more than 70 % of radial ooids consist of algally derived materials (mostly Girvanella derived peloids and even Nuia as nuclei; Fig. 43). Thus, the dark gray or black staining of radial ooids probably represents the algal staining during the decay of the algal filaments of Girvanella. Therefore, the dark gray radial ooid-bearing thick, planar cross-bedded sublithofacies, consisting of pellets and cryptocrystalline cement, and

radiaxial-fibrous cement, indicate the relatively low-energy, deep-oolitic shoal environment where Girvanella favorably colonized and stabilized the active oolitic sands. The occurrence of the radiaxial-fibrous cement along with the cryptocrystalline calcite cement represents the relatively low-energy cementation formed in voids or micro protected-sides of this packstone and grainstone units (see Chap. 12). Moreover, the presence of pellets in the radial ooid-bearing strata also further supports that the radial ooid-dominated sublithofacies of this formation indicates a relatively low-energy, subtidal-shoal depositional environment.

The light brown ooid-bearing subunits -- composed of isopachous marine cement, thin low-angle cross foresets, scattered dark-gray radial ooids, radial ooid- bearing intraclasts--symbolize a high-energy shoal environment. Thus, the light brown ooid bearing subshoal units, consisting of transported radial ooids and radial ooid-constituted intraclasts of low-energy, open-seaward extended shoals, are believed to have formed on the crests of oolitic bars where the turbulence and agitation level was at climax. This energy or turbulence level most commonly produces aragonitic tangential ooids (Loreau and Purser, 1972). As previously suggested, during high-energy storm events, the dark gray radial ooids and radial ooid-constituted intraclasts and semi-lithified patches within the light brown ooid-dominated sublithofacies characterize the sediment transportation from low- energy shoal to high-energy shoal during major storm events. In the transitional zones, alternating radial ooid- and light brown ooid-bearing forsets may have resulted from transportation by tidal flood and ebb-tide currents. Thus, the light brown ooid-dominated lithofacies represent the crests of the oolitic bars which probably produced a physical shield for tidal flood waves and a restricted back shoal. Therefore, in the light brown oolitic sublithofacies, the absence of radial ooids and radial ooid-bearing intraclasts can be correlative with the post-storm sedimentation events in the oolitic shoal of the AVL rather than sand flat deposits.

The coexistence of the radial calcitic and aragonitic ooids in the indicated-transitional sublithologic units between the lower and upper oolitic sublithofacies may suggest that the sedimentary processes were primarily responsible for the formation of

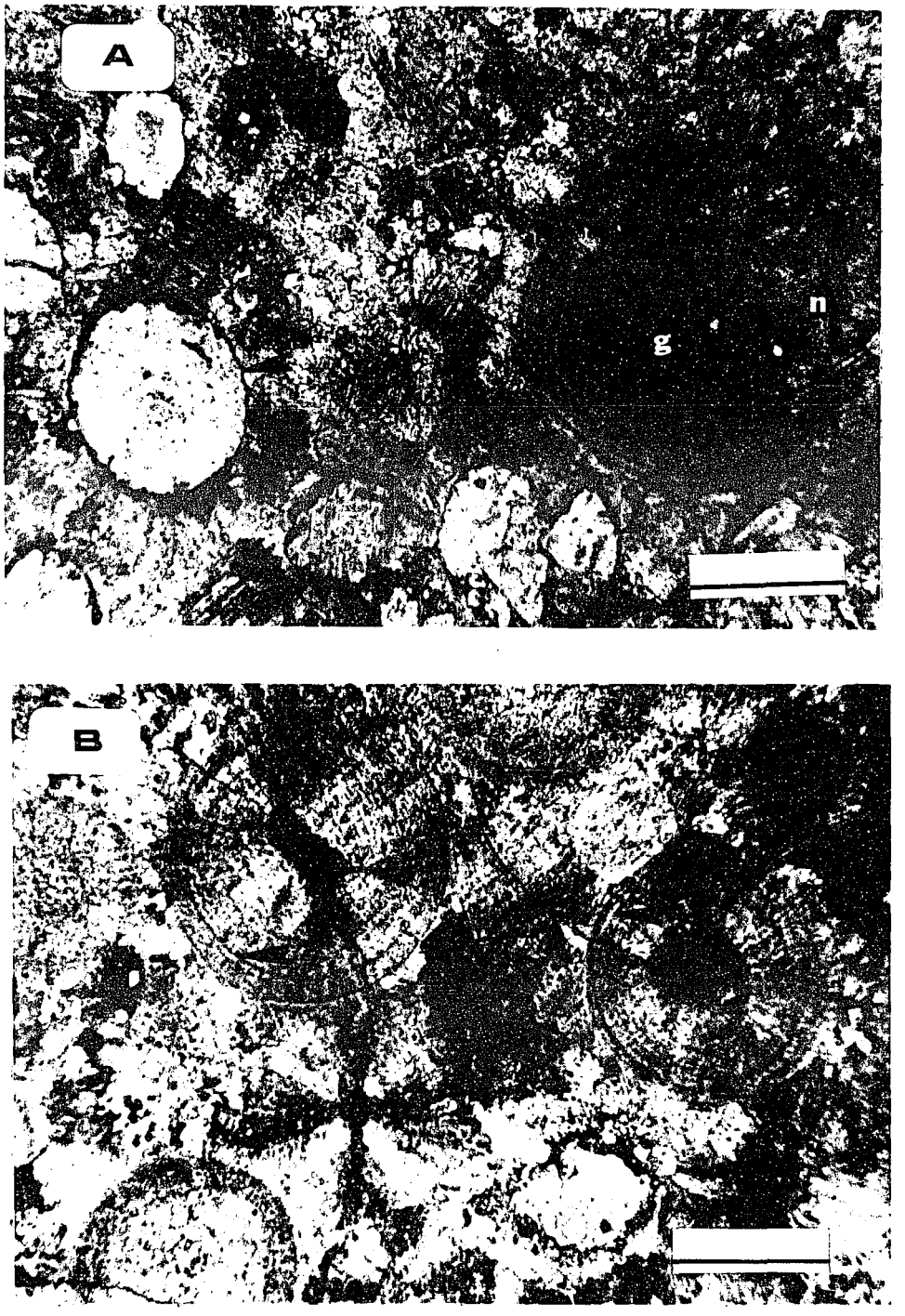


Figure 43- Photomicrographs of radial ooid-dominated grainstone. A) A large radial ooid consisting of dark Girvanella filaments (g) and a Nuia grain (n) as nuclei; arrowheads pointing to calcitized ooids. B) Radial ooids commonly contain a dark algal nucleus or a central core. Arrowheads indicate calcitized-tangential coatings of bimodal ooids along the truncated outline of larger radial ooids. With cross-polarized light; scales = 0.5 mm.

these ooid types and the associated sedimentary structures rather than hypersalinity and sea-level changes. All the evidence presented above suggests that the oolitic shoal of the AVL may have resulted from sedimentation at two subshoals: (1) Algally influenced (i.e., chemical influence by organic acid), low-energy subtidal shoal is assumed to have been linked to a Girvanella-dominated meadow or a shoal on the seaward extended-flank of oolitic bars; and (2) the high-energy, oolitic bar crest. This study suggests that the oolitic shoal settings of the AVL formed an open sea-shelf margin rather than an intra-cratonic shoal.

The influence of organic acids (humic acid) on sea water probably facilitates the formation of high-Mg calcite radial ooids (Davies et al., 1978). The formation of radial ooids and their high-Mg calcite composition have been demonstrated to have a close association with the organic acid and low-energy levels of depositional environment rather than constant Ca/Mg in Baffin Bay, Texas, (Land et al., 1979). On the basis of indicated relations by both studies above, for the AVL, it is possible to suggest that the low-energy, Girvanella- dominated open shoal probably organically influenced the composition of sea water which probably facilitated the formation of radial ooids with high-Mg calcite mineralogy. Especially, for the AVL, the pH level of the low-energy shoal environment (i.e., where radial ooids formed) appears to have been controlled by photosynthetic activity of Girvanella, Receptaculites, Sphaerocodium and other algae.

In this lithofacies, the large radial ooids with truncational outline coated by several outer concentric laminae (e.g. Heller et al 1980; Poncet, 1984) imply that initial radial ooids of the low-energy shoal facies were probably transported into the high-energy shoal environment where outer concentric laminae formed. Similarly, the large sparry calcite-filled ooids with truncational outline followed by two or three radial cortices (Figs. 40 C, 41 C) may suggest that these bimodal ooids (0.8 mm) initially formed in the crest of oolitic bars from which later they were transported into the radial ooid-forming, low-energy shoal either by the storm-counter currents or by the tidal ebbs.

Lithofacies 8: Peloidal Packstone and Grainstone

Description:

Light gray to gray skeletal and peloidal packstone and grainstone lithofacies show similar bedding forms with those of the oolitic packstone- and grainstone lithofacies. The calcite-filled ooids and micritized ooids are also common in this lithofacies. The micritized peloids are similar in size to the well-sorted radial ooids (Fig. 44 A and B). This lithofacies lies above and below the oolitic packstone and grainstone layers, gradually overlies the light brown upper oolitic subunits and grade upward into skeletal grainstone units (Figs. 36, 37). Beneath the oolitic grainstone, this lithofacies is usually thicker and has more crinoids than that of the same unit above the oolitic packstone- and grainstone unit. This peloidal lithofacies generally has more ostracods than the oolitic packstone and grainstone units.

In places, the crinoidal grainstone overlies this peloidal lithofacies with a sharp erosional contact and changes gradually upward into relatively dark gray peloidal packstone units. Yellow brown, elongated-or well-rounded mud intraclasts are locally present in these peloidal lithofacies. Except for color and composition, this peloidal lithofacies has very similar sedimentary structures and bed forms with the overlying underlying packstone- and grainstone units.

The approximated-average constituents of this lithofacies are, as follows: peloids 35-40 %, crinoids 8-25 %, ostracods 3-8 %, pellets 3-5 %, ooids 8 %, brachiopods and molluscs together 5-6 %.

In the Martin Ridge sections, two other distinct peloidal and skeletal packstone and grainstone lithofacies occur in the Anomalorthis zone. The first one occurs at intervals of 805 and 816 feet and is characterized by light gray to tan, thin-bedded units which include some chert nodules (Fig. 37; Appendix I-B). At these intervals, this lithofacies directly overlies the algal-flat deposits and changes gradually upward into the bioturbated wackestone to mudstone lithofacies of the restricted-platform interior lithofacies which grades farther upward into algal- flat lithofacies (Fig. 37; Appendix

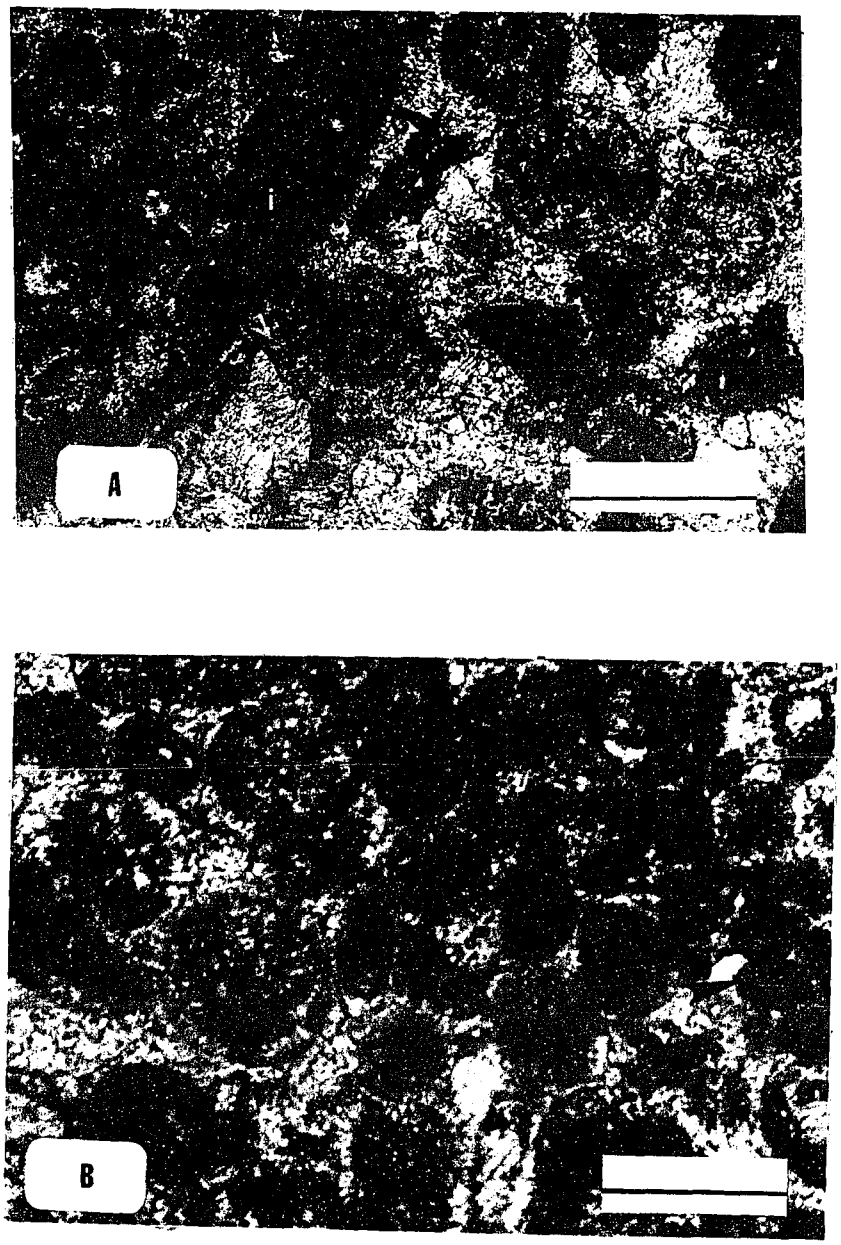


Figure 44- Photomicrographs of the peloidal packstone- and grainstone lithofacies. A) In oolitic grainstone unit, a peloidal intraclast is composed of micritized-radial ooids which are cemented by isopachous calcite cement. B) Peloidal packstone- and grainstone units are primarily composed of peloids or micritized radial ooids. With plane-polarized light; scales = 0.5 mm.

I-B). The second peloidal packstone units occur at the interval of 877 and 928 feet, and are composed of about 8 to 16-feet thick, gray to slightly light brownish gray, tabular cross-bedded skeletal and pelletal packstone units, which alternate with 3-5 feet of bioturbated-wackestone units in a cyclical manner (Fig. 37). These upper skeletal and peloidal packstone sublithofacies (in Martin Ridge) are laterally correlative with the oolitic and skeletal shoal facies at intervals of 1165 and 1186 feet in the Ninemile Canyon. Similarly, the lower peloidal packstone and grainstone sublithofacies is correlative with the bioturbated-oncolitic and skeletal packstone lithofacies directly overlying the stromatolitic mudstone units of intertidal and supratidal facies in the Ninemile Canyon section (Fig. 37; Appendix I-B).

The visual average percentages of constituents of this shoal lithofacies are, as follows: (1) for the lower unit, peloids (micritized ooids) 75-85 %, crinoids 5-10%, other skeletal fragments 5-8 %, glauconite 1 %, ostracods 3 % ; and (2) for the upper skeletal and peloidal shoal, crinoids 35-65 %, peloids 30-35 %, ooids 8 %, ostracods 5 %, and trilobites, brachiopods and gastropods altogether 5 %.

In the peloidal packstone lithofacies, ooids are smaller in grain size (about 0.2-0.3 mm) than the ooids of the oolitic packstone- and grainstone units. The peloids of the upper intervals of the Anomalorthis zone are mostly algally derived grains or Girvanella fragments, but the micritized ooids are most common in the lower peloidal packstone sublithofacies.

Interpretation:

This lithofacies containing more matrix-supported texture and bioturbation than the adjacent oolitic packstone- and grainstone units represents farther shoreward and open seaward extended-flanks of the active oolitic sand bars (e.g., Ball, 1967; Halley et al. 1983). The presence of ooids, as scattered in the skeletal grain-rich peloidal packstone- and grainstone units, indicates that deposition of this unit may have taken place at approximately 6 m of water depth in the shoal (below low-tide level) where ooids

gradually start to form. The increased micritiztion level of ooids due to organic activity and algal interactions (e.g., Ball, 1967; Bathurst, 1975; and Halley et al. 1983) and decreasing ooid content and grain size (Purdy, 1963 b) also suggest a lower energy subtidal environment than that of active ooid-forming shoal.

In the Martin Ridge section, peloidal and skeletal packstone- and grainstone units of the Anomalorthis zone are correlative with the oolitic packstone- and grainstone units of the Ninemile Canyon section. This relationship implies that the peloidal packstone lithofacies of the Martin Ridge section represents the open-seaward extension of the oolitic shoal facies during the indicated period.

Lithofacies 9: Crinoidal Packstone and Grainstone

Description:

Tan to light gray to tan crinoidal grainstone lithofacies is one of the most common lithofacies of the oncolitic shoal and oolitic and skeletal shoal. This lithofacies, in the Martin Ridge section, shows more bioturbation and slightly darker color than in the Ninemile Canyon.

In the oolitic and skeletal shoal, the crinoidal packstone- and grainstone lithofacies in places overlies oolitic and peloidal packstone- grainstone units with a sharp basal contact and gradually changes upward into relatively dark gray peloidal and skeletal packstone- and grainstone units.

In the Ninemile Canyon section, a gradational transition zone occurs at interval of 645 to 685 feet (Fig. 36; Appendix I-B) between
the small Receptaculites bioherms-bearing, crinoid-rich oncoidal packstone- and grainstone units of the oncoidal shoals and the overlying low-angle cross-bedded crinoidal grainstone- and packstone units of the oolitic and skeletal shoals (Fig. 45 A). In oncoidal shoals, two to three feet of thick-bedded, light gray crinoidal grainstone units occur on the top of the oncoidal bars and give rise to the initiation stage

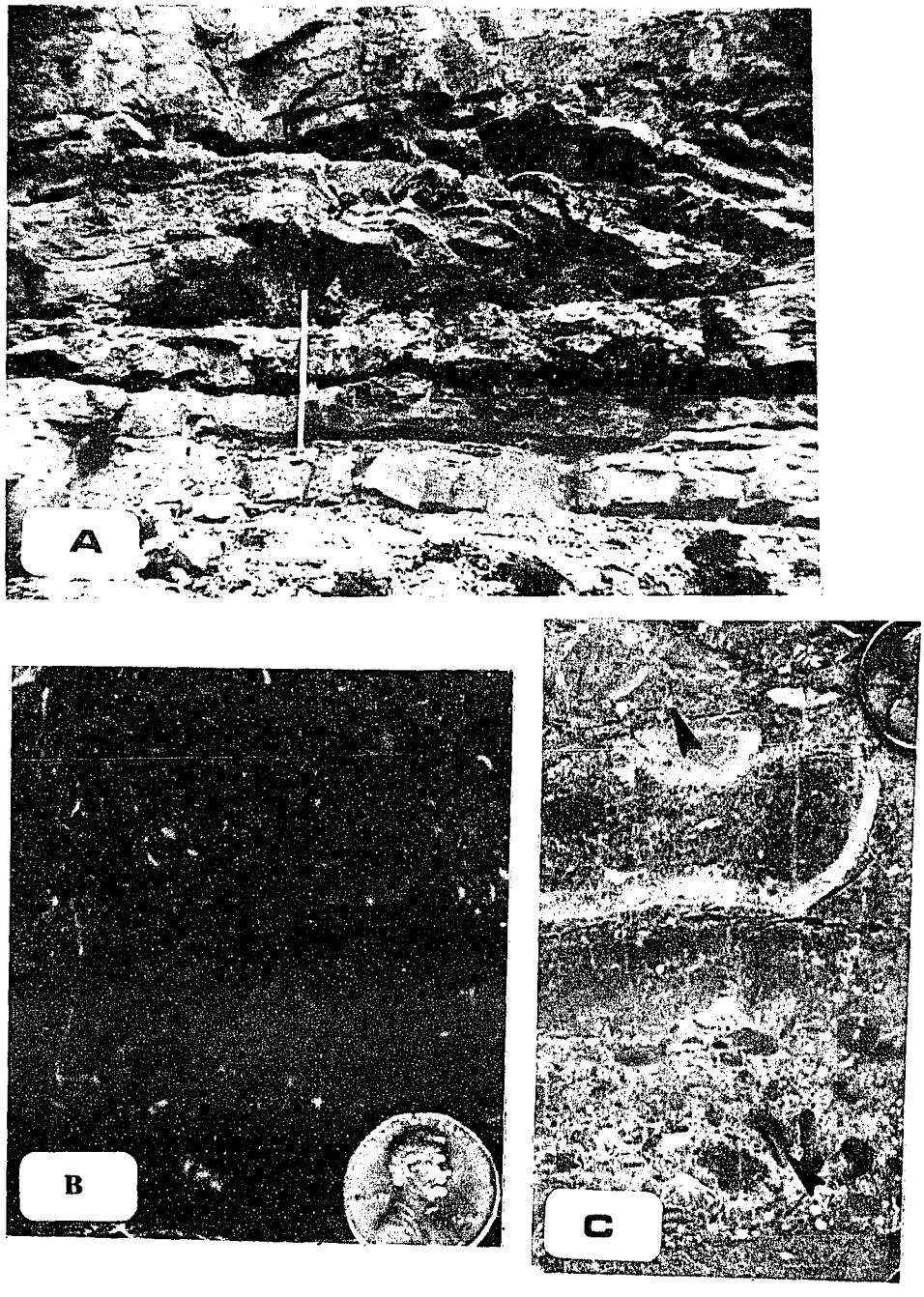


Figure 45- Crinoidal packstone- and grainstone lithofacies. A) An outcrop photograph of the low-angle, cross-bedded crinoidal grainstone lithofacies in the Ninemile Canyon section. B) Polished slab of crinoidal packstone-grainstone lithofacies shows that low-angle foresets formed by alternating crinoidal and oncoidal-rich sublayers indicated by arrowheads. C) A polished slab of the same unit shows that a concave-upward truncational contact separates the overlying, light gray crinoidal packstone- and grainstone unit from the dark gray oolitic and peloidal packstone- and grainstone unit. Penny for scale.

(stabilization and domination) of Receptaculites buildups (see Chap. 5). In addition, the crinoidal packstone- and grainstone units also occur at the top of the micritic, bryozoan-rich upper parts of these Receptaculites buildups, and as the flank deposits, they laterally change into thick-bedded oncoidal bar facies (see Chap. 5). The constituents of this crinoidal lithofacies in the oncoidal shoal and Receptaculites buildups are more algal-rich in composition than those of the crinoidal packstone grainstone lithofacies of skeletal and oolitic shoal. Especially, Girvanella oncoids, Nuia, Sphaerocodium, Receptaculites ossicles are the important algal constituents of this skeletal packstone- and grainstone lithofacies.

In the Ninemile Canyon section, thick-, tabular cross-bedded crinoidal grainstone units comprise a nearly 3 to 4 cm-thick cross-alternating foresets which sometimes are composed of alternating crinoidal packstone- and grainstone foresets and skeletal and ellipsoidal oncolitic and skeletal mixed layers (Fig. 45 C). The crinoidal packstone- and grainstone lithofacies of the Ninemile Canyon section are correlative with the oolitic shoal lithofacies of the Martin Ridge section (Fig. 36; Appendix I-B). In Martin Ridge, in cyclical successions, the light gray and clean crinoidal grainstones overlie bioturbated-wackestone lithofacies of the oolitic backshoal with a sharp and erosional basal contact and gradually change upward into the same bioturbated-wackestone units with a shallowing-upward feature (Fig. 36; Appendix I-B). Some crinoidal packstone- and grainstone units containing yellowish-brownish muddy intraclasts overlie the oolitic grainstone and packstone units with a sharp-erosional contact (Fig. 45 B, D). Furthermore, in the Lone Mountain section, particularly, at the upper Orthidella and lower Palliseria zones crinoidal grainstone gradually overlies the Nuia grainstone unit and gradually changes upward into a 10-foot thick oolitic packstone- and grainstone unit. In this lithofacies, crinoids constitute approximately 65 to 85 percent of whole allochems. Peloids, ostracods, gastropods, brachiopods and trilobites are also commonly present in this lithofacies. The grain size of crinoids varies between 0.15 and 2.5 mm.

Epitaxial overgrowth is the most common cement type in this lithofacies. Grain-boundary pressure solution and dolomitization are also common in the every

intervals of this lithofacies, in which crinoids and brachiopods are selectively chertified.

Interpretation:

Clean, well-sorted and well-rounded skeletal fragments within this packstone- and grainstone lithofacies represent the high-energy depositional environment or the skeletal shoal facies. The lowest level of wave base in shoals (initiation of high-energy Y zone) is widely accepted to be defined by the formation of skeletal packstone- and grainstone units (Irwin, 1965; Heckel, 1972).

In the skeletal shoal, the thick, low-angle tabular-cross beds with a sharp planar basal contact may represent a single, high-energy, storm-induced bedform (Ball, 1967; Bathurst, 1975; and Hine, 1977). In the thick tabular cross beds of this lithofacies, about 1 to 2 cm thick, alternating skeletal grain- and oncoid-dominated foresets (Fig. 45 C) indicate post-stormal reworking by waves and tidal currents.

Relatively dark gray crinoidal packstone / grainstone units at the base of oolitic shoals probably represent a relatively low-energy, deep-skeletal shoal in which the algal activities, and the infiltration of fine-grained sediments into the interparticle space are very common.

In the Ninemile Canyon sections, particularly at the Lower and Middle Palliseria subzones, thick crinoidal grainstone- and packstone units, correlative with the oolitic shoal units in the Martin Ridge, suggest that this eastward-thickening trend of skeletal shoal may have resulted from syndepositional tidal bar belts. These kinds of oolitic shoal-bar patterns likely produce a well to moderately well agitated back-shoal environment (Ball, 1967).

It the Ninemile Canyon section, the Antelope Valley Limestone-- with small Receptaculites buildups (patches) within the crinoidal packstone- and grainstone units--is comparable to the skeletal shoal lithofacies of the Middle Ordovician Rockdell Formation, Tennessee (Ruppel and Walker, 1982), and to the Devonian

Coeymans Formation, New York (Laporte, 1978).

On the other hand, in the Ninemile Canyon section, at the upper Palliseria zone, the skeletal shoal lithofacies are replaced by bioturbated-wackestone units of restricted-shelf facies which are correlative with the oolitic shoal lithofacies at the Martin Ridge section. These indicated relationships clearly show that a major change must have taken place by the evolution of syndepositional oolitic bar topography from the stage of tidal-bar belts to the stage of physical barriers or of mobile sand belts.

Crinoids, suspension feeders like Maclurites, Receptaculites, and bryozoans, usually attach themselves onto substrate and produce stabilized-firm grounds. Consequently, it can be suggested that in the oncoidal shoal facies, the crinoid meadows probably created favorable places or stabilized grounds for Receptaculites and helped Receptaculites to build the bioherms. The crinoidal packstone- and grainstone lithofacies, overlying the uppermost part of the Receptaculites mounds and laterally changing oncoidal lithofacies represent the flank deposits which most likely formed during strong storm events.

The common occurrences of 1 to 5-feet thick, light gray crinoidal grainstone- and packstone units with yellow, elongated mud intraclasts, overlying the oolitic packstone- and grainstone units with a sharp erosional contact, may indicate spill-over fans. In the backshoal and skeletal shoals, spill-over fans or lobes represent the landward movement of skeletal grain transportation by storm-induced currents. Similar phenomena in the modern shoal environments of the Bahama Bank and Florida have been noted during episodic storm events (Ball, 1967; Perkins and Enos, 1968). For instance, Hurricane Betsy's spill-over lobes overlie the pelletal platform interior sediments (Perkins and Enos, 1968).

Moreover, in cyclical successions, locally the crinoidal grainstone lithofacies, unconformably overlying the oolitic grainstone lithofacies and the bioturbated-wackestone lithofacies of backshoal, represent a short durational, relatively high-amplitude rise in sea level.

Lithofacies 5 A: Oncoidal Packstone of Oolitic Shoal

Description:

The brownish gray intraclast-rich oncoidal packstone lithofacies gradually overlies the skeletal packstone or the skeletal and peloidal grainstone units of backshoals. And these packstone units gradually change farther upward into the ostracod-rich, bioturbated- wackestone units of back-shoals.

The Girvanella-coated oncoids are moderately well sorted and rounded within this lithofacies, which is also composed of open marine fauna, and abundant Girvanella-derived intraclasts and peloids. The intraclasts have grain size ranging from 0.15 to 2.5 mm appear to be either derived from oncoids or from the uncoated-Girvanella fragments as bio-lumps. The oncoids of this lithofacies have multiple, symmetrical complete concentric laminae and regular outline, and their grain size ranges from 2.5 to 8 mm.

This oncoidal lithofacies consists of interparticle-rim cement as equant blocky and bladed-blocky cements but not the columnar-calcite cements, which are most commonly present in the oncoidal packstone- and grainstone lithofacies of the oncoidal shoal. In addition, this oncoidal lithofacies of the oolitic and skeletal shoal does not show any fining-upward texture which distinctly occurs in the oncoidal shoal lithofacies.

The approximated-average percentages of constituents of this oncoidal lithofacies are, as follows: oncoids 15-30 %, and intraclasts 20-35 %, peloids 8-25 %; crinoids 10 %, ostracods 8-10%, trilobites and brachiopods together 2 %, unbroken Maclurites 8-15 %, and pellets 5-12 %.

Interpretation:

In this lithofacies, the well-rounded oncoids with their continuous concentric laminae and regular outline, the presence of interparticle-rim cement and thick-shelled large gastropods imply that the formation of these oncoids probably took place in a moderately high-energy environment. The energy level of the indicated environment was strong enough to keep these grains in constant motion and to produce concentric algal laminae, as suggest by Logan et al. (1962). Moreover, like in the AVL, the well-rounded oncoids and ooids coexist at the back and windward flanks of oolitic bars in the Cambrian carbonates in Australia (Young, 1979). This environment may represent a moderately high-energy shoal facies.

The formation of oncoids in the backshoal and in stabilized tidal channels by turtle grass Thalassia has been reported in the modern carbonate environments (Bathurst, 1975, p. 135). This lithofacies appears to represent the modern, oncoid-forming environments. However, the grain-supported texture and the close association with oolitic shoal eliminates this possibility. Moreover, this oncoidal packstone lithofacies directly overlying the oolitic packstone- and grainstone units at the lower oolitic shoal sequence without a sharp erosional contact suggests that the moderately high-energy environment conditions occurred in the backshoal environment during the formation of the early skeletal and oolitic shoals. On the basis of the presence of interparticle-rim cement and the absence of columnar calcite cement and stratigraphic position of this lithofacies, we can suggest that the energy level of the environment (i.e., in the skeletal and oolitic shoal) was probably much greater than those of the oncoidal shoals. Moreover, in this lithofacies, upward-increasing ostracod-, gastropod- and irregular large oncoid contents correspond to a landward-increased restriction at backshoal.

C. Synthesis

In the Ninemile Canyon and Martin Ridge sections, the oncoidal shoal facies gradually changes upward into the skeletal and oolitic shoal facies which dominates the middle and upper Palliseria zones. However, the oolitic and skeletal shoals are absent in the Lone Mountain, Keystone Canyon, and Arrow Canyon (Stricker and Carozzi, 1977) sections and Meiklejohn Peak at the Nevada Test site (Ross, 1977), where Girvanella-dominated oncoidal subtidal bars or shoal facies are gradually overlain by the bioturbated-wackestone lithofacies of the shelf facies. Therefore, the submerged-shelf margin below the normal-wave base characterize the whole Palliseria and Anomalorthis zones at the Lone Mountain, Keystone Canyon, and Arrow Canyon sections and Meiklejohn Peak at the Nevada Test site.

In the Antelope Valley region, the Nuia shoal and oncoidal shoal units coincide with thick skeletal and oolitic shoal units in the same vertical sections. This suggests that the precursor topography might have had a great influence on the localization of the skeletal and oolitic shoal. The elevated topography of the precursor Nuia bars may have fostered relatively high sedimentation rates leading to the formation of oncoidal shoals and Receptaculites mounds. In the Antelope Valley region, high progradation, and sedimentation rates of oncoidal shoals compared to other regions may have been responsible for the establishment and evolution of the skeletal and oolitic shoals.

On the other hand, in the Keystone and Lone Mountain sections, the formation of thin oolitic skeletal shoal lithofacies on the top of oncoidal bar facies and Receptaculites buildups indicates a brief establishment of the initial stage of the high-energy skeletal and oolitic shoals.

The thick, well-winnowed skeletal shoal units with the Receptaculites bioherms in the Ninemile Canyon section are correlative with the dark radial ooid-dominated, lower oolitic shoal units of the Martin Ridge section. This lateral facies relationship can be attributed to a very well-circulated shelf behind the syndepositional topography of the oolitic tidal bars. Furthermore, the presence of the Receptaculites mounds at

inner platform site of the shoal (the skeletal shoal of the Ninemile Canyon section) can also be attributed to good circulation in the carbonate shelf behind the oolitic shoal bars.

In the upper oolitic shoal units of the Ninemile Canyon section, the restricted shallow-subtidal lithofacies gradually substitutes for the oolitic skeletal packstone and grainstone units and changes laterally westward into the oolitic packstone- and grainstone units in the Martin Ridge. These relations suggest a well-circulated nature of the shelf may have progressively been diminished by the progressive growth of the syndepositional oolitic barrier sands at the Martin Ridge section and adjacent area. In the Ninemile Canyon section, this evolutionary trend can also be supported by the transitional phase: the thin oolitic layers (a 4-foot thick) repeat in a cyclical fashion within the predominantly skeletal packstone- and grainstone shoal units. These features may indicate the farther landward-extended oolitic bars, more specifically the spill-over fans and lobes. The lateral and vertical facies relations described above imply that oolitic tidal bars dominated the shelf margin laterally and vertically grew up to the mobile sand belts in the Martin Ridge section whose syndepositional topographies (as physical barriers) left very restricted shelf facies behind during the late Palliseria zone at and early Anomalorthis zone.

In the Martin Ridge and Ninemile Canyon sections, the formation of the mobile-sand belt in the oolitic shoal may have created a protected shelf facies or platform interior and also a low-energy algal-flat paleoshoreline (Fig. 46). Like in the Whiterockian shelf margin, the similar progressive evolutionary changes from the tidal-bar belt to the syndepositional physical barrier (i.e., mobile sand belt) have been noted in the following shelf margins: in the Holocene Luyacan Formation by Beach and Ginsburg (1980), in the modern oolitic shoal of Joulter Cay by Harris (1979), and in the Miami Limestone by Evans (1984).

In both, Ninemile Canyon and Martin Ridge, sections, the algal flat deposits of the lower- and mid-Anomalorthis zone are overlain unconformably by the oolitic and skeletal and skeletal and peloidal shoal lithofacies (Fig. 37). These relationships suggest that the high-energy shoal environment migrated farther eastward by third-

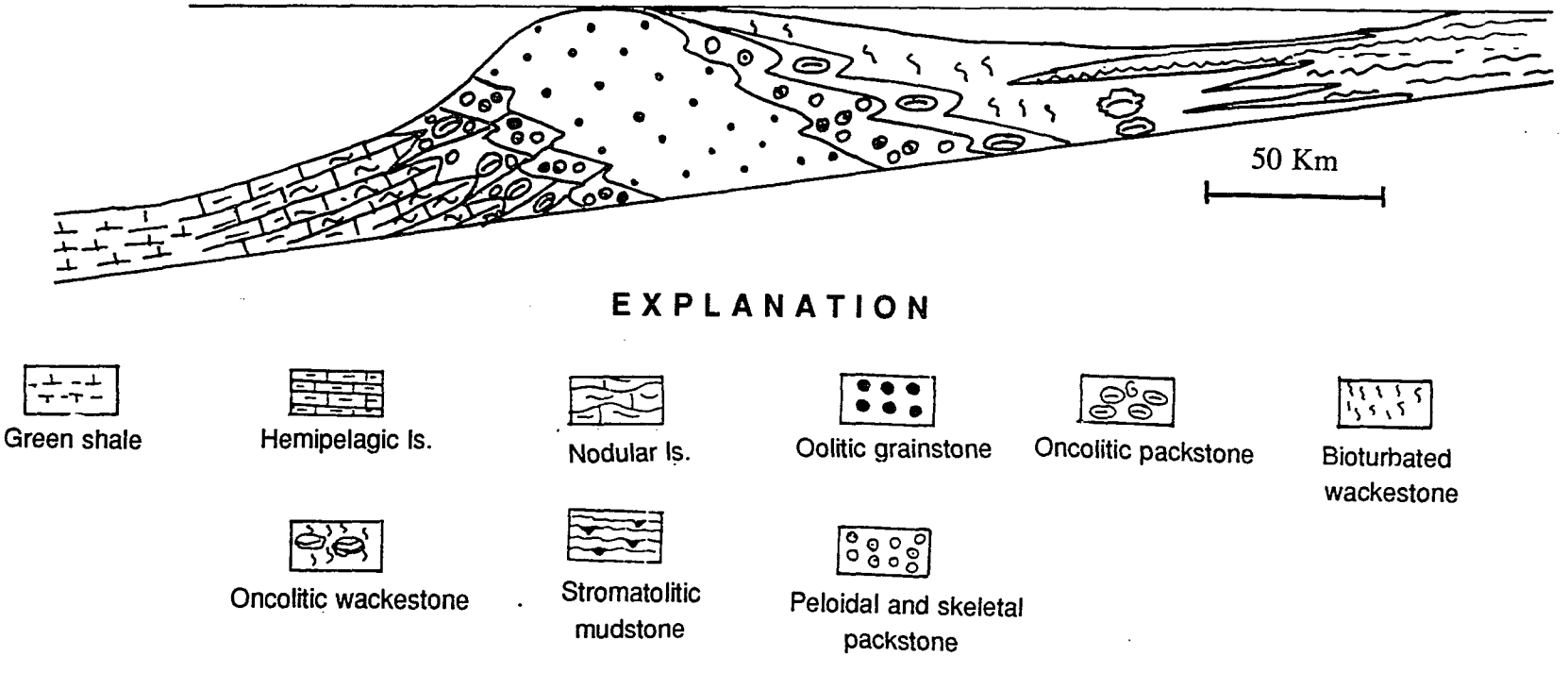


Figure 46- The suggested model for the oolitic shoal and related lithofacies of the AVL by this study.

order rise in sea level. As a result, this transgression probably altered the low-energy paleoshoreline into the high-energy shoreline where skeletal and peloidal nearshore bars separated the coastal lagoon from the well-circulated shelf (see Chaps. 10, 11).

In Martin Ridge and Ninemile Canyon sections, on the basis of the stratigraphic relations of skeletal and oolitic shoal lithofacies and their lateral variations and correlations, we can suggest that the incipiently rimmed-shelf margin facies probably evolved from the ramp margin during the deposition of the middle and upper Palliseria and continued until the end of Anomalorthis zone. However, at the same time, shelf margin profile at Lone Mountain, Keystone Canyon, Arrow Canyon sections and Nevada Test site probably represent the submerged-shelf margin below the normal wave base or incipiently drowned-shelf margin (see Chaps. 7, 10, 11).

In the same oolitic shallowing-upward cycles, the lower, dark gray radial ooid-bearing sublithofacies and the upper light brown ooid-bearing sublithofacies show gradual changes in sedimentary and compositional features. These relationships and the coexistence of calcitic radial ooids and calcitized-aragonitic ooids suggest that controls on ooid fabrics are primarily sedimentologic rather than due to changes in the chemistry of sea water (Wilkinson et al., 1978; Pigot and Mackenzie, 1982; and Sandberg, 1984).

This study also suggests that dark gray radial ooids represent in a low-energy shoal environment where algally produced acids influence the chemistry of sea water. On the other hand, calcitized ooids represent high energy shoal facies where turbulence and agitation level at its climax do not allow the formation of the any form of algae. Therefore, the high-energy levels at the crests of the oolitic bars favorably produced aragonitic ooids.

The dark gray radial ooids-constituted intraclasts represent the hardground crusts which were probably broken up and transported by a high-energy storms into the crest of the oolitic bar facies.

CHAPTER 7: SHELF FACIES BELT

This facies belt represents a depositional environment lying between the shoal and paleoshoreline. The bioturbated-wackestone and mudstone lithofacies is the predominant lithofacies of this facies belt. The bioturbated-wackestone and mudstone lithofacies represent the four different shelf facies (Appendix I-B): (1) Nuia shelf, in the Martin Ridge and Ninemile Canyon sections (Figs. 47-I, 19 in Chap. 4); (2) oncoidal shelf, in the Martin Ridge, Ninemile, Whiterock Canyon, Lone Mountain (Figs. 47-I, 28 in Chap. 5), and Keystone Canyon (Fig. 52 in this chapter) sections; (3) skeletal and oolitic shelf, in the Martin Ridge and Ninemile Canyon sections (Figs. 49-I, 36 & 37 in Chap. 6); and (4) inner shelf or lagoon, in the Martin Ridge and Ninemile Canyon sections (Figs. 49-I, 36 & 37 in Chap. 6).

A. Lithofacies

Lithofacies 10 A: Bioturbated-Wackestone Lithofacies of the Shelf Behind the Nuia Shoals

Description:

The Nuia-rich, bioturbated-wackestone lithofacies (Fig. 47-I, 47-II A, B) lies between the Nuia bars and the oncoidal packstone and grainstone units of the oncoidal shoal (Appendix. I-B). The light gray bioturbated-wackestone lithofacies in the Ninemile Canyon section grades into the dark gray wackestone lithofacies in the Martin Ridge section (Fig. 47-I). In cyclic successions, the bioturbated-wackestone shelf lithofacies (Fig. 47-II A), gradually overlie the subtidal Nuia bars and are

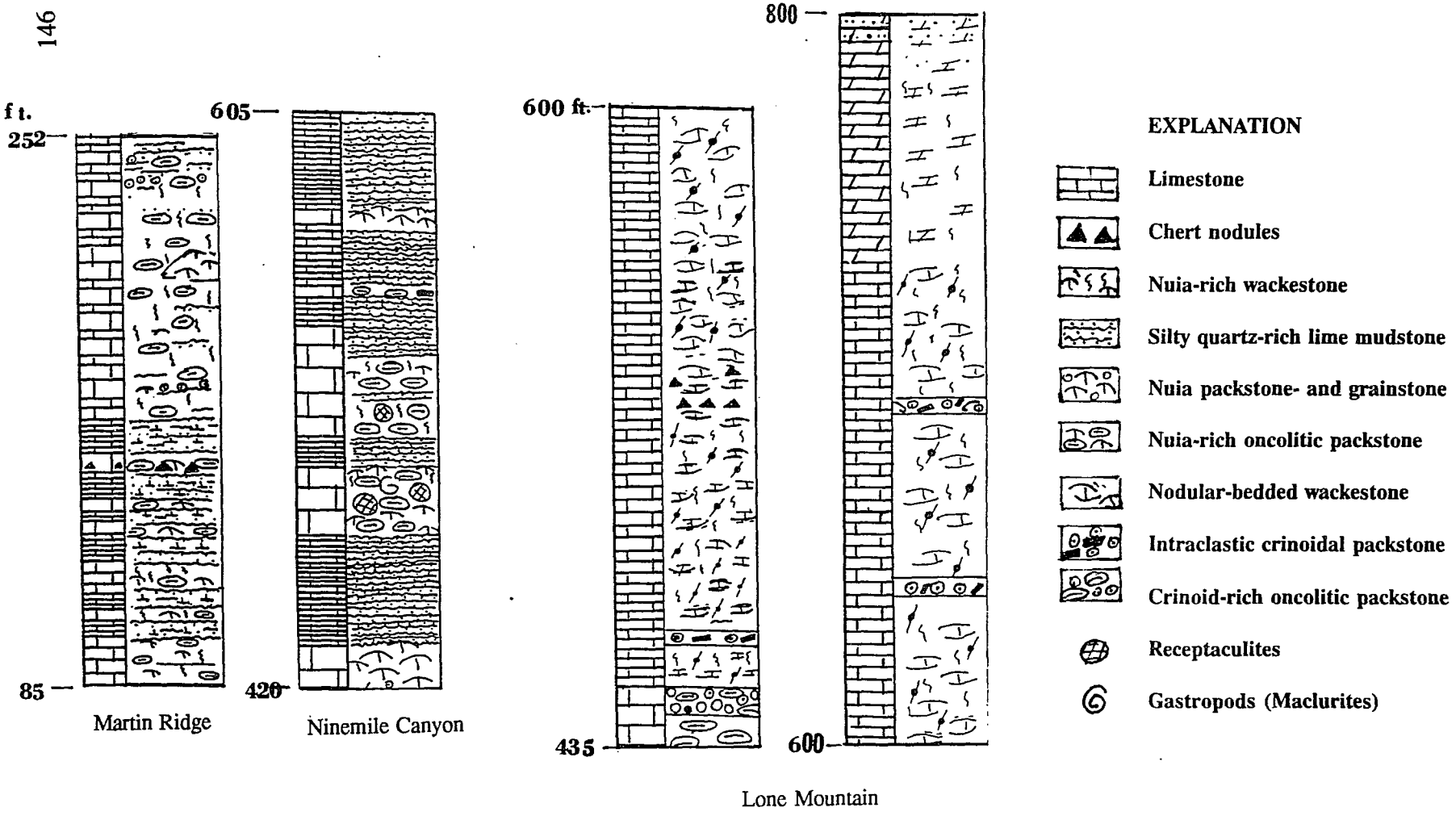


Figure 47 I- Vertical section showing the bioturbated-wackestone lithofacies and related lithologic units overlying the Nuia shoal units in the Antelope Valley region and oncoidal shoal units in the Lone Mountain section.

unconformably overlain by the sharp erosional basal contacts of the Nuia bars (see Fig. 19 in Chap. 4; Appendix I-B).

The Nuia-rich wackestone lithofacies are closely associated with the following lithologic subunits, in ascending order: (1) intensely bioturbated wackestone with homogenized-bedding forms; (2) in the thin-beds of the massive, amalgamated-bedded units, the basal oncoidal packstone to wackestone sublayers changing gradually upward into silty quartz-rich muddy blankets; (3) Nuia-rich peloidal, crinoidal, and oncoidal wackestone to packstone units in the Martin Ridge section; (4) about 3 to 5-feet thick, silty quartz-rich, parallel-laminated lime mudstone units of the Martin Ridge section which alternate with the Nuia-rich, bioturbated-wackestone lithofacies and grade eastward into the predominantly light gray to yellowish gray parallel-laminated, silty quartz-dominated pelletal lime mudstone units in the Ninemile Canyon section.

In both sections, bioturbation of this lithofacies ranges from moderate to intensive (Fig. 47-II C). Burrows are commonly filled by yellowish-brown silty mud and by the skeletal fragments (Fig. 48 A).

The Nuia-rich, thin-bedded skeletal packstone subunits are very common in this wackestone lithofacies and gradually overlain by the parallel-laminated silty quartz-rich lime mudstone subunits. The skeletal subunits with overlying fine-grained siliciclastic components show a fining-upward texture and commonly occur in the Nuia-rich, bioturbated-wackestone lithofacies with a sharp, slightly concave upward basal contact.

In addition, about 5-feet thick biohermlike Nuia-rich oncoidal-Receptaculites packstone units occur in the upper part of this shelf lithofacies and become more common particularly in the parallel-laminated, silty quartz-rich lithofacies of the Nuia shelf unit in the Ninemile Canyon section.

The visually approximated-average percentages of the constituents of the bioturbated-Nuia wackestone lithofacies are, as follows: Nuia 8-15%, crinoids 4-15 %, small ostracods 3-8 %, brachiopods 3-6 %, trilobites 3-5 %, mollusc fragments 2-3 %, silty quartz 8-15 %, and pellets 10 %. Micro-euhedral pyrite crystals are chiefly scattered in the siltstone and silty quartz-rich, parallel-laminated mudstone units.

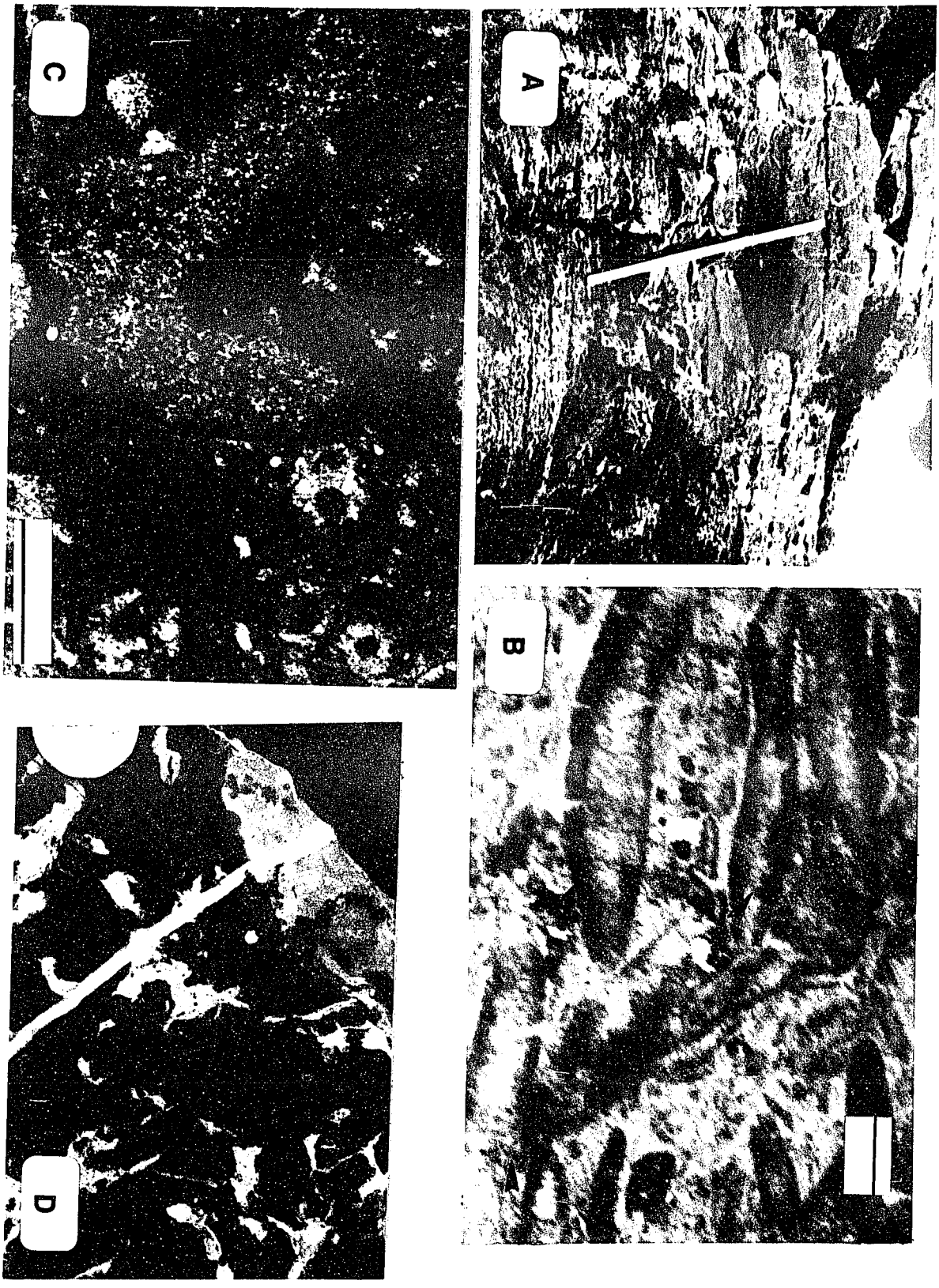
Interpretation:

The bioturbated-wackestone lithofacies, with a diverse benthic fauna and without any wave-induced sedimentary structures, reflect a low-energy subtidal depositional environment (a hydrologically well-circulated platform interior) where bioturbation commonly range from moderate to high. In this lithofacies, despite the paucity of diverse benthic fauna, the common presence of crinoids, brachiopods, trilobites, sponge spicules, with Nuia signify the open marine conditions, good-circulation, and normal salinity (Heckel, 1972). The submerged portions of the Great Pearl Barrier Bank in the Persian Gulf (e.g., Purser and Evans, 1972), which are composed of these skeletal sediments, is a good analogue for the Nuia shoal and related-shelf facies of the AVL. The restriction of the shelf behind the Great Pearl Barrier Bank increases progressively shoreward with the increasing shoaling, fine-grained siliciclastic influx, and salinity and daily temperature fluctuations. Similarly, this lithofacies changes eastward into the light gray to yellowish gray, silty quartz-rich, parallel-laminated lime mudstones of the upper mid and upper shelf. The lithology and color variations of this lithofacies correspond to a shoreward progressively shoaled and restricted, Nuia shelf. Therefore, the dark gray Nuia-rich, bioturbated-wackestone lithofacies in the Martin Ridge section represents a relatively deeper shelf environment than that of the shelf facies in the Ninemile Canyon section.

Silty quartz- and skeletal grain-filled burrows (Fig. 48 A) are closely related to storm deposits: The fine-grained siliciclastic suspensions of storm countercurrents probably filled previously open burrows during the quiescent storm periods; and the storm-resuspended shelly particles of shelf sediments probably filled open burrows during the rapid storm-phase sedimentation. Similar skeletal-burrow filling was reported in the Caicos platform after Hurricane Kate by Wanless et al. (1988 a).

Receptaculites and Girvanella mounds and local Nuia bars in this shelf facies, especially in the upper middle part of this shelf facies, probably represent topographically high areas, where high-energy environmental conditions may have locally been attained.

Figure 47 II- Bioturbated-wackestone lithofacies. A) An outcrop photograph of the bioturbated wackestone lithofacies (a). This lithofacies overlie the Nuia packstone- and grainstone lithofacies with a gradational basal contact, and its lowermost part includes rhythmically parallel, thin-bedded siltstone interlayers; a four-feet long stick for scale. B) Photomicrograph of Nuia-rich, bioturbated-wackestone lithofacies, (n) indicating Nuia grains, and (c) crinoid fragment. With plane-polarized light; scale= 0.5 mm. C) Polished slab of intensely bioturbated Nuia-rich wackestone. Burrows are filled by orange tan silty quartz-rich mud; penny for scale. D) Photomicrograph of unidentified objects, probably fecal pellets, indicated by arrowheads. These objects were only found in the bioturbated wackestone shelf facies of the oncoidal shoal; scale = 0.5 mm.


A
B
C
D

Lithofacies 10 B: Bioturbated-Wackestone Lithofacies of the Shelf behind the Oncoidal Shoals

Description:

Dark gray to black oncoid- and Maclurites-rich, intensely bioturbated wackestone gradually overlie dark gray subtidal oncolitic bars; however, this wackestone lithofacies are disconformably overlain by oncoidal packstone- and grainstone units in cyclical successions. In the Martin Ridge section, the bioturbated shelf lithofacies constitutes the upper component of the oncoidal shoal cycle, and its thickness ranges from 5 to 15 feet which eastward grades into the crinoid-rich oncoidal packstone units in the Ninemile Canyon section. In the Lone Mountain (Fig. 47-I) and Keystone Canyon sections, the dark gray to black bioturbated wackestone lithofacies is overlain by the Eureka Quartzite with a sharp unconformable contact, and by the Copenhagen Formation with a gradational contact (see Fig. 52).

In the Lone Mountain section (Fig. 47-I), this bioturbated lithofacies is composed of thin to medium, nodular-bedded units which are commonly alternating with 1- to 3-feet thick, parallel-laminated, silty quartz-rich lime mudstone intervals which commonly include dark-chert nodules.

In the Keystone Canyon section (see Fig. 52), the pervasively dolomitized lithofacies consists of nodular bedforms and alternates cyclically with fine-grained siliciclastic lithofacies, as found in the Lone Mountain section. From the lower part of this lithofacies, silty quartz-rich, parallel-laminated mudstone units cyclically repeat with basal oncoidal wackestone units. In cyclical successions, upwards the oncoidal subunits progressively become thinner and are replaced by dominantly silty quartz-free, bioturbated wackestone units.

In the Lone Mountain section, diverse open marine faunas, such as crinoidal, trilobite, brachiopod, sponge spicules, and conodont fragments, are common in all bedforms of this lithofacies. Also, in this lithofacies, bioturbation and fossil content tend to increase progressively upward. In the pervasively dolomitized shelf lithofacies

of the Keystone Canyon section, upward from the base of this lithofacies, the abundance of small gastropods and ostracods increases progressively along with the progressive dominance of fine-grained siliciclastics.

The average percentages of constituents of the bioturbated wackestone lithofacies in the Lone Mountain section, is as follows: silty quartz 4-20%, pellets 20-25%, ostracods 8-15%, crinoids 3-5%, brachiopods 2%, trilobites 3%, molluscan fragments 3-8%, broyozoans 2%, spicules 1%. Micropyrite crystals are usually scattered in the mudstone units and burrows.

In Lone Mountain section, an exceptionally peculiar allochem (Fig. 47-II D) which measures about 0.6 mm in width with 3.5-8 mm length have been noted at intervals 683-670 feet from the base of the sections within this wackestone lithofacies. This lithofacies at indicated intervals is primarily composed of ostracods 10-15 % and unidentified object between 30-35 %.

Interpretation:

This oncoidal shelf lithofacies represents a deeper shelf facies behind relatively deeply submerged oncoidal bars than that of the shelf facies formed behind the Nuia shoals. The nodular-beds, diverse open marine faunas, dark thin chert layers and nodules with abundant sponge spicules indicate a deep, hydrologically well-circulated middle shelf lithofacies. On the other hand, the presence of euhedral micropyrite in this lithofacies suggests that the stagnation level of the oncoidal shelf may have produced moderately reducing conditions.

In both Lone Mountain and Keystone Canyon sections, upward increase in bioturbation and frequency of the silty quartz-rich intervals characterizes a shoreward-progressive shoaling and restriction in a hydrologically well-circulated shelf. The cyclic repetitions of the silty quartz-rich lime mudstone units and the bioturbated oncoidal wackestone and the bioturbated wackestone lithofacies probably represent a storm countercurrent sedimentation during high sea-level stands. The storm

countercurrents are widely accepted as dynamic agents which can remobilize fine-grained sediments (e.g., Yancey, 1986; Chow and James 1987) and intermix them with the carbonates in the middle shelf during high-sea level stands.

Lithofacies 10 C: Bioturbated Wackestone Lithofacies of the Shelf behind the Skeletal and Oolitic Shoals

Description:

In the Martin Ridge and Ninemile Canyon sections, the dark gray bioturbated wackestone shelf lithofacies gradually overlie the oolitic and skeletal shoal lithofacies and are gradually overlain by the stromatolitic mudstone units of intertidal algal flat. In cyclical successions, this bioturbated wackestone shelf lithofacies is overlain by a truncational basal contact of the skeletal and oolitic shoal basal units of the subsequent oolitic shoal cycle (see Figs. 36 & 37 in Chap. 6).

This lithofacies in the backshoal usually shows a diverse normal-marine faunal content; however, this faunal content decreases upward in vertical sections. This faunal change coincides with a gradual increase in the concentration of ostracods and thin-shelled gastropods, hemispherical bryozoans, blackened intraclasts, pellets, and irregularly-laminated oncoids. Thick-shelled Maclurites and Palliseria, well-rounded oncoids, crinoids, and peloids are common within the transition zone between the oolitic shoal and this bioturbated shelf lithofacies. Thick-bedded skeletal packstone- and grainstone units occur at various stratigraphic levels of the bioturbated wackestone lithofacies with sharp planar lower and upper contacts.

The oncoidal wackestone sublithofacies with restricted faunas and irregularly coated oncoids occur in the transition zone between strictly restricted and moderately restricted subfacies of this shelf lithofacies. The restricted sublithofacies are represented by intensively bioturbated wackestone and pelletal limestone units which are primarily composed of abundant small, thin-shelled gastropods (10 %) and

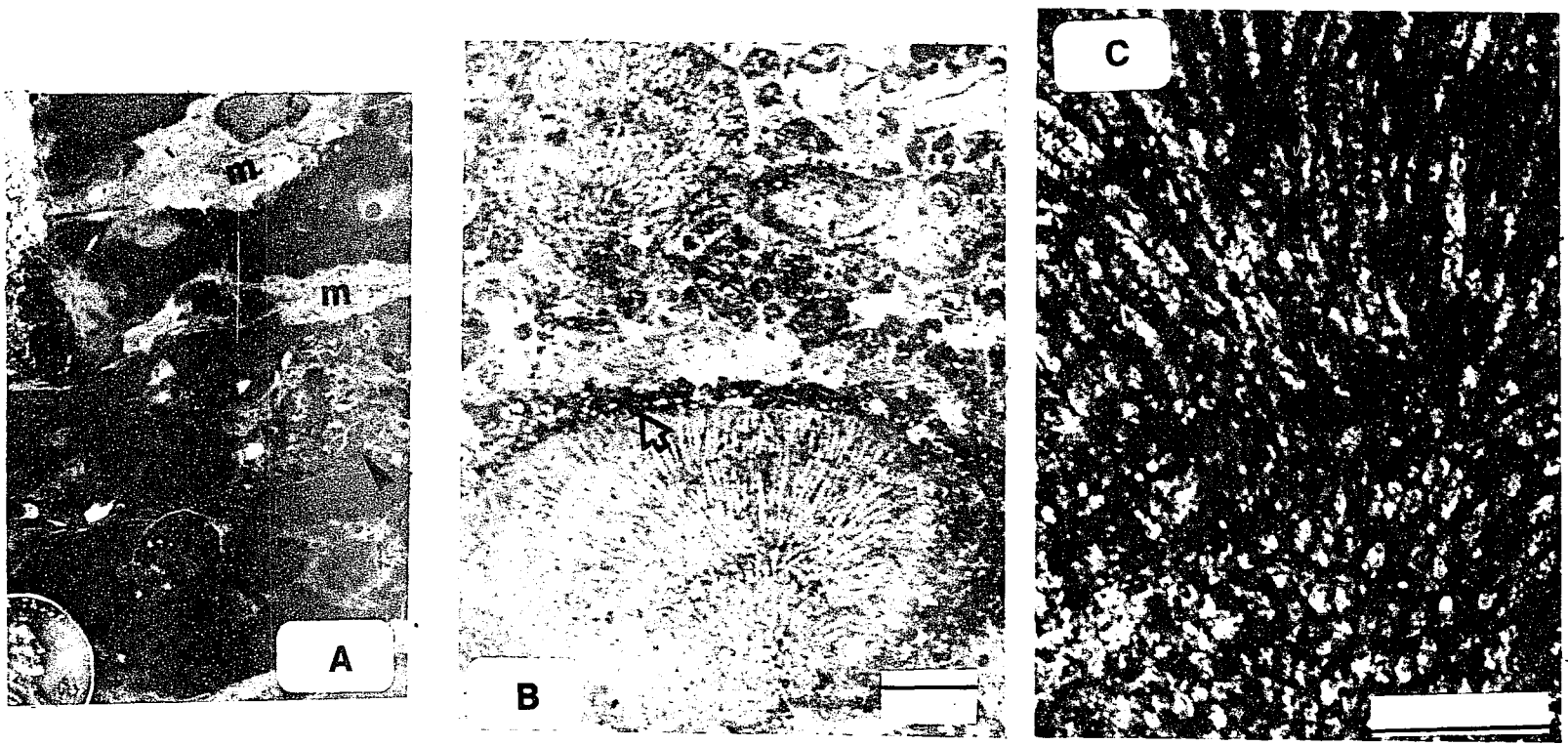


Figure 48- Bioturbated wackestone lithofacies in the Middle and Late Anomalorthis zone. A) Polished slab of bioturbated wackestone shows that burrows are filled by skeletal fragments indicated by arrowheads and by silty quartz-rich mud (m). B) Photomicrograph of semi-spherical bryozoans in the bioturbated-wackestone unit which is separated from the Copenhagen Formation by the peloidal nearshore bars; an arrow indicates baffled-, fine-grained silty quartz grains along outline of hemispherical bryozoa. C) Close-up photomicrograph of a semi-circular bryozoa. With plane-polarized light; scale = 0.5 mm.

ostracods (20 %). This restricted-sublithofacies gradually changes upward into stromatolitic algal mudstone units. In addition, the intraclastic wackestone- to packstone unit (about a foot thick), which is composed of well-rounded intraclasts with algal laminae, occurs in restricted wackestone to mudstone units and has a sharp erosional basal contact. In polished-hand specimens, the intraclasts do not show imbrication but display a fining-upward internal texture at the basal part (Fig. 48 D).

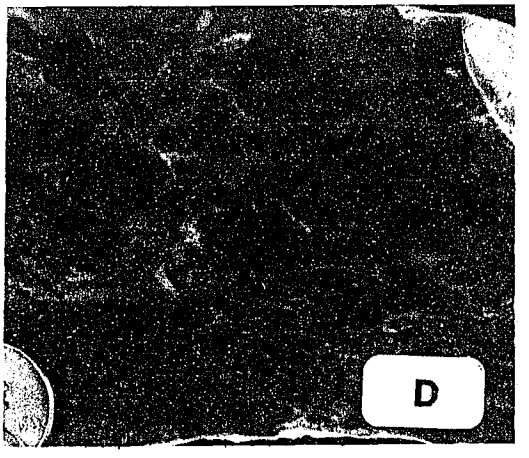


Figure 48 D- Polished slab of recycled flat-pebble conglomerate; arrow indicates a fining-upward texture in this unit.

The features described above for this lithofacies only correspond to the middle and upper Palliseria zone and lower to middle Anomalorthis zone in the Ninemile Canyon and Martin Ridge sections. At the same vertical sections, in the middle to upper Anomalorthis zone, the bioturbated-wackestone lithofacies with open marine faunas is bounded between the oolitic shoal (i.e., unconformably overlying intertidal algal deposits) and the peloidal nearshore bars which separate this bioturbated wackestone lithofacies from the interlayered-wackestone to mudstone and shale lithofacies (i.e., lagoonal lithofacies or the Copenhagen Formation; Figs. 49-II, 36 & 37).

The burrows in the bioturbated-wackestone lithofacies are commonly filled by

skeletal grains and silty quartz-rich mud (Fig. 48 A).

The approximated-average percentages of constituents in this lithofacies are, as follows: ostracods 8-15%, gastropods 5-9%, trilobites 2-3%, crinoids 8-10%, brachiopods 2%, bryozoans 3-5%, pellets 12-30%, and silty quartz 5-13%. Pyrite usually occurs as euhedral crystals which are commonly oxidized. The bryozoans are generally hemispherical and coated by Girvanella (Fig. 48 B, C).

Interpretation:

In this lithofacies, upward rapid decline in the abundance of normal marine fossils, and rapid increase in ostracods and small thin-shelled gastropods, and the stromatolitic mudstone characterize a restricted-shelf facies which formed behind the high topography of oolitic shoal bars. This physical barrier caused the formation of a restricted-shelf and low-energy, algal-flat environments (e.g., Purdy, 1963; Kendall and Skipwith, 1969; Purser and Evans, 1972; Harris, 1979; and Beach and Ginsburg, 1982).

Moreover, in this lithofacies, upward increase in the concentration of dark or blackened intraclasts is the result of algal staining, (e.g., Kendall and Skipwith, 1969). Irregularly coated oncoids with outer and inner skeletal concentric laminae also represent a low-energy, restricted-subtidal depositional environment.

In the intraclastic (rounded-algal chips) packstone- to wackestone sublithofacies, a fining-upward texture and sharp-erosional basal contact indicate a gradually waned energy level of the storm currents. The rounded-algal chips without imbricated texture suggest that this unit may have formed from storm countercurrents in a shallow-subtidal depositional environment. On the basis of the features presented above, oolitic shoals were physical barriers to open marine wave and currents, at the Martin Ridge section, and probably created a protected-shelf or platform-interior facies.

In the middle and upper Anomalorthis zone, the bioturbated-wackestone lithofacies

with normal-marine fauna represents a hydrologically well-circulated shelf facies which formed behind the oolitic shoal whose syndepositional topography was not completely a barrier to wave and currents.

Lithofacies 10 D: Interlayered Wackestone and Mudstone and Shale (Lagoonal or the Copenhagen Formation)

Description:

Light to dark gray, thin to medium-bedded wackestone to mudstone layers are interbedded with yellow-brown silty quartz-rich, dark gray to dark-green shale layers. In the Antelope Valley region, particularly at the uppermost part of the AVL, this lagoonal lithofacies is known as the Copenhagen Formation and lies between the underlying peloidal and skeletal nearshore bars and the Eureka Quartzite (Fig. 49-I). Commonly, in this lithofacies, shaley layers increase upward with decreasing thickness of the wackestone and mudstone layers. These medium-bedded lime mudstone- and wackestone layers most commonly consist of intraclastic, shelly thin sublayers which have a grain-supported texture (packstone texture) and concave upward truncational basal contact (Fig. 49-II A, B, C).

In addition to intraclasts, thin-shelled gastropods, large ostracods, and oncoids are also commonly present, and large ostracod shells rest on these packstone sublayers in a concave-upward position. In these shelly packstone sublayers of the medium-bedded mudstone to wackestone layers, the skeletal grain content gradually diminishes upward as quartz silt-rich muddy matrix increases, showing a fining-upward texture (Fig. 49-II A, B, C). Another diagnostic sedimentary structure in the mudstone and wackestone interlayers is that about 1-cm thick light skeletal fragment-rich sublayers gradually change upward into dark organic-rich sublayers and overlie one another with a truncational basal contact (Fig. 49-II C).

In the Ninemile Canyon section, the base of this lithofacies, which is intensively

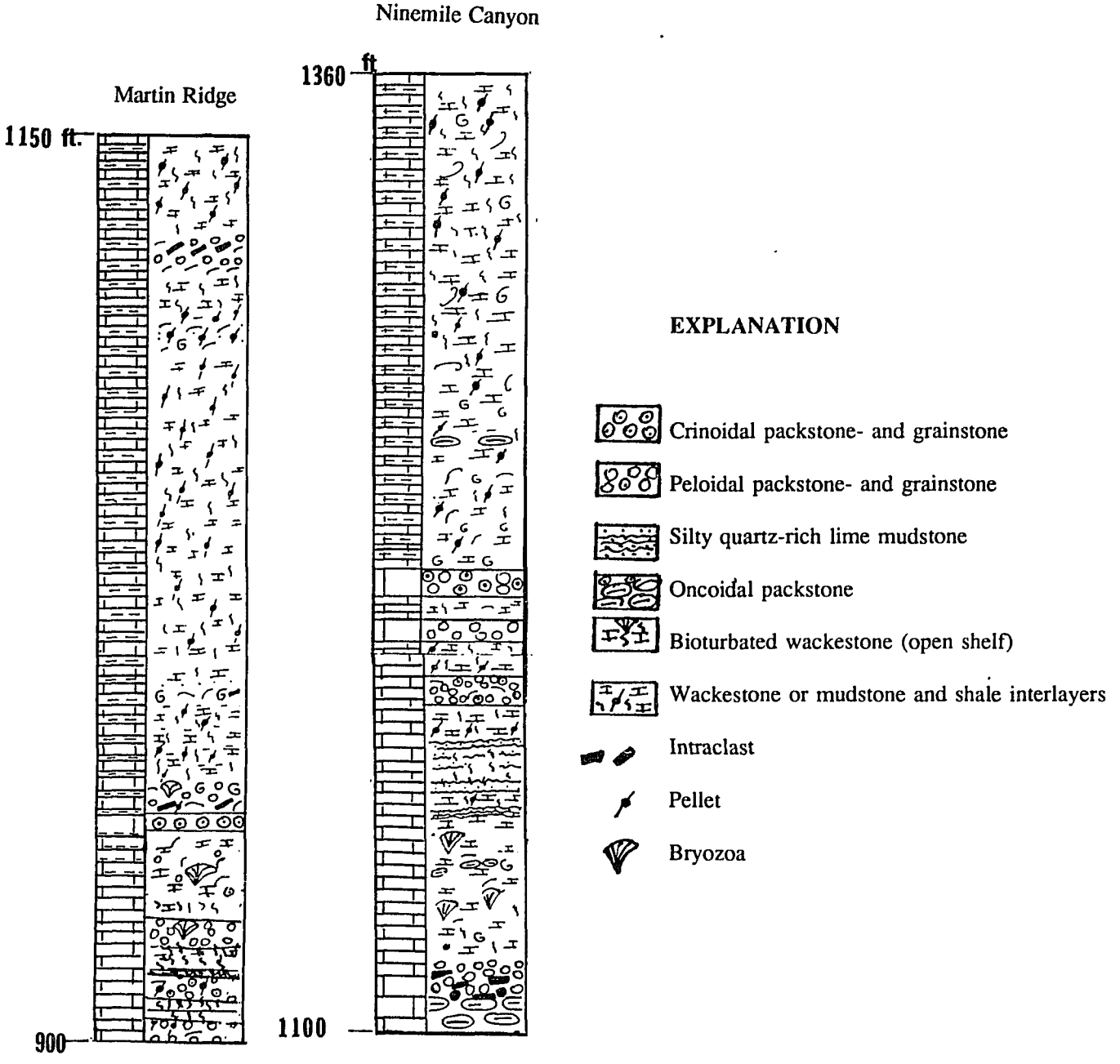
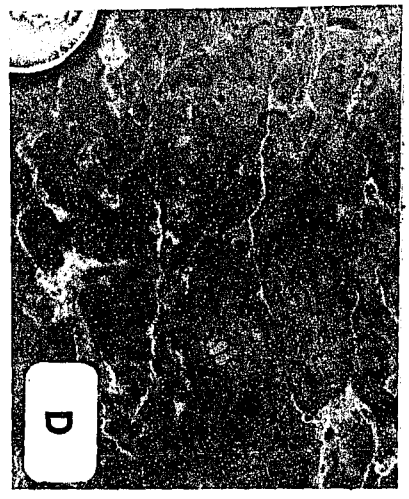


Figure 49 I- Vertical section showing the interlayered wackestone to mudstone and shale (Lagoonal lithofacies of the AVL) or the Copenhagen Formation.

Figure 49 II- Polished slabs of the lagoonal lithofacies of the AVL, or the Copenhagen Formation. A) Shelly inner sublayers within lime mudstone interlayers alternating rhythmically with shales; a large arrowhead indicating a concave upward truncational surface between a thin-shelled gastropod (g) and ostracod-rich inner shelly sublayers blanketed by silty quartz-rich lime mud (m). B) In the shelly sublayers, large ostracods show a concave-upward grain settlement, small arrowheads indicate a very thin mud concentration between two shelly substorm layers, and large arrowhead points to a sharp truncational basal contact of a shelly inner layer. C) Multiple light gray, thin, fine-grained shelly basal sublayers alternate with equally thick, dark-gray mud blankets, showing a fining-upward texture; arrowheads indicate sharp and truncational contacts between these thin layers. D) Thin-shelled, unbroken gastropod-rich restricted inner shelf or lagoonal lithofacies. Pennies for scale.


C


A


D


B

burrowed and homogenized, may be correlative with the moderately bioturbated units of this lithofacies in the Martin Ridge section. These lithofacies of the Martin Ridge section consist of silty quartz-rich lime mudstone and siltstone intervals.

The homogenized sublithofacies contain a 2-foot thick crinoidal grainstone which has sharp planar basal and upper contacts and which is a marker bed in the Martin Ridge and Ninemile Canyon sections. Partially chertified large crinoidal fragments and dolomitized peloids are the most common grain types in the crinoidal grainstone unit; ostracods and selectively chertified bryozoans are also common.

Homogenized sublithofacies at the base of this lithofacies gradually overlies about 10-feet thick peloidal and skeletal bars, which separate this interlayered lithofacies from well-circulated shelf lithofacies, and this sublithofacies changes upward into thin-shelled, gastropod-rich, interlayered, bioturbated wackestone subunit (Fig. 49-II D).

In the Clear Canyon and Keystone Canyon sections, this lithofacies consists of only thin rhythmically bedded-lime mudstone and equally thick shaley interlayers. In these southern localities, about 10-feet thick, fine-grained siltstone and silty quartz-rich, parallel-laminated lime mudstone similarly separates this lithofacies from the middle-shelf facies of the AVL. In the Clear Creek section, however, about 8-10 feet of light creamy medium grained quartz arenite (orthoquartzite) occurs in the lower Copenhagen Formation.

For the Martin Ridge and Ninemile Canyon sections, the approximated-average percentages of the constituents of the lithofacies are, as follows: ostracods 8-20%, gastropods 3-12%, bryozoans 2-5%, crinoids 2%, brachiopods 0-1%, trilobites 3-5%, oncoids 5-8%, and pellets 8-20%.

Interpretation:

In this bioturbated wackestone- and mudstone lithofacies, lack of any wave-induced sedimentary structures and abundant restricted-faunas along with minimal broken-open

marine shells symbolize a low-energy, restricted-subtidal environment. In the Martin Ridge and Ninemile Canyon sections, the truncational concave-upward basal contacts of the inner shelly sublayers with a fining-upward texture as well as large ostracods resting on a concave-upward position (Fig. 49-I A, B, C) clearly indicate a possible storm-induced sedimentation in a predominantly low-energy, restricted-subtidal environment or inner shelf (e.g., Kreisa, 1981; and Aigner, 1982; and Kreisa and Bambach, R., 1982).

The fine-grained siliciclastic lime mudstone intervals cyclically repeats within this lithofacies and indicate episodic siliciclastic sedimentation related to storm countercurrents or storm-enforced winds, as suggested by Hayes (1965) and Nelson (1982).

In vertical sections, upward-increasing thicknesses of the shaley interlayers indicate progradation and a shoreward-increasing dilution of carbonate deposition by fine-grained siliciclastic sediments. The thick-bedded crinoidal packstone- to grainstone unit (as a marker bed in this lithofacies) with its sharp upper and basal contacts indicates that it was very rapidly deposited from a high-energy storm current in a predominantly low-energy subtidal environment, as suggested by Aigner (1982), and Kreisa and Bambach (1982).

The homogenized or intensively bioturbated lithofacies implies that a relatively good circulation of inner shelf probably occurred in areas closer to nearshore bars where restriction was considerable reduced by the replenishment of relatively oxygen-rich water through bypass flows.

In the lime mudstone and wackestone layers, pellets, small gastropods, ostracods, and small oncoids suggest a shallow, low-energy, restricted-depositional environment.

Lithofacies 11: Fine-Grained Peloidal Packstone

Description:

In the Ninemile Canyon section, the light gray to tan, medium-bedded skeletal and peloidal packstone units occur with low-angle cross beddings at intervals of 1180-1889 and 1195-1204 feet from the base of this vertical section (see Fig. 37 in Chap. 6; Appendix I-B). About 7 to 9-feet thick peloidal packstone units occur at the uppermost part of the Antelope Valley Limestone, separating the Copenhagen Formation from

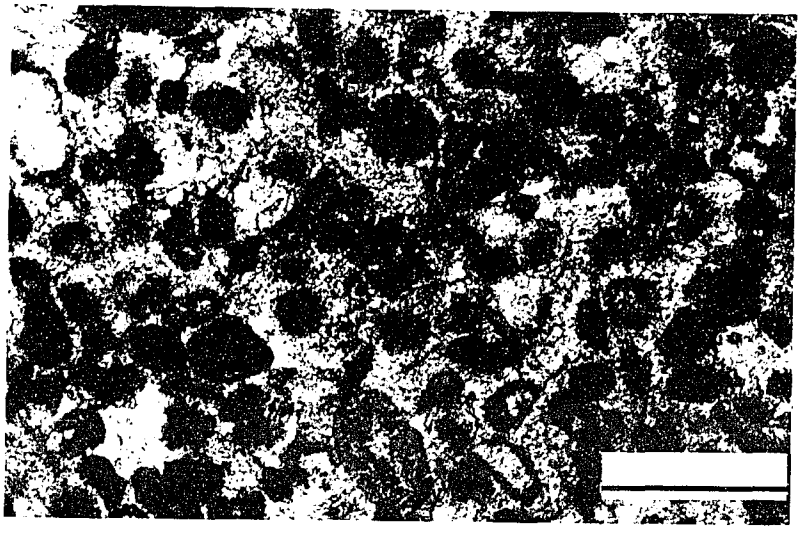


Figure 50- Photomicrograph of peloidal packstone lithofacies. Peloids appear to be well sorted micritized and partially calcitized ooids whose grain size ranges from 0.8 to 0.20 mm (average of 0.15 mm). Under plane-polarized light; scale= 0.5 mm.

the AVL. Interparticle cement is common among the moderately well sorted peloids (Fig. 50). The quartz silt-rich, intensively bioturbated or homogenized-lower units of the Copenhagen Formation gradually overlie this peloidal lithofacies. However, in cyclical successions, the peloidal packstone lithofacies overlies the homogenized units of the lagoonal lithofacies (Copenhagen Formation) with a sharp, erosional-planar basal contact.

The grain size of peloids ranges from 0.08-0.20 mm, and some of them are selectively dolomitized (Fig. 50). The visually approximated percentages of the most common constituents of this lithofacies are (1) peloids or small micritized-radial ooids 70-75 %, crinoids 8-10 %, and ostracods 5 %.

Interpretation:

This lithofacies, with its tabular-cross beddings, grain-supported textures and interparticle cement, indicates a high-energy environment. The recognizable, small-micritized ooids (Fig. 50) in the tabular cross bedded units probably represent the oolitic bars of a relatively low-energy shoal environment.

Since, stratigraphically these bars underlie the Copenhagen Formation and are separated from the active oolitic shoal facies by the bioturbated wackestone lithofacies with normal marine faunas, it can be suggested that these peloidal bars characterize a nearshore, high-energy environment in which the topography of these bars may have reached a level that left behind a restricted-inner shelf or coastal-lagoon facies.

Lithofacies 12: Fine Siliciclastics

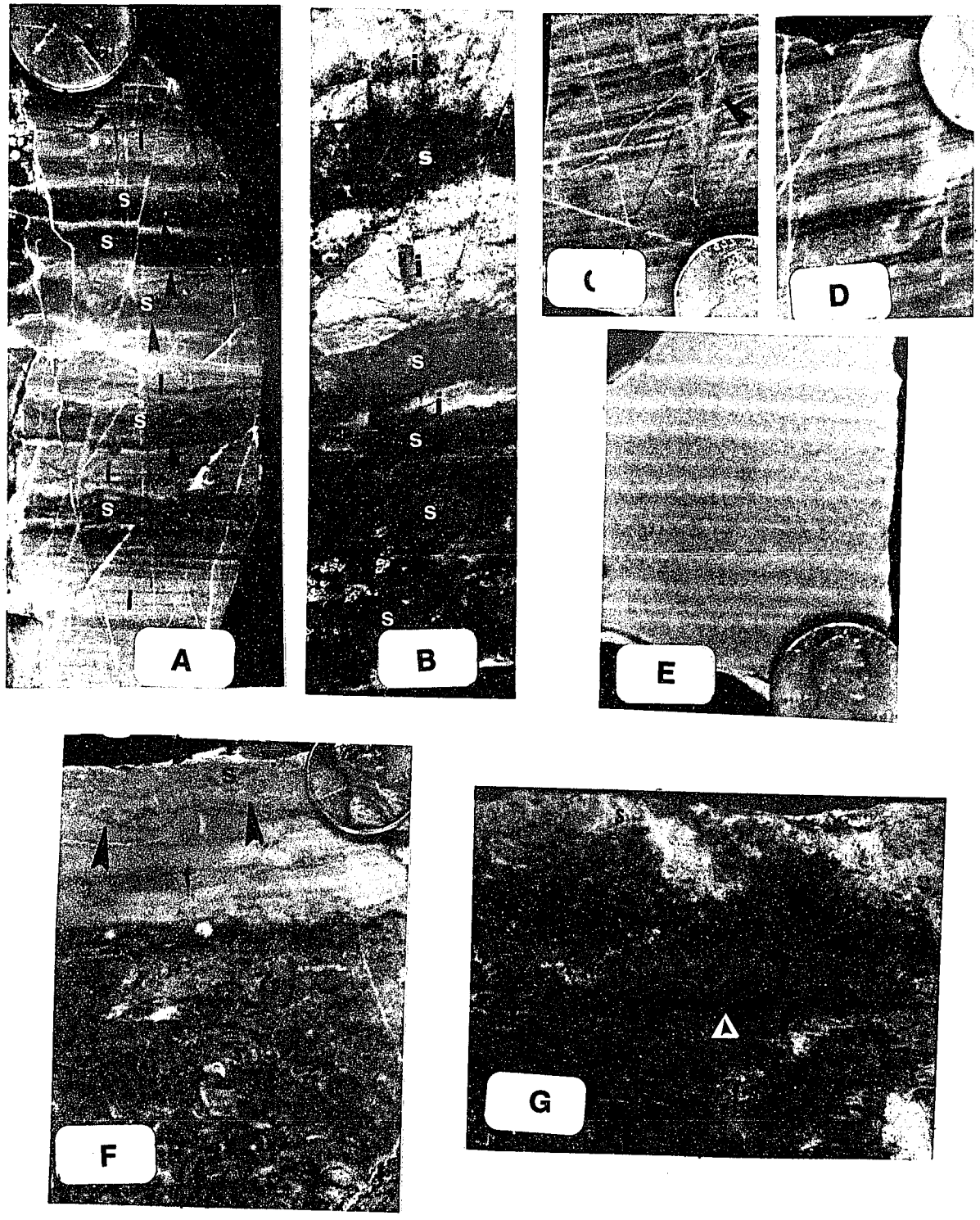
Lithofacies 12 A: Parallel-Laminated, Silty Quartz-Rich Lime Mudstone

Description:

Submillimeter to a few millimeters thick, even parallel laminated, silty quartz-rich laminae commonly occur in pelletal lime mudstone units (Fig. 51 A to G). Creamy to light gray color dominates these silty quartz-rich parallel-laminated lime mudstone lithofacies. In places, these parallel laminae show slight inclination as low- angle cross laminae (Fig. 51 D, E), but parallel, even laminae are predominant in this lithofacies (Fig. 51 A, B, C, G). These parallel laminae are occasionally burrowed and destroyed in their uppermost parts where silty laminae change gradually into dark gray lime mudstone laminae (Fig. 51 D to E). Usually, the thickness of this lithofacies range from about 2 to 15 feet, and they commonly repeat within the bioturbated-wackestone units of shelf facies. Commonly, these silty quartz-rich, parallel-laminated intervals are bioturbated and colonized mostly by brachiopods.

In the Ninemile Canyon section, the silty quartz-rich lithofacies dominate the uppermost part of the bioturbated-mudstone and wackestone of Nuia-shelf facies (Appendix I-B). And they locally comprise about 5-10 cm-thick skeletal packstone and grainstone units. On the other hand, in the Martin Ridge section, in the Nuia-rich bioturbated shelf lithofacies, the silty quartz-rich lithofacies occur in about 3-5 feet thickness and cyclically repeat within the bioturbated-wackestone lithofacies (see Fig. 49-I). Commonly, the Nuia-rich, tabular thin-bedded (about 2 to 5 cm) skeletal packstone units cyclically repeat within the parallel-laminated, silty quartz-rich lime mudstone lithofacies with a sharp, concave-upward basal contact (Fig. 51 B, G). These Nuia-rich shelly layers grade upward into fine-grained muddy blankets which commonly consist of parallel, even continuous silty quartz-rich laminae (Fig. 51 B, G). In the Lone Mountain section, the parallel-laminated, silty quartz-rich,

Figure 51- Rhythmically alternating silty quartz-rich parallel-laminated lime mudstone or thin siltstone and lime mudstone interlayers. A) and B) Polished and unpolished slabs show that parallel-laminated thin siltstone units (s) rhythmically alternate with parallel- laminated lime mudstone interlayers (I) and overlie them with sharp truncational basal contacts indicated by arrowheads. C), D), and E) Polished slabs show parallel- or slightly inclined laminae within the silty quartz-rich lime mudstone lithofacies. F) Polished slab shows that shelly basal subunits (s) are overlain directly by parallel-laminated, silty quartz-rich mud blankets (f), and display a fining-upward texture; arrowheads point to sharp, concave-upward truncational basal contacts of shelly basal sublayers. G) Shelly basal sublayers (s) overlie parallel-laminated silty quartz-rich lime mudstone sublayers (f) with a sharp truncational concave upward contact indicated by arrowhead. Pennies for scale.


A
B
C
D
E
F
G

massive-mudstone intervals with dark gray chert lenses usually repeat within the thin, nodular-bedded wackestone lithofacies of the deep-middle shelf facies formed behind the oncoidal shoals. In the Anomalorthis zone of the Martin Ridge section, this parallel-laminated lithofacies is not present; however, at the Ninemile Canyon section, it occurs only at the uppermost part of this formation (at intervals of 1150-1158 and 1161-1169 feet).

The parallel-laminated lithofacies most commonly occurs in and dominates the shelf facies of the oncoidal shelf in the Keystone Canyon and Clear Creek Canyon sections (Fig. 52). About 10-feet thick, silty quartz-rich, parallel-laminated lime mudstone units overlie about 10-15 feet thick oncoidal packstone units, and in cyclical successions, they are overlain disconformably by the oncoidal shoal facies. However, the oncoidal basal units of these cyclical occurrences upward become progressively thinner and are gradually substituted by the bioturbated-, detrital silty quartz-free wackestone intervals (Fig. 52). Most commonly, in cyclical successions, the parallel-laminated, silty quartz-rich lime mudstone units upward become thicker and more dominant than those of the basal components (i.e., these bioturbated-mudstone to wackestone units).

In addition, in the up sections of the Keystone Canyon and Clear Creek Canyon sections, the silty quartz-rich lime mudstone layers gradually become rhythmical thin-bedded, parallel-laminated, siltstone (about 2-3 cm thick) and parallel-laminated lime mudstone units (Fig. 52). These rhythmic couplets gradually change upward into massive-bedded, bioturbated-siltstone lithofacies (Fig. 52).

Interpretation:

The silty quartz-rich, parallel-laminated lime mudstone and parallel-laminated siltstone interlayers may represent a very rapid sedimentation from a suspension load of storm countercurrents in a predominantly low-energy subtidal environment. It is widely believed that these fine-grained detrital sediments of the middle shelf originate

from a nearshore area, especially during storm events by storm countercurrents. The preservation of the parallel and slightly inclined parallel laminae clearly represents three principal causes: (1) below-wave base sedimentary conditions; (2) rapid deposition, and (3) prevailing restricted-low energy subtidal environmental conditions during deposition of fine-grained siliciclastic sediments.

These fine-grained siliciclastic deposits also characterize hostile, stressed-environmental conditions in the open shelves for carbonate-producing benthic faunas. Under the indicated environmental conditions, the parallel even laminae would most likely be preserved. In addition, the absence of the bi-directional cross laminae usually indicates a relatively deep, open mid-shelf environment than intertidal and shallow-subtidal depositional environments.

In fact, in this fine-grained siliciclastic lithofacies, the straight, continuous parallel laminae (Fig. 51) and absences of parallel algal laminae (with convex and concave bulges) clearly rule out the possibility of a cryptalgal origin of these parallel laminae. Moreover, the colonization of the siltstone interlayers at their upper surface by inner faunas (chiefly brachiopods) also indicates an episodically stressed-subtidal sedimentation in this shelf facies.

The common occurrences of the thin, normal-graded shelly layers within the fine-grained siliciclastic lithofacies also represent the storm-induced sedimentation in the predominantly low-energy subtidal depositional environment (Mullin and Kelling, 1975; Kreisa, 1981; and Aigner, 1982). The sharp basal contacts of these shelly beds (Fig. 51 B, G) may have formed during the storm-peak phase and followed by deposition of the coarse-grained subunits (i.e., the resuspended-sediments of shelf floor) from the gradually waning of storm waves (Aigner, 1982; Kreisa and Bambach, 1982). On the other hand, the fine-grained, matrix-supported upper component of these thin shelly layers probably were deposited from the suspension loads of the storm countercurrents.

Upward increase in the thickness and frequency of the detrital, fine-grained sedimentation units characterize a shoreward mid-shelf facies. These detrital fine-sedimentation units commonly occur in the outer shoreward shelf and outer shelf

compared to relatively deeper middle shelves (Yancey, 1986).

Rhythmically uniformed fine-grained siltstone and mudstone sublithofacies, gradually change into the massive siltstone and represent episodical sedimentations from storm countercurrents in a shoreward mid-shelf environment. Facies similar to the thin-bedded siltstone and parallel-laminated lime mudstone have been reported about 30 km from the onshore area of the Bering Sea shelf by Nelson (1982).

In the Antelope Valley region, the scarcity of this fine-grained siliciclastic lithofacies in the shelf facies of the oolitic shoal clearly reflects a high-carbonate production rate in the oolitic shoals and existence of the intertidal-algal flat which stabilized and baffled the fine-grained detrital particles.

Lithofacies 12 B: Massive Siltstone

Description:

Tan to light gray, massive-siltstone units are entirely bioturbated and have gradual basal and upper contacts. Grain size of silt particles ranges from of 80 and 120 microns. About 10 feet-thick, this massive-bedded siltstone unit at the uppermost part of the Keystone Canyon and Clear Creek Canyon sections separates the Copenhagen Formation's interlayered shale and lime mudstone units from the silty quartz-rich, parallel-laminated, dolomitic mudstone units of the AVL (Fig. 52).

Thick-bedded siltstone units, without any internal sedimentary structures, usually have a massive-bedded appearance. These thick-bedded siltstone units gradually change downward into rhythmical, thin-bedded siltstone and parallel-laminated dolomitic mudstone units (Fig. 52).

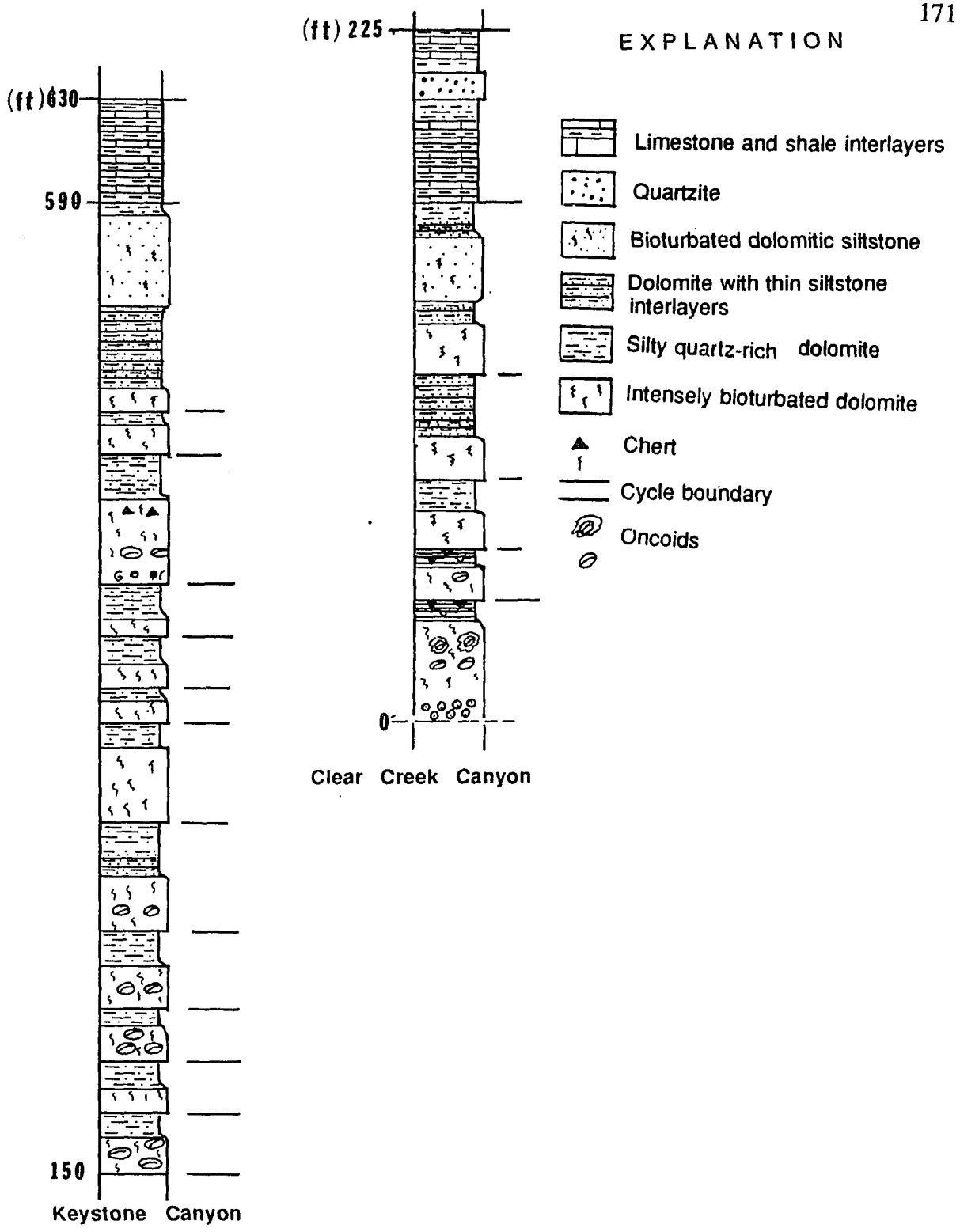
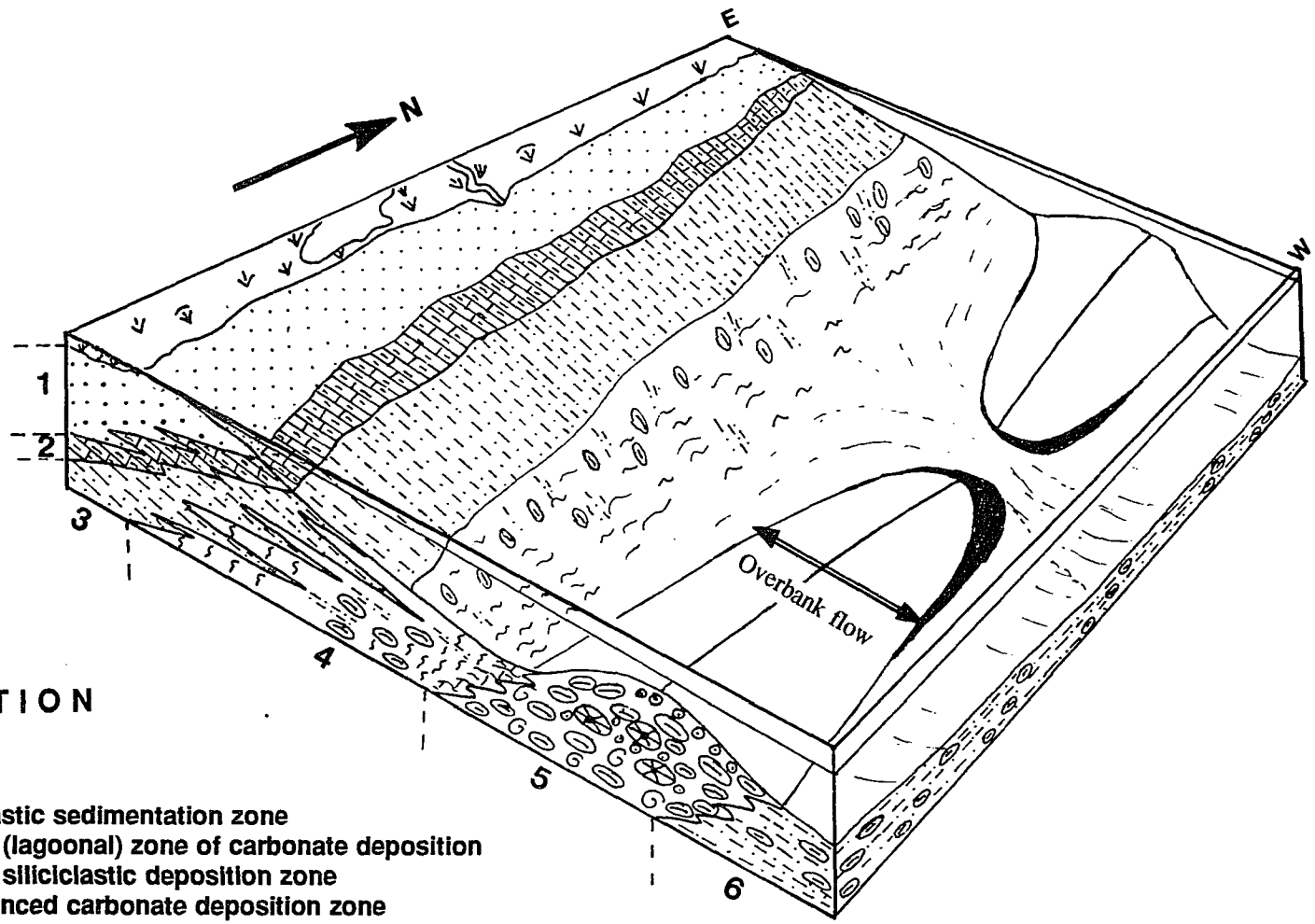


Figure 52- Cyclical successions of parallel-laminated, silty quartz-rich lime mudstone lithofacies within the bioturbated wackestone lithofacies, showing a nonshallowing-upward cyclic features in the Keystone Canyon and Clear Creek Canyon sections.

Interpretation:

The massive appearance of the siltstone unit without any sedimentary structures and its gradual contact relations with the rhythmical siltstone and lime mudstone couplets may suggest a further shoreward-extended shelf environment. Furthermore, the absence of bi-directional laminae and flaser beds in the massive siltstone lithofacies eliminate the possibility for the massive siltstone lithofacies being an intertidal-flat deposit. In the Keystone Canyon section, this massive siltstone unit gradually overlies the indicated rhythmical beds and gradually changes upward into thin-bedded non-fossiliferous mudstone and shale interlayers of the Copenhagen Formation (Figs. 52, 53). Therefore, on the basis of this stratigraphic observation, we can suggest that this fine-grained sandstone or siltstone may represent the mouth bars of the storm countercurrent channels. This interpretation can also be inferred from the stratigraphic position of this sublithofacies which is separated from the Eureka Quartzite by the rhythmical bedded shale and lime mudstone interlayers of the Copenhagen Formation (Fig. 52, 53). The occurrences of the rhythmical lime mudstone and shale lithofacies of the Copenhagen Formation between the Eureka Quartzite and this siltstone and silty-quartz dominated mid-shelf sediments of the AVL clearly indicate a storm-controlled siliciclastic sedimentation rather than progradation of the shoreline. In Figure 53, fine-grained siliciclastic sedimentation progressively increases from mid-shelf up to shoreward where the massive siltstone sublithofacies probably formed as storm-countercurrent mouth bars from storm-countercurrent channels. The carbonate sedimentation with calcareous shale interlayers (the Copenhagen Formation) dominates a farther shoreward, shallow-shelf environment which is interpreted to have formed between the depositional sites of the storm countercurrent channels' mouth bars and the shoreline siliciclastics (the Eureka Quartzite).

The indicated-sedimentation pattern is not consistent with progradating shoreline sediments and delta deposits, such as Pennsylvanian deposits in the Midland Basin, Texas and Midcontinent (cf., Mack and James, 1986; Heckel, 1986; and Yancey,



EXPLANATION

1. Coastal siliciclastic sedimentation zone
2. Nearshoreward (lagoonal) zone of carbonate deposition
3. Shoreward-fine siliciclastic deposition zone
4. Girvanella-enhanced carbonate deposition zone
5. Incipiently drowned oncoidal shoal
6. Fine-siliciclastic dominated-open shelf or upper slope

Figure 53- Model for the sedimentation of nonshallowing-upward fine-siliciclastic cycles in middle and outer open shelves. The coastal siliciclastic sediments (1) represents the Lower and Upper Eureka Quartzite members. Near Shoreward carbonates (2) represents the Copenhagen Formation. Lithologic units depicted by 3, 4, 5, and 6 represent the AVL.

1986), but it is principally controlled by strengths of the shoaling storm-flood and storm countercurrents, by the morphology of shelf and as well as by the quantity of dissecting storm-counter channels.

Similarly Hayes (1967), Kelling and Mullin (1977), and Nelson (1982) relate the fine-grained sedimentation in shelves to storm countercurrents-transported suspension. However, Morton (1983), using relatively recent oceanographic measurements and findings, relates the fine-grained sediment transportation to wind-forcing currents rather than storm countercurrents during storm events. Nelson (1982) illustrates that these two mechanisms are equally important for fine-grained sediment transport during storm events in the Bering Epicontinental Sea.

Lithofacies 12 C: Fine-Grained Massive Quartz Arenite

Description:

In the Clear Creek section, the laterally discontinuous, light pinkish quartzite (quartz arenite) overlies disconformably the rhythmical thin-bedded lime mudstone and shale units. The well-rounded, fine-grained sands and silts are cemented by micritic dolomite. This quartzite lithofacies generally has a massive appearance and does not show any internal texture; otherwise, it is similar to the Eureka Quartzite by the color and grain size of its fine-grained particles.

Interpretation:

The laterally discontinuous, fine-grained, massive quartzite (quartz arenite) probably represents storm-surge channel deposits in the near shoreward inner shelf. The lack of coarse grains and intraclasts agrees with this postulate. The color and grain types of this lithofacies are similar to the pinkish lowermost Eureka Quartzite; therefore, it is

possible to suggest that the fine-grained particles of this quartzite may have come from the sandy shoreline by storm-counter currents. Also it is possible that this quartzite may have been deposited in a farther shoreward-extended site of the inner shelf.

Lithofacies 13: Pelletal- and Oncolitic Wackestone

Description:

Dark gray, bioturbated, pellet-rich oncolitic wackestone units commonly occur in the shelf facies of the skeletal and oolitic shoal, oncoidal shoal as well as Nuia shoal. This lithofacies commonly lies between the restricted-shoreward shelf lithofacies and the moderately well-circulated shoalward shelf lithofacies (bioturbated wackestone).

About 2 mm to 2 cm irregularly coated, asymmetrical oncoids with outer and inner skeletal concentric laminae (Fig. 54 A to D) lie in the medium-bedded oncoidal sublayers showing a crude-normal grading.

The oncoids of this lithofacies generally have two kinds of nuclei: (a) algal core; and (b) skeletal core, containing mostly ostracod and gastropod fragments.

From the Martin Ridge section to Ninemile Canyon section, in the shelf facies of the skeletal and oolitic shoal, this oncolitic lithofacies increases eastward in thickness, whereas in the shelf of Nuia shoal, these oncolitic units become thinner in the same direction. In the Keystone Canyon sections, particularly in the shelf of the oncoidal shoal, this lithofacies cyclically intercalates with silty quartz-rich intervals. Usually, in mid-shelf facies, this lithofacies appears to have massive bedforms, but close examination of polished-hand specimens indicates that multiple thin-bedded units constitute the massive-bedded oncolitic sublithofacies. In these amalgamated bedforms, the oncoidal layers overlie another with a sharp-basal contact and show a fining-upward texture (Fig. 54 B).

There are two kinds of coating algae have been recognized in the oncoids of this oncolitic lithofacies: (1) Girvanella, most common (Fig. 54 C, D); and (2) Girvanella

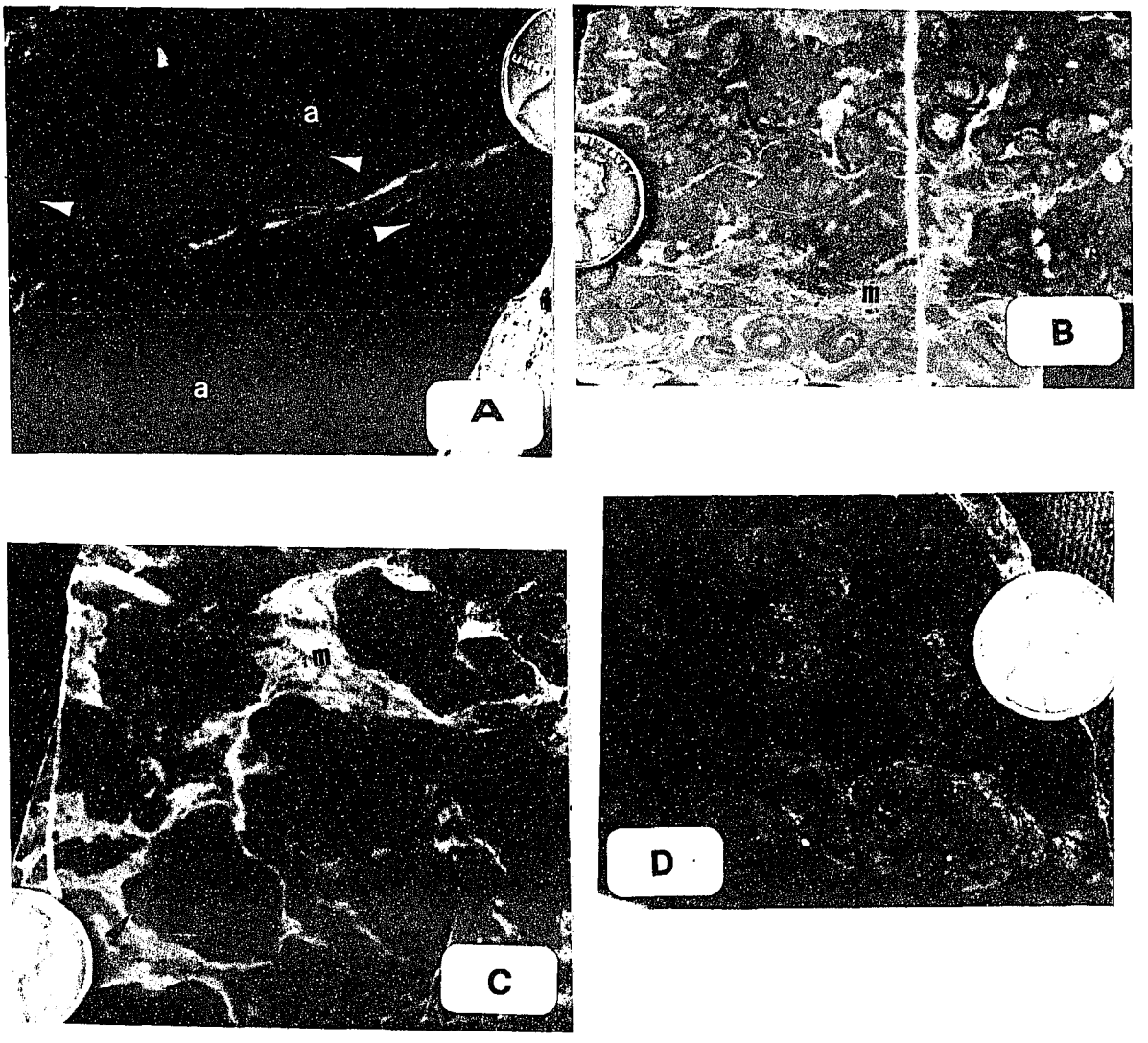


Figure 54- Oncolitic wackestone lithofacies of restricted-shelf. Polished slabs of the oncoidal wackestone lithofacies (A, B, C, and D). A) Oncoids of this oncoidal wackestone show two major coating types: (1) regular Girvanella coating; and (2) digitated-bryozoa coatings indicated by white arrowheads and (a). B) The oncoidal wackestone lithofacies consists of oncoids with irregular coatings and outlines; (m) indicating yellow-brown mud concentration. C) Oncoids show two different coating modes: (1) relatively well rounded inner coating indicated by small arrowheads; and (2) irregular outer coatings and outlines. (m) indicates yellow-brown, silty quartz-rich mud concentration. D) Dolomitized-oncolitic wackestone is composed of large oncoids characterized by skeletal inner laminae and digital outlines. Pennies for scale.

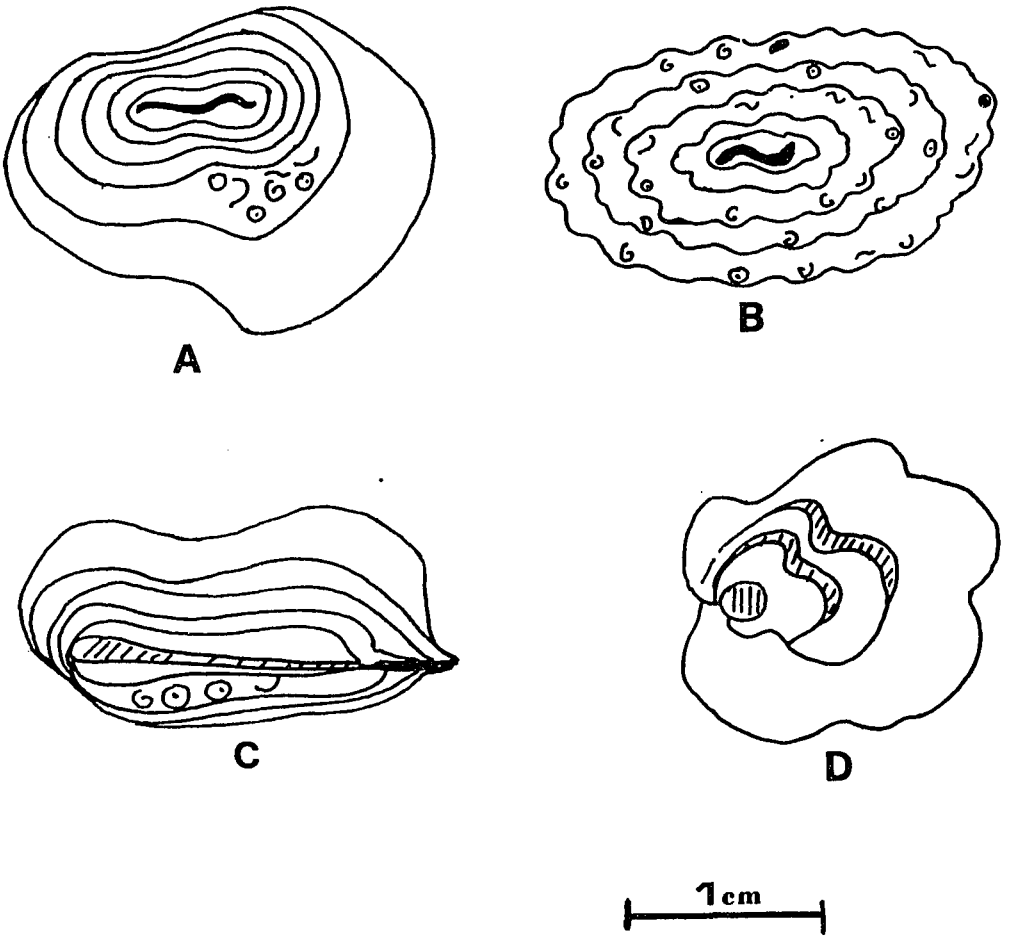


Figure 55- Forms of oncoids and their different kinds of laminae in the restricted-shelf facies. A) Two coating forms and outlines: (1) regular inner coating with or without skeletal laminae, and (2) irregular outline and non-symmetrical concentric coating. B) Skeletal laminae with digitated outline. C) Irregular and incomplete concentric inner and outer lamina and outline. D) Incomplete concentric laminae with digitated form and partial calcitic concentric laminae.

and bryozoans (Fig. 54 A), coating the uppermost half of the oncoids. Usually, the light gray bryozoan coating on the half of uppermost part of the oncoids can be clearly distinguished from the dark Girvanella-constructed oncoidal laminae. Figure 55 indicates the common oncoid types and concentric laminae in the restricted-, low-energy shelf. The oncoids in of this lithofacies usually have irregular inner and outer laminae and irregular outline. The inner and outer laminae of these oncoids most commonly consist of skeletal and detrital particles (Fig. 55). Microdolomite crystals commonly occur along the boundaries of concentric oncoidal laminae. These oncoids containing calcite-filled (or neomorphosed allochems) centers and fenestra-filling calcite cements are commonly replaced by dolomite euhedral spars.

The approximated average constituents of this lithofacies are oncoids 30-35 %, ostracods and gastropods 8-10 %, algal intraclasts or peloids 10-15 %, and pellets 12-15 %. Peloids seem to have been originated from algal fragments of 0.2-0.3 mm grain size.

Interpretation:

Especially, gastropod and ostracoda and bryozoa-rich bioturbated-wackestone and mudstone units generally indicate a restricted-subtidal, low-energy environment. The oncoids of this lithofacies -- with irregular outer outline, common presence of inner and outer skeletal laminae, with asymmetric coating and the absence of interparticle cement -- indicate that the deposition of this lithofacies may have taken place in the low-energy subtidal environment. Under the indicated environmental conditions, it can be explained that episodic moderate turbulence was strong enough to keep these oncoids in motion with a considerably short time compared to other shoal and backshoal oncoids. This interpretation can be substantiated by the common occurrence of skeletal grain-bearing, inner and outer concentric irregular laminae in oncoids of this lithofacies.

The silty quartz-rich, intensely bioturbated-upper muddy sublayers between the

oncolitic layers probably represent a post-stormal sedimentation. In general, for bioturbated-oncolitic sublayers, we can suggest that soft-bottomed, algal carpeting was destroyed as the algal balls were taken into suspension during episodic storm events. Then oncoids may have been deposited first while the storms were gradually loosing their strengths, and finally fine-grained sediments were probably deposited from the storm countercurrents or normal sedimentation. Consequently, the fining-upward texture and, the amalgamated-bedding forms are indicative of the multiple-waning currents and related sedimentation during short-lived, high-energy events.

The asymmetric concentric laminae of oncoids, with the skeletal grain-rich internal laminae, are believed to indicate relatively moderate-energy environmental conditions under which these oncoids were taken into suspension less frequently and rested on the sea floor relatively longer than their suspension periods (Logan et al., 1962; Dahanayake, 1977).

Coatings by two different organisms (Girvanella and bryozoan) suggest that oncoids were probably resting on the sea floor when bryozoas attached themselves on the upper surface of those oncoids and coated them.

The formation of the low-energy oncolitic units between relatively open-marine shelves represented by the normal marine bioturbated wackestone lithofacies and increasingly restricted shoreward shelf represented by pelletal mudstone can be analogous to the grapestone facies forming behind the emerged-oolitic shoal bars, as noted by Purdy (1963 a) and Winland and Matthews (1974). The algal coating or colonization and chemical cementation are primarily responsible for the formation of grapestone facies under the nondepositional or zero depositional, low-energy environmental conditions (Winland and Matthews, 1974). Similarly, Peryt (1981) suggests that formation of the Girvanella oncoids generally characterize low-sedimentation rather than bathymetry. Therefore, on the basis of this interpretation, it can be suggested that episodically moderate turbulence and low-sedimentation rate are prerequisite for the formation of this kind of oncolitic lithofacies within a predominantly low-energy, shallow-subtidal depositional environment.

B. Synthesis

The Nuia-rich, bioturbated wackestone lithofacies gradually overlies the Nuia packstone- and grainstone lithofacies. This wackestone lithofacies with open marine fauna represents a hydrologically well-circulated shelf facies formed behind the Nuia shoal. In this shelf facies, to eastward increase in the fine-grained siliciclastic sedimentation and in the tone of light color represents a shoreward progressive shoaling.

The good shelf circulation is assumed to have been provided primarily by overbank and interbank flows. The upper shelf facies containing the fine-grained siliciclastics represents the shoreward shelf as well as storm counter deposits formed during the incipiently drowned Nuia shoal facies.

The oncoid-rich bioturbated wackestone lithofacies with the nodular bedforms overlie the oncoidal shoal units. This lithofacies with indicated features also characterizes a hydrologically well-circulated, relatively deeper shelf than that of the shelf formed behind Nuia bars. In the oncoidal shelf, overbank flow appears to have been more effective and maintained a good circulation by the overbank flow of the Nuia shoal. The faunal and lithologic variations of this oncoidal lithofacies also represent progressively shoaled and restricted shelf which can be inferred from eastward upward increase in the concentration of the fine-grained siliciclastic particles.

The sedimentation rate in this shelf and the oncoidal shoal appears to have been outpaced by sea-level rise. These depositional conditions began after the deposition of the late Orthidella zone and continued until the end of the Anomalorthis zone due to the incipiently drowned carbonate bank and shelf conditions (Fig. 53).

Generally, the siliciclastic-free, bioturbated-wackestone lithofacies, which gradationally overlying the oolitic and skeletal packstone- and grainstone units and overlain by the algal-flat deposits, represent a restricted-shelf facies which may have formed behind the skeletal and oolitic shoals. This lithofacies, containing restricted-marine fauna, also indicates that the high-sedimentation rate of the oolitic

shoal kept pace and outpaced the sea-level rise, especially during the deposition of the middle and upper Palliseria and lower Anomalorthis zones. In this shelf facies, the oncoidal wackestone units, lying between the bioturbated wackestone of moderately well-circulated shelf and the pelletal lime mudstone of the restricted shelf, represent the grapestone lithofacies. In the late Palliseria and lower Anomalorthis zones, the thick algal-flat units, which commonly cap the shallow-subtidal units, represent the high-progradation rate of the tidal flat. This episode probably has a correspondence with the high-progradation rate of the siliciclastic shoreline sediments (the Eureka Quartzite at Lone Mountain and at the southern localities of this study).

Mudstone to wackestone limestone layers rhythmically alternate with thin shaley layers. The restricted-marine faunas dominate the limestone interlayers in the rhythmically bedded lithofacies which overlie the peloidal and siltstone nearshore bars. These rhythmical lithofacies are separated from the moderately well-circulated shelf by nearshore bars and the mouth bars of storm-countercurrent channels. Therefore, based on evidence, we can suggest this rhythmical lithofacies with restricted-marine fauna represents the lagoon or inner shelf facies. Eastward increase in progressive shoaling of this inner shelf can be inferred from the progressive increase in the thickness of fine-grained siliciclastic interlayers. The rapid sea-level rise at the beginning of the late Anomalorthis zone is assumed to have been the principal cause for the formation of this lagoonal lithofacies (the Copenhagen Formation) along with a well-circulated shelf and oolitic shoal at Ninemile and Martin Ridge region. However, the indicated relations above are not present at the other localities due to the configuration of the carbonate shelf profile and its positions with respect to mean-sea level (Fig. 53).

The absence of the Copenhagen Formation in the Lone Mountain section, about 20 miles north of the Antelope Valley region, is also related to the lower carbonate deposition rate and incipient drowning of the carbonate producing oncoidal bank. Therefore, the high-progradational rate of the coastal siliciclastics and their basinward migration may have caused the Eureka Quartzite to directly overlie the deep-shelf facies behind the oncoidal shoal.

CHAPTER 8: INTERTIDAL- TO SUPRATIDAL FACIES BELT

This facies belt ranges from upper subtidal- to intertidal algal-flat depositional environments. The stromatolitic lime mudstone lithofacies (Lithofacies 15) is the most important and thickest lithofacies of this facies belt, gradually overlying the pelletal and oncoidal mudstone- to wackestone lithofacies " Lithofacies 14" (Fig. 56-I).

The stromatolitic lime mudstone lithofacies, capping the shallowing-upward oolitic shoal cycles, are thicker and higher in number in the Ninemile Canyon section than those in the Martin Ridge section (Fig. 56-I).

The pelletal and oncoidal mudstone- to wackestone lithofacies (Fig. 56-I A) are not thick enough to be depicted in vertical columns; therefore, they are included into the stromatolitic lime mudstone lithofacies (Fig. 56-I).

A. Lithofacies

Lithofacies 14: Pelletal- and Oncoidal Mudstone and Wackestone

Description:

A tan to light gray bioturbated-pelletal mudstone unit gradually overlies tan to light gray the oncoidal mudstone and wackestone sublithofacies and gradually changes upward into the stromatolitic mudstone units. Usually, this lithofacies consists of pellets, discontinuous cryptalalgal laminae, ostracods, and small and thin-shelled gastropods (Fig. 56-II A).

The bean-shaped oncoids lie within discontinuous stromatolitic layers, and their

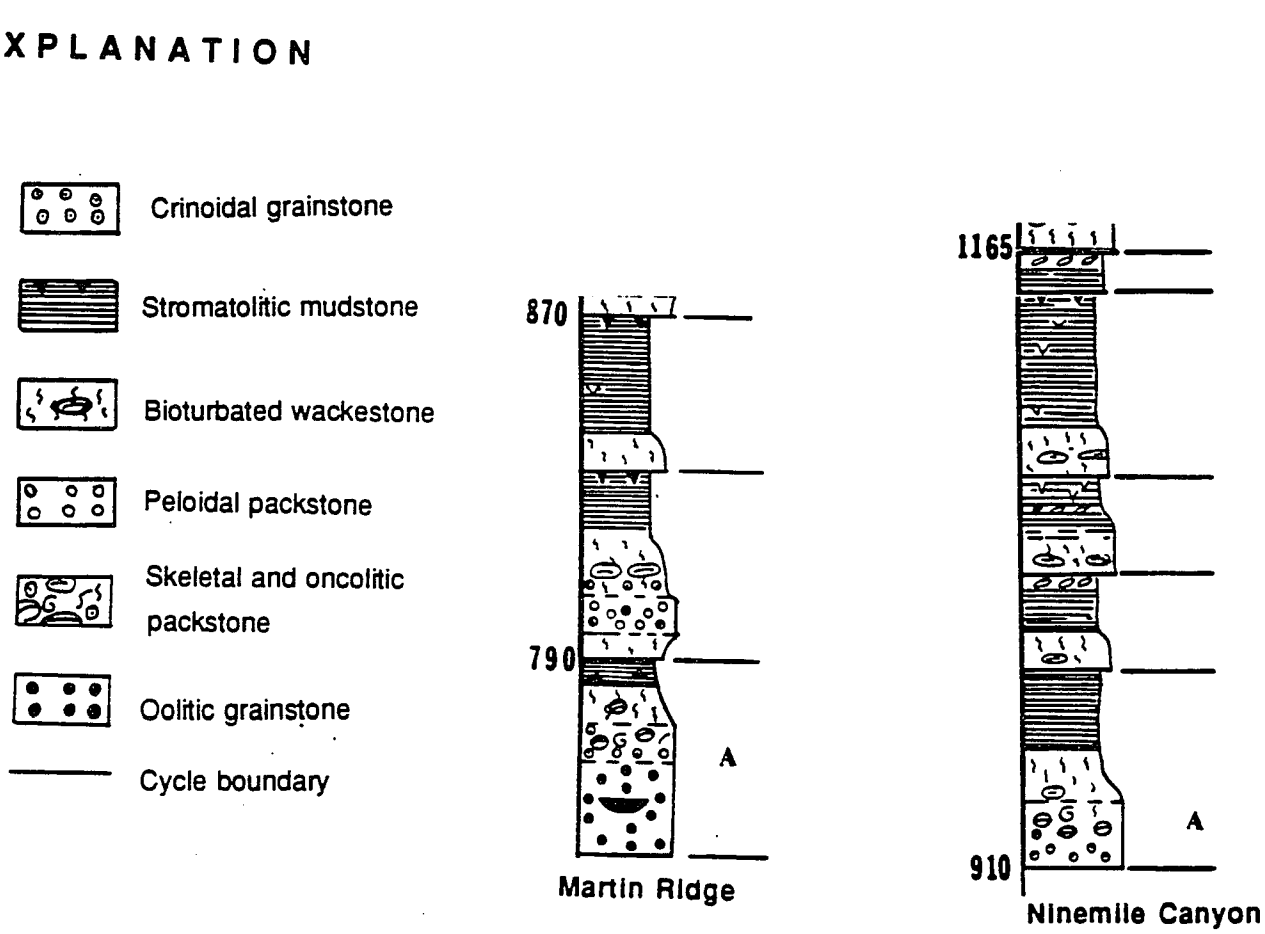


Figure 56 I- Vertical section showing the cryptalgal lime mudstone lithofacies and their cyclical successions in the Ninemile Canyon and Martin Ridge sections.

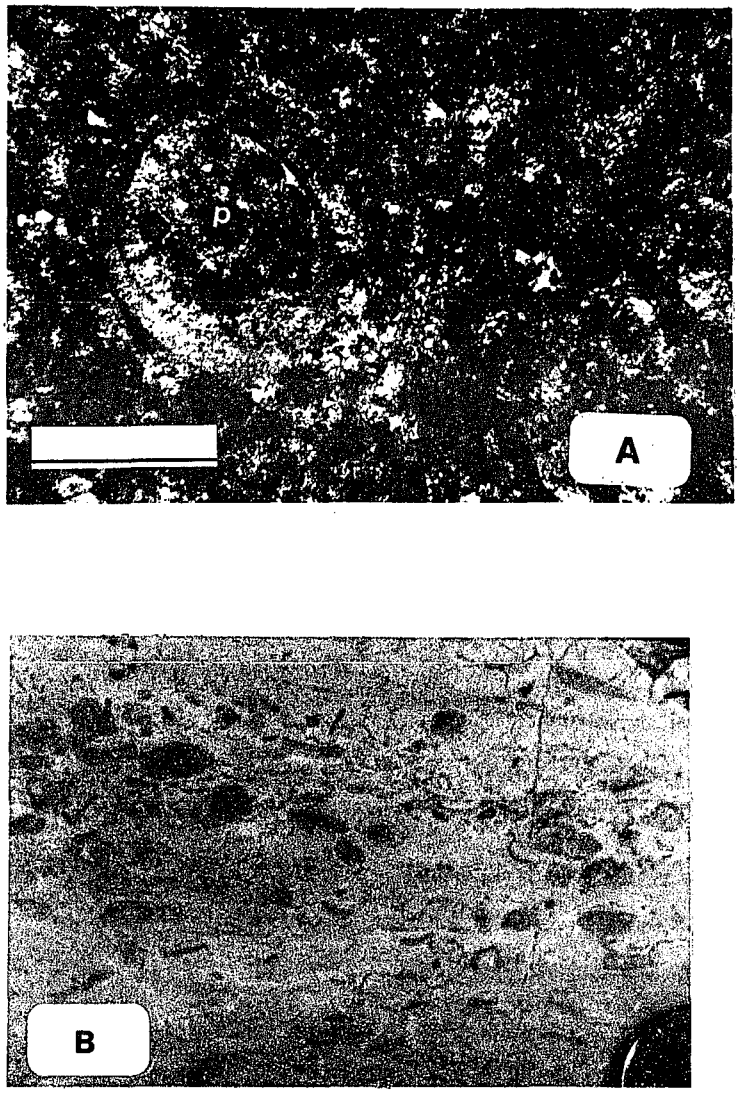


Figure 56 II- A) Photomicrograph of pelletal lime mudstone to wackestone lithofacies; ostracods are common along with pellets (p). With plane-polarized light; scale= 0.5 mm. B) The stromatolitic-oncoidal wackestone to mudstone unit; penny for scale.

longer axes are parallel to the disturbed-algal laminae (Fig. 56-II B). Tan to light gray oncolitic mudstone to wackestone is composed of elongated- and bean-shaped oncoids having gastropods and ostracods in their nuclei. The dark micritic concentric laminae of these oncoids commonly contain fenestral textures and scattered-micropyrite crystals. The grain size of these oncoids is in the range of 0.4-1 cm, an average grain size 0.5- 0.6 cm.

The approximated-average percentages of constituents of this oncoidal sublithofacies are (1) oncoids 25-30%, (2) pellet 10-15 %, (3) intraclasts 10 %, (4) peloid or small-algal fragments 10-5%, (5) ostracods 5%, and (6) gastropods 2%.

Interpretation:

Tan to light gray bioturbated-pelletal mudstone lithofacies, with discontinuous-cryptalgal laminae and predominant restricted faunas, represents a low-energy, lower intertidal depositional environment where grazing faunas were relatively more active. In such environment, the fluctuation of daily temperature and salinity probably creates very stressed-environmental conditions for normal-marine faunas. Therefore, only few restricted-faunas, ostracods and gastropods, contested and survived in this restricted environment.

Similar lithofacies have been described in modern tidal deposits of humid climate by Shinn (1969), Hardie (1977) and Ginsburg and Hardie (1979), and of arid climate by Kendall and Skipwith (1969), Kinsman (1969), Friedman et al. (1973), Logan et al. (1974) and Purser and Evans (1972).

The oncoidal sublithofacies change gradually upward into the pelletal stromatolitic mudstone sublithofacies and downward into the dark gray, pelletal bioturbated-wackestone units. The oncoidal sublithofacies probably represents a depositional environment ranging from upper subtidal to lower intertidal.

The oncoids of this sublithofacies, consisting of gastropods and ostracods as nuclei (Fig. 57 A), clearly indicate a very restricted-shallow subtidal environment. The

absence of imbrication of oncoid grains also indicates an environment ranging from low-energy shallow-subtidal and lower-intertidal depositional environments. Therefore, this oncoidal unit symbolizes similar environmental conditions under which modern oncoids commonly form (Ginsburg, 1960; Bathurst, 1975; and Flügel, 1982). The oncoids described in this lithofacies are very different from those described in the other parts of the AVL, such as lack of Girvanella filaments and common occurrences fenestral texture. Thus, the fenestral texture indicates a very close association between these oncoids and stromatolites which were probably the principal producer of these organo-sedimentary grains for this subunit. Finally, from the criteria above, it can be implied that periodic turbulence probably detached stromatolites and produced these organo-sedimentary grains.

The present day stromatolitic oncoids and stromatolites have been reported in the Hamelin Bay in the Shark Bay, Australia by Logan et al. (1962); in Joulters Cay by Gebelein (1969). In contrast to Girvanella oncoids, the subtidal stromatolites grow on the hard-ground surfaces (Monty, 1967; and Gebelein, 1969).

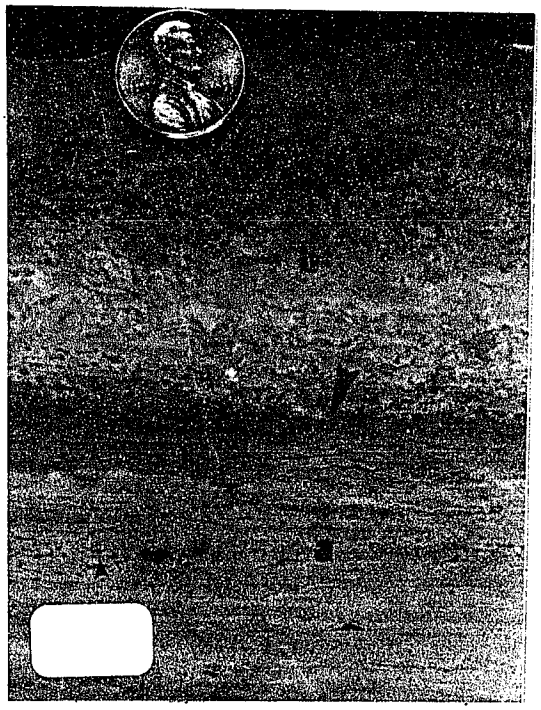
Lithofacies 15 : Cryptalgal Lime Mudstone

Description:

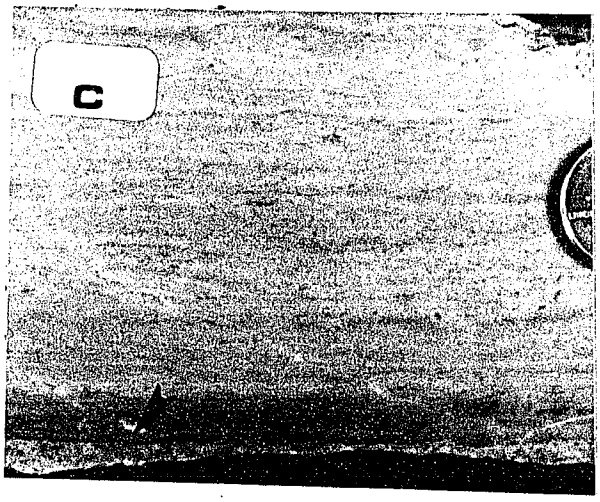
Tan to buff, parallel, thin (sub mm to mm) cryptalgal-laminated stromatolitic mudstone sublithofacies grade upward into the fenestral (birdseye) texture-dominated subunits, and grade downward into light gray mudstone lithofacies (i.e., relatively discontinuous parallel, algal laminae-dominated subunits).

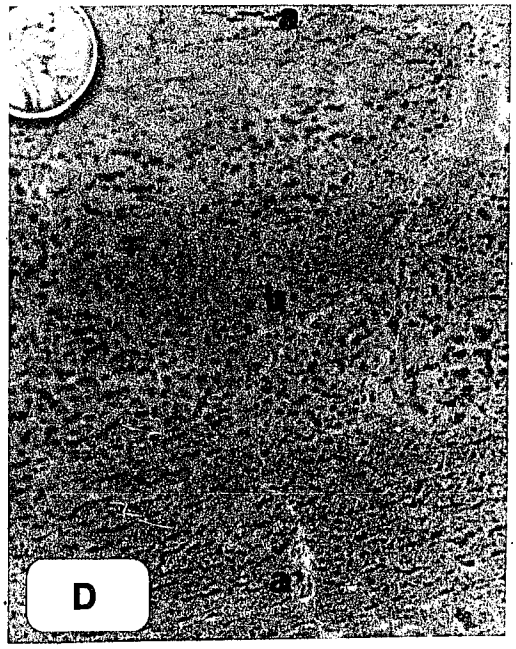
The parallel cryptalgal laminae are commonly crenulated (Fig. 57-I A, C). The polygonal mud cracks are also commonly found at the upper surface of this lithofacies. The polygonal-desiccation cracks (Fig. 57-II B) propagate downward with a 'V' shape

Figure 57 I- Cryptalgal mudstone lithofacies. A, C, and D are polished slabs and B is a photomicrograph. A) Parallel-laminated cryptalgal lime mudstone lithofacies. (a) represents nearly parallel and continuous cryptalgal laminated subunit which locally contains laminoid or fenestrae indicated by large arrowhead, and small arrowheads indicate calcite-filled spherical fenestrae or birdseye texture. (b) represents a mechanically disturbed cryptalgal subunit which upward becoming as a flat-pebble conglomerate; arrowhead indicates a sharp contact between these two subunits. B) Photomicrograph of the cryptalgal lime mudstone lithofacies. Euhedral pyrite crystals (p) are primarily scattered within the dark algal organic-rich sublaminae. With plane-polarized light; scale= 0.5 mm. C) The cryptalgal mudstone lithofacies shows stromatolitic laminae, and arrowhead indicates a sharp planar contact between the algal subunit and thin skeletal fragment-rich subunit. D) The cryptalgal mudstone lithofacies; parallel and elongated birdseye or fenestrae (a) changing upward into lensoidal birdseye texture (b). Pennies for scale.




B
p
p


C


D

and are filled by detrital, fine-grained silt. The well-developed, parallel-algal laminae gradually change upward into the poorly laminated mudstone subunits in which the elongated fenestrae are also present (Fig. 57-I A). These poorly laminated subunits are gradually overlain by darker stromatolitic subunits (about 1-4 cm) which rarely show a "scallop fabric" (tufted mud). The parallel laminae disappear in these subunits as thin fenestrae become continuous. The scallop-textured, thin darker, sublayers change upward into a subunit in which algal chips are parallel to the disturbed-algal laminae. The birdseye fabric is common in the interalgal chip space and gradually upward becomes dominant (Fig. 57-I A). Similarly, the laminated algal subunits show a transition from well-laminated algal (smooth mat) to poorly laminated to massive stromatolitic mudstone subunits (pustular mat) and further upward into predominantly laminoid or fenestral (birdseye) fabric-dominated subunits (Figs. 57-I D, 57-II A, B) as described in the algal flats of Hamelin Pool by Logan et al. (1974) and Hagen and Logan (1974).

The birdseye-algal mudstone subunits exhibit a transitional internal morphology (Fig. 57-I D). The elongated-fenestrae change upward into the randomly oriented, or isolated fenestrae. The similar textural relations have been described in algal mud under the experimental work (Shinn, 1967).

Under microscope, the cryptalgal laminae are seen as alternating calcitic and relatively thicker pelletal and silty quartz-rich sublayers (Fig. 57-I B). Microscopic examination of birdseye texture reveals that well-rounded and well-sorted algal peloids commonly occur in irregular clusters.

The algal-laminated units consist of thin-bedded skeletal and oolitic grainstone- to packstone layers (1 to 5-cm thick). These grainstone- and packstone units occur in the algal-laminated mudstone units with a sharp erosional, planar-basal contact and a sharp upper contact (Fig. 57-I C). The sharp planar upper contacts of these shelly layers are most commonly colonized by stromatolites, as noted on the Cacios Platform by Wanless et al. (1988 b).

Another common sublithofacies of this stromatolitic mudstone is the flat-pebble conglomerate, which is composed of stromatolitic intraclasts. The flat-pebble

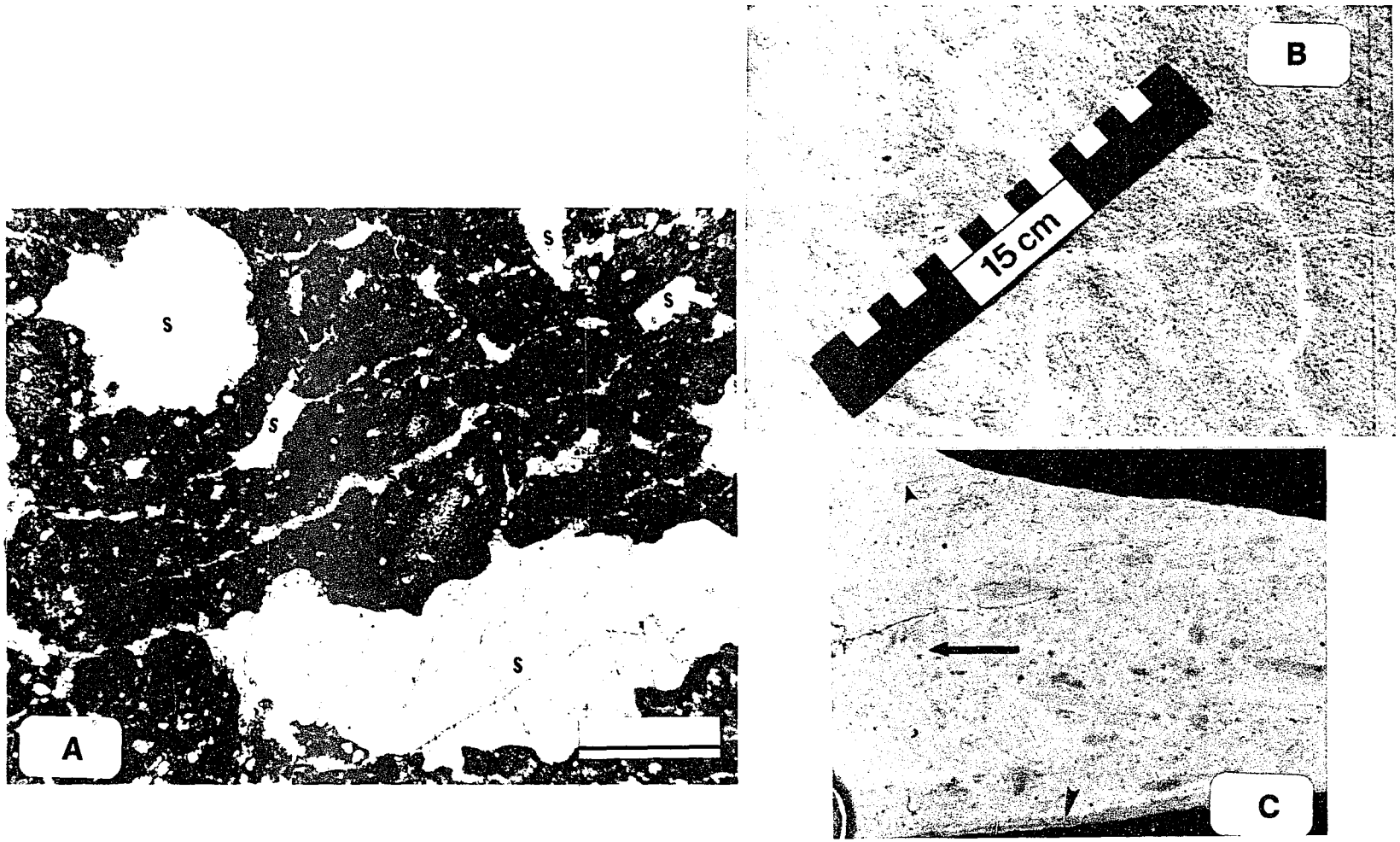


Figure 57 II- Cryptalgal mudstone lithofacies. A) Photomicrograph of birdseye texture. (s) indicates fenestra-filing sparry calcite cement. With plane-polarized light; scale= 0.5 mm. B) An close-up outcrop photograph of desiccation cracks in the cryptalgal lime mudstone lithofacies. C) Polished slab of flat-pebble conglomerate. Arrow indicates imbrication of algal clasts, and arrowheads point to sharp, planar basal and upper contacts of this subunit within the stromatolitic lime mudstone; penny for scale.

conglomerates overlie the parallel-laminated algal units with a sharp, erosional contact, and their algal chips clearly display imbrication (i.e., one pebble leaning over another; Fig. 57- II C). Like the shelly layers, the upper contacts of these conglomerates are sharp, planar and also colonized by stromatolites.

Due to the same light creamy color in both units, it is difficult to differentiate these conglomeratic units from the poorly laminated stromatolitic mudstone units even in the polished-samples. The oxidation of precursor iron minerals, such as pyrite, stains this units with slightly yellow-brown color.

Interpretation:

The study of modern carbonate intertidal depositional environments has provided enormous information which makes it possible to compare them to their ancient counterparts. The following studies deal with the humid climatic intertidal-modern carbonates by Ginsburg (1960), Shinn (1969), Ginsburg and Hardie (1977), Gebelein (1969), Monty and Hardie (1977), and Hardie (1977); and the arid tidal-flat modern carbonates in Shark Bay by Logan et al. (1974), and by Hagen and Logan (1974); in Persian Gulf by Kendall and Skipwith (1966), Kinsman (1969) and Evan and Purser (1972); in Red Sea by Friedman et al. (1973), Friedman and Krumbein (1985), and Friedman, et al, 1985).

The present-day stromatolites (blue-green algae or cyanobacteria) mostly grow in intertidal-algal flats where high salinity, daily temperature fluctuations, long subaerial exposure and siliciclastic influx reduce and eliminate benthic faunal activities. Only few organisms can contest with these harsh environmental conditions. Thus stromatolites preferentially grow where sediment mobility and the presence of grazing organisms are minimal (Monty, 1964; Gebelein, 1969).

In such environments, stromatolites attach themselves to firm grounds or hardground surfaces, bind, and baffle detrital sediments. According to Monty (1977), the

phototactic activity (movement of plants toward light) stromatolites determines the parallel algal laminae: During the day, algae grow upward and baffle detrital sediments; and algae grow laterally and form dark thin algal film or mat during the night. Similarly daily photosynthesis activities of the blue-green algae (cyanobacteria, see Friedman et al. 1992) caused the formation of biological organo-sedimentary lamination which are composed of alternating light acicular-aragonitic laminae and dark, thin cryptocrystalline laminae (Friedman et al., 1973): The light, aragonitic-fibrous laminae generally form during the night by withdrawal of CO_2 from the hypersaline water; and during days dark cryptocrystalline laminae (high-Mg calcite) form. Thus, these cryptalgal laminae are considered as bio-sedimentary structures rather than gravitational sedimentary structures.

Dolomite- and silty quartz-rich muddy laminae with relatively higher pyrite content are probably associated with the Mg-rich composition of the organic-rich sublayers. These organic laminae provide Mg during the formation of dolomites (Friedman et al. 1973; Gebelein and Hoffman, 1973). Microcrystalline pyrites indicate reducing microenvironments which were primarily created by daily activity of sulfur-reducing bacteria at the surface environments (Friedman and Sanders, 1978, p. 105). However, the absence of dark algal mud intervals probably related to extensive oxidation of algal laminae.

Logan et al. (1974), Hagen and Logan (1974), and Kinsman and Park (1977) indicate that smooth (parallel-cryptalgal laminae) and pustular-lime mud and fabrics characterize an upper intertidal environments in modern arid algal flats. On the other hand, in the humid climatic algal flats, the similar algal units represent the supratidal sequence (Shinn, 1968; Hardie, 1977; Shinn, 1984; and James, 1984).

Similarly, the cryptalgal-laminated (smooth and pustular) algal units characterize the humid climate's tidal-flat sequences, more specifically they represent upper intertidal and supratidal depositional environments.

Upward gradual disappearance of the cryptalgal laminae along with the formation of the elongated-continuous-fenestrae can be correlative with the farther landward part of tidal flat where relatively long periods of subaerial exposure and high-evaporation rate

dominate (Figs. 57-I D & 57-II A). In addition, the polygonal desiccation cracks (Fig. 57-II B) at the top of the birdseye-dominated stromatolitic sublithofacies (Fig. 57-II A) suggest a prolonged-subaerial exposure of an algal-flat environment or supratidal environment.

The formation of "loferite" or birdseye texture is attributed to expansion and contraction of algal mud during repeated-wet and-dry episodes (Fischer, 1964). The generation of the gas bubbles is due to algal decay during wet episodes (Fischer, 1964). Logan et al. (1974) have put forth the similar process for the formation of fenestrae. Logan et al. (1974) assume that fenestrae formed by algal decay are most commonly filled by late diagenetic cements. On the other hand, Monty and Hardie (1977) have observed in the modern algal flats of the Florida and Bahama Banks that the storm-transported peloids disturbed the algal mud by detaching and repacking them; these re-orientation or regrouping resulted in the formation of irregular or elongated openings due to following algal decay. Monty and Hardie (1977) also observed the aragonitic crusts on the upper surfaces of these layers indicate that contemporaneous cementation and early lithification are responsible for the preservation of the fenestrae and their calcite fillings. In the birdseye-dominated subunits of this lithofacies, the orientation of the fenestrae is also closely related to the packing mode of peloids (Fig. 57-II A). In addition, the fenestral subunits hardly have any angular algal chips except in the slightly disturbed algal layers (Fig. 57-I A) in which wedged-algal chips are parallel to algal laminae with sparry calcite-filled fenestrae. On the basis of detailed examination of textural relations, we can suggest that Monty and Hardie's (1977) hypothesis appears to provide the best explanation for the formation of the fenestral fabric in the AVL. Moreover, rounded, well-sorted algal peloids (Fig. 57-II A) and absence of any edgy algal chips or clasts disagree with the desiccation process-generated birdseyes texture. Therefore, it is possible suggest that desiccations can occur after the contemporaneous cementation or aragonite encrustation of algal muds.

Two kinds of fenestra-filling have been recognized in this study: (1) early fenestrae, occurring before the desiccation along the slightly disturbed algal laminae

(wedged-algal chips parallel to algal laminae), and (2) late fenestrae (elongated fenestrae), forming after the desiccation. The rounded-peloids with fenestral texture that indicate the formation of fenestral openings in this lithofacies may have taken place much earlier than the desiccation process.

Nearly, about 15-feet thick, birdseye texture-bearing algal sublithofacies with desiccation cracks (Fig. 57-II B) do not contain any evaporite minerals and their crystal molds. This most likely suggests that deposition of this lithofacies took place under humid-climatic conditions of supratidal environment.

The rapid colonization of these shelly storm layers is analogous to shelly storm layers in modern algal flats where these shelly layers are commonly colonized by blue-green algae (Cyanobacteria) in a very short period. The microbial colonization period generally ranges from 15 days to 5 months depending on algal or microbial type and thicknesses of storm layers (Wanless et al. 1988).

The presence of angular, or subrounded clasts, either parallel to bedding plane and / or imbricated, is indicative of cyanobacterial contraction during the dry seasons. The imbricated-flat pebbles in the monogenic flat-pebble conglomerate appear to have derived from algal flats and indicate the landward flow direction that must have been caused by stormal events. The occurrences of the algal flat-pebble conglomerate on the algal laminated-mudstone units are also indicative of the supratidal environment. The comparable imbricated-deposits have been noted in modern intertidal environments by Shinn (1969), in ancient limestone units by Laporte (1967), Braun and Friedman (1969), Schenk (1967).

Finally, the absence of calcrete facies (conglomerate, pisolite and massive calcrete subfacies), collapse breccias, and evaporite minerals and their crystal molds suggest that humid-paleoclimatic conditions prevailed during the deposition of the Antelope Valley Limestone.

B. Synthesis

The cryptalalgal-laminated units gradually change downward into very restricted-, shallow-subtidal lithofacies. And they grade upward into birdseye-dominated algal units which indicate a farther landward, upper intertidal depositional environment. The flat-pebble conglomerates and mud cracks represent the subaerial exposure of the algal-flat environment. The absence of evaporite-related collapse breccia, evaporite minerals and their crystal molds, and calcrete conglomerates suggest that the AVL was most likely deposited under humid climatic conditions.

CHAPTER 9: SLOPE- AND BASINAL-MARGIN FACIES BELT

Slope- and basinal margin facies extends from shelf margin or shelf edge to deep basin. For the AVL in the study area, this facies belt is represented in the Whiterock Canyon section, Mill and June Canyon sequences (in the Iks Canyon window), and in the Dry Creek Canyon, Toiyabe Peak, and Reeds Canyon sections of the Toiyabe Range. In addition, the upper slope subfacies is present in the lower part of the Lone Mountain section, but its relations with basinal subfacies are not observable due to intermountain basin-fill sediments. Figure 58 shows the kinds of lithofacies in this facies belt and their relationships in vertical sections.

A. Lithofacies

Lithofacies 16 A: Greenish Gray Shale

Description:

In the lowermost part of the June Canyon section, greenish gray calcareous shale locally consists of dark gray, very thin limestone interlayers (Fig. 59). Down section, the shales become darker in color and overlie dark gray, thin-bedded cherty limestones with a sharp contact. Parallel, even laminae are common in the dark-green shale and in the very thin, micritic limestone interlayers. Micropyrite crystals are scattered within the thin limestone interlayers.

The allochem constituents of this sublithofacies never exceed 2 % and are chiefly fine-grained skeletal fragments. Bioturbation in this lithofacies is rare.

At the base of the Whiterockian Canyon section is a 60-feet thick, olive-green to dark gray shale containing very thin lime mudstone interlayers and dark gray

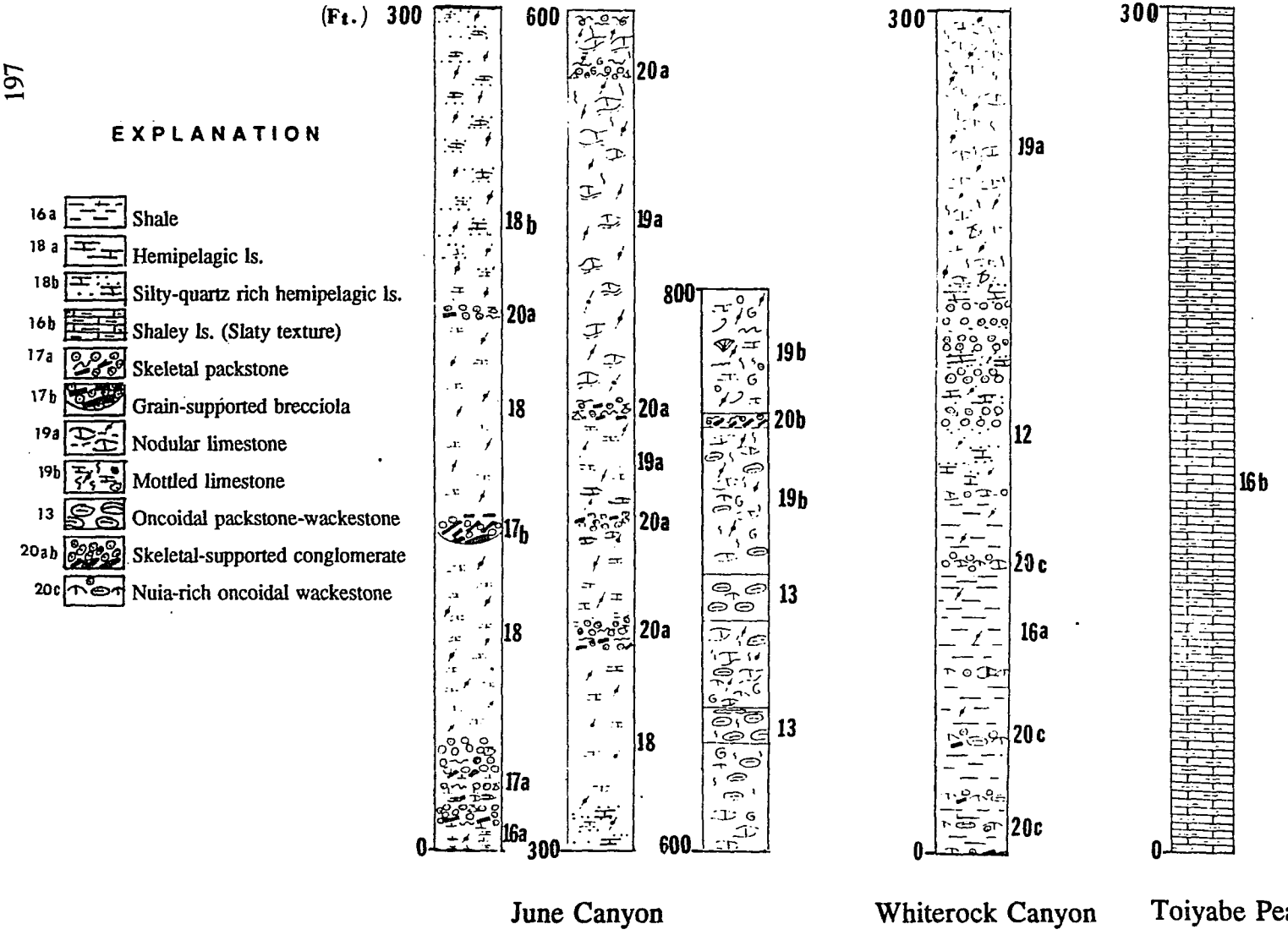


Figure 58- Lithofacies of the open shelf facies in the AVL, and their successions in the June Canyon, Whiterock Canyon and Toiyabe Peak sections. Numbers at the right side of the vertical columns represent the lithofacies numbers of this facies belt have been described in this chapter.

wackestone beds (20-cm thick) at intervals of 10 feet (Fig. 58).

Interpretation:

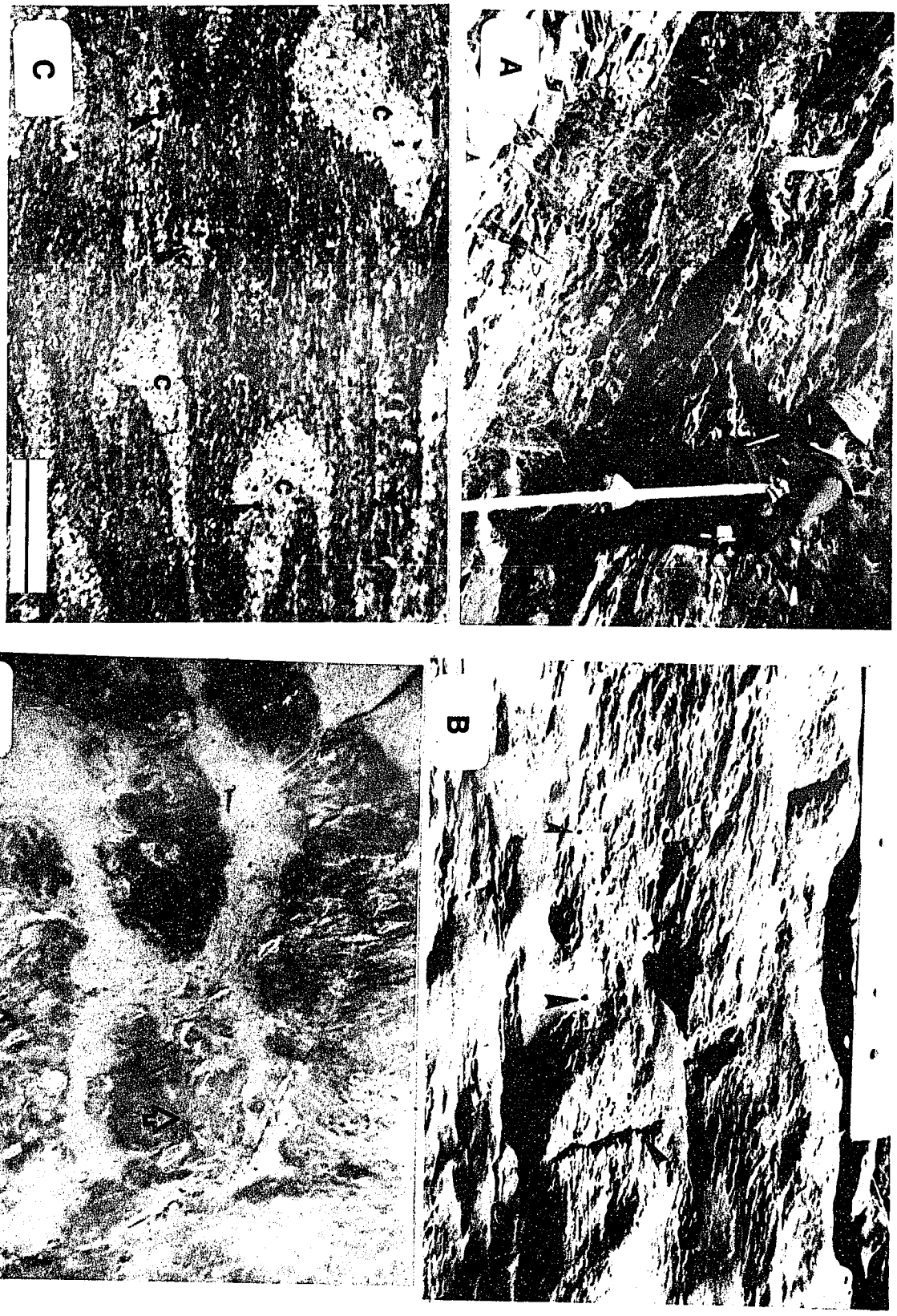
These lithofacies were probably deposited in the low-energy, basin margin in which anoxic or oxygen-minimum depositional conditions were responsible for the lack of bioturbation, presence of micropyrite, and preservation of parallel, even laminae (cf., Wilson, 1978). The absence of wave-induced sedimentary structures and preservation of thin, dark parallel laminae probably indicate a basinal environment (Heckel, 1972, and Byers, 1977). Their stratigraphic positions beneath the turbiditic layers, and their exposure at the westernmost extension of the Antelope Valley Limestone (AVL) within the westward deepening basin corroborate the interpretation.

Lithofacies 16 B: Shaley Limestone

Description:

In the Reeds Canyon section and the middle part of the Toiyabe Peak section (Fig. 58), black, thin-bedded limestone layers are separated from one another by thin shaley partings. Parallel, even laminae are common in both micritic and shaley interlayers. Under the microscope, the parallel laminae are seen as alternations of silty quartz-and clay-rich, very fine fragmented-skeletal grain-rich laminae with pellet-rich micritic laminae. In addition to large pyrite crystals, microeuhedral pyrite crystals are very common within the parallel-laminated, silty quartz-rich intervals. The even parallel laminae do not show any sign of bioturbation. This lithofacies consists of about 5-25 % silty quartz, 15-25 % pellets, and 2-3 % very fine skeletal fragments. The black, shaley micritic limestone units also occur in the Toiyabe Peak section and some intervals of the Dry Creek section. Generally, massive appearance of this lithofacies

Figure 59- Shaley limestone lithofacies. A) An outcrop photograph of slaty cleavage in the shaley limestone lithofacies. B) A close-up outcrop photographs of the silty quartz-rich layers in the slaty intervals of the shaley limestone lithofacies of the AVL; arrowheads point to late-diagenetic pyrite crystals; a 30-inch long ruler for scale. C) Photomicrograph of slaty texture. Arrows indicate pressure shadows, and arrowheads point to euhedral pyrites, and (c) designates locally recrystallized quartz and calcite crystals. With plane-polarized light; scale = 0.2 mm. D) An close-up outcrop photograph of a probable mollusc mound within shaley limestone (slate) units. Intermound spaces were filled by orange tan silty quartz-rich fine sediments.


C
A
D
B

without recognizable upper and basal contacts of individual units coincides with the development of axial plane or slaty cleavage (Fig. 59 A, B). Calcite-filled fractures are folded in this lithofacies. Products of pressure solution or microstylolites are commonly present along the parallel even laminae. Locally, skeletal laminae are composed of relatively large (up to 0.5 mm) crinoid spines.

The coarse-grained crinoids within the very fine-grained skeletal layers appear to have a pressure-shadow texture (Fig. 59 C) which probably resulted from rigid-body rotation of the larger allochems within the fine-grained interlayers. The slaty cleavage, one of the most prominent features of this lithofacies, can be recognized in microscopic and macroscopic scales. Under the microscope, preferentially oriented mica minerals, mostly sericite, and recrystallized quartz are found to be aligned in the direction of slaty cleavage, offsetting the pressure solution (i.e. parallel to thin even laminae). Euhedral micropyrite crystals are also aligned along these pressure solution laminae. In addition, the large euhedral pyrite crystals are randomly disseminated in this unit, poikilotopically including sparry calcite and replacive quartz.

The large pyrite crystals commonly occur in 5 to 10-feet thick, parallel-laminated, fine-siliciclastic intervals (Fig. 59 B). Another sublithofacies of this lithofacies includes the large mollusc-rich, black fossiliferous, massive units (Fig. 59 D) which alternate with relatively coarse pyrite-bearing beds. Upsection, this lithofacies grades into the uniformly rhythmic, thin-bedded limestone and shale units.

This lithofacies in the Dry Creek section alternates with thick crinoidal packstone units.

Interpretation:

The black color, evenly parallel laminae, lack of bioturbation, and scattered-, fine-grained pyrite crystals suggest that deposition of this lithofacies took place below the storm-wave base within an oxygen-minimum, deep-sea or basinal environment.

The black fossiliferous unit may represent either biohermal mounds in the mid-slope

area or sediments transported from the upper slope or platform-margin environments. However, its small, laterally discontinuous morphology eliminates the possibility of its being a debris flow. Most likely, it represents a deep-water lithoherm or mound. Oxygen supply in this environment for the bioherms may have been maintained by basinal, bottom-current systems, as suggested by Neumann et al.(1977) for the carbonate mounds found at depths of 600 to 700 m. The intercalation of silty quartz-rich, parallel-laminated, large pyrite-bearing beds and the dark, siliciclastic-free fossiliferous units may indicate fluctuations of oxygen level in this depositional realm. Large pyrite crystals are late diagenetic in origin and do not have depositional significance.

Advanced deformation, represented by ptygmatically- folded fractures, slaty cleavage, pressure shadow, elongated-micritic lenses and folding of the pre-existing, calcite-filled fractures, obliterated the original sedimentary textures and structures.

Lithofacies 17 A: Graded-Bioclastic Packstone

Description:

This lithofacies occurs only in the June Canyon sequence, approximately 90 feet from the tectonic contact between the AVL and the Devonian Shale (Fig. 58). Similar, thick skeletal packstone units in the Dry Creek section alternate with thick, slaty-cleaved units. However, their internal sedimentary structures were erased by the deformation. It is characterized by thick-bedded skeletal packstone units with erosional basal planar contacts (Fig. 60 A, C), but without any flute or tool marks. These units show a fining-upward texture as grain size decreases and fine matrix increases upward (Fig. 60 B). The several thick-bedded skeletal packstone units overlie one another with an erosional basal contact (Fig. 60 A, C). These thick-bedded units occur within black,

Figure 60- Bioclastic turbidites within the hemipelagics. A) An outcrop photograph of normal-graded, thick-bedded bioclastics within the hemipelagic lithofacies; arrows indicate the sharp-erosional, planar basal contacts of normal graded-bioclastic units. A 4-foot long stick for scale. B) Polished slab of normal-graded bioclastic packstone unit shows normal grading or a fining-upward texture. (i) designates hemipelagic intraclasts; penny for scale. C) An outcrop photograph of normal graded, thick-bedded bioclastics. Arrows indicate sharp planar basal contacts between normal-graded thick beds and underlying wackestone or hemipelagic units; a 4-foot long stick for scale. D) A close-up outcrop photograph of a classic turbidite sequence. a, b, and c respectively represent Ta, Tb and Tc of classic turbidites, and arrow indicates a truncational contact between two turbidite layers of two discrete high-density turbidity flow.


A
B
C
D
a
b
c
a
b
c
a

thin-bedded hemipelagics whose internal structures include ripple-cross laminae and parallel-even laminae (Fig. 60 A, C).

Approximately 2.5 to 4 feet of thick-bedded, normal-graded skeletal packstone units of this lithofacies alternate with a 3 to 5-feet thick interlayered wackestone and shale units (Fig. 60 B). Each packstone bed, about 1-foot thick, comprises grain-supported, rounded micritic clasts at the base which gradually disappear toward the upper part of these beds. The basal grain-supported parts of these beds are similar to the T(a) of Bouma sequence.

Some massive-looking thick beds of this lithofacies consist of multiple, thin-skeletal layers gradationally changing upward into the silty quartz-rich, relatively thin sublayers or by lenses of silty quartz. The silty intervals in places appear to be discontinuous and similar to dish structure (Fig. 61 A), as described by Walker (1977). The normal-graded basal part of the some thick beds are followed by parallel-laminated, grain-supported subunits which are similar to the Tb division of the classic turbidite grading upward into more undulatory laminae similar to rippled laminae or the division of Tc (Fig. 60 D). Between the overlying two thick-bedded units, locally about 4 cm-thick skeletal packstone occurs without normal gradation. About one to two-feet thick beds occur within the hemipelagic units at intervals of 110 and 190 feet, also having sharp erosional upper and basal contacts. In these intervals, three or four sublayers within each thick bed also exhibit a fining-upward texture and overlie one another with a sharp erosional basal contact and constitute these beds.

The visually approximated-average constituents of the normal-graded thick beds are, as follows: crinoids 40-45 %, trilobites 15 %, brachiopods 4-5 %, ostracods 3-4%, sponge spicules 2%, conodont fragments 1-2%, pellets 8-12 %, silty quartz 5-8%.

One thick-bedded subunit, particularly at the base of this lithofacies shows a different composition: trilobite 20-25 %, crinoids 15-20 %. Average percentages of other constituents are almost the same as in other units.

The approximate, average constituents of thin to medium, rhythmically alternating wackestone and shale layers between the two cyclical thick-bedded units are, as follows: trilobites and ostracods 8-12 %, crinoids 5 %, brachiopods 3%, pellets 15-20

%, sipicules 1-2 %, and conodonts less than 1 %.

Some thin beds within the thick-bedded grainstone-to-packstone units also show a completely different composition: peloidal grains nearly 60 % (similar to the radial ooids) and crinoids 5 %.

Interpretation:

In the thick beds, the graded-basal units grading upward into parallel-laminated, grain-supported subunits and then to undulose, or wispy-laminated subunits (Fig. 61 D) resemble, respectively, the Ta, Tb and Tc divisions of the Bouma sequence of the classic turbidites.

Turbidity currents are known to be triggered by earthquakes, resulting in episodic sediment movement on the slope (Cook and Mullins, 1984; and Middleton and Hampton, 1976). In the thick-graded beds, well-rounded intraclasts within the grain-supported calcarenite with a fining-upward texture suggest that these beds may have formed directly from high-density turbidity currents (Lowe, 1982).

Yellowish, silty quartz-rich welded beds and convex-upward local concentrations of fine sediments resemble dish structures or thin-welded beds (Fig. 61 A). In the thick skeletal packstone beds, multiple thin-welded beds probably indicate multiple high-density turbidity flows during the deposition of the massive-looking beds. Walker (1977) demonstrated that dish structures formed from a high-density fluidized flow: Coarse grains settle very rapidly from high-density turbidity flows, while water among the grains moves upward carrying fine grains and forming clay partings, lenses and water-escape pipes. Lowe (1982) suggested that liquefied flow could also be initiated from slumping leading to liquefaction on a slope if its gradient exceeds 3°/ km. Thus, it can be suggested that accelerated-slumps on high-angle slopes created turbidity currents from which thick graded-beds were deposited.

In the hemipelagic rhythmical beds, dark normal-graded, tabular, thick-bedded packstone units with parallel-laminated sublayers, welded beds and dish structures are

believed to represent submarine fans formed by rapid deposition from high-density turbidity currents or from fluidized-cohesionless particle flow (Walker, 1977; Keith and Friedman, 1977; Davies, 1977; Yurewicz 1977; Friedman and Sanders 1978; and Lowe, 1982). In this lithofacies, thick skeletal packstone units overlie one another with sharp-erosional contacts without shaley interlayers, probably implying that turbidity currents scoured the upper surface of the underlying turbidites and created erosional basal contacts.

Dark color of the packstone or grainstone units probably indicates that deposition of these units took place in an anoxic deep-water environment; and argillaceous clasts in these grain-supported units suggest that partially lithified hemipelagic units formed on the slope prior to high-density turbidity flow.

Trilobite-rich wackestone interlayers alternating with shales, between the thick-bedded crinoidal grainstone- and packstone units, probably represent the sediments of the distal-supra fan. Concentration of trilobites in these units was probably controlled by hydrodynamic factors: After the final deposition of normal-graded bioclasts, trilobites with lower density and higher-surface area were carried farther basinward by waning turbidity currents.

The presence of radial ooids in only a few sublayers indicates that oolitic shoals were not an important-sediment source of this lithofacies. The sediments of this lithofacies were probably derived from upper to middle slope mounds. However, the major grain types, crinoids, and other open-sea fauna were probably derived from crinoid meadows and crinoid-dominated sponge mounds on the open shelf margin or the upper slope. From these areas crinoids were perhaps swept into the basin by storm-induced counter currents. Later, these grains may have been transported farther basinward by the high-density turbidity currents which were originally accelerated-storm countercurrents (Hamblin and Walker, 1979). In the subunits of the submarine fans, absence of shelf- and shelf margin-derived clasts and sediments except for sparse radial ooid suggest that during the deposition of these units carbonate shoals or platforms were submerged for a long period. All the data support that these supra fans were most likely deposited in the anoxic lower-slope or marginal-basin

environment.

In the June Canyon sequence, the one foot-thick packstone to wackestone beds at intervals of 110 and 190 feet generally differ from the distal-storm units formed in the lower nodular-bedded units by sharp planar basal contacts and by their tabular bed forms. Therefore, this study suggests that these thick-bedded units at indicated intervals were probably deposited from very strong, storm-induced density currents below the storm-wave base.

Lithofacies 17 B: Skeletal Grain-Supported, Monogenic-Edgewise Conglomerate

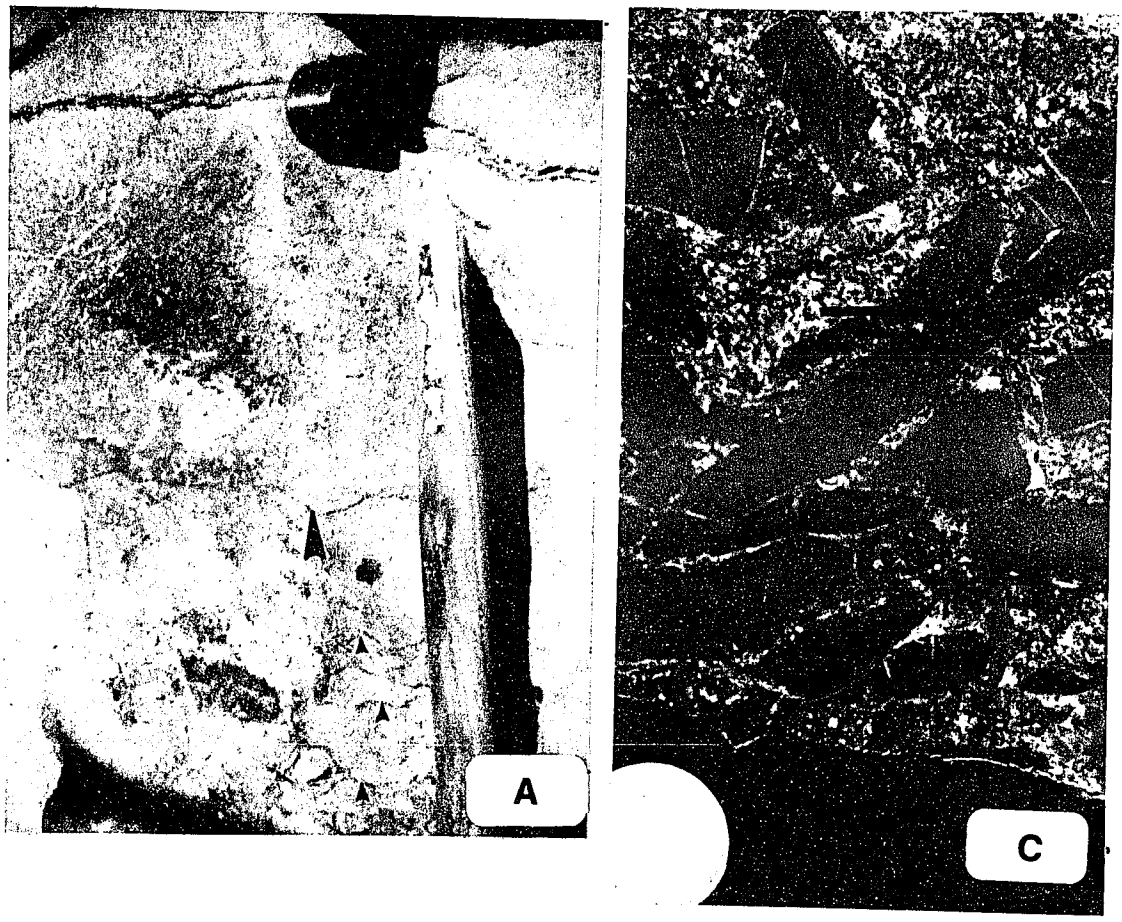
Description:

This lithofacies is about 1.5-feet thick, laterally continuous dark gray, skeletal grain-supported edgewise conglomerate or brecciola, found in the June Canyon sequence (Fig. 58). This conglomeratic lithofacies is composed of poorly sorted, dark micritic, parallel-laminated, large angular clasts (Fig. 61 B, C) and occurs within thin to medium-bedded hemipelagics with sharp erosional upper and basal contacts.

The thicknesses of individual clasts varies between 3-5 cm (average 3.5-4 cm) and their lengths range from 10 cm to 2 m (Fig. 61 B). The largest clasts usually lie at the bottom of this thick-bedded lithofacies, and clast size decreases upward (Fig. 61 B). Although the large clasts appear to be randomly oriented, the smaller clasts at the uppermost part of this unit indicate a crude imbrication (Fig. 61 C). Crinoidal grain-supported texture, the most prominent feature of this unit, does not change in lateral and vertical directions.

The visually approximated-average percentages of different constituents of this lithofacies are, as follows: crinoids 70-75 % of whole allochems; small-rounded intraclasts 3-5 %; ostracods 3 %; trilobites 5 %; brachiopods 3 %; Nuia grains 2-3 %; spicules 1-2 %; and fine quartz 3-4 %. The clast / grain ratio nearly equals to 1. The

Figure 61- Normal-graded, thick-bedded turbidite and skeletal grain-supported edgewise conglomerate (brecciola) lithofacies. A) A close-up outcrop photograph of a thick-bedded bioclastic unit shows welded beds and dish structures. A large arrowhead indicates a truncational contact between two welded-bed units, and small arrowheads point to welded beds or dish structure. Hammer for scale. B) A close-up outcrop photograph of the brecciola lithofacies shows that hemipelagic lime mudstone clasts are supported by skeletal grains; arrow indicates upward-decreasing clast size. C) Polished slab of the brecciola lithofacies shows that crinoid-supported hemipelagic intraclasts appear to exhibit imbrication in the direction of arrow. Penny for scale.


A
C


B

edgewise conglomerate is overlain by a one-foot thick, matrix-supported wackestone unit which comprises black, thin wackestone sublayers and yellowish-brown, silty quartz-rich smear zones.

Interpretation:

Imbrication and some degree of normal grading in clast size (Fig. 61 C) indicate the paleo-flow direction and waning of the high-density turbidity currents, respectively. Despite lack of tool and scour marks, the sharp planar basal contact of infra-formational conglomerate is consistent with rapid sedimentation from high-density turbidity currents. Similar grain-supported monogenic conglomerate with mainly hemipelagic clasts cyclically alternating with hemipelagics were studied by Cook and Taylor (1977) and Cook and Mullins (1983). Cook and Taylor (1977) reported them from the Cambro-Ordovician Hales Limestone of north central Nevada, and they traced them laterally into slump deposits.

This lithofacies is the only occurrence in the whole June canyon sequence which couldn't be traced into slump deposits in the field. Nevertheless, it is suggested that this unit started as a slump on a steep slope (slope> 3°/km) leading to high-density turbidity current. This, in turn, increased the turbulence, reworking, and rapid deposition; as a result, grain-supported conglomeratic units formed.

The large clasts were possibly derived from the underlying consolidated and semi consolidated hemipelagic units: As water-rich mud moved downward and broke up pieces from the parallel-bedded plane hemipelagics mudstone units, as in a manner suggested by Ensile (1974). Mullins (1983) reported a transitional relation between the mud-supported debris flows of the upper slope and grain-supported debris flow of the lower slope from the north of the Little Bahama bank. According to Mullins (1983), the muddy matrix was removed by turbulence as the flow traveled downslope.

The upper mud-supported conglomerate unit, approximately one-feet thick unit, that overlies the grain-supported edgewise conglomerate with a sharp contact suggests

that the grain-supported unit might have originated from similar downward moving slump which later turned into a high-density turbidity flow.

Unlike the skeletal grain-supported monogenic infra-formational conglomerate, grain-supported polygenic conglomerates within hemipelagic units have been interpreted as distal-talus deposits derived from shoals, reefs and the platform, perhaps from the upper slope (Hurst, 1985; 1983; Keith and Friedman, 1977; Cook and Taylor, 1977; and Cook and Mullins, 1983).

Therefore, the grain-supported monogenic conglomerate with black, parallel-laminated micritic clasts represents the basinward lower slope or basinal margin facies.

Lithofacies 18: Rhythmical Hemipelagics with Shale Interlayers

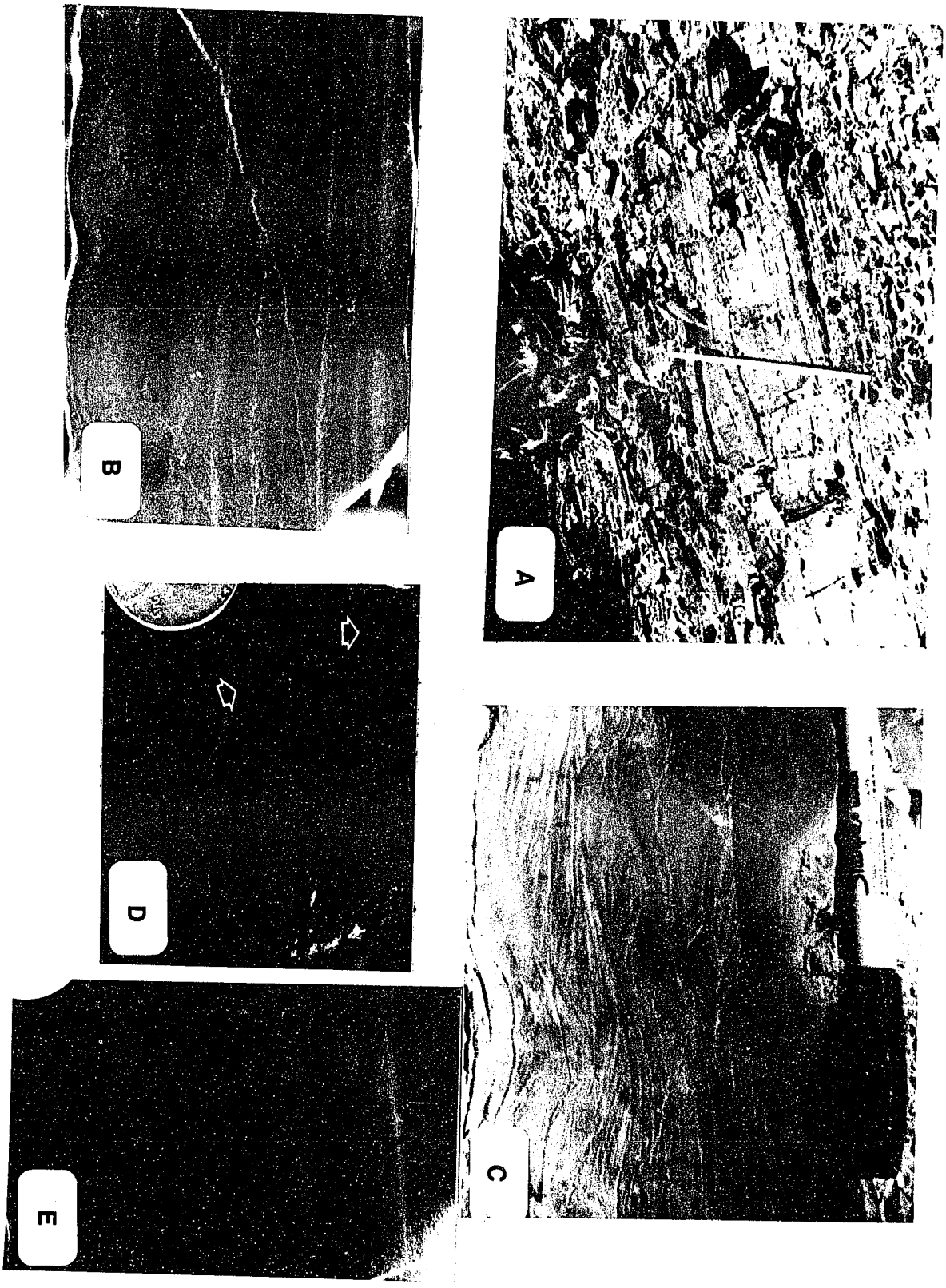
Description

Dark gray to black, parallel, thin-to medium-bedded pelletal lime mudstone interlayers, 3-6 cm thick, rhythmically alternating with dark greenish gray shaley layers from paper thin to 0.5 cm characterize this lithofacies (Fig. 62 A). And this lithofacies occurs only in the June Canyon sequence (Fig. 58). Evidence of bioturbation in these hemipelagic lime mudstone interlayers are very scarce.

Constituents of these black lime mudstone interlayers are, as follows: sponge spicules (the most common skeletal grains) 3-4 %, pellets 25-40 %, and abundant scattered-microeuhedral pyrite crystals.

Parallel even laminae with or without a crude-normal grading (Fig. 62 B), ripple-cross laminae (Fig. 62 C) and hummocky-cross laminae (Fig. 62 D, E) are commonly present in the black lime mudstone interlayers. The laminae are made up of silty quartz, fine-grained skeletal fragments and intercalating pelletal lime mud. In addition, relatively thick, gradational laminae are recognized in the lime mudstone

Figure 62- Hemipelagic lime mudstone beds and their sedimentary structures. A) An outcrop photograph of the rhythmical hemipelagics with shale interlayers; four-feet long stick for scale. B) Polished slab of hemipelagic mudstone shows normal-graded parallel laminae: light gray sublaminae representing shelly sublayers which change upward into mud-supported sublaminae; and each lamina separated from one another with a truncational basal contact of light gray shelly sublayers. Arrow indicates normal grading, and arrowheads point to normal-graded laminae. C) A close-up outcrop photograph of ripple-cross laminae. D) Polished slab of the hemipelagic lime mudstone shows hummocky-cross laminae, each of which separated from another with arched truncations indicated by white arrows. E) Polished slab of the hemipelagic lime mudstone shows hummocky-cross laminae without arching truncations; this sample was taken from a lithologic unit occurring between normal-graded parallel laminae- and hummocky-cross laminae-dominated intervals.


A
B
C
D
E

interlayers. These laminae generally start with a very light gray, fine-fragmented skeletal basal lamina which grades upward into the black muddy laminae, thus showing a fining-upward texture (Fig. 62 B). These parallel, normal-graded laminae overlie one another with sharp, planar basal contacts (Fig. 62 B).

About 390-400 feet from the base of the June Canyon section, parallel even laminae dominate the thin uniformly rhythmical hemipelagic-lime mudstone interlayers and show rare ripple-cross laminae. Graded-turbiditic beds and monogenic brecciolas are also restricted in this interval. At the interval of 400-490 feet, hummocky cross laminae-bearing hemipelagics alternate with bioturbated-mudstone and wackestone intervals of nodular beds. The inclined-parallel laminae tend to curve and arch upward as a transitional feature to the hummocky-cross strata, whereas some layers exhibit strong hummocky characteristics (Fig. 62 D, E). Figures 63 A & B show that hemipelagics are primarily made up of alternating silty quartz-rich and pellet-rich sublaminae as well as small, fragmented allochems.

Within the hemipelagics, the nodular appearance of beds becomes conspicuous upward along with increasing bioturbation. Microstylolites are most commonly at the outer margins of these thin beds where the pelmicritic components have been converted to microspar. In these hemipelagic lime mudstone beds, micro stylolites progressively decrease from outer margins to centerward.

Yellowish brown, parallel-laminated, silty quartz-rich hemipelagics are abundant in the interval of 210-330 feet from the base of June Canyon section (Figs. 58; 63 C). This interval consists of syndepositional faults (Fig. 63 C) and curved or gliding basal contact. From 330 to 500 feet from the base of June Canyon section, the limestone interlayers consist of yellowish brown, fine-grained, quartz-rich composition which gradually become thinner as bioturbation and nodular beds become more common. In the same interval, the silty quartz-rich hemipelagic layers in 1 to 5 feet thicknesses occur and repeat with the silty quartz-free interlayered-hemipelagics and nodular-bedded units in a cyclical manner, showing stair-step morphologies.

The silty quartz-rich interlayers usually overlie silty quartz-free interlayers with truncational basal contacts and sharp upper contacts (Fig. 63 C). Yellow brown, silty

quartz-rich hemipelagic interlayers exhibit parallel, even laminae which are also common in the silty quartz-free dark hemipelagic interlayers. In the uppermost part of (at 330 feet) this silty quartz-dominated hemipelagic units, unbroken brachiopods are very common.

Interpretation :

The black color, absence of benthic fauna, low bioturbation, preservation of parallel, ripple-cross laminae observed in this lithofacies have been described from low-energy, anoxic subtidal depositional environments elsewhere (Byers, 1977; Garrison and Fischer 1978; Yurewicz, 1977; and Wilson, 1978).

Pelletal mudstone and dark-greenish shale interlayers in the rock records generally show a close association with turbidites, such as graded bioclastics and grain-supported edgewise conglomerates (Cook and Taylor, 1977; Davis, 1977; Hopkins, 1977; Keith and Friedman, 1977; Yurewicz, 1977; and Hurst and Sheehan, 1983). It is widely believed that hemipelagic lime mud was derived from the shallow carbonate shelf and upper slope, transported farther basinward where it deposited from suspension alongside basinal pelagic sediments. Pelagic contribution by radiolarians, sponge spicules, graptolites to hemipelagic lime mud was very limited during the lower Paleozoic as in the present lithofacies, even before the Jurassic (Garrison and Fischer, 1978; Wilson, 1978).

Absence of bioturbation in these hemipelagics could be attributed to high-frequency deposition from suspension and to anoxic depositional environment (Byers, 1977). Storm-currents probably suspended the lime mud which were probably transported farther basinward as a suspension load by the strong storm- counter currents (Hamblin and Walker, 1979), or by the low-density turbidity flow (Lowe 1982), or by diluted-turbidity currents (Walker and Mutti, 1973). And the lime mud settled rapidly from suspension loads of the indicated currents.

The presence of the multiple thin to medium laminae with normal grading probably

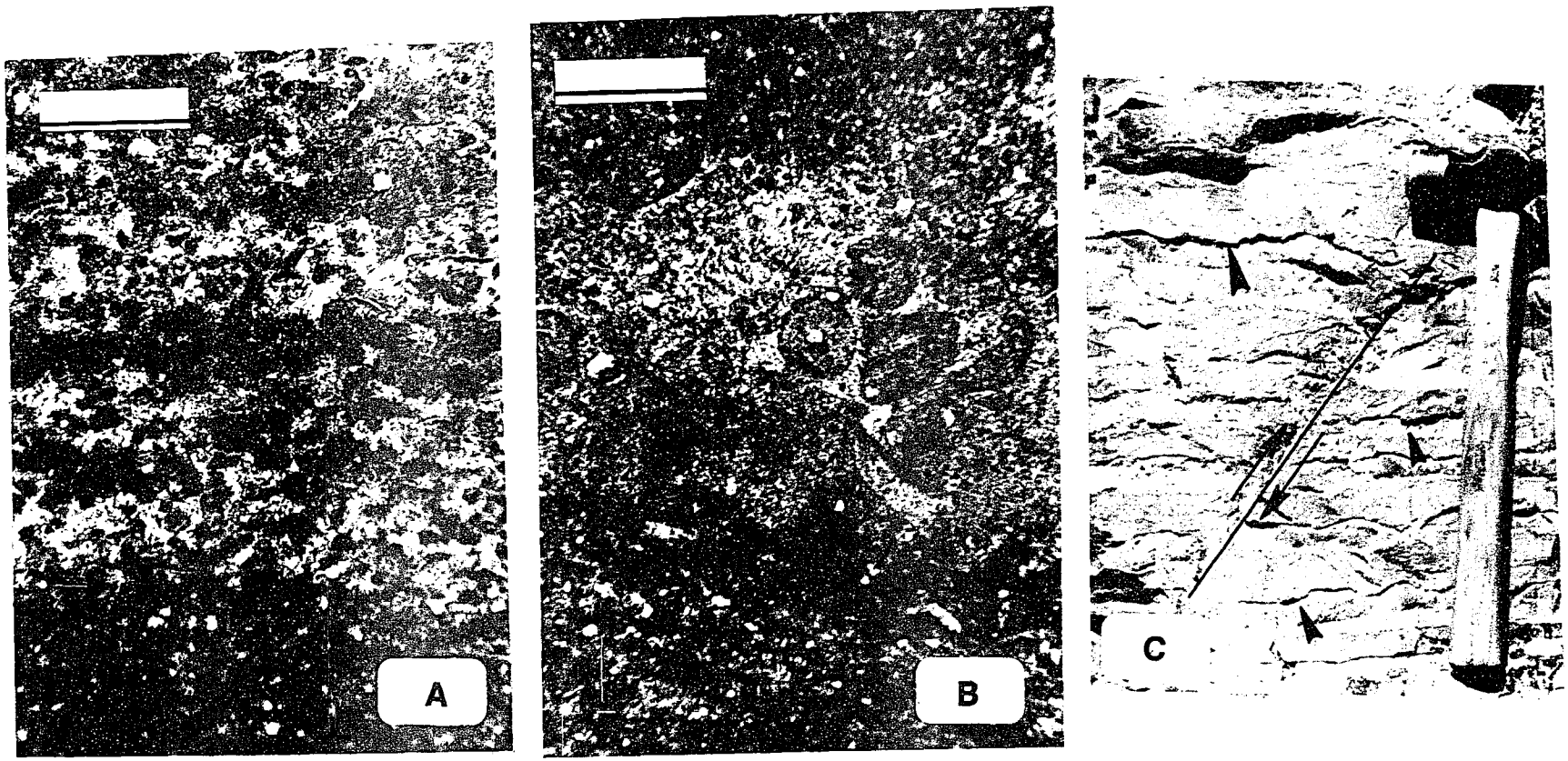


Figure 63- Photomicrographs of hemipelagic lime mudstone interlayers and outcrop photograph of silty quartz-rich hemipelagic intervals. A) Normal-graded parallel laminae of this unit consist of alternating pelletal-rich sublaminae and silty quartz-rich sublaminae; B) Micritic pellet-rich sublaminae alternating with allochem-rich sublaminae. With plane-polarized light, scale = 0.5 mm. C) A close-up outcrop photograph of silty quartz-rich hemipelagic intervals. Arrowheads indicate truncational contacts between silty quartz-rich interlayers and silty quartz-free hemipelagic interlayers, and straight line indicates syndepositional fault; hammer for scale.

represents multiple occurrence of low-density flow or diluted-turbiditic flow during the formation of the lime mud interlayers. The parallel laminae with a sharp, planar basal contact and normal grading suggest that each of these laminae represents an individual low-density turbidity current and rapid deposition from suspension. The parallel-laminated hemipelagic interlayers probably represent the basinal margin facies or lower slope facies (e.g., Schlager and Chermak, 1979). The common occurrences of low-angle laminae, hummocky cross laminae and ripple-cross laminae in the hemipelagic interlayers, in addition to parallel laminae, have also been reported by Yurewicz (1977), Handford (1985), and Hurst and Sheehan (1986) from other geologic formations.

Each of these laminae (parallel even, cross-ripple, hummocky cross laminae) in hemipelagic layers is believed to have formed from suspension by rapid deposition, and each lamina type may have resulted from the current reworking of the bottom. In the lower section of the hemipelagic interlayers, occurrences of ripple-cross laminae with a parallel even laminae may indicate a deep-basinal depositional environment. In the hemipelagic interlayers, the graded-parallel laminae become more and more common and further upward, parallel, slightly inclined lamination gradually changes to the hummocky cross-strata. This trend agrees with the observations and interpretations of Yurewicz (1977) and Hurst and Sheehan (1985). According to them, parallel laminae, hummocky-cross laminae, and ripple-cross laminae all form from rapid deposition of fine-grained sediments from the low-density turbidity current, but correspond to strong, intermediate, and weak traction of bottom-counter currents, respectively.

In the hemipelagics, the degree of dilution by extremely silty quartz-rich intervals was interpreted to be caused by the tectonic uplifting of the Toole arch in eastern Nevada and western Utah (Ross et al., 1989). However, in this study, silty quartz-rich intervals are believed to represent very rapid deposition from episodic storm countercurrents during the incipiently drowned carbonate platform or transgression (see cycles and their correlations in Chap. 9). The lower boundary of the silty quartz-rich hemipelagics represent slightly concave-upward or planar truncation probably due to

sliding on the slope environment. Differential compaction might have caused the syndepositional faulting this unit (Fig. 63 C).

Lithofacies 19 A: Nodular Limestone

Description:

About 4-6 cm thick, dark gray to black, nodular-bioturbated mudstone and wackestone (Fig. 64 A) layers alternating with thin shaley and silty layers characterize this lithofacies. This lithofacies are present in the June Canyon, Mill Canyon sequences and Whiterock Canyon section (Fig. 58; Appendix I-B). Some burrows are stained by iron oxide and selectively replaced by sparry calcite near their walls. Framboidal pyrite crystals occur in these replacive calcites. Under the microscope, burrows can easily be recognized by the arrangement of skeletal fragments along the burrow walls, by pyrite crystals and iron oxide staining of the skeletal-free micritic zone, and by calcitization of micrite (Fig. 64 B).

The boudinage structures along with bioturbation are the most prominent features in the wackestone interlayers. Parallel lamination, seen in the previously described units, appears to have been obliterated by burrowing in this lithofacies.

The visually approximated-percentages of the constituents of this lithofacies are, as follows: ostracods 4-5 %, gastropods 2-3 %, brachiopods 3-5 %, trilobites 3-4 %, crinoids 8-10 %, Nuia 2-3%, pellets 18-25 %,. Girvanella oncoids 2-3 %.

This lithofacies gradually changes upward into gastropod-and oncoid-rich wackestone to packstone units. Episodic storm deposits and biohermal deposits are also very common in this lithofacies. Bioherm facies are especially represented by sponge mounds which laterally change into the nodular-bedded units.

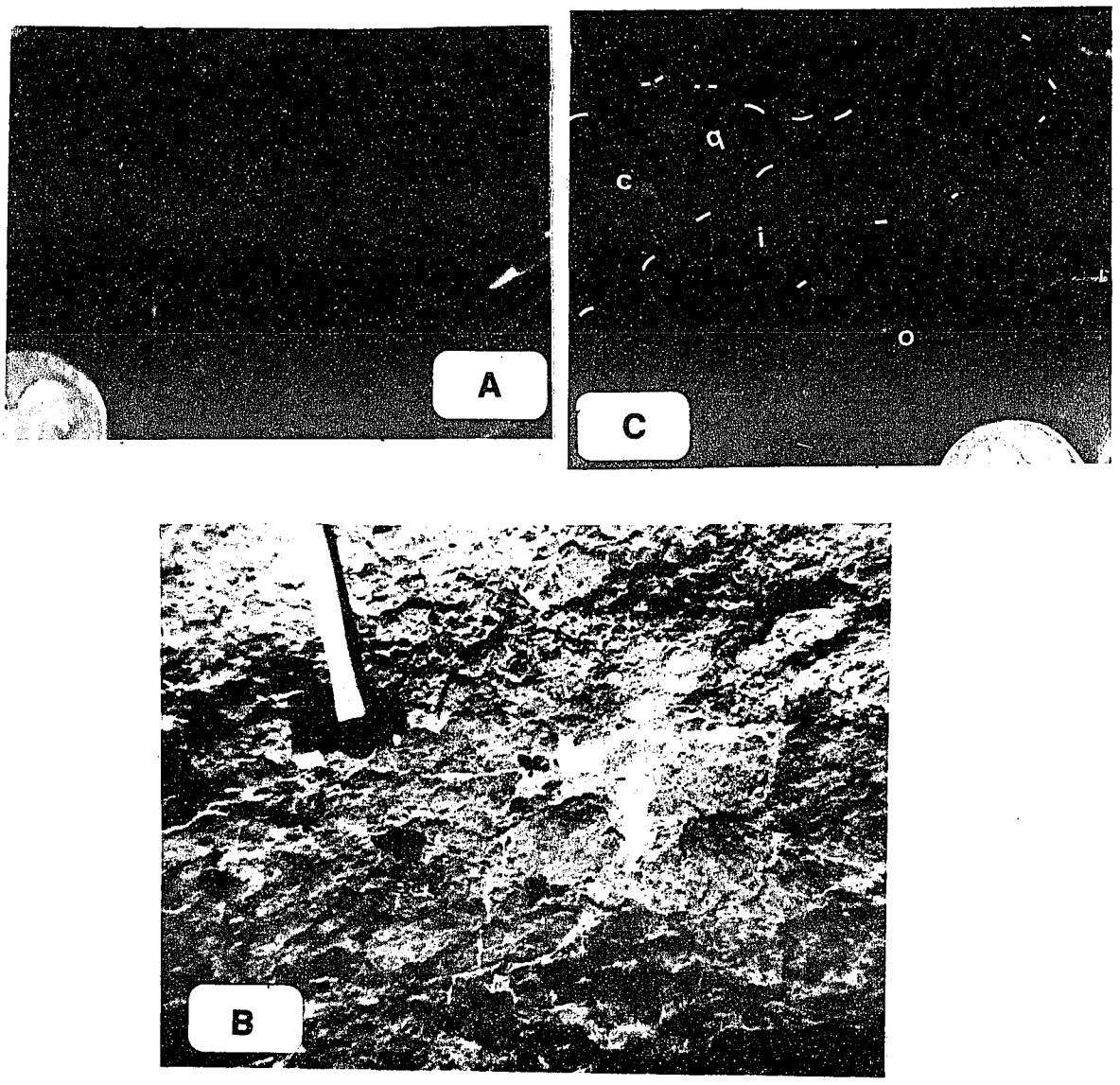


Figure 64- Nodular limestone and mottled-limestone lithofacies. A) Polished slab of the nodular limestone lithofacies shows that thin-shelled gastropods pointed by arrowheads and trilobites (t) are common in this unit; penny for scale. B) An outcrop photograph of the mottled-lime mudstone to wackestone lithofacies shows that intensive bioturbation obliterated bedforms and sedimentary structures. C) Polished slab of bioturbated nodular beds shows that skeletal grains, mostly trilobites (t), are aligned around burrows; (c) indicates the partially calcitized-central burrow, and (q) indicates iron oxide-stained burrow margins. Arrowheads point to oxidized zones locally consisting of smaller darker burrows, and (o) marking the outer margin of burrow. Penny for scale.

Interpretation:

In this lithofacies, evidence of bioturbation with bored and encrusted surfaces, and replacement of micrite by cryptocrystalline calcite in the burrows as well as iron staining (Fig. 64 B) may reflect the hardgrounds or hardground surfaces. In general, the hardgrounds represent the early cementation of sediments on the sea floor prior to deposition of overlying sediments (Bathurst (1975, p. 395). In the bioturbated units of the open sea facies of the Bahama bank, hardground surfaces display a gradual downward decrease in degree of early lithification at depths of 600 to 700 m caused by churning of sediments by boring and filling activities of organisms, and by cementation (Wilber and Neumann, 1977). The bioturbated-lime mud with abundant bivalve shells in deep shelf of the Persian Gulf, also exhibiting early cementation and hardgrounds, have been used as a modern analogy for the nodular-bedded, bioturbated-wackestone or mudstone of ancient limestones (Purser and Evans, 1972). Common occurrences of hardgrounds in grain-supported units suggest that winnowing by bottom currents are prerequisite for their formation which is reflected in better development of early cementation in the shoalward direction (Wilber and Neumann, 1977). On the slope of the Little Bahama bank, recently cemented nodular ooze displays a persistent down-slope decrease in the degree of cementation from hardground nodules to unlithified-periplatform ooze or hemipelagics (Mullins et al., 1983).

From the aforementioned modern examples, it can be inferred that the depositional environment of the nodular-bedded lithofacies probably ranged from similar hardground-forming zone to hemipelagics-forming realm, characterized by a well-circulated open-sea environment. This suggestion is corroborated by the presence of diverse-open marine fauna and early patchy cementation and lithification in bioturbated-mudstone and wackestone interlayers. From hemipelagic units to the nodular bedded units, gradual disappearance of the laminated-sedimentary structures can be attributed to biologic perturbations corresponding to increasing oxygen content from the lower to upper slope environments.

Within the burrows, precipitation of iron oxides and sparry calcite replacements (Fig. 64 B) indicate pre-burial oxidation and lithification. Increase in early cementation from this nodular-bedded lithofacies upward to the oncoid and gastropod-rich packstone to wackestone units can be explained by analogy the physical conditions presently operating on the slope of the Little Bahama bank.

Therefore, these dark gray, nodular mudstones and wackestones containing open-marine fauna (Fig. 64 A), alternating with the storm calcarenite and bioherm facies, changing gradually downward into the hemipelagics of lower slope environment and upward into the upper slope lithofacies indicate a deep ramp or a transitional basinal facies between the upper slope / basin margin or lower slope. Read (1980) and Markello and Read (1981) interpreted similar Middle Ordovician lithofacies as a deep-ramp lithofacies in the Appalachian basin.

Wanless (1979) suggested that differential compaction played a significant role on the formation of nodular beds. In this lithofacies, however, early patchy cementation and bioturbation appear to have been more important. Subsequent, compaction-induced stylolitization probably accentuated the nodular appearances of these beds.

Lithofacies 19 B: Mottled Limestone

Description

This lithofacies is represented by dark, yellow-brown silty quartz-rich, intensely bioturbated mudstone to wackestone units (nearly homogenized beds; Fig. 64 C) which change downward into the oncoid-and gastropod-rich wackestone and packstone lithofacies in the June Canyon sequence (Fig. 58). Close investigation of this massive-bedded unit shows that it has thin nodular beds alternating with thin siltstone interlayers at its gradual lower contact. In the upper part of this unit, thick shelly beds with a sharp basal and upper contacts are common. In this lithofacies, thick shelly beds are common with their sharp basal and upper contacts. Moreover, this lithofacies

appears to be an intensely bioturbated, nodular-bedded lithofacies.

The visually approximated-average percentages of the constituents of this lithofacies are, as follows: gastropods 6-7%; brachiopods 3-4 %; trilobites 5-6 %; crinoids 7%; ostracods 5-7%; bryozoas 3 %; and Nuia 2-3 %. Girvanella oncoids and intraclasts are also important components of this unit.

Interpretation:

Dark gray, bioturbated-wackestone units with high-silty quartz content probably indicate low-energy sedimentation below normal-wave base. The preservation of the silty quartz-rich components of the rhythmically bedded lower part of this lithofacies may have deposited from storm-induced currents. However, destruction of silty interlayers and wackestone interlayers by bioturbation indicates that deposition of this unit took place in the oxygen-rich below normal-wave base.

A well-circulated, open-marine environment can be inferred from the presence of diverse open marine fauna and intensive bioturbation which probably implies that this intensively bioturbated lithofacies may have formed in the well-oxygenated, upper-slope environment. Abundance of silty quartz-rich interlayers suggest a high rate of episodic, fine-grained siliciclastic influx probably transported by storm-counter currents or by wind-forced currents during sea-level rise.

Lithofacies 12: Parallel-Laminated, Silty Quartz-Rich Lime Mudstone

Description

This lithofacies was observed at the lower part of Lone Mountain (below the dolomitized Nuia bars) and Mill Canyon sequence (Fig. 65; Appendix I-B), and also in the upper hemipelagic intervals and lower-nodular bedded units of the June Canyon sequence of the Iks Canyon window (Fig. 58; Appendix I-B). In the Whiterock Canyon section, this lithofacies occurs within the nodular-bedded units in cyclical repetitions with the thick shelly layers (Fig. 58; Appendix I-B). In all these sections, these fine-grained siliciclastic intervals mostly occur in the Orthidella zone. The same lithofacies have also been described in the shelf facies of Nuia and oncoidal shoals (see Chap. 7). It consists of 1 to 5-feet thick, light gray, parallel-laminated silty quartz-rich lime mudstone units which gradationally overlie the oncolitic wackestone of the open-shelf facies (Fig. 65) in the Mill Canyon sequence (Iks Canyon section) and which occur within the thin-bedded mudstone to wackestone of the open-shelf facies in the Lone Mountain section.

In these sections, this lithofacies is interbedded with noticed lithofacies mentioned above. The constituents and lamination styles are very similar to the same lithofacies described in Nuia and oncoidal shelf (see Chap. 7) except their associations with outer shelf lithofacies and abundant chert layers and nodules.

In this lithofacies, chert nodules or thin discontinuous layers are usually white in the Lone Mountain section and black in the Mill Canyon section. Millimeter-thick, parallel even laminae appear to be preserved within these chert layers and nodules (Fig. 66 A). However, the chertified parts of the beds truncate the unchertified-parts of the same beds in which parallel, even laminae more conspicuous than the laminae within the chertified parts.

In this lithofacies, fine quartz silts are the most common grain types along with 45-60 % pellets. In the chert layers, abundant sponge spicules and radiolarians are

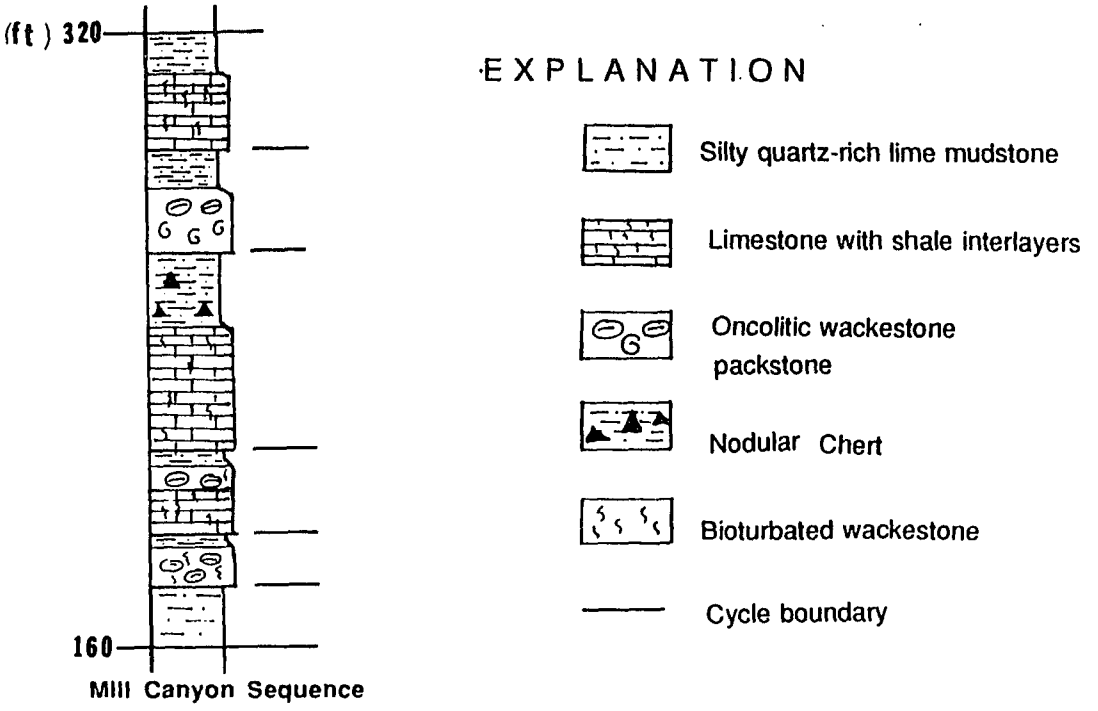


Figure 65- Cyclical successions of parallel-laminated, silty quartz-rich lime mudstone and oncoidal wackestone intervals of the open shelf facies of the AVL in the Mill Canyon sequence.

observable.

Interpretation:

The preservation of parallel laminae probably indicates sedimentation below the normal-wave base, and rapid sedimentation from the suspension load of storm countercurrents (see Chap. 7).

The presence of open marine fauna and concentrations of sponge spicules and radiolaria indicate an open-marine sedimentation. Dark to black chert layers in the Mill Canyon sequence (in the Iks Canyon section) may represent relatively deep, anoxic open-shelf environments.

These fine-grained siliciclastic sediments probably formed during the incipiently drowned carbonate platform stage. Storm-countercurrents carried these sediments across the shelf and over the drowned shoal into the open shelf where deposition from suspension inhibited light penetration and created unfavorable conditions for photosynthesis by algae and a hostile environment for the benthic fauna.

Lithofacies 13: Oncoidal Wackestone to Packstone

Description:

This lithofacies occurs at interval of 643-690 feet from the base of the June Canyon sequence of the Iks Canyon window (Fig. 58), at several intervals of lower Mill Canyon section (Fig. 65), and in the interval of 90 to 115 feet of the Lone Mountain section.

This oncoidal lithofacies consists of dark gray to black, oncoidal wackestone units which appear to comprise multiple, thin beds. Each of these thin beds is composed of thin (3 cm) basal oncoidal grading upward into thick silty quartz-rich mudstone or

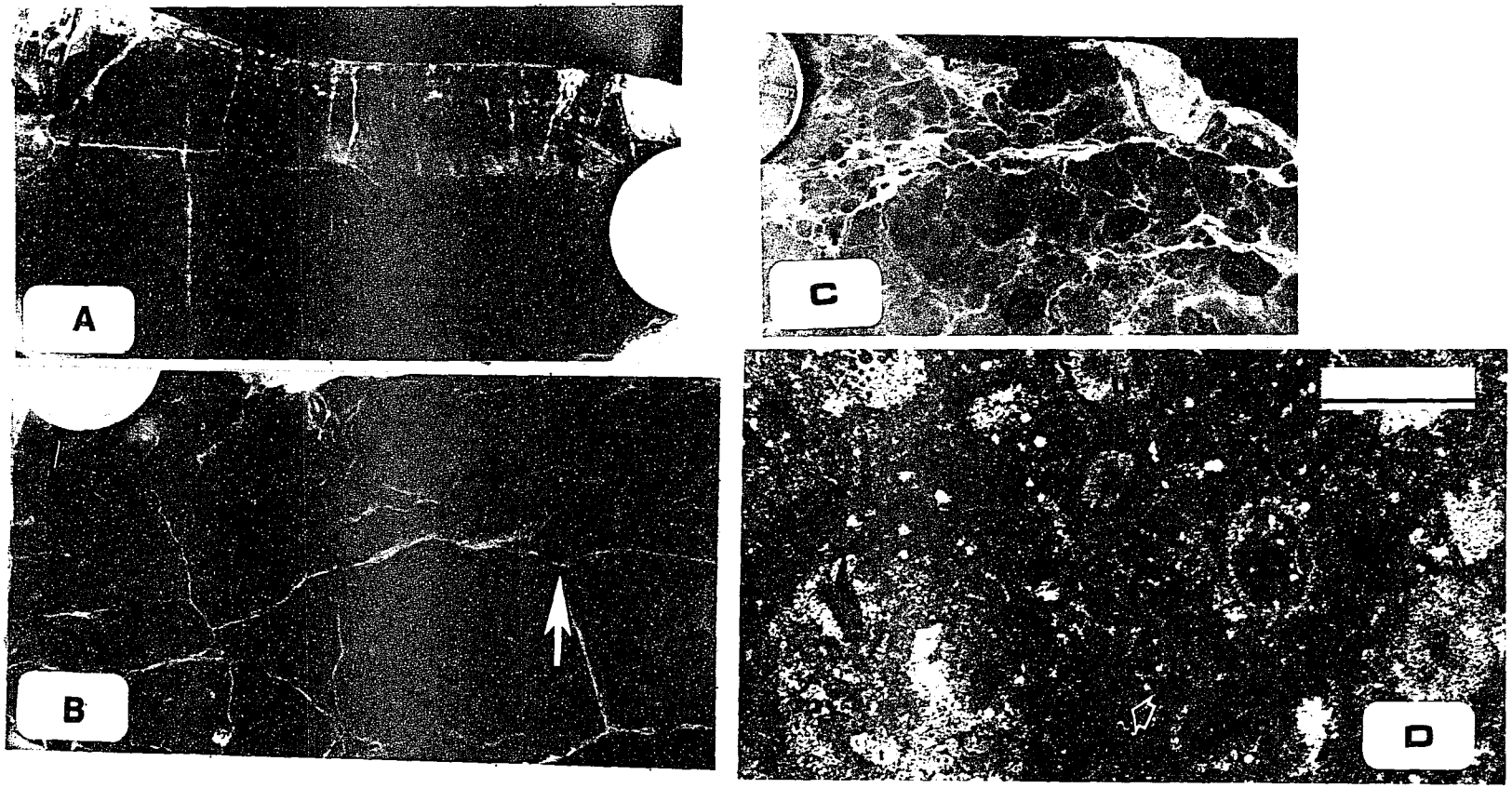


Figure 66- Oncolitic packstone-wackestone and parallel-laminated, silty quartz-rich lime mudstone units. A) Polished slab of parallel-laminated, silty quartz- rich lime mudstone unit. Arrowhead points to a diagenetic truncational contact between selectively chertified, and nonchertified parts of the parallel laminated silty quartz rich lime mudstone; penny for scale. B) In polished slab of oncoidal packstone- and wackestone unit, light arrow points to a fining-upward texture, and black arrow indicates a truncation between two thin oncoidal layers; penny for scale. C) Polished slab of oncoidal wackestone unit does not show a fining-upward texture. Penny for scale. D) Photomicrograph of oncoidal packstone- and wackestone lithofacies. (n) designates Nuia grains, and (g) indicates Girvanella oncoids which were constituted only by stacking growth form; with plane-polarized light, scale= 0.5 mm.

shaley interlayers (Fig. 66 B). Each individual oncoidal bed thus shows a fining-upward texture, overlain by a sharp erosional basal contact of the next oncolitic layers (Fig. 66 B).

In the Mill Canyon section, about two to five-feet thick oncolitic lithofacies repeat with about 5 to 10-feet thick, parallel-laminated, silty quartz-rich lime mudstone units (Fig. 65). In these cyclical successions, basal-oncoidal sublayers overlie the parallel-laminated, silty quartz-rich, partially chertified-lime mudstone units (Fig. 66 A) with a sharp erosional contact and commonly include intraclasts of the underlying mudstone units (Fig. 65). The oncolitic wackestone units do not exhibit a fining-upward texture (Fig. 66 C). Nuia grains are common in this lithofacies as independent grains and as nuclei for Girvanella oncoids (Fig. 66 D).

Unlike oncoids of the oncoidal shoal, the oncoids of the open-shelf lithofacies do not contain fabric- selective dolomites which commonly replace the calcitized nuclei and thick concentric laminae of oncoids in the oncoidal shoal lithofacies. Oncoids of this lithofacies consist of irregular and discontinuous, and radial or partially continuous concentric laminae (Fig. 67 A, B). The texture is matrix-supported and rich in micropyrite. Figure 68 shows the oncoid and lamina types in the open shelf facies.

In the June Canyon sequence, this oncolitic lithofacies stratigraphically occurs above the sponge-bearing strata of the AVL and gradually overlies gastropod-rich, nodular-bedded wackestone facies (Lithofacies 19 A), gradually changing upward into the mottled-wackestone lithofacies (Lithofacies 19 B). Small, thin-shelled gastropods are very common in this oncoidal unit, whereas thick-shelled gastropods, Maclurites and Palliseria, dominate the oncoidal packstone lithofacies of oncoidal and shoal units in the Antelope Valley region.

In the June Canyon sequence and Lone Mountain section, the oncoids are bean-shaped or ellipsoidal (Fig. 66 B), contain well-rounded Girvanella-derived peloids, and show nearly continuous concentric laminae. However, discontinuous laminae and skeletal inner laminae are commonly present in these oncoids. The nuclei of these oncoids are composed of skeletal grains of open-marine fauna, such as small, thin-shelled gastropods, brachiopods, trilobites, crinoids, and Nuia.

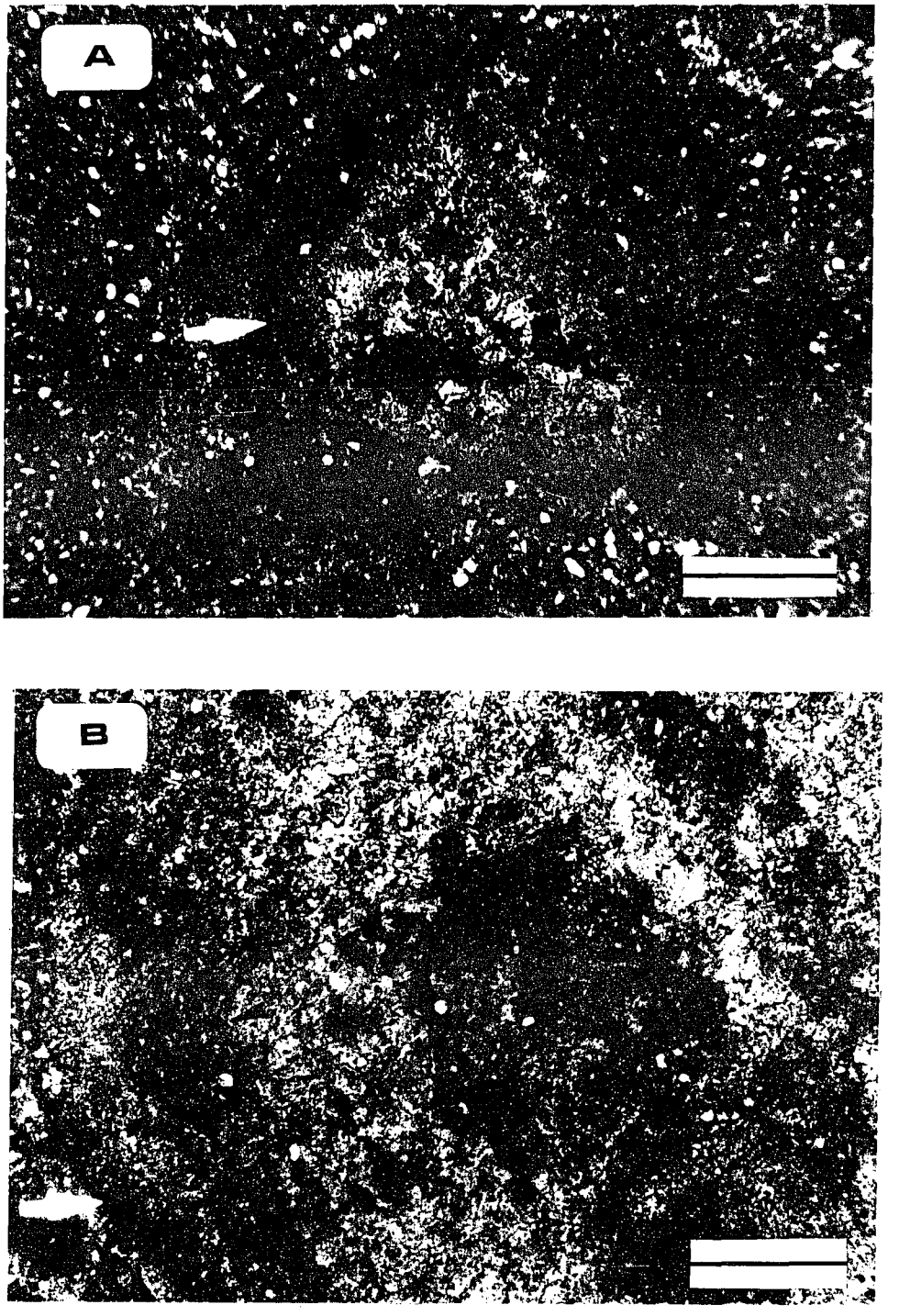


Figure 67- Photomicrographs of open shelf oncoids and their concentric laminae. A) Thin coating by tightly intertwined-Girvanella tubules with a matrix-supported texture. B) Oncoid is composed of silty quartz-rich lime mudstone as nucleus occurring within the matrix-supported texture. With plane-polarized light, scale = 0.5 mm.

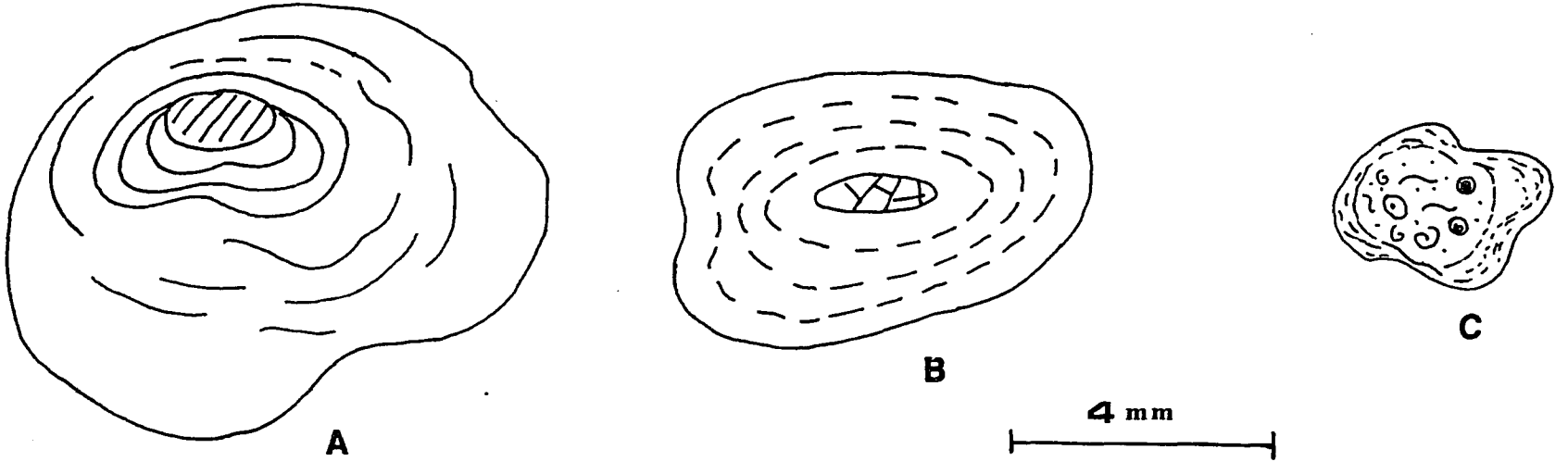


Figure 68- Oncoids of open shelf facies or deep ramp. A) An oncoid with a skeletal nucleus, discontinuous, and irregular concentric calcitized laminae and irregular outline. B) Similar to A but outline is regular within the matrix-supported texture. C) Skeletal fragments with silty-quartz rich matrix-supported texture are found as a nucleus.

In the June Canyon sequence, this oncoidal wackestone to packstone lithofacies appears to form amalgamated-massive bedforms (Fig. 66 B) in which each individual thin bed has relatively more grain-supported oncolitic basal part and relatively more matrix-supported upper part. Fig. 66 B shows that multiple thin oncolitic layers overlie one another with truncational basal contact and have fining-upward texture with columnar cement. Nuia grains are very important constituents (reaching 25 %), especially in the Girvanella peloid- and oncoid-rich basal layers of this lithofacies (Fig. 66 D).

Interpretation:

In the oncoidal wackestone interlayers, oncoids with irregular and partially concentric laminae, diverse marine fauna, and matrix-supported texture with abundant, dispersed micropyrite are indicative of a low-energy, open marine environment. The thick, irregular concentric laminae of oncoids represent long resting periods punctuated by short intervals of agitation for these organo-sedimentary grains on the sea floor. Therefore, one can suggest that the energy level of short-lived agitation probably was not strong enough to keep the oncoids in constant motion and to produce continuous, symmetrical-concentric laminae.

In the Mill Canyon section, the small amount of Nuia in the oncoidal sublayers can simply be attributed to their seaward transportation from the Nuia shoal or shelf by current and wave activities. Thin oncoidal layers capped by very thin silty and muddy blankets in the amalgamated beds probably indicate multiple, short-lived, relatively high energy events in this low-energy, deep-subtidal environment. Therefore, these thin oncoidal layers are believed to have formed during storm-induced agitation when the oncoids were transported a short distance in the leeward direction. During the post-storm quiescent stage, the oncoidal layers were probably capped by silty quartz-rich muddy blankets from the storm-generated suspension (Hayes, 1967; Reineck and Singh, 1972; and Kelling and Mullins, 1975).

Oncoids with thick micritic and irregular concentric laminae basal sublayers in this lithofacies in the Mill Canyon suggest that they were probably formed in a more open seaward environment than the depositional site discussed above. On the other hand, more regular and continuous concentric laminae with sheltered-columnar cement and greater grain-supported texture indicate a relatively higher energy and shallower depositional environment for these oncoidal beds in the June Canyon sequence and Lone Mountain sections. These findings contradict the general consensus that oncoids form from blue-green algae and commonly represents intertidal and upper-subtidal environments (Gebelein, 1969; Monty, 1977, and Flügel, 1984). This study suggests that blue-green algal oncoids, particularly Girvanella oncoids, can form in a wide range of bathymetry (cf., Peryt, 1981; Riding, 1975; 1977), from very shallow water to depths of up to 100 m. This lower depth range of the bathymetry can be inferred from the stratigraphic position of the Girvanella oncoid-bearing units which overlie the sponge-bearing strata in the June Canyon sequence.

In the Mill Canyon section, cyclical successions of oncoid-bearing intervals (5 to 10 feet) with parallel-laminated, silty quartz-rich lime mudstones suggest that Girvanella, as a pioneer organism, normalized the increasingly stressed environment by colonizing this environment and enhanced carbonate sedimentation after episodes of silt rain or deposition. Silt deposition from suspension most likely impeded the penetration of light, creating stressed-environmental conditions for benthic organisms and algae.

The parallel-laminated, silty quartz-rich lime mudstone units (Figs. 65, 66 A) have been inferred to represent sedimentation from storm countercurrents during high-sea level stands (see Chap. 7). Oncoidal intervals (Fig. 65), on the other hand, probably represent episodic storm sedimentation during late progradational or relatively lowered sea-level stages. Therefore, it seems that carbonate production kept pace with the rate of sea-level rise, and wider intertidal-algal flats formed during high stands and baffled these fine siliciclastics. Interactions between the rate of sea-level rise and sedimentation, more specifically carbonate production rate, thus were the principal factors controlling such environmental changes.

Slope- and Basinal Skeletal Storm Deposits

Lithofacies 20 A: Crinoidal Packstone to Wackestone Lithofacies

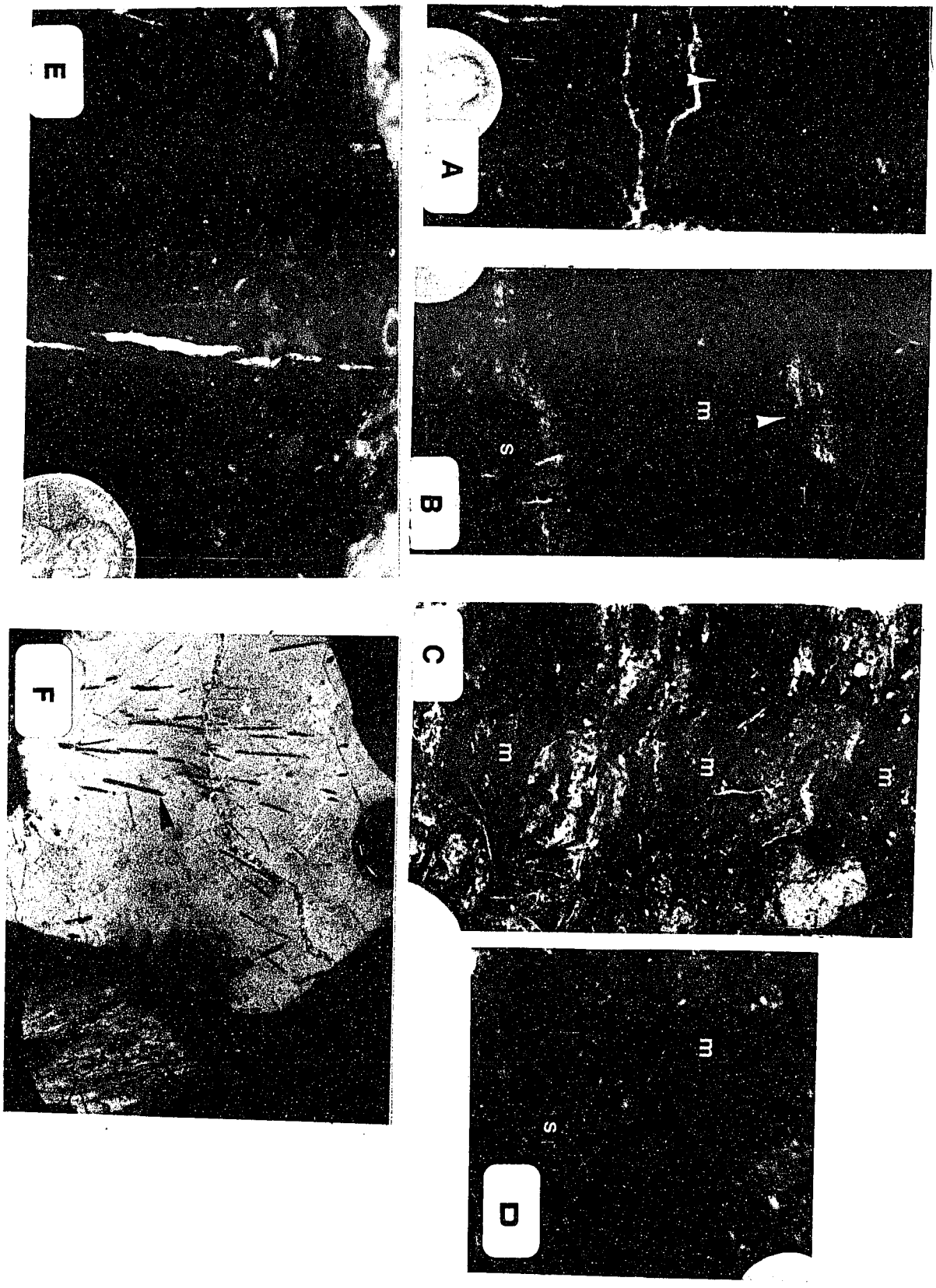
Description

This lithofacies consists of dark gray, thick-bedded grainstone to packstone units and occurs within the rhythmical nodular-bedded wackestone and mudstone units (Lithofacies 19 A) of the June Canyon sequence and Whiterock Canyon section (Fig. 58; Appendix I-B). With sharp upper and erosional basal contacts, thick and massive crinoidal packstone beds are composed of 3 to 5 cm thick layers. Each of these layers consists of a basal shelly unit with a packstone texture which grades and fines upward in to a matrix-supported wackestone to mudstone texture (Fig. 69 A, B, C). There thin multiple beds overlie one another with sharp and erosional, wavy basal contacts (Fig. 69). The thick-bedded packstone units appear to have lenticular bed forms which show lateral variation in their thickness. In the June Canyon sequence, this lithofacies shows a vertical change in overall texture. In the lowermost part of the Lithofacies 19 A, the texture of this lithofacies generally ranges from packstone to wackestone. However, within the upper part of Lithofacies 19 A, the rank of this lithofacies attains packstone to grainstone texture with thin mud covers.

Locally, black mud concentrations within the uppermost part of the basal grainstone- and packstone units are very common. These local mud lenses and upper muddy units of beds of this lithofacies commonly comprise large pyrite crystals.
Sheltered-columnar calcite cements occur between the basal shelly and the upper muddy blanketing layers, and under the protected side of skeletal grains in the shelly sublayers (Fig. 69 A to D).

Bioturbation is more evident in the wackestone and upper mudstone sublayers of individual beds. The muddy sublayers overlying the shelly units usually contain brachiopods and trilobites.

Figure 69- Storm layers of the slope and basinal facies. Polished slab of normal-graded packstone- to wackestone units (A, B, C, D, E) shows that shelly packstone sublayers change upward into mud-supported sublayers (fining-upward texture): A) Each shelly layer is separated from one another by mud blanket marked by white arrow; B) Thick muddy blankets (m) overlie relatively thinner shelly packstone to wackestone subunits; C) Multiple shelly packstone to wackestone sublayers with an equally thick muddy blankets; D) Patchy mud concentrations within thin crinoidal packstone basal layers and overlying thick mud blankets. E) A plan-hardground surface on the lower shelly units. F) Sponge tufts, sampled from the sponge mounds occur in the nodular-bedded units. Pennies for scale.


A
B
m
s
C
m
m
m
D
m
s
E
F

Alternating multiple beds within the amalgamated, thick beds with wavy erosional basal contacts appear to have boudinage or nodular bedding. And in places these sublayers are bounded by planar-hardground surfaces (Fig. 69 E).

Figure. 69 F-shows the sponge tufts within the wackestone unit which was sampled from the nodular-bedded lithofacies. At this interval, thick-bedded storm layers with the columnar cements are very common.

Crinoids are the most abundant constituents in the shelly sublayers amounting to 65 to 75 %, followed by trilobites, brachiopods, ostracods, and gastropods.

Interpretation:

The crinoidal packstone units with sharp erosional basal and upper contacts, occurring in a cyclical manner within the dark gray, nodular-bedded lithofacies, probably represent episodic, high-energy sedimentation in a predominantly low-energy, upper slope or ramp environment.

During storm events, the normal weather-wave base was lowered and affected the deeper sea floor of the basinward environments. Sharp erosional basal contact of each of beds of this lithofacies within the thick- amalgamated beds (Fig. 69 A to D) suggests that high-energy storm waves scoured the sea floor which resulted in suspension of sediments laying on the sea floor. The suspended sediments were most likely reworked and winnowed by storm waves. Winnowing and reworking of suspended sediments by high-energy storm waves was most likely followed by the settlement of larger grains first onto erosional surfaces followed by progressively lighter and smaller grains as the storm waned. Multiple layers of this kind in the thick-integrated (amalgamated) beds with their sharp, erosional, basal contacts and fining-upward textures thus indicate the multiple episodes of short durational high-energy storm conditions which occurred in the dominantly low-energy open shelf environment. The lenticular bedforms of the amalgamated-thick beds can distinguish them from the tabular-bedded, normal-graded turbidites (Kreisa, 1981). Comparable

relationships were described and interpreted to be storm deposits of various environments and geologic ages by Brenner and Davies (1973), Kelling and Mullins (1975), Kreisa (1981), Aigner (1982), and Miller et al. (1988).

The shell beds with abraded-and fragmented-skeletal grains probably represent storm deposits (e.g., Ball, 1971) rather than well-rounded shoal sediments.

The mottled lithofacies and parallel laminated, silty quartz-rich mudstone layers directly overlying the grainstone or packstone basal units suggest rapid sedimentation from suspension carried by storm countercurrents during the post-storm quiescent periods. For the benthic fauna, stressed physical environmental conditions may have resulted from the fine-grained siliciclastic sedimentation. Colonization of the fine-grained siliciclastic components of storm deposits by brachiopods is consistent with their capabilities to accommodate to rapid changes in the environment to restriction of the environment.

Dark gray to black muddy lenses within the grainstone and packstone units indicate infiltration of fine sediments during rapid deposition from storm counter currents. Pyrite formation in these lenses and burrows of muddy sublayers was probably caused by rapid deposition-induced reduction in this environment. Perched- and sheltered-columnar cement have been interpreted to result from storm events (Kreisa, 1981; Aigner, 1982).

Thin to medium, dark skeletal layers or shell beds intercalating with a thick, fine-grained muddy sublayers within the lower nodular-bedded units of June Canyon and Whiterock Canyon sections probably indicate the distal-storm deposits or distal tempestite (Aigner, 1982; Miller et al., 1988).

Lithofacies 20 B: Normal-Graded Conglomeratic Packstone

Description:

This lithofacies, observed in the lower part of the Lone Mountain section, consists of slightly dark gray, grain-supported, thick-bedded conglomerates with sharp erosional basal and upper contacts. It occurs in the mottled beds of open shelf facies in a cyclical manner at about 10-feet intervals.

In these two-feet thick beds, well-rounded, internally parallel-laminated micritic intraclasts are primarily supported by crinoidal grains and skeletal fragments of other open-marine faunas. The grain size of these intraclasts is approximately in the range of 0.5 to 2 cm. From the erosional basal contacts of these thick beds, intraclasts decrease upward in amount and size; therefore, the upper parts of these units appear to be skeletal grainstones in texture (Fig. 70 A, B). This thick-bedded lithofacies also comprises a few thin internal beds, similar to the integrated or amalgamated beds of Lithofacies 20 A.

In the June Canyon, about 40 cm of crinoid-supported conglomerate, consisting of parallel-laminated, silty quartz-rich micritic intraclasts, oncoids or algally derived peloids, is directly overlain by parallel-laminated, silty quartz-rich micritic layers. This lithologic unit clearly demonstrates a fining-upward texture: A conglomeratic basal unit gradually changes upward into moderately bioturbated-wackestone which is capped by parallel laminated, siliciclastic micrite.

Sheltered columnar cements occur in the lower part or the protected side of these siliciclastic-rich micritic intraclasts (Fig. 70 C; see Fig. 92 in Chap. 12 A).

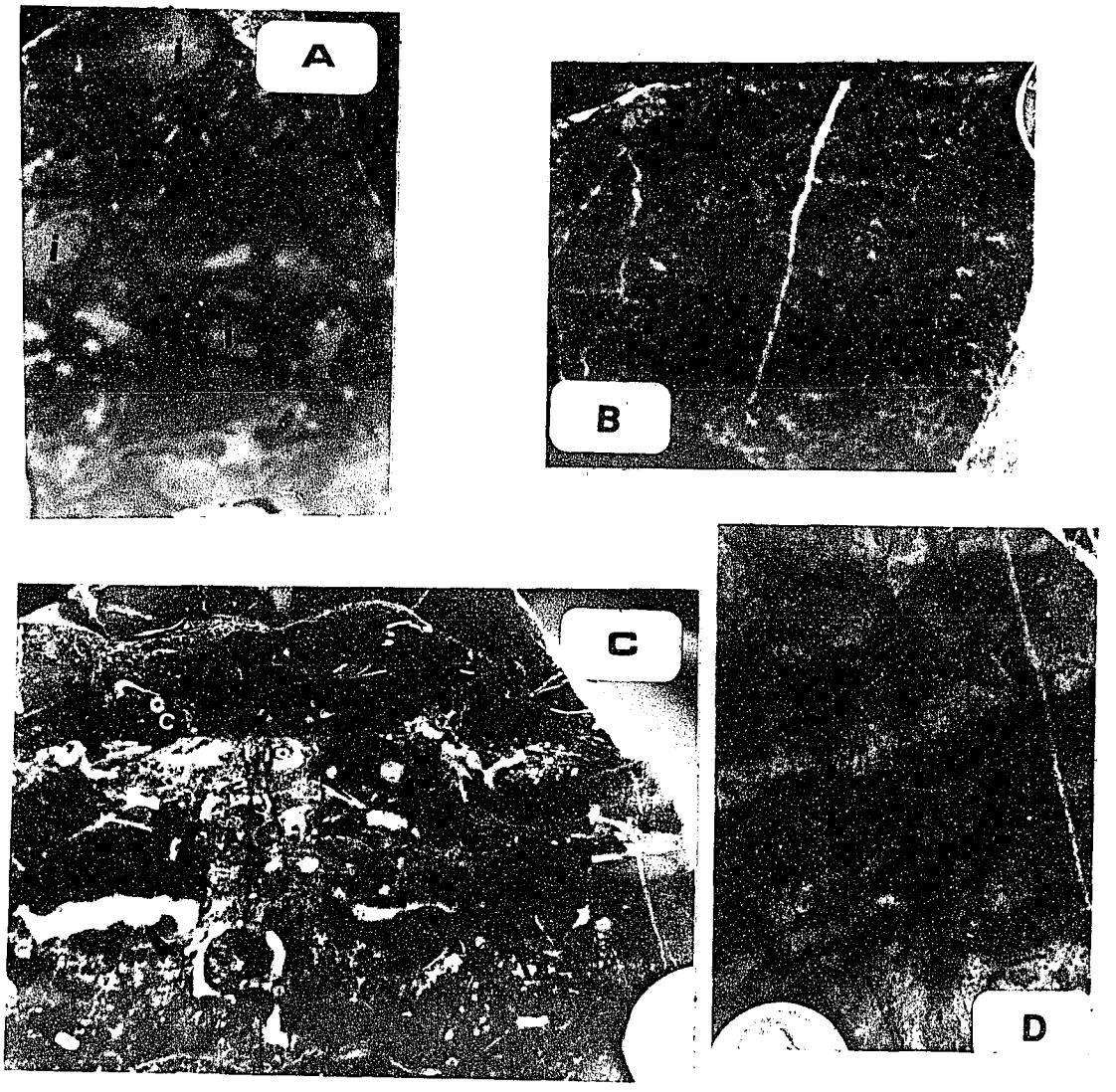


Figure 70- Grain-supported conglomerate and thin shelly packstone to wackestone units of the open shelf facies of the AVL. A) Polished slab of crinoid-supported monogenic conglomerate shows that intraclasts (i) are primarily parallel-laminated hemipelagic mudstone or pellmicrite. B) Polished slab of crinoid-supported intraformational conglomerate shows that grain size of intraclasts (i) decreases upward and indicates a fining-upward texture. C) Polished slab shows that sheltered-columnar calcite cement between the uppermost part of shelly sublayers and lower part of the mud blankets as arrowheads indicating; (c) designates muddy blanket. D) Polished slab shows that relatively thin shelly layers gradationally change upward into thick muddy blankets, and these shelly layers overlie one another with truncational, concave-upward basal contact. Pennies for scale.

Interpretation:

Storm-induced wave and currents probably scoured and eroded partially lithified, parallel-laminated lime mudstone from the underlying units in the sea floor. The clasts, without evidence of burrowing, with internal parallel laminae, characterize the contemporaneously lithified underlying sediments deposited below the normal wave-base. Intraclasts with grain-supported texture, without imbrication, algal lamination, and fenestral fabrics (e.g., Shinn, 1983) and the stratigraphic position of this lithofacies represent rapid sedimentation below the normal-wave base. Moreover, well-rounded clasts scattered within the normal-graded, grain-supported texture without imbrications also indicate high-energy events within a predominantly low-energy environment. At the peak phase of storm activities, the sea floor was scoured below the normal-wave base. During this stage, clasts and skeletal grains were taken into suspension which was followed by rapid redeposition in which the larger grains redeposited first.

Intraclasts of grain-supported conglomerates have been interpreted to represent contemporaneous partial cementation in the sediment water interface prior to storms (Kazmirczack and Goldring, 1978; Kelling and Mullins, 1975; Kreisa, 1981; Sepkoski, 1982). Submarine cementation in the slope and basinal modern carbonate deposits has been reported by Wilber and Neumann (1977) and Mullins et al. (1980). From the examples, it is believed that, early lithification of the sediments covering the sea floor played a major role for the formation of intraclasts in these crinoidal conglomerates.

Cyclical occurrences of conglomeratic units within the parallel-laminated and hummocky cross-laminated lithofacies (Lithofacies 19 A and B) suggest that depositional environment of these conglomeratic storm units probably occurred in a low energy deep-ramp or upper-slope depositional environment (Markello and Read, 1981; Kreisa, 1981; and Harms et al., 1975).

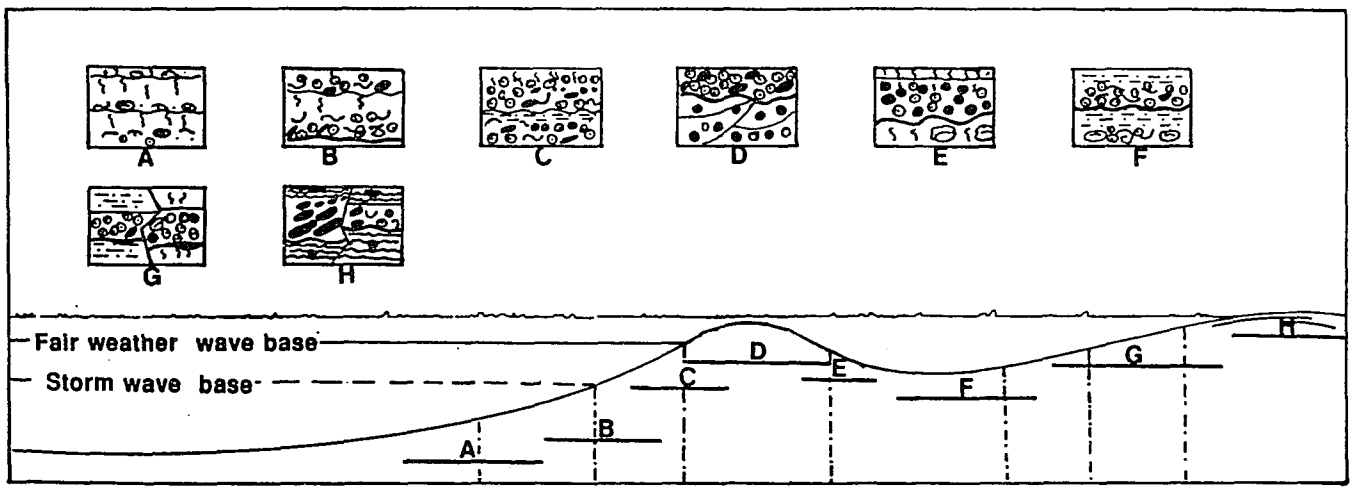
Lithofacies 20 C: Nuia-Rich Oncoidal Wackestone

Description:

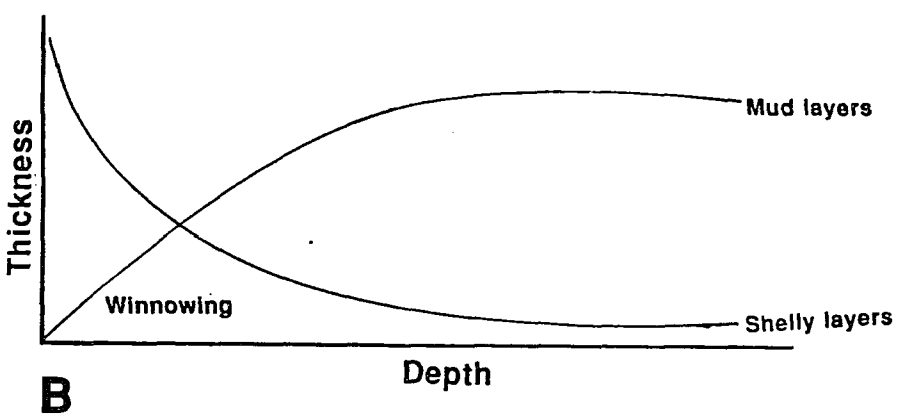
In the lowermost part of Whiterockian Canyon section, 20 to 30-cm thick, dark gray to black, wackestone units cyclically alternate with the dark green shale about 10 feet intervals. Each thick-bedded unit is composed of several thin wackestone interlayers which overlie one another with sharp erosional wavy contacts (Fig. 70 D). Thin wackestone interlayers are made up of a very thin shelly basal subunits overlain by thick muddy blankets. In addition to Nuia and Girvanella oncoids, the important allochems of the basal shelly or skeletal units are crinoids, trilobites, and brachiopods, and rarely Sphaerocodium. Besides scattered micropyrite, large euhedral pyrite crystals are common in the muddy subunits, poikilotopically enclosing calcite crystals. Planar hardground surfaces along with iron oxide-stained small intraclasts are also present at the base of the sublayers. Well-rounded oncoids usually have regular, continuous, concentric laminae, being similar to selectively dolomitized oncoids of the oncoidal shoal.

Interpretation:

Well-rounded oncoids of this lithofacies with continuous concentric laminae imply that these oncoids were imported from the Nuia shoals or their open seaward flanks where Girvanella oncoids more favorably formed. In this study, the Nuia shoals are interpreted to have formed under higher energy condition than those of the Girvanella oncoidal shoals. Therefore, these organo-sedimentary grains and Nuia were most likely transported into the low-energy, deep-shelf or basinal environment by the current and wave activities. Thin shelly (skeletal) sublayers followed by thick muddy sublayers within the thick-integrated beds represent multiple, high-energy events in such a low-energy setting. Increasing depth and decreasing winnowing are represented



A



B

Figure 71- A) Depositional model for the storm deposits of open shelf facies or deep ramp, and their comparison with storm layers in carbonate shelf: "A"= thin shelly wackestone to packstone units overlain by thick mud blankets; "B"= shelly packstone sublayers and overlying equally thick mudstone sublayers; "C"= thick packstone shelly layers with very thin mud blankets; "D"= skeletal packstone to grainstone units overlying oolitic packstone- and grainstone units; "E"= skeletal and oolitic packstone grainstone sheets overlying a bioturbated-wackestone units with sharp upper and basal contacts; "F" and "G"= relatively thin skeletal packstone unit overlying the parallel laminated, silty quartz rich lime mudstone or bioturbated-wackestone units; and "H"= flat-pebble conglomerate within the stromatolitic layers. B) Relations between winnowing level and water depth, and corresponding texture in storm layers.

by the thicker muddy blanket over the thin shelly sublayers (Fig. 71; also see Miller, 1988). Because such storm layers form below the normal-wave base, they have greater chance for preservation (Fig. 71).

Sharp, truncationally bounded thick layers in the dark green shale (the Ninemile Shale) suggest that the gradient of the slope was gentle in this region during the deposition of this lithofacies. From the alternation this lithofacies with the basinal Ninemile Shale, it can be suggested that this lithofacies was probably deposited in the lower slope or basin-margin facies from the storm-surge currents of the strongest storms.

Depositional Model for the Slope- and Basinal Storm Deposits

Lenticular, massive amalgamated beds with sharp basal and upper contacts within the hemipelagics and nodular-bedded lithofacies of the AVL have been attributed to open-shelf storm deposits. Each amalgamated massive unit contains multiple thin-bedded layers overlying one another with a sharp basal contact. Each of these thin layers consists of shelly packstone to wackestone sublayers and of mud blanket, showing a fining-upward texture.

The thickness of each sublayers in these thin layers can be controlled primarily physical conditions of environment whether these layers were deposited below the fair weather wave base or storm wave base or in between (Fig. 71 A). The water depth and winnowing level at the depositional site are the most important factors that control the thickness of mud and shelly sublayers. Winnowing or agitation level at depositional site decreases as depth increases (Fig. 71 A). As a result, the deeper the depositional site is, the thinner the shelly layers and thicker the mud sublayers will be; high-winnowing level corresponds thicker shelly sublayers and thinner mud blankets (Fig. 71. B).

Storm layers above the fair weather- wave base or in shoals are represented only by shelly layers, and each layer is separated from one another with a basal sharp

contact (see deposits designated "D" in Fig. 71 A). Storm layers in the inner shelves are similar to the storm layers of the open shelf, but they contain considerable amount of restricted marine fauna (see sedimentary units represented by E, F, G in Fig. 71 A).

B. Synthesis

Stratigraphically, these shelf lithofacies occur in the following ascending order: dark green shale (basinal), hemipelagics consisting of graded-turbidite units and infra-formational conglomerate, nodular-bedded units, mottled units, oncoidal shoal. In the June Canyon sequence, nodular-bedded lithofacies comprises sponge mounds and related-flank deposits, changing upward into bioturbated and mottled lithofacies which gradually change into oncoidal wackestone lithofacies representing the seaward extension of oncoidal subtidal bars or of oolitic bars. The submerged-flank of the oncoidal shoal is abruptly overlain by mottled-limestone lithofacies.
In the Whiterock Canyon section, however, oncoidal lithofacies represents oncoidal shoal, and the mottled units overlying the oncoidal units in the June Canyon sequence are missing in this section due to erosion. In the Mill Canyon section, basinal shale, and hemipelagics are not exposed; thin-rhythmical bedded lime mudstone or wackestone interlayers and more silty quartz-rich partings are probably equivalent to the nodular-bedded and mottled units of June Canyon and Whiterock Canyon sections. Therefore, the sediments of the Mill Canyon section are interpreted to have formed on a relatively shallow, intershoal-slope environment (i.e., between two submerged shoals) and to have been closer to the shelf edge or margin than the June Canyon section. The nodular-bedded lithofacies are commonly composed of the amalgamated-storm beds, such as crinoidal packstone and grainstone in the Whiterock Canyon and June Canyon sections and oncoidal wackestone units in the Mill Canyon section. All the type sections of Toiyabe Range are represented by basinal shale, and shaley lime mudstone

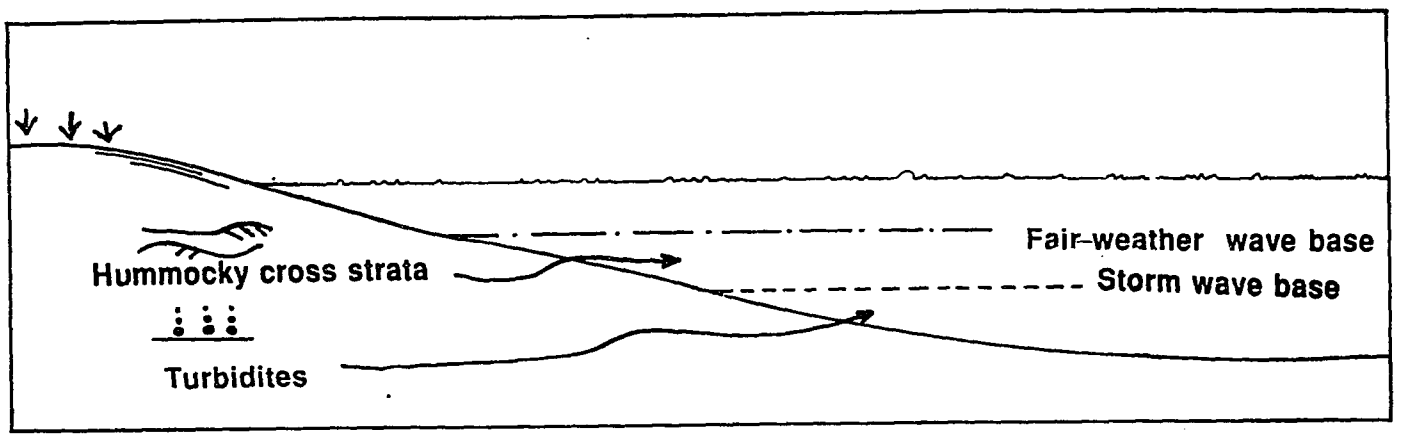


Figure 72- Model for strong storm currents-induced turbiditic deposits (Hamblin and Walker, 1977).

units that show slaty cleavage.

In the June Canyon sequence, parallel-laminated, silty quartz-rich, thick lime mudstone intervals are found in the transitional units between hemipelagics and nodular-bedded units of the middle slope to upper-slope facies, and within the nodular-bedded units of the same slope facies in all other sections. In the Toiyabe Peak section, 30 to 40 feet-thick silty quartz-rich, parallel-laminated lithofacies occurs at 250 feet above the base of the section.

This study suggests that fine-grained siliciclastic sediments or parallel laminated-, silty quartz-rich lime mudstone units of the ramp and upper slope facies are synchronous with siliciclastic sedimentation over the Nuia bars and shelf in the Ninemile Canyon and Martin Ridge sections. In the upper slope or deep ramp, this fine-siliciclastic sediments were deposited from storm countercurrents during the incipiently drowned carbonate-platform stage (the late Orthidella and early Palliseria zones). Carbonate shoal and shelf edge is generally submerged and does not act as physical barrier to storm countercurrents during incipient drowning stages. Therefore, this study disagrees with the suggestion of Ross et al. (1989) that tectonic uplifting of the land area and specifically the formation of Toole Arch may have been responsible for the formation of this lithofacies. Absence of a clastic wedge in the nearshore and shelf environments disagrees with Ross and others' suggestion.

In hemipelagic lime mudstone interlayers, parallel and hummocky-cross and ripple-cross laminae were probably produced by rapid deposition from suspension and by the storm-generated counter-bottom currents. The hemipelagic units in which the indicated laminae are preserved represent an anoxic, open-shelf environment. The graded-bioclastic lithofacies and skeletal grain- supported brecciola formed from high-density turbiditic flows caused by strong, storm-generated counter currents (Hamblin and Walker, 1979; Fig. 72). From hemipelagics to oncoidal wackestone lithofacies, increase in early submarine cementation and bioturbation can be attributed to increases in sea-floor current velocity and in oxygen content of the environment. In this study, formation of nodular-bedded lime wackestone or mudstone interlayers is primarily related to early cementation and secondarily to later differential compaction.

Crudely graded storm layers resulted from storm-induced currents in the upper slope. The source of skeletal (mostly crinoidal) layers was probably the open shelf crinoid meadows and sponge mounds. These massive sponge- and crinoid-framed bioherms laterally change into the nodular-bedded units and stratigraphically occur below the oncoidal wackestone units in the June Canyon sequence. Girvanella is present with other open marine faunas but not a major constituent of these bioherms. Nuia occurs only in the biostromes (2-3 percent or less), but not in these sponge mounds. Thus, this study suggests that Nuia had no affiliation with sponge mounds, and Girvanella had only minor a encrusting role. These findings contradict with the interpretation of Ross et al.(1989) and Alberstadt and Repetski (1989).

Girvanella-derived oncoidal lithofacies alternating with parallel-laminated, silty quartz-rich mudstone units and overlying the mottled lithofacies of the upper slope facies probably indicate water depth of least 40-45 m which clearly contradicts with the proposed shallow-water origin of the Girvanella oncoids by Flügel (1984) and others.

All these lithostratigraphic units with gradational contacts suggest that the Antelope Valley Limestone (AVL) was deposited on a very gentle slope profile which did not have any major break. This gentle slope gradient without platform talus deposits represents a ramp-type margin, not a rimmed-shelf margin. However, the ramp-type margins evolved into the rimmed-shelf only in the Martin Ridge and Ninemile Canyon sections. In other areas, ramp type depositional system prevailed after the initiation of the Palliseria zone and continued throughout the deposition of the Antelope Valley Limestone.

CHAPTER 10: CYCLICITY OF THE ANTELOPE VALLEY LIMESTONE

Introduction:

In the Antelope Valley Limestone, two kinds of short durational cycles have been described by this study: (1) cycles with shallowing-upward sequences, occurring in interpreted intertidal, shallow-subtidal and shoal facies; (2) cycles without shallowing-upward sequences, occurring at some intervals in middle and outer shelf facies. The short-durational cycles that show shallowing-upward features are asymmetrical in nature. The asymmetrical carbonate shelf cycles, with a shallowing-upward feature, start with an interpreted very rapid relative sea-level rise, and form during longer periods of marine progradation. Each of these shallowing-upward cycles shows progradational sedimentary features which are characterized by landward sedimentary lithofacies overlying open-seaward lithofacies. Similar asymmetrical carbonate shelf cycles (with shallowing-upward feature) have been noted by Ginsburg (1971), Wilson (1975), Wilkinson (1982), James (1981), Matthews (1984), Goodwin and Anderson (1985), Grotzinger (1986), James and Pratt (1986), Read et al. (1986), Bova and Read (1987), Chow and James (1987), and Koerschner and Read (1989), Elrick and Read (1991), Fischer and Bottjer (1991), and Osleger and Read (1991).

Shallowing-upward cycles usually start either with very thin-transgressive basal units or nondepositional, erosional-basal contacts, and are followed upward by the thick depositional or progradational components. These nondepositional or thin transgressional units represent a rapid deepening or flooding of carbonate platforms. The following progradational components signify a gradual and long durational shoaling (Wilson, 1975; Matthews, 1984; Grotzinger, 1986, and others).

Anyone of three possible mechanisms can be responsible for the shallowing upward

cycles: (1) allocyclicity, resulting from external forces, such as climate-forced sea-level changes (Matthews, 1984; Olson, 1985; Grotzinger, 1986; Read et al. 1986, Bova and Read, 1987; and Koerschner and Read, 1989); and (2) autocyclicity, resulting from progradation of carbonate platform (constant sea level is prerequisite); and (3) sediment loading-induced cyclicity due to progradation of clastic wedge. (Galloway, 1989).

Pleistocene eustatic sea-level changes due to fluctuations of ice volume can explain the sharp erosional basal contacts and thick depositional components of shallowing-upward cycles: the rapid decay of ice volume corresponds to a rapid transgression, and gradual growth of ice volume in longer periods corresponds to the progradational or depositional phase of these cycles (Hays, 1977; Imbrie, 1985). Ice-volume change or climate-forcing cyclicity have been applied to the short durational, shallowing-upward cycles (Grotzinger, 1986; and Read et al., 1986) and to the deep-ramp or basinal cycles by Roof et al. (1991) and Elrick and Read (1991).

Generally, 15-20 % of the cycle period is considered to be the "lag period" (Matthew, 1984; Read et al., 1986) corresponding to time elapsed between the rapid sea-level rise and the initiation of carbonate sedimentation. However, a lag period is less than 10 % of short durational sea-level rise (Quinn and Matthews, 1990). Lag depth is the minimum water depth necessary to initiate carbonate sedimentation (Quinn, and Matthews, 1990).

The shallowing upward cycles have been commonly noted in carbonates from Proterozoic to Holocene. Therefore, it is essential that one understands the environmental dynamics during the deposition of these high-frequency cyclical units in order to establish a basin-wide chronostratigraphy. The environmental dynamics, during the formation of these cycles, are principally controlled by interactions between sedimentation rates and patterns as well as by rates of short durational sea-level fluctuations, and by the effects of these short durational sea-level fluctuations on the third-order sea-level changes. Third-order sea-level changes in duration ranging from 1 to 10 m.y correspond to Vail curves (Vail et al.1977).

The objectives of this study, with respect to cyclicity, are the following: to

establish a basin-wide correlation for these short durational cycles, to investigate the relations between these fourth-order cycles and third-order cycles, and to estimate cycle parameters, such as cycle durations and progradation rates.

A. Shallowing Upward Cycles

A.1: Nuia Shoal Cycles

The major shallowing-upward cycles (Fig. 73) in this shoal are the following: (1) Type I, Nuia packstone and grainstone units of Nuia subtidal bars bounded between the planar cycle boundaries; (2) Type II, Nuia packstone and grainstone lithofacies of Nuia bars changing gradually upward into the relatively low-energy lithofacies, such as into the Nuia-rich oncoidal and peloidal Nuia packstone units of back-shoal facies and farther upward into the Nuia-rich wackestone units of the platform-interior lithofacies; (3) Type III, Nuia-rich and oncoidal packstone to grainstone basal subunits and overlying thick, parallel-laminated, fine-siliciclastic lime mudstone, or thick units which consist of rhythmical thin, parallel-laminated siltstone and lime mudstone interlayers.

Thicknesses of the shallowing-upward cycles range from 10 to 45 feet. A total of 21 Nuia shoal cycles in the Ninemile Canyon section and 11 cycles in the Martin Ridge section were described. The 11 uppermost cycles are correlative between these two sections and occur in equal number (see Fig. 76 in this chapter).

In the cyclical successions, these cycles overlie one another with sharp-erosional basal contacts (Fig. 74) which are also conformable with basal contacts of thick-bedded Nuia packstone- and grainstone units. In the upper cyclical sequences, Type III cycles, showing a stair-step morphology, were interpreted to result from the landward migration of Nuia shoals during cyclical rapid sea-level rises. In these cyclic successions, Nuia bars progressively become thinner upward, and the

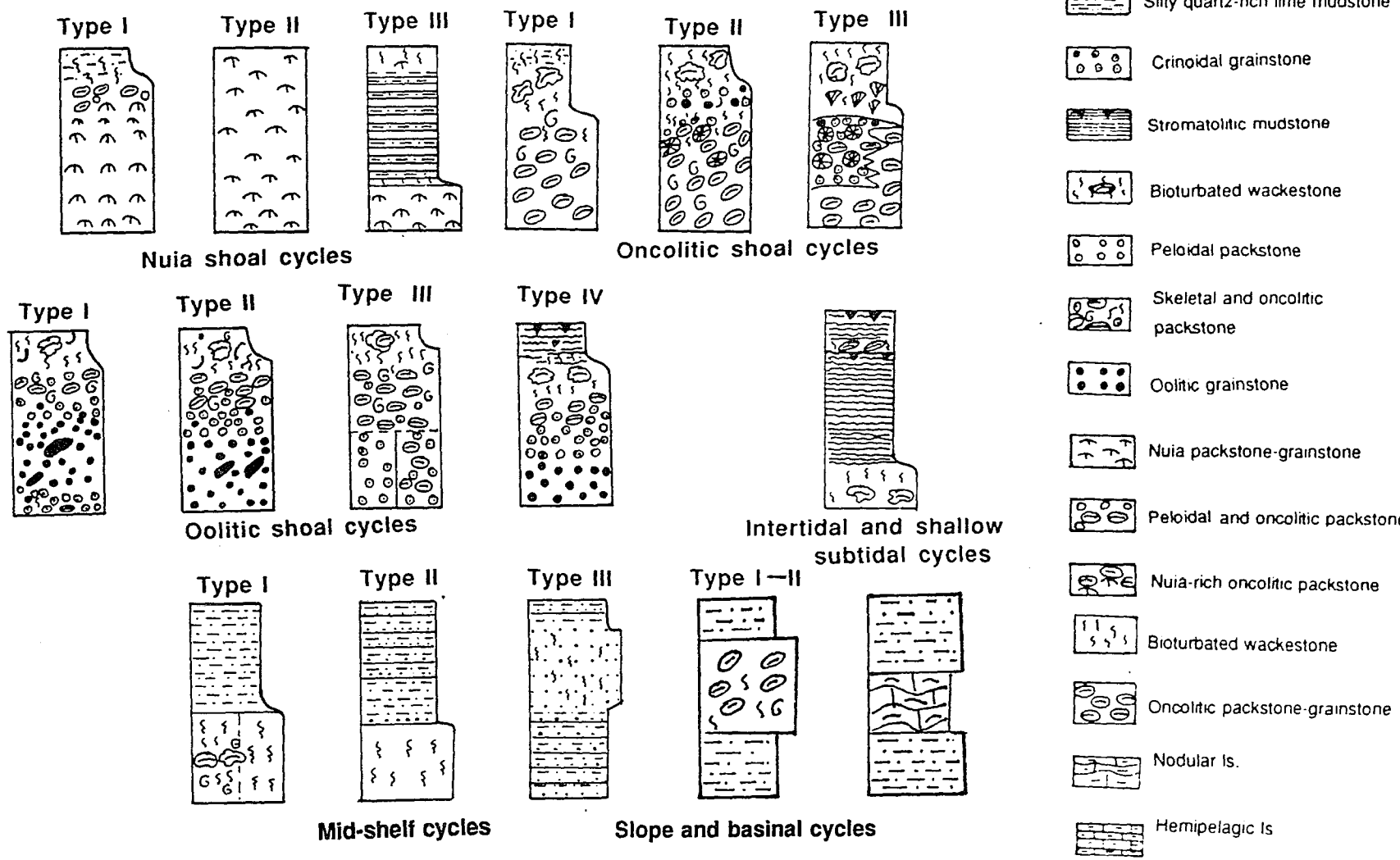


Figure 73- Major cycle types of the different depositional facies of the AVL.

siltstone and lime mudstone rhythmical interlayers become gradually thicker (Fig. 76).

A. 2: Oncolitic Shoal Cycles

The major cycle types (Fig. 73) are the following: (1) Type I, oncoidal packstone to grainstone gradually changing upward into the dark gray, bioturbated-wackestone subunits; (2) Type II, the oncoidal packstone-grainstone lithofacies gradually changing upward into the skeletal and radial ooid-rich pack to grainstone; (3) Type III, the oncoidal packstone- and grainstone overlain by crinoid-rich Receptaculites bioherm or biostrom facies which is gradually overlain by black to dark gray bryozoa-rich pelletal bioturbated-mudstone or wackestone lithofacies.

Shallowing-upward cycles of the oncoidal shoal facies display sharp basal contact relations with one another (Fig. 74). In the Lone Mountain and Keystone Canyon sections, the oncoidal shoal cycles without oolitic and skeletal shoal cycles represent the whole Palliseria zone. In this study, a total of 7 cycles in the Lone Mountain section and in the Martin Ridge section, 5 in the Ninemile Canyon section and 4 in the Whiterockian Canyon section were reported to range from 15 to 35 feet in thickness.

A. 3: Oolitic and Skeletal Shoal Cycles

Four types of cycles (Fig. 73) have been described: Type I generally consists of a shallowing-upward sequence, in ascending order, (a) bioturbated-oncoidal, peloidal, and skeletal packstone, (b) skeletal, peloidal and oolitic packstone to grainstone, (c) oolitic packstone and grainstone (i.e., shoal crest), (d) skeletal, and peloidal packstone to grainstone, (e) skeletal and oncoidal packstone, and (f) finally, bioturbated-wackestone unit. Type II begins with the dark gray radial ooid-bearing grainstone subunits and grades upward into the brown and light gray ooid-dominated

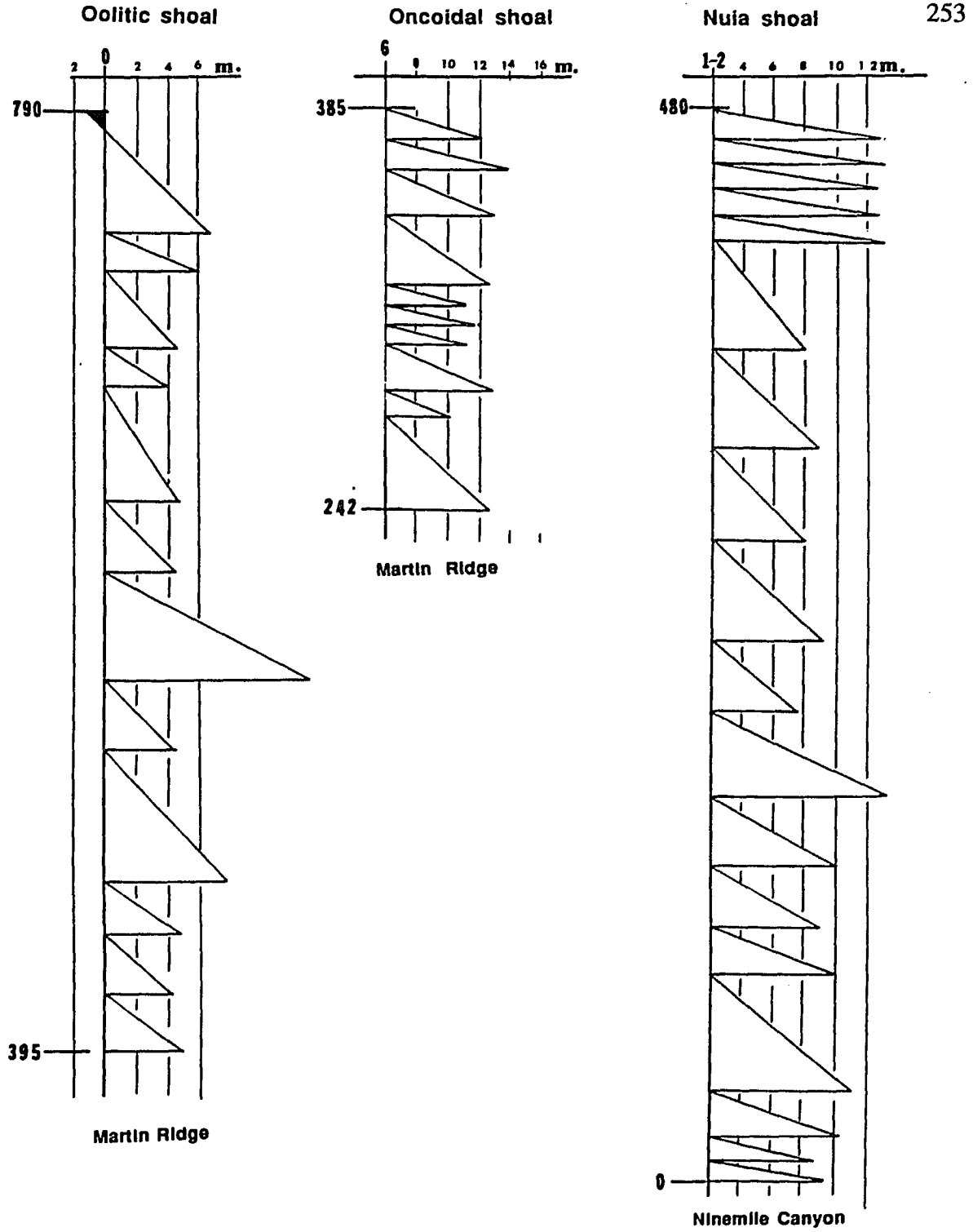


Figure 74- Interpreted approximate-initiation depth ranges of the following shallowing-upward cycles and their succession patterns in vertical sections: 1) Oolitic shoal in the Martin Ridge section; 2) oncoidal shoal in the Martin Ridge section, and 3) Nuia shoal in the Ninemile Canyon section.

subunits. This oolitic grainstone unit is upward followed by skeletal and peloidal packstone- and grainstone, skeletal and oncoidal packstone, and finally by bioturbated wackestone. Type III begins with either crinoidal packstone- and grainstone, or oncoid-rich crinoidal packstone- and grainstone units and does not have any oolitic subunits. Type IV, which begins either with oolitic basal grainstone units, or with crinoidal basal grainstone to packstone units, is capped by cryptalalgal-laminated mudstone lithofacies of intertidal and supratidal environments.

Oolitic and skeletal shoal facies are present only in the Martin Ridge and Ninemile Canyon sections (Antelope Valley region) with considerable thicknesses. In this shoal complex, shallowing-upward cycles have sharp erosional basal contact relations with one another (Fig. 74).

A total of 13 shallowing-upward cycles in the Martin Ridge and 7 in the Ninemile Canyon section range from 11 to 57 feet in thickness. In the Martin Ridge section, basal units of cryptalalgal-laminated mudstone-capped cycles are grain-supported and change eastward into the matrix-supported subtidal lithofacies in the Ninemile Canyon section. In the Martin Ridge and Ninemile Canyon sections, three oolitic and skeletal shoal cycles (about 7-10 feet thick) disconformably overlie the thick, intertidal-algal flat stromatolitic mudstone units during the upper Anomalorthis zone.

In addition, two more cyclical units of skeletal and peloidal packstone to grainstone units have been interpreted to be nearshore bar units ranging from 4 to 7 feet thick (with low- angle cross beds) which occur between the underlying well-circulated middle shelf lithofacies and the restricted inner shelf or coastal lagoon (i.e., the Copenhagen Formation). About 30 to 40-feet thick Eureka Quartzite disconformably overlie the lagoonal lithofacies in the Martin Ridge and Ninemile Canyon sections of the Antelope Valley region.

A. 4: Shallow Subtidal and Intertidal Algal-Flat Cycles

The shallowing-upwards cycles in these depositional realms vary from 24-48 feet in thickness. Each cycle, especially in the protected-shoreline depositional facies, starts with bioturbated wackestone or oncoidal wackestone and gradually changes upward into the tidal flat-cryptalgal lithofacies (Fig. 73). The cryptalgal-laminated upper component of these cycles are usually disconformably overlain by a basal subtidal or shoal basal subunits of subsequent cycles.

A total of five intertidal algal flat-capped, shallowing-upward cycles are found at the Ninemile Canyon section, and three at the Martin Ridge section (Fig. 75), and two at the Clear Creek Canyon section. The thicknesses of these tidal-flat caps in the shallowing-upward cycle range from 9-33 feet (3-11 m).

Thick algal flat-capped cycles characterize a protected, low-energy subtidal and low-energy shoreline sedimentation during deposition of the Upper Palliseria and Lower Anomalorthis zone.

B. Nonshallowing-Upward Cycles

The nonshallowing-upward cycles do not show a shallowing-upward sequence, instead these two-cyclical subunits were deposited in the same shelf during fine-grained siliciclastic-free and -rich episodes.

B. 1: Slope or Deep-Ramp Cycles

Two kinds of slope or deep-ramp cycles are recognized. Type I, observed in the Mill Canyon section, particularly in the Orthidella zone, is composed of approximately 8 to 10-feet thick oncoidal wackestone containing large intraclasts from underlying

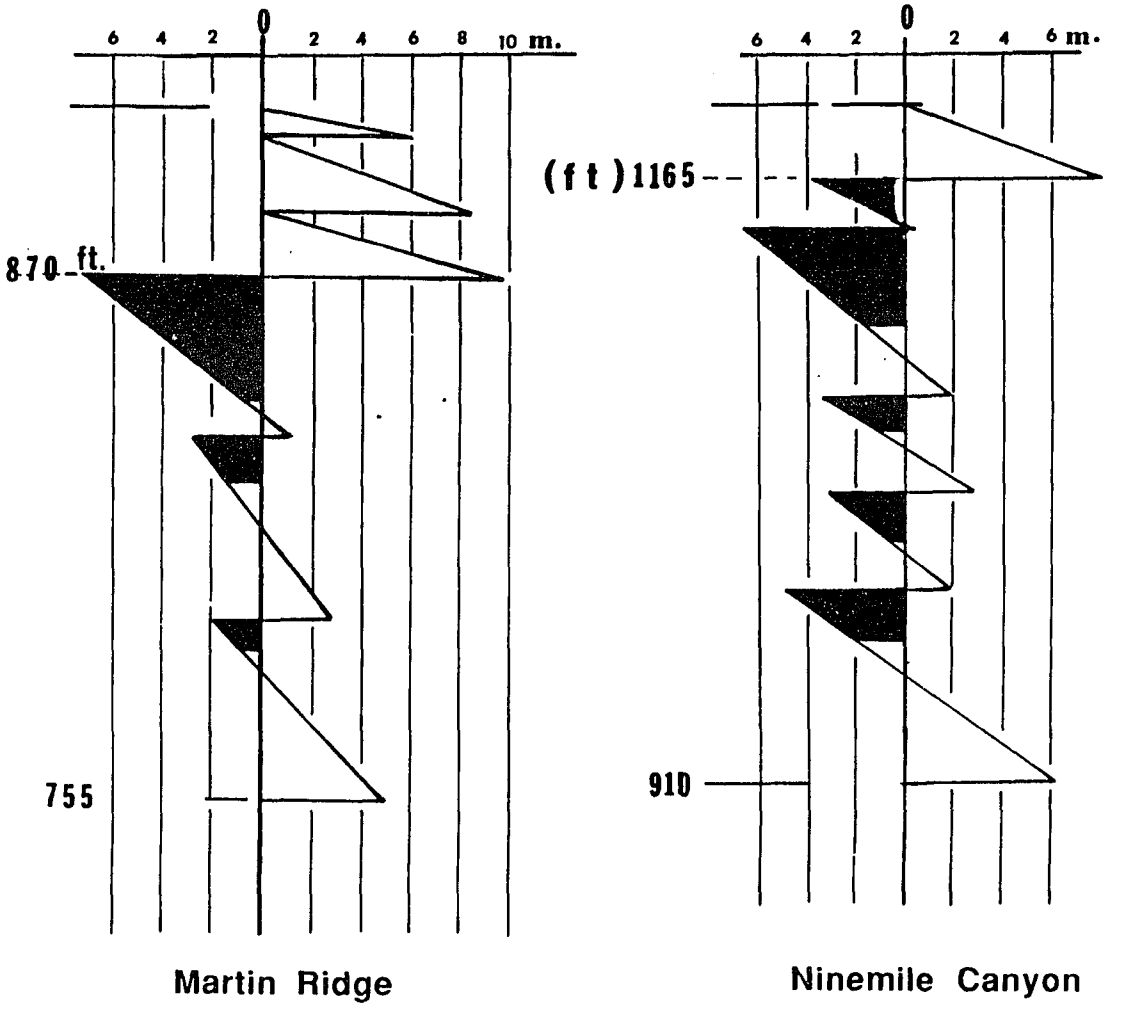


Figure 75- Algal flat-capped, shallow-subtidal cycles and algal flat cycles and their patterns in vertical sections.

lithofacies and the overlying parallel-laminated, silty quartz-rich lime mudstone lithofacies (5 to 15 feet). The oncoidal wackestone intervals gradually change upward into the parallel-laminated, silty quartz-rich lime mudstone units and overlie them with sharp-erosional basal contacts (Fig. 73).

Type II was observed in the June Canyon, Whiterock Canyon, and Lone Mountain sections. In the June Canyon section, particularly in the upper Orthidella zone, the parallel-laminated hemipelagics alternate with the siliciclastic free-hemipelagics at the interval of 279-330 feet and above. Cyclical repetition of the fine-siliciclastic sediments occurs in the nodular-bedded lithofacies at interval of 150 to 210 feet from the base of the Whiterock Canyon section. Such cyclic repetition occurs at interval of 40 to 105 feet from the base of the Lone Mountain section.

B. 2: Middle Shelf Cycles

In the Keystone Canyon and Clear Creek Canyon type sections, four kinds of shelf cycles were recognized. Type I cycles, occurring at the lower part of the shelf facies in the Keystone Canyon section, start with the basal bioturbated-oncoidal wackestone units which are overlain gradually by parallel-laminated, silty quartz-rich lime mudstone units (Fig. 73). Type II cycles start with bioturbated wackestone units which gradually change upward into the parallel-laminated, fine-siliciclastic lime mudstone units. Type III cycles, dominating the upsection of the middle shelf units in the Keystone Canyon and Clear Creek Canyon sections, start with thin-bedded, siliciclastic-rich lime mudstone and siltstone couplets and gradually change upward into thick, massive bedded siltstone units which exhibit a gradual transition upward into thin bedded-quartz silt-rich lime mudstone and siltstone couplets.

A total of 12 cycles in the Keystone Canyon section and 6 cycles in the Clear Creek Canyon sections were described.

Correlation of Shallowing-Upward Cycles

Occurrences of diachronous cyclical subunits in short durational, shallowing-upward cycles are far faster and shorter than the evolution of any biostratigraphic zonations; therefore, these cycles can not be used for biostratigraphic correlations (Wilson, 1975). The basal contacts of these cycles and the thin-transgressive units mark the rapid relative sea-level rise and flooding of the carbonate platform. Such contact relations can be used for an approximate time line for any correlation. These cycles can easily be correlated for a long distance if the cycles are found along the same depositional strike. However, the correlation of these cycles on the line perpendicular to depositional strike is comparatively difficult.

The following principal criteria have been applied to the correlation of these cycles: (1) lateral persistency of these cycle in closely spaced sections, (2) the sharp erosional basal contacts of shallowing-upward cycles, and (3) noting the basinward and shoreward facies change due to paleoenvironmental changes.

We are also aware of possible occurrences of the unnoticeable cycle couplets within the thick cycles which may have resulted from by nondepositional hiatus and erosional surfaces produced by low-amplitude, relative sea-level rises. Thus, the unnoticeable cycle couplets within thick cycles can easily cause miscalculations of cycle durations and basin-wide inaccurate cycle correlations.

The short durational shallowing-upward and non-shallowing upward cycles of the AVL in our study area have been correlated as much as 7-8 km in the Antelope Valley region, about 60 km between the Antelope Valley region and June Canyon sequence (allochthonous) in the Iks Canyon, and about 100 km between the Lone Mountain section and June Canyon sequence perpendicular to depositional strike. Similar distances are valid for correlations on the profile parallel to depositional strike.

Duration of Shallowing-Upward Cycles

The present thicknesses and the estimated-original thicknesses of sedimentary units during the Whiterockian stage are given in Table 1. Estimated-thicknesses of these units were calculated by the addition of 30 % decompaction to the present thicknesses (Table 1). The Whiterockian stage (from Latest Argelian to Llandelian time) is estimated to have lasted approximately 12 m.y (Ross et al. 1989).

Table 1- Decompacted and present day thickness of Middle Ordovician Rocks in the Antelope Valley Region.

Formations	Thickness ft.	m	Estimated Original Thickness in m. (30 % Decomapaction added)
Eureka Quartzite	150	46	60
Copenhagen Fm.	375	114	148
The AVL	1280	390	487
Ninemile Shale*	550	167	267
Total Thickness	2355	717	962

*50 % compaction added.

Average cycle durations can be calculated from the following equations given below:

(1)- Subsidence rate = Z / T

(2)- Approximated-average cycle duration = T / n

Z=total thicknesses of this formation

T=total duration of the formation

n= number of cycles

Subsidence rate = 962 m / 12 m.y; from this subsidence rate = 8 cm / 1000 years.

Total duration of the AVL with 30 % of compaction rate=

487 00 cm / 0.008 cm = 5.85 m.y

Average cycle duration= 5.85 / 58 + 5 = 92, 000 years.

Thicknesses of the shallowing upward cycles range from 6.5 m to 21 m with 30 % added decompaction. Average 13.5 m shallowing-upward units of this formation are estimated to have deposited in the 92, 000 years. The depositional periods of these cycles for 10 and 20 % of lag periods will be 82, 800 and 73, 000 years, respectively.

Several problems are associated with the calculations of average cycle durations. For instance, (1) constant subsidence rate is assumed for the deposition of entire Whiterockian units; (2) unnotified synchronously nondepositional surfaces caused by the low-amplitude, rapid sea-level rise are clearly responsible for longer cycle durations; (3) intensive calichification of this formation makes it very difficult to identify individual cycles on the basis of their erosional basal contact, (4) lateral variation in the lithology and texture of these cycles also makes the cycle correlation very difficult, (5) in comparison to Holocene examples, cycle durations of this formation are very long.

Despite all these, the longer cycle periods of this formation are usually corresponding to 100, 000 yrs periods of the eccentricity Milankovitch band which is ranging from 55, 000 to 413, 000 years (Imbrie, 1985).

Progradation Rate of the Intertidal-Algal Flat

Progradation rate can simply be calculated from the distance of progradation over the cycle duration. Ross et al. (1989) indicated that the Antelope Region, especially the Ninemile Canyon was located 125 miles (208 km) away from the paleoshoreline, and Martin Ridge may have been 215 km away from the same paleoshoreline. We assume that progradation had been effective in the area 30-35 km farther basinward

from the Martin Ridge area because, in the upper shallow subtidal and algal-flat cycles, stromatolitic mudstone units directly overlie very thin shallow-subtidal lithofacies without basal skeletal and oolitic shoal components of the shallowing upward cycles. Such relations suggest that progradation of algal flat and oolitic shoal deposits extended farther westward.

From this assumption, the approximate rate of progradation will be the following: Progradation rate of the tidal flats equals to 250 km / 92 x 0.8 = 3.5 km / 1000 years (0.8 is the 80 % of the depositional cycle period).

Progradation of the intertidal-algal flats is closely related to the gradient of the carbonate platform, and the rate of sea-level fall or rise as well as sedimentation rate. When these parameters together are taken into consideration, more accurate and higher progradation rates will be estimated. The lower estimated-progradation rate, due to unnoticed low amplitude shallowing-upward cycles, is still comparable to those progradation rates of regressive sequences. Thus, it is clear that this rate may represent the minimum progradation rate during that particular time.

Chronostratigraphy of the Shallowing-Upward Cycles and Their Relations with Third-Order-Changes in Sea-Level

In the Ninemile Canyon, at the beginning of the Nuia shoal complex, about four thin shoaling-upward cycles become gradually thicker upward. In cyclical successions, Nuia shoal units comprise stacked shallowing-upward cycles in which shoaling-upward sequences conformably overlie one another with a sharp- erosional contact (Fig. 76). These cyclic occurrences with little lithologic difference appear to have formed at similar depth. Absence of tidal-flat caps on these cycles, presence of conformable cycle boundaries, and predictable cyclic repetitions as well as extensive marine cements suggest that sedimentation and carbonate-production rates of Nuia shoal bars

kept pace with third-order rise of relative sea level. This stage, known as "Keep Up" phase, symbolizes a flat-topped carbonate platform, as suggested by Kendall and Schlager (1981).

In the uppermost Nuia shoal complex, however, Type III Nuia shoal cycles consist of thin, basal packstone to grainstone units which change upward into thick, parallel-laminated, silty quartz-rich lime mudstone. These Nuia cycles represent the landward lateral migration of Nuia bars, which was probably caused by rapid relative sea-level rise. Cyclic successions of Type III cycles forming a stair-step morphology suggest that each of this kind of cycle corresponds to landward migration of the high-energy environment during short durational high-amplitude, sea-level rises. Six cycles of type III (Fig. 76) indicate relatively rapid and short durational, high-amplitude, relative sea-level rises with a relatively longer lag time which may have resulted in the incipient drowning of the Nuia shoals and flooding of the intertidal algal flats. Therefore, during incipient drowning of Nuia shoals, the coastal and nearshore fine-siliciclastic sediments were suspended, remobilized, and transferred to middle shelve, shoals, and to farther basinward (specifically to the upper slope or deep-ramp depositional belts). These fine-grained siliciclastics have been interpreted to be deposited from storm countercurrents on the incipiently drowned Nuia-bar crests and in the outer-deep ramp or upper slope. Therefore, it is possible to suggest that fine-grained siliciclastic lime mudstone units of the Orthidella zone in the lower part of Mill Canyon, June Canyon, and Whiterock Canyon are synchronous and represent the incipiently drowned carbonate platform. Six thin type III Nuia shoal cycles (the uppermost six cycles of Nuia shoal; Fig. 76) suggest that six-superimposed, short durational, high-amplitude sea-level rises were responsible for these type III Nuia shoal cycles and the incipiently drowned carbonate platform stages. And these short durational, high amplitude relative sea-level rises which probably an initiated the third-order sea-level rise which outpaced the carbonate production rate and the growth rate of Nuia shoals.

The third-order high-sea level stand probably caused the formation of stressed-environmental conditions by rapid mobilization and sedimentation of

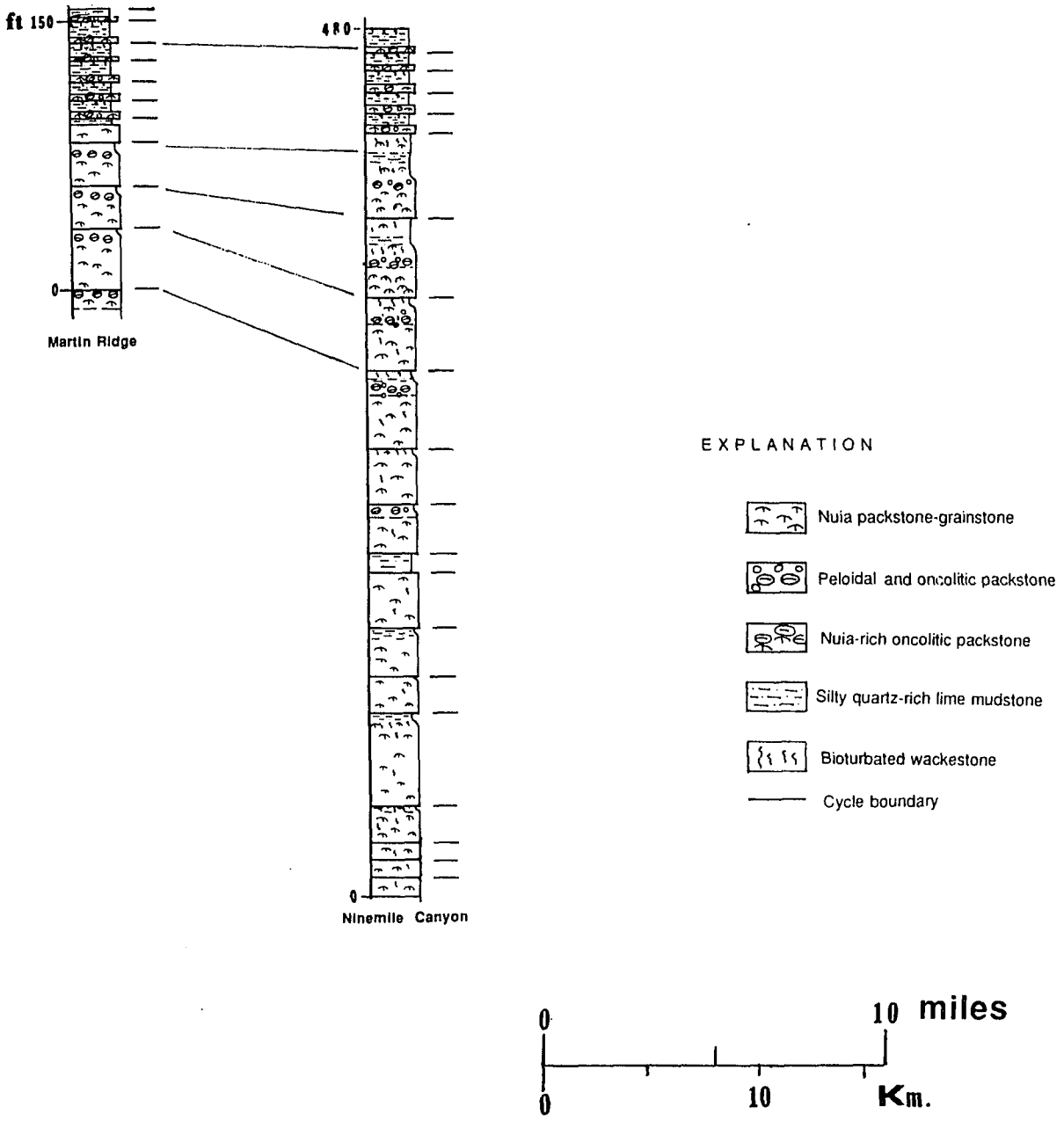


Figure 76- Correlation of short durational, shallowing-upward Nuia shoal cycles.

fine-grained siliciclastics from suspension of storm countercurrents. These fine-grained siliciclastics may have choked the Nuia meadows.

The onset of the oncoidal shoals is represented by formation of the oncolitic packstone lithofacies in the Martin Ridge and Ninemile Canyon sections. In both sections, Girvanella-constituted oncoids are the primary oragno-sedimentary grain type; Nuia is the second most important constituent, and particularly in the Ninemile Canyon section, Nuia's presence is considerably high in percentage. In addition, in the Ninemile Canyon section, nearly 35-feet thick Nuia shoal facies with gradually overlying subtidal shelf-facies is correlative with the two cycles in the Martin Ridge which are, in ascending order, (1) relatively more matrix-supported basal oncoidal shoal cycle, and (2) about 7 to 10-feet thick Nuia shoal cycle (Fig. 77). In the Ninemile section, the thick Nuia cycles, overlying oncoidal shoal units, may represent initiation of Nuia shoal facies in the farther-shoreward shelf facies to the point where Nuia shoal was forced to move by rapid, short durational, high-amplitude, sea-level rise. In addition, these Nuia-shoal cycle, overlying oncoidal shoal in the Ninemile Canyon and Martin Ridge sections (Fig. 77), probably represent a very brief "Catch Up" phase of the Nuia shoal (Fig. 77) at the indicated localities. In Antelope Valley region, formation of the oncoidal shoals marks the beginning of the Palliseria zone. Finally, we can suggest that Nuia-rich oncoidal shoal cycles at the Martin Ridge section are correlative with Nuia shoal cycles at the Ninemile Canyon section represent the basinward extension of Nuia shoal (Fig. 77).

Formation of the oncoidal shoals appears to have originated from the short durational, high-amplitude relative sea-level rise with relatively longer lag periods, which were primarily responsible for the drowning of the Nuia shoals. However, the previously indicated "Catch Up" phase of Nuia shoal units probably resulted from the rapid progradation of Girvanella-dominated shoal units during the relatively low-amplitude sea-level rise. In Antelope Valley region, after the short durational "Catch Up" phase of Nuia shoal, the following high-amplitude, sea-level rise, with a long-lag period, probably terminated the Nuia shoal and caused the formation and basin-wide domination of the very wide oncoidal shoal during the Palliseria zone. On

the other hand, in the Lone Mountain and Keystone Canyon sections, Nuia growth ceased by superimposed short durational high amplitude sea-level rises which coincided with the third-order sea-level rise even before the formation of oncoidal shoals. In these two sections, after Girvanella oncoidal shoal had taken over Nuia shoal, the oncoidal shoals with the Receptaculites bioherms represent the incipiently drowned shoal complex which prevailed through deposition of the entire Palliseria and Anomalorthis zones.

In the Antelope Valley region, the skeletal and oncolitic packstone units represent the shoreward component of the open seaward oncoidal shoal. The progradation of these skeletal and oncoidal packstone lithofacies appears to have played a significant role in leading to the formation of the skeletal and oolitic shoals in this region (Fig. 77). As seen in this example, formation of the skeletal and oolitic shoal is not a third-order rapid sea-level fall but a rise which may have resulted from the superimposed-short durational, high-amplitude sea-level rise. The oncoidal shoal units directly overlie the nodular-bedded lithofacies of deep ramp in the Whiterock Canyon sections where the oncoidal shoal units represent the Palliseria zone, and this relationship suggests that the oncoidal shoal appears to have become an open seaward extension of the oolitic shoal.

Except for Type IV oolitic and skeletal shoal cycles, other cycles mostly repeat with a sharp erosional contact without landward migration (in place) as in the aggradated-or stacked-Nuia shoal complex (Fig. 77). In cyclical successions of oolitic and skeletal shoal cycles, conformable cycle boundaries, short durational, abundant marine cementation, and low to moderate progradation rates as well as absence of tidal-flat caps on these cycles are indicative of the "Keep Up" phase of platform (i.e., flat-topped progradating platform, Kendall and Schlager, 1981). In addition, some oolitic and skeletal shoal cycles, starting with Type I, and Type III cycles, are usually thicker than those of the cycles starting with directly oolitic packstone to grainstone units. Therefore, both Type I and Type II cycle types correspond to the long "lag periods" and cycle periods which were probably caused by the high- amplitude rise in sea-level combined with a relatively high subsidence rate (Fig. 77).

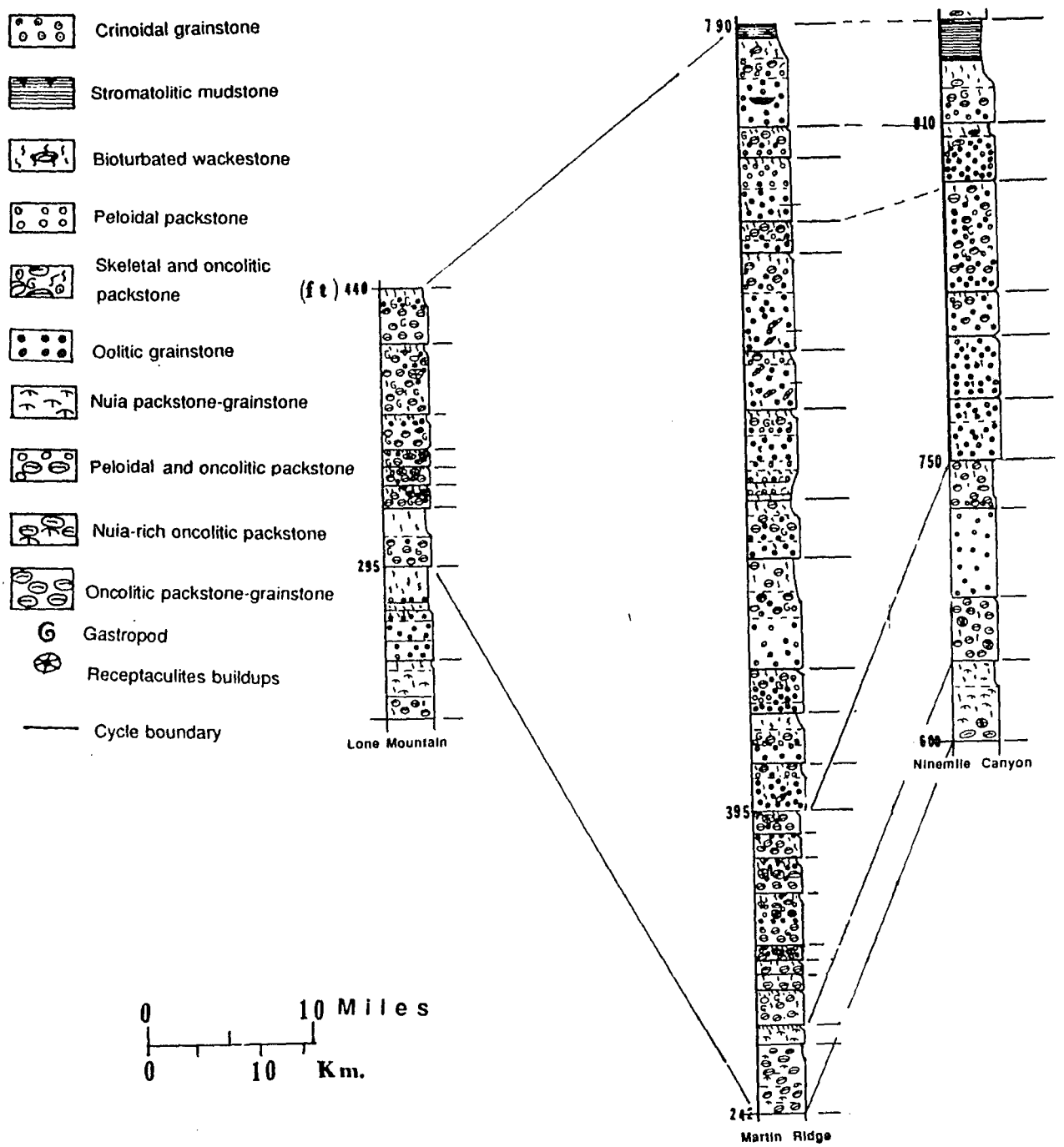


Figure 77- Correlation of short durational, shallowing-upward oncolitic and oolitic cycles.

Thick, algal flat-capped uppermost oolitic shoal cycles (Type IV) of the Palliseria zone and other shallow-subtidal cycles which characterize a high-sedimentation and progradation rate, were probably resulted from the high rate of lowering in third-order sea-level rise and low-subsidence rate of the carbonate platform (Fig. 77). Although the amplitudes of short durational sea-level rises were high, their cycle durations were probably shortened by considerably high sedimentation rate and by a very low-subsidence rate of the carbonate platform. As a result, the carbonate production rate may have reached its peak phase during the farther westward progradation of the intertidal algal flats and oolitic shoals. Fine-grained siliciclastic sedimentation was probably confined to the tidal flat-depositional belt during this peak progradation phase but not in the shelf and outer shelf. The evidence from the late Palliseria zone to the end of middle Anomalorthis zone indicates that progradation rate exceeded the subsidence rate of the carbonate platform and the third-order relative sea-level rises with a considerable rate. As a result, the thick intertidal algal flat lithofacies progradated as much as 250 km over the shelf and shoal sequence in the Antelope Valley region.

In June Canyon sequence, the oncoidal packstone and wackestone lithofacies of the Palliseria zone progradationally overlies the lithofacies of the Anomalorthis zone and even younger zones (e.g., Kay 1962 and Kay and Crawford, 1964). All the field evidence indicates that these oncoidal lithofacies of the June Canyon section are correlative with the algal-flat capped oolitic shoal cycles at the Martin Ridge section. Thus, it can be suggested that these oncoidal lithofacies represent the major progradation or regression during which these oncoidal shoal units, as open seaward extension of oolitic and skeletal shoals, progradated far-distant over the deep-ramp settings. Therefore, one can suggest that algal flat-capped oolitic shoal cycles and their correlative oncolitic shoal cycles at the farther basinward environments represent a third-order sea-level fall or regression. This regression may have resulted from the superimposition of high or low-amplitude sea-level rise with short-lag periods and from low-subsidence rate of the carbonate platform. In Antelope Valley region, this regressive period is represented by the subaerial-exposured features of the algal-tidal

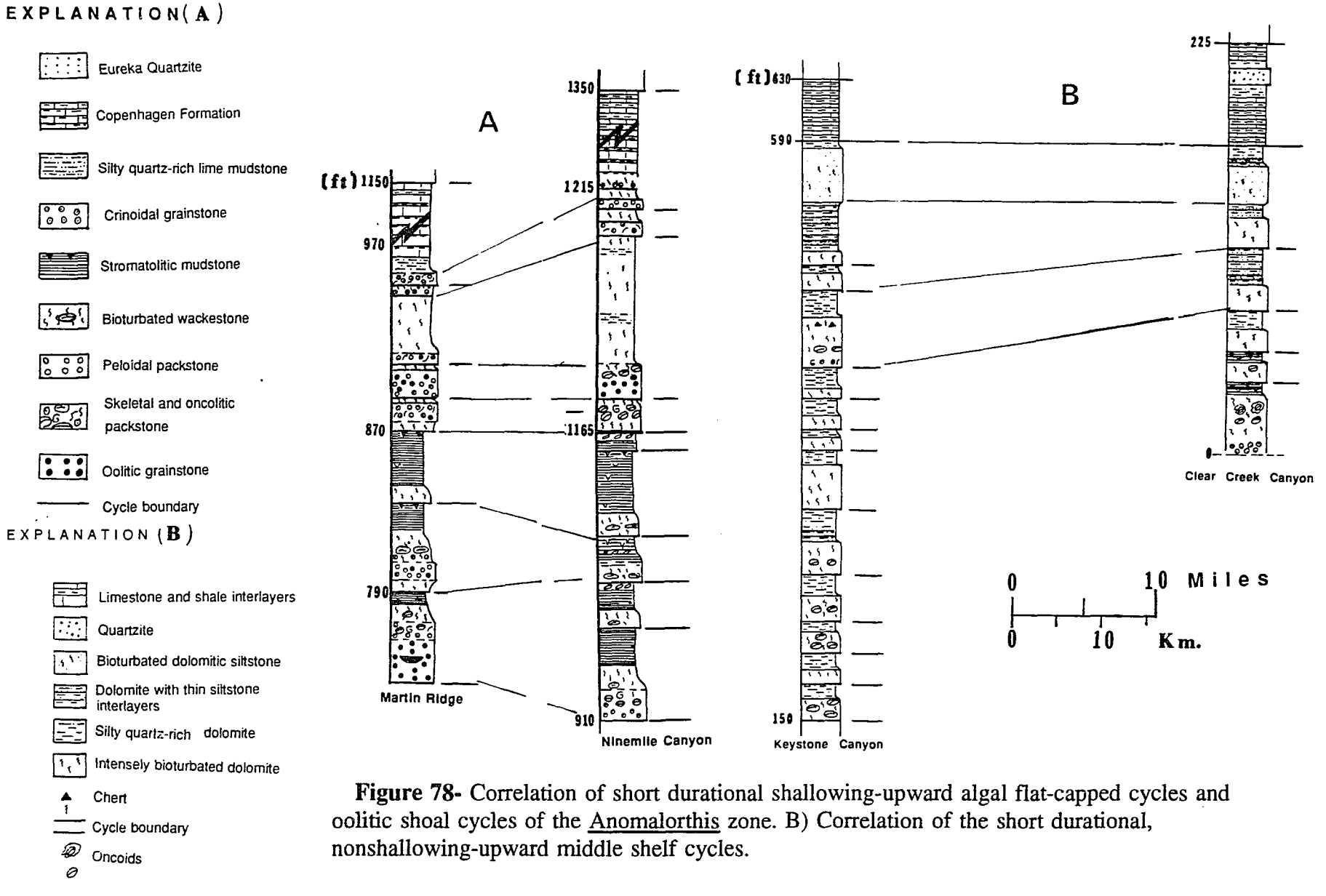


Figure 78- Correlation of short durational shallowing-upward algal flat-capped cycles and oolitic shoal cycles of the Anomalorthis zone. B) Correlation of the short durational, nonshallowing-upward middle shelf cycles.

flats which display desiccation cracks, birdseye, and flat-pebble conglomerates as well as considerable vadose-zone diagenesis.

In the Lone Mountain and Keystone Canyon sections, on the other hand, the fine-grained, siliciclastic-dominated shoreline sedimentation (the lower-quartzite member of the Eureka Quartzite) overlies the deep-shelf lithofacies of the oncoidal shoal and very thin lagoonal lithofacies, respectively. The farther-westward progradation of the coastal, fine-grained siliciclastics clearly represent a major regression in these places. The difference of progradation level at both sections clearly suggests that progradation rate of the siliciclastic-dominated shoreline was much higher in the Lone Mountain section than in the Keystone Canyon section. The high progradation rate in northerly regions (Lone Mountain) was controlled not only by closeness of the source region, but also by the gradient and width of shelf or combination of both.

In the Ninemile Canyon section, the uppermost oolitic shoal cycles of the upper Anomalorthis zone are correlative with the skeletal and peloidal cyclic units of the Martin Ridge sections. In both sections, these cyclical units unconformably overlie the thick, stromatolitic mudstone units of the algal flats (Fig. 78 A). In addition, two other cycles, the nearshore bars repeating with the lagoonal lithofacies occur in the Ninemile Canyon section, but they are not found in the Martin Ridge section (Fig. 78 A).

Considering that the cycle durations are considerably short, in turn, the subsidence of the carbonate platform alone can not yield the thick, tidal flat-capped cyclical occurrences into the depth range of submergence. Therefore, the transgressive oolitic and skeletal and peloidal shoal cycles overlying the algal flat deposits suggest that third-order sea-level rise may have resulted from several superimposed high-amplitude relative sea-level rises with a long lag period combined with a high subsidence rate. As a result, during the deposition of transgressive units of the AVL, the sea-level rise exceeded the sedimentation rate, caused flooding of the shelf, and lowered or inhibited the progradation rate of the intertidal-algal flats. In the Antelope Valley region, this transgression is interpreted to have turned algal flat-dominated shoreline facies into the siliciclastic shoreline.

This transgressive period is represented by the middle member of Eureka Quartzite, which is thin, rhythmical nodular-bedded limestone lithofacies of open shelf in Lone Mountain and which is composed of oncolitic packstone and Stromatoporoid-bioherm lithofacies in Keystone Canyon.

In the Antelope Valley region, the indicated nearshore bar cycles, thick lagoonal lithofacies and the coastal siliciclastic lithofacies (the Upper Eureka Quartzite) represent the high sedimentation and progradation rates which began exceeding the rate of short durational sea-level rise and subsidence rate during the late episode of previous transgression. Consequently, the progradational-shoreline siliciclastics and coastal lagoon lithofacies, overlying oolitic and skeletal shoal cycles and related sediments, represent a major regression which might have taken place after the relatively brief transgression.

The Upper quartzite member of the Eureka Quartzite progradated over the indicated transgressive lithofacies of middle member of Eureka Quartzite in Lone Mountain and Keystone Canyon sections and the Copenhagen Formation in the Martin Ridge section.

Figure 78 B- shows that nonshallowing-upward cycles of the well-circulated shelf (behind the incipiently drowned oncoidal shoal) are correlative in the Keystone Canyon and Clear Creek Canyon sections of the southern localities.

Origin of the Shallowing-Upward Cycles in the AVL

The features described above for the various forms of shallowing-upward cycles in the Antelope Valley Limestone (AVL) suggest that external or allogenic controls played a principal role during the formation of these cycles, rather than sedimentation rate and sediment production area-controlled subsidence (autocyclicity). For instance, in the shallowing upward cycles, the synchronous nondepositional surfaces or the sharp and erosional basal contacts of these cycles and their thick diachronous

depositional components characterize the basin-wide synchronous rapid deepening, flooding and gradual shoaling. This basin-wide synchronous rapid deepening can not be explained by partial, progradation-generated differential subsidence.

With constant sea level, the progradation of intertidal flat and unfilled-subtidal facies produces only a gradual subsidence which is also limited in a relatively local area rather than in basin-wide subsidence. Similarly, the shoal cycles without intertidal-flat capping can not be explained by the indicated tidal-flat progradation. Therefore, the rapid subsidence and synchronous deepening and following gradual shoaling events probably represent rapid, eustatic sea-level rise and gradual lowering sea-level rise or fall.

The basin-wide correlations of the cycles of the AVL on the profile perpendicular to paleoshoreline, their thickness, and lateral persistency and continuity support the allogenic force-induced cyclicity, as suggested by Goodwin and Anderson (1975), Heckel (1986), Read et al. (1986), Grotzinger (1986) Bova and Read (1987), Koerschner and Read (1989), Elrick and Read (1991), Fisher and Bottjer (1991), Osleger and Read (1991), and Roof et al. (1991).

The eustatic sea-level changes can be caused by the effects of the following three processes: (1) Glacio-eustacy, controlled by changing volume of the continental ice sheets (Hays 1977, Matthews, 1984, Grotzinger (1985) and Read et al., 1986); (2) geoidal eustacy, controlled by the change of geoids which are the equipotential sea-level surfaces of the combined rotational and gravitational potential fields (Morner 1976); and (3) tectonic eustacy, controlled by the spreading rate or changes in volume of the mid-oceanic ridges. However, generally, the spreading rate of 1 cm/1000 yrs is too low to produce rapid sea-level oscillations (Pitman, 1978).

The rapid, short durational sea-level rises and relatively long, gradual shoaling periods of the shallowing-upward cycles are related to rapid decay and slow growth of continental ice sheets (Hays, et al., 1977; Matthews, 1984; Grotzinger, 1986; and Read et al., 1986) and Roof et al. (1991). Therefore, of the indicated eustacy processes, the glacioeustatic sea-level changes were probably the major cause of the cycles of the Antelope Valley Limestone (AVL). Hence, allogenic cyclical mechanisms were

responsible for formation and evolution of these cycles throughout the Whiterockian stage.

By contrast, for autogenic cycle models (e.g. Ginsburg, 1971; Wilkinson, 1982, and James, 1984) the sedimentation rate and sediment producing area played a major role for the formation of the shallowing-upward cycles because the subsidence rate and sea-level changes are constant. The principal advantage of the auto cyclicity mechanism is that it explains small-scale cyclicity without sea-level changes, and the symmetrical cyclical repetitions (with respect to similar thicknesses of the cycles and their repetition at uniform intervals, such as every 10 feet) are commonly expected to form by this process. However, this cyclical model fails to explain the occurrences of non-tidal flat-capped cycles of Nuia, oncoidal, and oolitic and skeletal shoals as well as the mid-shelf and outer-shelf cycles. Because, according to auto cyclicity model, progradation of tidal flats and filled-shallow subtidal environments causes the subsidence and initiates the new cycle; however, during the formation of algal flat-uncapped shoal cycles, progradation rate of tidal flat was significantly lowered or inhibited.

In effect, very low-sedimentation and subsidence rates are believed to have prevailed during the incipiently drowned oncoidal shoals. Therefore, the only mechanism that could be responsible for the oncoidal shoal cyclicity was the glacio-eustatic, sea-level changes. Moreover, thick tidal-flat capping cycles and extensive fresh-water diagenesis can also not be explained by the autocyclic mechanisms (e.g. Read et al., 1986; and Grotzinger 1986): Because, in autocyclic models, sedimentation builds up to sea level then instant subsidence follows and initiates the next cycle.

About 150 miles (250 km) of basinward progradation of thick cryptalgal laminae-dominated cycles can not be interpreted by the sedimentation-generated subsidence because their thicknesses are too small to initiate the subsidence of carbonate platform (subsidence rate for passive margin is 20-40 mm/1000 yrs according to Grotzinger, 1986; and 50 to 100 mm /1000 yrs by Pitman, 1978) in a cyclical fashion with short durational intervals. In addition, in autocyclicity, subsidence

starts when sediments build up to the sea level; therefore, the formation of thick algal-flat deposits and their prolonged exposure to meteoric diagenesis are unlikely. Even for the thick algal-flat cycles, the glacio-eaustsy appears to provide best explanation.

Finally, the middle shelf and outer shelf cycles without shallowing-upward features can also only be explained by rapid relative sea-level rise because these cycles mostly consist of fine-grained siliciclastics and siliciclastic-free normal marine lithofacies. Particularly, parallel-laminated fine siliciclastics have been interpreted to represent the sedimentation from suspension loads of the storm countercurrents during the short durational, sea-level rise which inhibits the tidal-flat progradation.

The oolitic shoal cycles with and without tidal-flat capping have been interpreted by the noneustatic "island-tidal flat" model" as a mosaic of islands in an open sea (James and Pratt, 1986; and Chow and James, 1987). This suggested model is also an autogenic cyclical model, relating the irregularity of cycle assemblages to geographic configuration and extent of shoal complex and storms. Even, in the uppermost oolitic cycles of the AVL, the algal-flat deposits capping the thick, shallow-subtidal lithofacies of oolitic shoal cycles exclude the applicability of this model to oolitic shoal cycles of the AVL for the previously indicated reasons.

The short durational climatic cycles are closely related to changes decay and growth of continental ice sheets which are accepted to be controlled by the earth's orbital variations on solar insulations, namely Milankovitch cycles (Precession, Obliquity, and Eccentricity). Imbrie (1985) illustrates that Milankovitch cyclic bands range from 10.000 years to 400.000. Milankovitch cyclical periods have been applied to sedimentary cycles by many studies. However, Algeo and Wilkinson (1989) have argued that application of the earth's orbital variations-forced, sea-level fluctuations are questionable even though cycle durations coincide with the Milankovitch cycle bands, unless glaciers have been noted in that particular geologic time.

In the Mesozoic Newark Supergroup, sedimentary cycles are interpreted to have been produced by rises and falls of large lakes in response to periodic climatic changes coinciding with the Milankovitch cyclic bands (Olson, 1985). Olson related ice-free early Mesozoic Milankovitch-type changes to the precession which probably

altered the intensity of low-pressure cells and drove the monsoonal winds to the more southern areas. Similar explanations were adopted for the Cretaceous basinal limestone and marl cycles by Arthur et al. (1986).

For the cycles of the Antelope Valley Limestone, this mechanism may not be applicable. However, during the Mid-Ordovician global cooling may have been in progress because during the Late Ordovician the polar ice caps are widely known to have formed in the Sahara, Africa (Freidman and Sanders, 1978). The glacial deposits of Late Ordovician have been reported in the Sahara by Beuf et al. (1968) and Arbey (1968); Port Askaig tillite in the N.W. Scotland by Spencer and Pitcher (1968); and in South Australia by David, 1907, David and Browne (1950). Paleomagnetic data indicate that the Sahara was in the polar position during the Ordovician (Frzkes, 1979).

It is possible to suggest that climatic change-induced sea-level fluctuations may have begun during or even before the early Middle Ordovician time and resulted in cyclical sedimentation of the AVL. Precession and eccentricity-induced changes in the intensity and position of low-pressure cells at the subtropical regions may have been solely responsible for the indicated cycles of the AVL which was deposited within the area 10° south of the Equator (Ross, 1977).

CHAPTER 11: EVOLUTION OF WHITEROCKIAN CARBONATE PLATFORM

The Whiterockian carbonate platform resulted from nine-evolutionary phases which characterize the following-platform margin features: 1) keep up; 2) incipiently drowning; 3) onlap; and 4) off lap. In the Lone Mountain and Keystone Canyon sections, a total of seven phases represents the evolution of the carbonate platform, which, however, in the Ninemile Canyon and Martin Ridge sections, is represented by nine phases (Figs. 79, 80).

In the study area, the nature of these evolutionary phases have been determined by interactions among the sedimentation and subsidence rates, and rate in sea-level rises. These phases or the evolution of the Whiterockian carbonate platform correspond to two transgressions, two regressions, and two stand stills (Fig. 81).

Phase I:

This phase is represented by the transitional zone (75 to 100-feet thick), which occurs between the lower Orthidella zone of the Antelope Valley Limestone (AVL) and the Ninemile Shale in the Ninemile Canyon section. Greenish-gray, olive gray calcareous Ninemile Shale (550-feet thick) overlies the Goodwin Formation in the same section (Merriam, 1963). The upper part of the Goodwin Formation, consisting primarily of light gray crinoid-rich Nuia packstone and grainstone units (e.g., Mamet and Roux, 1982; and Gillet, 1983), represents a skeletal shoal facies. From the indicated-stratigraphic relations, the formation of the Ninemile Shale probably indicates the initiation of the major transgression which completely drowned the

skeletal shoals of the Goodwin Formation in the Antelope Valley region. Furthermore, this third-order sea-level rise may have caused a synchronous basin-wide deepening and prompted the formation of Nuia bank facies at the farther eastward shelf environment (Figs. 79, 80). On the other hand, the gradual trend between the lower AVL and the Ninemile shale (during the Upper Canadian and Early Orthidella zone) indicate progressive lowering in the rate of sea-level rise and progressive increase in sedimentation rate in this area.

In the Antelope Valley region, the commencement of the Nuia-subtidal bars probably represents the time period during which sedimentation rate of the Nuia shoal probably began to catch up with the rate of seal-level rise. However, a well-circulated deep shelf facies containing abundant fine siliciclastics (see Kellog, 1963; and Ross et al., 1989) implies that during the resumption of the Nuia shoal bars sedimentation rate in the backshoal and shelf as well as Nuia shoal lagged behind the sea-level rise (Figs. 79, 80).

Toward the end of Early Orthidella zone, in the Antelope Valley region, progressive increase in rate of sedimentation due to the accretion and westward progradation of the initial Nuia bars may have resulted in the formation of Nuia shoals. Moreover, in southern Nevada, particularly at the Meiklejohn Peak, the deep-ramp mounds formed from the same transgression (Ross, 1977). Therefore, in the Antelope Valley region, this phase is assumed to have formed during the late stage of that major transgression and continued until the sedimentation rate of Nuia shoal units established balance between the rate of sedimentation and sea-level rise.

Phase II:

This phase dominates most of the Orthidella zone and is represented by thick shallowing-upward cycles of the Nuia shoal, without intertidal-algal flat capping. These cycles occur in a predictable manner as the Nuia shoal bars overlie, in place, one an other or the upper component of these cycles (i.e., the Nuia-rich, bioturbated

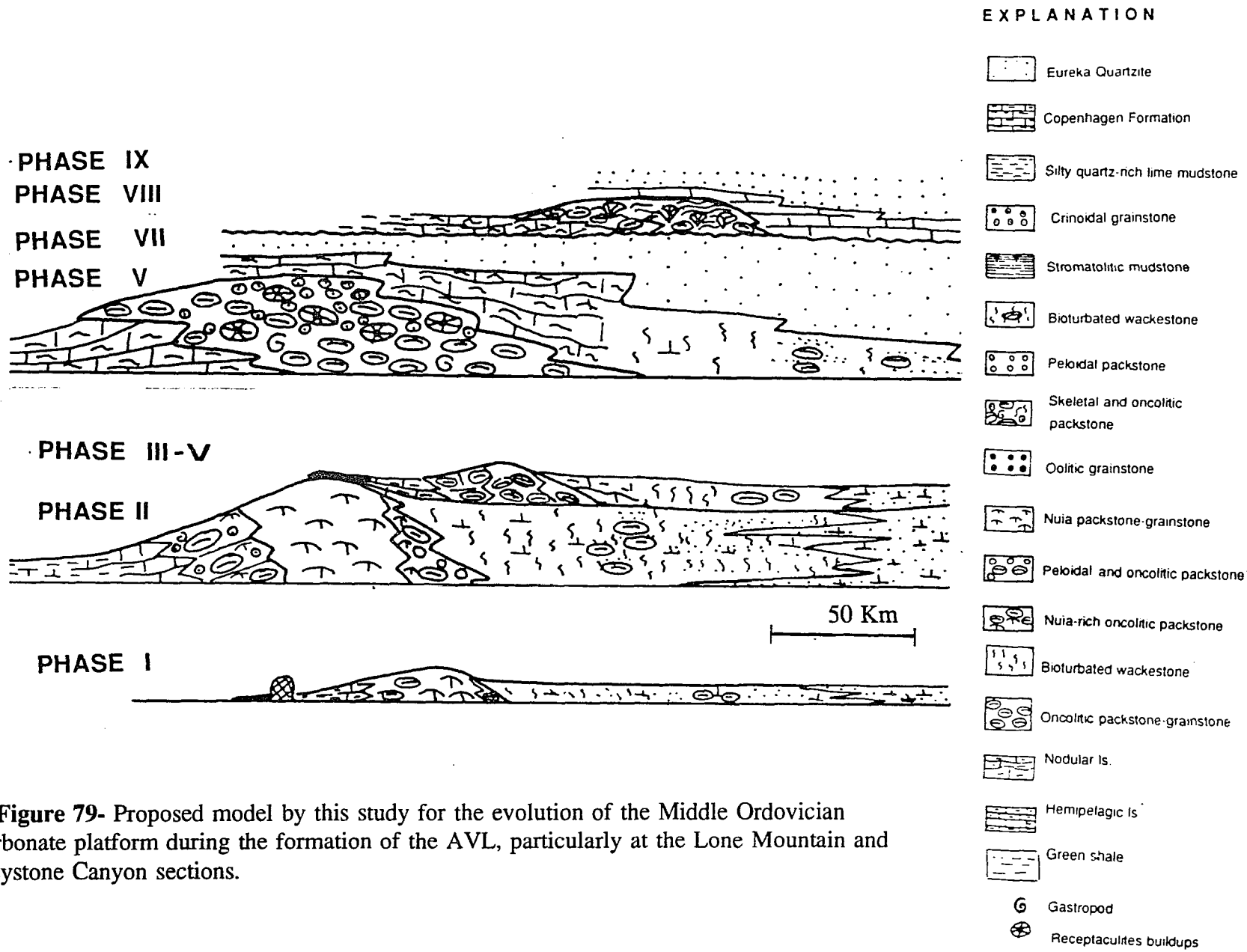


Figure 79- Proposed model by this study for the evolution of the Middle Ordovician carbonate platform during the formation of the AVL, particularly at the Lone Mountain and Keystone Canyon sections.

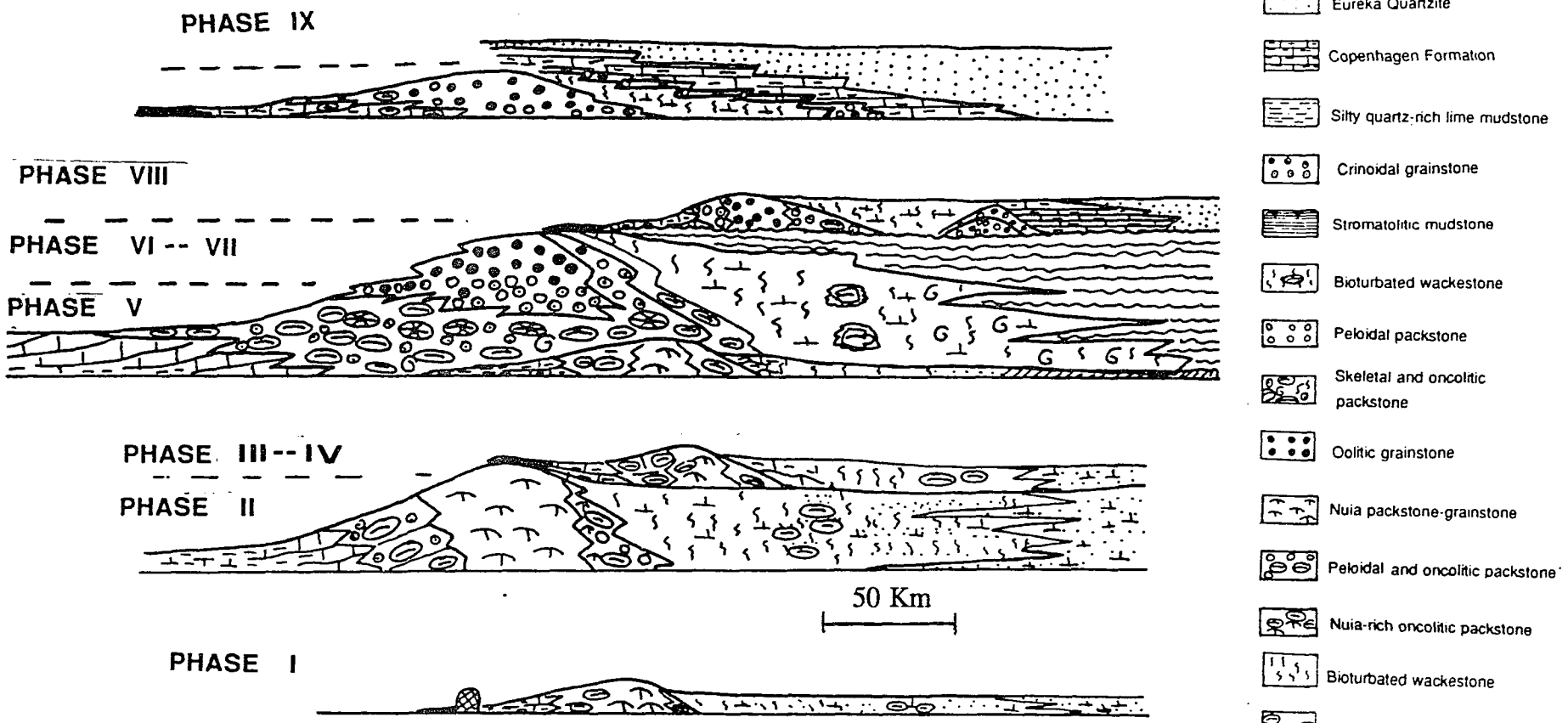


Figure 80- Proposed model by this study for the evolution of the carbonate platform at the Martin Ridge and Ninemile Canyon sections.

wackestone of the well-circulated shelf; see Nuia shoal cycles in Chapter 10) with sharp, erosional disconformable contacts.

The bank-top overflows and interbank flows at low areas between the Nuia banks are believed to have equally been responsible for the formation of the well-circulated deep shelf behind those Nuia banks. During this phase, sedimentation rate of the Nuia shoal units appears to have kept pace with the rising-sea level; as a result, Nuia bank deposits as a high-energy skeletal ramp (e.g. Read, 1982) probably progradated westward over the ramp-slope deposits (Fig. 79, 80). At the same time period, the balance established between the rate of sea-level rise and sedimentation probably inhibited or slowed the progradation of the algal-flat deposits.

From the interpretations above, it can be implied that throughout this phase, the short- durational, high-frequency, rapid sea-level rises and following progradations may have produced the thick accretionary Nuia-shoal complex (nearly 400-feet thick) on a gently declining shelf margin or ramp (Figs. 79, 80).

These progradationally and vertically accreted-cyclic occurrences (in place) resemble the "Keep Up" phase (Kendall and Schlager, 1981) and the "Stationary shelf-slope break" stage (James and Mountjoy, 1983) in the evolutionary carbonate platforms (Figs. 79, 80).

In addition, the normal-graded turbidites (Lithofacies 16 A and B) within the hemipelagics (Lithofacies 17) of the Orthidella zone below the level of the silty quartz-rich hemipelagic sublithofacies, tentatively suggest that these two lithofacies may have been deposited during the Phase II due to relatively high-carbonate production rate at shelf margin, at upper slope or deep ramp (Fig. 81). The crinoid meadows and calathid mounds at upper slope or deep ramp were probably the primary sources for these bioclastic turbidites.

Barnes (1984), on the basis of his biostratigraphic work, suggests a regression for the entire Orthidella zone in Canada. This study, however, has clearly demonstrated that the sedimentation and progradation rate of the Nuia shoal units never exceeded the rate of short durational, glacioeustacy-induced sea-level rises. Therefore, the suggested regression for the Orthidella zone by Barnes (1984) is not consistent with

the lithofacies associations of the Orthidella zone in our study area. As opposed to the suggestion of Barnes, Ross et al. (1989) suggest a probable transgression for the entire Orthidella zone. Similarly, Ross and others' suggestion also reflects an misrepresentation of the inter-relations between the sedimentation rate and pattern, and rate in sea-level rise.

In summary, one can suggest that Phase II or accretionary growth of the Nuia-shoal complex represents an evolutionary stage of carbonate platform: from the ramp-carbonate slope profile to an incipiently rimmed shelf margin (e.g. Read, 1982; and Mullins et al., 1989).

Phase III:

In the Antelope Valley region, this phase is characterized by back-stepping of the Nuia-bars which represent shoreward (eastward) migration of the high-energy ramp, Nuia bars, or incipient drowning of the Nuia shoal bars caused by short durational, rapid sea-level rises.

Relatively thin, dark gray, oncoid and peloid-rich Nuia bar lithofacies (1 to 5-feet thick) are overlain by thin, interbedded-siltstone and mudstone units, and thin, parallel-laminated, silty quartz-rich lime mudstone (Type III cycles of the Nuia shoals). These Nuia bars with overlying fine siliciclastic units repeat with the bioturbated-wackestone lithofacies in a cyclical manner and exhibit a stair-step morphology as back-stepping of bioherms and reefs (e.g., Logan, 1981).

The back-stepping of these Nuia bars is interpreted to have resulted from the short-durational, high-amplitude, sea-level rises with long-lag periods. Therefore, during Phase III, the combined effects of very low-subsidence rate and several superimposed, short-durational, high-amplitude sea-level rises outpaced the growth and sedimentation rate of the Nuia shoals of the AVL. It is possible to suggest that these superimposed-short durational, sea-level rises probably initiated a third-order sea-level

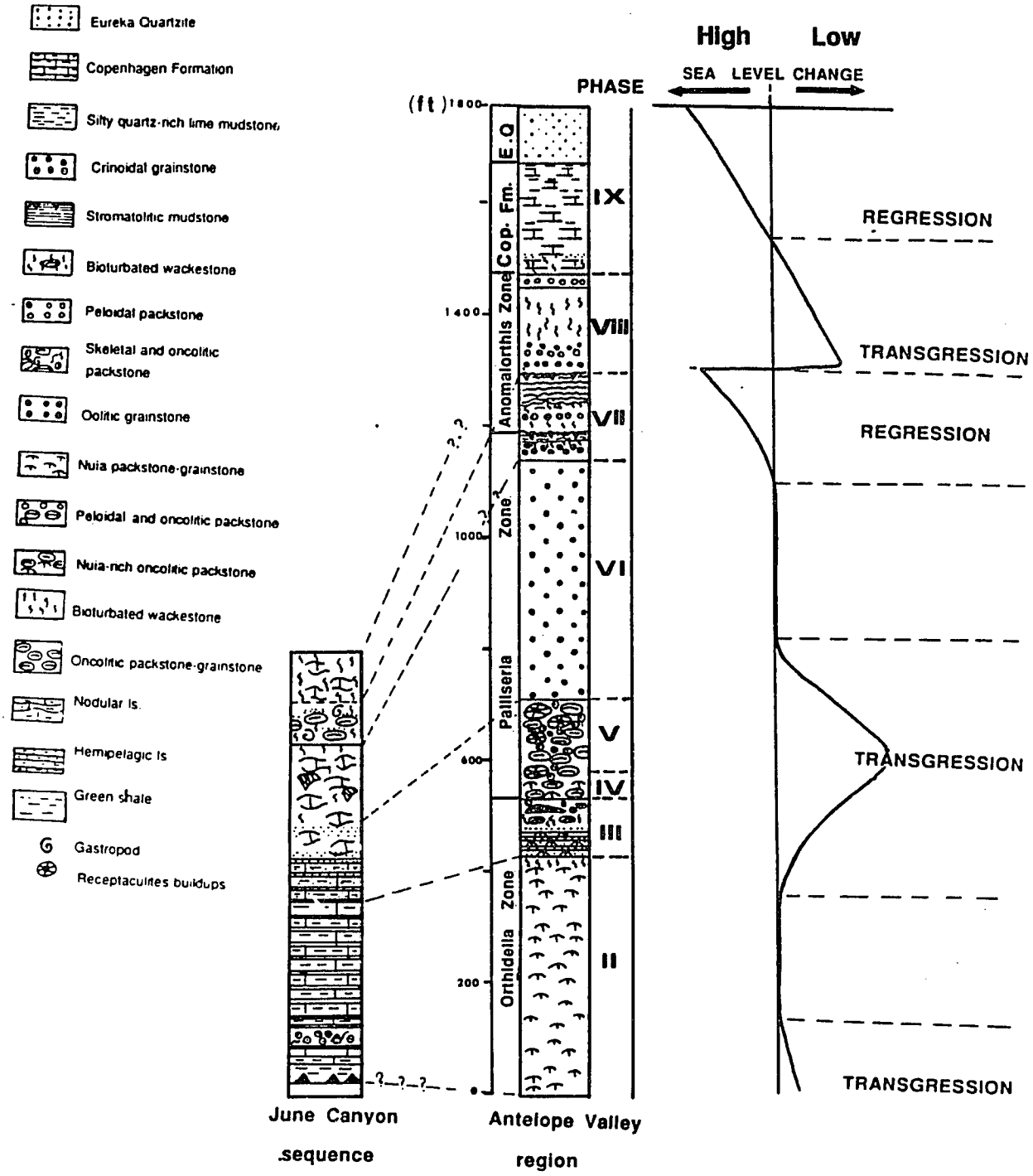


Figure 81- Relations between third-order changes in sea level and sedimentation patterns, and evolutionary phases during the formation of this formation and their correlatives.

rise which caused the formation of incipiently drowned Nuia shoal bars (Figs. 79, 80, 81).

Regressions have been suggested for the latest Orthidella zone of the AVL in the Antelope Valley region by Taban (1986) on the basis of the fine siliciclastics overlying the Nuia bars. He has also interpreted the fine-grained siliciclastic units as the algal-flat deposits. However, this study interprets that these fine siliciclastics were probably deposited from the suspension (i.e., re-activated- and remobilized-fine siliciclastics of nearshores or shores) of storm-counter currents during high-sea level stands.

In addition to the fine-siliciclastics of shelf and Nuia bars, the thick, fine-siliciclastic units in the open shelf, the Orthidella zone, facies in the Mill Canyon, June Canyon and Whiterock Canyon sections are also interpreted by this study to have resulted from short-durational sea-level rises generated by transgression or third-order sea-level rise (Fig. 81).

Phase IV:

This phase characterizes a very brief "Catch Up" phase (e.g. Kendall and Schlager 1981) of the Nuia shoal after the incipient drowning of the incipient accretionary Nuia-shelf rim. As previously indicated, Nuia-shoals were incipiently drowned and moved farther shoreward from their former positions on the shelf margin at Antelope Valley region.

At the base of oncoidal shoal (beginning of the Palliseria zone), the Nuia shoal units in the Ninemile Canyon section are correlative with the Nuia-rich oncoidal shoal units of the Martin Ridge section. This lithofacies association appears to represent the "Catch Up" phase (Kendall and Schlager, 1981) of the Nuia shoal. However, in the Lone Mountain and Keystone Canyon sections, this "Catch Up" phase has not been noted, and the only incipiently drowned oncoidal shoal units represent the whole

Palliseria zone.

In Antelope Valley region, on the other hand, the re-establishment of the Nuia shoals or "Catch Up" phase is believed to have resulted from high-amplitude, rapid sea-level rises with short-lag periods and relatively high sedimentation rate in these areas. This "Catch Up" phase is interpreted to have lasted very briefly because the following relatively high-amplitude sea-level rises with the long lag periods exceeded the sedimentation rate. Consequently, the Nuia shoals of the AVL at least in this region were once more incipiently redrowned (Figs. 80, 81). As a result, during this phase, a distally steepened ramp facies formed during the Phase III did not undergo significant modification in this region due to short duration of this "Catch Up" phase.

Phase V:

During Phase V, two types of shelf margin developed: (1) Oncoidal shoal in the Lone Mountain, Keystone Canyon, Martin Ridge, Whiterock Canyon sections and Arrow Canyon (Fig.79); and (2) oncoid-rich skeletal shoal in the Ninemile Canyon section (Figs. 80, 81).

Except at Ninemile Canyon section, the oncoidal shoal units represent the incipiently drowned oncoidal shoal stage which probably formed in the indicated sections above after the Phase III. According to Kendall and Schlager (1981), the incipiently drowned shoal stage was caused by rapid deepening of high-energy shoals within the euphotic zone that significantly decreased the carbonate production rate. Some incipiently drowned shoal examples from geological formations are (1) the Fonda and Wolf Hollow (Upper) Member of Tribes Hill Formation, Ordovician, (Braun and Friedman, 1969), (2) the Middle member of Chepultic Formation, Early Ordovician, (Bova and Read 1987), and (3) the Noncyclic units of the Rocknest Formation (Proterozoic) by Grotzinger (1986). These examples are comparable to the oncoidal shoal units of Palliseria zone of the Antelope Valley Formation (AVL), which

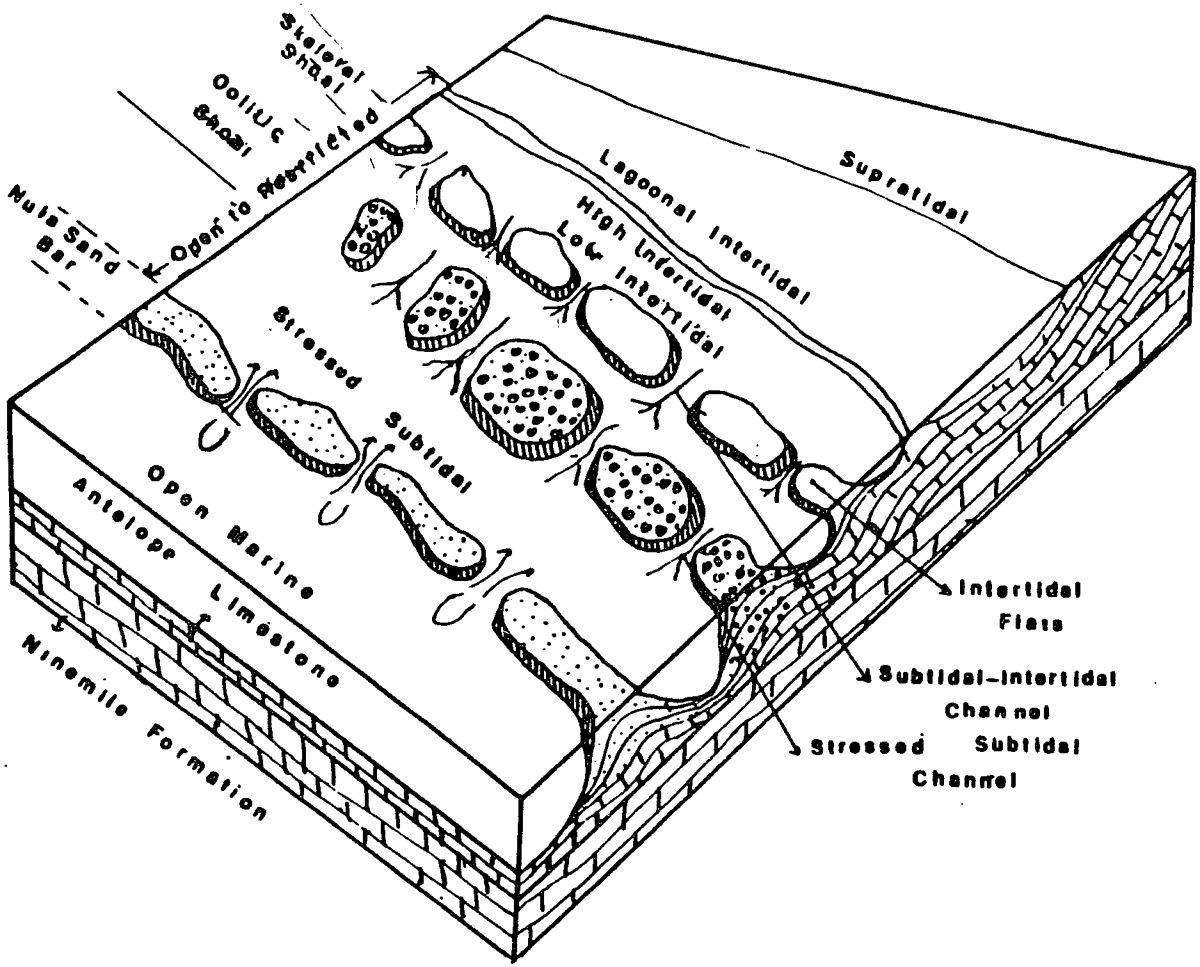


Figure 82- Depositional model of the Antelope Valley Limestone proposed by Taban (1986).

represent the sedimentation that occurred below the normal wave-base level or in the storm-dominated shoal (Figs. 79, 80, 81).

In the Martin Ridge section, Receptaculites and crinoids-built bioherm in the oncoidal shoal facies, indicating a moderately high-energy environment, are correlative with the oncoid-rich skeletal shoal facies of normal wave base in the Ninemile Canyon section. In these two sections, this trend clearly shows that oncoidal shoal units represent an open-seaward extension of skeletal shoal and westward gradually deepening shelf margin (see Chap. 10). The silty quartz-rich, parallel-laminated lime mudstone units, which predominate the shelf and open shelf or the upper slope facies of this formation are also representative of this phase. The cyclical fine siliciclastic sediments in shelf and deep-ramp or slope are interpreted to have formed from storm countercurrents during third-order sea-level rise which resulted from short durational, high-amplitude rises in sea level with long-lag periods (Fig. 81). During this phase, due to further submergence of the oncoidal shoal bars into the deeper part of the euphotic zone, the sedimentation rate at the Girvanella-constituted oncoidal shoal was probably extremely low, the progradation of the tidal flat was completely inhibited, and the incipiently drowned oncoidal shoal allowed the fine siliciclastics to be transported to the upper slope or deep ramp. Due to absence of the gully-cut slope patterns, shelf rim, and major subaerial exposure, these cyclical silty quartz-rich hemipelagics can not be explained by regression or third-order sea-level fall. These cyclical fine-siliciclastic intervals within the hemipelagics of deep-ramp facies may be analogous to the silty quartz-rich pelagic units of the interglacial periods reported on the modern ramp-slope profile of Gulf of Mexico, south west Florida (Gardulski et al., 1989; and Mullins et al., 1989). Despite lack of pelagics during the Lower Paleozoic formation, strong resemblance between the siliciclastic units of the AVL and the modern deep-ramp sediments indicate incipiently drowned oncoidal shoal and third-order sea-level rise.

Increasing sedimentation rate along with establishment of Receptaculites bioherms in the oncoidal shoals resulted in the formation of westward prograding oncolitic shoals which caused the oncoidal shoal units to overlie the nodular-bedded,

upper-slope deposits like at the Whiterock Canyon section. Therefore, initially distally steepened ramp depositional profile gradually evolved into the homoclinal ramp by continuous progradation and accretion (Fig. 79).

At the end of this phase, progressively increasing sedimentation rate began to keep up with the short-durational sea-level rises and resulted in progradation and vertical accretion of oncoidal bars which, in turn, produced optimum conditions for the oolitic shoal formation in the Martin Ridge and Ninemile canyons (Fig 80).

Striker and Carozzi (1977) suggest that in the AVL transition from Nuia subtidal bars to algal ball (oncoidal) subtidal bars resulted from subsidence of the nearly flat slope. However, sedimentation rate of Girvanella-oncoids is widely known to be very low (Riding, 1977; and Peryt, 1981). Hence, the subsidence of Nuia shoal units to the incipient drowning stage and cyclical repetition of the oncoidal shoal can not be explained by simple subsidence because sedimentation rate of Girvanella oncoids are too small to initiate that subsidence. Like in Phase III, we relate the initiation of this phase to a third-order sea-level rise which was caused by several superimposed-, short durational, high-amplitude rise in sea level with the long lag periods. Taban (1986) proposes three synchronous shoals (Fig. 82) -- the Nuia, oolitic, and skeletal shoals, without considering the evolutionary stages of carbonate platform of the AVL, and he did not recognize the oncoidal shoal. Taban (1986) further suggests that progradations of these shoal units produced the AVL and its stratigraphic zones. All the evidence of this study disagrees with the suggestion of Taban's three synchronous shoals, which do not correspond to the evolutionary trend of the AVL as we see it.

Ross et al. (1989) propose a regional evolutionary model for the AVL and the Middle Ordovician carbonate platform which includes four stages (Figs. 83, 84). Their Phase I includes formation of the calathid mounds formed by sea-level rise, but their Phase I does not comprise the evolutionary stages of the Phase II, III and IV of this study, more specifically formation of the Nuia-shoal complexes and their influences on the evolution of the carbonate platform. Their phase II starts with progradation and accretion of the Girvanella-oncoidal shoal, and at the same time sedimentation rate keeps up and exceeds the sea-level rise. The interpretations by Ross et al. (1989)

contradict with the incipiently drowned oncoidal shoal which very briefly reached the tide-dominated oolitic shoal conditions (see Chapter 5).

Phase VI:

This phase represents the establishment of skeletal shoal and oolitic shoal in the Antelope Valley region after termination of the incipient drowning of the oncoidal shoal on the carbonate platform. Sedimentation rate of this shoal appears to have kept pace with the relative sea-level rise during this phase. Thus, for the first time, the "Keep Up" phase in the evolution of the carbonate platform is believed to have been re-established during this phase after Phase II. The phase change from Phase V to Phase VI does not necessarily represent a third-order sea-level fall (Fig. 81), but it probably corresponds to high-sea level stand during which sedimentation rate of this shoal may have kept pace with rising sea-level.

In cyclical successions, the shoal units repeat in a predictable fashion as these oolitic and skeletal shoal cycles overlie one another in place with sharp, erosional basal contacts like in phase II. The skeletal shoal units are generally found in the Ninemile Canyon section and grade westward into the oolitic shoal units of the Martin Ridge section. The presence of oncoids in the westerly section suggest that the oolitic and skeletal shoals gradationally changed farther westward into the oncoidal shoals in the open shelf margin of the AVL.

Therefore, during this phase, "Keep Up phase or "Stationary shelf margin" probably evolved from the homoclinal ramp to incipient-shelf rim (Fig. 80). However, toward the end of the Phase VI, the vertical accretion of carbonate shoal complex and their westward progradation may have caused the sedimentation rate of the oolitic shoal to progressively increase and to exceed sea-level rise.

Phase VII:

This phase represents the stage during which sedimentation rate exceeded the rate of sea-level rise and combined effects of subsidence. During this phase, progradation and aggradation of the oolitic and skeletal shoals resulted in the formation of a syndepositional physical barrier on the shelf margin (parallel to shelf slope break with distinct topographic high) which separated the platform interior from the open shelf. As a result, the protected shelf and low-energy intertidal algal-flat deposits progradated farther westward, and the carbonate-producing area and sedimentation rate increased significantly. The very high rate of progradation may have caused the thick algal-flat deposits to cap the upper part of the oolitic shoal cycles (Fig. 80). During this phase, the oncolitic packstone to wackestone units, as representing the farther open-seaward extension of the oolitic bars, also progradated farther westward over the Anomalorthis zone of the June Canyon section. Therefore, the Phase VII clearly indicates the regressive stage or "Off Lap" type platform margin (Fig. 81), as suggested by James and Mountjoy (1983).

Particularly, in the Antelope Valley region, an incipient-shelf rim evolved into the rimmed-shelf stage (e.g., Wilson, 1975) during Phase VII.

However, the siliciclastic shoreline facies which prograded farther westward over the nodular-bedded lithofacies of the deep shelf occurred behind the incipiently drowned oncoidal shoal at the Lone Mountain section, and over the lowermost part of the Copenhagen Formation at the Keystone canyon section. In this case, relative lowering in the third-order sea level may have not induced grave change; on the other hand, high-sedimentation rate in siliciclastic-dominated shoreline sedimentation exceeded the rate of sea-level rise with a considerable rate, or high-sedimentation rate of siliciclastic shoreline deposits coupled with sea-level fall. As a result, an about 70-feet thick lower quartzite member of the Eureka Quartzite (Fig. 85) progradated westward as much as 250 km. Farther westward progradation of this quartzite member at Lone Mountain (the northerly region) compared to Keystone Canyon of the Hot

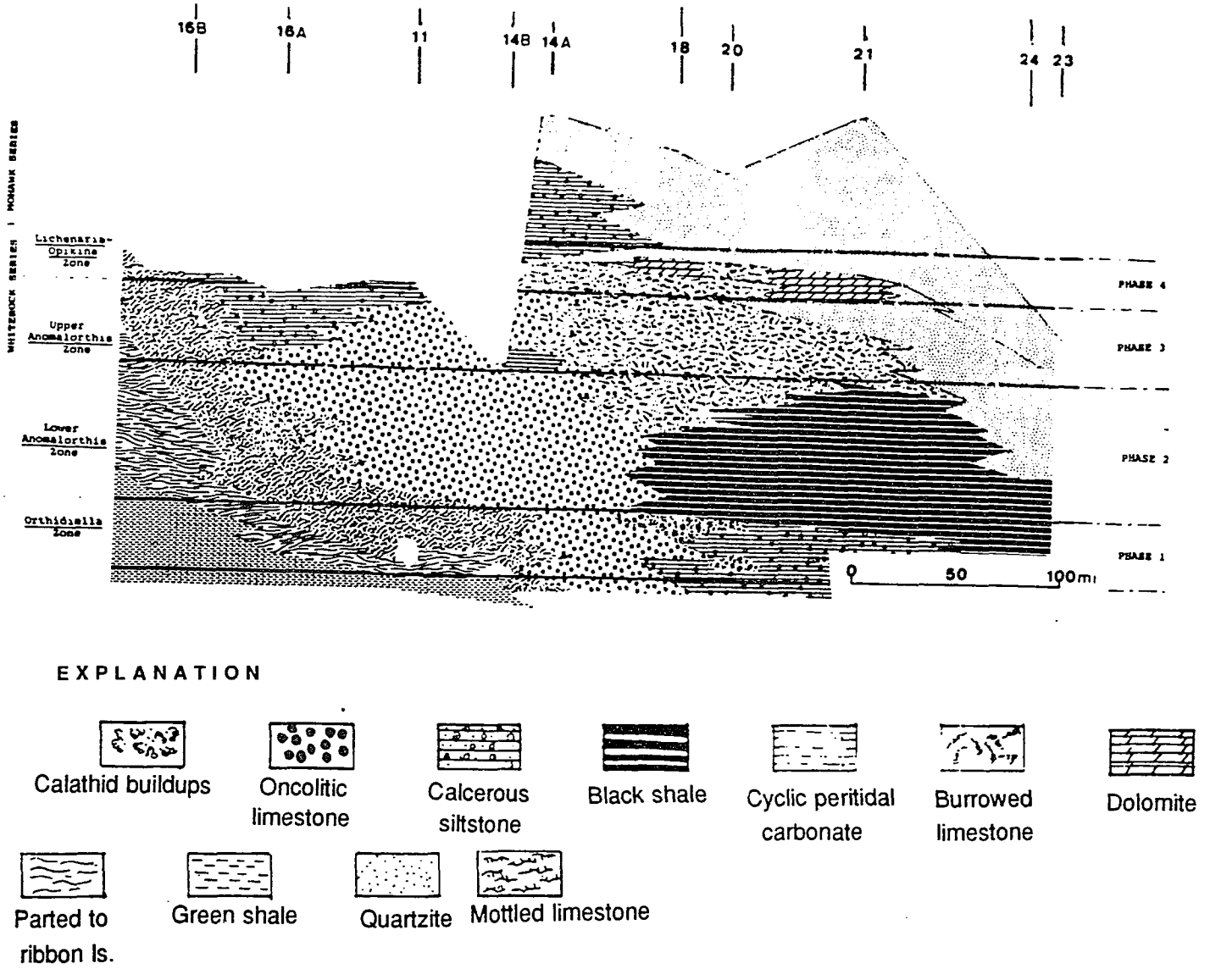


Figure 83- Regional Cross section of Whiterockian strata in western Utah and Nevada. Localities: 16A- Mill Canyon sequence (Iks Canyon), 16B- June Canyon sequence (Iks Canyon), 11- Callaghan Ranch, 14B-Whiterock Canyon, 14A-Martin Ridge, 18-Pogonip Ridge, 20- W. Steptoe Ranch, 21- Ibex Area, 24- Fillmore Richfield Area, and 23- M. Pavant Range (Ross et al., 1989).

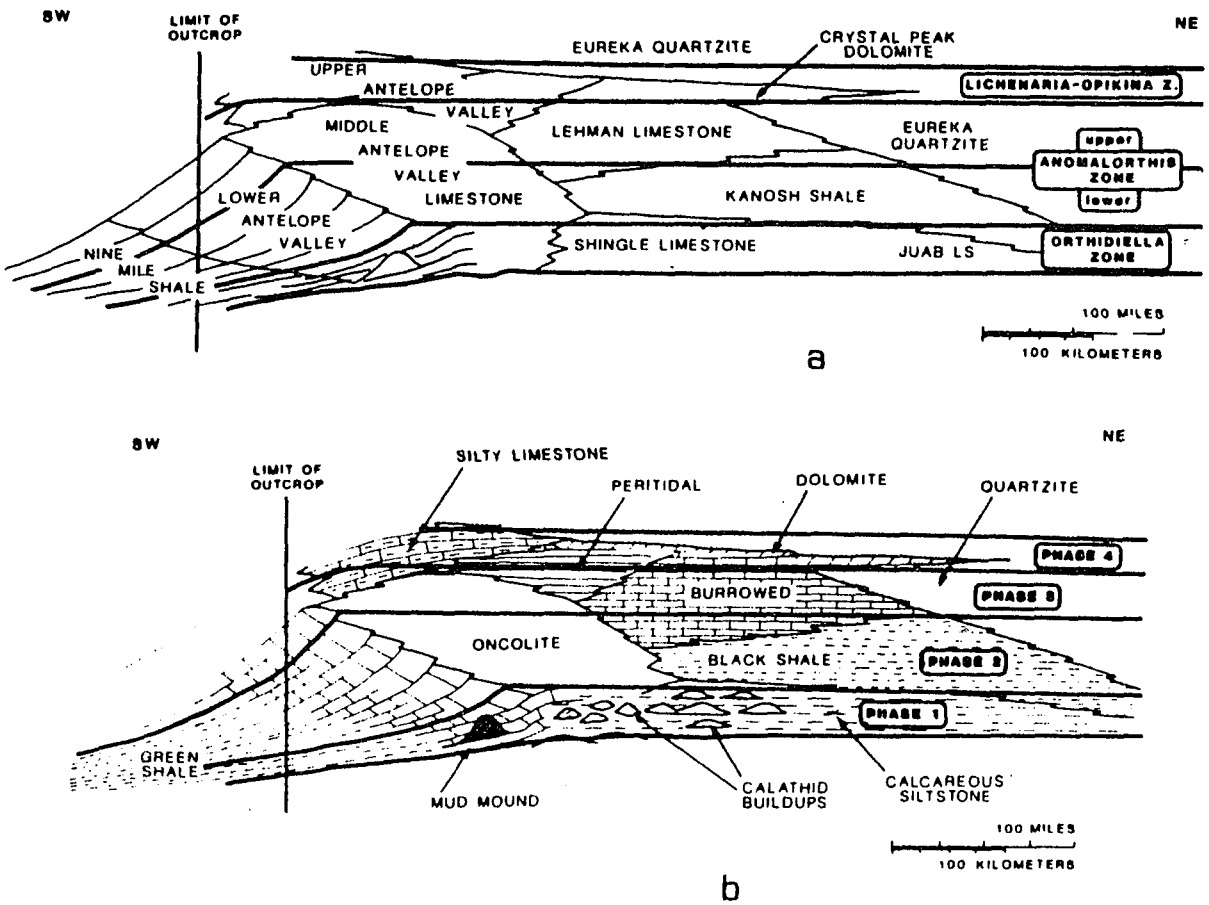


Figure 84- Model for evolution of the Middle Ordovician carbonate platform suggested by Ross et al. (1989).

Creek Canyon region (the southern region) was probably related to the width and depth of shelf, progradation rate of skeletal and oolitic shoal, and to the provenance of siliciclastic sediments.

Phase VIII:

In Antelope Valley region, this phase is represented by peloidal and skeletal and oolitic shoal units which unconformably overlie the stromatolitic lime mudstone lithofacies of intertidal-algal flat facies. These relations also characterize a farther eastward or landward moved, or a stepped-back, high-energy oolitic shoal. It can be considered that during this phase, the "Onlap" phase (Kendall and Schlager, 1981) of shelf margin was probably established, progradation of the algal flat was inhibited, and algal-flat dominated-shoreline transformed into the siliciclastic-dominated shoreline. In addition, the high-energy nearshore bars formed and separated the coastal lagoon (the Copenhagen Formation) from the well-circulated middle shelf of the AVL (Figs. 80, 81). Therefore, this phase represents a third-order sea-level rise which was primarily caused by superimposed-several, short durational, high-frequency, high amplitude sea-level rises.

In the Lone Mountain and Keystone Canyon, respectively, about 15 feet-thick of thin to medium rhythmically bedded wackestone and shaley interlayers and about 25- to 30-feet thick, dolomitized- stromatoporoitic bioherms (Fig. 85) within the oncoidal shoal represent the same third-order sea-level rise or transgression (Fig. 79). Particularly, in Keystone Canyon, the occurrences of the high-energy shelf edge facies suggest that this section was probably situated at the farther landward locality than the Lone Mountain section.

At the end of the Phase VIII, the shelf margin and slope profile of carbonate platform did not change in the Keystone and Lone Mountain regions. However, in the Antelope Valley region, the rimmed-shelf margin transformed into the incipient-shelf

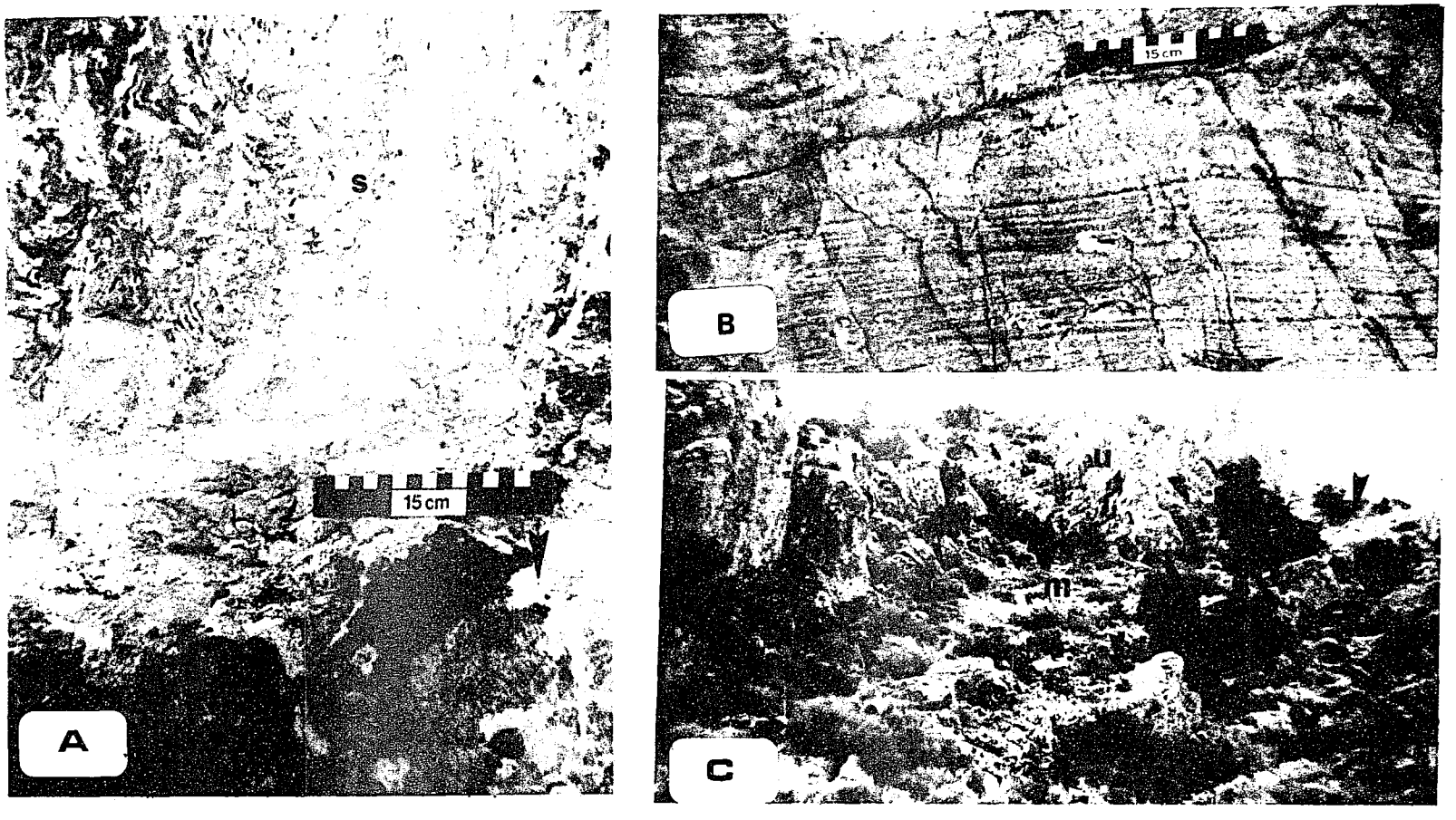


Figure 85- Areal view of the Eureka Quartzite. A) An outcrop photograph of the transgressive Middle carbonate member of the Eureka Quartzite shows that pervasively dolomitized early corals (arrowhead pointing to) and encrusting stromatoporoids (s). B) A close-up outcrop photograph of the Upper quartzite member of the Eureka Quartzite shows that low-angle cross beddings are the most common sedimentary structures in this member. C) Photograph of the Eureka Quartzite shows that the Middle carbonate member of the Eureka Quartzite separates the steep, cliff-forming upper and lower quartzite members of the Eureka Quartzite; arrowheads point to upper and lower boundaries of the Middle member of the Eureka Quartzite.

rim (Fig. 80). After the middle of this phase, the sedimentation rate began to exceed the sea-level rise; as a result, the nearshore bars and coastal lagoons as well as siliciclastic shoreline sedimentation probably migrated westward as far as to the Antelope Valley region.

Phase IX:

This phase is represented by considerably high sedimentation rate which exceeded the third- order sea-level rise and combined subsidence rate and resulted in considerably high progradation rate. As a result, whole regions were capped by the progradating siliciclastic-shoreline sedimentation, or the Upper Quartzite Member of the Eureka Quartzite (Fig. 85). Thinner quartzite beds (probably upper member of the Eureka Quartzite) in the Martin Ridge section compared to the indicate two other regions represent much different paleogeographic settings. All the evidence above suggest that this phase generally represents a third-order sea-level fall, or regression (Figs. 79, 80, and 81) for the whole region.

DEPOSITIONAL ENVIRONMENTS, DIAGENESIS, AND BURIAL HISTORY OF THE ANTELOPE VALLEY LIMESTONE (LOWER-MIDDLE ORDOVICIAN) IN THE GREAT BASIN, CENTRAL NEVADA

by

ALI KAYA

(VOLUME II)

A dissertation submitted to the Graduate Faculty in Earth and Environmental Sciences in partial fulfillment of the requirements for the degree of Doctor of Philosophy, the City University of New York.

1993

PART III: DIAGENESIS AND DIAGENETIC HISTORY OF THE ANTELOPE VALLEY LIMESTONE

- CALCITE CEMENTS
- DOLOMITE TYPES AND CHEMISTRY, AND MODEL FOR PERVASIVE DOLOMITIZATION
- DEDOLOMITIZATION
- QUARTZ AND CHERT CEMENTS
- TIMING AND SUMMARY OF DIAGENESIS

CHAPTER 12: CALCITE CEMENT

On the basis of texture, isotope composition, and timing, calcite cements were studied under three categories: marine, meteoric, and deep-burial. Radiaxial-fibrous, isopachous calcite, cryptocrystalline calcite, and columnar calcite cements are grouped under the marine cement. These marine calcite cements are found in the shoal and upper slope lithofacies. Pendant vadose, equigranular cement, drusy, syntaxial cements are representative of the meteoric cement. Pendant cement occur in the stromatolitic limestone units of the AVL as fenestra-filling calcite cement. Equigranular calcite mosaic is volumetrically the most important cement type in the shoal and shelf units. Syntaxial calcite cements are common in the crinoidal grainstone units of the shelf, shoal and upper slope units. Ooid-filling calcite, void- and fracture-filling calcite, intercrystalline calcite and neomorphic cements are grouped under the deep-burial cement. Void- and fracture-filling calcite cements are the most common deep-burial calcite cement type.

A. MARINE CEMENT

Radiaxial-Fibrous Cement

Description:

The radiaxial-fibrous cements can easily be recognized by their radially oriented, elongated-crystal forms which commonly have two-directional curved twin lamellas and display distally convergent crystal forms (Fig. 86 A, B; Bathurst, 1975; Kendall ,1985). The radiaxial-fibrous cements have rhombohedral crystal terminations and

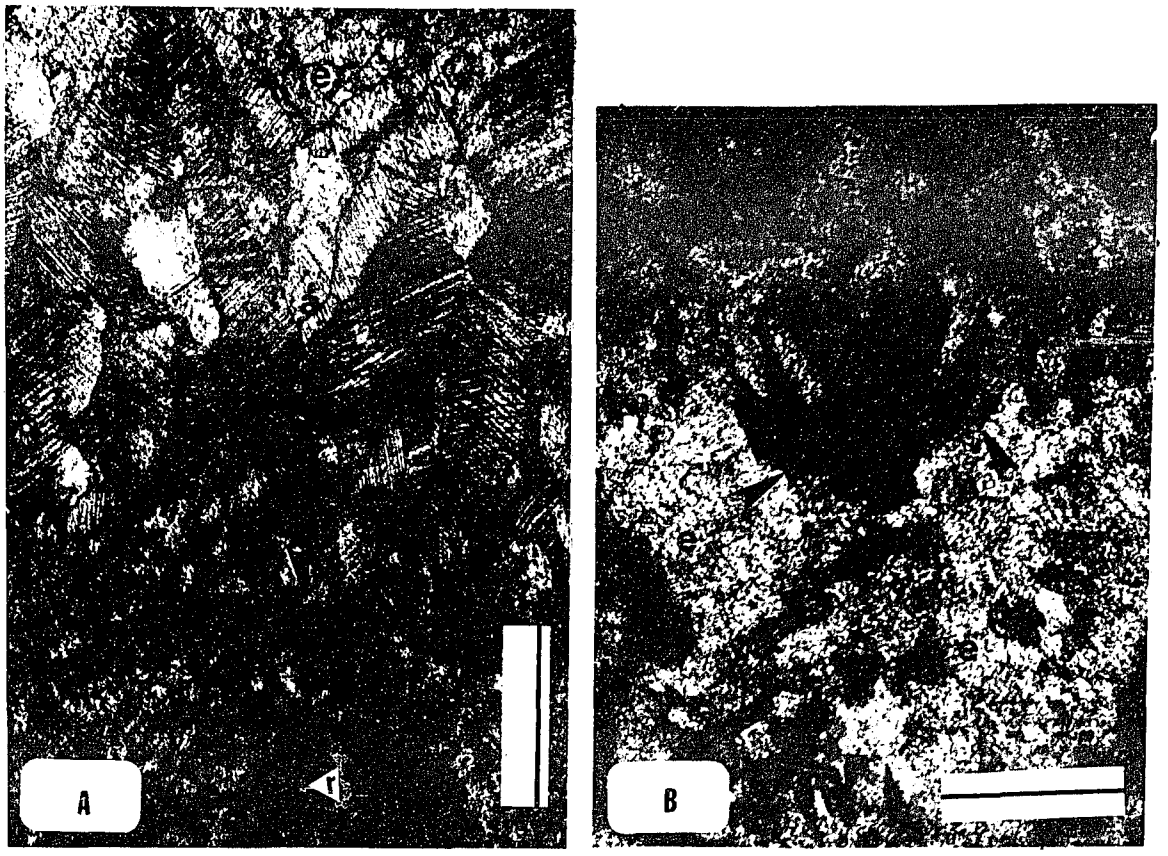


Figure 86- Photomicrographs of radiaxial-fibrous calcite cement. A) Bi-directionally twined and distally convergent radiaxial-fibrous calcite cements (a) filled primary voids in the radial ooid-dominated packstone and grainstone unit; arrowheads indicating a sharp, curvature-void wall between the radiaxial calcite-filled void and a cryptocrystalline calcite-cemented area (b); (r) indicates iron oxide-stained radial ooids within cryptocrystalline calcite zone. B) Radiaxial-fibrous cement within a gastropod. At the center of the void of a gastropod, radiaxial-fibrous calcite cements were replaced by neomorphic equant blocky calcite cement (e); arrowhead indicates a diagenetic replacive contact between these two cement types. With cross-polarized light; scales= 0.5 mm.

show undulose extinction. Extinction differs in distally convergent crystals from 10° to 15° (see Bathurst, 1975).

Radiaxial-fibrous cement is common in the oolitic shoal units of the AVL (Fig. 86 A). The elongated crystals are generally normal to void walls. Equant blocky calcite cements partially replaced the radiaxial-fibrous cement in the central part of voids (Fig. 86 B). The radiaxial-fibrous cements are common in primary pores in the radial ooid-bearing oolitic packstone- and grainstone subunits but not in the light brown ooid (calcite-filled ooids)-bearing subunits. The cryptocrystalline cement (see this chapter) occurs as thin rims along the inner walls of the voids in the oolitic packstone- and grainstone lithofacies and are followed pore centerward by radiaxial-fibrous cements which fill the most voids (Fig. 86 A). The radiaxial-fibrous cements are scarce in the Nuia packstone-and grainstone units of the Nuia shoals (Fig. 87 A, B). The occurrences of this cement in the Nuia units are only recognizable under cathode light. Moreover, the radiaxial-fibrous cements are also present in the empty gastropods' shells of the backshoal environment (Fig. 86 B). Relic cement forms, such as fibrous aragonite or aragonite needles, were not recognized in this cement type.

Radiaxial-fibrous cements commonly reveal a luminescence ranging from non-luminescence to dull and sometimes to yellow red.

Radiaxial-fibrous cement has the oxygen-isotope values ($\delta^{18}O$) of - 6.66 ‰ PDB; and carbon-isotope composition ($\delta^{13}C$) of -1.12 ‰ PDB based on one sample.

Interpretation:

Common occurrences of the radiaxial-fibrous cement in the radial ooid-bearing packstone- and grainstone and Nuia grainstone units indicate a relatively low-energy shoal, or marine-phreatic environment. In addition, the presence of this cement within empty gastropods in backshoals suggests that the radiaxial-fibrous cement probably characterizes a broad physical and chemical environmental spectrum which may extend to either side of high-energy shoal, leeward and windward. In the

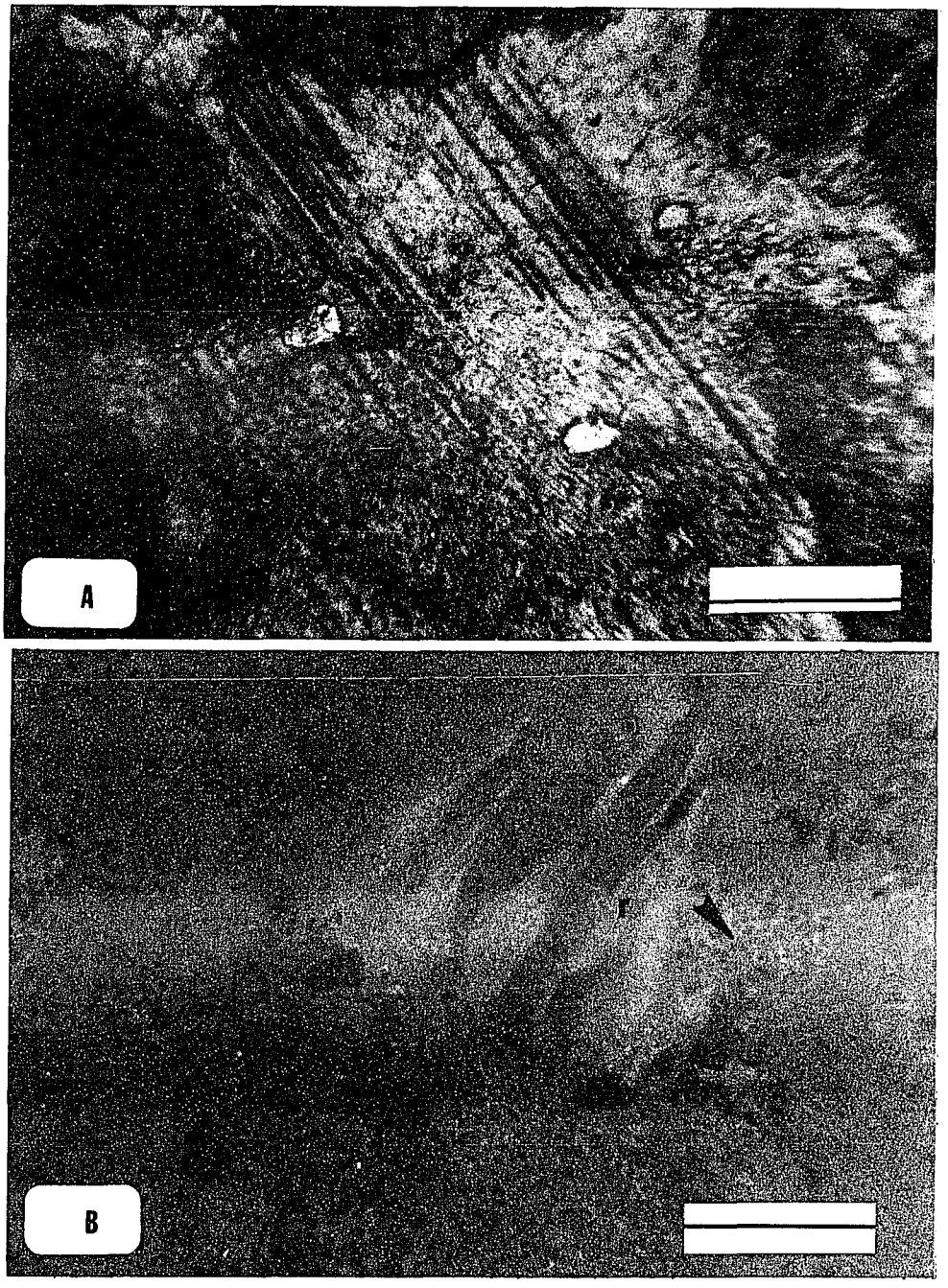


Figure 87- Photomicrographs of neomorphically altered radiaxial cement. A) Twinned- sparry interparticle calcite cement of the Nuia grainstone unit. Arrowhead points to granular neomorphic alteration of Nuia grains which appears to postdate the mechanically twinned-coarse calcite crystal; under plane-polarized light. B) Under cathode light, the twinned-, coarse crystal of interparticle calcite cement appears to be void-filling, radiaxial-fibrous cement (r). Scales= 0.25 mm.

indicated-depositional and diagenetic environment, void-filling, radiaxial-fibrous cement probably represents sheltered-microdiagenetic environments, such as primary voids and cavities.

The most common occurrences of the radiaxial-fibrous cement have been reported in the reef and bioherm voids, specifically in the fore-reef and reef-flat in marine-phreatic environments (Ross, et al., 1975; Asserto and Folk, 1980; Kendall, 1985; Henrich and Zankl, 1986; Kerans et al., 1986; and Reitner, 1986).

In the Devonian reefs of Australia, Kerans et al. (1986) observed that radiaxial-fibrous cements rapidly disappeared from reef-flats to back-reef subenvironments. Thus, the suggestion of this observation above is consistent with interpretation of this study that this radiaxial void-filling cement mostly occurs on the open seaward-extended shoal units or bars (see Chap. 6). The absence of these radiaxial cements in the high-energy shoal lithofacies (in the light brown ooid-bearing subunits representing oolitic bar crests) can be attributed to the energy level of environment. Because, in the high-energy shoal, wave and current reworking hinders the formation of primary voids which probably results from rapid sedimentation in the open-seaward extended flank of oolitic bars.

Close association between the radiaxial-fibrous cement and the cryptocrystalline rim-calcite cement in the primary voids (Fig. 86 A), particularly in the hardgrounds in the radial ooid-bearing subunits of fore-shoal facies, indicates probable marine-phreatic diagenetic origin for these two cements (see Chap. 6).

The formation of radiaxial-fibrous cement can be attributed to Mg-side poisoning effect of Mg-rich sea water (Ca / Mg = 1/5 ; see Folk, 1974; Bathurst, 1975; Macintire, 1977). The radiaxial-fibrous cements in the shoal lithofacies of the AVL probably resulted from sea water saturated with respect to $CaCO_3$ which replenished pores by active tide and wind pumping. Crystal morphology of radiaxial-fibrous cements, their rhombohedral crystal endings, absence of relic aragonite lathes as inclusions in them (see Mazzullo, 1980; Kendall, 1985; Sandberg, 1985) and presence of solid inclusions (probably microdolomite inclusions see Lohmann and Meyers, 1977) suggest that the radiaxial cements were originally of high-Mg calcite original

composition and are marine phreatic in origin. The high-Mg calcite original composition of this radiaxial cement can also be inferred from the preservation of the original radiaxial-fibrous texture. Because high-Mg calcite changes into low-Mg calcite without any textural changes during meteoric diagenesis a process is known as "paramorphic change" (Friedman, 1964); Gavish and Friedman, 1969). Therefore, the crystal forms and rhombohedral crystal endings of the radiaxial-fibrous calcites clearly indicate original high-Mg calcite precursor.

$\delta^{18}O$ value (-6.66 ‰ PDB) of this cement is generally more depleted compared to modern marine calcite cements and sediments; however, it is compatible with the estimated-$\delta^{18}O$ values of the Middle Ordovician marine calcite ranging from -6 to -7 ‰ PDB (Ross et al., 1977; Popp et al., 1986; and Lohmann and Walker, 1989). $\delta^{13}C$ value (-1.12 ‰ PDB) of the radiaxial-fibruous cement represents a slightly more depleted carbon-isotope composition than the estimated-$\delta^{13}C$ composition range (0 to 1 ‰ PDB) of the Middle Ordovician marine calcite. Such depleted-carbon isotope composition probably was caused by oxidation of plant materials by organisms and represents the diagenetic stabilization by a meteoric diagenetic water which probably had an oxygen-isotope value lying in the similar compositional range with the Middle Ordovician sea water at 25 °C (for further details see Columnar cement).

The radiaxial calcite cement fills the primary voids whose void walls were filled by cryptocrystalline calcite cement or by micrite in the lower oolitic shoal units, where the isopachous bladed-cement is the most common cement. On the basis timing relations, the radiaxial cement appears to have formed after the isopachous-bladed and cryptocrystalline cements.

Isopachous-Bladed Cement

Description:

Bladed cements commonly show a width/length ratio of 1:3; width of the blades ranges from 20 to 40 μm. In general, calcite blades are perpendicular to the substrate and occur as interparticle cement (Figs. 88, 89). They commonly show uniform extinction, and they are inclusion-free. In the AVL, bladed-calcite cements are most commonly found in the Nuia packstone- and grainstone units and in the oolitic packstone-and grainstone units (Fig. 88). In the Nuia grainstone units, intergranular pore spaces are isopachously filled by this cement type, which exhibits the polygonal rim cement boundaries (e.g., Longman 1980).

The isopachous cement in oolitic packstone- and grainstone units is still recognizable even though original texture of this cement appears to have been obliterated by intensive fresh-water alteration or neomorphism. In these shoal units, the best presentation of this cement type can be seen in the radial ooid-constituted intraclasts (Fig. 89 B).

Interpretation:

The morphology of bladed cements and their orientations on the substrate of particles, and the occurrence in peloidal intraclasts (Fig. 89 A) suggest that this cement type has a probable synsedimentary origin. In the Nuia grainstone units, the isopachous-bladed cement shows polygonal boundaries which are observable (Figs. 88, 89) and probably represent marine-phreatic diagenesis in the high-energy Nuia shoal (Longman, 1980). Under cathodoluminescence, the bladed-isopachous cements appear to have been changed into interparticle equant cements (in situ replacement by

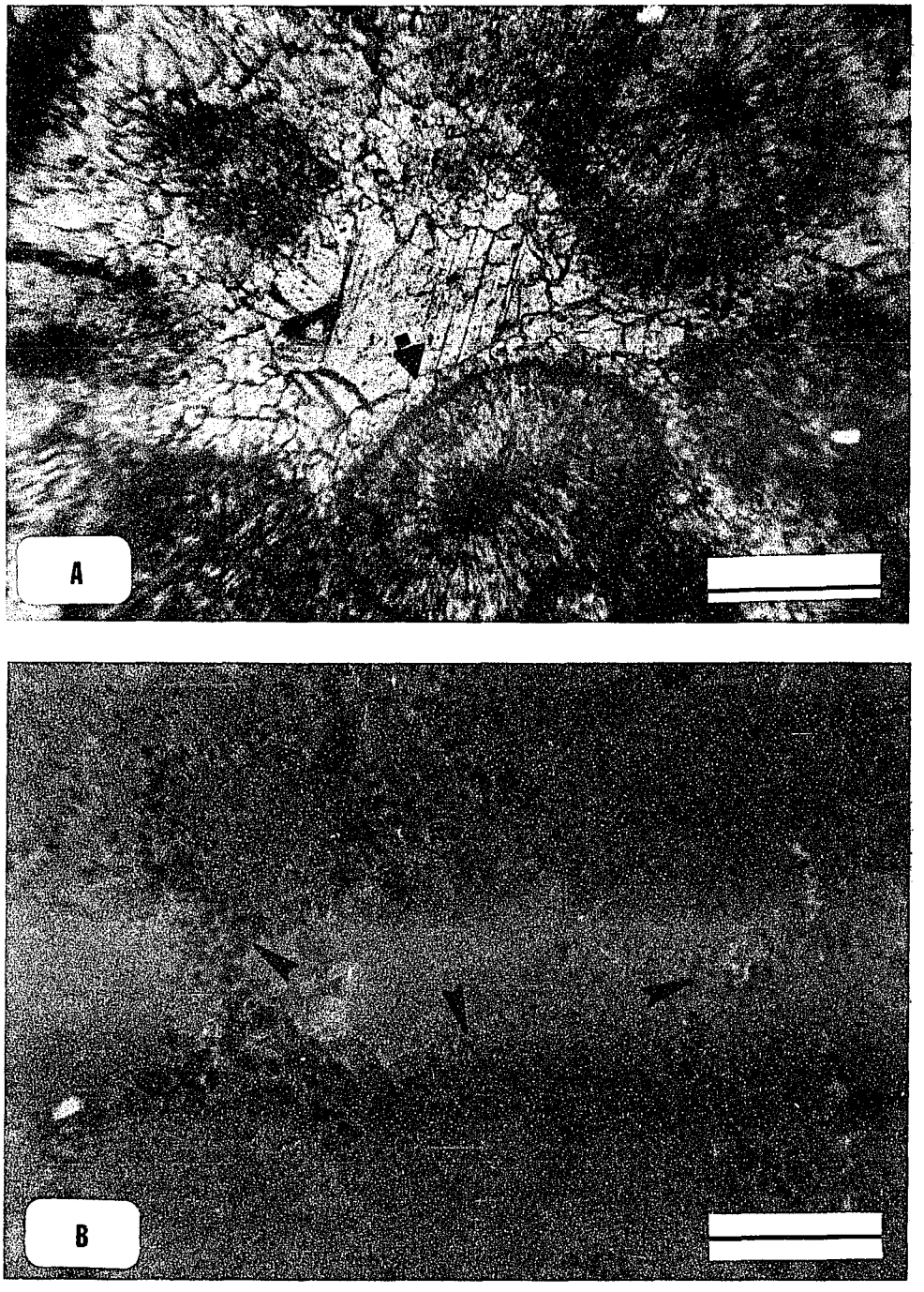


Figure 88- Photomicrographs of the interparticle, isopachous-rim cement of Nuia packstone- and grainstone unit. A) Interparticle-rim cement (arrow) and equant mosaic cement; under plane-polarized light. B) Same view under cathode light, the interparticle rim cements appear to be isopachous-bladed cement enveloping Nuia grains. Arrowheads point to nonluminescent rim cement whose crystals have rhombohedral terminations and uniform crystal size. Scales= 0.25 mm.

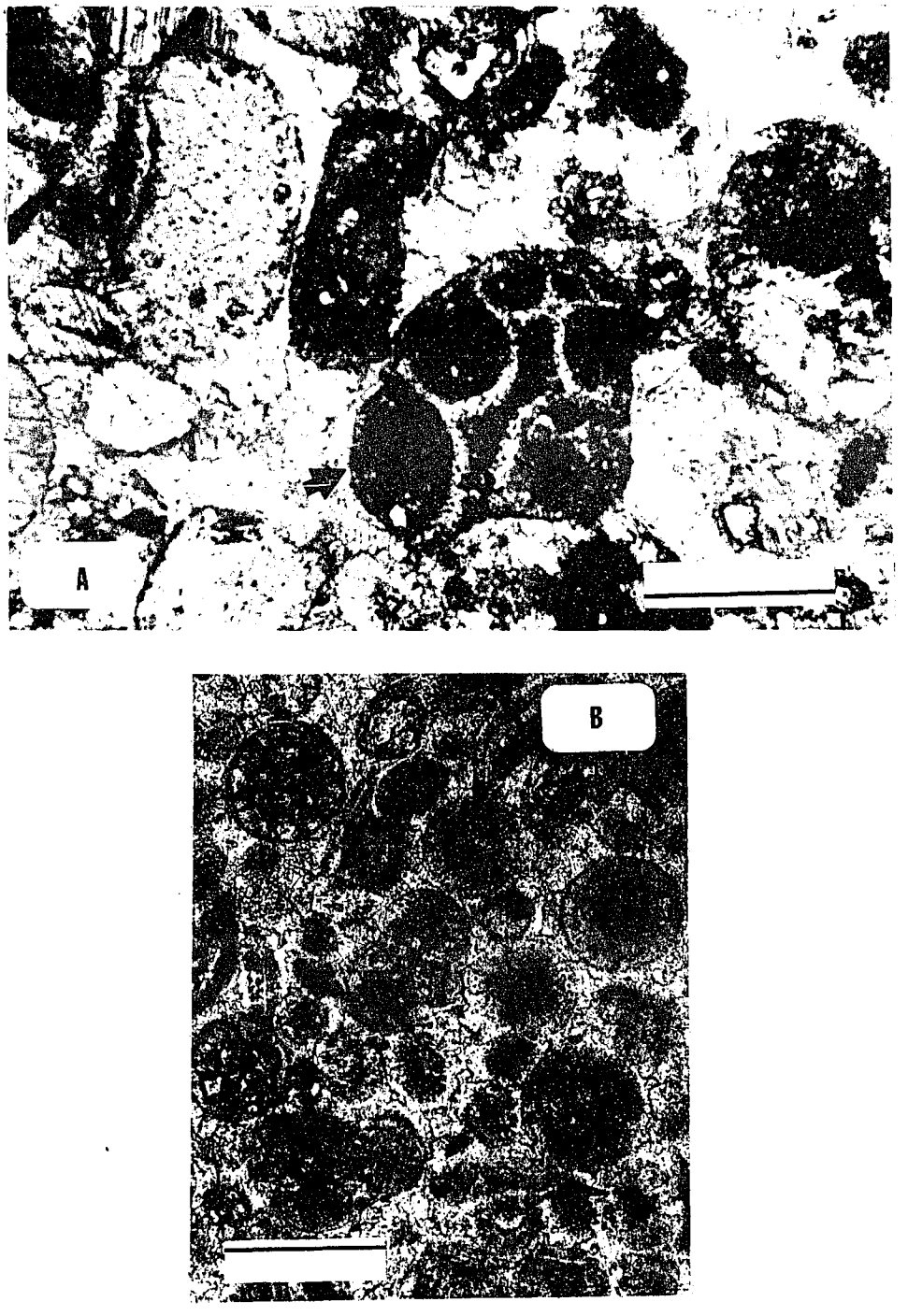


Figure 89- Photomicrographs of isopachous-bladed calcite cement. A) In skeletal and peloidal packstone unit, arrow points to an intraclast which is composed of peloids which are cemented by isopachous-rim cement. B) In oolitic grainstone unit, arrow indicates isopachous-bladed cement enveloping radial ooids. Arrowhead points to partially dolomitized radial ooids. Under plane-polarized light; scales= 0.5 mm.

simultaneous dissolution-precipitation); the original form of these cements can still be inferred from their morphology in spite of indicated diagenetic alteration mentioned above (Fig. 88 B). The preservation of bladed texture of this cement during transformation of high-Mg calcite to low-Mg calcite probably indicates that this calcite cement type originally was high-Mg calcite composition. However, in modern oolitic shoals, aragonitic tangential ooids are the major ooid forms, and isopachous-marine cement is also aragonitic in composition. Thus, the inferred high-Mg calcite original composition of this cement can be attributed to the presence of abundant organic matter and its influence on composition of sea water. Such influence by organic matters and acids is considered to be one of the most important factors that initiate formation of radial ooids of high-Mg calcite composition (see Chap. 6). Absence of the preserved isopachous-bladed cement in the calcitized (originally aragonitic tangential) ooid-bearing sublithologic units also provide additional support our suggestion about original mineral composition of isopachous-bladed calcite cement.

In addition, Cantrell and Walker (1985) also relate the original mineral composition of isopachous-bladed cement of the oolitic grainstone units of Ordovician carbonates in east Tennessee to the high-Mg calcite of marine phreatic diagenesis on the basis of the bladed-crystal morphology of this cement. Cantrell and Walker's suggestion is consistent with the explanation put forth in this study about the origin of the isopachous-bladed calcite cement. Furthermore, James et al. (1976) reported this cement in the open sea site of the Belize Reef and also related to the high-Mg calcite of marine phreatic diagenetic environment. In voids or cavities of reefs, the cryptocrystalline cements fill and make the initial rim which is followed by the bladed-calcite cements (Friedman et al., 1974; James et al., 1976; and Davies, 1977).

Marine phreatic origin of this cement type in reefs has also been supported by Schroeder (1973), Walls et al. (1979), Longman (1980), Kerans et al. (1986), Koch and Schorr (1986), and Reitner (1986).

Predominant occurrences of this cement type in the open seaward shoal or reef also suggest high-energy environment and strong and continuous water pumping into interparticle pores and voids.

Cryptocrystalline High-Mg Calcite Cement

Description:

Finely cryptocrystalline crystals are commonly misidentified as matrix material mechanically filling the interparticle and intraparticle pores of micron-size openings. This cement type for the first time was reported in bored walls of allochems by organisms in micritic envelope (Bathurst, 1958, 1964; Friedman 1964). In the modern carbonate environments, grain size of these cement ranges from 2 to 4 μm (Ginsburg et al., 1971).

In the AVL, this cryptocrystalline cement is present in the intraclast-bearing, radial ooid-dominated subunits of the oolitic shoal units, in which bladed-isopachous rim and radiaxial-fibrous cements are also common (Fig. 90). Fine-grained peloids are also scattered in the cryptocrystalline cements or cemented areas. Under cathode light, the cryptocrystalline cements show even dim or dull luminescence, similar to those of the ooids.

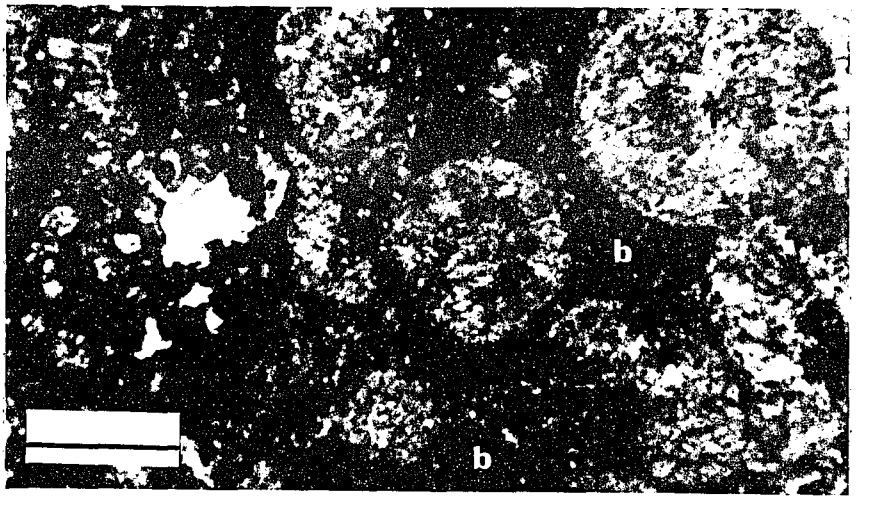


Figure 90- Photomicrograph of cryptocrystalline calcite cement. Slightly dark gray, micro-equigranular calcites (b) filled interparticle the pores of the radial ooid-dominated packstone and grainstone subunits. Under plane-polarized light; scales= 0.5 mm.

Parallel-laminated micritic intraclasts within the skeletal packstone- and grainstone storm layers and in the skeletal-grain supported brecciolas of the slope facies do not

exhibit any recognizable cement types other than micrite. Under standard microscope, it is considerably difficult to pin point which micrite is cement and which is matrix in these syndepositional, micritic intraclasts. SEM and cathodoluminescence petrography can be useful for such discrimination. Under cathode light, the marine cryptocrystalline cements are non-luminescent.

Interpretation:

Cryptocrystalline cement with high-Mg calcitic composition occurs in the modern reef environments as a cement and a matrix (Ginsburg et al., 1971; Friedman et al., 1974; James et al.,1976; and Friedman, 1985). Micritic high-Mg calcite cements occur if pore spaces are smaller than 15 μm in diameter (James et al,. 1976).

Organisms is believed to play important role for precipitating of this cement type (see Land and Goreau, 1970; Macintire, 1977). According to Ginsburg et al. (1971), high degree of agitation and low-sedimentation rate are prerequisite for the extensive development of submarine cementation by cryptocrystalline high-Mg calcite in reefs. The similar diagenetic environmental conditions as suggested by Ginsburg et al. (1971) can be adopted for the radial ooid-bearing sublithofacies of the AVL which is interpreted to have been deposited on open seaward-extended flanks of oolitic bars (see Chap. 6). The cryptocrystalline cement is common with other marine cements in the radial ooid-bearing units. It is possible to suggest that during the precipitation of this cement type sedimentation rate was low and radial ooid-bearing units were already stabilized by algal colonization and early cementation (by bladed-isopachous cement) like in the relic sands of the Holocene Lily bank (Hine, 1977).

Micritic intraclasts of the skeletal packstone units of storm layers in the upper slope and the skeletal grain-supported brecciola lithofacies of the lower slope depositional environment represent a relatively different submarine lithification and cementation. Cryptocrystalline calcite cement was also reported at the slope of the Little Bahama bank by Wilber and Neumann (1977) and Mullins (1983).

The micritic intraclasts of the AVL indicate early submarine cementation (e.g., Kazimercazk and Goldring, 1978; Sepkoski, 1982) in the open-shelf, anoxic diagenetic environment. From absence of other kinds of recognizable marine cements and syndepositional nature of the micritic intraclasts, it can be suggested that the cryptocrystalline cement may have precipitated directly from sea water under combined effects of winnowing-ocean bottom currents, interaction of organism and oxidation of organic matter by sulfur-reducing bacteria. Activities of benthic organisms appear to have been considerably limited because the preservation of parallel laminae in the hemipelagic intraclasts eliminates such possibility.

Columnar Cement

Description:

This cement is volumetrically the most significant interparticle cement in the oncolitic packstone- and grainstone units of oncolitic shoal facies (Fig. 91 A and B). Columnar calcite cements also commonly occur in the skeletal grain-supported, intraclastic storm layers (Fig. 92 A). In these storm units, columnar-calcite cements primarily occur on and under side of the intraclasts.

The columnar calcite crystals have planar crystal boundaries with rhombohedral crystal terminations (Figs. 91, 92). By these features, they can be readily distinguished from radiaxial-fibrous calcite cements. The columnar cements also appear to form as radiaxial fans on the high convexity of oncoidal grains (Figs. 91 A-B, 92 B). White, milky columnar calcite cement generally has uniform extinction. There are two kinds of columnar calcite crystals that are recognizable on the basis of their size and width / length ratio. The first kind is medium grained, cloudy columnar crystals sitting directly on the substrate and making isopachous rim (Fig. 91 A, B). The second kind columnar cement has coarse columnar crystals, generally ranging from 0.5 to 1 mm in length,

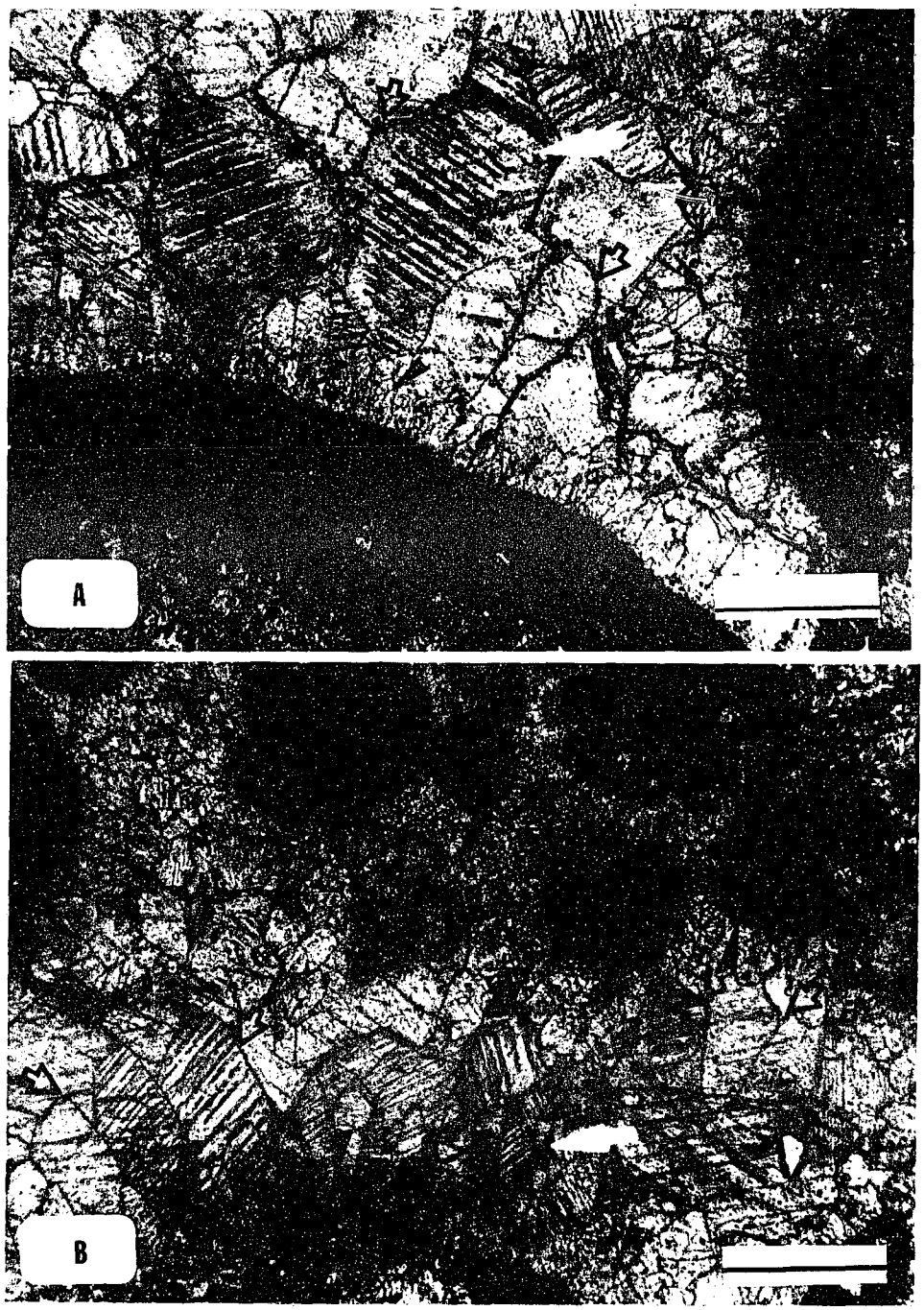


Figure 91- Photomicrographs of columnar-calcite cement in oncolitic packstone- to grainstone units. A) Columnar calcite cement, pointed by arrows, commonly filled the protected-side of oncoids or considerably large interoncoidal pores. Crystals of coarse columnar calcite cement are bidirectionally twinned and appear to have distally divergent crystal axis. Arrowheads point to medium-grained isopachous-columnar cements around oncoids. B) Distally divergent columnar calcite crystals show a fan-shaped crystal morphology. In this oncolitic packstone- and grainstone unit, arrowheads point to radial ooids commonly containing algal nuclei (Girvanella). Under plane-polarized light; scales= 0.5 mm.

and its w/l is 1/6. Some of the coarse crystals also show twins in two directions (Figs. 91, 92).

The coarse-grained columnar crystals often succeed the fine-grained columnar crystals; at the center of pores these coarse crystals commonly encounter other coarse columnar cements that developed from the other side of the same interparticle pores.

Some large columnar cements contain solid inclusions parallel to their scalenohedral crystal endings. In the columnar cements of the Precambrian Beck Spring Dolomite in California, similar inclusions were identified to be microdolomite rhombs under the SEM by Zempalich et al. (1988). The columnar calcite cements of the AVL reveal generally non-luminescence to dully luminescence.

The isotope values of this cement from two samples occur in the following range: $\delta^{18}O$ =-6.69 to -6.77 ‰ PDB, and $\delta^{13}C$= + 0.88 to -1.13 ‰ PDB.

Interpretation:

The absence of relic acicular aragonite lathes (Mazzullo, 1980; Sandberg, 1985), presence of dolomite rhombs (Zempalich et al., 1988), and rhombohedral terminations of these crystals suggests that the columnar calcite cements were originally of high-Mg calcite composition and of marine-phreatic origin. The columnar calcite cements of the oncoidal packstone-and grainstone lithofacies indicate that this cement may have precipitated in a moderately high energy environment where particularly algae-generated organic acid on sea-water composition was considerably important. Cementation of these lithologic units may have followed the final settlement of organo-sedimentary grains (oncoids).

In shelly storm layers, the grain-supported texture and columnar calcite cements represent moderately winnowed environmental conditions which were caused episodically by storm currents. Entrapment of $CaCO_3$-saturated sea water in storm deposits and downdip diffusion of the water was responsible for the formation of this calcite within the predominantly low-energy subtidal depositional environment. The

dull to non-luminescence of columnar cements also suggest an oxygen-rich marine diagenetic environment in both shoal and upper-slope depositional environments.

In the modern marine sediments, marine acicular cements commonly make isopachous rim around sedimentary particles and are composed of aragonite. These two metastable carbonate minerals are converted to low Mg-calcite by diagenesis. High-Mg calcite generally preserves its original texture during the diagenetic conversion to low-Mg calcite (Friedman, 1964; Bathurst, 1975). Conversely, allochems and cements with aragonitic composition lose their original fabrics by meteoric water conversion because this process is primarily dissolution of aragonite and precipitation of low-Mg calcite (Friedman, 1964; Gavish and Friedman, 1965; Bathurst, 1975; Mazzullo, 1981; and Sandberg, 1983 and 1985). Precipitation of high-Mg calcite as well as radial ooids is interpreted to be function of organism and their influence on sea-water composition by producing organic acid in the low-energy shoal facies (see Chap. 6 for further detail). The oncoidal shoal is a Girvanella-constituted shoal, and its energy level is believed to have ranged from moderate to moderately high. These environmental conditions are thus favorable for high-Mg calcite cementation in the oncoidal shoal facies (see Chap. 5).

The dolomitized-columnar, isopachous cements in the oolitic grainstone units and birdseye fillings in the stromatolitic limestone, were reported by Tucker (1983) and Zempalich et al. (1988). They interpreted these cements as a marine-phreatic cement on the basis of isopachous nature and isotope composition of the columnar cements. These case studies also provide additional support for the interpretation of this study about origin of columnar calcite cements.

Oxygen-isotope composition of columnar calcite cement (-6.69 to -6.77 ‰ PDB) is compatible with the estimated-$\delta^{18}O$ values (-6 to -7 ‰ PDB) of calcite directly precipitated from the Middle Ordovician sea water (Ross et al., 1977; Popp et al., 1986; and Lohmann and Walker, 1989). Such depleted oxygen-isotope compositions of marine calcite cements represent the Middle Ordovician warm sea water whose $\delta^{18}O$ value is estimated to have ranged from -3.71 to -4.71 ‰ SMOW for 25 °C surface temperature in the following expression of oxygen-isotope fractionation.

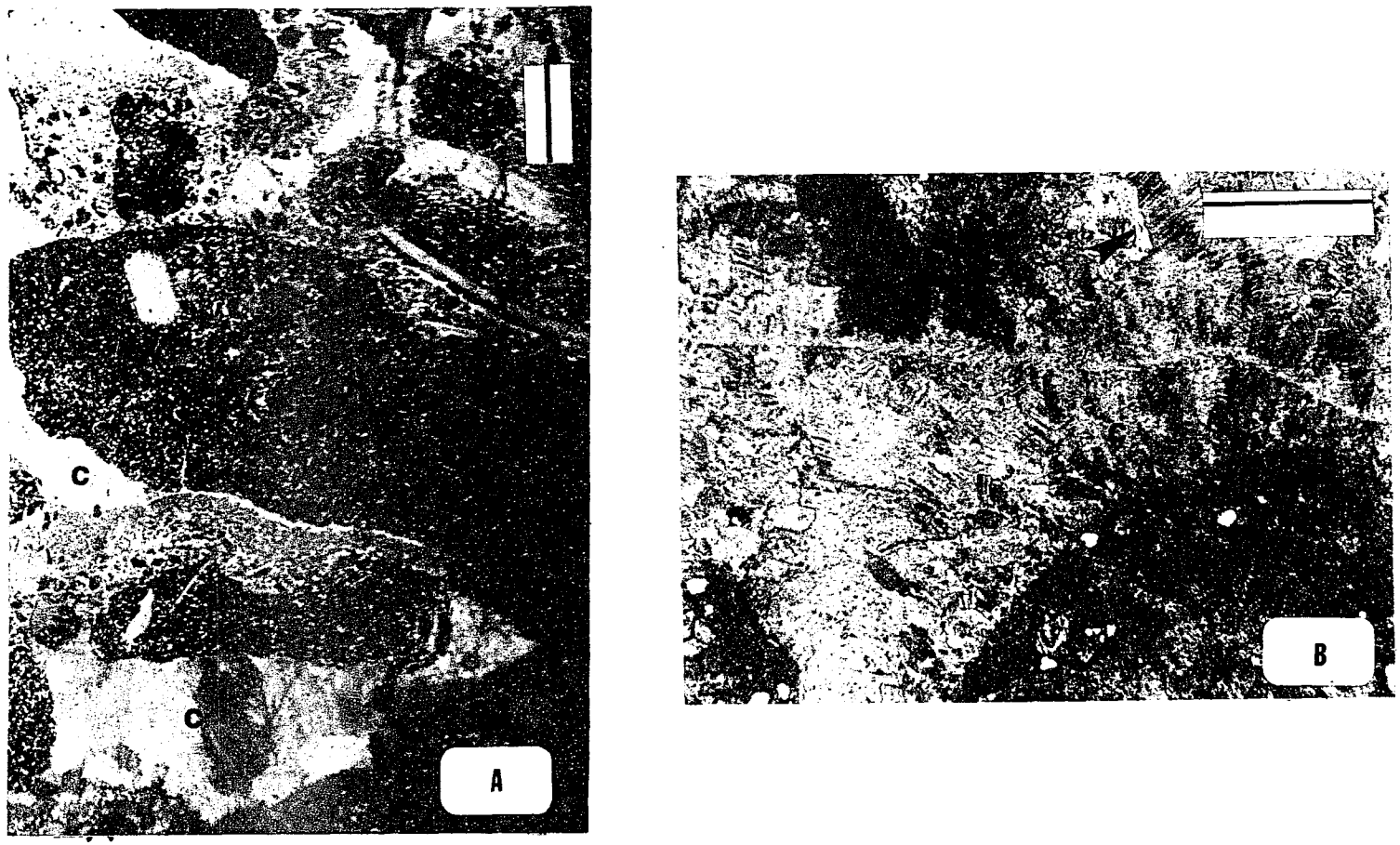


Figure 92- Photomicrographs of columnar calcite cement. A) In the grain-supported conglomeratic storm layers of open shelf, columnar calcite cements (c) filled the protected sites of silty quartz-rich lime mudstone intraclasts. B) Relict columnar cements after neomorphic alteration in the oncoidal packstone- and grainstone unit. Under plane-polarized light; scales = 0.5 mm.

$10^3 ln = 2.78 \times 10^6 T^{-2}$ *(°Kelvin)-2.89* (Friedman and O'Neil, 1977)

Textural features of this cement suggest a "paramorphic" diagenetic stabilization under meteoric diagenesis. Carbon-isotope composition of columnar calcite ranges -1.13 to +0.88 ‰ PDB. In this cement, $\delta^{13}C$ value (+0.88 ‰ PDB) occurs in the same carbon isotopic range with the estimated-$\delta^{13}C$ value of the Middle Ordovician marine calcite, which ranges from 0 to +1 ‰ PDB. However, $\delta^{13}C$ value (-1.13 ‰ PDB) of columnar calcite represent a slightly more depleted carbon-isotope composition which may have been caused by fresh-water phreatic or by mixed-diagenetic water-induced isotopic modifications. Slightly depleted $\delta^{13}C$ value of columnar calcite cement can be related to ^{12}C enrichment in the meteoric or mixed-diagenetic water due to generation of CO_2 by oxidation of organic matter.

In short, it can be concluded on the basis crystal morphology and isopachous nature and dolomite inclusions that these columnar cements may have precipitated in the marine-phreatic diagenetic environment, and they were diagenetically altered by the meteoric diagenetic waters which may have had comparable $\delta^{18}O$ value with the estimated-$\delta^{18}O$ composition of the Middle Ordovician sea water.

B. METEORIC CALCITE CEMENT

Pendant Calcite Cement

Description:

This cement is a coarse-grained, fenestra-filling calcite cement of the cryptalalgal-laminated limestone. Generally, the fenestral limestone sublithofacies is situated at the uppermost part of the cryptalgal lithofacies, in which mud cracks and other features of subaerial exposure are very common (see Chap. 8).

The fenestra-filling calcites generally vary from 0.1 to 2 mm in size (Fig. 93 A). The large calcite crystals commonly exhibit twins in two directions. The floors and roofs of fenestrae as well as host peloids commonly contain silt size, detrital quartz particles.

Under cathode light, the fenestrae of the cryptalgal lithofacies are filled by (1) zoned-luminescent calcite cements, and (2) dull luminescent, non-zonal calcite cement (Figs. 93 B, 94). Dull luminescent, non-zonal cements are volumetrically very important and constitute more than 85 % of the fenestra-filling calcite cement (Figs. 93, 94).

The fenestra-filling zoned cements appear to have initiated from the roofs of fenestral pores and to have grown toward the floors of the same pores in a competitive crystal growth habit (Fig. 93 B; see Bathurst, 1975).

Under cathode light, the fenestra-filling, zoned-calcite cements reveal that dark nonluminescent bands alternate with bright-orange red luminescent bands (Figs. 93 B,

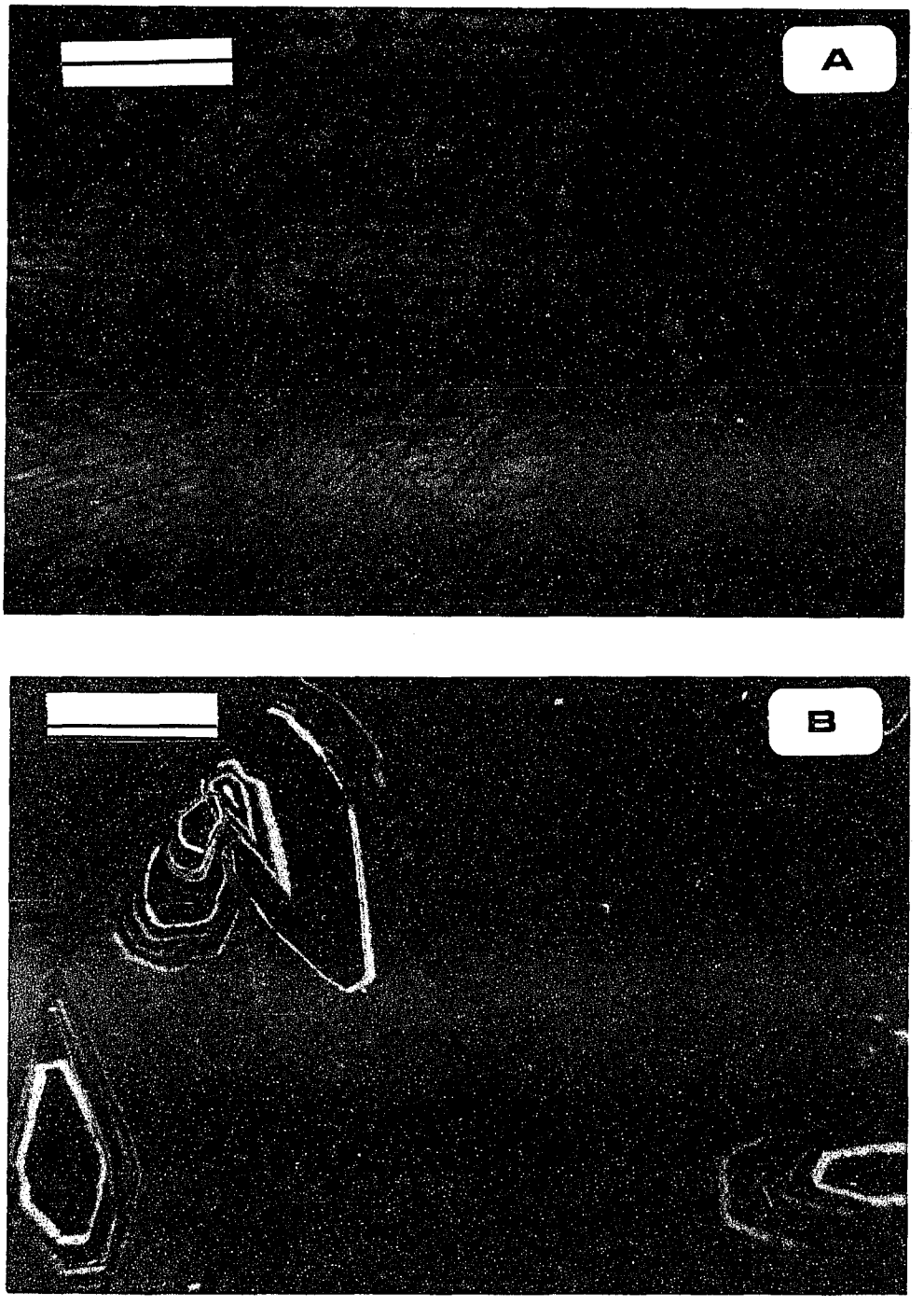


Figure 93- Photomicrographs of pendant or fenestra-filling calcite cement. A) Fenestra-filling sparry calcite cement; under cross-polarized light. B) The same view of photomicrograph A reveals a gravitational cement morphology and orange-red and alternating non-luminescent zones of pendant cement, and the rest of fenestra-filling calcite cement reveal dull luminescence. Scales= 0.25 mm.

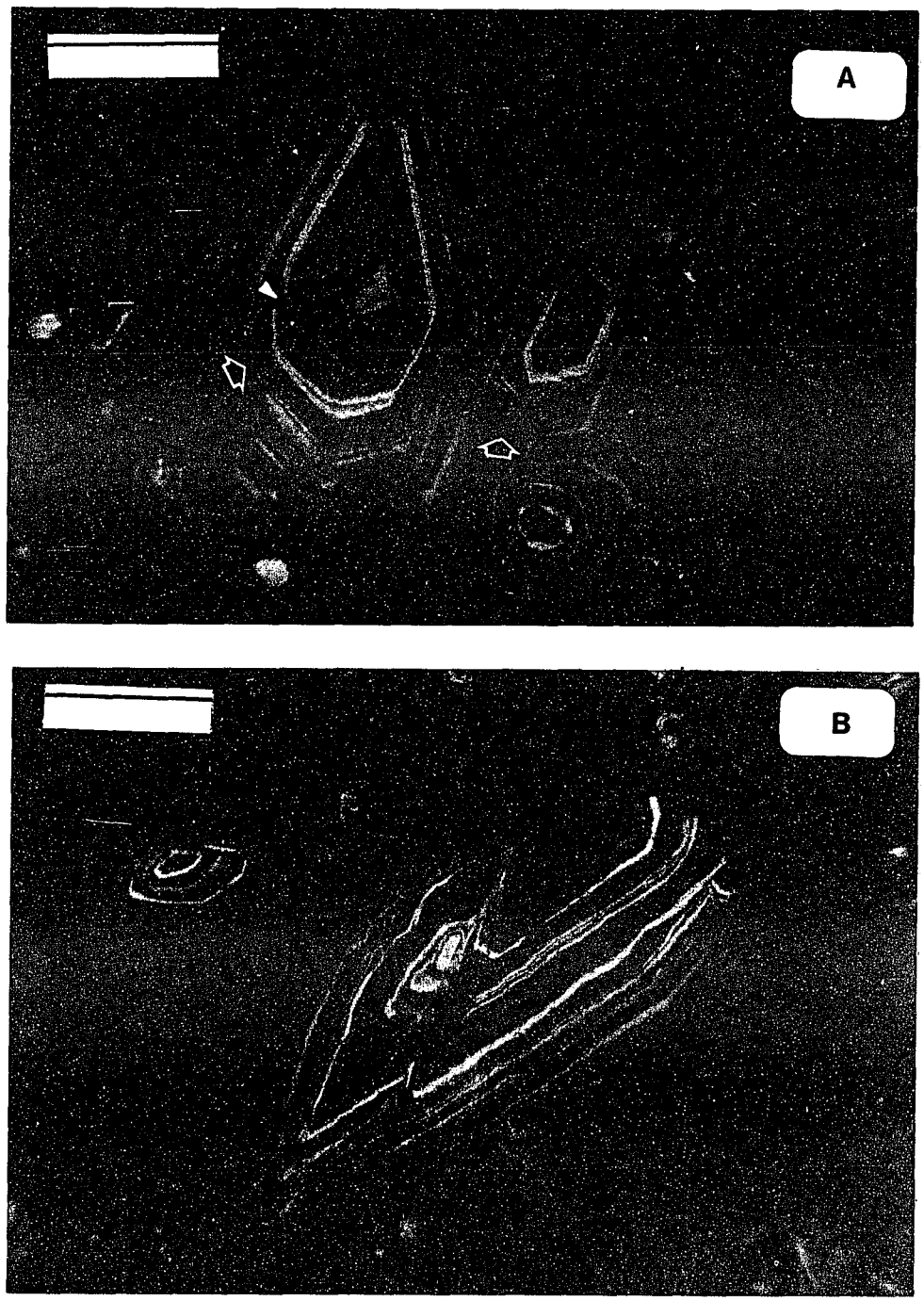


Figure 94- Cathodoluminescence photomicrographs of gravitational pendant cement. A) In pendant cement, arrow indicates discontinuous orange-red luminescent bands, and white arrowhead points to corrosion of a bright luminescent band and subsequent dark non- luminescent band. B) Pendant cement reveals continuous and regular luminescent bands. Under cathode light; scales= 0.25 mm.

94 A, B). In the zoned cements, transition from bright-orange red luminescent bands to nonluminescent bands appears to show dissolutional boundaries. On the other hand, in the zoned cements, transition from the dark, nonluminescent bands to the bright orange-red luminescent bands appears to be sharp but not dissolutional (Figs. 93, 94). Thickness of red zones are generally irregular and unequal.

The dull luminescent, fenestra-filling cement does not show any luminescent bands; it also locally truncates the zonal cements and their outermost bands (Fig. 94 A, B).

The bulk $\delta^{18}O$ composition of this cement based on one sample is -5.6 ‰ PDB, and its $\delta^{13}C$ composition is -0.94 ‰ PDB.

Interpretation:

Mud cracks, and fenestral fabrics clearly indicate the subaerial exposure of these upper intertidal and supratidal-lithologic sequences (see Chap. 9).

Concentrations of the detrital silty quartz on the floors and roofs of the fenestrae may be comparable with the phenomena described by Dunham (1969; 1971) and Grover and Read (1983). The fenestra-filling zoned cement can be considered as "pendant cement" on the basis of crystal morphology, close association with detrital quartz or feldspar silts within the upper intertidal to supratidal lithofacies of the AVL (see Dunham, 1969; 1971; and James and Choquette, 1984). Because these coarse calcite cements can only form either in deep-burial or meteoric diagenetic environments where Mg / Ca ratio is lower than 1 (Folk, 1974). Lithology and their features of subaerial exposure and their close association with detrital quartz and feldspar silts also represent a diagenetic environment of the fresh water-vadose zone (i.e., unsaturated-ground water zone). Vertical percolation of unsaturated-meteoric waters with respect to calcite in vadose zones may have been responsible for the formation of gravitational or "pendant cement" of the AVL (Müller, 1971; Longman, 1980; and James and Choquette, 1984).

The pendant cements commonly form in vadose-diagenetic environments of the

Quaternary carbonates (James and Choquette, 1984). The pendant cement specifically occurs in the interparticle pores of sediments and sedimentary rocks of vadose zones in which saturated-water droplets or films with respect to $CaCO_3$ cling to undersides of grains or grain boundaries by surface tensions (Müller, 1971; Dunham, 1971).

The formation of non-luminescent and luminescent bands in the zoned-pendant cements represents variations in oxidation and reducing states of pore waters in a vadose-diagenetic environment (Grover and Read, 1983). Bright luminescent bands represent the reducing conditions in pore waters (Carpenter and Oglesby, 1976; Frank et al., 1982); nonluminescent bands represent oxidizing pore water. The bright luminescent bands probably represent the late stagnant stage of the same pore water which became a reducing-pore water due to depletion of oxygen by organic activities (Grover and Read, 1983). Thus, the bands of the zoned-pendant cement probably formed from the same diagenetic water in diagenetic environments ranging from vadose to shallow-phreatic. The non-luminescent zones are the major, if not only, cement in near surface meteoric environment, in Shark Bay, Yucatan and Barbados (Grover and Read, 1983).

Under humid climatic conditions, a considerable amount of meteoric-water influx is required to keep the pore water being well oxidized in the organic-rich, tidal-flat deposits. The meteoric water can be provided from two sources: (1) direct precipitation; and (2) run off on land. Grover and Read (1983) have shown that the non-luminescent cement of the pendant cement in Ordovician peritidal deposits increases upward and decreases downward in the same region. In this study, the zoned-pendant cements were studied in two sections, but their zonal variations in vertical sections were not investigated. The thin, bright cement may have formed during the reduction of sulfate to sulfide where H_2S in solution causes iron to precipitate as an iron sulfide, FeS_2, (e.g., Krauskopf, 1979) and allows formation of Mn-rich cement. Particularly, the nonzoned-dull cement reflects the onset of redox potential which allows iron, as well as Mn^{+2} to be incorporated into calcite.

The gradual or conformable transitions from the non-luminescent bands to bright-orange red luminescent bands probably indicate that cyclical influx of

oxygen-rich fresh water progressively evolved into the oxygen-poor, reducing, stagnant stages by bacterial consumption of oxygen. However, at the initial stage of each influx, oxygen-rich water was probably under-saturated with respect to calcite and produced the micro-dissolutional surfaces between bright bands and non-luminescent bands (Fig. 94 A, B).

The dull cement truncating the zonal pendant cements probably indicate the phreatic or burial cementation formed during the relatively late-diagenetic events.

The oxygen isotope composition (-5.16 ‰ PDB) of the bulk pendant cement is more enriched in ^{18}O than the estimated-$\delta^{18}O$ values of the Middle Ordovician marine calcite, ranging from -6 to -7 ‰ PDB. A slightly more depleted $\delta^{13}C$ value of - 0.94 ‰ PDB compared to the estimated-$\delta^{13}C$ value of the Middle Ordovician marine calcite (from 0 to +1 ‰ PDB) may indicate meteoric water-induced depletion in ^{13}C. Such slightly depleted-$\delta^{13}C$ composition is considered to be enriched compared to the $\delta^{13}C$ composition of modern vadose calcite. This enriched-$^{\delta 1}3O$ composition of vadose calcite can be attributed to the absence of a developed-soil zone or to a rapid equilibration between rock-derived calcite and groundwater. $\delta^{18}O$ composition of this cement is believed to represent a meteoric diagenetic groundwater whose $\delta^{18}O$ composition is estimated to be equal to -3 ‰ SMOW at 25 °C equilibrium temperature from the isotopic fractionation equation of O'Neil and Friedman (1977).

Equant Blocky Cement

Description:

Volumetrically, equant blocky cement is the most significant cement type in the shoal and peritidal lithofacies of the AVL. In these lithofacies, equant cements most commonly occur in the form of equant blocky mosaic. The equant blocky mosaic is the most common interparticle cement of the AVL and generally occludes entire

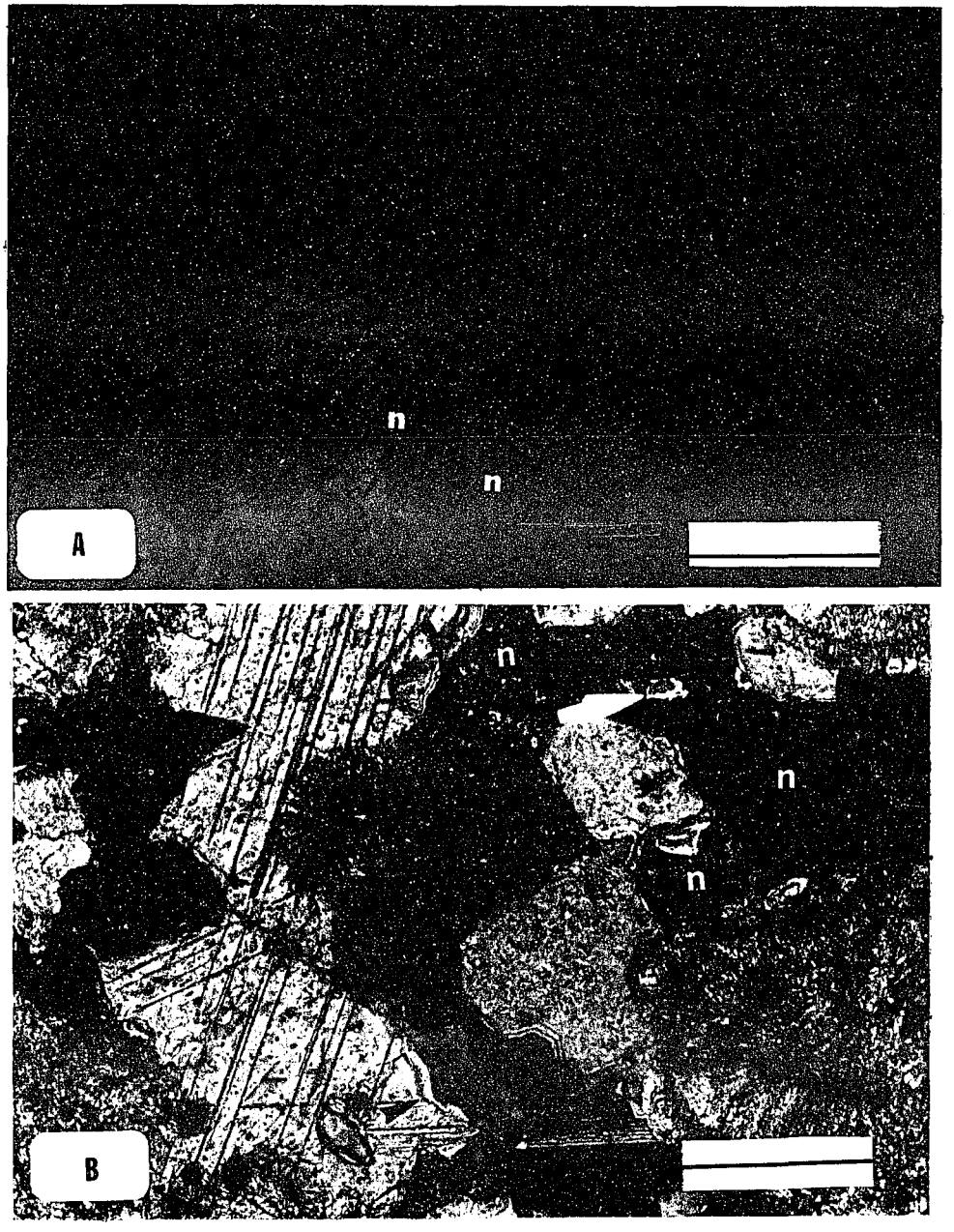


Figure 95- Photomicrographs of equant blocky interparticle cement in the Nuia packstone- and grainstone lithofacies. A) Twinned, large sparry calcite (a) was replaced by untwinned calcite cement crystals (black n) along nonplanar crystal boundaries. White (n's) indicate the replacive inclusions in large, twinned-sparry crystals of calcite cement. Arrowhead points to isopachous-rim cement preserved around Nuia grains, and arrows point to a replacive contact between two cements. B) Untwinned sparry crystals of calcite cement (n) replaced the twinned-sparry calcite cement along non-planar crystal boundaries. White arrow indicates an inclusion of twinned-calcite cement in the untiwinned calcite (white n), and black arrowheads indicate irregular and non-planar replacement fronts between twinned- and untwinned-calcite crystals. Under cross-polarized light; scales= 0.25 mm.

interparticle pores (Fig. 95 A, B).

The equant-bladed rim cements occur along the allochems of some packstone- and grainstone units of the shoal lithofacies. The equant blocky mosaic follows the equant-bladed rim cement pore centerward and shows a texture of increasing crystal size toward pore centers (Fig. 95).

With varying crystal sizes, the equant calcite cements commonly display planar crystal boundaries and very common occurrences of triple junctions and enfacial junctions (e.g., Bathurst, 1975, and 1983). These calcite spars are clear and relatively solid inclusion-free, and have a few two-phase fluid inclusions (Fig. 86). In some cases, two equant blocky cements side by side have common crystal boundaries; one shows relatively intensive mechanical twining features, whereas the other has no sign of mechanical twinning (Figs. 86, 95). Under cathode light, the equant cements generally show dull to bright-dull luminescence.

Furthermore, the equant cements are seldom replaced by syntaxial cements and by relatively large spars whose grain boundaries with other neighboring calcite spars vary from planar to nonplanar (Fig. 97 A). Commonly, the calcite-filled fractures cross-cut allochems and equant mosaics. The equant cements commonly exhibit uniform or homogeneous dull luminescence. In places, these interparticle equant rhombs of calcite mosaic are replaced by dolomite and quartz.

Interpretation:

Study of recent carbonate sediments and their diagenesis under the influence of meteoric diagenetic environment have been presented by many studies (Friedman, 1964; Gavish and Friedman 1967; Land et al., 1967; Plummer et al., 1976; Halley and Harris ,1979; and Bud, 1989), and review papers by Friedman (1975), Longman (1980), and James and Choquette (1984).

The equant cements, with blocky or bladed-crystal morphology, are volumetrically the most important cement types of the meteoric diagenesis in the AVL.

The fresh water phreatic origin of the equant calcite mosaic is likely to be justified by the following criteria: (1) planar crystal boundaries; (2) common enfacial and triple junctions; and (3) progressive increase in crystal size of equant blocky cement toward the pore center. These criteria have been noted in many ancient carbonate rocks by Friedman, 1964, Bathurst (1975, 1983), Loucks (1977), Prezbindowski (1985), and many others. All these studies suggest that the pore centerward-coarsening calcite texture is a distinctive feature of early cementation in the fresh water diagenetic environment. Bathurst (1983) demonstrated that the equant calcite cement could also be distinguished from the neomorphically altered mosaic of the skeletal fragments by the following criteria: (1) non-planar crystal boundaries of neomorphically calcitized molluscs and (2) absence of dusty inclusions or dirty cloudy spars (Bathurst, 1983). Therefore, clean, equant cements with a planar crystal boundaries can readily be separated from dusty inclusion-rich, neomorphically replaced molluscan shells.

The occlusion of interparticle pores by the equant cement mosaic showing a pore-centerward coarsening feature also suggests that this cement type represents a possible fresh-water phreatic origin.

Friedman (1964), Gavish and Friedman (1967) and Land (1967) suggest that cement precipitating in inter particle pores are of allochthonous origin. This suggestion clearly indicates that allochthonous cements originate either from dissolution of carbonate sediments at near-surface area or from the lateral ground water flow in large aquifer systems. Carbonate sediments, with aragonitic composition, may have been dissolved and reprecipitated as a cement downdip (see Longman, 1980). In the AVL, the absence of vadose cement in the equant cement-bearing units and absence of significant karst features or features of subaerial exposure probably eliminate the possibility of surface dissolution by vertically downward movement of meteoric water. Joulter Cay can be a good example for this (Halley and Harris, 1979), where ground water recharges into the phreatic zone from a run-off system at the farther shoreward or landward part of the sediments. During progradation of short durational cycles, fresh-water recharge was probably at maximum level in the shoal lithofacies of the AVL. And extensive phreatic cementation probably resulted from lateral ground-water

flow in the saturated zone of unconfined aquifer systems of the shoal facies.

James and Choquette (1984) demonstrate that Pleistocene carbonates in vadose zones are poorly cemented, while the same sediments in phreatic zones are limestone with a striking-mineralogical discontinuity developed near the water table. From this observation, it can be suggested that in the shoal lithofacies of the AVL, entirely occluded pores by equant blocky cements represent the phreatic-zone cementation. Absence of continuous isopachous cement in the oolitic, Nuia and other skeletal grainstone units of peritidal and shoal deposits indicates that cementation of this kind probably took place in the phreatic-diagenetic zones of humid and tropical climatical settings (e.g., Hird and Tucker, 1988).

Drusy Cement

Description:

Thin micritic rims outlining molluscs or other skeletal fragments commonly enclose an equant blocky calcite mosaic. Straight or planar crystal boundaries with a coarsening-pore centerward texture are the most prominent features of the intraskeletal pores. The coarsening-cement texture toward pore center is commonly called "drusy" cement (e.g. Bathurst, 1958, 1975; Friedman 1964).

This intraskeletal cement (Fig. 103 A in Chap. 12 C) is commonly distinguished from the interparticle mosaic by a very thin micritic rim or envelope outlining the skeletal fragments. This intraskeletal cement (Choquette and Pray, 1970) or skeletal moldic cement (Friedman, 1975) generally occurs in mollusc and ostracod fragments. However, mollusc fragments in the micrite-supported upper slope deposits appear to have a similar pore-centerward increasing cements which have non-planar crystal boundaries and dusty solid inclusion-rich calcite spars. Such drusy cement-like

occurrences are also commonly encountered within the oncoidal nuclei.

Under cathode light, drusy cements show the same luminescence with the equigranular interparticle mosaic.

Interpretation:

Skeletal molds filled by pore centerward-coarsening calcite spars, with planar crystal boundaries, probably represent a phreatic diagenetic environment (Bathurst, 1975; Loucks, 1977). Generally, pore-centerward coarsening texture of the packstone- and grainstone lithofacies of the shoal facies probably resulted from the competitive crystal growth (Bathurst, 1975).

According to Friedman and Sanders (1978), when skeletal fragments of aragonitic composition lies in the marine diagenetic environment, algae bore and micritize sedimentary fragments of aragonitic composition; then cryptocrystalline calcite crystals fill these microscopic borings prior to fresh-water diagenesis. Later carbonate sediments undergo fresh-water diagenesis where aragonitic allochems and cements are dissolved to yield moldic porosity (Bathurst 1975; Friedman, 1975). Relatively long range fluctuations of ground water due to short durational sea-level changes bring the strata under the influence of the unsaturated-phreatic zone to active phreatic zone in which cementation is very extensive and very rapid.

Syntaxial Cement

Description:

Volumetrically, this cement is by far the most important interparticle pore-filling calcite cement in the crinoidal packstone- and grainstone units of the shoal and upper

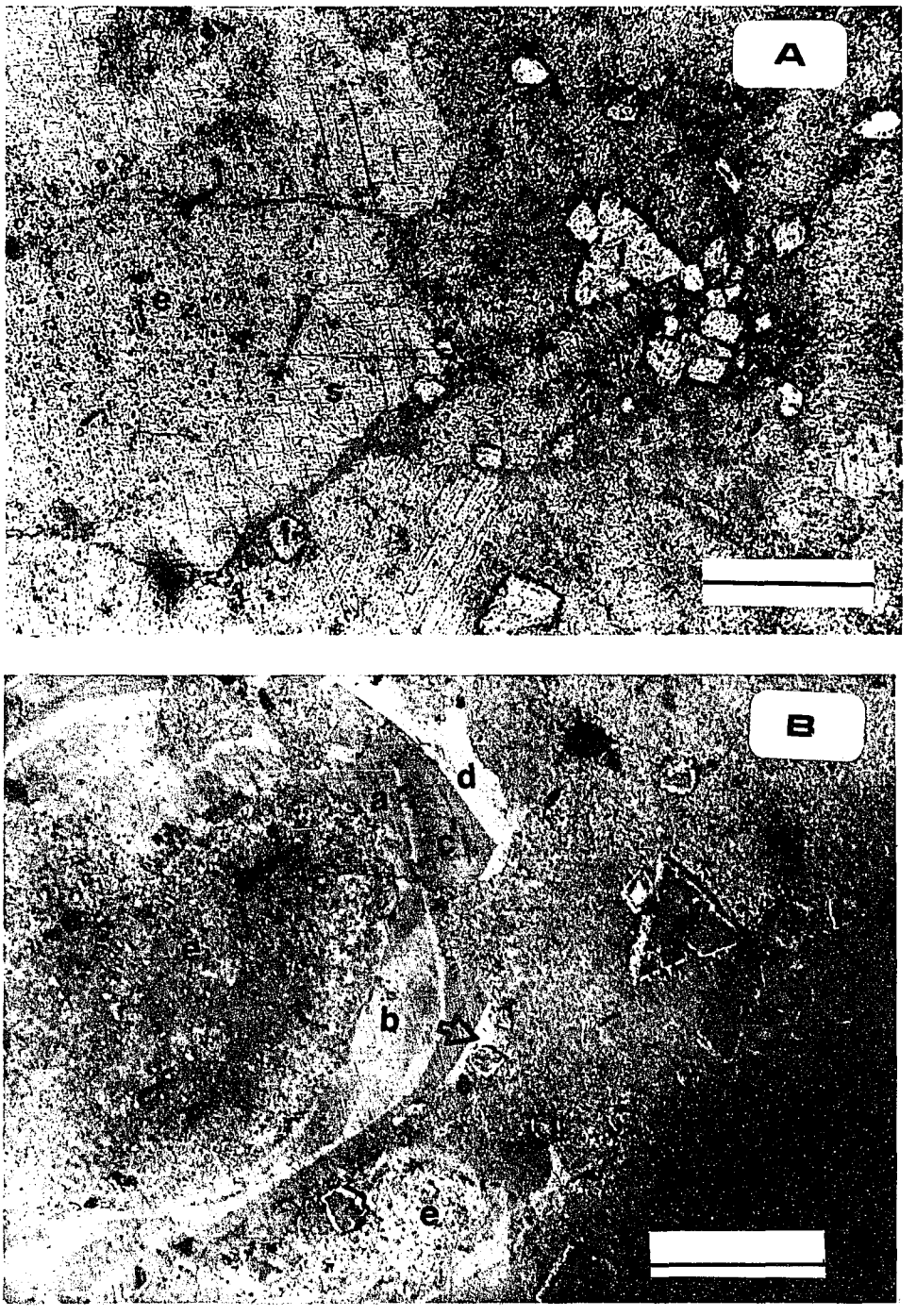


Figure 96- Photomicrographs of syntaxial cement. A) Crinoid (e) with syntaxial cement (s) and ferroan dolomites (f) in Nuia packstone and grainstone unit, under plane-polarized light. B) Crinoid containing microdolomite rhombs (e) and four syntaxial cement zones, (a), (b), (c), and (d), recognized under cathode light. Arrow indicates that ferroan dolomite postdated the latest syntaxial calcite cement zone (d). Scales= 0.25 mm.

slope facies. Syntaxial cements are also common in the Nuia shoal lithologic units even though crinoidal grains are rare.

Syntaxial cements occur around crinoids and can easily be recognized from the dusty, inclusion-rich host crinoids by their clean, inclusion-free rims (Fig. 96 A). The optical axes of syntaxial rim cements are the same with crinoidal grains; the host particles and syntaxial-rim cement reveal uniform extinction or single crystal extinction (Figs. 97, 103 B). This cement is uncommon on crinoidal fragments which are coated by micritic envelopes. The syntaxial cements seldom replace interparticle equant cements (Fig. 96 B).

Microdolomites (Fig. 96) are very common in host crinoid grains, and they appear to align on parallel, straight lines (Meyers and Lohmann, 1978). Under cathode light, these microdolomites reveal a bright red luminescence. Host crinoid grains are selectively replaced by chert, and microdolomites in the partially silica-replaced areas also show a uniform extinction with microdolomites of the unchertified part of host crinoids.

The zoned syntaxial cements were only observed in a few samples despite the fact that more than twenty samples were prepared. In the AVL, two kinds of zoned-syntaxial cements have been described by this study: (1) the zoned cement I, with discrete luminescent zones (in the crinoids of shoal units); and (2) the zoned cement II, showing almost homogeneous luminescence in the upper slope crinoidal packstones.

The syntaxial, zoned cement I was commonly observed in the Nuia and crinoid packstone- and grainstone units of the shoal facies. Four-discrete zones of syntaxial cement I within the Nuia in the crinoidal grainstone units of shoal facies (Figs. 95 B, 96 B) are, as follows:

1) non-luminescent zones (a), forming next to host crinoid;
2) bright yellow luminescent zones (b), relatively thin;
3) dull to non-luminescent zones (c).
4) bright yellow luminescence (d), replaced by dolomite rhombs.

These zones are generally conformable and do not have truncational boundaries

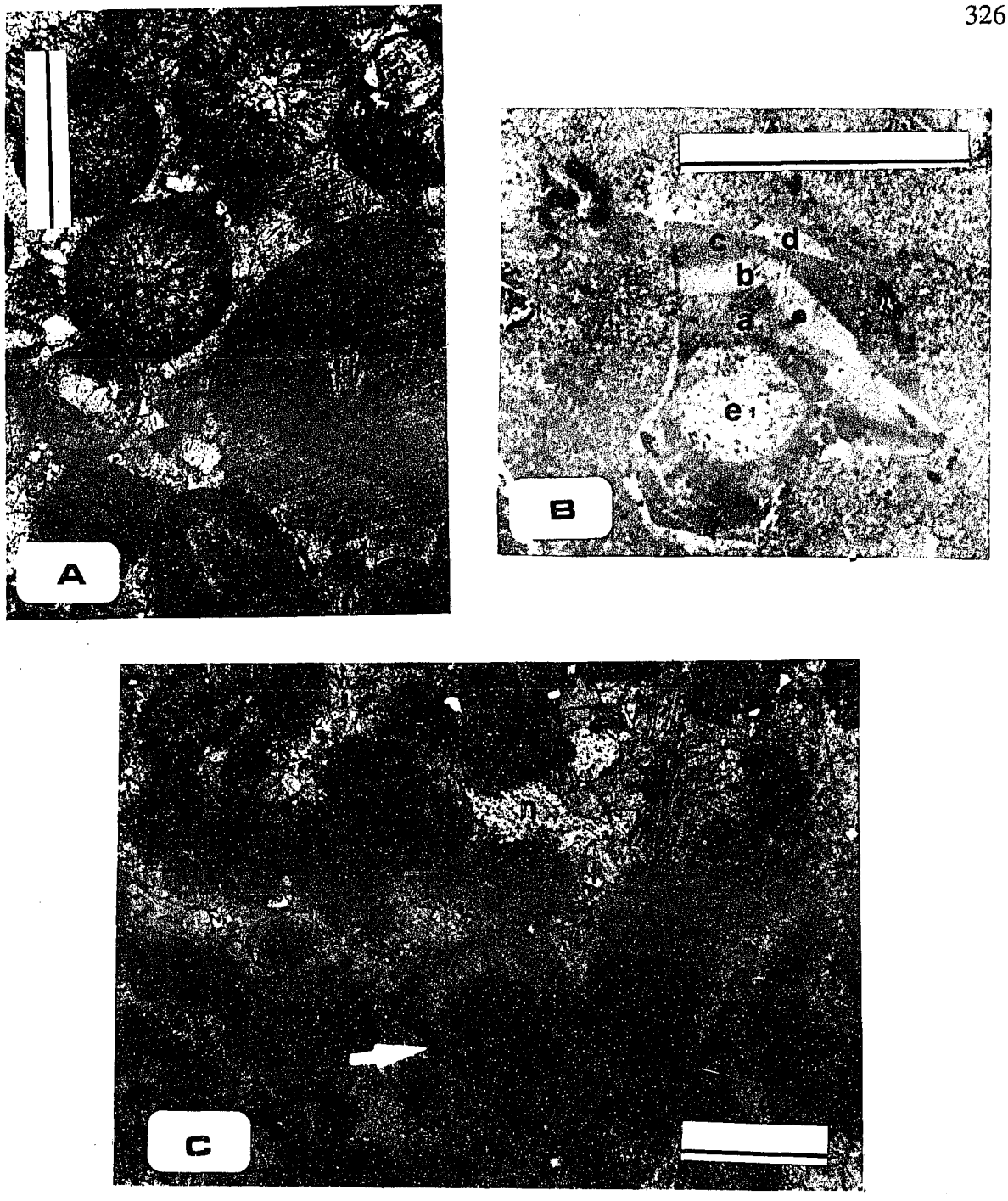


Figure 97- Photomicrographs of syntaxial cements. A and C show that syntaxial cement replaced the interparticle calcite cement in oolitic grainstone and Nuia packstone- and grainstone units, respectively; under plane-polarized light. B) Four syntaxial zones, (a), (b), (c), and (d), in Nuia grainstone unit, under cathode light. Scales = 0.5 mm.

among them. The sequential order in these four syntaxial zones is commonly continuous and complete. However, in places some zones (only first zone or last to two zones) are only present on one side of crinoids, and the complete four zones occur on the other side of the same grain. The normal sequential order of these zones is even unchanged in the pores filled by an incomplete sequence of zonal cements. Euhedral dolomite crystals of bright red luminescence with thin, bright yellow-red luminescent rim postdate all of these zoned-syntaxial cements. Figure 96 represents two different stratigraphic units of the same vertical section; each interval is separated by about 100 feet of vertical distance, yet they show almost the same zones. Generally, if pores are relatively large, the complete zones in a regular repetition appear to occur symmetrically on either side of crinoids.

In the storm layers of the upper slope facies, the zoned-syntaxial cement II can easily be recognized from inclusion-rich crinoids by their inclusion-free, red-bright luminescence syntaxial cement form. There appear to be three-discrete zones separated from each other by dull to red luminescent very thin hair-like zones; otherwise, three-differentiated zones nearly appear to have uniform or homogeneous bright-red luminescence.

Interpretation:

The same optical continuity and uniform extinction of syntaxial rim cements and crinoidal host grains evidently indicate the syntaxial nature of this rim cement (Evamy and Shearman, 1965; Bathurst, 1975).

Occlusion of large pores in many samples is associated with considerably greater growth rate of syntaxial cements as single large crystal compared to polycrystalline cement (Bathurst, 1975). The paucity of this cement around the crinoids with micritic envelope can probably be attributed to the presence of micritic and organic surfaces which may have a inhibiting effect on the crystal growth. Lack of syntaxial cements on the similar substrate has been also confirmed by Evamy and Shearman (1965) and

Meyers (1974).

Syntaxial cement, as a cement precipitated directly from calcite-saturated solutions, can be supported by their inclusion-free rim cements (solid-dolomite and others) and planar crystal faces as well as their pore-filling features.

The syntaxial luminescent zones clearly suggest compositional variations of pore-water chemistry with respect to trace element content. Each of these zones is interpreted to have formed synchronously from distinct pore water composition (Meyers, 1974 and 1978).

Four distinct cement zones of the AVL appear to show a continuous order from zone "a" to "b". However, in the same thin section, the incomplete sequence of these syntaxial zones clearly suggests that pore size and morphology of original grain as well as growth rate of the each zone probably plays a significant role in determining the completion of zones (Searl, 1988). Therefore, these incomplete regular zones are not unconformities on a microscopic scale, and they appear not to have resulted from dissolutional process.

Syntaxial zone (d), bright luminescence is postdated by Dolomite IV as indicated before. Therefore, on the basis of suggested criteria of cement stratigraphy by Meyers (1974), one can suggest that zoned-cements from "a" to "b" are the pre-dolomitic syntaxial calcite cements.

The syntaxial cement zones of the AVL are assumed to have commonly formed in phreatic to mixing-zone diagenetic environments and rarely formed in deep-burial environments. The absence of cloudy prismatic syntaxial cement in the AVL may be indicative of the mixing-zone diagenetic environment (see Lohmann and Meyers, 1977). Syntaxial-rim cements are commonly reported at phreatic diagenetic environments particularly for the Quaternary carbonate sediments of Israel (Gavish and Friedman 1969). According to Longman (1980), the syntaxial overgrowth is possible to form in modern marine environments, but it has not been observed.

Luminescent zones are generally interpreted to be Mn^{+2} rich, and nonluminescent

zones are Fe^{+2} rich in composition (Meyers 1974; Carpenter and Oglesby, 1976; Frank at al., 1982; Pierson, 1981; and Read and Grover 1983). Non-luminescent zones with a low-Mn^{+2} content suggest that they probably precipitated from diagenetic waters of high oxidizing potential (Frank et al, 1982). However, bright cement results from reduction of manganese due to decrease in redox potential or Eh of pore fluids (Oglesby, 1976; Frank et al., 1982; and Grover and Read, 1983). Under such conditions manganese readily substitutes for Ca^{+2} in calcite lattice, and Fe^{+2} forms pyrite. In dull cements containing both $Mn^{+}2$ and Fe^{+2}, the intensity of cathodoluminescence is proportional to the amount of Mn^{+2} and inversely proportional to amount of iron in calcite / dolomite (Carpenter and Oglesby, 1977; Pierson 1981; Frank et al., 1980; and Grover and Read, 1983). $Fe^{+}2$ and $Mn^{+}2$-bearing calcite form under more reducing conditions than bright luminescent zones because low-redox potential allows Fe^{+2} and Mn^{+2} incorporate into the lattice of calcite.

Homogeneous, red luminescent zones (cement II) in the crinoids of stormal shelly layers of upper slope facies may indicate that this cement is probably burial diagenetic in origin. This probably formed a few meters below the sediment-water interface. However, this red color represents more reduction or low-Eh environmental conditions due to sulfate reduction by microbiological activities.

In this study, the correlation of syntaxial zones is unlikely even though the intensity of luminescence in the syntaxial zones appear to be the same, and luminescent cements exhibit the same sequential order. In this study, we can not correlate the syntaxial zones basin-wide due to the absence of closely spaced vertical sections in which the syntaxial zones of the correlative lithologic units can be investigated.

C. DEEP-BURIAL CALCITE CEMENTS

Intraooid or Oomold-filling Calcite

Description:

This kind of cement is commonly found as an intraooid calcite cement in the light brown ooid-bearing packstone and grainstone sublithofacies, which stratigraphically overlie with a gradual contact the dark radial ooid-bearing packstone-and grainstone units (see Chap. 6).

Light-gray ooids are most commonly filled by single, large crystals of calcite and in places by several crystals (Fig. 98 A). The intraooid cement does not exhibit a pore-centerward coarsening texture. These ooid-filling spars commonly show uniform extinctions, are mechanically twinned, and occasionally display partial micritization which appears to penetrate from the outermost margin of ooids to inward (Fig. 98 B).

The ooid-filling crystals of calcite generally range from 0.15 to 0.6 mm in size. Some intraooid-calcite cements are broken and selectively replaced by ferroan dolomite. However, the unbroken megaspars, as intra-ooid cement, differ from the fragmented-intraooid cements by lack of twinning and inclusions. In places, the intra-ooid calcite crystals are coated by radial ooid cortices (see Chap. 6).

Calcite spar with and without twinning appear to be postdated by stylolites (Fig. 98 B). Ferroan dolomite rhombs selectively replaced the segmented-intraooid calcite crystals at the place where fragmentation of an original single intra-ooid spar is generally intensive.

Under cathode light, the crystals of calcite spar exhibit dull and moderately orange red luminescence, and some calcite spars show relatively bright inner luminescent cores. The dolomite, however, reveal generally non-luminescence with a bright red outer luminescent band (see Chap. 13 A).

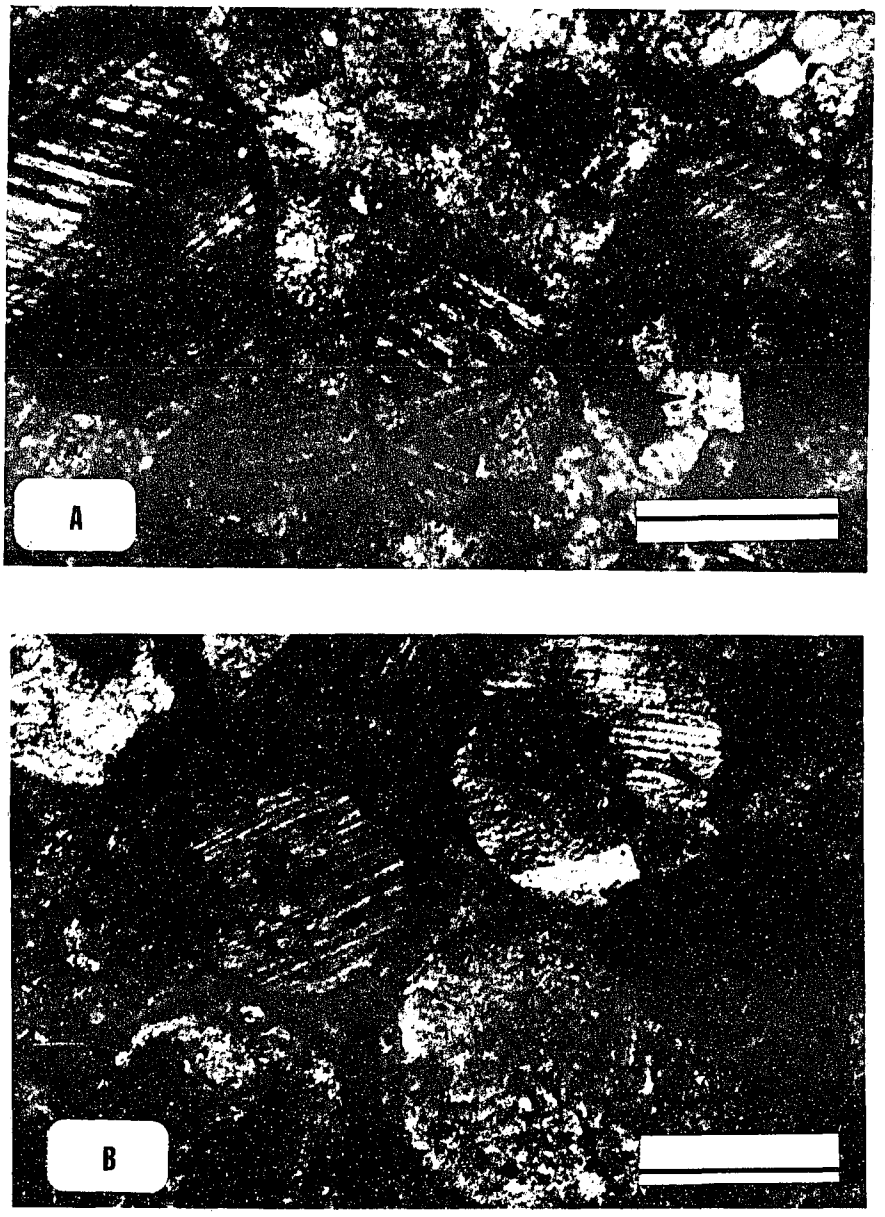


Figure 98- Photomicrographs of intraooid or oomold-filling calcite cement. A) Ooids of the light brown ooid-bearing oolitic packstone and grainstone sublithofacies (see Chap. 6) were filled by twinned-and untwinned-coarse sparry calcite cement crystals; arrowhead indicates euhedral ferroan dolomite crystals replaced the sparry crystals of calcite cement. B) Arrowhead shows a stylolite along sparry calcite-filled ooids. In both A and B photomicrographs, (m) indicates partial, late-micritization. Under plane-polarized light, scales = 0.5 mm.

The oxygen-isotope composition ($\delta^{18}O$) of this calcite cement is depleted with respect to ^{18}O and equal to -8.40 ‰ (PDB), and carbon-isotope composition ($\delta^{13}C$ is equal to -1.63 ‰ (PDB). The homogenization temperatures (T_h) of two-phase fluid inclusions from these calcite cements range from 164 to 179 °C.

Interpretation:

The absence of oomoldic porosity can probably be explained by two processes: (1) replacement of tangential ooids by calcite, as dissolution and reprecipitation advanced concomitantly along thin solution films; and (2) occlusion of oomolds by calcite cement during either meteoric or deep-burial diagenesis.

Oomolds of tangential ooids are believed to have formed during meteoric diagenesis of the AVL, and they may have been occluded by fresh-water calcite cements. However, the coarse intraooid calcite spars without equant blocky mosaic and pore centerward-coarsening texture do not represent the surface- and near-surface void-filling calcite cements. Therefore, it is likely that the oomoldic porosity of the AVL was occluded during the deep-burial diagenesis of this formation by the sparry calcites which probably precipitated from basinal solutions (Choquette and James, 1987; Halley, 1986). The absence of collapsed oomolds, however, can be attributed to pre-oomold, interparticle cementation by early phreatic diagenesis. Petrographic characteristics of the intraooid cements, their homogeneous dull yellow-red luminescence, absence of any relict inclusions, such as aragonite laths within them, high-homogenization temperatures of two-phase inclusions, and their very depleted-oxygen isotope composition (-8.04 ‰ PDB) suggest that all these criteria are consistent with late, deep-burial diagenetic origin of the oomold-filled calcite cements. Intra-ooid spars are believed to represent tangential ooids (Wilkinson et al. 1985; James and Klappa, 1983; Tucker, 1985; and Chow and James, 1988).

The non-twinned, oomoldic calcite crystals clearly predate the sutured stylolites which may have formed at greater burial depths of the AVL probably during the

Antler orogeny. Therefore, the intra-ooid calcite cement of this formation may have formed during the deep-burial diagenesis before the initiation of penetrative stylolites and the formation of synstylolitic replacive ferroan dolomites. With the high-T_h values and depleted-oxygen isotope compositions, this kind of calcite cement type may indicate a deep-burial diagenetic stage which probably took place just before or even during the early stage of stylolitization. In the AVL, the close association of this intraooid-calcite cement with fracture-filling calcite cement suggest the high-hydrostatic pressure before the stylolitization probably led to the formation of fractures which acted as conduits transporting basinal solutions from the deep part of basin to the platform.

Segmentation of an original single oospar probably caused by late mechanical fracturing allowed dolomitizing solutions to replace the intra-ooid cements along the segmented-calcite boundaries.

Partially micritized intraooid-calcite spars are closely associated with the most recent calichification.

Intercrystalline-Calcite Cement

Description:

This cement type has been commonly observed as intercrystalline calcite cement in some pervasively dolomitized intervals of the AVL. Under the microscope, the intercrystalline cements, as polyhedral-pore filling (e.g., Wardlaw, 1979), stained red with Alizarin-red and are readily distinguished from the mosaic dolomite (dolomite type VII). The intercrystalline calcite cement shows close relations with the post-dolomitic, fracture-filling calcite cement which have extremely depleted oxygen isotope values ranging from -27 to -31 ‰ PDB. This fracture-filling calcite cement and the intercrystalline calcite cements show the same luminescence ranging from

bright yellow to yellow-red. Size of the polyhedral calcite cements generally ranges from 0.05 to 0.1 mm. The intercrystalline calcite cement clogs the intercrystalline pores of the mosaic dolomite and makes this dolomite exceedingly tight. This cement type also shows nearly the same luminescence as the late fracture-filling calcite, and both calcite cements postdate the mosaic dolomites. Volumetrically, this calcite cements never exceeds 5-8% in these dolostones.

Interpretation:

The texture of this cement type, as an intercrystalline calcite within dolomite mosaics, and its compatible luminescence with the latest fracture-filling calcites strongly suggest that this intercrystalline calcite was synchronously precipitated from the same parent solutions of the late fracture-filling calcite cement. On the other hand, the presence of the intercrystalline cements only at some intervals of dolostones may also indicate that the intercrystalline calcite cement might have precipitated from progressively diluted dolomitizing fluids (Shukla, 1988).

Void-Filling, Poikilotopic Calcite Cement

Description:

This calcite cement appears to be a ferroan calcite as recognized by K-ferricyanide staining (Friedman, 1959; Dickson, 1969). This cement is inclusion free, not intensively twinned, and poikilotopically includes scalenohedral and columnar antecedent calcites crystals as inclusions. The void-filling cement is generally single calcite crystal with uniform extinction. Under cathode light, the poikilotopically

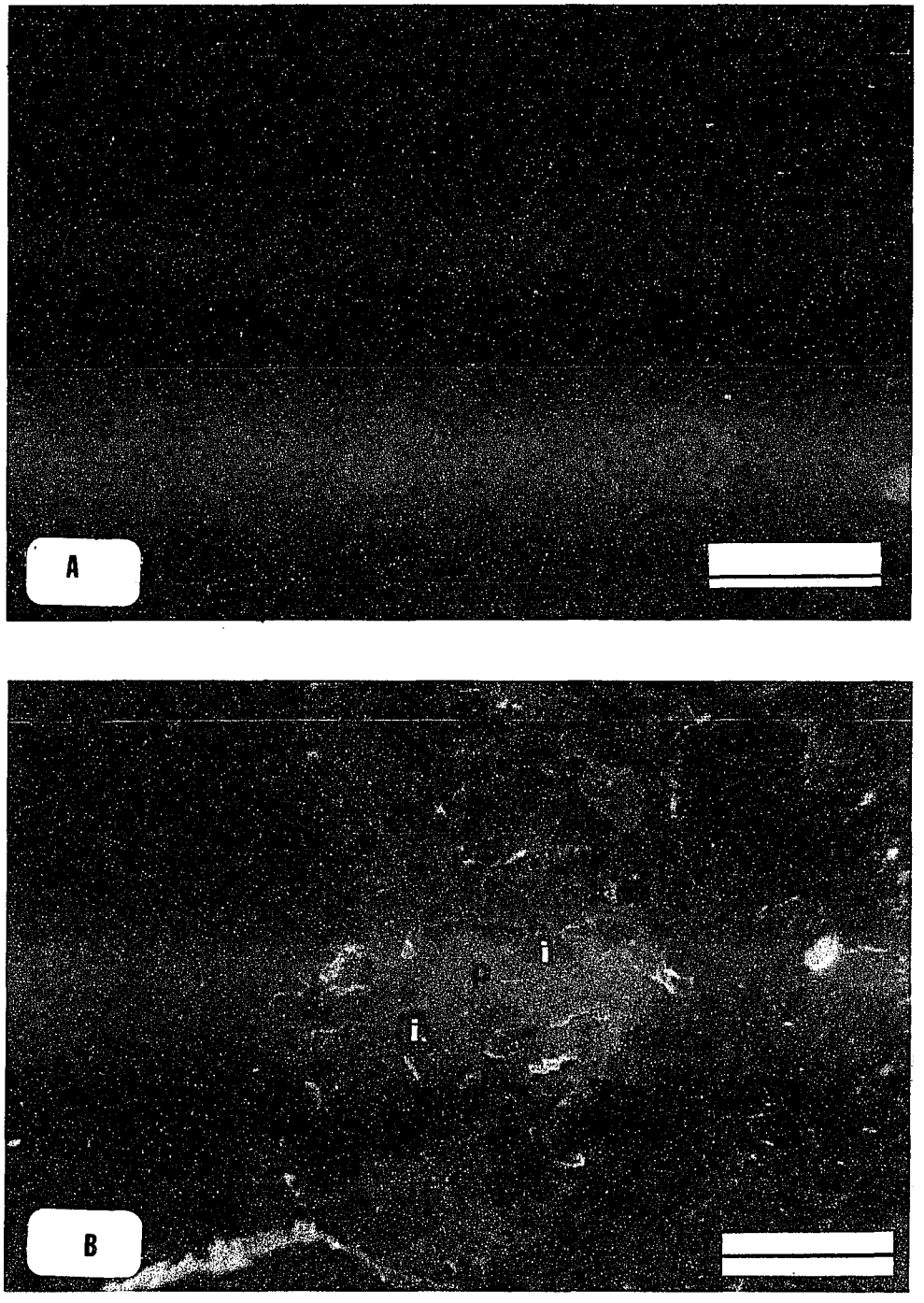


Figure 99- Photomicrographs of interparticle poikilotopic calcite cement. A) Coarse, untwinned-poikilotopic calcite cement (p) contains of inclusions (i) of early-calcite cement, under cross-polarized light. B) Interparticle poikilotopic calcite cement with a orange red luminescence contains inclusions of the non-luminescent early-calcites; under cathode light. Scales= 0.5 mm.

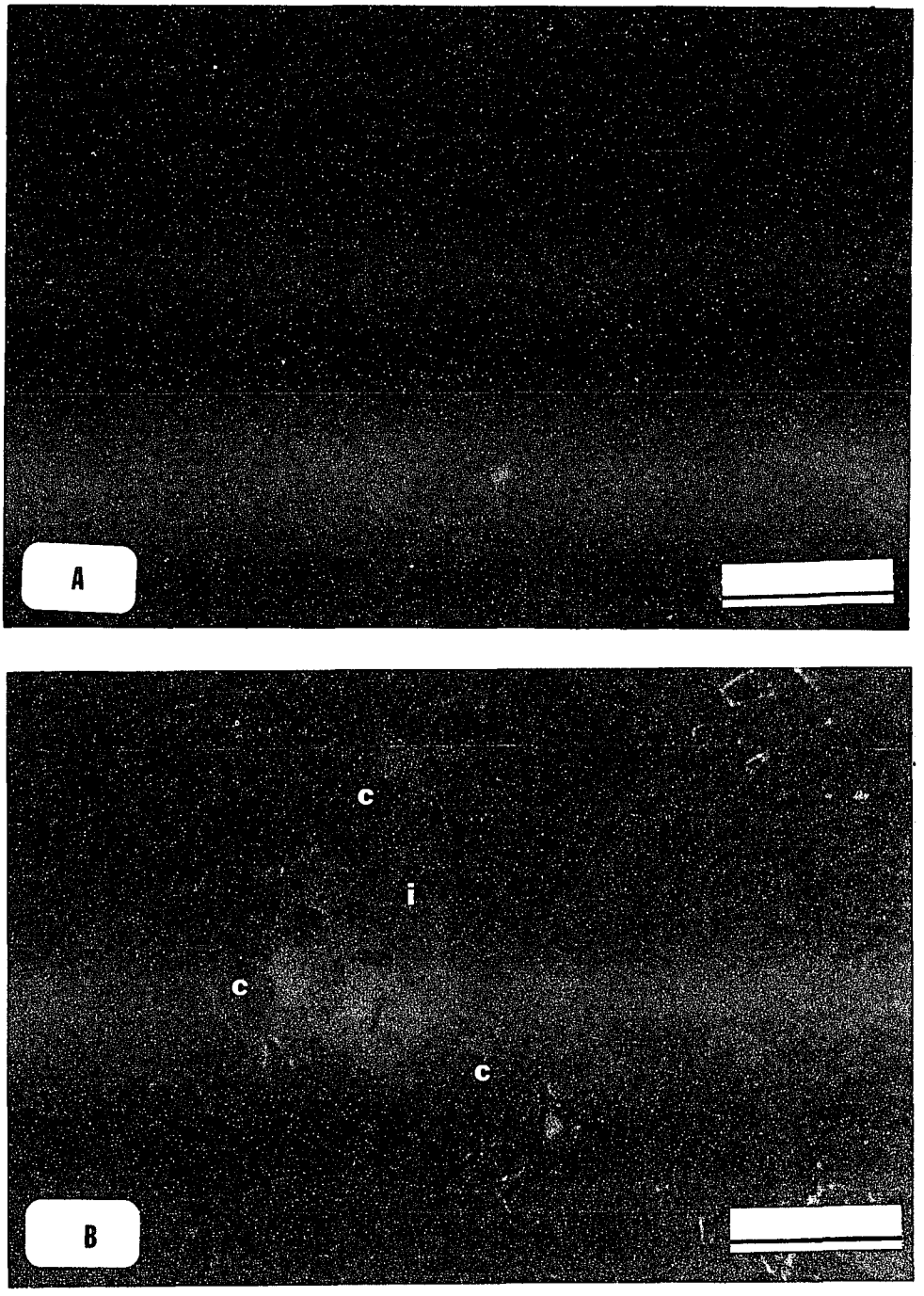


Figure 100- Photomicrographs of poikilotopic calcite cement. A) Untwinned-interparticle poikilotopic calcite cement (p) consists of inclusions of early-interparticle calcite cement (i), under cross-polarized light. B) Cathodoluminescence photomicrograph shows that non-luminescent interparticle pore-filling calcite cements appear to coarsen pore centerward, and were included as inclusions by dull to orange-red poikilotopic calcite cement. Scales= 0.5 mm.

included scalenohedral and columnar cements appear to reveal a pore centerward-coarsening texture (Fig. 99 A, B).

Figures 99 and 100 show that the contact of the void-filling poikilotopic cement and antecedent columnar cement (coarsening pore-centerward) is sharp

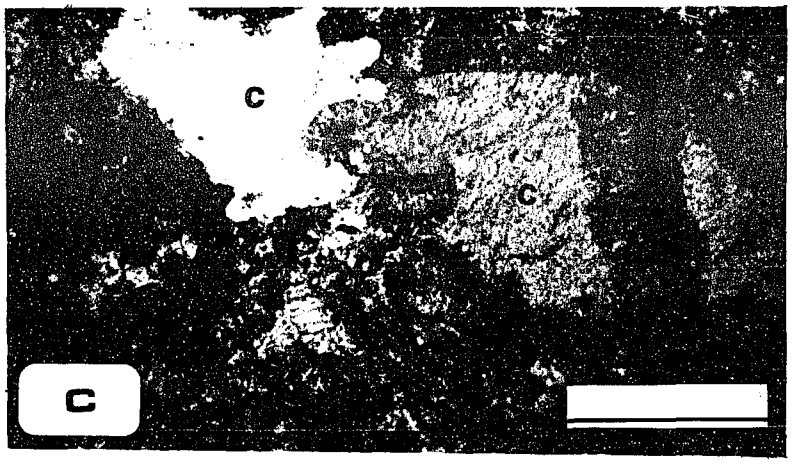


Figure 100- C) Photomicrograph of void-filling sparry calcite cement (c) in the Nuia packstone and grainstone units showing that void walls of this cement are generally sharp. Untwinned-, void-filling calcite cement appears to be a single, coarse calcite crystal and does not show a pore-centerward-coarsening texture. Under cross-polarized light; scale = 0.5 mm.

and truncational. In addition, the void-filling poikilotopic calcite cements appear to be genetically associated with late fracture-filling cement (Fig. 99 B).

Generally, the luminescence of void-filling calcite cements with and without poikilotopic texture is dull yellow-red, and the antecedent-void filling scalenohedral calcite cement reveals crystal growth zones with slight to nonluminescence.

The void-filling sparry calcite cements of the ooid and Nuia grainstone-packstone units, exhibit single grain or uniform extinction. These voids have dissolutional void walls which occur along allochems and pre-existing equant and blocky calcite cements (Fig. 100 C).

Interpretation:

Relative timing relations and close associations of the void-filling poikilotopic calcite cements with the late fracture-filling calcite cement (Fig. 99 B) and non-poikilotopic void-filling cement texture within dissolutional voids or vugs (Fig. 100 C) suggest that the void-filling coarse calcites with and without poikilotopic texture may have precipitated in the deep-burial diagenetic environment. In addition, the deep-burial diagenetic origin of this cement type can be inferred from this poikilotopic cement type, which truncates the scalenohedral cements of the fresh-water phreatic zone. Moreover, the large void-filling cements (Fig. 100 C), with or without poikilotopic texture, show a purple-red staining which indicates the ferroan-calcite composition which probably precipitated from Fe^{+2}-rich basinal solutions under somewhat reducing conditions. Fe^{+2} precipitated as pyrite crystals, and additional Fe^{+2} probably incorporated into the lattice of void-filling calcite cement under such reducing conditions. Dull orange-red luminescent of this calcite cement may indicate moderate Fe^{+2} concentrations in this cement type. The coarse void-filling calcite cements (non-poikilotopic) also show a syngenetic association with late fracture-filling cements which also show dull orange-red luminescence. This relationship suggests that the coarse void-filling calcites are not only late diagenetic, but also deep burial in origin.

Late diagenetic origin of these cements can also be inferred from the following textural relations:

1) dissolution of pre-existing calcite cement and allochems;

2) dissolutional and corrosional void or vug walls along large pores;

3) single crystal filling large pore spaces; and

4) in places inclusion of pre-existing calcite cement or allochems.

The (ferroan) poikilotopic calcite may have precipitated from basinal brines which were primarily ascending through unhealed fractures during the events of basinal dehydration. Consequently, pores directly connected to these brine-bearing fractures

were filled by this late diagenetic calcite cement. Late diagenetic poikilotopic calcite cements have been documented to be deep burial in origin and to be originating directly from the basinal brines (Mattes and Mountjoy, 1980; Moore and Druckman, 1981; Wong and Oldershow, 1981; Moore, 1985; Prezbindowski, 1985; Woronick and Land, 1985; Halley, 1986; and Choquette and James, 1988).

Absence of bitumen as an inclusion and bitumen staining (e.g., Prezbindowski, 1985) around the pore walls strongly suggests that formation of these pores may have not been related to oil migration. The opening of these late diagenetic pores is probably related to the following process: a) by mixing of fresh-phreatic water and sea water zone due to change in pH level (Kanuth, 1977); and b) by reaction of diagenetically modified basinal solutions of low-pH level with the AVL. In the AVL, even if the late diagenetic void or vug formations had occurred in the mixing zone, these voids or vugs were most likely to be occluded under deep-burial diagenesis.

Relatively dull yellow-red homogeneous luminescence probably indicates moderately reducing conditions during precipitation of these cements.

Neomorphic Equant Blocky Calcite

Description:

Equant blocky neomorphic megaspars with and without twins commonly replaced and truncated the radiaxial-fibrous cements of oolitic packstone- and grainstone units which commonly show two directional, slightly banded twinning (see Fig. 86 A in the Chap. 12 A). In the radial ooids, neomorphic equant spars replacing the radiating calcite prisms in the oolitic cortices are very common. In the center of radial ooids, these neomorphic crystals commonly aggradate into a relatively large neomorphic blocky calcite which in places contains euhedral microdolomite rhombs (see oolitic

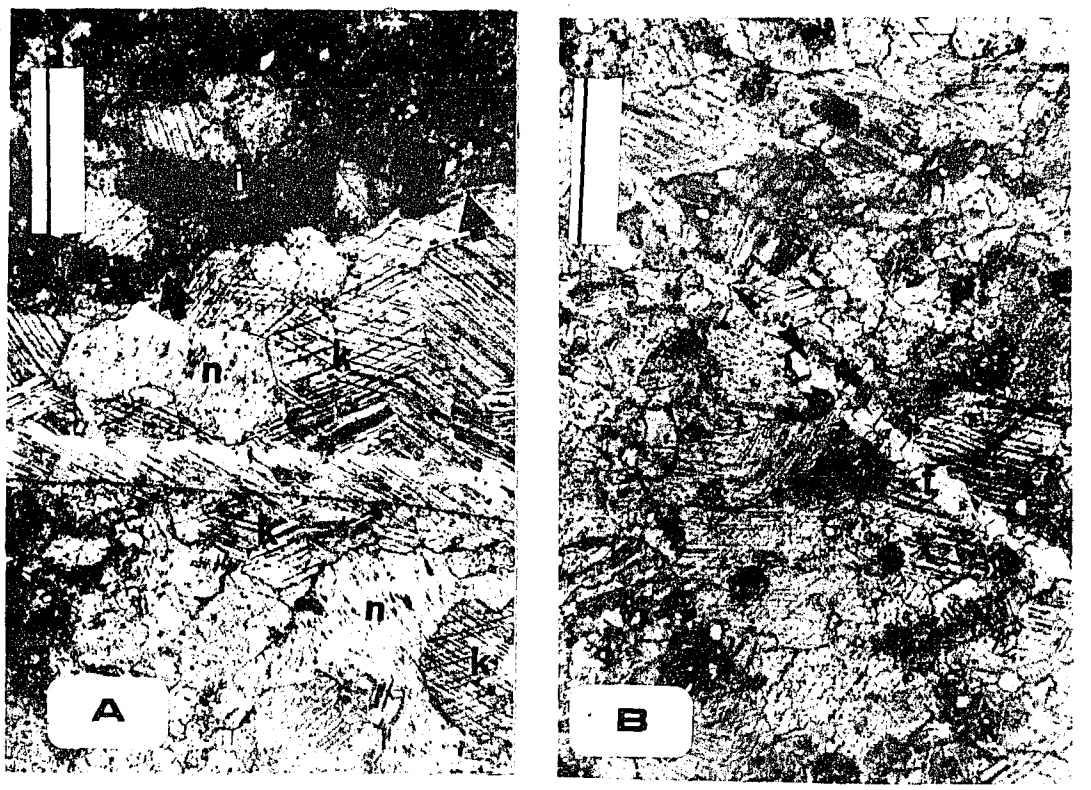


Figure 101- Photomicrographs of neomorphic blocky calcite cement. A) Untwinned-neomorphic equant blocky calcite cement (n) replaced the twined-columnar calcite cement (k) which was originally interparticle calcite. White letter (i) and large arrows point to a large intraclast. B) In peloidal packstone unit, arrowheads indicate that neomorphic equant calcite cement replaced the fracture-filling calcite cement (f). Under plane-polarized light; scales= 0.5 mm.

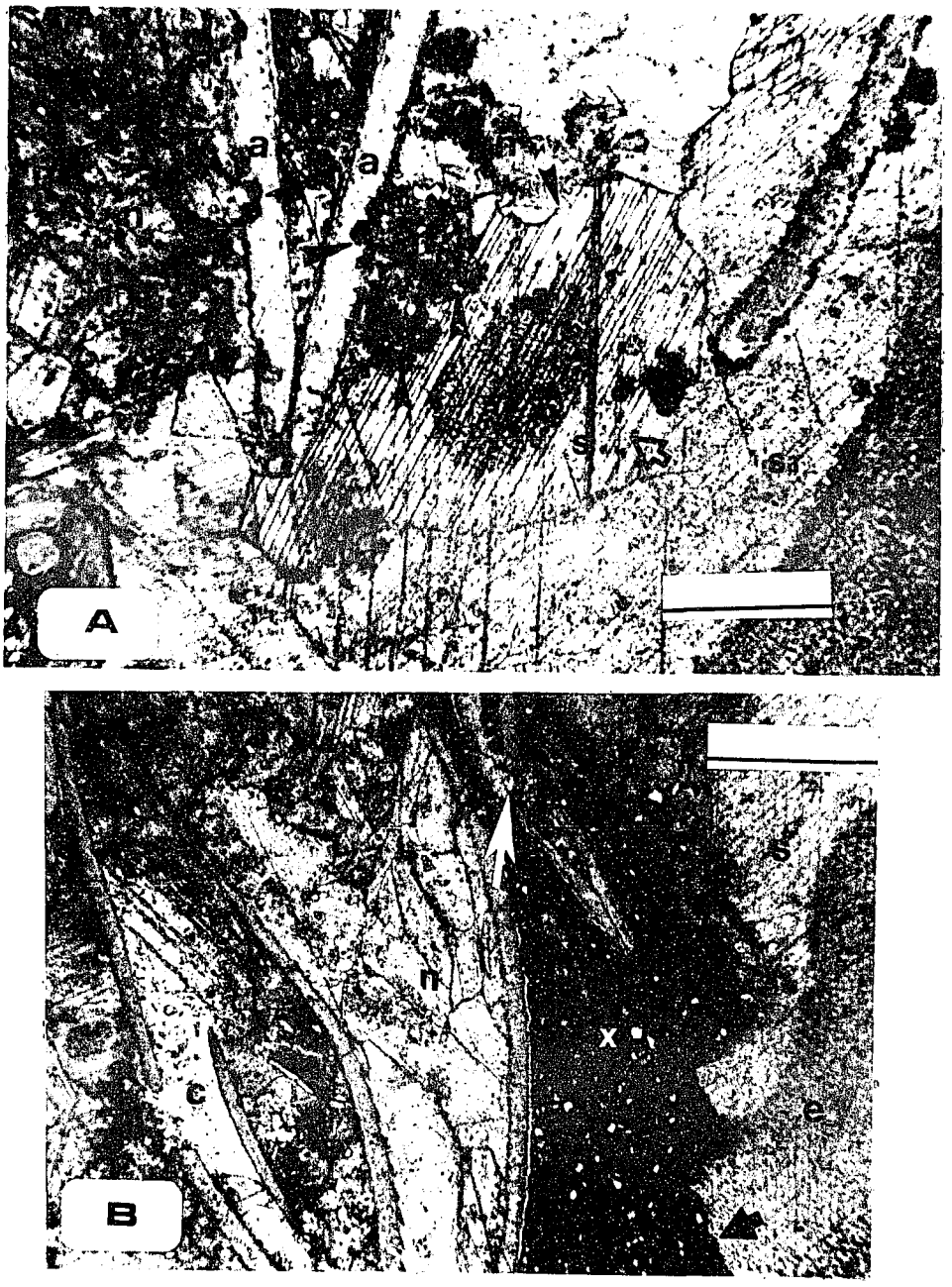


Figure 102- Photomicrographs of neomorphic blocky calcite cement of skeletal packstone units in the shelly substorm layers. A) Arrowheads point to replacement of syntaxial calcite cements (s, sa) and allochems (a) by neomorphic blocky calcite cement which appears to have originated from aggradational neomorphism of lime mud. Arrow points to optically continuous two syntaxial calcite cement crystals (sa, s). B) Neomorphic blocky calcite (n) was replaced by chert (c), and white arrow points to replacement of a mechanically broken allochem by this neomorphic blocky calcite. Silty quartz-rich mud concentration (x) in the skeletal packstone unit inhibited the formation of syntaxial cement (s) along a crinoid fragment (e). Under plane-polarized light; scales= 0.5 mm.

shoal, Chap. 6).

These cement forms are also commonly found in the neomorphic alteration of the columnar cements of the oncoidal shoal units (Fig. 101 A). The relatively large columnar cements are also terminated along the irregular crystal boundaries by coarse, equant-blocky cements (Fig. 101 A).

In the peloidal and skeletal packstone units of the back shoal, all the allochems were calcitized, and their relicts were included in sparry calcite crystals (Fig. 101 B). lack any porosity. In these cements, ostracods are identifiable by their organic-rich remnants or ghosts (Fig. 101 B). In figure 101 B, the equant neomorphic cement replaces and includes the crystals of the fracture-filling calcite cements. The calcite-filled fracture crosscuts allochems and cements (Fig. 101 B).

In the skeletal packstone units of the open shelf facies of the AVL, figure 102 A shows that the neomorphic equant cements replaced allochems and syntaxial cements of crinoids. In the same photomicrograph, arrowheads point to neomorphic calcite boundaries with unidirectionally twinned syntaxial clear calcite cement. In the same packstone units, figure 102 B shows neomorphic equant blocky calcites replacing interpreted ostracods and an iron-oxide stained, silty quartz-rich micrite concentration which includes mechanically broken spicules or trilobite; the broken edge of this allochem is selectively replaced by neomorphic equant blocky calcite crystals.

Interpretation:

The equant blocky neomorphic calcite replacing radiaxial-fibrous cement suggests that this neomorphic cement postdates the alteration of high-Mg calcite to low-Mg calcite stabilization which has been interpreted to be taken place in meteoric diagenetic environments.

The neomorphic, equant blocky cements postdating the mechanically broken ostracods and other skeletal grains suggest a neomorphism possibly postdating

mechanical fragmentation of allochems. Replacement of the inter-oncolitic columnar-void filling calcites generally coarse equant blocky cement also suggests a possible post-meteoric diagenetic neomorphic replacement. Neomorphic equant blocky spar appears to be poikilotopic and includes peloids in the backshoal lithofacies and postdates calcite-filled fractures
(Fig. 101 B). However, the extensive cementation of these units makes it very difficult for one to distinguish this cement type from early-diagenetic cements. The relict early cements are generally clear and have planar crystal boundaries, whereas neomorphically altered allochems display dusty and cloudy calcite cements and have curved crystal boundaries (see Bathurst, 1983).

The moderate twinning in the neomorphic equant calcites and their postdating calcite-filled fractures are consistent with shallow to intermediate burial depths. Neomorphic alteration of radial ooids probably may have occurred in similar diagenetic environments. The process of neomorphic replacement or alteration is going to be discussed in the neomorphic poikilotopic calcite.

Neomorphic-Poikilotopic Calcite

Description:

This poikilotopic calcite has straight to irregular (non-planar) crystal boundaries and shows uniform extinction. In places, these large calcite crystals include calcitized allochems (Figs. 103, 104). These neomorphic cements are generally clean and relatively solid inclusion free where they replace equigranular-calcite or columnar calcite mosaics (Fig. 103 B). The neomorphic poikilotopic calcite truncate interparticle equant-blocky mosaics with irregular crystal boundaries.

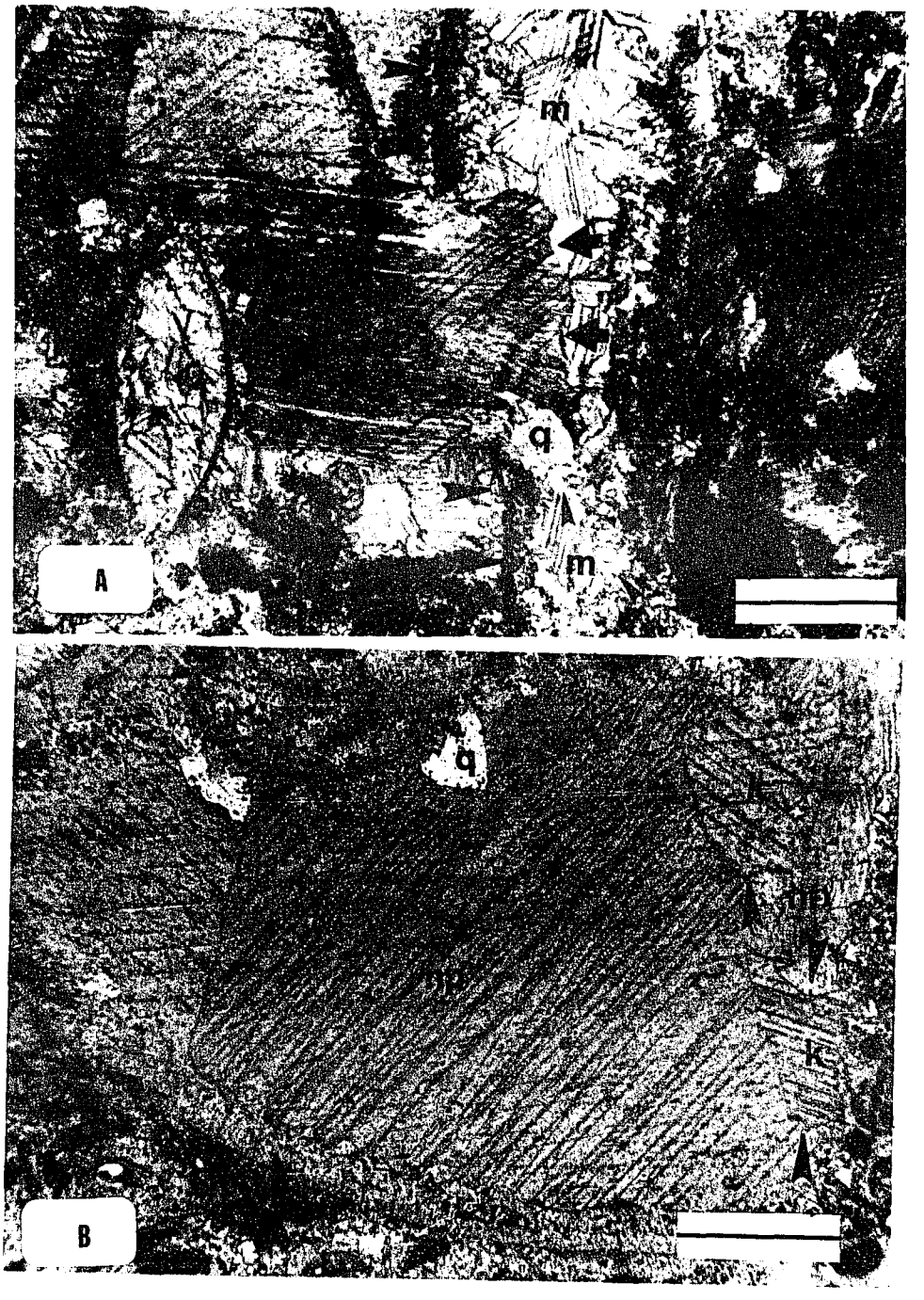


Figure 103- Photomicrographs of poikilotopic neomorphic cement in the skeletal and peloidal packstone to grainstone unit of the oolitic backshoal. A) Twinned-, poikilotopic calcite cement (np), containing drusy cement (d), penetrated into a neomorphically altered mollusc fragment (m) indicated by arrowheads. Arrows point to a penetrative crystal front of the neomorphic poikilotopic calcite cement. Under cross-polarized light. B) Coarse neomorphic calcite (np) crystal replaced and included the twined-columnar calcite cement indicated by arrowheads. (q) represents relatively late-diagenetic quartz which replaced this neomorphic poikilotopic calcite cement. Under plane-polarized light; scales= 0.5 mm.

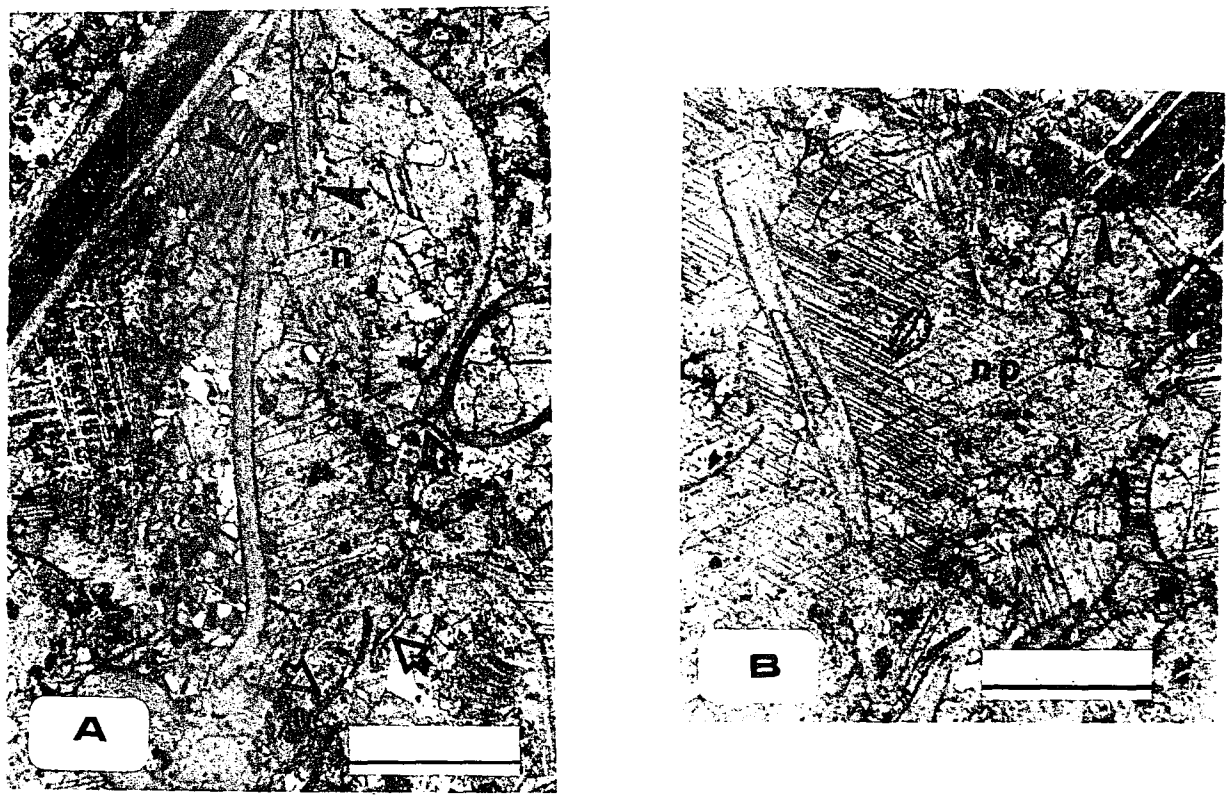


Figure 104- Photomicrographs of poikilotopic neomorphic calcite in skeletal packstone layers of the open shelf. A) Neomorphic calcite (n) replaced and poikilotopically included mechanically broken allochems indicated by arrowheads, and some ostracod fragments pointed by arrows. B) Neomorphic calcite cement poikilotopically (np) included allochems and replaced twined-crystals of calcite cement (c); arrowhead points to neomorphic replacive contact between these two cements. Under cross-polarized light; scales= 0.5 mm.

In peloidal, skeletal grainstone units, the coarse poikilotopic calcite crystals commonly include not only mechanically broken-ostracod remains but also ostracods with a drusy-cement fabric (Fig. 103 A). In addition, these neomorphic-poikilotopic calcite crystals postdate early neomorphic calcite crystals and were replaced by chert in mollusc fragments (Fig. 103 A). In oncoidal packstone- and grainstone units, coarse columnar calcite crystals coalesce into a much coarser poikilotopic calcite crystal which commonly includes and replaces precursor columnar calcite cements (Fig. 103 B).

Similar poikilotopic neomorphic calcite is common in storm layers and in the normal-graded, turbidite deposits of the slope facies and postdate the compactional grain breakage and grain-boundary microstylolites. These neomorphic calcite commonly include ostracods, and trilobites, but they do not show dissolution-precipitation fabrics (Figs. 103, 104). As indicated before, some allochems commonly occur as inclusions in neomorphic poikilotopic cement; however, there is no evidence to indicate a void-filling fabric (Fig. 104).

Under cathode light, these cements reveal a dull to slightly orange red luminescence.

Interpretation:

These neomorphic calcites are considered to be late diagenetic in origin. This inference can be substantiated from the following petrographic relations: The poikilotopic neomorphic crystals truncate the interparticle equigranular mosaics and include neomorphically altered allochems (Figs. 103, 104).

Patchy micro-equigranular calcites gradually diminish from neomorphically altered Nuia particles (Fig. 87 in Chap. 12 A). This relation indicates a gradually advanced neomorphic cementation which may have occurred along the advancing solution films. The neomorphic replacive front in places generated as a penetrative geometry into neomorphically altered mollusc fragments (Fig. 103 A). This penetrative texture also

provides additional evidence that the neomorphic poikilotopic calcites postdate neomorphically altered mollusc fragments. Thus, this neomorphic poikilotopic calcite can be considered as a late-diagenetic and deep-burial.

Formation of neomorphic cements probably resulted from thin dissolution films and simultaneous precipitation occurring along the advancing thin-solution films (Pingitore, 1976). Inclusion of some calcite cements and ghosts of skeletal fragments, and absence of dissolutional void walls and void-filling cement texture, can support a neomorphic origin of these poikilotopic cements (Folk, 1965; Bathurst, 1975; and Shroeder, 1986).

When skeletal fragments or ooids are subjected to neomorphic alterations as mentioned above, their outlines can be preserved. However, when aggradation of equant mosaics produces a neomorphic calcite spar, the neomorphic calcite do not preserve the outlines of precursor equant mosaic. For this reason, many neomorphic calcite replacing interparticle mosaic can often be interpreted as void-filling cements.

However, the presence of mechanically fractured allochems and equant spar as inclusions in neomorphic calcite spar suggests a shallow- to intermediate-burial depth for the formation of this neomorphic calcite. Selectively dolomitized peloids as inclusions in neomorphic calcites also suggest that this neomorphism event likely postdated fabric-selective dolomitization.

In the shelly subunits of storm beds and turbiditic deposits, the post-compactional poikilotopic neomorphic calcites and absence of pore centerward-coarsening texture suggest that these neomorphic calcites formed during late diagenesis at greater depths than the depth level where mechanical fractures commonly take place. However, in these slope deposits, neomorphism occurs in two forms, the first of which is equant blocky neomorphic calcites, and the second of which is coarse poikilotopic calcites (about 4 mm). The coarse poikilotopic calcites appear to have formed via neomorphic alteration of some allochems and aggradation of equant spars.

This study has shown that neomorphic calcite replacement is an important process from deep-phreatic to deep-burial diagenetic environments.

The three possible sources of solutions for these neomorphic cements are, as follows: (1) fluid inclusions, (2) remaining of diagenetic solutions from meteoric

diagenesis, or marine water entrapped in the pores, and (3) diagenetically modified formation water or basinal brine.

Generally, homogeneous dull-luminescence probably represents the moderately deep-burial diagenetic environments in which moderate reducing conditions prevail. Especially, presence of replacive quartz (chert) probably suggests the sulfate reduction by microbial activity or during the thermochemical sulfur reduction "TSR" (see Machel, 1987; 1989). The TSR which contemporaneously dissolves calcite and allows silica to precipitate. Lack of vugs or voids around these neomorphic solutions probably suggest that dissolved $CaCO_3$ during the silica precipitation probably advanced with addition of more dissolution calcite and simultaneously became supersaturated with respect to calcite. Eventually, the calcite-supersaturated solutions probably concomitantly reprecipitated behind the continuing dissolutional fluids.

CHAPTER 13: DOLOMITE TYPES AND CHEMISTRY, AND A MODEL FOR PERVASIVE DOLOMITIZATION

CHAPTER 13 A: DOLOMITE TYPES

On the basis of petrographic features, dolomite stoichiometry, stable-isotope geochemistry, and timing, nine kinds of dolomite have been recognized in the AVL. Dolomite I is a dull to non-luminescent euhedral dolomite in the stromatolitic lime mudstones. Dolomite II is brightly yellow luminescent euhedral dolomites found in the organic matter-rich, fine-grained concentrations of the skeletal packstone- and wackestone (Lithofacies 20 A) layers of the slope and deep-ramp facies in the Whiterock Canyon section. This dolomite type appears to be a synsedimentary marine dolomite in origin. Dolomite III selectively replaced the Girvanella oncoids of the oncoidal shoal lithofacies. Dolomite IV is a zoned dolomite, selectively replacing the calcite-filled ooids and syntaxial cements of the oolitic and skeletal shoal units in the Lone Mountain section. Dolomite V, also a zoned dolomite, is found in the Nuia-rich skeletal packstone units of the open-shelf facies of the Lone Mountain section. Dolomite VI, stylolitic and patchy ferroan dolomite, replaced organic-rich peloids, intergranular calcite mosaic, and oomoldic calcite in the shoal and shelf facies. Dolomite VII, replacive mosaic dolomite, is the dolostone units of the AVL and volumetrically is the most important dolomite type. Dolomite VIII is a fracture-filling dolomite and postdates the dolostone units of the AVL. Dolomite IX is a fracture-filling saddle dolomite, post dating the dolostone units (Dol. VII) of the AVL.

Dolomite Type I

Description:

Fine to medium-crystalline euhedral dolomite rhombs (Fig. 105) are scattered within fine-grained, silty and organic-rich concentrations which locally fills the interparticle spaces of the shelly basal sublayers of storm deposits of the upper slope- depositional environment (Lithofacies 20 A). Euhedral dolomite crystals with slightly brownish outline due to iron-oxide staining are scattered within the fine-grained matrix. The nearly uniform euhedral dolomite crystals in places show zones which have a relatively cloudy center and cleaner rims. Under the cathode light, these rhombs have a bright yellow luminescence (Fig. 105 B). Despite euhedral outline of these dolomite crystals, some dolomite rhombs appear to have been replaced by calcite cement (Fig. 105 B). The overall percentage of this dolomite is less than 5 % of partially dolomitized-shelly units, but in sheltered pores it is more than 60 %.

Interpretation:

Concentration of euhedral dolomite crystals within patchy, organic-rich fine matrix indicates a fabric-selective dolomitization (Fig. 105). Near-surface dolomitization models, such as mixing zone, sabkha or reflux seepage, can not be applied to these dolomites because the shelly units in which this dolomite type occurs represent open shelf or basinal facies. These shelly units were never exposed to meteoric diagenesis during sedimentation or early diagenesis.

Bright yellow luminescence indicates that they are Fe^{+2}-poor in composition. This can be confirmed by the syngenetic occurrence of pyrite and siderite with Dol. I. The brownish staining indicates late oxidation of pyrite or siderite. The petrographic vidence suggests that this dolomitization was early diagenetic in origin and took place

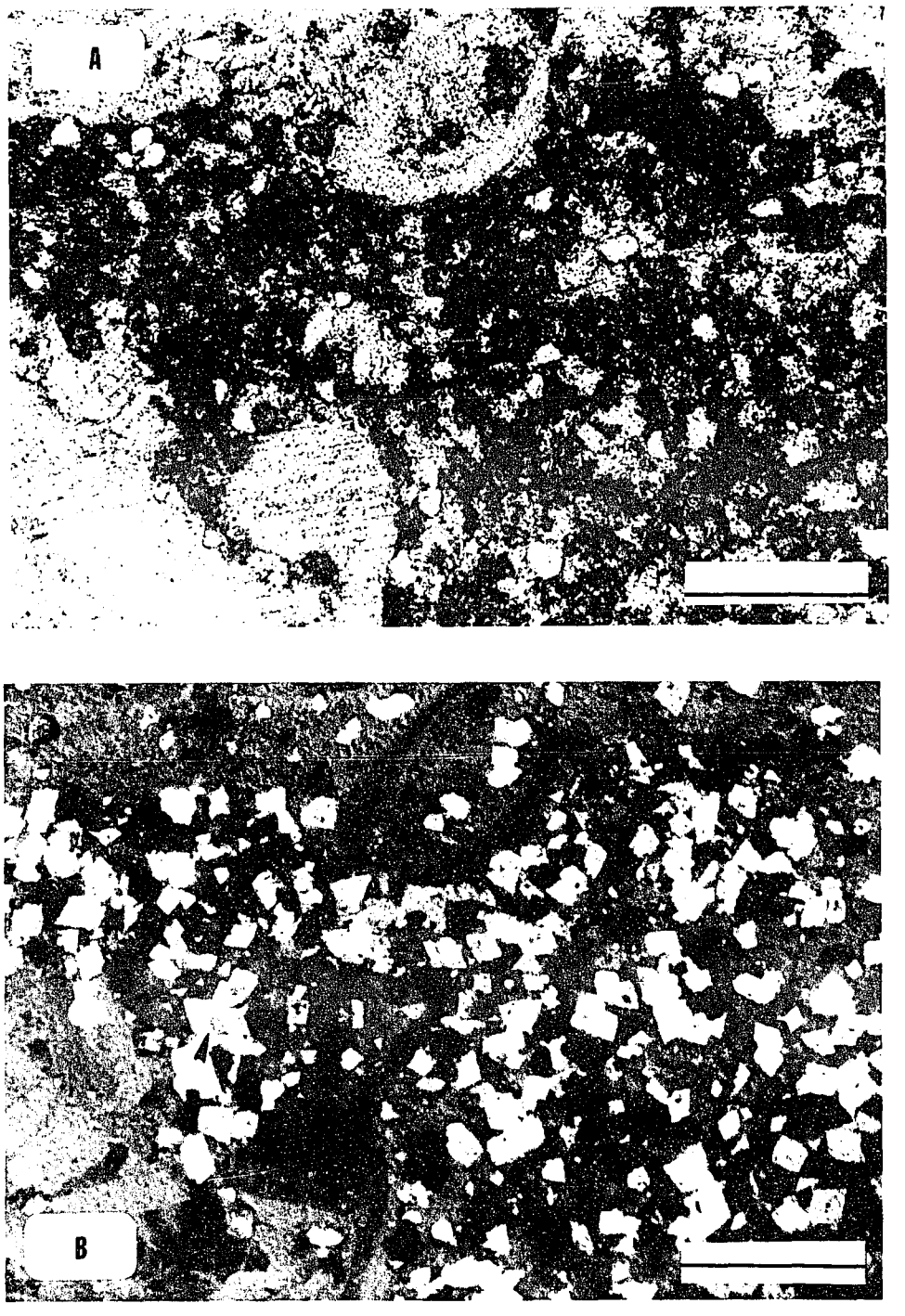


Figure 105- Photomicrographs of dolomite type I. A) Euhedral dolomite rhombs with slightly red brown-staining are within the locally concentrated fine-grained siliciclastics in the skeletal sublayers of storm beds. Plane-polarized light. B) The idiotopic dolomite crystals reveal bright yellow luminescence, and quartz silt particles are nonluminescent; arrowhead points to zoning in some dolomite crystals. Under cathode light; scales= 0.25 mm.

as replacement of organic matter-rich, fine-grained matrix in the lithofacies 20 A. Thus, this dolomitization process is a post-depositional feature (see Lumsden, 1990). Fe^{+2}-poor composition of these dolomites and their fabric-selective nature can be used to differentiate this kind of dolomite from Fe^{+2}-rich, source-dependent stylolitic dolomites (see Wanless, 1979; McHargue and Price, 1982).

Selective replacement of the fine matrix during early submarine diagenesis below the sediment-water interface can be related to available nucleation sites and greater surface areas of fine grain in the matrix compared to coarse-grained allochems (Sibley, 1982; Bullen and Sibley 1984; and Sibley et al., 1987). In this diagenetic environment, microbial activity eliminates the inhibiting effect of sulfate (in sea water) on dolomitization by simply reducing sulfate into sulfide (Kastner et al., 1977, Baker and Kastner, 1981; Baker and Burns, 1985; Burns et al., 1988; and Morrow and Ricketts, 1988). Sulfate reduction by microbial activity in organic-rich sediments can be initiated by oxidation of organic matter. This, in turn, raises the amount of HCO_3 in pore waters which leads to the process of dolomitization. Depth of dolomitization, in this process, is limited to either to the zone of diffusion of Ca and Mg into sediments from the overlying sea water or the maximum extent of SO^{-2}_4 reduction by microbial activities. Normally, if sediments contain high-organic carbon contents or sedimentation rates, sulfate is completely depleted in 100 meters (or less) from the sediment-water interface (Gieskes et al., 1984).

Authigenic dolomitization of this kind was first reported by Friedman (1964) from the Bermuda Apron, and in the hemipelagic and pelagics of the DSDP by Hein et al. (1981) and Garrison (1981). Matsumoto (1983) analyzed the DSDP pelagics and hemipelagics taken from the Blake Outer Ridge and found that dolomites and siderites of these modern sediments were authigenic. He also recognized two kinds of authigenic dolomite textures: (1) scattered, euhedral-calcian dolomites, and (2) ferroan dolomites with interlocking-crystal forms. On the formation of these dolomites, trace elements of Ca and Mg are assumed to have been incorporated into dolomite from sea water; Fe and Mn were derived under reducing conditions from detrital ferromanganese oxide-coated, fine-grained sediments (Matsumoto, 1983; and Burns et

al. 1988). Occurrences of fine-grained pyrite and oxidized-dolomite outlines confirm this assumption.

Dolomite Type II

Description:

Fine to medium, euhedral dolomite rhombs are scattered and aligned along the black organic-rich laminae of the stromatolitic mudstone units (Fig. 106). These dolomite rhombs range from 0.001 to 0.005 mm in size. They are also commonly found in the Girvanella coating, concentric-oncoid laminae, and in the organic-rich laminae of stromatolites. These dolomites are non-stoichiometric, with 45 mole % of $MgCO_3$ in their composition. Luminescence of this dolomite varies from bright dull red to nonluminescent.

Interpretation:

Preferential occurrences of these dolomites in the organic-rich (Fig. 106) laminae indicate that dolomitization of these sublayers are closely associated with composition of the organic-rich layers. Friedman et al. (1973) showed that organic-rich laminae in stromatolites are primarily high Mg-calcite in composition, and alternating layers are

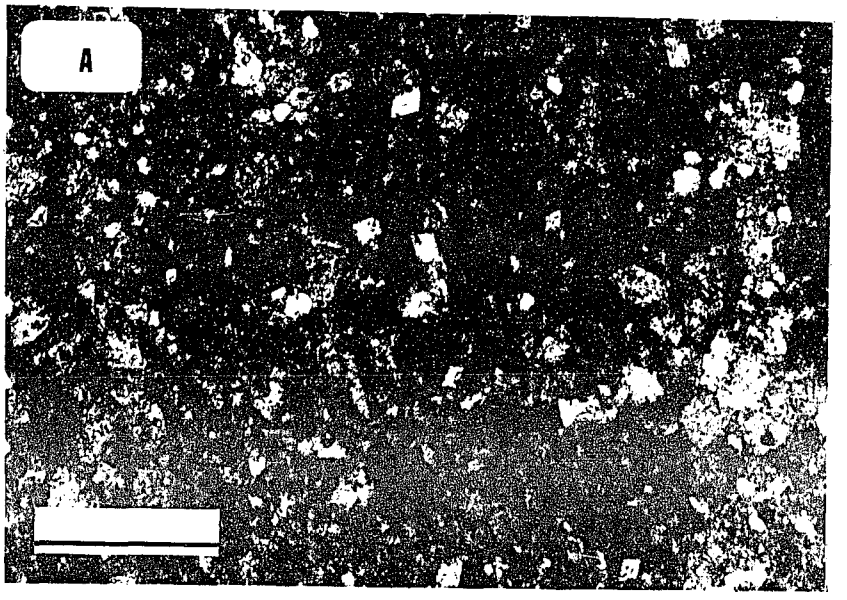


Figure 106- Photomicrograph of dolomite type II. Idiotopic dolomite rhombs scattered within the organic-rich laminae of cryptalgal laminae. Under plane-polarized light, scale= 0.5 mm.

aragonitic in composition. Thus, it can be inferred that Mg needed for dolomitization in dolomite Type II was obtained directly from the organic-rich laminae (Gebelein and Hoffman, 1973).

Non-stoichiometry of dolomite Type II suggests that it formed from early and near surface dolomitization (Morrow, 1982; Land 1985; and Sibley, 1990). Preservation of early nonstoichoimetry despite long burial history of the AVL also suggests possible early lithification and near-surface dolomitization. During the long course of burial, the dolomite type II-bearing units or subunits must have been closed to diagenetic fluids; otherwise, these non-stoichiometric dolomites would have converted to more ordered dolomite either due to replacement or neomorphism.

Therefore, dolomitization of the stromatolitic units in the AVL most likely took place either before or during lithification but not after. The various types of luminescence and their intensity can be related to the oxidation and reducing conditions of the environment or in other words, to the fluctuation of Eh level in the environment (Frank, 1982; Grover and Read, 1983).

Dolomite Type III

Description:

Medium- to coarse-grained dolomites are very common in the packstone lithofacies of oncoidal shoal, particularly at the Antelope Valley region. These medium to coarse-grained, euhedral dolomite crystals generally range in size from 0.1 to 0.30 mm and are commonly found in oncoids (Fig. 107). More specifically, they occur in the calcitized algal laminae at the center of oncoids, or along the boundaries of interoncoidal concentric laminae, or pressure-solution laminae boundaries.

Dolomite type III can easily be differentiated from the previously described dolomite type II by coarser crystal size, distinctive luminescence, and zonal textures (Fig. 107 A and C). Two distinct zones in these dolomites can be recognized under plain light-- a solid inclusion-rich cloudy center and a clear rim, but under cathode light, both are nearly homogeneous, bright-dull red. Rarely, the inclusion-rich zone shows a slightly brighter luminescence than that of clear rim.

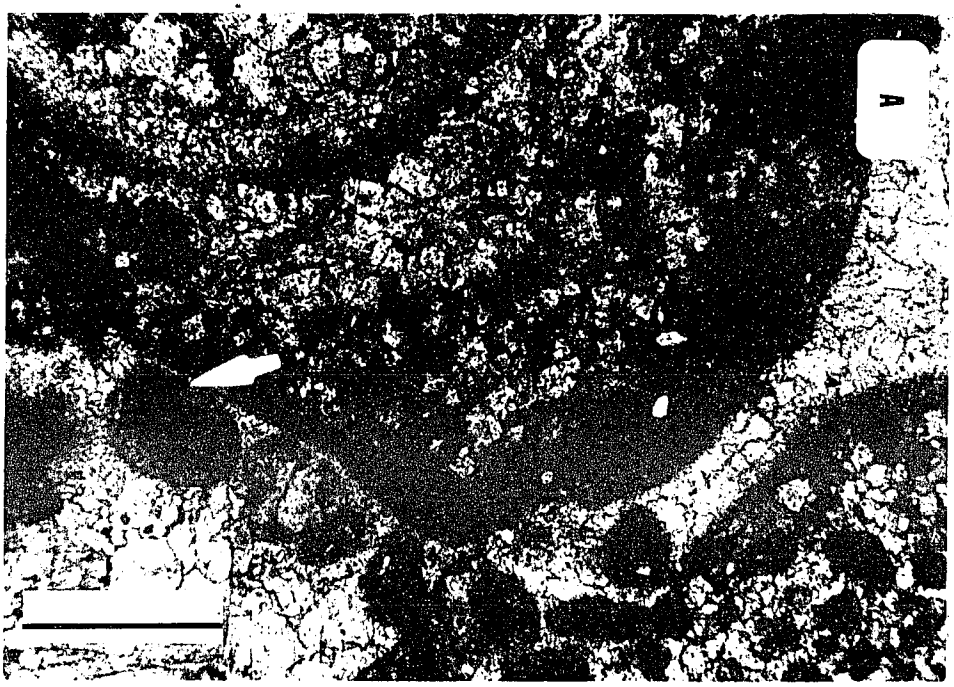
As indicated before, dolomite euhedra are generally restricted to oncoids, peloids or intraclasts of a possible Girvanella origin, and rarely in the calcite pseudomorphs in the core of oncoids, but not in the interparticle cement. Commonly, this dolomite type selectively replaced the partially calcitized, upward-growth form of Girvanella laminae, but not tightly intertwined encrusting-growth form of Girvanella laminae or peloids and intraclasts (see Chap. 5).

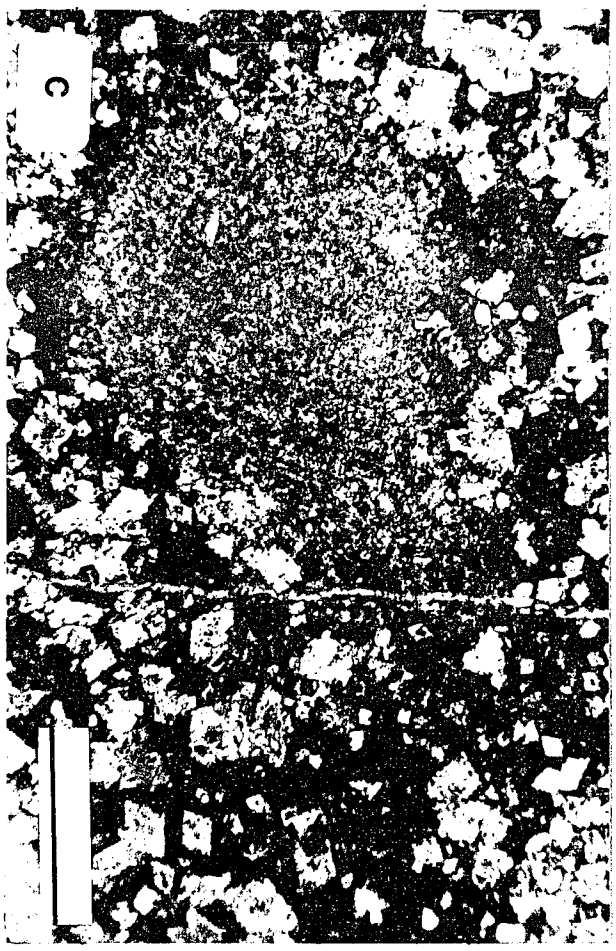
The petrographic relationship between this replacive, euhedral, zoned-dolomite type and other diagenetic products of the oncolitic packstone- and grainstone lithofacies are, as follows:

(1) These dolomites replaced the fracture-filling calcite cement that postdates both interparticle cement and oncoids (Fig. 107 B).

(2) Unhealed fractures cut across these euhedral dolomites, having been stained by organic residue of hydrocarbon.

Figure 107- Photomicrographs of dolomite type III. A) Zoned-euhedral dolomite rhombs selectively replaced allochems and calcitized-Girvanella filaments. White arrow points to a radial ooid containing an algal (Girvanella) nucleus which resisted to fabric-selective dolomitization. B) Type III dolomite replaced the fracture-filling calcite cement indicated by arrows, and this dolomite type is more common at the center of oncoids where upward-growth form of Girvanella are more prominent. White arrow points to authigenic quartz. C) Dolomite type III selectively replaced the upward-growth form of Girvanella at center of an oncoid; under plane-polarized light. Scales= 0.5 mm.


A


C


B

3) Some of the relatively fine, euhedral dolomite crystals are replaced by authigenic quartz (Fig. 107 B).

4) These dolomite crystals are commonly found along intraoncoidal laminae (Fig. 107 B).

Stable isotope composition of two samples of dolomite Type III ranges from -4.07 to -4.95 ‰ PDB for $\delta^{18}O$, and -0.50 to -0.55 ‰ for $\delta^{13}C$. Mole percentage of Mg CO_3 in these dolomites is 48%.

Interpretation:

Despite the presence of two zones in the euhedral dolomite crystals, relatively homogeneous luminescence in them implies that there is no compositional variation with respect to Fe^{+2} and Mn^{+2} in these zones.

Cloudy and solid inclusion-rich centers of dolomite crystals represent precipitation from a solution with a low Mg/Ca ratio, whereas the clear rims represent dolomitization from the same solution progressively enriched in Mg (high Mg / Ca ratio), at a very slow crystal growth rate. Ward and Halley (1985) and Humphrey (1988) have postulated for Holocene dolomites that as dilution of sea water progressively increases with respect to Mg/Ca, dolomitization follows the following order: dolomite, calcian dolomite and calcite. These studies show that dolomitization follows a different course from the progressively diluted-dolomitizing solutions with respect to Mg / Ca ratio proposed by Folk and Land (1975). For the zonal texture of dolomite Type III, it is proposed that progressive saturation of Mg in a dolomitizing fluid caused a transition from the cloudy, solid inclusion-rich dolomite to clear dolomite rim.

Selective dolomitization of partially calcitized upward growth forms of Girvanella or oncoidal laminae is probably related to relatively higher permeability of this growth form compared to the tight, nonporous concentric laminae of Girvanella.

Grain-size variations of euhedral dolomite crystals in the selectively dolomitized

areas are probably associated with spatial permeability variation in these microdiagenetic environments, and to flow directions of the dolomitizing fluids.

The close relations of this dolomite with intra-oncoidal, pressure solutions along concentric laminae of oncoids, post-fracture dolomitization, authigenic quartz replacement and bright-to-dull luminescence suggest that dolomitization was probably synchronous with pressure solution developed concentric oncoidal laminae and postdated the late fracture-filling calcite cement.

Therefore, a shallow to intermediate burial diagenetic environment can be inferred for this dolomite type from the above-mentioned sequence of diagenetic events. This inference is also consistent with the oxygen-isotope composition of this dolomite type.

An average $\delta^{18}OD_{ol.III}$ of -4.48 ‰ PDB represents much greater burial depth than surface and near-surface dolomitization. Such $\delta^{18}O$ composition is 1.7 ‰ PDB more enriched in ^{18}O than the estimated-$\delta^{18}O$ values of the Middle Ordovician marine calcite ranging from -6 to -7 ‰ PDB (Ross et al., 1977; Popp et al., 1986; and Lohmann and Walker, 1989). The Middle Ordovician $\delta^{18}O_{calcite}$ values in equilibrium at 25 °C reflect estimated-$\delta^{18}O_{water}$ values ranging from -3.71 to -4.71 ‰ SMOW for the Middle Ordovician sea water. By using the oxygen-isotope fractionation equation by Land (1983), the $\delta^{18}O$ value of dolomite in equilibrium with the Middle Ordovician sea water at 25 °C is estimated to have ranged from -1.89 to -2.80 ‰ PDB (average $\delta^{18}O$= -2.34 ‰ PDB).

$10^3 ln\alpha = 3.2 \times 10^6 T^{-2} - 3.3$ (Land, 1983).

Oxygen-isotope composition of Dolomite III is -2.2 ‰ more depleted the estimated-$\delta^{18}O$ value of dolomite in equilibrium with the Middle Ordovician sea water at 25 °C. This additional dilution could be associated with either meteoric-water origin or equilibration at high temperatures (either by neomorphic alteration of early dolomites or direct replacement by hot basinal solutions). In this study, however, no neomorphic replacement or textural relations in Dolomite III were observed (see Shelton and Gregg, 1989). $\delta^{13}C$ values of Dolomite III is slightly depleted and almost occurs in the range of the estimated-carbon isotope values (0 to +1 ‰ PDB). Thus, petrographic and isotopic data suggest that diagenetically modified pore-filling seawater was probably

responsible for the formation of Dol. III.

The $\delta^{18}O_{Dol.\ III}$ value of -4.905 ‰ PDB corresponds to 39 °C equilibration temperature by using the oxygen-isotope fractionation equation for dolomite (Land, 1983). For 20 °C surface temperature and 30 °C/km geothermal gradient, 39 °C equilibration temperature reflects a burial depth of 635 m during formation of this dolomite type.

Composition of the dolomite type III may be more stoichiometric than its measured stoichiometric composition of 47.8 mole percent of $MgCO_3$ if the dolomite type II are not present in oncoidal laminae. Thus, $dolomite_{(104)}$ reflection peaks of the dolomite type III reflect a combined composition of the dolomite type II (non-stoichiometric) and dolomite type.

Dolomitization of this type took place at the shallow- to intermediate-burial depths where Girvanella may have released Mg (e.g, Gebelein and Hoffman, 1973). Therefore, Mg was possibly derived from local sources rather than allochthonous basinal brine.

Dolomite Type IV

Description:

This zoned-dolomite was only observed in the ten-feet thick oolitic packstone and grainstone and in the three-feet thick crinoidal packstone and grainstone lithofacies, at the interval of 240 and 253 feet from the base of the Lone Mountain section. Euhedral-zoned dolomites are identified in the both lithologic shoal units by their coarse crystal sizes, cloudy centers and clear crystal rims (Fig. 108 A).

Oolitic lithofacies, cemented by bladed- and equant-blocky interparticle cement, consists of two types of ooids: (1) ooids filled by sparry calcite cement were selectively dolomitized by dolomite IV; and (2) radial ooids with an algal nucleus

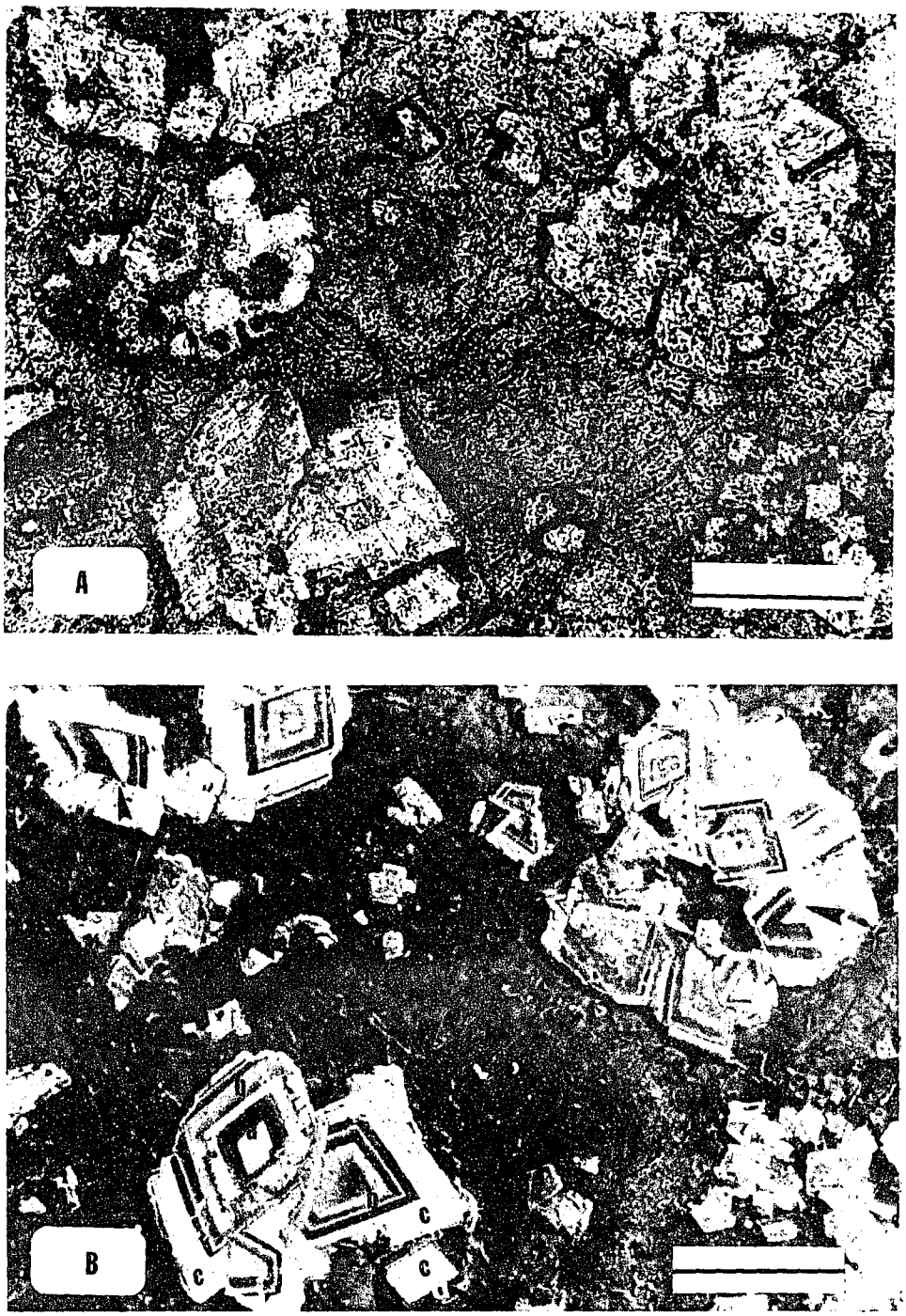


Figure 108- Photomicrographs of dolomite type IV. A) Selectively dolomitized oomold-filling calcite cement of oolitic grainstone units. (s) designates euhedral zoned-dolomite rhombs. Under plane-polarized light. B) Coarse euhedral dolomite crystals under cathode light reveal four major luminescent zones: a, b, c, and d. Arrowheads point to truncational contacts between zone b and c. Scales= 0.25 mm.

were neomorphically calcitized and were resistant to dolomitization. Relatively small euhedral, zoned rhombs replaced the algal core of radial ooids.

In crinoidal packstone- and grainstone units, dolomitization is of two kinds: (1) scattered-, micro-euhedral rhombs about 50 μm in crinoid grains (Fig. 109 A), (2) cement and replacive, euhedral-zoned dolomites of 0.2 to 0.5 mm within interparticle pores and along grain boundary pressure solutions, and patchy replacement of some allochems (Fig. 109 A). Major cement type in this skeletal grainstone unit is syntaxial cement with four-recognizable zones, all of which were replaced by replacive-zone dolomites, and remaining pores were occluded by the same dolomite cement of this kind (Fig. 109 A).

Dolomite zones:

Generally, the first-three luminescent zones in the dolomite crystals of oolitic lithofacies, and four continuous zones in the dolomite crystals of crinoidal packstone and grainstone lithofacies were differentiated by cathodoluminescence (Figs. 109, 110, 111, and 112).

Zone I (a):

This zone includes a very bright, orange-red, mottled-central dolomite rhomb, two moderately thick, nonluminescent bands separated by a moderately thick orange-red luminescent band. All the bands are regular and planar, and no truncations occur between them (Figs. 108 A, 109, 110, 111 and 112).

Zone II (b):

This zone consists of four bands: first of which is a dull luminescent and relatively thick band followed by non luminescent, moderately thick band which is separated from the similarly luminescent fourth band by a thin, bright-dull orange red band. Some crystals in places start with zone II (Figs. 109 B, 111 B).

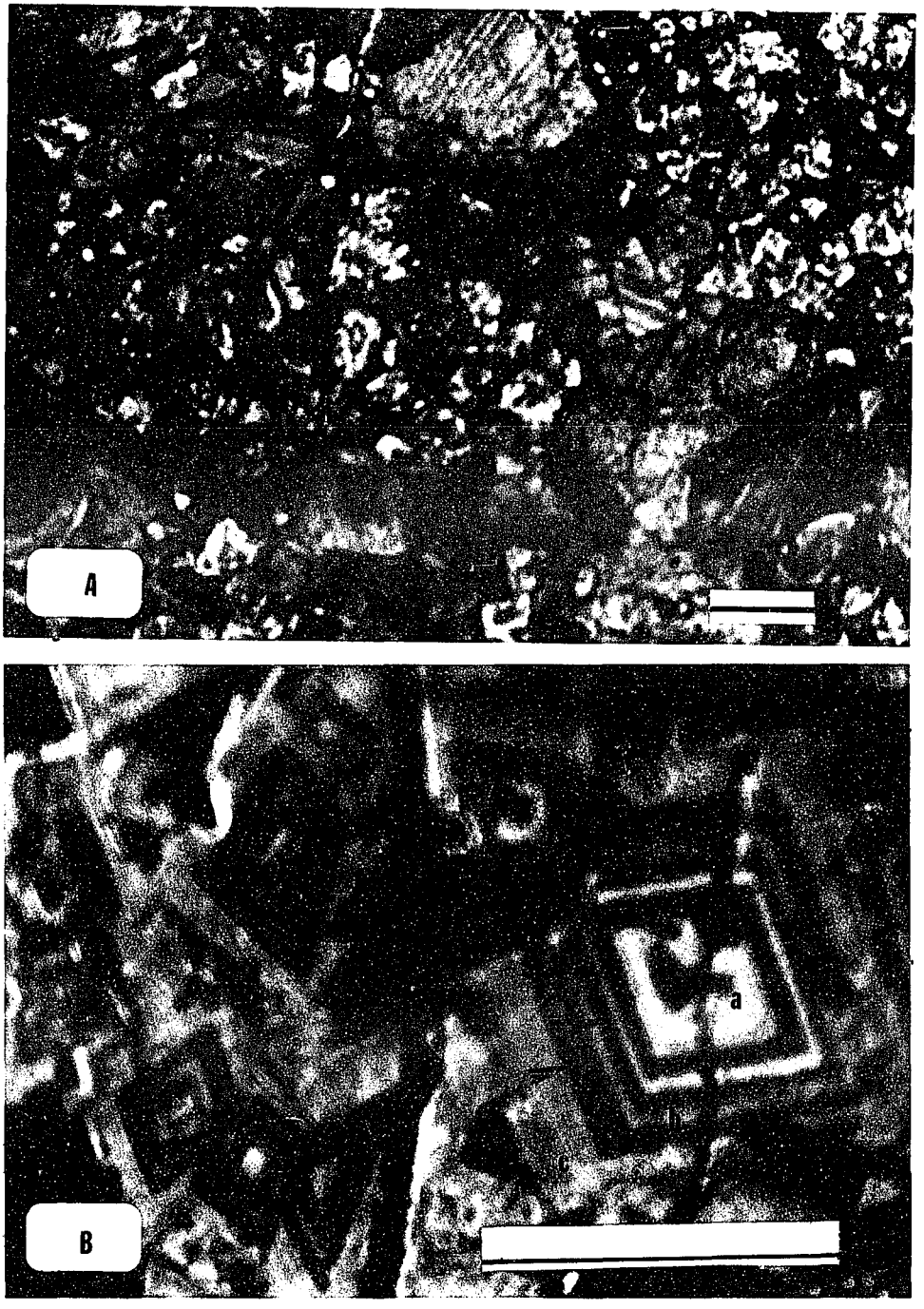


Figure 109- Cathodoluminescence photomicrographs of dolomite type IV. A) Zoned-euhedral dolomite rhombs contain continuous zones from (a) to (c), and all the zones of this dolomite type postdate the latest zone (4) of the syntaxial calcite cement in the crinoidal packstone-and grainstone unit. (1), (2), (3), and (4) are the zones of syntaxial calcite cement. B) Dolomite type IV rhombs selectively replaced the oomold-filling calcite cement in oolitic grainstone units and reveals the same continuous luminescent zones from "a" to "d", and arrowheads point to truncational contacts among the dolomite zones of "a" and "c", and "b" and "c". Scales= 0.25 mm.



Figure 110- Photomicrographs of dolomite type IV. A) Dolomite type IV selectively replaced an allochem; arrowheads point to zoned-dolomite rhombs. Under plane-polarized light. B) Close view of photomicrograph A under cathode light shows that zones (a, b, and c) of the dolomite type IV are regular and continuous, and no truncational contact in crystal level can be recognized among these discrete luminescent zones. Arrowheads indicate boundaries among the luminescent zones of a, b, and c. Scales= 0.25 mm.

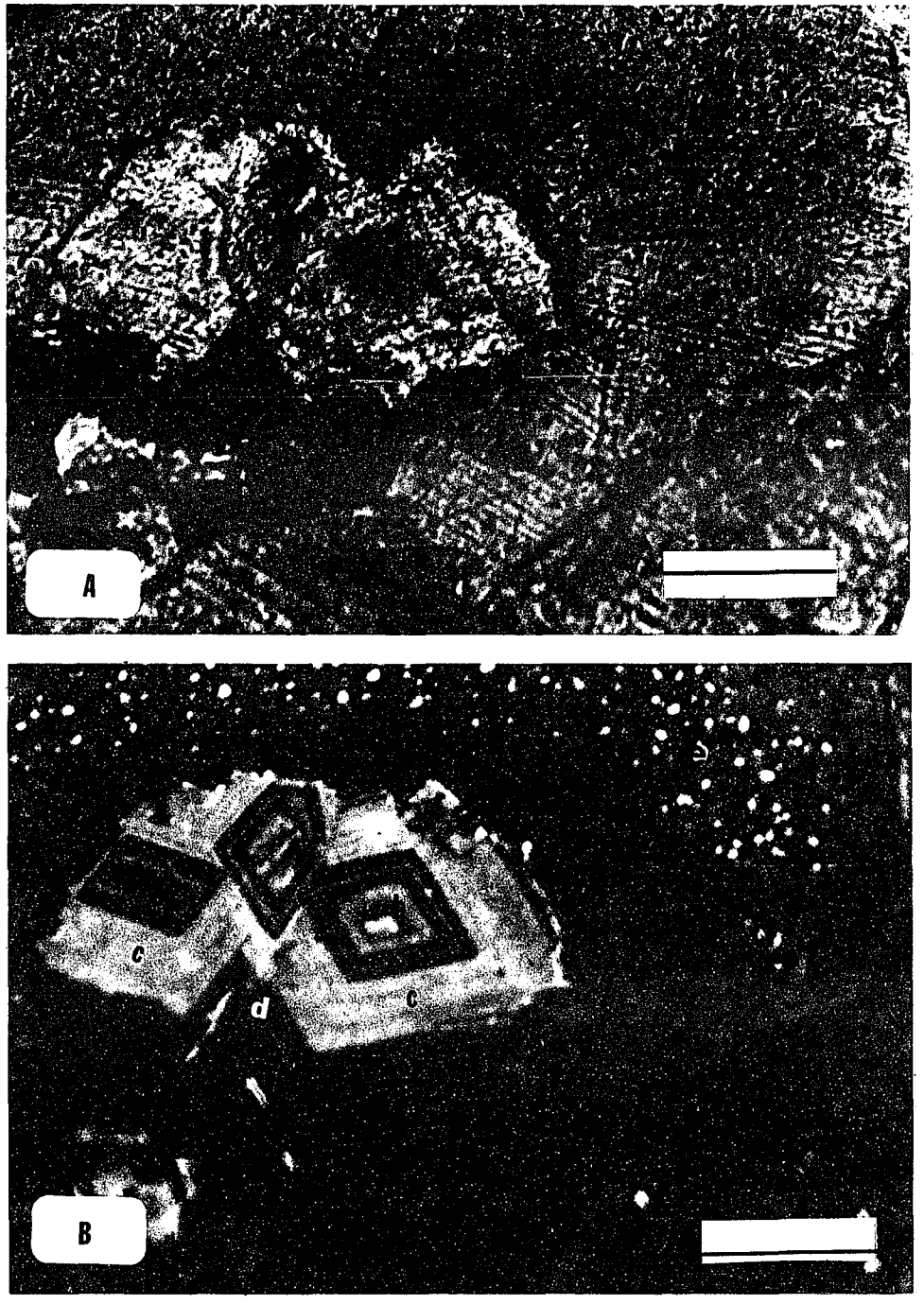


Figure 111- Photomicrographs of dolomite type IV. A) Dolomite type IV under plane-polarized light shows an inclusion-rich, dark cloudy center (d) and clear outer rim. B) The same view of photomicrograph A under cathode light reveals three discrete luminescent zones of b, c, and d. Zone "d", a dark and nonluminescent zone, is indicated by white letter (d). (e) designates the echinoderm fragment which consists of numerous bright red luminescent euhedral microdolomite rhombs indicated by arrowheads. Scales= 0.25 mm.

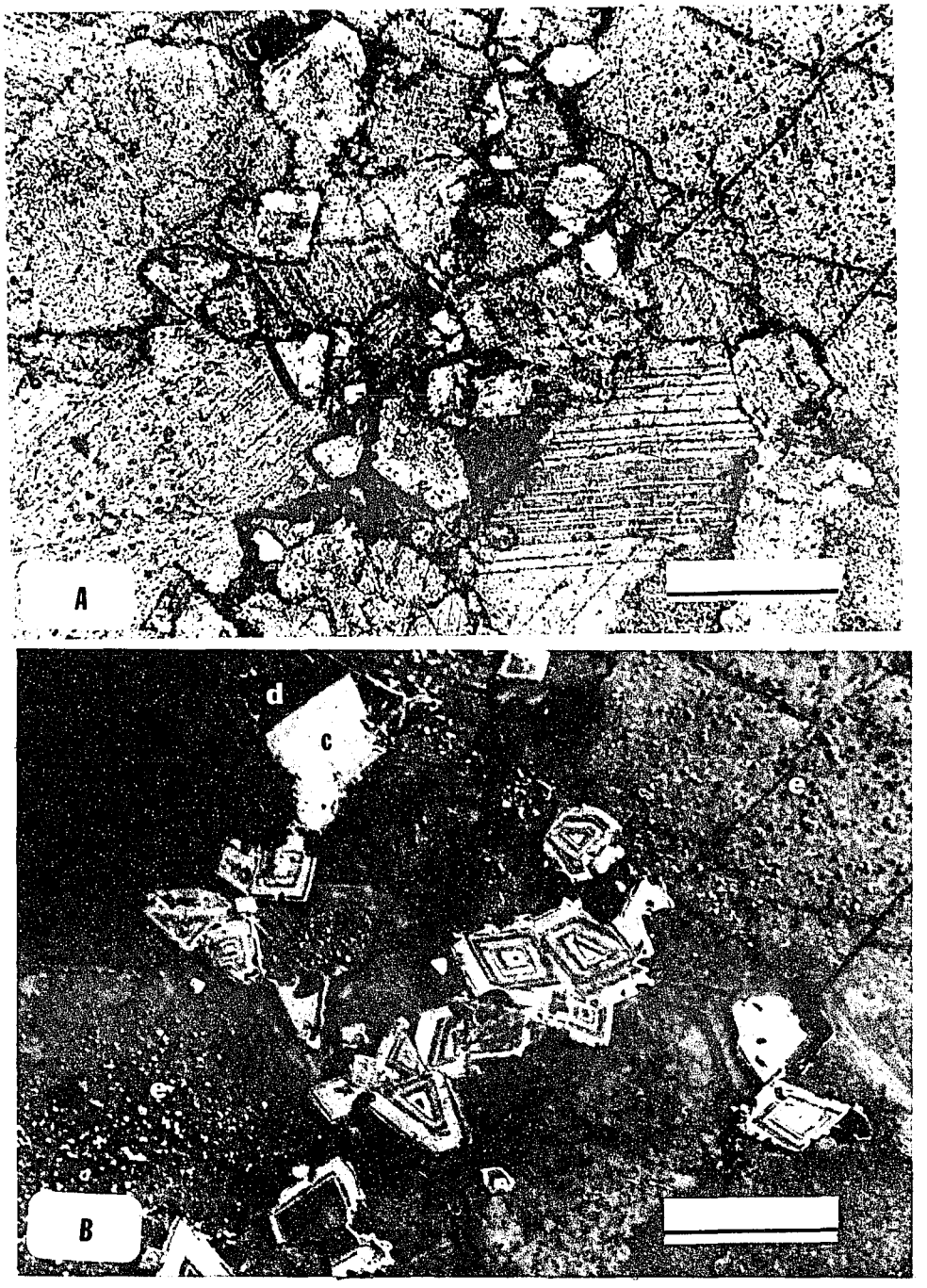


Figure 112- Photomicrographs of dolomite type IV in the crinoidal packstone- and grainstone unit. A) Dolomite crystals of dolomite type IV appear to have developed along interparticle grain boundary-pressure solution; under plane-polarized light. B) The same view of photomicrograph A under cathode light reveals that dolomite rhombs of this dolomite type show continuous and complete luminescent zones from a to d and that crinoids (e) contain of bright- red euhedral microdolomite rhombs. At the upper left center of this photomicrograph, this dolomite type is represented only by thick luminescent zones of c and d. Scales= 0.5 mm.

Zone III (c):

A single, considerably thick, bright-red luminescent band characterizes the zone III, which locally appears to have subzones which were separated by very thin (hairlike) nonluminescent partitions. This zone commonly exhibits a conformable contact with zone II (b); however, seldom does it truncate zone II with a sharp contact (Fig. 108 B).

Zone IV (d):

It is a single thick, nonluminescent zone, and a thin, bright-red luminescent band outlines this zone (Fig. 111 B and 112 B). It appears to be replacive in nature.

The first three zones of this dolomite type postdated and replaced the three identifiable zones of syntaxial cements (inclusion-rich, cloudy, non-luminescent and slightly yellow luminescent zones; Fig. 109). Dolomite as a cement appears to have precipitated along mechanically disturbed coarse grains or cements and even along grain-boundary pressure-solution contacts (Figs. 111, 112). In addition, these zoned dolomites also selectively replaced peloids and intraclasts, probably algal in origin (Fig. 110). Zone four, the latest zone, is Fe^{+2}-rich and replacive in nature, in places replacing the syntaxial cement alone without the three preceding dolomite zones. Relative abundance of the zoned dolomite crystals in skeletal and oolitic grainstones ranges from 8 to 15 %. Relations between stylolites and the zoned dolomites have not been directly observed; however, stylolites appear to be of relatively late diagenetic occurrence compared to the zoned dolomites. This relationship can readily be deduced from the relative time relations of other diagenetic events of the two lithologic units. The calcite-filled fracture that cross cuts oolitic lithofacies is postdated by stylolites, and its calcite cement crystals were replaced by very coarse-grained dolomite spars (Dol. VII) ranging from 1 to 2 mm in size (Fig. 113 A, B). These coarse, brightly luminescent replacive dolomites in fractures postdate the latest zone of the zoned dolomite type IV (Fig. 113 C, D).

Oxygen-isotope composition of the fracture-filling calcite and late replacive dolomite, and the zoned dolomites of the dolomite type IV are given in Table 2.

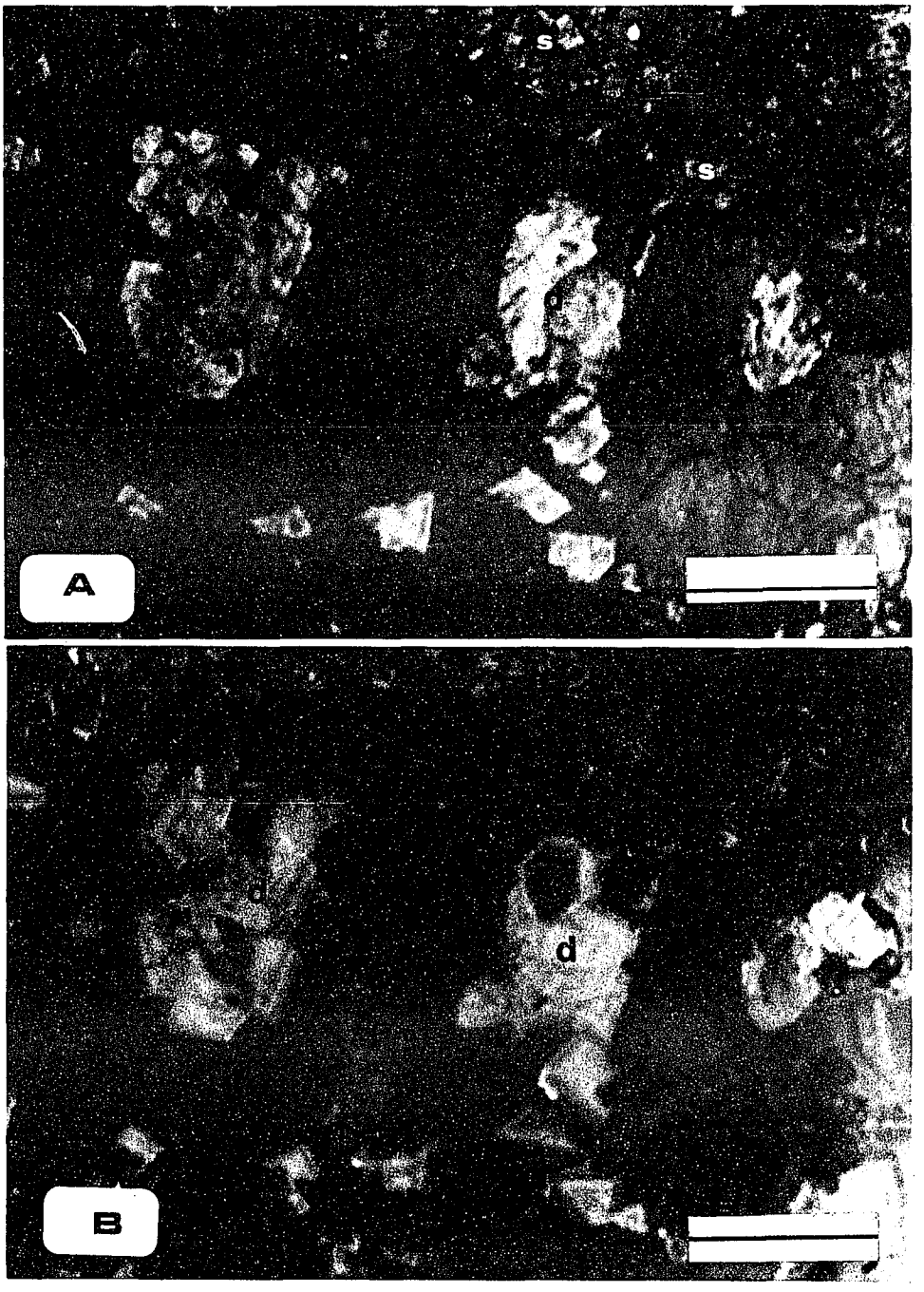


Figure 113- Photomicrographs showing timing relations among dolomite type IV, fracture-filling calcite cement, and late-replacive dolomite in the same fracture. A) A calcite-filled fracture cross-cuts the oolitic packstone- and grainstone unit in which calcitized ooids are selectively dolomitized (s); sparry dolomite crystals or Dol. VII (r) replaced the fracture-filling crystals of sparry calcite. Under plain-polarized light. B) The same view of photomicrograph A under cathode light shows that sparry dolomite crystals reveal bright red luminescence and that fracture-filling calcite cement reveals yellow-red luminescence. Arrows point to the walls of calcite-filled fracture in the oolitic packstone- and grainstone unit; scales= 0.5 mm.

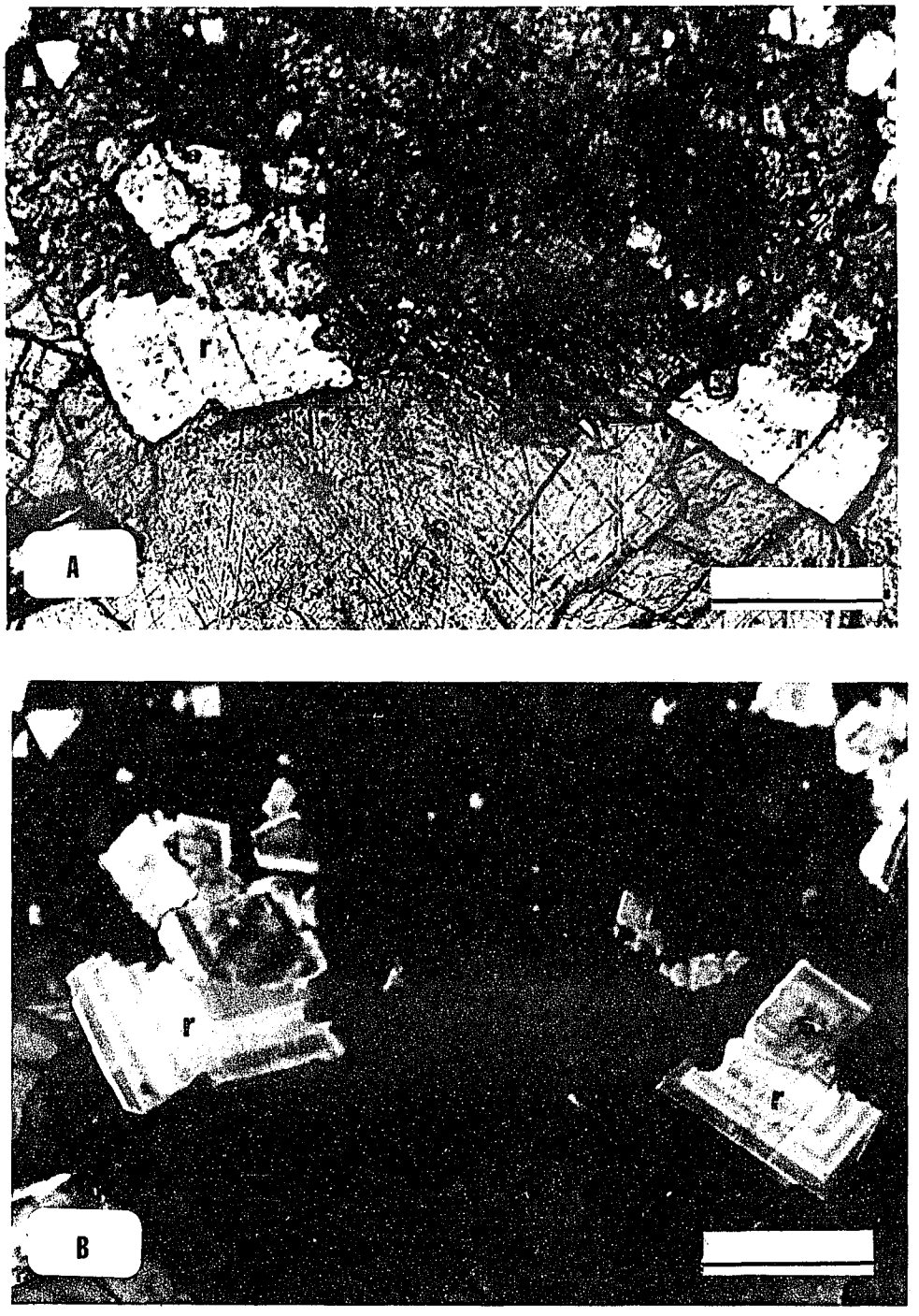


Figure 113 C- A close up photomicrograph shows that late-diagenetic dolomite (r) replaced the fracture-filling sparry calcite (c) and dolomite type IV (s); Under plane-polarized light. D) The same close up view of photomicrograph C under cathode light shows that zoned-dolomite crystals of dolomite type IV (s) appear to have been replaced and truncated by zoned, bright red and red luminescent, coarse sparry dolomite crystals (r) which replaced and postdate the fracture-filling calcite cement (c). Scales= 0.25 mm.

Table 2-Oxygen isotope composition of the dolomites and other diagenetic products in the crinoidal and oolitic packstone and grainstone units,

Samples	$\delta^{18}O$ ‰ PDB	$\delta^{13}C$ ‰ PDB
Dolomite type IV	-3.74	-0.38
Calcite (FC)	-11.25	-1.25
Dolomite (FD)	-10.37	-0.90

(FC) fracture-filling calcite, and (FD) dolomite replacing the fracture-filling calcite cement and dolomite IV.

This zoned dolomite is nearly stoichiometric ranging from 48.5 to 48.8 mole % of MgCO3.

Interpretation:

Even though some euhedral dolomite rhombs do not have the complete sequence of zones, they still show a regular continuous zonal order (Figs. 108 to 114). Truncation or crystal-level disconformity (e.g., Harris, 1982; Cander et al. 1988; Banner et al., 1988; Farr, 1989; and Voss and Gregg 1989) between these major zones were not recognized in this zoned dolomite. Therefore, completeness, continuity and regularity of these zones imply that all the zones of this dolomite may have been precipitated from the same parent dolomitizing solution. However, a sporadic truncation between zone II(b) and zone III(c) may indicate progressive dilution of the same parent solution with respect to Mg/Ca ratios as well as pH level of the same solutions in microdiagenetic environments.

Absence of major truncational boundaries among the major zones eliminates the possibility of multiple-fluid origins and dolomitizations during the growth of this

dolomite type. Truncational boundaries in zoned dolomites have been attributed to pulses of basinal fluid expulsion (e.g., Cathels and Smith, 1984), to meteoric water diagenesis during subaerial exposures (Voss and Gregg, 1989; Farr, 1989), and to sea-level fluctuations (Meyers, 1978; Harris, 1982).

Absence of zone I in some dolomite euhedra can be explained either by direction of fluid-migration path or by local variation in porosity and permeability during the dolomitization event.

It is possible to determine the flow directions of dolomitizing solutions if these zones are correlated across the basin. However, this attempt was not successful because these zoned cements were found only in one section. It is also impossible to determine on a microscopic scale since the indicated textural relations occur in a mm to cm scale in the microdiagenetic environments of the lithologic unit. These zonal variations were most probably related to local porosity and permeability-controlled dolomitization as well as to regional fluid- flow direction(s) of dolomitizing solutions. The zoned dolomites always end with a regular rhombohedral outline and terminate the adjacent zones of syntaxial cements. It implies that dolomitization postdated early calcite cements which have fresh-water phreatic or mixing-zone diagenetic origin. Mechanical compaction features, such as a fracturing or disturbance of cements, strong grain-boundary deformations and grain deformations are well developed in the lithologic unit containing zoned dolomites. The disturbed grains and early cement boundaries were probably the perfect sites for dolomite replacement.

In the oolitic packstone- and grainstone lithofacies (see description of this dolomite type), this dolomite selectively replaced the calcite-filled ooids which were presumably aragonitic in origin. Diagenetically, dissolution of aragonite occurs mostly in a meteoric-diagenetic environment and calcite filling may take place in the burial-diagenetic environment (Chow and James, 1987; Choquette and James, 1988). Therefore, on the basis of petrographic evidence it can be suggested that dolomite replacement may have taken place in the shallow- to moderate-burial depths. Selective replacement of organic-rich ooid core of radial ooids may be closely related to the presence of organic matters (e.g., Gaines 1980), which probably enhanced the

dolomitization process in a moderately deep, mesogenetic diagenetic environment (e.g., Choquette and Pray, 1970). Partially dolomitized-, fracture-filling calcite cements also suggest the possible shallow- to moderate- burial conditions for dolomitization. Probably this dolomitization took place shortly after mechanical fracturing and during the formation of early grain-boundary pressure solution.

$\delta^{13}C$ value (-0.38 ‰ PDB) of dolomite IV (see Table II) almost lies in the same $\delta^{13}C$ compositional range with the estimated-Middle Ordovician marine calcite. Such depletion may have resulted from oxidation of organic matter. $\delta^{18}O$ composition (-3.74 ‰ PDB) of this dolomite type is 2.76 ‰ PDB more enriched in ^{18}O than the estimated-Middle Ordovician marine calcite values (-6 to -7 ‰ PDB). $\delta^{18}OD_{ol.\ IV}$ composition of this dolomite is 1.4 ‰ more depleted than the estimated-average $\delta^{18}O$ composition (-2.34 ‰ PDB) of dolomite was in equilibrium with the Middle Ordovician sea water at 25 °C. This additional depletion $\delta^{18}O$ value of dolomite IV corresponds to 31.3 °C which reflects an estimated burial depth of 376 m based on 20 °C surface temperature and geothermal gradient of 30 °C/ km (for further details of these estimation see Dolomite type III).

Nearly stoichiometric composition of this dolomite and $\delta^{18}O$ values along with petrographic features are in agreement with replacement of calcite cements by warm dolomitizing fluids at shallow to intermediate depths.

Absence of evaporite minerals and evaporite-related textures eliminates the possibility of early diagenetic, near-surface dolomitization in a hypersaline shoreline (sabkha) environment (Butler, 1969; Kinsman, 1969; Friedman and Radke, 1979; Friedman, 1980; McKenzie et al., 1980; Hardie, 1987) or "Seepage Reflux" dolomitization (Adams and Rhodes, 1960).

One of the most recent studies on mixing-zone dolomitization by Ward and Halley (1985) shows that dolomite precipitated in the available pores and replaced the microcrystalline, low-Mg calcite but not sparry calcite cement, and this dolomitization took place during and after aragonite conversion to low-Mg calcite. On the basis of observations of Ward and Halley, it can be suggested that replacement of sparry calcite cement by this zoned dolomite represents a late diagenetic event even if

aragonitic ooid molds were filled during mixing-zone diagenesis not late-burial diagenesis. Thus, the replacement of intraooid-calcite spars probably occurred much later than the mixing-zone diagenesis.

Presence of the non-luminescent ferroan zone (the zone IV) in dolomite IV in the crinoidal grainstone lithofacies represents the process of dolomitization that probably took place below the SO_4-reducing zone of microbial activities. Therefore, such dolomitization eliminates the possibility of either coastal-mixing model (Land, 1973; Ward and Halley, 1985, and Humphery, 1988) or inland-mixing model (Hanshaw et al., 1971; Olson and Dunham, 1978). In addition, replacement of sparry calcite crystals in ooids or oomolds by dolomite crystals at near-surface conditions is almost impossible due to low temperature and lack of nucleation sites along large crystals (Sibley 1982; Bullen and Sibley, 1984; and Sibley et al, 1987). In addition to petrographic evidence, the oxygen-isotope composition of the zoned dolomites of dolomite type IV (average composition of -3.74 ‰ PDB; see Tab. 2) also indicates that this dolomite may have occurred in a shallow to intermediate burial depth.

Mg probably came from four possible sources: (1) trapped-sea water in pores, (2) Mg-rich allochems, particularly Girvanella-related peloids, (3) allochthonous from overlying and underlying lagoonal lime mud, and (4) from overlying sea water by diffusion.

Rapid drowning of the oolitic and crinoidal (skeletal) shoal facies of the Orthidella zone by third-order sea-level rise can be suggested during the formation of oncoidal shoal lithofacies (see Chapts. 10, 11). As a result, the pore water may have had mainly sea-water composition.

Formation of the outer nonluminescent, ferroan dolomites indicate a relatively deeper burial environment than the bacterial sulfate-reducing zone or depth range. Absence of extensive mixing-zone dolomitization in study area may be related to the following: (1) high PCO_2 in the intersitial solutions due to conversion of aragonite and high-Mg calcite to low-Mg calcite particularly in a humid climate (Sibley, 1980), (2) slow growth rate of dolomite under the low-temperature, near-surface conditions and (3) rapid-fluid flow rates due to sea-level change and seasonal variations (Machel

and Mountjoy, 1986; Hardie, 1987).

Dolomite Type V

Description:

This dolomite type was observed in the one- to five-feet thick shelly storm layers of the open shelf lithofacies (see Chap 9) which primarily consists of crinoids, Nuia, brachiopods, trilobites, oncoids, and intraclasts. Two dolomite types were recognized under plain light and cathodoluminescence: (1) fine-grained euhedral rhombs (0.01 to 0.05 mm) within the micritized intraclasts, revealing dark non-luminescent dolomite, similar to dolomite type II; and (2) zoned dolomite, occurring as replacive and cement and showing three major zones--here named dolomite type V.

Zone I(a):

Dark, non-luminescent, mottled center of the rhomb is enveloped in the following bands: a moderately thick dull-luminescent band, a moderately thick non-luminescent band, and a considerably thick dull luminescent band (Figs. 114 B, 115 B, and 116 A).

Zone II(b):

A very thin, orange yellow band separates two non-luminescent bands of zone I and zone II (Figs. 114 B, 115 B, and 116 A). Following this partition, zone II reveals three non-luminescent bands alternating with three orange-yellow bands all of which are moderately thick, straight, and planar (Figs. 114 B and 115 B).

Zone III (c):

The last, thick, nonluminescent to slightly dull band gradually changes into the dark-luminescent, void-filling dolomite cement (c). If this outermost band is not present, the corrosional or dissolutional boundaries are noted between the void-filling xenotopic dolomite and bright, orange-red luminescent bands of zone II (Fig. 117 B).

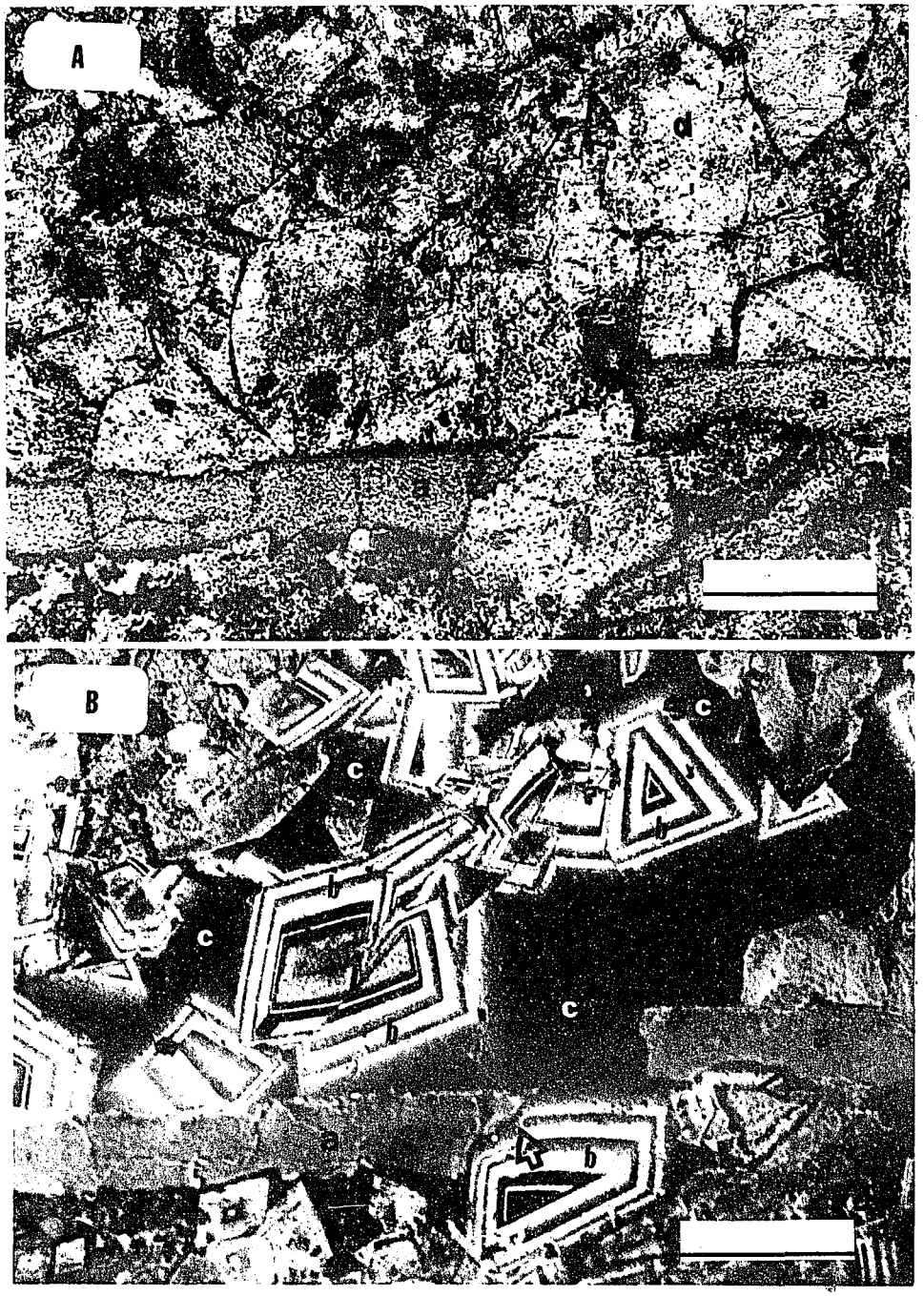


Figure 114- Photomicrographs of dolomite type V. A) Sparry dolomite crystals (d) replaced allochems and sparry calcite crystals postdate mechanically fractured allochems (a); under plane-polarized light. B) The same view of photomicrograph A under cathode light shows that dolomite crystals of dolomite type V consist of three discrete luminescent zones: a, b, and c. Zone a is dull and mottled dolomite nuclei, followed by zone b, which consists of orange-red bands alternating with thin non-luminescent bands. Zone c is the nonluminescent outermost zone; zone b zone b and c clearly postdate the mechanically fractured allochem indicated by arrows. Scales= 0.5 mm.

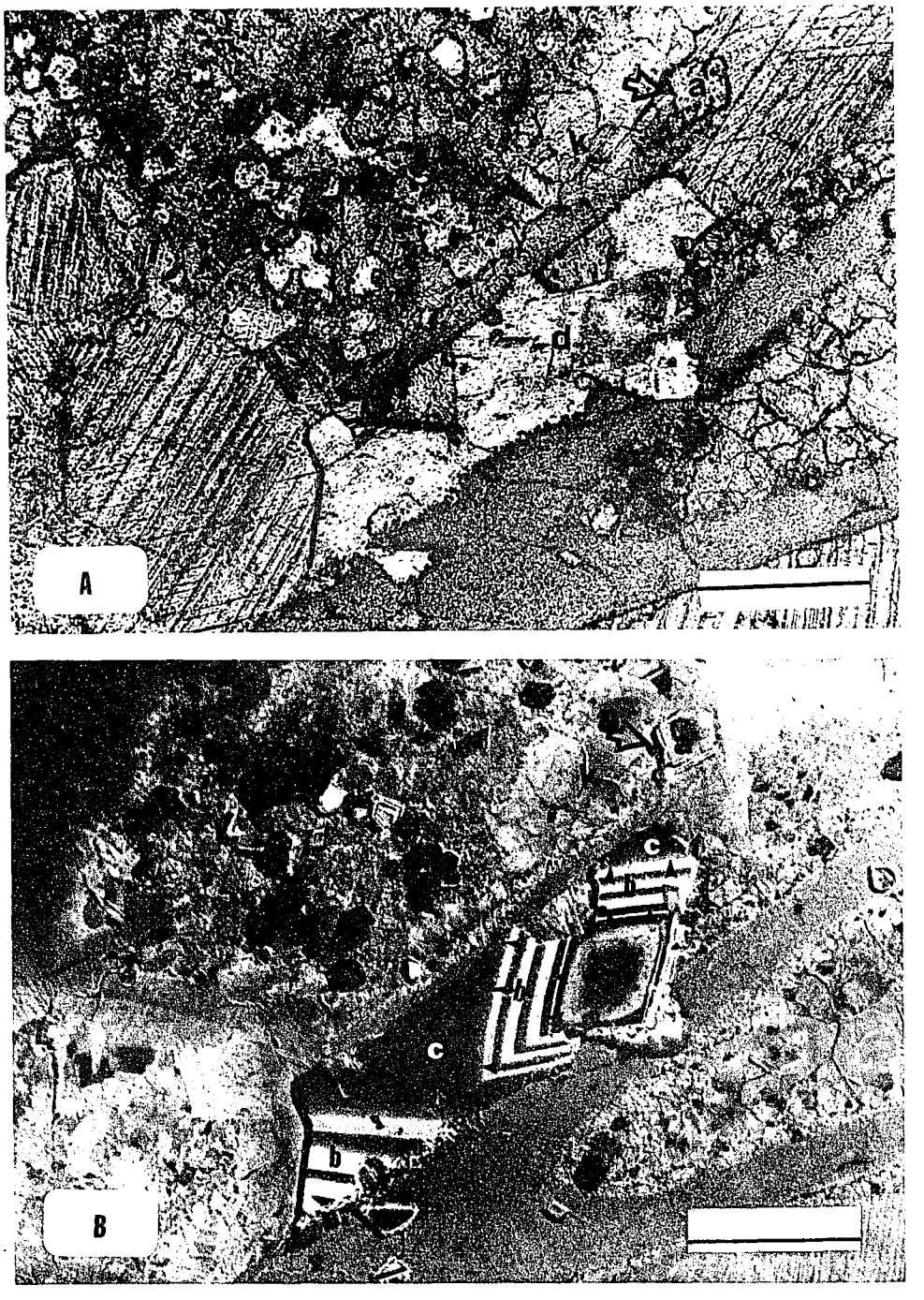


Figure 115- Photomicrographs of dolomite type V and its complete zones. A) Clean light dolomite crystals (d) replaced the allochem and twinned-calcite cement; arrowhead points to the replacement of allochems by neomorphic calcite (k) which also postdates the zone "a" of dolomite type IV. Under plane-polarized light. B) The same view of photomicrograph A under cathode light shows the major luminescent zones of dolomite type V; small arrowheads point to boundaries between zones "a" and "b" and "c", and the contacts among all these zones are regular without crystal level truncations. Scales: 0.25 mm.

Another important petrographic relation is that bright orange-red luminescent zones locally replaced the dark, generally dull, zone I (Fig. 117 A). Aerial distributions of this dolomite type and its zones are not known in other sections.

Comparison of the zones in Dolomite V with the zones in Dolomite IV shows that there are no comparable luminescent zones in terms of sequential order of dolomites, intensity of luminescence in distinct zones, and their distinct bands as well as number of bands present in each zone.

Zone I (a) of this dolomite type in places dominates a certain part of the pores or replacement sites where only this zone or an incomplete zone II (b) is present, at other sites zone II (b) dominates and includes the zone I(a). Zone I(a) and zone II(b) show some compactional features that formed during the crystal growth (Fig. 117 B). These zoned dolomites postdate mechanical compaction or grain breakage (Figs. 114 A, B, 115 A, B) and selectively chertified crinoids and brachiopods, and replaced the void-filling calcite cements.

Stable isotope composition of dolomite V in a bulk sample is -2.82 ‰ PDB, and -0.77 ‰ PDB for $\delta^{18}O$ and $\delta^{13}C$, respectively.

Interpretation:

Dolomite type V is also replacive and appears to have formed during or after the mechanical compaction at shallow-burial depth (Fig. 116 A, B). The replaced sparry calcite cement is probably of marine cement which precipitated from entrapped-marine pore water, or it may be neomorphic in nature (Figs. 114, 115). Dolomite bands of zone I (a) with a general non-luminescence appear to predate mechanical compaction or breakage of allochems. Perhaps, there are relatively early diagenetic replacements at the depth range of oxidation of organic matter by bacteria (Baker and Burns, 1985; Burns et al. 1988).

Oxidation of organic matter (due to reaction with sea water) may have been responsible for dissolution of calcite and produced HCO_{3-1} which incorporates the

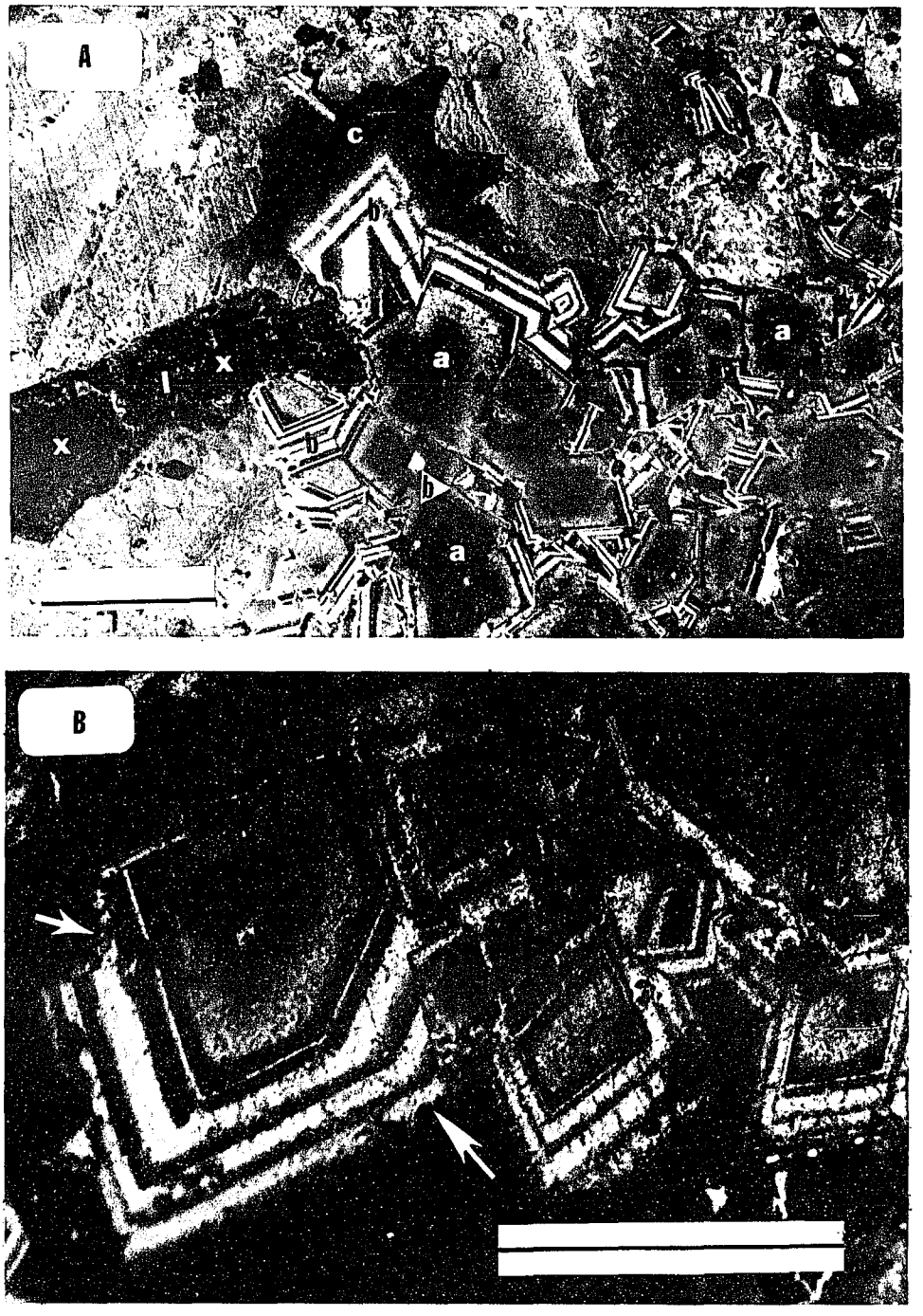


Figure 116- Cathodoluminescence photomicrographs of dolomite type V. A) Luminescent zones (a, b, and c) of dolomite type V have regular continuous contact relations, but white arrowheads with letter "b" point to the replacement of zone (a) by zone (b). (I) is a partially chertified brachiopod; (x's) point to chertified parts of the brachiopod. B) White arrows point to locally recognizable truncational contacts between zones (b) and (c) of dolomite type V. Scales= 0.25 mm.

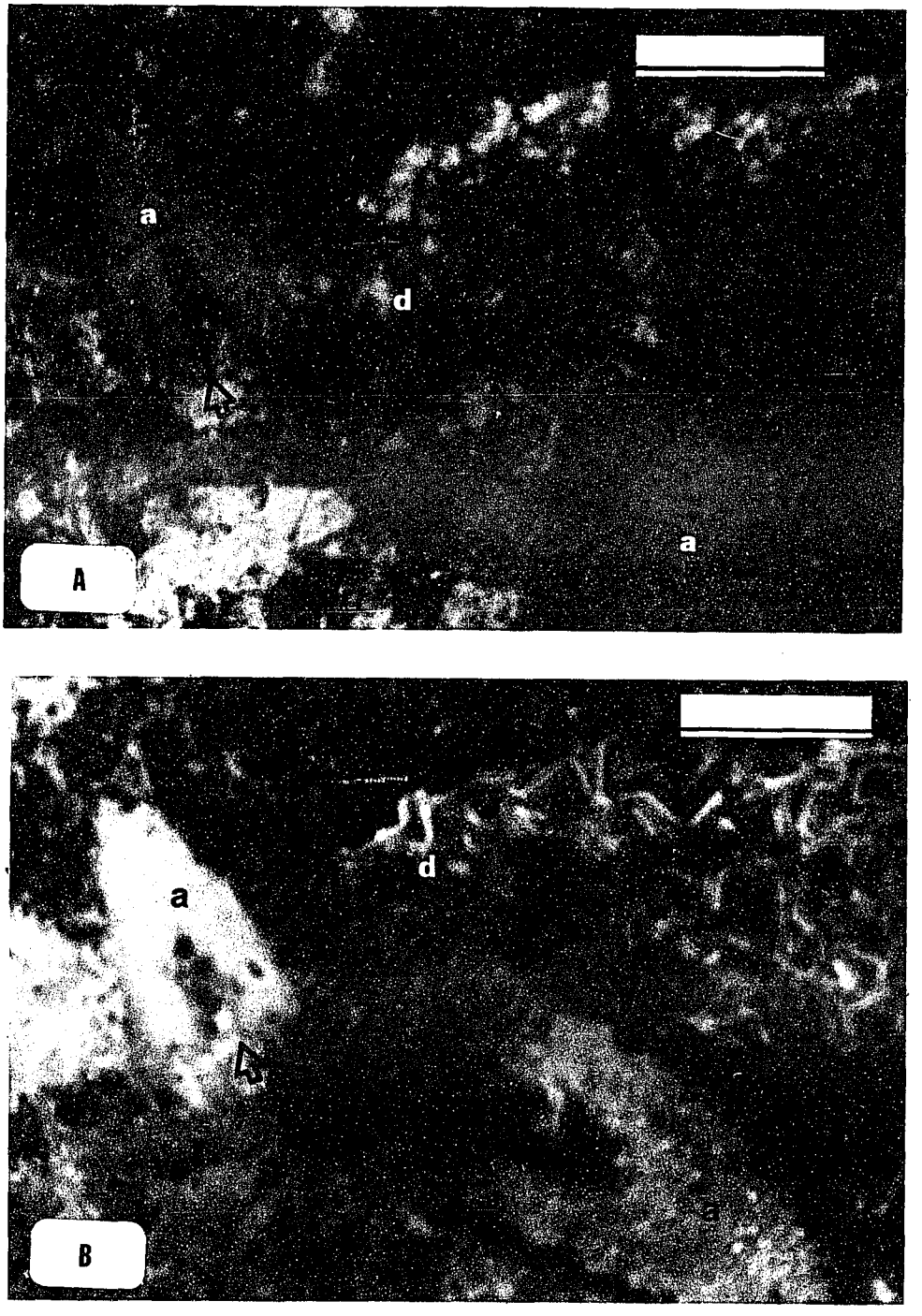


Figure 117- Photomicrographs showing diagenetic timing relations between a mechanically broken allochem and dolomite type V. A) Dolomite type V (d) replaced the parts of the mechanically broken allochem (a), and arrows point to replacement of allochem fragments (a) by this dolomite type. B) The same view of photomicrograph A under cathode light also shows that dolomite type V postdates the mechanical fragmentation of allochems. Scales= 0.25 mm.

composition of dolomite with Mg in dolomite zone I. Sea water was primary Mg supplier for dolomitization.

In zone II(b), alternating bright and non luminescent bands, with synchronous or slightly late mechanical breakage (Fig. 116 A, B) imply that dolomitization at this stage occurred in a shallow burial depth, probably also within the range of oxidation of organic matter by bacteria or microbial activities. As bacteria reduce SO_{4-2} by oxidizing organic matter, resultant HCO_{3-1} from the dissolution of calcite similarly incorporate Mg in composition of dolomites. Mg was probably derived from entrapped-sea water in the pores or from downdip diffusion of Mg-bearing sea water (Burns and Baker, 1985; Mullins et al., 1988).

The thick, slightly dull to non-luminescent outermost band, conformable transitional band between brightly luminescent zone II and dark, non-luminescent dolomite zone III (c) suggest that dolomitization was progressive and continuous. Even though, dolomitizing fluid was primarily the same diagenetically modified sea water, variation in Eh through time probably caused variation in dolomite zones and their trace-element composition.

The nonluminescent void-filling dolomite (zone III) probably represents a relatively deeper burial depth range than previous bands of zone II. Below the depth range of sulfate-reducing zone, entrapped-pore waters become enriched in Fe^{+2} which incorporates precipitating dolomite.

The measured-$\delta^{18}O_{Dol.V}$ composition is slightly more depleted than the estimated-average $\delta^{18}O$ value of dolomite which was in equilibrium with the Middle Ordovician sea water at 25 °C. $^{\delta 13}C_{dol.V}$ composition of this dolomite is slightly more depleted than the estimated-$\delta^{18}O$ value of the Middle Ordovician marine calcite, but it is much heavier than that of dolomite formed under sulfate-reducing conditions. Slightly depleted both $\delta^{18}O$ and $\delta^{13}C$ values suggest that diagenetically modified marine pore water was the possible dolomitizing fluid at a shallow-burial depth.

Sea water with a long reaction time is one of the most important dolomitizing fluids in sediments with considerable porosity and permeability (Hardie, 1987). In conclusion, downdip diffusion of sea water was probably responsible for Mg supply to

these zoned dolomites in the progressively deepening diagenetic environments. Non-luminescent, late dolomite probably precipitated from the entrapped-pore water (diagenetically modified sea water) and updip-moving early compactional solutions derived from underlying and overlying fine-siliciclastic sediments.

Deep-burial replacive dolomitization by updip-migrating basinal brine is not applicable for this dolomitization because of its close associations with an early mechanical compaction.

Dolomite Type VI

Description:

Euhedral, ferroan-dolomites most commonly occur along pressure-solution seams and as patchy selective replacement in the peloidal allochems and in the intraooid calcite cements. Dolomites associated with the stylolites have more euhedral crystal outlines and smaller crystal size than those of patchy ferroan dolomites. Formation of dolomite along the stylolites, particularly in micritic and mud-supported lithologic units, appears to be restricted to zones rich in silty quartz.

However, in both lithologic types, stylolite-induced dolomitization shows source-controlled patterns as the relative abundance of dolomite and pyrite progressively decrease away from pressure-solution seams. The patchy, Fe^{+2}-rich dolomites generally occur in an idiotopic and hypidiotopic crystal form.

In the Antelope Valley region, this dolomite type (Figs. 118, 119) is volumetrically second to mosaic dolomite. Its occurrence predates the mosaic dolomites (dolomite type VII). Both stylolitic and patchy dolomites of type VI are very common in the shelly stormal layers of the shoal and inner shelf. In the storm layers of these shelf units, the ferroan dolomites are accompanied by partially chertified allochems,

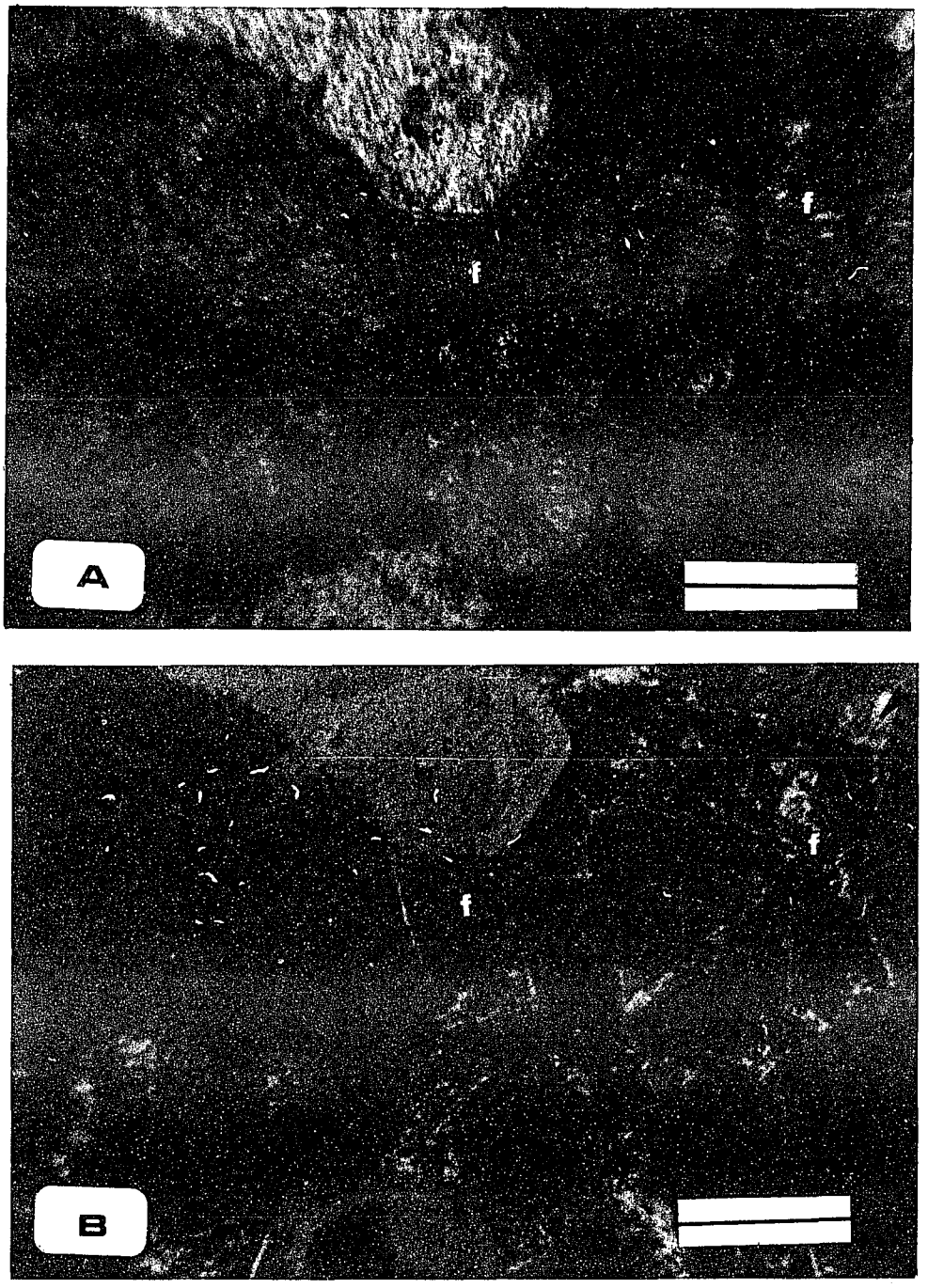


Figure 118- Photomicrographs of dolomite type VI (euhedral ferroan dolomite). A) Euhedral ferroan dolomite crystals (f) replaced the interparticle sparry crystals of calcite cement (c). Arrowheads point to dark gray to black iron-oxide rims around ferroan dolomite rhombs. Under cross-polarized light. B) The same view of photomicrograph A under cathode light shows that ferroan dolomites are nonluminescent and have mottled core and orange-red luminescent rim along non-luminescent ferroan dolomite outlines. Scales= 0.25 mm.

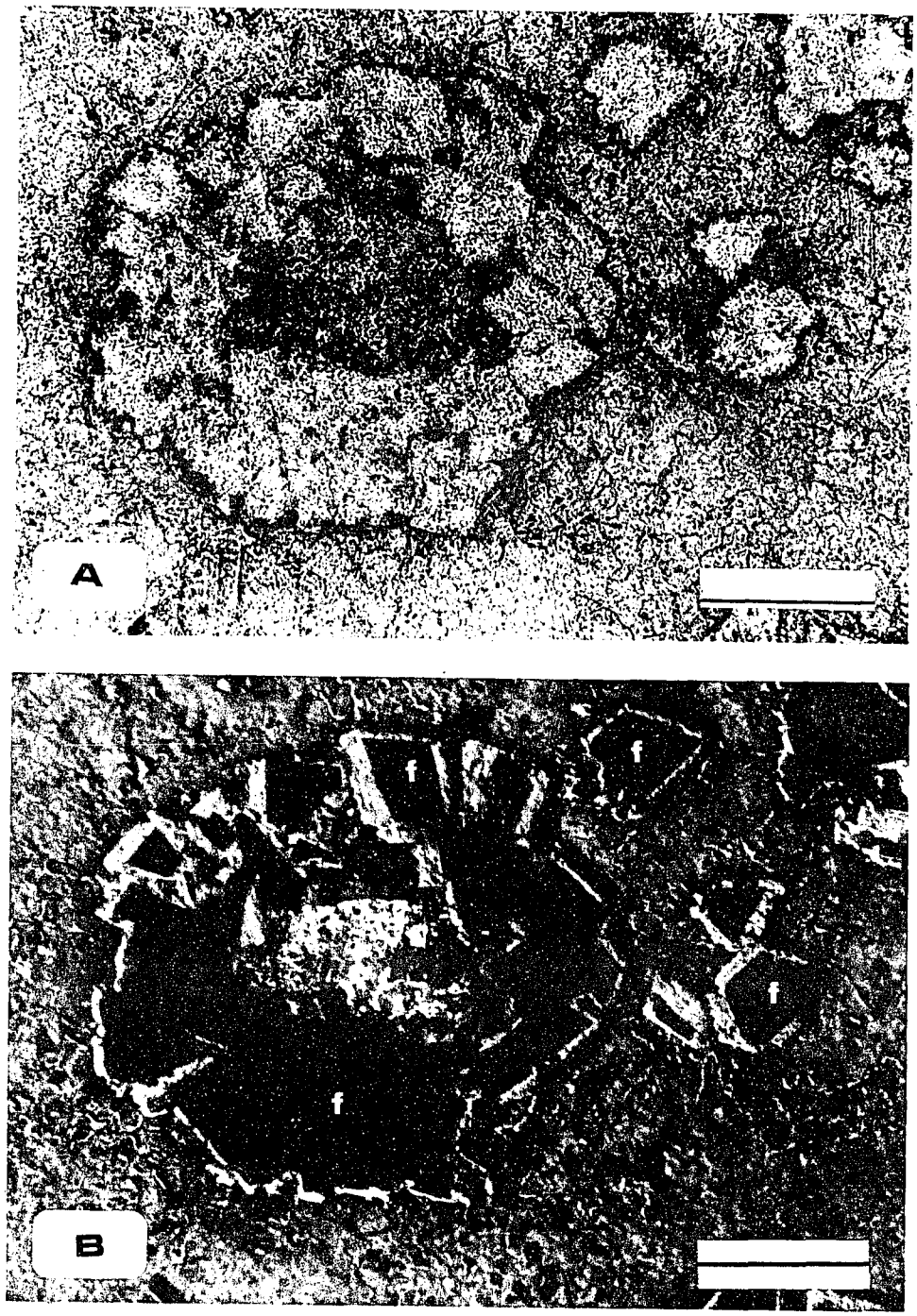


Figure 119- Photomicrographs of dolomite type VI in the oolitic grainstone unit. A) Euhedral ferroan dolomite crystals (f's) selectively replaced the oomold-filling calcite cement is (o). B) The same view of photomicrograph A under cathode light shows that ferroan dolomite rhombs are nonluminescent, and outer crystal rims of the dolomite crystals show a bright-red luminescence. Scales= 0.25 mm.

especially crinoid ossicles and bryozoa.

However, the relationship between chertification and the ferroan dolomites is rather complex: the ferroan dolomites postdate early, partial chertification but predate late chertification, particularly in broyozoans. Replaced-euhedral ghost rhombs of dolomite along with euhedral pyrite crystals are very common in late chertified allochems and cements.

In the shoal lithofacies, the patchy ferroan dolomites selectively replaced interparticle-, blocky-, even poikilotopic cements, intraooid-calcite cements, and peloidal grains (Figs. 118, 119). The intraooid calcite is a late cement in which measured homogenization temperatures of two-phase fluid inclusions range from 160 to 179 °C. The most common feature of these ferroan dolomites is that the outer rhombs under plain polarized light reveal a brownish red, staining along the crystal outlines (Figs. 118, 119). These stained zones under cathode light appear as thin, bright red luminescent zones, whereas the whole dolomite euhedra appear dark and non-luminescent.

The oxygen-isotope composition ($\delta^{18}O$) of dolomite Type V from two replacive dolomites on intraooid calcite ranges from -8.04 to - 9.7 ‰ (PDB). Carbon isotope composition ($\delta^{13}C$) ranges from -1.25 to -1.73 ‰ (PDB). These ferroan dolomites have 48.9 mole percent of $MgCO_3$ in their average composition.

Interpretation:

Partial dissolution of carbonates under increased pressure due to increased depth of burial either by sediment loading or tectonic loading is known as pressure solution (Bathurst, 1975). Therefore, applied forces or confining pressure are primarily responsible for dissolution of the carbonates in a varying depth range rather than dissolution induced by low pH solution.

Dunnington (1967) estimated depth range of 600 to 900 m for the formation of pressure solution. Under certain physical conditions, for instance, if pore water is

trapped between the impermeable barriers, rise in hydrostatic pressure will exceed the lithostatic pressure and pressure solution may not occur until depths of 3000 m is reached (Bathurst, 1980). In either case, dolomite associated with pressure solution is likely to have formed during deep-burial diagenesis when the limestone has already lost most of its porosity.

In the matrix-supported limestone, insoluble residue along wispy or stratiform stylolites (known as horse-tale stylolites) is commonly accompanied by relatively smaller dolomite euhedra (Wanless, 1979). In such example, the formation of dolomite took place much earlier than stylolitic dolomites of grain-supported units (Bathurst, 1975). In both stylolite forms, formation of ferroan dolomites indicates that dolomitization took place below the bacterial sulfate-reducing zone at elevated temperatures. Under such conditions, Fe^{+2} is directly incorporated into dolomite; and the excess Fe^{+2} of the dolomitizing solution goes into the formation of pyrite (Bathurst, 1980; and Machel, 1987). Sulfate reduction in the pore water and oxidation of organic matter by bacteria (BSR) takes place at up to 85 °C, whereas thermochemical sulfate reduction (TSR) is responsible for formation of pyrite at a temperature range of 85 to 135 °C (Machel, 1987; and 1989). The TSR's reaction range is equivalent to or greater than that represented by vitrinite reflectance level of 1.5 % Ro (Machel, 1989).

It is clearly seen that stylolitic dolomite and pyrite were cogenetic, and they resulted from dolomitization at the deeper burial depth than bacterial-sulfate reducing burial depths. For the formation of dolomite along pressure solutions, Mg was supplied from local sources either from Mg-rich calcite cements or allochems (Wanless, 1979). Insoluble residue, such as clay and organic matter, is believed to be a source of Mg source for stylolite-induced dolomitization, and Mg^{+2} released during smectite-illite transformation has been proposed as a major mechanism for dolomitization (McHargue and Price, 1982). McHargue and Price also suggested that dolomite formation in the clay-rich lithofacies occurs even earlier, specifically during mechanical compaction.

Absence of dolomites in the shaley limestone units of the June and Mill Canyon sections is probably related to formation of the chlorite (see Land, 1985). Relatively high chlorite occurrences were reported by X-ray analysis of these lithologic units (see

Chapter 20).

Fe^{+2}-rich composition of both stylolitic and patchy dolomites can be inferred from the non-luminescence of these dolomites. The outermost bright red luminescence may represent progressively depleted-Fe^{+2} concentration in dolomitizing solutions under the reducing diagenetic environment.

An average $\delta^{18}O$ value (-8.54 ‰ PDB) is considerably depleted in ^{18}O compared to the estimated average $\delta^{18}O$ value (-2.34 ‰ PDB) of dolomite in equilibrium with the Middle Ordovician sea water at 25 °C. This depleted-$\delta^{18}O$ composition of Dolomite VI may have resulted from hot basinal solutions at a great burial depth.

The patchy replacive dolomites are also late diagenetic and deep burial in origin which can be inferred from the replacement of late diagenetic, coarse sparry calcite cements (Zenger, 1983), high Fe content, excessively depleted isotope oxygen composition, and their nearly stoichiometric compositions.

In the near-surface diagenetic conditions, dolomites preferentially replace microcrystalline low-Mg calcite, or mixtures of aragonite and Mg-calcite mud (Lucia and Muray, 1967; Sibley, 1982; and Sibley et al. 1987). This is due to fine grain size of the components which provide very intensive nucleation sites, and high surface area for chemical reaction (Choquette and James, 1987). On the contrary, selective replacement of sparry crystals of calcite in the oomoldic cement most likely represent a late-diagenetic dolomitization in deep-burial diagenetic environments. The high temperatures and long-reaction periods facilitate this deep-burial dolomitization during which large surface areas of calcite crystals attract incoming ions into the crystal growth fronts (e.g., Lucia and Muray, 1967, Freeman, 1972; and Sibley et al. (1987).

The late, deep-burial dolomite replacement obliterates the original texture of carbonate precursors rather than preserve them as in near-surface dolomitization (Zenger, 1983; Gregg and Sibley, 1984; Bullen and Sibley, 1984). All the criteria mentioned above are in good agreement with the textural features of patchy and stylolitic ferroan dolomites, supporting a deep-burial origin for dolomite VI.

Relatively early diagenetic processes in shallow-burial depths that can produce ferroan dolomites by the following mechanism: (1) progressive depletion of H_2S

below the depth of SO_4-reducing zone (Pye, 1985), and (2) early compaction of basinal shale and early expulsion of basinal fluid (Taylor and Sibley, 1986). These processes may be count for dolomitization of the ferroan dolomite of dolomite type IV and V (zoned-dolomite I and zoned dolomite II). Dolomitization induced by pressure solution or smectite-illite transformation (McHargue and Price, 1982; and Sternbach and Friedman, 1984) can be adopted for dolomitization of patchy and stylolitic dolomites (Type VI), having taken place much later and at greater depths than mechanical compaction-induced dolomitization.

Dolomite Type VII (Mosaic Dolomite)

Stratigraphic Relations and Areal Distributions

Pervasively dolomitized Antelope Valley Limestone (AVL) intervals have been reported in the Antelope Valley and Hot Creek regions (Fig. 120). These intervals are nonstratiform dolostone units which characterize a tectonic-controlled dolomitization. Nolan et al. (1956) and Merriam (1963) have shown that two-directional normal faults (N-S and E-W) affected central Nevada considerably and caused the regional uplifting during the Middle Pennsylvanian time.

In the Martin Ridge section, pervasively dolomitized intervals occur along the E-W extending normal faults (Fig. 121 A), away from which dolomitization progressively decreases in either direction. Narrow zones of pervasive dolomitization along the faults are specifically well-developed when these faults encounter with fine-grained or matrix-supported lithofacies (Fig. 120). However, in the grained-supported lithofacies (Figs. 121 B, 123), laterally extensive, pervasively dolomitized zones occur between 50 and 100 m (150 to 300 feet) from these faults (Fig. 120; Appendix I-B). In the pervasively dolomitized units of the AVL, calcite-filled fractures, stylolites, and other lithologic features have been replaced and in places obliterated, and only relics of these diagenetic products are discernible (Fig. 123 A, B, C). The upper and lower contacts of these dolomite units are sharp. Along the lower sharp contacts of the dolomitized units, particularly near the fault zones, small breccia pockets were also noted.

In the Lone Mountain section, two pervasively dolomitized intervals of the AVL occur at intervals of 125 to 215 feet and 750 to 800 feet from the base of this section (Fig. 120; Appendix I-B). The basal and upper contacts of the lower interval are sharp but not gradational, and the E-W fault-controlled dolomitization has not been

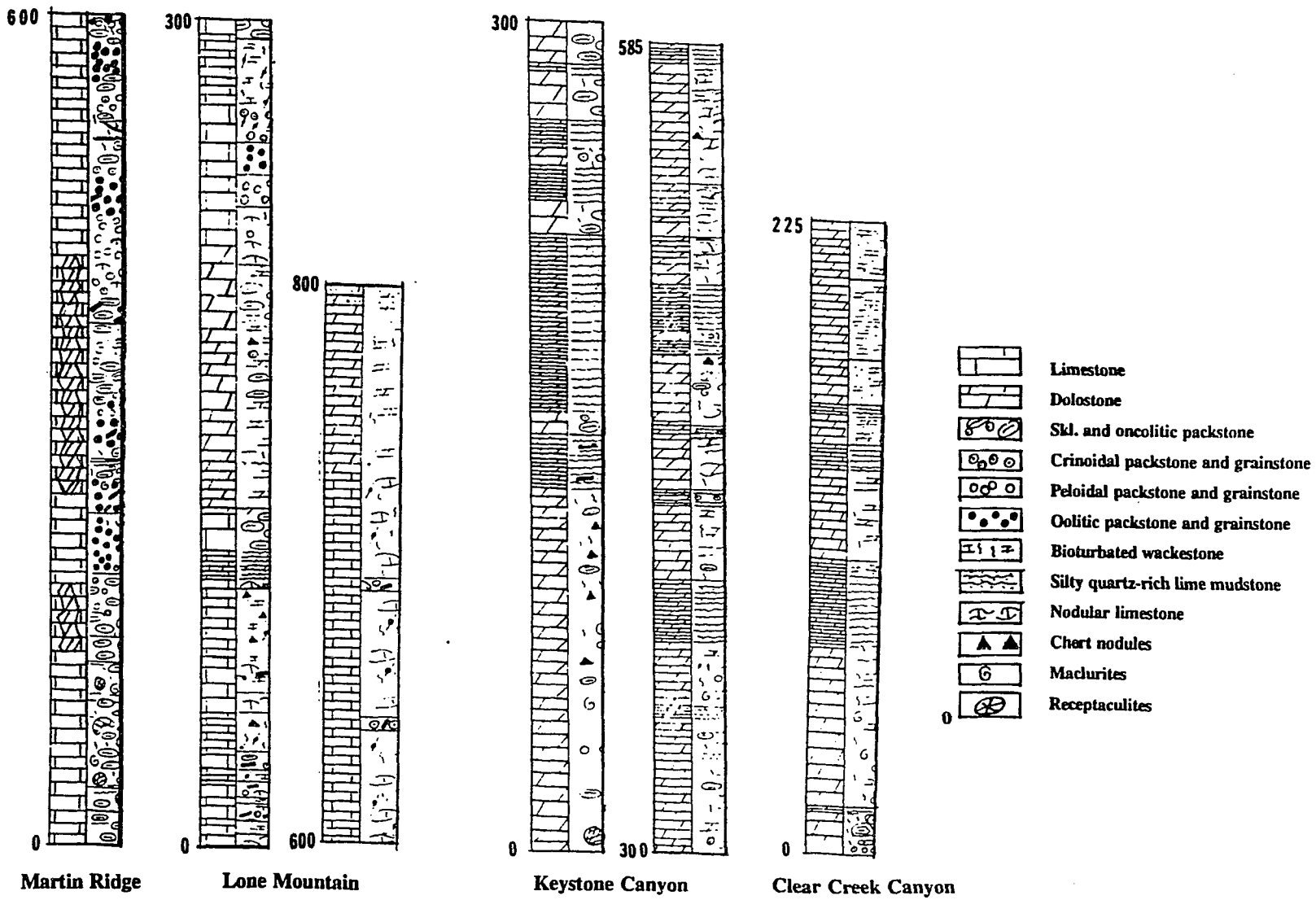


Figure 120- Pervasively dolomitized intervals (Dol. VII) of the AVL in the Martin Ridge, Lone Mountain, Keystone Canyon and Clear Creek Canyon sections.

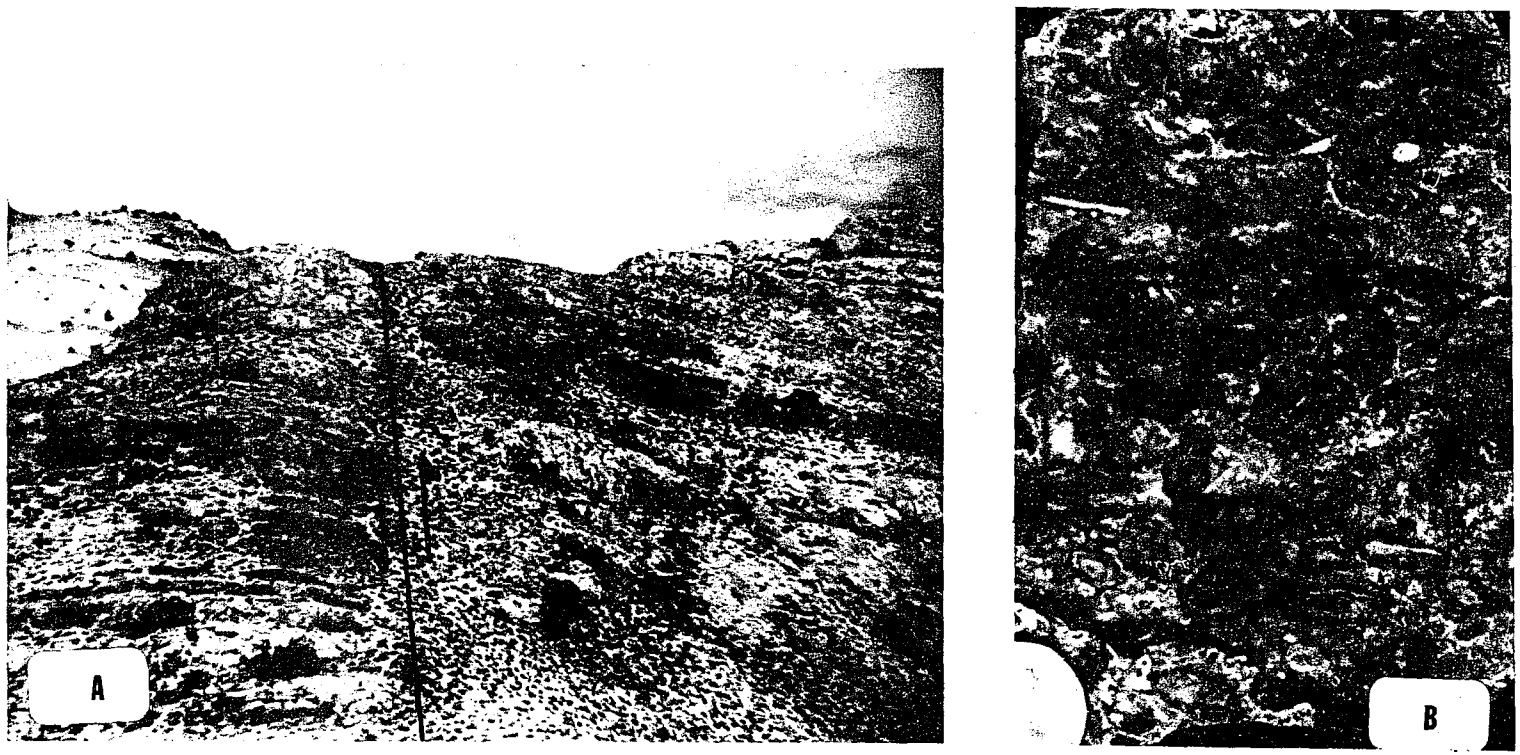


Figure 121- A) A field view of E to W trending normal faults in the Martin Ridge section. These faults are responsible for the fault-controlled pervasive dolomitization. B) A polished slab of the pervasively dolomitized oncolitic packstone- and grainstone lithofacies.

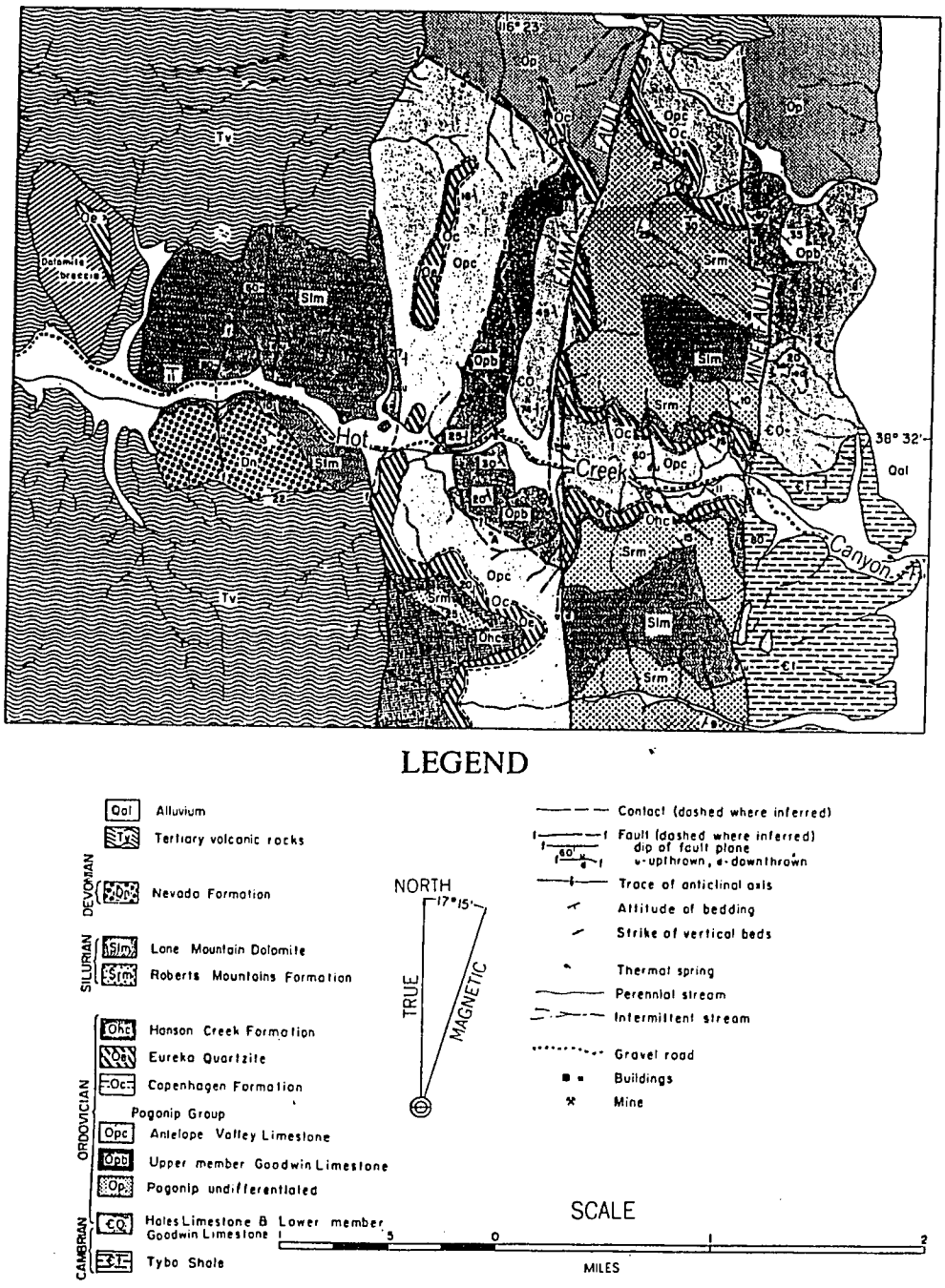


Figure 122 A- The geological map of the Hot Creek Canyon region shows the Antelope Valley Limestone (opc), and E to W and N to S-trending normal faults (Lowell, 1965).

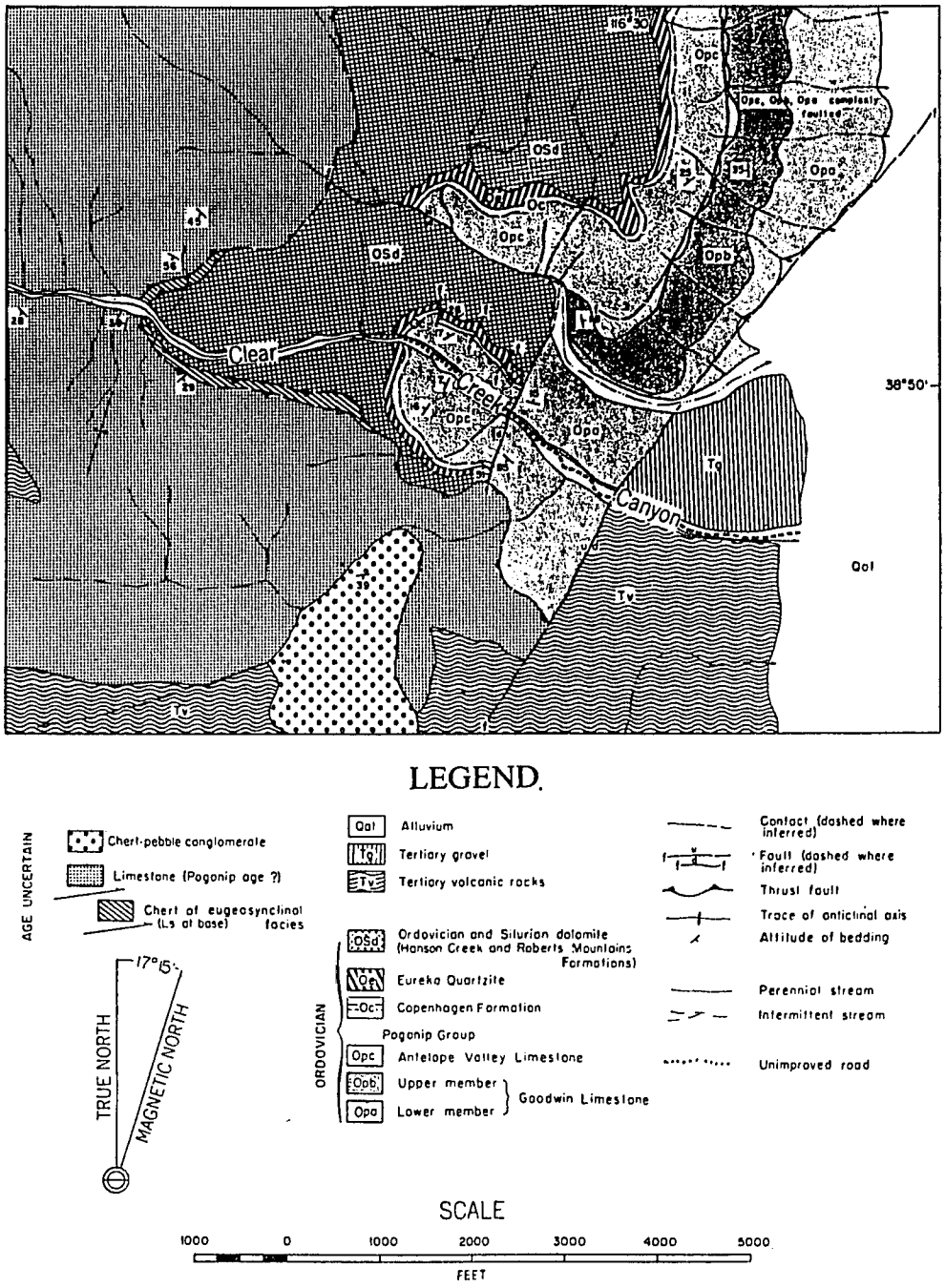


Figure 122 B- The geologic map of the east Clear Creek Canyon region shows the E to W and N to S-trending normal faults and the Antelope Valley Limestone (Lowell, 1965).

recognized. This is, in part, due to the fact that Lone Mountain is a small, isolated horst-like structure in the center of the inter-mountain basin where basin-filling sediments cover the dolomitized intervals and the lower part of the AVL. Thus, it is very difficult to relate this pervasive dolomitization directly to the faults in this vertical section. However, in the Lone Mountain section, the laterally restricted, pervasively dolomitized units and their contact relations appear to be the same as those of dolomitization features and stratigraphic relations of the dolostones of the Martin Ridge section. The upper dolostone interval of the AVL (Fig. 120) also shows a sharp basal contact but a gradational upper contact upward with the Eureka Quartzite. Morreale (1981) measured and sampled the AVL at the same locality about 500 m south of the section mentioned in this study, but he did not report any dolomitized units.

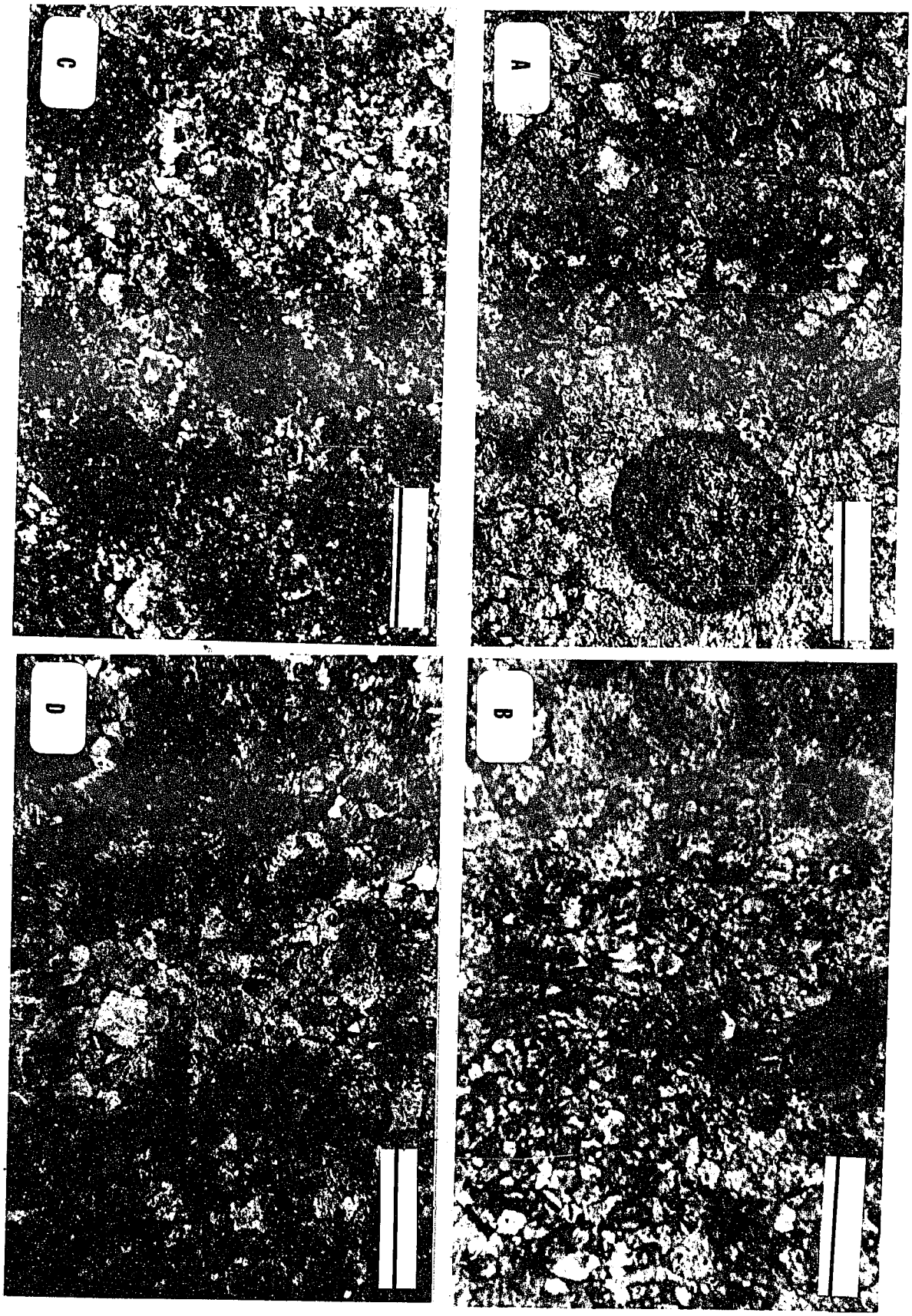
In the Hot Creek region, Keystone Canyon and Clear Creek Canyon sections (Figs. 120; 122 A, B), all the sequences of the AVL are pervasively dolomitized. Both N-S and E-W extending normal faults are clearly recognizable in these vertical regions (Fig. 122 A, B). Particularly, the N-S extensional faults are closely spaced, parallel to one another (Fig. 122 A). Some of the N-S faults offset even the Tertiary volcanic rock units. These faults postdate the Roberts Mountain thrusts and juxtapose the AVL against other Mid-Paleozoic formations and the Cambrian Tybo Shales (Fig. 122 A). In the Keystone Canyon, a 30-feet wide Upper Cretaceous intrusive dike cross cuts the (AVL) and the whole Paleozoic sequence.

All pervasively dolomitized intervals of the AVL in the Antelope Valley region and southern localities of this study occur in the autochthonous unit of the AVL.

Petrography:

Mosaic dolomite is volumetrically the most abundant dolomite type in the pervasively dolomitized units of the Antelope Valley Limestone (AVL) in the indicated localities. Fracture-filling dolomite cement and saddle dolomite are also

Figure 123- Photomicrographs of dolomitized oolitic grainstone units of the AVL. A) Euhedral ferroan dolomite crystals selectively replaced calcitized ooids (oomold-filling calcite cements). This sample represents the lithologic unit at least 50 m away from the E-W trending fault. B) Coarse, euhedral ferroan dolomite crystals and oomold-filling calcite were replaced by medium-grained mosaic dolomite (Dol. VII). Still some radial ooids are remained unaffected by the dolomitization. This photomicrograph represents the same oolitic unit which was collected about 15 to 20 m away the fault. C) Relatively medium- to coarse-crystalline mosaic dolomite (Dol. VII) become dominant as getting closer to the faults. In this mosaic dolomite, ghost ooids (g) and pointed by arrows still can be recognized due to fabric selective dolomitization (finer and darker euhedral dolomite crystals coarse crystalline, xenotopic host mosaic). Under cross-polarized light; scales = 0.5 mm. D) Close up view of photomicrograph C under polarized-plane light. Scale = 0.25.


C
A
D
B

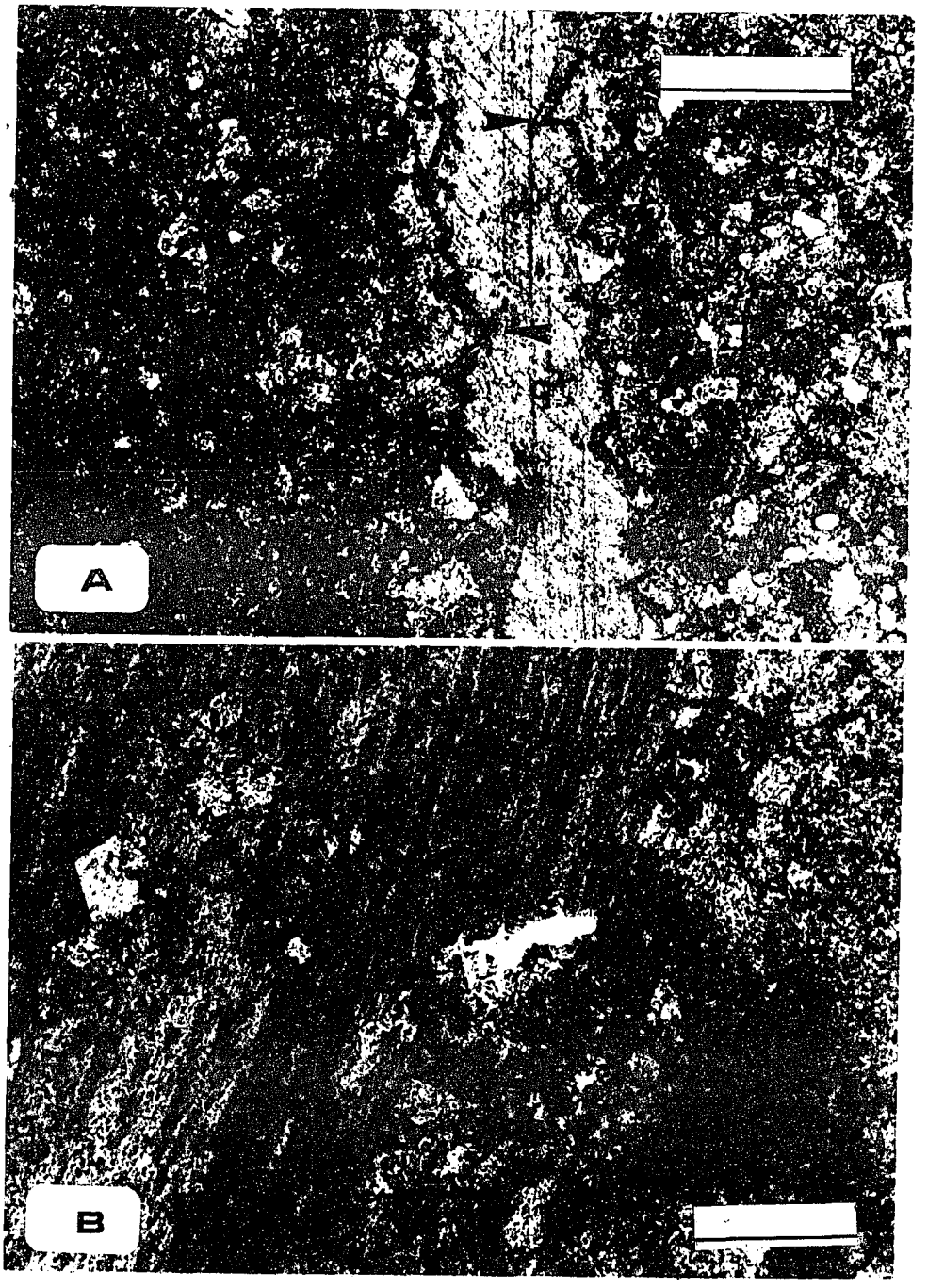


Figure 124- Photomicrographs showing dolomite type VII (mosaic dolomite) and its relationship with pre- and post-pervasive dolomitic, fracture-filling calcite cements. A) Dolomite type VII or mosaic dolomite replaced the fracture-filling calcite cement. Arrowheads point to a "saw-tooth" texture along the replacement front between mosaic dolomite and partially replaced, fracture-filling calcite cement. B) Post- pervasive dolomitic calcite cement (c) replaced dolomite crystal of the xenotopic mosaic. Arrowheads indicate the replacement of dolomite rhombs in the mosaic dolomite by the fracture-filling calcite cement crystals (c). White arrow points to quartz that partially replaced the late fracture-filling calcite crystals. Under cross-polarized light; scales= 0.5 mm.

present in the dolostone units of the AVL, but they are rare.

This mosaic primarily consists of xenotopic dolomites and insignificant amount of idiotopic and hypidiotopic dolomite crystal forms. Idiotopic (euhedral) dolomite crystals with hypidiotopic dolomite crystals are in places observed within some ghost allochems, such as ooids and peloids (Fig. 123 A, B). Idiotopic and hypidiotopic dolomite crystals are also present in places where dolomite replaces fracture-filling calcite cement and interparticle sparry calcite cement which resisted pervasive dolomitization. These late-replacement diagenetic features can simply be recognized as dolomite crystals along the replacement front showing a saw-tooth appearance in which dolomites have euhedral crystals ending toward the large relict calcite cement. The replacing dolomites, however, have hypidiotopic to xenotopic crystal outline ending toward the mosaic dolomite (Fig. 124 A). In addition, idiotopic dolomite crystals in mosaic dolomite occur in a sub-mm distances from xenotopic dolomites, and the euhedral dolomites are more prominent and appear to be locally concentrated with a patchy appearance.

The grain size of dolomites in this dolomite type varies from medium to coarse grain: (1) coarse-grained dolomite, ranging from 0.1 to 0.5 mm; and (2) medium to coarse-grained dolomite, ranging from 0.03 to 0.1 mm. Generally, whole dolomitic sequences have a coarse-grained xenotopic texture except in some silty quartz rich-subtidal lithofacies.

Two types of xenotopic dolomite crystals (Fig. 126 A) in the dolomite mosaic were recognized by their color and inclusion content: (a) gray, inclusion-rich core and clear rim, and (b) light, clear dolomite poikilotopically including some gray and cloudy dolomites and having corrosional or dissolutional crystal boundaries with the gray dolomites. These clear dolomites also show undulose extinction and account for about 8-15 % of total dolomite. These clear xenotopic dolomites probably represent the intercrystalline cement. In some dolostone intervals, gray, xenotopic-dolomite mosaics show an inclusion-rich, cloudy dolomite core and clear rim which are common petrographic textures in all localities. Xenotopic mosaics of dolostone units reveal undulose extinction without any exception.

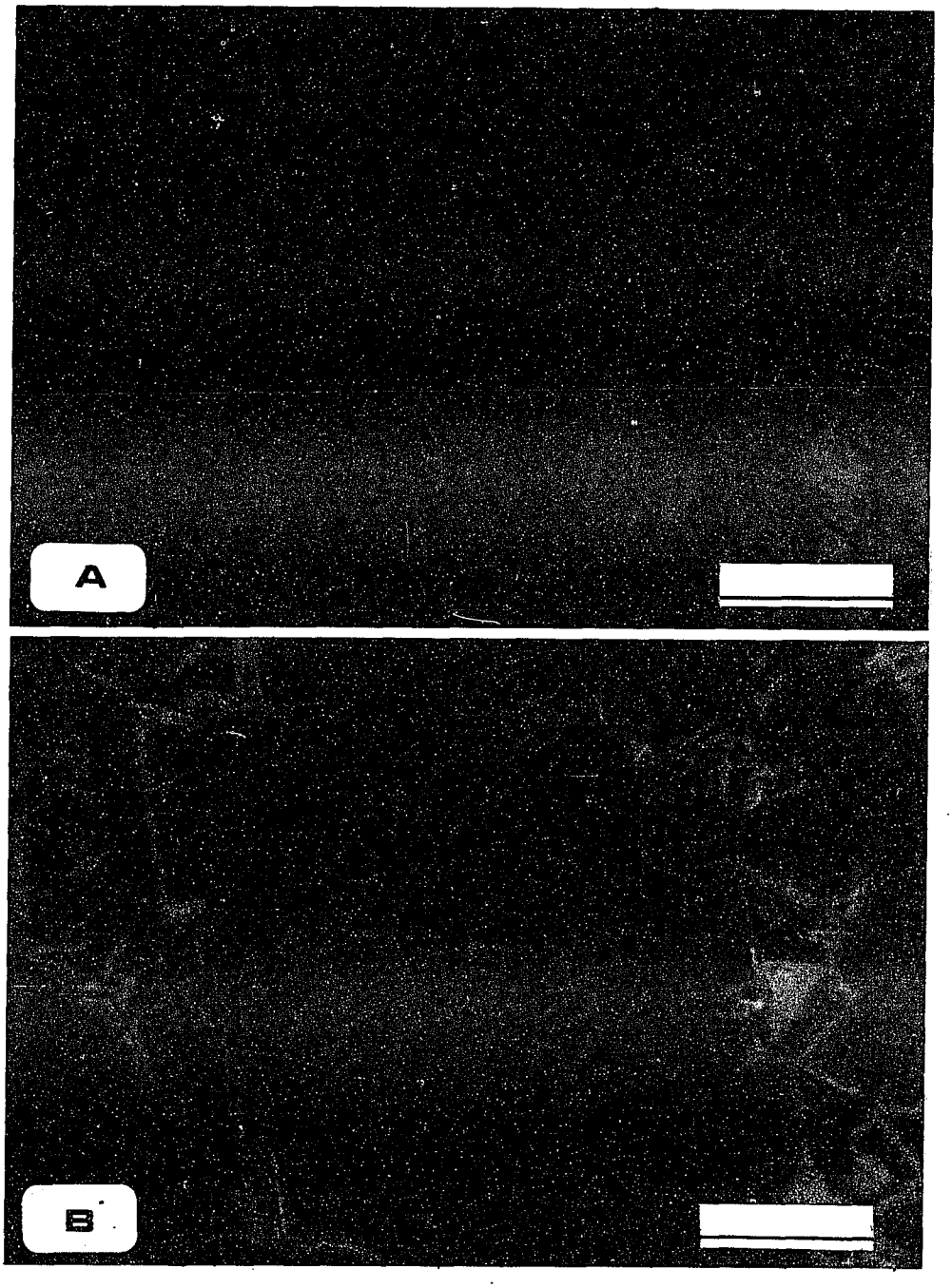


Figure 125- Photomicrographs of a mimicly replaced crinoid by mosaic dolomite. A) Within the xenotopic mosaic dolomite, a very coarse-euhedral dolomite crystal shows uniform extinction, has a circular cloudy and center and clear rim, and has reminiscence of dolomite replaced a single crinoid grain. Under cross-polarized light. B) The same view of photomicrograph A under cathode light shows that mimicly replaced crinoid reveals the same dull luminescence with that of mosaic dolomite, and the single, coarse, dull luminescent euhedral dolomite crystal is followed by orange red luminescence dolomitic cement. Scale= 0.25 mm.

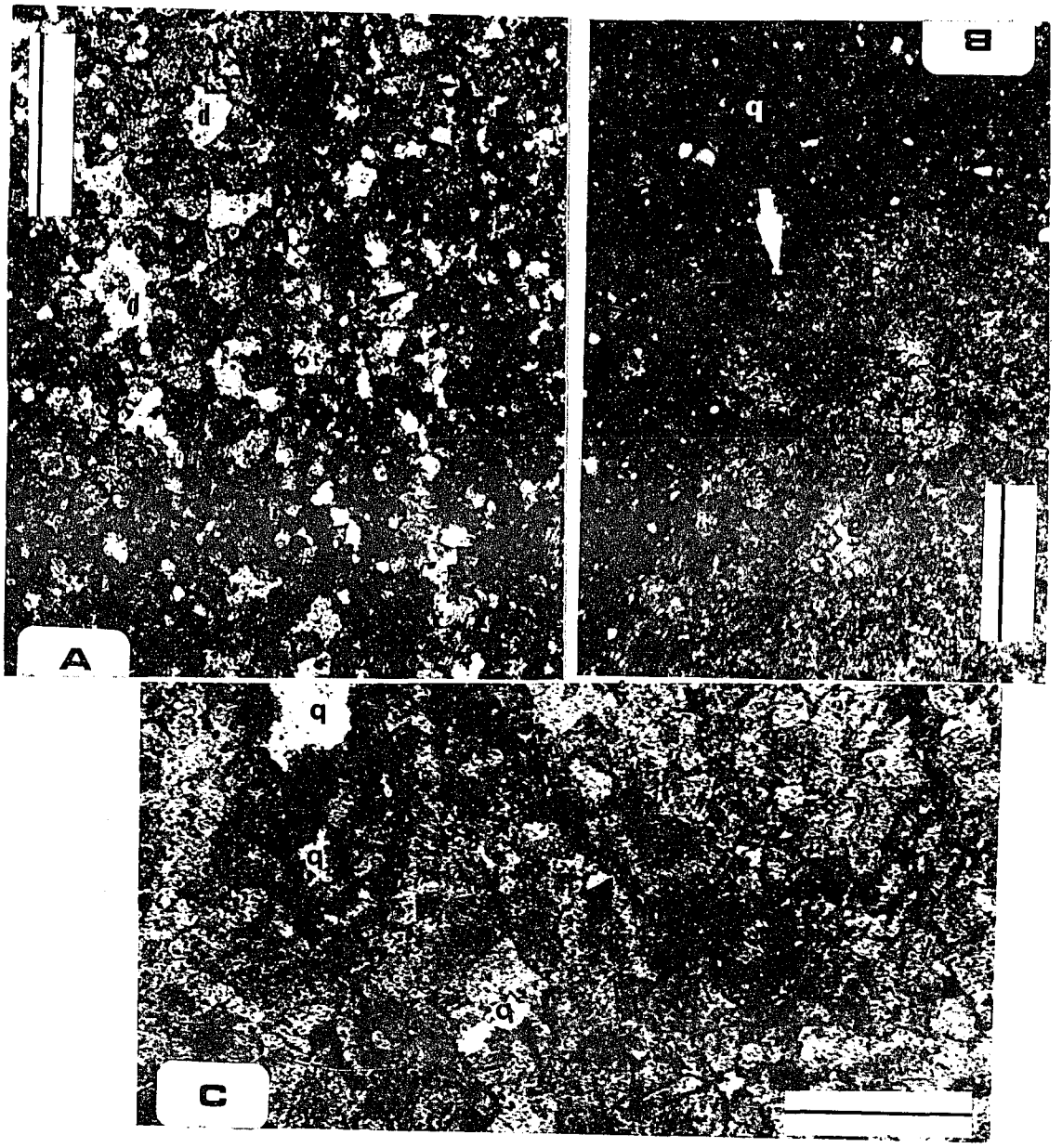


Figure 126- Photomicrographs showing mosaic dolomite (dolomite type VII) and its relation with stylolite. A) Mosaic dolomite postdates horsetail stylolites which are recognizable only by their very narrowed organic residues in the mosaic dolomite without stylolite-induced carbonate cements. (d's) indicate white sparry xenotopic dolomites of the mosaic dolomite. B) Post-pervasive dolomitic, hydrocarbon-stained stylolite pointed by arrows postdates and mosaic dolomites into texturally different two subunits: (1) relatively darker and fine crystalline mosaic dolomite; and (2) relatively lighter and coarse crystalline mosaic dolomite at the upper half of the photomicrograph. C) Pre-pervasive dolomitic stylolite; arrows point to stylolite which does not exhibit stylolite-induced cementation, but it can be recognized only by silty quartz concentrations along very narrow zone in the mosaic dolomite. (q) represents quartz cement which postdates the stylolite and mosaic dolomite. Under cross-polarized light; scales= 0.5 mm.

The xenotopic replacement mosaic erased and altered much of the texture of precursor limestone. Some mimic, and non-mimic replacements (e.g., Kaldi and Gildman, 1982; Bullen and Sibley, 1984; Sibley and Gregg, 1987) can still be recognized. The replacement of crinoid by single dolomite crystals is an example of mimic replacement (Fig. 125); and replacements of ooids, gastropod pseudomorphs, ostracods, and oncoids are example of nonmimic replacement.

In Martin Ridge and Keystone Canyon sections, the calcite-filled fractures are also present which cross-cut the xenotopic mosaic dolomites. Under plane-polarized light, the post-dolomitic, fracture-filling calcite cuts across dolomitic mosaics with a sharp contact, where dolomite does not show a saw-tooth morphology (Fig. 124). In addition, replacive dolomites of precursor calcite-filled, pre-dolomitic fractures can be easily distinguished from the gray mosaic dolomite by their distinct light, clear appearance and relatively larger crystal sizes.

In the dolomite mosaic, insoluble residue marks the stylolites which do not show pressure solution-induced calcite and euhedral dolomite cements, or source-dependent dolomitization (i.e., dolomitization decreases with increasing distance from stylolites; Figs. 126 A, B, C). In many thin sections, dolomite crystals of the mosaic dolomite (type VII) commonly postdate the narrow band of insoluble residue, and in some thin sections stylolites and related organic residue were completely replaced and obliterated (Figs. 126 A, C). However, one stylolite generation or chert-bearing stylolites postdate and partially replace the mosaic dolomites (Fig. 127 B). Chert cogenetically formed with stylolites includes dolomite inclusions and euhedral pyrite, and, thus, postdates the mosaic dolomite.

However, it is very difficult to determine whether the solution paths represented by the stylolites are relict-dissolution paths, or those reactivated by more acidic solutions or another generation of pressure solution formed during deeper-burial postdating mosaic dolomites.

Another type of chert predates pervasive dolomitization (Fig. 127 C), it is found in cores of ghost oncoids and ghost mollusc fragments and is comparable with early chert replacement in the partially dolomitized-, correlative limestones of the AVL in other

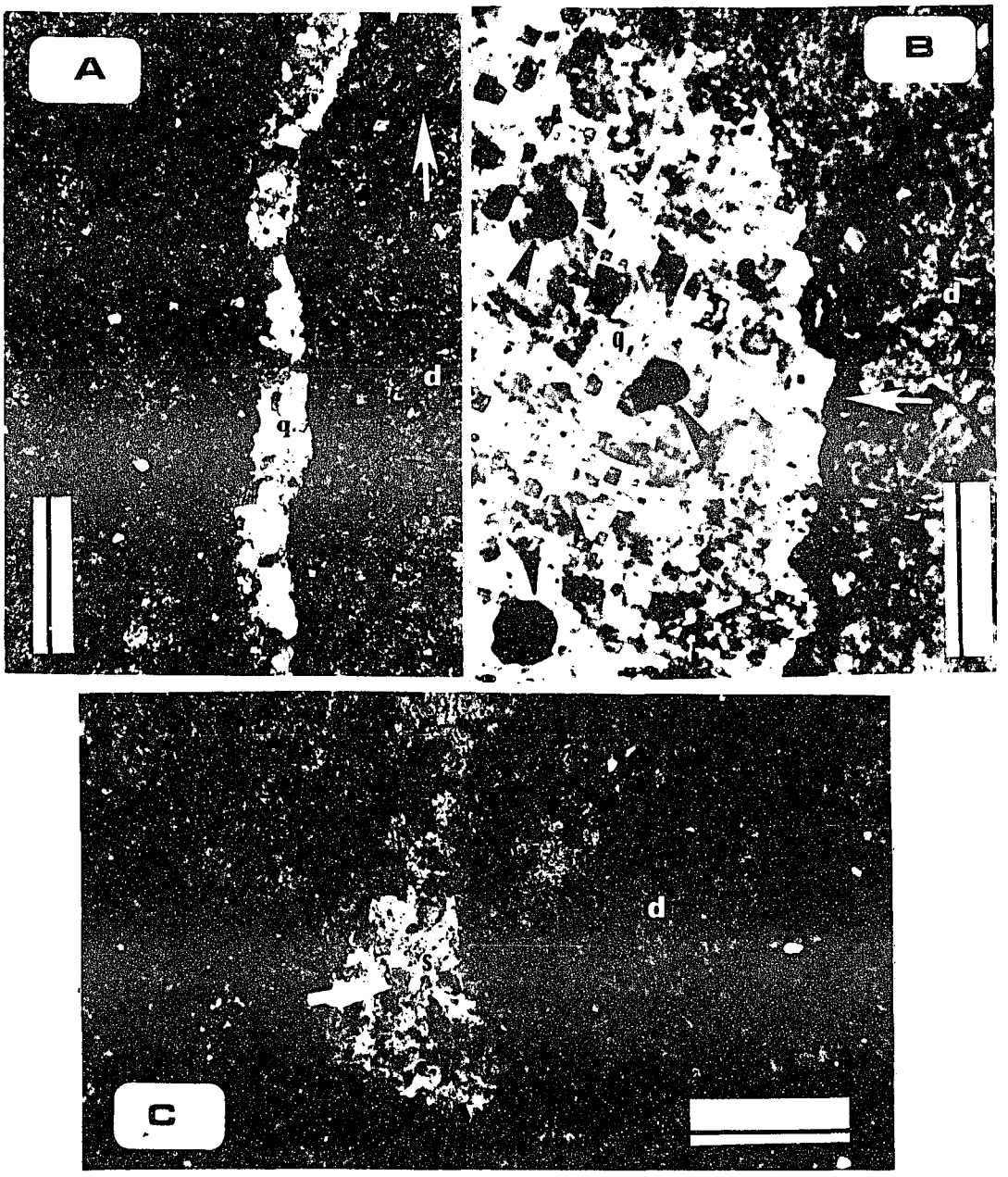


Figure 127- Photomicrographs of mosaic dolomite and intercrystalline quartz cements. A) A quartz-filled fracture postdates the hydrocarbon-bearing, post-pervasive dolomitic stylolite indicated by arrow. Quartz crystals of the fracture-filling quartz cement (q) poikilotopically included dolomite crystals of mosaic dolomite (d). B) Arrows point to the hydrocarbon-bearing, post-pervasive dolomitic stylolite along which quartz (q) replaced the xenotopic dolomite crystals of mosaic dolomite, and poikilotopically included them. Arrowheads point to euhedral pyrite crystals within the poikilotopic replacive quartz. C) Pre-pervasive dolomitic silica was replaced by Dol. VII. White arrow points to the replacement of quartz (s) by mosaic dolomite (d). Under cross-polarized light; scales= 0.5 mm.

sections.

Fractures filled by white sparry dolomites and saddle dolomites cross-cut pervasively dolomitized units. In addition to these, the late calcite, which postdates mosaic dolomite, late fracture-filling dolomites and saddle dolomites, is postdated by replacive quartz and fracture- and pore-filling quartz cement (Figs. 126 C, 127 A). Quartz as a cement fills intercrystalline pores and fractures, and poikilotopically includes some mosaic dolomite. Dissolutional contact relations occur between mosaic dolomite crystals and quartz.

Cathodoluminescence petrography:

Under cathode light, mosaic dolomite reveals a homogeneous, dull to bright-dull red luminescence. Although this homogeneous luminescence is the most common feature of the mosaic dolomite in the dolostones of the AVL, some thin sections reveal bright yellow to orange-red luminescence (Figs. 128 B, 129 B).

The bright red luminescence is volumetrically significant only in dolomite type VII (not more than 15 %); in other dolomites, it never exceeds more than 5 % of the total mosaic dolomite. Both clear and cloudy xenotopic mosaic dolomites have the same homogeneous luminescence. The late bright red luminescence locally produces euhedral crystal outlines within the homogeneously dull luminescent dolomite spar (Fig. 129). It appears to be a late replacive dolomite rather than intercrystalline pore-filling dolomite cement. Locally, euhedral dolomite patches with bright-red luminescence are partially replaced by quartz cements filling the intercrystalline pores (Fig. 128 and 130). The outer boundaries of the bright-red luminescent dolomites show a saw-tooth pattern within the homogeneously dull-red xenotopic mosaic dolomite (Fig. 131 C).

Dolomitized, formerly calcite-filled, fractures show nearly the same luminescence as of the xenotopic host mosaic, ranging from dull to bright, dull red (Fig. 131 A and B). Dolomites of these fractures reveal crystal growth bands of a saw-tooth growth pattern

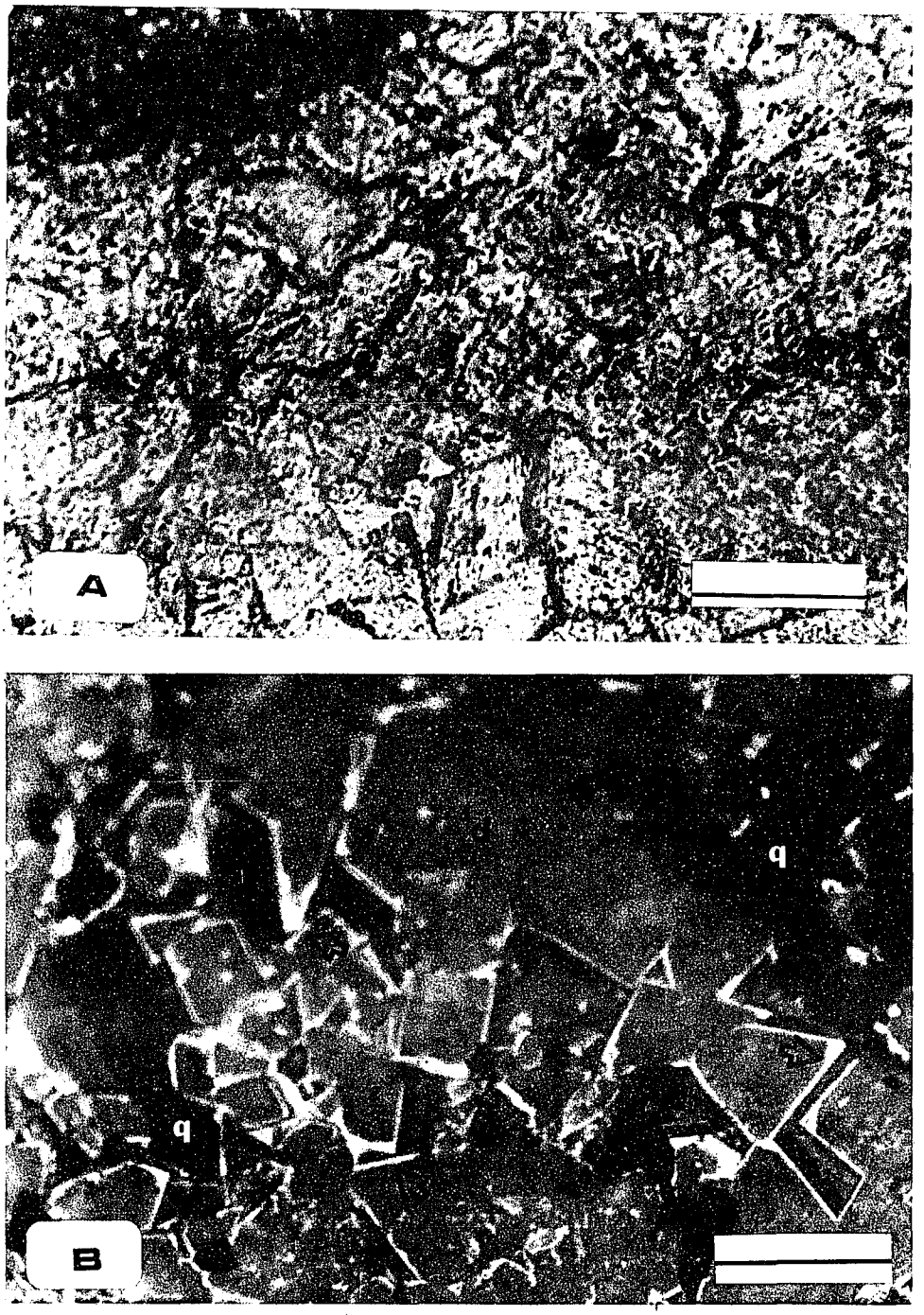


Figure 128- Photomicrographs of mosaic dolomite. A) Mosaic dolomite, under plane-polarized light. B) The same view of photomicrograph A under cathode light shows that mosaic dolomite reveals a dull-red luminescence (d) which is directly followed by orange-red, thin, luminescent rims indicated by arrows. The orange-red rims give an euhedral appearance to the xenotopic dolomite crystals of mosaic dolomite. Non-luminescent quartz (q) crystals replaced the dolomite crystals of mosaic dolomite along corrosional crystal boundaries. Scales= 0.25.

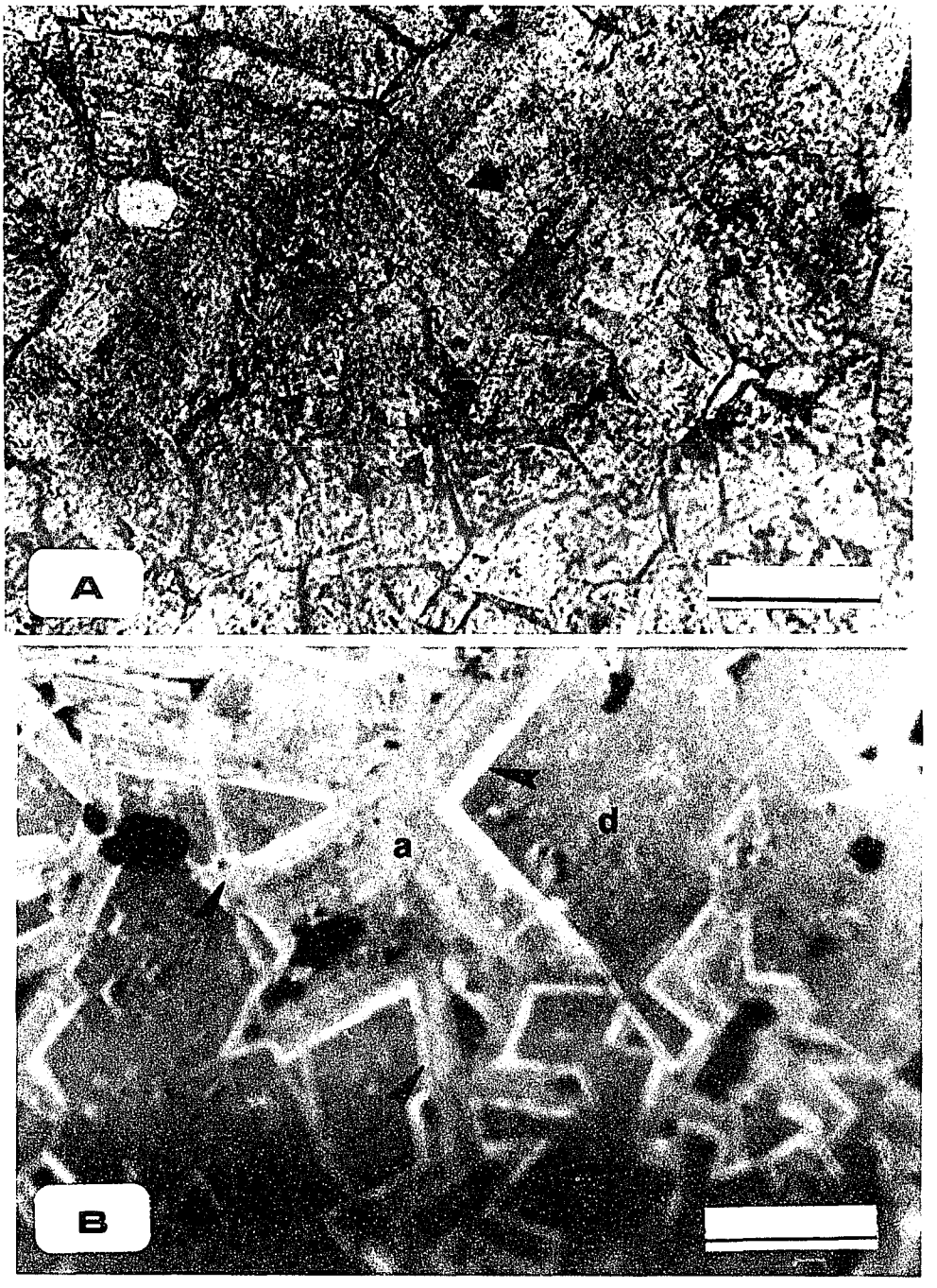


Figure 129- Close-up photomicrographs of mosaic dolomite. A) Mosaic dolomite, under plane-polarized light, shows that some dolomite crystals of mosaic dolomite have euhedral solid and two-phase fluid inclusions zones pointed by arrow despite their xenotopic outlines. B) The same view of photomicrograph A under cathode light shows that dull-red luminescent mosaic dolomite (d) with thin orange-red luminescent bands followed by bright dull-red luminescent cement (a). Arrowheads point to truncational contacts between thin orange-red bands and bright dull-red luminescent cement (a). Non-luminescent quartz cement replaced the mosaic dolomite and its luminescent zones (a) along corrosional contacts. Scales= 0.25 mm.

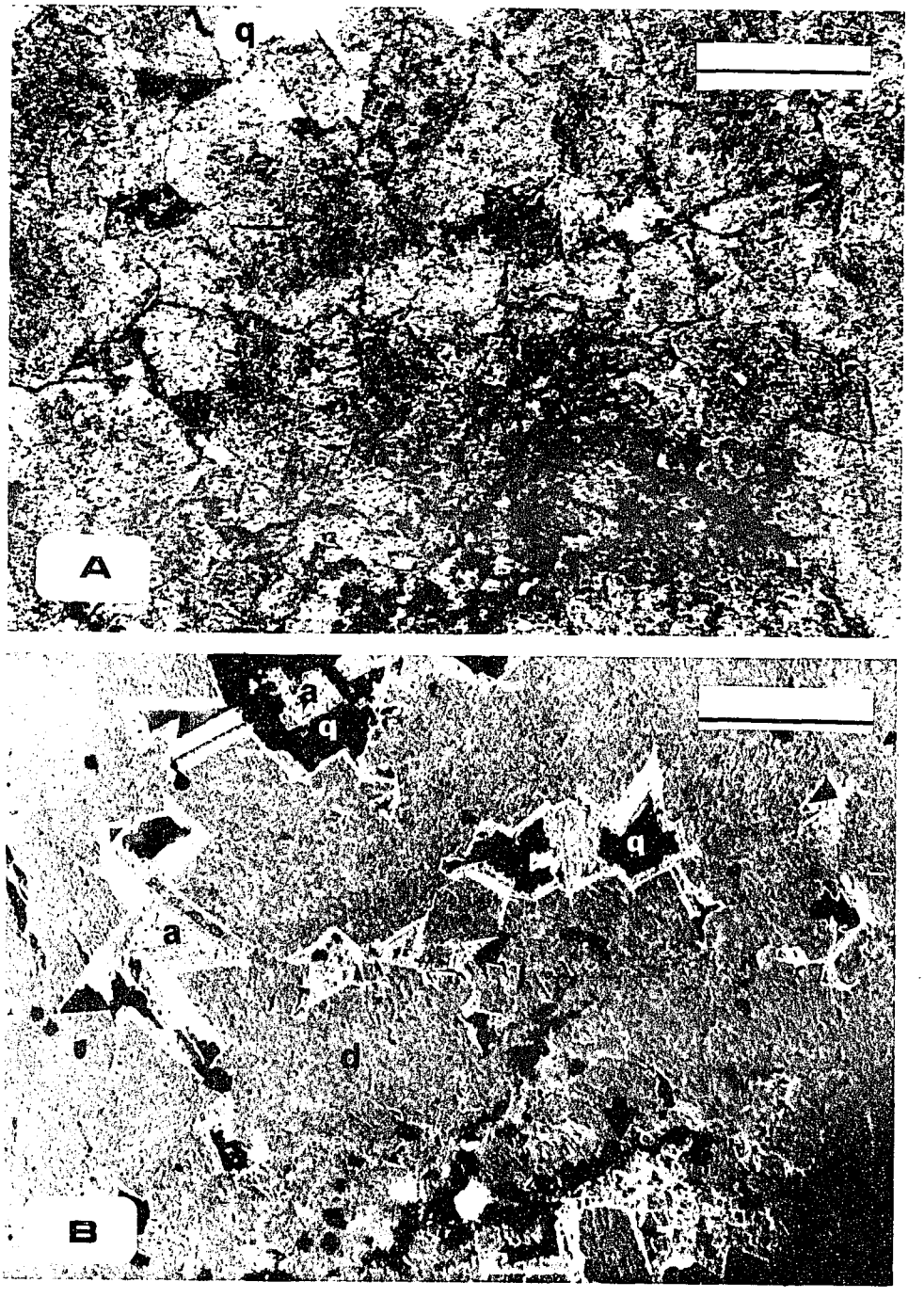


Figure 130- Photomicrographs of mosaic dolomite. A) In mosaic dolomite, arrow indicates a relict penetrative stylolite along which silty quartz (q) particles are concentrated; under plane-polarized light. B) The same view of photomicrograph A under cathode light shows that silty quartz concentration along the stylolite is non-luminescent pointed by arrow, and that quartz cement (q) replaced the mosaic dolomite (d) and bright dull-red luminescent zones (a) along corrosional contacts and poikilotopically included the crystals of the mosaic dolomite and related zones. Scales= 0.25 mm.

which developed from both fracture walls toward the center of the fractures (Fig. 131 B).

Fracture-filling dolomite cements (dolomite VIII) postdating mosaic dolomite " dolomite VII" (Fig. 132 A, B) generally have three zones and two types of textural relationship: (1) truncational or a sharp-contact relation between fracture-filling dolomite cement and mosaic dolomite; and (2) gradual or transitional contact as mosaic cement gradually fills or extends into the fracture. These fracture-filling dolomite cements and their relations will be discussed in the following section.

Fracture-filling calcites also show two types of luminescence: (1) orange-red luminescence revealed by pre-pervasive dolomitic, fracture-filling calcite cement; and (2) bright-yellow luminescence, revealed by fracture-filling calcite which postdates xenotopic mosaic dolomite and is postdated by bright-red luminescent dolomite, late inter-crystalline quartz cement, and late replacive quartz or chert (Fig. 131 C).

Quartz and other silica cements are non-luminescent, and intercrsytalline quartz cement have corroded-crystal boundaries with dolomite crystals of dolomite VII (Figs. 128, 129, 130).

Another important feature that has been noted by cathodoluminescence is the post-stylolitic pervasive dolomitization. Along the tracks of insoluble residue or relic stylolites, scattered, nonluminescent, ferroan-dolomite rhombs are found to be floating within bright dull mosaic dolomite (Fig. 132 A, B). Euhedral crystal outlines of stylolite-induced, non-luminescent ferroan dolomite are corroded and replaced by dull mosaic dolomites; as a result, their formerly straight crystal margins have been changed to nearly curved-and irregular crystal margins (Fig. 132 C).

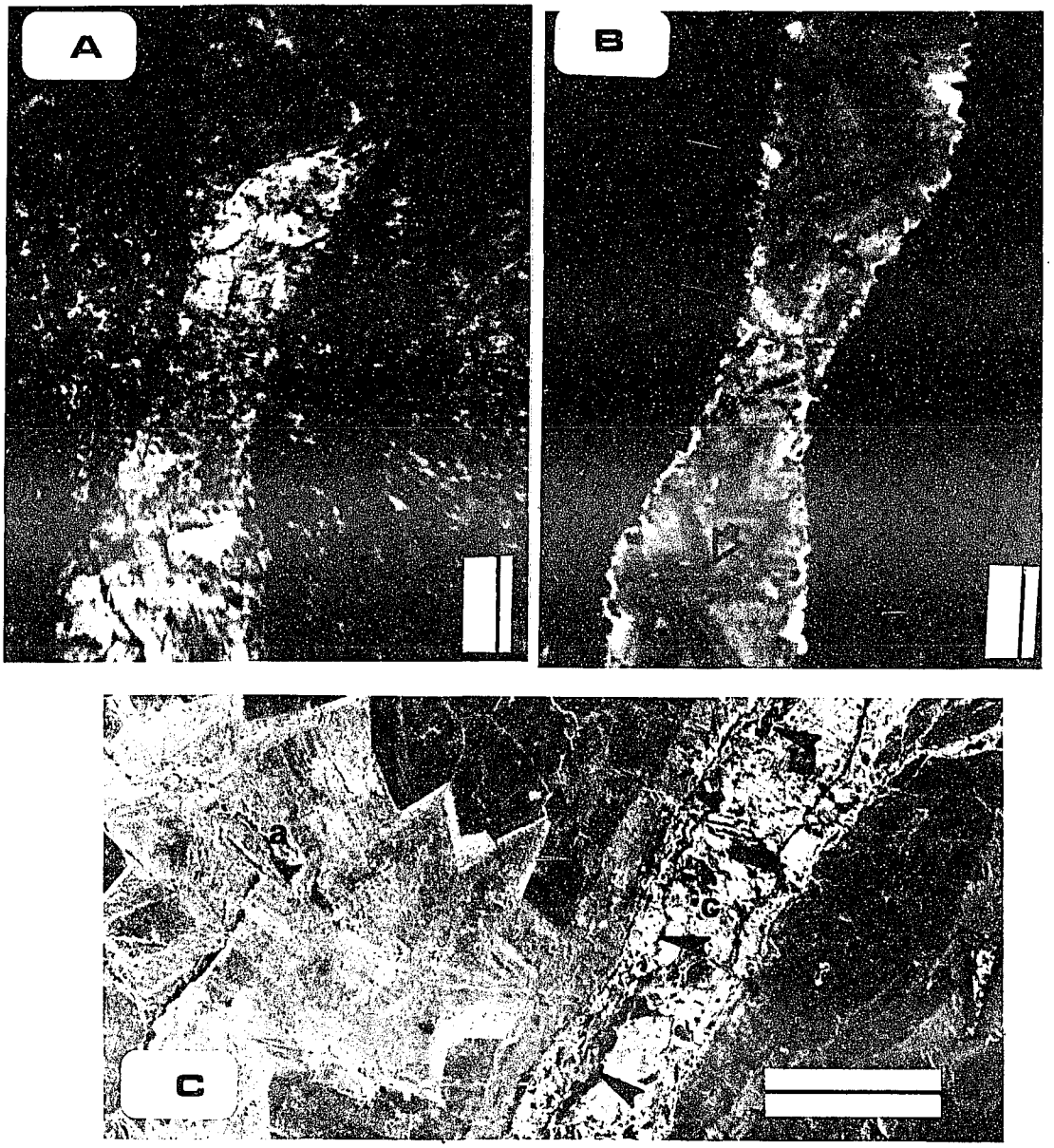


Figure 131- Photomicrographs of fracture-filling dolomite and calcite cements in the mosaic dolomite. A) Fracture-filling dolomite cement within mosaic dolomite shows uniform extinction with that of the host mosaic dolomite and appears to be a pre-pervasive dolomitic, fracture-filling calcite cement; under plane-polarized light. B) The same view of photomicrograph A under cathode light shows that mosaic dolomite and dolomite crystals of fracture-filing dolomite cement reveal nearly a homogeneous luminescence except bright orange-red luminescence at the walls of the dolomite-filled fracture. Arrows point to crystal growth fronts in the fracture-filling dolomite crystals. C) A cathodoluminescence photomicrograph of mosaic dolomite shows that a late-bright yellow luminescent calcite-filled fracture cross cuts mosaic dolomite (d), and is postdated by bright dull-red dolomite (a). Arrowheads point to the late-diagenetic replacement of the fracture-filling calcite cement by silica cement. Scales= 0.25 mm.

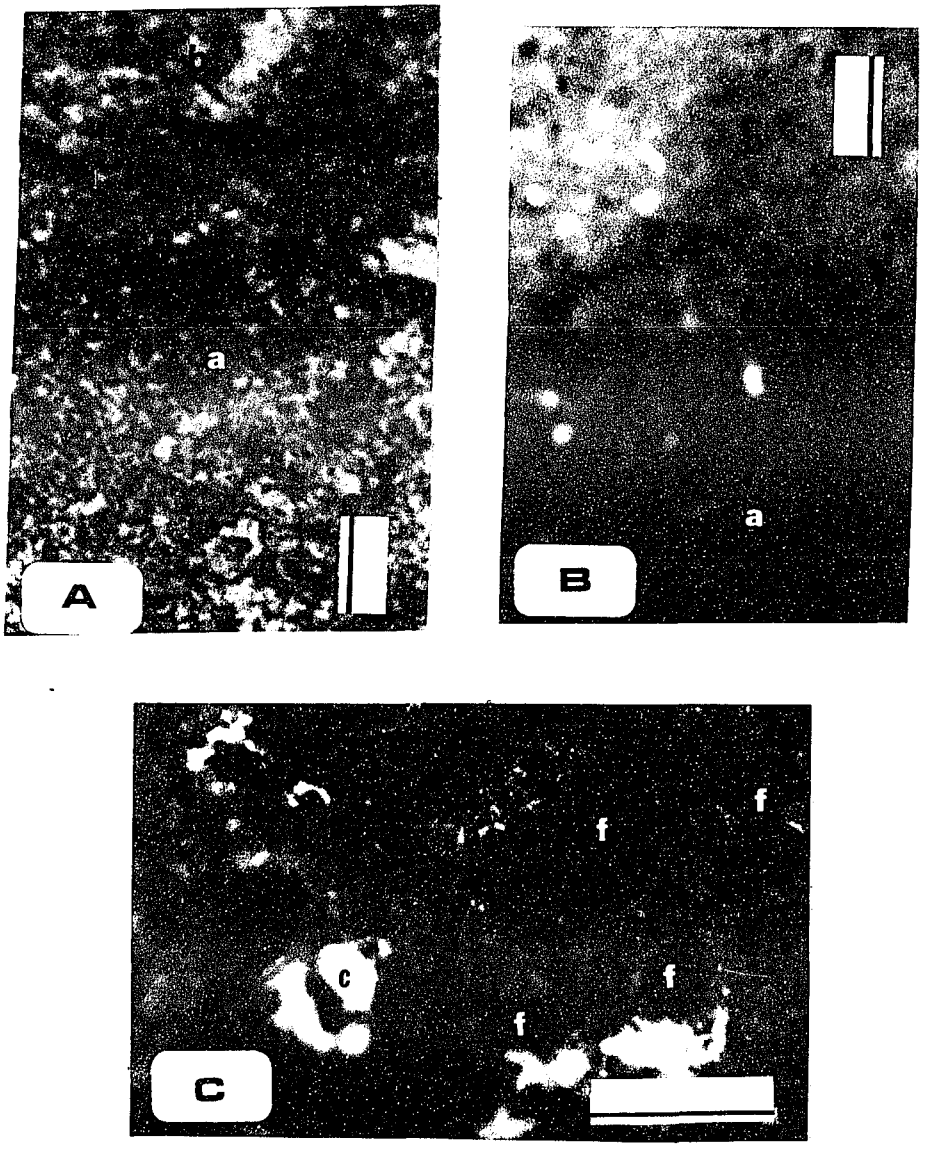


Figure 132- Photomicrographs of mosaic dolomite (Dol. VII) and stylolite-induced ferroan dolomite (VI). A) Arrowhead points to partially continuous relict stylolite within mosaic dolomite; under plane-polarized light. B) The same view of photomicrograph A under cathode light shows that stylolite-induced, nonluminescent dolomite rhombs are abundance in the one side of the stylolite (a). C) Close-up cathodoluminescence view of non-luminescent part of photomicrograph B shows that non-luminescent ferroan dolomites were poikilotopically included and replaced by the dolomite crystals of mosaic dolomite. Truncational contacts are pointed by arrowheads between originally euhedral dolomite rhombs and the mosaic dolomite. Scales= 0.25 mm.

Stable isotope chemistry:

Oxygen isotope composition of the mosaic dolomite generally ranges from -3.14 to -11.05 ‰ PDB (Fig. 133; Table 3).

Table 3- Oxygen and carbon isotope compositions of the late replacive mosaic dolomite VII of the Antelope Valley Limestone.

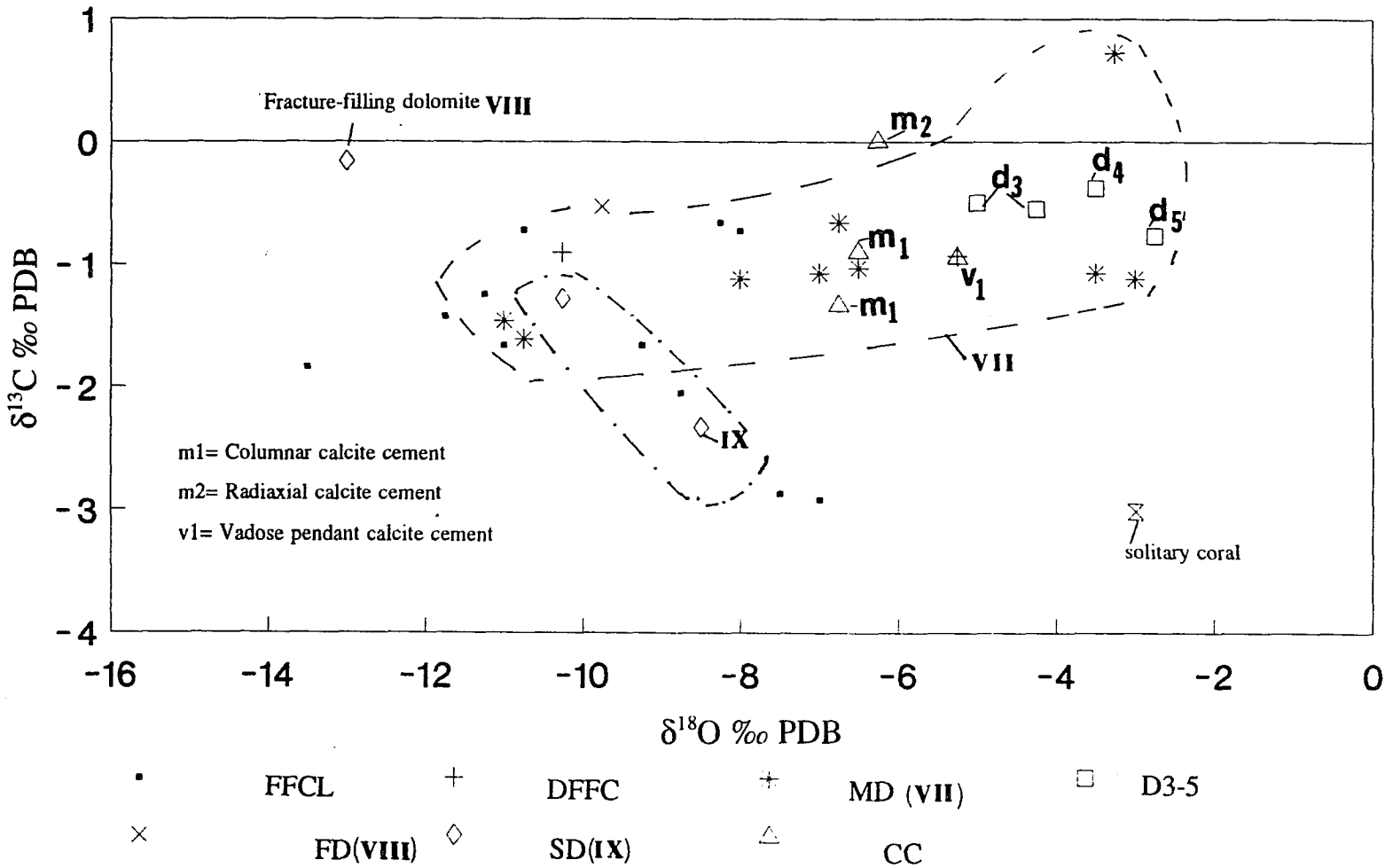
Samples	$\delta^{18}O$ ‰ PDB	$\delta^{13}C$ ‰ PDB	Samples	$\delta^{18}O$ ‰ PDB	$\delta^{13}C$ ‰ PDB
L.171	-3.14	+0.72	C.7 B	-10.84	-1.61
L.150	-5.25	-0.93	C.8 B	-11.05	-1.46
M.28 A	-7.10	-1.07	K.13 B	-8.10	-1.20
M.28 B	-6.88	-1.03	K.17	-3.42	-1.07
M.36	-6.83	-0.66			

In the individual section, the range of $\delta^{18}O$ values occurs in the following ranges: from -3.42 to -5.25 ‰ PDB in the Lone Mountain section; from -6.83 to - 7.10 ‰ PDB in the Martin Ridge section; from -10.84 to -11.05 ‰ PDB in Clear Creek Canyon section; and -3.42 to -8.10 ‰ PDB in the Keystone Canyon section. Carbon-isotope composition $\delta^{13}C$ generally ranges from -1.60 to + 0.72 ‰ PDB.

Stoichiometry of the mosaic dolomite:

A total of forty-three dolostone samples (dolomite VII) of the AVL were analyzed for nonstoichiometry. The nonstoichiometry of mosaic dolomite ranges from 48.8 to 51.2 mole percent of $CaCO_3$. In addition, about three samples have an ideal dolomite composition of 50 mole percent of $CaCO_3$.

Figure 133- Isotope composition of dolomite types and calcite cements of the Antelope Valley Limestone. FFCL= fracture-filling calcite cement in limestone, DFFC= fracture-filling calcite cement in dolostone, MD= mosaic dolomite, FD= ferroan dolomite, CC= calcite cements, SD= saddle dolomite, D3= dolomite type III, D4= dolomite type IV, D5= dolomite type V.



Interpretation:

Field relation of the dolostone intervals in the AVL suggests that dolomite VII (mosaic dolomite) is clearly related to the tectonic activity in central Nevada. Fault-controlled occurrence, sharp basal and upper contacts of the dolomitized intervals, presence of pockets of breccias close to faults, non-stratiform dolomitization, and relative age of the normal faulting--all these suggest that pervasive dolomitization of the AVL took place during late diagenesis when the AVL was buried to great depth and was affected by vertical faulting. Thus, pervasive dolomitization of the AVL can be considered as an epigenetic dolomitization. Absence of extensive early stratiform dolomitization is also consistent with deep-burial, epigenetic, replacive dolomitization which originated from hot basinal solutions. Fault-controlled dolomitization, as dolomitization progressively decreasing away laterally from these faults (Figs. 120, 123), appears to be dominant mechanism in the Antelope Valley region as well as in the Hot-Creek region (Fig. 122 A, B).

The absence of upward decrease in degree of dolomitization from basal contacts of the shoal units (overlying the basinal lithofacies) of the AVL argues against the possibility of thrust-induced dolomitization through expulsion of basinal solutions (Oliver, 1984; and Lee and Friedman, 1987) or early compaction-induced dolomitization (Mattes and Mountjoy, 1980; Quing & Mountjoy, 1988; and Machel and Anderson, 1989).

Mosaic dolomite with a coarse crystal size, xenotopic texture, undulose extinction and a predominantly homogeneous, dull luminescence indicates a late diagenetic, replacive dolomitization at elevated temperatures. Such dolomites are commonly attributed to high-temperature conditions (Morrow, 1982; Zenger, 1983; Gregg and Sibley, 1984; Gregg, 1985; Zenger and Dunham, 1988).

Xenotopic dolomite crystals in the mosaic with a cloudy core and a clear rim are believed to represent progressive enrichment of Mg in the dolomitizing solutions (e.g., Ward and Halley, 1985) rather than progressive dilution (e.g., Folk and Land, 1975).

Increased temperature in sedimentary environments is likely to be related to sedimentary or tectonic loading and resultant subsidence. The deep-burial and elevated-temperature conditions have several advantages over near-surface environments in causing dolomitization: (1) The rate of dolomite crystal growth at low temperature and in the near-surface diagenetic environments is exceedingly slow, whereas long reaction periods and high reaction rates are expected features of burial dolomitization (Mattes and Mountjoy, 1980; Machel and Mountjoy, 1986; Hardie, 1987); and (2) high temperatures overcome kinetic barrier or hydration of Mg which has an inhibiting effect on crystal growth (Mattes and Mountjoy, 1980; and Morrow, 1982).

During early diagenesis, less reactive, coarse-grained low-Mg calcite cements and allochems are unlikely to participate in dolomitization reactions. However, under increasing burial depth and temperature, coarse grained calcite cements and allochems become selectively dolomitized (Muray and Lucia, 1967; Freeman, 1972). Under high temperature conditions, low degree of supersaturation with respect to dolomite results in crystal growth rather than nucleation (Mattes and Mountjoy, 1980). In the AVL, the replacement of fracture-filling calcite cements by dolomite VII and nonfabric-selective dolomite replacements represent the high-temperature replacement features mentioned above.

However, it is not always easy to establish whether the late burial dolomite is a replacement product or due to neomorphism of early diagenetic, near-surface dolomites at elevated temperature. This neomorphism simply means re-equilibration or stabilization of the unstable dolomite phase to the stable phase, as from nonstoichiometric to stoichiometric dolomite. Petrographic lines of evidence for the late diagenetic replacive origin of the mosaic dolomite are going to be compared with results of other techniques, such as fluid inclusion microthermometry, stable isotope chemistry, stoichiometry, and reconstructed-burial history of the AVL.

(1) Texture and paragenesis of mosaic dolomite:

Gregg and Sibley (1984) proposed that xenotopic dolomite in nature and in lab experiments is closely associated with high temperatures ranging from 50 to 100 °C. According to them, xenotopic dolomite begins to form at temperatures of about 50 °C in sabkhas which they named the " critical roughening temperature" (CRT). Shukla (1986) argued that the coexistence of euhedral and xenotopic crystals on a submillimeter scale could not be attributed only to temperature control on the formation of xenotopic texture, but also to the saturation state of solutions and porosity and permeability of the host rock. He also proposed 35 °C for CRT of dolomite. In this study, the coexistence of the xenotopic mosaic and scattered idiotopic dolomite crystals.do not indicate different episodes of dolomitization by different dolomite solutions, but variation in saturation state of the solutions and porosity and permeability of the host.

Similarly, clear xenotopic dolomites occasionally including cloudy dolomite and having dissolutional contacts with gray dolomites probably represent a relatively late pervasive dolomitization which chiefly filled intercrystalline pores among cloudy xenotopic mosaic. The polyhedral pores may have formed during the pervasive dolomitization of the AVL by mole-to-mole replacement reactions. At the end of such reaction, 6-18 % porosity is expected to form (Friedman and Sanders, 1967; Morrow, 1982). Many replacive mosaic dolomites have calcite-filled polyhedral pores or just empty pores (see Shukla, 1986). The intercrystalline calcites probably results from the post-dolomitic calcite cementation or from the same progressively diluted dolomitizing solutions. In the AVL, homogeneous dull luminescence on both cloudy and clear xenotopic dolomite crystals of dolomite VII may indicate single parent solution which was probably diluted but potentially dolomitizing. It is also possible that clear xenotopic dolomite cements may have originated from different dolomitization events due to phases of dehydration or basinal pulses (Cathels and Smith, 1983) under similar burial conditions.

Various studies indicated that dolostones with a predominantly xenotopic texture represent high dolomitization temperatures. Some of the selected temperature ranges

are, as follows: (1) 120 °C (from mean T_h) in the Little Falls dolomite, New York, Zenger, 1981); (2) 150 to 200 °C in the Precambrian dolomite in Scotland (Fairchild, 1980); (3) 50 to 75 °C for the Keg River Formation, Alberta, Canada (Quing and Mountjoy, 1987); (4) 40 to 50 °C for Nisku Formation in Alberta, Canada (Machel and Anderson, 1989); (5) 207 °C for the Ellenburger Formation in the U.S.A. (Lee and Friedman, 1987). And in this study, dolomitization temperature of Antelope Valley Limestone (AVL) ranges from 100 to 160 °C. Some higher temperatures, 180 to 210 °C, were also measured, but major clustering occurs in a range from 120 to 160 °C. Assuming geothermal gradient of 25 °C/ km and an annual surface temperature 20 °C, this temperature range corresponds to a burial depth of 3.2-4.8 km.

2. Post-stylolitic pervasive dolomitization:

As observed in thin sections, very narrow insoluble residue, termination of this residue by replacive dolomite rhombs, absence of stylolite-induced dolomitization postdating dolomite VII, and presence of nonluminescent, ferroan dolomite inclusions (dolomite type VI, being interpreted to have formed during the smectite-illite transformation) within the dull luminescent mosaic dolomite--all these imply that pervasive dolomitization of the AVL postdates pressure solution.

Thus, this pervasive dolomitization is late diagenetic and deep burial in nature. Similar relationships have been reported in the Bonneterre Formation in Missouri by Gregg, (1989).

3. Partial replacement of the fracture or void-filling calcite cement:

Pervasive dolomitization with a saw-tooth morphology is a good argument for late replacement in a deep-burial environment rather than neomorphism.

4. Multi stage dolomitization in the partially dolomitized limestones:

Multi-stage dolomitization spanning early to late stages are commonly present in the correlative, partially dolomitized limestone units of the AVL; absence and scarcity of these multistage dolomitizations in dolostone (dolomite VII) is directly related to

obliterative effects of late, deep-burial diagenetic dolomitization (Mates and Mountjoy, 1980; Zenger,1983; Gregg and Sibley, 1984; Gregg, 1985; and Lee and Friedman, 1987).

Mimic replacement of crinoids and nonmimic replacement of pseudomorphs of allochems also suggest late-diagenetic, post-syntaxial cement dolomitization. Absence of microdolomite rhombs in the crinoids replaced by single large dolomite crystals can also be attributed to late, deep-burial diagenetic replacement.

Dolomitization of silicified-calcite pseudomorphs by dolomite mosaic also provides additional support for late diagenetic origin of this dolomite mosaic because silica replacement was interpreted to form at shallow burial depths after mechanical compaction.

5. Luminescence pattern of mosaic dolomite:

Homogeneous dull red luminescence is found in all the dolomitized units of the AVL in the studied sections. This luminescence type represents a nearly stable and long reaction by the solution(s) of the same or nearly same composition. Such luminescence is very common in many deep-burial cements (Mattes and Mountjoy, 1980; Lee and Friedman, 1987). A second luminescent cement, bright red to orange red in color postdates the homogeneous mosaic dolomite as well as saddle dolomite. The bright red luminescence indicates that in this dolomite the Fe/Mn ratio is lower than that in mosaic dolomite. Dolomite with such a different luminescence type may indicate precipitation from a different basinal solution at a relatively late stage.

Inclusions of nonluminescent ferroan dolomites with dissolutional crystal outlines within the dull luminescent mosaic dolomite (dolomite VII) clearly suggest that replacive mosaic dolomite postdates the pressure solutions-induced ferroan dolomites, and indicate that pervasive dolomitization of the AVL at the indicated areas took place much later and at the greater burial depths than those of the pressure solution-induced, ferroan dolomites.

6. Homogenization temperature of fluid inclusions:

Pressure-uncorrected homogenization temperatures (T_h) of two-phase inclusions from dolomite cement are clustered between 100 and 160 °C, although there are some scattered readings ranging from 180 to 240 °C. These very high T_h are interpreted to have been stretched or re-equilibrated. Th range between 100 and 160 °C is accepted for the minimum formation temperature (because the T_h readings are not corrected for pressure) of this dolomite. This temperature range corresponds to a depth range of 3.2 to 4.8 km (see texture and paragenesis of mosaic dolomite, Chapter 13 A).

7. Oxygen and carbon isotope chemistry:

Oxygen isotope composition ($\delta^{18}O$) of the mosaic dolomite ranges from -3.14 to -11.05 ‰ PDB. Mean value of $\delta^{18}O$ is -7.1 ‰ PDB (Fig. 134). If we exclude the two exceedingly depleted ^{18}O values, -10.84 and -11.05 ‰ PDB of mosaic dolomite from the Clear Creek Canyon section, then the composition ranges from -3.14 to -8.1 ‰ PDB with the mean isotope value of -5.57 ‰ PDB. The reason for the exclusion is that these two isotopic oxygen values represent the mosaic dolomites which have direct contact with the late diagenetic saddle dolomites. Therefore, it can be suggested that these exceedingly depleted-oxygen isotope compositions of mosaic dolomites may have resulted from re-equilibration of mosaic dolomite with the saddle dolomite-bearing relatively hot basinal fluids or brines. The mean isotope value of -5.57 ‰ PDB is very depleted compared to modern dolomites (e.g., McKenzie et al. 1980; Sibley, 1980; Pierre et al., 1984; Ward and Halley, 1985; and Mullins et al., 1988).

The relations between oxygen-isotope composition of dolomites and dolomitizing fluids are not well understood compared to calcite and calcitizing solutions. $\delta^{18}O$ values of dolomites are generally 3.8 ‰ PDB heavier than those of co-existing calcites in limestones (Land, 1980); similar relations have been documented in the epigenetic or fault-controlled Cool Creek Dolomites of Arbucle Group in Oklahoma (Friedman and Sanders, 1967; Friedman, 1992). Such isotopic enrichment is attributed to re-equilibration of isotopically depleted calcites by isotopically heavier and warmer basinal brines (Friedman and Sanders, 1967; Friedman, 1992).

The $\delta^{18}O$ values with a very wide compositional range and a very narrow $\delta^{13}C$ range have been reported in the fault-controlled dolomites of the Wabamun Group by Mountjoy and Halim-Dihradja (1991). They show that some mosaic dolomites of deep-burial diagenetic origin have more enriched $\delta^{18}O$ composition than an average $\delta^{18}O$ values of -3.9 ‰ PDB. They also relate the enriched-$\delta^{18}O$ composition to diagenetically heavier dolomitizing fluids which are assumed to have originated from the compactional brine which probably included some older Frasnian brine.

It is a well known fact that oxygen-isotope composition of dolomites is directly related to composition and temperature of the dolomitizing fluid. High temperature and dilution of dolomitizing fluid by meteoric water are responsible for depleted-oxygen isotope compositions (Land, 1980). He also suggested that dolomite with an isotope composition of less than -4 ‰ PDB could not form at near-surface conditions even if from Paleozoic sea water whose composition was estimated to range from -5 to -6 ‰ SMOW. Therefore, depleted oxygen isotope composition of dolomites may have originally formed during late, deep-burial diagenesis either by replacement of precursor limestone by hot basinal brine (Mates and Mountjoy, 1980; Quing and Mountjoy, 1989; Lee and Friedman, 1987; Kupcez and Land, 1991; Mountjoy and Halim-Dihardja, 1991; and Amthor and Friedman, 1992) or by stabilization (recrystallization) of early, near-surface dolostones (Morrow, 1982; Land, 1985; Moore et al., 1988; Gao and Land, 1991; 1992).

These oxygen isotope values of dolomites are less depleted than $\delta^{18}O$ values of calcites (-7.1 to - 7.8 ‰ PDB) in limestones of the Cool Creek Dolomite (Friedman and Sanders, 1967; Friedman, 1992). In the Cool Creek Dolomite, average oxygen isotope values range from -8.4, -9.0 ‰ and to -9.3 ‰ PDB which were measured from the fine-, medium-, and coarse-grained dolomite crystals, respectively (Gao and Land, 1991; 1992). These two different trends of $\delta^{18}O$ variations in the dolomites and calcites of the Cool Creek Dolomite have been attributed to diagenetic processes: Friedman and Sanders (1967) relate the relatively $\delta^{18}O$-enriched dolomite composition to the isotopic re-equilibration which might have occurred during the replacement of isotopically depleted limestone precursors by isotopically heavy or enriched-$\delta\underline{18}O$ hot

basinal solutions. The exceedingly depleted $\delta^{18}O$ values of the Cool Creek Dolomite are interpreted to have resulted from the modification of pre-existing sabkha dolomites which are inferred from relict anhydrite nodules replaced by chert (e.g. Moore et al., 1988; Gao and Land, 1991) by downward mowing meteoric diagenetic waters (Gao and Land, 1991; 1992). According to them, downdip-moving meteoric water is more dolomitizing due to progressive increase in temperature and concentration of Mg from unstable dolomites than progressively cooling, updip-moving basinal brines.

Petrographic and field evidence of the Antelope Valley Limestone (AVL) indicate that pervasively dolomitized (dolomite VII) units of this formation are late diagenetic replacement dolomites formed from high-temperature basinal fluids in a deep-burial diagenetic environment. Depleted-oxygen isotope values of -5.57 to -7.1 ‰ PDB (mean values of mosaic dolomites) are consistent with deep-burial dolomitization and (Fig. 133). Origin of such dolomitization is also supported by fluid-inclusion data and the reconstructed-subsidence curve.

The oxygen isotope composition of mosaic dolomites of the AVL occur in a wider range from -3.14 to -11.07 ‰ PDB compared to isotope compositions of calcite cements ranging from -6.6 to -6.79 ‰ PDB (from radiaxial and columnar calcite cements; Fig. 133) and of solitary coral (-3.12 ‰ PDB). Some mosaic dolomites have an enriched oxygen-isotope composition ranging from -3.14 to -3.42 ‰ PDB (Fig. 133) compared to $\delta^{18}O$ values of precursor calcites and some mosaic dolomites. Such isotopic enrichment with respect to ^{18}O is probably attributed to the following factors: (1) isotopic compositions of reactant limestones and dolomitizing solutions which are responsible under a given equilibrium temperature for the oxygen-isotope composition of newly replacive dolomite (Mattes and Mountjoy, 1980) since dolomitization is known as a dissolution and reprecipitation process (Katz and Matthews, 1977; Land, 1985); 2) isotopically heavy dolomitizing solutions (Friedman and Sanders, 1967; Mountjoy and Halim-Dihardja, 1991); 3) degree of tightness or variations in the porosity and permeability of mosaic dolomite after the pervasive dolomitization of the AVL and throughout the deep-burial diagenesis of this formation.

During the pervasive dolomitization of the AVL, the isotopically heavy basinal brine

probably contributed to the relatively enriched $\delta^{18}O$ values of mosaic dolomites (e.g., Friedman and Sanders, 1967; Mountjoy and Halim-Dihardja, 1991). The tight portions of mosaic dolomites due to extensive dolomitization may have been closed to hot dolomitizing brines at higher burial and temperature conditions after pervasive dolomitization. As a result, tight portions of mosaic dolomites probably did not undergo further modification. Similarly, Meyers and Lohmann (1985, p. 230) related the isotopically heavy bioherm micrites of the Lake Valley Formation, New Mexico to early-marine micritic cementation or to a diagenetically closed system. Therefore, this study also suggests that mosaic dolomites with enriched-$\delta^{18}O$ values (-3.14 to -3.42 ‰ PDB) represent the closure of tight portions of mosaic dolomites, whereas $^{\delta 18}O$ values of mosaic dolomites (-5.25 to -11.05 ‰ PDB) represent the relatively open systems in the same mosaic dolomite.

In the AVL, carbon isotope ($\delta^{13}C$) values of -1.61 to +0.72 ‰ occur in the sea water compositional range (Fig. 133; Table III). This isotopic composition range may indicate that formation water may have been the source of the mosaic dolomite, or the diagenetic modification of dolomitizing fluid nearly acquired the composition of sea-water.

The isotope compositional range of dolomitized strata in the Antelope Valley Limestone (AVL) is comparable with the following formations: (1) the Miette Dolomite, Canada (Mattes and Mountjoy, 1980); 2) Epigenetic dolomites of the Ste. Genevieve Formation (Choquette and Steinen, 1980); the Little Falls Formation, New York (Zenger, 1981); the Lost Burro Formation, California (Zenger, 1983); the Bonnetrre Dolomite, Missouri (Gregg 1985, 1988); Ellenburger Formation in Oklahoma (Lee and Friedman, 1987).

In summary, the $\delta^{18}O$ range in the AVL is consistent with coarse-grained xenotopic mosaic (Jackson and Fritz, 1971) and deep-burial epigenetic dolomitization which resulted from hot, basinal brine or heated, and modified-ground water.

Dolomite Type VIII (Fracture-Filling Dolomite)

Description:

In the Lone Mountain section, fractures filled with white sparry dolomites cross cut dolostone units. This fracture-filling dolomite (dolomite type VIII) does not have scalenohedral, curved crystal forms. Their crystal size ranges from 0.2 mm to 1 mm. The relationships between fracture-filling dolomite (dolomite VIII) and mosaic dolomite (dolomite VII) are of two types: (a) gradational, even though these fractures appear to postdate mosaic dolomite (Fig. 134); and (b) cross cutting, with a sharp contact (Fig. 136).

In figure 134, dull red-luminescent mosaic dolomites (m) grew into the fracture with euhedral crystals (a) from fracture walls which reveal the same dull-red luminescent with mosaic dolomite (dolomite VII). In the same fracture, the red luminescent euhedral crystals (b), poikilotopically consisting of dull-red luminescent euhedral dolomite crystals, grew toward the center of fractures, and the remaining open tetrahedral pores of the fractures were filled by a very distinct bright-yellow luminescent dolomite or calcian dolomite (c) which is also inclusion-rich and slightly stained by Alizarin red (Figs. 132, 135). Fracture-filling, dull-red luminescent euhedral dolomite crystals with bright yellow-red, thin luminescent rim (band) are similar to mosaic dolomites (Fig. 132).

The other fracture-and void-filling cements, with a sharp contact relations with mosaic dolomites, consist of two luminescent dolomites (Fig. 136 B): (1) bright-red luminescent dolomite (d); and (2) nonluminescent ferroan dolomite (e). The bright-red luminescent dolomites truncate mosaic dolomites and their void-filling component (a) and bright-yellow dolomites (c), and gradually change into the nonluminescent ferroan dolomite (e) see figure 136 B. In addition to fractures mentioned above, some fractures are filled by all the dolomites from a to e (Fig. 136 B).

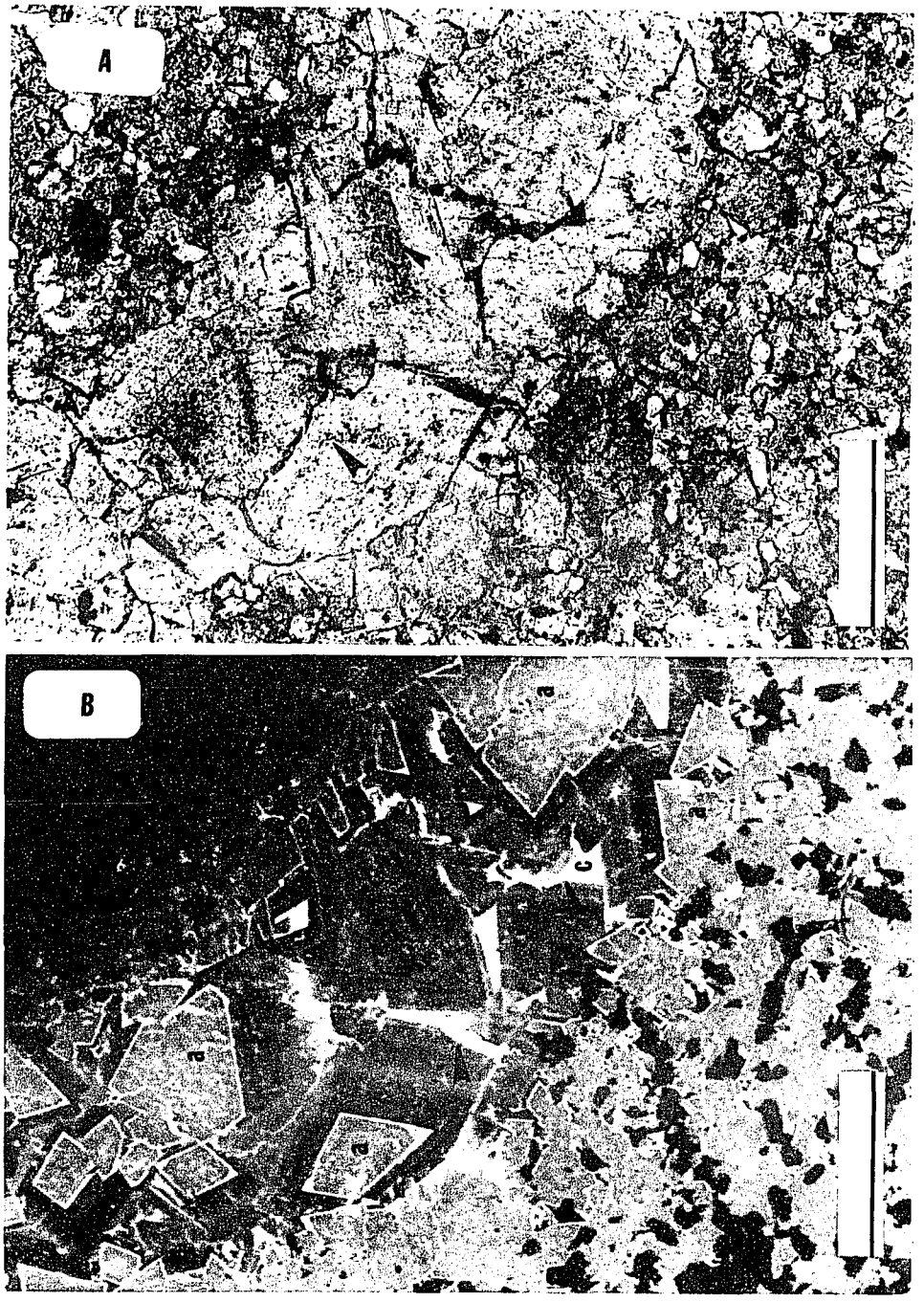


Figure 134- Photomicrographs of fracture-filling, white sparry dolomite (Dol. VIII). A) This dolomite consists of very coarse dolomite crystals which commonly show inclusion rich zones (arrowheads); under plane-polarized light. B) The same view of photomicrograph A under CL shows that Dol. VIII consists of three kinds of discrete luminescent dolomites: (1) bright dull-red luminescent euhedral dolomite crystals with very thin yellow luminescent rim (a's), having a gradational contact with mosaic dolomite; (2) red luminescent zones (b's), being major dolomite type in this fracture-filling dolomite cement and poikilotopically including the rhombs of zone "a"; and (3) thick bright-yellow luminescent dolomite or zone, truncating the zone b. Arrowheads point to truncational contacts between zones "b" and "c". Scales = 0.5 mm.

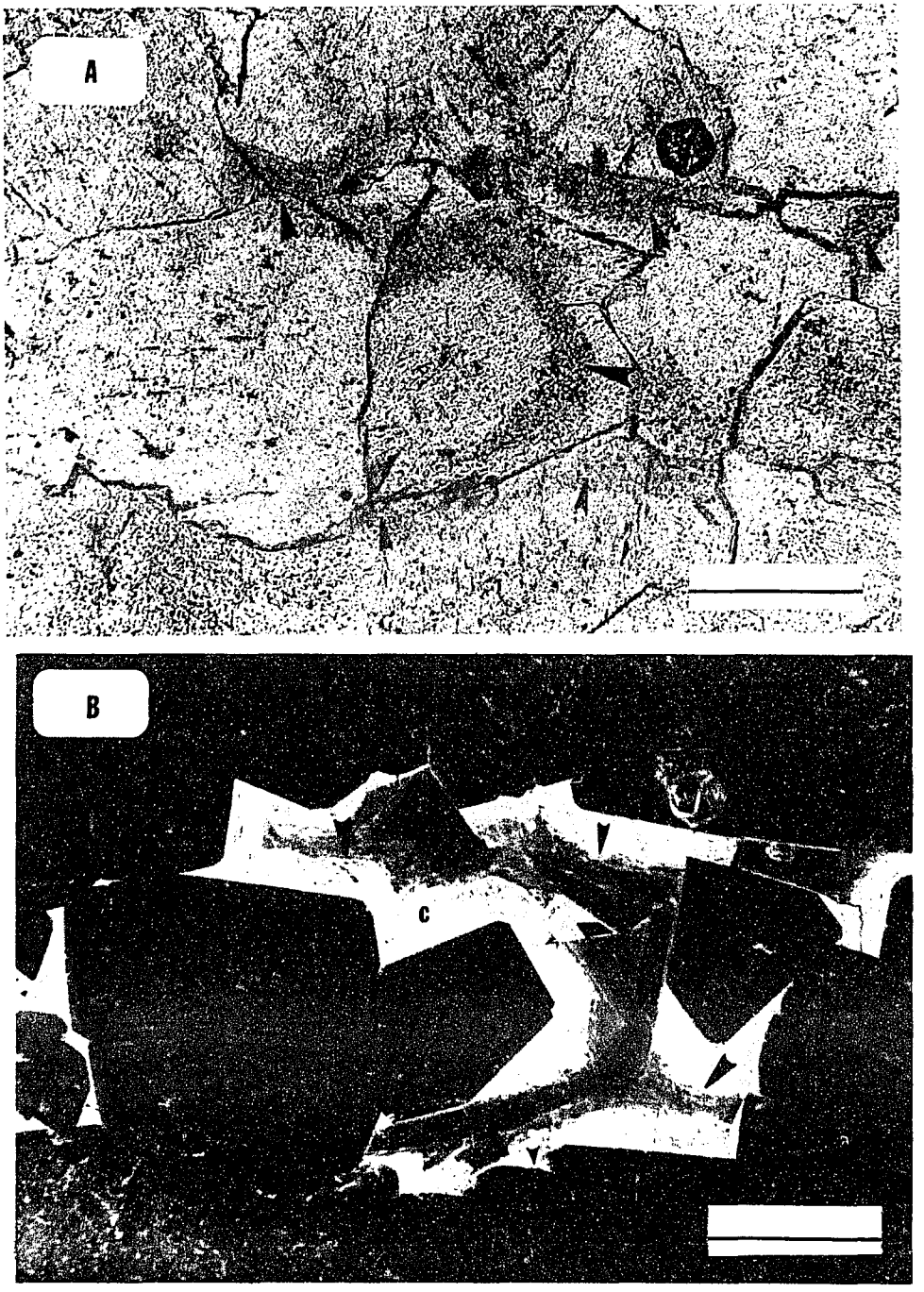


Figure 135- Close-up photomicrographs of inclusion-rich zones in the fracture-filling white sparry dolomite (Dol. VIII). A) In the fracture-filling white sparry dolomite crystals, arrowheads point to Alizarin red-stained, inclusion-rich zones. Under plane-polarized light. B) The same view of photomicrograph A under cathode light shows that the stained zones of this dolomite type reveal a bright-yellow luminescence (c). This bright yellow luminescent dolomite zone (c) truncates the red luminescent dolomite crystals (b); arrowheads point to dissolutional contacts between the "b" and "c" zones of the fracture-filling dolomite crystals. Scales= 0.25 mm.

Fracture-filling dolomite cements from a to c and d to e are optically continuous. However, three truncational or partially dissolved crystal boundaries have been recognized: between the mosaic dolomite and dolomite zone (d); between zone (b) and zone (c); and between zone (c) and zone (d) of dolomite cement (Figs. 135 B, 136 B). Some fractures and voids were filled by fracture-filling dolomites from (a) to (c), or (a) to (e), and only from (d) to (e) (Figs. 135 and 136).

The oxygen isotopic composition of this fracture-filling dolomite is very depleted. The $\delta^{18}O$ values of these late fracture-filling dolomites range from -10.37 to -13.11 ‰ PDB. And $\delta^{13}C$ values are in the range of -0.16 to -0.90 ‰ PDB. The homogenization temperatures (T^h) of two-phase fluid inclusions range from 110 to 160 °C. Melting temperatures (Tm) range from -17 to -25 °C, corresponding to a salinity range of 20 to 27 % NaCl equivalent (Potter et al., 1978).

Interpretation:

Fracture-filling dolomites types from (a) to (c) (Figs. 136, 137), their gradational relations with the host mosaic dolomite, and euhedral crystal outline (ending) of the mosaic dolomite crystals toward the center of fractures (Fig. 132), as well as optical continuity among fracture-filling dolomite cements -- all these suggest that dolomites (a to c) probably precipitated from the same parent solution which pervasively dolomitized the AVL at certain intervals. Therefore, it can be suggested that some fractures formed synchronously with mosaic dolomites and began to be healed by dolomite cements that precipitated form the same dolomitizing fluid. Despite indicated gradational petrographic relations between these two dolomite types, dolomite VIII has more depleted oxygen-isotope composition -10.37 to -13.11 ‰ PDB than dolomite VII (-5.57 to -7.1 ‰ PDB). This differences in isotopic signatures can be attributed to crystallization of dolomite VIII as a fracture-filling cement in the fractures directly from the hot, basinal dolomitizing solutions rather than replacement of relatively cold precursor limestones by the same solutions.

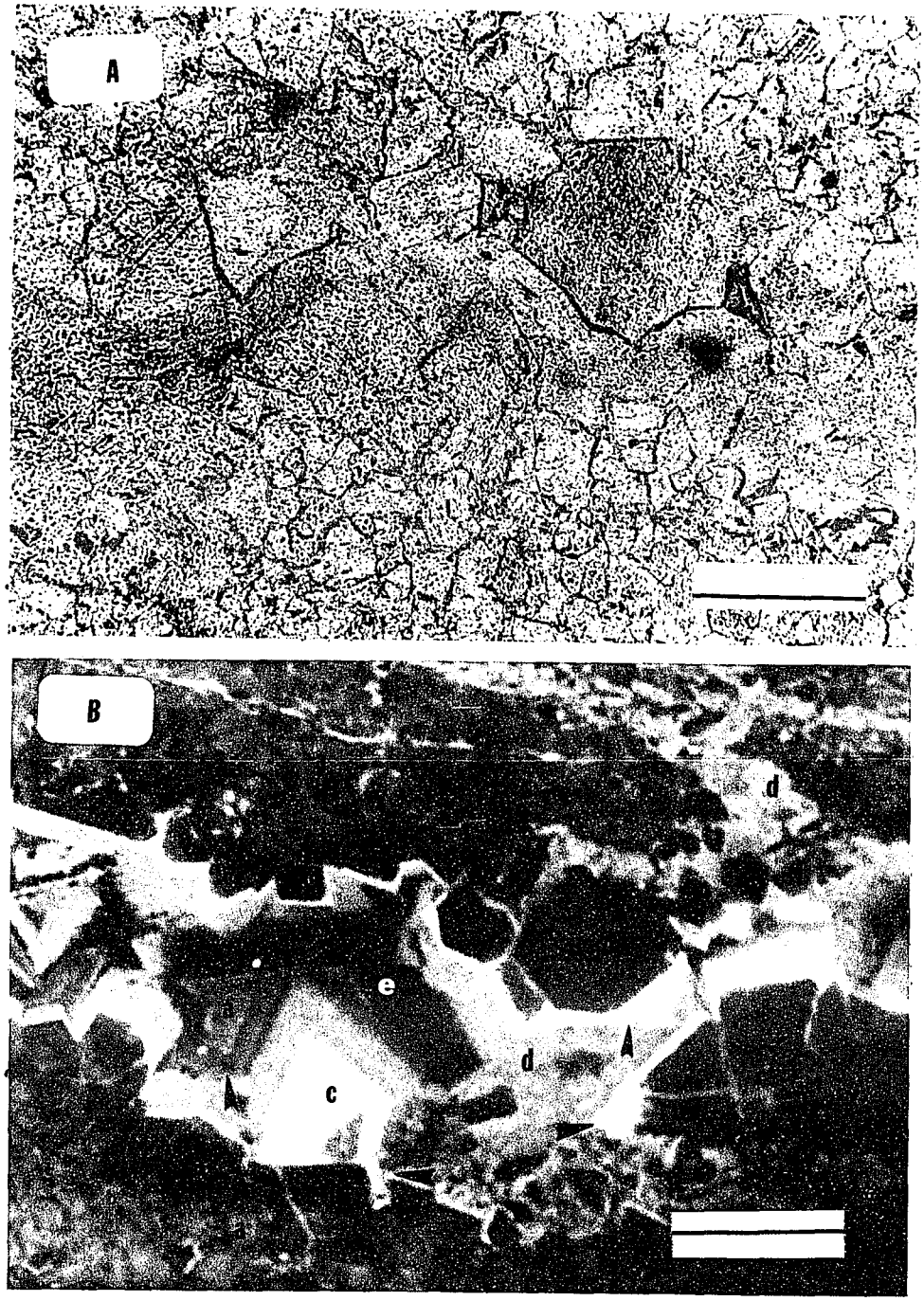


Figure 136- Photomicrographs of void-filling white sparry dolomite cement (Dol. VIII). A) Void-filling, white sparry dolomite cement under plane-polarized light. B) The same view of photomicrograph A under CL shows that in addition to zones of "a", "b", and "c", the bright-red luminescent dolomite zone (d) and ferroan dolomite zone (e) filled the post dolomitic fractures and voids. Arrowheads point to a truncational contact between zones "d" and "c", and "d" and (a). And gradational contact relations occur between zones "d" and "e". Scales= 0.25 mm.

Truncations between dolomite (a) and (d), (b) and (c), and (c) and (d) probably suggest that a second dolomitizing fluid was responsible for precipitating dolomites (d) and (e). Similar dissolutional boundaries or truncational zones are commonly related to multiple episodes of basin dehydration or solution expulsion (Gregg and Shelton, 1989; and Farr, 1989). Gradational contact between bright red luminescent cement (d) and non-luminescent ferroan dolomite (e) suggests a progressive evolution of the second dolomitizing fluid. The fracture type that contains only (d) and (e) dolomites probably represents a post-pervasive dolomitic fracture, later healed by the indicated second parent solution.

Progressive dilution of dolomite-bearing solutions with respect to dolomite probably caused some corrosion and dissolutional boundaries between the dolomites (b) and (c). As indicated before, three fracture-filling dolomite cements (a, b, and c) appear to have formed from the same solutions as progressive dilution with respect to Mg/Ca ratio finally led to calcitization. Alternatively, the dissolutional contact between b and c probably indicates a compositional difference between the two-different dolomitizing parent fluids.

Highly depleted oxygen-isotope compositions, high fluid-inclusion temperatures, and salinity of inclusions about 8 to 10 times that of normal sea water suggest that hot, hypersaline solutions were probably responsible for the fracture-filling dolomites as well as for pervasive dolomitization of the AVL. Since the pervasive dolomitization of the AVL formed synchronously with fracture-filling dolomites (a, b, and c), then it is likely to suggest that hot-basinal fluids in the deep-burial diagenetic environment were responsible for pervasive dolomitization of the AVL.

Dolomite Type IX (Saddle Dolomite)

Description:

This dolomite occurs as a late, fracture-filling dolomite cement which clearly postdates the pervasive mosaic dolomite (dolomite VII). In the field, particularly in the Clear Creek section, saddle dolomite-bearing fractures, 4 to 5 cm thick, cross-cut whole dolostone units and dolostone bedding planes (Fig. 137 A). In addition, small fractures with a zebra-dolomite filling (Mattes and Mountjoy, 1980) occur within dolomitized beds; they are parallel to bedding planes (Fig. 137 b).

Petrography:

The saddle dolomites have curved-scalenohedral crystals, curved twin lamellae and a sweeping extinction (Fig. 137 C). The curved-twin lamellae become gradually faded in some samples, particularly where bright-red luminescent cements replace dull-red luminescent saddle dolomites. Late quartz cement fills the intercrystalline pores among the saddle dolomite crystals. Saddle-dolomite also occurs as a pore-filling dolomite cement; in some cases saddle dolomite replaced mosaic dolomites and poikilotopically includes some small euhedral crystals.

Saddle dolomites generally reveal dull red luminescence, and were replaced by late bright-red luminescent dolomite. All these dolomite cements were replaced by intercrystalline pore-filling quartz cements.

Isotope chemistry:

The oxygen isotopes of this dolomite are highly depleted and $\delta^{18}O$ ranges from -8.44 to -10.23 ‰ PDB. Carbon isotope composition is slightly more depleted than sea



Figure 137- Fracture-filling saddle dolomite (dolomite type IX). A) An outcrop photograph of fracture-filling saddle dolomite pointed by arrowheads. Hammer for scale. B) A polished slab of saddle dolomite shows that very closely spaced, white saddle dolomite-filled fractures within the dark gray mosaic dolomite are similar to zebraic dolomites. Thin quartz vein (q) cross cuts the saddle dolomite. Penny for scale. C) Photomicrograph of saddle dolomite shows that scalonohedral saddle dolomite crystals with bi-directional twins were replaced by untwinned, neomorphic dolospars (n). under cross-polarized light; scales = 0.5 mm.

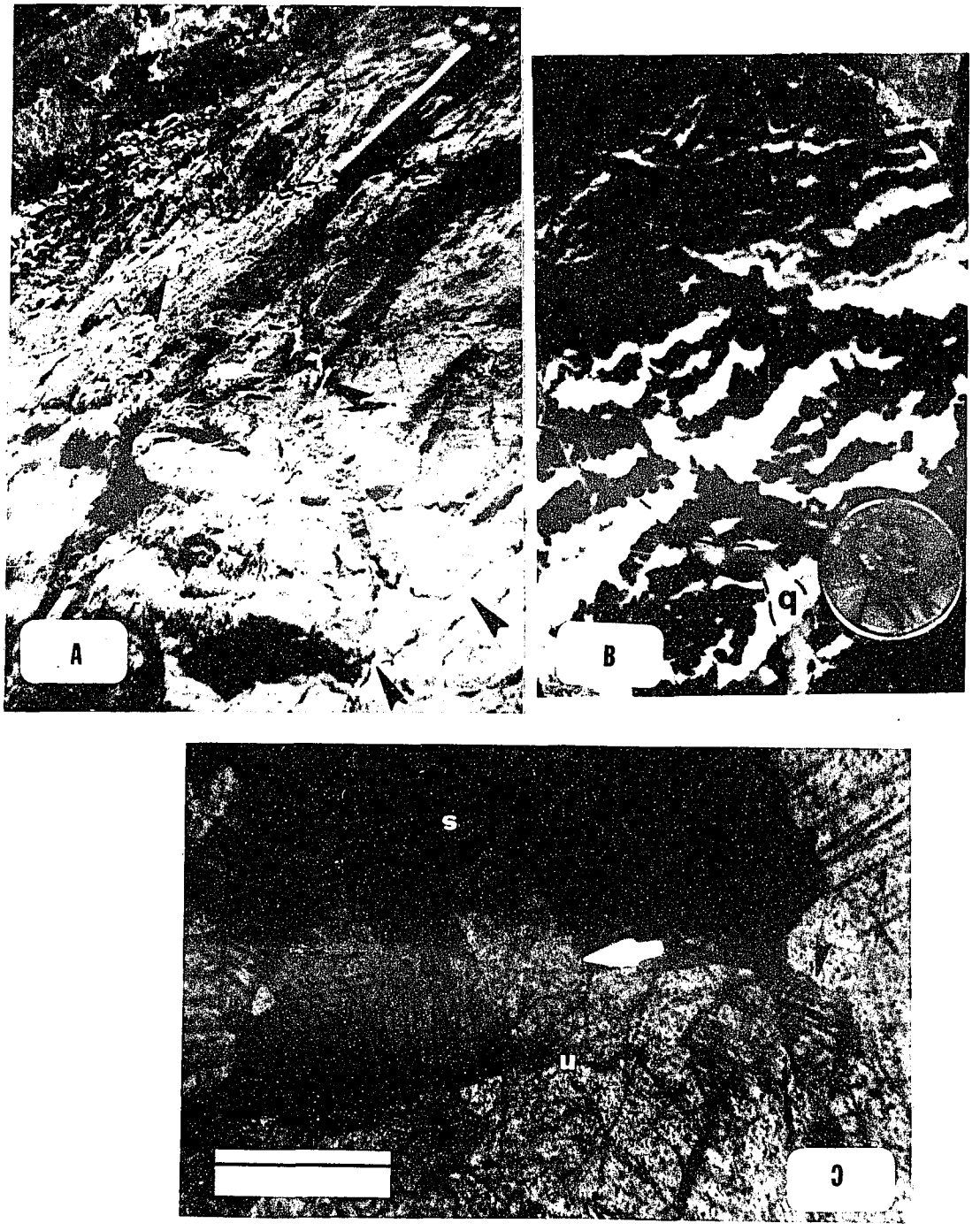


Figure 138- Photomicrographs of untwinned-saddle dolomites. A) Untwinned, (maybe neomorphic) saddle dolomites were replaced by intercrystalline pore-filling quartz (q), under plane-polarized light. B) The same view of photomicrograph A under CL shows that nonluminescent quartz cement replaced the dull mosaic dolomite (d) and bright red luminescent dolomite zone (a). Arrowheads point to corrosional contacts between quartz crystals, mosaic dolomite and bright red luminescent dolomite crystals. Intercrystalline quartz cement also poikilotopically included the latest bright-red luminescent neomorphic dolomite (a). Scales = 0.25 mm.

water, ranging from -1.28 to -2.33 ‰ PDB.

Interpretation:

Crystals with curved-twin lamellae are considered to be major characteristics of saddle dolomite (Radke and Mathis, 1980). Field and petrographic analysis and highly depleted oxygen isotope composition strongly suggest that the saddle dolomites of the AVL are late diagenetic, deep burial in origin. Formation of saddle dolomite directly from hot-basinal brine is widely accepted (Radke and Mathis, 1980; Bales and Hardie, 1980; Quing and Mountjoy, 1988; Machel, 1987; Lee and Friedman, 1987; Friedman, 1987; Kaufman, et al. 1990). Homogenization temperatures of two-phase fluid inclusions in the saddle dolomite are reported to range from 90 to 215 °C (Morrow et al., 1986; Lee and Friedman, 1987).

Two possible mechanisms may be responsible for the formation of saddle dolomite in the AVL: (1) expulsion of basinal fluid due to compaction of basinal shale or anhydrite via increased burial depth (Quing and Mountjoy, 1988, Machel, 1987), or orogeny (Lee and Friedman, 1987; Machel, 19787; Oliver, 1984); and (2) chemical compaction or stylolitization of dolomitic host rocks (Machel, 1987).

In addition to these two, downdip-flowing, diagenetically modified meteoric waters--saturated with respect to dolomite from dissolution of pre-existing dolostone--are assumed to produce fracture-filling dolomites, particularly during orogenic uplifting (Gao and Land, 1991); however, this is not the case for the AVL.

In this study, saddle dolomites primarily fill fractures and these fractures postdate the host dolostone units. Pressure solution can not account for the saddle dolomites of the AVL because formation of these fracture was primarily caused by very high hydrostatic pressure exceeding the confining pressure, unlike pressure solution in which dissolution of carbonate is primarily induced by confining pressure (Bathurst, 1980). Therefore, it is suggested that the saddle dolomites of the AVL precipitated from allochthonous basinal solution of unknown source.

Relative timing of saddle dolomite probably reflects a dolomitization event that took place during the Late Permian and Early Triassic Sonoma orogeny. Expulsion of the heavy basinal brine during the orogeny probably increased the hydrostatic pressure and eventually led to the formation of saddle-dolomite-bearing fractures.

CHAPTER 13-B: DOLOMITE STOICHIOMETRY

Introduction:

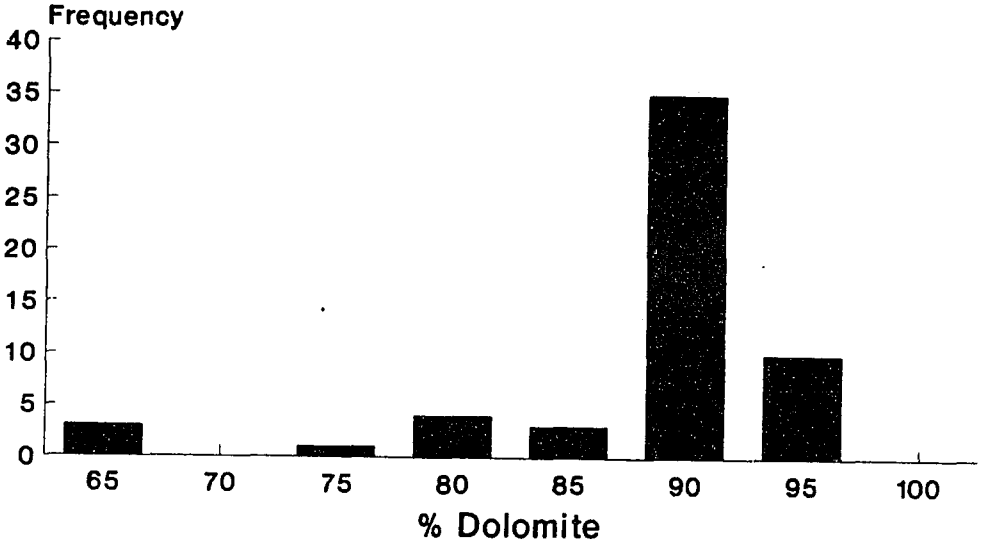
Approximately forty-three dolostone (dolomite VII) samples and a total of 13 dolomitic limestones were analyzed by X-ray difractometry in order to determine the mole percentages of $CaCO_3$ and $MgCO_3$ in dolomites of the AVL. Composition of ideally ordered or stoichiometric dolomite is $Ca_{0.50}Mg_{0.50}CO_3$ (Goldsmith and Graph, 1958). Any departure from the indicated mole concentration of this formula toward calcite is commonly considered to be a degree of calcitization. Therefore, the measure of calcite enrichment in dolomite composition can be used as a level of nonstoichiometry (e.g., Goldsmith and Graph, 1958; Lumsden and Chimahusky, 1980; Land, 1983). Generally, the mole percent of $CaCO_3$ in dolomites can be expressed as a degree of nonstoichiometry since common presence of trace elements, particularly Fe^{+2} and Mn^{+2} do not affect the nonstoichiometry.

Dolomite nonstoichiometry can be measured by the relationship between mole percent of $CaCO_3$ in dolomite (d_{104}) reflection peaks. When mole percentage of $CaCO_3$ is higher, d_{104} superstructure reflection become increasingly wider and $d_{(104)}$ spacing also increases (Goldsmith and Graph, 1958).

Dolostones

Results:

In the AVL, the dolomite content of dolostone units occurs in the range of 90 to 100 % with a few exceptions (Fig. 139). Generally mole percentage of $CaCO_3$ in dolomites of dolostones occur in a very narrow zone of 48.2 to 51.2 % (Figs. 140,



A total of 47 dolostones were analyzed for the stochiometric study

Figure 139- Dolomite percentages in dolostones of the Antelope Valley Limestone. The rest of the dolostone composition are mostly calcite, and a few samples are composed of considerably high fine-grained siliciclastics.

141; and see Table 4A). The average mole concentration of $CaCO_3$ for 39 samples is 50.9 % and this corresponds to 49.1 average mole percentages of $MgCO_3$.

Table 4A. indicating d-spacing and mole % of CaCO3 and MgCO3 in dolomite composition.

Number of Samples	Dolomite %	d-spacing Å	Mole % $CaCO_3$	Mole % $MgCO_3$
1 mosaic	65	2.888	50.9	49.1
2 "	75	2.889 - 2.892	51.2 - 52.2	48.8 - 47.8
2 "	85	2.887 - 2.888	50.3 - 50.6	49.7 - 49.4
5 "	90	2.885 - 2.888	49.7 - 51.6	50.5 - 48.4
29 "	100	2.882 - 2.888	48.8 - 51.5	51.2 - 48.5
		2.887 - 2.888	50.3 - 51.5	49.7 - 48.5
4 Saddle	100	2.887 - 2.893	52.1 - 52.5	47.8 - 47.5

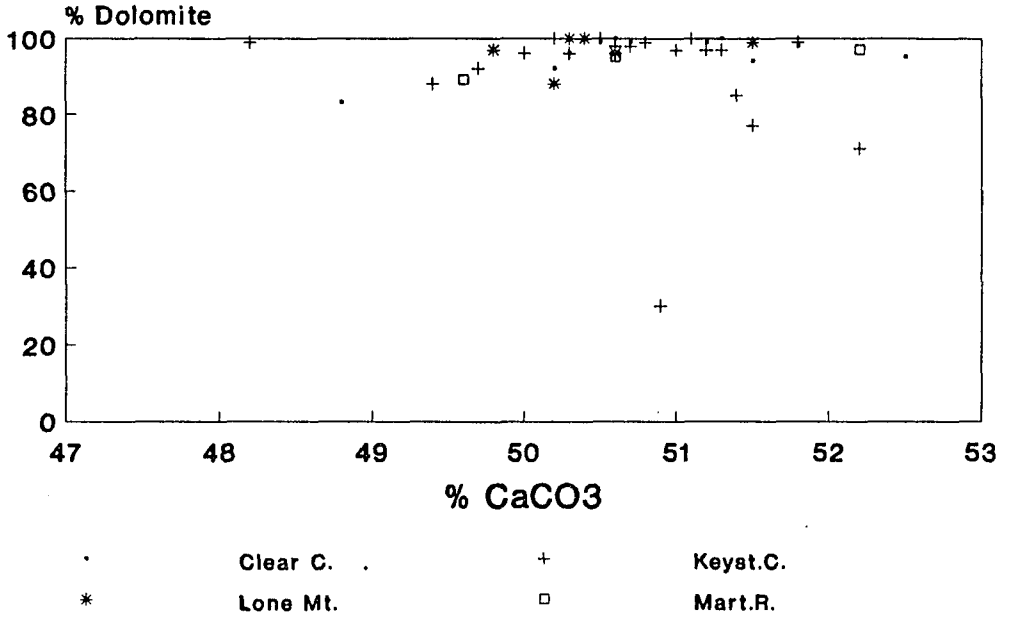
The mole concentration of $CaCO_3$ in four saddle dolomites ranges from 51.2 to 52.5 %, (Table 4A; average 52.2 %). Four dolostones with a recognizable Girvanella-derived oncoidal precursor, are considered to have had a formerly organic-rich composition; their $CaCO_3$ mole concentrations range from 49.7 to 51.5 % (average 50.6 %). Two dolostone units with mimic replacement on crinoid grains have 48.8 mole percent of $CaCO_3$; therefore, about 1.2 mole percent of $MgCO_3$ enrichment has been detected in these samples. Except for saddle dolomites, the various dolostone lithologies representing a very wide range of depositional spectrum show nearly the same $CaCO_3$ molar concentration (Table 4A), as indicated below:

(1) coarse-grained dolomite VII = 50.9 % .

(2) Silty quartz-rich, medium- to coarse-grained dolomite VII= 50.6%

(3) coarse-grained dolomite VII with oncoid relics= 50.6 % .

(4) coarse-grained dolomite VII with crinoid relics= 48.8 % .



Based on 47 dolostone samples

Figure 140- Mole percentages of $CaCO_3$ in the composition of dolomites of the dolostone units of the Antelope Valley Limestone.

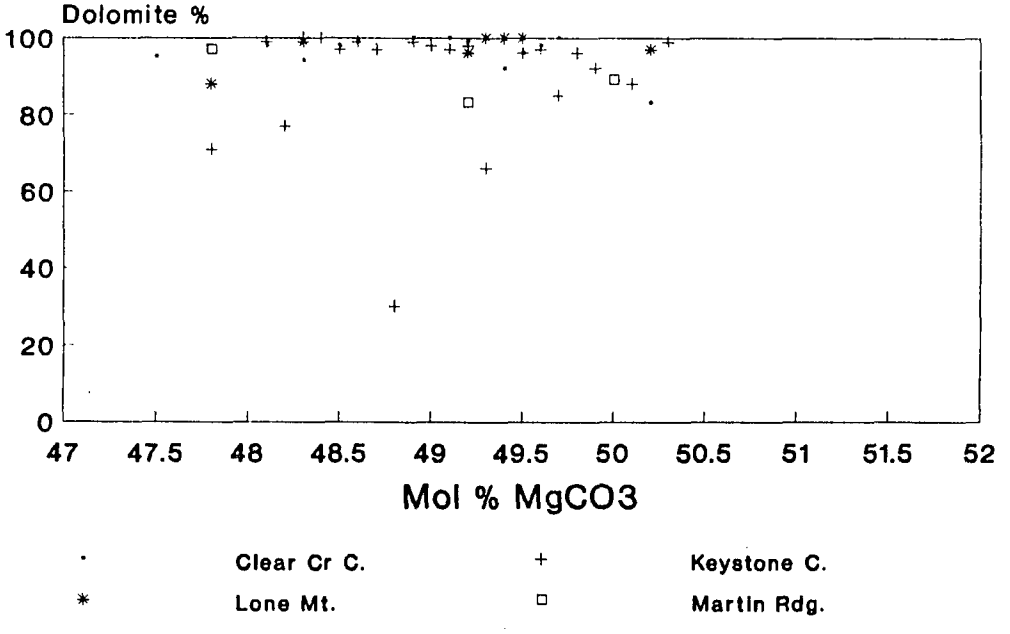


Figure 141- Mole percentages of $MgCO_3$ in the composition of dolomites of the dolostone units of the Antelope Valley Limestone.

(5) Saddle dolomite (dolomite IX)= 52.2 % .

In addition, dolomites of the dolostones of the AVL do not exhibit any variations in their stoichiometry with respect to the stratigraphic positions.

Interpretation:

Nearly ideal or the nearly stoichiometric dolomites are determined to be ranging from 50 to 52 mole % of $CaCO_3$ by Lumsden and Chimahusky (1980), and 51 mole % of $CaCO_3$ by Sperber et al.(1984). According to both ranges, dolomites of dolostones of the AVL are nearly stoichiometric because their average mole concentration of $CaCO_3$ is 50.9 %.

Nearly stoichiometric dolomite composition is consistent in all the dolostone intervals despite different grain sizes, and siliciclastic and organic-matter concentrations.

Non-stoichiometry of the dolomite in the dolostones of the AVL with respect to variations in grain size of dolomites, lithology types of dolostones, their stratigraphic positions and organic matter contents is in agreement with the findings of Lumsden and Chimahusky (1980) and Sperber et al. (1984). However, two dolostone samples that are assumed to have had crinoidal packstone and grainstone precursor show 1.2 mole % of $MgCO_3$ enrichment (48.8 % of $CaCO_3$) compared to ideal dolomites. Unlike in the work of Lumsden and Chimahusky (1980), this study relates such enrichment to the crinoid content of the precursor crinoidal packstone and grainstone units. About 1.2 mole % of $MgCO_3$ enrichment in dolomites of the dolostone of the AVL may have been directly related to the mode of early diagenesis: whether crinoids were altered by dissolution or by neomorphism. Because early diagenesis in near-surface environments by meteoric water often causes dissolution of crinoids (e.g., Dorobeg, 1987) and early dolomitization like in the Gate Hope Formation in Jamaica (Bullen and Sibley, 1984). Diagenesis of crinoids by dissolution probably produces crinoid molds which are likely to be filled by low-Mg calcite; therefore, this low-Mg

composition during late, diagenetic replacement at considerable depth does not contribute additional Mg to replacive dolomite. On the other hand, it can be suggested that crinoids with a high-Mg composition were neomorphically stabilized by meteoric water. As a result, crinoids retained their generally Mg-rich composition by neomorphism which resulted in the formation of euhedral microdolomites; then finally late diagenetic replacement of neomorphically altered crinoids and euhedral microdolomites by hot basinal, hypersaline solutions probably caused such enrichment in the composition of the replacive dolostone of the AVL.

The other important point, noted by this study, is that late fracture-filling dolomite cement and saddle dolomites are approximately 0.9 mole % more calcitic than dolomites of dolostones or pervasively dolomitized units of this AVL. Such more calcitic composition of late dolomites cement can be attributed either to fault-like crystal defects resulting from crystal growth (Reeder and Barber, 1982), or to the low-Mg / Ca ratio of basinal solutions (Sibley et al. 1987).

Absence of stratigraphy-controlled stoichiometry is probably related to non-hypersaline near surface dolomitization (Lumsden and Chimahusky, 1980).

Dolomites of dolostone units of the AVL are nearly stoichiometric at every stratigraphic level and position. The nearly stoichiometric dolomite composition of dolostones was probably closely associated with replacement of the AVL by hot basinal brines during deep-burial diagenesis.

Land (983, 1985) has shown that Cenozoic dolomites not related to evaporites are non-stoichiometric, Mesozoic dolomites are calcian and nearly stoichiometric, and Paleozoic and Precambrian dolomites are stoichiometric and nearly stoichiometric. Calcian, near-surface dolomites can change from nonstoichiometry to stoichiometry or metastable dolomites to stable dolomites by multiple recrystallization processes through geologic time (Morrow, 1982; Land, 1985; and Sibley, 1990). Stoichiometry of dolomites can also be reached in late-burial diagenesis or epigenetic dolomitization through replacement of precursor limestone by hot basinal brines. However, Land (1983, 1985) and Morrow (1982) suggest that dolomitization by hot basinal fluids at great depth is unlikely because of insufficient Mg in the composition of basinal brines.

Many recent studies, however, have reported epigenetic replacive dolomitization directly from hot, allochthonous basinal brines at elevated temperatures due to depth of burial. Our field study, petrography, fluid inclusions, clay diagenesis, isotope data, relative time relations of dolomitization, and burial history of the AVL are consistent with late diagenetic replacive dolomitization of this formation from hot basinal solutions.

Partially dolomitized limestones

Results:

Except for stromatolitic dolomites, average mole concentration of $CaCO_3$ of dolomites in partially dolomitic limestones of the AVL is equal to 52 % which is about 1.1 % more calcitic than dolomites of dolostones of the same formation (Table 4B).

Table 4B. The dolomite content of partially dolomitic limestones, mole percentages of $CaCO_3$ and $MgCO_3$ in the dolomites of dolomitic limestones of the AVL.

Number of Samples	Dolomite %	Mole % CaCO3	Mole % MgCO3
Dol. VI in skeletal psc.	30 - 32	51.2 - 51.5	48.8 - 48.5
Dol. III in oncolitic pcs.	7 - 18	52.2	47.8
Dol. IV in oolitic grs.	12 - 20	52.2 - 52.7	47.8 - 48.5
Dol. II in stromatolitic mst.	10	54.9	45.1

Pcs: Packstone
Grs: Grainstone
Mst: Mudstone

Interpretation:

Dolomites of dolomitic limestones are slightly enriched in $CaCO_3$ compared to dolomites of dolostones and are approximately 1.1 more calcian (with an exception of dolomites in stromatolitic limestone) than dolomites of the dolostones of the AVL. Despite 1.1 % of more calcitic composition, dolomites of the dolomitic limestones still lie in a nearly stoichiometric dolomite composition range (Table 4B). On the other hand, dolomites of the stromatolitic limestones are nonstoichiometric and more calcian (54.9 mole percent of $CaCO_3$; Table 4B). This bimodal nonstoichiometry of dolomites of the AVL may have resulted from two principal factors: (1) multiple generations of dolomites, and (2) porosity and permeability of host rock during and after dolomitization.

Dolomites of Type III of partially dolomitized oncolitic limestones, and of Type IV (Zoned dolomite I) of oolitic packstone and grainstone are replacive and interpreted to have formed in the intermediate-burial diagenetic environment. Their, nearly stoichiometric composition is consistent with indicated dolomitization process. Therefore, such stoichiometric composition may have resulted from both direct replacement and recrystallization under great burial depth.

Patchy, nonluminescent ferroan dolomites (dolomite VI) of shelly layers of storm beds are nearly stoichiometric and 1 to 1.2 % more stoichiometric than those of the Dolomite III and Dolomite IV. This nearly ideal stoichiometry is consistent with replacement of limestone under deep-burial conditions by hot basinal solutions.

Dolomites of type II dolomite in the stromatolitic mudstone lithofacies are believed to have formed during early, near-surface dolomite. Despite its early formation, nonstoichiometric composition of the dolomites of the stromatolitic lithofacies can be attributed primarily to closed diagenetic systems which were probably created during early lithification of the stromatolitic lithofacies of the AVL. Therefore, age and long-heating period can not be sufficient for stabilizing metastable dolomite if the system is closed to the diagenetic fluids (Sperber et al., 1984; Lumsden, 1988).

CHAPTER 13 C: B. DOLOMITIZATION MODEL OF THE DOLOSTONE UNITS IN THE ANTELOPE VALLEY LIMESTONE

In the Antelope Valley region, aerial distribution of nonstratiform-dolostone units of the Antelope Valley Limestone (AVL) is controlled chiefly by normal faults extending N-S and E-W. This relation was documented in detail in Martin Ridge, where fault-controlled pervasive dolomitization progressively decreases away from the faults.

In the Lone Mountain section, this study found a laterally discontinuous, 100-feet thick dolostone unit, which appears to be stratiform and overlies the open shelf and basinal facies of the AVL. Morreale (1981) studied the AVL in this section, about 500 m (1500 feet) away from the measured section of this study. However, he didn't mentioned this pervasively dolomitized interval. Since Lone Mountain is a small, isolated-horst-like structure within the inter-mountain valley, it is considerably difficult to note the fault-controlled pervasive dolomitization there. On the other hand, Taban (1986) reported an about 45-feet thick, pervasively dolomitized interval in the Ninemile Canyon section which was not found in this study.

In the southern localities of the AVL, in the Clear Creek Canyon and Keystone Canyon sections, the two-directional faults are more prominent and very closely spaced and appear to have played a primary role in pervasive dolomitization of the AVL.

In the Antelope Valley and Hot Creek Canyon regions, the N-S and E-W extending faults postdate and displace lithologic units of the Roberts Mountain thrusts (Nolan et al., 1956; Merriam, 1963; and Lowell, 1965). During the Late Middle Pennsylvanian and Early Late Pennsylvanian, a widespread-continental uplifting is believed have occurred and produced these normal faults in central Nevada (Nolan et al., 1956) and east central Nevada (Steel, 1960; Roberts, 1964; Yochelson and Fraser, 1973; and Ketner, 1977).

These post-Antler orogenic normal faults, covered by Tertiary volcanics, juxtapose Silurian, Devonian and Cambrian formations with the AVL (Figs. 121, 122). Unlike others, one of the N-S extending normal faults even postdates Tertiary units. This suggests that the Middle Pennsylvanian faults may have reactivated during the late Cenozoic extensional tectonics. At the beginning of the Antler orogeny, the maximum-burial depth of the AVL was estimated to be about from 2000 to 3750 m (6096 to 11,430 feet). After this orogeny, the AVL in central Nevada had a burial depth of approximately 6000 to 8000 m (18,328 to 24,484 feet). Thrusting can cause expulsion of significant amounts of basinal solutions from deeply buried basinal areas to the carbonate platform (Oliver, 1986). During thrusting events, increased hydrostatic pressure due to expelled hot basinal brine or solutions can also create fractures and microfracture systems which likely enhance permeability of platform carbonates. Laterally continuous, stratiform, pervasive dolomitization -- gradually diminishing upward -- is assumed to form generally at lower shoal and reef facies during updip migration of basinal brine by expulsion mechanism (e.g. Mattes & Mountjoy, 1980; Machel and Mountjoy, 1986; Machel and Anderson, 1987; and Quing and Mountjoy, 1988). If the migration of thrust-induced basinal solutions is responsible for the dolomitization of the AVL, laterally continuous, stratiform, pervasive dolomitization should have occurred, particularly in the Martin Ridge, Ninemile Canyon and Whiterockian Canyon sections. However, no such dolomitization was observed in these sections.

It has been interpreted that pervasive dolomitization of the AVL took place during Late Middle Pennsylvanian and early Late Pennsylvanian uplifting or with uplifting-generated normal faults rather than Antler orogeny. Even during the Middle Pennsylvanian, burial depth of the AVL was not less than 4 to 5 km (see the reconstructed-subsidence curve in Chapter 20); therefore, the epigenetic dolomitization took place in the deep-burial diagenetic environment. The following evidence points in favor of late, deep-burial dolomitization: coarse-grained, nonfabric-selective xenotopic mosaic, undulose extinction, late-diagenetic replacement of fracture-filling calcite cement by mosaic dolomite, post-stylolitic pervasive dolomitization (stylolite-induced

ferroan dolomites poikilotopically included in and chemically altered by the pervasive, mosaic dolomite), high homogenization temperature of two-phase fluid inclusions, very depleted-oxygen isotope composition, nearly stoichiometric dolomite composition, homogeneous dull luminescence, gradational textural relation with the post-fracture-filling dolomite cements.

Deep-burial epigenetic dolomitization, however, is not favored by many workers on account of professed Mg-deficiency in this environment and insufficient porosity and permeability of carbonates at great burial depths (Land, 1985; Morrow, 1982; Kupecz et al., 1988; and Kupecz, 1991).

Despite deficiency of Mg and inadequate porosity and permeability in deep-burial diagenetic environments, high temperature and reaction rate of the warm basinal brine and its much longer reaction time (Mattes and Mountjoy, 1980) can overcome the kinetic difficulty of dolomitization, which is caused by hydration of Mg. In addition, subsurface hydraulic flow maintains chemical stability, eliminates mass balance restrictions, and enhances the potential for slow formation of massive dolomites (Machel and Mountjoy, 1986, 1990). On the contrary, in the near-surface environment, inhibiting kinetic factors remain effective because of very rapid-flow rate and short durational, high-frequency changes in the hydrological equilibria of the systems.

It is very important that no matter how deeply the AVL was buried and heated, the host limestone would have remained unchanged unless an effective hydrologic system with adequate Mg-transfer mechanism existed. In the AVL, the pervasively dolomitized intervals must have been controlled by normal faults and related fractures which acted as conduits for updip flow of basinal fluids. All the lower and middle Paleozoic carbonates of central Nevada were interpreted to be dolomitized from mixing of fresh water and sea water under artesian water conditions (e.g., Hanshaw, 1981; Dunham and Olson, 1978). However, the mixing-zone dolomitization model (e.g., Hanshaw, 1971; Land, 1973; Badizomani, 1975; Dunham and Olson, 1978, 1980; Choquette and Steinen, 1980; Kaldi and Gildman, 1983; Ward and Halley, 1985; Baum et al., 1986; Coniglio et al., 1987; Humphery, 1989) is not applicable to the AVL. The absence of the following diagnostic stratigraphic and petrographic features

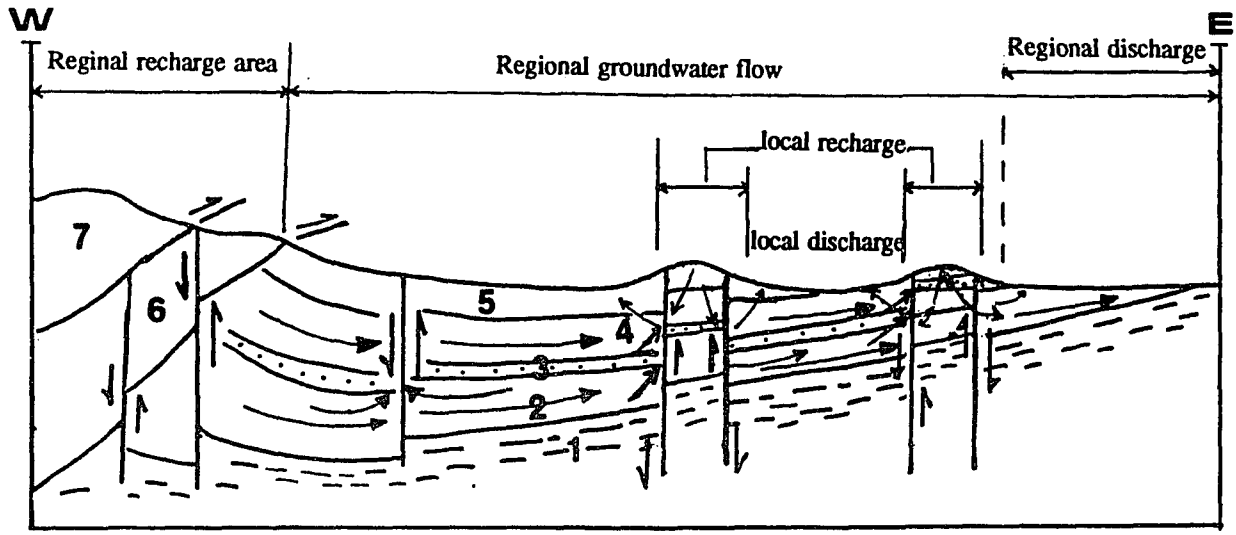


Figure 142- Deep-burial dolomitization model by topography-driven regional ground water, modified from Todh (1980), Hitchon (1984) and Garven and Freeze (1984). "7" Golconda thrusts (Late Permian-Early Triassic), "6" Roberts Mountains thrusts (Late Devonian-Early Mississippian), "5" Devonian, "4" Late Ordovician-Silurian, "3" Eureka Quartzite, "2" The AVL, and "1" Ninemile Shale.

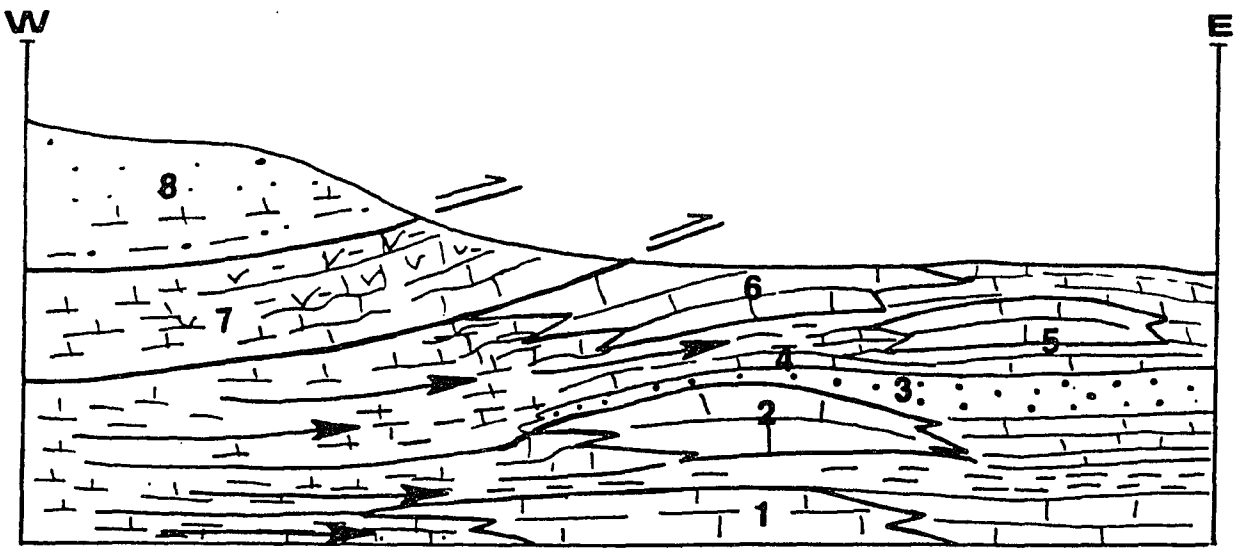


Figure 143- Deep-burial dolomitization model by compaction expelled basinal brine. "8" Golcanda thrusts, "7" Roberts Mountains thrusts, "6" Devonian, "5" Silurian, "4" Upper Ordovician, "3" Eureka Quartzite, "2" The AVL, and "1" Goodwin Limestone.

eliminates the mixing-zone model for the nonfabric-selective mosaic dolomites (Dol. VII) of the AVL: (1) absence of major unconformity or unconformity-controlled dolomitization, as dolomitization progressively decreases downward from the surface; (2) absence of karst and karst related topography (Hanshaw and Back, 1980; Back et al., 1986); and (3) absence of optically continuous, alternating dolomite and calcite rhombs of early fabric-selective replacement or pore-filling lipid dolomites (e.g., Cutiles, 1904; Ward and Halley, 1985; Machel and Mountjoy, 1986; and Humphrey, 1988).

The other models, such as "sabkha model" (e.g., Butler, 1969; Kinsman, 1969; Mackenzie (1980), Hardie, 1987) and "reflux seepage" (Adams and Rhodes, 1960), are also not applicable to dolomitization of the AVL because of absence of diagnostic diagenetic and sedimentary textures, such as evaporite minerals or their crystal molds, and any type of replacive or neomorphic cement indicating evaporite precursors (e.g., Radke and Friedman, 1979).

Thus, deep-burial, epigenetic dolomitization is the most appropriate model for the formation of mosaic dolomite in the AVL (Fig. 143). Although it is believed that much of the dolomitizing fluid came from basinal compaction, other sources might have been involved. After the expulsion of basinal solutions during the early compaction, shales and muddy units lose much of their water. Shale loses its porosity from 21 to 11 % at 3500 to 5200 m of burial depth (Dickey, 1975; Magara, 1980). Such fluids may not have been sufficient to pervasively dolomitize the AVL at the indicated-dolostone intervals if they had not been channeled directly into the faults. Dolomitizing fluid may have been derived from "topography-driven gravity flow" (Garven and Freeze, 1984), or "cross-formational flow" as in figure 142 (Tóth, 1980; Hitchon, 1984). Perhaps, greater uplifting in the western part of the Antler highland due to thrusting created a higher recharge area from which water may have moved laterally eastward. Mg was probably derived either from basinal brine, or from the interaction of modified-, more reactive, hot ground water with the host rocks.

Dolomitization of the AVL might have been affected by local topographies. During the Late Middle Pennsylvanian and Early Late Pennsylvanian uplift, normal

faults and related uplifting probably produced more local topographic variations toward the edge of the foreland basin. Relatively large volumes of fresh-water mixed at the non-basinal local recharge and discharge systems (e.g., Hitchon, 1984) of locally gravity-driven flow may have been responsible for the formation of the post-pervasive dolomitic fracture-filling calcite cements which have depleted $\delta^{18}O$ values of -27.00 ‰ PDB.

The Sonoma orogeny during Late Permian to Early Triassic probably caused renewed rapid updip expulsion of the basinal solutions eastward which probably caused the formation of the fracture-filling saddle dolomite.

With the Sonoma orogeny, clastic wedges migrated farther east on the Antler highland which probably caused the additional burial, and gravity-driven ground water probably caused the bright-red luminescent, mosaic dolomite and fracture- and intercrystalline pore-filling quartz cements as well as late chert replacement along the stylolites that postdates mosaic dolomite.

CHAPTER 14: DEDOLOMITIZATION

Introduction:

For the first time, Von Morolot (1948) used "dedolomitization" to define the replacement of dolomite by calcite, which is a reverse process of dolomitization (Evamy, 1967). Thus, dedolomite or dedolomitization as a term is principally restricted to the calcitization of dolomites.

In the Antelope Valley region, calcitization of dolomites is common but not extensive in scale. However, in some intervals of the AVL, dedolomitization is extensive and has completely obliterated dolomite rhombs. In these intervals, for instance, dolomites can be recognized only by their rhombohedral crystal molds or outlines. Two types of calcitized dolomite textures have been recognized: (1) replacement of dolomite rhombs by relatively late diagenetic calcite cements; and (2) fabric-selective dedolomitization along Fe^{+2} rich-zones and cleavage planes of dolomites.

Nonfabric-Selective Dedolomitization

Description:

In this kind of dedolomitization, dolomite rhombs are generally terminated by replacive calcite along irregular or jagged-crystal outlines (Fig. 144). Along such irregular front, calcite cements progressively replace dolomite rhombs, and dolomites' rhombohedral outlines gradually disappear by this replacement process. This replacement feature is common on both ferroan and nonferroan dolomites (Fig. 144).

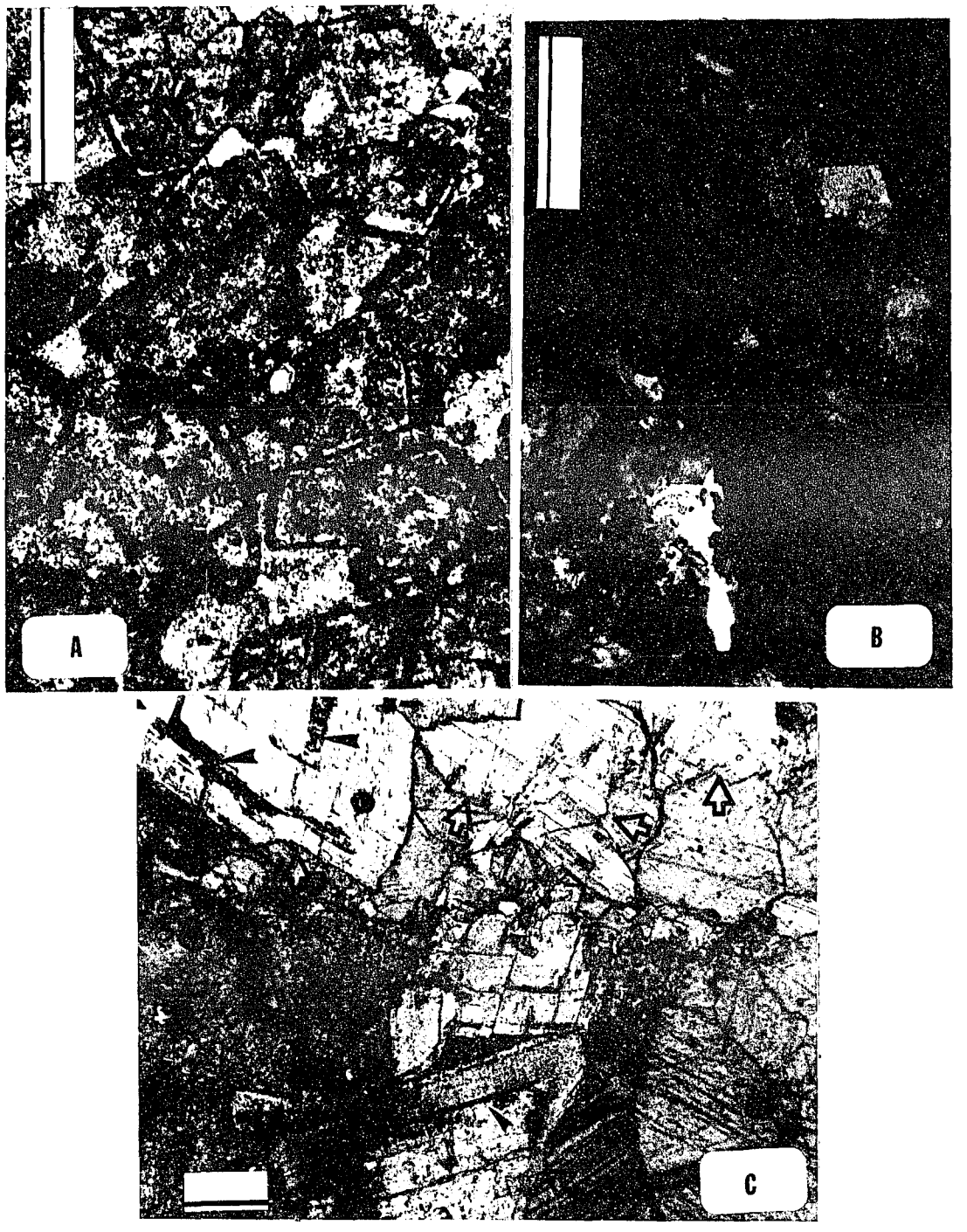


Figure 144- Photomicrographs of nonfabric-selective dedolomitization. A) Pervasively calcitized-euhedral dolomite crystals have iron oxide-stained rhombohedral outlines. B) Fracture-filing calcite replaced euhedral dolomite crystals (arrowheads). C) The replacement of late-diagenetic white sparry dolomite by sparry calcite crystals, and fabric selective dedolomitization along cleavage plains of sparry dolomites. Arrows indicate the nonplanar replacement front between sparry calcite crystals and originally euhedral dolomite crystals. Granular calcite (calichification) postdates both sparry calcite and dolomite. Under plane-polarized light, scales= 0.25 mm.

In figure 144 C, sparry calcite cements truncate and replace coarse-grained dolomites along the irregular sharp boundaries.

Interpretation:

Solutions responsible for such replacement mentioned above were probably under saturated with respect to dolomite and supersaturated with calcite. This replacement process appears to have occurred by progressive dissolution of dolomites and simultaneous precipitation of calcite which corresponds to migrating thin-solution film along the replacement front on dolomite substrate (see Pingitore, 1976). Fabric of dolomite crystals with indicated features above is the petrographic evidence for dedolomitization or replacement of dolomites by calcites (Fig. 144 A, B). If dolomites replaced pre-existing cements or matrixes, they tend to show a straight and planar crystal outlines (Katz, 1971). Therefore, the irregular crystal terminations of dolomite rhombs signify the opposite case of dolomite replacement by relatively late calcite cements (Fig. 144).

Fabric-Selective Dedolomitization

Description:

The fabric selective calcitization of dolomite or dedolomitization often occurs at the outermost surface, zones, and rhombohedral cores of ferroan dolomites as well as along cleavage planes of dolomites (Fig. 145). In the Nuia packstone- and grainstone units of the Martin Ridge section, whole dolomite rhombs are replaced by calcite cements which display iron oxide-stained rhombohedral rims (Fig. 144 A). In addition, some dolomites show crystal molds, and some others appear to be oxidized-dolomite

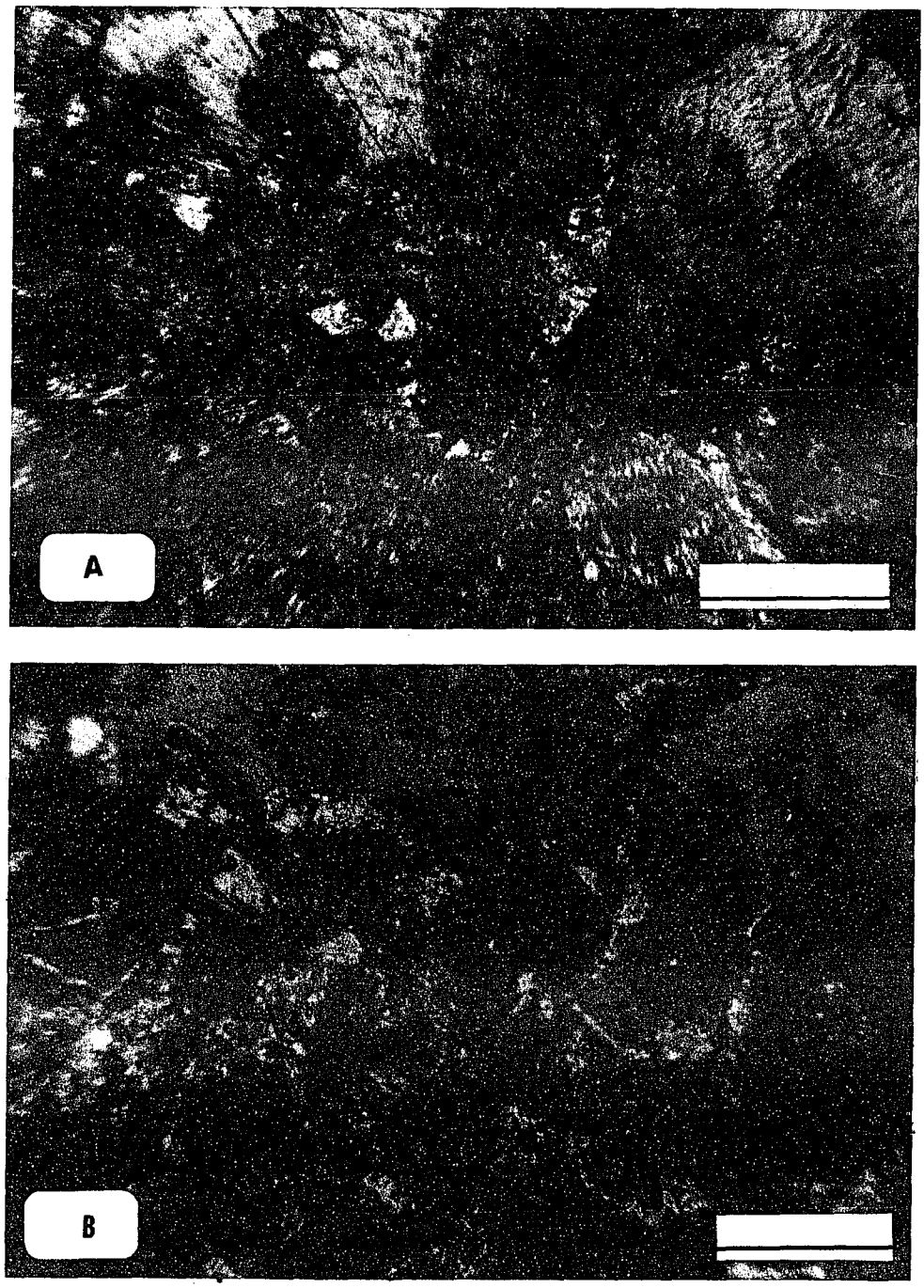


Figure 145- Photomicrographs of dedolomitized-euhedral ferroan dolomites. A) Euhedral ferroan dolomite (d) replaced sparry-calcite cements (c) in Nuia grainstone units. These cloudy dolomite crystals are rimmed by dark iron-oxide staining. Under plane-polarized light. B) The same view of photomicrograph A under CL shows that iron oxide-stained dolomite crystal outlines and the mottled parts of the dolomite crystals reveal a bright orange-red luminescence (arrow), whereas the unaltered-parts of ferroan dolomites are non-luminescent. Scales= 0.25 mm.

rhombs. Comparable textures, calcitization of entire dolomite rhombs, have been described by (Sibley, 1982). The textures of the fabric-selective dedolomitization of the AVL are comparable with the dedolomitization textures described by Evamy (1967), Katz (1971) Al-Hashimi and Hemingway (1973), Frank (1981), Harris (1982), and Theriault and Hutcheon (1987).

The fabric-selective dedolomitization can easily be recognized under plane-polarized light by oxidation color of the Fe^{+2}-rich zones and rhombs. The oxidation colors under plain light vary from yellow brown to dark brown, and oxidized zones reveal bright yellow-red luminescence under cathode light.

In addition to Fe^{+3} rich oxidation, often fine-grained iron oxides, hematite or goethite, are scattered within adjacent areas of dedolomitization (Fig. 146 A and B).

In Figure 144 C, the photomicrograph shows two types of dedolomitization: (1) nonfabric-selective dedolomitization by sparry calcite cement (see non-fabric selective dedolomitization); and (2) fabric-selective dedolomitization in Fe^{+2}-rich zones and along cleavage planes, and synchronous non-fabric selective dedolomitization and replacement of calcite by iron oxide and hydroxide-stained microgranular calcites.

Interpretation:

All the examples of fabric selective dedolomitization described above are closely associated with chemical and textural variations in idiotopic single dolospars and composition of reactant solutions. Particularly, in the AVL, dedolomitization of ferroan zones, rhombs, and single crystals imply that these ferroan-dolomite zones and crystals are more susceptible to such chemical alteration than non-ferroan dolomites. This is probably due to stability or stoichiometry of ferroan dolomites which are much less stoichiometric or stable than non-ferroan dolomites. However, in the non-ferroan dolomites, cleavage systems enable dedolomitizing fluids to penetrate into dolomite rhombs (Fig. 144 C). Thus, cleavages make dolomites more vulnerable with respect to dedolomitizing solutions as seen in figure 144 C.

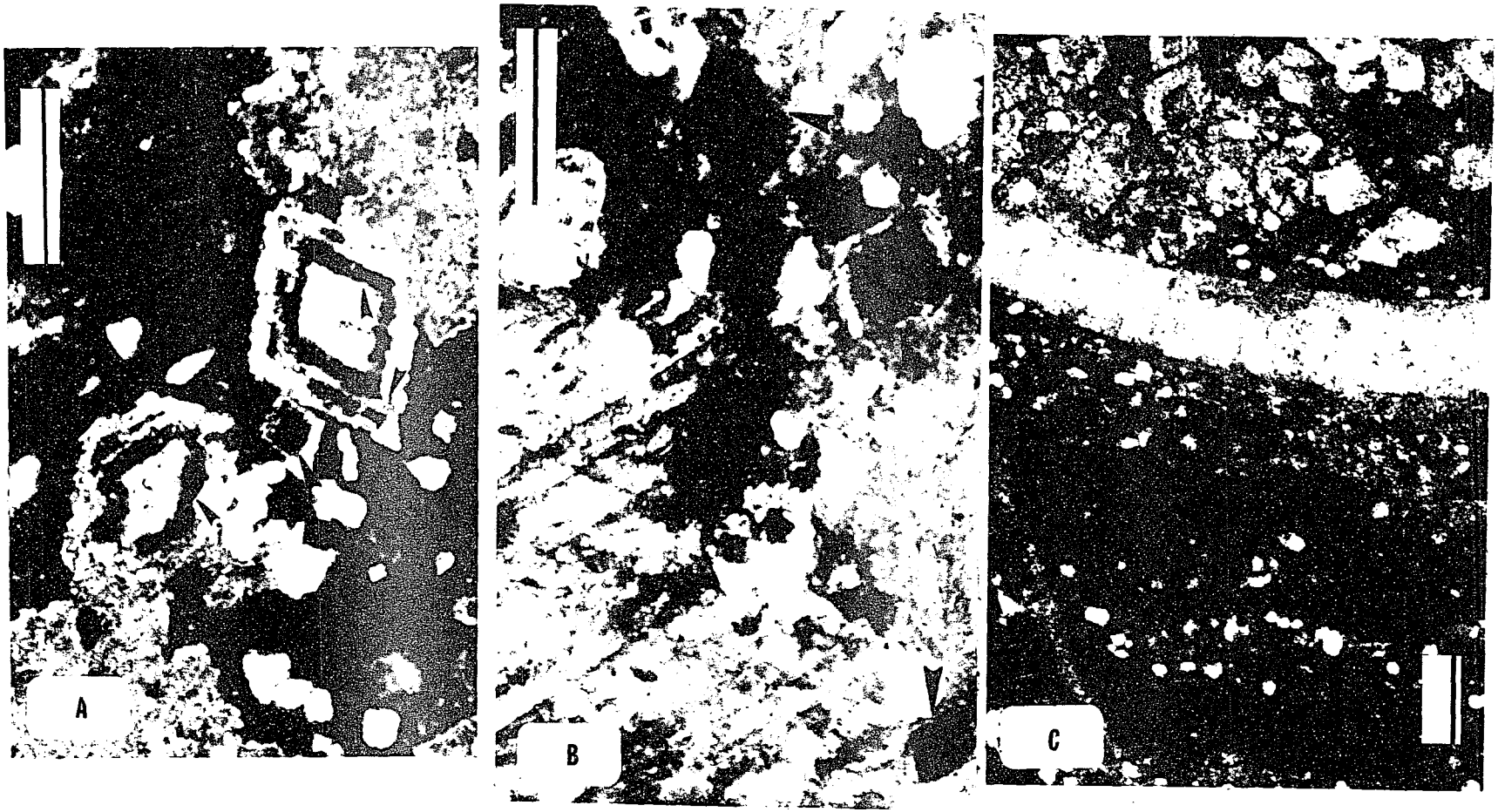


Figure 146- Photomicrographs of fabric-selective dedolomitization in zoned dolomite crystals. A) Arrowheads point to the fabric-selective dedolomitization along iron-rich, iron oxide-stained dolomite zones. B) Arrowheads indicate almost completely dedolomitized dolomite rhombs. C) In euhedral dolomite crystals, arrowheads point to Alizarin-red stained, inner calcitic rhombs. Under plane-polarized light; scales= 0.25 mm.

Compositional variations among the zones of the euhedral dolomites (Fig. 146 A, B, and C) correspond to changes in the chemistry of parent solutions (pH, and Eh levels) from which dolomite precipitated.

Petrographic examinations of dedolomite provide a significantly substantial evidence that Fe^{+3} iron oxides (may be hydroxide) co-exist with nonferroan calcites. Frank (1981) and Harris (1982) examined dedolomitized, iron oxide-stained zones under SEM, and demonstrated that calcites precipitated in these zones along with iron oxides, such as goethite. Therefore, it is likely to suggest that similar dedolomitization in the AVL could have resulted from the oxidation of $FeCO_3$ in the dolomite by reacting with meteoric water. It is believed that in near-surface and surface diagenetic environments, in unsaturated solutions with respect to dolomite, they react with ferroan dolomites or dolomitic zones more readily than non-ferroan dolomitic zones and produce Fe^{+3} oxides and low-Mg calcite (Evamy, 1967; Katz, 1971; Al-Hashimi and Hemingway, 1973; Frank, 1981; and Harris, 1982). As a result, these dedolomitizing solutions dissolve dolomite and oxidize Fe^{2+} to Fe^{+3}; calcites most likely precipitate simultaneously along thin-solution films which were very effective, especially, in dedolomitization of ferroan-dolomite zones of the AVL. The formation of calcitized dolomites along stylolites is also explained by this process (Fig. 146 C). From the foregoing discussion, it can be deduced that fabric-selective dedolomitization of the AVL may have occurred in relatively late diagenetic events during which the AVL was probably brought under the influences of fresh-water diagenesis at surface and near-surface environment or "telogenetic environments" (Choquette and Pray, 1970). For instance in Figure 144 C, dedolomitization was caused by the migration of caliche solutions along cleavage planes and dolospars in vadose-diagenetic environments (or in a weathering zone), and this is clearly one of the most recent diagenetic events. As a result, ferroan dolomite zones were oxidized, and initially high-Mg calcites precipitated in the Fe^{+3}-oxidized zones.

The other mechanism that can produce dedolomitization is oxidation of pyrite and formation of $CaSO_4$, which enhances solubility of dolomites at low PCO_2 and temperature below 50 °C (Yanta'eva, 1955; De Groot, 1967, see Evamy 1967).

Reactions of SO_4 ions in interstitial solutions with dolomite result in precipitation of calcite, $MgSO_4$, and dedolomitization (Evamy, 1967; Friedman and Sanders, 1967; Folkman, 1969; and Friedman and Radke, 1979). The sources of iron and SO_{4-2} ions are pyrite; however, paucity of pyrite in the shoal sediments of the AVL makes these reactions unlikely for dedolomitization. Therefore, this model is inapplicable to the dedolomitization of dolomites in the AVL.

CHAPTER 15: QUARTZ AND CHERT CEMENTS

In the AVL silica cements are represented in two forms: quartz and chert. Quartz cements are fracture- and intercrystalline pore-filling quartz, replacive quartz, and authigenic quartz. Quartz cements are common in the dolostone units of the AVL, but these cement forms are volumetrically insignificant. Authigenic quartz is commonly found in the dolostone units and in the oncoidal packstone- grainstone units of oncolitic shoal units in which authigenic quartz selectively replaced Dol. III in oncoids. Chert is volumetrically the most important silica cement type in the AVL. Chert occurs as replacement (microcrystalline quartz), and void-filling cement (chalcedony and megaquartz or quartz mosaic) in chert nodules or lenses. In the AVL's shelf and open-shelf facies, silty-quartz rich, parallel-laminated lime mudstone units are selectively chertified. Bio-allochems, such as crinoids, brachiopods, trilobites and bryozoans are selectively chertified.

I. Quartz Cements

A. Quartz Cement

Description:

This cement type commonly occurs as a fracture- and intercrystalline pore-filling cement (Figs. 147 A, B) in the dolostone units of the Antelope Valley Limestone (AVL), particularly in the Keystone Canyon, Clear Creek Canyon, and Lone Mountain and Martin Ridge sections.

In the Keystone Canyon section, the quartz cements postdates the fracture-filling saddle dolomite (see Fig. 137 C in Chap. 13A) and the post-dolomitic, fracture-filling

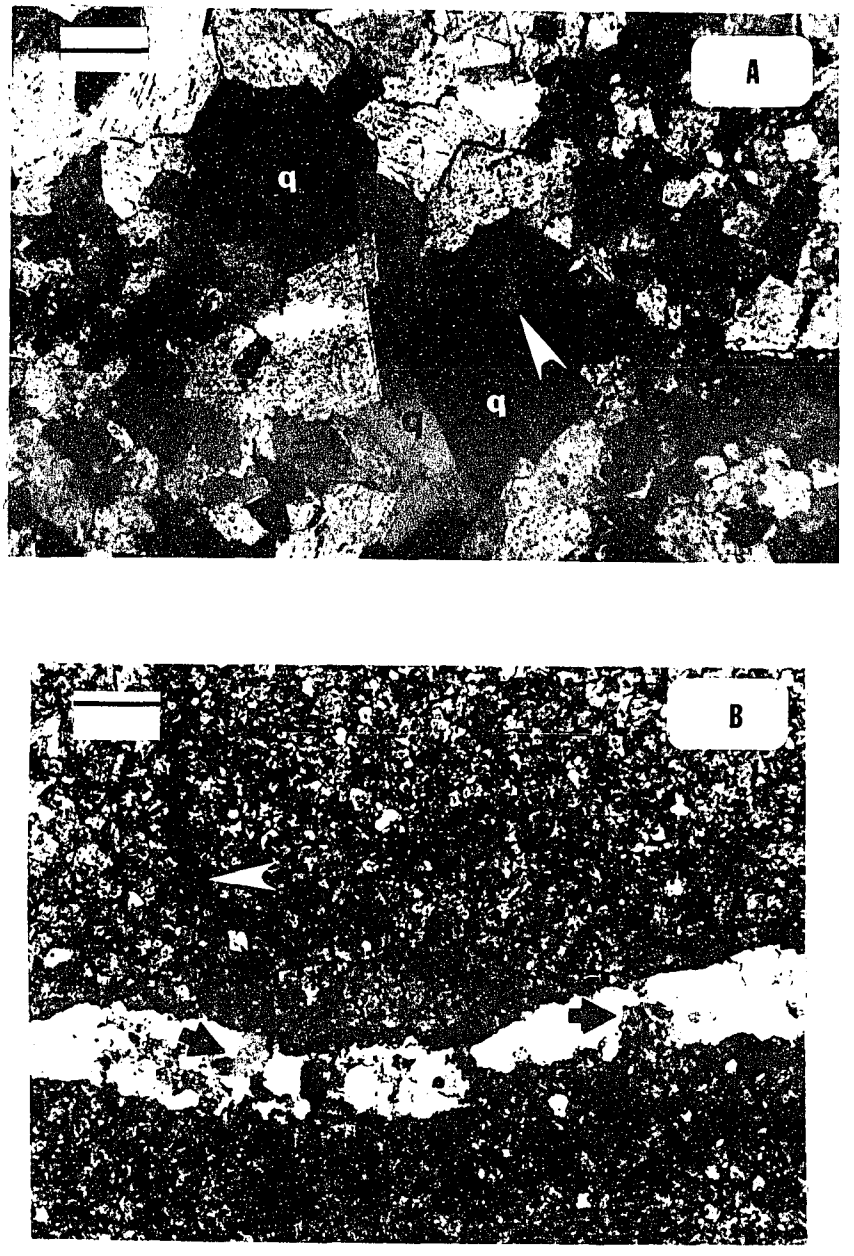


Figure 147 A, B- Photomicrographs of quartz cements. A) Intercrystalline pore-filling quartz cement (q) in mosaic dolomite postdates and poikilotopically included xenotopic dolomite crystals pointed by white arrow. B) Fracture-filling quartz cement postdates the mosaic dolomite and the latest hydrocarbon-stained stylolite indicated by arrows. Crystals of fracture-filling quartz poikilotopically included dolomite the crystals of the mosaic dolomite pointed by arrow. Under cross-polarized light; scales= 0.25 mm.

calcite cements. In the other sections, the fracture-filling quartz cements are not common; however, intercrystalline, pore-filling quartz cements have common occurrences in the dolostones of this formation.

The fracture- and intercrystalline pore-filling quartz cements are coarse-grained, ranging from 0.2 to 0.6 mm in size, clear and free of solid inclusions. They have planar crystal boundaries and uniform extinction. In addition, these quartz cements commonly contain abundant, two-phase fluid inclusions whose homogenization temperatures (Th) consistently range from 210 to 240 °C in all the type sections. In the Lone Mountain section, the intercrystalline pore-filling quartz cements commonly cut and terminate pre-dolomitic stylolites in mosaic dolomite VII (see Chap. 13 A; Fig. 131) and are irregularly scattered in mosaic dolomite. The dolomite-quartz crystal boundaries are irregular. In addition to irregular crystal boundaries with xenotopic dolomite crystals, the quartz cements poikilotopically include and corrode the latest, bright-red luminescent dolomite (see Dolomite VII). Under cathode light, these quartz cements are non-luminescent.

Interpretation:

All the petrographic criteria and timing relations of this cement with other late diagenetic products suggest that this quartz cement is late diagenetic in origin and appears to have formed under deep-burial diagenesis.

Both intercrystalline pore- and fracture-filling quartz cements probably had the same origin and may have formed under similar diagenetic conditions. The homogenization temperatures (T_h) of two-phase fluid inclusions lend support to the cogenetic origin of these two quartz cements. Pressure-uncorrected T_h values and fluid compositions of the two-phase inclusions are in similar temperature and composition ranges (see Fluid-inclusion microthermometry, Chap. 18). Thus, similar physical and chemical conditions, more specifically similar depths of burial, can be inferred from the similarity in fluid-inclusion data. The T_h and Tm (melting temperature) values in

the quartz cements are identical in three vertical sections, the Lone Mountain, Martin Ridge, Clear Creek Canyon sections, where there are no indications for igneous dikes or intrusions, like the one in the Keystone Canyon section. Comparable depth of burial from T_h values of these fluid inclusions also substantiate a deep-burial diagenetic origin of the quartz cements rather than a genetic link with deep-seated Cretaceous batholith and hydrothermal activities.

B. Replacive Quartz

Description:

In the dolostones of the AVL, two kinds of replacive quartz cements were observed (1) early, and (2) late. The early replacive quartz occurs in the core of oncoids, replacing gastropod or calcitized mollusc fragments (Fig. 147 C). This cement with the same textural relations have also been noted in the partially dolomitized oncolitic shoal limestones of the Whiterockian and June Canyon sections. The quartz replacement in neomorphically altered molluscs or drusy cement-like quartz initially starts along calcite crystal boundaries and progressively advances inward on neomorphic calcite crystals (see neomorphic calcite cements in Chap. 12 C). In dolostones, the early quartz appears to have resisted pervasive dolomitization (see mosaic dolomite in Chap. 13 A).

The late replacive quartz is much coarser than that of the early replacive quartz cement (Fig. 147 D) and formed cogenetically with the latest stylolites along which hydrocarbon staining is prominent. This quartz replaced the mosaic dolomite (Dol. VII) along irregular crystal boundaries and poikilotopically includes euhedral pyrite and dolomite crystals (Fig. 147 D). In addition, this cement replaced the post-pervasive dolomitic, late fracture-filling calcite.

In June Canyon, quartz replaced fracture-filling calcite crystals in the pelletal lime

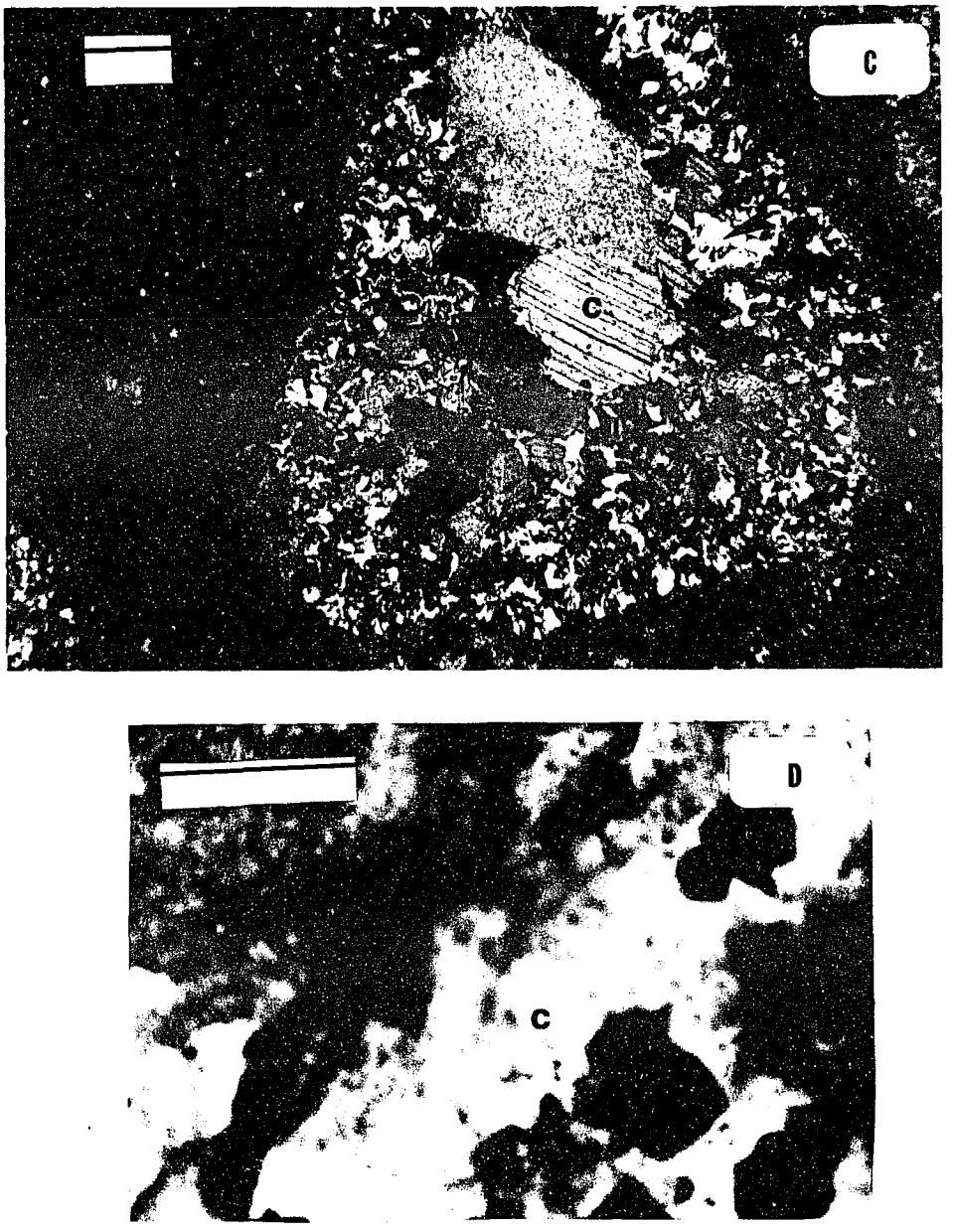


Figure 147 (C, D)- Replacive quartz cement. C) Quartz cement replaced the neomorphically altered allochem at the center of a Girvanella oncoid. White specks are replacive quartz indicated by arrowheads, and (c) indicates neomorphic sparry calcite crystals. D) Along the latest hydrocarbon-stained stylolite (post-pervasive dolomitic stylolite), quartz commonly replaced xenotopic crystals of mosaic dolomite and poikilotopically included them. In addition, the replacive quartz crystals poikilotopically include euhedral pyrite crystals which also postdate mosaic dolomite. Under cross-polarized light; scales= 0.25 mm.

mudstone units of the slope deposits which consist of calcitized sponge spicules.

Interpretation:

The late, replacive quartz cement may have formed during late hydrocarbon migration along late stylolites. During the hydrocarbon migration, H_2S and methane may have reduced pH levels and initiated dissolution of dolomite and then precipitation of the late replacive quartz. Presence of pyrite suggests that thermal sulfate-reducing reactions (TRS) occurred during silica replacement (Machel, 1989).

Early replacive quartz in the core of dolomitized oncoids of dolostones can be considered as a pre-pervasive dolomitic quartz replacement. This can be inferred from the similar replacive textural relations in the intraoncoidal, interparticle, and drusy calcites of the partially dolomitized units of the AVL. The interparticle calcite mosaics with drusy fabric are representatives of meteoric, phreatic diagenesis in limestones and dolomitic limestones of the shoal and peritidal sequence of this formation. Common occurrences of this post-phreatic zone (meteoric) quartz replacement in the shoal units of the AVL suggest that this replacement probably took place in shallow to relatively intermediate burial depths. However, it is difficult to quantify the range of possible burial depths of the early silica replacement in the AVL. Therefore, this early silica replacement represents a post-phreatic quartz replacement, and it can be considered as a product of the burial depth range of the AVL above, or of deep-mixing zone (e.g., Kanuth, 1979; Geezlin and Chafetz, 1981).

The partial replacement of fracture-filling calcite by quartz may have occurred after the lithification of the pelletal mudstone units of the slope deposits, probably under relatively deep-burial diagenetic conditions. In these slope deposits, diagenetic features do not indicate subaerial exposure. This also supports relatively late burial silicification and replacement of the fracture-filling calcite cements.

C. Authigenic Euhedral Quartz

Description:

Authigenic quartz is very common in the dolostones and oncoidal packstone and grainstone units of shoal facies. In the dolostone units, authigenic quartz is poikilotopically included in the xenotopic dolomites. In Girvanella oncoids, particularly in algal coatings, the euhedral quartz crystals commonly occur in two forms: (1) overgrowth on detrital quartz; and (2) replacement of dolospars. The latter shows dirty inner cores and clean outer zone (Fig. 148 B). Under cathode light, some of the authigenic quartz crystals display a bright-blue luminescence. Their grain sizes generally vary from 0.04 to 0.1 mm, and they have perfect, planar crystal faces, particularly, when authigenic quartz replaced euhedral dolomite rhombs. Overgrowth on detrital-quartz silt and authigenic quartz is usually completed as a whole crystal with a regular, planar-crystal outline. In places, this replacement or overgrowth by authigenic quartz is not complete; as a result, partially replaced detrital quartz apparently has one site with a irregular, non-planar crystal termination and the other half with a perfect, planar quartz crystal outline (Fig. 148 A). The euhedral quartz crystals contain solid inclusions of organic matter or dolomitic precursors (Fig. 148).

Interpretation:

Occurrence of authigenic euhedral quartz is common in carbonate rocks in which silica is believed to originate from two sources: (1) crystallization of silica, primarily derived from dissolution of radiolaria or sponge spicules; and (2) breakdown of pre-existing silicate minerals. In the AVL, the former was the possible source of silica for authigenic quartz replacement because detrital quartz grains do not show etched- or

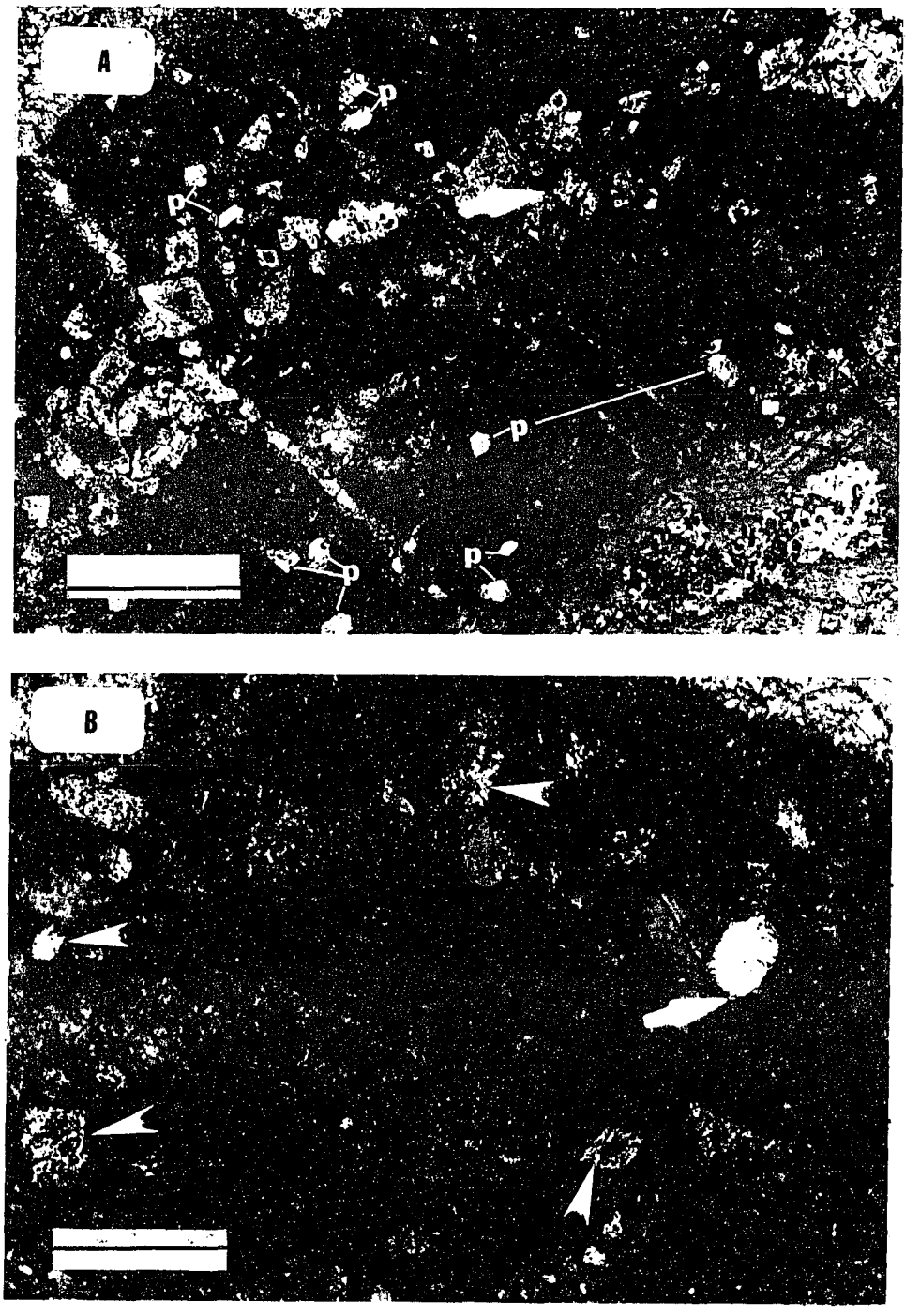


Figure 148- Photomicrographs of authigenic quartz (p). A) Authigenic quartz crystals in the selectively dolomitized portion of Girvanella oncoids replaced euhedral dolomite crystals. Scale = 0.5 mm. B) White arrow points to an authigenic quartz crystal which was an original euhedral dolomite crystal; arrowheads point to partially authigenic quartz replaced-euhedral dolomite rhombs. Under cross- polarized light; scale= 0.25.

dissolutional grain boundaries which would indicate the latter as a possible source. If the former was the possible source, silica derived from dissolution of radiolaria and sponge spicules under alkaline conditions would replace dolomite and nucleate and grow around the detrital quartz particles as pH dropped lower than 5 (Friedman and Shukla, 1980).

However, Friedman and Radke (1979) and Friedman and Shukla (1980) suggest that authigenic quartz is indicative of hypersaline environments in which evaporites, specifically gypsum crystals, are commonly replaced by authigenic quartz crystals. The Antelope Valley Limestone (AVL) does not consist of hypersaline lithofacies and does not have recognizable evaporite pseudomorphs. In nonevaporite-bearing carbonates, quartz replacement by calcite or calcite replacement by quartz or other silica forms has been primarily attributed to fluctuation of pH level in diagenetic solutions which is believed to be controlled by photosynthesis (or oxidation of organic matter by bacteria) and bacteria-induced sulfate-reducing reactions (Friedman and Sanders, 1978). According to Friedman and Sanders (1978), at pH level of 9 to 10 quartz dissolves and calcite precipitates.

Thus, any change in pH level of this environment is probably closely linked to the presence and abundance of organic matters and their oxidation by bacteria or by thermochemical reactions (e.g., Machel, 1987, 1989). Oxidation of the organic matters may produce a low-pH condition resulting in carbonate dissolution and silica precipitation in the microenvironment. In the AVL, replacement of dolomite type III by authigenic quartz and inclusions of the authigenic quartz in the xenotopic, coarse dolomites of dolostones (Dol. VII) suggests that authigenic quartz replacement predates pervasive dolomitization, but postdates dolomite. Thus, the formation of authigenic quartz in both Dol. III and Dol. VI is interpreted to have formed in a shallow to moderate burial-depth range and diagenetic environment. This inference can be supported by the petrographic relationships among fracture-filling calcite cement, dolomite type III and authigenic quartz (Fig. 184 A). In diagenetic sequential order, dolomite type III postdates fracture-filling calcite cements, but is replaced by authigenic quartz. Therefore, formation of this authigenic quartz can be attributed to

moderate burial depth ranges at which oxidation of organic matter by thermochemical reactions rather than sulfate-reducing bacteria (Machel, 1989) probably induced such a replacement.

In clastic sedimentary rocks, authigenic quartz fringing as overgrowth on detrital quartz silt was also interpreted to indicate a shallow- to intermediate deep-burial diagenetic environment (Helmod and Kamp, 1984).

II. Chertification

In the Antelope Valley Limestone, silicification by chert commonly occurs in two dominant forms: (1) selectively chertified skeletal grains or allochems; and (2) chert nodules and discontinuous chert layers.

Crinoids, brachiopods, bryozoans, and trilobites and their fragments are selectively chertified in the skeletal wackestone to grainstone lithofacies of shoal and upper slope facies (Figs. 148, 149). On the other hand, chert nodules and thin, discontinuous chert beds are chiefly confined to the silty quartz-rich lime mudstone lithofacies of the upper slope facies and to similar lithofacies of back shoal or shelf facies.

A. Selectively Silicified Allochems

a) Crinoids:

Crinoids are selectively chertified by quartzine or microcrystalline quartz (Fig. 149); however, their syntaxial cements most commonly escaped chertification. Dolomite rhombs are commonly present in the non-silicified crinoids, and under the cathode light, these microdolomite rhombs reveal bright-red luminescence, and they appear to

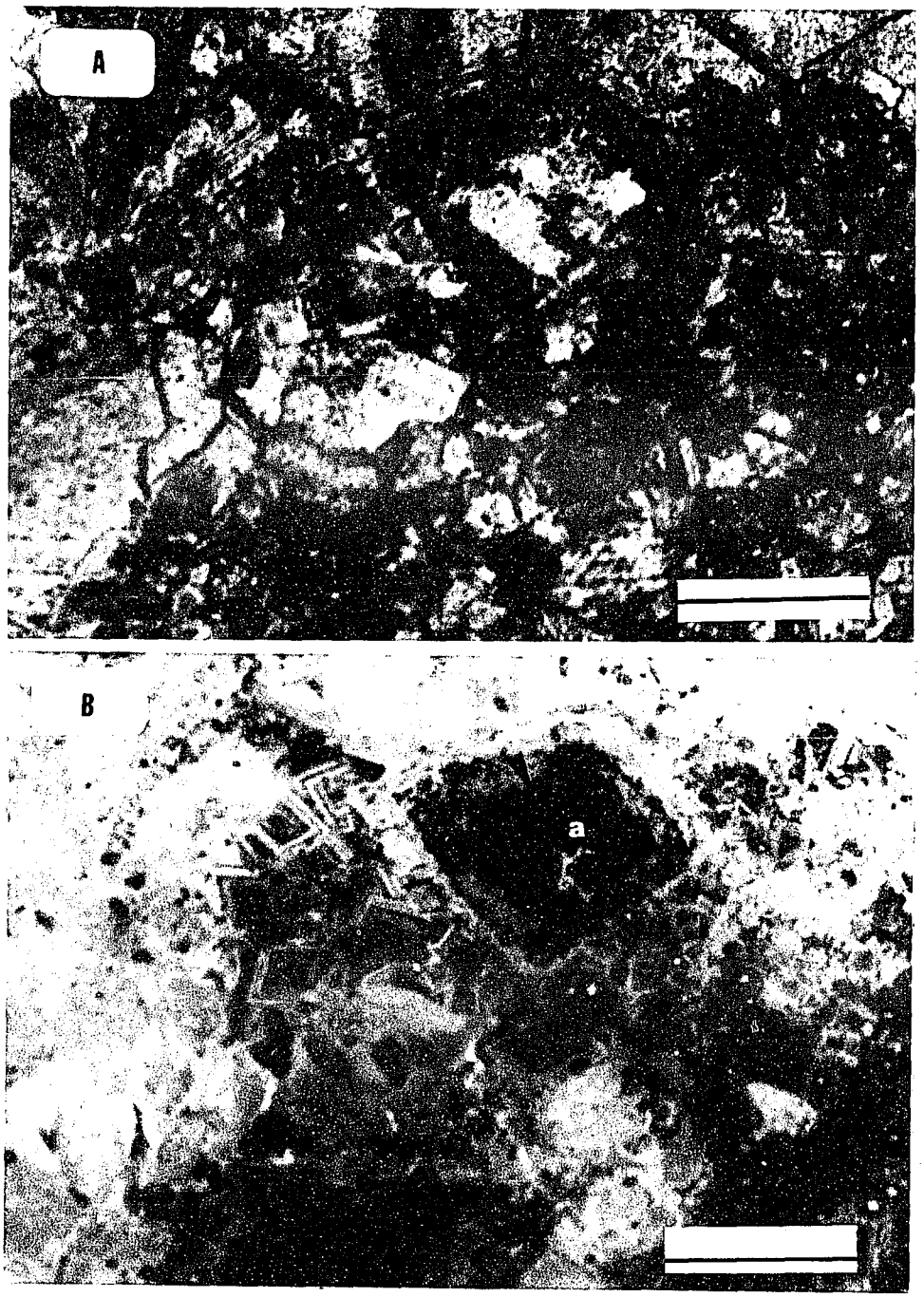


Figure 149- Photomicrographs of a selectively silicified crinoid grain. A) In a crinoid fragment, the white areas (a) represents the selectively chertified part of the crinoid grain. Under plane-polarized light. B) The same view of photomicrograph A under cathode light shows that the chertified areas reveal nonluminescence and consist of regularly ordered bright-red luminescent euhedral microdolomite rhombs indicated by an arrowhead. Scales= 0.5 mm.

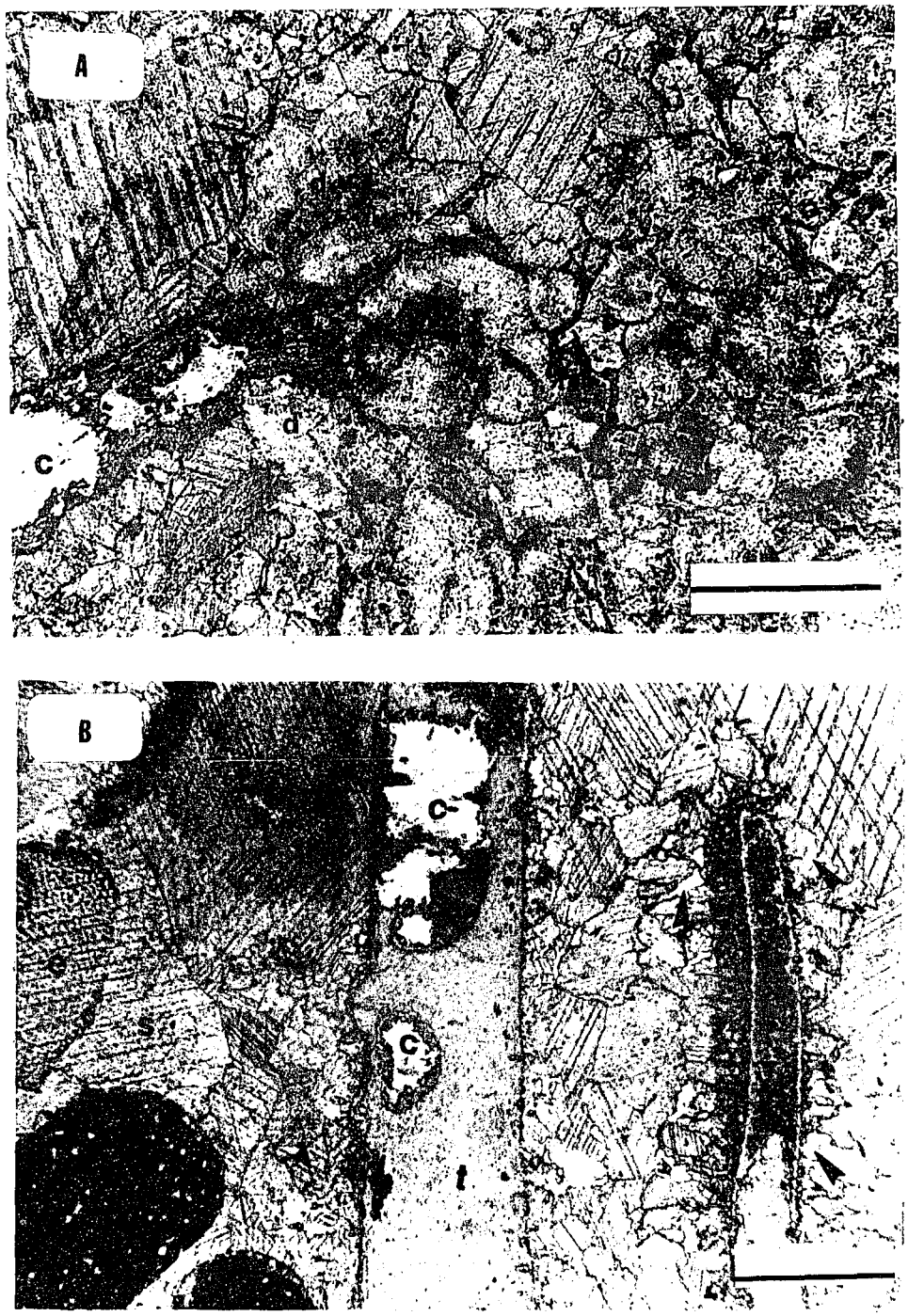


Figure 150- Photomicrographs of selectively-silicified allochems. A) Selectively chertified brachiopod (c) in a skeletal packstone unit. The internal texture of brachiopod appears to have been preserved in the chertified areas. B) Partially chertified trilobites (c') in the skeletal packstone units of open shelf. Arrowheads indicate the replacement of neomorphic calcite crystals along their crystal boundaries by silica cement. Under plane-polarized light; scale= 0.5 mm.

occur in regular, parallel lines (see Fig. 111 B in Chap. 13 A). Calcite crystals are also present in this microcrystalline replacive silica cement alongside microdolomite rhombs.

b) Brachiopods:

Brachiopod fragments are also selectively chertified; selective chertification is common particularly in thin-shelled brachiopods (Fig. 150 A) which are mainly found

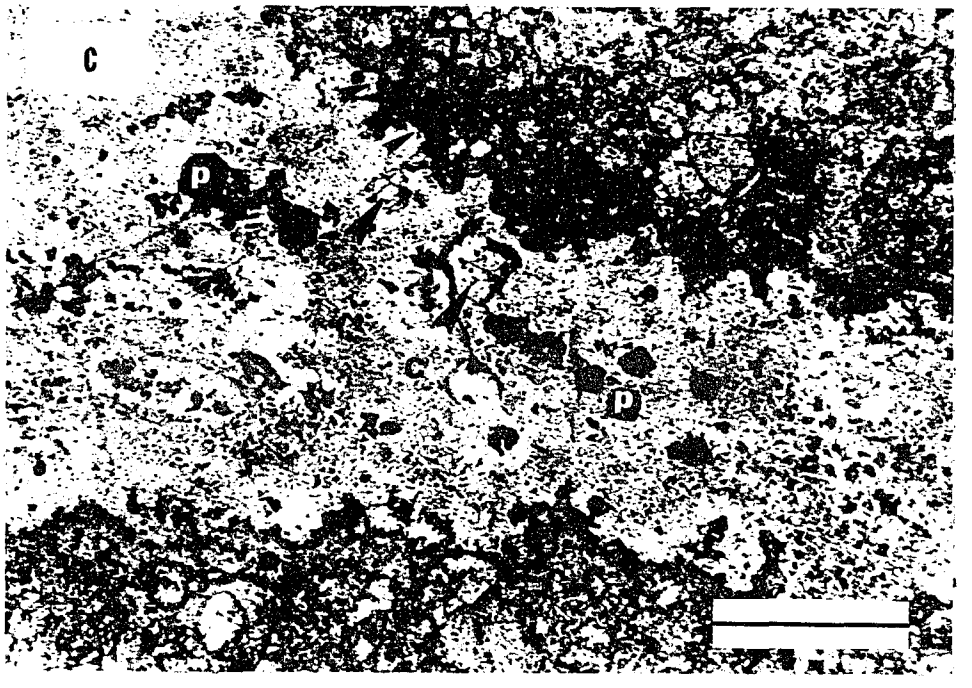


Fig. 150 C- Selectively chertified bryozoan in the skeletal and peloidal packstone- and grainstone unit of backshoal facies. Arrowheads point to chertified-ghost ferroan dolomite rhombs and euhedral pyrite crystals (p). Under plane-polarized light; scales= 0.5 mm.

in the siliciclastic, fine-grained sediments of the shelf facies that formed behind the Nuia shoals. Other brachiopods are also selectively chertified in the skeletal shoal

units and shelly storm layers of the upper slope facies.

c) Bryozoans:

Fragments of bryozoans are also selectively silicified by quartz polymorphs. Neomorphically calcitized bryozoans are often replaced by silica, and the silica-replacement commonly postdates some fracture-filling calcite cements as well as the patchy ferroan dolomites.

Figure 150 C- shows that in the peloidal packstone units of backshoal, ferroan dolomites of selectively replaced ooids or peloids are also replaced by silica (chert). Euhedral, moderate- to coarse-grained pyrite crystals accompany the silica replacement.

d) Trilobites:

Chertification of trilobites is generally seen in shelly storm layers of the upper slope facies. Generally, trilobite particles appear to have been dissolved, and these dissolution voids are filled by fibrous silica, especially by length-fast, botroidal or fibrous chalcedony (Fig. 150 B).

Interpretation:

Silica replacement along crystal boundaries of the neomorphic calcites in molluscs or drusy cement appears to have no relationship with quartz replacement in bryozoans. The replacive quartz cement along the crystal boundaries was interpreted to postdate meteoric diagenesis (see replacive quartz in foregoing section).

Replacement of the calcitized bryozoans and fracture-filling calcites, postdating intergranular calcite mosaics and calcitized bryozoans, as well as ferroan dolomites by

silica, suggests that silicification of bryozoa is rather a late diagenetic phenomenon which may have taken place after the completion of meteoric or deep-phreatic and mixing-zone diagenesis. Thus, the silicification events mentioned above were late and deep-burial diagenetic in nature; nevertheless, the events may not have been cogenetic because the replacement of ferroan dolomite by silica represents a post-stylolitic or very late diagenetic event. On the other hand, the fractures probably formed under shallow to intermediate burial conditions. Therefore, it is possible that these two silica replacement events may have been synchronous at the shallow to moderate burial depths.

Selective replacement of crinoids or echinoderm ossicles by silica is the most common type in all the lithologic unit except in oolitic packstone- and grainstone units. Despite the common occurrences, it is difficult to determine the timing of silicification of these grains. Restriction of silica replacement primarily in crinoids, not in syntaxial overgrowths, can not be used alone to determine whether silicification occurred during early diagenesis. This silicification must have some dependence on the original composition of crinoid fragments and their shell microstructures. They are generally high-Mg calcite in composition (e.g., Schole 1977) and include numerous porous plates (Horowitz and Potter 1972; Bathurst, 1975). Formation of dolomites in crinoids is associated with dissolution of high-Mg calcite crinoids during transformation of high-Mg calcite to low-Mg calcite (Lohmann and Meyers, 1977). However, Jake (1974) has related the microdolomite formation to replacement of high-Mg calcite by silica during which dolomite concomitantly occurred in Mg^{+2}-enriched areas of crinoid grains. However, parallel orientation of dolomite rhombs and dolomites within silicified and unsilicified parts of crinoids revealing a single-grain extinction (Jake, 1974; Hess, 1987) argue against Jake's thesis.

Existence of microdolomite rhombs in the low-Mg calcite, their parallel orientations, and single crystal extinction with the partially silicified crinoids suggest that formation of dolomite probably took place prior to chert replacement. Conversion from high-Mg calcite to low-Mg, or "polymorphic alteration", takes place in the meteoric phreatic environment (Friedman, 1964 and Gavish and Friedman 1969),

resulting in formation of dolomite during mixing-zone diagenesis (Lohmann and Meyers, 1977). From the information presented above, it is suggested that silicification of crinoids is post-microdolomitic or relatively late diagenetic at shallow- to intermediate-burial depth of the AVL.

Similarly, trilobites are partially replaced by chalcedony or length-fast chalcedony which replaces the syntaxial overgrowth on crinoids in the shelly packstone sublayers of the upper slope facies. For the indicated reason, it is inferred that silicification of trilobites was late diagenetic at shallow to moderate burial depth. Absence of interparticle chert or quartz cement or primary porosity-filling quartz cements can also indicate relatively deeper diagenetic environmental conditions than the mixing-zone chertification (Kanuth, 1977; Simonson, 1987).

Oxidation of organic matter by oxygen from sea water diffusion (Holdway and Calypool, 1982) can cause fluctuation of the pH level in sediment pores and initiate early silica replacement. However, the textural relations and precipitation of pyrite discussed above can be explained by a sulfate-reducing model. Sulfate reduction by microbial activities is believed to be common at intermediate burial depths where oxygen released from Mn^{+3} and Fe^{+3} no longer becomes available for oxidation of organic matters (Emerson et al 1980). Reduction of SO_4 by microbial activities results in generation of CO_2, while formation of H_2S decreases the alkalinity of water which becomes undersaturated with respect to calcite and over saturated with respect to silica. This process creates favorable conditions for concomitant formation of silica and pyrite (e.g., Noble and Stempvoort, 1989) as seen in selectively silicified bryozoans. In this case, pyrite probably precipitates from the same solutions relatively earlier than chert. Similarly, pyrite in calcite-filled sponge spicules may also be explained by the same process: high alkalinity led to dissolution of spicules concomitantly followed by pyrite and calcite precipitation. In the pelletal lime mudstones (hemipelagics) of the AVL, absence of collapsed-sponge spicule molds (e.g., Meyers, 1977) implies that concomitant occurrences of pyrite and calcite cement represent a shallow- to moderately deep-burial diagenetic environment.

Birnbaum and Wireman (1985) experimentally found that sulfate reduction by

bacteria produced: CO_2, H_2S and FeS. The same diagenetic products along with dolomite are also reported to have formed in the experiment of Baker and Kastner (1981). Maliva and Siever (1988) suggest that dissolution of calcite and precipitation of silica occur simultaneously and that silica replacement continues as the dissolution film of calcite progresses. As indicated above, except for chertification of bryozoa, silicification of other allochems can be explained by microbial sulfate reduction. Silicification of all these allochems appears to be post-meteoric diagenesis probably at shallow to shallow-intermediate burial depths which may range from 100's of meter to 1.5 or 2 km. This burial depth range is inferred from the suggestion of Machel (1987, 1989) -- by using 20 °C surface temperature and 30 °C/km for geothermal gradient-- that microbial sulfate reduction occurs up to 85 °C. However, silicification of bryozoa took place at greater burial depths than that of the microbial sulfate-reduction zone, probably in the thermal sulfate-reduction (TSR) zone which occurs at temperatures of about 135 °C (Machel, 1987, 1989).

B. Chert Nodules, Lenses and Beds

In the AVL, the parallel-laminated, silty quartz-rich lime mudstone lithofacies of the open shelf facies commonly have chert nodules and beds which consist of the following quartz polymorphs: (1) replacive microcrystalline equant quartz (Fig. 151 A and B) or microquartz (Wilson 1966; Folk and Pittman, 1971); (2) length-fast chalcedony or fibrous-spherulitic quartz, occurring as a void-or cavity-filling cement and seldom replacive (Figs. 151, 152 A, 153 A); and (3) megaquartz, as a void-filling quartz with a drusy cement fabric (Fig. 151 A, 153 A and B).

Parallel laminae of the mudstone lithofacies do not curves around chert nodules and are preserved in chert nodules (Blatt, 1982). In addition, the chertified parts of the silty quartz-rich, parallel-laminated lime mudstone beds are darker in color than unchertified parts of the same beds, and an irregular and truncational contact occurs

between these subunits.

a) Microcrystalline Granular Quartz

This is a replacive quartz and the major component of chert nodules and beds. The microcrystalline granular quartz has equant grains which are smaller than 10 μm (Folk and Pittman, 1971). Only in the Lone Mountain section, the replacive quartz includes inclusions of partially or completely replaced allochems, calcite cement, and dolomite rhombs. Completely replaced dolomites can be recognized in the microcrystalline replacive quartz as ghosts (relict structures), euhedral crystal outline of yellow-brown color.

Some replaced allochems can still be recognized; these include Nuia grains whose original structures are, in many cases, still preserved (Figs. 151 A, B). Crinoids are generally replaced, but their syntaxial cements appear less susceptible to silicification. Generally, large calcite spar also appears to have escaped silica replacement. Intraclasts or oncoids containing euhedral dolomite rhombs have been more commonly chertified (Fig. 155 B).

Zoned dolomites with bright red luminescence commonly occur in areas adjacent to chert margins in the partially chertified-parallel laminated, silty quartz-rich lime mudstone units. The replacement of dolomite by chert appears to show sponge-like advancing replacive zones. The bright-red luminescent coarse-zoned dolomites, which decrease in abundance and size from the chert margins, generally reveal two zones partially replaced and truncated simultaneously by chert and zoned-microdolomites (see Fig. 154).

In chertified limestone subunits or nodules, commonly microcrystalline-equant quartz mosaic consists of isolated chalcedony- and megaquartz-filling features which have a gradual contact with host microcrystalline equant quartz (Fig. 151 A, B).

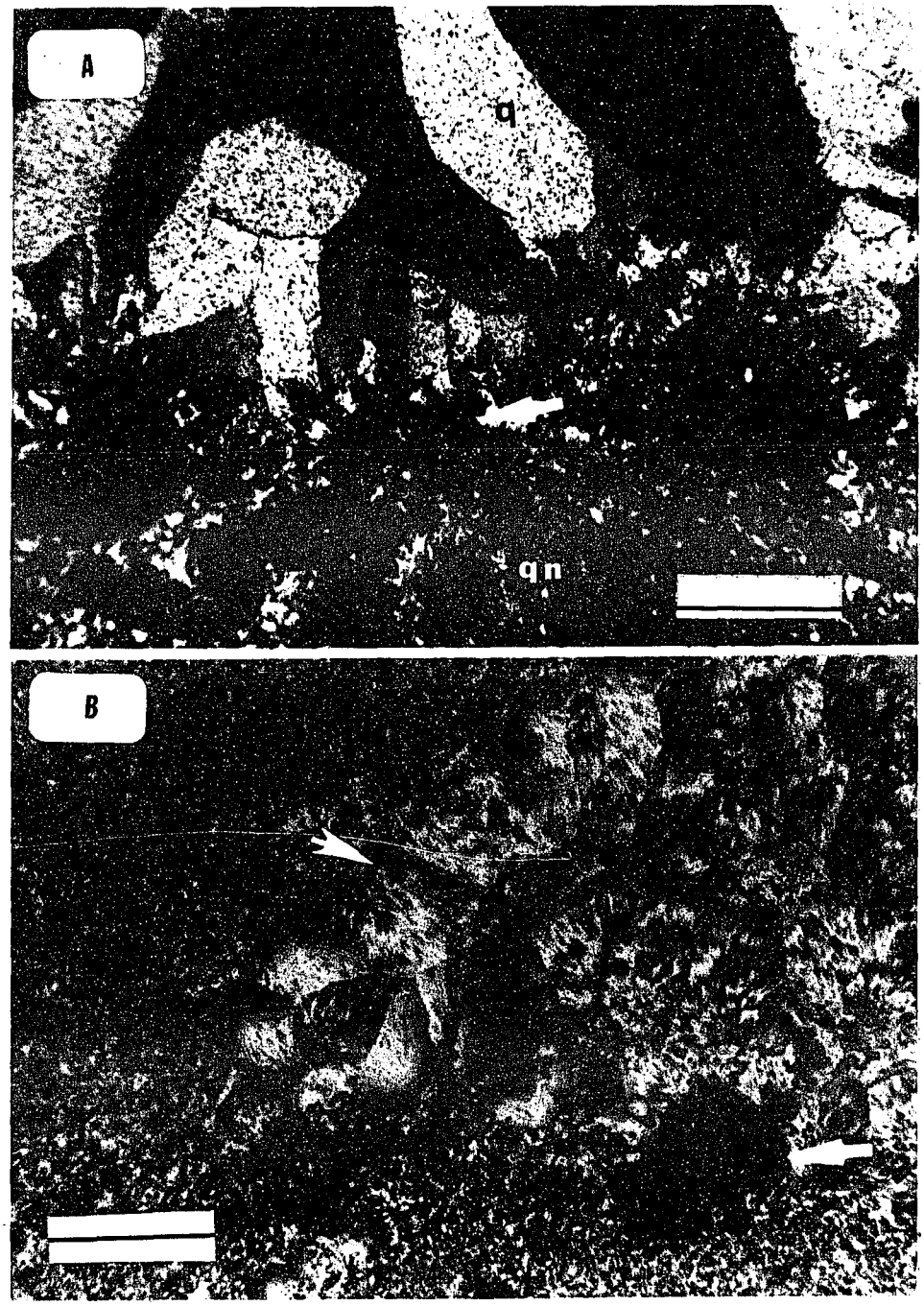


Figure 151- Photomicrographs of quartz cements in chert nodules and lenses. A) Photomicrograph of replacive microcrystalline granular quartz or chert (qn) and void-filling mosaic quartz or megaquartz (q). Microcrystalline granular quartz consists of some replaced allochems (ghost) indicated by white arrows and appears to have a sharp contact with the void-filling mosaic quartz (q) having a drusy- cement texture. B) Photomicrograph of microcrystalline granular quartz (qn) and length fast void-filling chalcedony (ch) shows that a sharp contact occurs between void-filling chalcedony and microcrystalline granular quartz cements indicated by white arrows. Under cross-polarized light; scales = 0.5 mm.

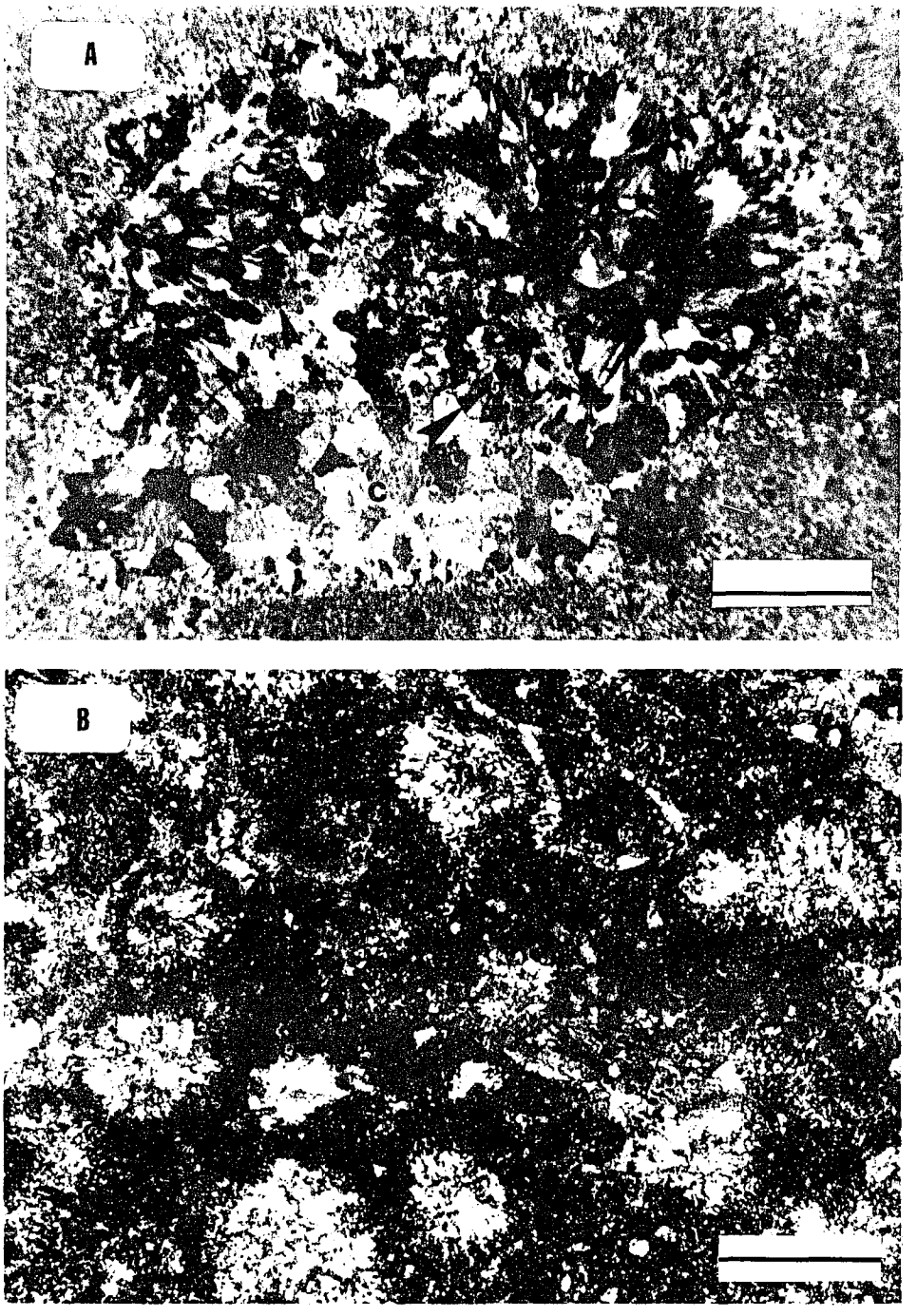


Figure 152- A) Photomicrograph of length-fast chalcedony at the calcitized center of a Girvanella oncoid. Arrowheads point to curvature, a sharp contact between calcite cement (c) and chalcedony (ch). B) Photomicrograph of pervasively silicified Nuia packstone- and grainstone unit. The microcrystalline quartz or chert replaced the matrix and intergranular cement among Nuia grains (n); however, Nuia grains replaced by quartz cement appear to have a mimic replacement texture. Under cross-polarized light; scales= 0.5 mm.

b) Length-Fast Chalcedony

In the chert layers, the length-fast chalcedony (LFC) is the most common cement. It is a fibrous, spherulitic, botryoidal, void-filling microquartz. Its extinction occurs perpendicular to the c-axis of the crystals (Figs. 151 B, 153 A). LFC is generally common in microcrystalline quartz mosaic with a void-filling texture (see Wilson, 1966). LFC also replaces oncoidal cores (Fig. 152 A and B), but such replacement is very rare and only observed in the nonchertified units of June Canyon section. Evaporite precursors are not recognized in this void-filling chalcedony (e.g., Folk and Pittman, 1971).

c) Megaquartz or Mosaic Quartz:

"Mosaic quartz" (e.g. Wilson, 1966) and "Megaquartz" (e.g., Folk and Pittman, 1971) represent the same fabric; however, the term "mosaic quartz" is preferred in this study because it is a better descriptive term than "megaquartz". Quartz crystals of mosaic quartz vary from 50 to 2000 μm in size and generally fill cavities and molds. Crystal boundaries are generally planar (Figs. 151 A, 153 A, B) are often visible in the texture of drusy cement (Bathurst, 1954; Friedman, 1964; and Wilson 1966). Quartz crystals are very clean and do not have any inclusions of calcite and dolomite cements. However, they contain various two-phase primary and secondary fluid inclusions.

Textural relations between mosaic quartz and chalcedony were not directly observed. However, in figure 151 A, prismatic-rim quartz crystals (probably original chalcedony) grade into the void-filling mosaic quartz. In drusy-like quartz mosaics (Fig. 153 A), coarsening of quartz crystals toward the center of pores is terminated by dolospar which has planar crystal boundaries with quartz crystals (Fig. 153 A).

The large-sparry dolomite crystals replaced coarse calcite spar which poikilotopically includes hematite or goethites (probably pseudomorphs of pyrite; Fig.

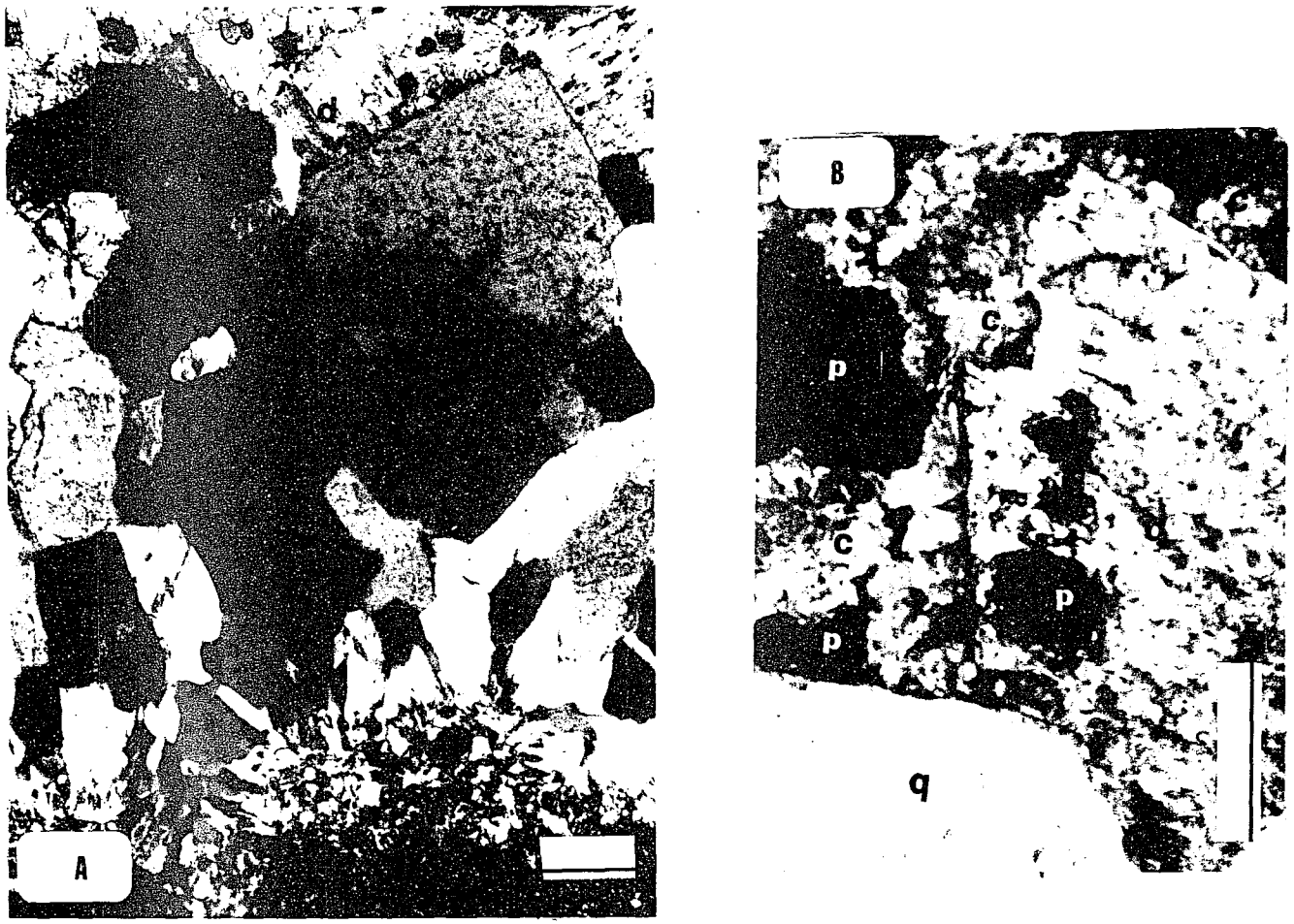


Figure 153- Photomicrographs of void-filling mosaic quartz and carbonate cements in chert nodules. A) In void-filling mosaic quartz cement, quartz crystals (q) coarsen toward the center of a precursor void and show a drusy-cement texture. White arrow points to a planar crystal boundary between dolomite (d) and megaquartz (q). The coarse, cloudy quartz crystal (q) with rhombohedral crystal form appears to be dolomite pseudomorph. B) Close view at contact relations between drusy-quartz mosaic (q), void-filling calcite (c), dolomite cements (d), and pyrite crystals (p). Arrowheads point to a planar contact between void-filling quartz and carbonate cements as well as pyrite crystals. Euhedral dolomite crystals replaced the calcite crystals which poikilotopically include pyrite crystals (p). Under cross-polarized light; scales= 0.25 mm.

153 A). Hematite appears to occur as perched grains in calcite without regular outlines, and also at the contact of coarse-calcite spar and coarse quartz crystals (Fig. 153 B).

Interpretation and Timing

Among the silica phases, opal A is the most soluble silica phase, and solubility decreases with increasing crystallinity; therefore, quartz is the least soluble silica phase (Meyers 1977). The difference of solubility between skeletal silica Opal-A and other diagenetic silica phases is probably the driving mechanisms for silica diagenesis (Meyers, 1977).

Quartz is expected to precipitate from the solution with 6-25 ppm dissolved silica and opal-CT from solutions with 25-125 ppm silica concentration (Mackenzi and Geas, 1971; Wise et al., 1972). During diagenesis of silicious rocks, silica phase generally transforms from opal-A (biological silica) to opal-CT and quartz (Murata and Larson, 1975; Meyers, 1977; and Williams et al., 1985). Late diagenetic origin of cherts in the AVL can readily be inferred from the parallel, continuous laminae within the chert and chert-free layers which do not curve around the chert nodules (see Fig. 66 D in Chap. 200; Blatt, 1982). The presence of irregular boundaries between chertified and unchertified parts of the same silty quartz-rich, parallel-laminated lime mudstone beds also provide evidence for late diagenetic replacement, but not syndepositional chert replacement. Moreover, replacement of allochems, such as Nuias, crinoids and oncoids or intraclasts by chert and inclusion of some partially replaced, calcite spars and relict dolomites strongly suggests that silicification in the AVL was a relatively late diagenetic event.

Replacement of siliceous spicules by calcite and absence of collapsed-spicule molds and early micrite fillings (e.g. Meyers, 1977), also suggest a possible post-lithification silica dissolution. Interparticle pore-filling silica was not observed in any thin section

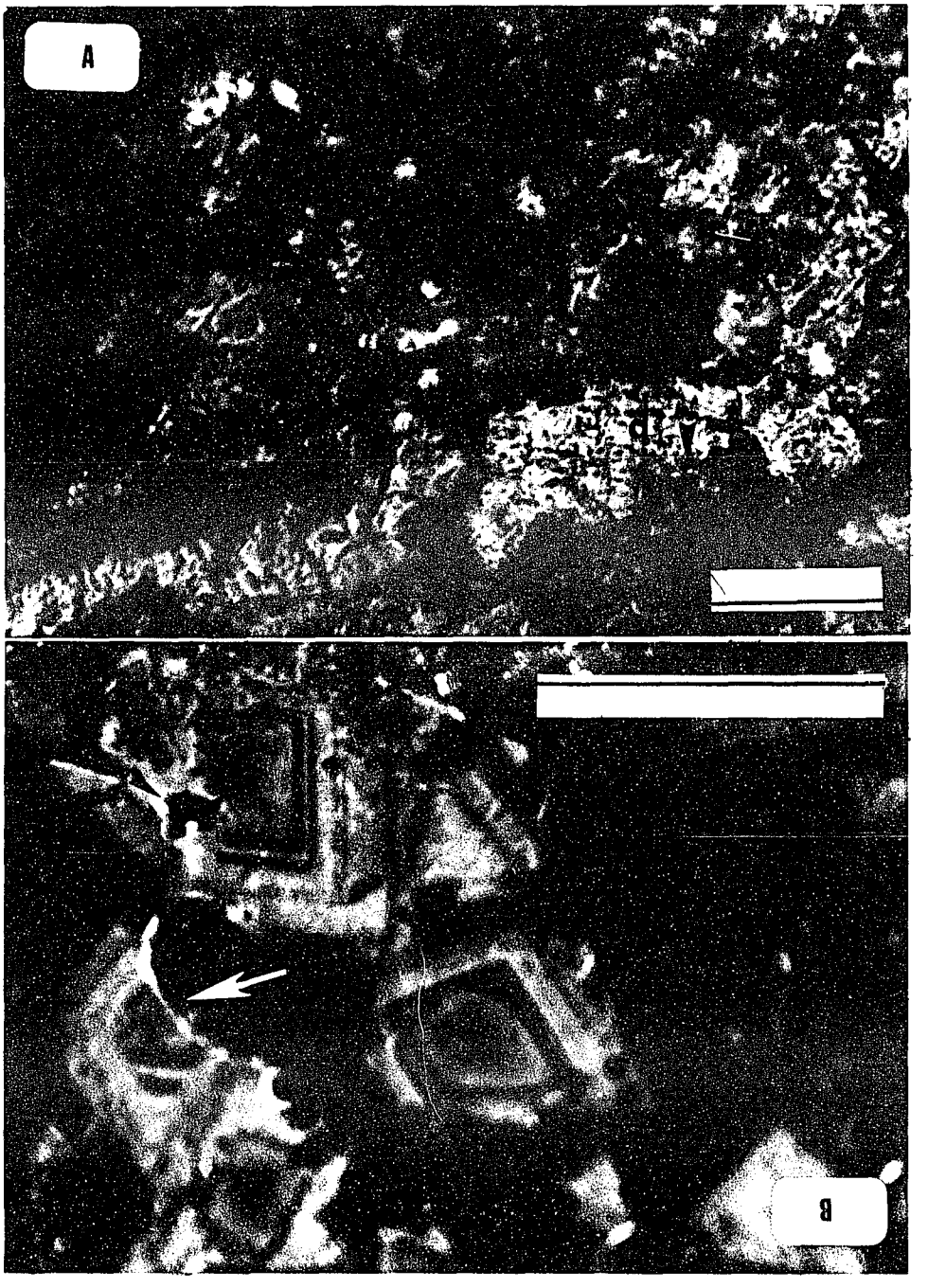


Figure 154- Photomicrographs of zoned-dolomite crystals replaced by quartz and zoned-microdolomite crystals at the margin of chert nodules. A) Chert replaced the selectively dolomitized part of the host limestone unit. Arrowheads point to corrosive crystal boundaries between dolomite crystals (d) and quartz crystals; under plane-polarized light. B) Close up view of photomicrograph A under cathode light shows that zoned-coarse dolomite crystals were replaced by quartz (q) and zoned-microdolomite crystals (m). A white arrow and small arrowhead point to corrosive crystal boundaries between quartz replacement and zoned-coarse dolomite crystals. A large arrowhead points to the replacement of zoned-coarse dolomite by micro-zoned dolomite crystals. Scales = 0.25 mm.

of silicified or silica-free packstone- and grainstone units. Therefore, all the evidence suggests post-depositional silica replacement and also late-silica replacement at shallow to intermediate burial depth.

The chalcedony within the replacive microcrystalline mosaic is a void-filling cement. It radiates from the walls of the cavities or molds, and grades into microcrystalline quartz mosaic. This might be indicative of contemporaneous precipitation and progressive dilution of silicifying solutions through time rather than replacement. Megaquartz cements with planar crystal boundaries in a drusy fabric and without any calcite and dolomite inclusions, unequivocally represent a void-filling cement rather than replacement. From the wall to the center of the quartz-filled voids or molds, the following sequential order is observed: microcrystalline quartz (replacive in nature) to bladed prismatic quartz to megaquartz crystals ending with parallel boundaries. This sequence may imply that microcrystalline quartz mosaic was the first to form followed by spherulitic chalcedony and finally by megaquartz spar. Silicification with a similar sequence has been reported by Meyers (1977) for the cherts of Lake Valley Formation of New Mexico and by Harris (1982) in the Burlington Limestone of Iowa. Such sequential order in quartz fabric is interpreted as a product of progressive dilution of silica-rich solutions (Jones and Segnit, 1971; Kastner et al., 1977).

In figure 153 B, the void-filling quartz mosaic, with a drusy texture (Fig. 153 A), is followed further pore-centerward by poikilotopic calcite spars which commonly contain irregular pyrite crystals ranging 0.25 to 0.5 mm in size. In the same photomicrograph, an euhedral dolomite spar (0.75 mm) also poikilotopically includes a nearly euhedral pyrite crystal (0.15 mm) and sparry calcites, and quartz crystals terminate planar crystal endings and cut calcite, dolomite, and pyrite crystals. Thus, large quartz crystals of the void-filling mosaic quartz exhibit replacement features along their contacts with calcite, dolomite, and pyrite crystals. The petrographic relations suggest that quartz was the first void-filing cement to precipitate and followed by pyrite, calcite, and dolomite. It is also possible that two diagenetic events may have been responsible for indicated diagenetic products and their timing: 1) the

first event, producing chalcedony or quartz, pyrite, and calcite; and 2) the second event, including replacive quartz, pyrite, and dolomite, respectively.

Kastner et al. (1977) and Baker and Kastner (1981) suggest that sulfate reduction by microbial activity promotes a cogenetic silica and dolomite precipitation. In their model opal-A to opal-CT transformation hinders dolomite formation; Mg^{+2} and OH^{-1} ions, incorporating into nucleations of opal-CT, enhance the formation of opal-CT. Dolomite is expected to form by the release of Mg^{+2} taken from opal-CT during the opal-CT to quartz transformation.

In the AVL, therefore, it is likely that quartz or opal-CT, pyrite, and calcite precipitation by microbial sulfate-reduction may have occurred in a shallow-burial depth where silica concentration was high in the solutions. The second diagenetic event may have taken place in a relatively deeper burial environment where hot, diluted silica-bearing solutions or recrystallization of opal-CT to quartz probably produced quartz, pyrite, and dolomite, respectively. In either case, precipitation of pyrites mark the major change in the composition of fluids form acidic (low pH) to alkaline (high pH) stages.

In figure 154 A, B, zoned-micro dolomite rhombs and quartz synchronously replaced the pre-existing large zoned-dolomite crystals. This probably represents the release of Mg during the opal-CT to quartz transformation (Kastner et al., 1977; Baker and Kastner, 1981). As demonstrated above, the petrographic evidence in this study strongly supports the diagenetic model for the progressive phase changes of silica and associated carbonate cement as well as pyrite precipitation proposed by Baker and Kastner (1981).

Quartz crystals have a planar contact with a dolomite crystal which clearly replaced sparry calcite and pyrites (Fig. 153 B). This petrographic relation suggests that quartz and dolomite formed cogenetically; by the precipitation of pyrite, dolomite began to replace precursor sparry calcite and pyrite crystals. However, replacement of dolomite by quartz (Fig. 153 B) probably represents a relatively late silicification of the AVL which probably did not result in precipitation of pyrite and dolomite. Similar chert dolomite association was noted by Deitrich et al. (1963) and Selleck (1985).

Absence of dolomite, on the other hand, in the silicified-lithologic units of the AVL is probably due to high SO_4 content in pore solution which was high enough to inhibit formation of dolomite, or Mg-supply was insufficient to promote dolomitization (see Selleck, 1985).

C. Source of Silica

The possible intraformational sources of silica for the chert nodules and discontinuous chert layers of the open-sea facies of the AVL are (1) volcanic ash, (2) dissolution of detrital quartz or feldspar, (3) sea water, (4) smectite-illite transformation, and (5) dissolution of siliceous organisms (spicules, radiolaria, diatoms).

Absence of volcanic ashes in the chertified units eliminates the possibility of a volcanic source for silica.

Feldspars are also not found in the chertified units and associated carbonate lithofacies as detrital particles. Silty quartz is abundant in some chert-bearing and chert-free layers, yet they do not show any dissolutional features. Therefore, detrital quartz and feldspars could not have been the source of dissolved silica.

Absence of diatoms before the Jurassic may have caused higher concentrations of dissolved silica in sea water; therefore, sea-water diffusion is believed to have probably caused silica to replace carbonate sediments of pre-Jurassic (Siever, 1988; Noble and Stempvoort, 1989). Since the appearance of diatoms, concentration of dissolved silica content is 1 ppm in normal sea water and 6 ppm in deep-sea water . Even if silica concentration in sea water was much higher during pre-Jurassic geologic time, very limited and selective nature of silicification in the AVL can argue against sea water as a possible source for silica.

Smectite-illite transformation in shale diagenesis was assumed to be the primary source of intraformational silica in the lower Cretaceous of the Gulf Coast (e.g., Perry

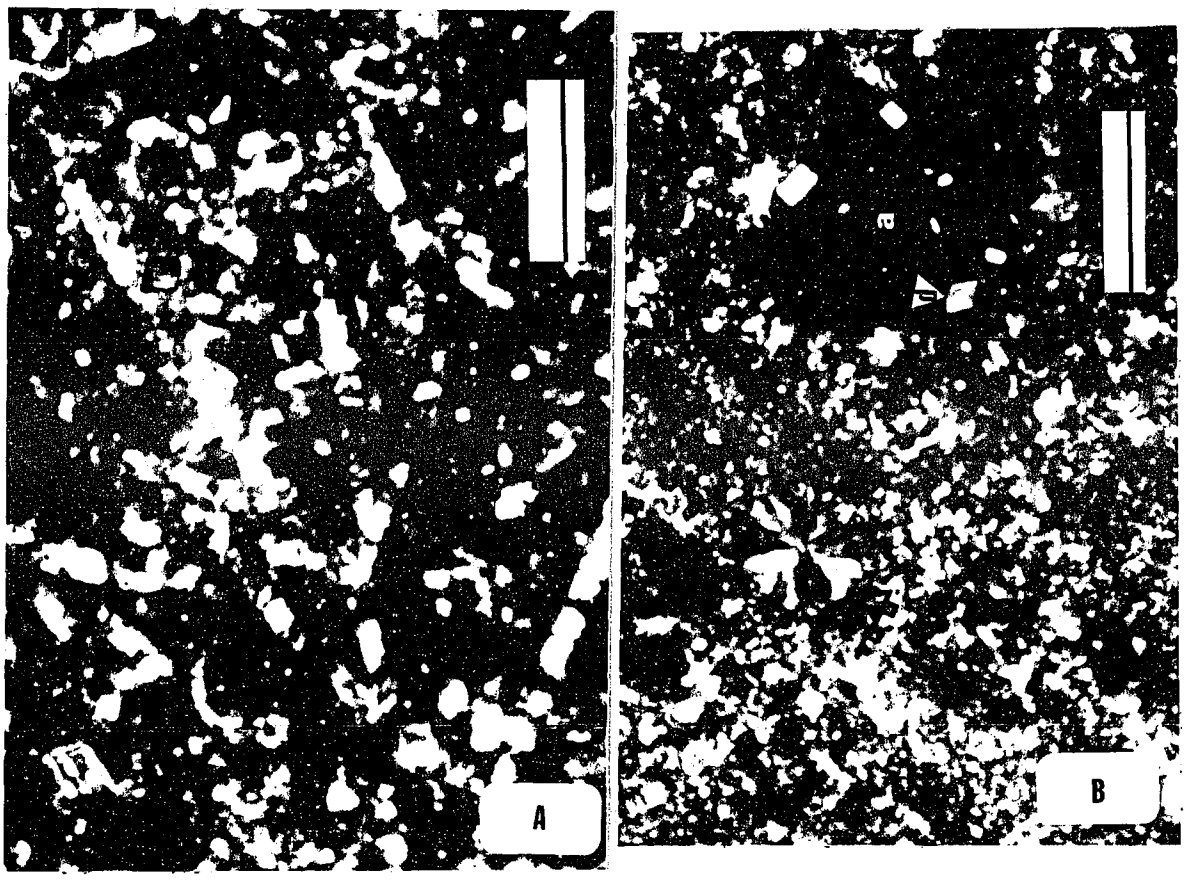


Figure 155- Photomicrographs of sponge spicules and radiolarias in chert nodules. A) Abundant silicified sponge spicules are recognizable within microcrystalline granular quartz cement. B) Arrow point to a radiolaria within the microcrystalline quartz cement. White arrowhead with (d) indicates ghost dolomites within a dark black allochem (a). Under cross-polarized light. Scales= 0.25 mm.

and Hower, 1972; Boles and Frank, 1979), and in the Southern Alps (Hess, 1988). Transformation of smectites would produce silica unless the released silica is used by other clay minerals, such as chlorite (Hess, 1988). X-ray analysis of the samples at Mill Canyon section shows very little chlorite, whereas in other sections, chlorite is common (see Chapter 20). Therefore, it can be suggested that smectite-illite transformation may have contributed to silica replacement in the AVL; however, it was not probably the primary source of silica.

Dissolution of biogenic opal from radiolaria and siliceous sponge spicules was probably the most important intraformational source for silicification or replacement of silty quartz-rich, parallel-laminated lime mudstone layers of the AVL. As mentioned above, sea water provides only 1-6 ppm dissolved silica; however, dissolved radiolaria and spicules produce silica-rich solutions with a silica content of 6 to 120 ppm (Baker and Kastner, 1981). Sponge spicules and radiolaria are considered to have been the primary source of chert nodules and silicified layers in limestones from early Paleozoic to Cretaceous (e.g., Meyers, 1977; Harris, 1982; Coniglio, 1987 and Maliva and Siever, 1988). By these studies, calcite-filled or replaced spicules and radiolaria and ghosts of these organisms (Fig. 155 A, B) were linked to the possible intraformational silica source or supply for the silicified units. However, it is often difficult to directly relate biogenic origin of cherts by standard petrography because intensive replacement obliterates original textures of cements and allochems. For example, in the Lone Mountain section, chert nodules and chertified-discontinuous layers show very few traces of radiolarians and sponge spicules (Fig. 155 A and B). The same thin section under cathode light shows very abundant radiolarian ghosts, very similar to those illustrated by Coniglio (1987).

In the AVL, abundant chert layers and nodules formed mainly in fine-grained storm layers of the open shelf. Thus, the formation of chert layers and nodules, in a way, was linked with paleocurrent-controlled accumulation and concentration of siliceous spicules and radiolarians.

TIMING AND SUMMARY OF DIAGENESIS

Timing relations of the diagenetic products or paragenesis in the Antelope Valley Limestone (AVL) are summarized in figure 156. In this diagram, some diagenetic products have been illustrated by the same bar, even though each of these diagenetic products show relative time differences in their occurrence. For instance, all the marine cements are represented by the same bar; however, in the oolitic shoal units, isopachous-marine cement is the first cement to form and is followed by cryptocrystalline low Mg-calcite and radiaxial-fibrous cements. Thus, for this reason, this diagram does not provide detailed-timing relations for the diagenetic products and features of each diagenetic environment as these relations have been discussed in detail in the appropriate chapters.

The position and length of each bar in figure 156 represents the relative timing relations and estimated duration of each diagenetic product compared to others. In addition, lengths of each bar or durations are somewhat arbitrary. For instance, the diagenetic products formed in the marine and near-surface diagenetic environments are represented by bars as long as those representing late and burial diagenesis, even though the AVL underwent a relatively short episode of near-surface diagenesis compared to a very long burial diagenesis.

The relative timing relations of these diagenetic products, on the other hand, are believed to be accurate. These relations have been primarily determined by field studies, standard petrography, and cathodoluminescence.

Some diagenetic products are represented by more than one bar, sometimes three or four bars which are used to determine multiple generations of the same diagenetic product. In each episode, these diagenetic products may represent somewhat different chemical compositions and textural relations due to changes in the physical and chemical conditions of the diagenetic environment.

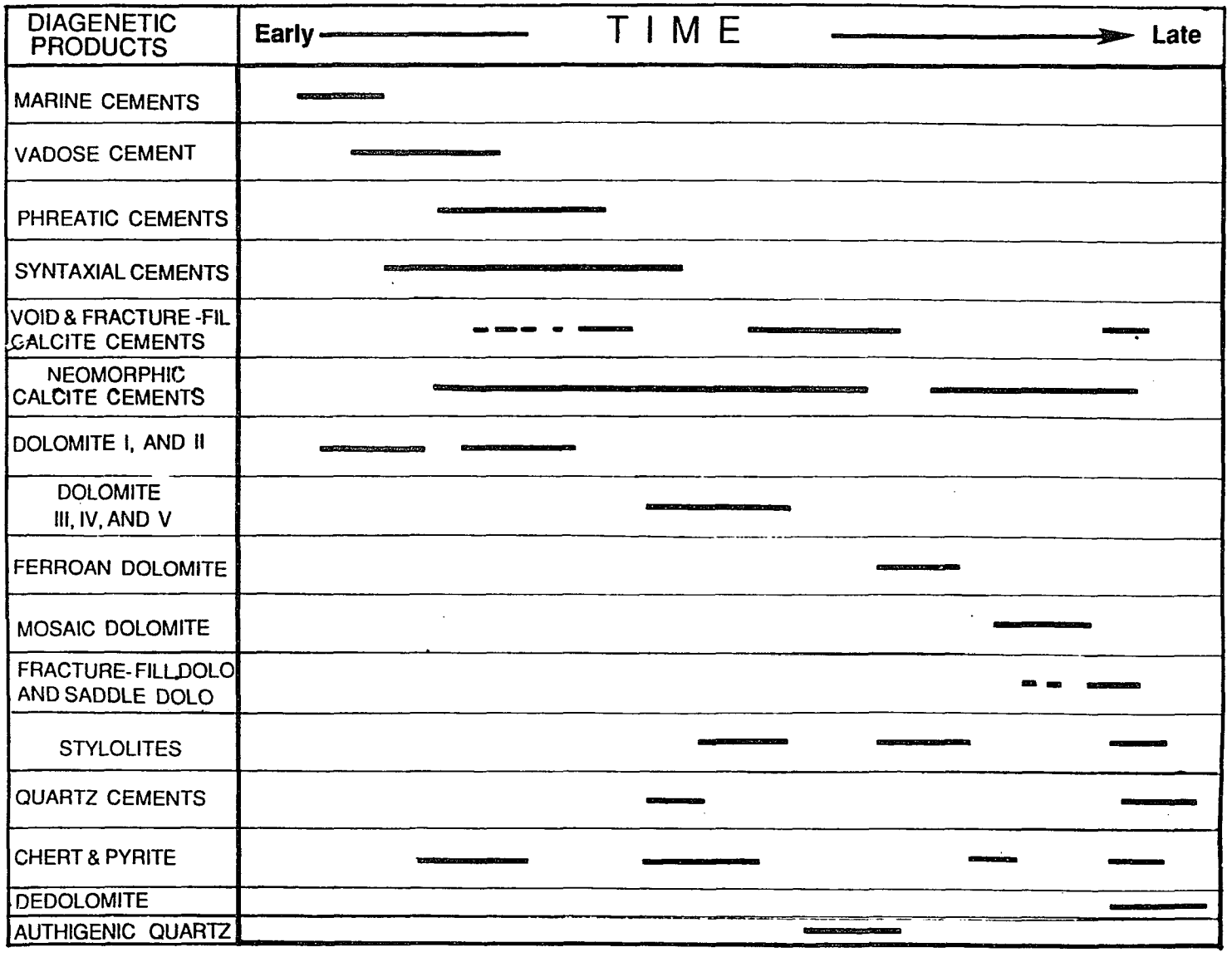


Figure 156- Paragenetic and diagenetic sequence of the Antelope Valley Limestone in the study area. The length of bars does not reflect the duration of diagenetic events and sequences, but these bars reflect the relative timing of diagenetic events.

PART IV: MAXIMUM BURIAL DEPTH RANGE OF THE ANTELOPE VALLEY LIMESTONE AND THERMAL HISTORY OF THE GREAT BASIN AT CENTRAL NEVADA

- ORGANIC METAMORPHISM (ORGANIC MATURATION OR THERMAL ALTERATION)
- OXYGEN-ISOTOPE THERMOMETRY
- FLUID-INCLUSION MICROTHEMOMETRY
- CLAY DIAGENESIS AND ILLITE CRYSTALLINITY
- COMPARING RESULTS OF GEOTHERMOMETRIES
- CONCLUSIONS
- APPENDICES
- REFERENCES

CHAPTER 16: ORGANIC METAMORPHISM (ORGANIC MATURATION OR THERMAL ALTERATION)

A. Introduction:

Fine-grained organic matter and remains are indigenous to all the sedimentary environments and sedimentary rocks. In most sedimentary rocks, organic matter is found in trace amounts; however, it is the major component of some rocks, such as oil shale, and coal.

After the deposition of organic debris within the sediments, the preservation and alteration of organic matter occurs in a very broad diagenetic and metamorphic realm. Some changes in the composition of disseminated-organic matter commonly start during sedimentation at the water-sediment interface, and these changes are primarily caused by microbial decomposing and zooplankton grazing (Barnes et al. 1984). Alterations below the water-sediment interface are also largely biochemical and caused by metabolism of fungi, bacteria, and other micro-organisms. These biochemical alterations can also be defined as bacterial-sulfur reduction and fermentation processes. Progressive increase in burial depths reflects progressively higher maturation or thermal alteration levels of organic matter. Therefore, thermal alteration level of organic substances or the LOM (level of organic metamorphism, see Hood et al., 1975) increases in response to increases in burial temperature and duration of heating.

Through progressive burial depths, fine-grained organic matter degrades, alters and transforms into oil, gas and finally to graphite in metamorphic media (Barnes, et al., 1984). Levels of thermal alteration of organic matter are grouped into three major diagenetic zones: Eogenesis, Catagenesis, and Metagenesis (Tissot and Welte, 1978).

Organic matter is much more sensitive to temperature changes than most inorganic mineral transformations, and they are not affected by interstitial solutions in the diagenetic environments (Dow, 1977; Price, 1983; Barnes et al. 1985; and Price and Barker, 1985). Moreover, all agree that diagenesis of organic matter is progressive and irreversible. Therefore, alteration or maturity level of organic matter can be used as an ideal tool for determining the thermal history of the sedimentary rocks in given sedimentary basins (Dow, 1977; Price, 1983; Price and Barker, 1985; and Barker, 1987). Heating duration, maximum depth of burial, geothermal gradient, heat capacity and thermal conductivity of sedimentary rocks are the controlling factors of the thermal alterations of organic matter or level of organic metamorphism.

For quantitative determination of thermal-maturation level of organic matter, two models are commonly used: (1) Lopatin's (1971) method, based on heating duration and temperature, and (2) maximum temperature model, based on maximum heating temperature (Tmax) which alone controls thermal maturation level of organic matter, but not heating duration at low temperatures. Time-temperature model (Lopatin (1971)'s model) updated by Waples (1980) is based on the rule that reaction rate is doubling for the each 10 °C temperature increase. In this model, the time-temperature relations in the process of organic maturation are concerned with heating at constant temperature or with integrating temperature effects over the entire burial history. Lopatin's model with respect to constant heating due to constant geothermal gradient is similar to the model of Hood et al (1975), which considers the combination of maximum temperature, effective heating time, and doubling reaction rate for the every 15 °C temperature increase instead of 10 °C.

Price (1983) demonstrates that there is a strong correlation between the increasing vitrinite reflectance (R_o %) data and increasing temperature, but there is no correlation between R_o% and increasing burial time. He also suggests that geologic time is not a controlling parameter in the thermal maturation of organic matter but maximum temperature is. Barker (1983) shows that at least 10^4 years are necessary for thermal alteration and stabilization of the organic matter in hydrothermal systems. Barker and Pawlewicz (1986), Barker (1989) and Barker and Goldstein (1990) illustrate a strong

correlation between Rm % and maximum temperature (Tmax), and they consider Tmax alone as a primary controlling factor on thermal alteration of sedimentary organic matter. According to Tmax model, during burial diagenesis, heating with maximum temperature (Tmax) can be sufficient for organic matter to reach maximum maturation level and to be stabilized. The steady effective heating time (Hood et al. 1975) should be more limited and not be considered. The organic maturation or organic metamorphism is irreversible so that the elapsed time, during constant temperature and declining-temperature, can not affect the organic-maturation level and elevate them to higher maturation levels. In addition to Tmax, the kinds of organic materials and depositional environment play an important role in the maturity level of kerogen (Price and Barker, 1985; Tissot et al., 1987).

The organic alteration level, particularly vitrinite reflectance, is commonly used with other geothermometries in order to determine maximum burial depth (Frey et al. 1980; Kisch, 1982; Duba and Williams-Jones, 1983; Friedman, 1987a,b; Friedman and Sanders, 1984; Levine, 1986; Cercone, 1984; Pollastro and Barker, 1986; Price 1983; Price and Barker, 1985; and Price et al. 1986).

In this study, thermal maturation level of sedimentary organic matter is based on microscopic observation of both color and structure alteration of organic debris--chiefly leaf cuticle and plant pollen because woody materials and land plants were absent during the early Paleozoic period.

Staplin (1969) used the color scale (yellow through brown to black) based on carbonization of spores and pollens and developed a similar color scale " Thermal Alteration Indices" (TAI). Staplin et al. (1974) correlated TAI with coal rank. Waples (1980) correlated TAI with vitrinite reflectance and TTI (Time Temperature Index).

B. Results:

Lone Mountain Sections

Data:

Two samples, L. 600, and L. 714, were taken from the deep lagoonal dark thin to medium, nodular limestone units. The kerogen types and percentages of these two samples are, as follows: (1)-Amorphous-sapropel (Am) 57 % ; and (2)- Degraded herbaceous 43 %. Thermal alteration indices (TAI) of these samples are equal to 2.7 in Staplin's thermal alteration scale. Equivalent Ro % values of these TAI values were obtained from Geochem Laboratories, Inc.'s calibration chart and corresponding vitrinite reflectance values are Rm %= 0.93 which corresponds to High Volatile Bitumen (HVB) coal ranges and 10.5 in LOM scale (sea the standard scale of Ro %, TAI, LOM, and Coal rank in Fig. 15 in Chapter 3).

Paleotemperature estimation from the equation in the Barker and Pawlewicz (1985) is 145 °C, and paleotemperature estimation from the Fig.19 of Price (1983) is 178 °C.

Interpretation:

These two samples represent a deep lagoonal facies which formed behind oncoidal shoals and where moderately anaerobic environmental conditions prevailed. These samples are stratigraphically separated from each other about 115 feet and both indicate the same thermal maturity level. Organic matter types and their relative abundance are the same in these samples. Absence of slight differences in the maturation rank of these samples can probably be attributed to the same kerogen type or organic matter types as well as to the same burial history.

Martin Ridge Section

Data:

Two samples, M.80 and M.35B, were taken from the same stratigraphic section, but M.35B is situated 700 feet below M.80. Kerogen types and relative abundance of the kerogen types in these samples are, as follows: (1) in M.35B, Amorphous materials (Am) 67 %, and degraded-herbaceous materials (H) 33 % ; and in M.80, Am 57 % and degraded-herbaceous materials (H) 43 %. The TAI values of these samples L.35B and M.80 are equal to 2.5 and 2.6, respectively. These TAI values 2.5 and 2.6 correspond to Ro% values, in turn, 0.85 and 0.90 which are equivalent of HVB in coal range and 10.2 and 10.5 in the LOM scale. Estimated paleotemperature from these Ro% values are 165 °C for M.35B and 175 °C for M.80 by using Price's (1983) equation.

Interpretation:

Despite M.35B being situated about 700 feet below M.80, the measured TAI value of M.35B is about 0.1 (R_o%= 0.05) less than that of M.80. Variations in the maturation level of these samples are not related to kerogen types because these two have almost identical organic composition. M.35B was deposited behind the restricted shelf margin where anaerobic conditions exist; M.80, on the other hand, was deposited in the shoreward extension of the coastal lagoon where aeration of the sediment-water interface was considerably higher.

It is widely known fact that well-drained depositional environments allow more oxygen concentration in sediments, whereas environments with anaerobic conditions are known to produce hydrogen-rich organic matter. Hydrogen-rich kerogen types usually give a lower reflectance than those of oxygen-rich kerogen types (Newman

and Newman, 1982; Price, 1983; Price and Barker, 1985; Price at al., 1986; and Tissot et al., 1987),

Therefore, we can conclude that variation in maturity rank of these samples is an environmental phenomenon and directly related to the oxygen and hydrogen content of the same organic matter because these two have the same thermal and geodynamic history.

Whiterockian Canyon Section

Data:

Two samples, W.5A and W.26, were examined for thermal alteration indices (TAI), and their kerogen types and relative abundance are, as follows: (1) in W.5A, (Am) 33 %, (H) 55 %, and inertinite (I) 12 %; and (2) in W.26, (Am) 57 %, and (H*) 43%. TAI values of W.5A and W.26 are 2.5 and 2.8, corresponding to Ro % values of 0.7 and Ro= 0.85, respectively.

W.5A is a dark black anaerobic lime mudstone and W.26 represents relatively thicker storm layers in the open shelf.

Interpretation:

Thermal maturity level of the organic matter in these samples are chiefly controlled by oxidation level of depositional environment, or whether these environments were anaerobic or not. For instance, W.26 was collected from the moderately oxygenated, upper slope-storm deposits, whereas W.5A represents the dark black thin mudstone unit within the green-gray basinal shale.

June Canyon Section

Data:

In this section, also two samples, I.12 and I.29, were taken from the anaerobic hemipelagic rhythmic limestone interlayers, separated from one another by about 150 feet in vertical section.

Kerogen types and their relative abundance in these samples are, as follows: (1) I.12, consisting of Am 33 %, H 44 %, and inertinite (I) 23 % ; and (2) I.29, consisting of Am 11 %, H 55 %, I 23 % and W 11 %. TAI values for I.12 and I.29 are 2.8 and 2.7, respectively, and their equivalent Ro % are 0.95 and 0.93. For these Ro % values, the estimated temperatures from the equation of Price (1983) are 181 °C and 178 °C, respectively.

Interpretation:

Both samples represent the same reduced-environmental conditions. Differences in the reflectivity values of these two samples (about 0.02) are believed to be associated with shale content of these samples (Duba and Williams-Jones, 1983). The sample with lower shale content has relatively low reflectivity.

Mill Canyon Sequence

Data:

Two samples, Ml.25 and Ml.29, were taken from dark gray wackestone units which represent a well-circulated open shelf environment. Kerogen types and their relative visual abundance in these samples are, as follows: (1) Ml.25, consisting of relict

amorphous-sapropel (Am*) 45 %, degraded-herbaceous materials (H) 33 %, and (I) 22 %; (2) Ml.29, consisting of Am* 67 %, and (H) 33 %. TAI values of these samples Ml.25 and ML.29 are 2.8 and 2.5, respectively, in the Staplin scale, and equivalent R_o% values, in turn, are 0.85 and 0.95. These R_o% values are correlative to the HVB (high volatile bitumen) in coal rank and 10.2 LOM (level of organic metamorphism). Estimated-maximum temperatures from Ro% values of 0.85 and 0.95 are corresponding to 181 °C and 166 °C, respectively.

Interpretation:

In the Iks Canyon window, the Mill Canyon sequence occurs on the lower slice of the lower thrust plate of the Roberts Mountain thrusts of Antler orogeny, and Mill Canyon sequence is overlain by June Canyon sequence, upper thrust slice of the lower thrust plate. The reflectivity index of these samples are dependent on the content of clay and fine-grained detritus of related sedimentary units. The higher the shale content in limestone is, the higher the reflectance values will be.

Ro% values of Mill Canyon sequence is lower than those of the upper tectonic slice (June Canyon sequence) despite the occurrences on the lower tectono-stratigraphic unit. In addition to organic matter type and lithology type, relative abundance of organic matter may have a significant effect on maturity level.

Toiyabe Range

Data:

Three samples, R.1, T.5, and T.2, were examined for determining the levels of thermal alteration index (TAI) ranging from 3.5, through 3.8 and 4.2, respectively.

These TAI values are equal to Ro% values of 1.63, 2.0 and 2.5, respectively, according to Geochem Lab's calibration; however, in Waples's conversion (1980) Ro% values correspond to TAI values of 1.62, 2.5 and 4.0, respectively.

The R_o% values of T.5, T.2, and R.1 are correlative with LVB (low volatile bitumen), anthracite and semi-anthracite coal ranks and respectively 12, 13.5 and 16 LOM (level of organic metamorphism). Two samples, T.5 and T.2, are of extremely inertinite-rich origin from 50 to 57 %, Am* 28-38 % and herbaceous kerogen about 12-15 % in total kerogen content. R.1 consists of 40 % of Am* and H, and 20 % of inertinite.

Estimated-maximum temperatures from the equation of Price (1983) are indicated R_o % values of 251 °C, 271 °C and 307 °C.

Interpretation:

In the Toiyabe Peak, the Antelope Valley Limestone (AVL) shows slaty cleavage or axial-plane cleavage which indicates a high degree of thermal alteration probably at the metagenesis stage. T.2 characterizes the cleaved-shaley limestone intervals, whereas sample T.5 represents less shaley intervals which do not display slaty cleavage texture on a mesoscopic scale and appear as a very massive unit. In this section, considerably high thermal alteration is not due to lithologic type and nature of organic matter, but is most likely linked to increased lithostatic pressure during the Antler and Sonoma orogenies and their eastward-advancing clastic wedges.

Abundance of inertinites, especially in T.5 and T.2, may have been caused by oxidation of organic matter by expelled-basinal fluid (e.g., Oliver, 1986). Therefore, increased oxygen content within the same organic compound and releasing of H^{+1} ions at the great-burial depths, probably during thrusting, can account for the high reflectivity or maturation level of organic matter.

Keystone Canyon Section

Data:

Three samples, K.2, K.15, and K.30, were examined for thermal alteration study. The TAI values of these samples are 2.5, 3.1 and 2.2, respectively on Staplin's scale, and these TAI values are equivalent of Rm% values 0.6, 1.13 and 0.5, respectively. These mean vitrinite reflectance values correspond to HVB of coal ranks and 10.2, 11.2 and 8.5 of LOM.

Kerogen types and their relative visual abundance are, as given below: (1) in K.2, Am 18 %, H 37 %, W 18 %, and I 27 %; (2) in K.15, Am 20 %, H 40 %, and I 40 %; and (3) in K.30, Am 37%, and H 63 %.

The calculated-Tmax values from the Ro% are, respectively, 166 °C, 202 °C and 120 °C.

Interpretation:

Sample K.15 has the highest R_o% value, representing silty quartz-rich, parallel-laminated dolomite. The difference between the TAI values of samples K.2 and K.30 appears to be environmental: K.2 represents the oncoidal shoal (oxygen-rich depositional environment); and K.30 represents the moderately reducing back-shoal or inner shelf. Much greater reflectivity in K.15 probably resulted from additional oxygen contribution from the iron oxide-coated, fine-grained siliciclastic sediments which were transported from the nearshore depositional environment to the depositional site by storm-counter currents.

Comparison of the Measured TAI and Estimated-Thermal Alteration Levels from TTI and Th (max)

From the sixteen samples, the measured-TAI values and their equivalent Ro% values usually indicate much lower thermal alteration levels than the estimated-thermal alteration values for the AVL by Lopatin's method (see Table 5A). In order to estimate approximate true thermal alteration value, Time Temperature Indices (TTI) were calculated from the reconstructed-basinal subsidence curve which was constructed based on the present-day stratigraphic units of the Antelope Valley region and Eureka district (see Table 5B). The effects of the Sonoma orogeny and its clastic wedges have not been taken into considerations because there post-Permian units have been reported other than the Cretaceous Newark Canyon Formation.

In the east of Antelope Valley, Table Mountain, Devils Gate, Lone Mountain and Roberts Mountain, the calculated-TTI values from the reconstructed-subsidence curve (see Table 5B) are, as follows: At the end of the Permian time, estimated-approximate TTI value is 15715 and equivalent to Ro %= 3.64. At the end of the Antler orogeny (Roberts Mountain thrusting), TTI value is 847.39 and corresponding to Ro % = 1.9. At the end of Devonian, TTI value is 143.39 and corresponding to Ro %=1.26. On the other hand, measured-TAI values for the two samples are equivalent Ro %= 0.93. Equivalent Ro % from the measured-TAI values of four samples in this region are 0.85, 0.93, and 0.95.

Table 5A- TAI values of the AVL and their correlative Ro%, LOM, Coal Rank values and the estimated temperature range from TAI for each vertical section.

S.No:	TAI	R_o%	LOM	Coal Rank	Estimated Temp. °C I	II
L.600	2.7	0.93	10.5	HVB	145	178
L.714	2.7	0.93	10.5	HVB	145	178
M.35B	2.5	0.85	10.2	HVB	130	165
M.80	2.6	0.90	10.5	HVB	140	173
W.5A	2.3	0.70	9.2	HVB	108	130
W.26	2.8	0.95	10.2	HVB	130	166
I.12	2.8	0.95	10.6	HVB	147	181
I.29	2.7	0.93	10.5	HVB	145	178
Ml.25	2.8	0.95	10.2	HVB	147	181
Ml.29	2.5	0.85	10.2	HVB	130	166
T.2	4.2	2.30	16.0	Anth.	271	307
T.5	3.8	2.00	13.5	S.Anth.	242	278
R.1	3.5	1.63	12.0	LVB	218	251
K.2	2.5	0.80	10.2	HVB	130	166
K.15	3.1	1.13	11.2	HVB	88	120
K.30	2.2	0.60	8.5	HVB*	170	202

Temperatures under group I were estimated from Barker and Pawlevicz (1986).
Temperatures under group II were estimated from Price (1983).

It is clearly seen that difference between the measured-thermal alteration values and estimated TTI values by Lopatin's method (Waples,1980) are almost two- to three-fold during Permian time.

Table 5.B- Estimation of TTI values from Lopatin method (see Waples, 1980).

Temperature Intervals °C	r^n	Time (m.y)	TTI Intervals	TTI Total
20-30	2^{-8}	4	0.015	0.015
30-40	2^{-7}	2	0.015	0.030
40-50	2^{-6}	21+2	0.36	0.39
50-60	2^{-5}	4	0.12	0.51
60-70	2^{-4}	4	0.25	0.76
70-80	2^{-3}	3	0.37	1.13
80-90	2^{-2}	4	1.00	2.13
90-100	2^{-1}	3	0.66	2.79
100-110	$2^{0}= 1$	14	14	16.79
110-120	2^{1}	8	16	32.79
120-130	2^{+2}	9	36	68.79
130-140	2^{+3}	13	104	172.79
140-150	2^{+4}	12	192	1364.79
150-160	2^{+5}	11	352	714.79
160-170	2^{+6}	17	1024	1730.79
170-180	2^{+7}	3	384	2712.79
180-190	2^{+8}	4	1024	3156.79
190-200	2^{+9}	4	2048	5194.79
200-210	2^{+10}	4	4096	9290.79
210-220	2^{+11}	3	6144	15434
220-230	2^{+12}	3	12288	27712

Table 5 C- For the AVL, estimated thermal alteration or maturation level of organic matter during the following geologic time periods calculated by Lopatin method from burial history.

Geological Time Periods	Time Temp. Index (TTI) Values	Equivalent	
		TAI	R_o %
Ordovician	0.015 - 0.3	2.0	0.3
Silurian	0.3 - 2.79	2.25	0.4
Devonian	2.79 - 186.79	2.25 - 3.3	0.4 - 1.36
Mississippian	186.79 - 1754.79	3.3 - 3.8	1.36 - 2.30
Pennsylvanian	1754.79 - 27738.79	3.8 - 4.0	2.3 - 4.1

Even just after the Antler orogeny, estimated-TTI values are at least twice as much as the measured-TAI values even though a high-geothermal gradient has been used for TTI estimation. If we integrate the clastic wedge of the Sonoma orogeny to the reconstructed-subsidence curve, the TTI values of these samples will be at least three to four times greater than the measured-alteration values.

Comparison of measured-organic maturation levels with the maximum homogenization temperature from two-phase fluid inclusions also shows that measured TAI values are much lower than the maximum temperature based on T_h values (max. T_h= 260 °C to 270 °C at the east end of the Antelope valley and Lone Mountain region). Under the max. T_h temperature range organic matter is assumed to equilibrate and become more stabilized and more mature. The T_h max. and thermal alteration relation under increased-temperature conditions can be explained by the expression of Barker and Goldstein (1990). This expression is ln R_o% = 0.0088 x Th - 1.26. By using this expression for 260 °C, Equivalent R_o% should be 2.8, and for 270 °C, it to 3.05.

As indicated above, calculated-TTI values and their corresponding R_o% values are at least three times greater than the measured-TAI values and their correlative R_o%

values during the Antler orogeny at the end of Permian time. Therefore, one can suggest that any paleotemperature estimation solely from the 100 % exinitic kerogen type always provides a low-temperature range. For this reason, it is not advisable to use any of those formulae by Price (1983) and Barker and Pawlewicz (1986) for the kerogen Type I and Type II. Paleotemperature estimations from the equation of Price (1983) generally provides higher temperature range than Barker and Pawlewicz (1986).

Paleotemperature estimation directly from the measured-maturation rank even by Price's expression is significantly lower than those of TTI values derived from the subsidence curve of the AVL in the Antelope Valley and Lone Mountain regions. As a result, this study suggests that it is necessary to compare measured-organic maturation levels with T_h values of two-phase fluid inclusions and estimated-organic maturation levels as TTI values which usually provide comparable results.

C. Synthesis

It is clearly demonstrated that measured maturation levels of the exinite-dominated organic matter do not reflect the expected-thermal maturation level of organic matter which progressively and irreversibly increase with increasing depth of burial. As indicated previously, measured-organic thermal alteration levels are almost two to three times lower than those of expected-maturation levels.

Type I and Type II kerogens are predominantly H-rich and show a considerably lower reflectivity index compared to oxygen-rich vitrinitic kerogen or kerogen type III (Tissot et al., 1988; and Price and Barker, 1985). Presence of reasonable amount of alginate materials in the vitrinitic material was interpreted to significantly suppress the reflectance (Hutton et al. 1980; Hutton and Cook, 1980; Price, 1983; Price and Barker, 1985; Price et al., 1986; and Tissot et al., 1988). If sedimentary units consist of 100 % H-rich exinitic (alginate) material, their reflective index is probably three to five times lower than the same units consisting of 100 % oxygen-rich vitrinitic kerogen (Hotten

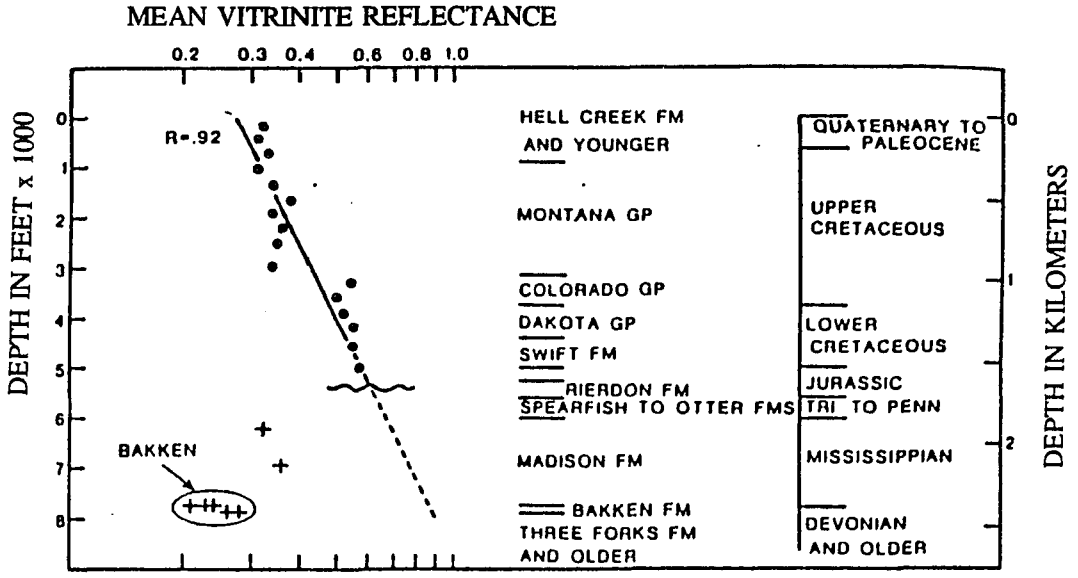


Figure 157- R_o versus depth relations of the samples from Well 6464 in Willistone Basin, Dunn County (Price et al., 1986).

et al., 1980, and Price and Barker, 1985). Our findings for the AVL are consistent with the suggestion of Price and Barker (1985) and support that two- to three-fold suppression of reflectivity is most likely to occur in the geological formation which predominantly contains kerogen type I.

On the other hand, differences in TAI values (from 0.02 to 0.70) at the indicated-type sections of this study are primarily related to oxygen level of depositional environment and lithology types.

In the Williston Basin, Thompson (1983) and Price and Barker (1985) showed that the vitrinite reflectance of the Mississippian Madison Group at the depth of 2.7 km decreases from Ro= 1.2 and 1.3 to Ro= 0.43 and 0.47 range in the Devonian Bakken Shale (Fig. 157). This suppression is chiefly controlled by changes from predominant vitrinitic kerogen to exinitic kerogen, and not to faults and major unconformities (see Dow, 1977). Similar phenomena were reported in Mississippi Salt Basin (Mississippi) and Los Angeles Basin (Price and Barker, 1985).

In order to estimate Ro% values for older and exinite-dominated lower Paleozoic units, Thompson (1983) extrapolated the linear reflectance (R_o%) plot (e.g Dow, 1977) from the Mississippian Madison Group through the Devonian Bakken Shale and further extended to the Ordovician Red River Formation (Fig.157).

This method is probably the best approximation method to determine true thermal-alteration level or reflectivity index for geologic formations chiefly composed of Type I, because high reflectivity or maturation level of organic matter will be encountered with increasing burial depths due to irreversible nature of organic metamorphism.

CHAPTER 17: OXYGEN-ISOTOPE GEOTHERMOMETRY

A. Introduction:

The $\delta^{18}O$ ($^{18}O/^{16}O$) values of carbonate cements have been widely used to determine the approximated-formation temperature of carbonates cements, particularly of calcite and dolomite (Prezbindowski, 1984; Woronick and Land, 1984; Moore, 1984; Urshel and Friedman, 1984; Gurney and Friedman 1987; Brockerhoff and Friedman, 1987a; Friedman, 1987b; Barker and Halley (1986).

Late-diagenetic burial carbonate cements (dolomite and calcite) directly precipitate from the diagenetically modified, isotopically enriched (with respect to heavy ^{18}O) hot-formation waters or basinal brines (Mattes and Mountjoy, 1980). Therefore, oxygen-isotope composition of deep-burial carbonate cements are generally depleted, whereas replaced precursor carbonates by deep-basinal solutions show a rather wide range oxygen isotope composition. As a result, oxygen isotope compositions of deep-burial carbonates occur in a very wide compositional range from +2 to -18 ‰ PDB. However, carbon isotope composition of this carbonate occur in comparatively narrow range from -2 to +4 ‰ PDB (e.g, Friedman and Sanders, 1967; Mattes and Mountjoy, 1980; Friedman, 1991; Mountjoy and Halim-Dihardja, 1991).

Application of $\delta^{18}O$ isotopes to determine the formation temperature of deep-burial carbonate cements requires that $\delta^{18}O$ values for cement and formation waters should be known.

Formation waters in sedimentary basins usually have two possible sources (1) diagenetically modified-meteoric water migrating downdip to the basin (like in the Illinois Basin); oxygen-isotope composition of this basinal water ranges from -8 to +4 ‰ SMOW (Clayton et al., 1966); (2) mixing meteoric and diagenetically modified sea water (Hitchon and Friedman, 1969; and Hanor, 1983). $\delta^{18}O_{water}$ values of formation water in the Alberta Basin, Canada, and Gulf of Mexico Coast range from -15 to +7

‰ SMOW and from + 0.5 to +15 ‰ SMOW and, respectively (Hitchon and Friedman, 1969; and Hanor, 1983).

The re-equilibration of carbonate sediments or a water of given composition reacting with carbonate and exchanging oxygen at the progressively deeper-burial diagenetic environments can produce a lighter oxygen isotopic composition for calcite and dolomite cements, and progressively higher salinity content in the isotopically heavy formation water as temperature increases due to progressive burial depth (Clayton et al., 1966; Dickson and Colleman, 1980; Hanor, 1987; Hitchon and Friedman, 1969; and Land and Prezbindowski, 1981). In a given sedimentary basin, maximum enrichment in $\delta^{18}O$ value of basinal fluid and maximum depletion in $\delta^{18}O$ values of calcites and dolomites are indicative of the highest salinity content and temperature at the greatest burial depth (Taylor, 1979).

Fracturing of lithologic units of sedimentary basins allows the hot-formation water to move upward very rapidly along fracture systems and prevent basinal solutions from re-equilibrating with oxygen-isotope composition and temperature of the ambient rock in these fractures. For this reason, late diagenetic, fracture-filling, isotopically depleted $\delta^{18}O$ values of blocky calcites and dolomites may indicate the formation temperatures of these cements.

On the other hand, excessively depleted $\delta^{18}O$ values in carbonate cements result from (1) progressive heating of formation water due to depth of burial, and (2) fresh water or meteoric water whose $\delta^{18}O$ values are significantly depleted. Consequently, the excessively depleted $\delta^{18}O$ values of carbonate cements should be treated with considerable care because such depleted-oxygen isotope compositions may have resulted from meteoric water. Thus, the cause of the extreme depletion of ^{18}O in carbonate cements can result from compositional variations of diagenetic solutions or burial temperatures of the related geologic formation. As a result, $\delta^{18}O$ values of carbonate cements should be compared with Th and salinity content of two-phase fluid inclusions from the same carbonate cement.

In this study, low-salinity content of two-phase fluid inclusions and excessively depleted $\delta^{18}O$ composition of fracture-filling calcite cement were used for indicating a

meteoric water origin of formation water. $\delta^{18}O_{water}$ values of +5 and +9 ‰ SMOW, which are believed to represent the oxygen-isotope composition of basinal brines, were used for estimating formation temperatures of carbonate cements. The paleotemperature calculations are chiefly based on the relationships between equilibrium fractionation of calcite or dolomite and the related formation water (Craig, 1965; Land, 1983; 1985; and for further details see methods in Chap. 3).

B. Results:

Lone Mountain Section

Data:

All the samples indicated on the Table 6 are representative of deep-burial diagenetic, fracture-filling calcite and dolomite cements of the Antelope Valley Limestone (AVL). L.250 A is fracture-filling sparry calcite replaced by white sparry dolomite (Dol. VII) occurring (L.250B*) in the same fracture system. L.150 probably represents the precursor calcite cements in the fractures replaced by pervasive mosaic dolomite (Dol. VII). These dolomite-filled fractures do not show cross-cutting relationships with the host dolomite. Thus these relations signify that the sparry dolomites in fractures may have been originally fracture-filling calcite cement in the precursor limestone. L.171 is fracture-filling, white dolomite (Dol. VIII) postdating the pervasively dolomitized host rock. $\delta^{18}O$ is considerably depleted in these dolomitic spars ranging from -10.37 to -13.5 ‰ relative to PDB (Table 6).

Host dolomite conversely has relatively heavier $\delta^{18}O$ and $\delta^{13}C$ values of, respectively, -3.4 ‰ (PDB) and of + 0.72 ‰ (PDB).

Land (1980) suggested that $\delta^{18}O$ values of late diagenetic dolomitizing fluids range from 0 to +10 ‰ SMOW, and Friedman (1986) and his colleagues chose +2 to +8 ‰

SMOW for $\delta^{18}O$ of Paleozoic rocks in New York State. In this study, +5 and +9 ‰ SMOW for $\delta^{18}O$ values of formation water are in the consistent range with other works.

Table 6- Estimated formation temperatures of the fracture-filling calcite and dolomite cements of the AVL by oxygen-isotope thermometry and comparison with T_h ranges in the Lone Mountain section.

Sam.No:	$\delta^{13}C_{cal\text{-}dol}$ ‰ PDB	$\delta^{18}O_{cal\text{-}dol}$ PDB ‰	SMOW ‰	TEMPERATURE	
				$\delta^{18}O_{water}$(SMOW) +5‰ °C	+9‰ °C	Hom. temp. (T_h) °C
L.250A	-1.25	-11.25	19.26	130	188	170 - 230
L.250B*	-0.90	-10.37	20.16	144	197	120 - 142
L.150*	-0.93	-5.25	25.14	94	138	
L.171A*	-0.16	-13.11	17.13	179	253	100 - 160
L.171	+0.72	-3.14				

* dolomite samples

The estimated formation temperatures for dolomite spar by $\delta^{18}O$ appear to be much higher than those of homogenization temperatures (T_h) of two-phase primary fluid inclusions which were measured from the same samples (Table 6).

By using measured $\delta^{18}O$ values and homogenization temperatures (T_h) in the equation of oxygen-isotope fractionation (see methods in Chap. 3), $^{18}O_{water}$ values of formation water can be calculated for the dolomite and calcite cements. The calculated-$\delta^{18}O$ values of formation water range from +2 to +7.2 ‰ (SMOW) for dolomite, and for calcite these values range from +6 to +11 ‰ (SMOW).

Generally T_h values of L.171 and L.250 B* are clustered between 120 and 140 °C and a few T_h readings are scattered at 160 °C. However, indicated T_h values are mostly lower than those of the estimated temperatures of dolomite from $\delta^{18}O$ values of

dolomite.

Table 7- Calculated-$\delta^{18}O$ values and salinity contents of the formation water of carbonate cements by using from T_h range in the isotopic fractionation equation as an equilibrium temperature.

Sam. No:	$\delta^{18}O_{cal\text{-}dol}$ ‰ PDB ‰ SMOW	Est. $\delta^{18}O_{water}$ ‰ SMOW	Salinity % From Tm	Homogen. Temp. (T_h) °C
L.250A	-11.25 19.26	+8 to +11		170 - 230
L.250B*	-10.37 20.16	+3 to +7.2	23-26	120 - 172
L.171A*	-13.31 17.33	0 to +2.5	24-28	120 - 160

* dolomite samples

For instance, estimated temperatures from $\delta_{18}O$ for dolomite range from 151 to 265 °C. Unlike estimated formation temperatures of dolomite by the oxygen isotope geothermometry, estimated temperatures of calcite from $\delta^{18}O$ appear to be consistent and are closer to the lower range of T_h values. Calculated $\delta^{18}O_{water}$ values of calcite cements are in the range of +6, and + 11 ‰ SMOW which are slightly higher than the approximated oxygen-isotope values (+5 to +9 ‰ SMOW) of formation water for carbonate cements by this study.

Interpretation:

These differences between the estimated temperatures and T_h primarily arise on the basis of choosing the higher isotope values for formation water than original isotopic composition of these solutions which were equilibrated with dolomite spars at formation temperatures. However, the opposite case is true for calcite: chosen $\delta^{18}O$ values of formation water +5 ‰ and +9 ‰ SMOW are much smaller than the calculated isotope values.

Oxygen isotope composition of the fluids and T_h values suggest that parent solutions of calcite cement are representative of more deeply buried environments than the environment where fracture-filling dolomite was precipitated. Therefore, dolomitization of the AVL indicates relatively late diagenetic periods during which basinal strata were uplifted to the extent where basinal brine and deep-meteoric water were mixed, or cooled adiabatically due to progressive pressure drop during updip flow of basinal solutions.

The $\delta^{13}C$ values of dolomite range from -0.93 to +0.72 ‰ PDB, indicating sea water compositions. Very slight depletion in $\delta^{13}C$ = -1.25 ‰ indicates that CO_2 presence in the dolomitizing and calcite-bearing solution was insignificant.

The Antelope Valley Region

Data:

M.32 is a late diagenetic oomoldic sparry calcite. Except A.19 from the Ninemile Canyon section, and the rest samples of calcite cements from the Martin Ridge section, all represent late diagenetic, fracture-filling calcite cement. An other two samples, M.28* and M.33* are dolomitized oncolitic interparticle cement (Dol. VII) and selectively dolomitized oomoldic cement (Dol. VI), respectively. Isotopic composition of these late diagenetic calcite cements, particularly $\delta^{18}O$ values range from -8.40 to -8.83 ‰ relative to PDB, and $\delta^{13}C$ values are in the range of -0.73 to -2.92 ‰ PDB. However, sample M.17 shows an exceptionally depleted oxygen isotope composition of $\delta^{18}O$ = -26.4 ‰ PDB and an enriched $\delta^{13}C$ value of +4 ‰ PDB. Isotopic composition of the dolomites: $\delta^{18}O$ ranging from -7.10 to -9.76 ‰ PDB and $\delta^{13}C$ ranging from -1.07 to +0.53 ‰ PDB.

Table 8- Estimated-formation temperatures of carbonate cements of the AVL by oxygen-isotope thermometry and comparison of these temperatures with T_h ranges of the same formation in the Antelope Valley region.

Sam. No:	$\delta^{13}C_{cal-dol.}$ ‰ PDB	$\delta^{18}O_{cal-dol.}$ PDB ‰	SMOW ‰	TEMPERATURE δ^{18}Owater (SMOW) +5 ‰ °C	+9 ‰ °C	Hom. Temp. (T_h) °C
A.19	-2.05	-8.83	21.75	103	149	190 - 270
M.75	-2.92	-8.71	21.87	102	148	130 - 190
M.33*	+0.53	-9.76	20.79	137	188	
M.32	-0.73	-8.40	22.50	97	140	97 - 179
M.28*	-1.07	-7.10	23.53	110	151	125 - 140
M.17	+4.00	-26.54	3.53	289	343	120 - 210

* Dolomite

The estimated formation temperatures of carbonate cements are in the following range for $\delta^{18}O_{water}$ values of +5 ‰ and +9 ‰ SMOW: (1) calcite, respectively, in the range of 98-109 °C and 147 and 185 °C, (2) dolomite respectively occurring in the range of 116 - 143 °C and 158-198 °C. Homogenization temperatures of calcite cements are higher than the estimated-temperature ranges for calcite. The calculated-$\delta^{18}O_{water}$ values for calcite occur in the range of +7 and +13 ‰ SMOW (Table 9). Unlike other calcites, T_h readings of M.17 ranging from 120 to 210 °C are much lower than those of the estimated-temperature range around 289-343 °C.

Table 9- Calculated-$\delta^{18}O$ values and salinity contents of the formation water of carbonate cements of the AVL by using from T_h range in the isotopic fractionation equation as an equilibrium temperature.

Sam. No:	$\delta^{18}O_{cal-dol.}$ ‰ PDB	‰ SMOW	Est. $\delta^{18}O_{water}$ ‰ SMOW	Salinity % From Tm	Homogen. Temp. (T_h) °C
A.19	-8.83	21.75	+10 to +14	19-25	190 - 270
M.75	-8.71	21.87	+8 to +12	8-19	130 - 230
M.32	-8.40	22.50			160 - 179
M.28*	-7.10	23.53	+7 to +8		125 - 140
M.17	-26.54	3.50	-12 to -6	3-8	120 - 210

*dolomite

Craig' expression (1966) is used for M.17 to calculate formation temperature of this calcite cement. The calculated $\delta 18O_{water}$ values of this sample range from -12 to -6 ‰ SMOW (Table 9). Salinity of M.17 is an average 3%, whereas other calcite cements have considerably heavy $\delta^{18}O$ values and high salinity contents ranging from 9 to 25 % (Table 9).

Interpretation:

The differences between the estimated temperatures and homogenization temperatures of calcite cements of the AVL (in the Antelope Valley region) are primarily due to the lower approximated $\delta^{18}O_{water}$ values of +5 and +9 ‰ SMOW. The estimated-dolomite temperatures of 116 and 158 °C are similar to those of T_h values of late diagenetic dolomite cements in the Loan Mountain section. In sample M.17, excessively depleted $\delta^{18}O$ values of calcite cements indicate that these calcites are not

associated with the high temperature because of their extremely depleted oxygen-isotope composition and less saline fluid composition determined from two-phase primary fluid inclusions. Low-salinity content about 3 %, low-T_h range, extremely depleted oxygen-isotope composition and calculated $\delta^{18}O$ value of formation water (-12 to -6 ‰ SMOW) suggest that $\delta^{18}O$ value of -26.54 ‰ PDB probably reflect a meteoric fresh-water in origin (cf., Aulstead et al., 1988). This extremely depleted, unusual oxygen-isotope composition of calcite cement is comparable with an oxygen-isotope composition ranging from -22 to -38 ‰ PDB of post-pervasive dolomitic, fracture-filling calcite cement of Manetoe Facies (diagenetic facies cross cutting Lower and Middle Devonian strata of the Elk Point Basin and Mackenzie shelf carbonates) in Alberta, Canada (Aulestead et al., 1988).

In sample M.17, the enriched $\delta^{13}C$ value of +4 ‰ probably resulted from dissolution of the host limestone by meteoric water and reprecipitation as a cement (Anderson and Arthur, 1983). In general, $\delta^{13}C$ composition ranging from -0.2 to -2.92 ‰ PDB is probably related to ^{12}C enrichment in pore waters or parent solution from CO_2 derived from oxidation of plant materials (Faure, 1977).

The Allochthonous Antelope Valley Limestone units in the Whiterock Canyon, June Canyon and Mill Canyon sections

Data:

Sample initials, W and Ml, are corresponding to the initials of type sections, such as W-Whiterock Canyon, Ml-Mill Canyon; however, (I) initial represents the June Canyon section. These three-type sections are representing the lower thrust plate of the Roberts Mountain thrusts. June Canyon section and Whiterock Canyon section are the part of the same tectonic stratigraphic unit as an upper thrust slice in the lower plate, whereas Mill Canyon occurs on the lower slice of the same thrust plate. All the

isotope values of $\delta^{18}O$ were derived from the fracture-filling, late diagenetic, deep-burial calcite cement, occurring in the two major ranges (Table 10): (1) first group, ranging from -8.12 to -13.2 ‰ PDB and being deep burial in origin; and (2) second group, ranging from -20.88 to -24.47 ‰ PDB representing surface and near-surface meteoric water origin.

Table 10- Estimated formation temperatures of carbonate cements of the AVL from the oxygen-isotope thermometry and their comparison with T_h ranges of the same formation in the allochthonous sections.

Sam. No:	$\delta^{13}C_{cal-dol.}$ ‰ PDB	$\delta^{18}O_{cal-dol.}$ PDB ‰	$\delta^{18}O_{cal-dol.}$ SMOW ‰	Estimated $\delta^{18}O_{wat.}$ ‰ SMOW	TEMPERATURE	
					δ^{18}Owater (SMOW) +5 ‰ °C	+9 ‰ °C	T_h °C
W.5A	-1.85	-13.20	17.25	+4 - +7	155	227	158-189
W.5b	-1.92	-20.88	9.33		219	267	
W.33	-2.84	-8.12	22.48	+1 - +9	97	140	134-172
I.10	-2.28	-24.47	9.91	-6, -1	262	314	120-186
I.23	-1.66	-9.31	21.26	+1 - +5	105	156	110-180
Ml.22	-1.48	-11.75	18.74		145	209	

Sparry calcites with a light red staining from potassium ferricyanide has $\delta^{18}O$ value of -20.88 ‰ PDB, and this fracture cross-cuts the other calcite-filled fractures whose calcite cements are stained with slightly bluish to purple and have $\delta^{18}O$ values range from -8.12 to -13.12 ‰ PDB.

Interpretation:

The estimated-formation temperatures of the first group calcite cements are in good agreement with T_h values of the same calcite cements. The estimated-temperatures of second group calcite cements, however, do not have a good correspondence with (T_h) of the same calcites. The estimated temperatures of the first group Fe^{+2}-rich deep-burial calcite cement which is inferred from red-purple staining, for $\delta^{18}O_{water}$ for +5 and +9 ‰ SMOW correspond to 105-155 °C and 156-227 °C, respectively. T_h range measured from the same samples occur in the range of 110-191 °C. The estimated temperatures for the excessively depleted $\delta^{18}O$ values of calcite cement occur in the range of 219-314 °C, whereas their homogenization temperatures of 120 to 186 °C are significantly lower than those of estimated temperatures by oxygen-isotope thermometry. Fracture-filling cements with the second group oxygen-isotope composition ranging from -20.88 to -24.47 ‰ PDB and Fe^{+2}-poor composition inferred from the light red staining by potassium ferricyanide characterize the meteoric water origin. These exceedingly depleted oxygen isotope compositions of the second group fracture-filling calcite cements can not be related to methane generated-calcite because its $\delta^{13}C$ values occur a very narrow range from -1.92 to -2.23 ‰ PDB (cf., Friedman, 1991). Therefore, the estimated temperature ranges from the second group, fracture-filling calcite by oxygen-isotopes thermometry are not reliable because these cements are believed to have originated from isotopically very depleted-meteoric waters with respect to $\delta^{18}O$ but not from hot basinal solutions.

The Toiyabe Peak Region

Data:

T.10 represents the recrystallized-calcite cement in the folded (similar to ptygmatic folding) and recrystallized intervals which are parallel to the axial plane cleavages of slate. On the other hand, T.3 characterizes the fracture-filling calcite cements which offset the slaty texture of this rock unit. D.7 A and D.7B represent the different fractures and are healed by very coarse sparry calcites. The former cross cuts the latter (D.7B). Sample D.13 also represents the fracture-filling sparry calcite cement. Large fractures in these sections, Dry Creek and Toiyabe Peak, are folded and axis of the small folds developed during the dynamic metamorphism resulted from the similar stress

Table 11- Estimated formation temperatures of carbonate cements of the AVL from the oxygen-isotope thermometry and their comparison with T_h ranges of the same formation in Toiyabe Peak region.

Sam. No:	$\delta^{13}C_{cal\text{-}dol.}$ ‰ PDB	$\delta^{18}O_{cal\text{-}dol.}$ PDB ‰	SMOW ‰	TEMPERATURE		
				δ^{18}Owater (SMOW) +5 ‰ °C	+9 ‰ °C	Th °C
T.10	-1.62	-11.60	18.90	135	194	210 - 290
T.3	-1.66	-28.30	1.69	312	368	210 - 240
D.7A	-0.05	-25.43	4.65	274	328	150 - 230
D.7B	-4.39	-26.40	3.65	287	341	
D.13	-4.39	-18.84	11.24	197	242	170 - 250
R.3	-0.17	-10.74	19.78	130	188	180 - 290

system which was responsible for the slaty cleavage (Fig. 158). Estimated temperatures from the extremely depleted $\delta^{18}O$ value of T.3 occur in the range of 312 to 413 °C. Similarly for the same $\delta^{18}O_w$ values, D.17A, D.17B and D.3 samples have an estimated temperature ranging between 197 and 341 °C. Homogenization temperatures for the each of these samples occur in a considerably lower range than those of estimated temperature ranges from $\delta^{18}O$ values for the same samples (see table 11). Three samples are significantly depleted ($\delta^{18}O$ ranging from -18.84 to 26.40 ‰ PDB) in the fracture-filling calcite cement. The cross-cutting fracture has more heavy oxygen depletion than that of fracture being cross cut. Sample R.3, from the Reeds Canyon section, has a $\delta^{18}O_c$ value of -10.74 ‰ PDB, and its estimated temperatures occur in the range of 118 to 185 °C. In this sample, T_h (homogenization temperatures) values measured from the two-phase fluid inclusions are greater than those of the estimated temperatures from $\delta^{18}O$ for R.3. The calculated $\delta^{18}O_w$ values for the three Dry Creek Canyon samples range from -9 to +4 ‰ SMOW, whereas for R.3, isotope value of formation water occur in the range of +9 and +13 ‰ SMOW. Carbon isotope composition of the samples are enriched in heavier 13C and ranging from -0.17 to -1.66 except for D.13 has $\delta^{13}C$ value of -4.39 (PDB).

Table 12- Calculated-$\delta^{18}O$ values and salinity contents of the formation water of carbonate cements of the AVL by using from T_h range in the isotopic fractionation equation as an equilibrium temperature.

Sam. No:	$\delta^{18}O_{cal\text{-}dol.}$ ‰ PDB	‰ SMOW	Est. $\delta^{18}O_{water}$ ‰ SMOW	Salinity % From Tm	Homogen.Temp. (T_h) °C
D.7A	-25.43	4.63	-8 to -3	6-25	150 - 230
D.13	-18.84	11.24	-0.2 to +4	4-25	170 - 250
R.3	-10.74	19.78	+9 to +12	19-24	180 - 290

Interpretation:

T.10 characterizes the metamorphic texture, thus it indicates that oxygen-isotope composition of calcite cements were equilibrated under the influence of very low-metamorphic physico-chemical conditions rather than a magmatic intrusion. The elevated temperatures and directed pressures which probably produced the very low-grade metamorphism were primarily controlled by tectonic heating of thrust plates during the Sonoma orogeny at end of Permian and beginning of Triassic.

The estimated temperatures of R.3 (deep burial in origin) occur in the lowest temperature of T_h range by using the approximated-, oxygen-isotope composition of formation water as indicated in the methods section. As suggested before, excessively depleted-oxygen isotope compositions of calcite may have not resulted from the higher temperature heating. However, T_h values and low-salinity contents of the solutions eliminates the possibility for this calcites being originated from a hot-basinal brine. Inclusions with a low T_h usually have the low-salinity contents than the inclusions with higher T_h values. $\delta^{13}C$ values usually occur in the range of -0.17 and-1.66 which is very closer to isotopic composition of marine carbonates ranging +0.56,- or +1.55 ‰ (Keith and Weber, 1964). But calcite cement of D.13 has a significantly depleted $\delta^{13}C$ value of -4 ‰ PDB; it may indicate a meteoric-water origin which was caused by presence of higher CO_2 probably derived from the oxidation of organic matters. Inclusions with high salinity contents and high T_h values in the same calcite cements indicate that possible re-equilibration probably took place under the high-temperature conditions during the thrusting events of the Sonoma orogeny. Therefore, isotope compositions of D.7A, D.7B and D.13 indicate that meteoric solutions filled the indicated fractures long before the Sonoma orogeny, probably during the Pennsylvanian uplifting. Isotope value of this solutions was estimated to range from -9 to -0.4 ‰ SMOW (Table 12).

Folding of the fracture system (Fig. 158) especially in this region suggests that fracture-filling calcite cements were probably recrystallized and re-equilibrated during

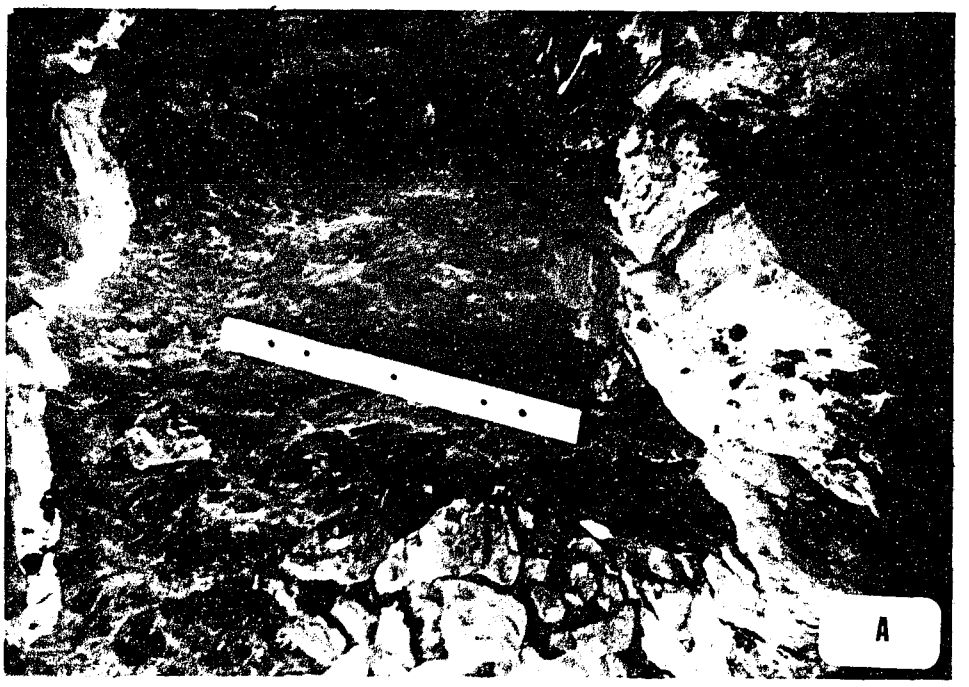


Figure 158- Intensely folded, calcite-filled large fractures within the slaty units of the Antelope Valley Limestone, which originally was a basinal shaley limestone lithofacies. These fracture-filling calcite cements are exceedingly depleted with respect to oxygen-isotopic composition ranging from -19 to -29 %. (PDB). A 30-cm long ruler for scale.

the Sonoma orogeny. Therefore, some inclusions were probably stretched and re-equilibrated under influences of elevated temperatures and pressures; as a result, these inclusions gained high T_h and salinity. T.3 , however, post dates slatey texture and significantly depleted in $\delta^{18}O$ also reflect the post-Sonoma orogenic uplifting, probably formed from the meteoric water- dominated diagenetic environment by the suggested-mixing process.

However, R.3 and T.10 have isotope values which are consistent with deeply buried calcite cements' isotopic composition. These fractures probably formed and healed before or during the Sonoma orogeny, but there are not any evidence to support accurate diagenetic sequential order for the formation of these deep-burial, fracture-filling cements relative to extremely depleted fracture-filling calcite cements.

Southern Localities (Keystone Canyon and Clear Creek Canyon)

Data:

In the Clear Creek Canyon section, isotope analysis were carried out on the saddle and host dolomites. Especially two samples, C.7A and C.8 A, were taken from the fracture-filling saddle dolomites which are post-dating the pervasively dolomitized host rock. On the other hand, C.7B and C.8B represent the host-dolomitic rocks having direct contacts with saddle dolomites, and they have more depleted-oxygen isotope composition than those of the adjacent saddle dolomites (Table 13). The estimated temperature of the saddle-dolomite range from 129 to 205 °C, and from 157 to 221 °C is estimated temperature range for host mosaic dolomite.

In the Keystone Canyon section, fracture-filling calcite cements of K.5, K.6, K.13 A, K.14, and K.18 show excessively depleted $\delta^{18}O$ values ranging from -27.12 to -30.72 ‰ PDB (Table 13A). These fractures postdate the pervasively dolomitized-host rocks, and their calcite cements have the oxygen-isotope composition ranging from

-2.83 to -3.42 ‰ relative to PDB and carbon composition ranging from -1.07 to -1.12 ‰ PDB.

Table 13- Estimated formation temperatures of carbonate cements of the AVL from the oxygen-isotope thermometry and their comparison with T_h ranges of the same formation in the Clear Creek Canyon and Keystone Canyon sections.

Sample No:	$\delta^{13}C_{cal\text{-}dol.}$ ‰ PDB	$\delta^{18}O_{cal\text{-}dol.}$ PDB ‰	SMOW ‰	TEMPERATURE δ^{18}Owater(SMOW) +5 ‰ °C	+9 ‰ °C	T_h °C
C.7A*	-1.28	-10.23	20.31	147	203	
C.7B*	-1.61	-10.84	20.31	154	213	
C.8A*	-2.33	-8.44	22.15	157	174	
C.8B*	-1.46	-11.05	19.04			
K.5	-2.70	-27.75	2.26			
K.6A	-1.88	-30.17	-1.98	345	404	150 - 210
K.13A	-0.83	-27.38	2.64	309	355	180 - 240
K.13*	-1.12	-8.10	22.50	124	170	
K.14	-0.27	-27.12	2.90	306	359	
K.18	-2.70	-27.69	2.30	312	359	
K.17	-1.07	-3.42	28.32	Host dolomite		
K.6B	-1.12	-2.83	27.93	" " "		

In addition, K.13 is represented by white, sparry dolomites filling the late fractures which also postdates the host dolomite, and it has oxygen isotopic composition value of -8.10 ‰ PDB, occurring in the same isotope compositional range with other white sparry fracture-filling dolomites. Estimated temperatures from the excessively depleted-$\delta^{18}O$ values of calcite (-27.1 to 30.72 %. PDB) range from 300 to 404 °C which is considerably higher than those of T_h values of 150-240 °C measured from the

two-phase fluid inclusions from the same samples.

Table 13A- Calculated-$\delta^{18}O$ values and salinity contents of the formation water of carbonate cements of the AVL by using from T_h range in the isotopic fractionation equation as an equilibrium temperature.

Sample No:	$\delta^{18}O_{cal\text{-}dol.}$ ‰ PDB ‰ SMOW	Est. $\delta^{18}O_{water}$ ‰ SMOW	Salinity % From Tm	Homogen. Temp. (T_h) °C
K.6A	-30.71 -1.98	-13 to -10	4-13	150 - 210
K.13A	-27.38 2.64	- 8 to - 5	3-15	180 - 240

Salinity content of these fluid inclusions occurs in the range of 3-15 ‰ equivalent of NaCl. For the calcite cements with the exceedingly depleted oxygen isotope composition, the calculated $\delta^{18}O$ values of formation water range from -5.5 to -13 ‰ SMOW (Table 13A).

Interpretation:

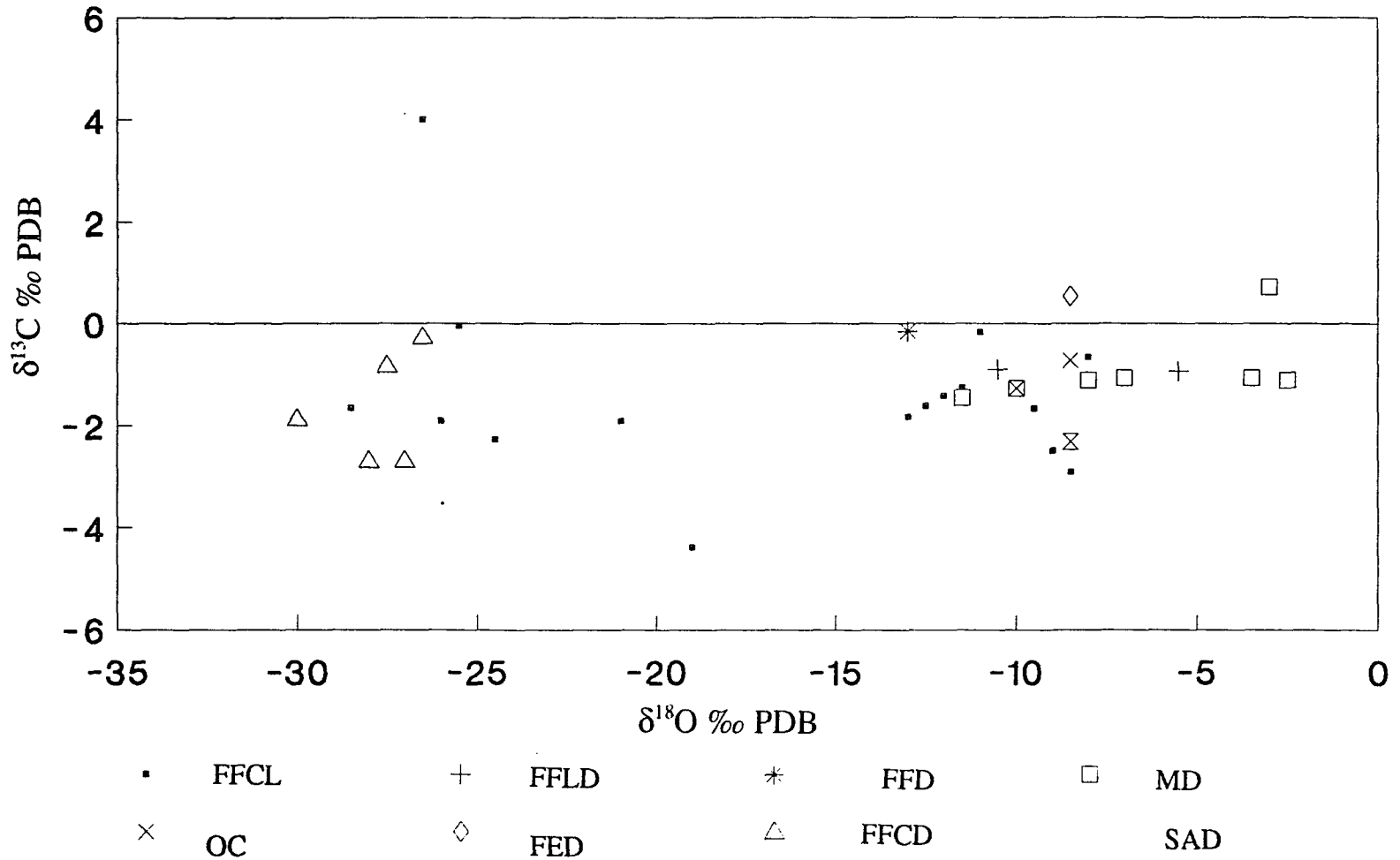
The estimated temperatures of the saddle dolomites from $\delta^{18}O$ values are higher than those of T_h ranges measured from the two-phase fluid inclusions of the same sample because the approximated-$\delta^{18}O_w$ values (+5 and +9 ‰ are higher than those of the calculated values. Considerably, lighter $\delta^{18}O$ values of calcite in the range of -27.12 to -30.72 ‰ PDB and low-salinity contents are likely to have originated from the meteoric water invasion of the pervasively dolomitized host rock in the subsurface environment.

C. Synthesis

Calcite cements in the late-diagenetic fracture systems of limestones and dolostones demonstrate two significantly different trends (Figs.159, 160) of $\delta^{18}O$ values ranging from: (1) -7 to -13 ‰ PDB; and (2) -18 to -30.72 ‰ PDB. The first isotopic compositional range in calcite cement with high salinity (11 to 25 %) and high-T_h values suggest that these fracture-filling calcite cements are deep burial in origin and predate dolomitization (Fig. 160). The second oxygen-isotope range of fracture-filling calcite cements, with a significantly light oxygen-isotope composition and with low-salinity content (3 to 11 %) is most likely to indicate a meteoric diagenetic origin of the parent solutions of these cements (Fig. 160). Estimated-oxygen isotope composition of the fluids from T_h values ranging from -5 to -13 ‰ SMOW were most likely to be responsible for the extremely depleted unusual oxygen-isotope composition of fracture-filling calcite cements. The approximated-oxygen isotope composition (+ 5 and + 9 ‰ SMOW) of parent fluid represents relatively more enriched in $\delta^{18}O$ composition of basinal brines than original isotope composition of meteoric waters. Therefore, the estimated oxygen-isotope values of these fluids represent rather equilibrated-oxygen isotope values of the meteoric fluids.

Hitchon and Krouse (1972) have shown that water samples from the Mackenzie River's drainage basin, particularly water samples of M-33 and M-37 have the isotopic values of -22 %. and -17 %. (SMOW). Surface waters of North and South Saskatchewan River drainage basin have isotopic composition ranging from -14.6 to -19.9 ‰ SMOW (Hitchon and Friedman, 1969). On the basis of two examples, it can be suggest that similar types of depleted meteoric water with respect to $\delta^{18}O$ may have been responsible formation of the indicated fracture-filling calcites with extremely depleted oxygen-isotope composition. Aulstead et al. (1988) also noted similar oxygen-isotope compositions in the post-dolomitic, fracture-filling calcite cements of the Manetoe Facies of Devonian in Alberta, Canada. Therefore, the isotopically extremely depleted (in $\delta^{18}O$) calcite cements of the AVL are consistent with Aulstead et al.

Figure 159- Oxygen-isotope compositions of fracture- and void-filling carbonate cements which have been used for oxygen-isotope thermometry to estimate the paleo-burial temperature range for the Antelope Valley Limestone. FFCL= Fracture-filling calcite cement in limestone, FFD=Fracture-filling dolomite, FFLD= Dolomite replaced fracture-filling calcite, MD= Mosaic dolomite, IOC= Ooid mold-filling calcite, FED= Ferroan dolomite, FFCD= Fracture-filing calcite in dolostones, and SAD= Saddle dolomite.



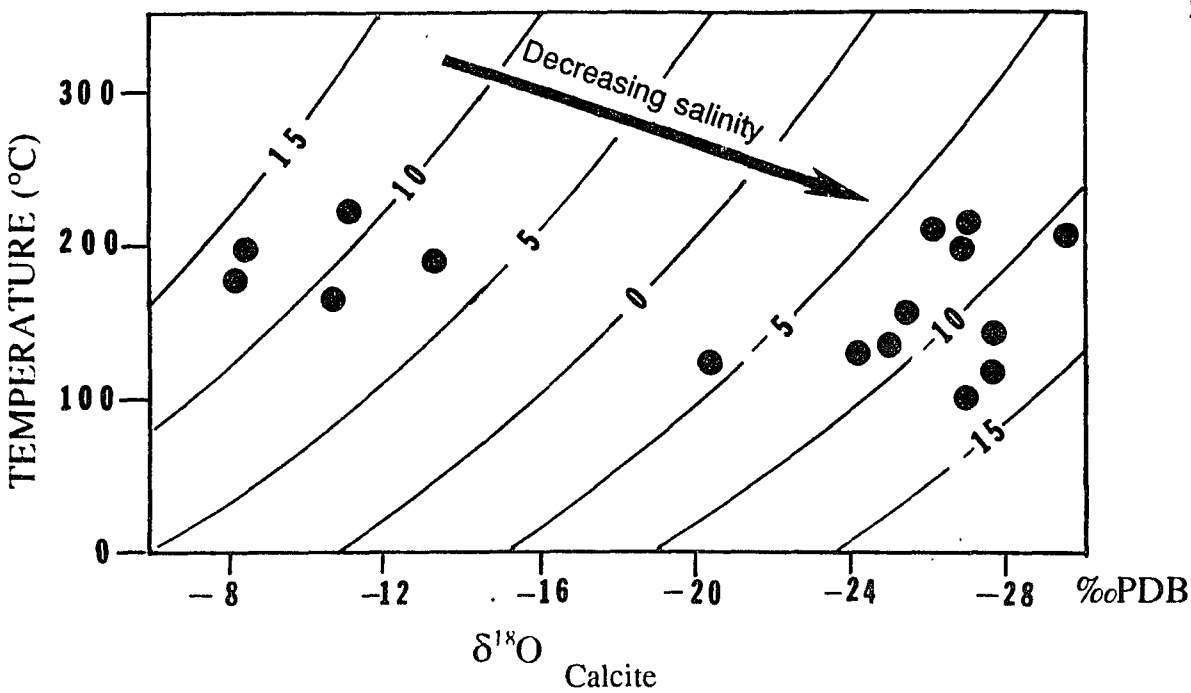


Figure 160- Plot of oxygen-isotope composition range of parent fluids of the fracture-filling calcite cements and their salinity content: oxygen-isotope composition of parent fluids estimated from the homogenization temperatures, and oxygen-isotope compositions of host calcite cements. Counter lines are in ‰ SMOW.

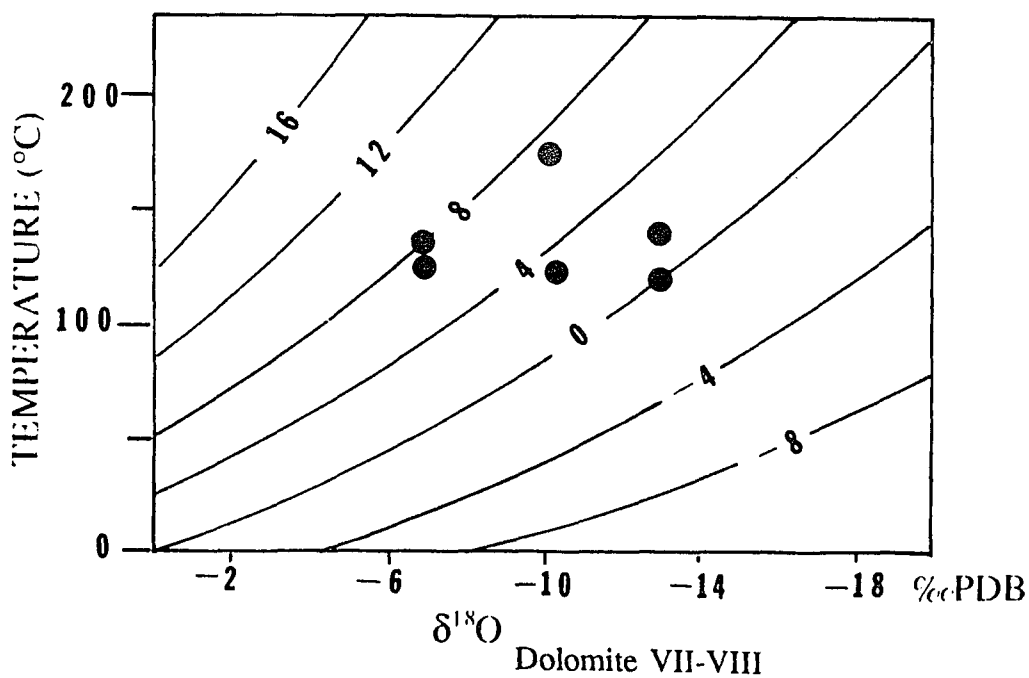


Figure 161- Plot of oxygen-isotope composition range of the dolomitizing fluids. Counter lines are in ‰ SMOW.

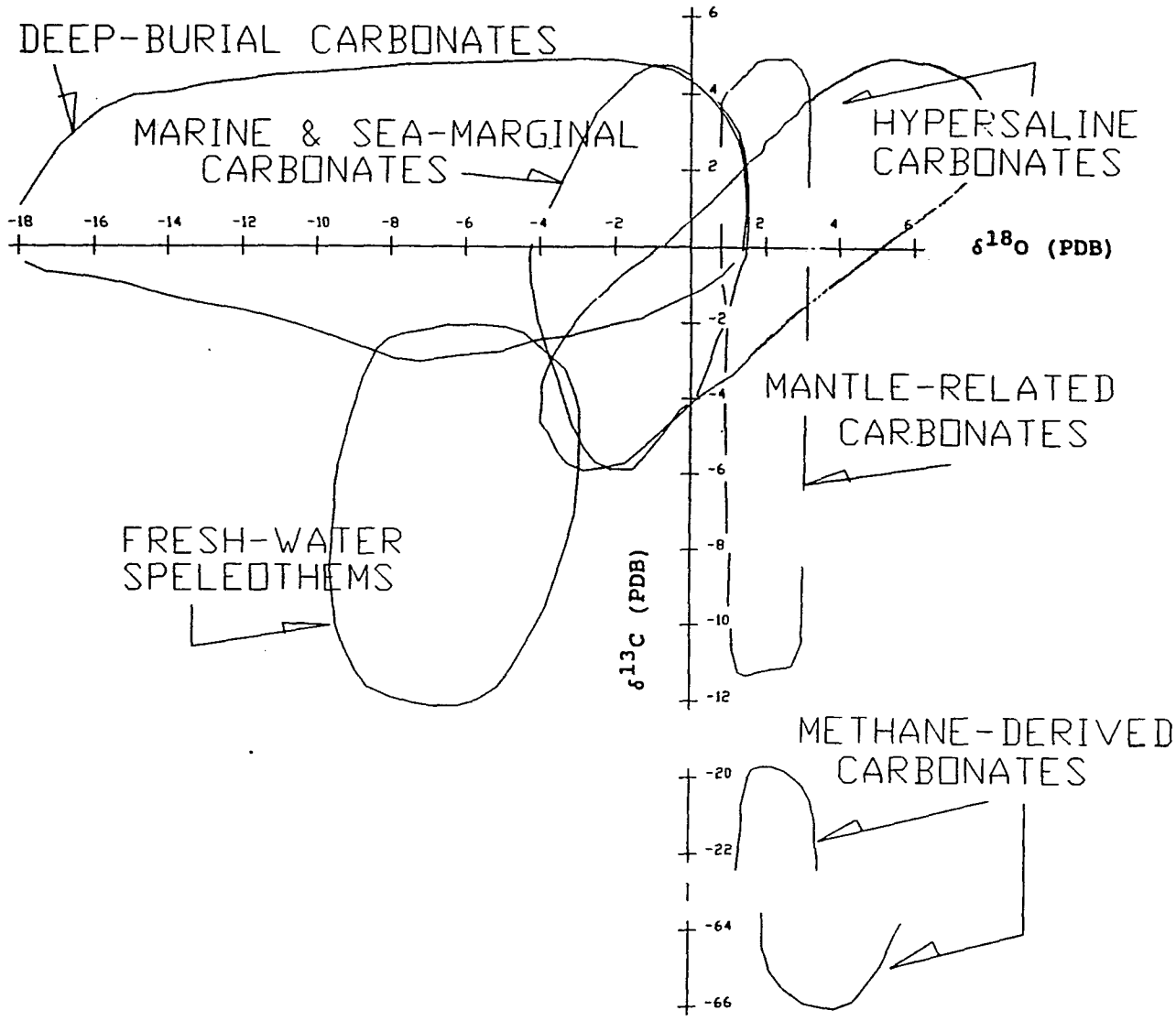


Figure 161 B- Oxygen and carbon-isotope composition range of carbonate rocks (Friedman, 1992).

(1988, Hitchon and Friedman (1969), and Hitchon and Krouse (1972). In a major fault zone, Fyfe et al. (1987) also reported extremely depleted oxygen-isotope compositions of three fracture-filling calcite cements ranging from +4 to +8 ‰ SMOW (or from -26.0 to -22.2 ‰ PDB). The same fracture-filling calcite cements have depleted-$\delta^{13}C$ values of -6 and -10 ‰ PDB. Fyfe et al. (1987) relate this isotopic compositional range to the mixing of deep-seated hydrothermal fluid and isotopically very negative fluids of meteoric origin.

Methane-induced cementation (e.g., Friedman, 1991) and deep-burial origin for such calcite cements indicated above can be eliminated (see Figure 161 B) with respect to their very wide oxygen-isotopic compositional ranges and very narrow carbon isotope ranges.

Deep-burial, late-diagenetic fracture-filling white sparry dolomite (Dol. VIII) and saddle dolomite (Dol. IX) have considerably depleted $\delta^{18}1O$ values of -8 to -13 ‰ PDB. Calculated- oxygen isotope values of the formation waters of dolomite cements from the T_h range from 0 to +8 ‰ SMOW (Fig. 161). These isotope values are much lower than the approximated-$\delta^{18}Ow$ values (+5, +9 ‰ SMOW); therefore, estimated temperatures of formation waters during precipitation of fracture-filling dolomites is much higher than those of T_h values measured from the same dolospars. Therefore, these fracture systems may have formed or experienced greater burial depths than those of fracture-filling dolomites and saddle dolomites.

The estimated temperatures are usually lower than those of T_h measured from the two-phase fluid inclusions of the same calcite cement because approximated $\delta^{18}O_w$ values are smaller than those of calculated-$\delta^{18}O_w$ values ranging from +6 to +13 ‰ SMOW (Fig. 160).

CHAPTER 18: FLUID INCLUSION MICROTHERMOMETRY

A. Introduction:

Two-phase fluid inclusions have been extensively used in the Mississippi Valley-type ore-bearing carbonate rocks for estimating the formation temperatures and compositions of parent fluids from which ore minerals, such as lead, zinc, barite, as well as host dolomites precipitated (Roedder, 1967, 1971; Leach et al., 1975; Roedder, 1976; 1979b; Zimmermann and Kesler, 1981; Taylor et al., 1983; McNaughton and Smith, 1986; Gratz and Misra, 1986; and Roedder and Howard, 1988). However, the methodology of fluid-inclusion microthermometry in carbonates is poorly investigated compared to quartz, sphalerite, fluorite, and halite (see review in Roedder, 1984). It is commonly believed that phase changes at high-temperature, particularly homogenization of liquid and vapor phases into a liquid phase represents the minimum-entrapment temperature (T_h) of fluids (see Appendix III-C1).

Experimental data suggest that T_h does not always represent the minimum-entrapment temperature of fluid inclusions from the original parent solution because these fluid inclusions may have been stretched or decrepitated in nature (Larson et al., 1973; Bodnar and Bethke 1984; Goldstein, 1986, 1987, 1988; Prezbindowski and Larse, 1987; Wilkins, 1986; and Meuiner, 1989). Bodnar and Bethke (1984), and Prezbindowski and Larse (1987) experimentally demonstrated that fluid inclusions entrapped in calcite cements might re-equilibrate by stretching during overheating beyond the certain limit of homogenization temperatures. The re-equilibration of fluid inclusion by stretching results in volume increase and in higher T_h which is no longer representative of the minimum-entrapment temperatures

of the host crystals. Fluid inclusions may re-equilibrate under higher temperature and pressure conditions than the formation temperature of these inclusions; therefore, T_h values of re-equilibrated inclusions correspond to re-equilibration temperatures rather than the formation temperatures of crystals or minimum-entrapment temperatures of fluid inclusions (Larson et al., 1973; Bodnar and Bethke, 1984; Roedder, 1984; and Shepherd,et al, 1985). For these reasons, T_h values of these inclusions do not provide essential information for diagenetic studies; however, they are more practical for studying maximum burial depths of the sedimentary basins.

Goldstein (1986) has shown that re-equilibration of T_h may also occur in calcite cements by hydrofracturing (i.e. leaking in and out or exchange of diagenetic fluids followed by rehealing). More recently, Barker and Halley (1989) have demonstrated that T_h measurements from the vadose cement of the Miami Limestone provide high-homogenization temperature ranges. Therefore, homogenization temperatures should be used carefully for diagenetic interpretations.

Homogenization temperatures (T_h's) of two-phase fluid inclusions trapped from a single homogeneous parent fluid are essential to establish a geothermometry as well as a geobarometry (Roedder and Bodnar, 1980; Roedder, 1984; and Shepherd,et al, 1985). In addition, low-temperature phase changes of two-phase fluid inclusions, such as eutectic temperature (Te) and melting temperature (Tm), provide information on both the formation temperature of cement and salinity and composition of the parent fluids (Aulstead and Spencer, 1985; Hazeldine et al., 1984; Aulstead et al., 1988; and Cercone and Lohmann, 1987). Moreover, in sedimentary basins, hydrocarbon-fluid inclusions have been commonly used to determine the temperature of oil migration (Burruss, 1981; Burruss et al., 1985).

Homogenization temperatures of two-phase fluid inclusions need to be interpreted with considerable care and caution because re-equilibration of these inclusions is possible by over heating in the lab, and nature due to increased burial depth. Fluid-inclusion microthermometry along with oxygen-isotope thermometry, organic maturation level and clay thermometry have commonly been used to determine the maximum burial temperature of geologic formations, sedimentary basins as well as

their burial history (Frey et al., 1980; Duba and Williams-Joans, 1983; Urschel and Friedman, 1984; Barker and Halley, 1986; Pollastro and Barker, 1986; Brockheroff and Friedman, 1987; Gurney and Friedman, 1987; and Friedman, 1987 a,b). In addition, Barker and Goldstein (1990) attempted to develop a calibration chart and diagram for T_h maximum and R_o%, and they were able to show a comparable results and correlations for organic maturation levels (vitrinite reflectance) and fluid-inclusion microthermometry. Lehermann (1990) compared the conodont-color alteration indices (CAI) with T_h range, and found them in a good correlation. The relationships between the depth and T_h range have not been sufficiently investigated, but still several studies worth mentioning are those of Narr and Currie (1982), Tillman and Barnes (1983), and Aulstead and Spencer (1985). These relationships can provide significant data that can help to unravel the burial and uplifting histories of sedimentary basins in sequential order.

The fluid-inclusion thermometry on calcite, dolomite and quartz in the AVL was used to determine:

1) T_h and Tm values of primary and pseudosecondary, two-phase fluid inclusions;

2) Possible re-equilibration either by stretching (only volume change) or by hydrothermal fracturing (decrepitation) as volume and compositional change on the T_h versus salinity figures;

3) Maximum-burial depths of the AVL from the maximum-T_h value, in central Nevada.

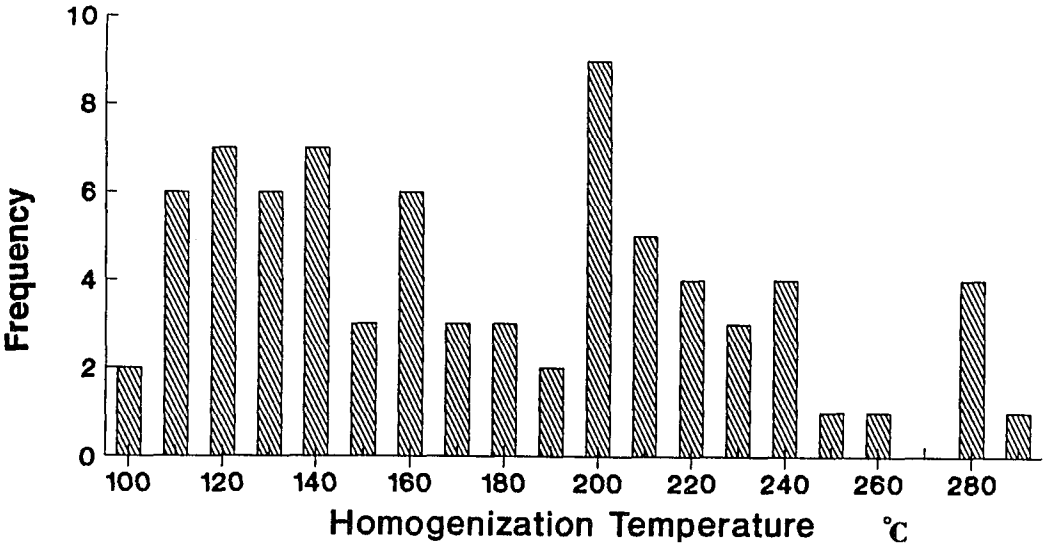
B. Results:

Lone Mountain

Homogenization (T_h) Data:

A total of 83 pressure-uncorrected homogenization temperatures (Fig. 162) were measured from five samples (L.250, L.150, L.171, L.570, and L.643). Samples, L.151 and L.171, are a fracture-filling, white-sparry dolomite which postdates the host dolostones. T_h values of these two samples generally range from 100 °C to 148 °C, and three additional T_h readings occur in the range of 218 to 254 °C (see Appendix III-C2). In L.250, the fracture-filling, late calcite cements are replaced by white sparry dolomite. In this sample, two-phase fluid inclusions of replacive dolomite (Dol. VII) have T_h values ranging from 125 to 140 °C (see Appendix III-C2) which is similar to the homogenization-temperature range of L.171. However, T_h values of a few two-phase fluid inclusions in the fracture-filling calcite cements of L.250 range from 160 to 228 °C (see Appendix III-C2), considerably greater range compared to replacive dolomite in the same fracture system.

T_h values of two other fracture-filling calcite samples are, as follow: (1) L.643, T_h values range from 170 to 242 °C; and (2) L.570, T_h values ranging from 88 to 289 °C (see Appendix III-C2). Particularly, in L.571, three-major subgroups of T_h range have been identified: (1) from 100 to 154 °C; (2) from 178 to 228 °C, and (3) from 260 to 289 °C for only a total of five readings (Fig. 162). Average T_h temperature of these samples is about 194 °C (from 100 to 289 °C); however, there are four-major subgroups that are considered to be important for the burial history of this formation (Fig. 162): (1) from 100 to 140 °C; (2) from 150 to 180 °C or 190 °C; (3) from 200 to 240 °C; and (4) 260-290 °C.



A total of 63 readings

Figure 162- Histogram of homogenization temperatures (T_h) of two-phase fluid inclusions from calcite and dolomite cements in the Lone Mountain section.

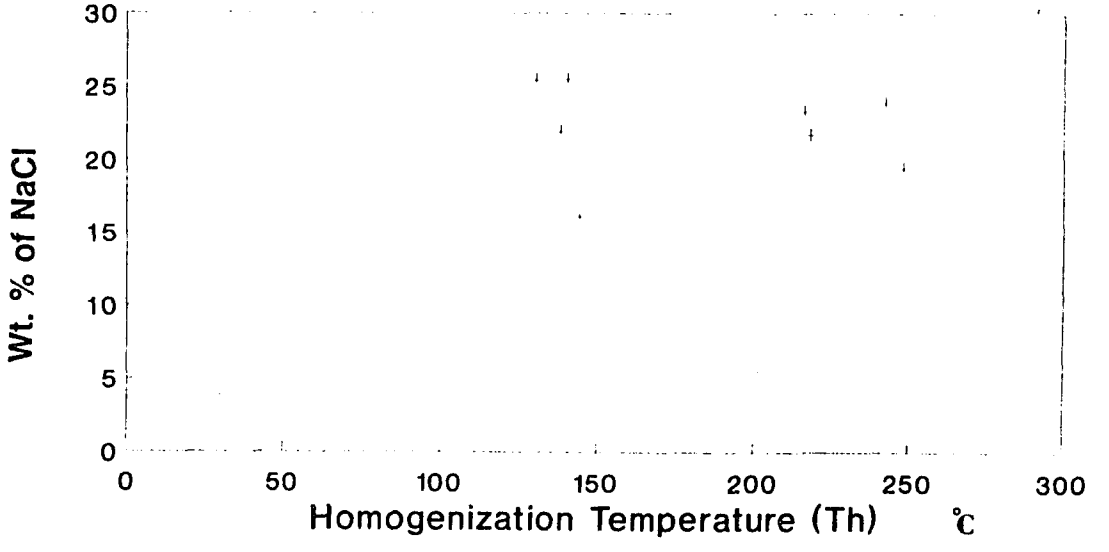


Figure 163- Plot of homogenization temperature (T_h) versus salinity content of primary two-phase fluid inclusions in fracture-filling dolomite cement in the Lone Mountain section.

Freezing Data:

Melting temperature of two-phase primary inclusions range from -12.1 to -27.5 °C (Fig. 163). The only melting temperature measured from fracture-filling calcite is -20.9 °C. The rest of the melting temperatures were measured from fracture-filling, white-sparry dolomite crystals of L.171 (Fig. 163; Appendix III-C2). Corresponding salinities of the Tm ranges are between 16.1 and 27.6 % wt. percent of equivalent NaCl. The first ice-melting temperatures (Te) of three inclusions range from - 47.4 to -52.8 °C.

Interpretation:

The oxygen-isotope compositions, and melting temperatures (Tm) of the fracture-filling dolomite in the L.171 and L.250 as well as petrographic examination suggest that the fracture-filling dolomites are late-diagenetic and deep-burial in origin. The fractures filled by late-diagenetic dolomite crosscut host dolostones. In L.250 and In sample L.171, two major T_h values, (1) 100-140 °C, and (2) 145-160 °C, are much lower than those of fracture-filling calcite, and a few readings range from 218 to 256 °C.

Fracture-filling calcite cements from samples L.250, L.570, and L.641 are believed to have formed under deep burial diagenesis. T_h values of these samples characterize much deeper burial environmental conditions than their burial depths during the formation of fracture-filling calcite cements. Because most of the fracture-filling calcites predate the pervasive dolomitization of the AVL and appear to have experienced greater burial depth than those of fracture-filling dolomite. Thus, T_h values of these calcites are likely to represent re-equilibration temperatures rather than minimum-formation temperatures of two-phase fluid inclusions. Petrographic evidence suggests that these fracture-filling calcite cements are pre-stylolitic, yet their T_h values correspond to greater burial depth than that of burial depth of approximately 4 km

during major stylolitization produced by the Antler orogeny (see Chap. 13).

Variations in T_h values and high-salinity content, dolomite-fluid inclusions may have formed from the mixture of the hotter, very saline basinal fluids and relatively colder deep-meteoric diagenetic waters (Zimmermann and Kesler, 1981; Taylor et al., 1983; and McNaughton and Smith, 1986); alternatively the same relationships may be related to periodic influx of basinal fluids of similar salinities (Gratz and Misra, 1987).

The pervasive dolomitization of the AVL is assumed have resulted from major continental uplifting-induced faulting which probably occurred during Late Middle Pennsylvanian (Nolan et al., 1956; Ketner, 1977). For the AVL, It is likely that progressive cooling of basinal solutions as a result of adiabatic cooling due to decreasing-confining pressure and heat exchange with cold host rocks during updip flow of basinal fluids may account for the wide range of T_h values (100 to 160 °C) during updip flow of deep-basinal solutions.

In the fracture-filling dolomite spar, Th values of two-phase inclusions ranging from 100 to 160 °C (Table 14) may indicate the minimum formation temperature of these deep-burial dolomite cements rather than maximum burial depth of the AVL. Therefore, T_h values of these readings from dolomite cements represent the formation temperature of dolomite crystals corresponding to the burial depth of the basin, especially during pervasive dolomitization of the AVL. For 20 °C surface temperature and 25 °C/Km of geothermal gradient, temperature range from 100 to 160 °C will represent respectively 3.2 km and 5.6 km (9753 to 17 068 ft), respectively (Table 14). For geothermal gradient of 30 °C/ km, the same temperature range corresponds to 2.6 and 4.6 km (7 924 to 14 020 ft) of burial depths, respectively (Table 14).
On the other hand, higher Th values of 218 and 256 °C in fracture-filling dolomite cements with a similar salinity probably indicate re-equilibration or elastic expansion of the walls of two-phase fluid inclusions due to depth of burial-induced heating which was far beyond the formation temperature of these inclusions (Fig. 163). The fluid inclusions of the high T_h values occur side by side with the two-phase, primary fluid inclusions ranging from 110 to 170 °C; therefore, the varying T_h values do not represent different generations of cements.

Table 14. T_h values of two-phase fluid inclusions and the corresponding maximum-burial depth range for the AVL in the Lone Mountain section.

Samp. No:	Homogenization Temp. T_h °C	Maximum Burial Depth (km)	
		25 °C /km	30 °C/km
L.250+	195 - 225	7.8 - 8.2	5.8 - 6.8
L.570+	190 - 205	6.8 - 8.2	5.6 - 6.1
L.643+	200 - 240	7.2 - 7.8	6.0 - 7.3
L.250*	125 - 140	3.4 - 4.8	2.8 - 4.0
L.171*	100 - 160 218 - 256	3.2 - 5.6 7.9 - 9.3	2.6 - 4.6 6.6 - 7.8
L.570+	260 - 290	9.6 -10.8	8.0 - 9.0

* fracture-filling dolomite, + fracture-filling calcite

They were probably re-equilibrated by decrepitation or leaked during the Sonoma orogeny and its eastward advancing clastic wedge (Fig. 163).

The maximum T_h values of 260 to 290 °C correspond to the maximum-burial depths of the AVL ranging from 8.0 to 9.0 km (24 834 to 27 432 ft) and from 9.6 to 10.8 km (29 261 to 32 918 ft) for, respectively, paleogeothermal gradients of 30 °C /km and of 25 °C and 20 °C surface temperature (Table 14). From the second highest temperature range from 240 °C to 256 °C, maximum-burial depth of the AVL ranges from 7.3 to 8.8 km (22 250 to 26 822 ft.) and from 7.8 to 9.4 km (23774 to 28651 ft.), respectively for the indicated paleogeothermal gradients and surface temperatures (Table 14). From the indicated maximum temperature range, the shallowest burial depth and the greatest burial depth can be used to indicate maximum burial depth range. For instance, 8.0 km and 10.8 km is the maximum burial depth range for the AVL for the temperature range of 260 to 290 °C. Similarly, maximum burial depth range from 7.3 to 9.4 km corresponds to the second highest T_h temperature range of 240 to 256 °C.

Ninemile Canyon

Homogenization Temperature (T) Data:

In this section, a total of 206 pressure-uncorrected homogenization temperatures (Fig. 164) and 37 melting temperatures were measured. Generally, T_h values range from 110 to 290 °C, and mean T_h is 200 °C for this section (Fig. 164). All the samples are fracture-filling late-diagenetic calcite cement, except sample A.65 which is representative of precursor vadose calcite cement in birdseyes fenestrae (see Appendix III-C2).

Considerably large numbers of inclusions with higher T_h values cluster particularly between 180 and 240 °C (Table 15). The ranges of T_h for the selected samples and their depths from the base of section are illustrated in Table 15. For the following samples, parenthesis proceeding the sample numbers include height (in feet) from the base of this vertical section from which samples were taken for the fluid-inclusion microthermometry. In sample A.14 (200 ft), T_h values range from 130 to 250 °C in which three clusters of T_h values range (1) from 150 to 175 °C, (2) from 180 to 230 °C (Table 15; Appendix III-C2), and (3) few T_h values are scattered below and above of these ranges. In sample A.18 (260 ft), T_h values generally range from 110 to 205 °C, including two clusters of T_h values ranging from (1) 110 to 160 °C, and (2) 180 to 205 °C (Table 15; Appendix III-C2). In sample A.19 (320 ft), T_h values range from 190 to 290 °C in which two major clusters occur in the following two ranges: (1) from 190-240 °C, and (2) from 260-290 °C (Table 15; Appendix III-C2). In sample A.48 (1000 ft), T_h values range from 185 to 230 °C, including two clusters are (1) 185-205 °C, and (2) 215 to 230 °C (Table 15; Appendix III-C2). Sample A.65 (1065 ft) is primarily composed of neomorphosed-precursor vadose cement in birdseyes fenestrae and T_h values of fenestral cement range from 120 to 150 °C(Table 15; Appendix III-C2). In sample A 84 (1200 ft), T_h values generally range from 125 to 230 °C in which two clusters of T_h values are, as follows: (1) from 140 to 160 °C,

and (2) 175-210 °C (Table 15; Appendix III-C2). Generally, in this section, three major T_h clustering ranges are (1) 110 to 160 °C, (2) 170 to 240 °C, and (3) 255 to 290 °C (Table 15; Fig. 164; and Appendix III-C2).

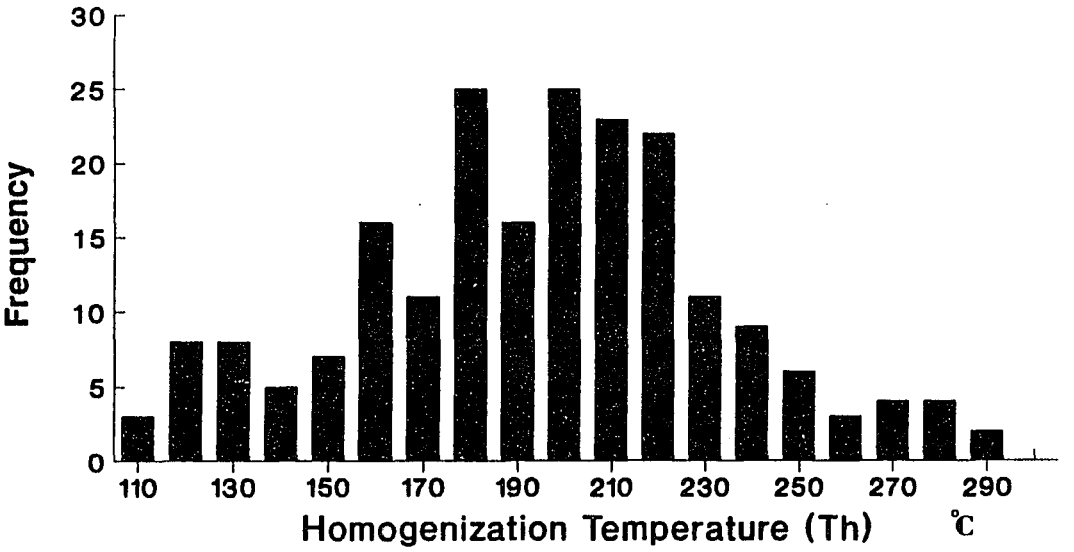
Table. 15. Three major clusters of T_h values and relative positions of the samples, from the base of section, in the Ninemile Canyon section.

Sample Number	From the base of section (Ft)	Homogenization Temp. (Th) Range °C		
		Cluster I	Cluster II	Cluster III
A.84	1200	140 to 160	170 to 205	
A.65	1000	120 to 150		
A.48	830		180 to 205 185 to 230	
A.19	320		190 to 240	255 to 290
A.18	260	120 to 160	180 to 205	
A.14	200		160 to 230	

Freezing Data:

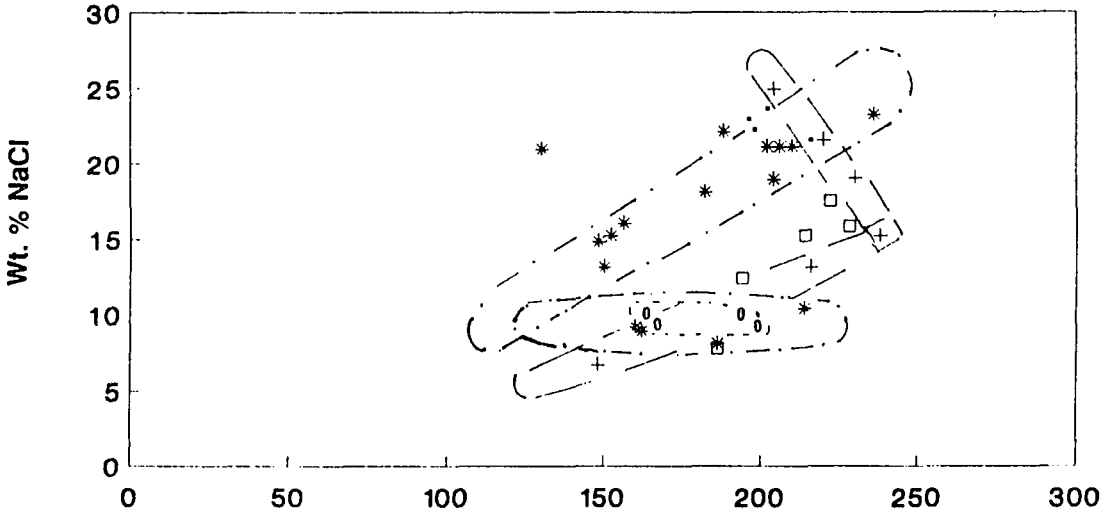
Final-melting temperatures (Tm) of two-phase fluid inclusions from this section range from -5 to -24 °C. First-melting temperatures (Te) were commonly measured from relatively large inclusions. Te values range from -27.2 to -48.5 °C.
In Figure 165 A, T_h versus salinity for each selected sample indicates the following relationships:

In sample A.18, Th values range from 149 to 214 °C, and Tm ranges from -4.9 to -6.3 °C which are equivalent to 7.8 to 9.6 wt % of NaCl. Figure 165 A, T_h versus salinity plot, shows that salinity of inclusions of this sample generally exhibit a horizontal trend or a parallel trend to T_h axis. In horizontal trends, salinity of fluid



A total of 208 readings

Figure 164- Histogram of homogenization temperatures (T_h) of primary two-phase fluid inclusions from fracture-filling calcite cement in the Ninemile Canyon section.



· A. 19	+ A. 14	0 A.18
* A. 84	□ A. 48	

Figure 165- Plot of T_h versus salinity content of primary two- phase fluid inclusions in Ninemile Canyon section.

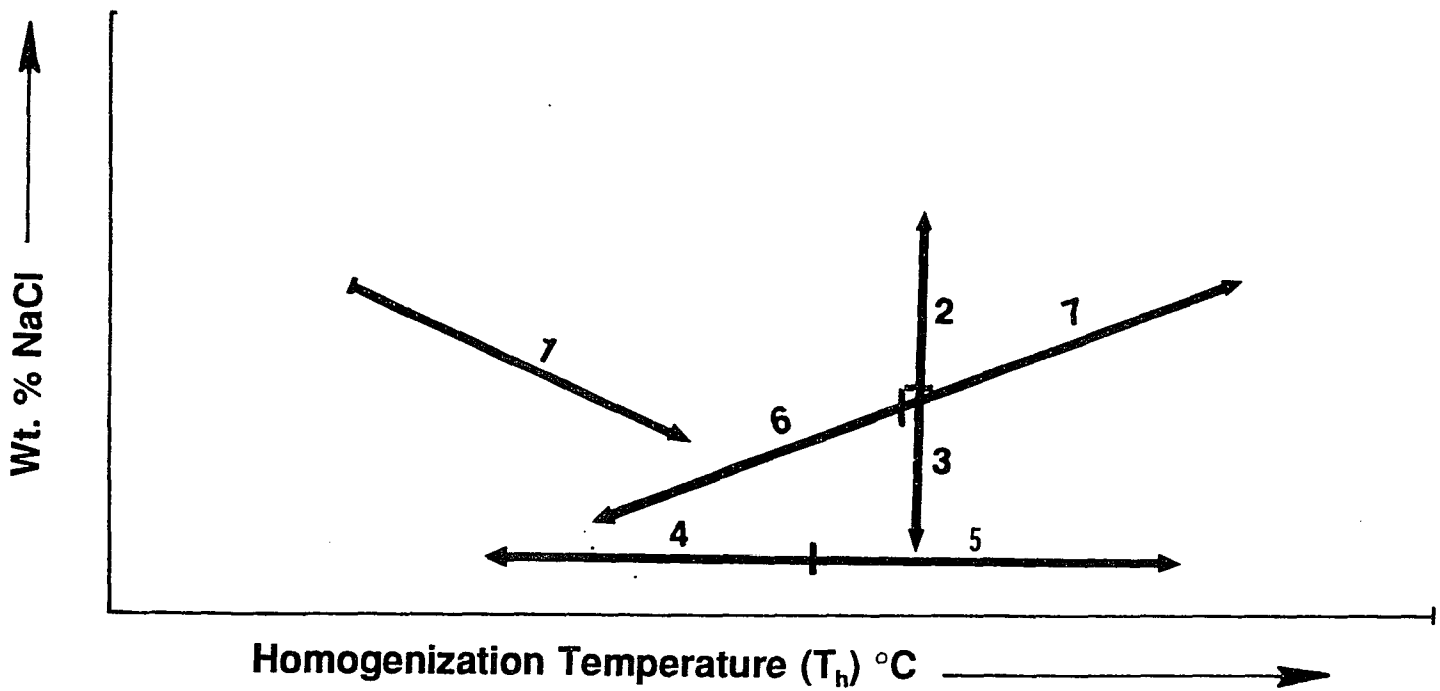


Figure 165 A- Plot of T_h versus salinity content explains volumetric and compositional changes on fluid inclusions and suggests possible processes for indicated changes after Shepherd et al. (1985) and Goldstein (1988). Trends in the T_h versus salinity plot may indicates the following processes: "4" and "5" necking down or stretching; "2" and "3" isothermal fluid mixing, "7" leaking and mixing of fluid inclusions with high-temperature basinal brine, "6" leaking and mixing with colder less saline solutions, and "1" leaking and mixing with high temperature low salinity solutions or probably hydrothermal fluids.

inclusions remains constant with progressively increasing T_h values (see the salinity and T_h values of samples A.18 and A.84 in Fig. 165).

Diagonal trends in figure 165 are represented by samples A.14, A.48, and A.84, indicating that salinity of inclusions changes as temperature of inclusions increase or decrease. In sample A.14, homogenization temperatures range from 131 to 238 °C, and Tm values of the two-phase fluid inclusions of the same sample (A.14) range from -9.2 to -23.2 °C which are equal to 13.1 to 24.9 wt. % of NaCl (Fig. 165 A). For this sample, two diagonal trends are recognizable: (1) T_h values falling from 238 to 131 °C coinciding with a progressive decrease in salinity; and (2) T_h values falling from 238 to 170s °C coinciding with progressive increase in salinity content of inclusions. T_h= 238 °C and 24.9 % salinity on figure 165 represent an intersection point of these two diagonal trends.

Sample A.19 is represented by only four Tm measurements (Fig. 165 A; see Appendix III-C2), and the distribution of T_h and Tm demonstrate nearly a horizontal trend with respect to increasing T_h. For T_h values from 197 to 216 °C, final-melting temperatures are in the range of -18.4 to -21.4 °C corresponding to 21.5 and 23.6 wt. % of equivalent NaCl, respectively.

In sample A.84, a relatively large number of Tm measurements range from -5.1 to -24.1 °C and corresponding to 8.1 to 25.4 wt. % of equivalent NaCl. In figure 165, the distribution of T_h and salinity values of fluid inclusions for sample A. 84 occurs in a diagonal trend (salinity increasing with increasing T_h values) and a horizontal trend (salinity being constant and parallel to T_h axis). These two trends appear to intersect or converge at 155-165 °C and form a shape of recumbent letter V: diagonal upper trend, and lower horizontal trend.

Interpretation:

The fluid inclusions with homogenization temperature values of 110 to 160 °C occur side-by-side with the inclusions which have much higher T_h values in the same crystal. They are only a few microns apart and do not show any observable textural

change in the crystals, such as kinking or twining etc. However, in some calcite crystals, smaller inclusions with relatively low-T_h and salinity values are commonly found at the solid inclusion-rich center of calcite crystals, whereas a few larger inclusions having high T_h values and higher salinity contents are found in the clean, relatively solid inclusion-free outer rims or zones of calcite crystals (e.g., Kaufman et al. 1989; and Abegg, 1990). This textural relation clearly indicates that the crystal growth of calcite cement probably occurred at great burial depths and resulted in formation of a different generation of fluid inclusions. In the inclusion-rich central part of calcite crystals, some inclusions with high T_h and salinity values may have been re-equilibrated by reheating during indicated crystal growth stage. This process may have resulted in either stretching, or leaking (i.e., exchange of diagenetic solutions) followed by rehealing (Roedder, 1984; Burruss, 1987; 1988; and Goldstein, 1988).

Composition of two-phase fluid inclusions is estimated from Te values of -27.2 to -- 48.5 °C to be reflecting the following chloride salts: Kcl_2. $NaCl_2$ and $MgCl_2$. NaCl (see Crawford, 1981).

In Figure 165, for sample A.84, the horizontal and diagonal trend between T_h and salinity content converge and appear to be intersected at temperature range of 155-165 °C. However, in general, T_h values of this sample range from 140 to 210 °C. Thus, it is likely that low-T_h values and low-salinity contents at the convergence point (Fig. 165), where horizontal and diagonal trend intersect, probably represent the original composition and minimum entrapment temperature of the parent fluid from which host crystals formed. The relationship between T_h values and salinity contents of fluid inclusions in sample A.84 (Fig. 165) appears to be a diagonal trend which is similar to the trend indicated by "7" in figure 165 A, which indicates that progressive increase in T_h corresponds to progressively higher salinity content of fluid inclusions. It is believed that diagonal trend indicate the possible re-equilibration of fluid inclusions caused by possible compositional (leaking) and volume changes "stretching" (see Roedder, 1984; and Goldstein, 1988) under the deeper burial depth range than that of the burial depth under which original inclusions formed. Samples A. 48 and sample A.14 also display a diagonal trend (similar to that of trend described above for sample

A.84) between T_h values and salinity contents of fluid inclusions in the T_h versus salinity plot (Fig. 165). Therefore, the same re-equilibration mechanism (leaking or compositional change) may have been responsible for the above indicated trend in samples A.14 and A.48. Under progressively increasing burial depth, microfractures may have opened some inclusions and caused the original fluid of these inclusions to leak. These partially drained-fluid inclusions were probably refilled or mixed by hotter and more saline basinal solutions. These refilled inclusions were probably later rehealed.

Horizontal trend (constant salinity corresponding to a very wide range of T_h values; see Figs. 165, 165 A) probably indicates only volume changes by stretching (Goldstein, 1988) which probably results from expansion of inclusion walls due to the increased-burial depth of the AVL (Bodnar and Bethke, 1984). Thus, T_h values higher than temperature of 160 °C for samples A.18 and A.84 may not represent the minimum formation temperature of calcite crystals or the temperature of parent fluid during the crystallization. Therefore, the wide range of T_h values probably represents re-equilibrated temperatures which were probably caused by stretching of some two-phase fluid inclusions due to greater burial depths of the AVL after the formation of these calcite cement. The horizontal trends "4" and "5" in figure 165 A is also believed to result from "necking down" process (see Appendix III-C1), as suggested by Roedder (1984), and Shepherd et al. (1985).

The other diagonal trend in sample A.14 is that progressive decrease in the salinity content of fluid inclusions corresponds to progressively increasing T_h values (Fig. 165). This diagonal trend between salinity contents and T_h values of fluid inclusions is depicted by trends "1" and by "6" (Fig. 165 A). Such trends suggest that inclusions were re-equilibrated by leaking and following refilling processes. It is likely that in trend "1" inclusions were probably refilled or mixed by hotter and less saline solutions and that in trend "6", inclusions were probably refilled or mixed by colder and less saline solutions.

The above indicated trends clearly suggest that multiple re-equilibration events appear to have affected two-phase fluid inclusions and that each event of re-

equilibration probably indicates different physical environmental conditions than others.

For 20 °C surface temperature and 25 °C/km and 30 °C/km paleogeothermal gradient, a T_h value of 160 °C corresponds to 5.6 km (17 068 ft) and 4.6 km (14 020 ft) of burial depth during the formation of fracture-filling cements. Thus, two fracture-filling calcite cements represented by samples A.18 and A.84, may have formed cogenetically at the different stratigraphic levels by the same tectonic or dynamic process. The two-phase fluid inclusions in the sample A.84, collected at about 1000 feet above the A.18-bearing strata, have relatively greater T_h values than those in sample A.18. These relations between A.18 and A.84 suggest that the formation of the fractures represented by sample A.84 (collected at 1200 feet from base of this section) and their healing took place first when the AVL was more deeply buried than during the healing of fractures represented by sample A.18 (collected at 260 feet from base). Therefore, the indicated altitudes and T_h values imply that formation and healing of these fractures correspond to gradual uplifting due to high erosional rate induced by faulting or by isostatic unroofing or readjustment.

Sample A.48 shows a diagonally increasing T_h values of 190 to 230 °C and salinity content of 7 to 17 wt. % NaCl (Fig. 165). Such diagonal trend between Th values and salinity contents similar to the trend "7" in figure 165 A indicates re-equilibration of two-phase fluid inclusions by leaking and rehealing (compositional change) during an increased burial depth.

In figure 165, the fluid inclusions in samples A.19 and diagonal trend "1" (Fig. 165 A) of A.14 usually have very consistent high-salinity contents and high-T_h values. Consequently, these two appeared to be different from the other selected samples, and the fractures represented by A.19 and A.14 were probably formed at great burial depth or probably during the maximum-burial depth of the AVL.

Sample A.65 is a fenestra-filling vadose cement; however, its two-phase fluid inclusions have Th values as much as 150 °C which clearly does not correspond to the temperature conditions of vadose diagenetic environments, but re-equilibration temperature of two-phase fluid inclusions (Burruss, 1987; 1988; Goldstein, 1986;

1988; 1989; and Barker and Halley, 1988) at great burial depth of AVL.

Table 16. Estimated-maximum burial depth range of the AVL from the pressure-uncorrected, maximum T_h values, from the Ninemile Canyon section.

Samp. No:	Homogenization Temp. T_h °C	Maximum Burial Depth (km)	
		25 °C /km	30 °C/km
A.14	160 - 230	5.6 - 8.4	4.6 - 7.0
A.18	180 - 205	6.4 - 7.4	5.3 - 6.1
A.19	190 - 240 255 - 290	6.8 - 8.4 9.4 - 10.8	5.6 - 7.3 7.8 - 9.0
A.48	190 - 230	6.8 - 8.4	5.6 - 7.0
A.84	170 - 205	6.0 - 7.4	5.0 - 6.1

From the subsidence curve (see Chap. 20), the AVL is estimated to have been buried as much as 3.7 to 4.0 km (11 277 to 12 192 ft.) at the end of the Devonian or initiation of the Antler orogeny. This burial depth range has correspondence with the T_h range of 110 to 160 °C for 30 °C/km geothermal gradient.

For the AVL, the maximum burial depth is estimated from the T_h values of 255-290 °C to be ranging between 9 and 10.8 km (24 432 to 32 918 ft), for surface temperature of 20 °C geothermal gradient of 30 °C/km and 25 °C/km, respectively (Table 16). An average burial depth for 200 °C corresponds 6 to 7.2 km (18 288 to 21 945 ft) respectively for the indicated-geothermal gradients.

For 30 °C/km and 25 °C/km and 20 °C surface temperature, the second highest T_h of 240 °C corresponds to the maximum-burial depth of 7.3 to 8.8 km (22 250 to 26 822 ft), respectively (Table 16). Thrust plates may have caused an additional heating (Oxborough and Trocotte, 1974). However, these T_h values are not pressure corrected and do not represent the maximum formation and equilibration temperatures of these fluid inclusions. Therefore, we can suggest that maximum-burial depth range of the

AVL in this region probably occurred between 7.3 and 10.8 km (22 250 to 32 918 ft).

Martin Ridge

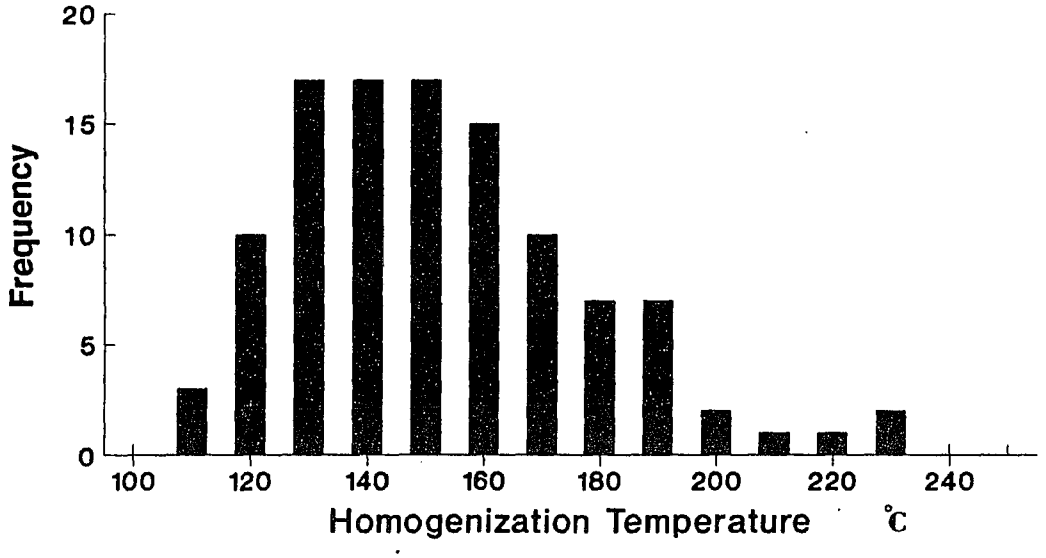
Homogenization-Temperature Data:

A total of 103 pressure-uncorrected T_h readings (Fig. 166) were measured from a total of 15 samples(14 fracture-filling calcite and one fracture-filling dolomite). Homogenization temperature values of this section occur in two ranges (1) from 110 to 160 °C and (2) 170 to 230 °C. In sample M.28 (fracture-filling dolomite), T_h values range from 128 to 138 °C. In addition to a general temperature range of dolomite (from 100 to 140 °C), two other T_h occur between 158 and 173 °C.

Sample M.32 is the late diagenetic ooid-filling calcite cement (Deep-burial, intraooid calcite cement) which white sparry dolomite (Dol. VI) replaced. T_h values measured from oomoldic calcite spar of M.32 occur in the range of 162 to 179 °C. Oxygen isotope values of the calcite and dolomite cements are very depleted with respect to heavy oxygen (^{18}O) and consistent with indicated T_h value range. However, sample M.17 (fracture-filling calcite) has excessively depleted $\delta^{18}O$ composition of -26.54 ‰ PDB and enriched carbon isotope composition $\delta^{13}C$ ‰ PDB; its T_h values range from 160 to 200 °C (see Chap. 17). A few T_h values are as high as 230 °C; the rest of T_h as indicated above are much lower than this maximum T_h value.

Freezing Data:

In this section, last-ice crystal-melting temperatures (Tm) range from -0.6 to -17.8 °C corresponding to 1.1 % to 21.0 wt. percent of equivalent NaCl. Tm values of M.17 occur in the range of -0.1 and -5.1 °C; T_h values versus salinity contents of fluid



A total of 103 readings

Figure 166- Histogram of homogenization temperatures (T_h) of primary two-phase fluid inclusions from fracture-filling calcite cement in the Martin Ridge section.

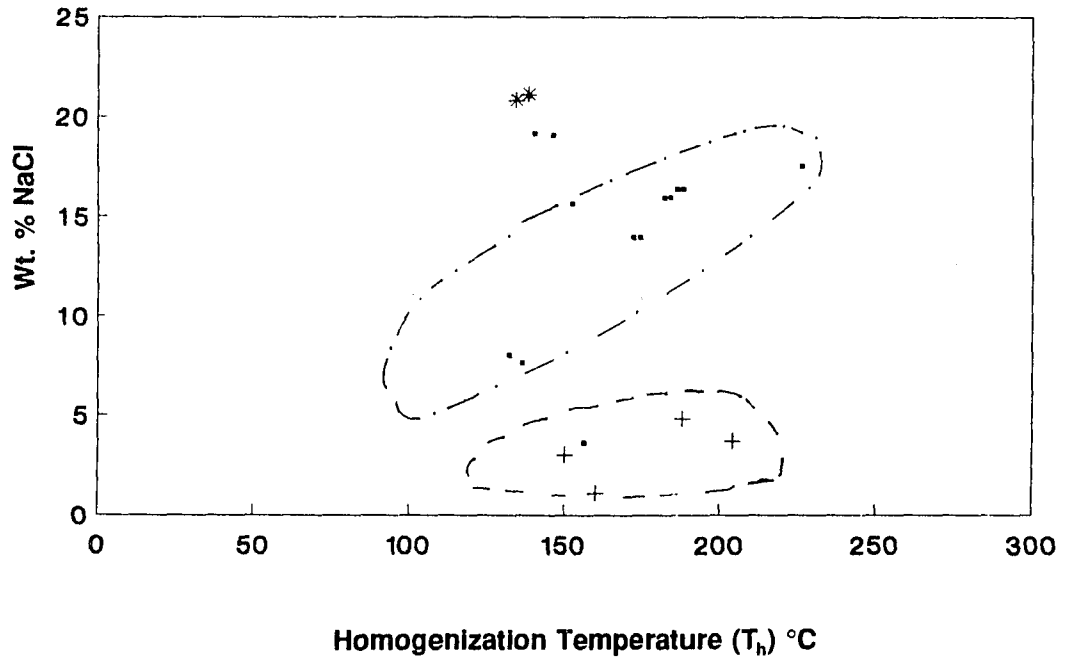


Figure 167- Plot of T_h versus salinity content of primary two-phase fluid inclusions in the Martin Ridge section.

inclusions of sample M.17 in figure 167 appear to show a horizontal trend or parallel trend to T_h axis (see Fig. 165 A). In the same figure, increase in homogenization temperature generally coincides with nearly constant salinity content. T_h values and salinity contents of fluid inclusions in sample M.75 appear to shows a diagonal trend (Fig. 167) which is similar to the diagonal trend depicted by 7 (Fig. 165 A). In sample M.28 (dolomite), two Tm values range from -17.5 to -17.8 °C corresponding to salinity content of 20.8 and 21 wt. % of equivalent NaCl, respectively (Fig. 167). These Tm values are compatible with Tm values of dolomite in the Lone Mountain section.

Interpretation:

Like in the Lone Mountain section, variations in T_h values of dolomite cement ranging from 120 to 140 °C with identical salinity contents may indicate similar a dolomitization mechanism as suggested before (see the Lone Mountain section in this chapter).

The T_h values of 158 and 173 °C in the same dolomite crystals probably represent the re-equilibrated T_h values other than minimum-formation temperatures of these dolospars. The horizontal trend between T_h values and salinity contents of sample M.17 (salinity remains nearly constant with increasing T_h; Fig. 167) implies that these inclusions were re-equilibrated by stretching process. Fracture-filling calcite cement of M.17 shows excessively depleted-$\delta^{18}O$ composition of -26.54 ‰ PDB and considerably enriched $\delta^{13}C$ composition of +4 ‰ PDB; very low-salinity content may indicate that this fracture-filling calcite cement may have originated from meteoric diagenetic fluids during the Late Devonian unconformity prior to Antler orogeny. Consequently, T_h values of M.17 also represent the re-equilibration temperature rather than the minimum entrapment temperature of related fluid inclusions in calcite cements. It is likely to suggest that the lower T_h range of 140 °C also represent the re-equilibration temperature of calcite crystals in this fracture-filling calcite. On the other hand, in sample M.75, T_h range of 140 to 230 °C and increase in Th values

corresponding progressively increasing higher salinity suggest re-equilibration of fluid inclusions through leaking of original fluids and the following refiling or mixing with relatively high salinity and high temperature basinal brines at great burial depths of the AVL.

Table 17. Estimated-maximum burial depth of the AVL from the pressure-uncorrected T_h values at the Martin Ridge section.

Sample Number	Homogenization Temp. T_h °C	Maximum Burial Depth (km)	
		25 °C /km	30 °C/km
M.8	110 - 160	3.6 - 5.6	3.0 - 4.6
M.17	160 - 200	5.6 - 7.2	4.6 - 6.0
M.32	160 - 180	5.6 - 6.4	4.6 - 5.3
M.75	160 - 230	5.6 - 8.4	4.6 - 7.0

Homogenization temperature ranges of each sample and their corresponding burial depths for 25 °C/km and 30 °C/km paleogeothermal gradient and surface temperatures of 20 °C are listed in Table 17. An average T_h values of 180 °C corresponds to 6.4 km and 5.2 km (19 507 and 15 844 ft) of burial depth for the geothermal gradient of 25 °C/km and 30 °C/km, respectively. The maximum-burial depth range of this formation is estimated from T_h values of 200 and 230 °C which correspond to 7.2 and 8.4 km (21 945 and 25 603 ft) and 6.0 and 7 km (18 288 and 21 336 ft) for the same geothermal gradients mentioned above (Table 17). The burial depth between 7.2 and 8.4 km (21 945 and 25 603 ft) appears to represent the maximum burial depth of the AVL at the Martin Ridge section because T_h values greater than 230 °C have not been reported any samples of the AVL in the Martin Ridge section.

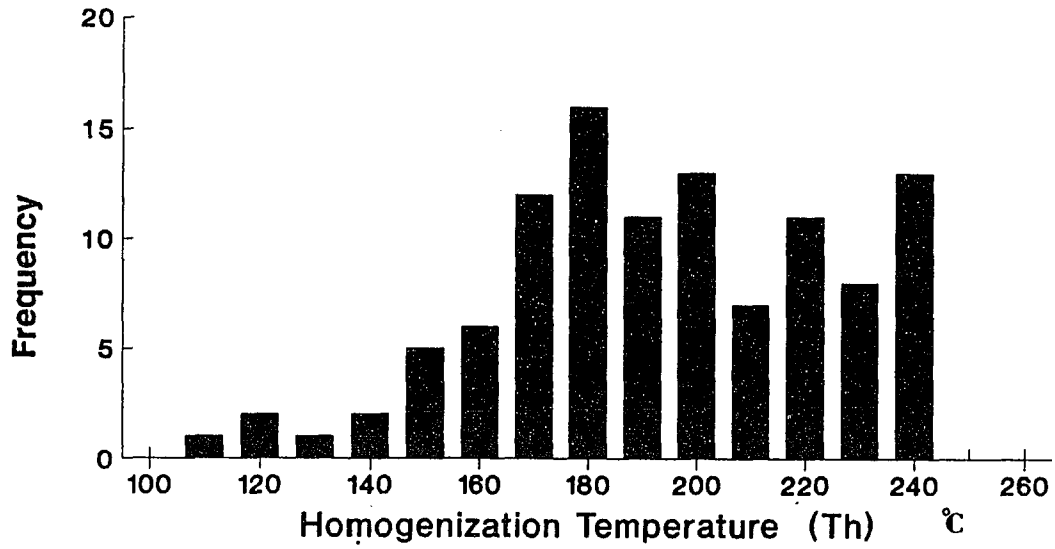
Keystone Canyon

Homogenization-Temperature Data:

A total of 106 pressure-uncorrected homogenization temperatures (Fig. 168), ranging from 110 to 240 °C, were measured from samples of fracture-filling calcite cements (samples K.6, K.10, K.13, K. 19 and K.27; Table 18). Th values commonly occur in the range of 180 to 240 °C (Appendix III-C2), but T_h values of K.13 cluster in two-major ranges: a) from 110 to 160 °C, and b) from 175 to 240 °C. These calcite-filled fractures crosscut pervasively dolomitized unit; they are commonly postdated by the quartz-filled latest fractures. In K.5, two-homogenization temperatures of two-phase, fluid inclusions of this quartz cement range from 163 to 206 °C (Appendix III-C2). The isotope values of the late fracture-filling calcites are excessively depleted ($\delta^{18}O$ values of -27 ‰ PDB; see Chap. 17).

Freezing Data:

A total of 23 melting temperatures were measured from samples K.6 and K.13. Two-phase fluid inclusions of fracture-filling calcite cements have considerably high T_h values and a very low-Tm ranging from -1.1 to -11.4 °C (Appendix III-C2). This Tm range corresponds to 3.7 and 15.3 wt % of equivalent NaCl (Fig. 169). Their eutectic temperatures or first-ice melting temperatures (Te) values vary from -12.3 to -24.5 °C. T_h versus salinity diagram shows that generally salinity content of inclusions decreases as T_h values decrease (Fig. 169). Except for three readings, their lower T_h values coincide with a high-salinity concentration (Fig. 169).



A total of 108 readings

Figure 168- Histogram of homogenization temperatures (T_h) of primary two-phase fluid inclusions from the fracture-filling calcite cement in the Keystone Canyon section.

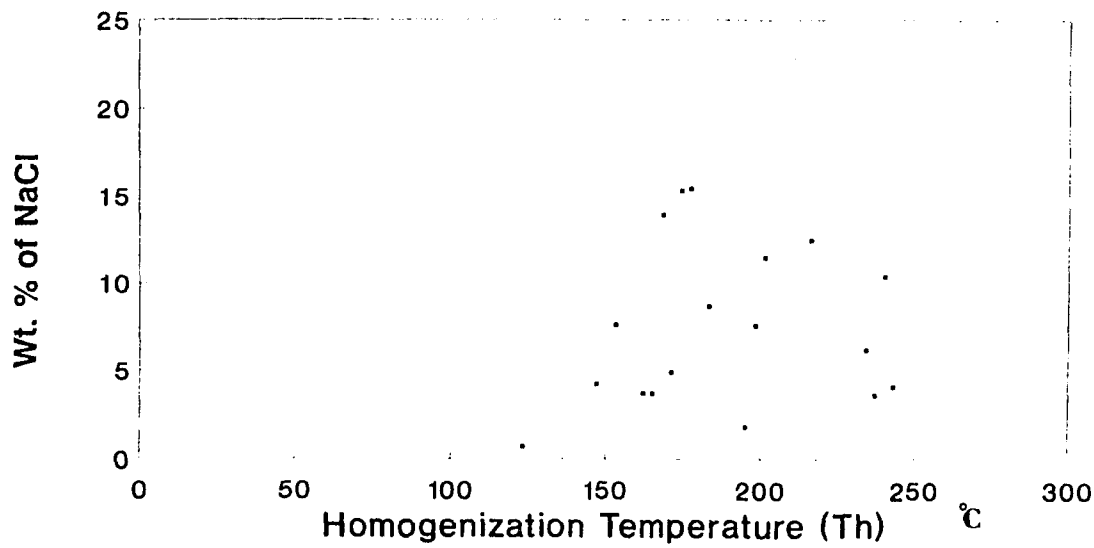


Figure 169- Plot of T_h versus salinity content of primary two-phase fluid inclusions in the Keystone Canyon section.

Interpretation:

These two-phase fluid inclusions with a low-salinity content between 3.7 to 15.3 wt. % of NaCl are consistent with their eutectic temperatures (Te) which are corresponding to a NaCl and NaCl.Kcl types of chlorine salt in fluids (Crawford, 1981).

On the basis of extremely depleted oxygen-isotope composition and very low salinity content of two-phase fluid inclusions, the probable meteoric water origin for the late fracture-filling calcite cement can be inferred. Similar isotopic composition and salinity relations were observed from late diagenetic, fracture-filling calcite cements postdating the pervasively dolomitized units in the Pine Point lead and zinc ore deposits, Alberta, Canada (Aulstead et al., 1988).

Despite considerably high-T_h values, low-salinity fluid composition of two-phase fluid inclusions and exceedingly depleted oxygen-isotope composition of calcite cements generally indicate meteoric origin of parent solutions from which these calcite cements initially formed (see Chap. 17). The high T_h values of the low-salinity fluid inclusions are most likely to represent the re-equilibration temperatures rather than minimum-entrapment temperatures of the indicated-fluid inclusions.

Thus, these fractures may have initially filled by meteoric water, but later their two-phase inclusions were probably re-equilibrated due to increased burial depth during the Sonoma orogeny or its eastward-advancing clastic wedges.

At this location, the ranges of maximum-burial depth for the AVL can be estimated from the following temperature range: (1) Th values from 190 to 240 °C correspond to 6.8 and 8.8 km (20 726 and 26 823 ft) of burial dept of the AVL for surface temperature 20 °C, and geothermal gradient 25 °C/km, and 5.6 to 7.1 km (17 068 and 21 640 ft) for 30 °C/km (Table 18).

Clear Creek Canyon

Homogenization-Temperature Data:

A total of 34 pressure-uncorrected homogenization temperatures were measured from the latest quartz cement within the intercrystalline pores of the saddle dolomite "Dol. IX" (Fig. 170). Quartz cements show the dissolutional or etched rims around saddle dolomite crystals, and poikilotopically enclose saddle dolomite crystals as an inclusion (see Chap. 13).

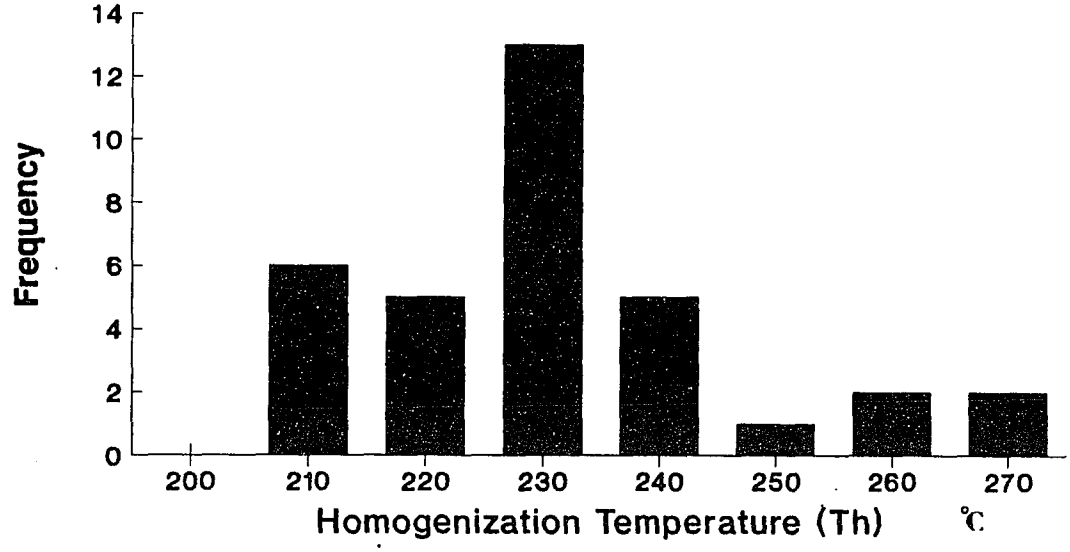
T_h values of two-phase fluid inclusions range from 210 to 270 °C (Fig. 170), but major clusters of T_h values occur in the range of 210-240 °C degrees. No other lower T_h values were measured from the two-phase primary inclusions of quartz cements.

Freezing Data:

Melting temperatures of the two-phase fluid inclusions of quartz cements commonly vary between -5.7 and - 20 °C corresponding to 8.9 and 22.7 wt. % of equivalent NaCl (Fig. 171). Te values generally range from -36 to -43.9 °C. Two-major ranges of the melting temperature "Tm"s for these inclusions are the following: (1) -5.7 to -11 °C, and (2) -18 to -20 °C (Fig. 171).

Interpretation:

Indicated Te values are correlative with a $MgCl_2$, and $NaCl.MgCl_2$ salt composition (e.g Crawford, 1981). The variations in "Tm"s and salinity composition of these inclusions (Fig. 171) were probably related to replacement of saddle dolomite by quartz crystals because inclusions with high-salinity content and inclusions with low-salinity content occur in the same quartz cement side-to-side with a few microns separating them. Thus, fluid inclusions salinity probably represent the original fluid



A total of 34 readings

Figure 170- Histogram of homogenization temperatures (T_h) of primary two-phase fluid inclusions from intercrystalline pore-filling quartz cement in the Clear Creek Canyon section.

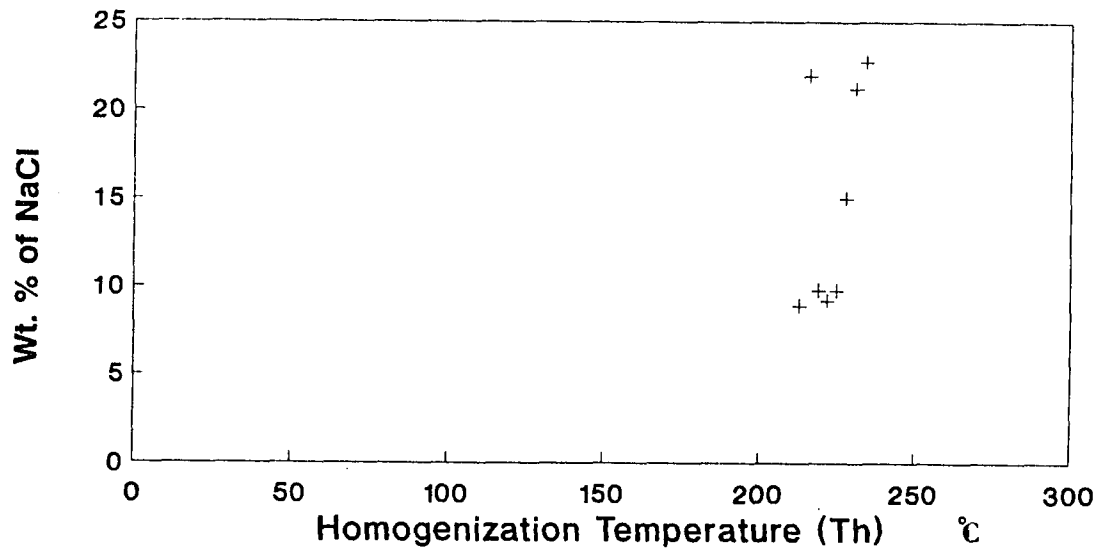


Figure 171- Plot of T_h versus salinity content of primary two-phase fluid inclusions in the Clear Creek Canyon section.

inclusions of the replaced dolomite crystals, and during the replacement of dolomite crystals by quartz, some inclusions may have unchanged compositionally due to irregularities of crystal structure or rate of replacement process. Probably, the original dolomitic inclusions within quartz crystals were re-equilibrated by volume change or stretching under increased burial depth.

Moreover, Tm values of the two-phase inclusions in the saddle dolomite elsewhere ranging from -20 to -28 °C may have been compositionally changed by exchanges of fluids with quartz-bearing basinal solutions during the replacement of dolomite. Therefore, re-equilibrated and newly formed inclusions could have cogenetically formed in the same quartz crystals with microns apart. In quartz crystals, the coexistence of high- and low-salinity inclusions and their comparable T_h values suggest that mixing of diagenetically two different fluids is unlikely because Th and salinity contents of fluid inclusions do not show a wide range (Fig. 171). In addition, quartz has a considerable strength and resistance against stretching and leaking (see Roedder, 1984). Consequently, necking down (e.g., Roedder, 1980) and leaking can be ruled out for quartz cement due to physical characteristics of this mineral. Therefore, preservation of fluid inclusions of some precursor dolomite during the replacement by quartz dolomites appears to be the primary cause of the salinity variation.

Alternatively, low-salinity content can also be explained by formation of solid salt crystals, "hydrohalite," (Roedder, 1963, 1972 ,1984). In this case, intercrystalline pore- and fracture-filling quartz cements with considerably high-T_h values and varying salinity concentrations probably derived from the same silica-rich, deep-basinal solution during expulsion of basinal fluid by the activities of Sonoma orogeny.

Estimated-maximum burial depth of the AVL in this section range from 7.0 to 10.0 km (21 336 to 30 048 ft); see Table 18 for detail.

Table 18- Estimated-maximum burial depths of the AVL from the maximum T_h ranges at the Keystone and Clear Creek Canyon sections (surface temperature 20 °C).

Vertical Type Section	Sample Numbers	Homogenization Temp. (T_h) °C Clusters	Max. Burial Depth (km)	
			25 °C/km	30 °C/km
Keystone Canyon	K.5, K.6	110 - 140	3.6 - 4.8	3.0 - 4.0
	K.6, K.13, K.19, K.27	150 - 180	5.2 - 6.4	4.4 - 5.3
	K.5, K.6, K.10, K.13, K.13, K.19, K.27	180 - 200	6.4 - 7.2	5.3 - 6.0
	K.6, K.10, K.13, K.27	210 - 240	7.6 - 8.8	6.3 - 7.3
Clear Creek Canyon	C.7	210 - 240	7.6 - 8.8	6.3 - 7.3
	C.6, C.7	250 - 270	9.2 -10.0	7.6 - 8.3

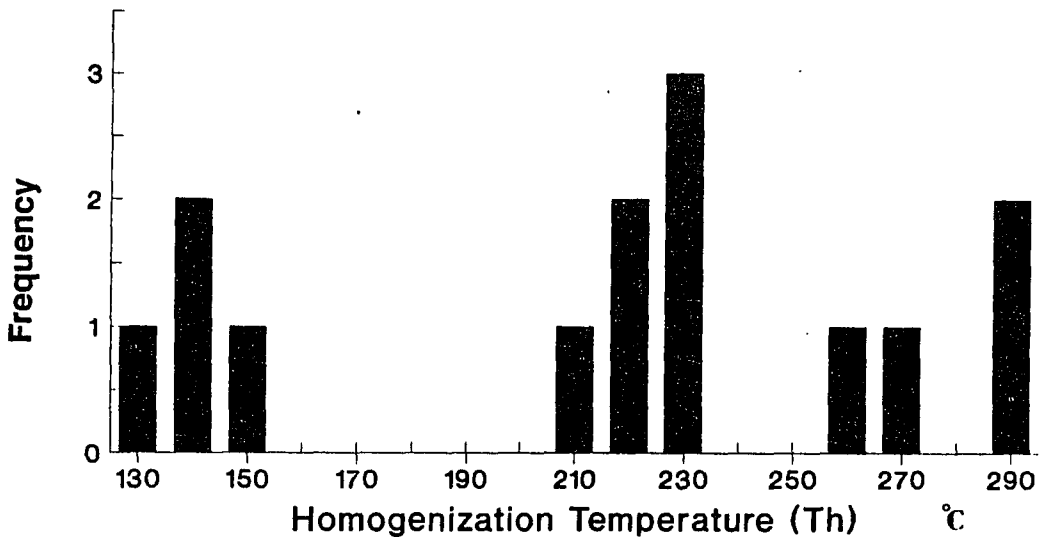
The Toiyabe Range

1. Toiyabe Peak

Homogenization Temperature Data:

In this section, a total of 14 pressure-uncorrected homogenization temperatures were measured from two fracture-filling calcite samples (Fig. 172). On a mesoscopic scale, these fractures are folded and show similar deformation with the axial-plane cleavage (slaty cleavage) of the shaley limestone of the AVL. (see Fig. 158 in Chap. 17).

Melting temperatures of relatively larger inclusions could not be measured because



A total of 14 readings

Figure 172- Histogram of homogenization temperatures (T_h) of primary two-phase fluid inclusions from fracture-filling calcite cement in the Toiyabe Peak section.

of darker background of inclusion walls. Despite paucity of two-phase fluid inclusions, fourteen T_h values are clustered in the three-major temperature ranges: a) from 130 to 160 °C, b) from 210 to 230 °C, and c) from 260 to 290 °C (Fig. 172; Appendix III-C2)

Under a microscope, the fracture-filling calcite shows recrystallization, and pressure shadow and preferred orientation of sericite (phengite) along with quartz. Moreover, in individual calcite crystals, twinning, kinking and new calcite-crystal formation along the sheared twins and kinking are prominent. The AVL in this section is overlain by four thrust units as much as 3280 m (10 000 ft), ranging from Ordovician to Permian in age (Washburn, 1969).

Interpretation:

The petrographic and isotopic study of the AVL suggests that fracture-filling calcite in the folded large mesoscopic fractures are late diagenetic in origin, but these fractures appear to have formed prior to maximum burial depth of the AVL. Therefore, the formation of fractures and their healing by calcite probably took place much earlier than the dynamic metamorphism, but they were most likely deformed synchronously with slaty cleavage during the emplacement of thrust plates of the Sonoma orogeny.

Oxygen-Isotope composition ($\delta^{18}O$= -28.30 ‰ PDB) of fracture-filling calcite suggests that this cement probably originated from probable meteoric water (see further detailed information in isotope section). Therefore, indicated, high-T_h ranges probably correspond to the re-equilibrated T_h which was caused by much greater burial depth of the AVL than burial depth during the minimum entrapment temperature of these two-phase fluid inclusions.

Table 19- Estimated burial depth range of the AVL from T_h ranges, in the Toiyabe Peak (Average surface temperature= 20 °C)

Homogenization Temp. T_h °C	Maximum Burial Depth (km)	
	25 °C /km	30 °C/km
110 - 160	3.6 - 5.6	3.0 - 4.6
210 - 240	7.6 - 8.8	6.3 - 7.4
260 - 290	9.6 - 10.8	8.0 - 9.0

It is very difficult to suggest that the T_h values, ranging from 110 to 160 °C, represent the original formation temperature of the fracture-filling calcite cement, because increased temperature and pressure during maximum-burial depth of the AVL by tectonic loading and eastward advancing clastic wedge of the Sonoma orogeny created much greater burial temperature than 160 °C. Thus, the T_h range of 110 to 160 °C may represent the post-metamorphic hydrofracturing of inclusion and rehealing of these inclusions during the post-Sonoma orogeny. For the AVL, the T_h range from 210 to 240 °C corresponds to 7.6 - 8.8 km (23 164 - 26 822 ft) and 6.3 - 7.4 km (19 202 - 22 555 ft) of burial depths for a geothermal gradient of 25 °C /km and 30 °C/km, respectively. Maximum burial depth of this formation is estimated to range from 8.0 to 10.8 km (24 384 to 32 918 ft), see Table 19. Maximum T_h value of 290 °C corresponds to 9 km of burial for the AVL by using a 30 °C/km geothermal gradient. All these T_h values are most likely to be re-equilibration temperatures of the previously formed two-phase fluid inclusions. Thus, the pressure-uncorrected T_h values indicate a shallower-burial depth ranges than max. burial depth of the AVL.

Thrusting probably produced additional heat; the heat transfer during thrusting is believed to be convectional rather than conductional (Oxborough and Trocotte, 1979; Karabinos, 1987). Therefore, this process probably required a higher geothermal

gradient than geothermal gradients used in this study.

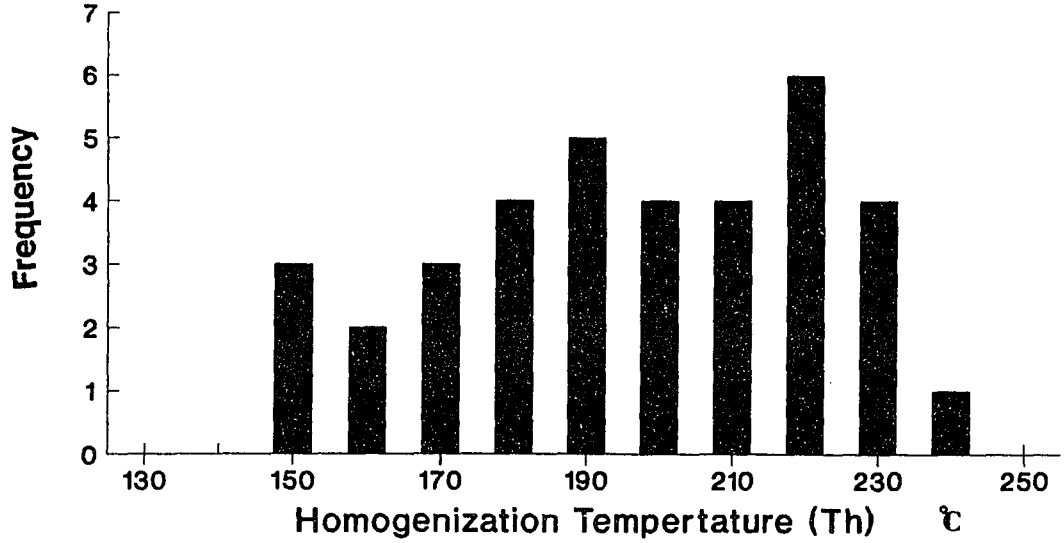
2. Dry Creek Section

Homogenization-Temperature Data:

A total of 36 pressure-uncorrected homogenization and 13 melting temperatures were measured from two fracture-filling calcite samples in this section (Fig. 173). Calcite cements are intensively twinned, and kinked and smaller calcite crystals are formed along the kinking similar to those of the Tioyabe sections. In general homogenization temperatures range from 150 to 240 °C. Oxygen-isotope composition of the fracture-filling calcite cements (folded fractures) is extremely depleted with respect to heavy oxygen, such as $\delta^{18}O$ ranging from -18 to-27 ‰ with respect to PDB.

Freezing Data:

Two-phase inclusions with homogenization temperature values between 150 and 180 °C, or less than 200 °C, usually have melting temperatures (Tm) ranging from -1.3 to -7.6 °C which correspond to salinity ranging from 2.2 to 11 wt. % equivalent NaCl (Fig. 174; Appendix III-C2). Inclusions with homogenization temperatures greater than 200 °C have freezing-temperature ranges from -13 to -24 °C which correspond to salinity contents of 17.6 to 25 wt % equivalent NaCl (Fig. 174; Appendix III-C2), respectively. The average melting temperature (Tm) of -17 °C corresponds to 21 wt. % of equivalent NaCl. The eutectic temperatures (Te) occur in two ranges: (1) from -12.3 to -20.8 °C, and (2) from -42 to -53 °C. The T_h versus salinity plot of this section shows a diagonal trend (Fig. 174).



A total of 36 readings

Figure 173- Histogram of homogenization temperatures (T_h) of primary two-phase fluid inclusions from fracture-filling calcite cements in the Dry Creek Canyon section.

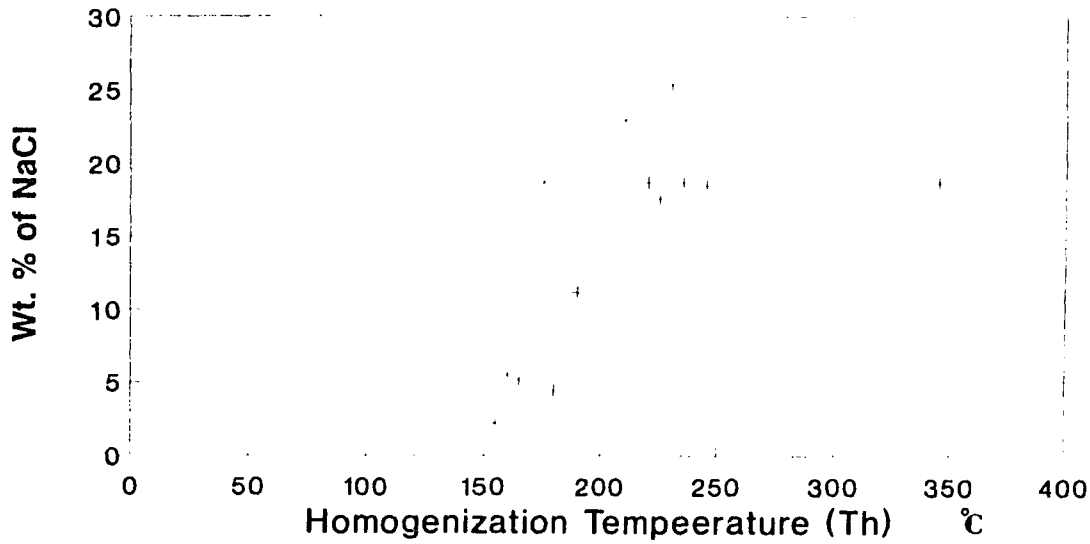


Figure 174- Plot of T_h versus salinity content of primary two-phase fluid inclusions in the Dry Creek Canyon section.

Interpretation:

The very depleted oxygen isotopic composition ($-\delta^{18}O$= -25 ‰ PDB) of fracture-filling calcites, lower salinity and mesoscopically folded fractures suggest that these fractures formed and healed before the major deformation caused by major thrusting events of the Sonoma orogeny. The extremely depleted oxygen-isotope composition of calcite cements and low-salinity content of fluid inclusions are compatible with the meteoric water origin of parent solutions for these calcite cements. Figure 174 shows that Tm or corresponding salinity increases diagonally with the increasing T_h values. This diagonal trend certainly suggests that the minimum-homogenization temperatures of the two-phase inclusions were probably re-equilibrated at greater burial depths than their formation depths.

Table 20- Estimated-maximum burial depth range of the AVL from the max. T_h range, in the Dry Creek Canyon.

Homogenization Temp. T_h °C	Maximum Burial Depth (km)	
	25 °C /km	30 °C/km
150 to 180	5.2 - 6.2	4.3 - 5.3
190 - 240	6.8 - 8.8	5.6 - 7.3

T_h values of two-phase inclusions range from 150 to 230 °C. Maximum depth of burial range were estimated from T_h values ranging from 190 to 240 °C which correspond to 6.8 to 8.8 km (20 726 to 26 822 ft) of maximum-burial depth for the AVL (see Table 20). T_h values of 290 °C of Toiyabe Peak section was not recorded in this section, this T_h value can be used for determining the max. burial depth of the AVL at the Dry Creek section. Since these two sections are very close to each other, it is likely that both sections experienced the same burial history.

3. Reeds Canyon Section

Homogenization-Temperature Data:

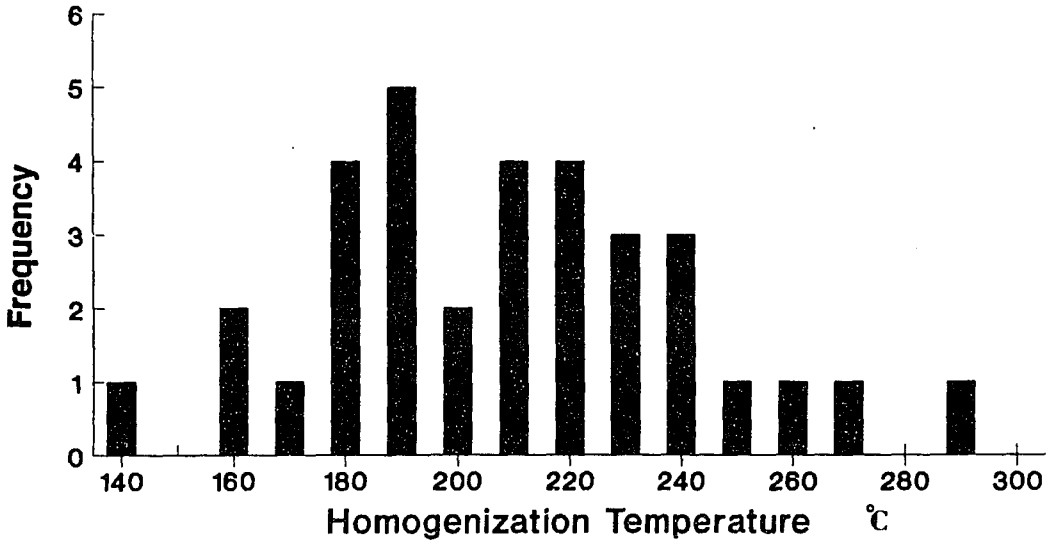
A total of 33 pressure-uncorrected homogenization temperatures were measured from two fracture-filling calcite samples (Fig. 175; Appendix III-C2) which are represented by a fracture-filling calcite cements. Homogenization temperatures generally range from 140 to 290 °C; however, most of the Th values clustered between 160 to 240 °C (Fig. 175). Isotope compositions of these fracture-filling calcites ($\delta^{18}O$= -10.74 ‰) differ from those of fracture-filling cement in the Dry Creek and Tioyabe Peak sections. Vertical distance between these two fractures is approximately 170 feet, and no significant temperature differences can occur in their calcite cements.

Freezing Data

First ice-melting temperatures (Tm) of these inclusions range from -37 to -50 °C corresponding to the last ice-melting temperatures ranging from -12.3 to -21.9 °C which reflect an approximate salinity range of 16.3 to 24 wt. % of equivalent NaCl (Fig. 176).

Interpretation:

The isotopic composition of the fracture-filling calcites ($\delta^{18}O$= -11 ‰ PDB), high T_h values and high-salinity content of two-phase fluid inclusions suggest that calcite-filled fractures may have formed at greater burial depth, probably during the thrusting events of Sonoma orogeny. Therefore, some T_h values of these fluid inclusions may represent the minimum-formation temperatures of these fracture-filling calcite cements in this



A total of 33 readings

Figure 175- Histogram of homogenization temperatures (T_h) of primary two-phase fluid inclusions from fracture-filling calcite cement in the Reeds Canyon section.

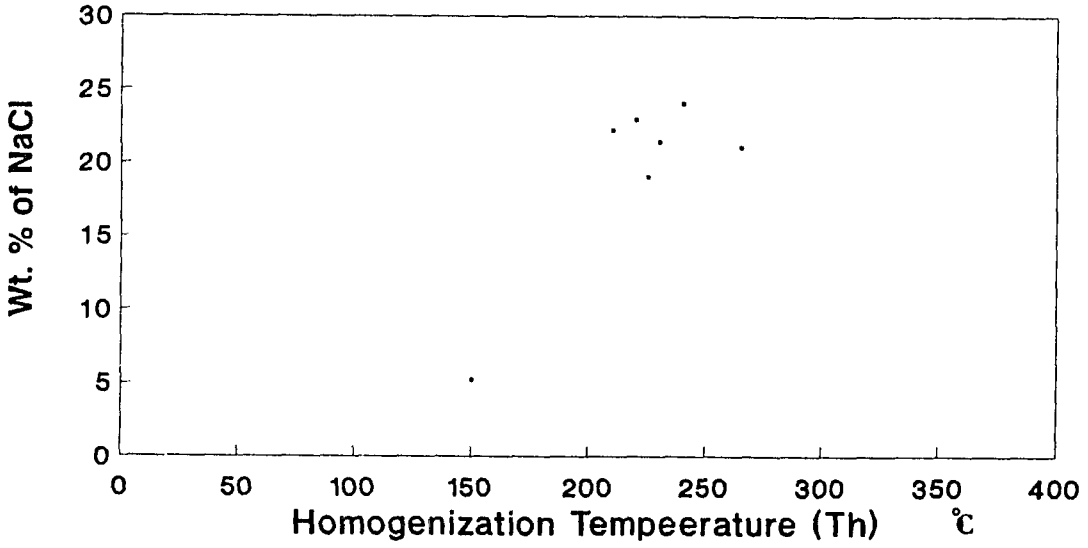


Figure 176- Plot of T_h versus salinity content of primary two- phase fluid inclusions in the Reeds Canyon section.

type section. From the same calcite crystal, high-melting temperature of -3.2 °C coincides with a homogenization temperature of 150 °C (Fig, 176). With this inclusion, the salinity contents and T_h values of fluid inclusions of this section exhibit a diagonal trend in figure 176. And this diagonal trend (characterizing the trend "6" in figure 165 B) suggests that the fluid inclusion with low salinity and Th values was most likely re-equilibrated by solution exchange due to hydrofracturing and following rehealing during the post-Sonoma orogeny uplifting.

Te values are correlative to chlorine salt composition of MgCl and NaCl.MgCl (e.g, Crawford, 1981).

Th ranges of 180 to 200 °C, 210 to 240 °C, and 290 °C can be used for determining the maximum burial depth of the AVL (Table 21).

Table 21- Estimated maximum-burial depth of the AVL from the T_h values, in the Reeds Canyon.

Homogenization Temp. T_h °C	Maximum Burial Depth (km)	
	25 °C /km	30 °C/km
180 - 200	6.4 - 8.0	5.3 - 6.0
210 - 240	7.6 - 8.8	6.3 - 7.3
290	10.0	9.0

Max. burial depth of the AVL in this section is estimated to range from 9.0 to 10.8 km (27 432 to 32 918 ft) for 290 °C (Table 21). The second-highest burial range has been estimated to occur in the range of 6.3 to 8.8 km (19 202 to 26 822 ft); see Table 21 for further detail.

Allochthonous Units of the Roberts Mountain Thrusts

I. Upper Tectonic Slices of The Lower Plate

I. 1) Whiterock Canyon Section

Homogenization-Temperature Data:

In this section, a total of 10 pressure-uncorrected homogenization temperatures ranging from 110 to 190 °C were measured from three fracture-filling calcite samples (Fig. 177; Appendix III-C2). Two major cluster ranges of T_h values occur between 110-140 °C and 160-190 °C. No melting temperatures were measured because two-phase fluid inclusions were very small.

I. 2) June Canyon Section

Homogenization-Temperature Data:

A total of 36 pressure-uncorrected homogenization temperatures were measured from five fracture-filling calcite samples (Fig. 178; Appendix III-C2). In this section, the homogenization temperatures of the two-phase inclusions are identical to those of inclusions measured from the Whiterock Canyon section, and they occur in similar ranges, such as from 110 to 190 °C, showing very similar clusters of T_h values from 110 to 140 °C and from 160 to 190 °C with the Whiterock Canyon section (Fig. 178).

Isotope values of these fracture-filling calcite cements show two generations of fracture-filling calcites. Particularly samples W.5 and I.10 are very depleted with respect to $\delta^{18}O$ values, varying between -20 to -25 ‰ PDB, respectively. T_h values range from 110 to 160 °C.

Interpretation:

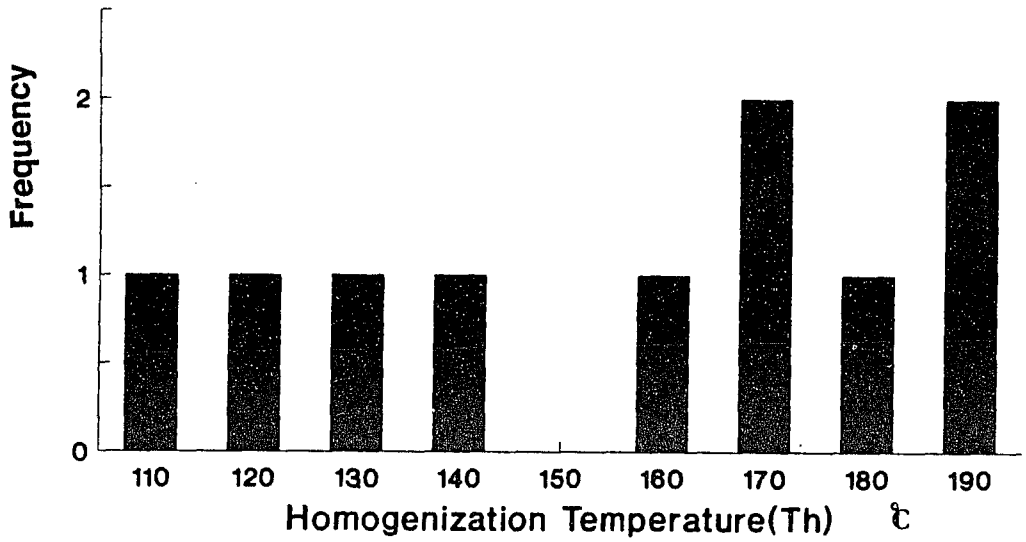
The homogenization-temperature ranges in these two-thrust plates are identical, and the calcite-filled fractures may have formed during the same tectonic events by similar diagenetic processes. The oxygen isotope-composition of fracture-filling calcite cements of the samples I.10 and W.5 probably indicate a meteoric diagenetic water as an original parent fluid. The exceedingly depleted $\delta^{18}O$ compositions differ from the other fracture-filling cements which appear to have formed at great burial depth, or during the thrusting events.

Table 22- T_h ranges and the corresponding burial-depth ranges, in the Whiterock Canyon section and June Canyon sequence.

Homogenization Temp. T_h °C	Maximum Burial Depth (km)	
	25 °C /km	30 °C/km
140 - 160	4.8 - 5.4	4.0 - 4.6
140 - 190	4.8 - 6.8	4.0 - 5.6

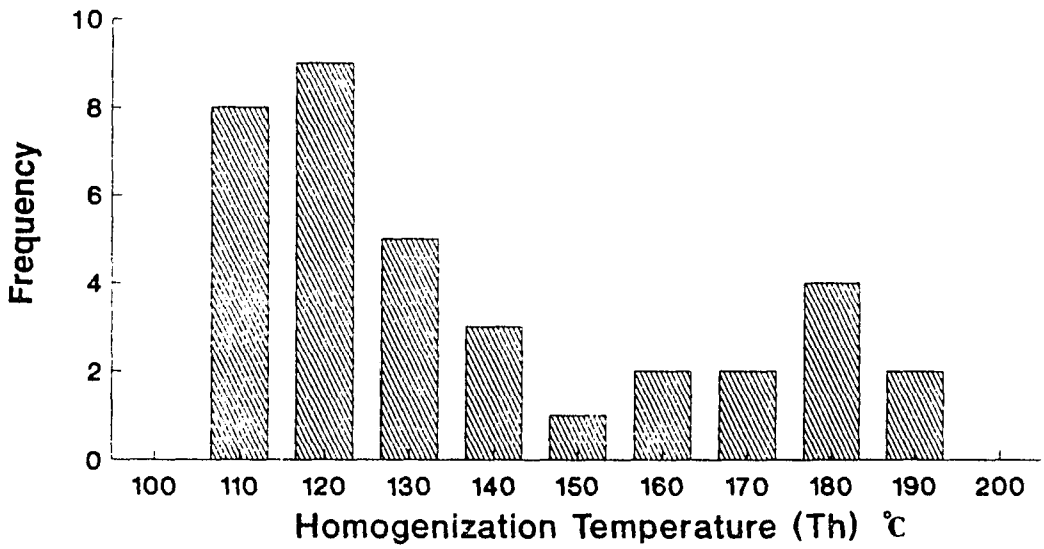
Therefore, T_h values ranging form 110 to 140 °C from calcite cements with excessively depleted oxygen-isotope composition may have formed before thrusting, and then post- thrusting subsidence probably re-equilibrated these inclusions.
It is possible to suggest that this meteoric water influenced-calcite cement may have formed during the Middle Pennsylvanian uplifting. As a result, it can be suggested that this regional uplifting affected not only east-central and central Nevada, but west-central Nevada as well.

Estimated maximum burial depth of the AVL represents the post-Devonian burial depth range which is estimated to range from 5.6 to 6.8 km (17 248 to 20 726 ft); see Table 22.



A total of 10 readings

Figure 177- Histogram of homogenization temperatures (T_h) of primary two-phase fluid inclusions from fracture-filling calcite cement in the Whiterock Canyon section.



A total of 36 readings

Figure 178- Histogram of homogenization temperatures (T_h) of primary two-phase fluid inclusions from fracture-filling calcite cement in the June Canyon sequence at Iks Canyon.

II. Lower Tectonic Slice of the Lower Thrust Plate

1. Mill Canyon Section

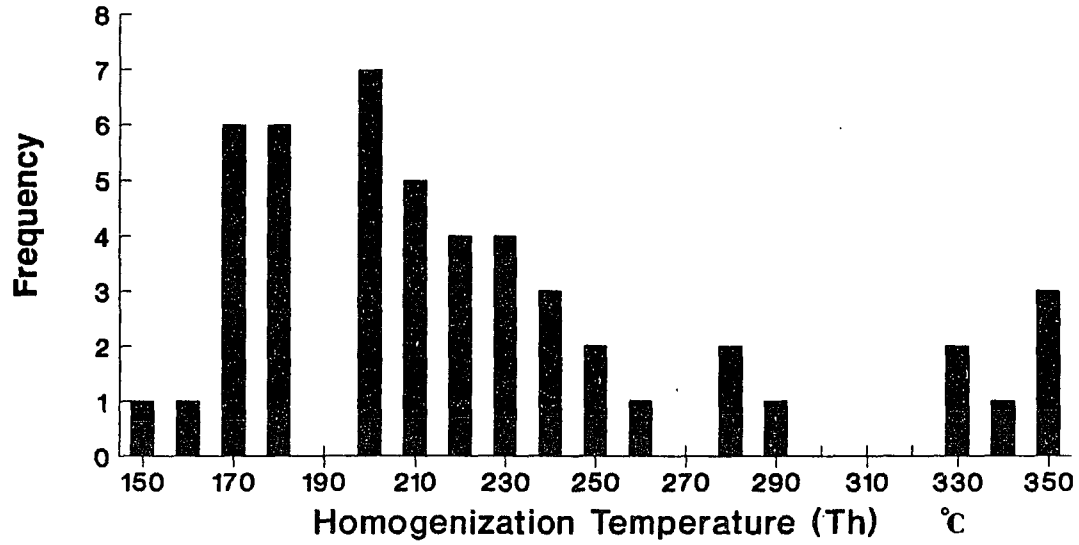
Homogenization-Temperature Data:

A total of 49 pressure-uncorrected homogenization temperature measurements were recorded from three fracture-filling calcite samples, and T_h values of these two-phase fluid inclusions generally range from 160 to 350 °C (Fig. 179). Four major T_h clusters occur in the following intervals: (1) from 160 to 180 °C, (2) from 200 to 260 °C, (3) 280-290 °C, and (4) 330-350 °C. The highest temperatures, ranging from 330 to 350 °C, represent stretched inclusions during heating experiments.

The temperatures range from 280 to 290 °C have been measured from inclusions with dark walls. Th values ranging from 200 to 260 °C generally occur near crystal boundaries where smaller two-phase fluid inclusions are scarce.

Freezing Data:

A total of ten last-melting temperatures ranging from -5.3 to -21.0 °C were measured. Indicated-melting temperature range corresponds to salinity content of 8.3 to 23.5 wt. % of equivalent NaCl (Fig. 180). The high T_h values have correspondence with a high salinity content of these inclusions. Eutectic temperatures (Te) range from -36 to -48 °C. The T_h values ranging from 160 to 200 °C have salinity content of 10 to 15 %; further increase in T_h corresponds to higher salinity in a diagonal trend (Fig. 180).



A total of 49 readings

Figure 179- Histogram of homogenization temperatures (T_h) of primary two-phase fluid inclusions from fracture-filling calcite cement in the Mill Canyon sequence in Iks Canyon.

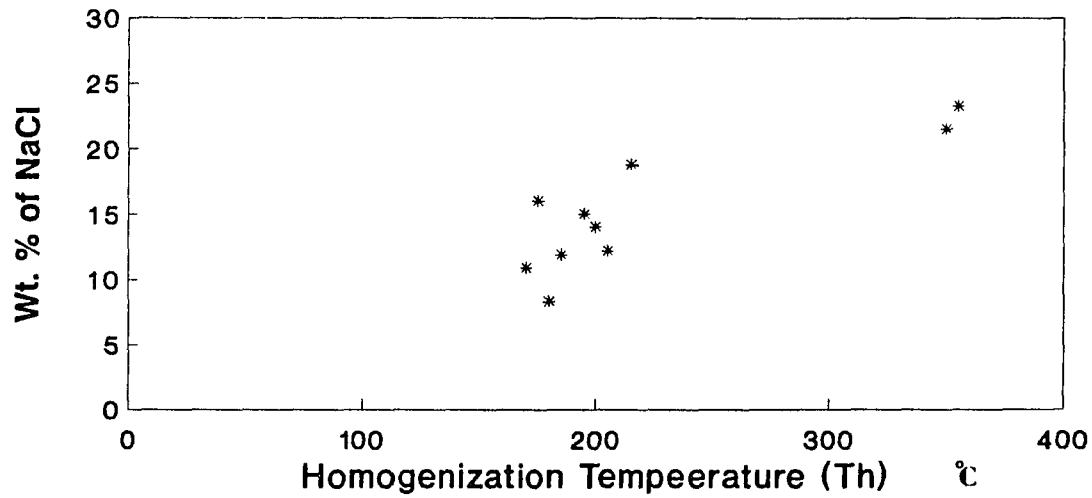


Figure 180- Plot of T_h versus salinity content of primary two- phase fluid inclusions in the Mill Canyon sequence in Iks Canyon.

Interpretation:

The isotopic composition and salinity content of the two-phase inclusions suggest that the fracture-filling calcite cements are late diagenetic and deep burial in origin.

In figure 180, the diagonal trend of T_h values and salinity contents suggests that two-phase fluid inclusions with T_h values of 160 to 180 °C from calcite cement had probably formed initially, and then were re-equilibrated by volume and compositional changes due to much greater burial depths than formation depth of these inclusions. The indicated-burial depth range was primarily caused by tectonic loading and westward-advancing clastic wedges of two orogenies, Antler orogeny and Sonoma orogeny, respectively.

Table 23- Estimated-maximum burial depths of the AVL from T_h values, in the Mill Canyon sequence.

Homogenization Temp. T_h °C	Maximum Burial Depth (km)	
	25 °C /km	30 °C/km
160 - 180	5.6 - 6.4	4.6 - 5.3
200 - 260	7.2 - 9.6	6.0 - 8.0

Composition of final solutions after re-equilibration is NaCl. MgCl can be inferred from the eutectic temperatures measured from two-phase fluid inclusions of this section (Crawford, 1981).

The estimated-maximum burial depths occur in the range of 6.0 km and 9.6 km (18 288 and 29 260 ft) from T_h values ranging from 200 to 260 °C. The maximum burial depth range from 8.0 to 9.6 km (24 384 to 29 360 ft) is estimated from 260 °C for geothermal gradients 30 C/km and 25 C/km, respectively. Th values ranging from 280 to 290 °C were not used for the fluid-inclusion microthermometry because of their darker boundaries which made the measurements difficult.

CHAPTER 19: CLAY DIAGENESIS AND ILLITE CRYSTALLINITY

A. Introduction:

Illite (water-free interlayers) and montmorillonite (water-bearing interlayers) mixed-layers commonly occur by alteration of the pre-existing micas and illites, hydrothermal reactions, alteration of volcanic glasses, and diagenetic modifications of montmorillonite (Weaver and Pollard, 1973). Illite has a lattice similar to mica. Illite becomes stable and commonly forms in an environment where the waters have a high K/H ratio (Garrels and Christ, 1965).

Changes in the composition of mixed-layer illite and smectite and ordering levels in their structure significantly vary from deep-burial diagenetic environments to metamorphic realms. The variations in these parameters are the responses to changes in the physical conditions of environments rather than geologic age and lithology. Perry and Hower (1970, 1972), Weaver and Beck (1971), Dunoyer de Segonzack (1970), Aoyagi and Kazama (1980), Sorodon and Erbel (1984), Elliot and Aronson (1986) and, Jennings and Thompson (1986) have shown that illite content progressively increases within the mixed-layers illite and smectite as the depth of burial increases. Aoyagi and Kazama (1980) have correlated the phase changes of these mixed layers with diagenetic alteration of zeolites and silica diagenesis under increased burial depth.

Generally, four-major assemblages and diagenetic sequences of I/S mixed layers have been recognized by these studies: (1) montmorillonite (Mo), (2) highly expandable mixed-layer minerals (ML_r and ML_o), (3) low-expendability minerals and frequently allevardite which contains 40-30 % expandable layers (ML_{ss}), and (4) IMII type ordering (also R3 or ISII ordering after Sorodon and Erbel, 1984), which contains 15-5 % expandable layers (Fig. 181).

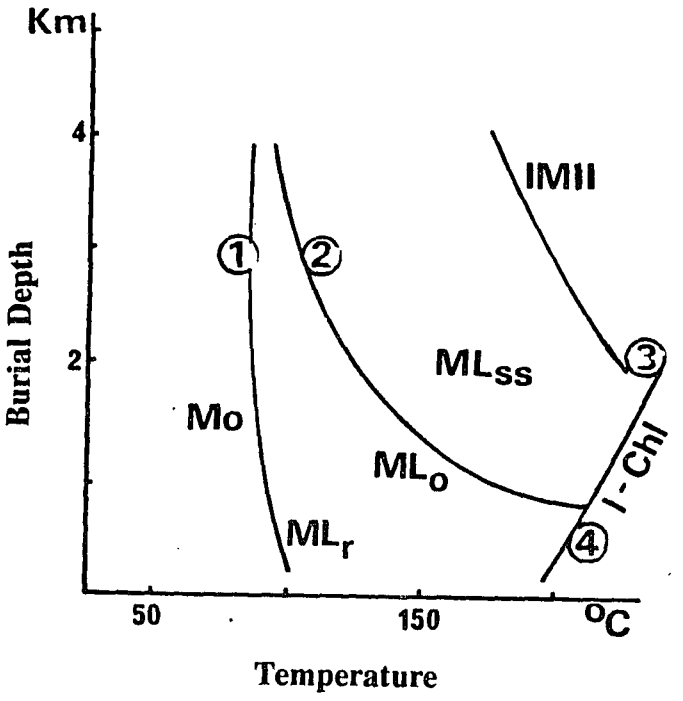


Figure 181- Diagenetic evolutionary phases in the Illite Smectite-mixed layers (Velde, 1981). Mo= fully expandable phases, ML_o= ordered-mixed layer structure, ML_{ss}=allevardite-type ordering, IMII= four-layer ordered (15-5) expandable structure, I= illite, Chl= chlorite, and numbers refer to phase field boundary.

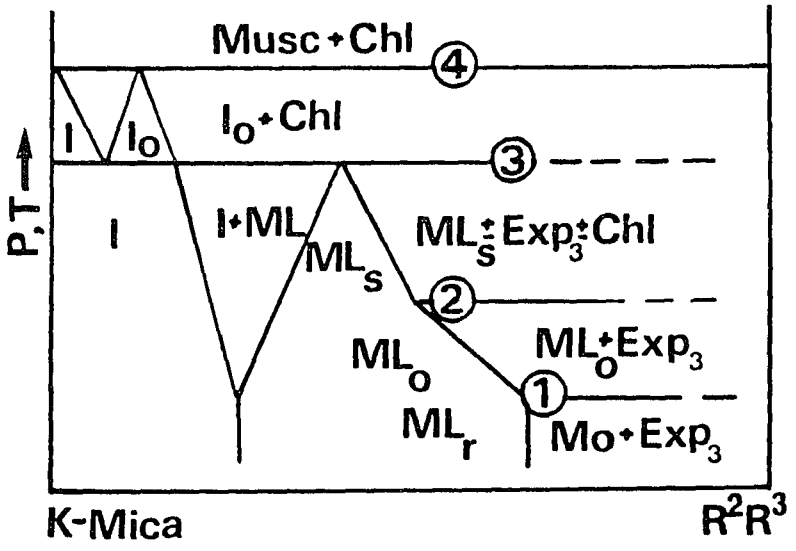


Figure 182- Generalized phase diagram and phase changes in non-binary chemical coordinates between muscovite-phengite (K-mica) and aluminous mineral such as chlorite (R^2R^3) through progressively increasing heat and pressure (Velde, 1981). I°=IMII-type phase. Exp_3= expandable trioctahedral minerals. Other symbols are the same in Fig. 181.

In illite and smectite-mixed layers, the presence of expandable layers (between 60-30 %) generally corresponds to temperature ranges of 80-120 °C (Weaver and Beck, 1971). The IMII type ordering represents the highest temperature range and the lowest expandable layers in the I/S mixed layers. Unexpandable chlorite minerals are commonly present in these mixed layers (Fig. 182; Velde, 1981).

The following studies attempted to determine the physical conditions at the upper limit of the IMII zone: 200 °C and 6 km of depth of burial (Hower et al., 1976); and 210 °C for 4 km (Boles and Frank, 1979).

In the diagenetically modified clay-mineral assemblages, the presence, gradual disappearance and total loss of kaolinite can also be indicative of certain temperature conditions as clay mineral index (Weaver and Pollard, 1973; and Jennings and Thompson, 1986). In this conjunction, kaolinite becomes metastable, starts to decompose at 150 °C and transforms into chlorite and illite; at 210 °C complete kaolinite loss occurs (Jennings and Thompson, 1986). As a result, clay-mineral assemblages become chiefly illite and chlorite with considerably less amount of smectite.

Furthermore, Nadeu and Reynolds (1981) showed that illitic composition increases with increasing proximity to intrusive rocks and decreases progressively away from these intrusives.

Weaver (1960), Kubler (1967), and Dunoyer de Segonzack (1970) observed that the shape of 001 illite reflections becomes sharper and narrower as the burial depth of clay-bearing lithofacies increase. It is well known fact that as temperature increases due to progressive depth of burial, not only does illite content increase, but also illite becomes well ordered and crystallized in the mixed-layer phase. The sharpening of the basal reflections of 001 illite peaks is probably due to increasing K_2O content in the phase (Dunoyer de Segonzack, 1970).

Illite crystallinity indices are commonly used for indicating the onset and end of Anchizone, which is a transitional zone between deep-burial diagenetic environments and the lower metamorphic zone "Epizone" (Kubler, 1967). Al/Fe+Mg ratios increase with crystallization of illite in the anchizone to epizone (Dunoyer de Segonzack,

1970). This trend has been confirmed by Kisch (1980), and Weaver and Broekstra (1984).

The indicated clay zones above were correlated with vitrinite-reflectance data by Kisch (1980), addition to these vitrinite reflectance, fluid-inclusion microthermometry by Frey et al. (1980), Duba and Williams-Jones (1983), and Pollastro and Barker (1986). I/S ratio and fission-track method for similar reasons were applied by Johnsson (1986).

Decrease of expandable layers in the I/S mixed-layers is comparable with an increasing maturation level of diagenetically irreversible organic matters. Guthrie et al. (1986) compared vitrinite reflectance with illite crystallinity and sharpness ratio to determine the generation and destruction of oil zones in the spectrum of sharpness ratio and crystallinity indices.

In this study, illite and smectite mixed-layers and their relative abundance, level of ordering, and corresponding assemblages have been determined and compared with fluid-inclusion and oxygen-isotope thermometry. The illite crystallinity indices and sharpness ratios and their aerial distribution have been used to determine aerial distribution and boundaries of anchizone and epizone in this region. Esquiven charts have also been used to determine the relationships among crystallinity indices, burial depths, and Al/Mg+Fe ratios.

B. Results:

In this study, clay particles of 2 μm and smaller were used for determining the illite crystallinity indices because 6-20 μm size particles might be derived from igneous and metamorphic unaltered-, and mixed-clastic mica. Therefore, the coarser fractions usually show much narrower peaks than fine-grained clay fractions, whereas 2μm and finer fractions are more authigenic fractions which represent diagenetic alterations (Kisch, 1980).

a) Peak Positions of Illite

Illite 001 peaks are invariably located in the range of 8.70-8.84° 2θ corresponding to 9.99-10.15 Å d-spacing (Fig. 183). At the same time, the 002 illite peaks are located between 17.68° and 17.78° 2θ corresponding to 5.01 and 4.99 Å (d-spacing, respectively (Fig. 183).

b) Peak Positions of Chlorite and Kaolinite

Chlorite peaks are most commonly located at the following ranges (Figs. 184, 185, 189): 001 chlorite peaks between 6.14 and 6.18° 2θ corresponding to 14.2-Å d-spacing; 002 chlorite peaks usually at 12.36° and 12.40° 2θ corresponding to 7.11-7.13 Å d-spacing; and 003 chlorite peaks between 18.60° and 18.70° 2θ corresponding to 4.74-4.75 Å d-spacing. Chlorites, in I.9, generally show weaker odd reflections as 001 and 003 compared to 002 even peaks (Fig.184) which can be explained as an increase in Fe/Mg ratio in the composition of the chlorite (e.g., Moore and Reynolds, 1987).

Kaolinite peaks usually occur at 12.28-12.32° 2θ and corresponding d-spacing is 7.20-7.17 Å (Figs. 185, 189). In the diffractograph, presence of first order chlorite reflection at 6.2° 2θ and third order reflections at 18.8° 2θ help to identify kaolinite form chlorite (Moore and Reynolds, 1987). In this study, 002 kaolinite peaks can not be defined because X-ray analyses were run between 3 and 19° 2θ.

c) Clay Mineral Assemblages

Clay-mineral composition commonly varies in the same vertical section due to different lithological composition; on the other hand from Whiterock Canyon to Toiyabe Peak kaolinite progressively disappears in clay-mineral assemblages due to increased burial depths. The percentages of each clay mineral on the Table 24 was

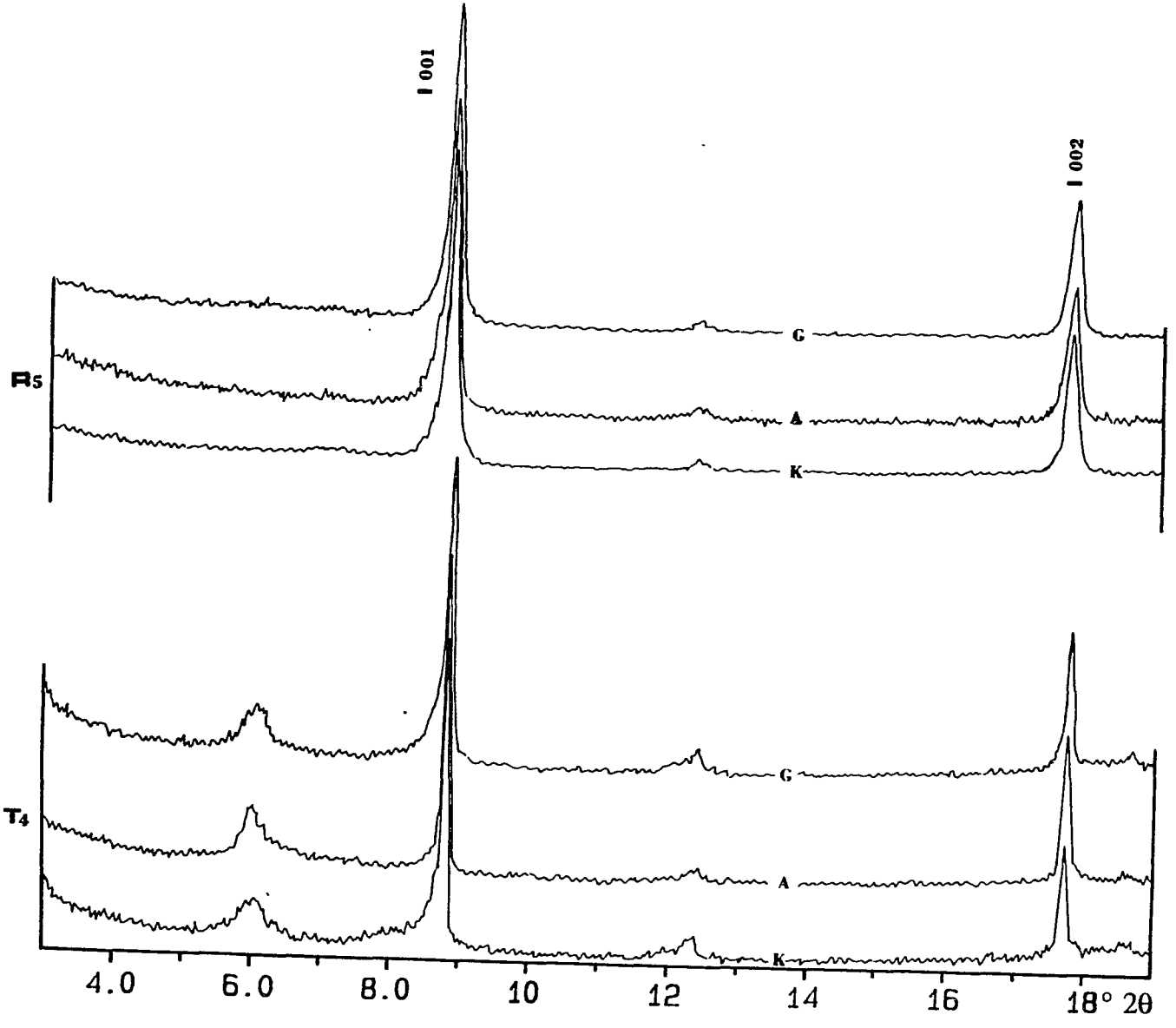


Figure 183- Position of illite peaks and effects of glycolation (G) on 001 illite peak position (10 Å) of air-dried samples (A), and effects of potassium (K) saturation on the 001 illite peak (10 Å).

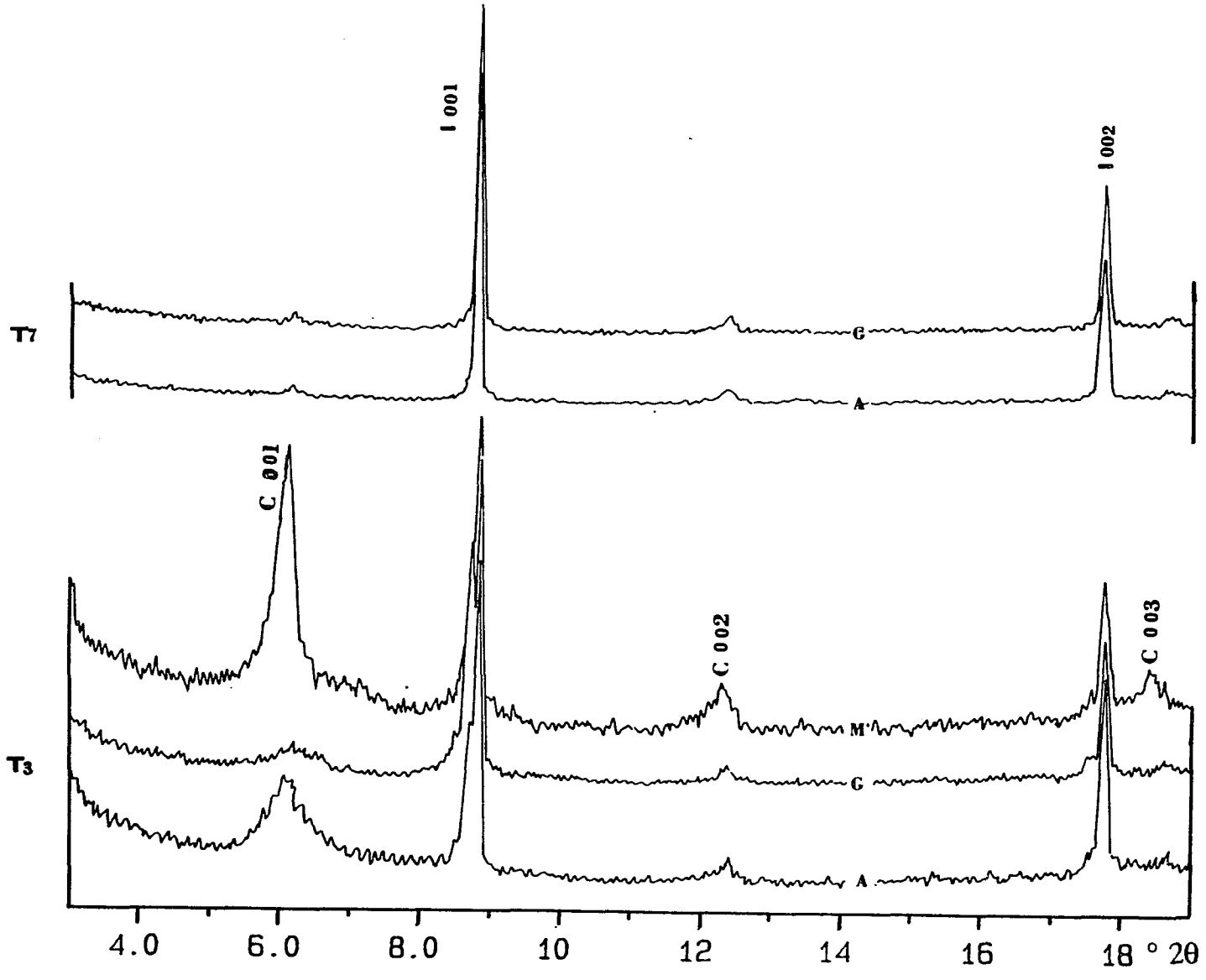


Figure 184- Position of illite peaks and effects of glycolation (G) and magnesium saturation (M) on the 001 illite peaks (10 Å) of air-dried samples (A).

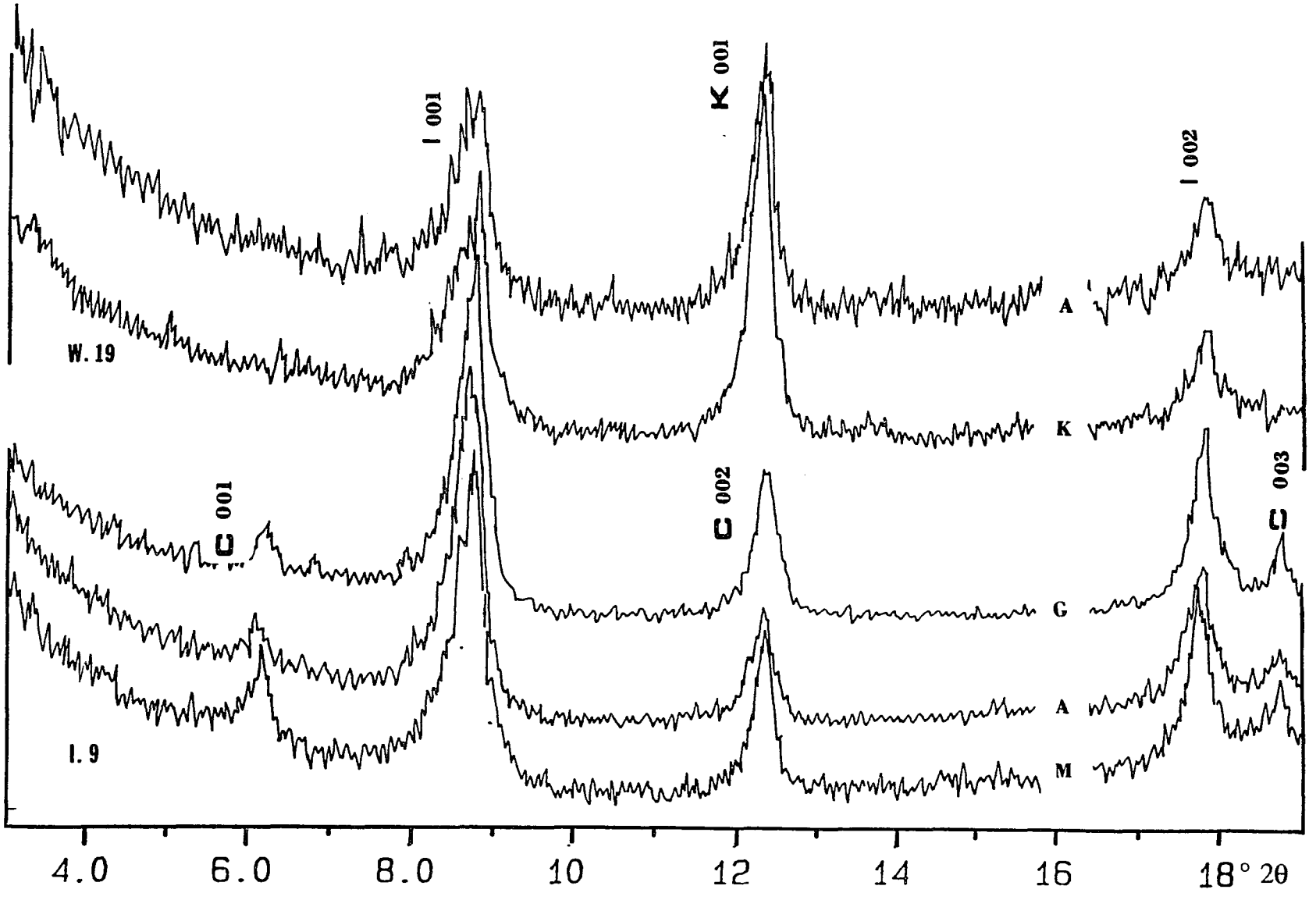


Figure 185- Position of illite (**I 00**), chlorite (**C 00**), and kaolinite (**K 00**) peaks, and the effects of K and Mg saturations (K, and M), and glycolation (G) on the position of their peaks in air-dried samples.

calculated from its intensity in the total amount (see Moore and Reynolds ,1987).

Table 24. Relative abundance of clay mineral assemblages in the various sections.

Sections & Samples	Muscovite (Phengite) %	I/S %	Chlorite %	Kaolinite %
K.14		45	25	15
W.19		43	7	50
I.5		30		70
I.7		46	25	29
I.9		67	22	11
I.37		47	48	5
Ml.4		100		
Ml.15		95	5	
R.1	100			
R.5	100			
T.2	91		9	
T.3	90		10	
T.4	95		5	
T.5	91		9	
T.6	65		35	
T.7	94		6	
T.10	90		10	

d) Effects of KCl and MgCl Treatments on 001 Illite Peaks: Variations in Illite Crystallinity.

Usually K-treated samples from the Tioyabe Range show sharper and narrower 001 illite peaks than the same peaks of the unsaturated- or air-dried samples. The difference in illite crystallinity indices by indicated methods range from 0.001 to 0.045°2θ (Figs.183, 184, 185). However, some samples in this Range also show the

broadening of 001 illite peak about in the range of 0.004 to 0.045° 2θ (Table 24).

Three samples were treated by $MgCl_2$. Two illite peaks of the Mg-saturated samples are sharper and narrower than Kcl-treated samples' 001 illite peaks, and one sample, especially in the Tioyabe Peak section, showed wider crystallinity indices than Kcl-treated 001 illite peaks (Figs. 183, 184).

In general, the widths of 001 illite peaks of air-dried samples are closer to those of K-saturated samples, but 001 illite peaks of the Mg-saturated samples are wider than the K-saturated samples' 001 illite peaks. This is probably caused by vermiculite and montmorillonite layers which are interlayered with illite.

Strong peak broadening by K^{+1} cation saturation is also attributed to the collapsed-expandable phases or interlayers in I/S mixed layers, which probably represent weathered illites with the strong cation deficiency (probably Ca and Na between the layers), or which was probably caused by the early HCl and H_2O_2 treatment (Kisch, 1980).

Kisch (1980) further suggested that half widths of 10.1 Å illite peaks of air-dried samples with grain size < 2 μm size fractions are not suitable for studying illite crystallinity because effects of acid extraction of these very fine-gained fractions is more effective than those of coarse illite fractions. For the indicated reasons, this study used the K-saturated illite 001 peaks and their half widths.

e) Effects of Glycolation

KCl-saturated samples were selectively treated with ethylene glycol in order to determine the content of expendable layers in I/S mixed layers, and they were heated until 350 °C. As a result of these processes, the following changes were observed on 001 first order illite peaks: in the Toiyabe Range, two samples show the broadening of 001 illite peaks in the range of 0.001-0.113° 2θ; and narrowing of the same peaks occur in the range of 0.002-0.046° 2θ (see Table 25, and Figs.183, 184, 185). For other regions, 001 illite peaks remained unchanged, or very slight changes occurred, such as in I.7 narrowing by as much as 0.019° 2θ. On the other hand, in W.19

broadening of this peak was as much as 0.400° 2θ.

All these above suggest that these samples are considerably higher in illitic composition within the I/S mixed layers; approximate illite content ranges from 85 to 90 % in the I/S mixed-layer structure (see Table 25).

Table 25- Effects of K^{+1}, Mg^{+2} cations and glycolation on 001 illite peaks, illite crystallinity indices (CI) and sharpness ratio from KCL-treated samples (WI).

Samp. No:	CI from air-dried samp. °2θ	CI from KCl-treated samp. °2θ	mm	CI from Glycol-treated samp. °2θ	CI from $MgCl_2$-treated samp. °2θ	WI °2θ
I.5A	0.700	0.698	8.8			2.1
I.7	0.659	0.618	7.8	0.618	0.539	2.2
I.9	0.530	0.478	6.0	0.459	0.458	2.5
I.37	0.478	0.518	6.5			2.3
Ml.4	0.780	0.379	4.8			4.0
Ml.15	0.278	0.359	4.5			4.5
K.14	0.438	0.518	6.5			2.3
W.19	0.577	0.960	12.0	1.359		1.9
R.1	0.156	0.152	1.9			16.2
R.5	0.217	0.195	2.5	0.196		10.8
T.2	0.135	0.150	1.9			10.8
T,3	0.154	0.172	2.2	0.295	0.254	12.8
T.4	0.150	0.154	1.9	0.152		12.8
T.5	0.172	0.130	1.6			26.0
T.6	0.196	0.151	1.9			20.0
T.7	0.147	0.146	1.8	0.100		21.0
T.10	0.156	0.150	1.9			17.4

f) Ordering Level of Illite and Composition of the I/S Mixed Layers

In all type sections, illite ranges from 90-100 % in the mixed layers I/S; this compositional range usually indicates a highly ordered texture (R=3 or R3), as seen in Table 26. Therefore, in all the sections, illite composition of I/S mixed layers varies between 85-95 percent which indicates a high degree of illitization. Illite percentages within the I/S mixture can be estimated from Table 7.3 of Moore and Reynolds (1987, p. 251), especially from the °2θ which is the difference between °2θ of 001 and 002 illite peak positions. In the Toiyabe Range, all the peaks of measured samples indicate a composition range from phengite to muscovite (e.g. Dunoyer de Segonzack, 1970).

Table 26- Illite content in the composition of mixed layers and its ordering level (R).

Samp. No:	Illite %	R	001 / 002		002 / 003		2Δ=°2θ(001)-°2θ(002)
			d(Å)	°2θ	d(Å)	°2θ	
I.7	90	3	10.04	8.80	5.00	17.72	8.92
I.9	95	3	10.10	8.74	5.00	17.72	9.02
I.15	90	3	10.08	8.76	5.00	17.72	8.94
I.37	95	3	10.08	8.76	5.00	17.70	8.92
K.14	90	3	10.11	8.74	5.00	17.68	8.94
Ml.4	100	3	10.06	8.78	5.00	17.72	8.94
Ml.5	100	3	10.06	8.78	5.00	17.70	8.92
W.19	90	3	10.04	8.80	5.00	17.72	8.92

g) I 002/ I 001 Ratio and Esquiven Charts

Esquiven in 1969 introduced a plot in which crystallinity indices versus intensity ratio of second-order 002 illite peaks and first-order 001 illite peaks correspond to the

ratio of Al/Mg+Fe (Dunoyer de Segonzack, 1965; and Kisch, 1980). The high concentration of Al in octahedral layers and of Na in interlayers reflects high

Table 27 Crystallinity indices (CI), sharpness ratio (WI) and intensity ratio of 5 Å and 10 Å illite reflections (I 002/I 001).

Samp. No:	CI from air-dried samp. °2θ	CI from KCl-treated samp. °2θ	mm	WI from KCl-treated samp. °2θ	Intensity Ratio (002 / I001)
I.5A	0.700	0.698	8.8	2.1	0.55
I.7	0.659	0.618	7.8	2.2	0.49
I.9	0.530	0.478	6.0	2.5	0.48
I.37	0.478	0.518	6.5	2.3	0.48
Ml.4	0.780	0.379	4.8	4.0	0.42
Ml.15	0.278	0.359	4.5	4.5	0.43
K.14	0.438	0.518	6.5	2.3	0.44
W.19	0.577	0.960	12.0	1.9	0.45
R.1	0.156	0.152	1.9	16.2	0.40
R.5	0.217	0.195	2.5	10.8	0.46
T.2	0.135	0.150	1.9	10.8	0.58
T,3	0.154	0.172	2.2	12.8	0.66
T.4	0.150	0.154	1.9	12.8	0.48
T.5	0.172	0.130	1.6	26.0	0.51
T.6	0.196	0.151	1.9	20.0	0.54
T.7	0.147	0.146	1.8	21.0	0.47
T.10	0.156	0.150	1.9	17.4	0.52

Table 27 clearly shows that I 002/I 001 ratio increases with increasing illite crystallinity (CI) and sharpness ratios (WI) from 0.42-0.43 in the Mill Canyon

Figure 186- Plots of illite crystallinity index and I 002/ I 001 ratio (Esquiven chart): relations between Al / Fe+Mg ratio and clay diagenetic and metamorphic zones.

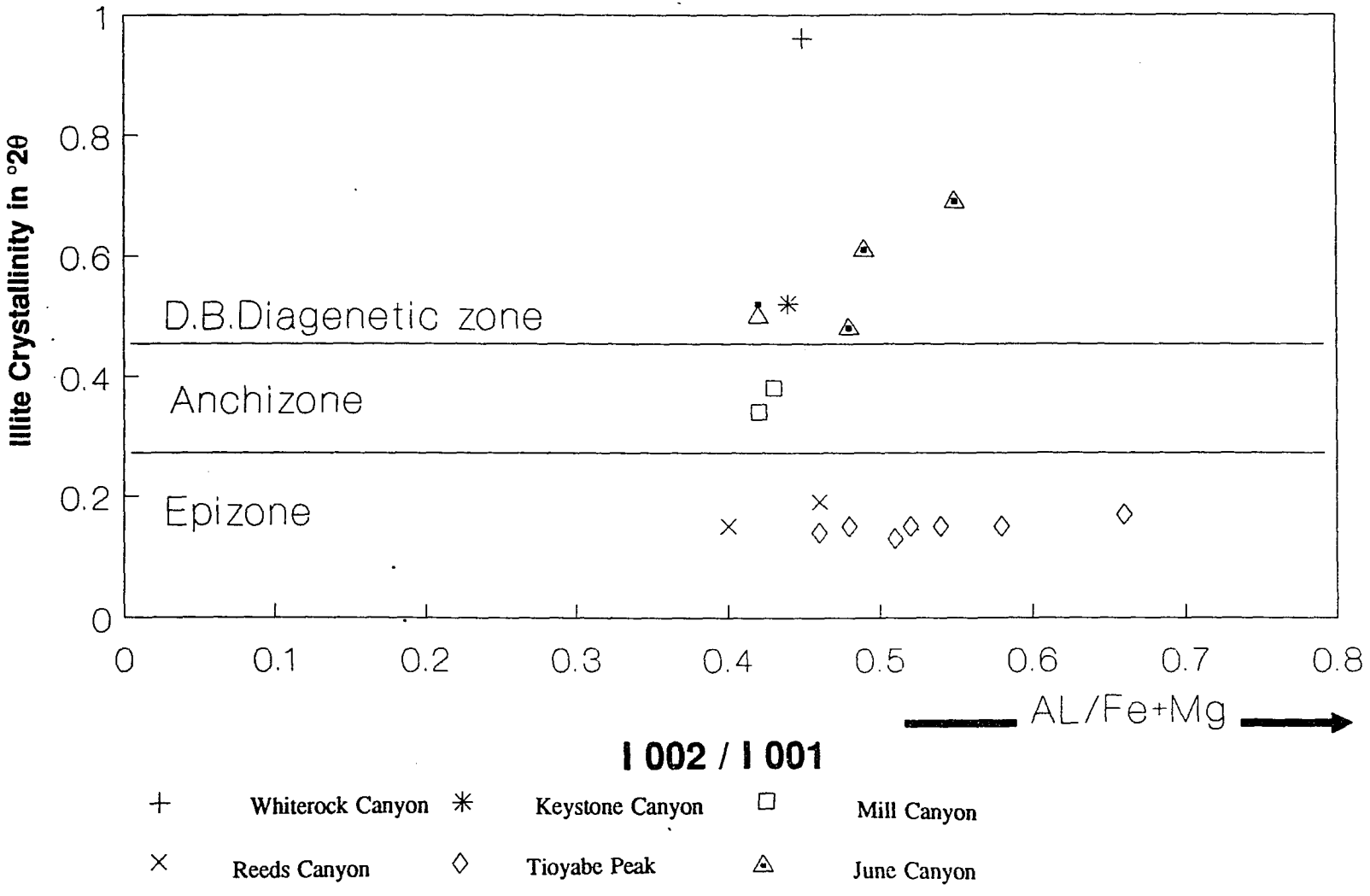
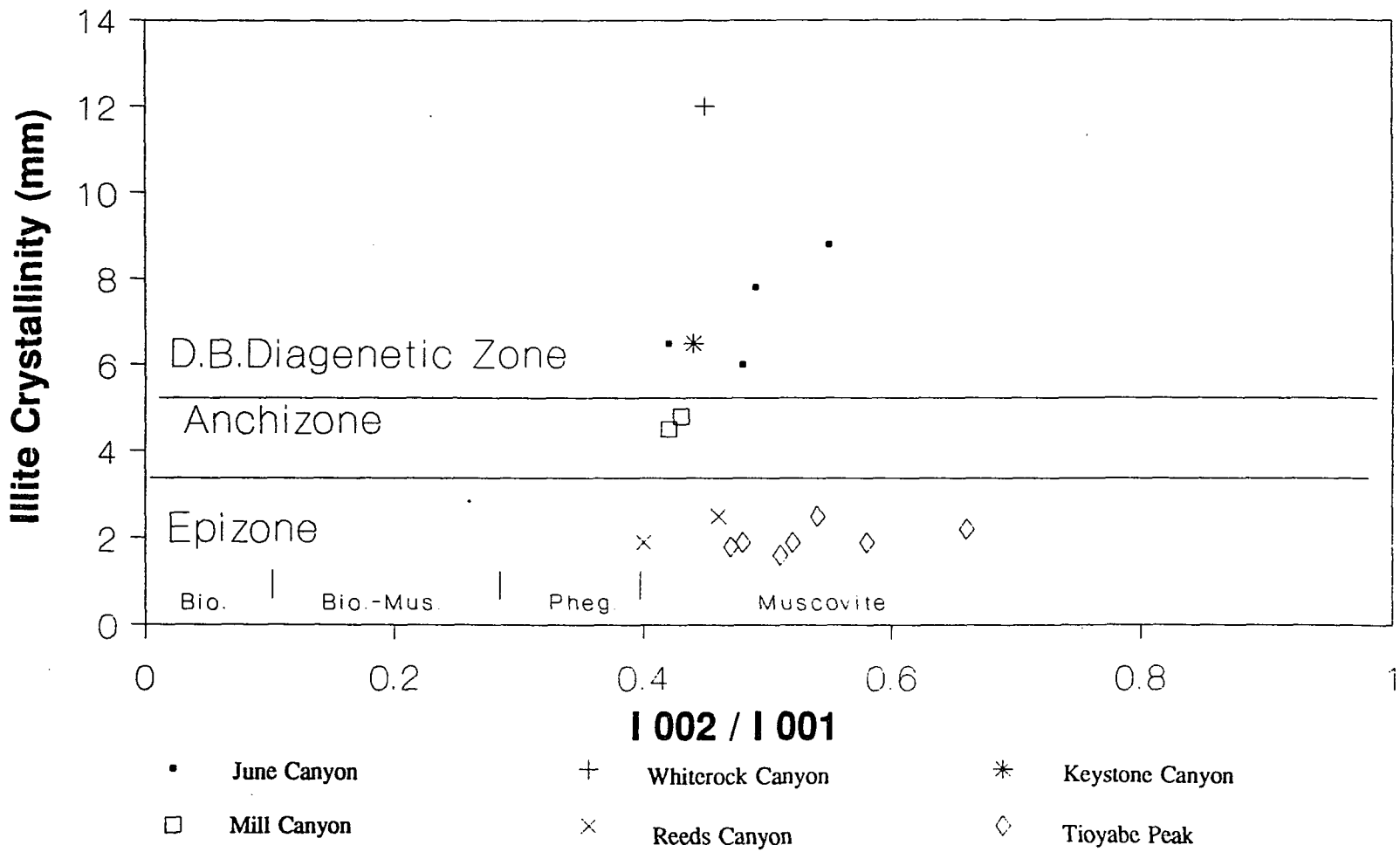


Figure 187- Plots of illite crystallinity index and I 002/ I 001 ratio (Esquiven chart): Mineral composition of mica minerals in epizone.



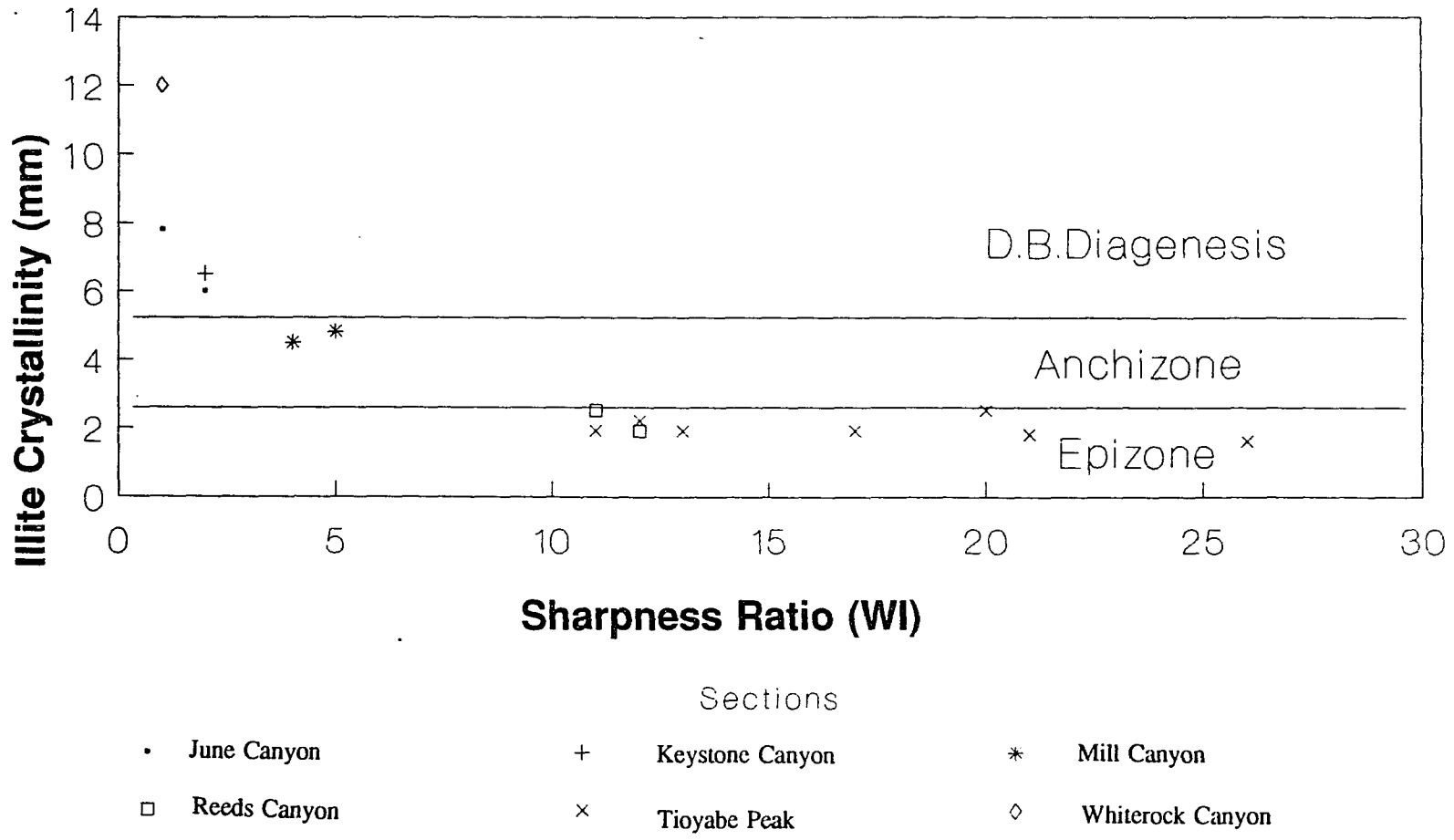


Figure 188- Plots of illite crystallinity index of Kubler (1966) and sharpness ratio of Weaver (1960): Boundaries of clay diagenetic and metamorphic zones.

sequence to 0.40-0.66 in the Toiyabe Range. Except two samples from the Reeds Canyon section have relatively low I 002/I 001 intensity ratio, ranging from 0.41 to 0.46, with a higher crystallinity indices between 0.152° 2θ (1.9 mm.) and 0.195° 2θ (2.5 mm).

From the Mill Canyon sequence in the Toquima Range to the Toiyabe Range, crystallinity indices, sharpness ratio of 10-Å illite reflections, and intensity ratio of I 002/I 001 exhibit an increasing Al/Mg+Fe ratio with increasing diagenetic and incipient metamorphic heating (Fig. 186).

Figure 187 shows that in the Reeds Canyon section intensity ratio of illite peaks corresponds to 0.4 which is considered to be low even though illite crystallinity of samples marks the beginning of muscovite and just the end of the phengite compositional zone (the anchizone). However, Tioyabe Peak samples primarily characterizes muscovite composition of the epizone, particularly "sericite" or paragonitic muscovite.

Figure 188 clearly demonstrates that parameters such as illite crystallinity indices (IC) of Kubler and the sharpness ratio (WI) of Weaver are consistent for indicating the diagenetic and submetamorphic zones.

Regional Distribution of Clay-Mineral Assemblages and Their Relations With Illite Crystallinity

a) Deep-Burial Diagenetic Zone

From Whiterock Canyon only one sample examined for clay diagenesis and crystallinity indices and sharpness ratio represents a moderate depth of burial. In W.19, despite high-ordering level (R3) of illites of the I/S-mixed layers, 10-Å illite peak has a low CI value of 0.90° 2θ (12 mm), and kaolinite content in clay mineral assemblages is significantly high about 50 % along with a 7 % of chlorite (Table 25).

Similarly, I.5 of the June Canyon sequence also shows low crystallinity index (CI) value of 0.7 °2θ (8.8 mm) and has 70 % of kaolinite in its assemblages (Fig. 189)

In other samples I.7, I.37 and K.14, and I.9, crystallinity indices, sharpness ratio and clay-mineral assemblages generally characterize the deepest part of deep-burial diagenetic environments, where diagenetic changes progressively transform into the anchizone (Fig. 189). As illite crystallinity indices of these four samples range from 0.61 to 0.47 °2θ, kaolinite content of these samples occurs in small amounts (5-29 %). Thus, these relatively high illite crystallinity indices are correlative with high illite and chlorite contents in clay- mineral assemblages. For this reason, clay-mineral assemblages and CI characterize a diagenetic zone which can be considered as an illite and chlorite zone. In the clay-mineral assemblages, types of the chlorites are still expandable in nature.

An other important trend being noted by this study is that the samples, particularly I.37, K.14 and I.9, show progressive narrowing and sharpening of 001 chlorite peaks 14.2 Å and this trend has correspondence with the crystallinity indices (CI) of the same samples (Table. 28).

As it indicated above, except for I.7, the rest of three samples characterize the transition zone between diagenetic and anchizone. This transition zone is chiefly characterized by predominance of illite and common occurrences of chlorite in the clay-mineral assemblages.

In addition to increasing depth of burial, precursor compositions of the carbonates are still important, and they had a great deal of influence on the composition of nonsoluble residue of shaley limestones, even though diagenetic changes are gradually becoming free from the dependence on lithology. In the June Canyon section, illite crystallinity indices of 10-Å illite reflections vary between 0.47 °2θ and 0.70 °2θ in four samples, not showing any appreciable relationship with increasing burial depth (Table 28).

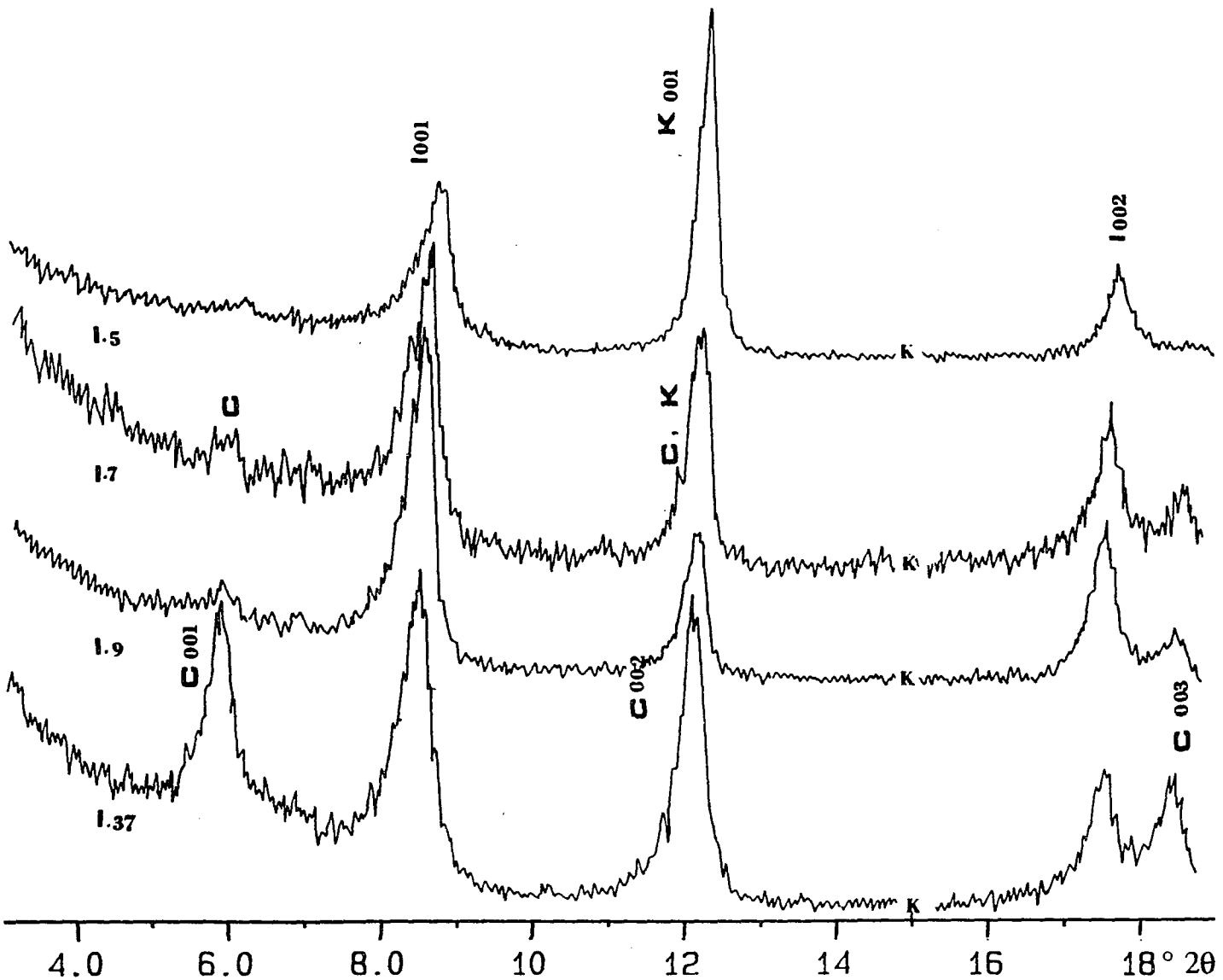


Figure 189- Position of illite peaks and assemblages of clay minerals in the K-saturated samples and their correspondence with clay content of the shale limestone samples from the June Canyon sequence.

Table 28- Illite crystallinity indices and half width of chlorite peaks at half height; June Canyon sequence (I), and Keystone Canyon section (K).

Sample No:	Crystallinity Index Chlorite °2θ	Illite °2θ	Sample No:	Crystallinity Index Chlorite °2θ	Illite °2θ
I.7	0.920	0.70	I.9	0.538	0.51
I.37	0.559	0.51	K.14	0.538	0.48

For example, I.37 was sampled at 700 feet above the base of the June Canyon section, whereas I.5 was sampled 20 feet above the base of the same section. Nevertheless, illite peaks from I.37 still retain about 0.20° higher crystallinity indices and narrower peaks than those of 10 Å peaks measured from I.5. This is believed to have been caused by original lithology types. For instance, in the AVL, samples from shaley limestone or shaley interlayers within the rhythmical beddings have greater CI's than those from the limestones and shaley limestones as well as dolomites. Carbonate rocks commonly exhibit a retarded-illite crystallinity because they are low in K^{+1} and Al^{+3} and high in Ca^{+2} and commonly low in permeability (Frey et al., 1980). In conjunction with this suggestion of Frey and others, this study suggests that high concentrations of fine-grained nonsoluble fractions intensify during compaction along the pressure solutions or stylolites which probably can function as only permeable paths allowing K^{+1} and Al^{+3} ions react with nonsoluble residue. However, lack of nonsoluble fine-grained fractions in the limestone enhances the neomorphism, without any permeability. Hence, the possibility of formation of new phases in clay-mineral assemblages is most likely to be impeded by very low permeability.

Permeability-enhanced high-crystallinity indices and assemblages have been noted in the sandstone and shaley units by Dunoyer de Segonzack (1970) and Duba and Williams-Jones (1983). Even though shale has a high Al and K content, it has lower

CI compared to sandstone and siltstone due to its lower permeability.

Presence and proportion of kaolinite in the clay-mineral assemblages is a significantly important indicator along with other parameters, such ordering level of illite (Rechivite= "R"), or presence of other expandable layers. Weaver and Beck (1971), and Weaver and Pollard (1973) show that kaolinite changes into illite and chlorite at 200 °C. A considerable amount of kaolinite conversion to illite and chlorite occurs at 180-194 °C, and at 210 °C kaolinite completely changes into more stable phases of clay minerals (Jennings and Thompson, 1986).

From the given information above, this study assumed that I.9 composed of a 5-9 % kaolinite may correspond to 190 to 210 °C degree temperature range, even a little higher than the indicated range above, and I.37, and I.7 probably represents a 180 to 194 °C temperature range. Since all the four samples underwent almost the same burial depths and physical conditions, we can take the highest crystallinity index of I.9 as the representative of the maximum burial depth of the AVL in the June Canyon sequence at Iks Canyon. The lower limit of R3 ordering of illite is believed to be at a 4.5 km depth range (Pollastro and Barker, 1986). The upper limit of the IMII or R3 ordering of illite is believed to occur in 200 °C and 6 km depth of burial (Hower et al., 1976); and 210 °C for 4 km (Boles and Frank, 1979). In the Central Poland Basin, Sorodon (1984) showed that illitization reaction considerably slowed down, after reaching the R3 (ISII) ordering and 10 % of expandable layers which are persistent at 200 °C and correlative with 3 % vitrinite reflectance.

As indicated above by various studies, the end of the deep-burial diagenetic zone and the onset of the anchizone may occur in the range of 210 to 220 °C. These temperature ranges from clay diagenesis and illite crystallinity show good agreement with pressure-uncorrected homogenization temperatures of this section ranging from 180 to 190 °C.

b) Anchizone

The anchizone is a transitional zone between the deep-burial diagenetic zone and metamorphic epizone. In the Mill Canyon sequence, two samples, Ml.4 and Ml.15, both have crystallinity ranging from 0.37 to 0.35 °2θ corresponding to 4.8 to 4.5 mm (Fig. 190), respectively. These crystallinity indices are much less than Kubler's CI value of 0.42 °2θ that marks the onset of the anchizone. Chlorite content is considerably less compared to June Canyon sequence ranging between 0 to 5 %. Intensity ratio of I 002 / I 001 peaks increases from the Iks Canyon region to the Tioyabe Peak region where CI is just below the 0.25 °2θ (see Kubler 1967) which is the lower boundary of the anchizone zone. In both samples Ml.4 and Ml.15, illite and phengite are the major constituents of the clay-mineral assemblages with a very small amount of the chlorite (Figs. 186, 190)

Illite + I/S = Al-Illite (muscovite) + chlorite **(I)**

The replacement of chlorite and calcite by mica makes the composition of the mica minerals change into phengite rather than illite (Weaver and Broekstra, 1984). This clearly explains why chlorite assemblages of the deeply buried facies (zone) almost entirely disappeared. At temperature range of 200 to 250 °C, illite become metastable, whereas phengite becomes stable (Weaver and Broekstra, 1984).

c) Epizone

This zone is characterized by the transformation of Al-rich illite to sericite (white mica). Illite crystallinity index (CI) of 0.25 °2θ marks the onset of this zone. Illite particles in micron size are generally transformed the micas (0.1 mm grain size) by re-arrangement of the ions in the lattice as well as by neomorphism of mica by crystal

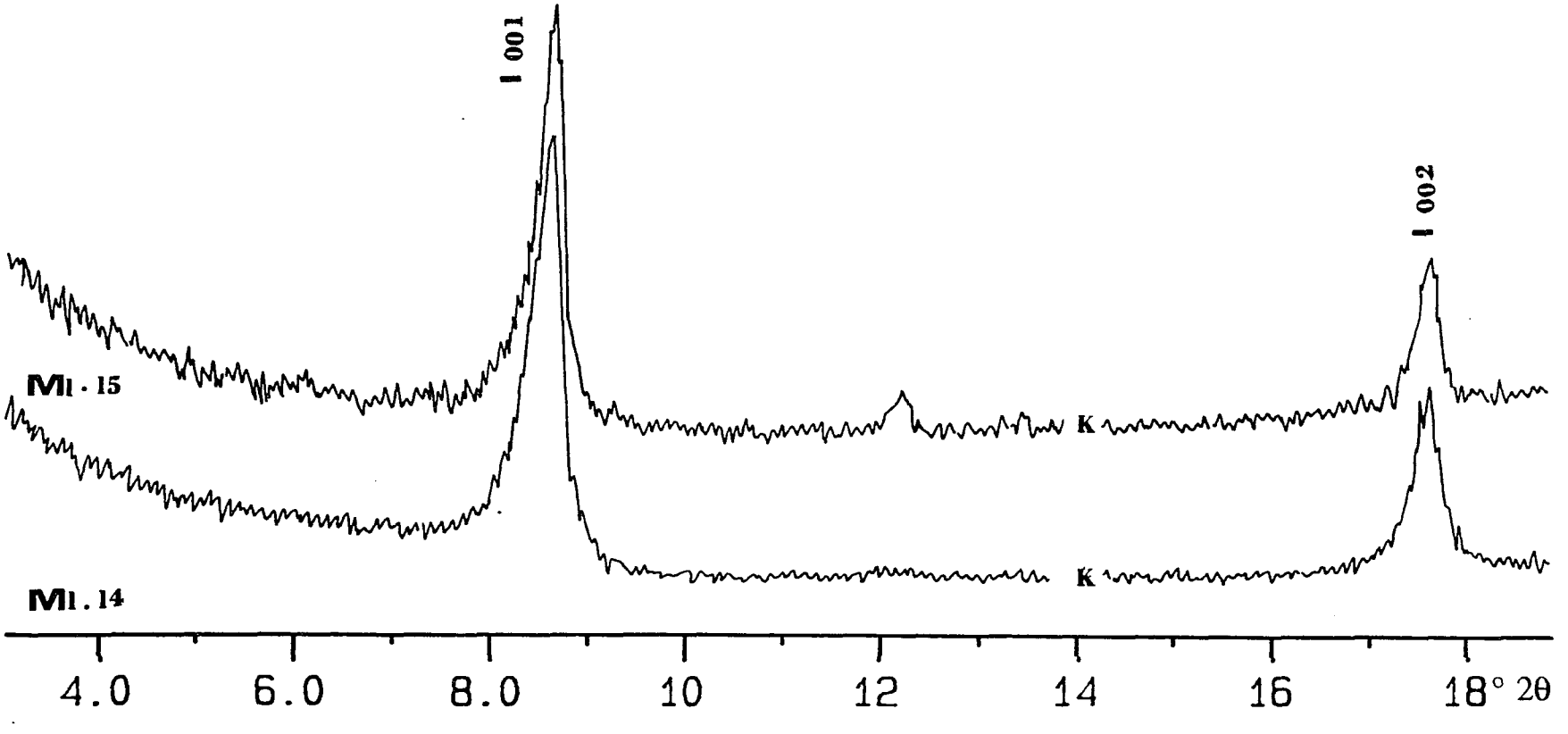


Figure 190- Position of illite peaks from K-saturated samples representing the anchizone of this formation in the Mill Canyon sequence.

growth (Dunoyer de Segonzack, 1970).

Al-illite + chlorite = Phengite + Al-chlorite (II)

The crystallinity indices (CI) of the nine samples from the Reeds Canyon and Tioyabe Peak section show highly crystalline indices ranging from 0.15 to 0.192 °2θ corresponding to a range from 1.9 to 2.5 mm (see Tables 25, 27). The variations in crystallinity indices prevail in both in spite of variations in depths and composition of shaley limestones. The indicated CI range ,thus, can not be attributed to the higher grade of metamorphism, but to the relative abundance of the illite and phengites (Kisch, 1980).

Chlorites are present in some samples with varying proportions generally in the range of 5 to 10 %, but one sample has nearly a 35 % of Al-rich chlorite (Table 24). Two samples from the Reeds Canyon section, samples R.1 and R.5, have intensity ratio 002/001 of 0.4 to 0.45 which probably represents the lower epizone (Tables. 25, 27; Figs. 186, 187, 188, 191). Other samples, intensity ratio I 002/ I 001 generally ranges from 0.48 to 0.66 represents muscovite compositions which are probably paragonitic Na-rich muscovites (Dunoyer de Segonzack, 1970; and Weaver and Broekstra, 1984).

Petrographic analysis of the samples, especially from the Toiyabe Peak, shows mica (sericite) or phengite lath, which are aligned with quartz minerals along the axial plain cleavage plain or slaty cleavage and postdate stylolites.

In addition to quartz and sericite, chlorite is an important component in the composition of shaley limestone that was identified from the X-ray diffractograph. Therefore, the epizone in the Tioyabe Peak region is represented by Illite + Quartz + Chlorite paragenesis which predominates the noncarbonate composition of the shaley limestone.

Calcite veins are usually intensely folded and calcite-filled fractures indicate an intensified granulation and new-mineral formation along the twin lamellae and kinking (Figs. 192 and 193). Moreover, along the calcite lamellae, new calcite minerals form, and rotation of the crinoidal fragments causing the formation of pressure shadows which are characteristic of the dynamic metamorphic zones and also indicate the

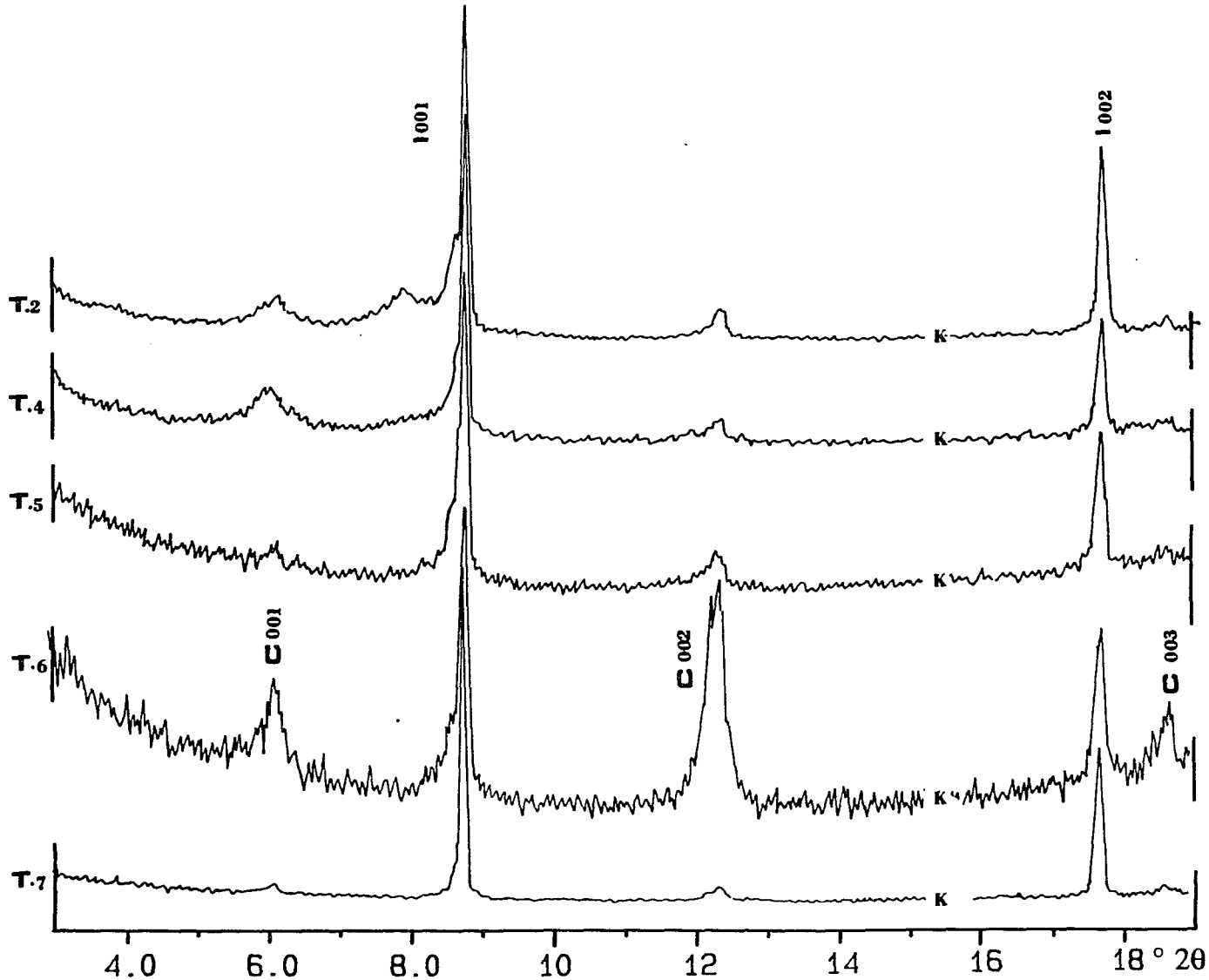


Figure 191- Position of 001 illite peaks (10 Å) and clay-mineral assemblages from K-saturated samples, representing the epizone, of this formation in the Toiyabe Peak.

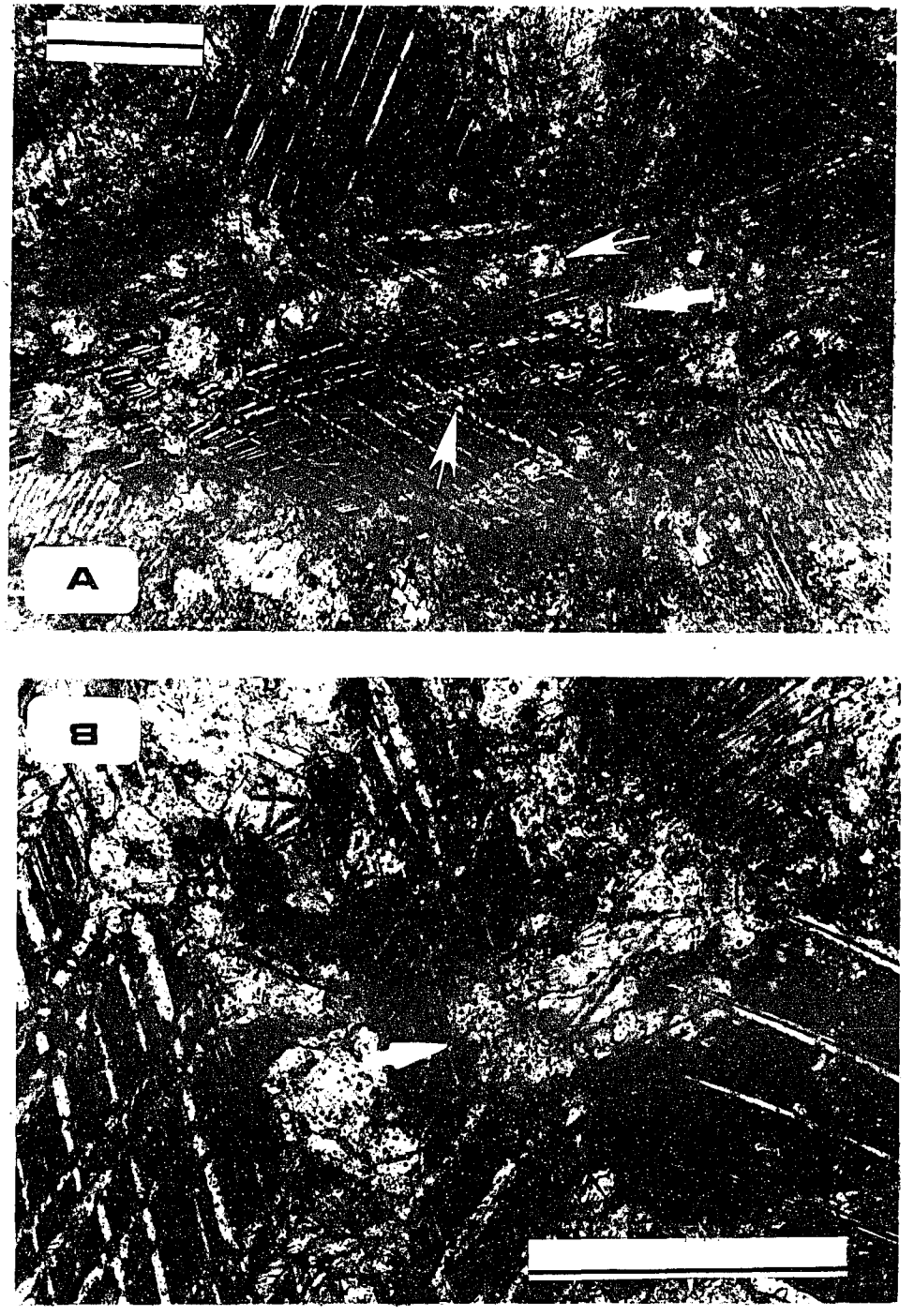


Figure 192- Photomicrographs showing advanced deformation and recrystallization on fracture-filling calcite cement. A) Arrows point to new calcite crystals which formed along the twinning and kinking zones. B) Highlighted view of kinking zone where relatively smaller calcite crystals forming and replacing the intensely twinned and kinked megacalcite crystals. Under cross-polarized light; scales= 0.5 mm.

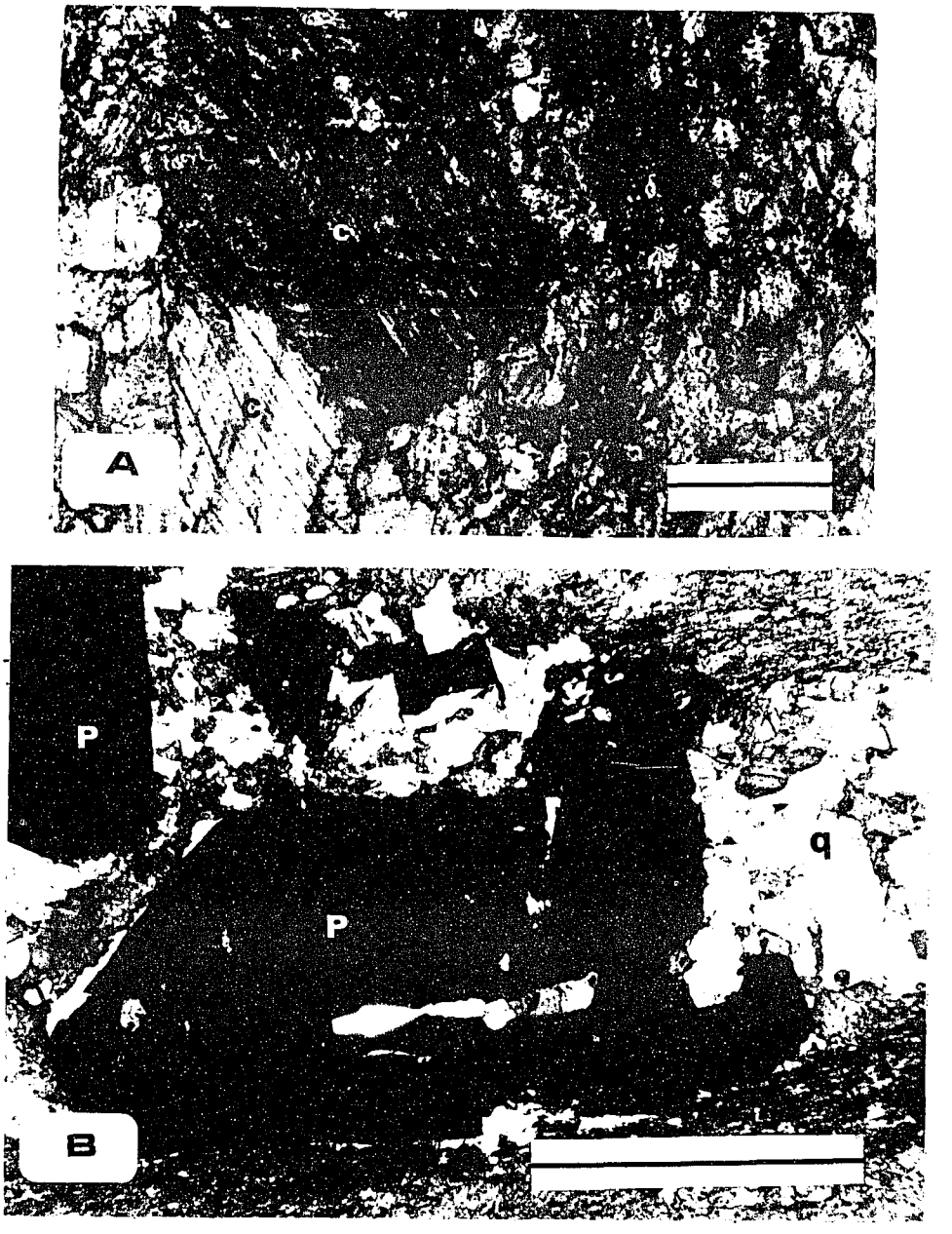


Figure 193- Photomicrographs showing deformation of calcite crystals, slaty texture, and related mineral paragenesis. A) Advanced-deformation on calcite crystals of the crinoidal packstone units of the slaty limestone occurred by elastic grain diminution (c_g) of large calcite spars or allochems (c). B) Authigenic pyrite crystals (P) scattered within the slaty AVL and poikilotopically included the recrystallized quartz (q) which also has planar crystal boundaries with the recrystallized quartz mosaic. Under plane-polarized light, scales= 0.5 mm.

increased deformation far beyond the field of diagenesis.

Formation of large euhedral pyrite crystals (Fig. 193 B) was probably related to expulsion of hot-basinal fluids during the thrusting events of the Sonoma orogeny. These pyrite crystals also poikilotopically include recrystallized quartz and calcite crystals (Fig. 193 B). The clay-mineral paragenesis of the AVL in the Toiyabe Peak indicates the pre-green schist mineralogic assemblage that is commonly seen in slaty units. Chlorite polymorphs in this paragenesis are likely to be Al-rich chlorites which coincide with the lithological change from shale to slate or transition of 1M to 2M polymorph illite or mica types. These assemblages especially with the dominance of 2M polymorph type indicate 7th metamorphic grades of Hoffman and Hower (1979), which correspond to burial temperature of 300 °C for the upper Mesozoic and lower Tertiary rocks.

C. Synthesis

In sedimentary basins, diagenetic heating is a function of the magnitude of burial depths and geothermal gradients. In addition to normal sedimentation-induced subsidence, thrust-induced pressure and expulsion of K^{+1}1 and Al^{+3} rich water from the shaley units are also equally important during the course of diagenetic and high-grade transformations (e.g., Elliot and Aronson, 1987; and Oliver, 1986).

Sorodon and Erbel (1984) showed that reaction time and composition of rock- and pore fluid with respect to K^{+1} also play a significant role for the illitization of mixed layer and transformation of the metastable clay minerals into the more stable phases. For example, abundance of K^{+1} and their reactions in the Gulf Coast were compared with the Central Polish Basin, and they found that semectite-illite transition in the Gulf Coast ceases when expandable layers reaches 20 % in composition. On the other hand; in the latter, expendable layers are consumed up to less than 10 percent (Sorodon and Erbel, 1987). This trend in the central Polish Basin is attributed to the abundance of

K^{+1} supply in the basinal mudstone which is composed of detrital clay-rich minerals and K-feldspars.

On the basis of all these case studies indicated above, this study suggests that combined effects of thrusting and depth of burial played a considerably important role for illitization of the mixed-layers and phase transitions from diagenetic, through anchizone and to epizone. Probably K^{+1}-rich basinal brine flushed into this region by thrusting during the Antler and Sonoma orogenies. However, we do not have any evidence to support this suggestion on the regional scale.

Kisch (1980) indicated that onset of the anchizone occurs at the illite peak 0.40° 2θ which corresponds to 2.6 % vitrinite reflectance. Frey et al. (1980) have shown that onset and end of the "anchi"-metamorphic zone occurs in the following illite crystallinity (IC) ranges: 7-9 mm correlative with Rm % of 2.5 and 3 % which was assumed to represent the minimum temperature at 200 °C; the end of anchizone CI 4.5-5 mm and 4.5 to 5 Ro %, the high-grade anchizone, corresponding to 270 °C. Duba and Williams-Jones (1983) have indicated that anchi-metamorphic zone occurs between 0.42 and 0.24 °2θ illite crystallinity index, and 0.24 °2θ CI correlative to R_o% = 4.6 which corresponds to 300 °C and marks the end of the anchi-metamorphic zone. Distinction between diagenesis and first metamorphic zone (anchizone) in pelitic rocks is based on CI value of 0.42 °2θ and borders between anchizone and epizone, defined at CI value of 0.25 °2θ (Kubler, 1966; and Weaver and Broekstra, 1984). The temperature range of the indicated crystallinity indices (CI) for the onset and end of the anchizone is estimated to occur in the range of 250 to 280 °C and 360 °C, respectively (Weaver and Broekstra, 1984). Expandable illite/ smectite mixed layers are estimated to be 10 % end of the diagenetic zone and gradually decreases to 0 % at the end of the anchizone and onset of the epizone (see Weaver and Broekstra, 1984).

In this study, the boundaries of the anchizone are estimated to occur in the following temperature ranges:

Diagenetic zone to Anchizone = 220 ± 10 °C;

Anchizone = from 220 ± 10 to 320 ± 10°C;

Epizone = 320 ± 10 °C and above.

Table 29- Clay mineral assemblages and illite crystallinity indices and corresponding pressure-uncorrected T_h values.

Measured Sections	Ill. Cryst. (CI) Aver. °2θ	Max. °2θ	Temperature °C CI	T_h	(R)	Clay Mineral Assemblages
Keystone Can.	0.51	----	200-210	-------	R3	I, I/S, Chl, Ver
Whiterock	0.96	----	170-190	170-190	R3	I, I/S, Kao
June Can.	0.57	0.47	200-210	170-190	R3	I, I/S, Chl, Kao
Mill Can.	0.36	0.35	220-280	240-260		I, Phengite
Reeds Can.	0.17	0.15	320-360	240-290		Mica (Ser), Chl
Tioyabe Peak	0.16	0.14	320-360	240-290		Mica (Ser), Chl

Therefore, estimated paleotemperature values of the anchizone for the AVL at the indicated sections occur in a closer range with the estimated-temperature range suggested by Frey et al. (1980) and Duba and Williams-Jones (1983). However, these suggested-temperature ranges, including this study, are considerably lower than those of temperature ranges suggested by Weaver and Broekstra (1984). It is likely that indicated temperature differences on the onset and end of anchizone can be attributed to lithology type, to the composition of interstitial fluids, and to geothermal gradient.

Illite crystallinity, intensity ratio of I 002 / I 001, and clay-mineral assemblages of the Antelope Valley Limestone at the Toiyabe Range and Mill Canyon sequence of the Toquima Range characterize epizone and anchizone, respectively. The maximum, pressure-uncorrected homogenization temperature of two-phase fluid inclusions is 260 °C which is consistent with the estimated-temperature range in the anchizone. In this study, estimated temperature marking the end of the anchizone is believed to occur at 320 °C, which is slightly higher than 300 °C suggested by Duba and Williams-Jones (1980), but lower than 360 °C (e.g., Weaver and Broekstra, 1984).

In the June Canyon sequence, the highest temperature reported indicates threshold of the anchizone with crystallinity index of 0.47 °2θ. CI values and pressure-uncorrected maximum T_h value of 190 °C of two-phase fluid inclusions appear to be consistent. This temperature range is closer to temperature ranges of 200 °C and 220 to 240° C for the onset of anchizone suggested by Frey et al. (1980) and Duba and Williams-Jones (1980), respectively. In this study, it is suggested that TAI levels are not reliable, particularly in the lower Paleozoic rocks Nevertheless, large numbers of T_h values from two-phase fluid inclusions and illite-crystallinity data can provide more reliable geothermometry ranges than those of geothermometries established from illite crystallinity or sharpness ratio and oxygen-isotope thermometry (e.g., Weaver and Broekstra). Also in this study, it has been clearly shown that there are serious problems in application of oxygen-isotope thermometry (see Chap. 17). For the indicated reasons, temperature ranges for the onset and end of the anchizone offered by this study appear to have advantages over the proposed-temperature ranges by Weaver and Broekstra, 1984).

In this formation, similarly high T_h values were reported elsewhere in the study area; however, absence of the high-crystallinity level can probably be attributed to absence of dynamic metamorphism at that particular region which was primarily created by superimposed multi-thrust plates of Antler and Sonoma orogenies. Thus, thrust-induced directed pressure along with increasing lithostatic pressure probably enhance the transformation by expulsion of K^{+1}, $Al^{+3,}$ and Fe^{+2}-rich interstitial solutions.

CHAPTER 20: COMPARING THE RESULTS OF GEOTHERMOMETRIES

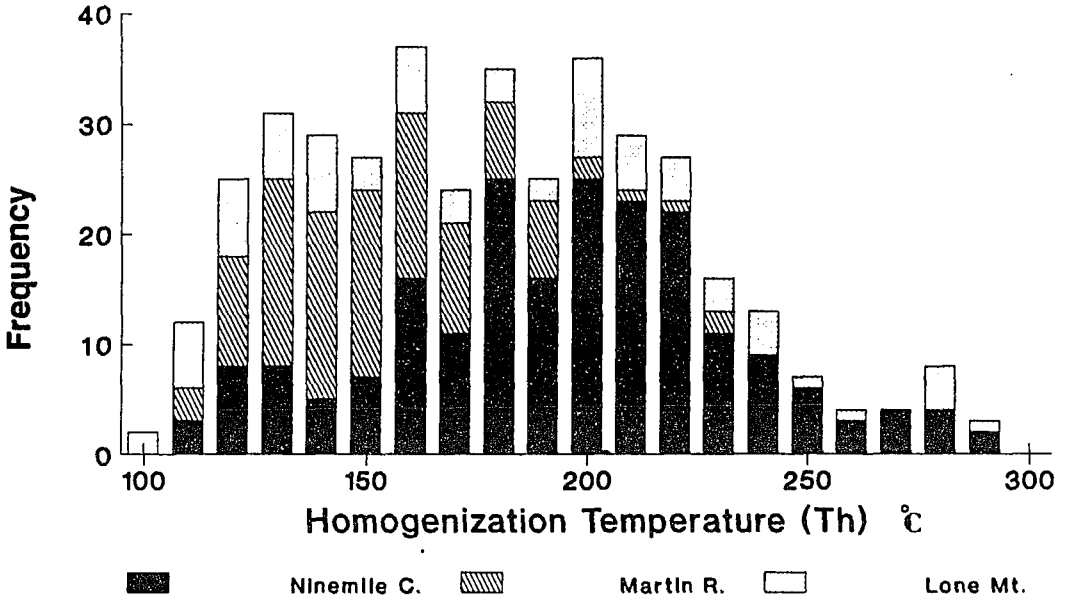
A. Results:

The Antelope Valley region

As indicated before, determination of maximum paleo-burial temperature range for the Antelope Valley region was primarily based on homogenization temperatures of two-phase fluid inclusions (Table 31; Fig. 194). Other geothermometries, such as oxygen isotope and thermal alteration level of organic matter, used along with fluid-inclusion microthermometry are inconsistent with T_h range and maximum burial-depth range of the AVL estimated from the subsidence curves reconstructed from the regional stratigraphic units (Table 31).

Table 31- Maximum-burial temperatures of the AVL estimated from various geothermometries in the Antelope Valley region.

Vertical Type Sections	TEMPERATURE				
	Fluid Inc. (T_h) °C	$\delta^{18}O_{water}$ SMOW +5 °C	+9 ‰ °C	**Organic Met.** Measured °C	Esti. °C
Lone Mountain	218 - 256 260 - 290	130 179	188 253	178	319
Martin Ridge	160 - 230	102 137	148 188	173	319
Ninemile Canyon	190 - 240 255 - 290	103	143		319



A total of 393 readings

Figure 194- Histogram of homogenization temperatures (T_h) of primary two-phase fluid inclusions from fracture-filling carbonate cements in the Antelope Valley region.

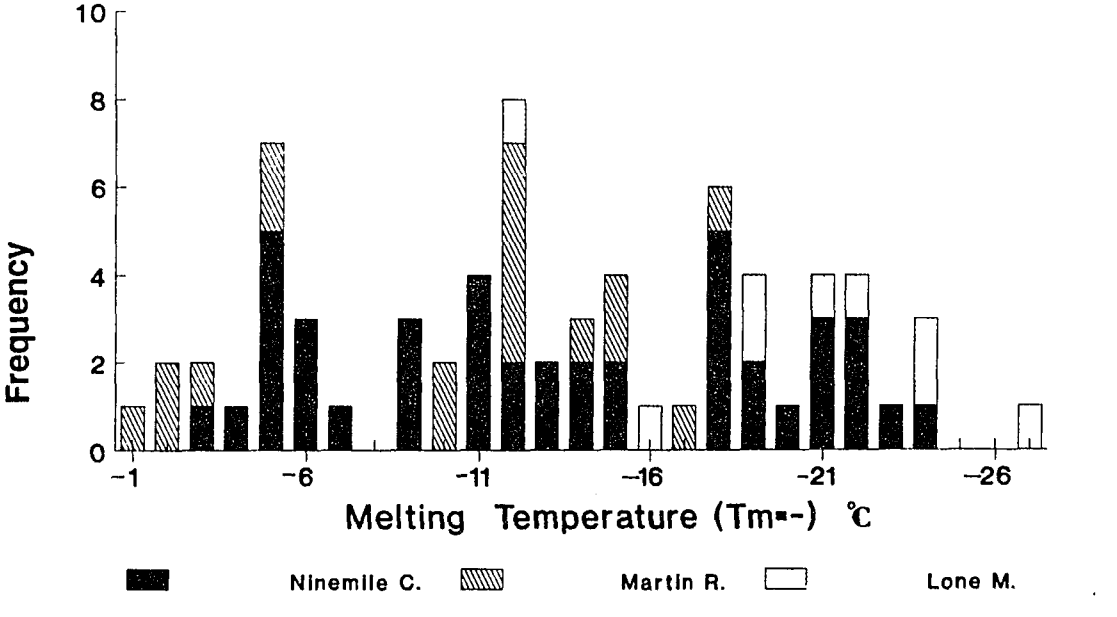


Figure 195- Histogram of Melting temperatures (Tm) of primary two-phase fluid inclusions from fracture-filling carbonate cements in the Antelope Valley region.

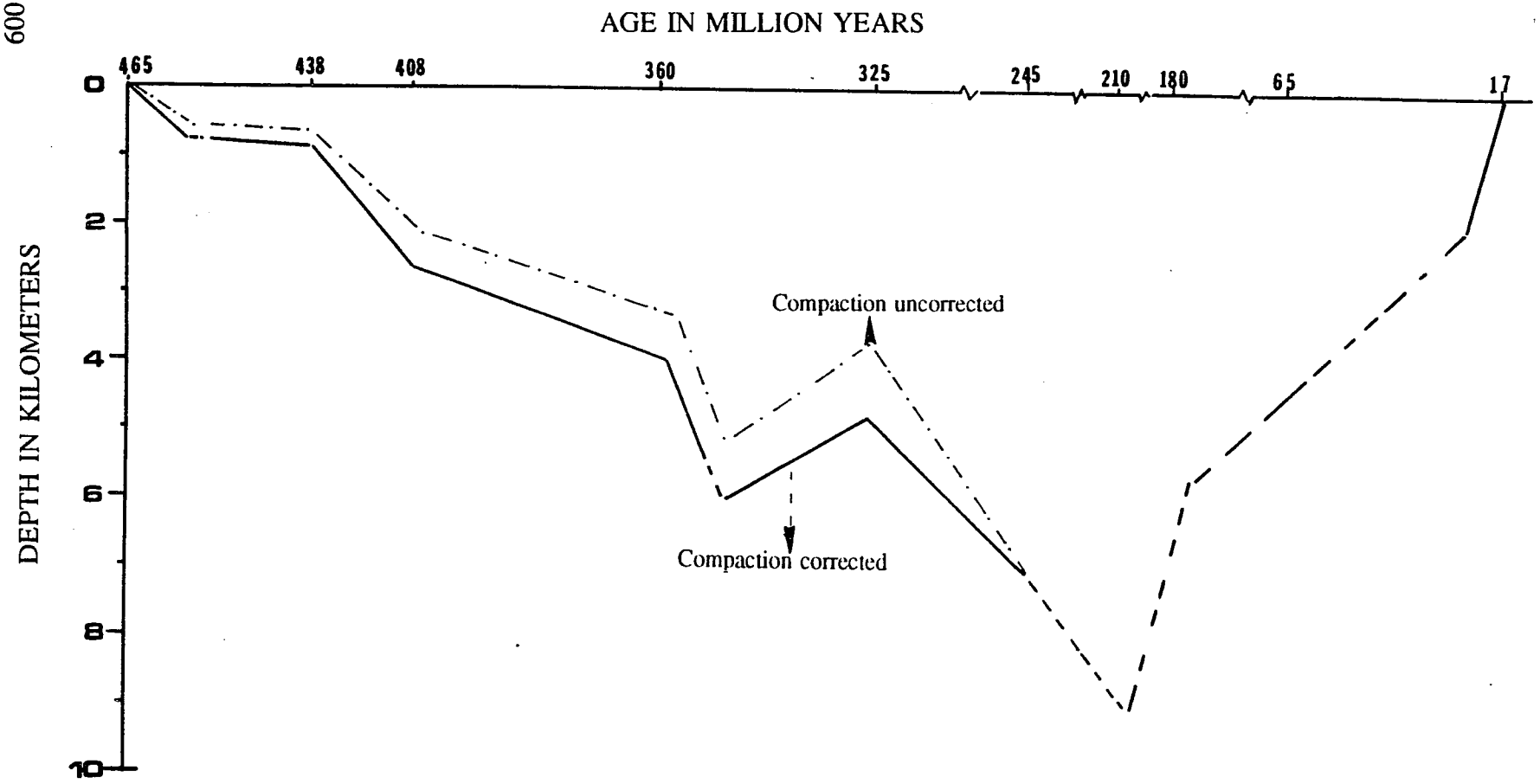


Figure 196- Burial-history diagram of the Antelope Valley Limestone in the Antelope Valley region and Eureka district. The compaction-corrected subsidence curve was constructed on the basis of calculations given in Angevine and Heller (1987).

General T_h values for the Antelope Valley region range from 100 to 290 °C (Fig. 194), and melting temperatures of these fluid inclusions cluster in three ranges (Fig. 195): (1) -1 to -8 °C; (2) -10 to -16 °C; and (3) -18 to -23 °C.

Maximum burial depth of the AVL from the pressure-uncorrected T_h maximum values of 260 to 290 °C is estimated to have ranged from 8.0 to 9.0 km for 30 °C/km and surface temperature of 20 °C (Table 32). The burial depth range of 8.0 to 9.0 km is also in a good agreement with the maximum burial depth of the AVL in the reconstructed-subsidence curve (Fig. 196). In the Antelope Valley region, the removed post-Devonian strata are almost equal to 4.3 to 5.3 km in thicknesses (Table 32).

A total uplifting of Middle Ordovician Antelope Valley Limestone at the present elevations in the Lone Mountain, Ninemile Canyon and Martin Ridge sections is estimated to range from 10.1 to 11.1 km, 10.5 to 11.5 km, and 10.1 and 11.1 km, respectively (Table. 32).

Table 32- Maximum burial depths of the AVL, removed post-Devonian strata, and total uplifting of the AVL estimated from maximum T_h range and other geothermometries in the Antelope Valley localities.

T_h Range °C	Maximum Burial Depth of the AVL (km)	Maximum Removed Post-Devonian Strata (km)	A Total Uplifting Range of the AVL (km)
260-290	8.0 to 9.0	4.3 to 5.3	10 to 11

Compaction-corrected maximum-burial depth range of this formation from the reconstructed subsidence curve is about 7 km which is very close to 9 km of maximum burial depth range estimated from T_h max. range (Fig. 196). The second highest Th is 260 °C which corresponds to 9.6 km of burial depth for geothermal gradient 25 °C/ km. Therefore, 9 km of burial depth is a conservative estimate for the maximum burial depth of the AVL. The reconstructed-subsidence curve is based on the present-day stratigraphic unit, including Permian age and older but not Triassic and

Jurassic rocks (Fig. 196) because these stratigraphic units were eroded and are not present in the study area and vicinity. According to geodynamic history of this region, the maximum burial-depth range of the AVL was reached after the Lower Triassic or may be during the Triassic due to an eastward-advancing clastic wedge which originated from the Lower-Triassic Upland produced by the Golconda thrusts during the Sonoma orogeny of Late Permian and Lower Triassic (Steward, 1980).

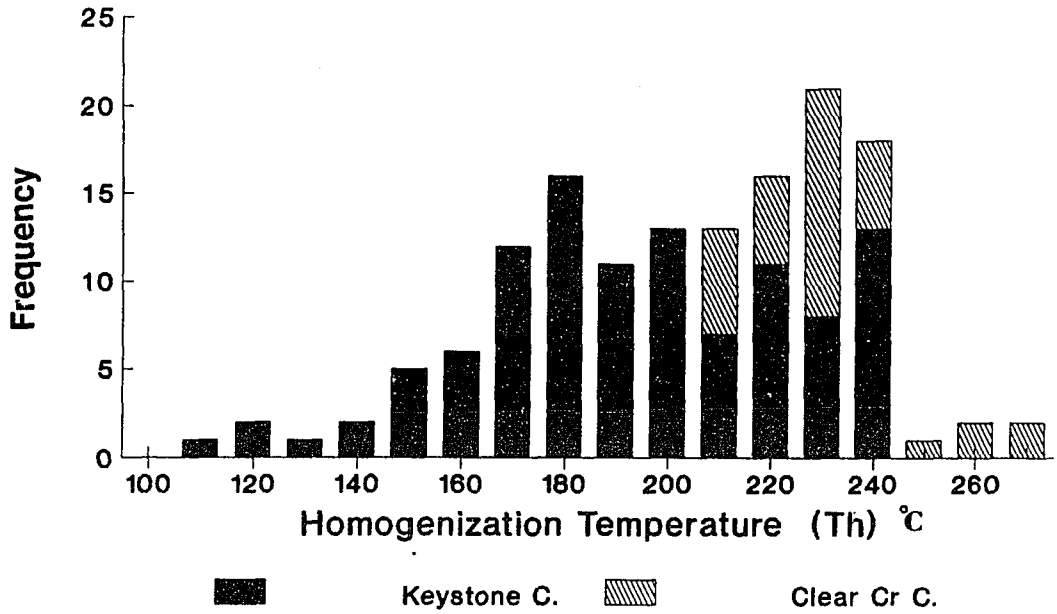
Southern Localities: The Keystone Canyon and Clear Creek Canyon Sections

Figure 197 shows the measured-T_h ranges from 110 to 270 °C, and figure 198 exhibits the melting-temperature range of -1 to -20 °C of the two-phase fluid inclusions. Table 33 shows that high T_h values range from 180 to 240 °C and from 210 to 240 °C for the Keystone Canyon and Clear Creek Canyon sections, respectively. However, burial temperatures estimated from the oxygen-isotope composition of carbonate cements are not consistent in both sections with fluid-inclusion thermometry and other thermometries (see Table 33).

Table 33- Maximum-burial temperatures of the AVL estimated from various geothermometries at southern localities (Keystone Canyon and Clear Creek Canyon sections) of this study.

Vertical Type Sections	TEMPERATURE			
	Hom. temp. (T_h) °C	$\delta^{18}O_{water}$ +5 °C +9 ‰ °C	Org. Met. °C	Illite Cryst. (CI) °C
Keystone Canyon	180 - 240	125 171	202	210
Clear Cr. Canyon	210 - 240 240 - 270	147 203		

*$\delta^{18}O_{water}$ values are in SMOW.



A total of 92 readings

Figure 197- Histogram of homogenization temperatures (T_h) of primary two-phase fluid inclusions from fracture-filling calcite cement and intercrystalline pore-filling quartz in the southern localities of this study.

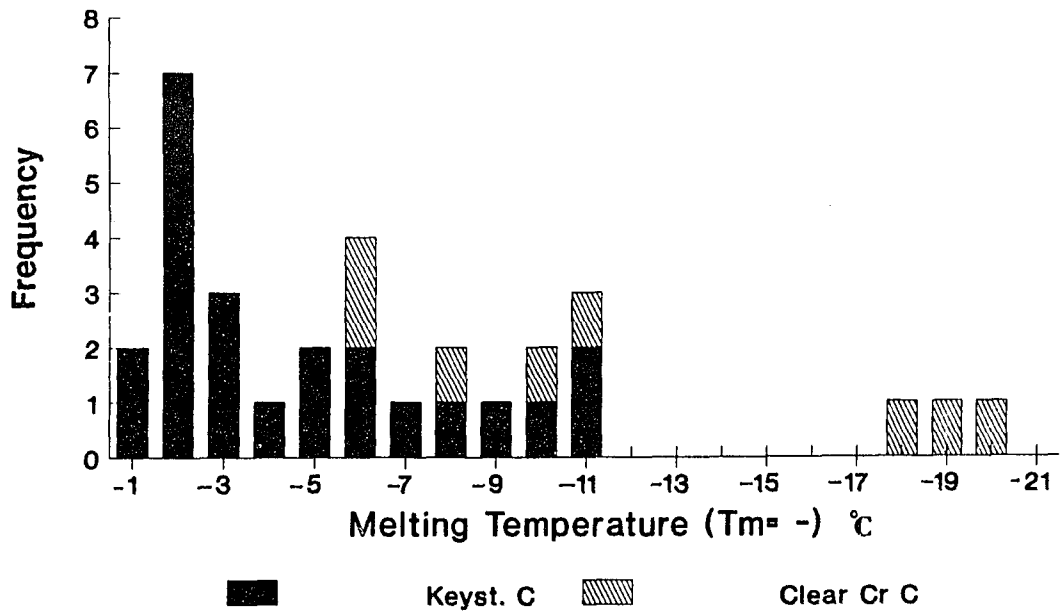


Figure 198- Histogram of melting temperatures (Tm) of primary two-phase fluid inclusions from the indicated cements in the southern localities of this study.

In Keystone Canyon section, the estimated-burial temperature range of 202 and 210 from organic metamorphism by Price's formula (1983) and illite crystallinity indices, respectively, occur in the lower T_h range (Table 33).

In the Keystone Canyon section, the fracture-filling, post-mosaic dolomitic calcite cements have excessively depleted-$\delta^{18}O$ compositions which range from -27.38 to -30.71 ‰ (PDB). In addition, two-phase fluid inclusions of these calcite cements usually have a very low-salinity content (Fig. 198). These fracture-filling calcite cements are believed to have formed from late-diagenetic meteoric waters (see Chap. 17).

Table 34- Maximum burial depths of the AVL, removed post-Devonian strata, and total uplifting of the AVL in the Keystone Canyon and Clear Creek sections, estimated from the range of maximum T_h values and other geothermometries.

T_h Range °C	Maximum Burial Depth of the AVL (km)	Maximum Removed Post-Devonian Strata (km)	A Total Uplifting Range of the AVL (km)
240-270	7.3 - 8.3		9.2 - 10.2

Estimated-maximum burial-depth ranges of the AVL in the southern localities, particularly, in the Keystone Canyon and Clear Creek Canyon sections, are based on the maximum homogenization-temperature values of two-phase fluid inclusions (Table 34). Other geothermometries did not provide the comparable temperature ranges, except illite crystallinity index of one sample indicates the lower range of the maximum burial of this formation (Table 33).

The maximum range of T_h values of 240 and 270 °C, with geothermal gradient of 30 °C/km and surface temperature (20 °C), corresponds to 7.3 to 8.3 km of maximum burial depth for the AVL, respectively (Table 34). Present elevation of the AVL on the measured sections about 1.9 km above sea level suggests that 9.2 and 10.2 km of total

uplifting probably took place up to present day from the indicated-maximum burial depths of this formation (Table 34).

The Toiyabe Range

Three sections of this mountain range are 1) Toiyabe Peak (T), 2) Dry Creek Canyon (D), and 3) Reeds Canyon (R).

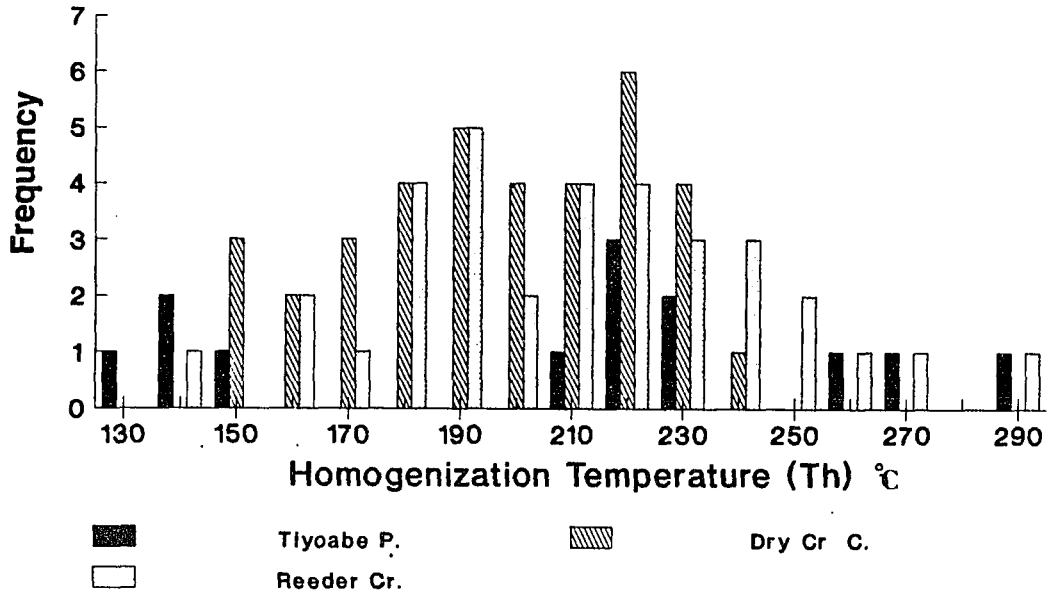
Figure 199 shows that T_h values of the AVL range from 120 to 290 °C, and figure 200 shows that the melting temperature ranges of two-phase fluid inclusions (from the AVL) range from -3 to - 24 °C.

Table 35- Maximum-burial temperatures of the AVL estimated from various geothermometries in the Toiyabe Peak region.

Vertical Type Sections	TEMPERATURE			
	Hom. temp. (T_h) °C	$\delta^{18}O_{water}$ +5 °C +9 ‰ °C	Org.Met. °C	Illite Cryst. (CI) °C
Tioyabe Peak	210 - 240 260 - 290	135 194	281 - 301	350
Dry Cr. Canyon	190 - 240			
Reeds Canyon	240 - 290	131 188	251	320

*$\delta^{18}O_{water}$ values are in SMOW.

Oxygen-isotope compositions of calcite cements occur in the two-discrete areas: (1) from -10.74 to-11.60 ‰ PDB, indicating deep-burial origin of the fracture-filling calcites; (2) -18.40 to -28.30 ‰ indicating meteoric origin for the second-group calcite cements.



A total of 92 readings

Figure 199- Histogram of homogenization temperatures (T_h) of primary two-phase fluid inclusions from fracture-filling calcite cement in the Toiyabe Range.

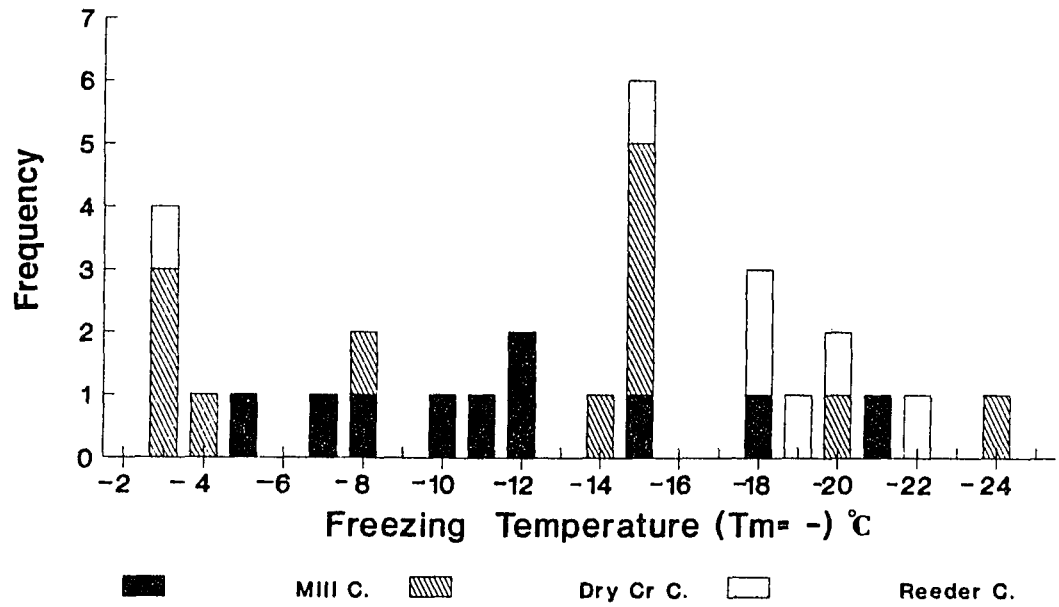


Figure 200- Histogram of melting temperatures (Tm) of primary two-phase fluid inclusions from fracture-filling calcite cement in the Toiyabe Range.

Temperatures estimated by the oxygen-isotope thermometry are generally lower than measured-T_h ranges, and they can only extend into the lowest range of the maximum T_h range (Table 35). Therefore, these temperatures are very limited in the use of paleotemperature estimation and determination of maximum-burial depths of the AVL, as seen in almost all the vertical sections of this study.

In the Toiyabe Range, thermal alteration levels (TAI) of organic matters range from 3.0 to 4.2 are correlative with R_o % of 1.63 to 2.5 (see Chap. 16). This vitrinite reflectance range (from primarily kerogen type I) corresponds to the temperature range of 252 to 301 °C (see Table 35) according to Price's formula (1983).

This estimated-temperature range form the TAI or correlative R_o% range shows a good correlation with the range of pressure-uncorrected T_h values of 240 to 290 °C (Table 35) as well as the range of illite crystallinity indices (from 0.15 to 0.20° or 1.9 to 2.5 mm which correspond to the range of sharpness ratio between 10.8 and 21.0 mm; see Chap. 19). These parameters characterize the epizone of metamorphic zones in which crystallinity levels of illite characterize the phengite, muscovite, chlorite, recrystallized-quartz and calcite paragenesis. In this study, the onset of the slate facies (axial-plane cleavage) of the AVL is believed to have occurred at a temperature range of 310 to 320 °C (see Table 35, and Chap. 19). Therefore, maximum burial temperature of the AVL was much higher than the maximum homogenization temperature (T_h) value of 290 °C which is believed to represent the minimum entrapment or re-equilibration temperatures of two-phase fluid inclusions (Table 35).

However, the temperature range of 310 to 320 °C was not yielded by the maximum burial depth of the AVL alone due to progressive sedimentation or subsidence. Thrust loading not only increased the burial depth of this formation, but also directed a great deal of pressure on to the AVL in a relatively short period. Thus, thrust-induced directed pressure might have facilitated high-reaction rate and deformation in the shaley limestone lithofacies of the AVL. Consequently, thrust-induced, advective-heat flow probably played an important role for elevating temperatures of the deeply buried sedimentary rocks, specifically the AVL, into the rank to epizone along with some effects of conductive heat flow.

In the Tioyabe Peak region, the maximum burial depths of the AVL, estimated from T_h range of 240-290 °C for geothermal gradient of 30 °C/km and surface temperature of 20 °C, are given in Table 36, ranging from 7.3 to 10 km; the removed post-Permian strata are estimated to have ranged from 4.3 to 7.0 km.

Table 36- Maximum burial depths of the AVL, removed post-Devonian strata, and total uplifting of the AVL estimated from the range of maximum T_h values and other geothermometries at Toiyabe Peak region.

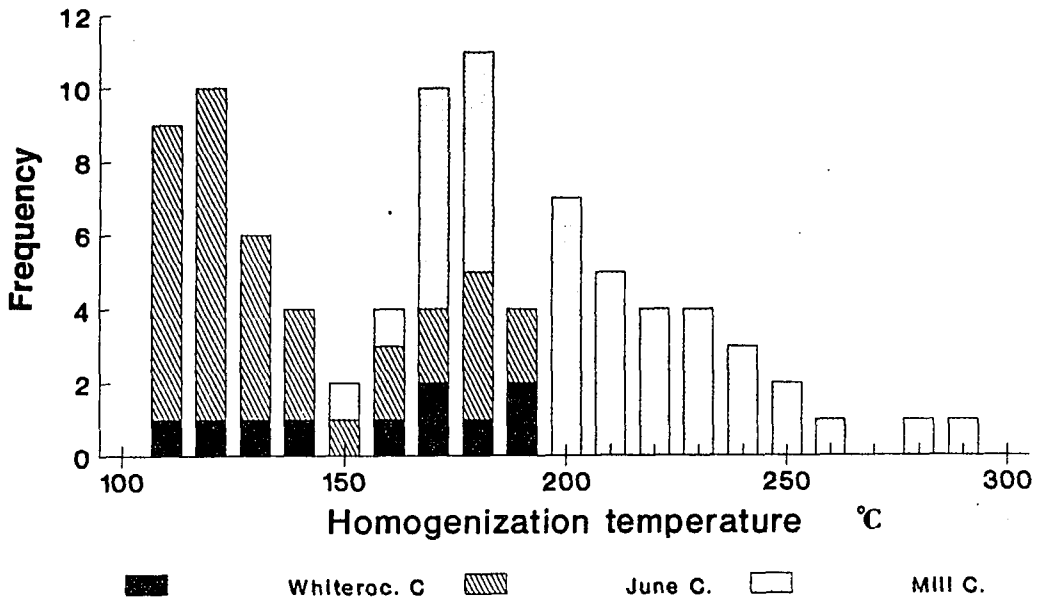
T_h Range °C	Maximum Burial Depth of the AVL (km)	Maximum Removed Post-Devonian Strata (km)	A Total Uplifting Range of the AVL (Km)
240-290	7.3 - 9.0	4.3 - 6.0	9.5 - 11.2 D,R 10.3 - 12.0 T
310-320	9.6 - 10.0	6.6 - 7.0	11.8 - 12.2 D,R 12.6 - 13.8 T

Estimated-maximum total uplifting of the AVL in the Dry Creek (D), Reeds Canyon (R), and Toiyabe Peaks (T) sections is estimated to range from 11.2 to 13 km.

Allochthonous Units: Whiterock Canyon section, June Canyon and Mill Canyon sequences

Three allochthonous AVL units were observed in the following sections: Whiterock Canyon in the Monitor Range; June Canyon sequence, and Mill Canyon sequence in Iks Canyon, Toquima Range.

Figure 201 shows that T_h values of two-phase fluid inclusions range from 120 to 190 °C in the Whiterock Canyon section and June Canyon sequence, two of which



A total of 97 readings

Figure 201- Histogram of homogenization temperatures (T_h) of primary two-phase fluid inclusions from fracture-filling calcite cement in the lower plates of Roberts Mountain thrusts.

represent upper thrust slice of the lower thrust plate of the Roberts Mountain thrusts; T_h values range from 150 to 270 °C in the Mill Canyon sequence, representing the lower thrust slice in the same lower thrust plate.

Table 37- Maximum-burial temperatures of the AVL estimated from various geothermometries in Whiterock and Iks Canyon regions.

Vertical Type Sections	TEMPERATURE			
	Hom. temp. (T_h) °C	$\delta^{18}O_{water}$ +5 +9 ‰ °C °C	Org.Met. °C	Illite Cryst. (CI) °C
Whiterock Canyon	160 - 190	156 227	120 - 166	
June Canyon Sequence	160 - 190	105 156	178 - 181	220 - 230
Mill Canyon Sequence	160 - 180 200 - 260		166 - 181	250 - 270

*$\delta^{18}O_{water}$ values are in SMOW.

Only in the Whiterock sections, the estimated-formation temperatures of fracture-filling calcite cements by oxygen-isotope thermometry occur in the range and above the homogenization temperature ranges for the AVL (Table 37).

In both June Canyon and Mill Canyon sections, measured TAI values occur nearly in the same range with the maximum-temperature range of 166 to 181 °C in spite of these two thrust units showing significantly different T_h ranges (Table 37). In the June Canyon sequence, the maximum illite crystallinity indices of 0.47° 2θ (6.0 mm) and sharpness ratio of 3.5 mm (see Chap. 19) mark almost the beginning of anchizone which probably corresponds to an initiation temperature of 210 or 230 °C (Table 37). In the Mill Canyon sequence, illite crystallinity indices of the AVL (CI) occur in the range of 0.35 to 0.35° 2θ (4.5-4.8 mm; Chap. 19), and T_h maximum is 260 °C (Table 37). Therefore, in this study, the maximum-estimated burial depths from temperature

ranges of 220 to 270 °C are conservative and reflect relatively lower maximum burial depths than actual maximum burial depth for the AVL. For instance, in the Mill Canyon sequence, pressure-uncorrected T_h maximum is 260 °C, but 270 °C for the maximum burial temperature is chosen for this formation.

Table 38- Maximum burial depths of the AVL, removed post-Devonian strata, and total uplifting of the AVL estimated from maximum T_h range and other geothermometries in the Whiterock Canyon (W), June Canyon (J), and Mill Canyon (M) sections.

T_h Range °C	Maximum Burial Depth of the AVL (km)	Maximum Removed Post-Devonian Strata (km)	A Total Uplifting Range of the AVL (km)
180-220	5.3 - 6.6	2.3 - 4.5	7.5 - 8.8 W 7.6 - 8.9 J
260-270	8.0 - 8.3	5.4 - 5.7	10.0 - 10.3 M

Maximum-burial depth of this formation in the Whiterock Canyon section and June Canyon sequence is estimated to be ranging from 5.3 to 6.6 km (Table 38). In the same sections, the removed post-Devonian strata range from 2.3 to 5.3 km, and total uplifting of the AVL in these sections occurs in the range of 8.8 to 8.9 km, respectively (Table 38).

In the Mill Canyon sequence, the maximum-burial depth of the AVL, the removed post-Devonian strata, and total-uplifting of the AVL are estimated to range from 8.0 to 8.3 km, 5.4 to 5.7 and 10.0 to 10.3 km, respectively (Table. 38).

Differences in the maximum-burial depth range of these two thrust slices do not correspond to the present-day thicknesses of rock units separating them.

B. Synthesis

Fluid-inclusion thermometry is a very useful method and maybe one of the most important geothermometries for lower Paleozoic rocks. Because during this geologic

period woody organic matters was absent, and exinitic organic matters were predominant. Under the same thermal and burial history, maturation level from kerogen type I and II always corresponds to at least three-fold lower temperature range than thermal maturation level of 100 % woody organic matter (see Chap. 16).

Fluid-inclusion microthermometry is the only available and reliable technique to determine the maximum-burial depth of the AVL, particularly at the regions where shaley units of this formation are not present. In addition, salinity content of two-phase fluid inclusions along with oxygen isotope composition also provide great help to determine the origin of the fracture-filling calcite cement whether meteoric or deep-burial in origin.

T_h values in the Toquima Range and Toiyabe Range show good correlation with the maximum temperatures estimated by illite crystallinity and clay diagenesis.

The estimated-formation temperatures of fracture-filling calcite cements by oxygen-isotope thermometry (from the approximated-$\delta^{18}O_{water}$ values = +5 ‰ and +9 ‰ SMOW) are significantly lower than the values of homogenization-temperatures of two-phase fluid inclusions.

Oxygen-isotope composition of fracture and vug-filling, dolomite cements are more depleted with respect to ^{18}O than those of fracture-filling calcite cements of deep-burial origin. The estimated-formation temperatures of these dolomite cements by oxygen-isotope thermometry are estimated to range from 179 to 253 °C; these estimated temperatures from $\delta^{18}O$ values are much greater than the measured-homogenization temperature (T_h values ranging from 120 to 160 °C of the same dolomite cement types from the same samples). The differences between the estimated-temperature range and homogenization-temperature range were probably caused by isotopic re-equilibration of carbonate cements and selection of non-representative oxygen-isotope composition for parent fluid from which carbonate cement precipitated.

In addition, the excessively depleted ^{18}O values ranging from -20.00 to -30.00 ‰ PDB of the fracture-filling, post-mosaic dolomitic calcite cements with a low-salinity fluid-inclusion composition, are interpreted to have formed from meteoric water (see

isotope section for further detail). Therefore, the paleotemperature estimation from such composition is certainly misleading because the indicated depletion in oxygen isotope composition was not caused by burial depth-induced heat but by excessively depleted oxygen-isotope composition of meteoric waters. Indicated such oxygen-isotope composition range will provide a significantly high-formation temperature range from 289 to 343 °C (see Chap. 17).

Similarly, thermal alteration levels of organic matter are also not comparable with the maximum homogenization temperatures (T_h) of two-phase fluid inclusions. Measured-TAI values and correlative parameters, such as coal rank, R_o%, and LOM, indicate that thermal alteration level corresponds to lower temperatures than those of homogenization temperatures measured from two-phase fluid inclusions. The low reflectivity or maturation level of organic matter is primarily related to exinite-rich kerogen type, kerogen types I and II (see Chap. 16). Estimated alteration or maturation levels of organic matter TTI (temperature-time index), using the subsidence curve of the AVL in the Antelope Valley and Lone Mountain regions, are significant and consistent with the T_h range. For instance, the estimated-maturation levels (R_o%) of organic matter at the end of the thrusting of Antler orogeny and the Late Permian period are 1.9 and 3.64 corresponding to burial temperatures of 234 and 316, respectively (see Chap. 16). Estimated paleotemperatures of 234 and 316 °C by TTI are very close to the pressure-uncorrected maximum T_h range of 260 to 290 °C.

Illite crystallinity indices, on the other hand, show good correlation with the maximum T_h values. Even though corresponding temperatures of illite crystallinity indices are 20 to 30 °C greater than pressure-uncorrected maximum T_h values, estimated temperatures by illite crystallinity may indicate the formation temperature or maximum re-equilibration temperatures of these two-phase fluid inclusions.

Therefore, this study suggests that in the lower Paleozoic rocks paleotemperature determination should be carried out primarily by fluid-inclusion microthermometry and illite crystallinity and clay diagenesis, but not organic maturation and oxygen-isotope geothermometries.

CONCLUSIONS

The results of this study were obtained from field study, petrographic, geochemical, and geothermometry analysis of the Antelope Valley Limestone (AVL). They can be grouped under the following categories: (A) depositional environment and evolution of carbonate platform; (B) diagenesis; and (C) maximum burial depth and burial history of the AVL in the study area.

A. Depositional Environment and Evolution of Carbonate Platform

(1) The lithofacies of the AVL characterize the depositional facies belts which range from intertidal- and supratidal shoreline facies to lagoonal, shelf, and shoal to slope and basinal facies.

(2) Texture, faunal content, degree of fine siliciclastic mixing and sedimentation patterns of the lithofacies in the indicated depositional facies belts were chiefly controlled by interactions between sedimentation rate, growth rate of the syndepositional topography of shoals, and rate in sea-level changes.

(3) In the AVL, three major shoals have been recognized, in ascending stratigraphic order: (a) Nuia shoal; (b) Girvanella-constituted oncoidal shoal; and (c) oolitic and skeletal shoal. All these shoal facies appear to have been closely associated with a gently declining slope or ramp without any major break.

(4) Nuia particles, finger-like-segmented problematical algal remains, are the major constituents of the Nuia shoal lithofacies, which represent a moderately high to high-energy, storm- and tide-dominated shoal-bar facies. A well-circulated shelf formed behind the subtidal bars of the Nuia shoals through the bank overflow and interbank flow of oxygen-rich open sea water.

(5) Open seaward and shoreward-extended flanks of the Nuia shoal bars provided a favorable, relatively low-energy, sheltered-shoal environment where Girvanella flourished along with Nuia.

(6) Absence of ooids and oolitic units within the Nuia shoal lithofacies can be attributed to a very flat shelf margin, high degree of fine-siliciclastic dilution and to the localities of subtidal Nuia bars which were probably a few to 10 km away from the site where strong ocean currents began to shoal, such as seen in Halimeda shoals in the Marquesas Keys, Florida.

(7) Oncoidal shoal lithofacies characterize the sedimentation below the normal wave base and storm-dominated shoal facies, which probably created a well-circulated, deep middle shelf behind the subtidal-oncoidal bars. The oncoidal shoals represent a moderately high energy, incipiently drowned shoal which allowed storm-counter currents to transport fine-siliciclastics from nearshore to middle shelf and to open shelf. In this respect, the Girvanella-constituted oncoidal shoals are analogous to the incipiently drowned shoals of the Serrinella bank of Nicaragua Rise. Receptaculites bioherms on the top of subtidal bars of the oncoidal shoal indicate 6 to 12 m of bathymetry.

(8) In the lower oolitic shoal intervals, the radial ooid-bearing sublithofacies are prominent and represent a tidal bar belt-type shelf margin; however, the upper oolitic shoal intervals consist of both radial ooid-bearing subshoal units and gradually overlying calcitized ooid-bearing subshoal units. The upper oolitic shoal intervals represent the syndepositional topographic shoal barriers or mobile sand-belt types of shelf margin.

(9) Radial ooids of high-Mg calcite composition represent an organically influenced low-energy shoal facies or open-seaward extended flanks of oolitic bars, whereas calcitized ooids (believed to have had original aragonitic composition)-bearing sublithofacies represent a high-energy shoal, particularly at the crest of oolitic bars.

(10) Girvanella oncoids represent a very low sedimentation rate rather than bathymetry because of their common occurrence in shallow subtidal, shelf, shoal, and open shelf.

(11) Stromatolitic lime mudstone units with birdseye texture, and desiccation cracks characterize the subaerial exposure of the AVL; however, absence of evaporite minerals and molds, paleocalichi surfaces, and calcrete breccias imply that tropical and subtropical climatic conditions prevailed during deposition of the AVL.

(12) The Copenhagen Formation is the lagoonal facies of the Antelope Valley Limestone (AVL) and separated from the middle shelf facies of the AVL by nearshore peloidal bars and storm-counter current channels' mouth bars.

(13) The Upper and Lower member of the Eureka Quartzite represent the progradational siliciclastic shoreline facies of the AVL; on the other hand, the Middle member of Eureka Quartzite represents transgressive shoal or bioherm facies.

(14) Shallowing-upward cycles of the AVL are correlative as far as 40 km normal to depositional strike and about 60 km along depositional strike. These cycles appear to represent the climate-forcing cyclicity or glacioeustacy with an average cycle duration of 82.000 yrs.

(15) In the study area, after the major transgression, the Nuia shoal units initiated the formation of the AVL, and during the late Orthidella zone, in place or stacked shallowing-upward Nuia shoal cycles reached 450 feet of thickness and evolved into an incipiently rimmed shelf margin from a homoclinal ramp. In this stage, strong storm-counter currents induced the high-density turbidity currents which, in turn , resulted in deposition of graded bioclastics in deep ramp or lower slope environments.

(16) The end of the Orthidella zone is represented by considerably thin Nuia shoal units and overlain by fine-grained siliciclastic-rich lime mudstone units. The cyclical successions of these Nuia shoal units and bioturbated back-shoal lithofacies exhibit a stair-step morphology which is believed to represent incipiently drowned Nuia shoals due to short durational sea-level rises causing a third-order sea-level rise.

(17) At the beginning Palliseria zone, Nuia shoals were briefly re-established following the drowning of Nuia shoals; however, the following high-amplitude, short durational rises in sea level redrowned the Nuia shoals which were replaced by Girvanella-constituted oncoidal shoals. At this stage, domination of the Nuia shoals by Girvanella represents the incipiently drowned shoal or distally steepened ramp which

evolved from an incipiently rimmed shelf. As a result, incipiently drowned Nuia shoals (at the uppermost Orthidella zone) and Girvanella-dominated shoals did not act as a physical barrier to the storm-counter currents which transported near-shore fine-siliciclastics to the middle shelf and to upper slope and deep ramp.

(18) These fine-grained siliciclastic depositional episodes created a stressed-depositional environment; Girvanella, as a pioneer organism, normalized and utilized the environment for benthic fauna and enhanced carbonate sedimentation.

(19) Only in the Martin Ridge and Ninemile Canyon sections, oncolitic shoal gave rise to oolitic and skeletal shoals, but not in the southern and northern localities of this study. The vertically stacked oolitic shoal cycles gradually yielded a syndepositional topographic barrier which left a restricted-shelf facies behind, converted the fine siliciclastic-dominated shoreline sediment into intertidal algal flats, and elevated the distally steepened ramp to the incipiently rimmed shelf. During this stage, the intertidal algal flats progradated farther westward over the place where the oolitic shoals reached considerable thicknesses, and oncolitic wackestone to packstone units of the open-seaward extended flank of oolitic shoals progradated farther westward over sponge mounds-bearing, nodular-bedded units in the June Canyon sequence.

20) At the same time, in the oncoidal shoal-dominated ramp at the Lone Mountain (northern locality) and Keystone Canyon (southern locality) sections, the siliciclastic-dominated shoreline sediments (the Lower quartzite member of Eureka Quartzite) progradated farther west over the deep-middle shelf facies of the oncoidal shoals in the Lone Mountain section and over the shoreward shelf facies of the AVL in the southern localities of this study. Thus, the progradation rate of shoreline sedimentation of the AVL in the northern localities was much greater than that of the southern locality.

(21) In Martin Ridge and Ninemile Canyon sections, the following rapid third-order sea-level rise converted incipiently rimmed shelf into a distally steepened ramp and intertidal algal flat-dominated shoreline sediment into a siliciclastic-dominated sediment, and created a well-circulated shelf which was separated from the lagoonal Copenhagen Formation by nearshore peloidal bars of the AVL.

(22) The Middle biohermal or carbonate member of the Eureka Quartzite probably resulted from the same third-order rise in sea level as described above which is believed to have lagged behind the rate of sedimentation and progradation of fine shoreline siliciclastics as well as carbonates. As a result, the Upper quartzite member of Eureka Quartzite prograded westward as far as the Antelope Valley region, even farther.

B. Diagenesis

(1) Submarine cementation played an important role in every interval of the AVL. Isopachous-rim cement and radiaxial-fibrous cement in the lithofacies of oolitic and Nuia shoals; the columnar-calcite cement in the oncoidal shoal and shelly storm beds of the open shelf; and cryptocrystalline calcite cement from shallow-subtidal, shoal, and to basinal facies. The $\delta^{18}O$ composition of columnar- and radiaxial-fibrous calcite cements ranges from -6.66 to -6.77 ‰ PDB which is consistent with the estimated-$\delta^{18}O$ composition of the Middle Ordovician marine calcite values.

(2) The following cement types of meteoric diagenesis have been recognized in the AVL: fenestra-filling, gravitational pendant calcite cement of vadose zone, and equant granular and blocky mosaic, drusy cement, and syntaxial overgrowth of phreatic zone. The equant mosaic is volumetrically the most important meteoric cement type in the AVL.

(3) Syntaxial cements are generally represented by four discrete luminescent zones, all of which are postdated by dolomite type IV.

(4) The void-filling or poikilotopic calcite cement, intraooid-filling large calcite spar, and intercrystalline pore-filling calcite cements in dolostones are deep burial in origin which can be inferred from their close association with late fracture-filling cements, depleted-oxygen isotope compositions, and high-T_h values.

(5) The neomorphic replacement of precursor meteoric and shallow-burial calcite cement appears to be an important process in deep-burial diagenetic environments.

(6) Dolomite I, with bright-yellow luminescence, in the shelly storm layers of the upper slope facies represents early dolomitization on the sea floor.

(7) Dolomite II, non-luminescent and non-stoichiometric, represents relatively early selective dolomitization in Mg-rich algal laminae of stromatolites and Girvanella oncoids.

(8) Dolomite III, a fabric-selective dolomite in the partially calcitized upward-growth of Girvanella, postdates fracture-filling calcites and represents the intermediate- to deep-burial diagenetic environments.

(9) Dolomite IV, with bright red and nonluminescent bands constituted zonal dolomites, selectively replaced calcite-filled ooids in the oolitic packstone- and grainstone units and four zones of syntaxial calcite cements in the crinoidal grainstone units, representing the shallow- to intermediate-burial diagenetic environments.

(10) Dolomite V, with orange red and nonluminescent band-constituted zonal dolomites, postdates mechanically broken allochems and probably represents shallow- to intermediate-burial diagenetic environments.

(11) Dolomite VI, ferroan dolomite, selectively replaced deep-burial calcite cements, and occurs along stylolites, and may have formed by expulsion of basinal brine during Antler orogeny.

(12) Dolomite VII (mosaic dolomite), the dolostones of the AVL, represents deep-burial, epigenetic dolomitization which may have formed during Late Middle Pennsylvanian and Early Permian uplifting or normal faulting.

(13) Dolomite VIII, fracture-filling sparry dolomite, appears to be synchronous with and postdates the host mosaic dolomite.

(14) Dolomite IX, saddle dolomite, occurs in fractures which crosscut the host dolostones, probably having formed during the Sonoma orogeny by the expulsion of basinal brines.

(15) In mosaic dolomite (dolostones), two kinds of major luminescence have been recognized: a) dull-red luminescence of mosaic dolomites, and b) bright red luminescence, characterizing post-pervasive dolomitic fracture-filing dolospar. Mosaic dolomites with bright-red luminescence postdate saddle dolomite; therefore, they

probably formed during the westward advancement of the clastic wedges of the Sonoma orogeny.

(16) In the study area, two possible mechanisms can be responsible for the formation of dolostone intervals in the AVL during the Late Middle Pennsylvanian and Early Permian normal faulting: a) expulsion of basinal brine, and b) gravity-driven, diagenetically altered groundwater regional flow.

(17) Some fracture-filling calcite cements (also postdating mosaic dolomites) with extremely depleted oxygen-isotope composition of about -20 to -30 ‰ PDB are believed to have precipitated from meteoric diagenetic parent fluids.

(18) Dedolomitization in the AVL represents late-diagenetic, near-surface diagenesis and occurs in two categories: a) non-fabric selective calcite replacement, and b) fabric-selective calcitization along ferroan dolomite zones.

(19) Silicification of the AVL shows a very wide diagenetic spectrum: from early to late diagenesis. Selectively chertified allochems are fragments of crinoids, brachiopods, bryozoans and trilobites. Chert replacement in bryozoans is generally late diagenetic in nature and postdates fracture-filling calcite cements and replacive ferroan dolomites.

(20) Chert nodules generally consist of three kinds of silica cements: cryptocrystalline quartz, chalcedony, and megaquartz. The fine siliciclastic-rich, parallel-laminated limestones of the open-shelf facies were selectively replaced by chert or cryptocrystalline quartz. Formation of chert nodules is late-diagenetic in nature and replacement of limestones is believed to have been caused primarily by fluctuations in pH level of solutions due to sulfate-reducing reactions either by microbioal activities or by thermal sulfur-reducing reaction (TSR).

(21) In chert nodules, presence of euhedral pyrite crystals in poikilotopic calcite and replacement of calcite by sparry dolomite which appears to be syngenetic with meagaquartz suggests that silica precipitation occurs at low pH levels, precipitation of pyrite initiates high pH and the precipitation of calcite, and formation of replacive dolomite is believed to have occurred by release of Mg^{+2} during chalcedony-quartz transformation or precipitation of quartz from diluted silica solutions.

(22) Siliceous sponge spicules and radiolarias are the primary source of silica.

(23) Authigenic quartz usually replaced the dolomite type III and indicates an intermediate- to deep-burial diagenetic environment rather than a hypersaline, near-surface diagenetic environment.

(24) Fractures and void-filling quartz cements represent the latest diagenetic event postdating the latest hydrocarbon-bearing stylolites and cogenetic silicification.

(25) Dolomites of dolostone are nearly stoichiometric or nearly ideal. Saddle dolomites are slightly more calcitic than those of mosaic dolomites.

(26) Dolomites of stromatolitic lime mudstone are nonstoichiometric, even though they are early diagenetic in origin. This nonstoichiometry is believed have resulted from the presence of closed-diagenetic systems within the stromatolitic lithofacies after the formation of these dolomites.

C. Maximum-Burial Depth Range and Burial History of The AVL

Multiple geothermometric methods have been employed to determine the maximum burial depth of the AVL. For this, the results of geothermometries have been compared with one another along with the subsidence curve reconstructed from the presently available sedimentary and tectono-stratigraphic units in the Antelope Valley and Lone Mountain, Devils Gate and Eureka regions.

(1) Organic maturation level by measured TAI values and their correlative vitrinite reflectance values are at least two to three times lower than thermal alteration levels estimated from fluid-inclusion thermometry, illite crystallinity, and TTI. This low-organic maturation level is the primary function of the algal organic matter which constitute kerogen types I.

(2) Therefore, this study suggests that the organic-maturation level of lower Paleozoic rocks should not be used for geothermometry because kerogen type I predominate in sedimentary rocks of that geologic time.

(3) In the AVL, differences in alteration levels of organic matter (from 0.02 to 0.7

Ro %) in the same sections are related to abundance of oxygen level in the depositional sites and lithology types.

(4) Oxygen-isotope thermometry is also not a practical method to determine the maximum-burial depths of the AVL: for calcite cements, estimated temperatures by using $\delta^{18}O_{water}$ composition of +5 ‰ and + 9 ‰ SMOW are much lower than T_h values; and for dolomite cements, the estimated temperatures by this geothermometry are much higher than T_h values. This is believed to have resulted from the inaccurately approximated oxygen-isotope composition of parent fluids: oxygen isotope values of parent fluids of dolomite and calcite cements have been calculated to range from 0 to +8 ‰ and +7 to +13 ‰ SMOW, respectively.

(5) Some fracture-filling calcite cements having a $\delta^{18}O$ composition ranging from -20 to -30 ‰ and a low-salinity fluid inclusion composition are believed to have formed from diagenetic meteoric waters whose estimated-oxygen isotope values ranged from -5 and -13 ‰ SMOW.

(6) Fluid-inclusion technique is a very important method to study geothermometry and fluid chemistry. The salinity versus T_h diagrams have been used to determine the physical and chemical evolution of two-phase fluid inclusions whether two-phase fluid inclusions were stretched (volumetrically changed) or decrepitated (compositionally changed). In histograms, statistical clusters of T_h values represent various heating events during the burial history of the AVL, and maximum T_h values correspond to the maximum burial depth of the same formation.

(7) Homogenization temperatures or (T_h) values represent the minimum entrapment and re-equilibration temperatures of two-phase fluid inclusions. The pressure-uncorrected maximum T_h values occur in a comparable range with illite crystallinity (CI) and are generally 20 °C to 30 °C lower than temperatures corresponding to the illite crystallinity level.

(8) Clay-mineral assemblages, and illite-crystallinity indices (CI) are very practical techniques for determining the maximum-burial temperatures of shale and shaley limestone units of the AVL. Illite crystallinity (CI) and its correlative temperature ranges are in better agreement with the maximum T_h ranges compared to other

geothermometries.

(9) Lithology type has great influence on CI of illite and composition of clay-mineral assemblages: limestones with less clay content correspond to much lower illite-crystallinity levels and clay-mineral assemblages of lower temperature equivalent than those of shaley limestone layers of the same intervals.

(10) In this study, the estimated boundaries of diagenetic zone, anchizone and epizone occur in the following temperature ranges, respectively: 220-230 °C; and 230 to 320 °C.

(11) In the Antelope Valley region, for 30 °C/km geothermal gradient and 20 °C surface temperature, T_h values of 260 to 290 °C correspond to 8 to 9 km (24 834 to 27 432 ft) of burial depth for the AVL, to about 4.3 to 5.3 km (13 106 to 16 154 ft) of removed post-Devonian strata, and 10.1 km to 11.5 km (30 784 to 35 052 ft) of total uplifting of the AVL estimated from their present elevation.

(12) In southern localities for the indicated geothermal gradient and surface temperature above, from T_h of 240 to 270 °C corresponds to 7.8 and 8.3 km (23 774 to 25 298 ft) of maximum-burial depth, and to 9.2 to 10.2 km (28 041 to 31 089 ft) of the total uplifting of for the AVL.

(13) In the Toiyabe Range, maximum T_h ranging from 240 to 290 °C (CI corresponding to 320-350 °C) corresponds to 7.3 to 9.0 km (22 250 to 27 423 ft) of burial depth and 9.2 to 12.0 km (28 041 to 36 576 ft) total uplifting of the AVL, and to 4.3 to 6.0 km (13 106 to 18 288 ft) of removed post-Devonian strata. Average 335 °C from CI represents about 11 km (33 528 ft) of maximum burial depth for the AVL in this region.

(14) In allochthonous units, particularly the Whiterock Canyon section and June Canyon sequence, maximum burial temperature by T_h technique ranges between 160 and 190 °C and from CI values ranges from 220 to 230 °C. The indicated T_h values correspond to 5.3 and 6.6 km (16 154 to 20 116 ft) of maximum-burial depth and to 7.5 to 8.9 km (22 860 to 27 127 ft) of total uplifting of the AVL to present position, and to 2.3 to 4.5 km (7 010 to 13 716 ft) of removed post-Devonian strata. In Mill Canyon sequence, maximum T_h of 260-270 °C (CI in the same temperature range)

corresponds to 8 to 8.3 km (24 384 to 25 298 ft) of depth of burial, about 10 to 10.3 km (30 480 to 31 394 ft) of total uplifting of the AVL, and to 5.4 to 5.7 km (16 459 to 17 373 ft) of removed post-Devonian strata.

(15) By using Max T_h, instead of temperature values of CI, maximum burial depth ranges of the AVL represent a generally conservative range.

APPENDIX IA: THE MEASURED-VERTICAL SECTIONS AND THEIR LOCATIONS

a) Ninemile Canyon Section

This section, the easternmost locality of this study, is located at the western front of the Antelope Range (Fig. 1), found in the uplifted-fault block of the Ninemile Canyon fault. In this section, the Antelope Valley Limestone (AVL) has a gradual basal contact with the Ninemile Shale and a gradual upper contact with the Copenhagen Formation; a total of 1220 feet of Antelope Valley Limestone (Fig. 202; p. 630-634 in Appx. IB) and about 180-foot thick strata of the Copenhagen Formation were measured. The remaining upper part of Copenhagen Formation is covered by volcanics. Ninemile Canyon is located on the Horse Haven Quadrangle, Eureka County, and its coordinates are R 51 E and T 15 N.

b) Keystone Canyon Section

This section, the southernmost locality of this study, is located on the northern wall of Keystone Canyon (Fig. 1) in the Hot Creek Range. The lower contact of Antelope Valley Limestone (AVL) is juxtaposed with Goodwin Formation by Emma fault and its upper contact is gradually overlain by thin Copenhagen Formation, underlying the Eureka Quartzite. In this section, about 600 feet of pervasively dolomitized AVL (Fig. 202; p. 635-636 in Appx. IB) was measured and this formation is crosscut by Jurassic dikes. This section is located four miles away from the mouth of Hot Creek Canyon, which is on the Hobble Canyon Quadrangle, Nye County.

c) Lone Mountain Section

This section, the northernmost locality of this study, is located in the southeastern front of Lone Mountain (Fig.1). In this section, the lower contact of the AVL is not

exposed and this formation is directly overlain by the Eureka Quartzite with sharp and erosional contact. About 800 feet-thick strata of the Antelope Valley Limestone (Fig. 202; p. 237-239 in Appx. IB) was measured. Lone Mountain is on the Bartine Ranch Quadrangle, Eureka County, and its coordinates are R 51 E and T 20 N.

d) Martin Ridge Section

This vertical section is located in the Antelope Valley region, particularly at Martin Ridge in the eastern front of the Monitor Range (Fig. 1). In this type section, about 240 feet of the Copenhagen Formation and 970 feet of the Antelope Valley Limestone (Fig. 202; p. 640-643 in Appx. IB) were measured. Martin Ridge is located on the Horse Haven Quadrangle of Eureka County, and Its coordinates are R 49 E and T 15 N.

In the same coordinates, about one mile south of the Martin Ridge type section, approximately 450-foot thick another vertical section (Fig. 202; p. 644-645 in Appx. IB) was measured for comparison.

e) Clear Creek Canyon Section

This section is located on the north wall of Clear Creek Canyon near its mouth at the eastern front of the Monitor Range (Fig. 1). This section occurs on the uplifted-fault block. In this section, a total of 227 feet-thick strata (Fig. 202; p. 646 in Appx. IB) of pervasively dolomitized Antelope Valley Limestone were measured. Clear Creek Canyon is on the Danville Quadrangle, Nye County, and its coordinates R 49 E and T 11 N.

f) Whiterockian Canyon Section

This section represents allochthonous strata of the lower thrust plates of Roberts Mountain thrusts and consists of the Ninemile Shale and Antelope Valley Limestone

(AVL). It is located on the northeastern wall of Whiterockian Canyon (Fig. 1) about one and half miles from Copenhagen Canyon in the Monitor Range. In this section, the AVL formation gradually overlies greenish calcareous shaley strata of the Ninemile Shale, which is separated from underlying Devonian units by a thrust plane. A total of 440 feet thick strata of the AVL (Fig. 202; p. 647-648 in Appx. IB) were measured. Whiterockian Canyon is located on the Horse Haven Quadrangle, Eureka County, and its coordinates are R 49 E and T 16 N.

g) June Canyon Sequence (Iks Canyon)

This vertical section is located on the southern slope of the Copper Mountain, near the Iks Canyon mouth (Fig. 1). In this section, the Antelope Valley Limestone (AVL) gradually overlies the Ninemile Shale and is conformably overlain by the unnamed Middle Ordovician Limestone. This section represents the June Canyon sequence on the lower tectonic plate of the Roberts Mountain thrusts, overlying Devonian strata of the Mill Canyon sequence with a tectonic contact. In this section, approximately 800 feet of the AVL (Fig. 202; p. 649-651 in Appx. IB) was measured. Location of this section is on the Dianas Punch Bowl Quadrangle, Nye County, and its coordinates are R 46 E and T 15 N.

h) Mill Canyon Sequence (Iks Canyon)

This section is also located in the Iks Canyon mouth (Fig.1). Its location is also in the Dianas Punch Bowl Quadrangle and it has the same coordinates as the June Canyon section. In this section, the basal contact of the AVL is not exposed, and its upper contact is unconformably overlain by the Silurian Masket Shale. The AVL is approximately 510-feet thick (Fig. 202; p. 652-653 in Appx. IB).

i) Toiyabe Peak Section

Toiyabe Peak is also located in the Toiyabe Range on the Austin Quadrangle, Lander County (Fig. 1). In this section, about 400 feet of the AVL (Fig. 202; p. 654-655 in Appx. IB) was measured from its base, but from that point the upper part of this section could not be measured. Toiyabe Peak is an inaccessible section; it can only be reached to the base of this section through Fork Canyon. Its coordinates are R 43 E, and T 18 N.

j) Reeds Canyon Section

This section is located at the western front of the Toiyabe Range, and is also one of the westernmost localities of this study (Fig. 1). In this section, a total of 170 feet of strata of the AVL (Fig. 202; p. 656 in Appx. IB) were measured. Reeds Canyon is also on the Austin Quadrangle, Lander County, and its coordinates are R 42 E and T 17 N.

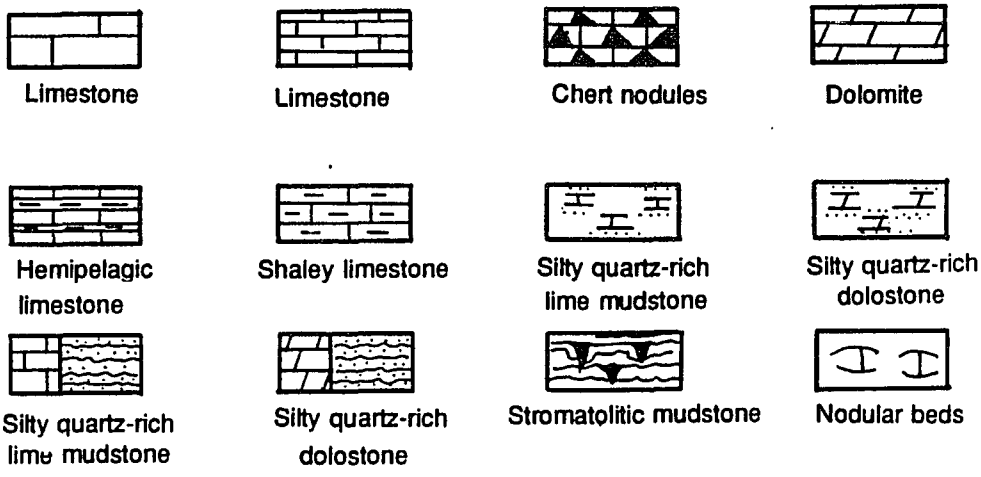
K) Dry Creek Canyon Section

Dry Crek Canyon section is one of the westernmost localities of this study and located at the western front of Toiyabe Range (Fig. 1). In this section, the lower contact of this formation is not exposed and its upper contact is overlain by the Silurian Masket Shale. In the Dry Creek Canyon section, about a 300 feet-thick strata of this formation (Fig. 202; p. 657 in Appx. IB) were measured. This vertical section is on the Austin Quadrangle, Lander County, and its coordinates are R 43 E and T 18 N.

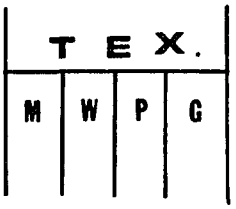
APPENDIX I-B: TEXTURAL AND LITHOLOGIC VARIATIONS OF THE ANTELOPE VALLEY LIMESTONE IN THE MEASURED SECTIONS

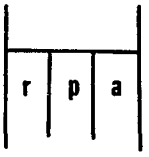
Figure 202- Lithology types, sedimentary structures, textures, and faunal and floral contents of the AVL in the measured sections.

EXPLANATION FOR MEASURED SECTIONS



- Peloids
- Ooids
- Crinoids
- Pellets
- Oncoids
- Intraclasts
- Gastropods
- Bryozoans
- Trilobites
- Brachiopods
- Burrows
- Ostracods

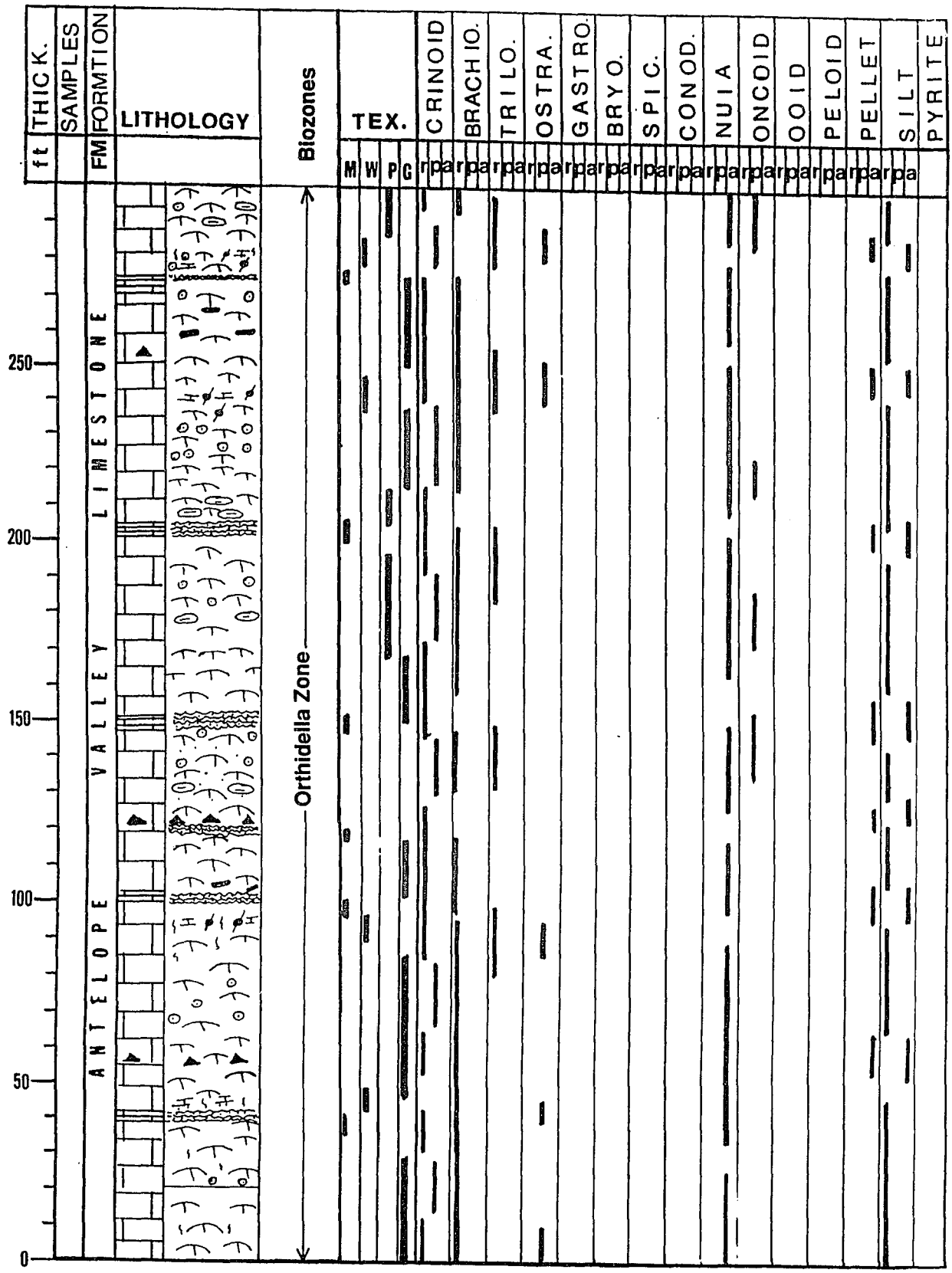




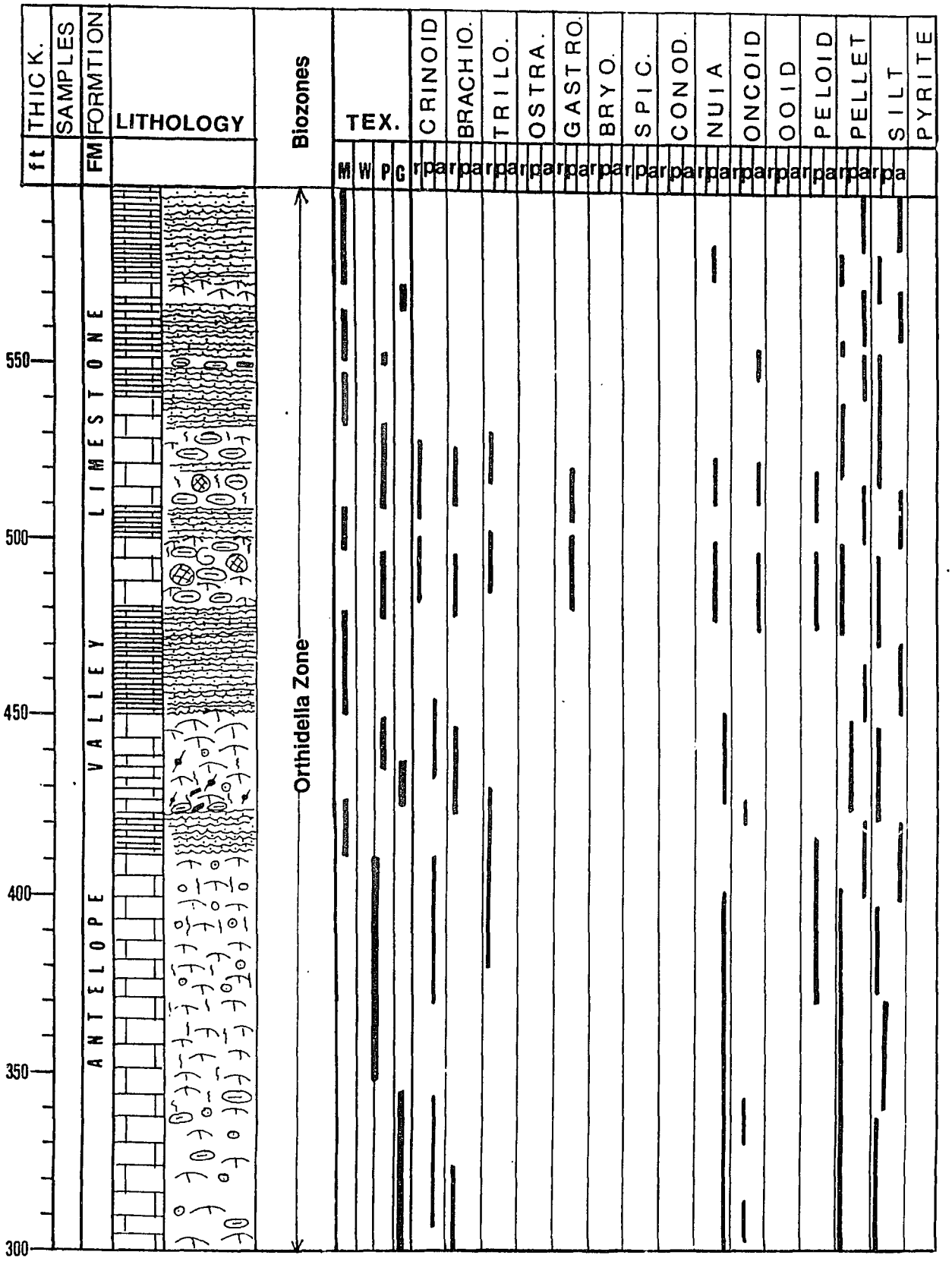
Relative abundance of allochems
r: rare
p: present
a: abundant

TEX.: Texture

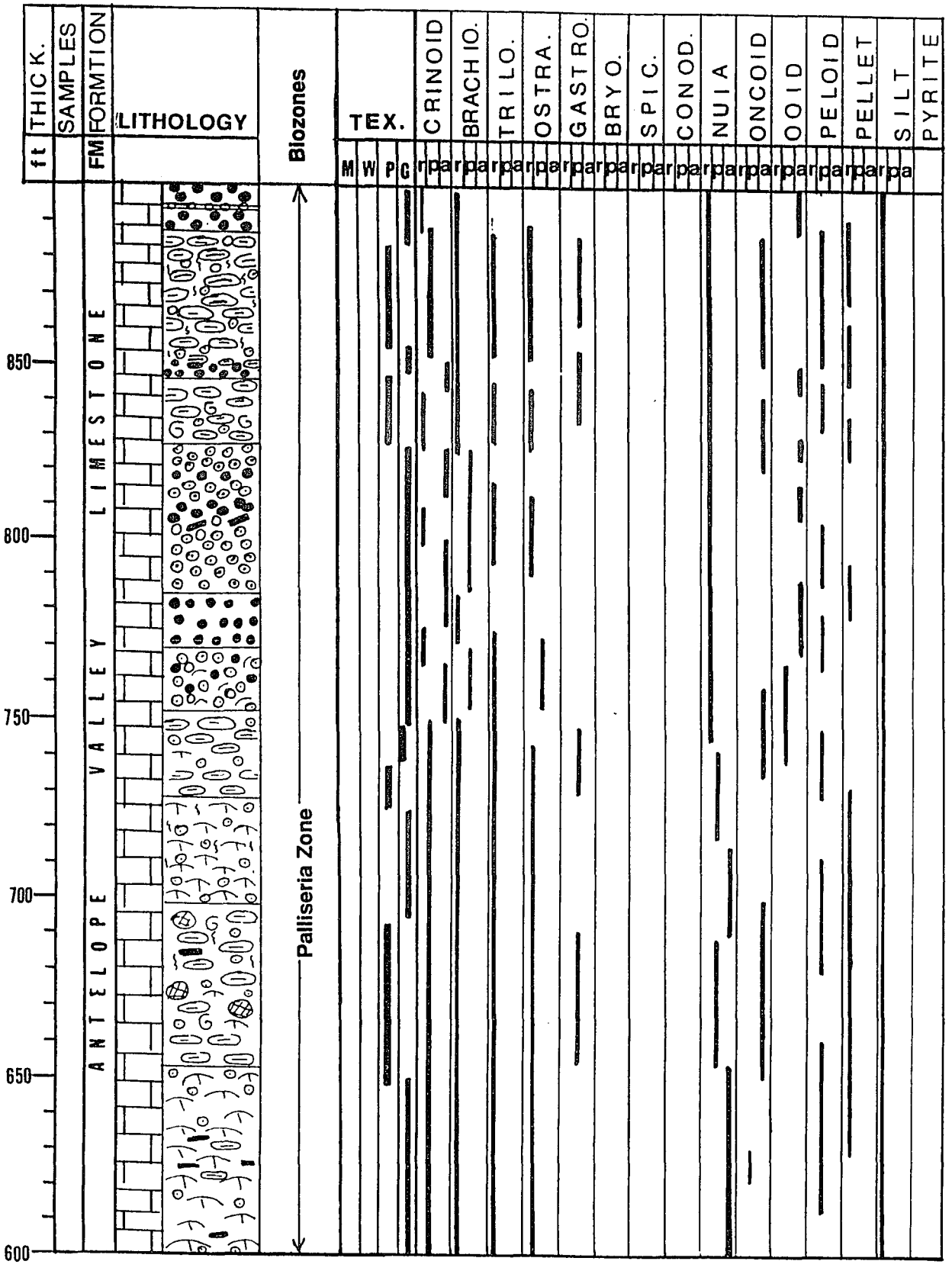
M: Mudstone **P:** Packstone
W: Wackstone **G:** Grainstone



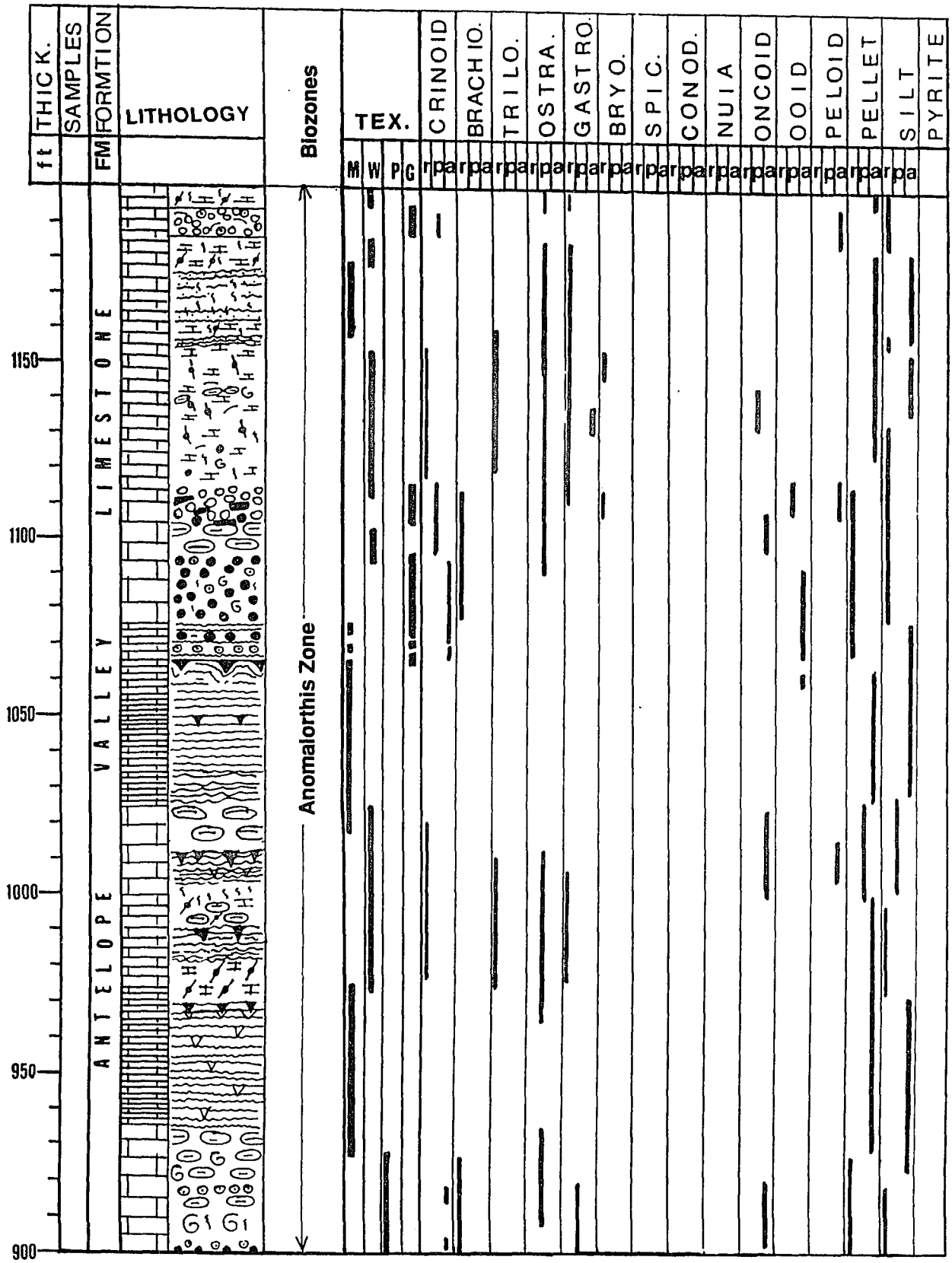
Ninemile Canyon Section



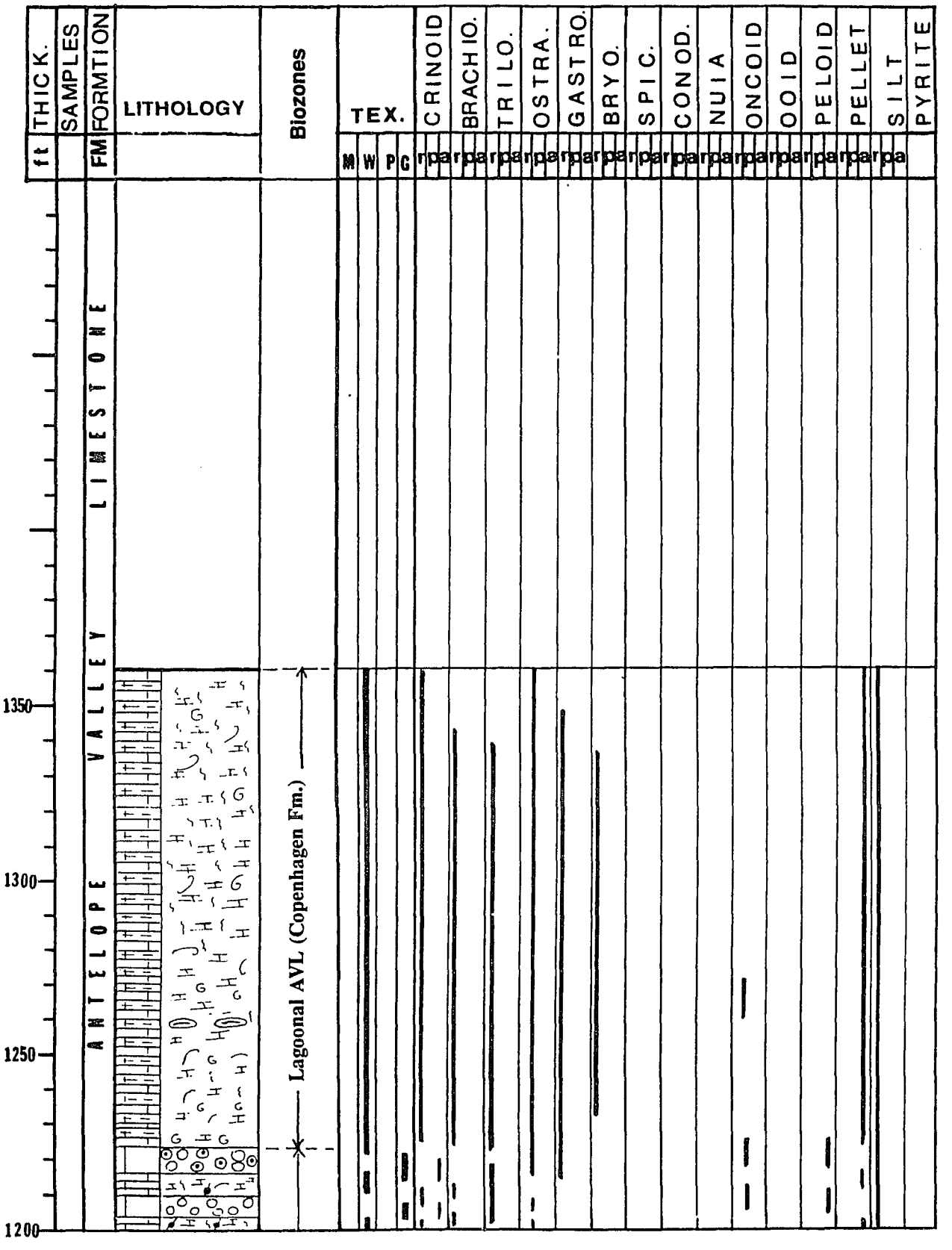
Ninemile Canyon Section



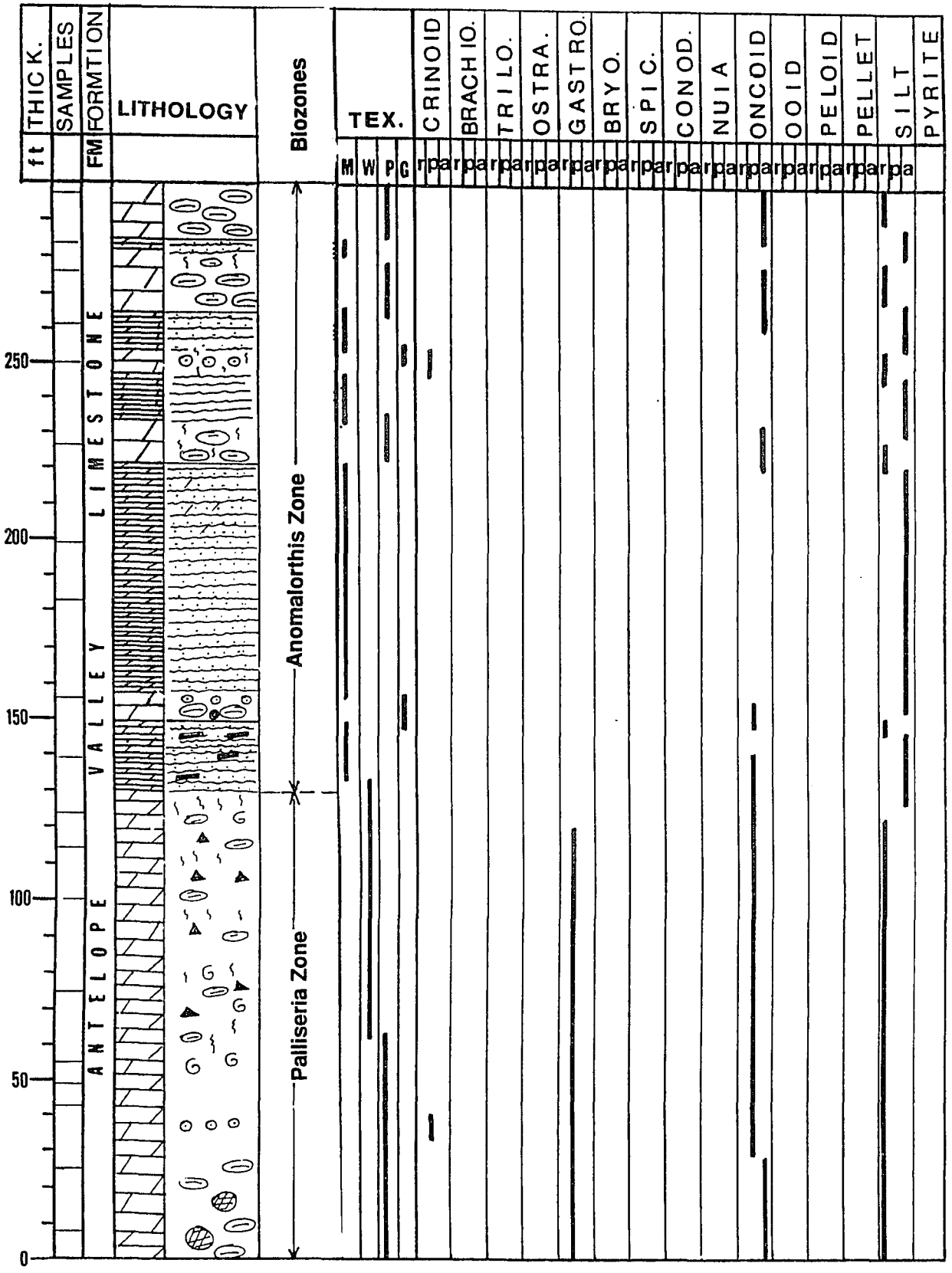
Ninemile Canyon Section



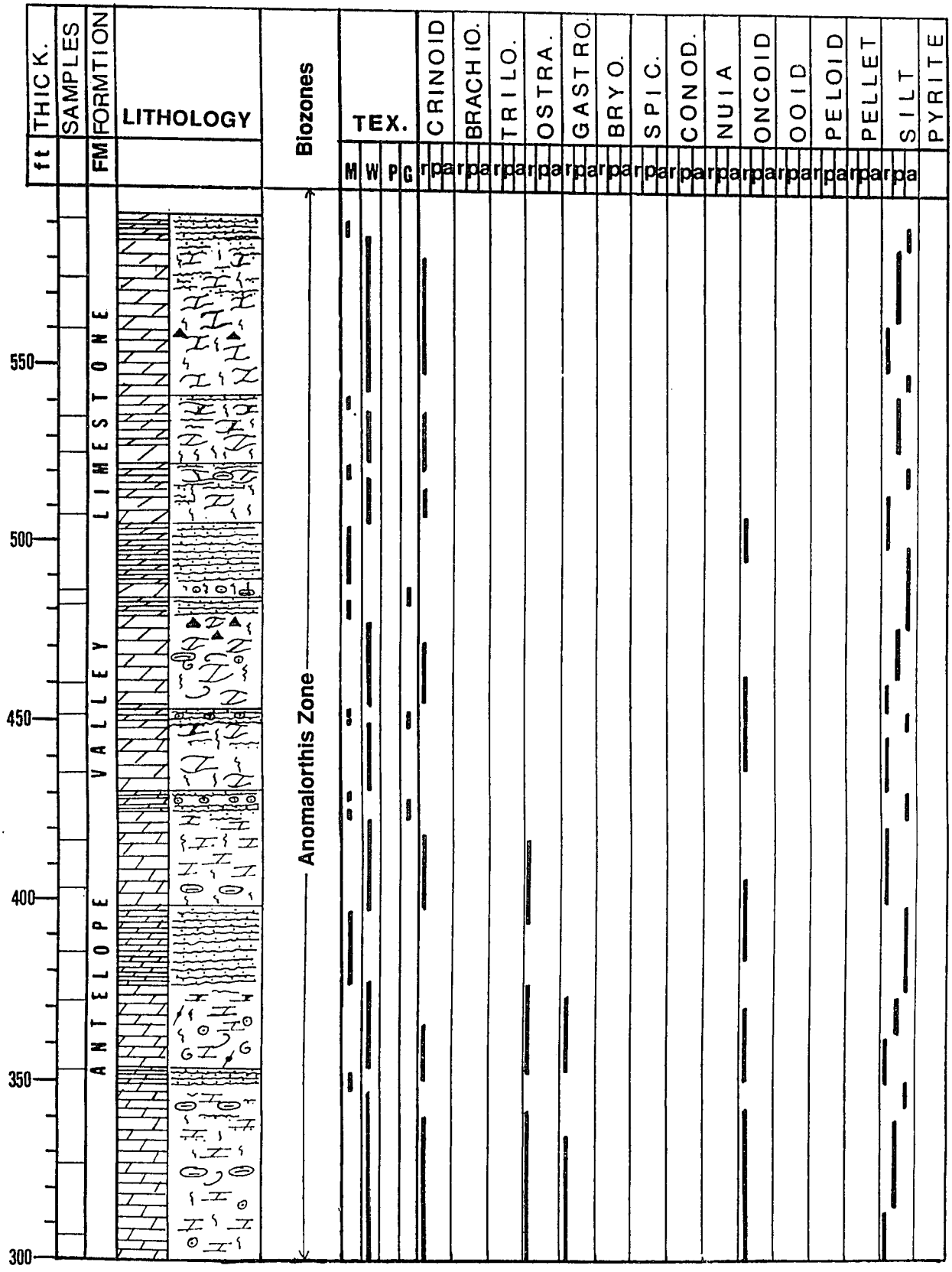
Ninemile Canyon Section



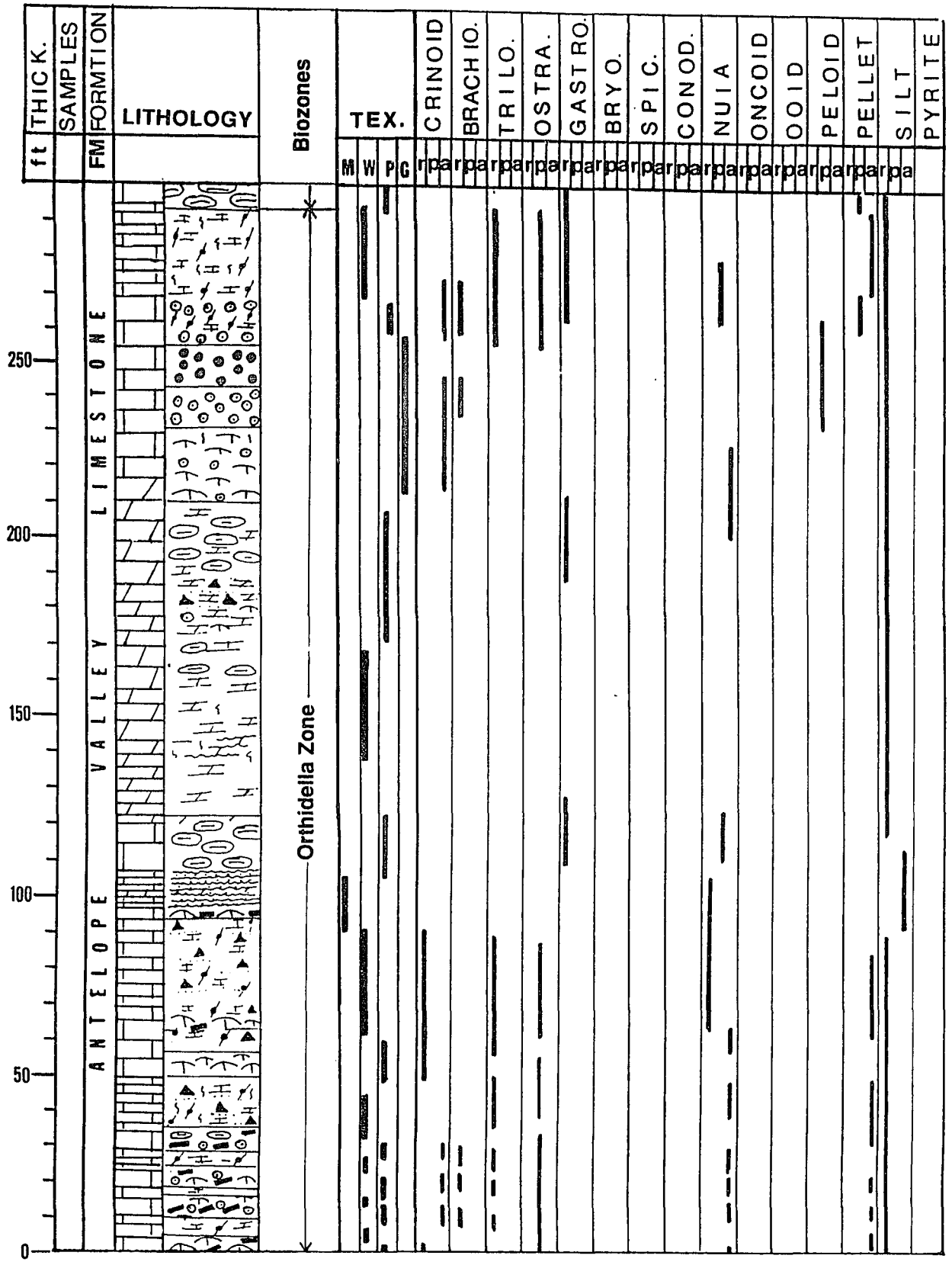
Ninemile Canyon Section



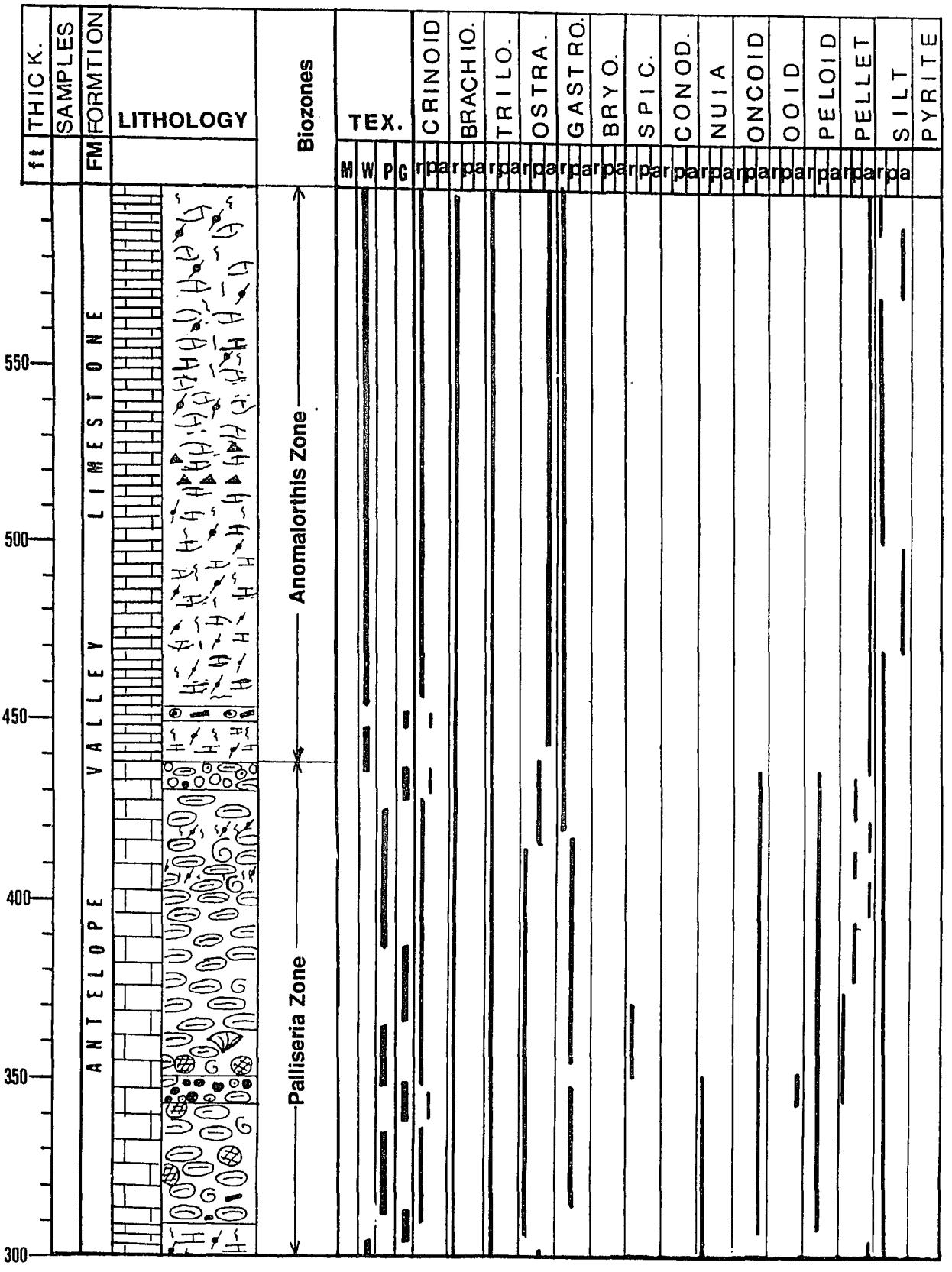
Keystone Canyon Section



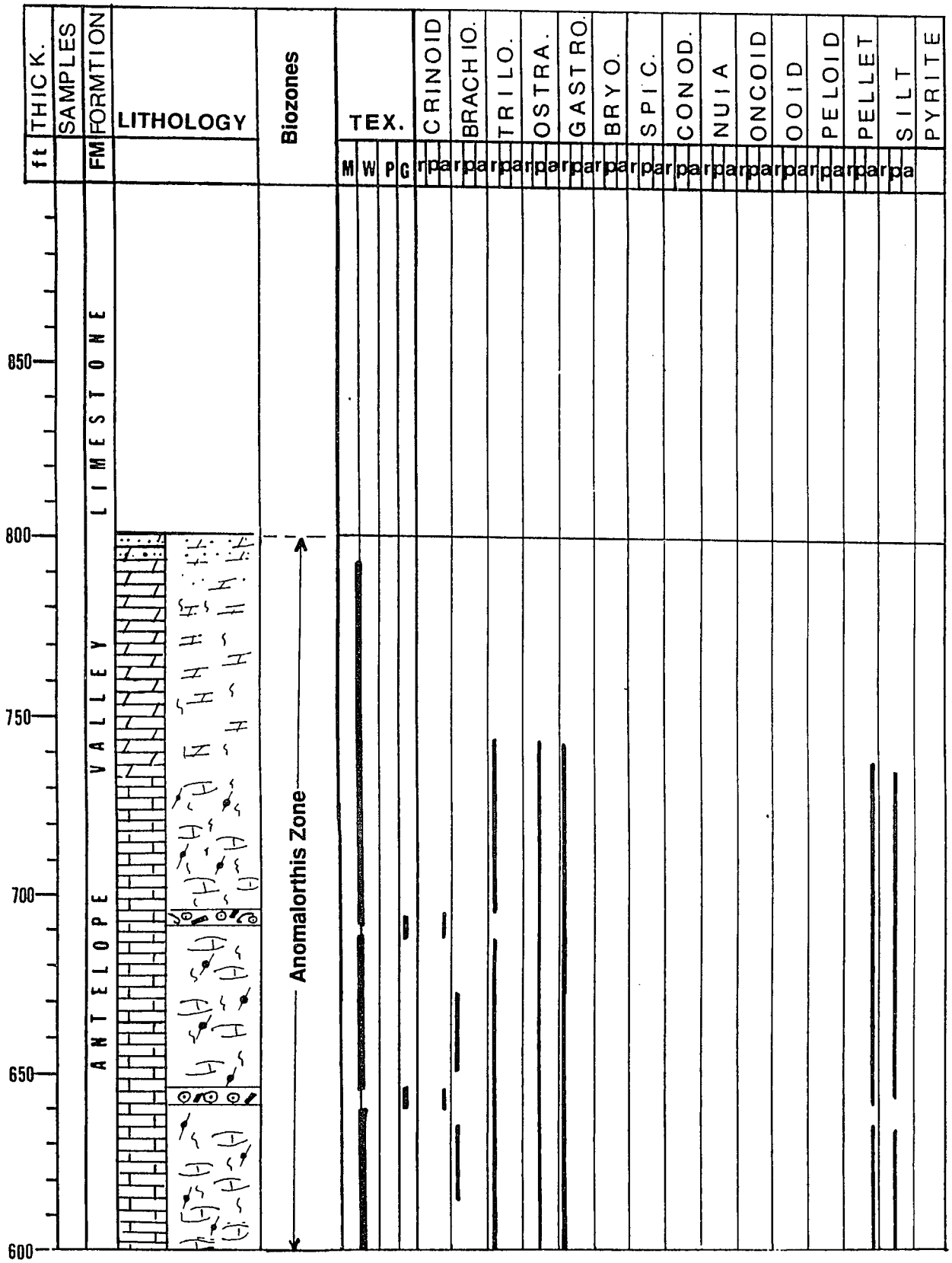
Keystone Canyon Section



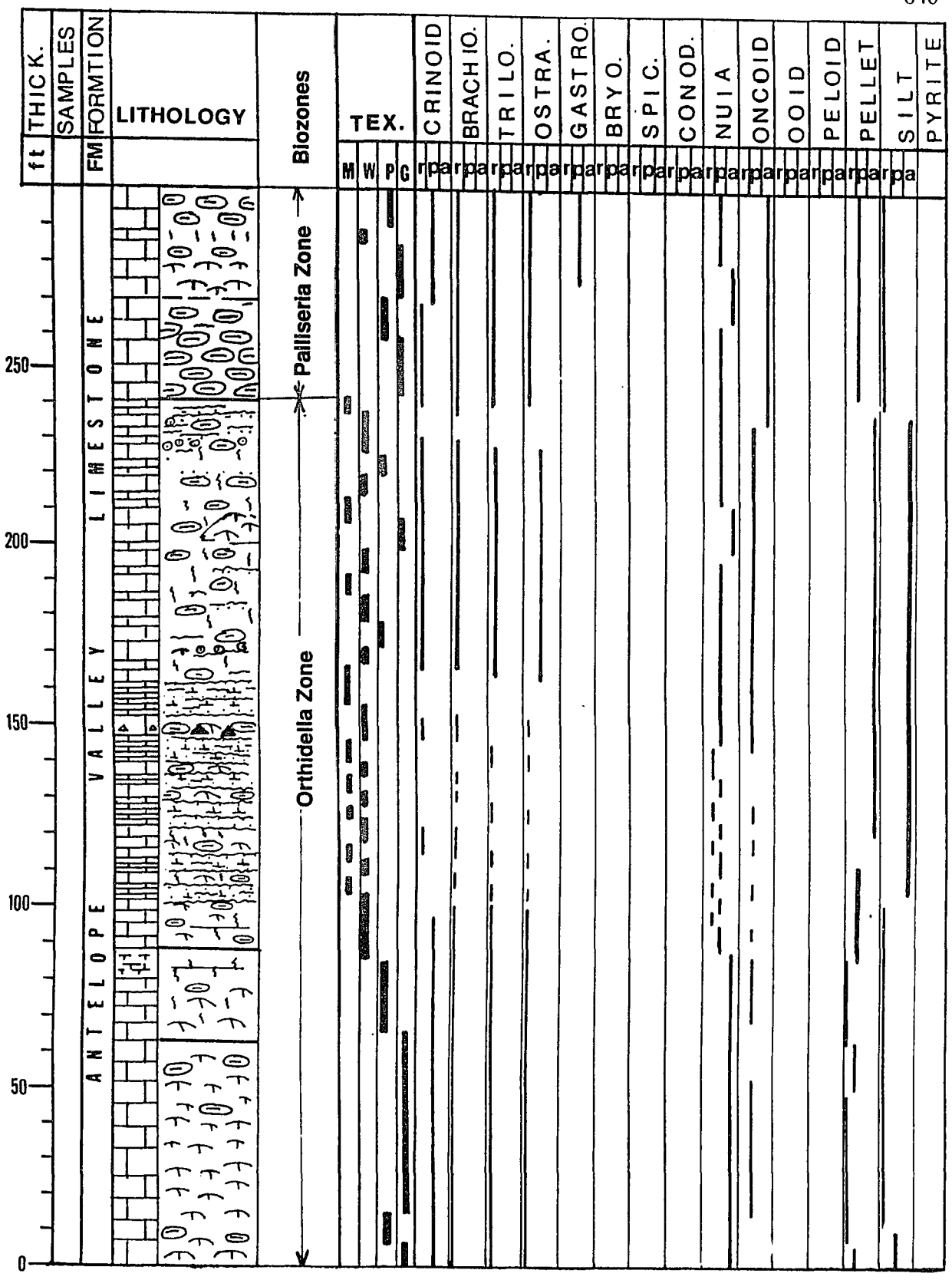
Lone Mountain



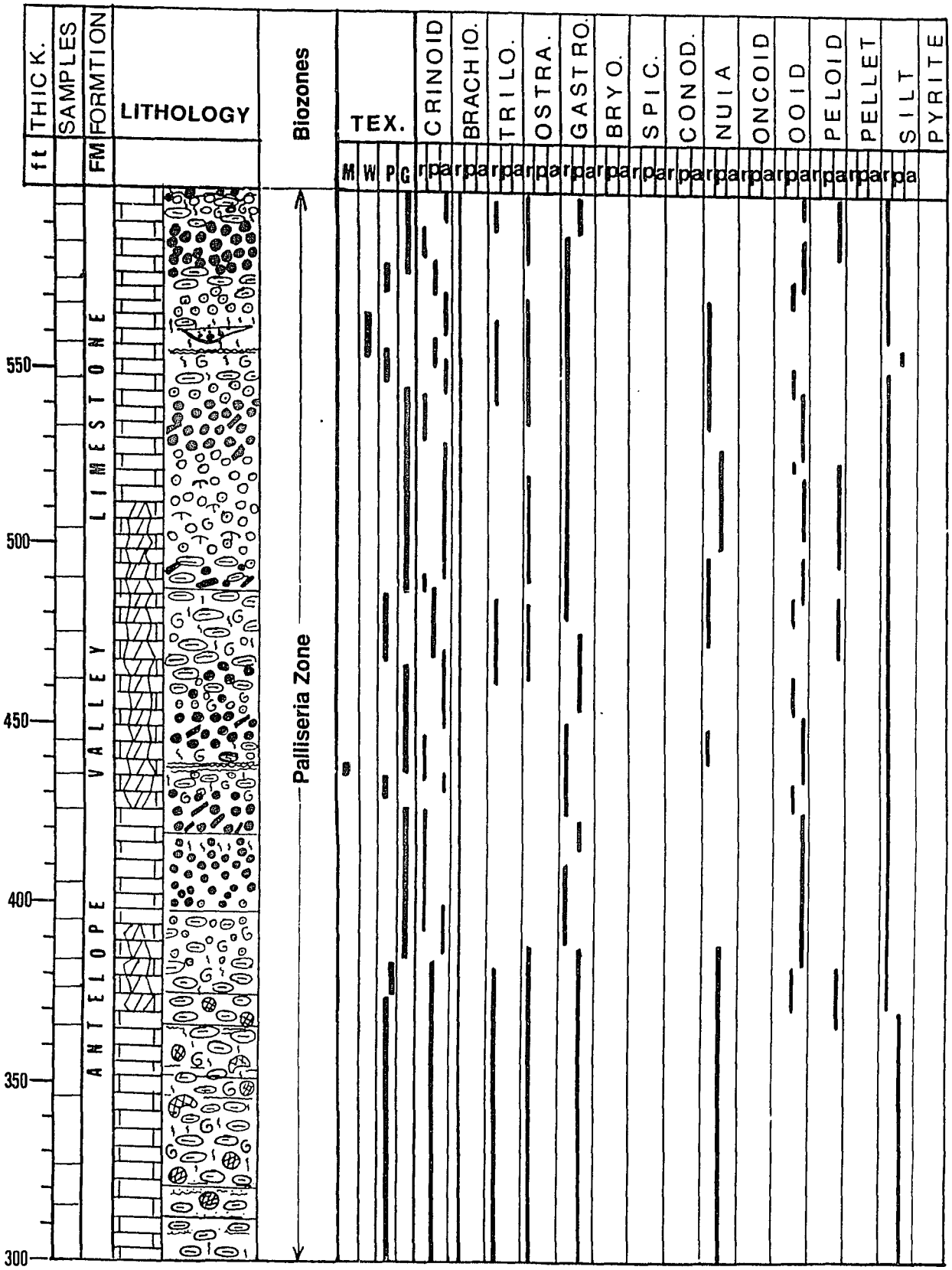
Lone Mountain



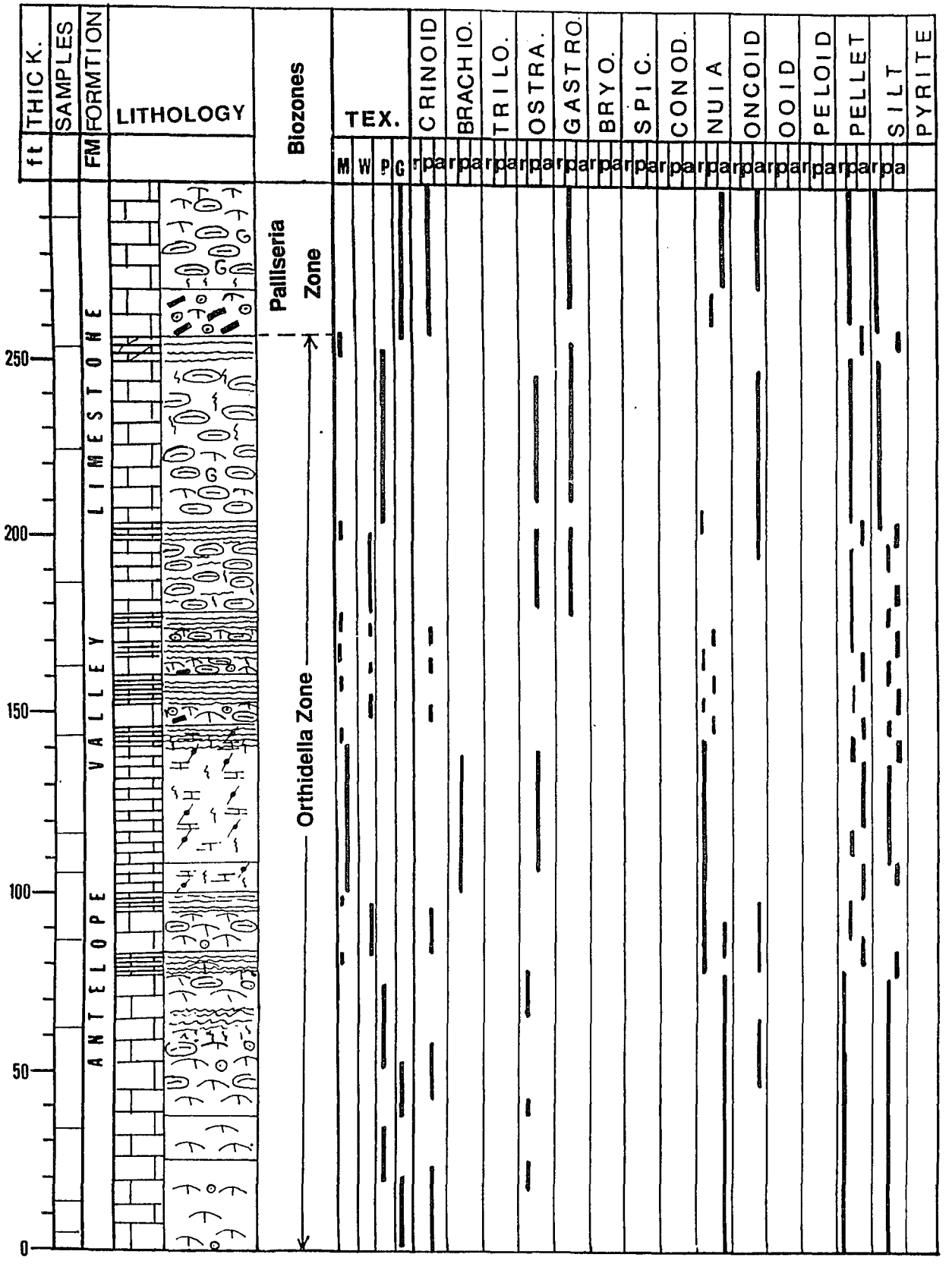
Lone Mountain Canyon



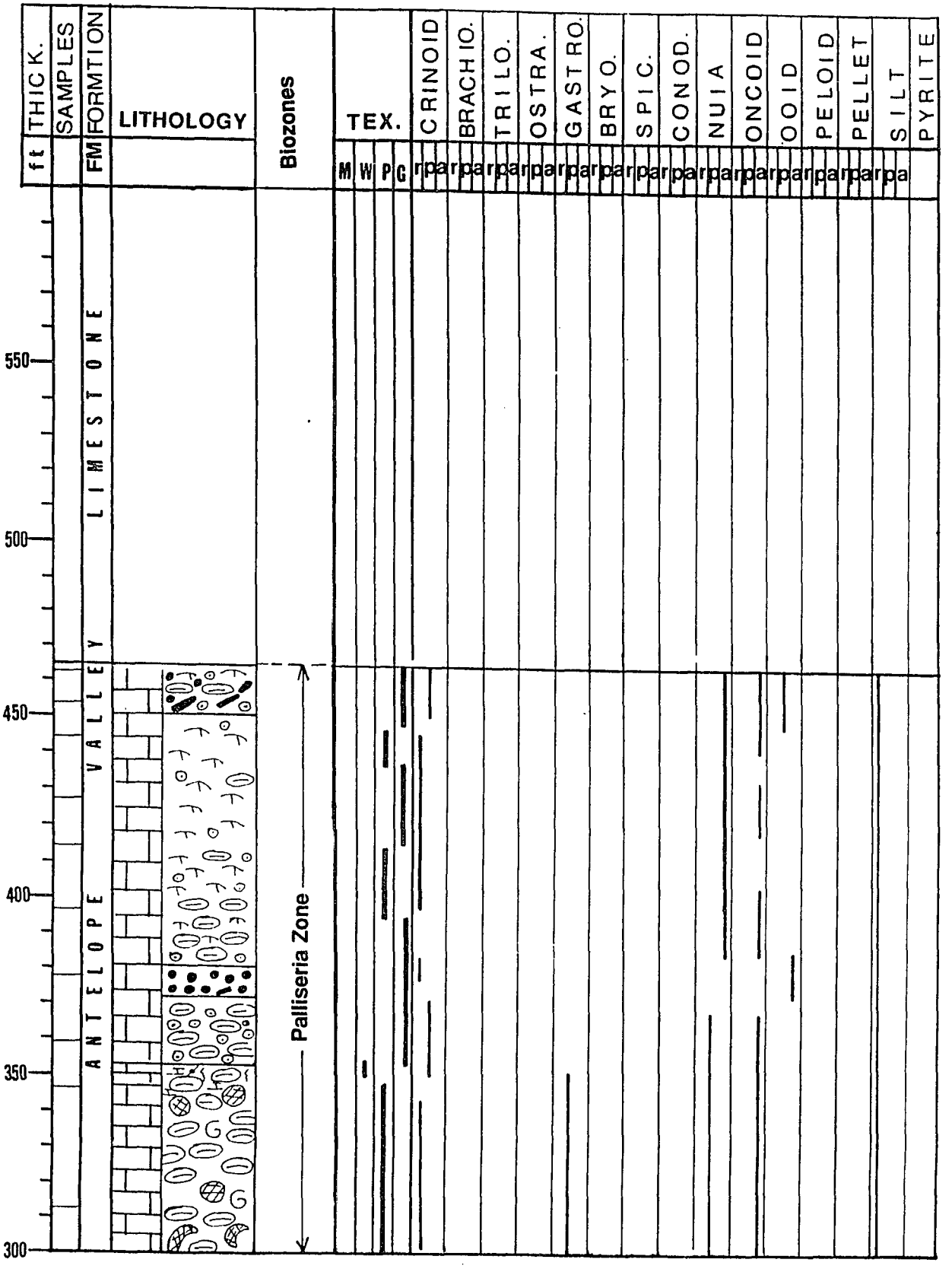
Martin Ridge Section



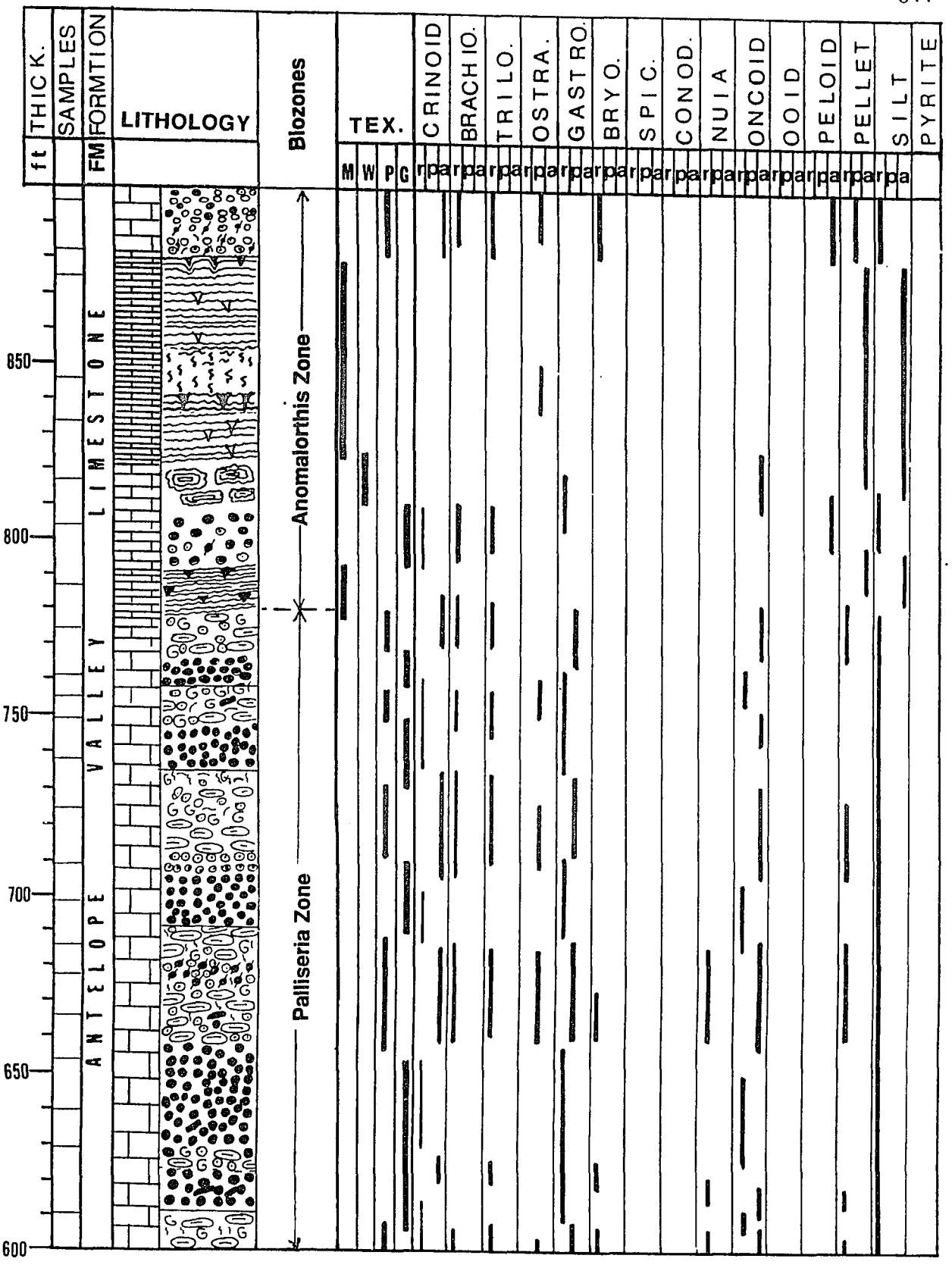
Martin Ridge Section



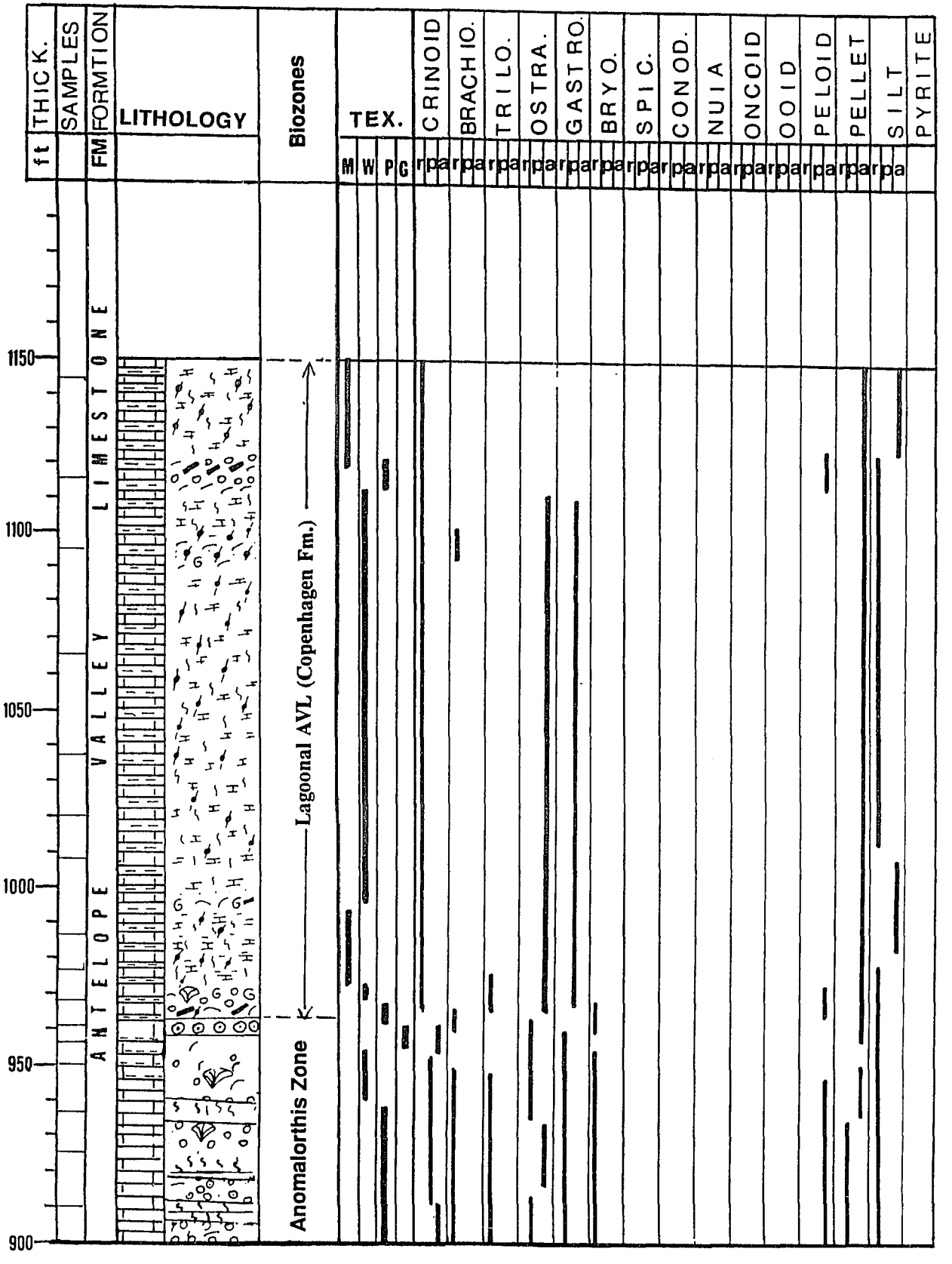
Martin Ridge Section II



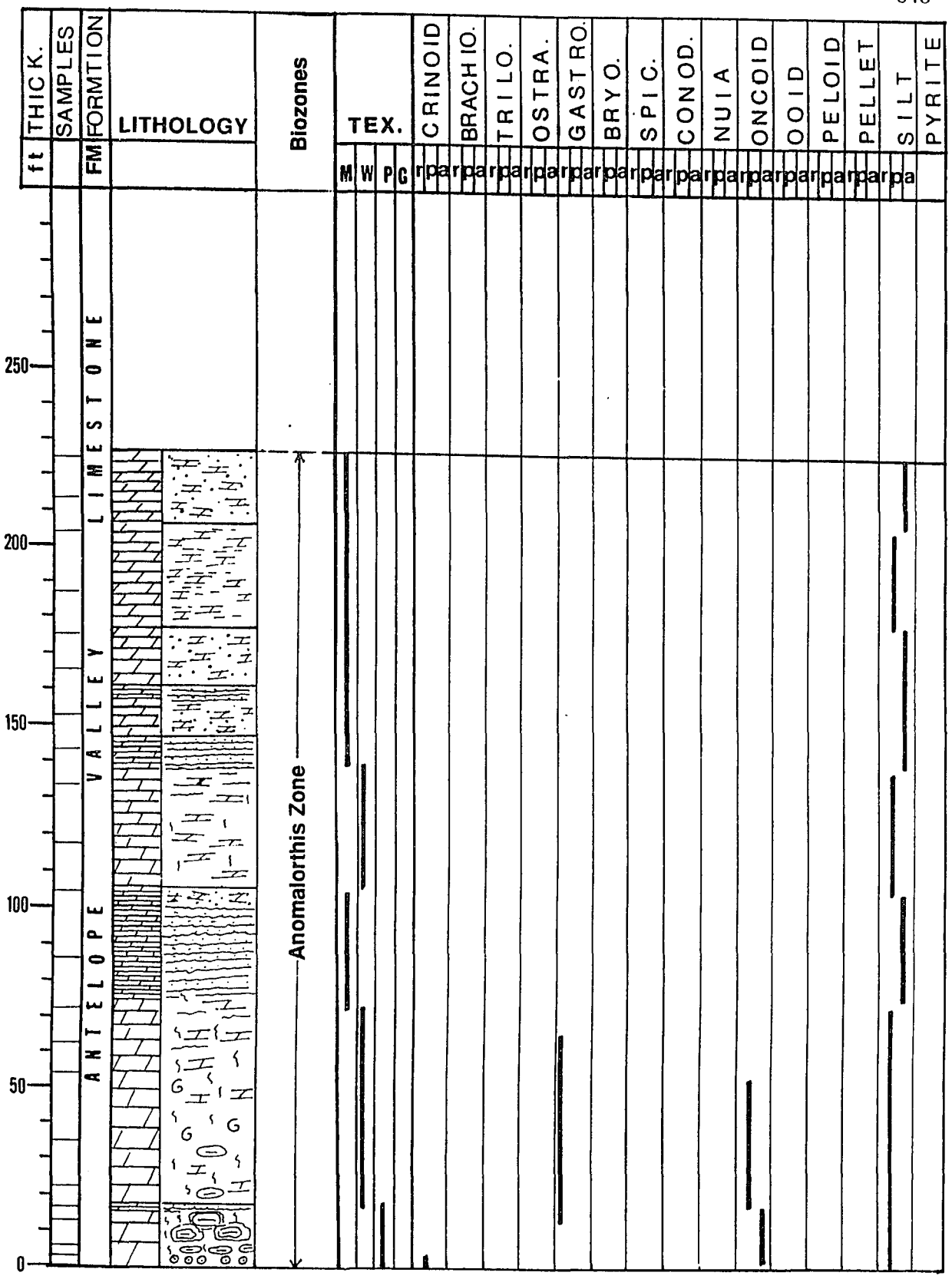
Martin Ridge Section II



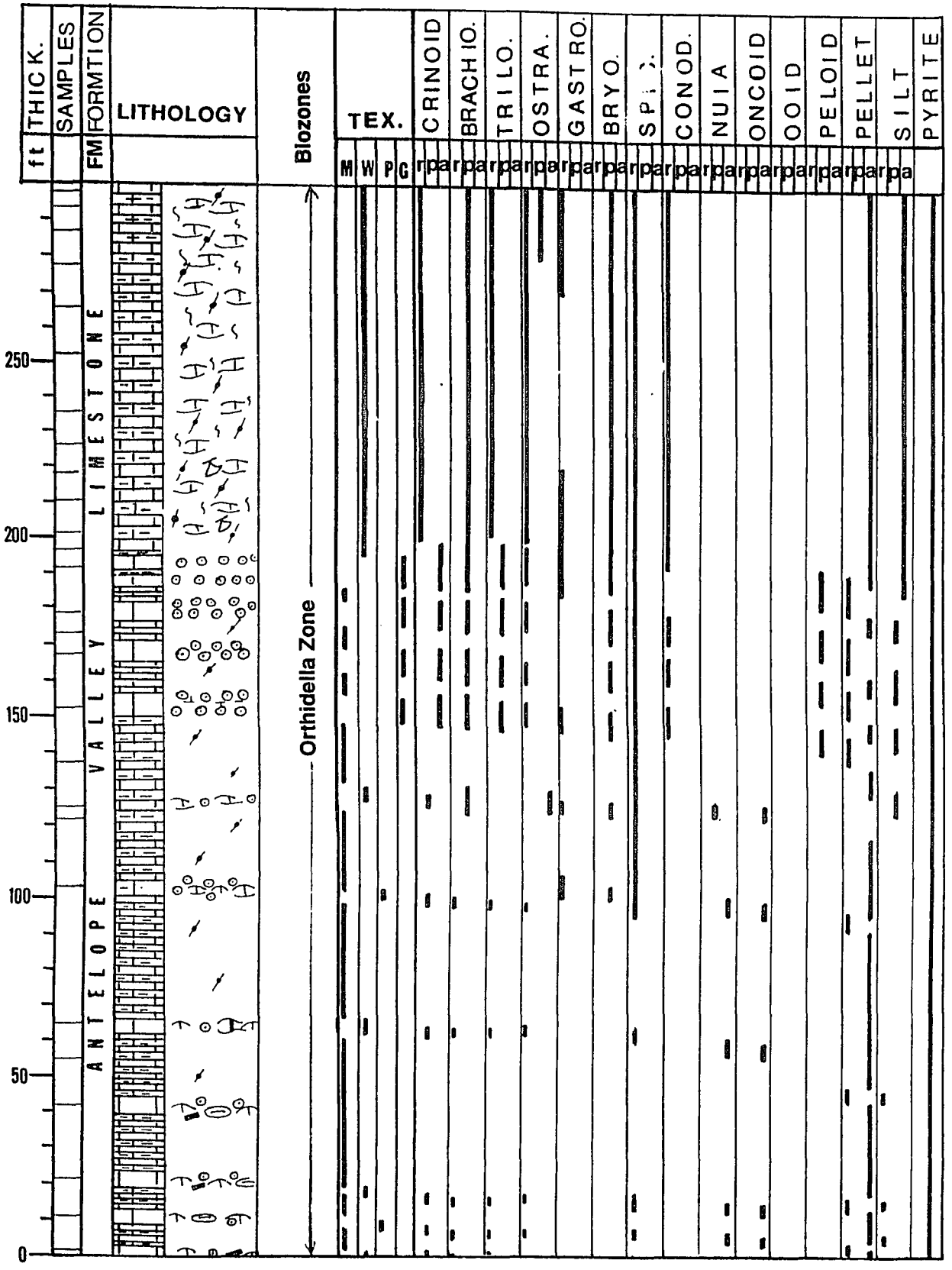
Martin Ridge Section



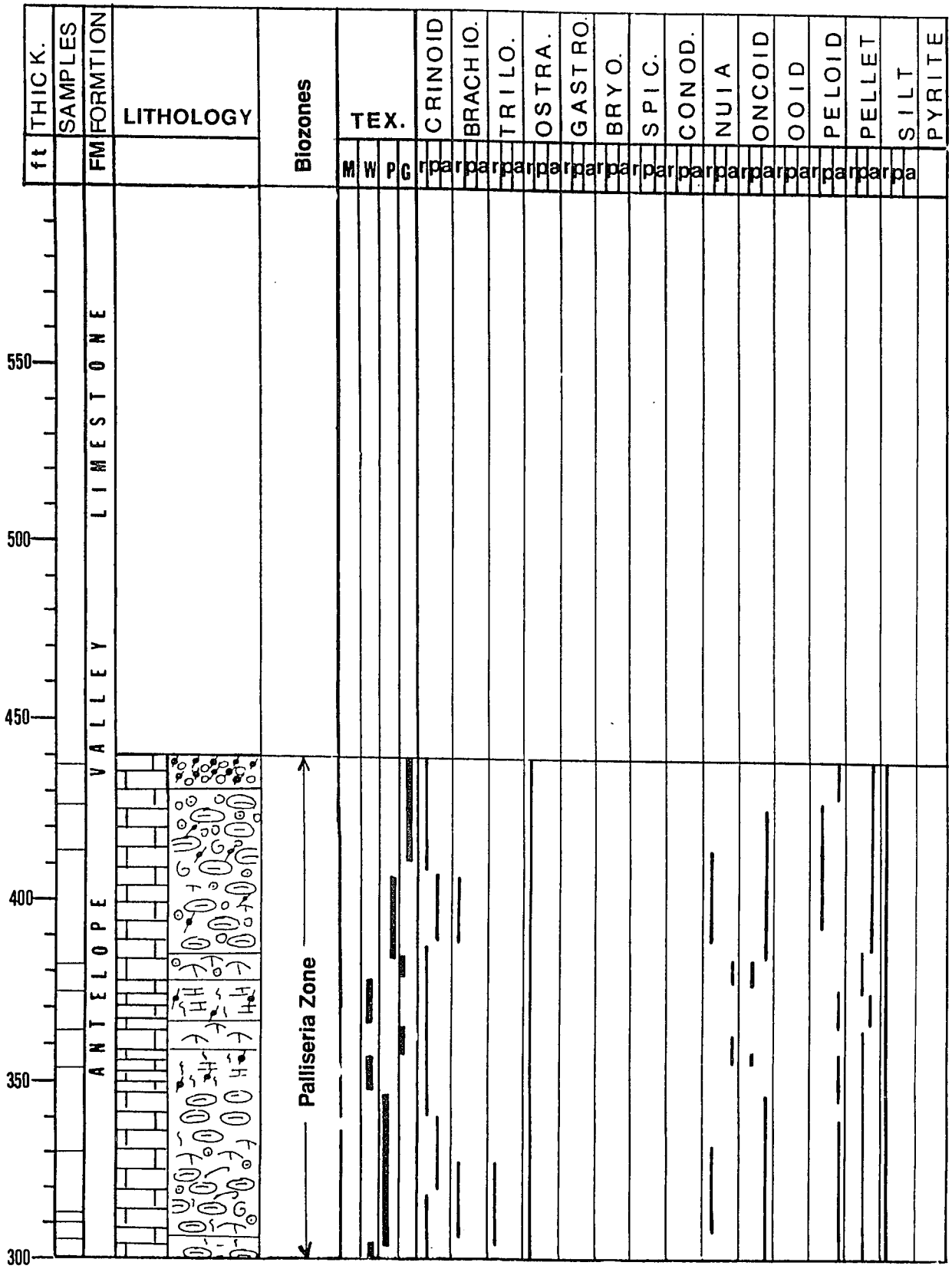
Martin Ridge Section



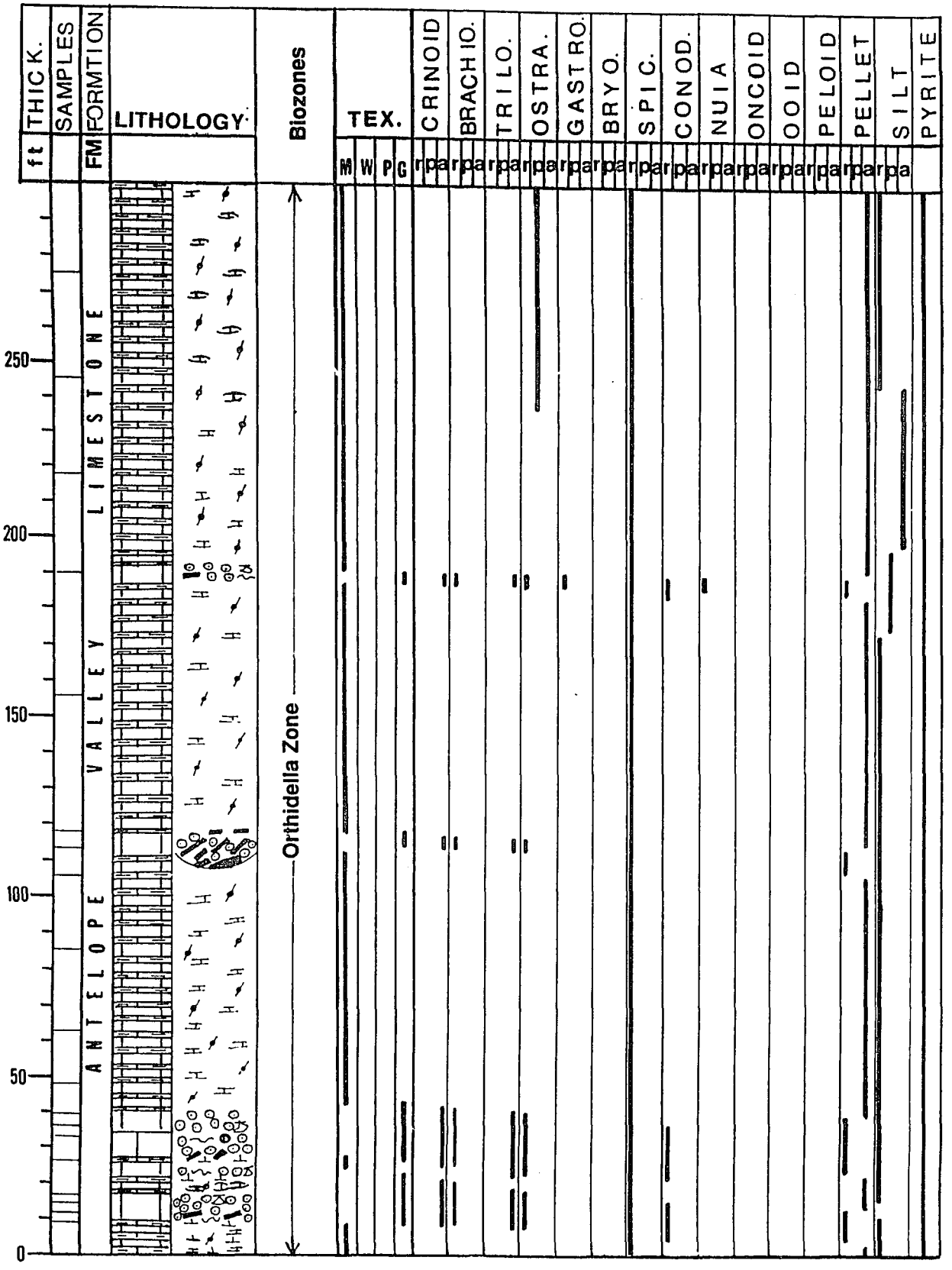
Clear Creek Canyon Section



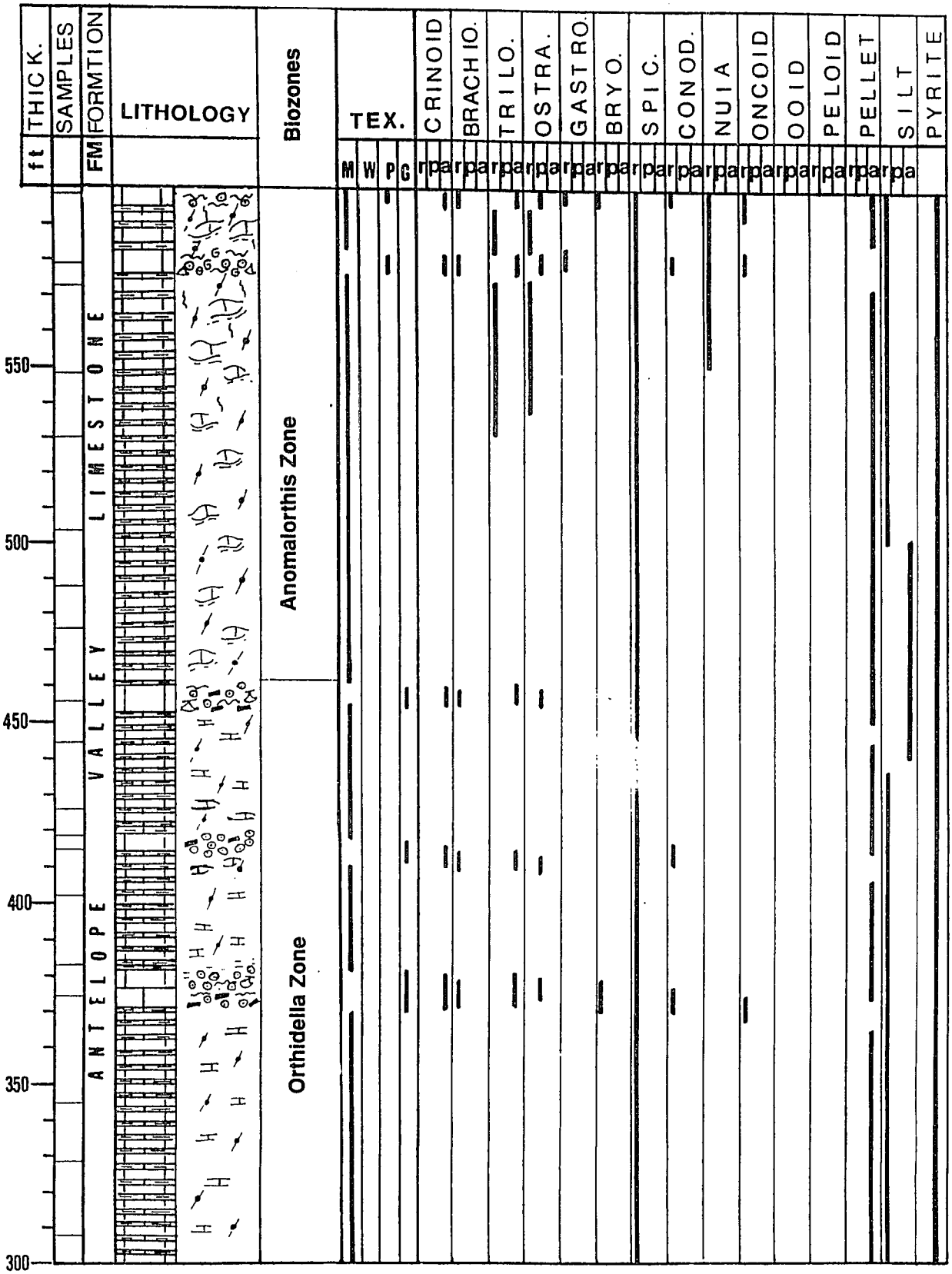
Whiterock Canyon Section



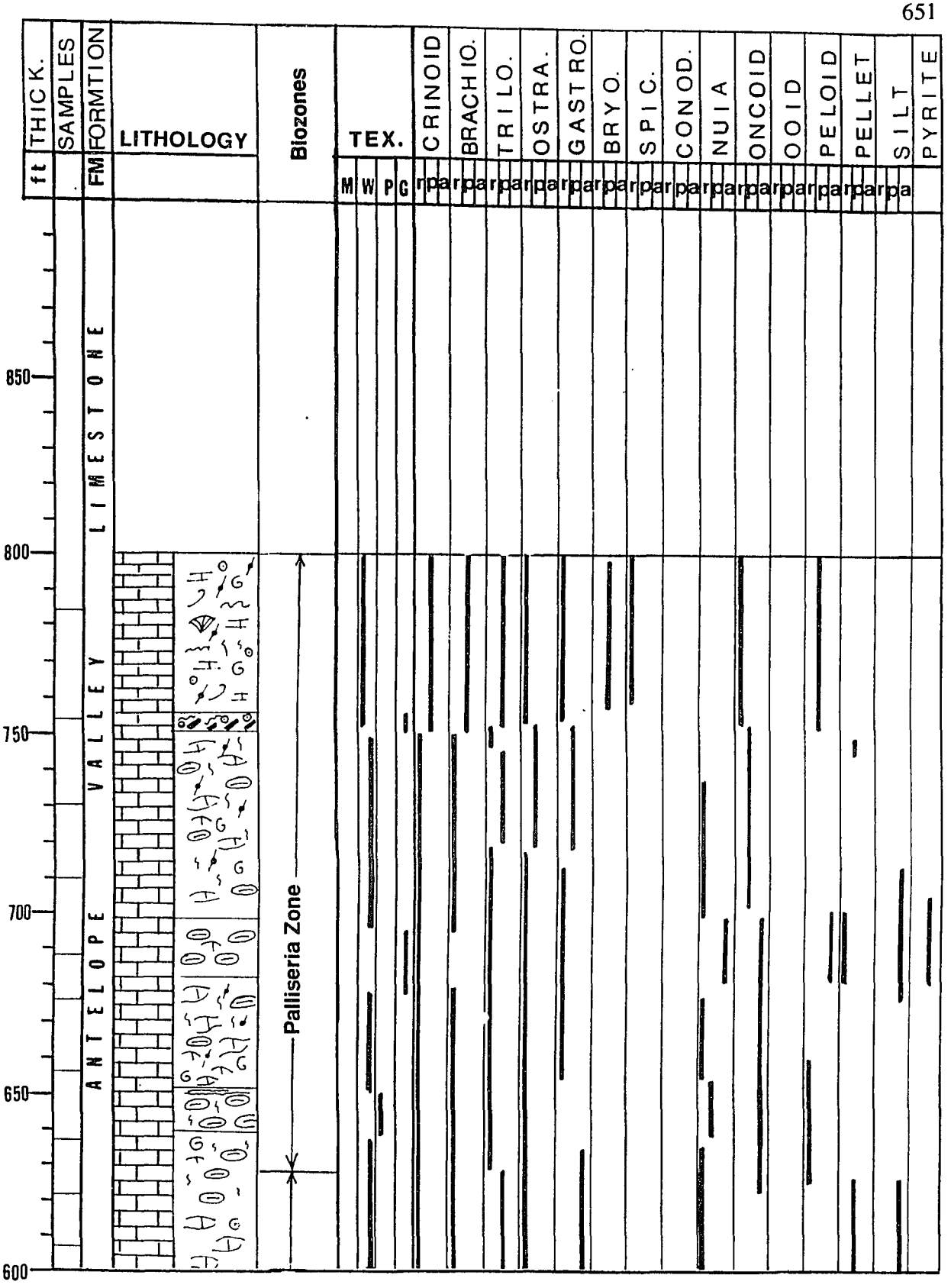
Whiterock Canyon Section



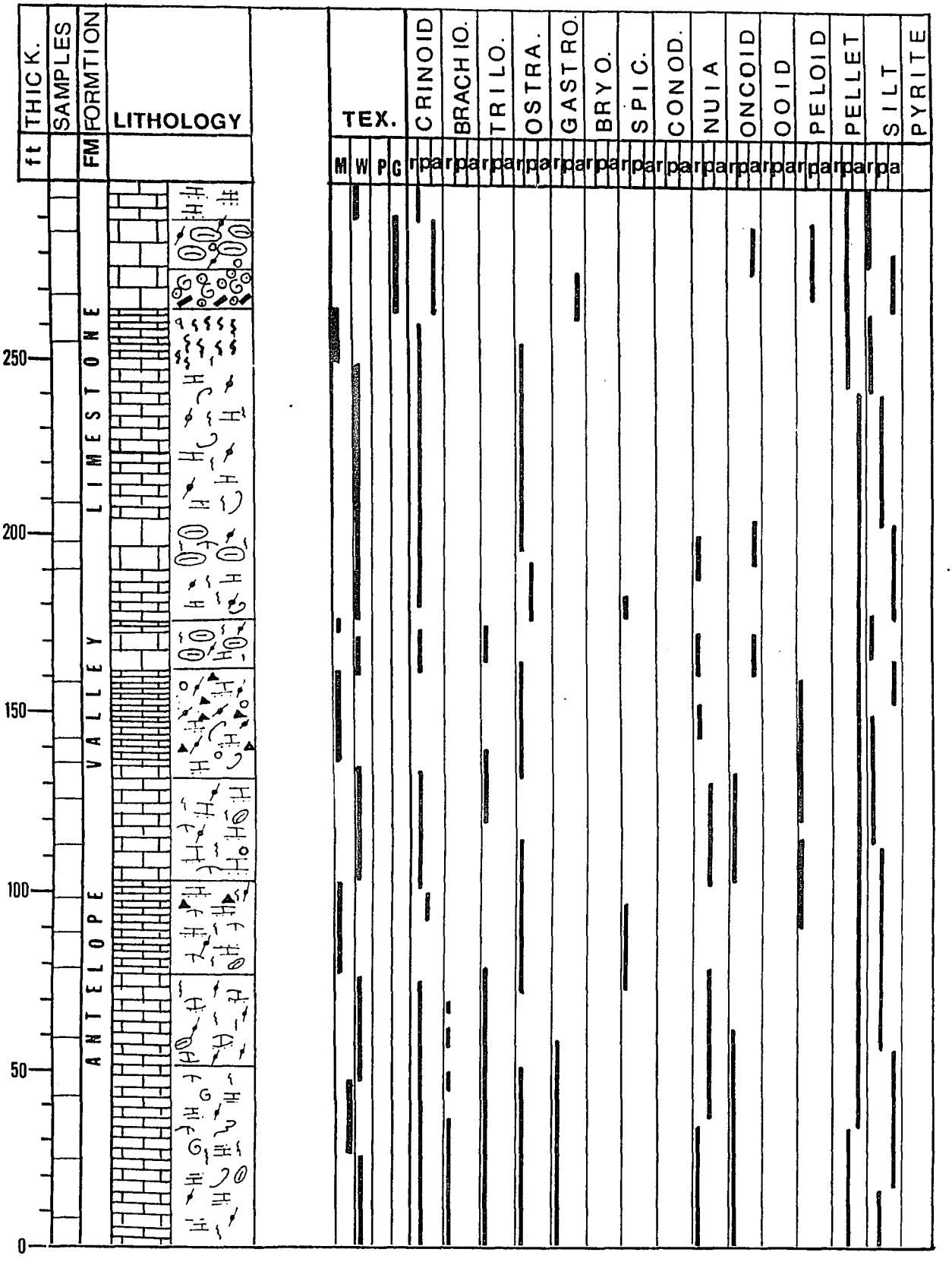
June Canyon Sequence (Iks Canyon)



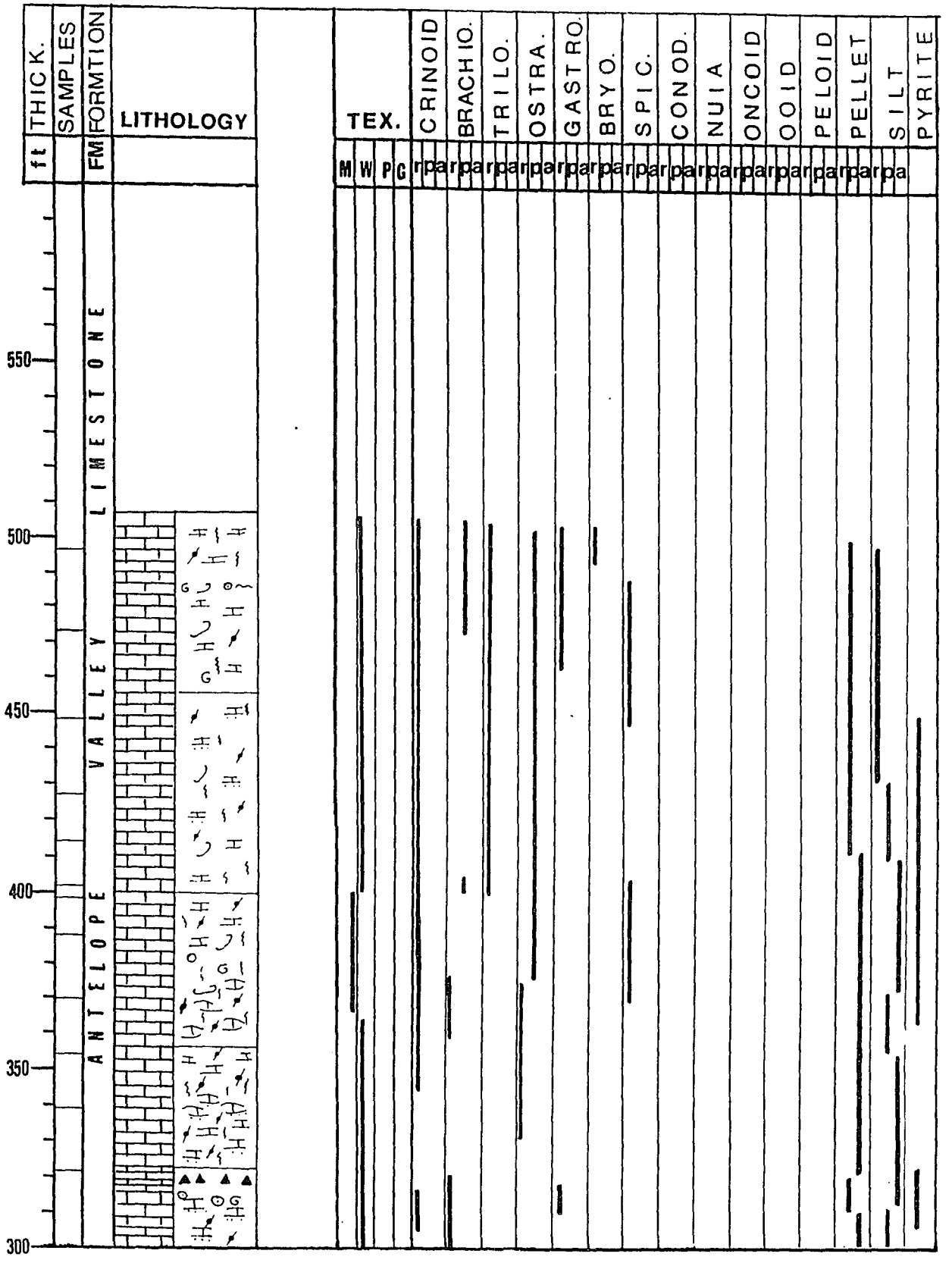
June Canyon Sequence (Iks Canyon)



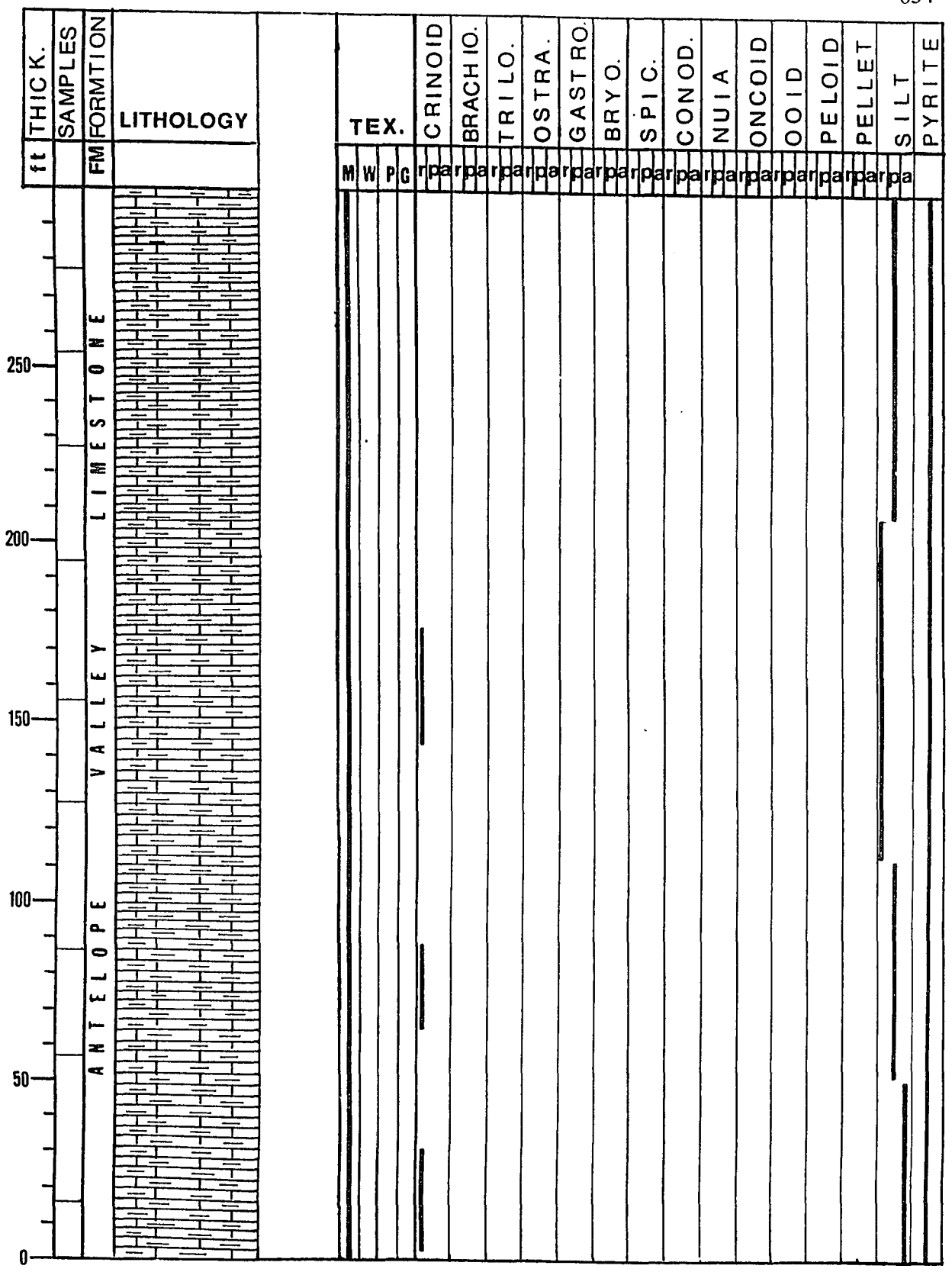
June Canyon Sequence (Iks Canyon)



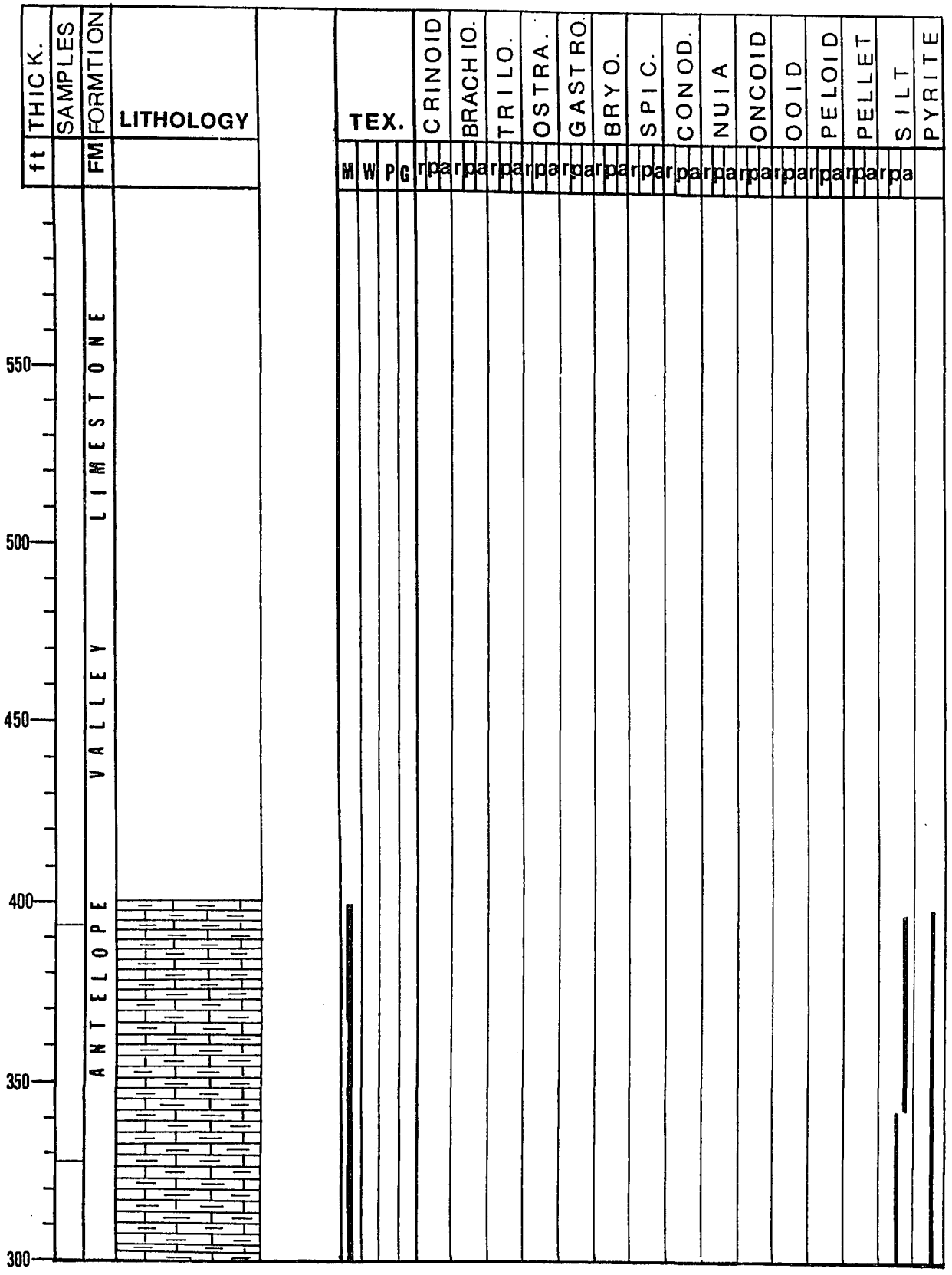
Mill Canyon Sequence (Iks Canyon)



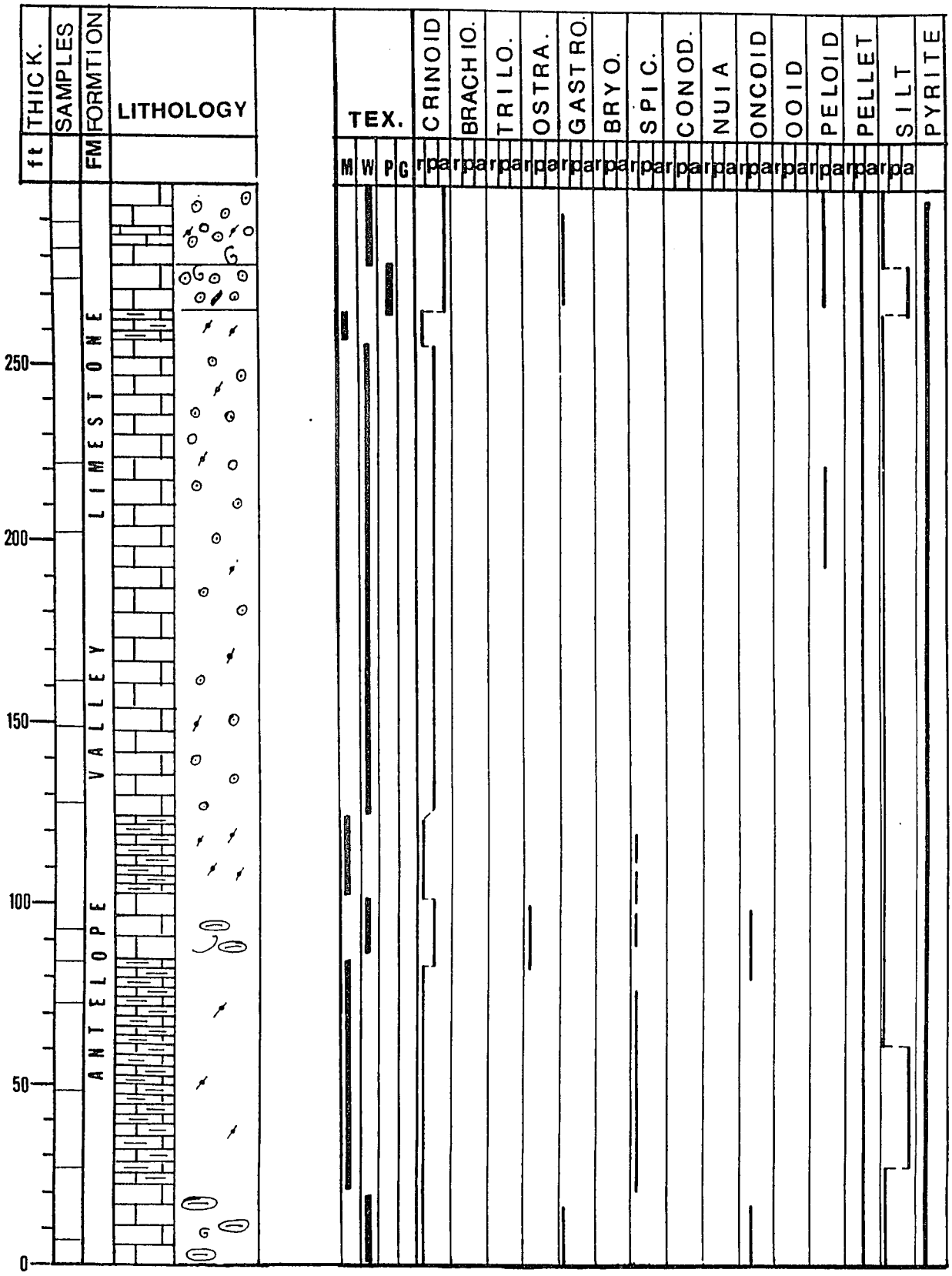
Mill Canyon Sequence (Iks Canyon)



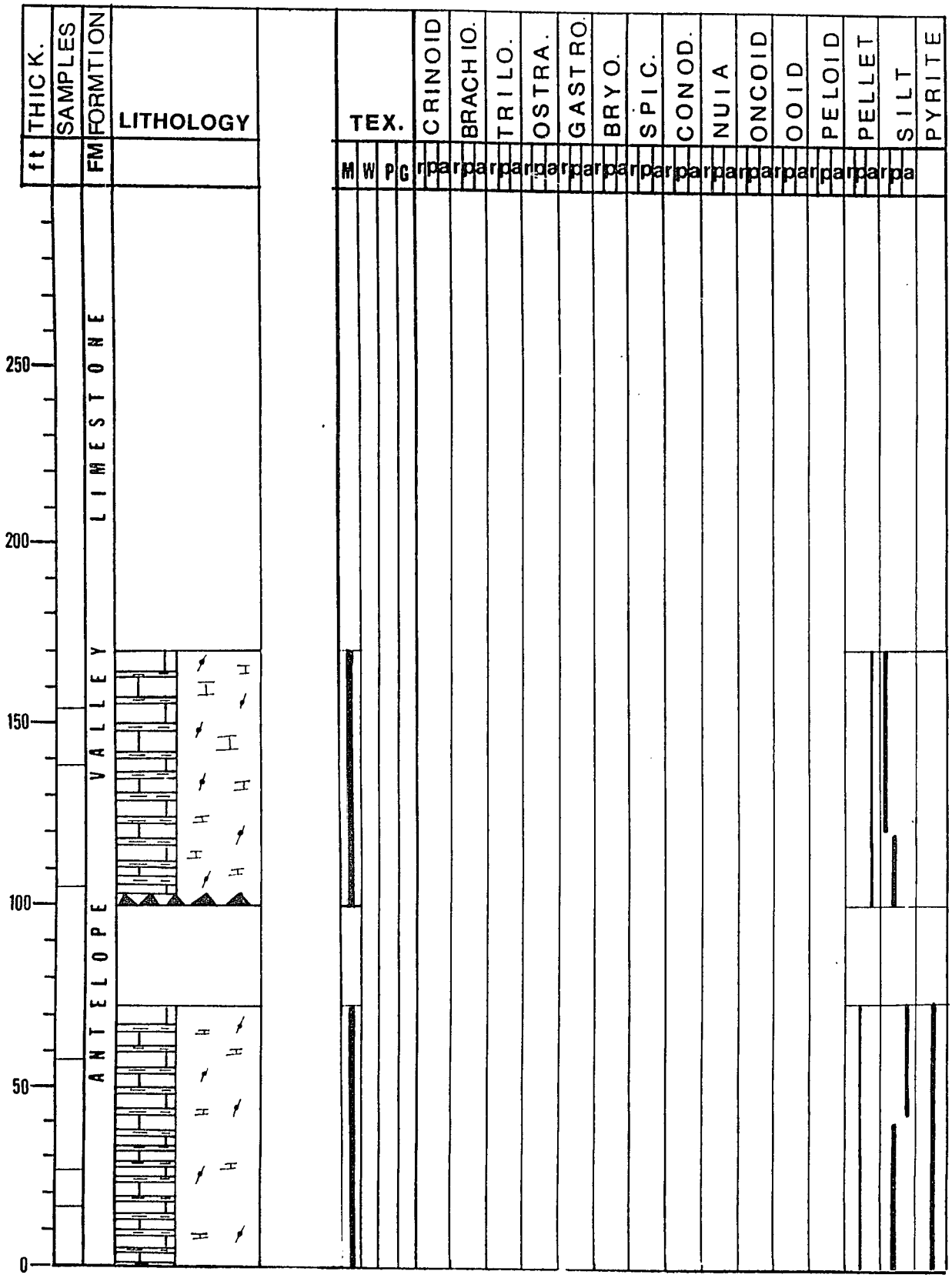
Toiyabe Peak Section



Toiyabe Peak Section



Dry Creek Canyon Section



Reeds Creek Canyon Section

APPENDIX I-C: OCCURRENCE AND GROWTH FORMS OF NUIA (PROBLEMATIC ALGAE)

A. Occurrences and Geographical Distribution of Nuia

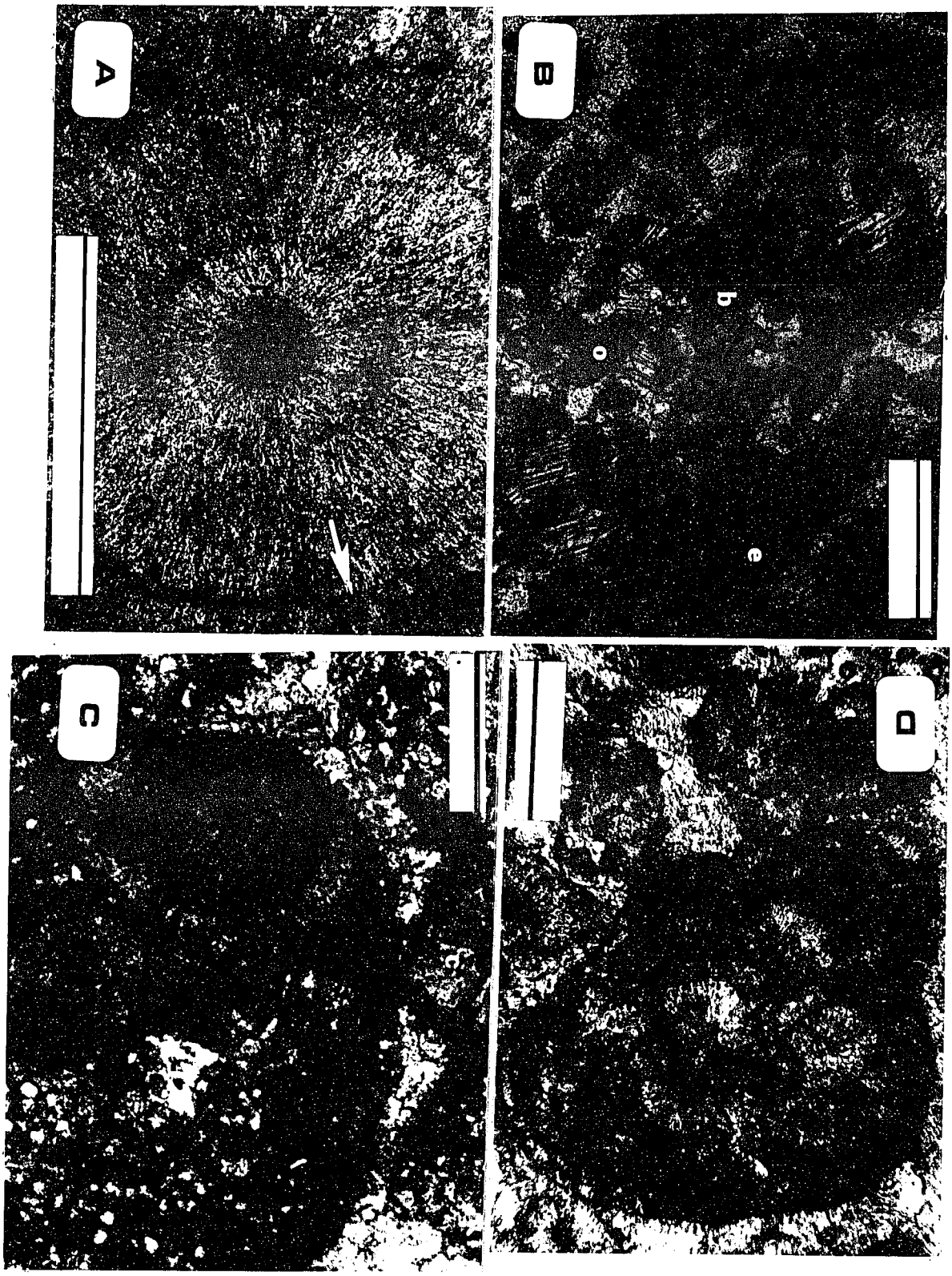
Nuia, the remains of the problematic calcareous algae, for the first time was noted by Maslow (1954) in the Middle Ordovician rocks of Kazakhstan and Siberia. With a dark micritized-central canal and radiating calcite crystals within the circular-wall forms, Nuia appears similar to radial ooids (Fig. 16 A). This form of Nuia has been identified by many workers as a deformed-radial ooid or just radial ooid (see Braun and Friedman, 1969). For instance, in the Antelope Valley region, Nuia-bearing strata were interpreted as oolitic shoal units by Morreale (1981).

The occurrences of these algal remains and their close association with Girvanella have been reported in the Lower Cambrian through Middle Ordovician rocks. Girvanella, a blue-green algae, commonly bores and coats Nuia (Toomey and LeMone, 1977). It is commonly believed that Nuia like other floras might have lived and flourished in a photic zone where oxygen is sufficient for photosynthesis. This can be inferred from the close associations between these two algae.

Algal experts disagree over the origin of Nuia and which algal group Nuia belongs to (Toomey and Klement, 1966). Thus, it has been called problematical algae. On the other hand, Ross et al. (1988) considered Nuia as a dasycladacean (green algae) and the functional equivalent of the modern Halimeda. They concluded this on the basis of morphologic features, segmentary appearances, and branching nature of Nuia.

Nuia-bearing strata were reported in the US and other countries by the following studies: in the Lower Ordovician Monitu Formation, in Colorado by Sweet (1964); (2) in the Cambro-Ordovician Dagger Flag Formation in Texas by Johnson (1966); (3) in the sponge mounds of the Lower Ordovician strata of the El Paso Group in Franklin

Figure 203- Photomicrographs of various growth forms of Nuia in the AVL. A) One wall-structured Nuia, scale= 0.25 mm. B) Oblique (o) and elongated (e) cross sections of normal dichotomy and budding-growth forms (b) of Nuia. C) Girvanella-coated, multiwall-structured Nuia or encasing-growth form of Nuia. D) Undescribed Nuia growth form by Mamet and Roux (1982). Arrows indicate two central canals in a multiwall-structured Nuia. With plane-polarized light; for B, C, and D, scales= 0.5 mm.


A
B
b
o
e
C
D

Mountain, Texas, by Toomey and Klement (1966)--Toomey and Klement also reported the multi wall-structured Nuia; (4) Receptaculites in the Nuia and Girvanella-rich biostromes with gastropods, bryozoans, brachiopods, ostracods, and trilobites in the Bromide Formation, Oklahoma by Toomey (1967); (5) within the Chazian mounds of the Lake Champlain region by Toomey and Finks (1969); (6) in the Lower Pogonip Group, probably in the Antelope Valley Limestone in the Arrow Canyon Range in Clark County, Nevada by Stricker and Carozzi (1977); (7) in the Chazian mounds of Quebec, Lake Champlain and Vermont by Shalaby (1983), and Roux (1985); (8) in the Orthidella zone of the Antelope Valley Limestone (AVL) at the Martin Ridge and Ninemile Canyon sections by Taban (1986), and in addition to these two sections, in the Lone Mountain and Whiterock Canyon sections, and in the Mill Canyon and June Canyon sequences by Kaya and Friedman (1987), and in the other type sections of the central and southern localities of the AVL by Ross et al. (1988); (9) in the Orthidella zone and lower part of the Palliseria zone of the Antelope Valley Limestone (AVL) at the Antelope Valley region in this current study; (10) in the Lower Ordovician strata of Argentina by Gnoli and Serpagli (1980); and (11) in the Whiterockian shallow-water carbonates of the Auchensoul Limestone in Scotland by Ince (1984).

B. Description of Nuia and Its Growth Forms

Nuia is the remains of the problematical calcareous algae with a dark micritic-central canal and wall structures composed of several concentric layers of radial calcite crystals (Fig. 16 A), and in places Girvanella commonly coats Nuia (Fig. 16 C). Nuia particles are similar in cross sections to those of the radial ooids, yet they are significantly different from them by their elongate sections. The following criteria can be used to differentiate radial ooids and Nuia remains: the in Nuia radiating-calcite crystals are continuous through successive wall layers

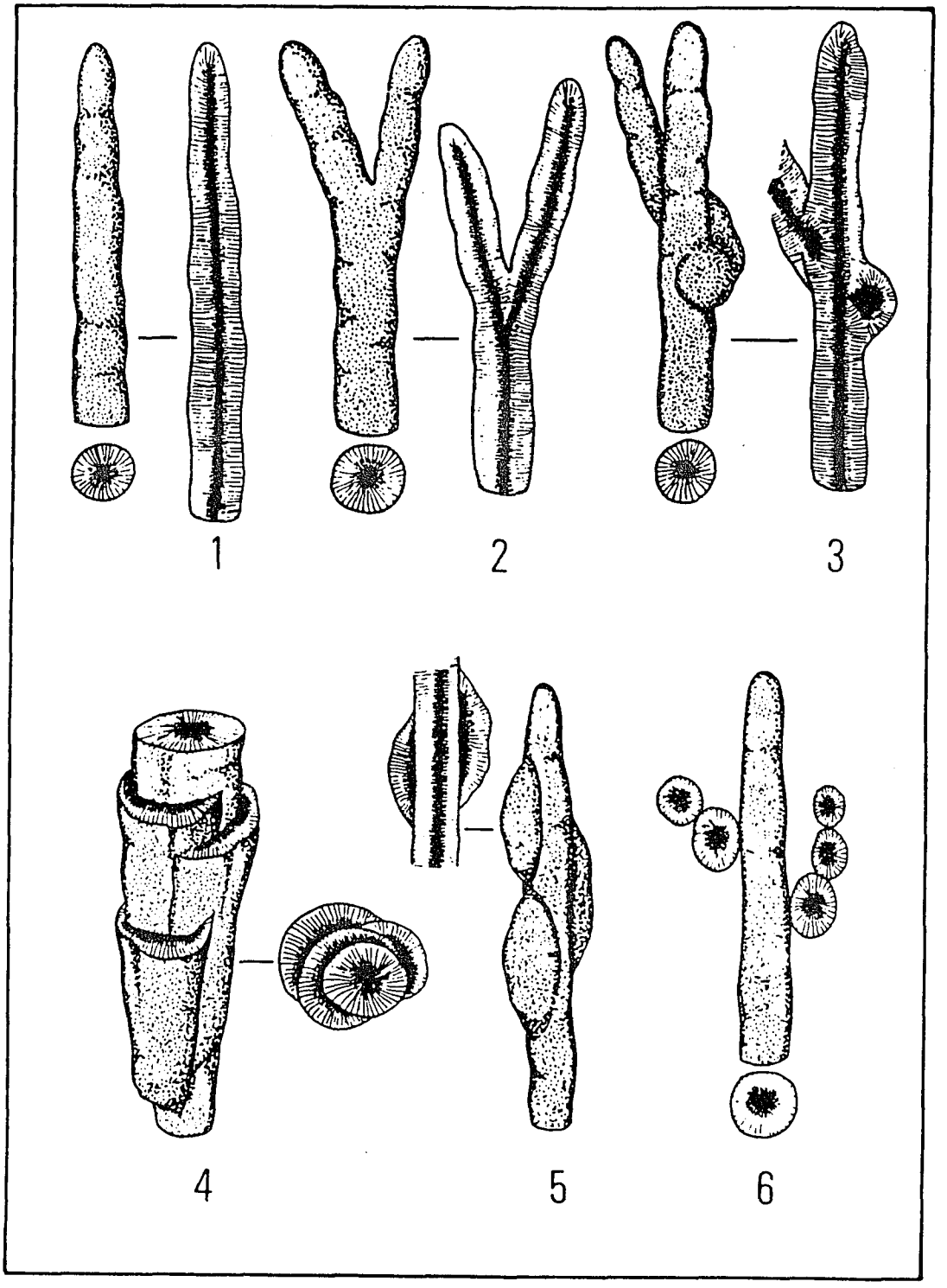


Figure 204- Reconstructed-growth forms of Nuia by Mamet and Roux (1982): 1) Normal growth; 2) normal dichotomy; 3) embracing dichotomy; 4) encasing growth; 5) external-veneering growth; and 6) budding growth.

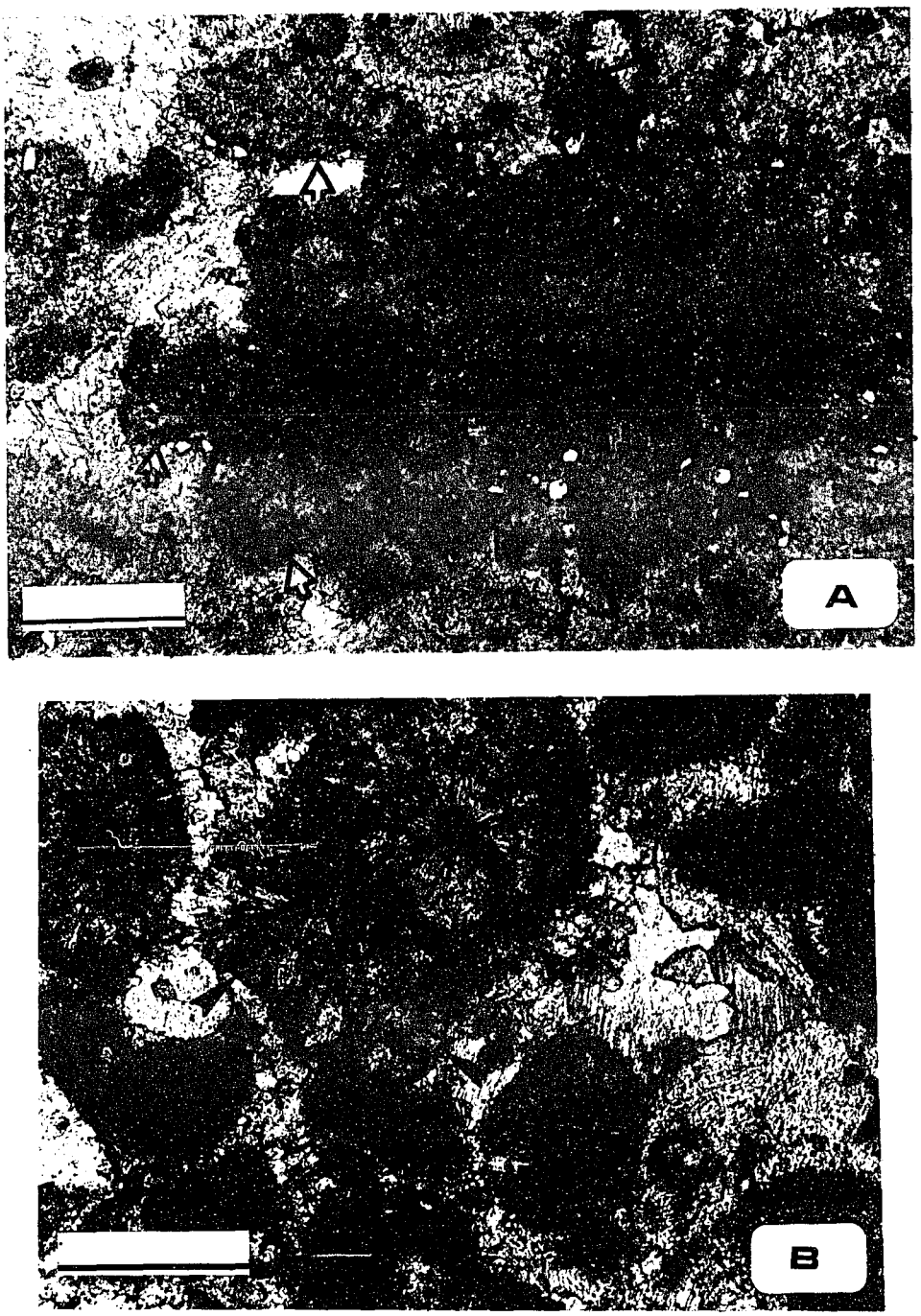


Figure 205- Photomicrographs of Nuia growth forms which were not described by Mamet and Roux (1982). A) A multiwall-structured Nuia with an elongated-micritic central canal is similar to the encasing growth form, but it is different from third growth form by its multiple-digitated branches (arrows). B) A combined-growth form of Nuia by normal- (indicated by arrow) and branching normal dichotomy-growth forms. With plane-polarized light, scales = 0.5 mm.

(Fig. 16 A, B); in radial ooids, however, the radiating-calcite crystals are commonly constrained to each concentric lamina (cortice) representing different episodes of grain growth.

Nuia particles with one-and two-wall structure are the most common types of these problematic algal remains. However, multi-wall structured Nuia remains (Fig. 16 C, D) are relatively rare. Thus, they have been interpreted to be a new species by Johnson (1966). But Toomey and Klement (1966), and Mamet and Roux (1982) interpreted the multi-wall structured Nuia as another growth form rather than a new species. In the Antelope Valley Limestone (AVL), Nuia particles appear to be circular, oval, and elongated and range from two- to multi-layered in their wall structures. This evidence suggests that Nuia particles represent originally 4 to 6-mm long cylindrical, fingerlike segments. When these fingerlike segments are cut along the different axes (Fig. 16 D), the cross sections of the indicated fingerlike segments result in the circular, ellipsoidal and elongated appearances. The grain size of these algal remains vary significantly for each type of Nuia in thin sections: (1) circular cross sections ranging from 0.1 to 0.5 mm, with an average grain size of 0.2 to 0.3 mm; (2) oval or ellipsoidal cross sections having the same diameter as seen in the circular Nuia, but their longer axis varying between 0.3 and 0.5 mm. Grain size of two-wall structured Nuia remains range between 0.5 and 1.5 mm, but the most common grain size of the two wall-structured Nuia ranges from 0.6 to 0.7 mm. The average grain size of the elongated-Nuia forms is 3 to 4 mm in length and have a diameter similar to the circular and oblique cross sections (Fig. 16 B).

Mamet and Roux (1982) defined six-growth forms of this organism (Fig. 17): (1) normal growth; (2) normal dichotomy; (3) embracing dichotomy; (4) encasing growth; (5) external veneering growth; and (6) budding growth. However, Figure 18 shows two Nuia growth forms in this formation which were not described by Mamet and Roux (1982).

APPENDIX II: SEMI-QUANTITATIVE X-RAY DIFFRACTOMETRY ANALYSIS FOR THE STOICHIOMETRY OF DOLOMITE

A total of 47 powdered-dolostone samples from the Keystone Canyon, Clear Creek Canyon, Lone Mountain, and Martin Ridge sections were analyzed for X-ray diffractometry.

A. Peak position, d-spacing, and intensity of dolomites and calcites of the dolostones of the AVL from X-ray diffractograms.

Keystone Canyon

Sample No:	Peak	°2θ	d-sp. (Å)	I(Rel)	I(Cps)	FWHM
K.15	1	29.410	3.0346	9.70	214.3	0.230
	2	30.950	2.8870	100.00	2210.2	0.179
K.3	1	29.440	3.0315	1.23	40.0	0.327
	2	30.960	2.8861	100.00	3254.1	0.189
K.34	1	29.410	3.0346	17.25	413.4	0.179
	2	30.940	2.8879	100.00	2396.3	0.179
K.33	1	29.420	3.0335	0.69	44.6	0.216
	2	30.940	2.8879	100.00	6464.2	0.168
K.14	1	29.410	3.0346	31.27	118.0	0.188
	2	30.920	2.8897	100.00	377.2	0.259
K.13	1	29.410	3.0346	27.63	137.4	0.189
	2	30.640	2.9155	23.88	118.7	0.120
	3	30.930	2.8888	100.00	497.2	0.259
K.16	1	29.430	3.0325	13.72	552.6	0.188
	2	30.980	2.8843	100.00	4027.4	0.179
	3	31.690	2.8212	1.79	79.0	0.229

Explanation: **I (Rel)**= Relative intensity; **I(Cps)**= Intensity in count per second; and **FWHM**= Full width half maximum.

Sample No:	Peak	°2θ	d-sp. (Å)	I(Rel)	I(Cps)	FWHM
K.10	1	29.390	3.0366	3.54	166.4	0.410
	2	30.920	2.8897	100.00	4704.3	0.179
K.5	1	29.430	3.0325	100.00	1757.8	0.179
	2	30.930	2.8888	42.05	739.1	0.288
K.1	1	29.430	3.0325	4.81	216.9	0.189
	2	30.950	2.8870	100.00	4508.7	0.179
K.27	1	29.420	3.0335	3.59	142.3	0.198
	2	30.940	2.8879	100.00	3959.5	0.189
	3	31.460	2.8413	0.93	36.7	0.109
K.22	1	30.920	2.8897	100.00	3700.2	0.199
K.23	1	29.360	3.0396	4.28	209.2	0.198
	2	30.920	2.8897	100.00	4892.1	0.188
K.35	1	29.550	3.0205	0.69	33.5	0.170
	2	31.020	2.8806	100.00	4852.1	0.179
K.16	1	29.430	3.0325	13.72	552.6	0.188
	2	30.980	2.8843	100.00	4027.4	0.179
	3	31.690	2.8212	1.79	72.0	0.229
K.28	1	29.370	3.0386	40.68	988.6	0.187
	2	30.890	2.8925	100.00	2430.2	0.229
K.12	1	30.950	2.8870	100.00	4907.5	0.188
K.17	1	29.430	3.0325	4.16	191.0	0.178
	2	30.950	2.8870	100.00	4590.5	0.198
K.11	1	29.390	3.0366	2.10	104.9	0.209
	2	30.930	2.8888	100.00	4997.0	0.188
K.8	1	29.400	3.0356	4.84	196.3	0.209
	2	30.930	2.8888	100.00	4054.4	0.209
K.10	1	29.410	3.0346	0.85	42.0	0.227
	2	30.930	2.8888	100.00	4913.2	0.179

Sample No:	Peak	°2θ	d-sp. (Å)	I(Rel)	I(Cps)	FWHM
K.36	1	29.430	3.0320	2.10	40.0	0.250
	2	30.930	2.8888	100.00	2155.0	0.188
K.31	1	29.480	3.0275	1.16	41.8	0.209
	2	30.900	2.8915	100.00	3601.0	0.189
K.39	1	29.420	3.0335	4.39	104.1	0.257
	2	30.960	2.8861	100.00	2372.4	0.179
Clear Creek Canyon						
C.1	1	29.490	3.0256	20.98	440.6	0.189
	2	31.000	2.8824	100.00	2100.2	0.189
C.2	1	29.430	3.0325	4.82	152.9	0.248
	2	30.950	2.8870	100.00	3173.1	0.179
C.3	1	29.390	3.0366	7.32	299.2	0.167
	2	30.910	2.8906	100.00	4085.2	0.199
C.4	1	29.390	3.0366	1.28	55.6	0.218
	2	30.920	2.8897	100.00	4330.8	0.209
C.5	1	29.380	3.0376	3.17	141.3	0.168
	2	30.900	2.8915	100.00	4456.8	0.210
C.6	1	30.920	2.8897	100.00	6265.3	0.179
C.7	1	29.340	3.0416	7.56	332.6	0.157
	2	30.880	2.8934	100.00	4402.5	0.198
C.8	1	29.400	3.0356	8.40	429.7	0.168
	2	30.950	2.8870	100.00	5115.4	0.179
C.9	1	29.410	3.0346	0.77	57.1	0.189
	2	30.940	2.8879	100.00	7381.5	0.189
C.10	1	29.420	3.0335	2.78	94.3	0.209
	2	30.950	2.8870	100.00	3386.8	0.199
C.11	1	30.950	2.8870	100.00	5532.1	0.179

Sample No:	Peak	°2θ	d-sp. (Å)	I(Rel)	I(Cps)	FWHM
C.13	1	30.930	2.8888	100.00	3529.0	0.199
C.19	1	29.420	3.0335	2.83	90.3	0.167
	2	30.940	2.8879	100.00	3185.5	0.189

Lone Mountain

L.145	1	29.430	3.0325	3.83	140.6	0.269
	2	30.940	2.8879	100.00	3670.4	0.169
L.150	1	30.950	2.8870	100.00	9430.5	0.178
L.171	1	29.470	3.0285	14.69	496.5	0.190
	2	31.000	2.8824	100.00	3378.8	0.188
L.185	1	30.950	2.8870	100.00	5249.5	0.179
L.205	1	29.380	3.0375	14.12	339.3	0.180
	2	30.890	2.8925	100.00	2402.8	0.238
L.759	1	29.430	3.0325	0.45	20.4	0.109
	2	30.910	2.8906	100.00	4432.1	0.179
L.764	1	30.950	2.8870	100.00	5649.8	0.178

Martin Ridge

Sample No:	Peak	°2θ	d-sp. (Å)	I(Rel)	I(Cps)	FWHM
M.28	1	29.420	3.0335	6.34	286.8	0.170
	2	30.940	2.8879	100.00	4522.0	0.179
M.36	1	29.370	3.0386	3.29	66.6	0.217
	2	30.890	2.8925	100.00	2026.7	0.199
M.39	1	29.430	3.0325	12.62	497.7	0.169
	2	30.970	2.8852	100.00	3945.1	0.179

B. Peak position, d-spacing, and intensity of dolomites and calcites of the dolomitic limestones of the AVL from the X-ray diffractogram.

Ninemile Canyon

Sample No:	Peak	°2θ	d-sp. (Å)	I(Rel)	I(Cps)	FWHM
A.62	1	29.360	3.0396	100.00	2194.1	0.188
	2	30.800	2.9007	11.12	244.0	0.249
	3	31.420	2.8449	2.84	62.4	0.175
A.39	1	29.380	3.0376	100.00	2433.6	0.179
	2	30.876	2.8943	25.86	629.3	0.258
A.52	1	29.400	3.0356	100.00	3122.3	0.178
	2	30.890	2.8925	14.06	438.9	0.238
A.79	1	29.380	3.0376	100.00	2526.0	0.177
	2	30.910	2.8906	48.35	1221.4	0.309
A.48	1	29.400	3.0356	100.00	3295.5	0.178
	2	30.910	2.8906	3.81	125.7	0.127
A.28	1	29.380	3.0356	100.00	1930.2	0.319
	2	30.920	2.8897	43.83	845.9	0.236
A.60	1	29.400	3.0356	100.00	3218.4	0.179
	2	31.450	2.8422	2.12	68.3	0.125
A.14	1	29.390	3.0366	100.00	3278.8	0.188
	2	31.400	2.2843	2.38	78.2	0.154

Lone Mountain

Sample No:	Peak	°2θ	d-sp. (Å)	I(Rel)	I(Cps)	FWHM
L.320	1	29.370	3.0386	100.00	2773.9	0.179
	2	30.890	2.8925	22.23	616.5	0.248
L.392	1	29.410	3.0346	100.00	3028.2	0.179
	2	30.890	2.8925	8.36	253.3	0.196
L.342	1	29.390	3.0356	100.00	3218.4	0.179

	2	31.440	2.8431	2.58	80.1	0.125
L.417	1	29.410	3.0345	100.00	3196.1	0.179
	2	30.910	2.8906	13.80	441.1	0.270

Martin Ridge

Sample No:	Peak	°2θ	d-sp. (Å)	I(Rel)	I(Cps)	FWHM
M.21	1	29.370	3.0386	100.00	3189.6	0.188
M.20	1	29.370	3.0386	100.00	3392.9	0.177
	2	30.900	2.8915	19.32	655.6	0.238

C. Mole percentage of $MgCO_3$ and $CaCO_3$ of dolomite of the dolostones of the AVL estimated from X-ray diffractogram.

Keystone Canyon

Sample No:	Lithology	% Dolomite	% $MgCO_3$	% $CaCO_3$
K.1	Mosaic dol.	96	49.7	50.3
K.3	"	99	50.0	50.0
K.5	"	30	49.1	50.9
K.8	"	97	49.1	50.9
K.9	"	97	48.8	51.2
K.10	"	99	49.1	50.9
K.11	"	98	49.1	50.9
K.12	"	100	49.7	50.3
K.13	"	66	49.1	50.9
K.14	"	77	48.8	51.2
K.15	"	92	50.3	49.7
K.16	"	78	50.6	49.4
K.17	"	97	49.7	50.3
K.22	"	100	48.8	51.2
K.23	"	97	48.8	51.2
K.27	"	98	49.4	50.6
K.28	"	71	47.8	52.2
K.33	"	100	49.3	50.7

K.34	"	85	49.4	50.6
K.35	"	99	51.8	48.2
K.36	"	99	49.1	41.9
K.39	"	96	50.0	50.0

Clear Creek Canyon

Sample No:	Lithology	% Dolomite	% $MgCO_3$	% $CaCO_3$
C.1	Mosaic dol.*	83	51.2	48.8
C.2	"	96	49.7	50.3
C.3	"	94	48.5	51.5
C.4	"	99	48.8	51.2
C.5	"	98	48.2	51.8
C.6	"	100	48.8	51.2
C.7	Saddle dol.	95	47.5	52.5
C.8	Mosaic.dol.	92	49.7	50.3
C.9	"	100	49.4	50.6
C.10	"	98	49.7	50.3
C.11	"	100	49.7	50.3
C.13	"	100	49.1	50.9
C.19	"	99	49.4	50.6

Lone Mountain

Sample No:	Lithology	% Dolomite	% $MgCO_3$	% $CaCO_3$
L.145	"	96	49.4	50.6
L.150	"	100	49.7	50.3
L.171	"	97	51.2	48.8
L.185	"	100	49.7	50.3
L.205	Frac.fil.dol.	88	47.8	52.2
L.764	Mosaic dol.	100	49.7	50.3
L.759	"	99	48.5	51.5

Martin Ridge

Sample No:	Lithology	% Dolomite	% $MgCO_3$	% $CaCO_3$
M.28	"	95	49.4	50.6
M.36	"	97	47.8	52.2
M.39	"	89	50.4	49.6

C. Mole percentage of $MgCO_3$ and $CaCO_3$ of dolomites of the partially dolomitized limestones of the AVL estimated from X-ray diffractogram.

S.No:	Lithology	% Dolomite	% $MgCO_3$	% $CaCO_3$
L.417	Onc.pcgr.	12	47.8	52.2
L.320	"	18	47.8	52.2
L.392	"	7	47.8	52.2
M.20	"	16	48.2	51.8
A.28	Silt.qtz lms.	30	48.8	51.2
A.39	Nuia wackst.	20	47.3	52.7
A.48	Peloid pack.	3	48.5	51.5
A.52	Oolit. pcgr.	12	47.8	52.2
A.62	Stromatolitic ls.	10	45.1	54.9
A.79	Crinoidal pgr.	32	48.5	51.5

Explanations for abbreviations which are used in the lithology types of dolostones and partially dolomitized limestone units:

pack.= packstone; pcgr.= packstone-and grainstone; oolit= oolitic;
oncol.= oncolitic; Silt.qtz.= silty quartz-rich; lms.=lime mudstone; dol.=dolomite; frac. fil.= fracture-filling;
wackst.= wackestone.

APPENDIX III-A

Table 39- Summary of Organic Carbon and Visual Kerogen Data

GEOCHEM SAMPLE NUMBER	CLIENT IDENTIFICATION NUMBER	ORGANIC MATTER TYPE	VISUAL ABUNDANCE NORMALIZED PERCENT					ALTERATION STAGE	THERMAL ALTERATION INDEX	VITRINITE REFLECTANCE (% Ro)
			Al	Am	H	W	I			
3558-001	L-714	Am;H*;-	0	57	43	0	0	2+ to 3-	2.7	0.93
3558-002	L-600	Am;H*;-	0	57	43	0	0	2+ to 3-	2.7	0.93
3558-003	T-2	I;Am**;H	0	28	15	0	57	4-	4.2	2.5
3558-004	T-5	I;Am**;H	0	38	12	0	50	3+	3.8	2.0
3558-005	I-12	H;Am;I	0	33	44	0	23	2+ to 3-	2.8	0.95
3558-006	I-29	H;I;Am-W	0	11	55	11	23	2+ to 3-	2.7	0.93
3558-007	R-1	Am**-H;I;-	0	40	40	0	20	3 to 3+	3.5	1.63
3558-008	M-80	Am;H*;-	0	57	43	0	0	2+	2.6	0.9
3558-009	K-15	H-I;Am;-	0	20	40	0	40	3- to 3	3.1	1.13
3558-010	K-30	H;Am**;-	0	37	63	0	0	2	2.2	0.6
3558-011	W-5A	H;Am;I	0	33	55	0	12	2 to 2+	2.3	0.7
3709-017	K2	H;I;Am-W	0	18	37	18	27	2 to 2+	2.5	0.85
3709-032	W-26	Am;H*;-	0	57	43	0	0	2 to 2+	2.5	0.85
3709-033	M1.29	Am**;H*;-	0	67	33	0	0	2 to 2+	2.5	0.85
3709-034	M.35b	Am;h*;-	0	67	33	0	0	2 to 2+	2.5	0.85
3709-035	M1.35	Am*;H*;I	0	45	33	0	22	2+ to 3-	2.8	0.95

LEGEND:

KEROGEN KEY

Predominant;	Secondary;	Trace
60-100%	20-40%	0-20%

Al = Algal
Am = Amorphous-Sapropel
Am* = Relic Amorphous-Sapropel
H = Herbaceous-Spore/Pollen
H* = Degraded Herbaceous
W = Woody-Structured
U = Unidentified Material
I = Inertinite
C = Coaly

APPENDIX III-B: OXYGEN- AND CARBON-ISOTOPE DATA

Listed $\delta^{18}O$ and $\delta^{13}C$ values of dolomite and calcite cements at the first rows are uncorrected, and parentheses next to carbon-and oxygen-isotopic compositions of dolomite and calcite cements represent a correction factor for each sample. Underlined $\delta^{18}O$ and $\delta^{13}C$ values at the second rows represent the corrected-isotope values of calcite and dolomite cements with respect to PDB.

A total of 46 samples were analyzed to determine the oxygen- and carbon-isotope compositional range of the AVL. The following abbreviations describe the selective samples: FFCC= Fracture-filling calcite cement; Dol.= Dolomite type; RAFC= Radiaxial-fibrous calcite; Col.Calcite= Columnar calcite cement; Fen. FCC= Fenestra-filling calcite cement; and OMCC= Oomoldic calcite cement.

Sample No:	**Description of samples**	$\delta^{18}O$ ‰	$\delta^{13}C$ ‰
L.320 A	Col. Calcite	-5.075 -6.774	-2.009 -0.883 PDB
L.320 B	Dol. III	-4.907	-0.556 PDB
L. 250 A	FFCC	-9.55 (.05) -1.25	-2.36 (.02) -1.25 PDB
L.250 B	Dol. VII	-8.67 (.04) -10.37	-2.14 (.04) -0.90 PDB
L.253	Dol. IV	-2.05 (.07) -3.74	-1.44 (.04) -0.38 PDB
L.2	Dol. V	-1.12 (.03) -2.82	-1.78 (.02) -0.77 PDB
L.150	Dol. VII	-3.56 (.06) -5.25	-2.00 (.05) -0.93 PDB

Sample No:	Description of samples	$\delta^{18}0$ ‰	$\delta^{13}C$ ‰
L.171 A	Dol. VIII	-11.42 (.04) -13.11	-1.53 (.03) -0.16 PDB
L.171 B	Dol. VII	-1.55 (0.8) -3.14	-0.30 (.02) +0.72 PDB
L.417 A	Col. Calcite	-4.990 ( ) -6.69	-2.23 ( ) -1.13 PDB
L.417 B	Dol. III	-2.37 (.09) -4.07	-1.61 (.01) -0.55 PDB
A.65	Fen. FCC	-3.46 (.03) -5.16	-2.01 (.02) -0.94 PDB
A.19	FFCC	-7.12 (.00) -8.83	-3.16 (.01) -2.05 PDB
A.84	FFCC	-0.88 (.01) -2.59	-3.74 (.01) -2.05 PDB
M.75	FFCC	-7.00 (.03) -8.71	-3.98 (.01) -2.92 PDB
M.32 A	RAFC	-4.97 (.01) -6.66	-1.17 (.03) -0.01 PDB
M. 32 B	OMCC	-6.35 (.02) -8.04	-1.90 (.02) -0.73 PDB
M.36	Dol. VII	-5.14 (.00) -6.83	-1.81 (.02) -0.66 PDB
M.33	Dol. VI (replaced OMCC)	-8.07 (.02) -9.76	-1.23 (.05) +0.53 PDB
M.17	FFCC	-24.898 (.01) -26.54	+2.21 (.02) +4.30 PDB

Sample No:	Description of samples	$\delta^{18}0$ ‰	$\delta^{13}C$ ‰
M.28 A	Dol. VII (dolomitized columnar cement)	-5.40 (.06) -7.10	-2.38 (.01) -1.07 PDB
M.28 B	Dol. VII	-5.18 (.02) -6.88	-2.15 (.04) -1.03 PDB
C.7 A	Dol. IX	-8.53 (.02) -10.23	-2.49 (.03) -1.28 PDB
C.7 B	Dol. VII	-9.14 (.06) -10.84	-2.84 (.03) -1.61 PDB
C.8 A	Dol. IX	-6.73 (.04) -8.44	-3.42 (.01) -2.33 PDB
C.8 B	Dol. VII	-9.35 (.05) -11.05	-2.69 (.04) -1.46 PDB
K.5	FFCC	-26.049 (.07) -27.69	-3.876 (.02) -2.170 PDB
K.6 A	FFCC	-29.01 (.02) -30.71	-3.66 (.00) -1.88 PDB
K.6 B	Dol. VII	-1.31 (.06) -2.83	-2.10 (.04) -1.12 PDB
K.13 A	FFCC	-25.71 (.00) -27.38	-1.06 (.03) -0.83 PDB
K.13	Dol. VII	-6.40 (.05) -8.10	-2.27 (.05) -1.12 PDB
K.14	FFCC	-25.43 (.06) -27.12	-2.08 (.03) -1.27 PDB

Sample No:	Description of samples	$\delta^{18}0$ ‰	$\delta^{13}C$ ‰
K.17	Dol. VII	-1.72 (.02) -3.42	-2.08 (.04) -1.07 PDB
K.18	FFCC	-25.98 (.04) -27.69	-4.37 (.02) -2.70 PDB
W.5A-A	FFCC	-11.502 (.02) -13.208	-3.116 (.01) -1.848 PDB
W.5A-B	FFCC	-19.178 (.06) -20.882	-3.425 (.02) -1.919 PDB
W.33	FFCC	-6.427 (.05) -8.123	-1.848 (.02) -0.665 PDB
Ml.22	FFCC	-10.049 (.03) -11.75	-2.68 (.02) -1.66 PDB
Ml.32	Solitary coral	-2.10 (.08) -3.82	-3.97 (.05) -3.07 PDB
I.10	FFCC	-22.765 (.05) -24.472	-3.880 (.01) -2.284 PDB
I.23	FFCC	-7.60 (.05) -9.31	-2.82 (.01) -1.66 PDB
T.3	FFCC	-27.593 (.06) -29.301	-2.82 (.01) -1.66 PDB
T.10	FFCC	-9.897 (.02) -11.601	-2.860(.01) -1.627 PDB
D.7 A	FFCC	-23.749 (.04) -25.435	-1.82 (.02) -0.50 PDB
D.7 B	FFCC	-24.737 (.01) -26.439	-3.595(.08) -1.913 PDB

D.13	FFCC	-17.119 (.02) -18.846	-5.677 (.01) -4.395 PDB
R.3	FFCC	-9.053 (.02) -10.749	-1.979 (.02) -0.717 PDB

APPENDIX III-C1: PRINCIPLES OF FLUID INCLUSION THERMOMETRY

Fluid-Inclusion Thermometry

Irregularity in crystal growth results in trapping of infinitesimal portions of the parent fluids in crystals (Roedder, 1984). The fluid-filled irregular spaces are sealed off by latter crystal growth. Fluid inclusions formed during crystal growths are called primary inclusions which are alone, randomly distributed and isolated in host crystals. Therefore, the microthermometric data derived from primary inclusions are representative of the composition, pressure, and temperature of the parent fluids. For this reason, primary inclusions are by the far most important tools that can primarily be preferred for microthermometric analysis (Roedder, 1984).

Pseduosecondary inclusions are similar yet different from primary inclusions as they form along fractures which are primarily confined in the host crystals. Pseudosecondary inclusions originate from the same parent solution of host crystals as primary inclusions.

Unlike primary and pseudosecondary inclusions, secondary inclusions are usually found in healed fractures, transcending the crystal boundaries. Thus, they postdate the host crystals. These relations imply that secondary fluid inclusions may have been trapped millions of years apart from host crystals and grossly differed from their fluid compositions. Further criteria for the type and origin of fluid inclusions have been summarized by Roedder (1962, 1963), Roedder and Coobs (1967), Roedder (1972, 1976, 1979a, 1984), and Shepherd et al. (1985).

The minute fluids in the two-phase fluid inclusions originate from a boiling homogeneous fluid at the time of crystal formation; the formation of inclusions from a single homogeneous solution (i.e. coexistence of vapor and liquid as single phase) is likely to be followed by temperature drop and cooling which generally cause the shrinkage of liquid and the formation of vapor bubbles as well as immiscibility between the vapor and liquid phases (Roedder, 1962, 1963, 1972; Roedder and

Bodnar, 1980; Roedder, 1984; and Shepherd et al., 1985). The temperature at which entrapment of inclusions occurs is called the "temperature of trapping" (Tt), and the formation temperature of immiscibility of two phases as gas and liquid is called homogenization temperature and designated with Th (1980; Roedder, 1984; Shepherd et al., 1984). It is widely believed that homogenization temperatures most likely represent the minimum- entrapment temperatures of two-phase fluid inclusions (see the reviews by Roedder, 1984; Shepherd et al., 1985). The material trapped in inclusions from the homogeneous fluid is representative of the bulk of the parent fluid which was present during crystal growth (Roedder, 1984). Despite its two formation temperatures "Tt" and T_h, two-phase fluid inclusions from a single homogeneous parent fluid are useful for geothermometry (Roedder and Boadnar, 1980; Roedder, 1984).

Principles of Fluid-Inclusion Microthermometry

Principal assumptions for the fluid-inclusion thermometry were summarized by Roedder (1962, 1963, 1972, 1976, 1979a, and 1984), as follows: (1) Parent fluid entrapped in the fluid inclusions during the formation of crystals was a single homogeneous phase. (2) The Cavity in which fluid was trapped has not changed since the formation of inclusion. (3) Nothing has been added into or lost from the inclusions after sealing. (4) Effects of pressure are insignificant or are known. (5) Origin of fluid inclusions is known (primary, secondary, pseudosecondary). (6) Determined-T_h values are accurate.

Conditions required in (1) and (2) are closely related to the constancy of shape and volume as well as composition of the fluid inclusions. Changes in the shapes of fluid inclusions are attributed to the necking-down process which causes large and irregular inclusions to split up into the series of smaller and more regular inclusions. This mechanism has been observed in the soluble salts, and it contributes a significant error to homogenization temperatures (see further detail in Roedder, 1984, and

Shepherd et al., 1985). After the trapping, constancy of the volume of fluid inclusions is of primary importance for geothermometry (Roedder, 1984, p.84).

Two-major exceptions about volume constancy of fluid inclusions are (A) reversible and (B) irreversible changes.

A. Reversible Changes

Reversible changes do not have a significant effect on T_h measurements, and they are (1) crystallization or formation of the daughter product on the walls of inclusions, (2) thermal contraction of minerals, and (3) dilational changes by the following processes: (a) enlargement of entire fluid inclusion within the inclusion cavities as a result of reduction in confining pressure due to uplifting, (b) dilation of host crystal especially surrounding part of the inclusion. Roedder (1979) suggests that dilational changes may cause 4 to 6 °C temperature increase for each additional kbar for quartz crystals. In their previous work, Rodder and Bodnar (1980) rejected the possible temperature increase for each kbar, but Roedder still believes that his previous suggestion of about 4 to 6 °C increase for each kbar is true (Roedder, 1984, p.71).

B. Irreversible Changes or Permanent Changes

Two most important mechanisms associated with irreversible or permanent deformation of fluid inclusions are decrepitation and stretching ((Bodnar and Bethke, 1984; Roedder, 1984; and Shepherd et al., 1985). The fundamental cause of these mechanisms is the high internal pressures of fluid inclusions that exceed the external pressures of the same inclusion during overheating either in laboratory or nature (Bodnar and Bethke, 1984; Roedder, 1984; Shepherd et al., 1985; Goldstein, 1986; and Burruss, 1987).

1. Decrepitation

Roedder and Skinner (1968) have shown that leakage by microfractures on the walls of fluid inclusions can be introduced by sample preparation or during the experiment. However, in nature, fractures form on the walls of the fluid inclusions due to greater internal pressures of fluid inclusions. Consequently, the inclusions' fluid can be leaked out, and fluids of other systems or generations can be allowed to refill (leak in) the emptied inclusions. This process is known as " decrepitation" (Roedder, 1984). It is apparent that decrepitation processes do yield volume changes and also compositional changes (Roedder,1984; Goldstein, 1986; and Burruss, 1987). Consequently, any microthermometric measurements on these inclusions will produce data which do not entirely correspond to the formation temperature and composition of host crystals. Differences in internal and external pressures of fluid inclusions can vary widely, particularly with the size of inclusions and mineral strength of host crystals. Bodnar and Bethke (1984) showed that smaller inclusions are commonly more resistant to decrepitation than larger inclusions.

In nature, overheating can be maintained by igneous activities and by deep-burial depth. Hydrothermal or basinal fluids rise along faults and related microfractures which open many or most pre-existing inclusions and refill them (Roedder, 1984; Goldstein, 1986; and Burruss, 1987). In vadose-calcite cements, considerably high T_h values represent the re-equilibrated formation temperature of fluid inclusions either by decrepitation and following healing or by stretching (Goldstein, 1986). Therefore, microthermometric data from these fluid inclusions can not be used by diagenetic studies and purposes, but can preferably be used to determine the maximum depth of burial of given formations and composition of ore fluids.

2. Stretching:

Stretching refers to an irreversible deformation, but it is less obvious permanent

deformation than decrepitation (Roedder, 1984; Shepherd, 1985). Generally, it occurs without any visible cracks in the soft minerals, such as fluorite and calcite. Stretching is primarily caused by ductile expansion of soft crystals around the inclusion walls (Bodnar and Bethke, 1984). Therefore, stretching usually results in a volume increase of fluid inclusions as a result of increased-internal pressures of fluid inclusions that exceed the external pressures of the same inclusions (Bodnar and Bethke (1984). Possible stretching during the microthermometry measurements are caused by the following two processes: (1) overheating of fluid inclusions beyond the certain limit causes the minute fluid of inclusions to expand and increases the internal pressure beyond the counterbalance of external pressure (Bodnar and Bethke (1984); and (2) during the freezing stage, formation and expansion of the ice crystals exerts a force on fluid inclusion walls which may cause a permanent deformation, particularly on soft minerals, such as fluorite, sphalerite and calcite (Lawler and Crawford, 1983).

The stretching may be evidenced by a regular rise in T_h during subsequent runs. Like decrepitation, smaller fluid inclusions and more resistant minerals are more resistant to stretching than larger inclusions in the softer minerals (Bodnar and Bethke, 1984). The concept of stretching was introduced, for the first time, by Larson et al. (1973). They discovered permanent deformation during their interlaboratory calibration and standardization, and they also demonstrated that T_h of fluorite had raised as much as 71 °C from 118 to 189 °C.

Prezbindowski and Larse (1987) experimentally demonstrated that fluid inclusions entrapped in calcite might re-equilibrate by stretching during the natural overheating due to increased depth of burial.

Fluid-Inclusion Microthermometry

Fluid-inclusion microthermometry comprises two stages: (1) heating the inclusions to their homogenization temperatures, and (2) freezing the fluid inclusions until they

become completely frozen, and then gradually heating the same inclusions to observe phase changes (Roedder, 1984; Shepherd, 1985).

Two-phase fluid inclusions are chiefly used to determine the minimum-entrapment temperature (T_h), and the first ice crystal-melting temperature (Te) and last ice crystal -melting temperature (Tm), respectively during heating and freezing/heating stages. For fluid-inclusion microthermometry, it is essential to determine origin of inclusions in the sequential order and their relations with host crystals (Roedder, 1972; 1976; 1979a; 1984; and Shepherd, 1985).

Heating Stage:

Two-phase fluid inclusions show immiscibility at room temperature as liquid and vapor (bubble). As two-phase fluid inclusions are heated, fluid will expand and refill the inclusions. Consequently, these two phases, vapor and liquid, will be homogenized in the liquid stage when temperature reaches the point where two phases become miscible (Liquid + Vapor = Liquid). Thus, the homogenization temperature represents minimum-entrapment temperature of fluids from the parent solution during the formation of host crystal (Roedder, 1984; Shepherd,et al, 1985).

During heating events of two-phase inclusions, vapor bubbles gradually decrease in size as temperature reaches the homogenization temperature (T_h), the final disappearances of vapor bubbles mark the homogenization temperature (see Roedder, 1984; Shepherd et al., 1985). Therefore, homogenization temperature refers to the temperature at which liquid and vapor phases become completely miscible.

The temperature difference between the maximum entrapment temperature (Tt) and homogenization temperature (T_h) is called "pressure correction" (= $Tt-T_h$), which is chiefly function of density of fluid, magnitude of pressure, and pressure types -- hydrostatic versus lithostatic (Potter, 1977; Roedder and Bethke, 1980; Roedder, 1984; and Shepherd et al., 1985). Volume and compositional constancy must be the prerequisite for pressure correction. First attempt to determine pressure correction was made by Lemmlin and Klevtsow in 1961 (Roedder, 1984). Their technique and graphs

of pressure correction have been practically used from 1961 to 1977. Potter (1977) presented the new-pressure correction graphs covering range of 20-400 °C for 1, 5, 15, 20, 20, 25 % NaCl solutions and to 2000 bars. These corrections can precisely be consistent if only (1) inclusion contains a pure NaCl, (2) salinity content "weight % NaCl equivalent" (Potter et al., 1978) of inclusion is determined considerable accuracy range, (3) estimated pressure should be compatible with the magnitude of pressure and type of pressure during the formation of host crystals, (4) two-phase fluid inclusions homogenize into a liquid phase. The salinity of fluid inclusions is determined as weight % NaCl equivalent because Na and Cl^{-1} are the most abundant component of basinal brines. Potter and Clynne (1978) have shown in their brine experiments that in Na, K, Mg, Ca, Cl^{-1}, Br^{-1}, SO_4, and H_2O systems, the P, V, T, X properties of brines were predicted within ± 1.0 % differences from the properties of NaCl solutions having the same value for the last ice crystal-melting temperature (Tm).

Composition or salinity content of fluid inclusions and geopressure at the time of fluid entrapment have a considerable effect on formation temperatures of fluid inclusions. Figure 203 shows that increase in NaCl content (i.e., density) of fluid inclusions causes not only critical point to rise, but also fluid-vapor curves to extend into high temperature ranges, as changing the slope of isochores (Roedder and Bodnar, 1980; Roedder,1984; and Shepherd et al., 1985). Isochores are the constant density lines in figure 203, and density change indicates a different slope angle of isochores. Density of fluids in fluid inclusions at T_h can be calculated form volumetric relations of inclusions or degree of fill (Haas, 1976; Roedder, 1984; and Shepherd et al., 1985).

Fluid isochores with independent geothermometers are commonly used to estimate geologic pressure (Gt) during the entrapment of fluid inclusions. Potter and Brown (1977) have shown that the density of NaCl solutions is function of pressure and temperature in the range of 1-25 wt % NaCl, 100-2000 bars and 25 - 500 °C. After determining T_h, Tm and fluid density, trapping temperatures (Tt) of fluid inclusions can be estimated from pressure-independent geothermometers which include partition of trace element, mineral compositions, and stable-isotope geothermometers (Roedder, 1984; Shepherd et al., 1985). In order to estimate accurate trapping temperatures (Tt),

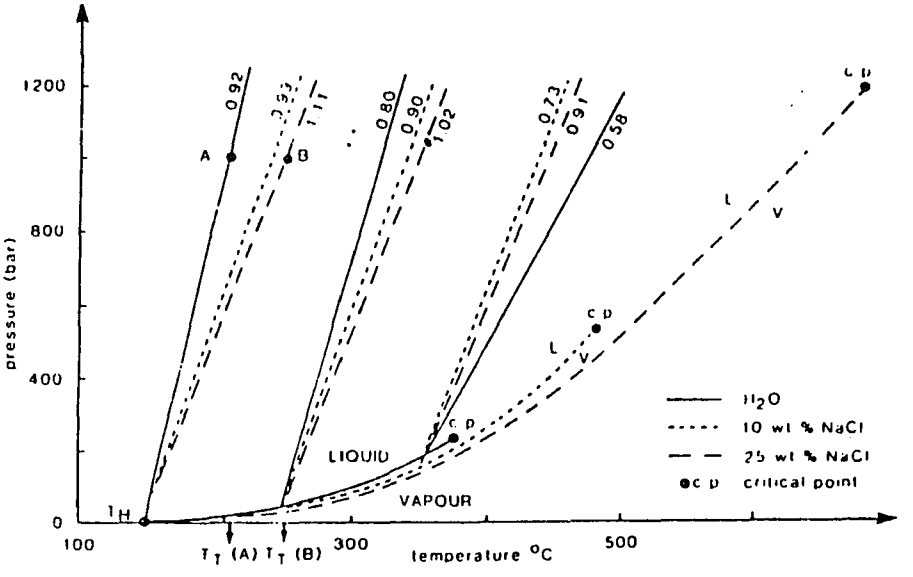


Figure 206- Influence of salinity on the positions of the liquid-vapor curves and slope of the isochores in the liquid field for H_2O- NaCl system (Roedder, 1984; Shepherd et al., 1985).

geopressure during the formation of fluid inclusions must be known; otherwise, it is almost impossible. In figure 203, formation or trapping temperatures Tt (A) and Tt (B) of fluid inclusions are derived from pressure-independent geothermometer on the NaCl-adjusted isochores which give temperature differences between the values of $Tt-T_h$. This difference is considered to be pressure correction.

Freezing / Heating Stage:

The second type of microthermometry involves supercooling of two-phase fluid inclusions around -100 °C and their phase changes under gradual warming. When inclusions are frozen, a variety of new solid phase forms: ice crystals, hydrohalites, and clathrates "compound of carbon dioxide hydrates" (Roedder, 1962, 1963, 1984). As a result of a gradual reheating, first liquid forms from the melting of ice crystals. This is also termed as "first-melting temperature of ice" (Te) or eutectic temperature. (Te) or first-melting temperature can commonly be estimated from the fluid inclusions when inclusions have granular appearance (Roedder, 1962, 1963, 1972, 1984; Shepherd et al., 1985). The temperature of Te is indicative of the chlorite salt types in the fluids of the inclusions (Roedder, 1963; Crawford, 1981). The following Te ranges particularly correspond to typical composition of chlorite salts in the fluids (from Crawford, 1981):

KCl	-10.6 °C	KCl.NaCl	-22.9 °C
NaCl	-20.8 °C	$MgCl_2$. NaCl	-35.0 °C
$MgCl_2$	-33.6 °C	$CaCl_2$. NaCl	-52.0 °C
$CaCl_2$	-49.8 °C	$MgCl_2$. $CaCl_2$.NaCl	-57.0 °C

As the temperature gradually increases, the ice crystals in fluid inclusions continuously melt and turn into a liquid phase; at the same time, vapor phases (bubbles) gradually become larger and larger. Ultimately, when the last ice crystal melts, for the first time, a vapor bubble is freed from its stationary position and will

start to move freely; this temperature of last ice melting is called melting temperature "Tm" (Roedder, 1962, 1963, 1972, 1984).

Hydrohalite + liquid are slow to coalesce into a crystal. As temperature increases, hydrohalite progressively melts and final melting of hydrohalite occurs at relatively higher melting temperature, as much as up to +0.10 °C. Hydrohalite melting has less practical value compared to Tm (ice + liquid).

The last ice-melting temperature gives the approximated-total salinity content of fluid inclusions; therefore, melting temperature (Tm) is a direct function of fluid composition because increasing salinity depresses the freezing point of fluids (Potter et al., 1978).

APPENDIX III-C2: HOMOGENIZATION- AND FREEZING-TEMPERATURE AND SALINITY DATA FROM TWO-PHASE FLUID INCLUSIONS

Homogenization Temperature Data (°C) from Two-Phase Fluid Inlusions.

Listed-Th values (°C) under each sample number indicates that all the homogenization temperatures were measured from the same sample. The following abrivations have been used to designate cement types: (1) FFC, fracture-filling calcite cement; (2) FFD, fracture-filling dolomite; (3) FFSD, fracture-filling saddle dolomite; and Fen.FC, fenestra-filling calcite cement.

Ninemile Canyon Section

A.14 (FFC)

172	166	207	218	195	194	184	230	178	180	203
215	197	181	175	146	198	186	190	246	194	171
238	190	217	178	204	176	216	205	213	183	163
214	194	221	241	131	161	214	194	221	205	196
171	185	215	218	208	166	182	221	227	205	198
210	175	221	185	204	227					

A.18 (FFC)

123	125	146	117	109	136	163	179	157	160	149
180	128	166	156	107	117	208	214	198	117	135
126	119	189	175							

A.19 (FFC)

202	203	248	242	236	224	221	237	285	205	245
230	286	217	272	160	279	295	251	209	215	260
203	208	253	267	229	223	246	248	229	292	248
288	276	221	218	282	190	246	302	193	163	216
219	269	241	259	233	267	197	197	201	198	216

A.48 (FFC)

161	229	205	220	199	201	206	180	219	207	286
201	205	252	207	240	189	185	194	187	225	229
235										

A.65 (Fen.FC)

162	143	123	129

A.84 (FFC)

137	114	133	224	150	149	160	149	152	186	124
146	186	219	201	190	183	158	182	188	165	183
237	176	210	178	167	159	163	167	218	204	229
215	156	205	150	178	207	182	180	200	178	187
184	214	187	206	186						

Keystone Canyon

K.5 (FFC)
163 206 106
K.6 (FFC)
192 217 237 241 212 242 226 229 211 234 231
238 202 194 166 189 217 238 239 232 236 241
235 238 244
K.10 (FFC)
202 207 192 185 200 245 246 231 221 223 214
196
K.13 (FFC)
158 156 189 143 136 146 152 176 177 169 124
177 184 187 168 183 181 177 205 149 199 200
203 172 164 175 188 168 174 161 176 156 198
180 169 219 223 224 219 181 157 175 195 153
123 174 182 174 191 180 179 182 225 194
K.19 (FFC)
205 181 244 211 197 201
K.27 (FFC)
186 209 165 239 217 188 213 218

Mill Canyon Sequence (Iks Canyon)

ML.4 (FFC)
190 155 198 208 196 151
ML.26 (FFC)
197 230 174 178 173 171 202 173 202
ML.32 (FFC)
228 172 160 167 245 231 216 224 218 229 224
218 200 178 183 201 205 215 208 183 245 241
351 357 204 249 214 286 267 180 177 146 210
338 334 293 348 255

June Canyon Sequence (Iks Canyon)

I.13 (FFC)
156 160 116 117 135 135 128 124
I.23 (FFC)
137 108 183 170 181 104 133 114 104 125 128
119 112 150 118 112
I.41 (FFC)
112 194 191 137 140 116 176 186 179 125 123
120

Martin Ridge

M.6 (FFC)
133 167 149 150 132 152
M.8 (FFC)
154 160 140
M.13 (FFC)
132 140
M.17 (FFC)
105 137 125 159 149 157 189 174 203 161 143
126 153 124 125 149 150 156 122 179 142 190
198 176 209 192 140 186 128 163 162 180 136
202 159
M.28 (FFD)
129 135 129 158 128 136 173 138
M.31 (FFC)
154 132 126 156 141 127 123 165 150 228 226
M.35 (FFC)
92
M.49 (FFC)
165 163 115 143
M.50 (FFC)
127,
M.53 (FFC)
137
M.75 (FFC)
145 152 140 180 160 127 148 149 133 155 136
143 130 136 138 180 177 164 174 175 173 187
140 153 168 227 160 185

Clear Creek Canyon

C.6 (FFD)
232 224
C.7 (FFSD)
209 210 248 226 272 215 257 263 222 223 225
218 214 228 245 272 231 245 230 236 228 235
215 216 229 230 236 240 246 231 243 234

Whiterock Canyon

W.5 (FFC)

106 159 173 179 191 189

W.13, W.33 (FFC)

143 122 136 172

Lone Mountain

L.150 (FFD)

150 137 136

L.171 (FFD)

102 100 105 116 119 138 122 143 140 130 148
144 111 125 242 218 254

L.250 (FFC and Replacive Ddolomite)

179 181 283 206 203 204 216 223 198 123* 198
169* 164* 142*
*dolomite

L.570 (FFC)

88 99 109 159 166 132 178 113 134 107 118
162 115 154 159 143 174 142 142 221 178 192
260 289 192 204 278 279 278 205 213 206 228

L.643 (FFC)

170 242 200 207 234 218 237 240 227 208

Toiyabe Peak

T.3, T.4 and T.9 (FFC)

139 149 142 216 131 225 236 229 269 217 225
257 288

Reeds Canyon

R.1 (FFC)

166 188 289 269 229 225 228 170 157 189 221
210 252 243 218 228 212 200 181

R.3 (FFC)

211 188 140 264 188 196 181 179 177 189 237
222 213 249 240

Dry Creek Canyon

D.7 (FFC)

188	227	218	231	205	217	204	184	168	154	152
158	161	183	184	169	161	189	215	193		

D.13 (FFC)

190	207	210	224	194	208	180	204	217	150	221
228	226	234	169	246						

Homogenization (T_h) and melting temperatures (Tm) and composition of two-phase fluid inclusions (Total weight % of NaCl calculated from melting temperatures (see Potter et al., 1978).

Ninemile Canyon

Sample No:	T_h (°C)	Tm (°C)	Wt % of NaCl
A.14			
1	204	-23.2	24.9
2	131	-17.6	20.9
3	230	-15.3	19.0
4	238	-11.2	15.2
5	217	- 9.2	13.1
6	149	- 4.2	6.7
A.18			
1	166	- 3.0	4.9
2	214	- 4.9	7.7
3	198	- 5.9	9.1
4	160	- 6.3	9.6
A.19			
1	197	-20.3	22.9
2	201	-21.4	23.6
3	198	-19.3	22.2
4	216	-18.4	21.5
A.48			
1	213	-11.2	15.2
2	221	-13.6	17.5
3	187	- 5.0	7.8
4	229	-11.8	15.8
5	194	- 8.6	12.4
A.84			
1	149	-10.8	14.8
2	152	-11.2	15.2
3	182	-24.1	25.4
4	188	-21.5	23.7
5	237	-20.7	23.2
6	204	-15.2	18.9
7	156	-12.0	16.0
8	131	-17.6	20.9
9	214	- 6.9	10.4
10	205	- 5.3	8.3
11	160	- 6.3	9.2

12	163	- 5.8	8.9
13	205	-17.9	21.1
14	150	- 9.2	13.1
15	207	-17.9	21.1
16	182	-14.2	18.1
17	187	- 5.2	8.1
18	187	-19.2	22.1

Martin Ridge

Sample No:	**T_h (°C)**	**Tm (°C)**	**Wt % of NaCl**
M.28*			
1	135	-17.5	20.8
2	138	-17.8	21.0
M.17			
1	189	- 2.9	4.8
2	203	- 2.3	3.7
3	150	- 2.4	3.0
4	161	- 0.6	1.1
5	155	- 2.3	3.6
M.75			
1	133	- 5.1	8.0
2	136	- 4.8	7.6
3	149	-15.3	19.0
4	173	- 9.8	13.9
5	187	-12.3	16.3
6	140	-15.4	19.1
7	185	-11.9	15.9
8	153	-11.6	15.6
9	173	- 9.8	13.9
10	187	-12.3	16.3
11	227	-13.6	17.5
12	185	-11.9	15.9

*dolomite

Clear Creek Canyon

Sample No:	**T_h (°C)**	**Tm (°C)**	**Wt % of NaCl**
C.7			
1	222	- 6.0	9.2
2	223	- 8.0	11.7
3	230	-18.0	21.2
4	230	-20.0	22.7
5	216	-19.0	21.9

6	218	-11.0	15.0
7	214	- 5.7	8.9
8	223	- 9.8	12.7

Mill Canyon Sequence

Sample No:	**T_h (°C)**	**Tm (°C)**	**Wt % of NaCl**
Ml.32			
1	200	-10.0	14.0
2	178	-12.0	16.0
3	183	- 8.3	11.9
4	201	-11.0	15.0
5	214	-15.0	18.8
6	205	-12.2	16.2
7	180	- 5.3	8.3
8	177	- 7.3	10.9
9	351	-18.3	21.5
10	357	-21.2	23.5

Keystone Canyon

Sample No:	**T_h (°C)**	**Tm (°C)**	**Wt % of NaCl**
K.6			
1	238	- 2.2	3.6
2	239	- 6.9	10.4
3	232	- 6.0	9.2
4	217	- 8.7	12.5
5	235	- 3.8	6.2
6	244	- 2.4	4.1
K.13			
1	146	- 2.5	4.2
2	152	- 4.8	7.6
3	176	-11.3	15.3
4	177	-11.4	15.4
5	169	-10.0	13.9
6	124	- 0.4	0.7
7	199	- 4.8	7.6
8	200	- 7.8	11.3
9	172	- 3.0	4.9
10	162	- 2.3	3.7
11	161	- 3.3	5.3
12	176	- 2.2	3.6
13	181	- 2.2	3.6
14	175	- 1.7	2.8
15	174	- 3.1	5.1

16	182	- 5.6	8.7
17	194	- 1.1	1.8

Lone Mountain

Sample No:	T_h (°C)	Tm (°C)	Wt % of NaCl
L.250			
1	216	-20.9	23.3
L.171			
1	140	-23.9	25.3
2	242	-21.8	23.9
3	130	-24.0	25.4
4	138	-18.9	21.9
5	143	-12.1	16.1
6	125	-27.5	27.6
7	218	-18.7	21.7
8	254	-15.8	19.4

Reeds Canyon

Sample No:	T_h (°C)	Tm (°C)	Wt % of NaCl
R.1			
1	229	-18.3	21.4
2	151	- 3.2	5.2
3	228	-15.3	19.0
R.3			
1	211	-19.3	22.2
2	264	-17.8	21.0
3	237	-21.9	24.0
4	222	-20.3	22.9

Dry Creek Canyon

Sample No:	T_h (°C)	Tm (°C)	Wt % of NaCl
D.7			
1	224	-13.8	17.6
2	180	- 2.7	4.4
3	234	-15.0	18.7
4	169	- 3.7	6.0
5	188	- 7.6	11.2
6	154	- 1.3	2.2
7	158	- 3.4	5.6
8	161	- 3.2	5.2
9	208	-20.9	23.0
D.13			
1	228	-24.0	25.4

2	334	-15.0	18.7
3	246	-14.7	18.7
4	227	-15.0	18.7
5	158	- 3.4	5.5

APPENDIX III-D: SEMI-QUANTITATIVE X-RAY DIFFRACTOMETRY ANALYSIS FOR CLAY MINERALS

Air-Dried Samples

Sample No:	°2θ	d-spa.(Å)	I(Rel)	I(Cps)	FWHM
I.5A					
1	6.080	14.5249	46.81	64.7	0.540
2	8.000	10.0405	47.50	57.7	0.273
3	12.320	7.1786	100.00	138.2	0.260
4	17.720	5.0013	40.44	49.1	0.219
5	18.180	4.8758	51.90	71.7	0.354
I.7					
1	6.160	14.3384	62.37	111.6	0.820
2	8.780	10.0633	87.44	156.5	0.659
3	12.300	7.1554	100.00	178.9	0.439
4	17.760	4.9901	75.27	134.7	0.699
5	18.700	4.7413	34.61	61.9	0.500
I.9					
1	6.120	14.4300	21.43	88.2	0.538
2	8.740	10.0033	100.00	411.8	0.418
3	12.360	7.1554	27.94	115.0	0.240
4	17.760	4.9901	51.81	188.6	0.500
I.15					
1	8.800	10.0405	63.30	90.2	0.700
2	17.720	5.0013	60.04	83.0	0.355
I.37					
1	6.140	14.3831	60.70	104.2	0.538
2	8.820	10.0178	93.74	132.7	0.479
3	12.400	7.1342	100.00	141.6	0.418
4	17.740	4.9957	56.21	79.6	0.280

Explanation: **I(Rel)**= Relative Intensity; **I(Cps)**= Intensity in count per second; and **FWHM**= Full With Half Maximum in °2θ.

Sample No:	°2θ	d-spa.(Å)	I(Rel)	I(Cps)	FWHM
Ml.14					
1	8.870	10.0633	100.00	212.1	0.899
2	17.740	4.9957	65.54	141.1	0.940
Ml.15					
1	8.220	10.7476	16.23	35.8	0.100
2	8.800	10.0405	100.00	240.4	0.278
3	12.320	7.1786	17.22	37.9	0.292
4	17.520	5.0579	25.01	55.1	0.095
5	17.740	4.9957	49.67	109.5	0.218
K.14					
1	6.140	14.3831	60.70	104.2	0.538
2	8.760	0.0863	100.00	171.7	0.438
3	9.340	9.4612	67.34	115.6	0.417
4	12.340	7.1670	59.31	101.8	0.418
5	17.700	5.0069	65.59	112.6	0.380
6	18.600	4.7666	47.85	82.2	0.280
W.19					
1	8.700	10.0178	71.44	143.3	0.577
2	12.280	7.2019	100.00	200.6	0.417
3	17.740	4.9957	47.72	95.7	0.340
R.1					
1	8.780	10.0833	100.00	868.1	0.156
2	17.720	5.0013	43.34	376.2	0.214
R.5					
1	8.760	10.0863	100.00	935.7	0.217
2	17.680	5.0125	45.01	421.2	0.258
T.2					
1	6.180	14.2901	19.94	137.5	0.580
2	8.820	10.0178	100.00	689.5	0.135
3	12.380	7.1439	14.79	102.0	0.700
T.3					
1	6.160	14.5728	28.53	232.9	0.759
2	8.840	9.9952	100.00	816.5	0.154
3	17.780	4.9845	64.08	523.2	0.152
T.4					
1	8.820	10.0178	100.00	1262.0	0.150
2	17.760	4.9901	53.49	673.3	0.153

Sample No:	°2θ	d-spa.(Å)	I(Rel)	I(Cps)	FWHM
T.5					
1	6.100	14.1773	14.15	287.3	0.760
2	7.110	12.3701	1.25	86.3	0.520
3	8.820	10.0178	100.00	2030.7	0.130
4	12.360	7.1139	6.39	129.7	0.180
5	17.740	4.9957	4.07	1114.2	0.158
T.6					
1	6.140	14.3831	14.92	121.6	0.460
2	8.800	10.0405	100.00	815.4	0.151
3	12.380	7.1439	24.74	201.8	0.398
4	17.740	4.9957	47.25	385.2	0.174
5	18.680	4.7464	13.81	112.6	0.736
T.7					
1	6.140	14.3831	5.19	94.1	0.519
2	8.820	10.0178	100.00	1814.0	0.147
3	12.360	7.1554	6.98	126.6	0.719
4	17.740	4.9957	49.65	900.6	0.153
5	18.660	4.7514	4.03	91.2	0.259
T.10					
1	6.140	14.3881	11.73	59.2	0.340
2	8.820	10.0178	100.00	504.9	0.156
3	12.320	7.1786	26.31	132.8	0.180
4	17.760	4.9901	63.83	322.3	0.174

Illite Peaks From KCl-Treated Samples

Sample No:	°2θ	d-spa.(Å)	I(Rel)	I(Cps)	FWHM
I.5A					
1	8.760	10.0863	42.53	315.5	0.618
2	17.700	5.0069	23.83	176.9	0.500
I.7					
1	8.800	10.0405	100.00	232.8	0.698
2	17.720	5.0013	49.31	114.3	0.460
I.9					
1	6.120	14.4300	24.99	115.7	0.478
2	8.740	10.1093	100.00	462.9	1.020
3	12.320	7.1786	50.94	235.8	0.377
4	17.720	5.0013	48.73	225.6	0.478

Sample No:	°2θ	d-spa.(Å)	I(Rel)	I(Cps)	FWHM
I.37					
1	8.760	10.0863	100.00	431.0	0.518
2	17.700	5.0069	41.88	180.6	0.299
MI.14					
1	8.780	10.0683	100.00	599.9	0.379
2	17.720	5.0013	42.18	294.0	0.319
MI.15					
1	8.780	10.0633	100.00	447.5	0.356
2	17.700	5.0066	43.39	194.2	0.720
K.14					
1	8.740	10.1094	100.00	406.8	0.518
2	17.680	5.0125	44.49	181.0	0.800
W.19					
1	8.800	10.0405	74.72	275.2	0.960
2	17.720	5.0013	34.19	125.9	0.480
R.1					
1	8.800	10.0405	100.00	1586.3	0.152
2	17.720	5.0013	40.95	649.6	0.195
R.5					
1	8.780	10.0863	100.00	1929.7	0.195
2	17.700	5.0069	46.08	889.1	0.215
T.2					
1	8.820	10.0178	100.00	1557.7	0.150
2	17.760	5.9901	57.2	899.1	0.153
T.3					
1	8.760	10.0863	100.00	836.2	0.172
2	17.760	4.9901	63.34	554.8	0.276
T.4					
1	8.780	10.0633	100.00	886.7	0.154
2	17.740	5.0013	48.19	427.0	0.157
T.5					
1	8.820	10.0178	100.00	604.5	0.172
2	17.740	4.9957	50.70	306.5	0.175
T.7					
1	8.820	10.0178	100.00	1941.7	0.146
2	17.740	4.9957	6.74	907.6	0.150
T.10					
1	8.840	9.9952	100.00	1225.6	0.150
2	17.760	4.9901	52.72	271.8	0.176

Illite Peaks from Glycolated Samples

Sample No:	°2θ	d-spa.(Å)	I(Rel)	I(Cps)	FWHM
I.9					
1	8.760	10.0863	100.00	423.2	0.459
2	17.740	4.9957	61.90	262.0	0.420
MI.15					
1	8.780	10.0633	100.00	468.8	0.338
2	17.720	5.0013	48.39	226.7	0.519
W.19					
1	8.800	10.0405	68.27	230.3	1.359
2	17.740	4.9957	43.35	142.6	0.460
R.5					
1	8.780	10.0653	100.00	1966.1	0.196
2	17.700	5.0069	44.35	871.9	0.199
T.3					
1	8.760	10.0863	100.00	740.8	0.295
2	17.760	4.9901	76.12	563.9	0.155
T.4					
1	8.820	10.0178	100.00	1008.8	0.152
2	17.740	4.9957	43.68	440.7	0.175
T.7					
1	8.820	10.0178	100.00	1835.1	0.100
2	17.740	4.9957	48.08	822.4	0.152

Illite Peaks from MgCl-Treated Samples

Sample No:	°2θ	d-spa.(Å)	I(Rel)	I(Cps)	FWHM
I.7					
1	8.800	10.0405	74.40	168.7	0.539
2	17.760	4.9901	61.78	135.1	0.500
I.9					
1	8.800	10.0405	100.00	341.5	0.458
2	17.760	4.9957	49.14	167.8	0.720
T.3					
1	8.820	10.0178	100.00	531.6	0.254
2	17.760	4.9901	58.41	319.6	0.175

REFERENCES

Abegg, F.E., 1990, Fluid-inclusion analysis of dolomite in lithoclasts from the Morgan Creek Limestone (Upper Cambrian) of central Texas: The Compass--Sigma Gama Epsilon, v. 67, p. 135-146.

Adams, J.E., and Rhodes, M.L., 1960, Dolomitization by seepage refluxion: Am. Assoc. Petrol. Geologists Bull., V. 44, p. 1913-1920.

Ager, D.V., 1974, Storm deposits in the Jurassic of the Moroccan High Atlas: Paleogeogr. Paleoclimatol. Paleoecol., v. 15, p. 83-93.

Ahfeld, F., and Branisa, L., 1960, Geologia de Bolivia: Instituto Boliviano del Petroleo. La Paz.

Ahr, W.M., 1973, The carbonate ramp: an alternative to the shelf model: Trans. Gulf Coast Assoc. Geol. Soc., v. 23, p. 221-225.

Aigner, T., 1982, Calcareous tempestites: Storm-dominated stratification in Upper Muschelkalk Limestones (Middle Trias, SW Germany), p. 180-197, in Einsele, A., and Seilacher, G., eds., Cyclic Event Stratification: New York, Springer Verlag.

Aitken, J.D., 1967, Classification and environmental significance of cryptalalgal limestones and dolomites with illustrations from Cambrian and Ordovician of southwestern Alberta: Jour. Sedimentary Petrology, v. 37, p. 1163-1187.

Alberstadt, L., and Repetski, J.E., 1989, A Lower Ordovician sponge/algal facies in the Southern United States and its counterparts elsewhere in North America: Palios, v. 4, p. 225-242.

Alberstadt, L.P., and Walker, K.R., 1976, A Receptaculitid-echinoderm pioneer community in a Middle Ordovician reef: Lethaia, v. 9, p. 262-272.

Alberstadt, L.P., and Walker, K.R., and Zurawski, R.P., 1974, Patch reefs in the Carter Limestone (Middle Ordovician) in Tennessee, and vertical zonation in Ordovician Reefs: Geo. Soc. America Bull., v. 85, p. 1171-1182.

Algeo, T.J., and Wilkinson, B.H., Periodicity of mesoscale Phanerozoic sedimentary cycles and role Milankovitch orbital modulation: Jour. Geology, v. 93, p. 313-322.

Al-Hashimi, W.S., and Hemingway, J.E., 1973, Recent dolomitization and the origin of rusty crusts of Northumberland: Jour. Sedimentary Petrology, v. 43, p. 82-91.

Allan, J.R., and Matthews, R.K., 1977, Carbon and oxygen isotopes as diagenetic and stratigraphic tools: Surface and subsurface data, Barbados, West Indies: Geology, v. 5, p. 16-20.

Allan, J.R., and Matthews, R.K., 1982, Isotope signatures associates with early meteoric diagnosis: Sedimentology, v. 29, p. 797-817.

Amthor, J.E., and Freidman, G.M., 1992, Early-to late diagenetic dolomitization of platform carbonates: Lower Ordovician Ellenburger Group, Permian Basin, west Texas: Jour. Sedimentary Petrology, v. 62, p. 131-144.

Amieux, P., 1982, La Cathodoluminescence: methode d'etude sedimentologique des carbonates: Bulletin Centres Rexherche Exploration Prod: Elf- Aquitaine, v. 6, p. 437-483.

Anderson, G.M., 1975, Precipitation of Mississippi Valley-type ores: Econ. Geol., v. 70, p. 937-942.

Anderson, G.M., and Macqueen, R.W., 1982, Ore deposit model-6, Mississippi Valley-type lead zinc deposits: Geoscience Canada, v. 9, p. 108-117.

Anderson, T.F., and Arthur, M.A., 1983, Stable isotopes of oxygen and carbon and their application to sedimentologic and paleoenvironmental problems, p.1-11, in Arthur. M.A., Anderson, T. F., Kaplan, I. R, Veizer, J. and Land, L. S., eds., Stable Isotopes in Sedimentary Geology: Soc. Econ. Paleon. Mineralogists Short Course no. 10, 436 p.

Angevine, C.A., and Heller, P.L., 1987, Quantitative Sedimentary Basin Modeling: Geol. Soc. America Short Course. 37 p.

Aoyagi, K., and Kazama, T., 1980, Transformational changes of clay minerals, zeolites, and silica minerals during diagenesis: Sedimentology, v. 27, p. 179-188.

Arbey, F., 1968, Structures et dépôts glaciares dans l'Ordovician terminal des chaines d'Ougarta (Sahara algérien): Acad. Sci., Paris, Comptes Rendus, Ser. D., v. 266, p. 76-78.

Armstrong, R.L., 1968, Sevier orogenic belt in Nevada and Utah: Geol. Soc. America Bull., v. 79, p. 429-458.

Arthur, M.A., Anderson, T.F., Kaplan, I.R., Veizer, J., and Land, L.S., 1983, Stable Isotopes in Sedimentary Geology: Soc. Econ. Paleon. Mineralogists Short Course no. 13, 436 p.

Arthur, M.A, Bottjer, D.J., Dean, W.E., Fisher, A.G., Hattin, D.E., Kauffman, E.G., Pratt, L.M., and Scholle, P.A., 1986, Rhythmic bedding in Upper Cretaceous pelagic carbonate sequences: Varying sedimentary response to climatic forcing: Geology, v. 14, p. 153-156.

Asserto, R., and Folk, R.L., 1980, Diagenetic fabric of aragonitic and dolomite in an ancient peritidal-splenenan environment: Triassic Calcare roso Lombardia, Italy: Jour. Sedimentary Petrology, v. 50, p. 371-394.

Aulstead, K.L., and Spencer, R.J., 1985, Diagenesis of the Keg River Formation, northwestern Alberta: Fluid inclusion evidence: Bull. Can. Petrol. Geol., v. 33, p. 167-183.

Aulstead, K.L., Spencer, R.J., and Krouse, H.R., 1988, Fluid inclusion and isotopic evidence on dolomitization, Devonian of Western Canada: Geochimica et Cosmochimica Acta, v. 52, p. 1027-1035.

Back, W., Hanshaw, B.B., Herman, J.S., and van Driel, J.N., 1986, Differential dissolution of a Pleistocene reef in the ground-water mixing zone of coastal Yucatan, Mexico: Geology, v. 14, p. 137- 140.

Badizomani, K., 1973, The Dorag dolomitization model--application to the Middle Ordovician of Wisconsin: Jour. Sedimentary Petrology, v. 43, p. 965-984.

Ball, M.M., 1967, Carbonate sand bodies of Florida and the Bahamas: Jour. Sedimentary Petrology, v. 37, p. 556-591.

Ball, S.M., 1971, The Westphalia Limestone of the Northeastern Midcontinent: A possible ancient storm deposit: Jour. Sedimentary Petrology, v. 41, p. 217-232.

Banner, J.B., Hanson, G.N., and Meyers, W.J., 1988, Determination of initial Sr isotopic composition of dolostones from the Burlington-Keokuk Formation (Mississippian): Constraints from cathodoluminescence, glauconite paragenesis and analytical methods: Jour. Sedimentary Petrology, v. 58, p. 673-687.

Barnes, M.A., Barnes, W.C., and Bustin, R.M., 1984, Diagenesis 8: Chemistry and Evolution of Organic Matter: Geosciences Canada, v. 11, p. 103-114.

Barnes, C.R., 1984, Early Ordovician eustatic events in Canada, p. 51-63, in Bruton, D.L., ed., Aspect of the Ordovician System: Paleontologic Contributions of University of Oslo, Universitetsforlaget, No. 295.

Baker, P.A., and Burns, S.J., 1985, The occurrence and formation of dolomite in organic-rich continental margin sediments: Am. Assoc. Petroleum Geologists Bull., v. 69, p. 1917-1930.

Baker, P.A., and Kastner M., 1981, Constraints on the formation of sedimentary dolomite: Science, v. 213, p. 214-216.

Barker, C.E., 1983, Influence of time on metamorphism of sedimentary organic matter in liquid-dominated geothermal systems, western North America: Geology, v. 11, p. 384-388.

Barker, C.E., 1988, Temperature and time in thermal maturation of sedimentary organic matter, p. 73-98, in Naeser, N.D. and McCulloh, T.H., eds., Thermal History of Sedimentary Basins: Berlin, New York, Springer-Verlag.

Barker, C.E., and Goldstein, R.H., 1990, Fluid-inclusion technique for determining maximum temperature in calcite and its comparison to the vitrinite reflectance geothermometer: Geology, v. 18, p. 1103-1106.

Barker, C.E., and Halley, R.B., 1986, Fluid inclusion, stable isotope, and vitrinite reflectance evidence for the thermal history of the Bone Spring Limestone, southern Guadalupe Mountains, Texas: in Gautier, D.L., ed.), Roles of Organic Matter in Sediment Diagenesis: Soc. Econ. Paleon. Mineral. Spec. Pub. 38, p. 189-203.

Barker, C.E., and Halley, R.B., 1988, Fluid inclusions in vadose cement with consistent vapor liquid ratio, Pleistocene Miami Limestone (southeastern Florida): Geochimica et Cosmochimica Acta, v. 52, p. 1019-1025.

Barker, C.E., and Pawlewicz, M.J., 1986, The correlation of vitrinite reflectance with maximum temperature in organic matter, p. 79-93, in Buntebarth, G. and Stegena, L., eds., Paleogeothermics, lecture notes in earth sciences, v. 5: Berlin, Springer-Verlag.

Basler, R.S., 1941, The Nevada Early Ordovician (Pogonip) sponge fauna: U.S., Natl. Mus. Proc., v. 91, p. 91-102.

Bathurst, R.G.C., 1958, Diagenetic fabrics in some Brithish Dinantian Limestone: Liverpool, Mannchester Geol. J., v. 2, p. 11-36.

Bathurst, R.G.C., 1975, Carbonate Sediments and Their Diagenesis: Amsterdam, Elsevier, 658 p.

Bathurst, R.G.C., 1980, Deep crustal diagenesis in limestone: Revista del Instituto de Investigaciones Geologicas Diputacion Provincal, Universidad de Barcelona, v. 34, p. 89-100.

Bathurst, R.G. C., 1983, Neomorphic spar versus cement in some Jurassic grainstones: significance for evaluation of evolution and compaction: Jour. Geol. Soc. London, v. 140, p. 229-237.

Beach, D.K., and Ginsburg, R.N., 1980, Facies succession of Pliocene -- Pleistocene carbonates, Northwestern Great Bahama Bank: Jour. Sedimentary Petrology, v. 64, p. 1634-1642.

Beadle, S.C., 1988, Dasyclads, Cycbrinitids and Receptaculitids: comparative morphology and Paleoecology: Lethaia, v. 21, p. 1-12.

Beuf, S., Biju-Duval, B., Stevaux, J., and Kulbicki, G., 1966, Ampleur des glaciations "Siluriennes" au Sahara: leurs influences et leurs consequences sur la sédimentation: Inst. Francias de Pétrol., Rév., v. 21, p. 363-381.

Biddle, K., 1983, Girvanella oncoids from Middle to Upper Triassic, allochthonous boulders of dolomite Alps, Northern Italy, p. 390-397, in Peryt, T.M., ed., Coated Grains: Berlin, Heidleberg, Springer Verlag, 655 p.

Birnbaum, S.J., and Wireman, J.W., 1985, Sulfate-reducing bacteria and silica solubility: a possible mechanism for evaporite diagenesis and silica precipitation in banded-iron formations: Can. Jour. Sci., v. 22, p. 1904-1909.

Bissel, H.J., and Barker, H.K., 1977, Deep-water limestones of the Great Blue Formation (Mississippian) in the eastern part of the Cordilleran Miogeosyncline in Utah, p. 171-186, in Cook, H.E., and Enos, P., eds., Deep-water carbonate environments: Soc. Econ. Paleontologists and Mineralogists, Special Publ. No. 25

Blatt, H., 1982, Sedimentary Petrology: W. H. Freeman and Company, San Francisco, 564 p.

Bodnar, R.J., 1983, A method of calculating fluid inclusion volumes based on vapor bubble diameters and P-V-T-X properties of inclusion fluids: Econ. Geol., v. 78, p. 535-542.

Bodnar, R.J., and Bethke, P.M., 1984, Systematics of stretching of fluid inclusions I: fluorite and sphalerite at 1 atmosphere confining pressure: Econ. Geol. v. 79, p. 141-161.

Boles, J.R., and Franks, S.G., 1979, Clay diagenesis in Wilcox Sandstones of southwest Texas: Jour. Sedimentary Petrology, v. 49, p. 55-70.

Bosselini, A., 1984, Progradation geometries of carbonate platforms: examples from Triassic of the Dolomites, northern Italy: Sedimentology, v. 31, p. 1-24.

Bossellini, A., and Ginsburg, R.N., 1971, Form and internal structure of recent algal nodules (rhodololites) from Bermuda: Jour. Geology, v. 70, p. 669-682.

Bova, J.A., and Read, J.F., 1987, Incipiently drowned facies within a cyclic peritidal ramp sequence, Early Ordovician Chepultepec interval, Virginia Appalachians: Geol. Soc. America Bull., v. 98, p. 714-727.

Braun, M., and Friedman, G.M., 1969, Carbonate lithofacies and environments of the Tribes Hill Formation (Lower Ordovician) of Mohawk Valley, New York: Jour. Sedimentary Petrology, v. 39, p. 113-135.

Brenner, R.L., and Davies, D.K., 1973, Storm-generated coquinoid sandstones: Genesis of high-energy marine sediments from the Upper Jurassic of Wyoming and Montana: Geol. Soc. America Bull., v. 84, p. 1685-1097.

Brockerhoff, F.G. and Friedman, G.M., 1987, Paleo-depths of burial of Middle Ordovician carbonates in New York state and Vermont: Northeastern Geol., v. 9, p. 51-58.

Brookfield, M.E, 1982, Glacio-eustatic sedimentary cycles in Trenton Limestone (Middle Ordovician) of southern Ontario: Am. Assoc. Petroleum Geologists Bull., v. 66, p. 1165.

Brookfield, M.E., and Brett, C.E., 1988, Paleoenvironments of the Mid-Ordovician (Upper Canadian) Trenton Limestones of southern Ontario, Canada: Storm sedimentation on a shoal-basin shelf model: Sed. Geology, v. 57, p. 75-105.

Bud, D.A., and Land, L.S., 1989, Geochemical imprint of meteoric diagenesis in Holocene ooid sands, Schooner Cays, Bahamas: Correlation of calcite cement geochemistry with extant ground waters: Jour. Sedimentary Petrology, v. 60, p. 361-378.

Bullen, S.B., and Sibley, D.F., 1984, Dolomite selectivity and mimic replacement: Geology, v. 12, p. 655-648.

Burns J.P., Baker, P.A., and Showers, W.J., 1988, The factors controlling the formation of dolomite in organic-rich sediments: Miocene Drakes Bay Formation, California, p. 41-52, in Shukla, V., and Baker, P.A., eds., Sedimentology and Geochemistry of Dolostones: Soc. Econ. Paleontologists and Mineralogists Spec. Publ. No. 28.

Burchfiel, B.C., and Davis, G.A., 1971, Nature of Paleozoic and Mesozoic thrust faulting in the Great Basin area of Nevada, Utah, southern California: Geol.Soc. America Abstracts with Programs, v. 3, p. 88-90.

Burruss, R.C., 1981, Hydrocarbon fluid inclusions in studies of sedimentary diagenesis, p. 138-156, in Hollister,L.S. and Crawford, M.L., eds., Short Course in Fluid Inclusions, application to petrology: Toronto, Mineral. Assoc., Canada.

Burruss, R.C., 1987, Diagenetic paleotemperatures from aqueous fluid inclusions: Re-equilibration of inclusions in carbonate cements by burial heating: Mineral. Magazine, v. 51, p. 477-481.

Burruss, R.C., 1988, Paleotemperatures from fluid inclusions: Advances in theory and technique, p. 119-131, in Naeser, N.D. and McCulloh, T.H., eds., Thermal History of Sedimentary Basins, Methods and Case Histories: New York, Berlin, Springer-Verlag.

Burruss, R.C., Cercone, R.K., and Harris, P.M., 1985, Timing of hydrocarbon migration - evidence from fluid inclusions in calcite cements tectonics and burial history, p. 277-289, in Schneidermann, N., and Harris, P.M., eds., Carbonate cements: Soc. Econ. Paleontologists and Mineralogists Spec. Pub. No. 25.

Butler, G.P., 1969, Modern evaporite deposition and geochemistry of coexisting brines, the sabkha, Trucial Coast, Arabian Gulf: Jour. Sedimentary Petrology, v. 39, p. 70-89.

Byers, C.W., 1977, Biofacies patterns in euxinic basins: a general model, p. 5-17, in Cook, H.E., and Enos, P., eds., Deep-water carbonate environments: Soc. Econ. Paleontologists and Mineralogists, Special Publ. No. 25.

Calvert, S.E., 1971, Composition and origin of North Atlantic deep-sea cherts: Contr. Miner. Petrol., v. 33, p. 273-288.

Cander, H.S., Kaufman, J., Daniels, D.L., and Meyers, J.W., 1988, Regional dolomitization of shelf carbonates in the Burlington-Keouk Formation (Mississippian) Illinois and Missouri: Constraints from cathodoluminescent zonal stratigraphy, p. 129-144, in Shukla, V., and Baker, P.A., eds., Sedimentology and Geochemistry of Dolostones: Soc. Econ. Paleontologists and Mineralogists Spec. Publ. No.28.

Cantrell, L., and Walker, K.R., 1985, Depositional and diagenetic patterns, ancient oolite, Middle Ordovician, Eastern Tennessee: Jour. Sedimentary Petrology, v. 555, p. 518-531.

Carozzi, A.B., 1963, Half-moon oolites: Jour. Sedimentary Petrology, v. 33, p. 633-645.

Carpenter, A.B., and Oglesby, T.W., 1976, A model for the formationof luminescently zoned calcitic cement and its implications: Geol. SOc. America. Abstracts with program, v. 8, p. 469-470.

Cathels, L.M., and Smith, A.T., 1983, Thermal constraints on the formation of Mississippi Valley-ty pe lead and zinc deposit genesis: Econ. Geology, v. 78, p. 983-1002.

Catolov, G.A.,1983, Triassic oncoids from the central Balkanides, p. 389-408, in Peryt, T.M., ed., Coated Grains: Springer Verlag, Berlin, Heidleberg, 655 p.

Cercone, K.R., 1984, Thermal history of Michigan Basin: Am. Assoc. Petroleum Geologists, v. 68, p. 130-136.

Cercone, K.R., and Lohmann, K.C., 1986, Diagenetic history of Union 8, Pinniacle reef (Middle Silurian) Northern Michigan, USA, p. 381-398, in J.h. Schroeder and B. H. Purser, eds., Reef Diagenesis: Springer-Verlag, Berlin, Heidelberg, 455 p.

Choquette, P.W., and James, N.P., 1987, Diagenesis # 12. Diagenesis in limestones-3. The deep-burial environment: Geoscience Canada, v. 14, p. 3-35.

Choquette, P.W., and Pray, L.C., 1970, Geologic nomenclature and classification of porosity in sedimentary carbonates: Am. Assoc. Petroleum Geologists Bull., v. 54, p. 207-250.

Choquette, P.W., and Steinen, R.P., 1980, Mississipian non-supratidal dolomite, Ste. Genevie Limestone, Illinois Basin: Evidence for mixed-water dolomitization, p. 163-196, in D.H. Zenger, J.B. Dunham, and R.L. Ethington, eds, Concepts and models of dolomitization: Soc. Econ. Paleontologists and Mineralogists, Spec. Pub. No. 28.

Chow, N., and James, N.P., 1987, Facies-specific calcitic and bimineralic ooids from Middle and Upper Cambrian platform carbonates, western Newfoundland: Jour. Sedimentary Petrology, v. 57, p. 907-921.

Chow, N., and James, N.P., 1987, Cambrian grand cycles : a northern Appalachian perspective: Geol. Soc. America Bull., v. 98, p. 418-429.

Churkin, M., Jr. 1974, Paleozoic marginal ocean basin volcanic arc systems in the Cordilleran fold belt, p. 174-192, in Dott, R. H. Jr., and Shaver, R. H., eds., Modern and ancient geosynclinal sedimentation: Soc. Econ. Paleontologists and Mineralogists Spec. Pub. No. 19.

Claypool, G.E., and Threlkeld, C.N., 1983, Anoxic diagenesis and methane generation in sediments of the Blake Outer Ridge: Initial Reports of the D.S.D.P., v. 87, p. 263-296.

Clayton, R.N., Friedman, I., Graf, D.L., Mayeda, T.K., and Shimp, N.F., 1966, The origin of saline formation waters, I. Isotopic composition: Jour. Geophys. Res., v. 71, p. 3869-3882.

Coniglio, M., 1987, Biogenic chert in the Chow Head Group (Cambro-Ordovician), western Newfoundland: Sedimentology, v. 34, p. 813-823.

Coniglio, M. and James, N.P., 1985, Calcified algae as sediment contributors to early Paleozoic limestones: Evidence from deep-water sediments of the Cow Head Group, western Newfoundland: Jour. Sedimentary Petrology, v. 55, p. 746-754.

Coniglio, M., and James, N. P., 1988, Dolomitization of deep-water sediments, Cow Head Group (Cambro-Ordovician), western Newfoundland: Jour. Sedimentary Petrology, v. 58, p. 1032-1045.

Coniglio, M., James, N.P., and Aissaoui, D.M., 1988, Dolomitization of Miocene carbonates, Gulf of Suez, Egypt: Jour. Sedimentary Petrology, v. 58, p. 100-119.

Cook, E.H., and Mullins, H.T., 1983, Basin Margin environment , p. 539-617, in Scholle, P.A., Bebout, D.G., and Moore, C.H., eds., Carbonate Depositional Environments: Am. Assoc. Petroleum Geologists, Memoir 33, 708 p.

Cook, H.E., and Taylors, M.E., 1977, Comparison of Continental slope and shelf environments in the Upper Cambrian and Lowest Ordovician of Nevada, p. 51-81, in Cook, H.E., and Enos, P., eds., Deep-water carbonate environments: Soc. Econ. Paleontologists and Mineralogists Spec. Publ. No. 25.

Cooper, G.A., 1956, Chazian and related brachiopods: Smithsonian Misc. Colln., v. 127, pts. 1 and 2, 1245 p.

Craig, H., 1965, The measurements of oxygen isotope paleo-temperatures, p. 161-182, in P Tongioni, E., ed., Stable Isotopes in Oceanographic Studies and Paleotemperatures: Consiglio Nazionale delle Richerche, laboratorio de Geologia Nucleare, Pisa.

Crawford, M.L., 1981, Phase equilibrium in aqueous fluid inclusions, p. 75-100, in Hollister, L.S. and Crawford, M.L., eds., Short Course in Fluid Inclusions, application to petrology: Mineral. Assoc. Canada Short Course Hand Book No. 6.

Crowder, D.F., McKee, E.H., Ross, D.C., and Krauskoph, K.B., 1973, Granitic rocks of the White Mountain area, California--Nevada-- Age and regional significance: Geol. Soc. America, v. 84, p. 285-296.

Cullis, C.G., 1904, The atoll of Funafuti. Boring into a coral reef and the results: The Royal Soc. London, p. 392-393, 404-415, 420 Plate F.

Curtis, R., Evans, A., Kinsman, D.J.J., and Shearman, D.J., 1963, Association of dolomite and anhydrite in recent sediments of Persian Gulf: Nature, v. 197, p. 679-680.

Curtis, C.D., 1978, Possible links between sandstone diagenesis and depth-related geochemical reactions occurring in enclosing mudstones: Jour. Geol. Soc. London, v. 135, p. 107-117.

Dahanayake, K., 1977, Classification of oncoids from the upper Jurassic carbonates of the French Jura: Sed. Geology, v. 18, p. 337-358.

Dahanayake, K., 1983, Grivanella oncoids from the Middle to Upper Jurassic oncoids, p. 377-388, in Peryt, T.M, ed., Coated Grains: Springer Verlag; Berlin, Heidleberg, 655 p.

David, T.W.E., and Browne, W.R., 1950, The geology of the Commonwealth of Australia: London, Edward Arnold and Co., v.1, 747 p.; v.2 , 618 p. v.3, colored geology maps.

Davies, G.R., 1977, Former magnesian calcite and aragonite submarine cements in upper Paleozoic reefs of the Canadian Arctic: a summary: Geology, v. 5, p. 11-15.

Davis, G.R., 1977, Turbidites, debris sheets, and truncation structures in upper Paleozoic deep- water carbonates of Sverdrup Basin, Arctic Archipelago, p. 221-244, in Cook, H.E., and Enos, P., eds., Deep-water carbonate environments: Soc. Econ. Paleontologists and Mineralogists Spec. Publ. No. 25.

Davies, P.J., Bubela, B., and Ferguson, J., 1978, The formation of ooids: Sedimentology, v. 25, p. 120-122.

Dickson, J. A. D., 1966, Carbonate identification and genesis as revealed by staining: Jour. Sedimentary Petrology, v. 36, p. 491-505

Dickson, J. A. D., and Coleman, M. L., 1980, Changes in carbonate and oxygen isotope composition during limestone diagenesis: Sedimentology, v. 27, p. 107-118.

Dietrich, R.V, Hoobs, C.R.B., and Lowry, W.D., 1963, Dolomitization interrupted by silicification: Jour. Sedimentary Petrology, V. 33, p. 646-663.

Dikey, P.A., 1975, Possible primary migration of oil from source rock in oil phase: Am. Assoc. Petroleum Geologists Bull., v. 60, p. 543-553.

Dorobek, S.L., 1987, Petrography, geochemistry and origin of burial diagenetic facies, Siluro-Devonian Helderberg Group (carbonate rocks), Central Appalachians: Am. Assoc. Petrol. Geol. Bull., v. 71, p. 492-514.

Dorobek S.L., and Read J.F., 1986, Sedimentology and basin evolution of the siluro - Devonian Helderberg Group, central Appalachian: Jour. Sedimentary Petrology, V. 56, p. 601-613.

Dow, W.G., 1977, Kerogen studies and geological interpretations: Journal of Geochemical Exploration, v. 7, p. 79-99.

Dow, W. G., 1982, Kerogen maturity and type by reflected light microscopy applied to petroleum exploration, p. 133-159, in Staplin, F. L., et al., eds., How to Assess Maturation and Paleotemperature: Soc. Econ. Paleontologists and Mineralogists, Short Course No. 7.

Dravis, J.J., 1979, Rapid and widespread generation of recent oolitic hard grounds on a high energy Bahamian platforms, Eleuthera Bank, Bahamas: Jour. Sedimentary Petrology, v. 49, p. 195-208.

Duba, D., and Williams-Jones, A.E., 1983, The application of illite crystallinity, organic matter reflectance and isotopic techniques to mineral exploration: a case study in southwestern Gaspe, Quebec: Econ. Geol., v. 78, p. 1350-1363.

Dunham, R. J., 1962, Classification of carbonate rocks according to depositional texture, p. 108-121, in W.E. Han, ed., Classification of Carbonate Rocks: Am. Assoc. Petroleum Geologists, Memoir 1, 279 p.

Dunham, R.J., 1969, Early vadose silt in Townsend mound (reef) New Mexico, p. 139-181, in Friedman, G. M., ed, Depositional environments in carbonate rocks: Soc. Econ. Paleontologists and Mineralogists, Spec. Pub. No. 28.

Dunham, R.J., 1970, Stratigraphic reefs versus ecologic reefs: Am. Assoc. Petroleum Geologists Bull., v. 54, p. 1931-1932.

Dunham, R.J., 1971, Meniscus cement, p. 297-300, in Bricker, O.P., ed., Carbonate Cements: Johns Hopkins Univ. Studies in Geology No. 19.

Dunham, J.B., and Olson, E.R., 1978, Diagenetic dolomite formation related to Paleozoic paleogeography of the Cordillerian miogeocline in Nevada: Geology, v. 6, p. 556-559.

Dunham, J.B., and Olson, E.R., 1980, Shallow subsurface dolomitization of subtidally deposited carbonate sediments in the Hanson Creek Formation (Ordovician-Silurian) of central Nevada, p. 139-162, in D.H. Zenger, J. B. Dunham, and R.L. Ethington, eds., Concepts and Models of Dolomitization: Soc. Econ. Paleontologists and Mineralogists, Spec. Pub. No. 28.

Dunnington, H.V., 1967, Aspect of diagenesis and shape change in stylolitic limestone reservoirs: World Petrol. Congr., Proc., Mexico, 2: p. 339-352.

Dunoyer de Segonzac, G., 1970, The transformation of clay minerals during diagenesis and low grade metamorphism: a review: Sedimentology, v. 15, p. 281-346.

Eardley, A.J., 1938, Sediments of Great Salt Lake, Utah: Am. Assoc. Petroleum Geologists, v. 22, p. 1305-1411.

Einsele, G., 1982, Limestone-marl cycles (periodites): diagenesis, significance, causes-- a review, p. 8-53, in Einsele, G., and Seilacher, A., eds., Cyclic Event Sedimentation: Berlin, New York, Springer-Verlag, 536 p.

Elliott, W.C., and Aronson, J.L., 1987, Alleghanian episode of K-bentonite ilitization in the southern Appalachian Basin: Geology, v. 15, p. 735-739.

Elric, M., and Read, J.F., 1991, Cyclic ramp-to-basin carbonate deposits, Lower Mississippian, Wyoming and Montana: a combined field and computer modelling: Jour. Sedimentary Petrology, v. 61, p. 1194-1224.

Emerson, R.J. Jahnke, R., Bender, M., Froelich, P., Klinkhammer, G., Bowser, C., and Setlock. G., 1980, Early diagenesis in sediments from the equatorial Pacific 1: Pore water nutrient and carbonate results: Earth Planet. Sci. Lett., v. 49, p. 57-80.

Enos, P., 1983, Shelf environment, p. 268-295, in Scholle, P.A., Beabout, D.G., and Moore, C.H., eds., Carbonate Depositional Environments: Am. Assoc. Petroleum Geologists, Memoir 33, 707 p.

Evamy, B.D., 1967, Dedolomitization and the development of rhoboheadral pores inlimestones: Jour. Sed. Petrology, v. 37., p. 1204- 1215.

Evamy, B.D., 1969, The precipitational environment and correlation of some calcite cements deduced from artificial staining: Jour. Sedimentary Petrology, v. 39, p. 787-821.

Evamy, B.D., and Shearman, D.J., 1965, The development of overgrowths from echinoderm fragments: Sedimentology, v. 5, p. 211-233.

Evans, I., and Kendall, C.G., ST.C., 1977, An interpretation of the depositional setting of some deep-water Jurassic carbonates of the central High Atlas Mountains Morocco: Soc. Econ. Paleontologists and Mineralogists Spec. Publ. No. 25, p. 249-261.

Evans, C.C., 1984, Development of an ooid shoal complex: The importance of antecedent and syndepositional topography, p. 392-429, in Harris, P.M., ed., Carbonate Sands-A Core Workshop: Soc. Econ. Paleontologists and Mineralogists Core Workshop No. 5, 464 p.

Fairchild, I.T., 1980, Stages in Precambrian dolomitization, Scotland: Cementing versus replacement textures: Sedimentology, v. 27, p. 631-650.

Farr, M.R., 1989, Compositional zoning characteristics of late dolomite cement in the Cambrian Bonneterre Formation Missouri: Implications for parent fluid migration pathways: Carbonate and Evaporites, v. 4, p. 177-194.

Faure, G., 1977, Principles of Isotope Geology: John Wiley & Sons, New York, 464 p.

Finks, R.M., and Toomey, D.F., 1969, The paleoecology of Chazian (Lower Middle Ordovician) "Reefs" or mounds: New York State Geological Association Field Guide Book, p. 93-120.

Fischer, A.G., and Bottjer, D.J., 1991, Orbital forcing and sedimentary sequences: Jour. Sedimentary Petrology, v. 61, p. 1063-1069.

Flügel, E., 1982, Microfacies Analysis of Limestones: Springer Verlag, Berlin, 633 p.

Folk, R.B., 1974, The natural history of crystalline calcium carbonate: effect of magnesium content and salinity: Jour. Sedimentary Petrology, v. 44, p. 40-53.

Folk, R.B., and Land, L.S., 1975, Mg/Ca ratio and salinity: two controls over crystallization of dolomite: Am. Assoc. Petroleum Geologists Bull., v. 56, p. 434-453.

Folk, R.L., and Pittman, J.S., 1971, Length slow calcedony: A new testament for vanished evaporites: Jour. Sedimentary Petrology v. 41, p. 1045-1058.

Frank, J.,T., 1981, Dedolomitization in the Sauk Limestone (Upper Cambrian) southeast Missouri: Jour. Sed. Petrology, v. 51, p. 7-17.

Frank, J.T., Carpenter, A.B., and Oglesby, T.W., 1982, Cathodoluminescence and composition of calcite cement in the Taum Sauk Limestone (Upper Cambrian) southeast Missouri: Jour. Sedimentary Petrology, v. 52, p. 631- 638.

Frape, S.K., and Fritz, P., 1982, The chemistry and isotopic composition of saline ground waters from Sudbury Basin, Ontario: Can. Jour. Sci., v. 19, p. 645-661.

Freeman, T., 1962, Quiet water oolites from Laguna Madre, Texas: Jour. Sedimentary Petrology, v. 32, p. 475-483.

Freeman, T., 1972, Sedimentology and dolomitization of Muschelkalk carbonates (Triassic), Iberian Range, Spain: Am. Assoc. Petroleum Geologists Bull., v. 56, p. 434-443.

Frey, M., Teichmuller, M., Teichmuller, R., Mullins, J., Kunzi, B., Breitschmid, A., Gruner, U., and Schwizer, B., 1980, Very low-grade metamorphism in external parts of the Central Alps: Illite crystallinity, coal rank and fluid-inclusion data: Eclogae Geol. Helv., v. 73, p. 173-203.

Friedman, G. M., 1959, Identification of carbonate minerals by staining methods: Jour. Sedimentary Petrology, v. 29, p. 87-97.

Friedman, G.M., 1964, Early diagenesis and lithification in carbonate sediments: Jour. Sedimentary Petrology, v. 34, p. 777-813.

Friedman, G.M., 1965, Terminology of crystallization textures and fabrics in sedimentary rocks: Jour. Sedimentary Petrology, v. 35, p. 643-655.

Friedman, G. M., 1975, The making and unmaking of limestones or the downs and ups of porosity: Jour. Sedimentary Petrology, v. 45, p. 379-398.

Friedman, G.M., 1980, Dolomites is an Evaporite Mineral: Evidence from rock record and from sea-marginal ponds of the Red Sea, p. 69-80, in Zenger, D.H., Dunham, J.B., and Ethington, R.L., eds., Concepts and models of dolomitization: Soc. Econ. Paleontologists and Mineralogists Spec. Pub. No. 28.

Friedman, G.M., 1985, The problem of submarine cement in classifying reef rock: An experience in frustration, p. 117-121, in Schneidermann, N. and Harris, P.M., eds., Carbonate cements: Soc. Econ. Paleontologists and Mineralogists Spec. Pub. No. 36.

Friedman, G. M., 1987a, Vertical movements of the crust: case history from northern Appalachian Basin: Geology, v. 15, p. 1130-1133.

Friedman, G.M., 1987b, Deep-burial diagenesis: its implication for vertical movements of the crust, uplift of the lithosphere and isostatic unroofing - a review: Sed. Geology, v. 50, p. 67-94.

Friedman, G.M., Amiel, A.J., Braun, M., and Donald Miller, 1973, Generation of particles and laminites in algal muds-example from sea-marginal hypersaline pool, Gulf of Aqaba, Red Sea: Am. Assoc. Petroleum. Geol., Bull., v. 57, p. 541-557.

Friedman, G.M., Amiel, A.J., and Schneidermann, N., 1974, Submarine cementation in reefs-- example from the Red Sea: Jour. Sedimentary Petrology, v. 445, p. 816-823.

Friedman, G.M., Cataffe, J. and Borak,B., 1984, Deep-burial diagenesis of the Hunton (Late Ordovician to Early Devonian) carbonates in the Anadarko Basin, p. 183-199, in Hinds, N.J., ed., Limestones of the Mid-continent: Tulsa Geol. Soc. Spec. Pub.

Friedman, G.M., and Radke, B., 1979, Evidence for Sabkha overprint and conditions of intermittent emergence in Cambro-Ordovician carbonates of North America and Queensland, Australia: Northeastern Geology, v. 1, p. 18-42.

Friedman, G.M., Reeckmann, S.A., and Borak, B., 1981, Carbonate deformation mechanism in the world's deepest wells (~9km): Tectonophysics, v. 74, p. 15-19.

Friedman, G.M., and Sanders, J.E., 1967, Origin and occurrences of dolostones, p. 267-348 in Chilingar, G.V., Bissel, H.J., and Fairbridge, R.W., eds., Carbonate rocks, developments in Sedimentology, 9A. The Netherlands, Elsevier Publ. Co., 471 p.

Friedman, G.M., and Sanders, J. E, 1978, Principles of sedimentology: New York, John Wiley & Sons, 795 p.

Friedman, G.M., and Sanders, J. E , 1982, Time-temperature-burial significance of Devonian anthracite implies former great (6.5km) depth of burial of Catskills Mountains, New York: Geology, v. 10, p. 93-96.

Friedman, G.M., Sanders, J.E., and Kopaska-Merkel, D.C., 1992, Principles of sedimentary deposits: stratigraphy and sedimentology: Macmillan Publ. Co., Nev York, 717 p.

Friedman, G.M., Sneh, A., and Owen, R.W., 1985, The Ras Muhammad Pool: implications for the Gavish Sabkha, p. 218-237, in Friedman, G.M., Krumbein, W.E., eds., Hypersaline echosystems. The Gavish Sabkha. Ecological Studies 53: New York, Springer-Verlag, 484 p.

Friedman, G.M., and Shukla, V, 1980, Significance of authigenic quartz euhedra after the sulfates: examples from the Lackport Formation (Middle Silurian) of New York: Jour. Sedimentary Petrology, v. 50, p. 1299-1304.

Friedman, G.M., and Sternbach, C.A., 1985, Dolomites formed under deep-burial conditions: Hunton Group carbonate rocks (Upper Ordovician to Lower Devonian) in deep Anadarko Basin of Oklahoma and Texas: Am. Assoc. Petroleum Geologists Bull., v. 69, p. 1317 (abstr.).

Friedman, I., and O'Neil, J.R., 1977, Compilation of stable isotope fractionation factors of geochemical interest, in Fleischer, M., ed., Data of Geochemistry, 6th ed., U.S. Geol. Survey Professional Paper, 440 p.

Fritz, P., and Smith, D.G.W., 1970, The isotopic composition of secondary dolomite: Geochimica et Cosmochimica Acta, v. 34, p. 1161-1173.

Frykman, P., 1986, Diagenesis of Silurian bioherms in the Klintberg Formation, Gotland, Sweden, p. 399-423, in Schroeder, J.H., and Purser, B.H., eds., Reef Diagenesis: Berlin, Heidelberg, Springer-Verlag, 455 p.

Fyfe, W.S., Kerrich, R., Hicock, S.R., and Colloza, F.C., 1987, Lithoprobe: Faults and fluids: Geoscience Canada, v. 14, p. 75-81.

Gaines, 1980, Dolomitization kinetics: Recent experimental studies, p. 81-86, in Zenger, D.H., Dunham, J.B., and Ethington, R.L., eds., Concepts and Models of Dolomitization: Soc. Econ. Paleontologists and Mineralogists Spec. Publ. No. 28.

Galloway, W.E., 1989, Genetic stratigraphic sequence in basin analysis I: architecture and genesis of flooding surface-bounded depositional units: Am. Assoc. Petroleum Geologists, v. 73, p. 143-154.

Gao, G., and Land, S.L., 1991, Early Ordovician Cool Creek Dolomite, Middle Arbuckle Group, Slick Hills , SW Oklahoma, U.S.A: origin and modification: Jour. Sedimentary Petrology, v. 61, p. 161-173.

Garrels, R.M., and Christ, C.L, 1965, Solutions, Minerals, and Equilibria: Harper, New York, 450 p.

Garrison, R.E., 1981, Diagenesis of oceanic carbonate sediments: A review of the DSDP perspective, p. 181-207, in Warme, J.E., Douglas, R.G., and Winterer, E.L., eds., The Deep Sea Drilling Project: A Decade of Progress: Soc. Econ. Paleontologists and Mineralogists Spec. Publ., No. 32.

Garrison, E.R., and Fischer, A.G., 1978, Deep-water limestones and radiolarites of Alpine Jurassic, p. 192-227, in Cys, J.M., and Mazzullo, S.J., eds., Sedimentary Processes: Depositional processes in ancient carbonates: Soc. Econ. Paleontologists and Mineralogists, Reprint series, No. 7.

Graven, G., and Freeze, A.R., 1984, Theoretical analysis of role of groundwater flow in the genesis of stratabound ore deposits I. Mathematical and numerical model. 2. Quantitative results: Amer. Jour. Sci., v. 284, p. 1085-1174.

Gavish, E., and Friedman, G. M., 1969, Progressive diagenesis in Quaternary to late tertiary carbonate sediment - sequence and time scale: Jour. Sedimentary Petrology, v. 39, p. 980-1006.

Gawthrope, R.L., 1987, Burial dolomitization and porosity development in a mixed-carbonate clastic sequence: an example from the Bowland Basin, northern England: Sedimentology, v. 34, p. 533-558.

Gebelein, C.D., 1969, Distribution, morphology, and accretion rate of Recent subtidal algal stromatolites, Bermuda: Jour. Sedimentary Geology, v. 39, p. 49-69.

Gebelein, C.D., 1977, Open marine subtidal and intertidal stromatolite (Florida, the Bahamas and Bermuda, p. 381-389, in Walter, M.R., ed., Stromatolites: Development in Sedimentology: Elsevier, 790 p.

Gebelein, C.D., and Hoffman, P., 1973, Algal origin of dolomite laminations in stromatolitic limestone: Jour. Sedimentary Petrology, v. 43, p. 603-613.

Geeslin, J.H., and Chafetz, H.S., 1982, Ordovician Aleman ribbon cherts: An example of silicification prior to carbonate lithification: Jour. Sedimentary Petrology, v. 52, p. 1283-1293.

Gevirtzman, D.A., and Mount J.F., 1984, Paleoenvironments of an earliest Cambrian (Tommotian) shelley found in the southwestern Great Basin, U.S.A.: Jour. Sedimentary Petrology, v. 56, p. 412-421.

Gieskes, J.M., 1981, Deep-sea drilling interstial water studies: implications for chemical alteration of the oceanic crust, Layers I and II, p. 149-167, in Warme, J.E., Douglas, R.G., and Winterer, E.L., eds., The Deep Sea Drilling Project: A Decade of Progress: Soc. Econ. Paleontologists and Mineralogists Spec. Publ., No. 32.

Gilbert, G.K, 1880, Contributions to the history of Lake Bonniville: U.S. Geol. Survey, 2nd Ann. Rep., p. 169-200.

Gillet, S.L., 1983, Major through-going stylolites in the Lower Ordovician Goodwin Limestone, southern Nevada: Petrography with dating from Paleomagnetism: Jour. Sedimentary Petrology, v. 51, p. 209-219.

Ginsburg, R.N., 1960, Ancient analogus of recent stromatolites: Inter. Geol. Congress, 21st. Norden, 1960, Repts. Pt. 22, p. 26-35.

Ginsburg, R.N., 1971, Landward movement of carbonate mud: new model for regressive cycles in carbonates (Abstract): Am. Assoc. Petroleum Geologists Bull., v. 55, p. 340.

Ginsburg, N.P., Shinn, E.A., and Schroeder, J.H., 1971, Recent synsedimentary cementation in subtidal Bermuda reefs, p. 54-59, in Bricker, O.P., ed., Carbonate Cements: Johns Hopkins Univ. Press, Studies in Geology, v. 19, 376 p.

Given, K.R., and Wilkinson, B.H., 1985, Kinetic contol of morphology , cpomposition, mineralogy of abiotic sedimentary carbonates: Jour. Sed. Petrology, v. 55, p. 109-118.

Given, K.R., and Wilkinson, B.H., 1987, Dolomite abundance and stratigraphic age: constraints on rates and mechanisms of Phanerozoic dolostone formation: Jour. Sedimentary Petrology, v. 57, p. 1068-1078.

Gnoli, M., and Serpagli, E., 1980, The problematical micro-organism Nuia in the Lower Ordovician of Precordillerian Argentina and its paleogeographic significance: jour. Paleontology, v. 54, p. 1245-1251.

Goldsmith, J.R., and Graf, D.C., 1958, Relation between lattice and constants and composition of the Ca-Mg Carbonates: The American Mineralogist, v. 43, p. 84-101.

Goldsmith, J. R., and Graf, D. L., 1958, Structural and compositional variations in some natural dolomites: Jour. Geology, v. 66, p. 678-693.

Goldstein, R.H., 1986, Re-equilibrium of fluid inclusions in low-temperature calcium-carbonate cement: Geology, v. 14, p. 792-795.

Goldstein, R.H., 1988, Cement stratigraphy of Pennsylvanian Holder Formation, Sacramento Mountains, New Mexico: Am. Assoc. Petroleum Geologists, v. 72, p. 425-438.

Goldstein, R.H., 1989, Petrographic and geochemical evidence for origin of paleospleothems, New Mexico implications for application of fluid inclusions to studies of diagenesis: Jour. Sedimentary Petrology, v. 60, p. 282-292.

Goodwin, P.W., and Anderson, E.J., 1985, Punctuated aggradational cycles: a general hypothesis of episodic stratigraphic accumulation: Jour. Geology, v. 93, p. 515-533.

Gratz, J.F., and Misra, K.C., 1987, Fluid inclusion study of the Gordonsville zinc deposit, central Tennessee: Econ. Geol., v. 82, p. 1790-1804.

Gregg, J.M., 1985, Regional epigenetic dolomitization in the Bonneterre Dolomite (Cambrian), southeastern Missouri: Geology, v. 13, p. 503-506.

Gregg, J.M., 1988, Origins of dolomite in the offshore facies of the Bonneterre formation (Cambrian), southeast Missouri, p. 67-84, in Shukla, V., and Baker, P.A., eds., Sedimentology and Geochemistry of Dolostones: Soc. Econ. Paleontologists and Mineralogists Spec. Publ. No. 28.

Gregg, J.M., and Shelton, K.L., 1990, Dolomitization and dolomite neomorphism in the back reef facies of the Bonneterre and Davis Formations (Cambrian) southeastern Missouri: Jour. Sedimentary Petrology, v. 60, p. 549-562.

Gregg, J.M., and Shelton, K.L., 1989, Minor and trace element distributions in the Bonneterre Dolomite (Cambrian), southeast Missouri - evidence for possible multiple basin fluid sources and pathways during lead-zinc mineralization: Geol. Soc. America Bull., v. 101, p. 221-230.

Gregg, J.M., and Sibley, D.F., 1984, Epigenetic dolomitization and the origin of xenotopic dolomite texture: Jour. Sedimentary Petrology, v. 54, p. 908-931.

Gregg, J.M., and Sibley, D.F., 1986, Epigenetic dolomitization and origin of xenotopic dolomite texture - reply: Jour. Sedimentary Petrology, v. 56, p. 735-736.

Grotzinger, J.P., 1986, Cyclicity and paleoenvironmental dynamics, Rocknest platform, Northwest Canada: Geol. Soc. America Bull., v. 79, p. 1208-1231.

Gurney, G.G., and Friedman, G.M., 1987, Burial history of the Devonian Cherry Valley carbonate sequence, Cherry Valley, New York: Northeastern Geol., v. 9, p. 1-11.

Guthrie, J. M., Houseknecht, D. W., and Johns, W. D., 1986, Relationships among vitrinite reflectance, illite crystallinity and, organic geochemistry in Carboniferous strata, Quachita Mountains, Oklahoma and Arkansas: Am. Assoc. Petroleum Geologists Bull., v. 70, p. 26-33.

Grower, G., and Read, J.F., 1983, Paleoaquifer and deep-burial related cements defined by regional cathodoluminescence patterns, Middle Ordovician carbonates, Virginia: Am. Assoc. Petroleum Geologists, v. 67, p. 1275-1303.

Hagen, G.M., and Logan, B.W., 1974, History of Hutchinson embayment tidal flat, Shark Bay, Western Australia, p. 283-315, in Logan, B.W, Read, J.F., Hagen, J.P., Hoffman, P., Brown, R.G., Woods, P.J., and Gebelein, C.D., Evolution and diagenesis of Quaternary carbonate sequence: Am. Assoc. Petroleum Geologists Memoir 22, 358 p.

Halley, R., 1977, Ooid fabric and fractures in the Great Salt Lake and the geologic record: Jour. Sedimentary Petrology, v. 47, p. 1099-1120.

Halley, R.B., 1987, Burial diagenesis of carbonate rocks, p. 1-15, in Halley, R.B., and Matthews, R.K., eds., Carbonate Depositional Environments -- Part 6: Diagenesis 2: Colorado School of Mines Press, Golden, Colorado.

Halley, R.B., and Harris, P.M., 1979, Fresh-water cementation of a 1,000-year old oolite: Jour. Sedimentary Petrology, v. 47, p. 565-581.

Halley, R.B., Harris, P.M., and Hine, A.C., 1983, Bank environment, p. 463-506, in Schole, P.A., Beabout, D.G., and Moore, C.H., eds., Carbonate depositional environments: Am. Assoc. Petroleum Geologists, Memoir 33, 707 p.

Hallock, P., Hine, A.C., Vrago, G.A., Elrod, J.A., and Jaap, E.W., 1988, Platforms of the Nicaraguan Rise: examples of sensitivity of carbonate sedimentation to excess trophic resources: Geology, v. 16, p. 1104-1107.

Hamblin, A.P., and Walker, R.G., 1979, Storm-dominated shallow marine deposits: the Ferine Kootenay (Jurassic) transition, southern Rocky Mountains: Can. Jour. Earth Sci., v. 16, p. 1673-1690.

Handford, C.R., 1986, Facies and bedding sequence in shelf-storm-deposited carbonates --Fayetteville Shale and Pitkin Limestone (Mississippian), Arkansas: Jour. Sedimentary Petrology, v. 56, p. 123-137.

Handford, C.R., 1988, Review of carbonate sand-belt deposition of ooid grainstone and application to Mississippian reservoir, Dame field, southern Kansas: Am. Assoc. Petroleum Geologists Bull., v. 72, p. 1184-1199.

Hanor, J.S., 1979, The sedimentary genesis of hydrothermal fluids, p. 137-172, in Barnes, H.L.Jr., ed., Geochemistry of Hydrothermal Ore Deposits, 2nd edition: New York, John Wiley & Sons, 798 p.

Hanor, J.S., 1987, Origin and Migration of Subsurface Sedimentary Brines: Soc. Econ. Paleon. Mineral. Short Course No. 21, 247 p.

Hanshaw, B.B., Back, W., and Deike, R.G., 1971, A geochemical hypothesis for dolomitization by ground water: Econ. Geol., v. 66, p. 710-724.

Hardie, L.A., 1987, Dolomitization: a critical view of some current views: Jour. Sedimentary Petrology, v. 57, p. 166-183.

Harms, J.C., Southard, J.B., Spearing, D.R., and Walker, R.G., 1975, Depositional environments as interpreted from primary sedimentary structures and stratification sequence: Soc. Econ. Paleontologists and Mineralogists, Short Course 2, 161 p.

Harris, D. C., 1982, Carbonate cement stratigraphy and diagenesis of the Burlington Limestone (Mississippian), S. E. Iowa, W. Illinois: Unpublished Master thesis, State University of New York at Stony Brook, 297 p.

Harris, P.M., 1979, Facies anatomy and diagenesis of a Bahamian ooid shoal: Miami, Fla., Univ. Miami, Sedimenta VII, Comparative Sedimentology Lab., 163 p.

Harris, P.M., 1984, Cores from a modern carbonate sand body; the Joulters ooid shoal, Great Bahama Bank, p.429-464, in Harris, P.M., ed., Carbonate Sands-A Core Workshop: Soc. Econ. Paleontologists and Mineralogists Core Workshop No. 5, 464 p.

Harris, P.M., Kendall, C.G. St. C., and Lerche, I., 1985, Carbonate cementation: a brief review, p. 79-95, in Schneidermann, N. and Harris, P.M., eds., Carbonate cements: Soc. Econ. Paleontologists and Mineralogists Spec. Pub., No. 25.

Hass, J.L, 1976, Physical properties of the co-existing phases and the thermochemical properties of H_2O component in boiling NaCl solutions: U.S. Geol. Survey Bull., v. 1421-A, 73 p.

Haszeldine, R.S., Samson, I.M., and Cornford, C., 1984, Dating diagenesis in a petroleum basin, a new fluid inclusion method: Nature, v. 307, p. 354-357.

Hayes, M.O., 1967, Hurricanes as geological agents, south Texas coast: Am. Assoc. Petroleum Geologists, v. 51, p. 937-942.

Hays, J.D., Imbrie, J., and Shackleton, J.J., 1976, Variations in the earth's orbit: pacemaker of the ace ages: Science, v. 194, p. 1121-1132.

Heckel, P.H., 1972, Recognition of ancient shallow marine environments, p. 226-286, in Rigby, J.K. and Hamblin, W.K., eds., Recognition of ancient sediment environments: Soc. Econ. Paleontologists and Mineralogists Spec. Publ. No. 16.

Heckel, P.H., 1986, Sea-level curve for Pennsylvanian eustatic marine transgressive-regressive depositional cycles along Midcontinent outcrop belt, North America: Geology, v. 14, p. 330-334.

Hein, J.R., Vallier, T.L., and Allan, M.A., 1981, Chert petrology and geochemistry, Mid-Pacific mountains and Hess Rise, DSDP Leg 62, Init. Report Deep See Drilling Project, v. 62, p. 711-748.

Heller, P.L., Komar, P.D., and Pevear, D.R., 1980, Transport process in ooid genesis: Jour. Sedimentary petrology, v. 50, p. 943-952.

Helmod, K.P., and van de Kamp, P.C., 1984, Diagenetic mineralogy and controls on albitization and laumonitic formation in Paleogene arkoses, Santa Ynez Mountains , California, p. 239-276, in McDoland, D.A., and Surdam, R.C., eds., Clastic Diagenesis: Am. Assoc. Petroleum Geologists Memoir 37.

Henrich, R., and Zankl, H., 1986, Diagenesis of Upper Triassic Wetterstein Reefs of the Bavarian Alps, p. 245-268, in Schroeder, J.H., and Purser, B.H., eds., Reef Diagenesis: Berlin, Heidelberg, Springer-Verlag, 455 p.

Hess, R., 1987, Selective and reversible carbonate-silica replacements in the Lower Cretaceous carbonate-bearing turbidites of Eastern Alps: Sedimentology, v. 34, p. 1055-1077.

Hess, R., 1988, Diagenesis # 13--Origin of chert: Diagenesis of biogenic silicious sediments: Geoscience Canada, v. 15, p. 1718-1732.

Hill, P.R., and Nadeau, O.C., 1989, Storm dominated Sedimentation on the inner shelf of the Canadian Beaufort Sea: Jour. Sedimentary Petrology, v. 59, p. 655-968.

Hine, A.C., 1977, Lily Bank, Bahamas: History of an active oolites sand shoal: Jour. Sedimentary Petrology, v. 47, p. 1554-1581.

Hine, A.C., and Mullins, H.T., 1983, Modern carbonate shelf-slope breaks, p. 169-188, in Stanley, D.J., and Moore, G.T., eds., The Shelfbreak Critical Interface on Continental Margins: Soc. Econ. Paleontologists and Mineralogists, Spec. Publ. No. 33.

Hird, K., and Tucker, M.E., 1988, Contrasting diagenesis of two Carboniferous oolites from South Wales: a tale of climatic influence: Sedimentology, v. 35, p. 587-602.

Hitchon, B., 1984, Geothermal gradients, hydrodynamics, and hydrocarbon occurrences, Alberta, Canada: Amer. Assoc. Petroleum Geologists Bull., v. 68, p. 713-743.

Hitchon, B., and Friedman, I, 1969, Geochemistry and origin of formation waters in the western Canada sedimentary basin I: Stable isotopes of hydrogen and oxygen: Geochimica et Cosmochimica Acta, v.33, p. 1321-1349.

Hitchon, B., and Krouse, H.R., 1972, Hydrogeochemistry of the surface waters of Mackenzie River dranige basin, Canada. III. Srtable isotope of oxygen, carbon, sulphur: Geochim. Cosmochim. Acta, v. 35, p. 567-598.

Hoffman, J. and Hower, J., 1979, Clay mineral assemblages as low grade metamorphic geothermometers - application to the thrust-faulted disturbed belt of Montana, USA, p. 55-79, in Scholle, P.A. and Schluger, P.R., eds., Aspects of Diagenesis: Soc. Econ. Paleontologists and Mineralogists Spec. Pub. No. 26.

Hoffman, P., 1977, Stromatolite morphogenesis in Shark Bay, western Australia, p. 261-271, in Walter, M.R., ed., Stromatolites: Development in Sedimentology: Elsevier, 790 p.

Holdaway, H.K., and Clayton, C.J., 1982, Preservation of shell microstructure in silicified brachiopods from Upper Cretaceous Wilmington Sands of Devon: Gel. Mag., v. 119, p. 371-382.

Hollister, L.S., 1981, Techniques for analyzing fluid inclusions, p. 272-277, in Hollister, L.S. and Crawford, M.L., eds., Short Course in Fluid Inclusions: application to petrology: Toronto, Mineral. Assoc. Canada.

Hood, A., Gutjahr, C.C.M., and Headcock, R.L., 1975, Organic metamorphism and generation of petroleum: Am. Assoc. Petroleum. Geologists Bull., v. 59, p. 986-996.

Hopkins, J.C., 1977, Production of foreslope breccia by differential submarine cementation and downslope displacement of carbonate sand, Miette and ancient wall buildups, Devonian Canada, p. 155-170, in Cook, H.E., and Enos, P., eds., Deep-Water Carbonate Environments: Soc. Econ. Paleontologists and Mineralogists Special Publ. No. 25

Horowitz, A.S., and Potter, P.E., 1972, Introductory Petrography of Fossils: New York, Springer-Verlag, 302 p.

Houseknecht, D.W., and Matthews, S.M., 1985, Thermal maturity of Carboniferous strata, Ouachita Mountains: Amer. Assoc. Petroleum Geologists Bull., v. 69, p. 335-345.

Howard, J.D., and Reineck, H.E., 1979, Sedimentary structures of "high energy" beach-to-offshore sequence; Ventura-Port Hueneme area, California (abstr): Geol. Soc. America Bull., v. 63, p. 468-469.

Hower, J., Eslinger, E., Hower, M.E., and Perry, E.A., 1976, Mechanism of burial metamorphism of argillaceous sediments: I. Mineralogical and chemical evidence: Geol. Soc. America Bull., v. 87, p. 725-737.

Hudson, J.H., 1985, Growth rate and carbonate production in Halimeda Opuntia: Marquesas Keys, Florida, p. 257-264, in Toomey, D.F., and Nitecki, M.N., eds., Paleoalgology: Contemporary Research and Applications: Berlin, Heidelberg, Springer-Verlag.

Humphrey, J.D., 1988, Late Pleistocene mixing zone dolomitization, southeastern Barbados, West Indies: Sedimentology, v. 35, p. 327-348.

Hurley, N.F., and Lohmann, K.C., 1989, Diagenesis of Devonian reefal carbonates in the Oscar Range, Canning Basin, Western Australia: Jour. Sedimentary Petrology. v. 59, p. 127-146.

Hurst, J.M., and Sheehan, P.M., 1985, Depositional environments along carbonate shelf to basin transect in the Silurian of Nevada, USA: Sed. Geology, v. 45, p. 143-171.

Hurst, J.M., and Surlyk, F., 1983, Depositional environments along a carbonate ramp to slope transitons in the Silurian of Washington Land, North Greenland: Can. Jour. Earth Sci., v. 20, p. 473-499.

Hurst, J.M., and Surlyk, F., 1984, Tectonic control of Silurian carbonate-shelf margin morphology and facies, North Greenland: Am. Assoc. Petroleum Geologist Bull., v. 68, p. 11-17.

Hutton, A.C., and Cook, A.C., 1980, Influence of alginite on the reflectance of vitrinite from Jodaja, SW, and some other coals and oil shales containing alganite: Fuel, v. 59, p. 711-714.

Hutton, A.C., Kantsler, A.,J., Cook, A.C., and McKirdy, D.M., 1980, Organic matter in shales: Journ. Austral. Petrol. Explor. Assoc., v. 20, p. 44-63.

Imbrie, J., 1985, A theoritical framework for the Pleistocene ice ages: Jour. Geol. Society, v. 142, p. 417-432.

Ince, D., 1984, Sedimentation and tectonism in the Middle Ordovician of Girvan district, SW Scotland: Royal Soc. Edinburgh, Transactions, v. 75, p. 223-237.

Irwin, M.L., 1965, General theory of epriric clear water sedimentation: Am. Assoc. Petroleum Geologists Bull., v. 49, p. 445-459.

Isaacs, C.M., 1982, Influence of rock composition on kinetics of silica phase changes in Monterey Formation, Santa Barbara area, California: Geology, v. 10, p. 304-308.

Jake, A.D., 1974, Replacement of fossils by length-slow chalcedony and associated dolomitization: Jour. Sedimentary Petrology, v. 44, p. 421-427.

Jackson, M.L., 1979, Soil Chemical Analysis -- Advanced Course, 2nd. ed., published by author, Madison, Wisconsisn, 580 p.

James, N.P., 1977, Facies models 8 -- Shallowing-upward sequences in carbonates: Geoscience Canada, v. 4, p. 126-136.

James, N.P., 1981, Depositional model for carbonate rocks, p. 289-348, in Parker, A., and Sellwood, B.W., eds., Sediment Diagenesis: Nato ASI series, Mathametical and Physical Series, v. 115, 536p.

James, N.P., and Choquette, P.W., 1983, Diagenesis 5. Limestones: Introduction, Geoscince Canada, v. 10, p. 159-161.

James, N.P., and Choquette, P.W., 1983, Diagenesis 6. Limestones: The sea floor diagenetic environment: Geoscince Canada, v. 10, p. 162- 179.

James, N.P., and Choquette, P.W., 1984, Diagenesis. 9; Limestone- Meteoric diagenetic environment: Geoscience Canada, v. 11, p. 161-194.

James, N.P., Ginsburg, R.N., Marszalek, D.S., and Choquette, P.W., 1976, Facies and fabric specifically of early subsea cements in shallow Belize (British Honduras) reefs: Jour. Sedimentary Petrology, v. 46, p. 523-544.

James, N.P., and Klappa, C.F., 1983, Petrogenesis of Early Cambrian reef limestone, Labrador, Canada: Jour. Sedimentary Petrology, v. 53, p. 1051-1096.

James, N.P., and Mountjoy, E.W., 1983, The Shelf-slope break in fossil carbonate platforms: an overview, p. 189-206, in Stanley, D.J., and Moore, G.T., eds., The Shelfbreak: Critical Interface on Continental Margin: Soc. Econ. Paleontologists and Mineralogists Spec. Publ. No. 33.

Jennings, S., and Thompson, G.R., 1986, Diagenesis of Plio-Pleistocene sediments of Colorado River delta, Southern California: Jour. Sed. Petrology, v. 56, p. 89-98.

Johnson, J.H., 1966, Late Cambrian algal geneus Nuia from Brewster County, Texas: Jour. Paleontol. v. 10, p. 432-452.

Johnsson, M.J., 1986, Distribution of maximum burial temperatures across northern Appalachian Basin and implications for Carboniferous sedimentation patterns: Geology, v. 14, p. 384-387.

Jones, J.B., and Segnit, E.R., 1971, The nature of opal I. Nomenclature and constituent phases: Geol. Soc. Australia Jour., v. 18, p. 57-68.

Kahle, C.F., 1965, Possible roles of clay minerals in the formation of dolomite: Jour. Sedimentary Petrology, v. 35, p. 448-453.

Kahle, C.F., 1974, Ooids from Great Salt Lake, as an analogue for the genesis and diagenesis of ooids in marine limestones: Jour. Sedimentary Petrology, v. 44, p. 30-39.

Kaldi, J., and Gildman,J., 1982, Early diagenetic dolomite cements: examples from the Permian Lower Magnesian Limestone of England and the Pleistocene Carbonates of Bahama: Jour. Sedimentary Petrology, v. 52., p. 1073-1085.

Kanuth, L.P., 1979, A model for the origin of chert in Limestone: Geology, v. 7, p. 274-277.

Karabinos, P., 1988, Heat transfer and fault geometry in the Taconian thrust belt, western New England, p. 35-45, in Mitra G., and Wojtal, S., eds., Geometries and Mechanisms of Thrusting with Special Refernce to Appalachian: Geol. Sos. America Special Paper No. 222, 232 p.

Kastner, M., Keene, J.B., and Gieskes, J.M., 1977, Diagenesis of siliceous oozes I: Chemical controls on the rate of opal-A to opal-CT transformation-an experimental study: Geochimica et Cosmochimica Acta, v. 41, p. 141-159.

Katz, A., 1971, Zoned-dolomite crystals: Jour. Geology, v. 79, p. 38-51.

Katz, A., and Matthews, A., 1977, The dolomitization of $CaCO_3$: An experimental study at 252-295 °C: Geochimica et Cosmochimica Acta, v. 41, p. 297-308.

Kaufman, J., Cander, H.S., Daniels, L.D., and Meyers, W.J., 1988, Calcite cement stratigraphy and cementation history of the Burlington-Keokuk Formation (Mississippian), Illinois and Missouri: Jour. Sedimentary Petrology, v. 58, p. 312-326.

Kaufman, J., Meyers, W.J., and Hanson, G.N., 1990, Burial cementation in the Swan Hills Formation (Devonian) Rosevear Field, Alberta, Canada: Jour. Sedimentary Petrology, v. 60, p. 918-939.

Kay, M., 1962, Classification of Ordovician Chazyan shelly and graptolitic sequence from central Nevada: Geol. Soc. America, v. 73, p. 1421-1430.

Kay, M., and Crawford, J.P., 1964, Paleozoic facies from the Miogeosynclinal to Eugeosynclinal Belt in thrust slices, central Nevada: Geol. Soc. America Bull., v. 75, p. 425-454.

Kaya, A., and Friedman, G.M., 1987, Depositional environment and diagenesis of Middle Ordovician Nuia-rich units, Antelope Valley Limestone, central Nevada: Geol. Soc. America Programs with Abstract, p. 722-723.

Kaya, A., and Friedman, G.M., 1988, Epigenetic and deep-burial dolomitization of Middle Ordovician Antelope Valley Limestone (Pogonip Group), central Nevada: Am. Assoc. Petroleum Geologists, v.72, p. 205, Abstract.

Kazimierczak, J., and Goldring, R., 1978, Subtidal flat-pebble conglomerate from Upper Devonian of Poland: A multiprovenant high-energy product: Geol. Mag., v. 115, p. 359-366.

Keith, B.D., and Friedman, G.M., 1977, A slope-fan-basin plain model Taconic sequence, New York and Vermont: Jour. Sedimentary Petrology, v. 47, p. 1220-1241.

Kelling, G., and Mullin, P.R., 1975, Gradded limestones and limestone quartzite couplets: possible ancient storm deposits from the Moroccan Carboniferous: Sed. Geology, v. 13, p. 161-190.

Kellog, G.E., 1963, Paleozoic stratigrphy of the southern Egan Range: Geol. Soc. America Bull., v. 74, p. 685-708.

Kendall, A.C., 1977, Fasicular-optic calcite: a replacement of bundled acicular carbonate cements: Jour. Sedimentary Petrology, v. 47, p. 1056-1062.

Kendall, A.C., 1985, Radiaxial-fibrous calcite: a reapprisal, p. 59-77, in Schneidermann, N. and Harris, P.M., eds., Carbonate Cement: Soc. Econ. Paleontologists and Mineralogists Spec. Pub., No. 25.

Kendall, A.C., and Tucker, M.E., 1973, Radiaxial fibrous calcite: a replacement after acicular carbonate: Sedimentology, v. 20, p. 365-389.

Kendall, C.G. St.C., and Schlager, W., 1981, Carbonates and relative changes in sea level: Marine Geology, v. 44, p. 181-212.

Kendall, C.G. St.C., and Skipwith, Sir P.A.d'E., 1969, Holocene-shallow water carbonate and evaporite sediments of Khor al Bazam, Abu Dhabi, Southwest Persian Gulf: Am. Assoc. Petroleum Geologists Bull., v. 53, p. 841-869.

Kerans, C., Hurley, N.F., and Playford, P.E., 1986, Marine diagenesis in reef complexes of the Canning Basin, Western Australia, p. 257-380., in Schroeder, J.H., and Purser, B.H., eds, Reef Diagenesis: Berlin, Heidelberg, Springer-Verlag, 455 p.

Ketner, K. B., 1977, Deposition and deformation of lower Paleozoic western facies rocks, northern Nevada, p. 251-258, in Stewart, J. H., Stevens, C. H., and Fritshe, A. E., eds., Paleozoic Paleogeography of the western United States: Soc. Econ. Paleontologists and Mineralogists, Pacific Sec. Pacific Coast Paleogeography symposium 1.

Ketner, K.B., and Smith, J.F.Jr., 1974, Folds and overthrusts of Late Jurassic or Early Creatceous age in northern Nevada: U.S. Geol. Survey Jour. Research, v. 2, p. 417-419.

Kinsman, D.J.J., 1969, Modes of formation, sedimentary associations, and diagonastic features of shallow-water and supratidal evaporites: Am. Assoc. Petroleum Geologists, v. 53, p. 830-840.

Kinsman, D.J.J., and Park, R.K., 1977, Algal belt and coastal sabkha evolution, Trucial coast, Persian Gulf, p. 421-433, in Walter, M.R., ed., Stromatolites: Development in Sedimentology: Elsevier, 790 p.

Kisch, H.J., 1980, Incipient metamorphism of Cambro-Silurian clastic rocks from the Jamtland Supergroup, central Scandinavia Caledonides, western Sweeden: Illite crystallinity and vitrinite' reflectance: J. Geol. Soc. London, v. 137, p. 271-288.

Koch, R., and Schorr, M., 1986, Diagenesis of Upper Jurassic sponge algal reefs in SW Germany, p. 224-244, in Schroeder, J.H., and Purser, B.H., eds., Reef Diagenesis: Berlin Heidelberg, Springer-Verlag, 455 p.

Koerschner, W.F. III, and Read, J.F., 1989, Field and modelling study of Cambrian carbonate cycles, Virginia Appalachians: Jour. Sedimentary Petrology, v. 59, p. 654-687.

Kreisa, R.D., 1981, Storm-generated sedimentary structures in subtidal marine facies with examples from the Middle and Upper Ordovician of southern Virginia: Jour. Sedimentary Petrology, v. 51, p. 823-848.

Kreisa, R.D., and Bambach, R., 1982, The role of Storm processes in generating shell beds in the Paleozoic shelf environments, p. 200-207, in Einsele, G., and Seilacher, A., eds., Cyclic Event Stratification: Berlin, Heidelberg, Springer-Verlag.

Kubler, B., 1967, La cristallinitie de l'illite et les zones tout a fait superieures du metamorphisme: Etage tectoniques, A la Baconniere, Neuchatel (Suisse), p.105-121.

Kubler, B., 1968, Evaluation quantitative du metamorphisme par la cristallinite de l'illite; etat des progres realises annees: Bull. Centre due Recherches de Pau, v.2, p. 385-397.

Kupecz, J.A., Kerans, C., and Land, L.S., 1988, Deep-burial dolomitization in the Ordovician Ellenburger Group Carbonates, West Texas and southeastern New Mexico: Jour. Sedimentary Petrology, v. 58, p. 908-910.

Kupecz, J.A., and Land, L.S., 1991, Late stage dolomitization of the Lower Ordovician Ellenburger Group, west Texas: Jour. Sedimentary Petrology, v. 61, p. 551-574.

Land, L.S., 1967, Diagenesis of skeletal carbonates: Jour. Sed. Petrology, v. 37, p. 914-930.

Land, L.S., 1973, Holocene meteoric dolomitization of Pleistocene limestones by meteoric water, North Jamica: Jour. Sedimentary Petrology, v. 20, p. 411-424.

Land, L.S., 1980, The isotopic and trace element geochemistry of dolomite: the state of the art, p. 87-110, in Zenger, D.H., Dunham, J.B., and Ethington, R.L., eds., Concepts and Models of Dolomitization: Soc. Econ. Paleontologists Mineralogists Spec. Publ., No. 28.

Land, L.S., 1982, Dolomitization: Am. Assoc. Petroluem Geologists, Education Course Note Series, No. 24, p. 20.

Land, L.S., 1983, The application of stable isotopes to studies of the origin of dolomite and to problems of diagenesis of clastic sediments, p.4-1--4-22, in Arthur, M.A., Anderson, T.F., Kaplan, I., Veizer, J., and Land, L.S., eds., Stable Isotopes in Sedimentary Geology: Soc. Econ. Paleontologists and Mineralogists Short Course No. 10, 436 p.

Land, L.S., 1985, The origin of massive dolomite: Jour. Geological Education, v. 13, p. 112-124.

Land, L.S., Behrens, E.W., and Frishman, S.A., 1979, The Ooids of Baffin Bay, Texas: Jour Sedimentary Petrology, v. 49 p. 1269-1278.

Land, L.S., and Goerau, T.F., 1970, Submarine lithification of Jamaican reefs: Jour. Sedimentary Petrology, v. 40, p. 457-462.

Laporte, L.F., 1967, Carbonate deposition near mean sea-level and resultant facies mosaic, Manlius Formation (Lower Devonian) of New York state: Am. Assoc. Petroleum Geologists Bull., v. 51, p. 73-101.

Laporte, L.F., 1978, Recognition of a transgressive carbonate sequence within a eperic sea: Helderberg Group (Lower Devonian) of New York state, p. 54-75, in Cys, J.M., and Mazzullo, J.S., eds., Sedimentary Processes: Depositional processes in ancient carbonates: Soc. Econ. Paleontologists and Mineralogists, Reprint series, No. 7.

Larson, L.T., Miller, J.D., Nadeau, J.E., and Roedder, E., 1973, Two sources of error in low temperature inclusion homogenization determination and corrections on published temperatures for east Tennessee and Laisvall deposits: Econ. Geol., vol. 68, p. 113-116.

Lawler, J.P., and Crawford, M.L., 1983, Stretching fluid inclusions resulting from a low-temperature microthermometric technique: Econ. Geol., v. 78, p. 527-529.

Leach, D.L., Nelson, R.C., and Williams, D., 1975, Fluid inclusion studies in the northern Arkansas zinc district: Econ. Geol., v. 70, p. 1084-1091.

Leckie, D.A., and Walker, R.G., 1982, Storm- and tide-dominated shorelines in Cretaceous Moosebar-Lower Gates interval-outcrop equivalents of Deep Basin gas trap in western Canada: Am. Assoc. Petroleum Geologists Bull., v. 66, p. 138-157.

Lee, Y.I., and Friedman, G.M., 1987, Deep-burial dolomitization in the Ellenburger Group Carbonates, western Texas and southeastern New Mexico: Jour. Sedimentary Petrology, v. 57, p. 544-557.

Lee, Y.I., and Friedman, G.M., 1988, Deep-burial dolomitization in the Ordovician Ellenburger Group Carbonates, West Texas and Southeastern New Mexico - Reply: Jour. Sedimentary Petrology, v. 58, p. 910-913.

Leheramnn, D.J., 1990, Study of fluid inclusions and conodont color alteration index from carbonate strata of the Road Canyon Formation (Permian) of southwest Texas: The Compass--Sigma Gama Epsilon, v. 67, p. 147-153.

Levin, J.R., 1986, Deep burial of coal bearing strata, Anthracite region, Pennsylvania: sedimentation or tectonics: Geology, v. 14, p. 577-580.

Lopatin, N.V., 1971, Temperature and geologic time as factors in coalification: Akademiya Nauk SSSR Izvestiya, Seriya Geologicheskaya, No. 3, p. 95-106.

Lohmann, K.C., and Meyers, W.J., 1977, Microdolomite inclusions in cloudy prismatic calcites: a proposed criterion for former high-Mg calcite: Jour. Sedimentary Petrology, v. 47, p. 1078-1088.

Lohmann, K.C., and Walker, 1989, The $\delta^{18}O$ record of Phanerozoic abiotic marine calcite cement: Geophys. Res. Lett., v. 16, p. 319-322.

Logan, B.W., Hoffman, P., and Gebelein, C.D., 1973, Algal mats, cryptalgal fabrics and structures, Hamelin Pool, Western Australia, p. 140-194, in Logan, B.W, Read, J.F., Hagen, J.P., Hoffman, P., Brown, R.G., Woods, P.J., and Gebelein, C.D., Evolution and diagenesis of Quaternary carbonate sequence: Am. Assoc. Petroleum Geologists Memoir 22, 358 p.

Logan, B.W., Rezak, R., and Gingsburg, R.N., 1962, Classification and environmental significance of Algal Stromatolites: Jour. Geology, v. 72, p. 68-83.

Longman, M.W., 1980, Carbonate diagenetic textures from nearsurface diagenetic environments: Am. Assoc. Petroleum Geologists Bull., v. 64, p. 461-487.

Longman, M.W., 1981, A process approach to recognizing facies of reef complexes, p. 9-40, in Toomy, D.F., ed., European Fossil Reef Models: Soc. Econ. Paleontologists and Mineralogists Spec. Publ. No. 30.

Loreau, J.P., and Purser, B. H., 1972, Distribution and ultra structure of Holocene ooids in the Persian Gulf, p. 279-328, in Purser, B.H., ed., The Persian Gulf. Holocene carbonate sedimentation in a shallow epicontinental sea: New York-Heidelberg-Berlin, Springer-Verlag, 471 p.

Loucks, R.G., 1977, Porosity development and distribution in shallow water carbonate complex-subsurface Pearsal Formation (Lower Cretaceous) south Texas, p. 97-126, in Beboutt, D.G., and Loucks, R.G., eds., Cretaceous Carbonates of Texas and Mexico: Austin, Univ. Texas, Bureau Econ. Geol. Rept. Invest. No. 89.

Lowe, D.R., 1982, Sediment Gravity flows: II--Depositional models with special reference to the deposits of high density Turbidity currents: Jour. Sedimentary Petrology, v. 52, p. 279-297.

Lowell, J. B., 1965, Low and Middle Ordovician history in the Hot Creek and Monitor Ranges, central Nevada: Geol. Soc. America Bull., v. 786, p. 257-266.

Lumsden, D.N., 1988, Characteristics of deep-marine dolomite: Jour. Sedimentary Petrology, v. 58, p. 1023-1031.

Lumsden, D.N., and Chimahusky, J.S., 1980, Relationship between dolomite nonstoichiometry and carbonate facies parameters, p. 123-138, in Zenger, D.H., Dunham, J.B., and Ethington, R.L., eds., Concepts and Models of Dolomitization: Soc. Econ. Paleontologists and Mineralogists Spec. Pub. No. 28.

Machel, H.G., 1985, Cathodoluminescence in calcite and dolomite and its chemical interpretation: Geoscience Canada, v. 12, p. 139-147.

Machel, H.G., 1987, Saddle dolomite as a by-product of chemical compaction and thermochemical sulfate reduction: Geology, v. 15, p. 939-940.

Machel, H.G., 1989, Relationships between sulphate-reduction and oxidation of organic compounds to carbonate diagenesis, hydrocarbon accumulations, salt domes, and metal sulfate deposits: Carbonate and Evaporites, v. 4, p. 137-151.

Machel, H.G., and Anderson, J.H., 1989, Pervasive subsurface dolomitization of Nisku formation in central Alberta: Jour. Sedimentary Petrology, v. 59, p. 891-911.

Machel, H.G., and Mountjoy, E.W., 1986, Chemistry and environments of dolomitization - a reappraisal: Earth. Sci. Review, v. 23, p. 175-222.

Macintire, I.G., 1977, Distribution of submarine cements in a modern Caribbean fringing reef, Galeta Point, Panama: Jour. Sedimentary Petrology, v. 47, p. 503-516.

Mack, H.G., and James, W.C., 1986, Cyclic sedimentation in the mixed siliciclastic-carbonate Abo-Hueco transitional zone (Lower Permian), southwestern New Mexico: Jour. Sedimentary Petrology, v. 56, p. 635-647.

Mackenzie, F.T., and Gees, R., 1971, Quartz: synthesis at Earth-surface conditions: Science, v. 173, p. 533-534.

Mackenzie, F.T., and Pigott, J.D., 1981, Tectonic controls of Phanerozoic rock cycling: Jour. Geological Society, v. 138, p. 183-196.

Magara, K., 1976, Water expulsion from clastic sediments during compaction-direction and volumes: Am. Assoc. Petroleum Geologists Bull., v. 60, p. 543-553.

Magara, K., 1980, Agents for primary hydrocarbon migration: a review, p. 33-45, in Roberts III, W.H., and Cordell, R.J., eds., Problems of Petroleum Migration: Am. Assoc. Petroleum Geologists Studies in Geology No. 10.

Major, R.P., Halley, R.B., and Lukas, K.J., 1988, Cathodoluminescent bimineralic ooids from the Pleistocene of Florida continental shelf: Sedimentology, v. 35, p. 843-855.

Maliva, R.G., and Siever, R., 1988, Mechanism and controls of silicification of fossils in limestones: Jour. Geology, v. 96, p. 387-398.

Maliva, R.G., and Siever, R., 1989, Chertification histories of some late Mesozoic and middle Paleozoic Platform carbonates: Sedimentology, v. 36, p. 907-926.

Mamet, B., and Roux, A., 1982, Sur le mode de croissance de Nuia Algue incerte sedis: Geobios, v. 15, p. 959-965.

Markello, J.R., and Read, J.F., 1981, Carbonate ramp-to-deeper shale shelf transitions of an Upper Cambrian intra shelf basin, Nolichucky Formation, southwest Virginia Appalachians: Sedimentology, v. 28, p. 573-597.

Marshall, J.F., and Davies, P.J., 1975, High-magnesium calcite ooids from the Great Barrier Reef: Jour. Sedimentary Petrology, v. 45, p. 285-291.

Maslow, V.P., 1954, On the Lower Silurian of eastern Siberia in Problems of the geology of Asia: Akad. Nauk. S.S.S.R., v. 11, 495-529.

Matsumoto, R., 1983, Mineralogy and geochemistry of carbonate diagenesis of the Pliocene and Pleistocene hemipelagic mud on the Blake Outer Ridge, Site 533, Leg 76, p. 411-426, in Sheridan R.E., and Gradstein , F.M., et al., eds., Init., Repts. DSDP, 76: Washington (U.S. Govt. Printing Office).

Mattes, B.W., and Mountjoy, E.W., 1980, Burial dolomitization of the Upper Devonian Miette buildup, Jasper National Park, Alberta, p. 259-297, in Zenger, D.H., Dunham, J.B., and Ethington, R.L., eds., Concepts and Models of Dolomitization: Soc. Econ. Paleontologists and Mineralogists Spec. Pub. No. 28.

Matthews, A., and Katz, A., 1977, Oxygen isotope fractionation during the dolomitization of calcium carbonate: Geochimica et Cosmochimica Acta, v. 41, p. 1431-1438.

Matthews, R.K., 1984, Dynamic Stratigraphy: 2nd. edition: Englewood Cliffs, NJ, Prentice-Hall Inc., 489 p.

Mazzullo, S.J., 1980, Calcite pseudospar replacive of marine acicular aragonite cement diagenesis: Jour. Sedimentary Petrology, v. 50, p. 409-422.

McHargue, T.R., and Price, R.C., 1982, Dolomite from clay in argillaceous or shale-associated marine carbonates: Jour. Sedimentary Petrology, v. 52, p. 873-886.

McKee, E. H., 1976, Northern part of the Toquima Range, Lander, Eureka, and Nye Counties: Nevada, U.S. Geol. Survey Prof. Paper, 931, 49 p.

McKee, E. H., and Ross, R. J. Jr., 1969, Stratigraphy of eastern assemblage rocks in a window in Roberts Mountain thrust, northern Toquima Range, central Nevada: Am. Assoc. Petroleum Geologists Bull., v. 53, p. 421-429.

McKenzie, J.A., Hsu, K.J., and Schneider, J.F., 1980, Movement of subsurface waters under the sabkha, Abu Dhabi UAE and its relations with evaporitive dolomites, p. 11-30, in Zenger D.H, Dunham, J.B., and Ethington, R.L., eds., Cocepts and Models of Dolomitization: Soc. Econ. Paleontologists Mineralogists Spec. Publ. No. 28.

McNaughton, K., and Smith, T.E., 1986, Fluid inclusion study of sphalerite and dolomite from the Nanisivik lead-zinc deposit, Baffin Island, Northwest Territories, Canada: Econ. Geol., v. 86, p. 713-720.

McRae, S.G., 1972, Glauconite: Earth Sci. Rev., v. 8, p. 397-440.

Merriam, C. W., 1963, Paleozoic rocks of Antelope Valley, Eureka, and Nye Counties: U.S. Geol. Survey Prof. paper 423, 67 p.

Merriam, C.W., and Anderson, C.A., 1942, Reconnaissance survey of the Roberts Mountains, Nevada: Geol. Soc. America Bull., v. 53, p. 1675-1728.

Meunier, J.D., 1989, Assessment of low temperature fluid inclusions in calcite using microthemometry: Econ. Geol., v. 84, p. 167-170.

Meyers, W.J., 1974, Carbonate cement stratigraphy of the Lake Valley Formation (Mississippian), Sacramento Mountains, New Mexico: Jour. Sedimentary Petrology, v. 44, p. 837-861.

Meyers, W.J., 1977, Chertification in Mississippian Lake Valley Formation, Sacramento Mountains, New Mexico: Sedimentology, v. 24, p. 75-105.

Meyers, W.J., 1978, Carbonate cements: their regional distributions and interpretation in Mississippian limestones of southwestern New Mexico: Sedimentology, v. 25, p. 371-400.

Meyers, W.L., and Hill, B.E., 1983, Quantitative studies of compaction in Mississippian skeletal limestones, New Mexico: Jour. Sedimentary Petrology, v. 231-241.

Meyers, W.J., and Lohmann, K.C., 1978, Microdolomite-rich syntaxial cements: proposed meteoric-marine mixing zone phreatic cements from Mississippian Limestones, New Mexico: Jour. Sedimentary Petrology, v. 48, p. 475-488.

Meyers, W.J., and Lohmann, K.C., 1985, Isotopic geochemistry of regionally extensive calcite cement zones and marine components in Mississippian limestones, New Mexico, p. 223-239, in Schneidermann, N. and Harris, P., eds., Carbonate Cements: Soc. Econ. Paleont. Mineralogists Spec. Pub., 36.

Middleton, G.V., and Hampton, M.A., 1976, Subaqueous sediment transport and deposition by sedimentary gravity flows, p. 197-218, in Stanley, D.J., and Swift, D.J.P., eds., Marine Sediment Transport and Environmental Management: Wiley, New York.

Miller, K.B., Brett, C.E., and Parsons, K.M., 1988, The paleoecologic significance of storm-generated disturbance within a Middle Devonian muddy epiric sea: Palios, v. 3, p. 35-52.

Milliman, J.D., and Barretto, H.T., 1975, Relict magnesian calcite oolite and subsidence of the Amazon shelf: Sedimentology, v. 22, p. 137-145.

Monty, 1967, Distribution and structures of recent stromatolitic algal mats, eastern Andros Island, Bahamas: Soc. geol. Belg. Bull., v. 90, p. 55-100.

Monty, C.L.V., 1972, Recent algal stromatolitic deposits, Andros Island, Bahamas. Preliminary report: Geol. Rundsch, v. 61, p. 742-783.

Monty, C.L.V., 1977, The origin and development of cryptalgal fabrics, p. 193-249, in Walter, M.R., ed., Stromatolites: Development in Sedimentology: Elsevier, 790 p.

Monty, C.L.V., and Hardie, L.A., 1977, The geological significance of the fresh water blue-green algae calcerous marsh, p. 447-477, in Walter, M.R., ed., Stromatolites: Development in Sedimentology: Elsevier, 790 p.

Moore, C.H., 1985, Upper Jurassic subsurface cements: A case history, p. 291-308, in Schneidermann, N., and Harris, P.M., eds., Carbonate Cements: Soc. Econ. Paleontologists and Mineralogists Spec. Pub. No. 25.

Moore, C.H., and Druckman, Y., 1981, Burial diagenesis and porosity evaluation, Upper Jurassic Smackover, Arkansas and Louisiana: Amer. Assoc. Petroleum Geologists Bull., v. 65, p. 597-628.

Moore, C.H., Chowdhury, A., and Chan, L., 1988, Upper Jurassic platform dolomitization, northwestern Gulf of Mexico: A tales of two waters, p. 175-190, in Shukla, V., and Baker, P.A., eds., Sedimentology and Geochemistry of Dolostones: Soc. Econ. Paleontologists and Mineralogists Spec. Publ. No.28.

Moore, D.M., and Reynolds, R.C.Jr., 1989, X-ray Diffraction and the Identification and Analysis of Clay Minerals: Oxford Univ. Press, Oxford, New York, 332 p.

Morner, N., 1976, Eustasy and geoid changes: Jour. Geology, v. 84, p. 123-151.

Morreale, S.A., 1981, Depositional environments and diagenesis of the Lower-Middle Ordovician Antelope Valley Liomestone, Eureka and Nye Counties, Nevada: Unpublished Master's thesis in University of Missouri, Colombia, 66p.

Morrow, D.W., 1982, Dolomite-Part 1: Dolomitization and dolomite precipitation: Geoscince Canada, v. 9, p. 5-13.

Morrow, D.W., 1982, Dolomite-Part 2: Dolomitization models and ancient dolostones: Geoscince Canada, v. 9, p. 95-107.

Morrow, D.W., and Ricketts, B.D., 1988, Experimental investigation of sulfate inhibition of dolomite and its mineral analogues, p. 25-39, in Shukla, V., and Baker, P.A., eds., Sedimentology and Geochemistry of Dolostones: Soc. Econ. Paleontologists and Mineralogists Spec. Publ., No. 28.

Mount, J.F., 1984, Mixing siliciclastic and carbonate sediments in shallow shelf environments: Geology, v.12, p. 432-435.

Mountjoy, E.W., and Halim-Dihardja, M.K., 1991, Multiple phase fracture and fault controlled burial dolomitization Upper Devonian Wabaumun Group: Jour. Sedimentary Petrology, v. 61, p.590-612.

Mullins, H.T., 1983, Modern carbonate slopes and basins of the Bahamas, p. 101-139, in Cook, H.E., Hine, A.C., and Mullins, H.T., eds., Platform Margin and Deep Water Carbonates: Soc. Econ. Paleontologists and Mineralogists Short Course No. 12.

Mullins, H.T., Dix., G.R., Gardulski, A.F., and Land, L.S., 1988, Neogene deep-water dolomite from Florida-Bahamas platforms, p. 235-244, in Shukla, V., and Baker, P.A., eds., Sedimentology and Geochemistry of Dolostones: Soc. Econ. Paleontologists and Mineralogists Spec. Publ. No. 28.

Mullins, H.T., Gardulski, A.F., Hinchey, E.J., and Hine, A.C., 1988, The modern carbonate ramp slope of central west Florida: Jour. Sedimentary Petrology, v. 58, p. 273-290.

Mullins, H.T., and Neumann, A.C., 1979, Deep carbonate bank margin structure and sedimentation in the northern Bahamas, p. 165-192, in Doyle, L.J., and Pilkey, O.H., eds., Geology of Continental Slopes: Soc. Econ. Paleontologists and Mineralogists Spec. Publ., No. 27.

Mullins, H.T., Neumann, A.C., Wilber, R.J., and Boardman, M.R., 1980, Nodular carbonate sediment on Bahama Slopes: possible precursors to nodular limestones: Jour. Sedimentary Petrology, v. 50, p. 117-131.

Murata, K.J., and Larson, R.R., 1975, Diagenesis of Miocene siliceous shales, Temblor Range, California: U.S. Geological Survey Journal of Research, v. 3, p. 553-566.

Muray, R.C., and Lucia, F.J., 1967, Cause and control of dolomite distribution by rock selectivity: Geol. Soc. America Bull., v. 78., p. 21-35.

Narr, W., and Currie, J.B., 1982, Origin of fracture porosity -- Example from Altamont field, Utah: Am. Assoc. Petroleum Geologists, v. 66, p. 1231-1247.

Nelson, C.H., 1982, Modern shallow water graded sand layers from storm surges, Bearing shelf: A mimic of Bouma sequence and turbiditic systems: Jour. Sedimentary Petrology, v. 52, p. 537-546.

Neumann, A.C., Kofoed, J.W., and Keller, G.H., 1977, Lithoherms in Straits of Florida: Geology, v. 5, p. 4-11.

Nevel, N.D., Purdy, E.G., and Imbrie, J., 1960, Bahamian oolitic sand: Jour. Geology, v. 68, p. 481-497.

Newman, J., and Newman, N.A., 1982, Reflectance anomalies in Pike River coals: evidence variability in vitrinite type, with implications for maturation studies and "Suggate rank": New Zealand Journ. Geol. Geophys., v. 25, p. 233-243.

Nitecki, M. H., 1972, The paleogeographic significance of Recepteculitids: Inter. Geol. Congress, Section 7, p. 303-309.

Noble, J.P.A., and van Stempvoort, D.R., 1989, Early burial quartz authigenesis in Silurian Platform carbonates, New Brunswick, Canada: Jour. Sedimentary Petrology, v. 59, p. 65-76.

Nolan, T.B., Merriam, C.W., and Williams, J.S., 1956, The stratigraphic section in the vicinity of Eureka, Nevada: U.S. Geol. Survey Prof. Paper 276, 77 p.

Northrop, D.H., and Clayton, R.N., 1966, Oxygen isotope fractionation in systems containing dolomite: Jour. Geology, v. 74, p. 174-196.

Odin, G.S., and Matter, A., 1981, De glauconiarum origine: Sedimentology, v. 28, p. 611-641.

Odom, E., 1984, Glauconite and celadonite minerals, p. 545-572, in Bailey, S.W., ed., Micas: Mineralogical Soc. America, Reviews in Mineralogy, v. 13, 584 p.

Oliver, J., 1986, Fluids expelled tectonically from orogenic belts: their role in hydrocarbon migration and other geologic phenomena: Geology, v. 14, p. 99-102.

Olsen, P.E., 1986, A 40-million-year lake record of early Mesozoic-orbital climatic forcing: Science, v. 234, p. 842-848.

Osleger, D., and Read, J.F., 1991, Relation of eustasy to stacking patterns of meter- scale carbonate cycles, Late Cambrian, U.S.A.: Jour. Sedimentary Petrology, v. 61, p. 1225-1252.

Parkinson, R.W., 1989, Decelerating Holocene sea-level rise and its influence on southwest Florida coastal evolution: A transgressive / regressive stratigraphy: Jour. Sedimentary Petrology, v. 59, p. 960-972.

Perkin, R.D., and Enos, P., 1968, Hurricane Betsy in the Florida-Bahama area--Geological effects and comparison with Hurricane Donna: Jour. Geology, v. 76, p. 710-717.

Perry, E.A., and Hower, J., 1970, Burial diagenesis in Gulf Coast pelitic sediments: Clays and Clay Min., v. 18, p. 165-177.

Perry, E.A., and Hower, 1972, Late stage dehydration in deeply buried pelitic sediments: Am. Assoc. Petroleum Geologists Bull., v. 56, p. 2012-2021.

Peryt, T.M., 1981, Phanerozoic oncoids - an overview: Facies, v.4, p. 197-21

Peryt, T.M., 1983, Oncoids: Comment to recent developments in coated grains, p. 273-275, in Peryt, T.M., eds., Coated Grains: Berlin, Heidelberg, Springer-Verlag, 655 p.

Pierre, C., Ortieb, L., and Person, A., 1984, Supratidal evaporitic dolomite at Ojo de Liebre Lagoon: Mineralogic and isotopic arguments for primary crystallization: Jour. Sedimentary Petrology, v. 54, p. 1049-1061.

Pierson, B.J., 1981, The control of cathodoluminescence in dolomite by iron and manganese: Sedimentology, v. 28, p. 601-610.

Pierson, B.T., and Shinn, E.A., 1985, Cement distribution and carbonate minerals stabilization in Pleistocene limestones of Hogsty Reef, Bahamas, p. 153-168, in Schneidermann, N. and Harris, P.M., eds., Carbonate Cements: Soc. Econ. Paleontologists and Mineralogists Spec. Pub. No. 36.

Pingitore, N., 1976, Vadose and phreatic diagenesis: products and their recognition in corals: Jour. Sedimentary Petrology, v. 46, p. 985-1006.

Pitman, W.C., III, 1978, Relationship between eustacy and stratigraphic sequence of passive margins: Geol. Soc. America Bull., v. 89, p. 1389-1403.

Plummer, L.N., Vacher, H.L., Mackenzie, F.T., Bricker, O.P., and Land, L.S., 1976, Hydrogeochemistry of Bermuda: a case history of ground-water diagenesis of biocalcareneite: Geol. Soc. America Bull., v. 87, p. 1301-1316.

Pollastro, R.M., and Barker, C.E., 1986, Application of clay-mineral, vitrinite reflectance, and fluid inclusion studies to the thermal burial history of the Pinedale Anticline, Green River Basin, Wyoming, in Gautier, D.L., ed., Roles of Organic Matter in Sediment Diagenesis: Soc. Econ. Paleontologists Mineralogists Spec. Pub. No. 38, p. 73-84.

Poncet, J. 1984, Microfabric and origin of Cambrian carbonate ooids -- Examples from the Cambrian oolite of Carteret (Northestern Armorican Massif, France): Sed. Geology., v. 39, p. 273-280.

Poole, F.G., 1974, Flysch deposits of Antler foreland basin in Western United States, p. 58-82, in Dickinson, W.R., ed., Tectonics and sedimentation: Soc. Econ. Paleontologists and Mineralogists Spec. Publ. No. 22.

Popp, B.N., Anderson, T.H., and Sandberg, P.A., 1986, Brachiopods as indicators of original isotopic compositions in some Paleozoic limestones: Geol. Soc. America Bull., v. 97, p. 1262-1269.

Potter, R.W.II, 1977, Pressure corrections for fluid inclusion homogenization temperatures based on volumetric properties of system NaCl-H_2O: Jour. Res., U.S. Geol. Surv., v. 5, p. 603-607.

Potter, R.W.II, and Brown, D.L., 1977, The volumetric properties of vapor saturated aqueous sodium chloride solutions from 0° to 500 °C at pressure 2000 bars based on regression of the available literature data: U.S. Geol. Surv. Open-file Rept. 76-243.

Potter, R.W.II, and Clynne, M.A., 1978, Pressure corrections for fluid inclusion homogenization temperatures: Abst. with Programs, Int. Assoc., Genesis Ore Deposits Symp., Alta, Utah, p. 146.

Potter, R.W.II, Clynne, M.A., and Brown, D.L., 1978, Freezing point depression of aqueous sodium chloride solutions: Econ. Geol., v.73, p.284-285.

Pratt, B.R., and James, N.P., 1982, Cryptalgal-metazoan bioherms of Early Ordovician age in the St. George Group, western Newfoundland: Sedimentology, v. 29, p. 543-569.

Prezbindowski, D.R., 1985, Burial cementation - is it important? A case study, Stuart City trend south central Texas, in N. Schneidermann, and P.M. Harris, eds., Carbonate cements: Soc. Econ. Paleontologists and Mineralogists Spec. Pub. No. 36.

Prezbindowski, D.R., and Larese, R.E., 1987, Experimental stretching of fluid inclusions in calcite - implication for diagenetic studies: Geology, v. 15, p. 333-336.

Price, L. C., 1983, The geologic time as parameter in organic metamorphism and vitrinite reflectance as an absolute paleogeothermometer: Jour. Petroleum Geology, v. 6, p. 5-38.

Price, L.C., and Barker, C.E., 1985, Suppression of vitrinite reflectance in amorphous-rich kerogen - a major unrecognized problem: Jour. Petroleum Geology, v. 8, p. 59-84.

Price, L.C., Daws, T., and Pawlewicz, M., 1986, Organic metamorphism in the Lower Mississippian-Upper Devonian Baken Shales--Part 1: Rock-eval pyrolisis and vitrinite reflectance: Jour. Petroleum Geology, v. 92, p. 125-162.

Purdy, E.G., 1963a, Recent calcium carbonate facies of the Great Bahama Bank. 1-Petrography and reaction groups: Jour. Geology, V.71 p. 334-335.

Purdy, E.G., 1963b, Recent calcium carbonate facies of the Great Bahama Bank 2-Sedimentary facies: Jour. Geology, v. 71, p. 472-494.

Purser, B.H., and Evans, G., 1973, Regional sedimentation along the Trucial Coast, SE Persian Gulf, p. 211-231, in Purser, B.H., ed., The Persian Gulf. Holocene carbonate sedimentation in a shallow epicontinental sea: New York-Heidelberg-Berlin, 471 p.

Pye, K., 1985, Electron microscope analysis of zoned dolomite rhombs in the Jet Rock Formation (Lower Toarcian) of the Whitby area, U.K.: Geological Magazine, v. 122, p. 279-286.

Quing, H., and Mountjoy, E.W., 1989, Multistage dolomitization in Rainbow Buildups, Middle Devonian Keg River Formation, Alberta, Canada: Jour. Sedimentary Petrology, v. 59, p. 114-126.

Quinn, T.M., and Matthews, R.K., 1990, Post-Miocene diagenetic and eustatic history of Enevetak Atoll: Model and data comparison: Geology, v. 18, p. 942-945.

Radke, B.M., and Mathis, R.L., 1980, On the formation and occurrence of saddle dolomite: Jour. Sedimentary Petrology, v. 50, p. 1149-1168.

Reeder, R. J., 1983, Crystal chemistry of the rhombohedral carbonates, p. 1-47, in Reeder, R. J., ed., Carbonates: Mineralogy and Chemistry: Reviews in Mineralogy 11, Mineralogical Soc. America, 393 p.

Reeder, R.J., and Barber, D.J., 1982, Lattice defects in saddle dolomites: an explanation for crystal distortion: Geol. Soc. America, Abstract with Programs 13, 536.

Read, J.F., 1977, Calcretes and their distinction from Stromatolites, p. 55-71,

Read, J.F., 1980, Carbonate ramp-to-basin transition and foreland basin evolution, Middle Ordovician, Virginia Appalachians: Am. Assoc. Petroleum Geologists Bull., v. 64, p. 1575-1612.

Read, J.F., 1982, Geometry, facies development of Middle Ordovician carbonate build ups, Virginia Appalachians: Am. Assoc. Petrol. Geologists Bull, v. 66, p. 189-209.

Read, J.F., 1982, Carbonate platforms of passive (extensional) continental margin types, characteristics and evolution: Tectonophysics, v. 81, p. 195-212.

Read, J.F., Grotzinger, J.P., Bova, J.A., and Koershner, W.F., 1986, Models for generation of carbonate cycles: Geology, v. 14, p. 107-110.

Reineck, H.E., and Singh, I.B., 1972, Genesis of laminated sand and graded rhythmites in storm-sand layers of shelf mud: Sedimentology, v. 18, p. 123-128.

Reinhart, J., 1977, Cambrian off-shelf sedimentation, central Appalachians, p. 83-112, in Cook, H.E., and Enos, P., eds., Deep-Water Carbonate Environments: Soc. Econ. Paleontologists and Mineralogists, Special Publ. No. 25.

Rezak, R., 1985, Local carbonate production on a terrigenous shelf: Trans. Gulf Coast Assoc. Geol. Soc., v. 23, p. 477-483.

Reitner, J., 1986, A compositive study of diagenesis in diaper influenced reef atolls and fault block reef platform in the Late Albian of Vasco-Cantabrian Basin (Northern Spain), p. 187-209, in Schroeder, J.H., and Purser, B.H., eds., Reef Diagenesis: Berlin, Heidelberg, Springer-Verlag, 455 p.

Rich, M., 1982, Ooid cortices composed of Neomorphic Pseudo Spar: Possible evidence for ancient originally aragonitic ooids: Jour. Sedimentary Petrology, v. 52, p. 843-847.

Richter, D.K, 1972, Authigenic quartz preserving skeletal material: Sedimentology, v. 221-225.

Riding, R., 1975, Girvanella and other algae as depth indicators: Lethaia, v. 8, p. 173-197.

Riding, R., 1977, Skeletal stromatolites, p. 57-60, in Flügel, E., ed., Fossil Algae, Springer Verlag, Berlin.

Roberts, R.J., 1964, Stratigraphy and structure of the Antler Peak quadrangle, Humboldt and Lander Counties, Nevada: U.S. Geol. Survey Prof. Paper 459-A, 93 p.

Roedder, E., 1962, Studies of fluid inclusions I: low temperature application of dual-purpose freezing and heating stage: Econ. Geol., v. 57, p. 1045-1061.

Roedder, E., 1963, Studies of fluid inclusions II: Freezing data and their interpretations: Econ. Geol., v. 58, p. 167-211.

Roedder, E., 1967, Environment of deposition of stratiform (Mississippi Valley-type) ore deposits from studies of fluid inclusion: Econ. Geol. Monographs 3, p. 339-369.

Roedder, E., 1971, Fluid-inclusion evidence on the environment of formation of mineral deposits of the southern Appalachian Valley: Econ. Geol., v. 66, p. 777-791.

Roedder, E., 1972, Composition of fluid inclusions: U.S. Geol. Surv. Prof. Pap. 440JJ, 164 p.

Roedder, E., 1976, Fluid-inclusion evidence on the genesis of ores in sedimentary and volcanic rocks, p.67-110, in Wolf, K.H., ed., Handbook of Stratabound and Stratiform Ore Deposits: Amsterdam, Elsevier.

Roedder, E., 1979a, Fluid inclusions as samples of ore fluid, p.684-737, in Barnes, H.L., ed., Geochemistry of Hydrothermal Ore Deposits, John Wiley & Sons, New York.

Roedder, E., 1979b, Fluid inclusion evidence on the environments of sedimentary diagenesis -- A review, p. 88-107, in Scholle, P.A., and Schlager, P.R., eds., Aspect of Diagenesis: Soc. Econ. Paleontologists and Mineralogists Spec. Publ., No. 26.

Roedder, E., 1984, Fluid Inclusions, in P.H. Ribbe, ed., Reviews in Mineralogy No. 12: Mineralogical Soc. America, 643 p.

Roedder, E., and Bodnar, R.J., 1980, Geologic pressure determinations from fluid inclusion studies: Ann. Rev. Earth Planet. Sci., v. 8, p. 263-301.

Roedder, E., and Howard, K.W., 1988, Taolin Zn-Pb-fluorite deposit, People's Republic of China: an example of some problems in fluid inclusion research on mineral deposits: Jour. Geol. Soc. Lond., v. 145, p. 163-174.

Roedder, E., and Skinner, B.J., 1968, Experimental evidence that fluid inclusions do not leak: Econ. Geol., v. 63, p. 715-730.

Roof, S.R., Mullins, H.T., Gartner, S., Huang, T.C., Joyce, E., Prutzman, J., and Tjalmsa, L., 1991, Climatic forcing of cyclic carbonate sedimentation during the last 5.4 million years along the west Florida continental margin: Jour. Sedimentary Petrology, v. 61, p. 1070-1089.

Ross, R. J. Jr, 1964, Relations of Middle Ordovician time and rock units in the Basin Ranges, western United States: Am. Assoc. Petroleum Geologists Bull., v. 48, p. 1526-1554.

Ross, R.J.Jr., 1970, Ordovician brachiopods, trilobites, and stratigraphy in eastern and central Nevada: U.S. Geol. Survey Prof. Paper 639, 103 p.

Ross, R. J. Jr, 1977, Ordovician paleogeography of the western United States, p. 19-38, in Stewart, J. H., Stevens, C. H., Fritshe, A. E., eds., Paleogeography of the Western United states: Soc. Econ. Paleontologists and Mineralogists, Pacific Section, Pacific Coast Paleogeography, Symposium 1.

Ross, R.J. Jr., and Shaw, F.C., 1972, Distribution of the Middle Ordovician Cophenhagen Formation and its trilobites in Nevada: U.S. Geological Survey Prof. Paper 749. 33 p.

Ross, R.J.Jr., James, N.P., Hintze, L.F., and Poole, F.G., 1989, Architecture and evolution of a Whiterockian (Early Middle Ordovician) Carbonate Platform, Basin Ranges of Western U.S.A., p. 167- 185, in controls on Carbonate platform and Basin Development: Soc. Econ. Paleontologists and Mineralogists, Spec. Publ. No. 44.

Ross, R.J.Jr., Jaanson, V., and Friedman, I., 1975, Lithology and origin of Middle Ordovician Calcerous mud mound at Meiklejohn Peak, southern Nevada: U.S. Geol. Survey Prof. Paper No. 871, 45 p.

Ross, R.J.Jr., Valusek, J., and James, N.P., 1988, Nuia and its environmental significance: New Mexico Bureau of Mines, Mineral Resources Memoir 44, p. 115-121.

Roux, A., 1985, Introduction á l étude des algues fossiles Paléozoïques (De la bacterie á La tectonique des plaques): Elf-Aquitaine, v. 9, p. 465-699.

Ruppel, S.C. and Walker, K.R., 1982, Sedimentology and distinction of carbonate build-ups, Middle Ordovician, east Tennessee: Jour. Sedimentary Petrology, v. 52, p. 1055-1071

Sandberg, P.A., 1975, New interpretations of Great Salt Lake ooids and of ancient non-skeletal carbonate mineralogy: Sedimentology, v. 22, p. 497-537.

Sandberg, P.A., 1985, Aragonite cements and their occurrences in ancient limestones, in Schneidermann, N. and Harris, P.M., eds., Carbonate Cements: Soc. Econ. Paleontologists and Mineralogists, Spec. Publ., No. 25, p. 33-57.

Sandberg, P. A., and Hudson, J.D., 1983, Aragonite relic preservation in Jurassic calcite replaced bivalves: Sedimentology, v. 30, p. 879-892.

Schenk, P.E., 1967, The Macumber Formation of the Maritime Provinces, Canada--A Mississippian analogue to recent strand-line carbonates of Persian Gulf: Jour. Sedimentary Petrology, v. 37, p. 365-376.

Schlager, W., and Chermak, A., 1979, Sediment facies of platform basin transition, Toung of Ocean, Bahamas, p. 193-208,in Doyle, L.J., and Pilkey, O.H., eds., Geology of Continental Slopes: Soc. Econ. Paleontologists and Mineralogists Spec. Publ. No. 27.

Scholle, P.A., 1977, Chalk diagenesis and its relation to petroleum - exploration: Oil from chalks, a modern miracle?: Am. Assoc. Petroleum Geologists Bull., p. 982-1009.

Scholle, P.A., 1978, Carbonate Rocks and Constituents, Textures, Cements and Porosities: Am. Assoc. Petroleum Geologists Memoir 27, 241 p.

Scholle, P.A., and Halley, R.B., 1985, Burial Diagenesis: Out of sight, out of mind, p. 277-289, in Schneidermann, N., Harris, P.M., eds., carbonate cements: Soc. Econ. Paleontologists and Mineralogists Spec. Pub. No. 25.

Schroeder, J.H, 1986, Diagenetic diversity in Paleocene Coral Knobs from the Bir Abu El-Husein area, South Egypt, 132-158, in Schroeder, J.H., and Purser, B.H., eds., Reef Diagenesis: Berlin, Heidelberg, Springer-Verlag, 455 p.

Schroeder, J.H., and Purser, B.H., 1986, The diagenesis of Reefs: a brief review of our understanding, p. 424-446, in Schroeder, J.H., and Purser, B.H., eds., Reef Diagenesis: Berlin, Heidelberg, Springer-Verlag, 455 p.

Searl, A., 1988, The limitations of "cement stratigraphy" as revealed in some Lower Carboniferous oolites from South Wales: Sed. Geology, v. 57, p. 171-183.

Sears, S.O., and Lucia, F.J., 1980, Dolomitization of northern Michigan Nigara Reefs by brine refluxation and sea water / fresh water mixing, p. 215-236, in Zenger, D.H., Dunham, J.B., and Ethington, R.L., eds., Concepts and Models of Dolomitization: Soc. Econ. Paleontologists and Mineralogists, Spec. Pub. No. 28.

Selleck, B.W., 1985, Chert and dolomite in the Onondaga Limestone (Devonian) of New York state: Northeastern Geology, v. 7, p. 136-143.

Selwood et al. 1989, Origin of late cements in oolitic reservoir facies: Fluid inclusion and isotope study, Mid-Jurassic Scotland England: Sed. Geology, v. 61, p. 223-237.

Sepkoski, J.J.Jr., 1982, Flat pebble conglomerates storm deposits, and the Cambrian bottom fauna, p.371-385, in Einsele A., and Seilacher G., eds., Cyclic Event Stratification: Berlin, Heidelberg, Springer-Verlag.

Shearman, D.J., Twyman, T., and Karimi, M.Z., 1970, The genesis and diagenesis of oolites: Proc. Geol. Assoc. v. 81. p. 561-575.

Shepherd, T. J., Rankin, A. H., and Alderton, D. H. M., 1985, A Practical Guide to Fluid Inclusion Studies: London, Blockie, 239 p.

Shinn, E.A., 1968, Practical significance of birdeye's structure in carbonate rocks: Jour. Sedimentary Petrology, v. 38, p. 215-223.

Shinn, E.A., 1983, Tidal flat environment, p. 171-210, in Scholle, P.A., Beabout, D.G., and Moore, C.H., eds., Carbonate Depositional Environments: Am. Assoc. Petroleum Geologists, Memoir 33, 707 p.

Shinn, E.A., Holmes, C.W., Hudson, J.H., Robbin, D.M., and Lids, B.H., 1982, Non-oolitic, high energy carbonate sand accumulation: the quicksands, southwest Florida Keys: Am. Assoc. Petroleum Geologists, v. 66, p. 629-630, Abstract.

Shinn, E.A., Lidz, B.H., and Holmes C.W., 1990, High energy carbonate-sand accumulation, the Quicksands, south west Florida: Jour. Sedimentary Petrology, v. 60, p. 952-967.

Shukla, V., 1986, Epigenetic dolomitization and origin of xenotopic dolomite texture - discussion: Jour. Sedimentary Petrology, v. 56, p. 733-734.

Shukla, V., 1988, Sedimentology and Geochemistry a regional dolostone: Correlation of trace elements with dolomite fabrics, p. 145-159, in Shukla, V., and Baker, P.A., eds., Sedimentology and Geochemistry of Dolostones: Soc. Econ. Paleontologists and Mineralogists Spec. Publ. No. 28.

Shukla, V., and Friedman, G.M., 1983, Dolomitization and diagenesis in a shallowing-upward sequence: the Lockport Formation (Middle Silurian) of New York state: Jour. Sedimentary Petrology, v. 53, p. 703-717.

Sibley, D.F., 1980, Climatic control of dolomitization, Seroe Domi Formation (Pliocene) Bonaire, N.A., p. 247-258, in Zenger, D.H., Dunham, J.B., and Ethington, R.L., eds., Concepts and Models of Dolomitization: Soc. Econ. Paleontologists and Mineralogists, Spec. Pub. No. 28.

Sibley, D.F., 1982, The origin of common dolomite fabrics : clues from Pleistocene: Jour. Sed. Petrology, v. 52, p. 1087-1100.

Sibley, D.F., 1991, Unstable to stable transformation during the dolomitization: Jour. Geology, v. 98, p. 739-748.

Sibley, D.F. Dedoes, R.E., and Bartlett, T.R., 1987, Kinetics of dolomitization: Geology, v. 15, p. 112-114.

Sibley, D.F., and Gregg, J.M., 1987, Classification of dolomite rock textures: Jour. Sedimentary Petrology, v. 57, p. 967-975.

Silberling, N.J., 1973, Geologic events during Permian-Triassic time along the Pacific margin of the United States, p. 345-362, in Logan, A., and Hills, L.V., eds., The Permian and Triassic systems and their mutual boundary: Alberta Soc. Petroleum Geol., Calgary, Alberta, Canada.

Siedlecka, A., 1972, Length-slow calcedony and relics of sulphates evidence of evaporitic environments in the Upper Carboniferous and Permian beds of Bear Island, Svalbard: Jour. Sedimentary Petrology, v. 42, p. 812-816.

Siever, R., 1982, Evolution of the silica cycle: Goldschimit confrence, Baltimore, Maryland: Programs and Abstracts, p.74.

Simone, L., 1980, Ooids: a review: Earth. Sci. Reviews, v. 16, p. 319-355.

Simonson, B.M., 1987, Early silica cementation and subsequent diagenesis in arenites from Four Early Proterozoic Iron formations of North America: Jour. Sedimentary Petrology, v. 57, p. 494-511.

Smith, J.G., McKee, E.H., Tatlock, D.B., and Marvin, R.F., 1971, Mesozoic granitic rocks in northwestern Nevada: a link between the Sierra Nevada and Idaho batholiths: Geol Soc. America Bull., v. 82, p. 2933-2944.

Soegaard, K., and Eriksson, K.A., 1985, Evidence of tide, storm and wave interaction on a Precambrian siliciclastic shelf: The 1,700 m.y. Ortega Group, New Mexico: Jour. Sedimentary Petrology, v. 55, p. 672-690.

Sorodon, J., and Eberl, D.D., 1984, Illite, p. 495-544, in Bailey, S.W., ed., Micas: Mineralogic Soc. America, Reviews in Mineralogy, v. 13, 584 p.

Speed, R.C., 1971, Golconda thrust, western Nevada--Regional extend :GSA Abstracts with Programs, v. 3, p. 199-200.

Speed, R.C., 1977, Island-arc and other paleogeographic terrains of late Paleozoic age in the western Great Basin, p. 349-362, in Stewart, J.H., Stevens, C.H., and Fritsche, A.E., eds., Paleozoic paleogeography of the western United States: Soc., Econ., Paleontologists and Mineralogists, Pacific Sec., Pacific Coast Paleogeography Symposium 1.

Speed, R.C., 1979, Collided microplate in the Western United States: Jour. Geology, v. 87, p. 279-292.

Sperber, C.M., Wilkinson, B.H., and Peacor, D.R., 1984, Rock composition, dolomite stoichiometry, and rock water reactions in the dolomitic carbonate rocks: Jour. Geology, v. 92, p. 609-622.

Spencer, A.M., and Pitcher, W.S, 1968, Occurrence of the Port Askaig Tillite in northeastern Scotland: Geol. Soc. London Proc. No. 1650, p. 195-198.

Staplin, F.L., 1969, Sedimentary organic matter, organic metamorphism, and oil and gas occurrences: Can. Petrol. Geol. Bull., v. 17, p. 47-66.

Staplin, F.L., 1977, Interpretation of thermal history from color of particulate organic matter - a review: Palynology, v. 1, p. 9-18.

Steele, G., 1960, Stratigraphic interpretation of the Pennsylvanian-Permian stratigraphy of east-central Nevada and adjacent Utah, in Geology of east-central Nevada: Intermountain Assoc. Petroleum Geologists, 11th Ann. Field Conf., Guidebook, p. 91-113.

Sternbach, C.A., and Friedman, G.M., 1984, Ferroan carbonates formed at depth require porosity well log corrections: Hunton Group, Deep Andarko Basin (Upper Ordovician to Lower Devonian of Oklahoma and Texas): Transactions Southwest Section Am. Assoc. Petroleum Geologists, p. 167-173.

Sternbach, L.R., and Friedman, G.M., 1984, Deposition of shoals to the Late Cambrian Proto Atlantic (Ipetus Ocean) in New York and Alabama, influence on the Interior Shelf, p. 2-19, in Harris, P.M., ed., Carbonate Sands-A core workshop: Soc. Econ. Paleontologists and Mineralogists Core Workshop No. 5.

Stewart, J. H., 1980, Geology of Nevada: Discussion to accompany the geologic map of Nevada: Nevada Bureau of Mines and Geology, Spec. Pub. 4, 136 p.

Stewart, J. H., and Poole, F. G., 1974, Lower Paleozoic and upper most Precambrian Cordilleran miogeocline, Great Basin, Western United States, p. 28-52, in Dickinson, W. R., ed., Tectonics and Sedimentation: Soc. Econ. Paleontologists and Mineralogists Spec. Pub. 22.

Stricker, G.D., and Carozzi, A.V., 1973, Carbonate micro facies of the Pogonip Group (lower ordovician) Arrow Canyon Range, Clark County, Nevada, U.S.A.: Bull Centre Rech. Pau, v. 30, p. 499-541.

Stubblefield, W.L., McGrail, D.W., and Kersey, D.G., 1984, Recognition of transgressive and pot-transgressive sand ridges on the New Jersey Continental Shelf, , p. 1-24, in Tillman, R.W. and Siemers, C.T., eds., Siliciclastic Shelf Sediments: Soc. Econ. Paleont. Mineralogist, Spec. Publ., No. 34.

Swett, K., 1964, Petrology and paragenesis of Ordovician Manitou Formation along the Front Range, Colorado: Jour. Sedimentary Petrology, v. 34, p. 615-624.

Swift, D.J.P., McKinney, T.F., and Stahl, L., 1984, Recognition of transgressive and post-transgressive sand ridges on the New Jersey Continental Shelf: Discussion, p. 25-36, in Tillman, R.W. and Siemers, C.T., eds., Siliciclastic Shelf Sediments: Soc. Econ. Paleontologists Mineralogists Spec. Publ., No. 34.

Swirydezuk, K., 1988, Mineralogical control on porosity type in Upper Jurassic Smackover Ooid grainstones, southern Arkansas and Northern Louisiana: Jour. Sedimentary Petrology, v. 58, p. 339-347.

Taban, O., 1986, Stratigraphy, lithology, depositional and diagenetic environments of the Antelope Valley Limestone at the Antelope Range and Martin Ridge section in central Nevada: Unpublished Master thesis, 181 p.

Taylor, H.P.Jr., 1979, Oxygen and hydrogen isotope relationship in hydrothermal mineral deposits, p. 236-277, in Barnes, H.L., ed., Geochemistry of Hydrothermal Ore Deposits, 2nd edition: New York, John Wiley & Sons, 798 p.

Taylor, M., Kesler, S.E., Cloke, P.L., and Kelly, W.C., 1983, Fluid inclusion evidence for fluid mixing, Mascot-Jefferson City zinc district, Tennessee: Econ. Geol., v. 78, p. 1425-1439.

Taylor, M., Kesler, S.E., Cloke, P.L., and Kelly, W.C., 1985, Fluid inclusion evidence for fluid mixing, Mascot-Jefferson City zinc district, Tennessee--Reply: Econ. Geol., v. 80, p. 1442-1443.

Taylor, T.R., and Sibley, 1986, Petrographic and geochemical characteristics of dolomite types and the origin of ferroan dolomite in the Trenton Formation, Michigan Basin: Sedimentology, v. 33, p. 61-86.

Theriault, F., and Hutcheon, I., 1987, Dolomitization and calcitization of Devonian Grosmont Formation, Northern Alberta: Jour. Sedimentary Petrology, v. 57, p. 955-966.

Thompson, K.F.M., 1983, Classification and thermal history of petroleum based on light hydrocarbons: Geochimica et Cosmochimica Acta, v. 47, p. 303-316.

Tillman, J.E., and Barnes, H.L., 1983, Deciphering fracturing and fluid migration histories in the northern Appalachian Basin: Amer. Assoc. Petroleum Geologists Bull., v. 67, p. 692-705.

Tissot, B.P., Pelet, R., and Ungerer, Ph., 1987, Thermal history of sedimentary basins, maturation indices and kinetics of oil and gas generation: Am. Assoc. Petroleum Geologists Bull., v. 71, p. 1445-1466.

Tissot, B.P., and Welte, D.H., 1978, Petroleum Formation and Occurrence, A New Approach to Oil and Gas Exploration: Springer-Verlag, Berlin, 538 p.

Toomey, D.F., 1970, An unhurried look at Lower Ordovician mount horizon southern Franklin Mountains, West Texas: Jour. Sedimentary Petrology, v. 40, p. 1318-1334.

Toomey, D.F., and Finks, R.M., 1969, Chazian mounds, southern Quebec, Canada-- A Summary: New York State Geological Assoc. Field Guide book, p. 120-134.

Toomey, D. F., and Klement, K. W. A., 1966, Problematical micro-organism from the El Paso Group (Lower Ordovician) of west Texas: Jour. Paleontology, v. 40, p. 1304-1311.

Toomey, D.F., and LeMone, 1977, Some Ordovician and Silurian Algal form selected areas of southeastern United States, p. 351-359, in E. Flügel, ed., Fossil Algae: Berlin, Springer-Verlag.

Tóth, J., 1980, Cross-formational gravity-flow of groundwater: a mechanism of transport and accumulation of petroleum (Generalized hydraulic theory of petroleum migration, p. 121-167, in Roberts III, W.H., and Cordell, R.J., eds., Problems of Petroleum Migration: Am. Assoc. Petroleum Geologists Studies in Geology No. 10.

Triffleman, N.J., Hallock, P., Hine, A.C, Vrago, G.A., and Gorrett, J., 1988, Serranella bank (southwestern Caribbean): an enigma of chloralgal sedimentation in an oceanic setting: Geol.Soc. America, Abstract with programs, p. 209.

Tucker, M.E., 1983, Diagenesis, geochemistry, and origin of a Precambrian dolomite: the Beck Spring Dolomite of eastern California: Jour. Sedimentary Petrology, v. 53, p. 1097-1119.

Tucker, M.E., 1984, Calcitic, aragonitic and mixed calcitic-aragonitic ooids from the Mid-Proterozoic Belt Super Group, Montana: Sedimentology v. 31, p. 627-644.

Tucker, M.E., 1985, Calcitized-aragonitic ooids and cements from the Precambrian of Southern Norway: Sed. Geology, v. 43, p. 67-84.

Ulrich, E.O., 1938, Ozarkian and Canadian Brachiopoda: Geol. Soc. America Spec. Paper 13, 323 p.

Ulrich, E.O., and Cooper, G.A., 1936, New genera and species of Ozarkian and Canadian brachiopods: Jour. Paleontology, v. 10, p. 616-631.

Urschel, S.F., and Friedman, G.M., 1984, Paleodepth of burial of Lower Ordovician Beekmantown carbonates in New York state: Compass, Sigma Gamma Epsilon, v. 61, p. 205-215.

Vail, P.R., Mitchum, R.M. Jr., and Thompson, S. III, 1977, Seismic stratigraphy and global changes of sea level, Part 4: Global cycles and relative changes of sea level, p. 83-97, in Payton, C.E., ed., Seismic Stratigraphy: applications to hydrocarbon exploration: Am. Assoc. Petroleum Geologists Memoir No. 26, 516 p.

Van Houtten, F.B., and Purucker, M.E., 1984, Glauconite peloids , and chamosite ooids favorable factors, constraints, and problems: Earth and Sci., Rev., v. 20, p. 211-243.

Veizer, J., 1983, Trace element and the isotopes in sedimentary carbonate, p. 265-299, in Reeder, J. R., ed., Carbonates: Mineralogy and Chemistry: Reviews in Mineralogy No. 11: Mineralogical Soc. America, 393 p.

Velde, B., 1981, Diagenetic reactions in clays, p. 215-268, in Parker, A., and Sellwood, B.W., eds., Sediment Diagenesis, Nato ASI Series C: Mathamatic and Physical Sciences: D. Reidel Publ. Comp., v. 115, 427 p.

Visser, W., 1982, Maximum diagenetic temperature in a petroleum source-rock from Venezuela by fluid inclusion geothermometry: Chemical Geology, v. 37, p. 95-101.

Voss, R.L., Hagni, R.D., and Gregg, J.M., 1989, Sequential deposition of dolomite and its relationship to sulfide mineral paragenetic sequence in the Viburnum trend, southeast Missouri: Carbonate and Evaporites, v. 4, p. 195-209.

Walker, A., 1982, Comparison of anomlously low reflectance values with other thermal maturation indices at Playa del Rey oilfield, California: Unpublished Master's thesis, University of Washington, 190 p.

Walker, R.G., 1977, Facies model 8: Turbiditic and associated coarse clastic deposits: Geoscience Canada, v , p. 91-101.

Walker, R.G., and Mutti, E., 1973, Turbidite facies and facies associations, p. 119-157, in Middleton G.V., and Bouma, A.H., eds., Turbidites and Deep-Water Sedimentation: Soc. Econ. Paleontologists and Mineralogists Pacific section, Los Angles, California.

Walls, R.A., Mountjoy, E.W., and Fritz, P., 1979, Isotopic composition and diagenetic history of carbonate cements in Devonian Golden Spike Reef, Alberta, Canada: Geol. Soc. America Bull., v. 90, p. 921-927.

Wanless, H.R., 1979, Limestone response to stress: pressure solution and dolomitization: Jour. Sedimentary Petrology, v. 49, p. 437-462.

Wanless, H.R., 1981, Burial Diagenesis, p. 319-417, in Parker, A., and Sellwood, B.W., eds., Sediment Diagenesis: Nato ASI series, Mathametical and Physical Series, v. 115, 536p.

Wanless, H.R., Tedesco, L.P., and Tyrell, K.M., 1988, Production of Subtidal tubular and surfacial tempestites by Hurricane Kate, Caicos Platform, British West Indies: Jour. Sedimentary Petrology, v. 58, p. 739-751.

Wanless, H.R., Tyrell, K.M., Tedesco, L.P., and Dravis, J.J., 1988, Tidal-flat sedimentation from Hurricane Kate, Caicos Platform, British West Indies: Jour. Sedimentary Petrology, v. 58, p. 724-738.

Waples, D., 1980, Time and temperature in petroleum formation: application of Lopatin's method to petroleum exploration: Am. Assoc. Petroleum Geologists Bull., v. 64, p. 916-926.

Ward, W.C., and Halley, R.B., 1985, Dolomitization in a mixing zone of near-seawater composition, Late Pleistocene, Northwestern Yucatan Peninsula: Jour. Sedimentary Petrology, v. 55, p. 407-420

Wardlaw, N.C., 1976, Pore geometry of carbonate rocks as revealed by pore casts and capillary pressure: Am. Assoc. Petroluem Geologists Bull., v. 60, p. 245-257.

Washburn, R. H., 1970, Stratigraphy of the Toiyabe Range, southern Lander County, Nevada: Am. Assoc. Petroleum Geologists Bull., v. 54, p. 275-284.

Weaver, C.E., 1960, Possible use of clay minerals in search for oil: Am. Assoc. Petroleum Geologists Bull., v. 44, p. 1505-1518.

Weaver, C.E., and Beck, K.C., 1971, Clay-water diagenesis during burial: how mud becomes gneiss: Geol. Soc. America Spec. Paper 134, 96 p.

Weaver, C.E., and Pollard, L.D., 1973, The chemistry of clay minerals. Developments in Sedimentology 15: Elsevier, Amsterdam, 213 p.

Weaver, C.E., and Broekstra, B.R., 1984, Illite-mica, p.67-98, in Weaver, C.E., and Associates, eds., Shale-Slate Metamorphism in Southern Appalachians: Development in Petrology 10, Elsevier, 239 p.

Webb, G. W., 1958, Middle Ordovician stratigraphy in eastern Nevada, western Utah: Am. Assoc. Petroleum Geologist. Bull., v. 42, p. 2335-2377.

Weiss, M.P., 1969, Oncolites, Paleoecology and Laramide tectonics, central Utah: Am. Assoc. Petrol Geologists Bull., v. 53, p. 1105-1120.

Wenk, H.R., Barber, D.J., and Reeder, R.J., 1983, Microstructures in carbonates, p. 301-367, in Reeder, R.j., ed., Carbonates: Mineralogy and chemistry: Mineralogical Soc. America, Review in Mineralogy, v. 11., 394 p.

Wilber, R.J., and Neumann, A.C., 1977, Porosity controls in subsea cemented rocks from deep-flank environment of Little Bahama Bank: Am. Assoc. Petroleum Geologists Bull., v. 61, p. 841.

Williams, L.A., and Cerar, D.A., 1985, Silica diagenesis II. General mechanism: Jour. Sedimentary Petrology, v. 55, p. 312-321

Wilkinson, B.H., 1982, Cyclic cratonic carbonates and Phanerozoic calcite seas: Geol. Education, v. 30, p. 189-203.

Wilkinson, B.H., Bucyznski, C., and Owen, R.M., 1984, Chemical control of carbonate phases: Implications from Upper Pennsylvanian calcite-aragonite ooids of southeastern Kansas: Jour. Sedimentary Petrology, v. 54, p. 932-947.

Wilkinson, B.H., Smith, A.L., and Lohmann, K.C., 1985, Sparry calcite marine cement in Upper Jurassic Limestone of southeastern Wyoming, p. 169-184, in Schneidermann, N. and Harris, P.M., eds., Carbonate cements: Soc. Econ. Paleontologists and Mineralogists Spec. Pub. No. 36.

Wilson, J. L., 1975, Carbonate Facies in Geological History: New York, Springer-Verlag, 471 p.

Wilson, J.L., 1978, Microfacies and sedimentary structures in "Deep-water" limestones, p. 176-181, in Cys, J.M., and Mazzullo, S.J., eds, Sedimentary Processes: Depositional processes in ancient carbonates: Soc. Econ. Paleontologists and Mineralogists, Reprint series, No. 7.

Wilson, J.L., and Jordan, C., 1983, Middle Shelf environment, p. 297-343, in Scholle, P.A., Beabout, D.G., and Moore, C.H., eds., Carbonate Depositional Environments: Am. Assoc. Petroleum Geologists, Memoir 33, 707 p.

Wilson, R.C.L., 1966, Silica diagenesis in Upper Jurassic limestones of southern England: Jour. Sedimentary Petrology, v. 36, p. 1036-1049.

Winland, H.D., and Matthews, R.K., 1974, Origin and significance of grapestone, Bahama Islands: Jour. Sedimentary Petrology, v. 44, p. 921-927.

Wiman, S.K. and McKendree, 1975, Distribution of Halimeda plants and sediments on and around a patchy reef near Old Rhodes Key, Florida: Jour. Sedimentary Petrology, v. 45, p. 415-421.

Wise, S.W., Bute, B.F., and Weaver, F.M., 1972, Chemically precipitateed cristobalite and the origin of chert: Geol. Helv., v.65, p. 157-163.

Wong, P.K., and Oldershaw, A., 1981, Burial cementation in the Kaybob Reef complex, Alberta, Canada: Jour. Sedimentary Petrology, v. 51, p. 507-520.

Woronick, E.R., and Land, S.L., 1985, Late burial diagenesis, Lower Cretaceous Pearsall and Lower Glen Rose Formations, South Texas, p. 265-275, in Schneidermann, N., and Harris, P.M., eds., Carbonate cements: Soc. Econ. Paleontologists and Mineralogists Spec. Pub. No. 36.

Yancey, E., 1986, Mixed carbonate-terrigenous clastic sedimentation on a ramp-topped shelf (distally-steepened ramp), the eastern shelf of the Midland Basin, Texas: West Texas Geol. Soc., v. 25, p. 4-10.

Young, B.C., 1978, Petrology and depositional environments of the Middle Cambrian Wirrealpa and Aroona Creek Limestone (south Australia): Jour. Sedimentary Petrology, v. 48, p. 63-74.

Yochelson, E.L., and Fraser, G.D., 1973, Interpretation of depositional environment in the Plympton Formation (Permian), southern Pequop Mountains, Nevada, from physical stratigraphy and a faunule: U.S. Geol. Survey Jour. Research, v. 1, p. 19-32.

Yurewicz, D.A., 1977, Sedimentology of Mississippi basin facies carbonates, New Mexico and west Texas -- The Rancheria Formation, p. 203-219, in Cook, H.E., and Enos, P., eds, Deep- water carbonate environments: Soc. Econ. Paleontologists and Mineralogists, Special Publ. No. 25.

Zempalich, G.W., Wilkinson, B.H., and Lohmann, K.C., 1988, Diagenesis of Late Proterozoic Carbonates: the Beck Spring Dolomite of eastern California: Jour. Sedimentary Petrology, v. 58, p. 656-672.

Zenger, D.H., 1972, Significance of supratidal dolomitization in the geologic record: Geol. Soc. America Bull., v. 83, p. 1-11.

Zenger, D.H., 1981, Stratigraphy and petrology of the Little Falls Dolostone (Upper Cambrian) east-central New York: Map and Charts 34, New York State Museum, The University of the State of New York, The StateEducation Department, 138 p.

Zenger, D. H., 1983, Burial dolomitization in the Lost Burro Formation (Devonian), east-central California, and the significance of late diagenetic dolomitization: Geology, v. 11, p. 519-522.

Zenger, D.H., and Dunham, J.B., 1980, An Introduction, p. 1- 11, in Zenger, D.H., Dunham, J.B., and Ethington, R.L., eds., Concepts and Models of Dolomitization: Soc. Econ. Paleontologists and Mineralogists, Spec. Pub. No. 28.

Zenger, D.H. and Dunham, J.B., 1989, Dolomitization of Siluro-Devonian limestones in a deep core (5,350 m), southeastern New Mexico, p. 161-175, in Shukla, V., and Baker, P.A., eds., Sedimentology and Geochemistry of Dolostones: Soc. Econ. Paleontologists and Mineralogists, Spec. Pub. No. 43.

Zimmermann, R.K., and Kesler, S.E., 1981, Fluid inclusion evidence for solution mixing, Sweetwater (Mississippi Valley-type) district, Tennessee: Econ. Geol., v. 76, p. 1134-142.